FLOW PATTERNS IN UPWARD TWO-PHASE FLOW IN SMALL DIAMETER TUBES

A thesis submitted for the degree of Doctor of Philosophy

by

Lejun Chen

School of Engineering and Design
Brunel University

December, 2006

Abstract

Two-phase flow in small tubes and channels is becoming a common phenomenon in industrial processes. However, the study of two-phase flow regimes in small tubes is still at its infancy. The previous studies are reviewed and discussed in the literature section. The problems and inconsistencies encountered in the earlier studies are presented and discussed.

The experimental facility is introduced in the chapters that follow. They include a section on the design of the experimental system and the test sections, the selection of the experimental parameters and the introduction of the purposely-developed programs to control the experiments and collect and process the data. The methodology of the calibration and the uncertainty analysis, the problems encountered and their solutions and the single-phase validation experiments are also described.

In this project we studied the effect of tube diameter and fluid flow parameters on flow patterns in small tubes using R134a as the working fluid. The tested tube diameters were 1.10, 2.01, 2.88 and 4.26 mm; the fluid pressures were 6, 10 and 14 bar; the liquid and gas superficial velocities covered a range of 0.04-5.0 m/s and 0.01-10.0 m/s respectively.

The observed flow patterns included bubbly, dispersed bubble, confined bubble, slug, churn, annular and mist flow. Twelve integrated flow maps are sketched in this report. The obtained results were compared with earlier experiments by other workers and with existing models, with obvious differences in the prediction of the transition boundaries. A set of new models and correlations were developed, based on the new data for boiling R134a presented in this thesis, to predict the effect of tube diameter and fluid properties on the transition boundaries. Some also agreed with the limited data available from earlier studies for adiabatic air-water flow in small to normal size tubes.

Declaration

The research presented in this thesis is the original work of the author except where otherwise specified, or where acknowledgements are made by references. This project was carried out at the Department of Engineering Systems, London South Bank University and later the School of Engineering and Design, Brunel University, under the supervision of Prof. T. G. Karayiannis and Dr. Y. Tian.

The work has not been submitted for another degree or award to any other institution.

Acknowledgements

This project would not be finished successfully without the help from many people. Firstly I would like to express my gratitude to my supervisor, Prof. T. G. Karayiannis, for his trust, support and encouragement. Without his close guidance and invaluable advice throughout the project, the study might not gain such progress and success. This thesis also required a lot of his time and energy for corrections.

I also would like to thank my second supervisor Dr. Y. Tian. He selflessly imparted me his knowledge, skill and experience. His constructive suggestions greatly facilitated the present work. Thanks are also to my friend Dr. L. Cheng for his useful discussions and help.

I'm grateful to Mr. R. Mills, Mr. J. Khaled, Mr. C. Openshaw, Mr. A. Redhead, Mr. B. Phillip and other technicians in the workshop of London South Bank University for their support and help during my research. I also greatly appreciate the excellent work on the experimental rig of my colleague Dr. X. Huo.

Thanks are also due to London South Bank University for awarding me a three-year Research Scholarship.

My heartfelt thanks go to my parents, brothers and sisters for their love, moral support and encouragement. My special thanks go to my parents and parents-in-law who took care of my daughter during my study.

Finally, I would like to express my great thanks to my wife and daughter for their patience, understanding, encouragement and love. Especially in the last three years of my study, my wife almost independently looked after our daughter whilst supporting the whole family with love and affection. My daughter also filled the home with laughter and hope which helped us to face all difficult tasks.

Contents

List of Figures

List of Tables

Nomenclature

A	area (m^2)
A_b	bubble surface area (m^2)
A_l	liquid section area (m^2)
Bo	Bond number, $Bo=(\Delta\rho g D^2/\sigma)^{1/2}$
B_X	systematic uncertainty for variable X
C	coefficient in Equations 4.12, 7.7, 7.21, 7.27 and Appendix C Chisholm parameter
C_I	experimental coefficient for inertia force, Equation 2.6
C_i	experimental coefficient for shear force, Equation 2.5
CK	dimensionless parameter, CK=Co*Ku
CK_g	dimensionless parameter based on gas superficial velocity, $CK_g=Co*Ku_g$
CK_l	dimensionless parameter based on gas superficial velocity, $CK_l=Co*Ku_l$
C_l	state coefficient, $C_l=16$ for laminar flow and $C_l=0.046$ for turbulent flow
C_{lt}	lift coefficient, $C_{lt}=0.4\text{-}1.2$, Appendix B Table B.1
Co	Confinement number, $Co=(\sigma/\Delta\rho g D^2)^{1/2}$
C_0	distribution parameter, Appendix B Table B.1 constant
C_1	experimental coefficient for slug-churn boundary, Equation 7.24
C_2	experimental exponent for slug-churn boundary, Equation 7.24
C'	constant, Equation 7.7
C'_d	experimental coefficient, Equation 2.12
C^*	dimension coefficient for slug-churn boundary, Equation 7.25
c_p	specific heat capacity at constant pressure (J/kg.K)
c_{pl}	liquid specific heat capacity at constant pressure (J/kg.K)
c_1	experimental coefficient for critical void fraction on bubbly-slug boundary, Equation 7.9
c_2	experimental coefficient for critical void fraction on bubbly-slug boundary, Equation 7.9
D	tube diameter (m)
D_c	critical diameter (m)
D_h	hydraulic diameter (m)

D_{in}	inside diameter (m)
D_{out}	outside diameter (m)
d	bubble diameter (m)
d_c	critical bubble diameter (m), $d_c=\min(d_{cb}, d_{cd})$
d_{cb}	the critical bubble diameter that bubbles tend to deform and coalesce easily (m)
d_{cd}	the critical bubble diameter that a bubble's buoyancy in the radial direction is equal to the turbulent fluctuation force (m)
d_{min}	minimum bubble diameter (m)
d_{st}	the stable maximum diameter in turbulent field (m)
E	energy (J)
E_{in}	internal energy (J)
E_{sur}	surface energy (J)
ΔE	energy change (J)
Eö	Eötvös number, $Eö=(2\pi)^2\sigma/\Delta\rho g D^2$
F	force (N)
F_B	buoyancy (N), Equation 2.4
F_I	Inertia force (N), Equation 2.6
F_i	shear force between gas and liquid phases (N), Equation 2.5
Fr	Froude number, $Fr=u/(gD)^{1/2}$
Fr_{gs}	Froude number based on gas superficial velocity, $Fr_{gs}=u_{gs}/(gD)^{1/2}$
Fr^*_{gs}	Modified Froude number based on gas superficial velocity, $Fr^*_{gs}=u_{gs}(\rho_g/\Delta\rho g D)^{1/2}$
Fr_h	Froude number based on homogeneous velocity, $Fr_h=u_h/(gD)^{1/2}$
F_S	surface tension (N), Equation 2.7
F_T	turbulent force (N), Equation 2.8
f	friction factor
f_h	friction factor based on homogeneous velocity
f_i	friction factor between gas and liquid phases
f_l	friction factor based on liquid superficial velocity
G	mass flux (kg/m^2s)
G_{gs}	gas phase mass flux (kg/m^2s)
G_{ls}	liquid phase mass flux (kg/m^2s)
Gr	Grashof number, $Gr=g\beta(T_w-T_a)L^3/\nu^2$
g	gravitational acceleration (m/s^2)
g_c	gravitational constant, $g_c=1\ m/s^2$

h	enthalpy (J/kg) convection heat transfer coefficient ($W/m^2.K$)
h_{fg}	latent heat of evaporation (J/kg)
h_g	gas enthalpy (J/kg)
h_{in}	inlet enthalpy (J/kg)
h_l	liquid enthalpy (J/kg)
h_3	fluid enthalpy at the inlet of the heating section (J/kg)
h_4	fluid enthalpy at the inlet of the observation section (J/kg)
Δh	liquid level lift (m)
Δh_l	change of liquid enthalpy (J/kg)
I	current (A)
I_{max}	maximum current (A)
K	thermal loss coefficient (W/ K), Equation 4.23
Ku	Dimensionless Kutdelaze number, $Ku=u(\rho/(\Delta\rho g\sigma)^{1/2})^{1/2}$
Ku_g	Dimensionless Kutdelaze number based on gas superficial velocity, $Ku_g=u_{gs}(\rho_g/(\Delta\rho g\sigma)^{1/2})^{1/2}$
Ku_l	Dimensionless Kutdelaze number based on liquid superficial velocity, $Ku_l=u_{ls}(\rho_l/(\Delta\rho g\sigma)^{1/2})^{1/2}$
k	correctional coefficient for void fraction, Table 7.3 thermal conductivity (W/m.K)
k_p	thermal conductivity of tube wall (W/m.K)
L	length (m)
ΔL	length difference (m)
L_E	entrance length (m)
L_1	distance between the observation point and the pressure transducers P4 (m)
L_2	distance between the observation point and the pressure transducers P0 (m)
l	length (m)
m	mass flow rate (kg/s)
m_g	gas phase mass flow rate (kg/s)
m_l	liquid phase mass flow rate (kg/s)
N	sample size
Nu	Nusselt number, $Nu=hD/k$
$N_{\mu l}$	viscosity number, $N_{\mu l}=\mu_l(\rho_l\sigma)^{-1/2}(\sigma/g\Delta\rho)^{-1/4}$
n	state exponent, n=1 for laminar flow and n=0.2 for turbulent flow

Pr	Prandtl number, $Pr = c_p\mu/k$
p	pressure (Pa)
p_b	pressure in bubble (Pa)
p_{sat}	saturated pressure (Pa)
p_0	outlet pressure of the observation section (Pa)
p_4	inlet pressure of the observation section (Pa)
Δp	pressure drop/difference (Pa)
Δp_{dc}	pressure difference due to different density (Pa)
Δp_f	friction pressure drop (Pa)
Δp_l	the calculated pressure drop based on liquid superficial velocity (Pa)
Q	heating power (W)
	cooling capacity (W)
	volume flow rate (m^3/s)
Q_{max}	maximum heating power (W)
ΔQ	thermal loss (W)
q	heat flux (W/m^2)
R	tube radius (m)
	resistance (Ω)
	thermal resistance (K/W)
R_a	thermal resistance of surrounding air (K/W)
R_p	thermal resistance of tube wall (K/W)
Re	Reynold number, $Re = \rho u D/\mu$
Re_{gs}	Reynold number based on gas superficial velocity, $Re_{gs} = \rho_g u_{gs} D/\mu_g$
Re_h	Reynold number based on homogeneous velocity, $Re_h = \rho_l u_h D/\mu_l$
Re_{ls}	Reynold number based on liquid superficial velocity, $Re_{ls} = \rho_l u_{ls} D/\mu_l$
Re^*	Modified Reynold number, $Re^* = \rho_g u_{gs}^2 D/\mu_l u^*_l$
r	experimental result
S_{Bx}	standard deviation estimate for the systematic uncertainty for variable X
S_X	standard deviation estimate for the random uncertainty for variable X
s	distance (m)
T	temperature (K)
T_a	ambient temperature (K)
T_f	fluid temperature (K)

T_{in}	inside temperature (K)
T_{out}	outside temperature (K)
T_{ref}	referent temperature (K)
T_{sat}	saturated temperature (K)
T_w	tube wall temperature (K)
T_3	inlet temperature of the heating section (K)
T_7	outlet temperature of the preheater (K)
$\overline{T}$	average temperature (K)
$\Delta\overline{T}$	average temperature difference (K)
Δt	time interval (s)
t_{95}	distribution coefficient with 95% confidence level
U	uncertainty
	velocity (m/s)
Ugs	gas superficial velocity (m/s), see the comment below
Uls	liquid superficial velocity (m/s), see the comment below
U_{95}	uncertainty with 95% confidence level
u	velocity (m/s)
u_c	combined standard uncertainty
u_d	bubble drift velocity (m/s)
u_g	gas velocity (m/s)
u_{gs}	gas superficial velocity (m/s)
u_h	homogeneous velocity (m/s), $u_h = u_{gs} + u_{ls}$
u_{ls}	liquid superficial velocity (m/s)
u_{max}	maximum velocity (m/s)
u_r	bubble rise velocity (m/s)
u'_r	bubble turbulent velocity (m/s), $u'_r = (f_l/2)^{1/2} u_l$
u'_{gs}	actual gas superficial velocity (m/s)
u'_{ls}	actual liquid superficial velocity (m/s)
u^*	dimensionless velocity
u^*_{gs}	dimensionless gas superficial velocity, $u^*_{gs} = u_{gs}(\rho_g/\Delta\rho g D)^{1/2}$
u^*_l	reference liquid velocity used in Re^* (m/s)
u^*_{ls}	dimensionless liquid superficial velocity, $u^*_{ls} = u_{ls}(\rho_l/\Delta\rho g D)^{1/2}$
V	volume (m^3)
ΔV_{act}	actual volume difference (m^3)

ΔV_{cal}	calculated volume difference (m^3)
W	weight (kg)
	work (J)
We	Weber number, $We=\rho u^2 D/\sigma$
We_b	Weber number based on bubble diameter and velocity, $We_b=\rho_g u_h^2 d_c/\sigma$
We_{gs}	Weber number based on gas superficial velocity, $We_{gs}=\rho_g u_{gs}^2 D/\sigma$
We_{ls}	Weber number based on liquid superficial velocity, $We_{ls}=\rho_l u_{ls}^2 D/\sigma$
W_F	mechanical work done by the turbulent force from liquid (J)
W_p	mechanical work done by liquid pressure (J)
X	Lockhart-Martinelli parameter, $X=(\Delta p_{ls}/ \Delta p_{gs})^{1/2}$
X_i	single reading of variable X
$\overline{X}$	mean of variable X
x	quality
Y	dimensionless coefficient, $Y=(\rho_l-\rho_g)g\sin\theta/\Delta p_g$
	measured variable
Y_B	average distance from the heating wall to the tip of bubble (m)
y	distance to tube wall (m)

Note:

In the diagrams produced in EXCEL or Paint, Ugs and Uls, instead of u_{gs} and u_{ls}, are used to present gas and liquid superficial velocity because subscript format is not available.

Greek symbols

α	void fraction
α_{act}	actual void fraction
α_c	critical void fraction
α_{cal}	calculated void fraction
α_l	liquid holdup, $\alpha_l=1-\alpha$
α_s	void fraction in liquid slug
α_{sc}	maximum table liquid holdup, $\alpha_{sc}=0.48$
β	volume flow ratio, $\beta=x\rho_l/(x\rho_l+(1-x)\rho_g)$
	volumetric thermal expansion (1/K), $\beta=1/T$ for idea gas

Δ	difference
δ	liquid film thickness (m) distance between two parallel plates (m)
ε	roughness (m) emissivity
γ	distortion coefficient, γ=1.1-1.5
φ^2_l	square root of two-phase multiplier
κ	energy dissipation per unit mass (m^2/s^3), Appendix B Table B.1.
λ	dimensionless coefficient, $\lambda=(\rho_g\rho_l/\rho_{gref}\rho_{lref})^{1/2}$
μ	dynamic viscosity (kg/m.s)
μ_g	gas dynamic viscosity (kg/m.s)
μ_l	liquid dynamic viscosity (kg/m.s)
μ_{lref}	reference liquid dynamic viscosity (kg/m.s)
ν	kinematics viscosity (m^2/s)
ν_l	liquid kinematics viscosity (m^2/s)
θ	inclination angle
θ_c	critical inclination angle
ρ	density (kg/m^3)
ρ_g	gas density (kg/m^3)
ρ_{gref}	reference gas density (kg/m^3)
ρ_l	liquid density (kg/m^3)
ρ_{lp}	liquid density in the connecting tube to differential pressure transmitter (kg/m^3)
ρ_{lref}	reference liquid density (kg/m^3)
ρ_{lt}	liquid density in test section (kg/m^3)
$\Delta\rho$	density difference (kg/m^3), $\Delta\rho = \rho_l - \rho_g$
Σ	total
σ	surface tension (N/m) Stefan-Boltzmann constant, 5.67×10^{-8} $W/m^2.K^4$
σ_{ref}	reference surface tension (N/m)
τ	shear stress (N/m^2)
τ_i	shear stress between gas phase and liquid phase (N/m^2)
τ_w	shear stress between liquid phase and tube wall (N/m^2)

υ	specific volume (m^3/kg)
υ_g	gas specific volume (m^3/kg)
υ_{gref}	reference gas specific volume (m^3/kg)
υ_l	liquid specific volume (m^3/kg)
υ_{lref}	reference liquid specific volume (m^3/kg)
ψ	dimensionless coefficient, $\psi=(\sigma_{ref}/\sigma)(\rho_{lref}/\rho_l)^{2/3}(\mu_l/\mu_{lref})^{1/3}$

Abbreviations

A	annular flow
B	bubble flow
CH	churn flow
CJC	cold junction compensation
CMF	Coriolis mass flow meter
DB	dispersed bubble flow
EB	elongated bubble flow
F.S.	full scale
H	horizontal
I	intermittent flow inclined
ID	inside diameter
OD	outside diameter
rdg	reading
rng	range
S	stratified flow
SL	slug flow
SS	stratified smooth flow
SW	stratified wavy flow
V	vertical

Chapter 1 Introduction

1.1 Background

Gas-liquid two-phase flow, a universal natural phenomenon, has been studied for a number of years owing to its wide application in industry. As early as the seventeenth century, air-water two-phase flow was utilized to produce compressed air and possibly the earliest publication on two-phase flow is that "*On the shape and motion of a bubble of air in a liquid of constant density*" published in 1830 by Thermin (Chisholm 1983). Since then, engineers began their scientific work in this area and thousands of papers were published.

In the last hundred years, there were many inventions that related to the applications of two-phase flow in the field of energy, chemistry, petroleum industry and domestic appliances. Later, with the rapid development of the nuclear industry, researchers focused on the safety and the stability of two-phase flow. The study of flow patterns received increasing attention because it can reveal the mechanism of the heat transfer processes in two-phase flow. The accuracy of correlations for heat transfer and pressure drop greatly depends on the precise prediction of flow patterns. According to Taitel (1990), the earliest flow map was plotted by Baker in 1954. Since then, numerous experimental data on flow patterns were collected, lots of flow maps were sketched and a large number of the correlations were published. Based on the above works, some models and correlations were put forward and could predict or explain the transition of flow patterns reasonably. However, these studies were mostly concerned with centimetre-scale tubes until recent years when this situation changed due to the development of micro-devices and micro-systems.

Flow boiling heat transfer in small channels, a highly-efficient heat transfer method, has found important use and applications in industries such as compact heat exchangers, cooling devices for nuclear reactors, air-conditioning and refrigeration systems, thermal control devices in spacecrafts, chemical processing systems and high power electronic device cooling systems. (Fukano and Kariyasaki 1993, Wongwises et al. 2000, Zietlow and Pedersen 1998). Large or super large-scale integrated circuits, for instance, may create a great quantity of heat in a narrow space, which requires a highly-efficient and compact heat exchanger to carry the energy away to protect such electronic equipment. Therefore, it is imperative that designers have a complete understanding of two-phase flow in small channels as this is the key in creating high quality thermal exchange equipment, where the accurate prediction of flow patterns significantly contributes to improve production performance, enhances heat transfer rate and reduces energy consumption. Such systems may also contribute to the depression of equipment noise and overall to the reduction in environmental pollution. Accurate prediction and control of pressure drop will also be possible.

However, up to now, the study of two-phase flow regimes in small diameter tubes is still at an early stage though there are a significant number of reports in this field. The present author examined the previous studies for small channels and concluded that the majority of them dealt with adiabatic air-water in rectangular channels with a hydraulic diameter range of 1 to 5 mm and flow flux range of 1 to 1×10^4 kg/m^{2}s, see Appendix A. Although researchers agree that surface tension becomes an important parameter with the decrease of the channel dimension (Oya 1971, Barnea et al. 1983, Fukano and Kariyasaki 1993, Hibiki et al. 1993, Lin et al. 1998, Coleman and Garimella 1999), the flow pattern transition mechanisms for small channels are quite vague and disputable. Therefore, it is still problematic or impossible to predict the flow patterns for small channels due to lack of adequate experiment data and theoretical analysis.

There are two main study methods for two-phase flow patterns: The experimental method (e.g. Barnea et al. 1985, Mao and Dukler 1989, Hout et al. 1992, Andreussi et al. 1999) and a different approach which focuses on establishing physical models (e.g. Taitel and Dukler 1976, Taitel et al. 1980, Mishima and Ishii 1984, McQuilian and Whalley 1985, Barnea et al. 1982, Barnea 1986, 1987). The earlier studies concentrated on standard size tubes (order of centimetre) as was the industry requirement at the time. Later studies (Sue and Grifith 1964, Oya 1971, Barnea et al. 1983, Graska 1986, Damianides and Westwater 1988) found that the existing correlations developed from standard size tubes could not predict properly flow regimes down to millimetre size tubes, and the deviation became more pronounced with the decrease of channel dimension. The reported flow maps for small tubes (Damianides and Westwater 1988, Mishima and Hibiki 1996, Coleman and Garimella 1999) showed large deviations when compared with the predicted maps by the existing models for normal tubes (Taitel and Dukler 1976, Taitel et al. 1980, Mishima and Ishii 1984, Barnea et al. 1982). To date, models for two-phase flow in small tube are not complete and also the corresponding experimental data are still scarce. Therefore, the present project is an experimental study of two-phase flow patterns in small tubes and further proposes to contribute to the development of new theoretical models and correlations.

1.2 The proposed project

The purpose of the proposed research is to elucidate the effect of channel dimension and fluid flow parameters (pressure and as a consequence fluid properties such as density, viscosity and surface tension) on flow patterns in small tubes. Compared to the current state of research in two-phase flow in small diameter tubes, the work includes and adds more experimental data and the development of flow regime maps. The results are compared with the previous predictions, quantitatively analysing the effect of tube diameter and fluid parameters. The ultimate aim is the establishment of new physical models and correlations for predicting two-phase flow regime boundaries in small tubes.

In particular, the objectives of the present study include:

1. Review the past work on the study of two-phase flow patterns in small tubes; summarize the existing findings/conclusions and identify unsolved problems or discrepancies.
2. Modify an experimental rig to satisfy the need of the current study. This must be suitable for long term flow boiling heat transfer and flow visualization research with multi fluids and wide parameter range.
3. Calibrate the measuring instruments and contribute to the commissioning of the experimental system. Validate the rig with single-phase experiments.
4. Study the effect of tube dimension and fluid flow parameters on flow boiling regimes and transition boundaries. Provide new flow pattern maps which include the effect of tube diameter and fluid parameters.
5. Develop and validate theoretical models and correlations describing flow regimes.

In order to achieve the above objectives, an advanced, highly sophisticated and accurate experimental facility has been built and commissioned. Four test sections with different diameters are used to study adiabatic flow patterns with high precision. A digital high-speed camera was used to objectively record flow patterns avoiding subjective observation. The experiments cover a wide range of temperature, pressure, mass flux and quality. The obtained data are enough to complete the integrated flow maps using various parameters to assess their relative importance. The new models and correlations suitable for small diameter tubes were developed through analysing and comparing the present experimental data and those from other researchers.

The range of parameters that were tested in the adiabatic flow pattern experiments are summarised below:

Fluid	R134a
Pressure (bar)	6, 10, 14
Temperature (°C)	21.56, 39.40, 52.45
Diameter (mm)	1.10, 2.01, 2.88, 4.26
Orientation	Vertical upward
Vapour superficial velocities (m/s)	0.01 - 10.0
Liquid superficial velocities (m/s)	0.04 - 5.0
Quality	0.0 – 1.0

1.3 Outline of this thesis

A detailed literature review was carried out and presented in Chapter 2. It discusses several basic concepts such as the definition of small tube or channel and the classifications of flow patterns. The parameters and factors which affect flow patterns are analysed and the existing discrepancies and unexplored problems are discussed. Chapter 3 introduces the existing experimental facility in detail, which includes system functions, experimental parameters and range, test sections and newly developed programs. The analysis of the experimental accuracy is presented in Chapter 4. The problems occurred in commissioning and the solutions are described in this chapter. The facility was validated using single-phase experiments which are described in the last part of this chapter. Chapter 5 presents the observed flow patterns in the experiments.

Twelve flow maps are sketched and compared. The effect of tube diameter and experimental pressure is qualitatively analysed. Chapter 6 compares the obtained data with the existing flow maps and correlations. Flow maps using the different coordinate systems are also discussed. In Chapter 7, the new models and correlations for predicting the flow patterns in small diameter tubes are developed based on the present data and compared with results from earlier studies. Chapter 8 presents the conclusions of the current study and the presentation of future work. In addition, some relative information is included in Appendixes to support the current work.

Chapter 2 Literature review

Although a great number of papers have been published on two-phase flow patterns, most of them concern normal size tubes. There is a lack of experimental data and theoretical analysis for small tubes in which flow shows notably different characteristics so it is vital to conduct research in this area. A literature review is presented in this chapter to clarify the present status of the study of flow patterns in small tubes and to provide the background for the present project.

2.1 Definition of small channel

Engineers used to regard tubes of diameter in the order of centimetre and millimetre as normal and small-scale tubes respectively. Now many researchers think the criterion ought to be based on the combination of channel size, fluid thermo-hydraulic properties and gravity field rather than only on channel dimension. For instance, Brauner and Moalem-Maron (1992) reported that large conduits exhibit some characteristics of small channel under reduced gravity field. However, a widely accepted standard to define small tubes has not yet been agreed. Kew and Cornwell (1997) used the confinement number Co, see Equation 2.1, to differentiate traditional and small size tubes. Two-phase flow exhibits different flow and heat transfer characteristics from normal size tube when Co>0.5. For instance, isolated bubbles prevail when Co>0.5 and cause a typical flow regime in small tube identified as confined bubble flow. Brauner and Moalem-Maron (1992) recommended Eötvös number Eö, see Equation 2.2. They stated that surface tension dominates when Eö>1 and this marks the boundary for small passages. Triplett et al. (1999) found that stratified flow became impossible when Eö>100 in their experiments. Hatori and Bretherton (cited from Wadekar 2002) theoretically derived and later experimentally verified a quantitative criterion for the free bubble rise velocity to be zero, i.e. Eö $\geq$ 11.71. They concluded that the narrowness of a channel leads to bubble stagnation and suggested the proposed criterion as a rational basis for bubble confinement. Akbar et al. (2003) summarized the previous studies and concluded that the buoyancy effect could be negligible when Bond number Bo, given by Equation 2.3, is less than 0.3, in which condition flow regimes are insensitive to channel orientation. Kandlikar (2002) summarized the previous studies on flow boiling and recommended the following criteria to differentiate channels, i.e. 3 mm and 200 μm are the critical diameters of traditional channels to mini-channels (small tube) and mini-channels (small tube) to micro-channels, respectively.

$$Co = \frac{1}{D}\sqrt{\frac{\sigma}{g(\rho_l - \rho_g)}} \tag{2.1}$$

$$E\ddot{o} = \frac{(2\pi)^2 \sigma}{(\rho_l - \rho_g)D^2 g} = (2\pi\ Co)^2 \tag{2.2}$$

$$Bo = D\sqrt{\frac{g(\rho_l - \rho_g)}{\sigma}} = \frac{1}{Co} \tag{2.3}$$

In fact, all coefficients Co, Eö and Bo consider the effect of fluid densities, surface tension and channel size to two-phase flow. Therefore, the criteria are not only influenced by channel dimension (D), but also by gas-liquid parameters. Table 2.1 illustrates the different calculated results given by the above five criteria, i.e. the size of a tube that indicates deviation from normal size behaviour.

Table 2.1 The different criteria for small tubes.

Parameters	Air/water	R-134a		
Pressure (bar)	1.0	6.0	10.0	14.0
Temperature (°C)	25.0	21.6	39.4	52.5
Surface tension (mN/m)	71.98	8.39	6.15	4.61
Gas density (kg/m³)	1.185	29.04	49.06	70.7
Liquid density (kg/m³)	997.0	1218.2	1148.3	1090.2
	Critical Diameter (mm)			
Criterion based on Eö=1	17.1	5.3	4.7	4.3
Criterion based on Co=0.5	5.4	1.7	1.5	1.4
Criterion based on Eö=11.71	5.0	1.6	1.4	1.2
Criterion based on Eö=100	1.71	0.53	0.47	0.43
Criterion based on Bo=0.3	0.81	0.25	0.23	0.20

As seen in the table, the discrepancy is quite significant (e.g. for air/water the critical diameter ranges from 0.81 to 17.1 mm) due to the different hydrodynamic mechanisms and there is a need for further work to clarify this. Fukano and Kariyasaki (1993) experimentally investigated the effect of diameter using air-water flow in 1 to 9 mm tubes at atmospheric conditions. The direction of flow was vertical upward, horizontal and vertical downward. They found the critical diameter, at which the surface tension surpasses the gravity, is between 5 to 9 mm and the effect of diameter dominated over flow direction when the tube diameter was smaller than 6 mm. The conclusions agreed with the result of Kew and Cornwell (1997) or Hatori and Bretherton (cited from Wadekar 2002), seen in the table above, i.e. 5.4 or 5.0 mm for air and water.

Despite the great discrepancies between the actual values, the common characteristics exhibited in small tubes have been recognized by the various researchers (Oya 1971, Damianides and Westwater 1988, Barajas and Panton 1993, Fukano and Kariyasaki 1993, Mishima and Hibiki 1996, Triplett et al. 1999, Lin et al. 1999) and are summarized below:

(1) Higher heat transfer capability.
(2) Surface tension becomes dominant force.
(3) Flow patterns are less affected by channel orientation and flow patterns tend to be axisymmetric in horizontal or inclined tubes.
(4) Bubbles tend to be regular in shape, i.e. round.
(5) Some special flow patterns emerge (not reported in normal size tubes).
(6) Some typical flow patterns in normal size tubes may be absent.
(7) Intermittent flow appears easily and stratified flow is suppressed.
(8) Confined bubble flow becomes a typical regime.
(9) There is thinner liquid film around plug bubbles.
(10) There is lower bubble drift velocity in vertical flow.

The significance of differentiating small from normal size tube is that flow pattern transition mechanisms change significantly in small channels due to growing restriction from the channel wall. It indicates that new physical models and mathematical correlations must be built for small channels in order to get more precise prediction of flow patterns. For instance, Takamasa et al. (2003) experimentally studied the axial development of local flow parameters such as void fraction, interfacial area concentration and gas velocity. The project used air-water bubbly flow in a vertical 9 mm diameter tube with the purpose of revealing the true transfer mechanism in two-phase flow. In their experiments, they found that the relatively small tube increases the probability of a trailing bubble to be within a projected area of a preceding bubble which will accelerate the trailing bubble and facilitate the merger. On the other hand, since the radial motion of bubbles is restricted by the presence of tube wall, bubble coalescence due to bubble random collision that frequently happens in normal size tubes is unlikely to occur in small tubes. Therefore, the major mechanism of bubble coalescence in small tubes is totally different from that in normal size tubes.

However, two-phase flow behaviour departs from that exhibited in small tubes as the channel size decreases further to the order of hundreds of microns and defined as microchannel. Kawahara et al. (2002) recently investigated two-phase flow of nitrogen and water through a 100 μm horizontal circular channel and reported significant differences in the flow regime maps from those previously described for small channels with about 1 mm diameter. In particular, some unique flow patterns, like liquid-ring flow and serpentine-like gas core flow which have not been observed in small tubes, were reported in their study. On the other hand, dispersed bubbly, churn and fully developed annular flow were absent under their experimental conditions. Chung and Kawaji (2004) also investigated the effect of micron-scale tube diameter on two-phase flow to distinguish microtubes from small tubes. Experiments were conducted with a mixture of nitrogen and water in circular channels of 526, 250, 100 and 50 μm diameter. In the 530 and 250 μm tubes, two-phase flow patterns were similar to those in small tubes, i.e. bubbly, slug, churn, slug-annular and annular. However, only some variations of slug flow, including the abovementioned liquid-ring flow and serpentine-like gas core flow, were observed in the 100 and 50 μm tubes. The authors also observed that the level of interfacial deformation was much smaller in the 100 and 50 μm channels. Kawahara et al. (2002), Chung and Kawaji (2004) attributed these new flow characteristics exhibited in the microchannels to the stronger effect of surface tension and laminar liquid flow. Apparently, their studies indicated that the critical size to differentiate small and micro tubes is between 100 to 250 μm when using nitrogen-water as working fluid. Feng and Serizamw (1999), Serizawa and Feng (2001) and Serizawa et al. (2002) also reported that flow patterns exhibited greatly different characteristics when tube diameter is smaller than 100 μm in their air-water flow experiments. However, the effect of different fluids on this criterion has not as yet been studied conclusively.

2.2 Flow patterns in small channels

Flow patterns reveal the shape and the distribution of the interface between different phases. A two-phase mixture may flow through a conduit in a variety of flow patterns depending on the range of system parameters, i.e. flow rate, fluid or conduit properties, heat transfer rate, pressure drop. Therefore, an appreciation of flow patterns is necessary and important.

2.2.1 Classifications of flow patterns

An accurate identification of flow patterns and transition boundaries is quite difficult due to lack of agreement in classification and the subjectivity of observers. Some researchers like to use very detailed classifications, which result in a large number of flow patterns. Others prefer less detailed divisions because the extremely detailed classifications are insignificant in engineering. Taitel (1990) reported that the trend was to minimize the number of flow patterns to the minimum essential with the desire to reach standardization so that data from different laboratories could be correctly interpreted and compared.

Although there are still arguments on the classifications of flow patterns, most researchers agreed to categorise flow patterns into four main classes: stratified flow, intermittent flow, annular flow and bubble flow. Each main class could be subdivided into several subclasses. Table 2.2 lists the typical descriptions for the flow patterns.

The factors affecting flow patterns are numerous and complex. The transition from one flow pattern to another may be abrupt but in most cases it is a gradual development process in which case the transition boundary becomes a transition zone. Within the transition zones the flow patterns possess characteristics of more than one of the flow patterns described above. The identification of flow patterns in transition zones is not easy and sometimes causes considerable confusion. For instance, a typical problematic zone is the region near slug, annular and stratified wavy flow in a horizontal tube. In this region the flow can be observed as either slug, wavy or annular flow, depending on the attitude of observers. Nicholson et al. (1978) termed this region as "Proto Slug", Lin and Hanratty (1986) named it as "Pseudo Slug" while Taitel and Dukler (1976) called it "Wavy Annular flow".

Table 2.2 Classification and description of two-phase flow patterns.

Main class	Subclass for normal tubes	Subclass for small tubes	Flow orientation
Stratified flow	Stratified smooth	Stratified wavy	Horizontal
	Stratified wavy		Horizontal
Bubble flow	Bubbly	Bubbly	Vertical / All
	Dispersed bubble	Dispersed bubble	All
Intermittent flow	Plug (Elongated Bubble)	Plug (Confined Bubble or Elongated Bubble)	Horizontal / All
	Slug (Taylor Bubble)	Slug (Taylor Bubble)	All (Vertical)
	Churn	Churn	Vertical
		Pseudo-slug (Wavy Annular)	Horizontal
Annular flow	Annular	Annular	All
	Mist	Mist	All
	Wispy annular		All

The typical flow patterns sketched in early researches are presented in Figures 2.1-2.5. Figure 2.1 shows the effect of gravity on flow patterns in normal size tubes, see stratified smooth and stratified wavy in horizontal tubes and elongated bubble and slug bubble in inclined tubes in which liquid flows at the bottom of conduit with gas at the top. Comparatively the distribution of gas and liquid phase is more uniform in bubble and annular flows which indicates that gravity is not as dominant force as the increase of gas/liquid velocity. The effect of surface tension on bubble configuration is significant in small diameter tubes. The typical flow characteristics in small tubes such as regular and round bubbles were clearly exhibited in plug flow in Figure 2.2. The typical flow patterns in vertical normal tubes were reported by Taitel et al. (1980), which included bubble (named as dispersed bubble in the current study), slug, churn and annular flows, see Figure 2.3. The flow patterns under microgravity conditions are presented in Figure 2.4 and discussed in Section 2.3.2 (6). Mishima and Hibiki (1996) studied air-water flow in 1 to 4 mm vertical tubes and reported several particular flow patterns which were never reported in normal tubes, as shown in Figure 2.5.

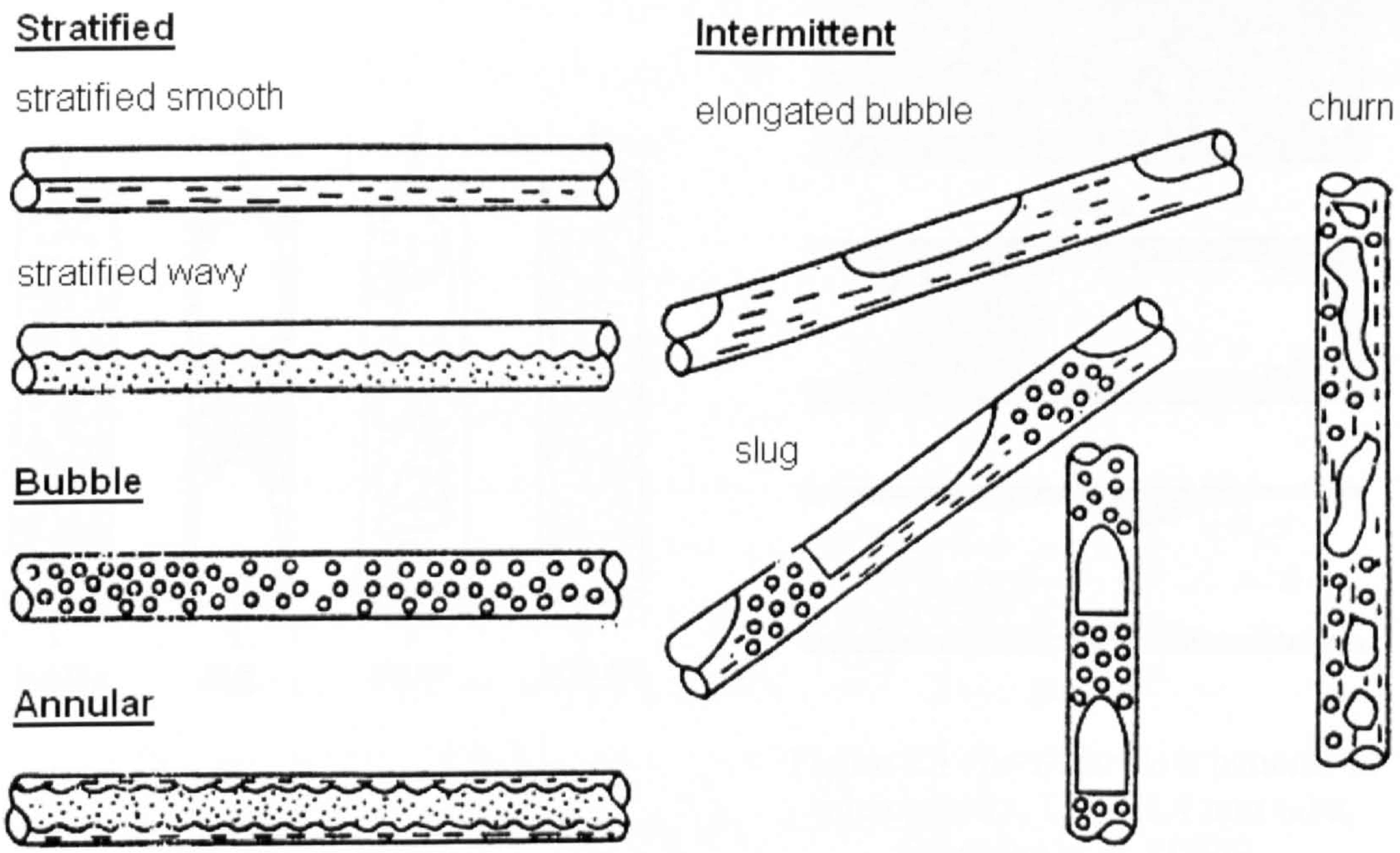

Figure 2.1 Flow patterns in normal size tubes, Taitel (1990).

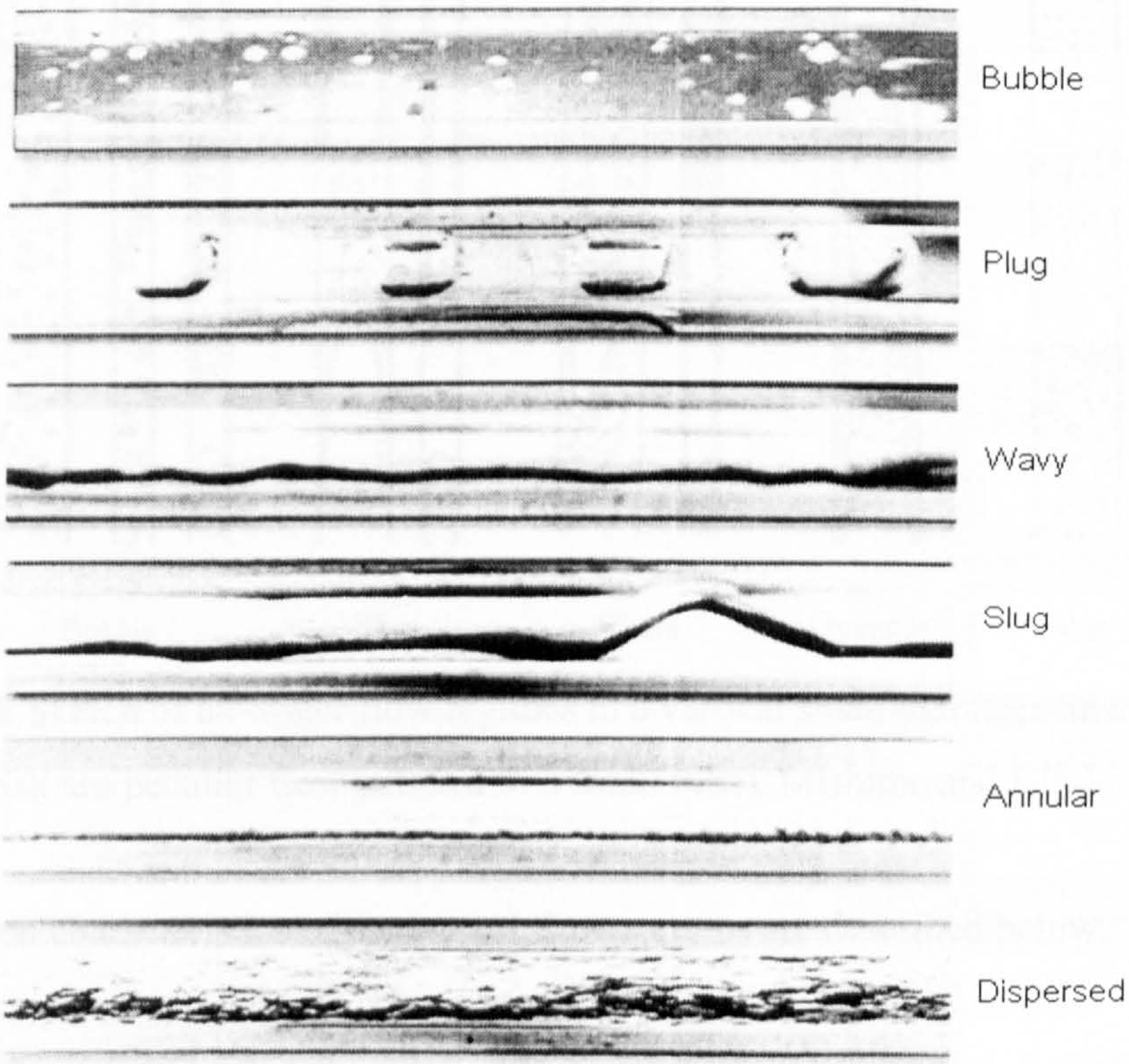

Figure 2.2 Photographs of air-water flow patterns in 3.0 mm horizontal tube, Yang and Shieh (2001).

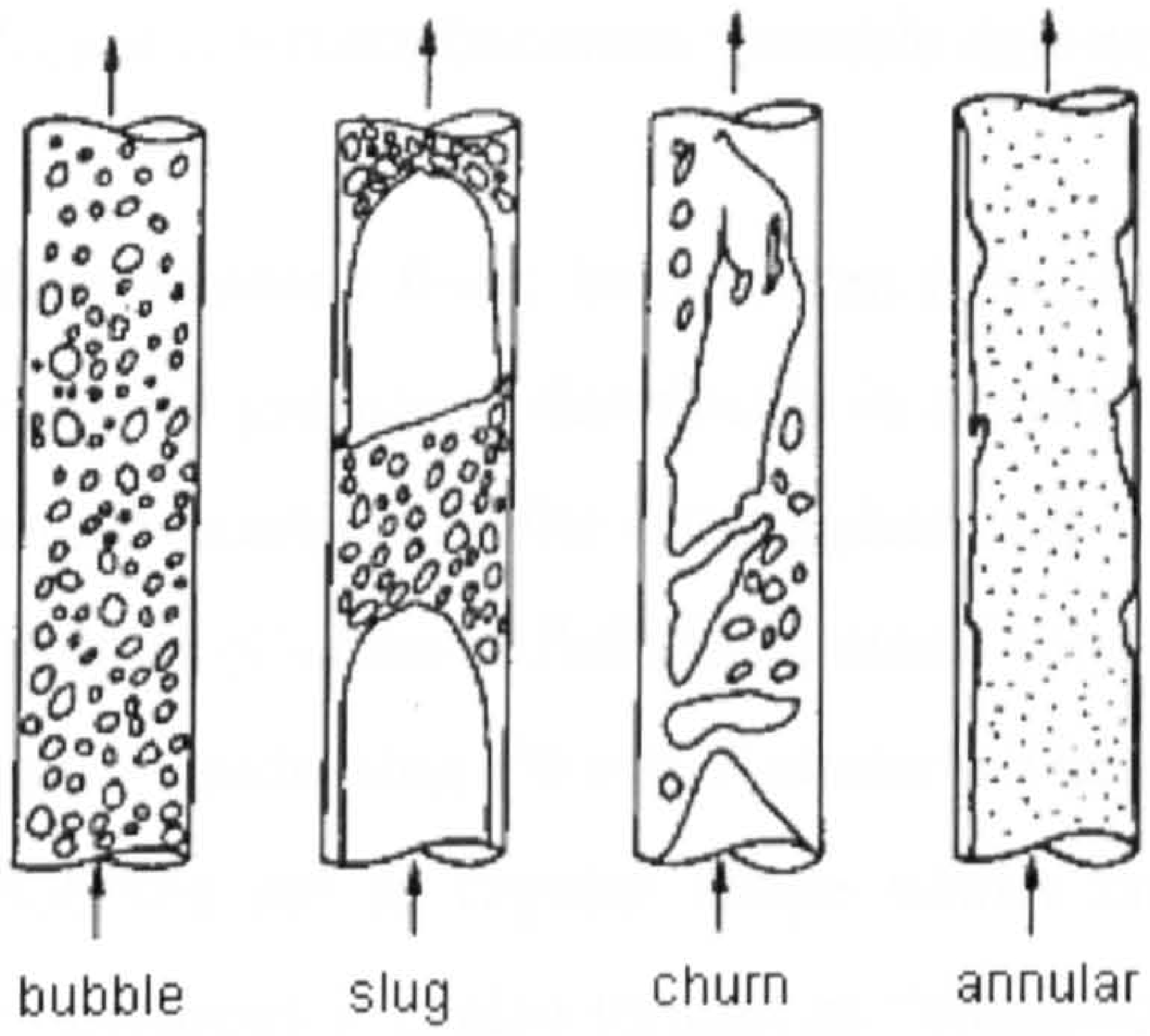

Figure 2.3 Flow patterns in vertical upwards air-water flow, 50 mm tube, Taitel et al. (1980).

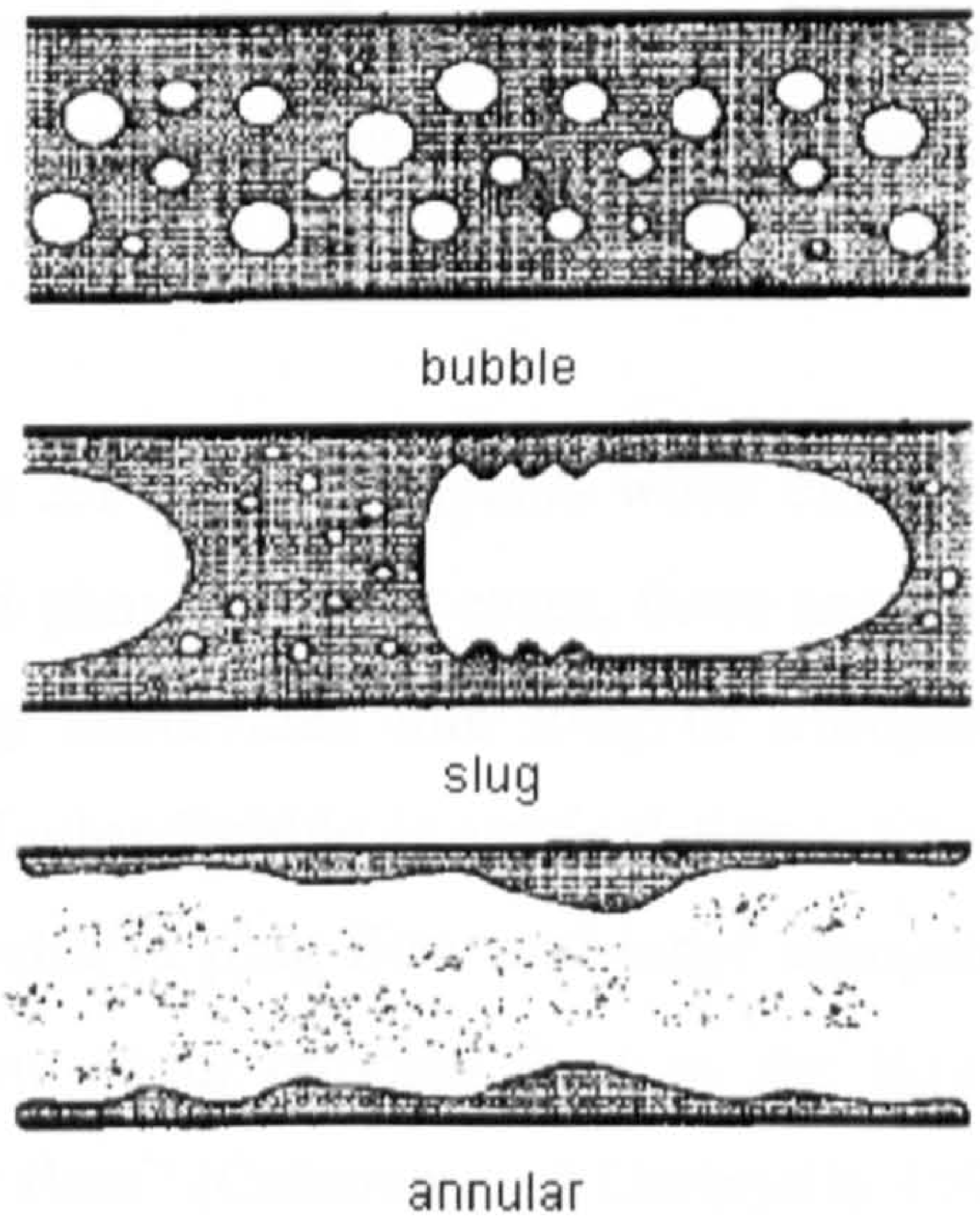

Figure 2.4 Air-water flow patterns in microgravity, 12.7-25.4 mm tube, Bousman et al. (1996).

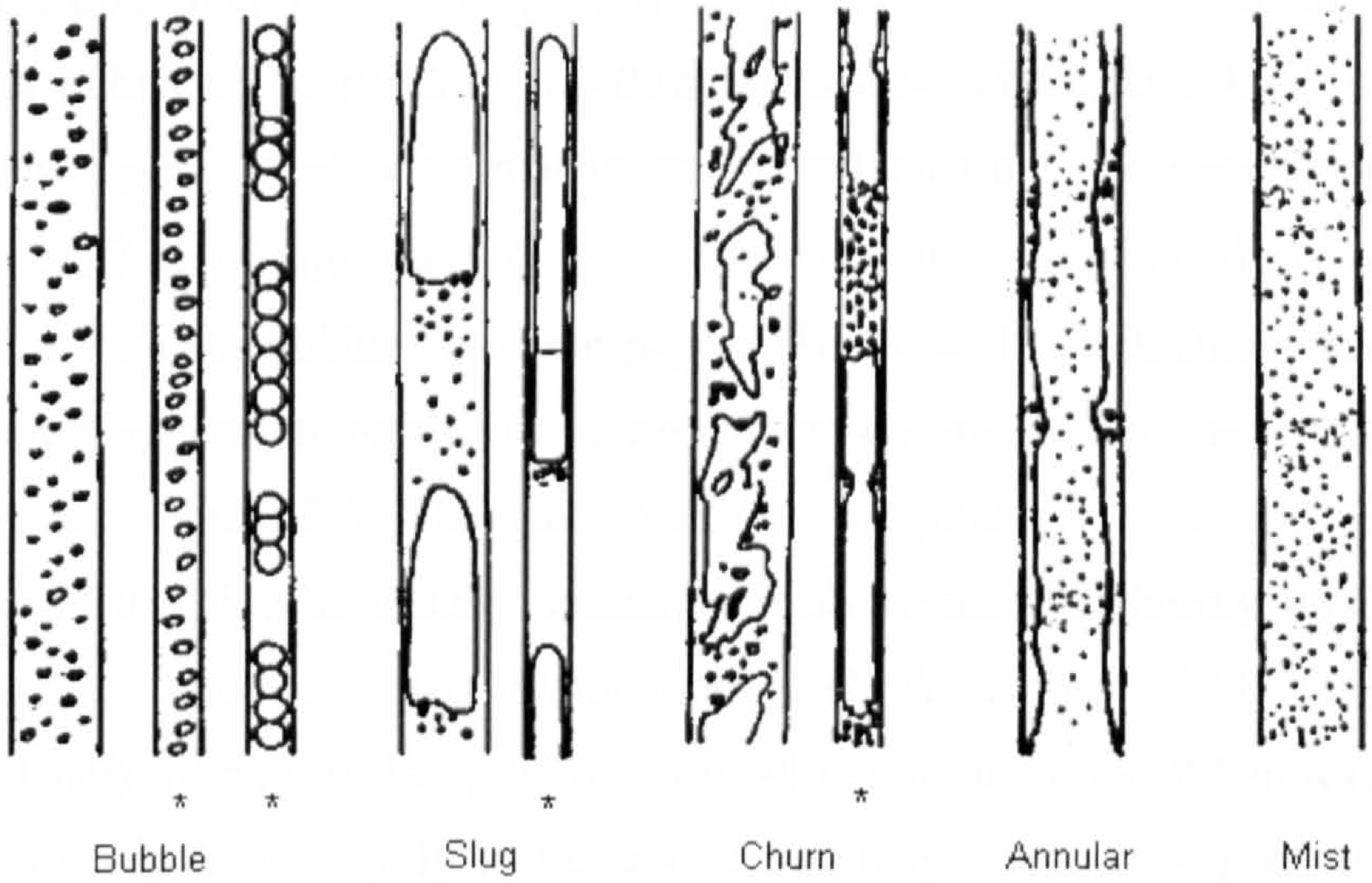

Figure 2.5 Sketch of air-water flow regimes in a vertical small diameter tube (marked by asterisk are peculiar flow patterns to a small tube), Mishima and Hibiki (1996).

The common characteristics of the typical flow patterns are described below.

Stratified flow: In stratified flow, liquid flows at the bottom of conduit with gas at the top due to the action of gravity, see Figure 2.1. It is observed mainly in horizontal or downward inclined flow. Stratified flow can be subdivided into stratified smooth and stratified wavy. In stratified smooth, both liquid and gas flows are laminar and there is no obvious fluctuation on the gas-liquid interface. It is hardly ever observed in small tubes because surface tension dominates gravity. Stratified wavy indicates that the gas-liquid interface becomes unstable and wavy.

Intermittent flow: Intermittent flow, see Figures 2.1 and 2.2, appears when elongated discrete gas-phase distributes in continuous liquid-phase. In most cases, there are many small bubbles in the liquid-phase. It is normally subdivided into Plug or Elongated Bubble (Confined Bubble in small tube), Slug (Taylor Bubble in vertical flow), Churn and Pseudo-slug (Wavy Annular). The flow is calm in plug flow and large elongated bubbles are in regular shape whilst none or few small bubbles float in the liquid. Sometimes it is also termed as "elongated bubble flow" (Coleman and Garimella 1999, Taitel 1990) or "confined bubble flow" in small tubes (Lin et al. 1999). Confined bubbles have spherical cap and bottom and the length is greater than tube diameter. This flow occurs in any flow orientation and direction and indicates that surface tension has grown into a dominant force. In slug flow, liquid is aerated and contains large as well as many small bubbles. It appears in any flow orientation. These large bubbles generally float on the upper part of horizontal tubes. In vertical flow, the large bubbles are in bullet shape. They occupy most of the cross-sectional area of conduit and are also designated as "Taylor bubble" in some papers (Taitel et al. 1980, Brauner and Barnea 1986). Churn flow resembles slug flow, but is more chaotic, frothy, distorted and highly oscillatory, see Figure 2.3. The gas phase has irregular interface and tends to be continuous. Churn flow is usually associated with vertical or sharply inclined tubes. Pseudo-slug or Wavy annular (Damianides and Westwater 1988, Coleman and Garimella 1999) are typical flow patterns in small horizontal tubes. When wave surfaces in stratified wavy flow amplify to the extent that they touch the top of tube wall or liquid slugs tend to be penetrated through by gas phase, Pseudo-slug flow is formed. This flow pattern can be regarded as the transition zone of slug, stratified wavy and annular.

Bubble flow: The most notable difference between bubble flow and intermittent flow is that the bubble size in bubble flow is smaller than the conduit dimension, see Figures 2.1-2.5. Bubbles, especially bigger bubbles, tend to concentrate in the centre of conduit in vertical flow. But for horizontal or inclined flow, bubbles usually float on the upper part of conduit. Bubble flow appears as bubbly flow at lower liquid and gas flow rates in which case the discrete bubbles are comparable with the conduit dimension. Bubbly flow turns into dispersed bubble flow when liquid flow rate increases and bigger bubbles are broken into fine bubbles. Dispersed bubble flow can appear at any flow orientation.

Annular flow: In annular flow liquid film flows at conduit wall and gas phase flows continuously in the core, see Figures 2.1-2.5. In some cases, gas phase contains entrained liquid droplets. Annular flow can exist in all flow orientations. Wispy annular flow means that the entrained liquid droplets concentrate into lumps at high liquid flow rate. Mist flow occurs in the case of high gas flow rate. Liquid and gas mix so tempestuously that causes liquid droplets to become quite small, i.e. like mist.

Summarizing the published reports, the basic flow patterns are now sketched and are presented in Figures 2.6-2.9 for normal size tubes and Figures 2.11-2.13 for small tubes.

(1) Horizontal flow in normal size tubes

Figure 2.6 illustrates the basic flow patterns in normal size horizontal adiabatic tubes. They are stratified smooth, stratified wavy, dispersed bubble, plug, slug, annular, mist and wispy annular.

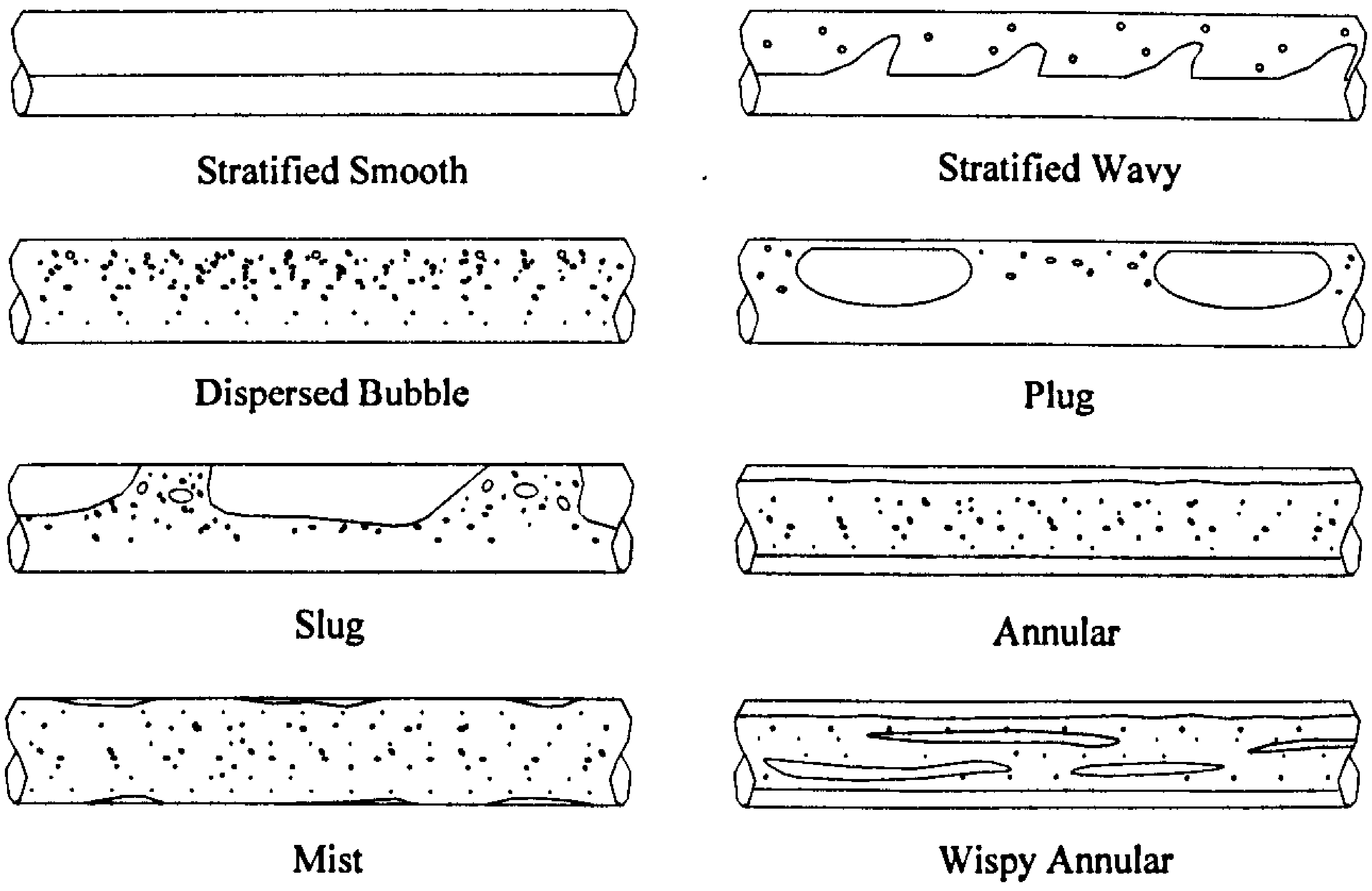

Figure 2.6 The basic flow patterns in normal horizontal adiabatic tubes.

Figure 2.7 illustrates the transformation process of the flow patterns in normal size horizontal tubes with heat flux at tube wall, i.e. flow boiling. With increasing quality, the possible flow patterns could be bubble, plug, slug, stratified wavy, annular and mist in turn. However, the dividing lines between the flow patterns are not clear.

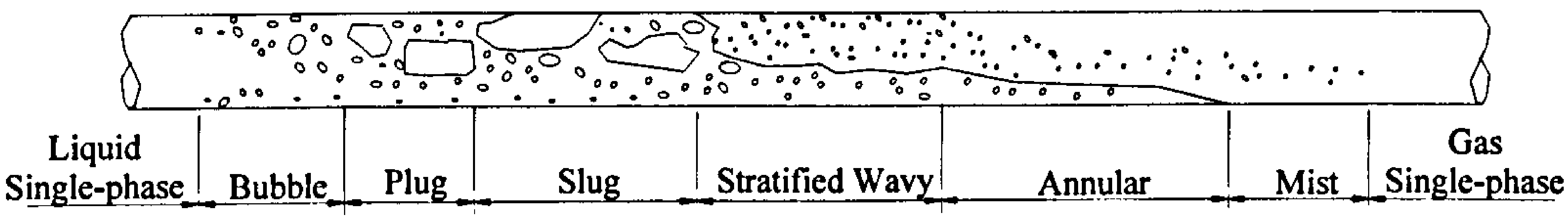

Figure 2.7 The transition flow patterns in horizontal flow boiling in normal size tubes.

(2) Vertical flow in normal size tubes

Figure 2.8 shows the basic flow patterns in normal size vertical adiabatic tubes. They include dispersed bubble, bubbly, slug (Taylor bubble), churn, annular, mist and wispy annular.

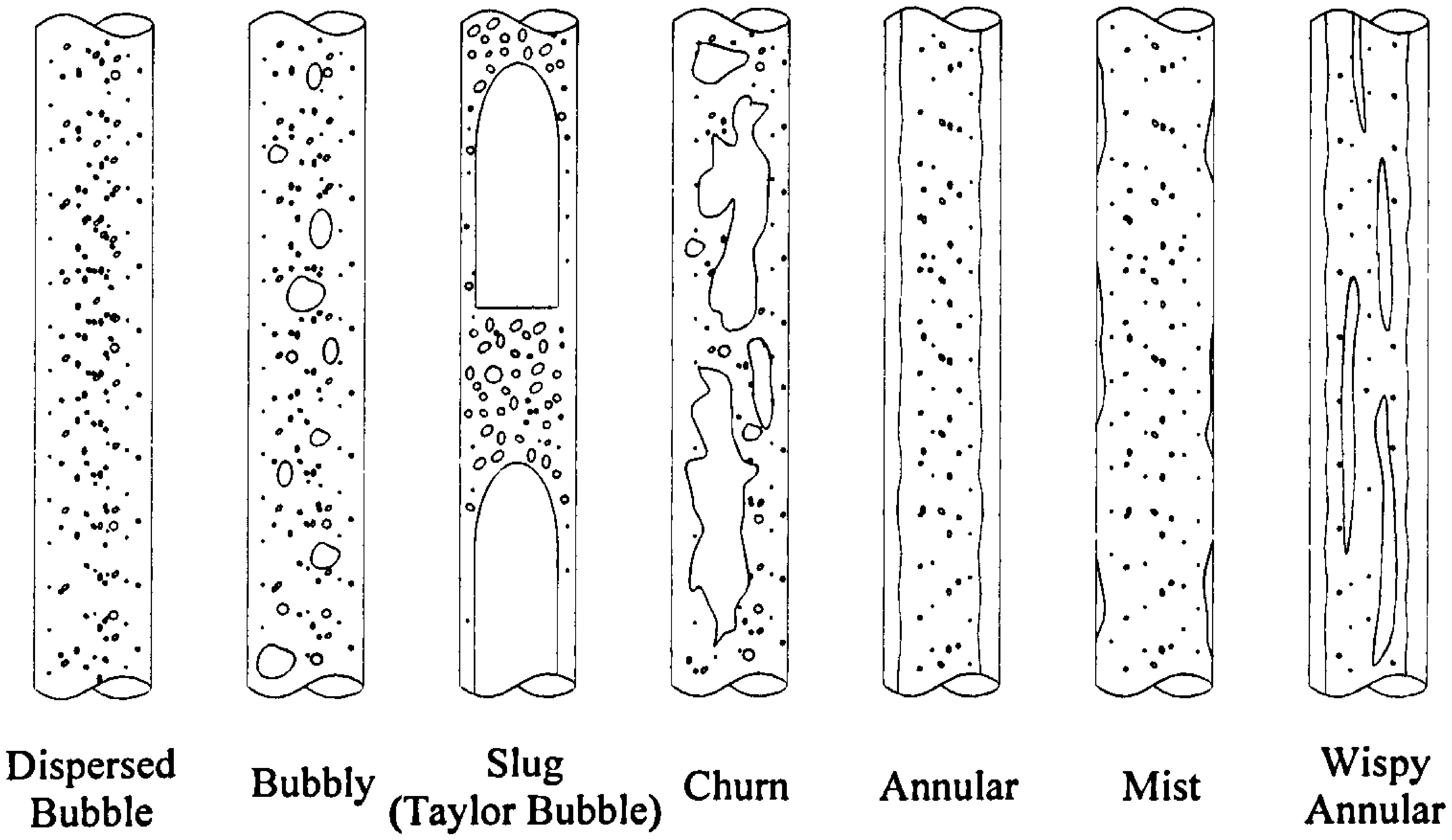

Figure 2.8 The basic flow patterns in normal size vertical adiabatic tubes.

Figure 2.9 shows the flow regimes in vertical flow boiling in normal size tubes. The flow patterns take turns to be bubble, slug, churn, annular and mist as quality increases.

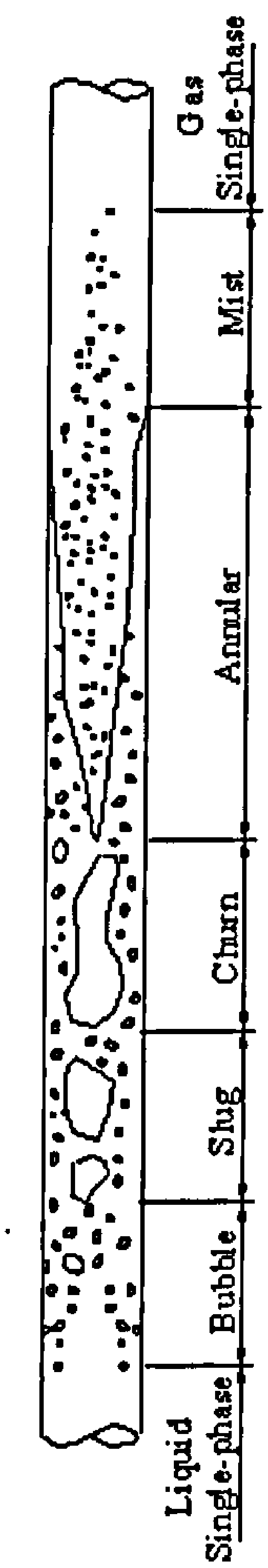

Figure 2.9 The basic flow patterns in vertical flow boiling in normal size tubes.

As tube diameter decreases, some particular flow patterns, which were never reported in normal size tubes emerged in small tubes; for example, spiral or intermittent bubble train flow, long bubble slug flow and long bubble churn flow reported by Mishima and Hibiki (1996), see the flow patterns marked with asterisk in Figure 2.5. In addition, the definitions and classifications of flow patterns in small tubes are more vague and non-unique. Some flow patterns were rarely reported in more than one experimental report. For instance, Granular-lumpy bubble and Fish-scale type slug flow reported by Oya (1971) were seldom observed by other researchers, see Figure 2.10. Some flow patterns, like confined bubble which are rarely reported in normal size tubes, become the prevailing regime in small tubes (Watel, 2003). Here, only general flow patterns in small tubes are presented based on the evaluation of the reports presented in the literature.

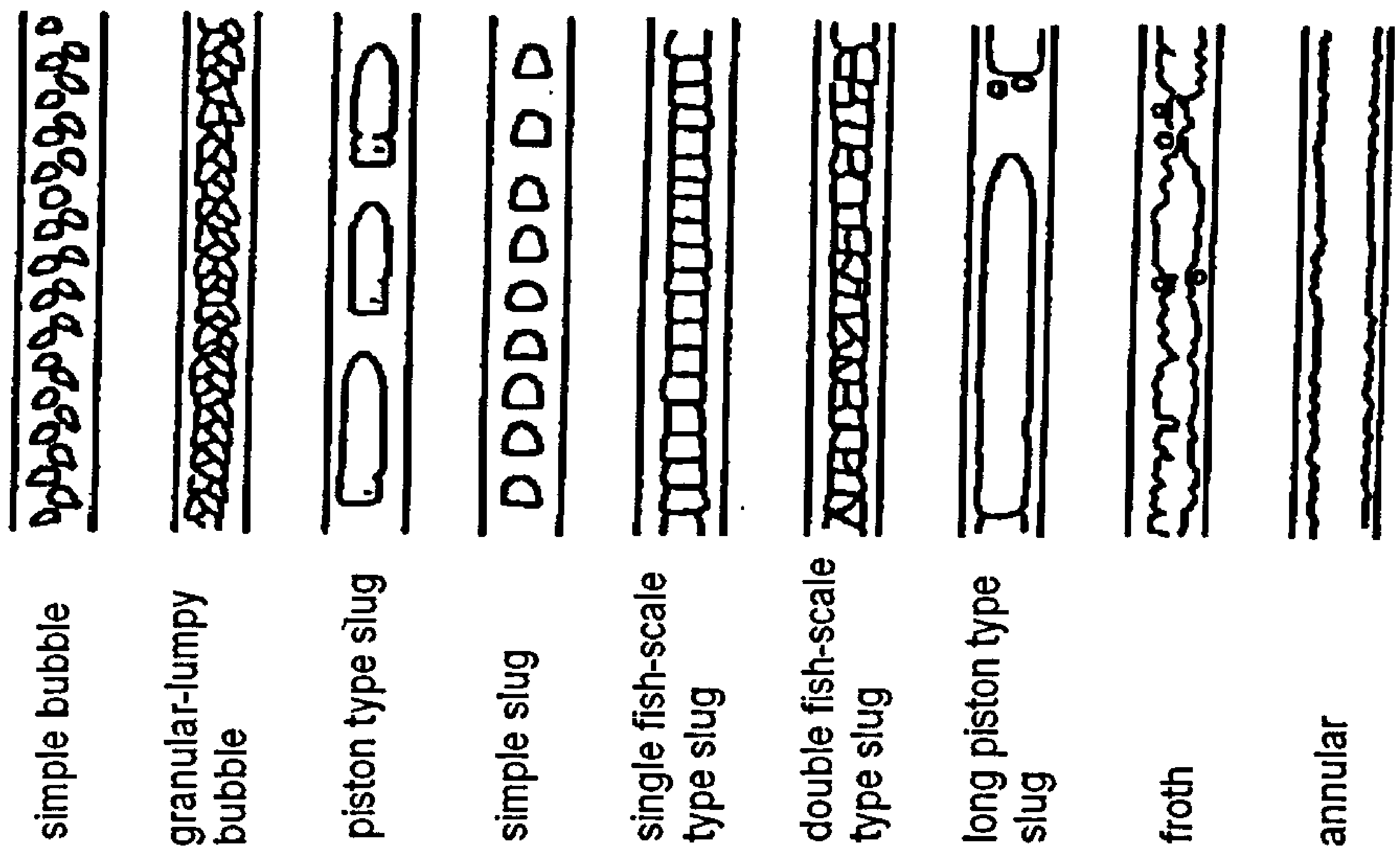

Figure 2.10 Air-water flow patterns observed in Oya (1971) experiments.

(3) Horizontal flow in small tubes

The typical flow patterns in horizontal small adiabatic tubes include bubbly, dispersed bubble, plug (confined bubble), slug, stratified wavy, pseudo-slug (wavy annular), annular and mist, see Figure 2.11.

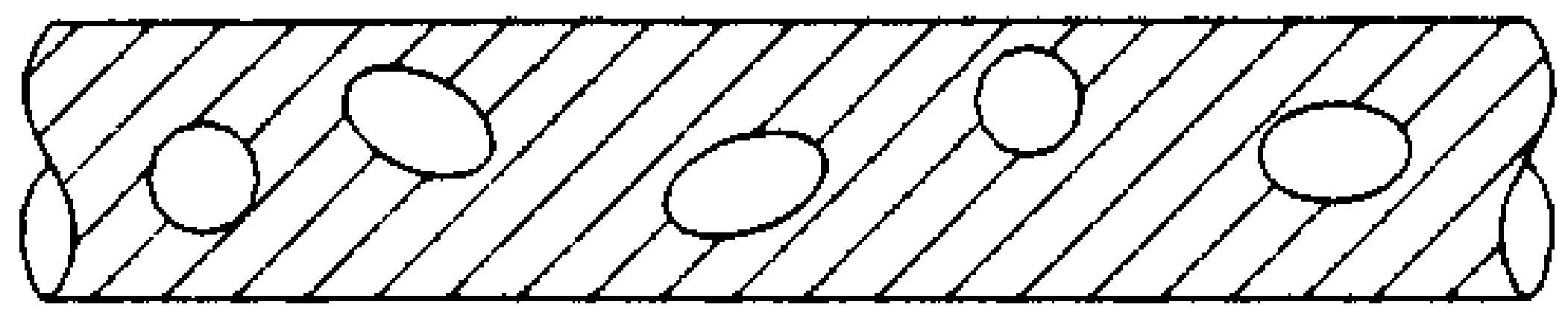
Bubbly

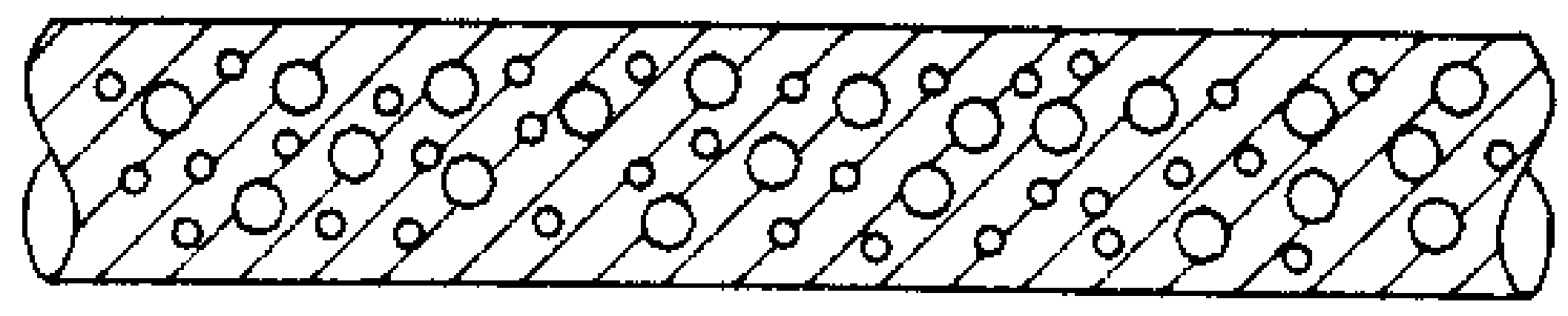
Dispersed Bubble

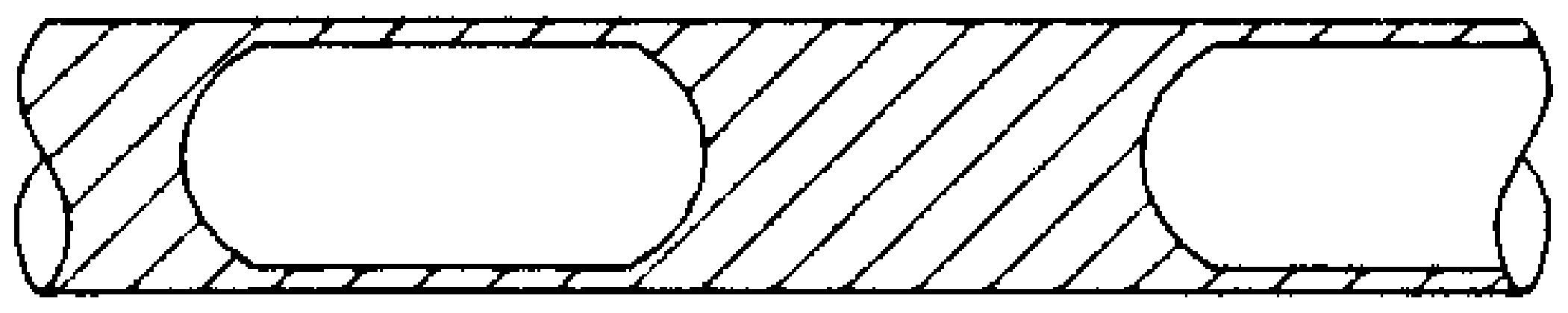
Plug (Confined Bubble)

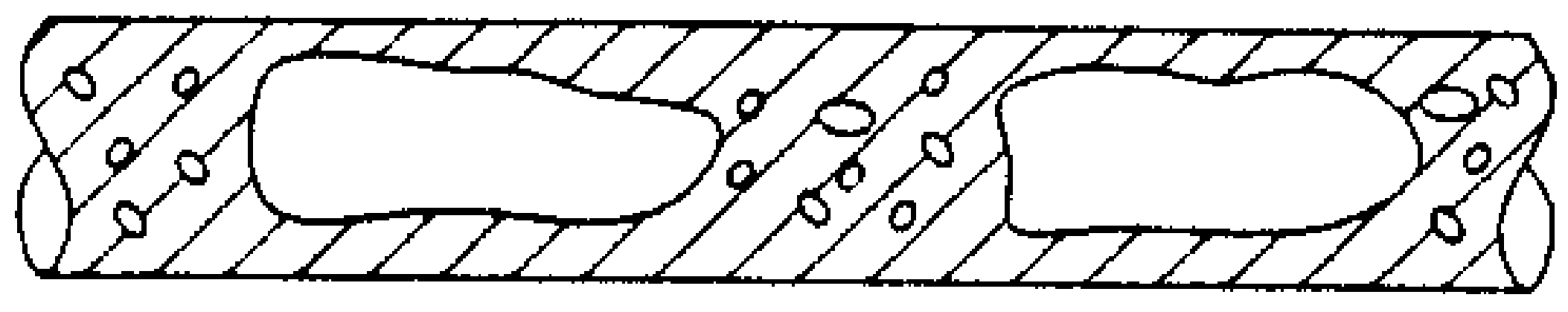
Slug

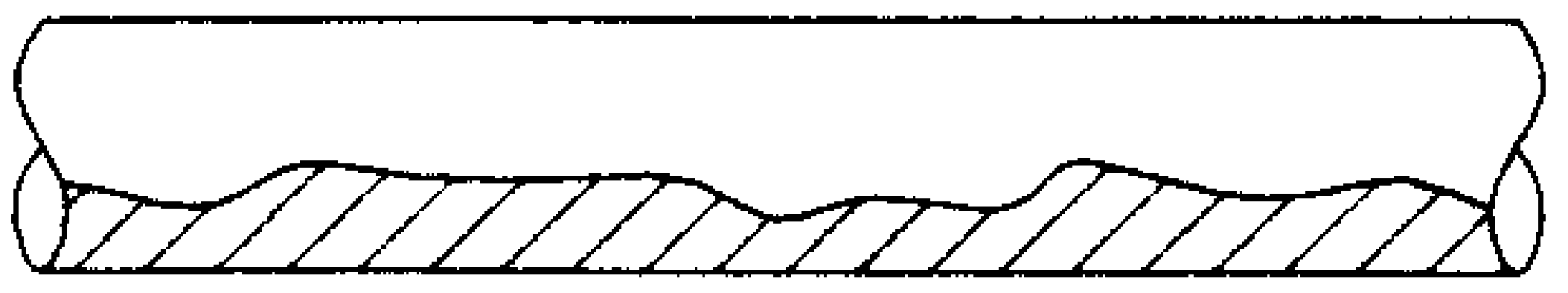
Stratified Wavy

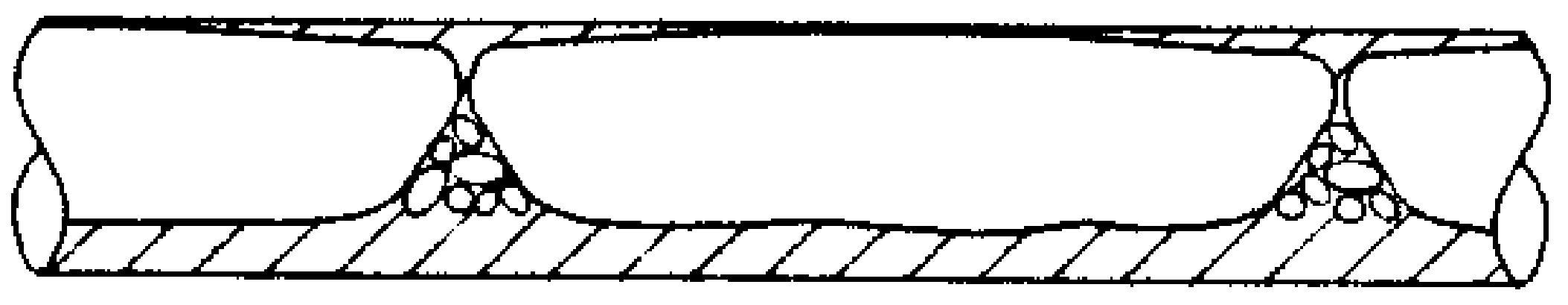
Pseudo-slug (Wavy Annular)

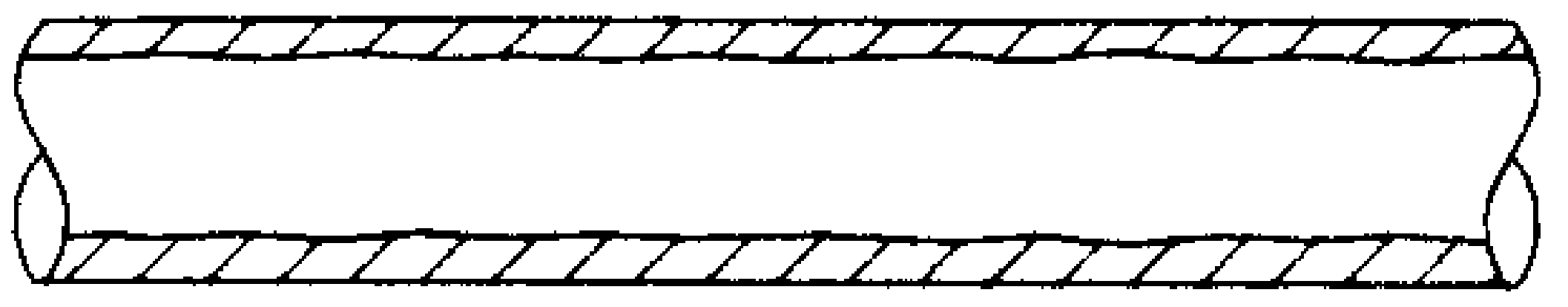
Annular

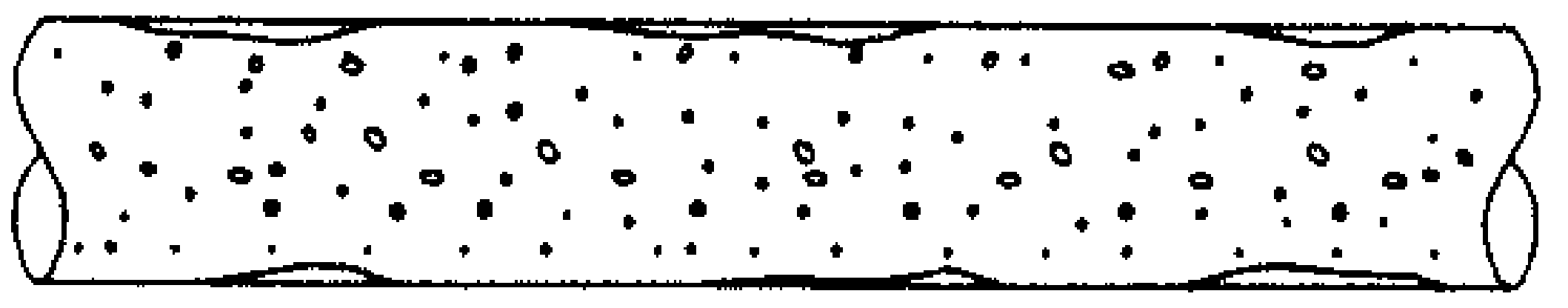
Mist

Figure 2.11 The basic flow patterns in small horizontal adiabatic tubes.

(4) Vertical flow in small tubes

The typical flow patterns in vertical small adiabatic tubes are presented in Figure 2.12.

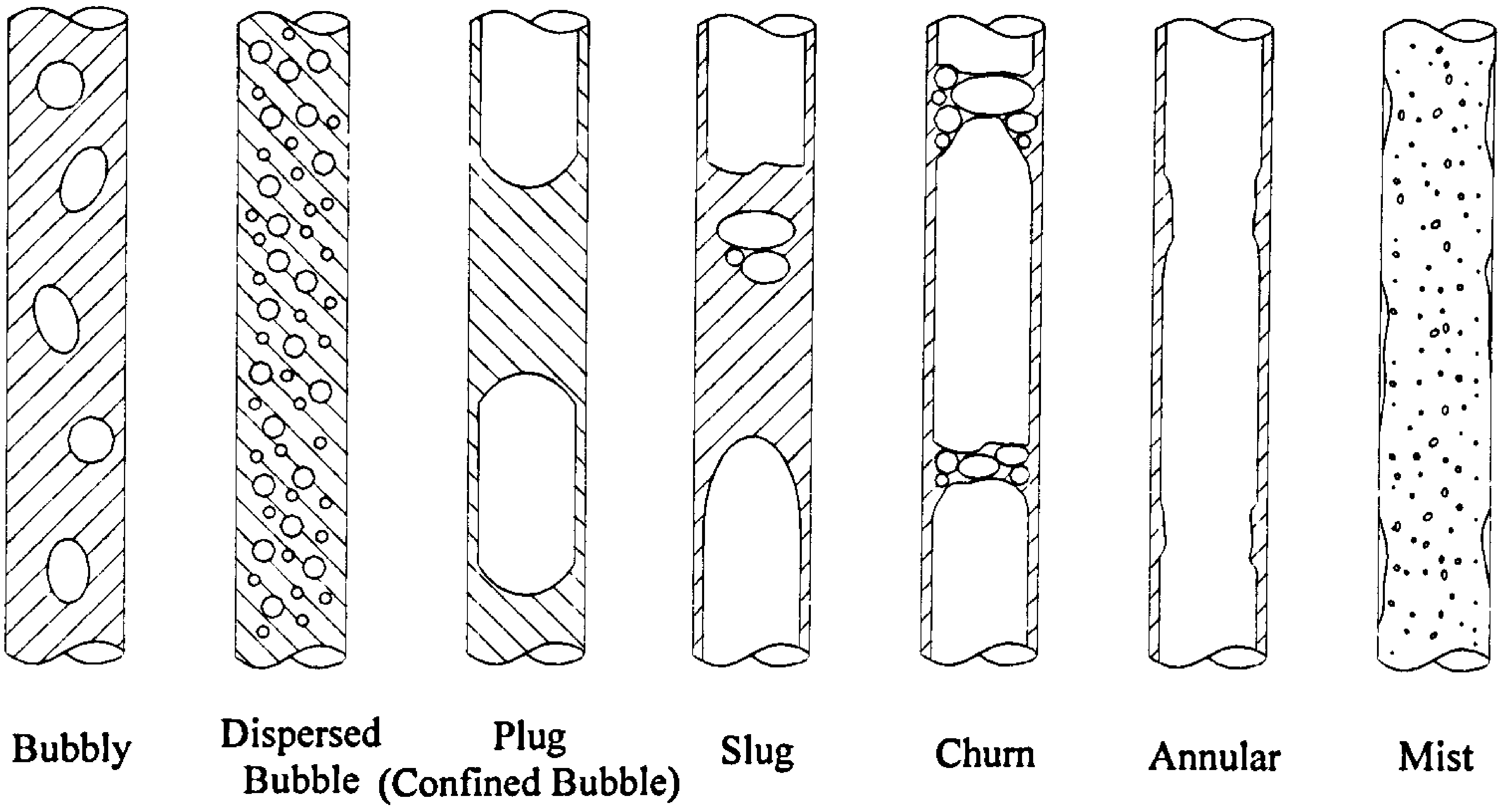

Figure 2.12 The basic flow patterns in small vertical adiabatic tubes.

Figure 2.13 drawn by author is based on the previous observations and illustrates the possible flow boiling patterns in small vertical tubes.

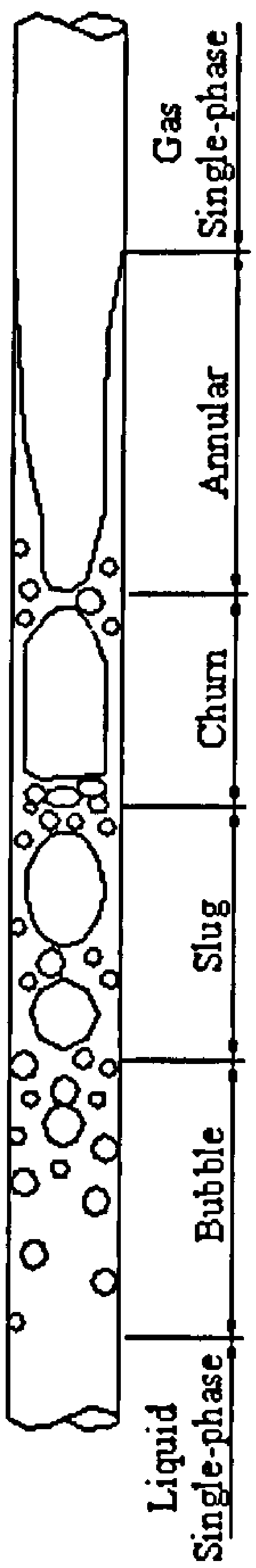

Figure 2.13 The possible flow patterns for flow boiling in small vertical tubes.

2.2.2 Flow maps

Pressure loss, heat and mass transfer, flow stability and component/system safety are strongly dependent on flow patterns. An accurate prediction of flow patterns has important actual significance. The most accepted tool to predict flow patterns are flow maps, which are initially sketched based on experimental data and then are hopefully predicted by correlations.

The first flow map may be that sketched by Baker in 1954 (Taitel 1990). Since then, various maps with different coordinate groups were proposed in an attempt to obtain general and accurate prediction of flow regimes. However, the aim has not been reached yet. Some flow maps were drawn in terms of dimensionless parameters, whereas others were based on dimensional parameters. The most popular coordinate parameters are gas and liquid superficial velocities. However, the dimensionless coordinate groups might be more general and effective since each coordinate can contain a group of parameters.

The coordinate groups in the published flow maps from various researchers have been summarized by Chisholm (1983), Troniewski and Ulbrich (1984) and are given below:

(1) u_{gs} vs. u_{ls}

(2) $\left(\frac{\upsilon_{gref}}{\upsilon_g}\right)^{1/3}\left(\frac{\upsilon_{lref}\sigma_{ref}}{\upsilon_l\sigma}\right)^{1/4} u_{gs}$ vs. $\left(\frac{\upsilon_{lref}\sigma_{ref}}{\upsilon_l\sigma}\right)^{1/4} u_{ls}$

(3) G_{gs}/λ vs. $G_{ls}\psi$

$$\lambda = \sqrt{\frac{\rho_g\rho_l}{\rho_{gref}\rho_{lref}}} \qquad \text{and} \qquad \psi = \frac{\sigma_{ref}}{\sigma}\left[\frac{\mu_l}{\mu_{lref}}\left(\frac{\rho_{lref}}{\rho_l}\right)^2\right]^{1/3}$$

(4) $\frac{G_{ls}}{G_{gs}}\lambda\psi$ vs. $\frac{G_{gs}}{\lambda}$

(5) u_h vs. β

(6) G_{gs} vs. G_{ls}

(7) $u_{gs}\left[\frac{\upsilon_l}{Dg(\upsilon_g-\upsilon_l)}\right]^{1/2}$ vs. α

(8) $\frac{u_{gs}}{u_{ls}}$ vs. u_{ls}

(9) $\frac{u_{gs}}{u_{ls}}$ vs. u_l

(10) Fr_h vs. β

(11) G vs. x

(12) $u_{ls}^2\rho_l$ vs. $u_{gs}^2\rho_g$

(13) m_l vs. m_g

(14) Re_{gs} vs. Re_{ls}

(15) We_{gs} vs. We_{ls}

(16) X vs. Y

$$Y=\frac{(\rho_l-\rho_g)g\sin\theta}{\Delta P_g}$$

(17) $u_{gs}\left(\frac{\rho_g}{g\sigma}\right)^{1/4}$ vs. $u_{ls}\left(\frac{\rho_l}{g\sigma}\right)^{1/4}$

(18) $u_{gs}\sqrt{\frac{\rho_g}{gD(\rho_l-\rho_g)}}$ vs. $u_{ls}\sqrt{\frac{\rho_l}{gD(\rho_l-\rho_g)}}$

(19) $u_{gs}\sqrt{\frac{\rho_g}{\sqrt{g\sigma(\rho_l-\rho_g)}}}$ vs. $u_{ls}\sqrt{\frac{\rho_l}{\sqrt{g\sigma(\rho_l-\rho_g)}}}$

(20) $\frac{u_{gs}}{D}\sqrt{\frac{\rho_g}{\sqrt{g\sigma(\rho_l-\rho_g)}}}\sqrt{\frac{\sigma}{g(\rho_l-\rho_g)}}$ vs. $\frac{u_{ls}}{D}\sqrt{\frac{\rho_l}{\sqrt{g\sigma(\rho_l-\rho_g)}}}\sqrt{\frac{\sigma}{g(\rho_l-\rho_g)}}$

The typical flow maps reported are shown in Figures 2.14-2.17 for normal and small size tubes at vertical or horizontal orientation. The significant effect of channel dimension can be detected from the aforementioned maps. For example, comparison of Figures 2.14 and 2.16 shows that stratified smooth flow occupies a large area in the 25 mm diameter tube but disappears in the 2.0 mm tube. This is one example of the many that urged researchers to explore flow regimes for small tubes. In addition, the flow maps for vertical and horizontal flow exhibited significant differences in both normal and small tubes, which indicates that gravity still is an important factor in flow regimes. For example, stratified flow (SS and SW) is a main flow pattern in horizontal normal size tubes but it completely disappears in vertical normal size tubes. On the other hand, churn flow (CH) can only be observed in vertical tubes. For small tubes, Damianides and Westwater (1988) observed bubble, dispersed bubble, plug, slug, pseudo slug, wavy and annular flow in small horizontal tubes as shown in Figure 2.16. However, Mishima and Hibiki (1996) only reported bubbly, slug, churn and annular flow in vertical small tubes, see Figure 2.17.

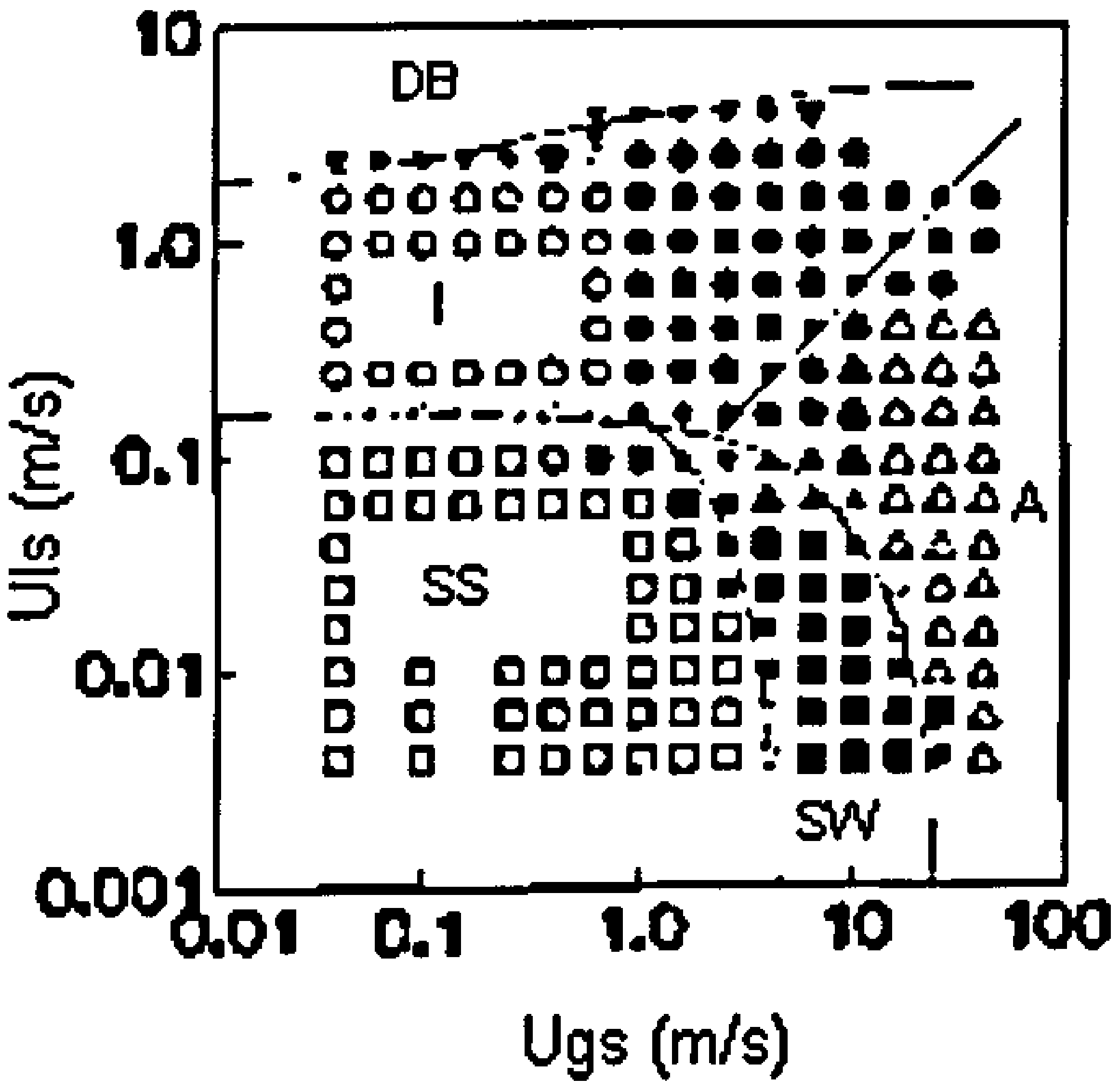

Figure 2.14 Flow patterns reported by Barnea et al. (1985) for 25 mm diameter horizontal tube, air-water at atmospheric conditions (25 °C, 1 bar), compared with the theoretical lines proposed by Taitel and Dukler (1976).

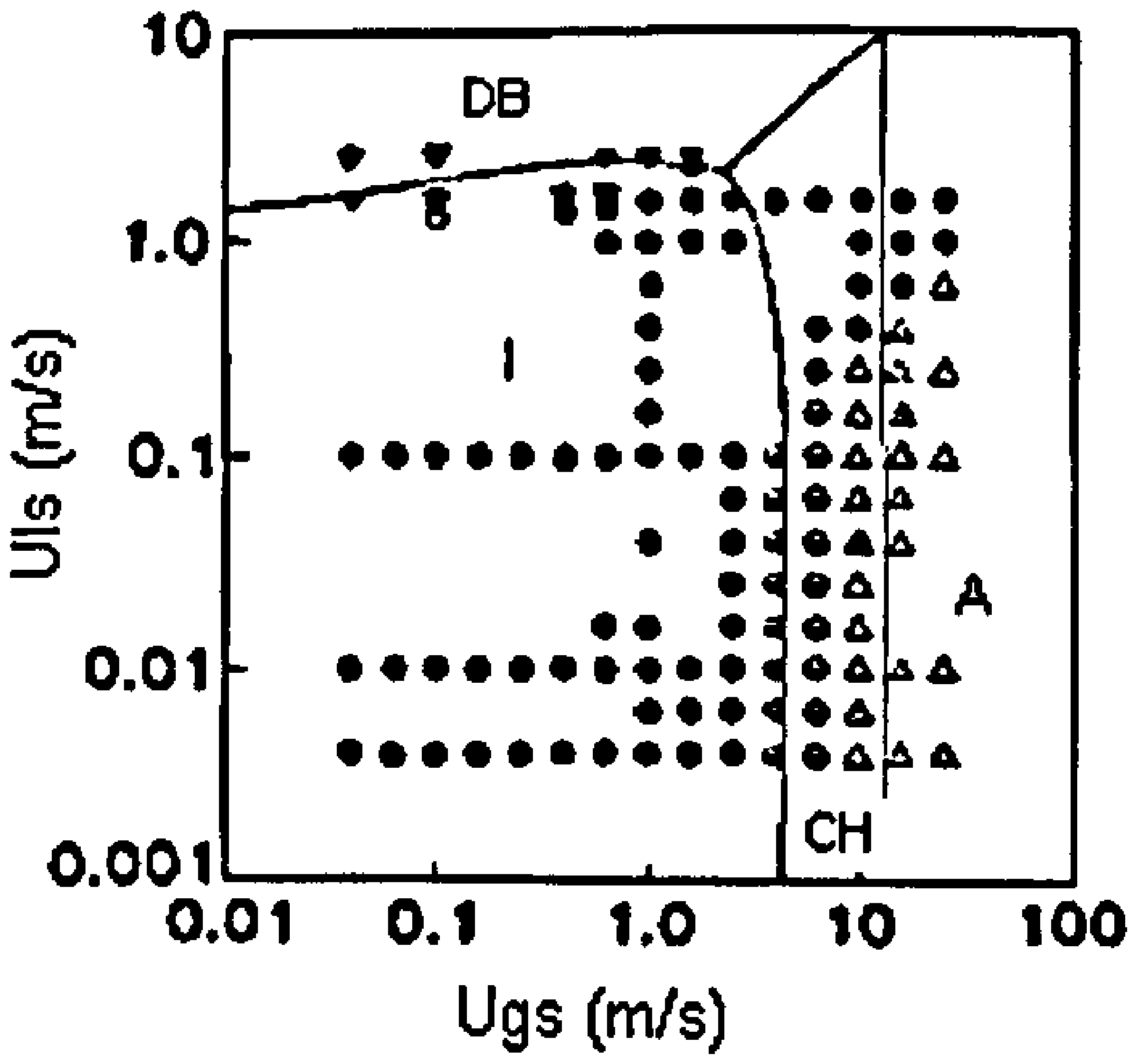

Figure 2.15 Flow patterns reported by Barnea et al. (1985) for 25 mm diameter vertical upward tube, air-water at atmospheric conditions (25 °C, 1 bar), compared with the theoretical lines proposed by Taitel et al. (1980).

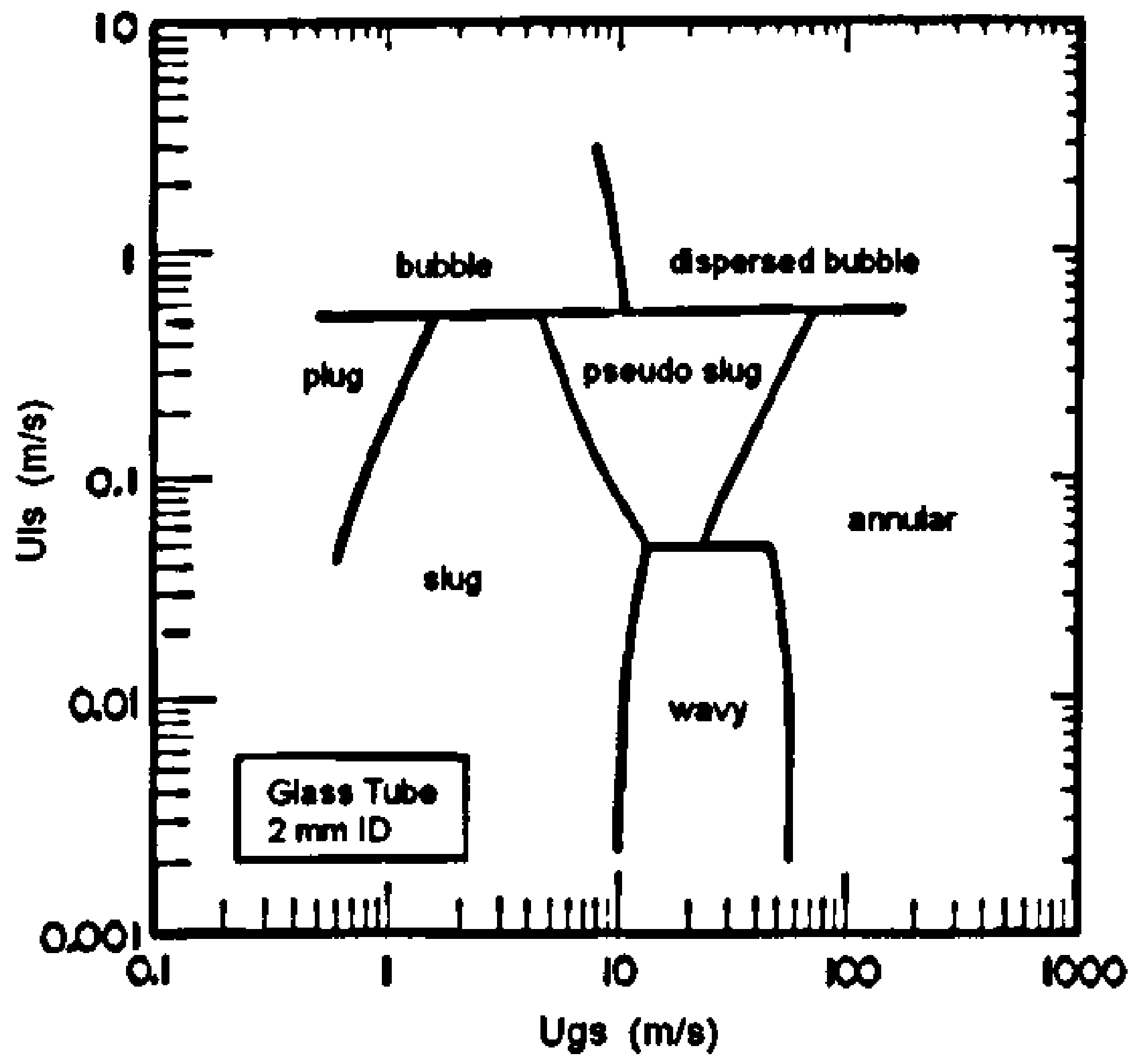

Figure 2.16 Flow pattern reported by Damianides and Westwater (1988) for 2 mm diameter horizontal tube, air-water at atmospheric conditions (10-25 °C, 1 bar).

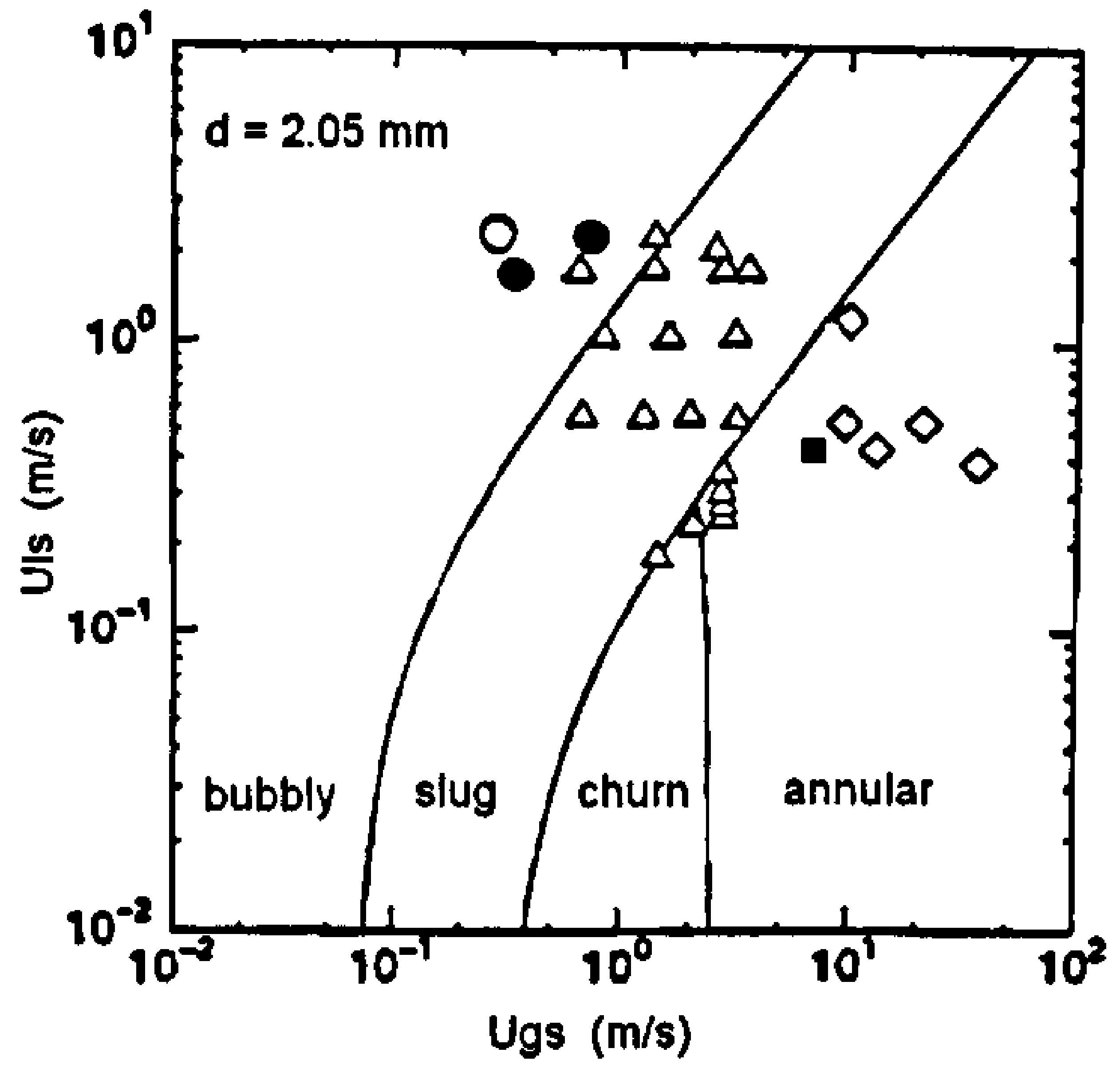

Figure 2.17 Flow pattern reported by Mishima and Hibiki (1996) for 2.05 mm diameter vertical upward tube, air-water at atmospheric conditions. The solid line is the prediction by the model of Mishima-Ishii (1984).

2.2.3 Transition models and correlations

The initial method to predict flow patterns was to correlate experimental data and plot them on a "flow pattern map". However, this method requires a great deal of experimental data and can hardly help obtain general correlations. In the 80's, attempts were required to develop physical models that allow an analytical prediction of the transition boundaries (Barnea 1986). These models try to simplify the description of physical phenomena so that a mathematical simulation is possible. However, a complete physical understanding of the phenomena related to flow pattern transitions is still not available. Most models are restricted to a specific range and thus give only a partial view of the transition mechanisms in tubes (Barnea 1987).

The models for normal size tubes have been presented for the following particular situations:

(1) Horizontal and slightly inclined tubes (Taitel and Dukler 1976, Husain and Weisman 1978, Kadambi 1982, Lin and Hanratty 1986)
(2) Vertical upward flow (Taitel et al. 1980, Mishima and Ishii 1984, McQuillan and Whalley 1985)
(3) Vertical downward flow (Barnea et al. 1982)
(4) Inclined upward flow from 0 to 90° (Barnea et al. 1985)
(5) Inclined downward flow from 0 to -90° (Barnea et al. 1982)
(6) Complete range of inclined flow from -90 to 90° (Barnea 1987)

Based on the previous studies, Taitel summarized and presented a "Unified Model" which can predict flow patterns reasonably at any angle of inclination. This model incorporates the effect of fluid properties (density, viscosity and surface tension), tube size and inclination angle. The prediction of the model agrees with the experimental results of 50.1 mm tube in the whole range of tube inclination (Taitel 1990). However, it was based solely on the experimental data for normal tubes and might not consider the effect of surface tension adequately. Therefore, the unified model is only valid for normal size tubes and a revision for small tubes is needed.

Barnea et al. (1983) verified experimentally the model of Taitel and Dukler (1976) for horizontal flow and Taitel et al. (1980) for vertical upward flow by using 4-12 mm tubes. The comparisons are shown in Figures 2.18 and 2.19 for horizontal flow and upwards vertical flow respectively. For the horizontal flow in Figure 2.18, the Taitel and Dukler's model (1976) could predict Barnea's data properly except for the stratified-intermittent transition boundary, which exhibit the enhanced effect of surface tension in small tube. For the vertical flow in Figure 2.19, the Taitel's model (1980) generally agreed with Barnea's data but the deviation was obvious at the boundaries of slug-churn and churn-annular at high u_{ls} region, which might be attributed to the different identification of churn flow. However, Damianides and Westwater (1988) sketched flow maps for 1-5 mm tubes in their experiments and found that the Taitel and Dukler's model (1976) could hardly predict any transition boundaries. For example, the stratified flow could not be observed in the Damianides and Westwater's experiments but it is a main flow pattern in the Taitel and Dukler's model, see Figures 2.20 and 2.21. It indicated that the existing models are not valid when tube diameter is less than 5 mm for air-water at atmospheric conditions because surface tension begins to dominate as tube diameter decreases.

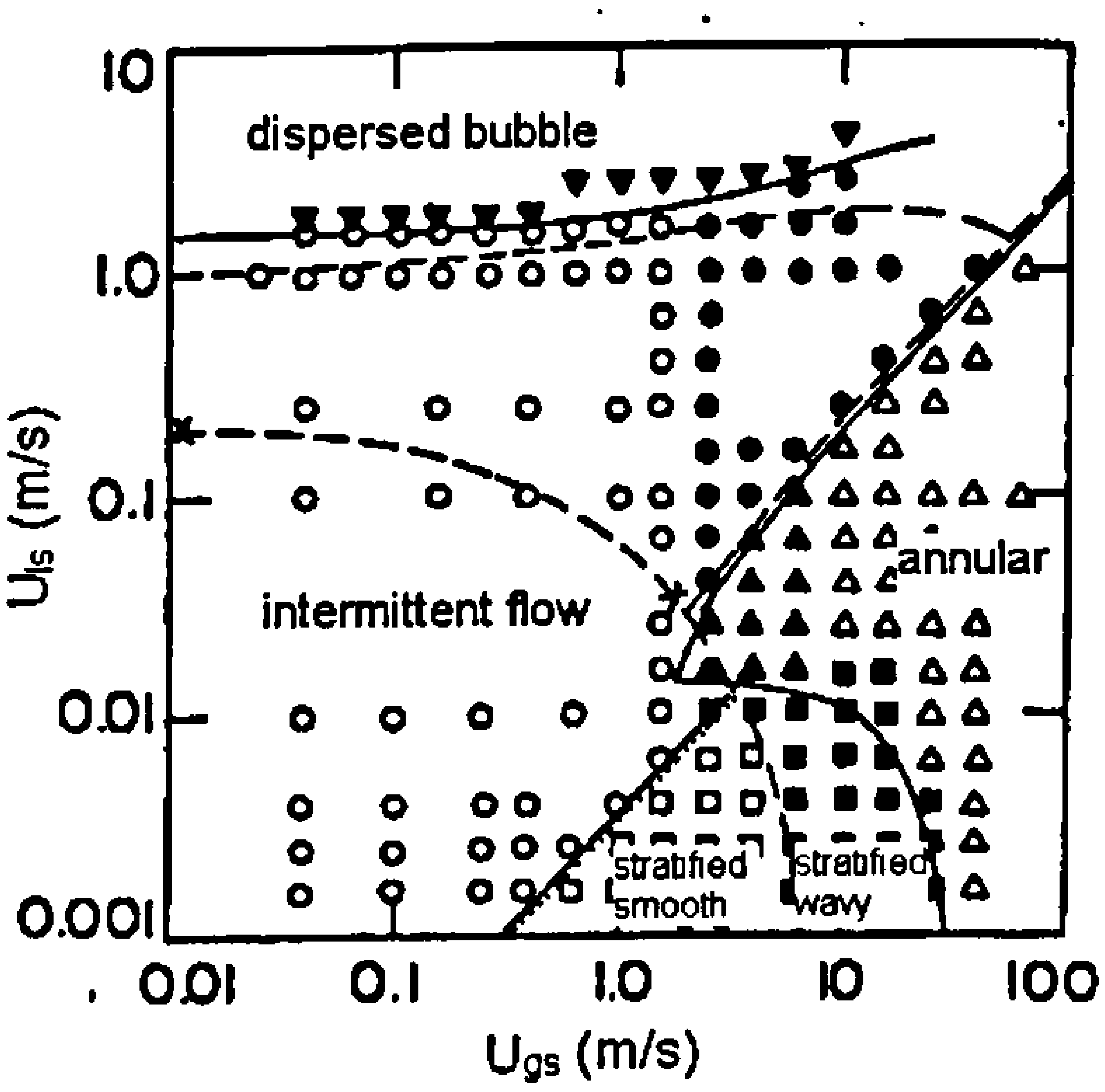

Figure 2.18 Comparison between the 4 mm horizontal air-water flow map at atmospheric conditions (25 °C, 1 bar) presented in the solid lines and the model of Taitel and Dulkler (1976) presented by the broken lines, (Barnea et al. 1983).

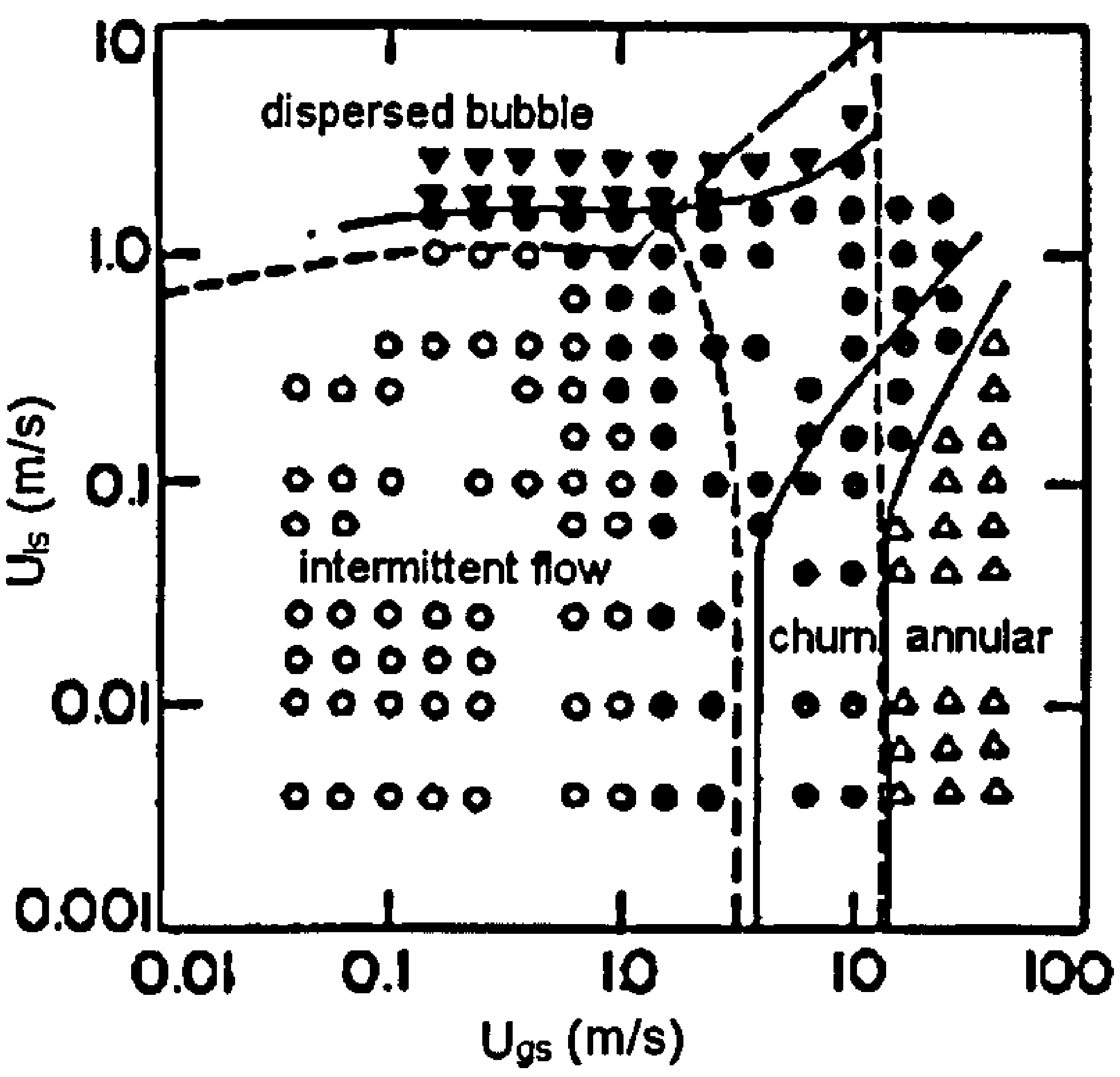

Figure 2.19 Comparison between the 4 mm upwards vertical air-water flow map at atmospheric condition (25 °C, 1 bar) presented in the solid lines and the models of Taitel et al. (1980) presented by the broken lines, (Barnea et al. 1983).

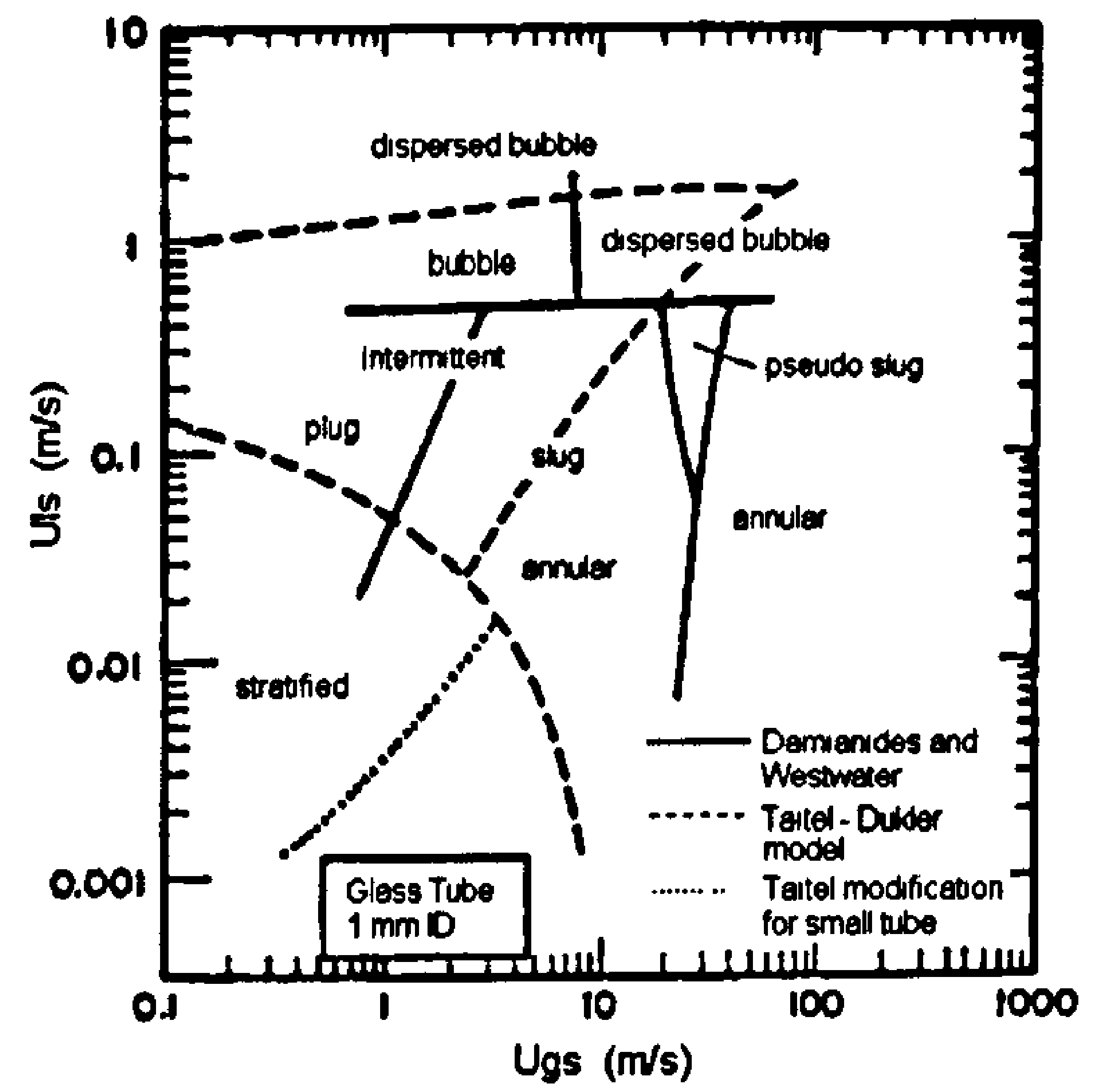

Figure 2.20 Comparison between the 1 mm horizontal air-water flow map at atmospheric conditions (10-25 °C, 1 bar) and the models of Taitel and Dukler (1976), (Damianides and Westwater 1988).

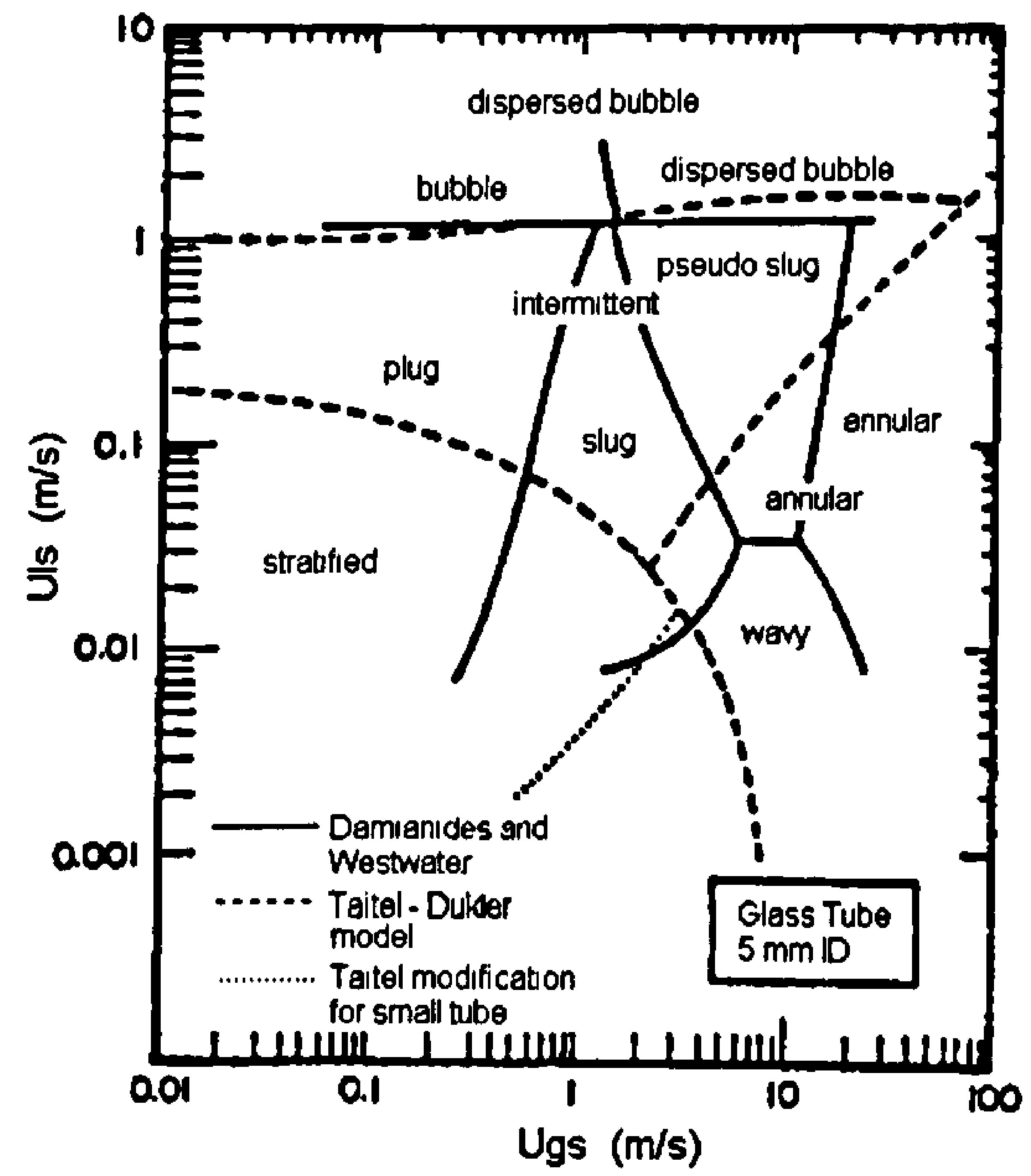

Figure 2.21 Comparison between the 5 mm horizontal air-water flow map at atmospheric conditions (10-25 °C, 1 bar) and the models of Taitel and Dukler (1976), (Damianides and Westwater 1988).

The maps depicted in Figures 2.22 and 2.23, are sketched according to the "Unified Model" model cited from Taitel (1990). The relevant equations are given in Appendix B. Obviously, it results in an inconsistent prediction for small tubes because there is a region where intermittent-churn and churn-annular transition boundaries cross, see Figure 2.23.

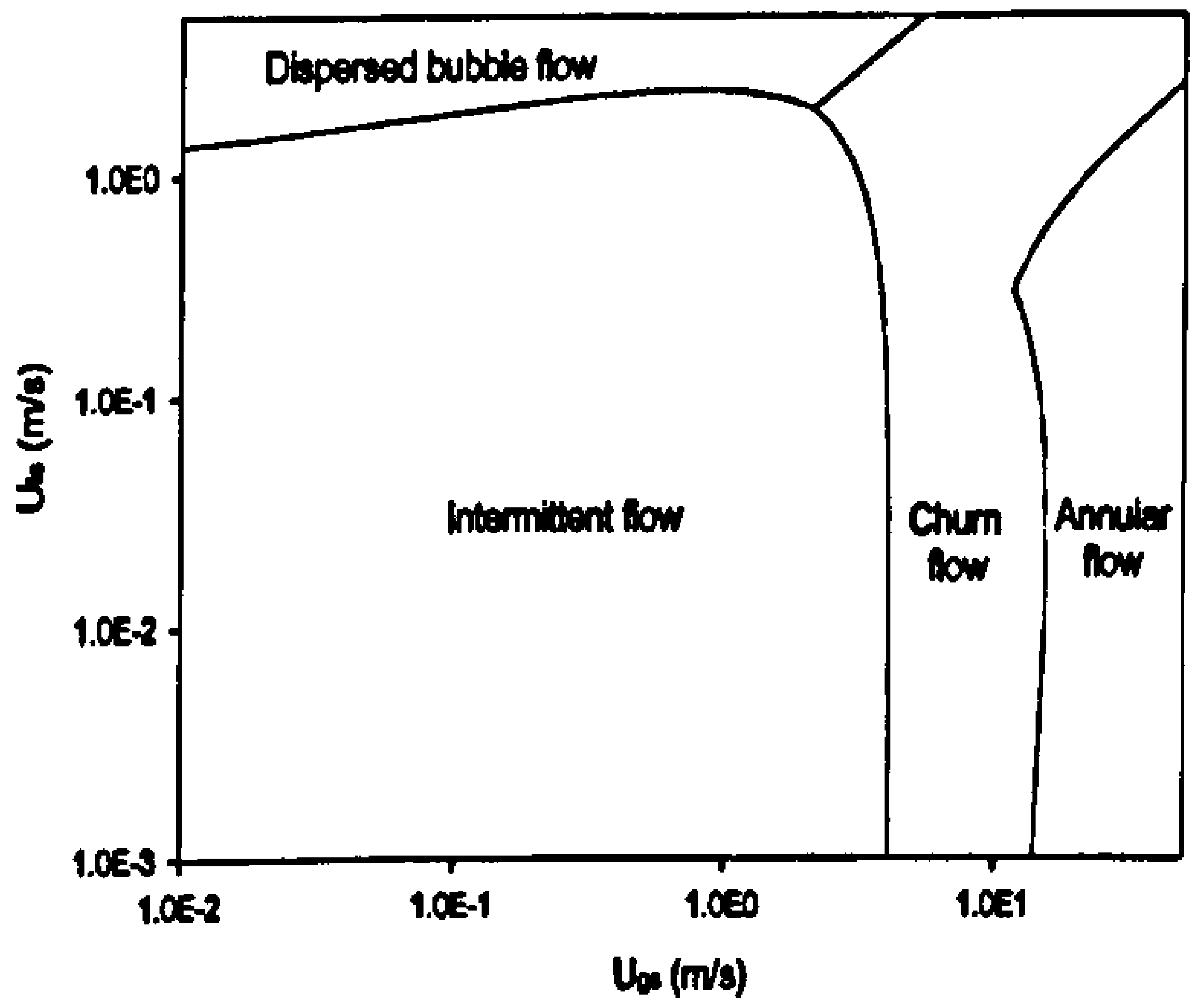

Figure 2.22 Flow map for vertical upward flow, air-water, 0.1 MPa, 25 °C, 25.4 mm tube based on Unified Model (Taitel 1990).

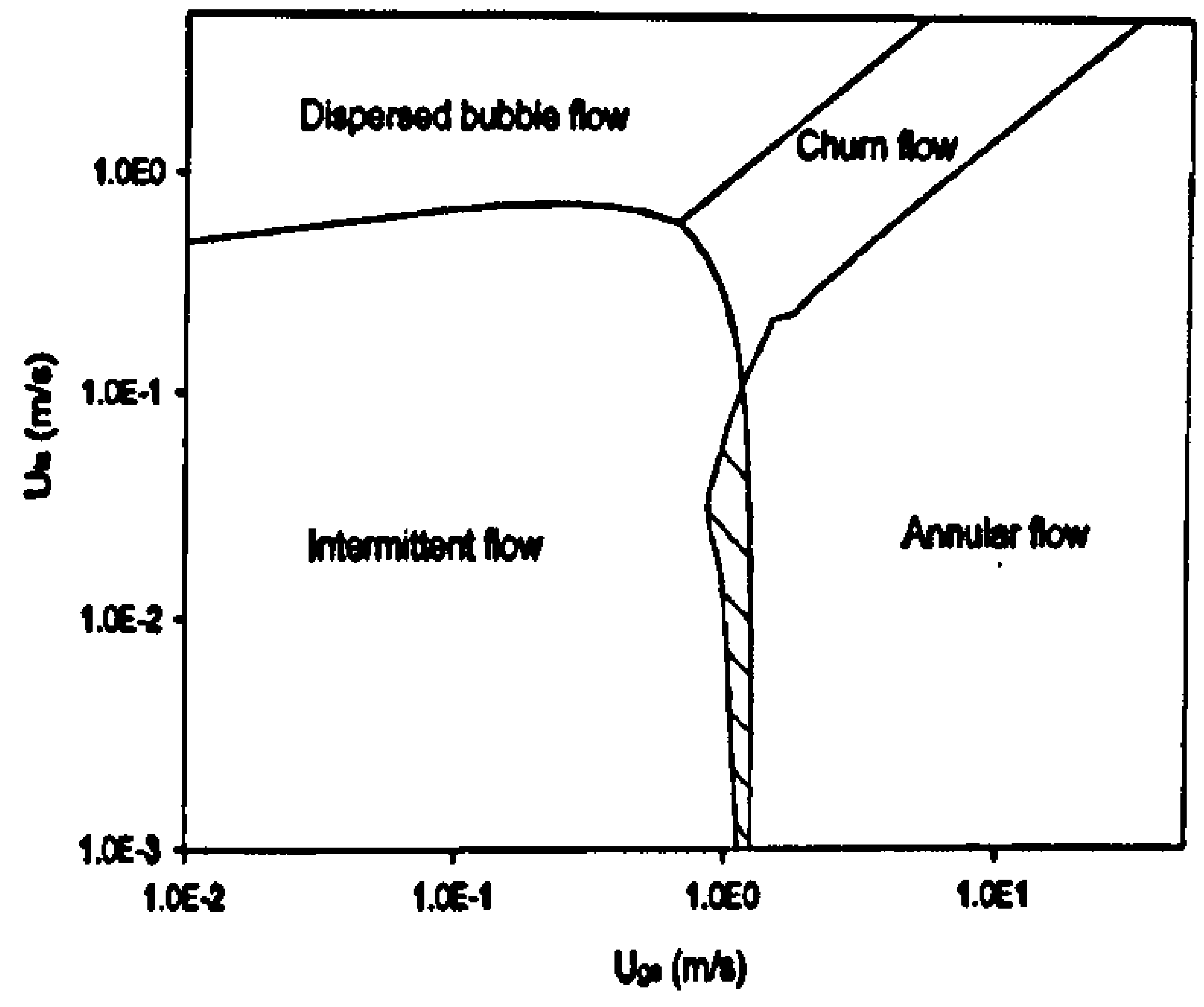

Figure 2.23 Flow map for vertical upward flow, R134a, 0.293 MPa, 0 °C, 2.0 mm tube based on Unified Model (Taitel 1990).

To date, the special transition models and correlations for small channels have not been established. Therefore, revising the existing models and correlations for normal size tubes or developing new models and correlations for small tubes is one of the main aims in current two-phase flow research. Although the existing models and correlations developed from normal size tubes have been proved by most researchers not to be suitable for small tubes (Sue and Griffith 1964, Oya 1971, Barnea et al. 1983, Graska 1986, Damianides and Westwater 1988), they can provide some indications of the boundaries or possibly provide the basis for the new developed models and correlations for small tubes. Therefore, it was considered necessary to present these models and correlations. Appendix B shows the equations of the models given by Taitel et al. (1980), Mishima and Ishii (1984), McQuillan and Whalley (1985) and, as mentioned above, the unified model summarized by Taitel (1990).

Unlike the traditional flow maps, in which the transition boundaries are sketched based on gas-liquid interface configuration, flow regimes for small tubes or in microgravity situations are depicted according to force analysis in the work of Akbar et al. (2003). They divided the entire flow map into four regions for small tubes:

(1) Surface tension-dominated region, including bubbly, plug and slug.

(2) Inertia-dominated zone 1, including annular and wavy-annular regimes.

(3) Inertia-dominated zone 2, including dispersed flow regime.

(4) Transition zone.

Akbar et al. (2003) proposed four semi-empirical correlations to predict the above four regions based on the previous experimental data for small channels, see Appendix B. The correlations use Weber numbers as the coordinate which represent the ratio of surface tension and inertia. The sketch transition lines agreed with the relevant data for air-water like fluid in circular and near-circular small tubes with about 1 mm hydraulic diameter at ambient conditions. The comparative result is presented in Figure 2.24. Akbar et al. also suggested that the applicability of the correlations needed further validation.

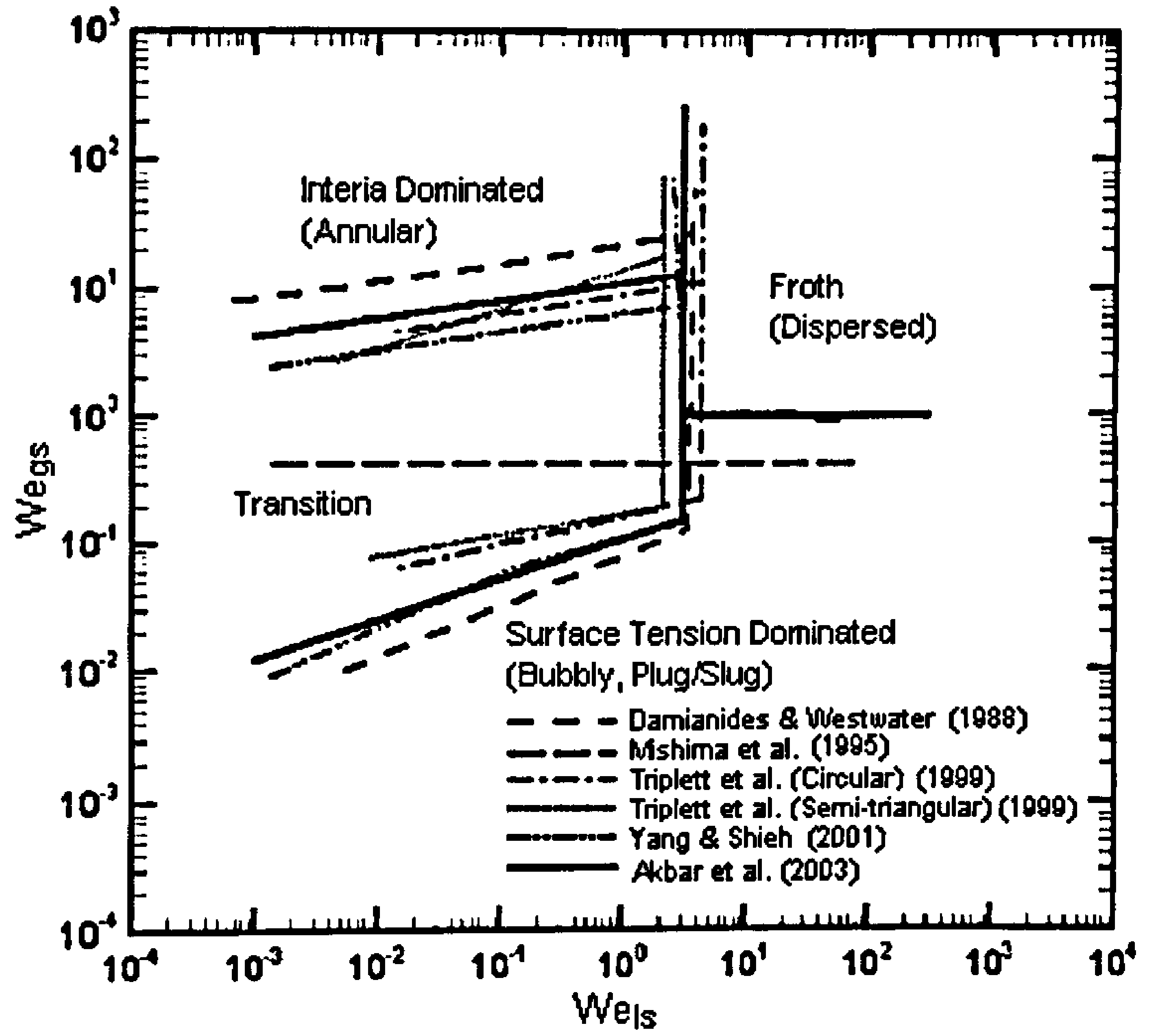

Figure 2.24 Comparison between the correlations proposed by Akbar et al. (2003) and the experimental data for circular and near-circular channels with about 1 mm diameter.

2.3 The factors affecting flow patterns

2.3.1 Force analysis

The particular flow regime established by a given combination of liquid and gas velocities depends upon the interaction of gravity, shear stress, inertia force, surface tension and turbulent force. It is believed that the flow mechanisms in small tubes are different from those in larger tubes primarily due to the different relative magnitudes of these forces (Coleman and Garimella 1999). The forces that act on a separate bubble can be defined quantitatively as follows:

(1) Buoyancy (gravity)

Buoyancy originates from the gravity acceleration and the difference of gas and liquid density. It causes the separation of gas and liquid thus is an important factor in forming stratified flow in horizontal flow. In inclined flow, buoyancy facilitates bubble accumulation and coalescence at the top of conduit, which leads to bubble flow transition into intermittent flow. It is given as:

$$F_B = \frac{\pi}{6} d^3 (\rho_l - \rho_g) g \tag{2.4}$$

i.e. the force is proportional to $d^3 (\rho_l - \rho_g) g$.

(2) Shear stress (friction)

Shear stress at the gas-liquid interface can maintain the liquid film in annular flow and can also intensify the disturbance of gas-liquid interface, which causes stratified smooth flow and slug flow change to stratified wavy flow and churn flow respectively. It is given as:

$$\tau_i = f_i \frac{\rho_g (u_g - u_l)^2}{2}$$

$$F_i = C_i \times \pi d l \times f_i \frac{\rho_g (u_g - u_l)^2}{2} \tag{2.5}$$

If the bubble's length l is proportional to the bubble diameter d, the shear force between gas and liquid phases is proportional to $d^2 f_i \rho_g (u_g - u_l)^2$.

(3) Inertia force

Inertia force keeps bubbles moving at their original track, direction and velocity. Liquid bridge is broken at higher gas velocity to facilitate the transition of churn to annular flow due to the large inertia force. In addition, turbulence flow can be formed at large inertia force and accordingly promote the emergence of churn flow.

$$F_I = C_I \times \frac{\pi}{8} d^3 \rho_g \times \frac{u_g^2}{d} \tag{2.6}$$

i.e. it is proportional to $d^2 \rho_g u_g^2$

(4) Surface tension

Surface tension takes an important role in small bubbles, i.e. it facilitates the formation of regular and round bubbles and enhances the rigidity and anti-coalescence of bubbles. Another reason surface tension becomes an important factor in small tubes is that the size and the shape of bubbles are not anymore negligible in flow pattern studies. The enhanced effect in small tubes makes the liquid film in churn flow thinner so as to facilitate the rebuilding of liquid bridge in annular flow. The resulting force is proportional to the bubble size and surface tension, i.e.

$$F_S \propto d\sigma \tag{2.7}$$

(5) Turbulent force

Turbulent force drives bubbles to move in a zigzag way (Levich 1962). It increases collision frequency among bubbles. It also prevents bubbles from accumulating at the top of conduit in inclined flow. It is given as:

$$F_T = \frac{1}{2}\rho_l u'^2_r \frac{\pi d^2}{4}$$

where

$$u'_r = u_l\left(\frac{f_l}{2}\right)^{1/2}$$

Therefore,

$$F_T = \frac{\pi}{16} d^2 \times f_l \rho_l u_l^2 \tag{2.8}$$

i.e. this force is proportional to $d^2 f_l \rho_l u_l^2$.

Figure 2.25, which is a plot of the ratio of the forces act on a bubble and the bubble surface area, i.e. F/A, qualitatively exhibits the influence of bubble size on buoyancy and surface tension, which shows that surface tension dominates over buoyancy when the bubble size is less than a certain value.

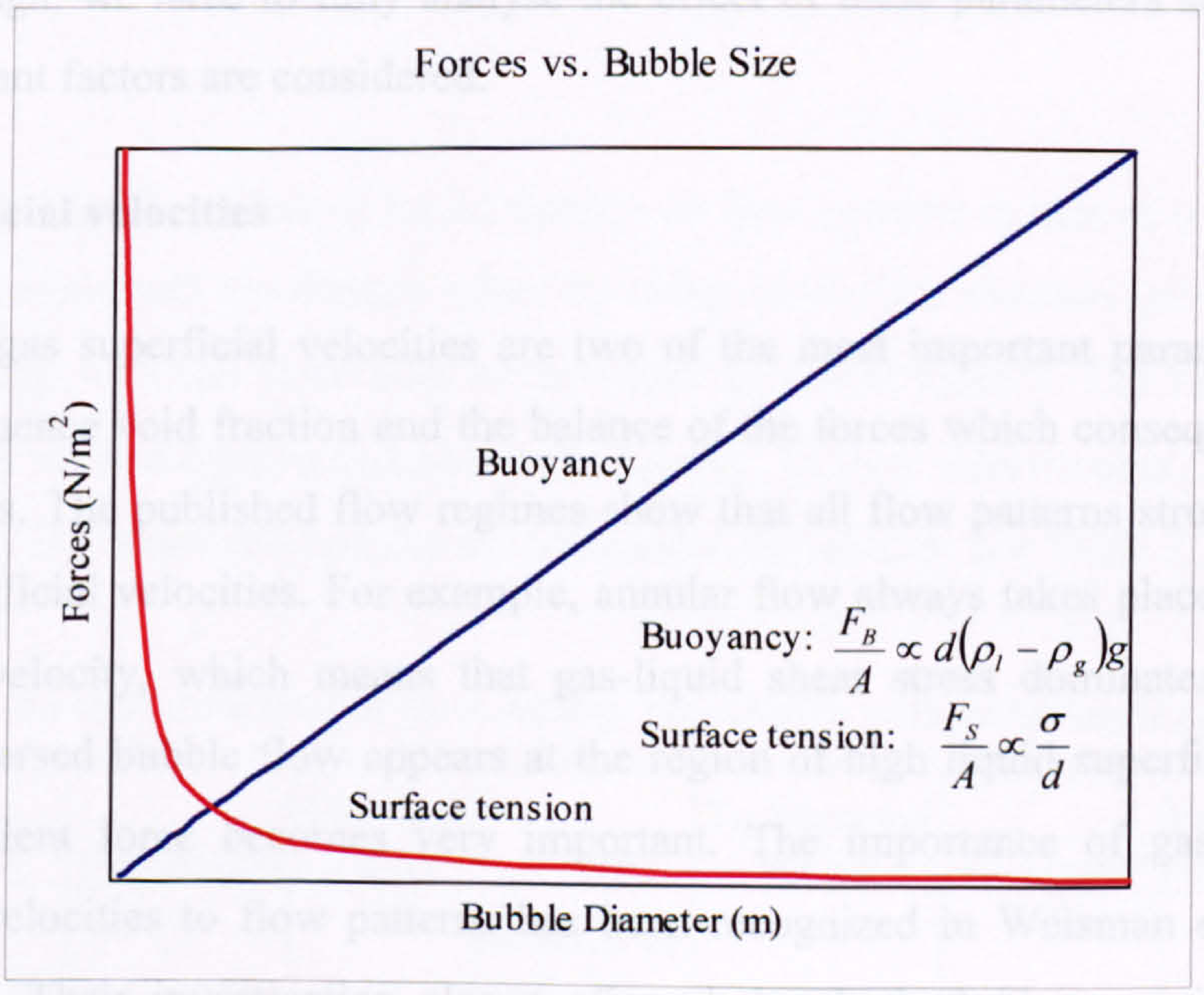

Figure 2.25 The relationship between forces and bubble size.

2.3.2 Parametric analysis

Based on the aforementioned dynamic analysis and Taitel's (1990) summary, it can be concluded that the following parameters directly affect flow patterns:

(1) liquid, gas superficial velocity u_{ls}, u_{gs}
(2) liquid, gas density ρ_l, ρ_g
(3) liquid, gas dynamic viscosity μ_l, μ_g
(4) conduit dimension, D
(5) gravitational acceleration g and conduit inclination angle θ
(6) surface tension, σ
(7) tube roughness, ε
(8) heat flux, q (only for flow boiling)
(9) enthalpy h_g, h_l and latent heat of evaporation h_{fg} (only for flow boiling)

Although the above parameters can be simplified to eight parameters in vertical adiabatic two-phase flow in smooth tube at the normal gravitational conditions, i.e. u_{ls}, u_{gs}, ρ_l, ρ_g, μ_l, μ_g, D, σ, it is still quite impractical to find a relation for them based on experimental data or theoretical analysis. In order to establish an appropriate mechanistic model that is sufficiently close to the natural phenomena as well as being simple enough, we have to fully analyse the effect of these parameters so that finally only important factors are considered.

(1) Superficial velocities

Liquid and gas superficial velocities are two of the most important parameters. They directly influence void fraction and the balance of the forces which consequently affect flow patterns. The published flow regimes show that all flow patterns strongly depend on the superficial velocities. For example, annular flow always takes place at high gas superficial velocity, which means that gas-liquid shear stress dominates over other forces. Dispersed bubble flow appears at the region of high liquid superficial velocity where turbulent force becomes very important. The importance of gas and liquid superficial velocities to flow patterns has been recognized in Weisman et al. (1979) experiments. Their investigation also confirmed that both fluid properties and tube diameter have only moderate influences compared with the superficial velocities. The effect of the superficial velocities on flow patterns is also explained by the effect on void fraction. Barnea and Brauner (1985), Hout et al. (1992) and Taitel et al. (2000) reported that the void fraction in liquid slug, α_s, is a function of homogeneous velocity u_h, where $u_h=u_{gs}+u_{ls}$, see Figure 2.26, and that α_s is a vital criterion that distinguishes intermittent flow, i.e. plug (or elongated bubble), slug and churn, see Figure 2.27.

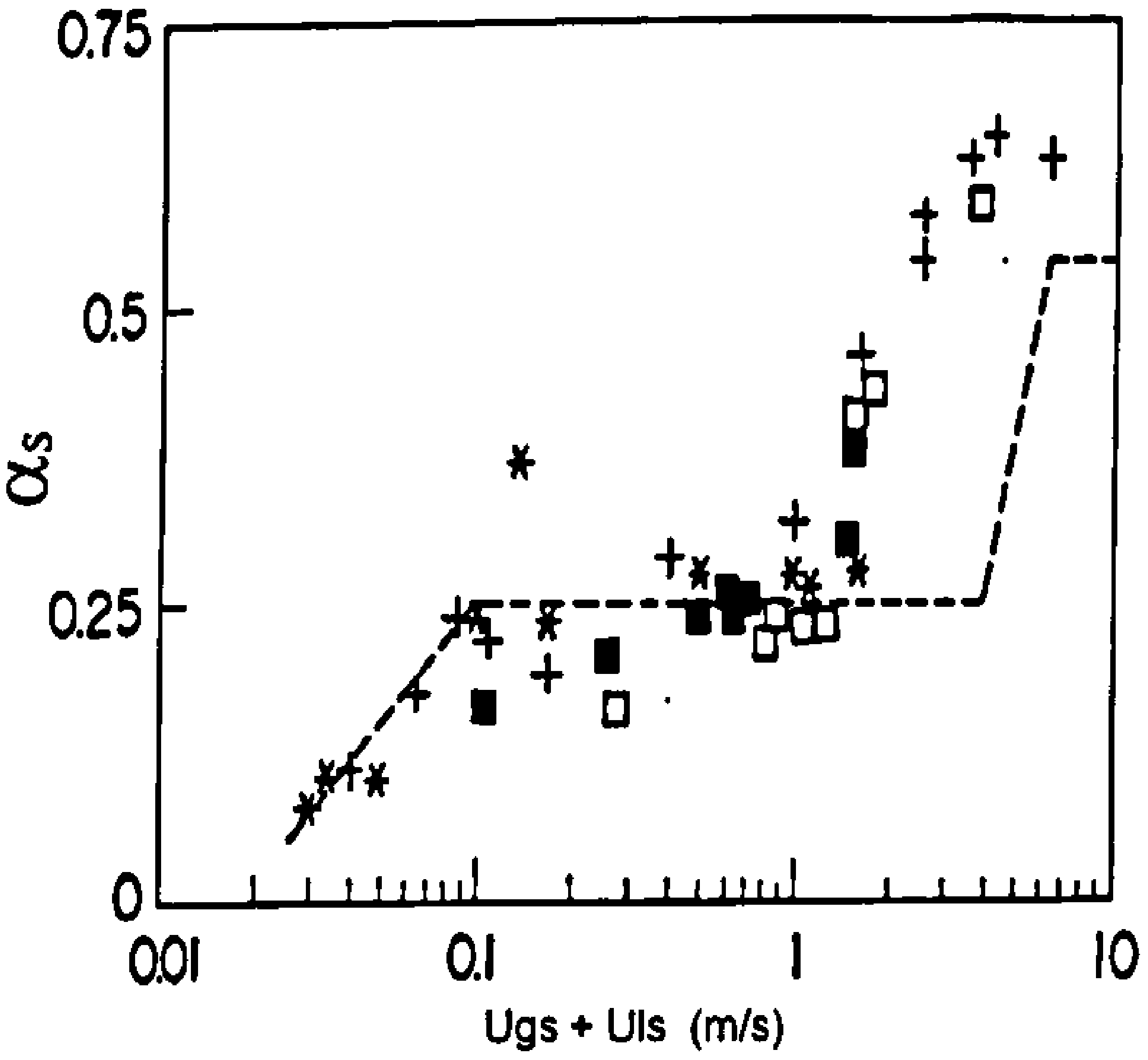

Figure 2.26 Void fraction in liquid slug, Hout et al. (1992).

- ■ Hout et al. (1992)
- + Barnea and Shemer (1989)
- * Fernandes (1981)
- □ Mao and Dukler (1989)
- ------- Barnea and Brauner (1985)

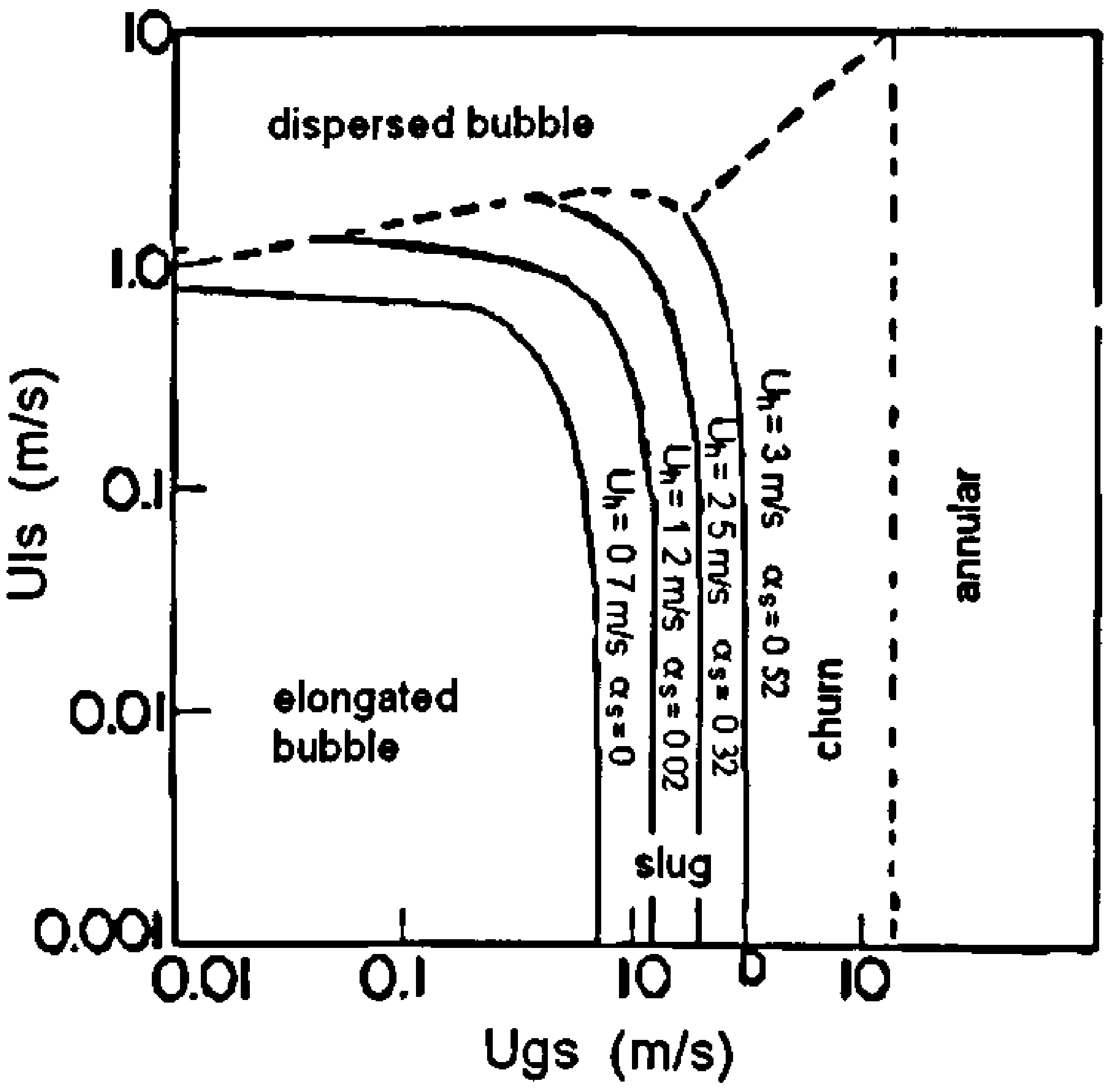

Figure 2.27 The different value of α_s in intermittent flow region, Barnea and Brauner (1985).

(2) Density

Published work on the effect of liquid density on flow patterns is indeed rare. Weisman et al. (1979) examined the density effect by using air-K_2CO_3 solution (ρ_l=1420 kg/m^3) and comparing with the flow map of air-water (ρ_l=1000 kg/m^3). The relative liquid viscosity and surface tension changed only slightly. In their experiments, it seems that liquid density has little effect on the main transient boundaries, see Table 2.3.

Table 2.3 The shift direction of flow pattern boundaries with reducing liquid density.

Researcher	Orientation	Diameter (mm)	Fluid	To dispersed bubble	To annular	Intermittent – stratified flow
Weisman et al. (1979)	horizontal	51	air-water vs. air-K_2CO_3 solution	little effect	little effect	little effect

The compressibility of gas is normally much bigger than that of liquid, and gas density can vary significantly compared with liquid. Therefore, it has more practical significance to study the effect of gas density on flow patterns. Gas density strongly depends on fluid pressure within a definite temperature range in incompatible gas-liquid fluids such as air-water flow. Other parameters, such as liquid density, gas and liquid dynamic viscosity, and surface tension, are less dependent on pressure. Thus, the effect of pressure on flow patterns reflects the effect of gas density indirectly. This effect could be variable in different fluids depending on the sensitivity of the gas density to pressure. However, the situation is much more complex for vapour-liquid type fluids such as steam-water or two-phase R134a flow used in the proposed experiments. The fluid temperature, i.e. the saturated temperature, is a function of the fluid pressure. The densities cannot be isolated from other parameters to study their exclusive effect only. Table 2.4 presents such relationship between fluid parameters and pressure.

Table 2.4 The effect of fluid parameters on their properties*.

	R134a			Steam-Water			Air-Water					
Pressure (bar)	6	10	14	1	10	100	1	10	100	1		
Temperature (°C)	21.6	39.4	52.5	99.6	179.9	311.0	20			0	50	99.6
Gas/Vapour Density (kg/m^3)	29.0	49.1	70.7	0.59	5.15	55.43	1.21	12.1	-	1.29	1.07	0.95
Liquid Density (kg/m^3)	1218	1148	1090	958	887	688	998	999	1003	1000	988	958
Gas/Vapour Dynamic Viscosity (μPa.s)	11.7	12.6	13.3	12.4	15.0	20.5	18.1	-	-	17.2	19.5	21.7
Liquid Dynamic Viscosity (μPa.s)	210.2	170.8	147.3	282.0	153.9	81.1	1071	1071	1065	1791	547.1	282.0
Surface Tension (mN/m)	8.4	6.2	4.6	59.0	42.2	11.8	72.8	-	-	75.6	67.91	58.9

*: Based on the information from Nagano, H.(1990), Schmidt, E. and Grigull, U.(1981), Rogers, G.F.C. and Mayhew, Y.R.(1988), and www.udel.edu/pchem/C446/Experiments/exp1.pdf.

Even with the above problems, the influence of gas density can be investigated qualitatively through a force analysis. High gas density evidently enhances gas-liquid shear stress and gas inertia force which facilitates churn or annular flow forming at lower gas velocity. Some experimental results support this analysis. For example, Weisman et al. (1979) evaluated the effect of vapour density by using R113 at 1 bar

(ρ_g=14 kg/m^3) and 4 bar (ρ_g=44 kg/m^3). Considering the change from the variation of viscosity and surface tension, the higher vapour density made the transition to annular flow to occur at lower gas superficial velocity but had little effect on the boundaries of stratified flow and intermittent flow, see Table 2.5. McQuillan and Whalley (1985) predicted the transition boundaries of plug-churn and churn-annular slightly shift towards the region of lower gas flow rate for vertical tubes when the pressure increases in their model. The agreement between the theoretical predictions and the experimental observations was generally good. Figure 2.28 shows the comparison of the McQuillan and Whalley's model with the steam-water flow maps sketched by Bergles and Suo (1966) at the pressures of 34.5 bar (ρ_g=17.28 kg/m^3) and 69.0 bar (ρ_g=35.95 kg/m^3) (McQuillan and Whalley 1985). However, the flow maps only support the prediction of churn to annular transition boundary, see Table 2.5 and Figure 2.28.

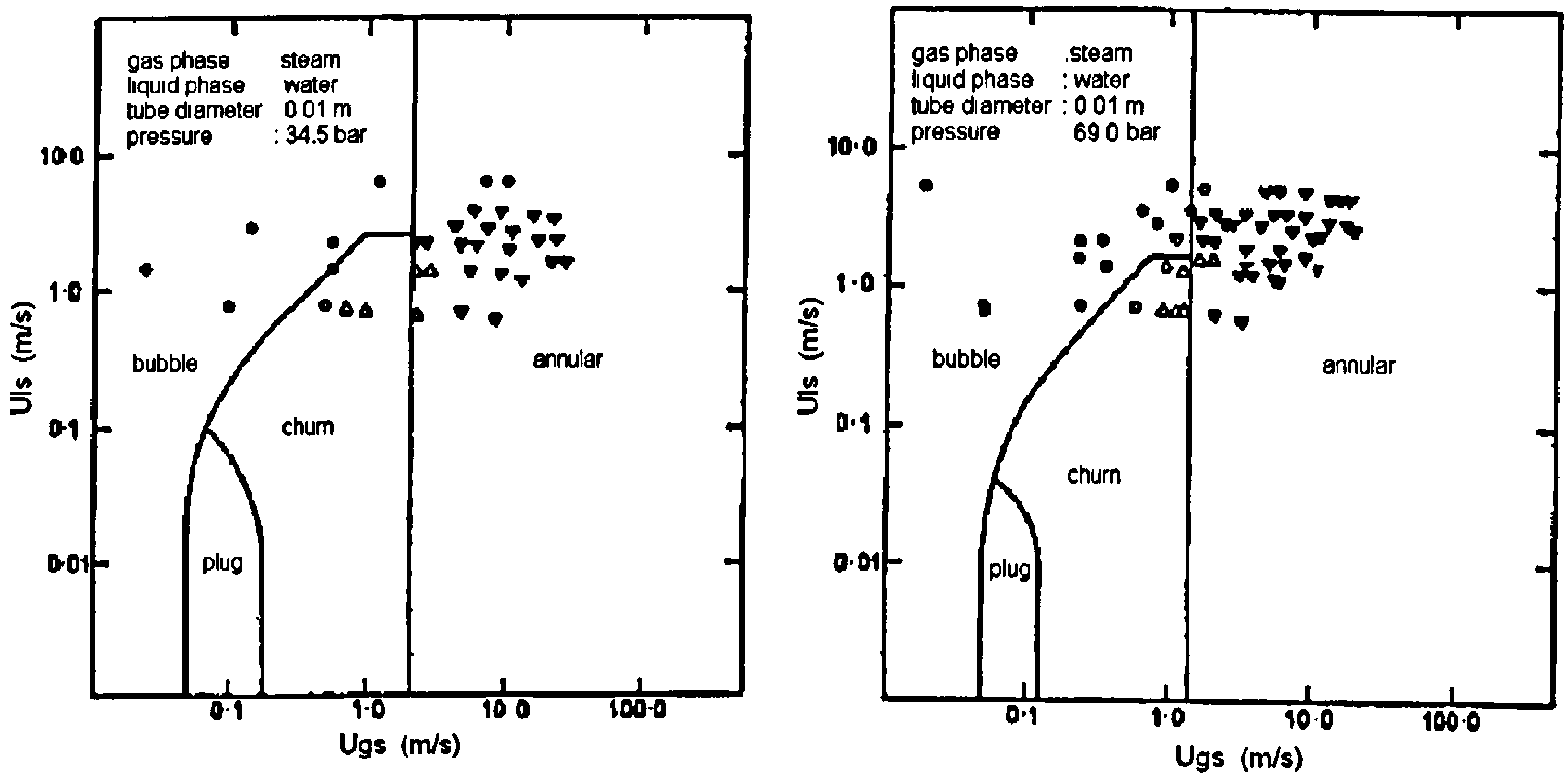

Figure 2.28 Comparison of the steam-water flow maps from Bergles and Suo (1966) and the model of McQuillan and Whalley (1985) at different pressures.

Table 2.5 The shift direction of flow pattern boundaries with reducing vapour density by decreasing fluid pressure.

Researcher	Orientation	Diameter (mm)	Fluid	Pressure	To annular	Intermittent - stratified
Weisman et al. (1979)	horizontal	25, 51	R113	1.0 vs. 4.0 bar	higher u_{gs}	little effect
Bergles and Suo (1966)	vertical	10	steam-water	36.5 vs. 69.0 bar	higher u_{gs}	N/A

The above works were based on large tubes. Yang and Shieh (2001) experimentally investigated two-phase flow patterns for refrigerant R134a and air-water in horizontal small tubes with the inside diameters from 1.0 to 3.0 mm. Compared to the air-water flow regime, an increase of vapour density in R134a flow leads to a shift of slug to annular transition to lower gas velocity. The authors attributed the phenomenon to the difference of surface tension since the surface tension of air-water is much larger than that of R134a. However, some researchers (Reinarts 1993) gave a different explanation to the above phenomenon. They suggested that the change of vapour density might be the key factor.

(3) Viscosity

A series of experiments were carried out by Weisman et al. (1979) to examine the effect of liquid viscosity on flow pattern transitions in 51 mm horizontal tube. The fluids used were air-water (μ_l=1.071 mPa.s) and air-glycerol solutions (μ_l=75 mPa.s and 150 mPa.s). Glycerol solution has an advantage of allowing the liquid viscosity to be varied while the surface tension and the density are nearly constant. The experimental results showed that the liquid viscosity affects the transition boundaries of dispersed bubble and annular but has little effect on stratified - intermittent boundary, see Table 2.6.

Bousman et al. (1996) experimentally studied the effect of liquid viscosity on flow patterns in 12.7 mm and 25.4 mm tubes at microgravity conditions. Air and two liquids, water (1 mPa.s) and glycerine-water solution (6 mPa.s), were tested at 21 °C. They concluded that liquid viscosity affects slightly the slug-annular boundary but had an effect on the bubble-slug boundary only for the larger diameter tube, see Table 2.6.

Furukawa and Fukano (2001) investigated the effect of liquid viscosity on the flow patterns of upward air-liquid flow in a 19.2 mm vertical tube. Three different liquids, including water and 53% and 72% glycerol-water solutions with the viscosities of 5.7 and 14.7 times that of water and little change on the density and the surface tension, were employed. Figure 2.29 shows the photographs of the three fluids under the same flow velocities (u_{gs}=0.2m/s, u_{ls}=0.3m/s). This clearly demonstrates the effect of viscosity on the flow patterns, i.e. small bubbles coalescence is easy to occur in the case of larger liquid viscosity. Similarly liquid viscosity has a great impact on the transition boundaries of slug-churn and churn-annular. For example, with a decrease of liquid viscosity, the slug-churn and churn-annular boundaries move towards lower u_{gs}, see Table 2.6 and Figure 2.30.

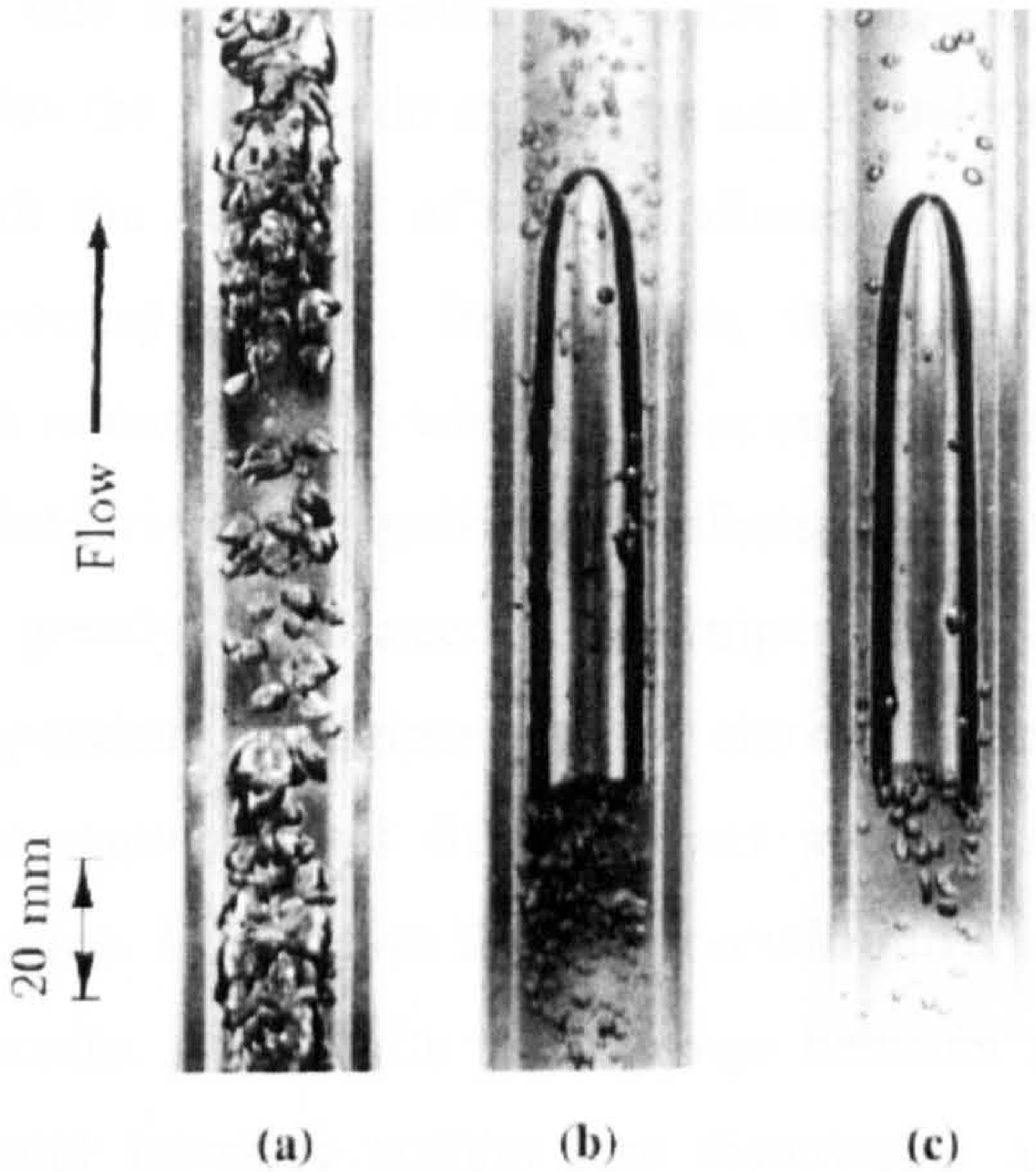

Figure 2.29 The flow patterns in three different fluids at the same conditions (u_{gs}=0.2m/s, u_{ls}=0.3m/s), Furukawa and Fukano (2001).
(a) bubble-slug, water (b) slug, 53% glycerol (b) slug, 72% glycerol

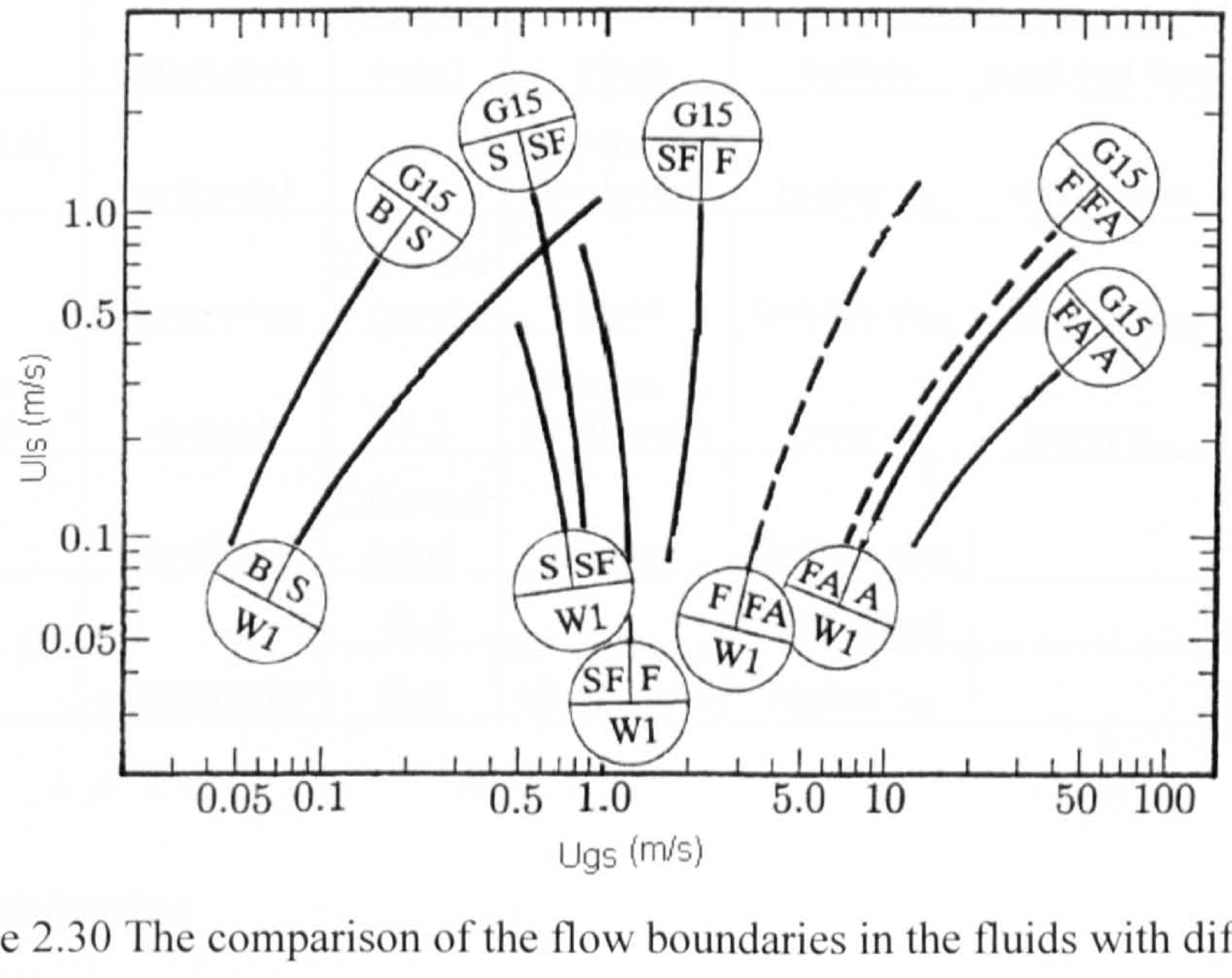

Figure 2.30 The comparison of the flow boundaries in the fluids with different viscosities, Furukawa and Fukano (2001).
(W1 – water, G15 - 72% glycerol, B – bubble, S – slug, SF – slug/churn, FA – churn/annular, A – annular)

Table 2.6 demonstrates conflicting information among the past reports. For instance, Furukawa and Fukano (2001) and Bousman et al. (1996) gave different results on the dependence of change of bubble-slug boundary on viscosity. Therefore, further work is necessary to explore this area. According to force analysis in Section 2.3.1, fluid viscosity, which decides the magnitude of friction and turbulent force, could become a dominating factor with the decrease of channel dimension because the gravitational force is depressed correspondingly. In addition, the thickness of hydrodynamic boundary layer, which is comparable with micro or small channel, is also decided by viscosity. Therefore, fluid viscosity significantly affects flow field. Viscosity, especially liquid viscosity is greatly influenced by temperature. Other parameters are comparatively less dependent on temperature, as shown in Table 2.4. Therefore, the effect of viscosity on vapour-liquid flow patterns may be explored indirectly by changing fluid temperature. It is known that friction will grow as the dominating force with increases in viscosity. This limits the slippage between gas and liquid phases. Therefore, the gas-liquid interface suffers less disturbance and the turbulent flow patterns such as churn flow may hardly appear in high viscosity fluids.

Table 2.6 The shift direction of flow pattern boundaries with reducing liquid viscosity.

Researcher	Orientation	Diameter (mm)	Fluid	To dispersed bubble	Intermittent – stratified flow	To annular
Weisman et al. (1979)	horizontal	51	air-water vs. air-glycerol	higher u_{ls}	little effect	lower u_{gs}
Researcher	Orientation	Diameter (mm)	Fluid	Bubble-slug	Slug-churn	To annular
Furukawa and Fukano (2001)	vertical	19.2	air-water vs. air-glycerol	lower u_{ls}	lower u_{gs}	lower u_{gs}
Researcher	Condition	Diameter (mm)	Method	Bubble-slug		Slug-annular
Bousman et al. (1996)	microgravity	12.7	air-water vs. air-glycerin	little effect		little effect
		25.4		higher u_{ls}		little effect

(4) Surface tension

Theoretically, surface tension minimizes the interfacial area of bubbles. It tends to keep bubbles retaining their circular shape and also to keep the liquid holdup to retard the transition from intermittent flow to annular flow (Yang and Shieh 2001). However, the study of surface tension on flow patterns was hardly carried out in normal size tubes because the size of bubbles tends to be larger in the absence of the confinement of tube wall and the effect of surface tension can be neglected when compared with other forces such as gravity, as shown in Figure 2.25 and the equations in Section 2.3.1. Therefore, in earlier studies the effect of surface tension is mostly indirectly demonstrated through a reduction in tube diameter, and rarely directly by changing surface tension itself. One of exceptions was that Bousman et al. (1996) who investigated its effect in 12.7 mm and 25.4 mm tubes in microgravity conditions. They mixed a small quantity of Zonyl FSP into water, which can reduce air-water surface tension from 72 mN/m to 21 mN/m without significantly affecting other physical properties. The results of experiments indicated that reducing surface tension resulted in a shift in the bubble-slug transition to lower u_{ls} at the same u_{gs}, i.e. higher void fraction. It had no significant effect on the slug-annular transition, see Table 2.7. The researchers explained that the reduced surface tension in the air-water/Zonyl FSP could reduce the probability of coalescence when bubbles contacted each other thus shift the bubble-slug boundary to lower liquid superficial velocity. Their result, that surface tension has little effect on the slug-annular transition boundary, was reported to be in agreement with Reinarts (1993) but in contrast with the analysis of Yang and Shieh (2001). The above phenomenon specified could be explained by the fact that the inertial force which relates closely to fluid velocity grows as a dominant force at the region of slug to annular flow. By comparison, the surface tension is not strong enough to influence the flow regime significantly at high liquid velocity. A similar experiment was also carried out by Weisman et al. (1979) using air-water (σ=68 N/m) vs. air-Aliguat 221 solution (σ=38 N/m) in a horizontal tube. They reported that surface tension had significant effect on the wavy to stratified boundary. Their experimental results are summarized in Table 2.7.

Table 2.7 The shift direction of flow pattern boundaries with reducing surface tension.

Researcher	Orientation	Diameter (mm)	Method	To dispersed bubble	To annular	Intermittent - stratified	Wavy - stratified
Weisman et al. (1979)	horizontal	11.5, 25, 51	air-water vs air-aliguat 221	little effect	little effect	little effect	higher u_{gs}
Researcher	Condition	Diameter (mm)	Method	Bubble-slug	Slug-annular		
Bousman et al. (1996)	microgravity	12.7, 25.4	air-water vs air-zonyl	Lower u_{ls}	little effect		

Bang et al. (2004) studied photographically vertical subcooled boiling flow using R134a in 4 x 5 mm rectangular channel. They reported that the higher pressure made the size of bubbles smaller, whilst higher subcooling caused faster bubble collapse, as shown in Figures 2.31 and 2.32. It indicates that dispersed bubble flow is easily formed in higher pressure, i.e. bubbly to dispersed bubble transition boundary may shift toward lower liquid superficial velocity. The transition mechanism of dispersed bubble to bubbly may relate to surface tension more rather than to the effect of vapour density as mentioned in the above section.

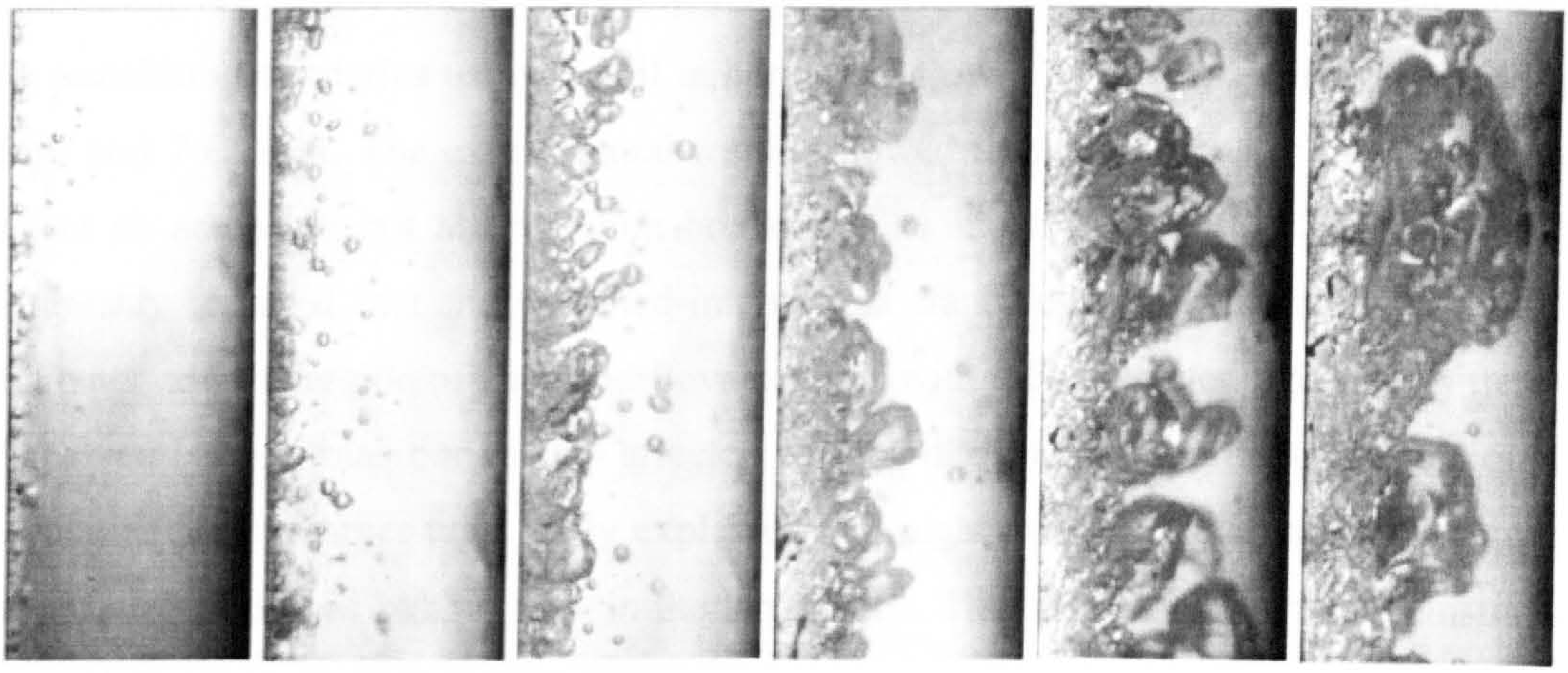

Figure 2.31 Effect of flow parameters on boiling phenomena at 7.0 bar, 2000 kg/m^{2}s, 137 to 955 kW/m^2, -13.8% to -11.5% quality.

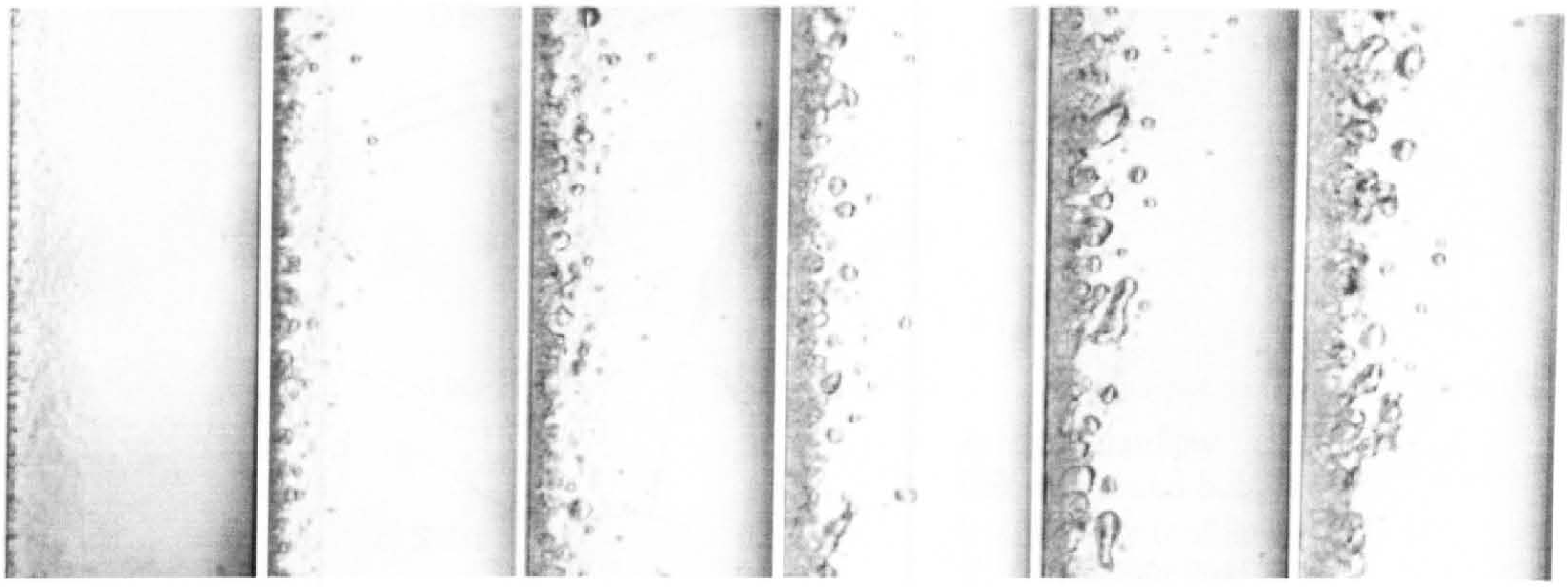

Figure 2.32 Effect of flow parameters on boiling phenomena at 14.5 bar, 2000 kg/m^{2}s, 478 to 873 kW/m^2, -24.6% to -23.3% quality.

(5) Channel dimension

One of main objectives in the present experiments is to elucidate the effect of channel dimension on flow patterns. Many previous studies proved that surface tension becomes an important parameter with the decrease of tube dimension (Oya 1971, Barnea et al. 1983, Fukano and Kariyasaki 1993, Hibiki 1993, Lin et al. 1998, Coleman and Garimella 1999). In small tubes, bubble size and shape can no longer be ignored and surface tension is a vital factor on deciding bubble size and shape.

Some transition boundaries are very sensitive to tube diameter and others are not. Kokal and Stranislav (1989) studied experimentally the effect of tube diameter (normal range) on transition boundaries using air-oil in horizontal flow. The tube diameters were 25.8, 51.2 and 76.3 mm. The experimental results showed that tube diameter had a distinct effect on some but not all transition boundaries as shown in Figure 2.33. Kokal and Stranislav reported that the stratified-intermittent transition is quite sensitive to tube diameter and the region of stratified flow expands with tube diameter. The intermittent-dispersed bubble transition is also affected by tube diameter and shifts to higher liquid velocities for the larger tube. They explained that higher turbulence level was required to produce dispersed bubble flow in the larger tube. The intermittent-annular transition was relatively insensitive to tube size.

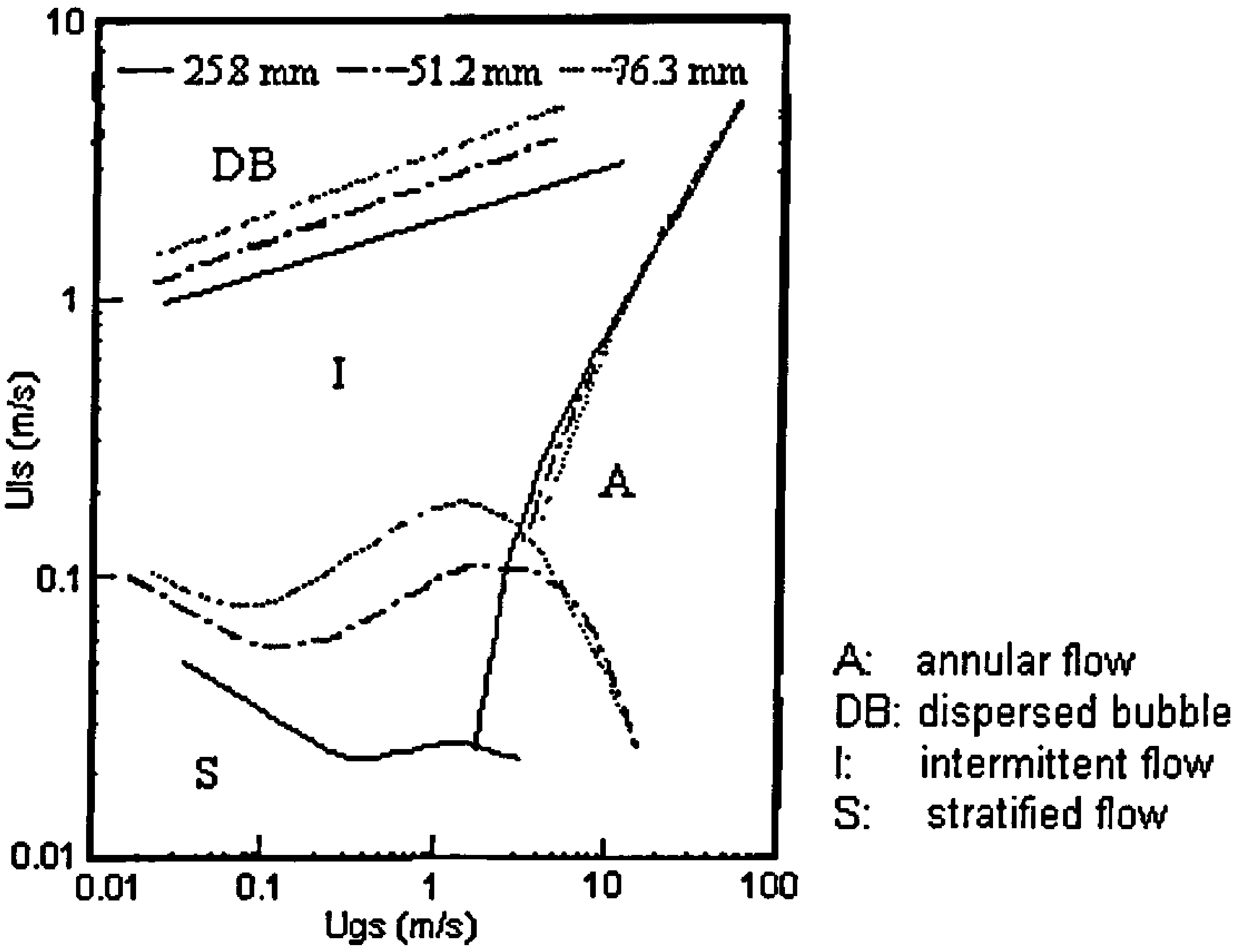

Figure 2.33 The effect of tube diameter on flow patterns for air-oil flow Kokal and Stranislav (1989).

Some studies focused on small tubes. Sue and Griffith (1964) studied two-phase flow in 1.0 and 1.6 mm horizontal tubes. They observed that the characteristics of slug flow in the horizontal small tube were quite similar to that in the vertical small tube. Therefore they concluded that surface tension dominates over gravity in small tubes. Oya (1971) investigated experimentally the developing flow patterns of air-water, air-gasoline two-phase flow in vertical upward flow. The tube diameters were 2, 3 and 6 mm and the experimental conditions were 10-40 °C and atmospheric pressure. He found that the flow patterns were much affected by tube dimension and surface tension. For example, fish-scale type slug flow appeared at higher u_{gs} in the smaller tubes. Some special flow patterns (granular-lumpy bubble and fish-scale type slug) were first reported in his experiments, see Figure 2.10.

Barnea et al. (1983) compared the experimental data of 4-12 mm vertical and horizontal tubes with the physical models for normal tubes (Taitel and Dukler 1976, Taitel et al. 1980), see Figures 2.18 and 2.19. They reported satisfactory comparisons except for the stratified-intermittent transition boundary in horizontal flow. They argued that the deviation between theory and experiment is attributed to the increasing effect of surface tension in small tubes, which makes surface tension, not Kevin-Hemholtz type instability, responsible for the transition from stratified flow to intermittent flow. However, the results disagreed with Damianides and Westwater (1988) and Fukano and Kariyasaki (1993) who considered that flow characteristics transform completely when tube diameter is less than 5 mm in air-water flow, see Figures 2.20 and 2.21.

Damianides and Westwater (1988) presented a set of typical air-water flow maps for horizontal small tubes. The experimental conditions were 10-25 °C and atmospheric pressure. They studied flow patterns in five tubes ranging from 1 to 5 mm and concluded that surface tension becomes a very important factor in the transition mechanisms when the tube diameter is less than 5 mm. Some common tendencies can be discovered by comparing the five flow maps, see Figure 2.34. The intermittent-dispersed bubble transition boundary moves to the region of lower liquid flow rate with decreasing tube diameter whilst the intermittent-annular transition boundary moves to regions of higher gas flow rate with decreasing tube diameter. The stratified flow region gradually shrinks with decreasing tube diameter until it vanishes completely in the 1 mm tube.

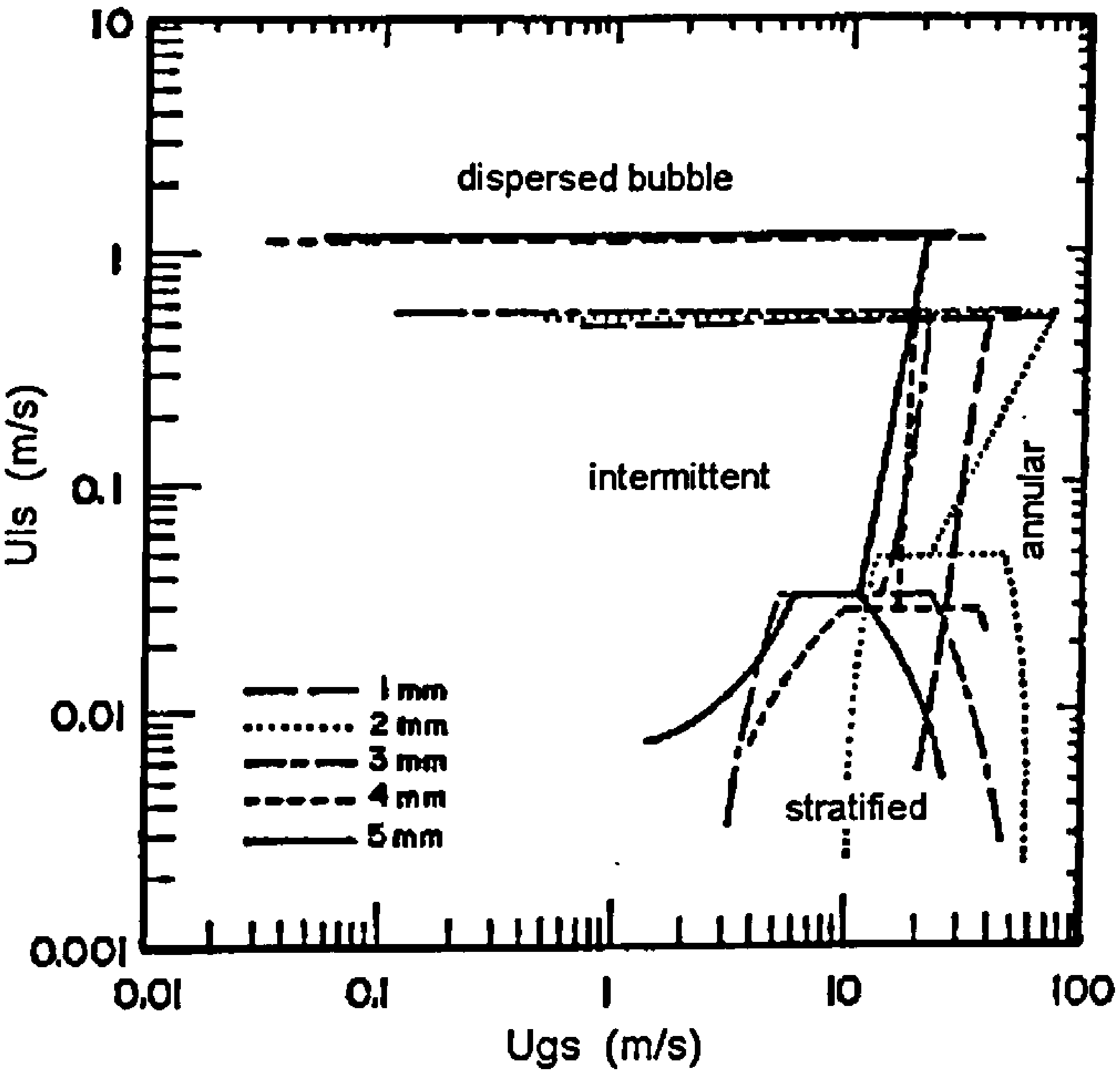

Figure 2.34 Comparison of air-water flow maps for small tubes, atmospheric conditions, Damianides and Westwater (1988).

Fukano and Kariyasaki (1993) studied air-water flow patterns and pressure loss in 1, 2.4, 4.9, 9 and 26 mm tubes at atmospheric conditions. The flow orientations were vertical upward, horizontal and vertical downward. In their experiments, the flow patterns were not severely affected by flow direction as a result of the strong effects of surface tension. Fukano and Kariyasaki presented some common characteristics of flow patterns in small tubes. For example, flow patterns are more axisymmetric, stratified flow is hardly observed, and small bubbles usually do not exist in liquid slugs and liquid films. They also concluded that the critical tube size at which surface tension surpasses gravity was between 5 and 9 mm for air-water mixture. The above conclusion is consisted with the criteria proposed by Kew and Cornwell (1997) or Hatori and Bretherton (cited from Wadekar 2002), as seen in Table 2.1.

Mishima and Hibiki (1996) observed air-water flow patterns, measured void fraction, slug bubble rise velocity and pressure loss in 1 to 4 mm vertical tubes at atmospheric conditions. Their results are shown in Figure 2.35 for the 2.05 and 4.08 mm tubes. They found that the transition boundaries were predicted well by the Mishima-Ishii's model (1984). The solid lines in Figure 2.35 present the prediction by the Mishima-Ishii's model. They also predicted void fraction and rise velocity by the revised drift flux model. The drift flux model indicated that gas velocity u_g can be calculated as a function of homogeneous velocity u_h and drift velocity u_d, i.e. $u_g = C_0 u_h + u_d$. Mishima and Hibiki considered the effect of tube diameter and corrected the distribution parameter C_0 as $C_0 = 1.2 + 0.51e^{-0.691D}$. Although the researchers drew the boundaries in the flow maps, examination of the maps indicates that the conclusion need to be validated further because of the limited number of data, see the map for the 2.05 mm tube. Therefore, the actual effect of diameter on flow patterns is not clear in these experiments.

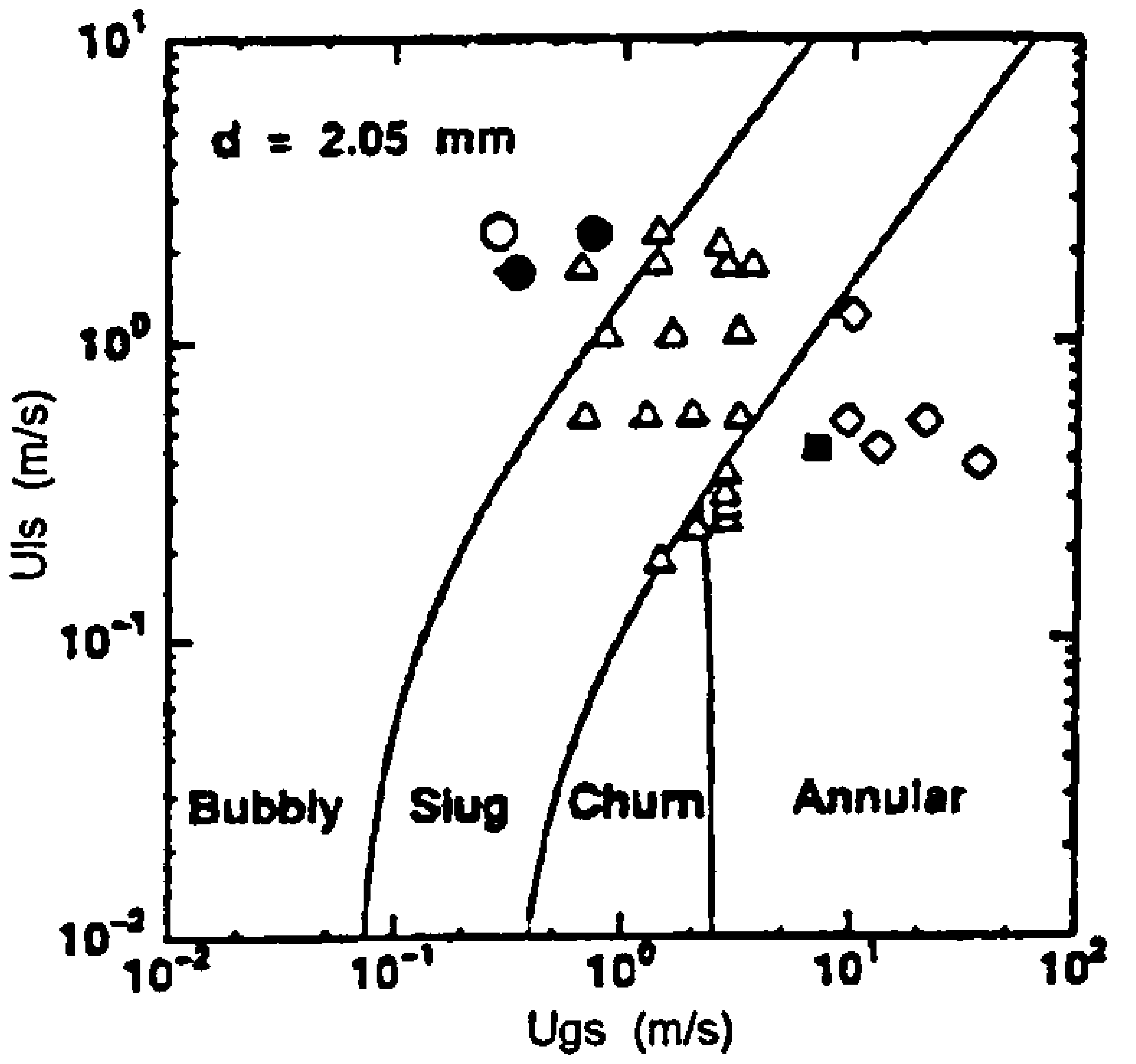

Figure 2.35 Air-water flow pattern maps at atmospheric conditions Mishima and Hibiki (1996).

Lin et al. (1998) studied air-water flow patterns in 0.5-4.0 mm vertical tubes at the conditions of 20 °C and 1 bar. The observation methods included direct observation, high-speed camera and differential pressure transducer. They observed that the transition boundaries of slug-churn and churn-annular shift toward the region of higher gas flow rate when the tube diameter decreases from 2.36 to 1.0 mm. However, the developed dimensionless flow maps were not in agreement with Barnea et al. (1983). For example, the transition of slug to churn and churn to annular occurred at lower u_{gs} in the experiments of Lin et al. compared with the flow map for the bigger tube (4.0 mm diameter) from Barnea et al. (1983), see Figures 2.36-2.38.

— — — — data for the 4.0 mm tube from Barnea et al. (1983)
———— data for the 1.0 or 2.36 mm tubes from Lin et al. (1998)
◇ confined bubble □ bubble ✕ annular
○ churn △ slug
◆ transition between confined bubble and slug
● transition between churn and annular

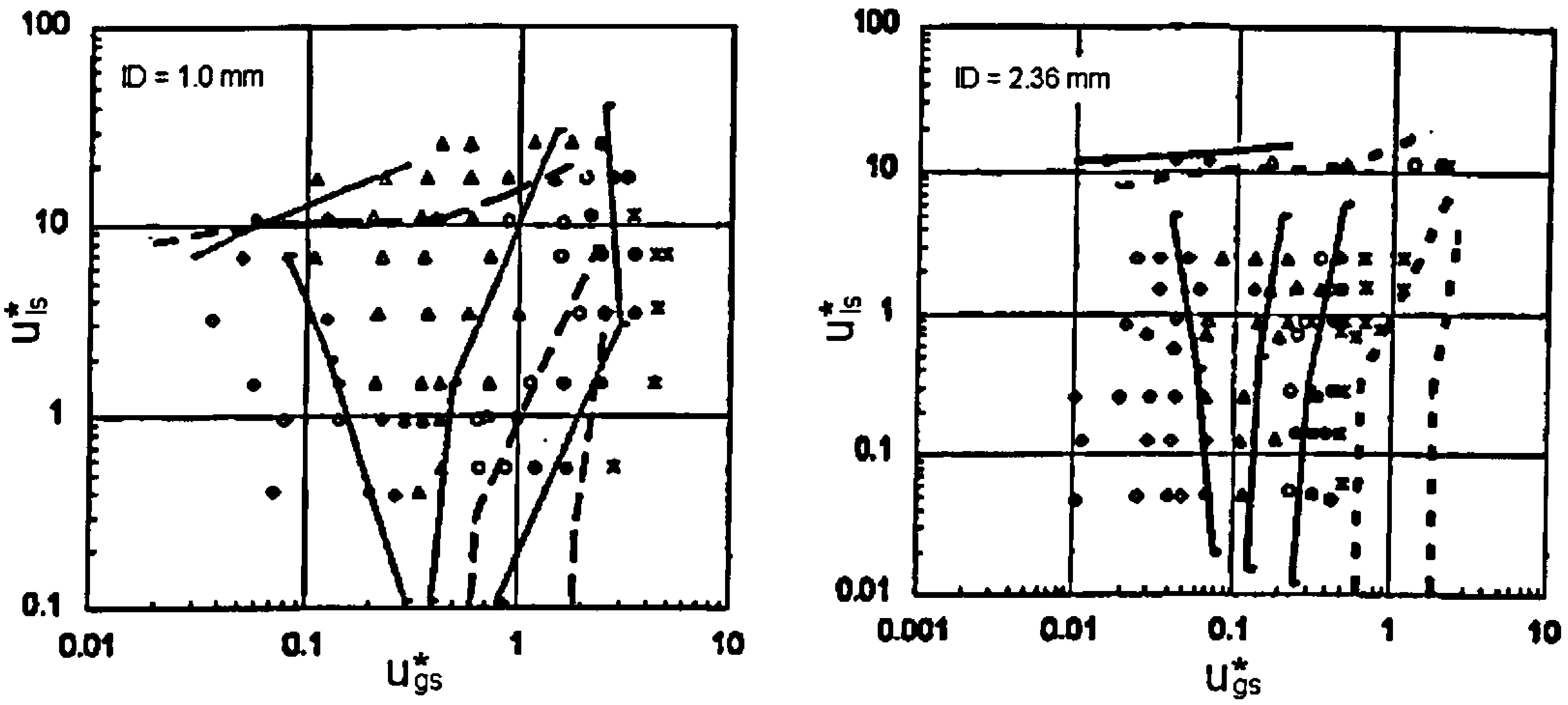

Figure 2.36 Air-water vertical flow maps using dimensionless superficial velocities, 20 °C 1 bar, Lin et al. (1998).

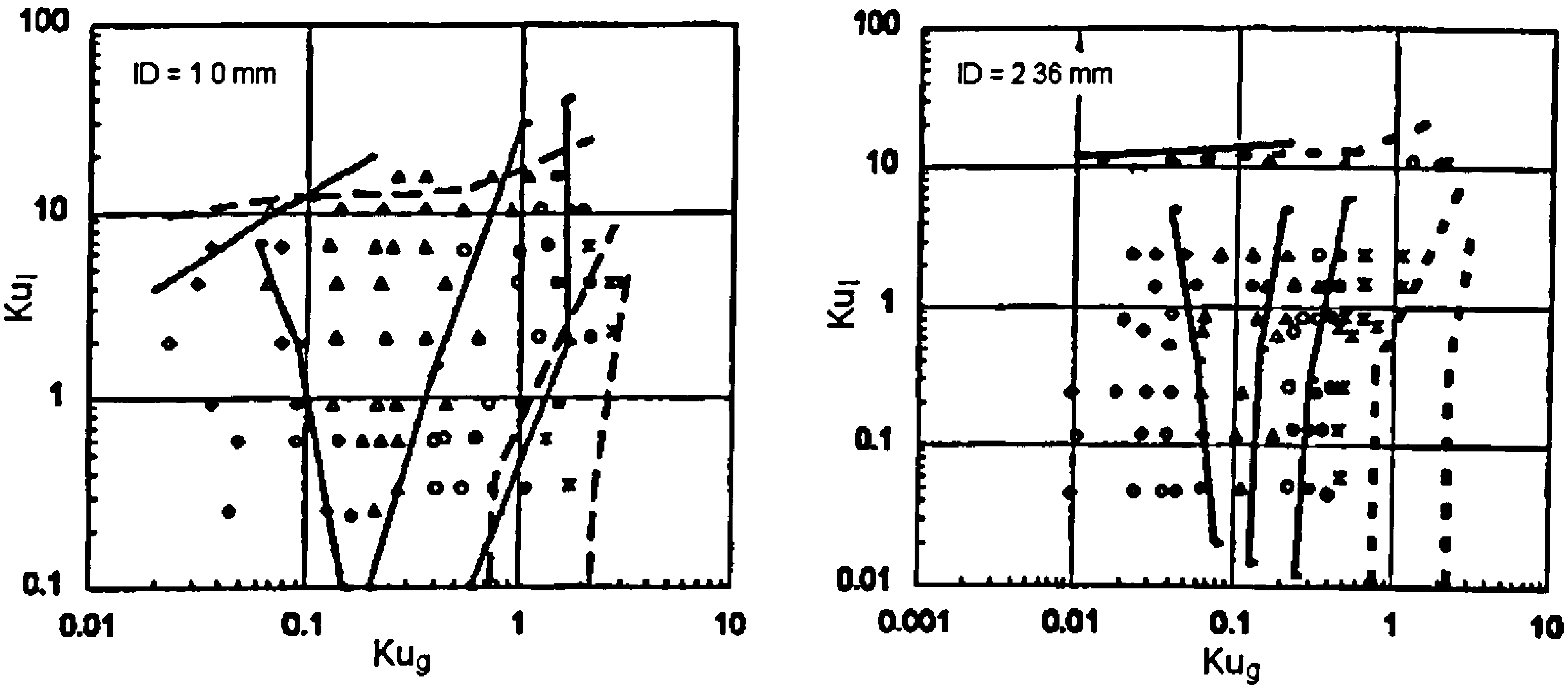

Figure 2.37 Air-water vertical flow maps using dimensionless Kutdelaze numbers, 20 °C 1 bar, Lin et al. (1998).

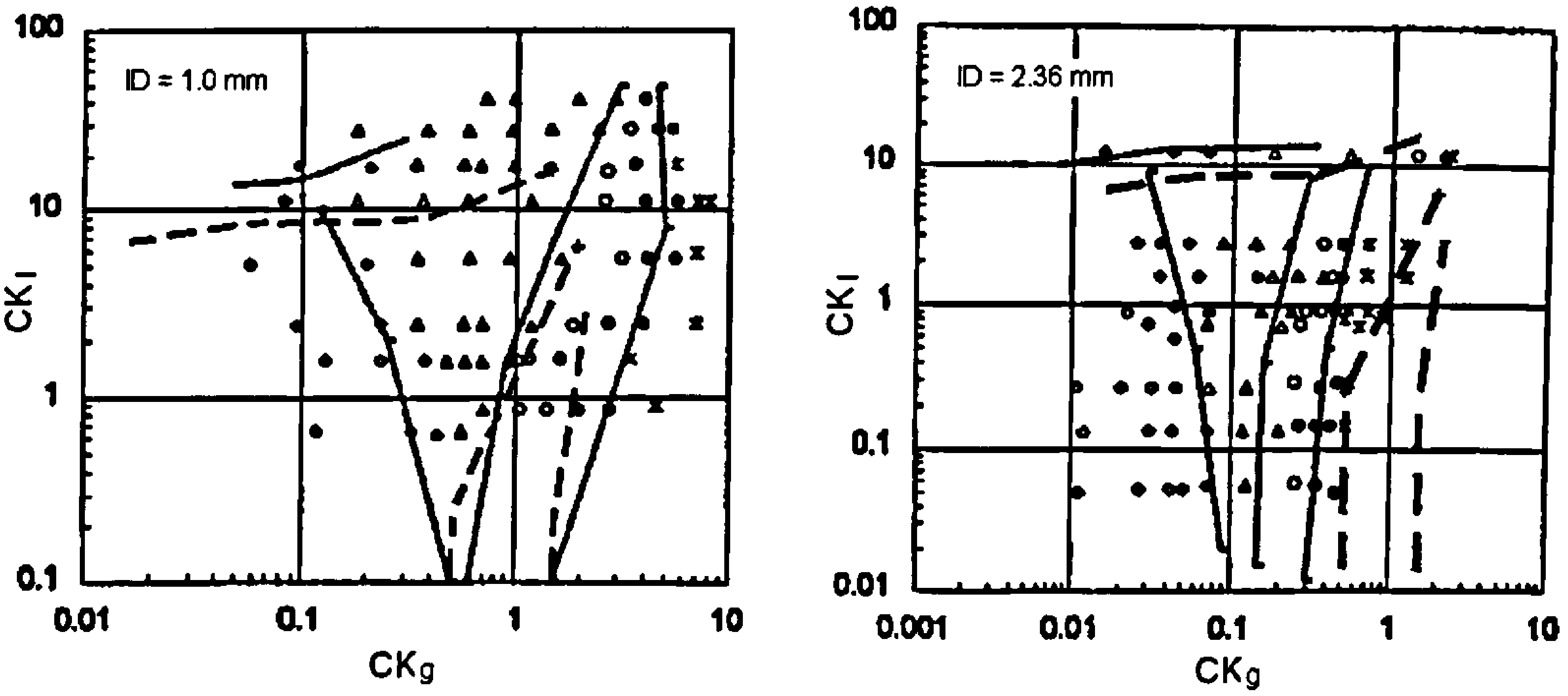

Figure 2.38 Air-water vertical flow maps using dimensionless parameter CK, 20 °C 1 bar, Lin et al. (1998).

Zietlow and Pedersen (1998) sketched several flow maps for refrigerant R134a in parabolic cross section channels with a hydraulic diameter of 0.74 mm. The detailed configuration of flow patterns was hard to observe because of the limitation of the observation method (fibre probe), which may have caused some confusion and these data are marked as "assumed" in Figure 2.39. Therefore further study is needed to complete the flow maps for R134a two-phase flow in small channels. Figure 2.39 shows the comparison of the experimental data of Zietlow and Pedersen (1998) with that from Damianides and Westwater (1988). As seen in the figure, a number of flow patterns that were observed by Zietlow and Pedersen fall in the region of slug flow in the Damianides and Westwater's map.

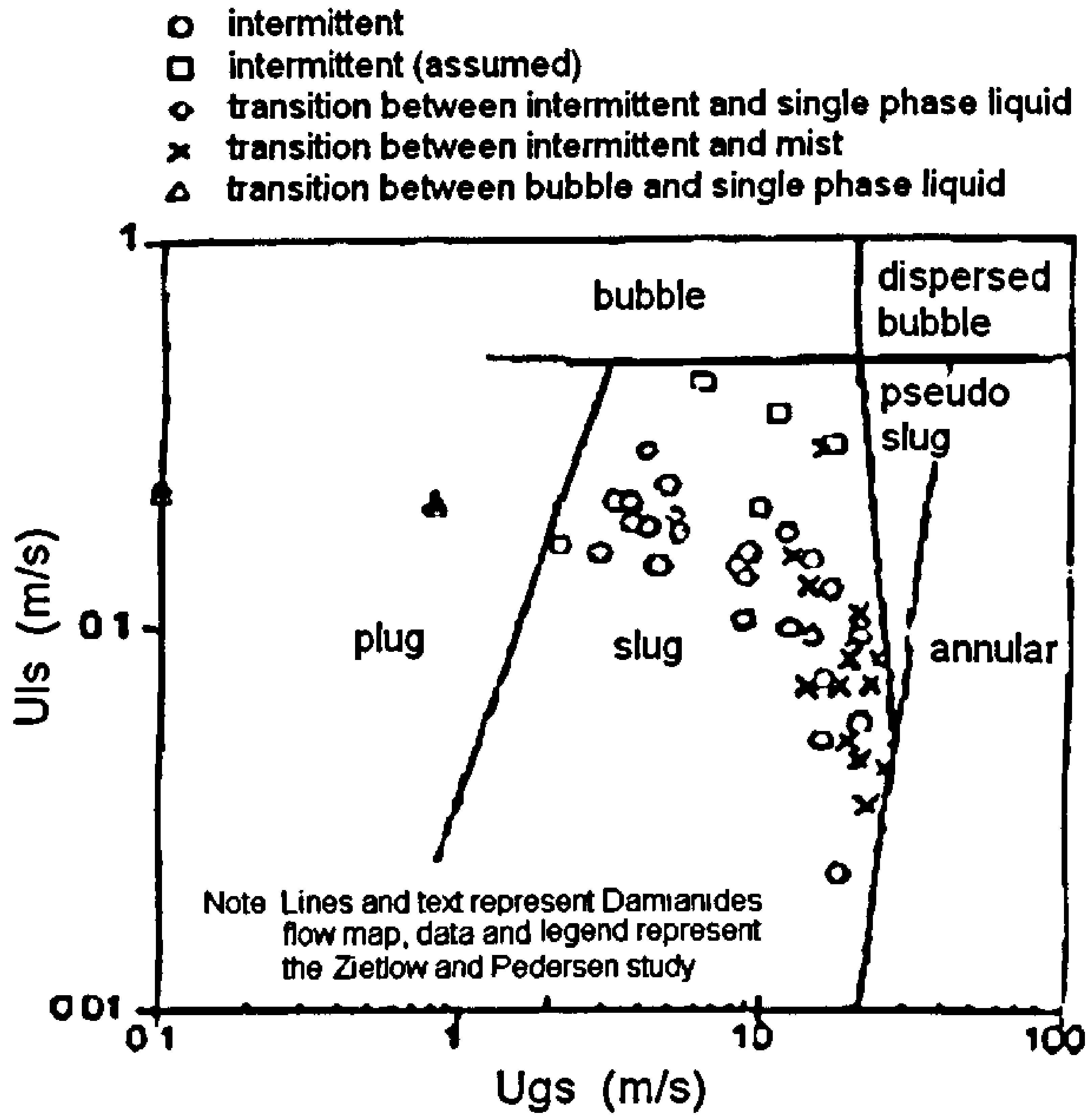

Figure 2.39 The comparison of Zietlow and Pedersen's data for R134a two-phase flow with the Damianides and Westwater's map for air-water flow (1988) (solid lines).

The effect of tube diameter on transition boundaries was also investigated by Coleman and Garimella (1999). Air-water was used in horizontal round and rectangular tubes with 1.3 to 5.5 mm hydraulic diameters at atmospheric conditions. As seen in Figure 2.40, the results clearly show that the tube diameter has a significant effect on the transition boundaries. For example, the transition boundary of intermittent flow to bubble and dispersed flow shifts significantly as the tube diameter change from 5.50 mm to 1.30 mm. However, the tendency of the above boundary moved to higher u_{ls} with decreasing diameter, contradicts with the results of Damianides and Westwater

(1988) depicted in Figure 2.34. Damianides and Westwater (1988) showed that the transition of dispersed bubble to intermittent flow happened at the lower u_{ls} in the smaller diameter tubes.

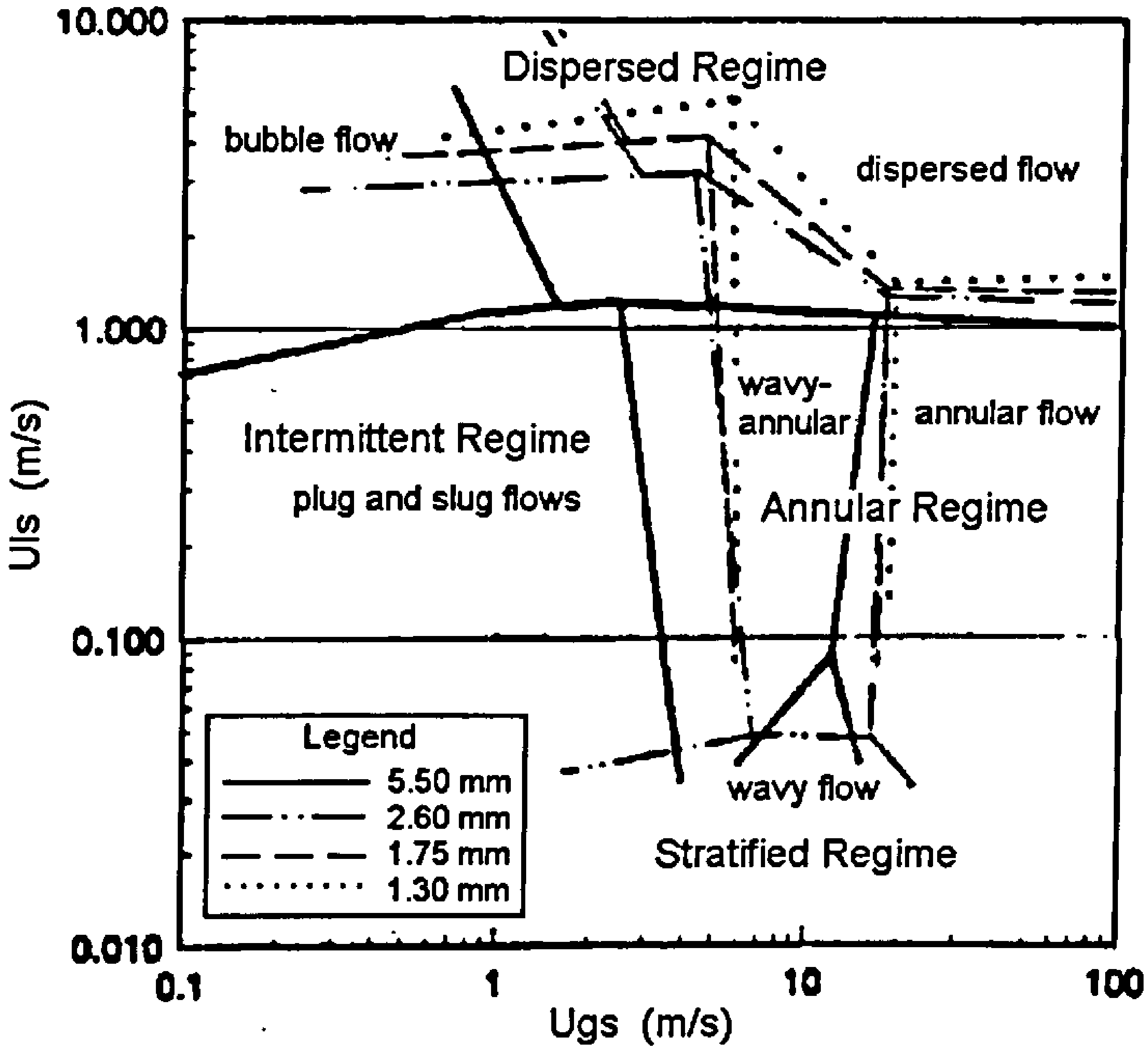

Figure 2.40 Comparison of air-water flow regimes for the 1.3 to 5.5 mm tubes at atmospheric conditions, Coleman and Garimella (1999).

Triplett et al. (1999) studied air-water flow regimes in 1.1 and 1.45 mm circular tubes as well as 1.09 and 1.49 mm hydraulic diameter semi-triangular conduits. Overall, the influence of surface tension on the flow patterns is significant but the flow maps were similar because of the limited change of the tube diameters. The author reported that the experimental data roughly agreed with the existing flow maps for small tubes (Damianides and Westwater 1988, Kukano and Kariyasaki 1993), see Figures 2.41 and 2.42. For example, the region of the annular flow in the flow map in Figures 2.41 from Triplett et al. (1999) is consisted with that from Damianides and Westwater (1988). The bubble-intermittent boundary sketched by Kukano and Kariyasaki (1993) shows excellent agreement with Triplett et al. (1999) as shown in Figure 2.42. They explained that the inconsistencies, such as bubbly-dispersed boundary in Figure 2.41 and intermittent-annular boundary in Figure 2.42, could be mainly attributed to the confusion on appropriate identification.

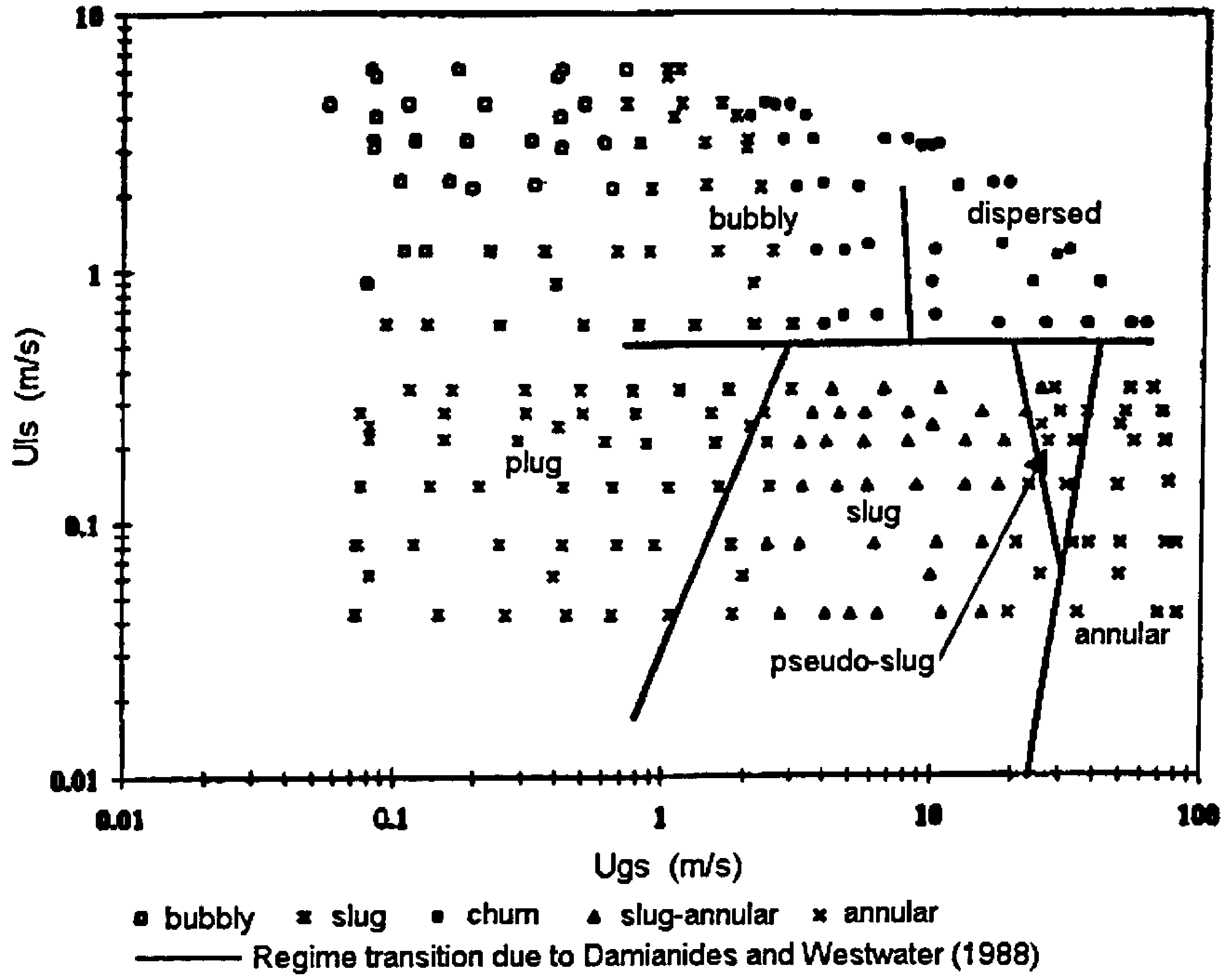

Figure 2.41 Comparison of air-water flow regimes for the 1.1 mm tube from Triplett et al. (1999) with the 1 mm experimental flow pattern transition limes from Damianides and Westwater (1988).

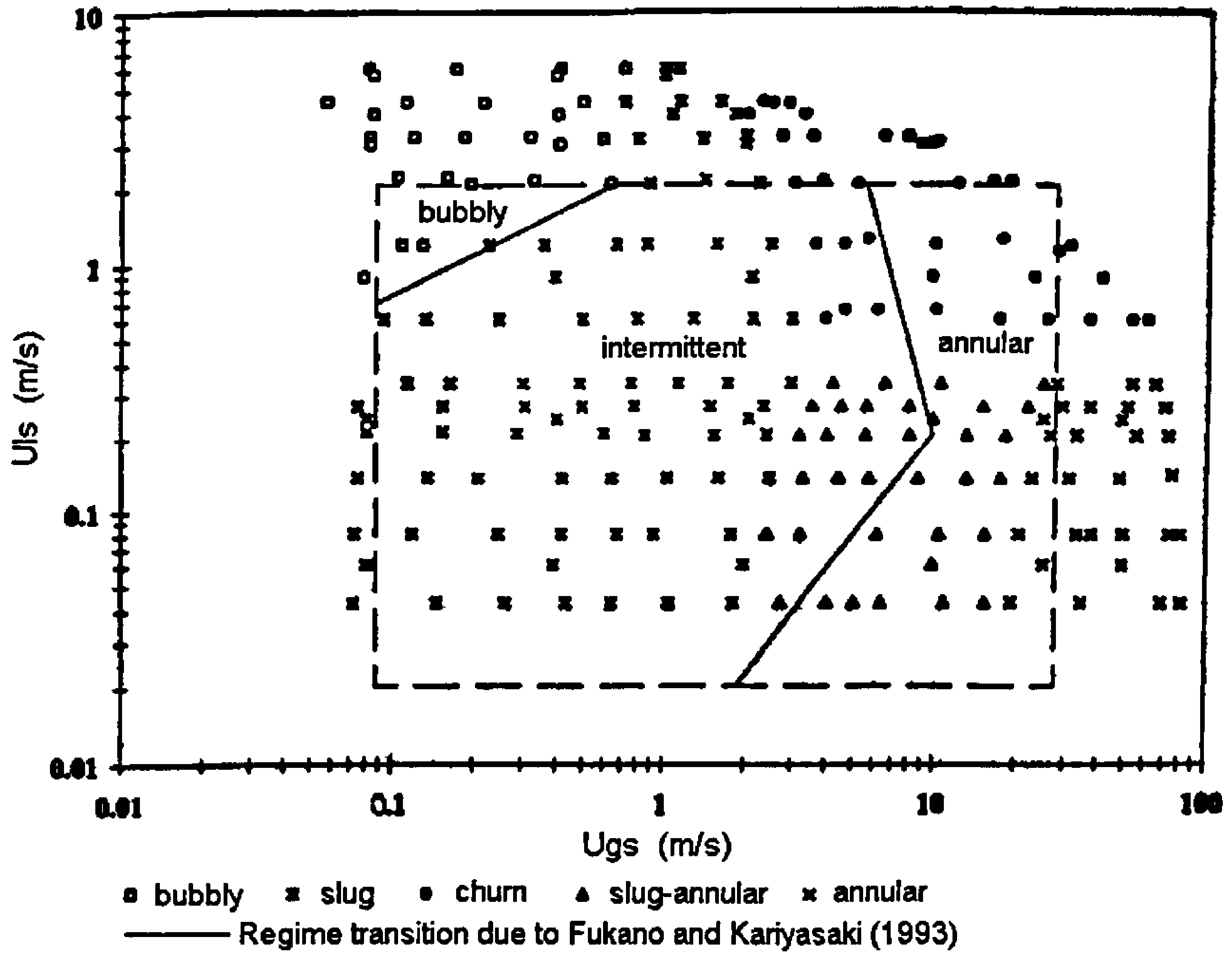

Figure 2.42 Comparison of air-water flow regimes for the 1.1 mm tube from Triplett et al. (1999) with the 1 mm experimental flow pattern transition limes from Fukano and Kariyasaki (1993).

Zhao and Bi (2001) investigated experimentally the characteristics of co-current upward air-water two-phase flow patterns in vertical equilateral triangular channels with hydraulic diameters of 2.886, 1.443 and 0.866 mm. The experimental results show that the typical flow patterns, such as dispersed bubble, slug, churn and annular flow, were observed in the 2.886 and 1.443 mm hydraulic diameter channels. However, dispersed bubble flow pattern was not found in the smallest channel (D_h=0.866 mm). Moreover, a new flow pattern - capillary bubbly flow was reported in the 0.866 mm channel. The flow maps, see Figure 2.43, presented the effect of channel dimension on flow patterns. For instance, dispersed bubbly flow shifted to a higher liquid superficial velocity whilst churn and annular flow occurred at higher gas superficial velocity as the channel dimension was reduced, see Figure 2.43 (a), (b) and (c). This tendency is in agreement with Lin et al. (1998), see Table 2.8. Their study also revealed that the existing models given by Taitel et al. (1980) and Mishima and Ishii (1984) could not predict flow patterns in small triangular channels.

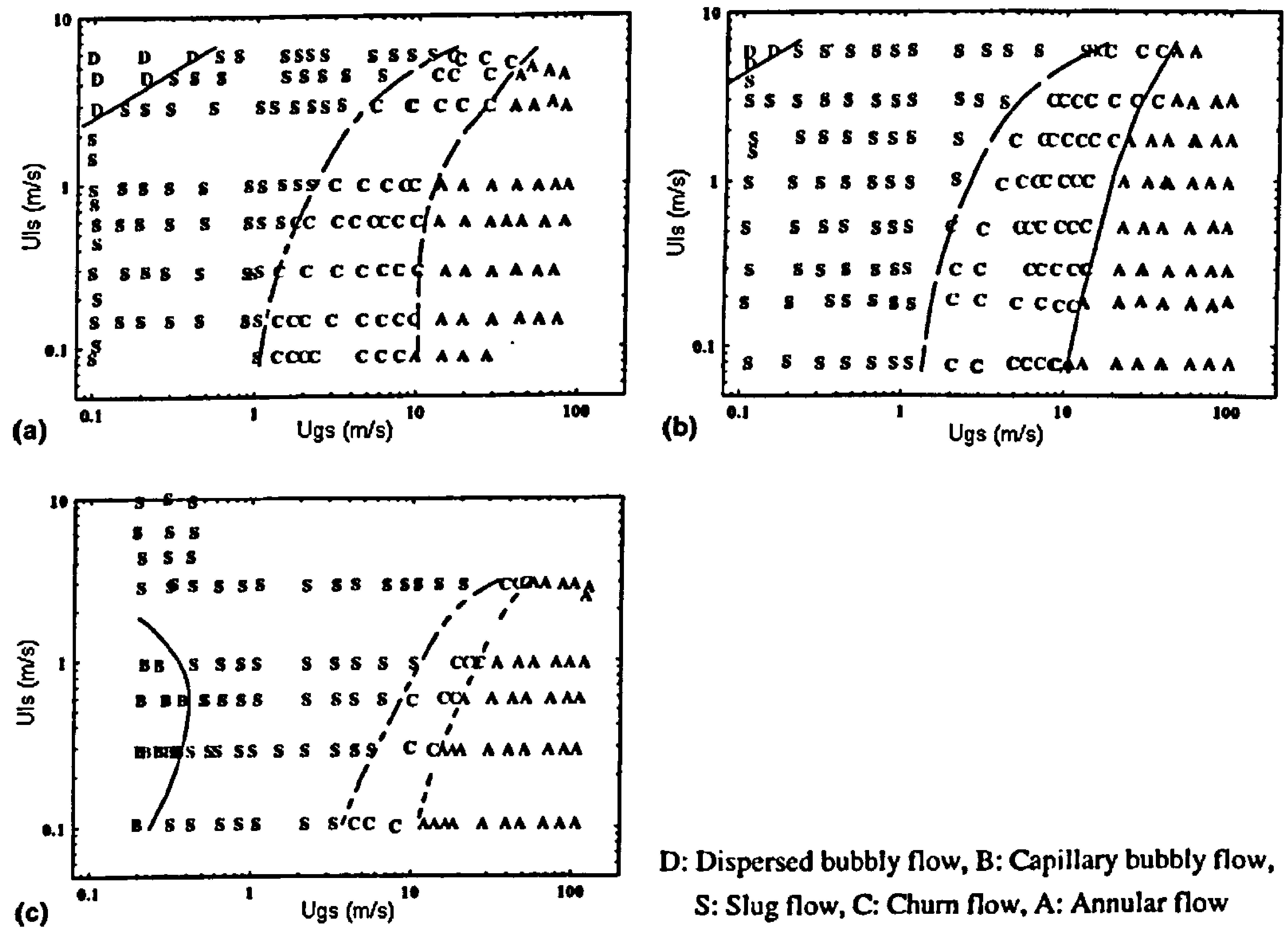

Figure 2.43 Flow regimes for upward flow in mini triangular channels, Zhao and Bi (2001). (a) side length is 5 mm (D_h = 2.886 mm); (b) side length is 2.5 mm (D_h = 1.443 mm); (c) side length is 1.5 mm (D_h = 0.866 mm)

Table 2.8 summarise the findings in the previous researches mentioned above. As seen in the table, the researchers gave same conclusions on the effect of tube diameter on some boundaries but on the other hand they could not agree with each other on other boundaries. For example, both Kokal and Stranislav (1989) and Damianides and Westwater (1988) reported that the boundary of intermittent to dispersed bubble moved toward lower u_{ls} with a decrease of tube diameter in horizontal flow, which is in total contradiction with the finding in the Coleman and Garimella's experiment (1999). Lin et al. (1998) and Zhao and Bi (2001) reported a same effect of tube diameter on the boundaries of slug to churn and churn to annular in vertical flow. However, the flow maps given by Lin et al. (1998) were in poor agreement with Barnea et al. (1983)

Table 2.8 The direction of boundaries shift with reducing channel dimensions.

Researcher	Orientation	Diameter (mm)	Fluid	Stratified-intermittent	Intermittent-dispersed bubble	Intermittent-annular	Stratified flow region
Kokal and Stranislav (1989)	horizontal	25.8, 51.2, 76.3	air-oil	lower u_{ls}	lower u_{ls}	little effect	
Damianides and Westwater (1988)	horizontal	1, 2, 3, 4, 5	air-water		lower u_{ls}	higher u_{gs}	smaller
Coleman and Garimella (1999)	horizontal	1.3, 1.75, 2.6, 5.5	air-water		higher u_{ls}	higher u_{gs}	smaller

Researcher	Orientation	Diameter (mm)	Fluid	Slug-churn	To dispersed bubble	To annular	
Lin et al.(1998)	vertical	0.5 - 4	air-water	higher u_{gs}		higher u_{gs}	
Zhao and Bi (2001)	vertical	0.87, 1.44, 2.89	air-water	higher u_{gs}	higher u_{ls}	higher u_{gs}	

***: Intermittent flow: include plug and slug flow for horizontal tube.**

The above studies involved the channels with the hydraulic diameters near or above 1 mm. Further changes in two-phase flow characteristics are expected for micro-channels as the diameters are in the order of hundreds micrometers. As we discussed in Section 2.1, the flow patterns observed in the previous experiments exhibited greatly different characteristics when the tube diameters were smaller than 100 to 250 μm in air-water flow, which indicates that the critical diameter to distinguish small and micro tubes is between 100 to 250 μm.

(6) Gravity and tube inclination

Gravity cannot be neglected in normal tubes but its effect diminishes in small tubes and might be neglected in micro channels as seen in Figure 2.25. Gravity makes flow patterns possess intensive directional characteristic. At low- or micro-gravity conditions, two-phase flows are essentially much simpler than those at normal gravity (Bousman et al. 1996 and Zhao et al. 2001). Therefore, the distinguishable flow patterns may be less and simpler in the absent of gravity.

Cheng and Lin (2001) experimentally observed air-dextran aqueous solution flow in 2-8 mm diameter tubes at horizontal, inclined and vertical orientations. The gravitational effect on gas bubbles is significant but is fading in smaller tubes under their experimental conditions (0.168-0.672 m/s liquid superficial velocity and 0.04-0.32 m/s gas superficial velocity). It indicates that gravity cannot be neglected entirely in bubble and slug flow for small tubes.

Flow orientation is not important in micro-gravity conditions and some studies showed that the flow maps under micro-gravity condition are similar with those in small tubes because surface tension, not gravity, dominates. For example, Nash et al. (1992) studied nitrogen-water two-phase flow regimes in a horizontal annular tube with 1.35 mm gap. They discovered that the flow maps were in agreement to those under micro-gravity conditions, see the boundaries of dispersed bubble and slug to annular flow in Figure 2.44. Again, the same conclusion was reached by Galbiati and Andreini (1994). Air-water flow in the 1 mm horizontal capillary tubes was tested in their experiments. The pressures in the test section were varied from 10 to 50 bar. Two flow regimes were substantially observed: slug and annular flow. The flow maps were in agreement with the data collected in a normal size tube at microgravity conditions by Dukler et al. (1988), which were carried out in microgravity "equivalent system" under normal earth conditions. Therefore, they concluded that two-phase flow in the 1 mm capillary tube could reasonably simulate the microgravity "equivalent system" under normal earth conditions.

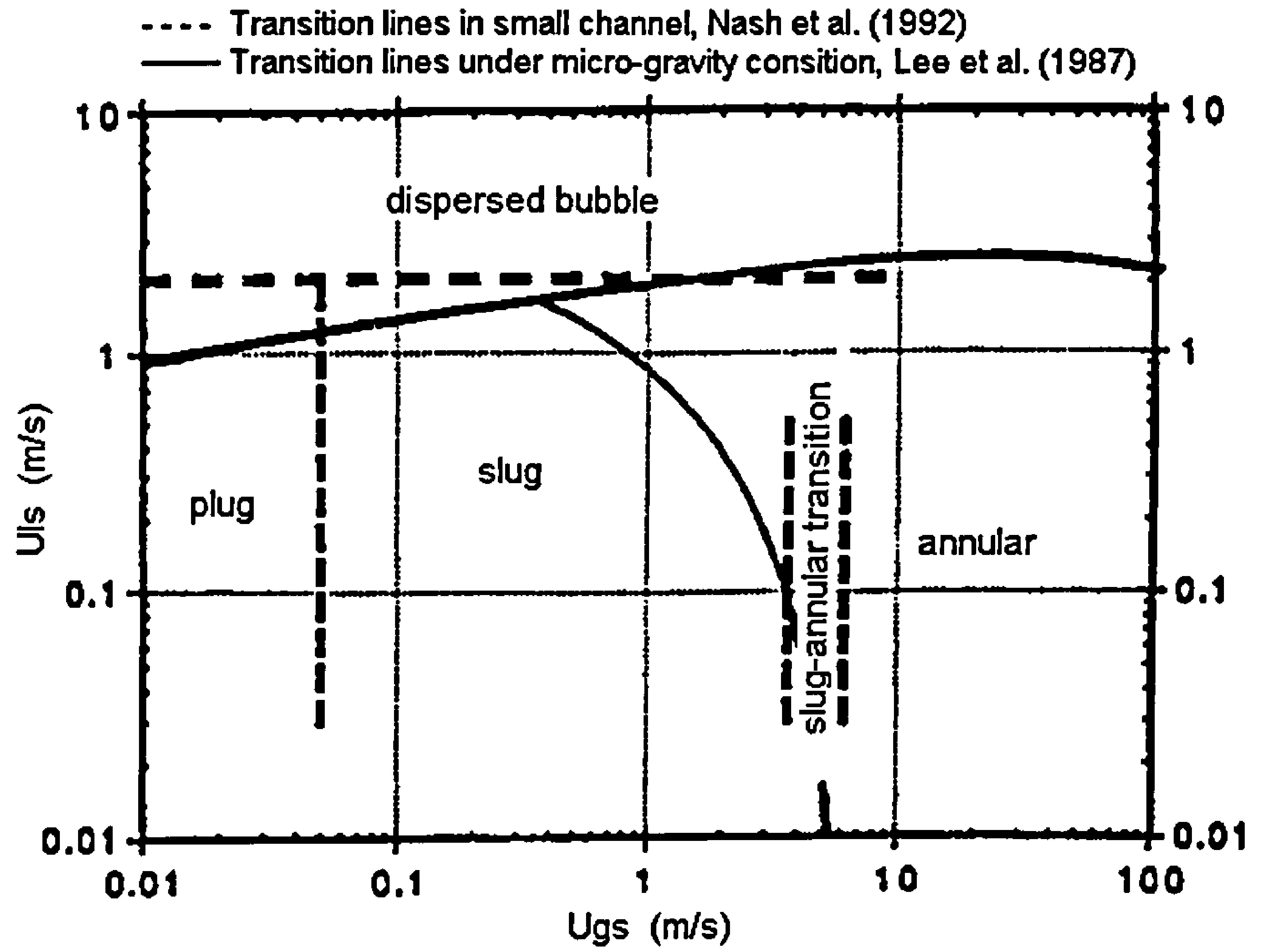

Figure 2.44 Comparison of nitrogen-water flow regime for 1.35 mm gap circle tube from Nash et al. (1992) with the microgravity flow map from Lee et al. (1987).

Bousman et al. (1996) studied flow patterns under microgravity in 12.7 and 25.4 mm diameter tubes. They observed only three flow patterns (bubble, slug and annular) in their experiments indicating that the types of flow patterns will be reduced when fewer forces act on two-phase flow, see Figure 2.4. Zhao et al. (2001) experimented in the microgravity environment of Mir Space Station (no more than 10^{-5} g). The working fluids were air-Carbogal and the tested tube was 10 mm diameter and 356 mm in length. The observed results were similar to those of Bousman et al. (1996) but they classified in more detail, namely dispersed bubble, bubble, slug, slug-annular and annular.

Two-phase flow transition models under micro-gravity conditions were developed by Zhao and Rezkallah (1993), Rezkallah (1996), Lowe and Rezkallah (1999) and summarised by Akbar et al. (2003). The models based on the Weber numbers, which consider that inertia and surface tension are the dominant forces in micro-gravity two-phase flow. They argued that the entire flow regime map could be divided into three zones, see Appendix B Table B.2. Zhao and Rezkallah (1993) suggested $We_{gs} = 1$ as the upper bound for surface tension-dominated zone, and $We_{gs} = 20$ as the lower bound for the inertia-dominated zone. Rezkallah (1996) and Lowe and Rezkallah (1999) modified the above criteria by the transition line of $We_{gs} \propto We_{ls}^{0.25}$. Similar to the microgravity case, surface tension and inertial forces are likely to determine, or at least play significant roles on the flow regimes in small tubes. Therefore, a similar transition mechanism should be expected and requires further investigation.

A great number of studies were carried out to discover the influence of inclination angle on flow patterns in normal tubes. Based on these works, some physical models were proposed and eventually developed to a "Unified Model" which can predict reasonably flow patterns in normal size tubes at any angle of inclination (Taitel 1990). In the case of micro-gravity or small tubes, the effect of gravity is reduced so that the flow regimes are less affected by inclination angle. Following from that, annular flow and dispersed bubble flow where shear stress, inertia force or turbulent force dominate over gravity do not depend on angle of inclination even in normal tubes (Taitel 1990, Kokal and Stainislav 1989).

(7) Roughness

To the best of the author's knowledge, none of the past experiments included a study on the effect of tube roughness on flow patterns. Tube roughness may intensify the turbulence of two-phase flow within the flow boundary layer. According to the boundary layer theory, the hydrodynamics mechanisms inside the boundary layer are totally different from that at the outside of the boundary layer. The significance of roughness and its effect on flow patterns needs to be investigated further as it is expected to rise in importance with diminishing diameter.

(8) Heat flux

The great majority of the studies on flow patterns were performed in adiabatic processes. However, boiling flow is a frequent phenomenon in industry. Frankum et al. (1997) reviewed the existing experiment data in flow boiling and compared them with the adiabatic flow maps and the adiabatic correlations. The conclusion indicated that the existing adiabatic flow pattern maps and the correlations agreed well with those obtained for flow boiling.

However, following a theoretical analysis, the flow regimes in boiling flow must be different from those in adiabatic flow. Heat flux influences both the distribution of void fraction and the liquid viscosity. This is certainly the conclusion of an earlier study by Dukler and Taitel (1991) which contradicts the work of Frankum et al. (1997). Dukler and Taitel experimentally verified the effect of heat flux on flow patterns. As seen in Figure 2.45, intermittent flow shrinks to a small area compared with adiabatic flow. One reasonable explanation is that flow boiling is a developing two-phase flow and the separated bubbles need time to coalesce.

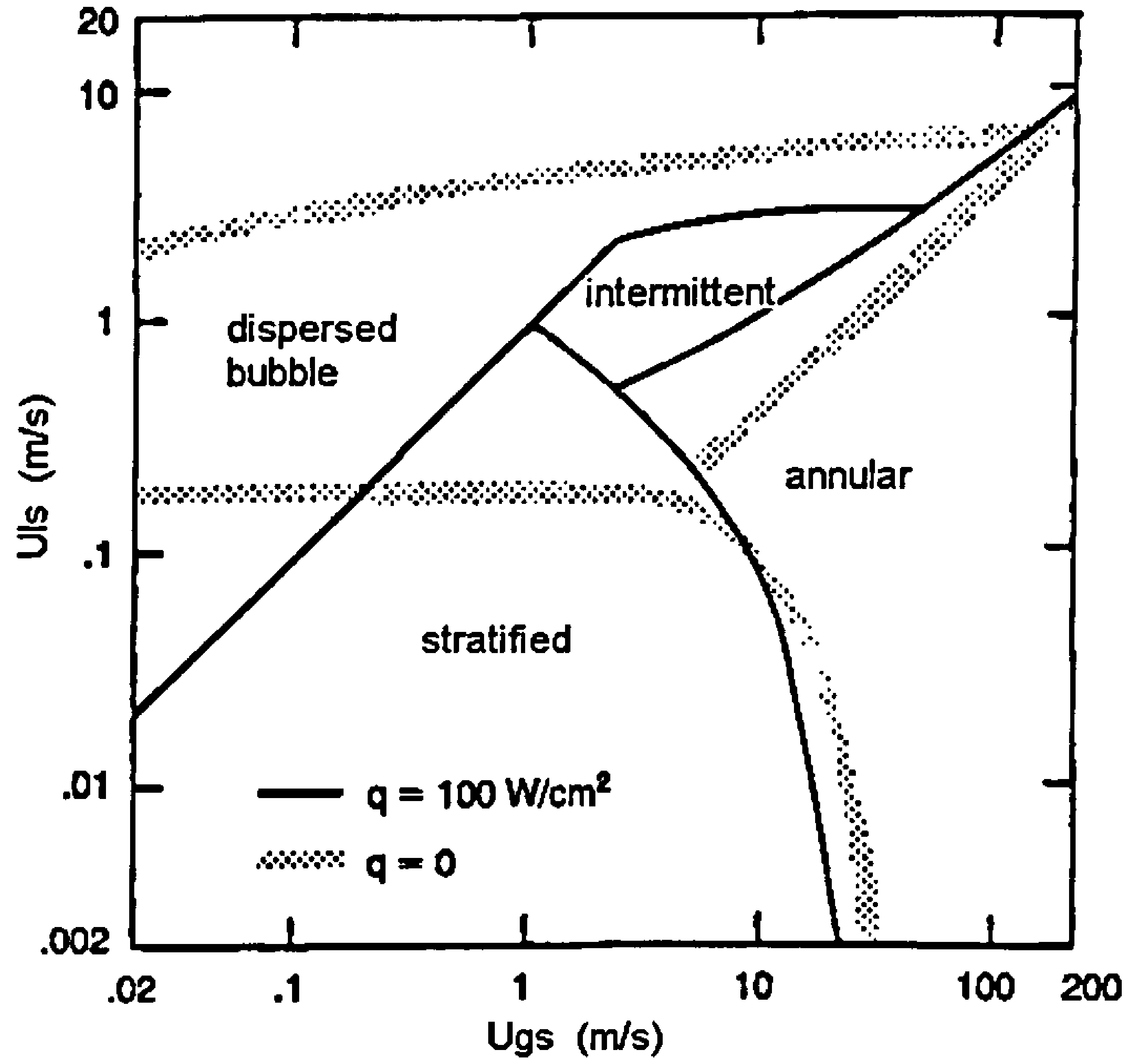

Figure 2.45 Flow pattern map for flow boiling of water in the 25 mm diameter horizontal tube at atmospheric pressure, Duckler and Taitel (1991).

(9) Enthalpy of vaporization

Cole and Rohsenow proposed a modified correlation give below for the bubble size at departure from a heating surface in 1969 (cited from Tong and Tang, 1997). The correlation appears to work quite well for a large variety of ordinary liquids in saturated pool boiling. The calculated bubble diameter at departure (d) relates closely to density, surface tension, specific heat, saturated temperature and latent heat, as seen in Equation 2.9 reference. Comparing to other parameters, the enthalpy of vaporization may be the most important parameter. For example, the enthalpy of vaporization of water is as much as 15 times of that of R134a at 14 bar so that the calculated bubble diameter for R134a is much smaller than that in water, see the comparison in Table 2.9.

$$\left[\frac{g(\rho_l - \rho_g)d^2}{g_c \sigma}\right]^{1/2} = C'_d \left(\frac{\rho_l c_p T_{sat}}{\rho_g h_{fg}}\right)^{5/4} \qquad (2.9)$$

$C'_d = 0.00015$ (for water)

$= 0.000465$ (for other liquids)

Table 2.9 Bubble size at departure in pool boiling.

Fluid	Unit	R134a			Water
Pressure	bar	6	10	14	1
Constant		0.00047	0.00047	0.00047	0.00015
Liquid density	kg/m^3	1218.17	1148.32	1090.19	958.4
Vapour density	kg/m^3	29.04	49.06	70.7	0.5903
Specific heat at constant pressure	J/kg.K	1412	1500	1594	4215
Saturated Temperate	K	294.71	312.55	325.6	336.78
Latent heat of evaporation	J/kg	181076	163985	149210	2257900
Surface tension	N/m	0.0084	0.0062	0.0046	0.0589
Bubble diameter	mm	0.37	0.21	0.14	6.79

The actual bubble size departing from a heated wall in flow boiling should be smaller than that in pool boiling. From Table 2.9, we can find the bubble size in saturated water is in the order of millimetres and is much bigger than that in R134a. Therefore, in small tubes the flow boiling regimes of R134a may develop from dispersed bubble flow whilst flow boiling in water starts from bubbly or slug flow.

2.3.3 Effect of other factors on flow patterns

The following factors may also affect flow patterns in small tubes although their effect may be smaller than those mentioned above.

(1) Channel shape

Damianides and Westwater (1988) compared the flow map in a 2 mm round tube with that in a 1.74 mm hydraulic diameter labyrinth type compact heat exchanger. They concluded that the flow patterns in the compact heat exchanger could not be predicted from the knowledge based on the straight round tubes. Another experiment was performed later by Wölk et al. (2000) for upwards vertical air-water flow through one circular and four different non-circular channels (with rectangular, rhombic and equilateral triangular cross-sections) with an equivalent hydraulic diameter of 6 mm. Three flow patterns were identified and named as dispersed bubble, slug and churn flow. Overall, the flow regimes were similar but the cross-section geometry did directly influence the transition boundaries, see Figure 2.46. As seen in the figure, the slug flow in the equilateral triangular tube occupies a smaller area in the flow map than that in the circular tube. The main reason for the shifting on the transition boundaries results from the turbulent secondary flow that occurs in non-circular channels and from the steeper radial distribution of the phase and/or velocities, according to the explanation by Wölk et al.

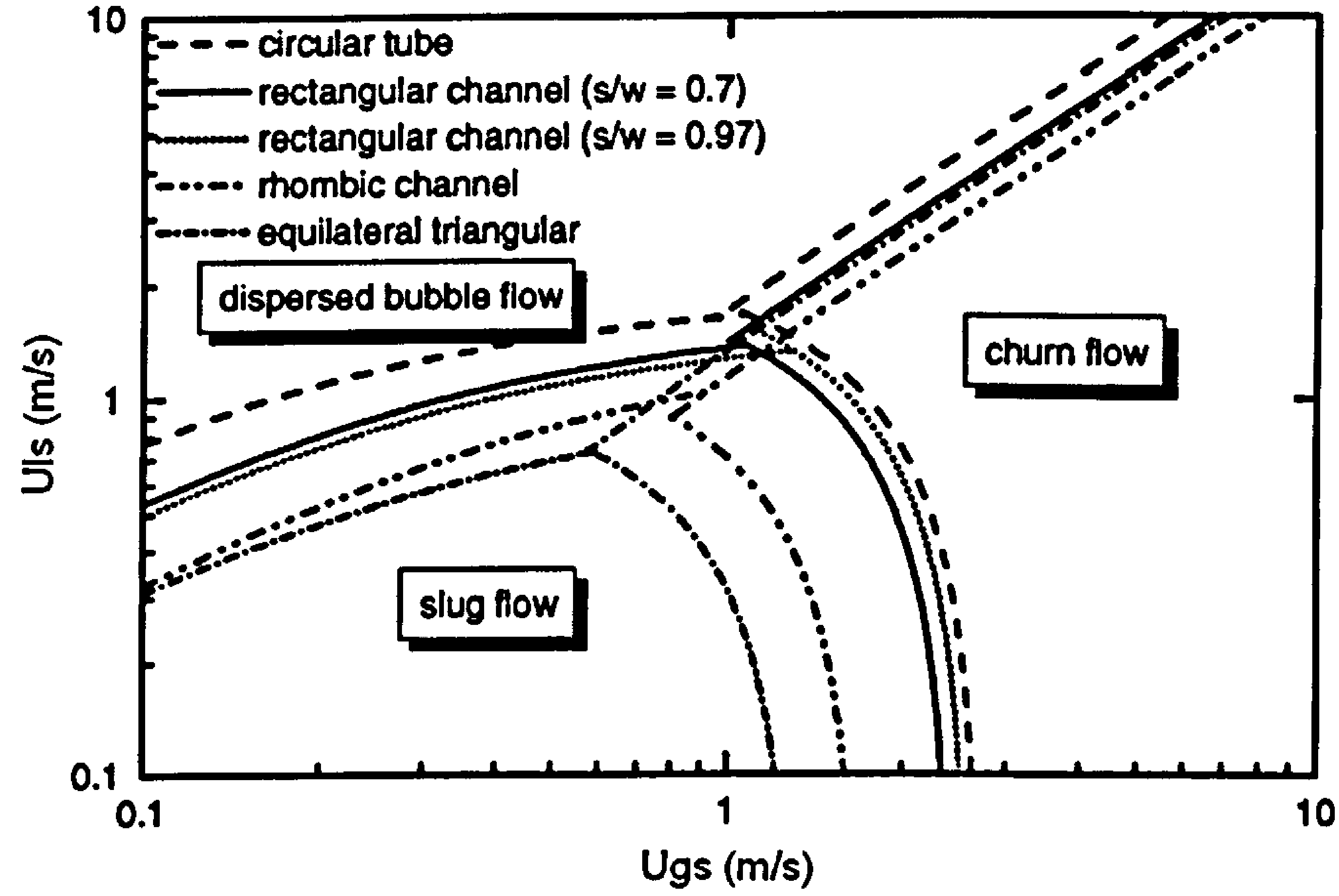

Figure 2.46 Comparison of the flow pattern transition boundaries with the different cross-sections, Wölk et al. (2000).

However, Coleman and Garimella (1999) also investigated the effect of channel shape using a 5.5 mm round tube and a 5.36 mm hydraulic diameter rectangular channel with an aspect ratio of 0.72. The experiment was carried out in horizontal air-water flow at atmospheric conditions and the two flow maps were similar. Triplett et al. (1999) reached a similar conclusion by comparing the experimental results of the 1.10 and 1.45 mm round tubes with those of the 1.09 and 1.49 mm semi-triangular channels.

There is still very limited work in this area to enable us to draw firm conclusions. The research so far indicates that when compared to circular passages straight conduit shape does not affect flow regimes significantly while complex channels such as labyrinth channel strongly affect them. Further work is necessary to reach final conclusions.

(2) Developed and developing flow

Oya (1971) experimentally investigated developing air-water and air-gasoline flow patterns in vertical 2, 3 and 6 mm tubes. He found that the flow patterns are hardly affected by the flow state. Barnea and Taitel (1993) established a model for liquid slug length. The model was based on bubble overtaking mechanism, i.e. bubbles behind short slugs travel faster than those behind long slugs. The process of overtaking is terminated once all slugs are long enough such that the velocity profile at the back of long slugs is fully developed and all bubbles flow at the same velocity. They reported that the required distance for fully developed flow is about 10-15 m in 50 mm tubes. No similar research has reported for small tubes yet. It can be expected that bubbles will grow continually before reaching fully developed state, and bubble flow in a developing stage may finally grow into slug flow in fully developed flow.

(3) Channel inlet conditions and bubble generation methods

Flow patterns are inevitably disturbed by channel inlet conditions and bubbling methods thus a long calming section is required to reduce this disturbance and expect to obtain a fully developed flow. Galbiati and Andreini (1992) studied experimentally the effect of inlet mixing method and calming section length on flow pattern transitions for vertical downward two-phase flow in 0.5, 1.1 and 2.0 mm tubes. The experimental results show that the inlet mixing method and the calming section length have a significant effect on the flow patterns in what they called capillary tubes. For instance, vertical downward stratified flow in small tubes with the internal diameter smaller than 3 mm, which was reported by Biswas and Greenfield (1985), was never observed in their experiments because of the fact that the mixing method was improved. Prasser et al. (2002) observed that the bubble size distributions were still strongly depended on the primary size after a calming section equal to 60 times the diameter at lower superficial gas velocity, e.g. 0.125 m/s in their experiments. At higher superficial gas velocities (e.g. at $u_{gs} = 0.5$ m/s) the bubble distribution became independent on the gas injection device. However, an adequate calming section is not always used in experiments due, for example, to space limitations. A calming section with 50 to 100 times diameter length usually is installed before the test section in flow pattern experiments.

2.4 The relationship between heat transfer and flow patterns

Heat transfer is closely related to flow patterns because gas and liquid possess different heat transfer characteristics. The control of flow regimes within a desired range is an effective way in engineering applications to improve heat transfer rates, avoid heat transfer deterioration and protect heat exchangers and plants.

At present, the flow boiling mechanisms in small tubes are not clarified since only a few papers related heat transfer with flow patterns. The existing researches are mostly restricted in qualitative analysis without the material correlations to link heat transfer with flow patterns (Kandlikar, 2002). For example, Laborie et al. (1999) experimentally proved that the length of gas slugs increased with decreasing tube dimension and the frequency of gas slugs decreased with decreasing tube dimension, which indicates that smaller tube may dry out intermittently in slug flow. Yu et al. (2002) studied experimentally the effect of flow patterns on heat transfer. They reported that the heat transfer coefficient generally keeps changing as the flow patterns changed along an evaporator tube. Agostini and Bontemps (2004) concluded that the bubble confinement led to higher heat transfer coefficients while dry-out happened easily in their flow boiling experiments in 11 parallel rectangular mini-channels (3.28 x 1.47 mm) with R134a. Frankum et al. (1997) described qualitatively the heat transfer mechanisms by observing the detailed configurations of flow patterns. They discussed the fact that the liquid film around vapour slug possesses better convective heat transfer characteristics than that of liquid slug in plug flow. This makes the wall temperature located in the area of vapour slug lower than that of liquid slug. Therefore, nucleate boiling is the main heat transfer mode in liquid slug region and convective heat transfer dominates in vapour slug region. Extending the above postulate, convective heating likely dominates in annular flow and nucleate boiling likely dominates in bubble flow. They coexist in intermittent flow and the heat transfer characteristics strongly relate to void fraction.

2.5 Summary

Numerous parameters, not well defined or vague concepts, subjectivity and the limitation of experimental techniques are vital factors that caused discrepancies in the results among different investigators. The flow maps sketched by different researchers may be dissimilar even though they use similar tubes under similar conditions. For instance, the vertical upward flow maps by Oya (1971), Barnea et al. (1983), Fukano and Kariyasaki (1993), and Mishima and Hibiki (1996), the horizontal flow maps by Barnea et al. (1983), Damianides and Westwater (1988), Fukano and Kariyasaki (1993), Coleman and Garimella (1999), and Triplett et al. (1999) are not in good agreement.

Some researchers thought that the existing models or empirical maps for normal size tubes could predict flow patterns in small tubes except for a few transition boundaries. For example, Mishima and Hibiki (1996) sketched air-water flow maps for 1 to 4 mm vertical tubes in their experiments and found that the transition boundaries were predicted well by Mishima-Ishii's model (1984). On the contrary, most researchers agreed that two-phase flow patterns in small tubes could not be properly predicted by the existing correlations developed for normal size tubes. In addition to the above disagreement, contradictory conclusions were also reported on the effect of conduit dimension. For horizontal flow, Damianides and Westwater (1988) discovered the intermittent-dispersed bubble transition boundary shifts towards the lower liquid flow rate region with decreasing tube diameter. However, this is completely contrary to the conclusion of Coleman and Garimella (1999). For vertical flow, both Lin et al. (1998) and Zhao and Bi (2001) found that the transition boundaries of slug-churn and churn-annular move to higher gas superficial velocity with decreasing tube size in their experiments. Mishima and Ishii (1984) obtained the same result by theoretical analysis. However, Oya (1971) argued that the flow maps sketched using superficial velocity coordinates are scarcely affected by tube dimension for both vertical and horizontal flow.

One of the distinctive characteristics of two-phase flow in small tubes is that flow patterns are less affected by channel orientation due to the fact that the relative effect of gravity is reduced. However, researchers still process their experimental data using horizontal or vertical flow maps separately that show notable orientation characteristics.

It seems that researchers followed the traditional classifying methods used in normal size tubes. Another possible reason is that the tubes examined were not small enough to neglect gravity completely even when they were recognized or reported as small tubes. Based on force analysis, annular and dispersed bubble flow in small tubes should be independent of inclination angle where gravity is a weaker force compared with other forces like shear stress, inertia force and turbulent force. Therefore, the transition boundaries in horizontal or vertical flow should be similar or at least the effect of tube diameter on them should be the same. However, the existing experimental results from different laboratories showed conflicting conclusions. For example, Damianides and Westwater (1988) found that the transition boundary of dispersed bubble in horizontal flow shifted towards lower liquid superficial velocity as the channel dimension decreases whilst Zhao and Bi (2001) found the tendency was toward higher superficial velocity for vertical air-water flow.

The effect of heat flux on flow patterns is another controversial point. Theoretically, the flow regimes in flow boiling must be different from those in adiabatic flow. However, in an experimental work, Frankum et al. (1997) concluded that the existing adiabatic flow pattern maps and correlations agree well with boiling flow. On the contrary, Dukler and Taitel (1991) obtained different conclusion in their experiments.

The effects of some parameters and conditions on flow patterns were rarely investigated in the previous studies. They are density, viscosity, surface tension, roughness, enthalpy of vaporization, and channel inlet conditions. Their influence on flow patterns were hardly analysed qualitatively or quantitatively or included in the correlations. Therefore, so far it has been difficult to obtain a general correlation and further work is needed.

In addition to above identifiable and objective factors, sometimes the discrepancies between different investigations can be attributed to subjectivity rather than any limitation in the experimental technique. Therefore, clear, universal definitions and classifications for flow patterns can effectively reduce subjectivity. Also the use of picture instead of description can be helpful. In the proposed experiments, a digital high-speed camera will be used to record the experimental process and the descriptions of flow patterns will be backed by photographs.

Chapter 3 Design of the Experimental Facility

The current status and literature available on two-phase flow patterns in small channels have been reviewed in Chapter 2. A number of arguments and disagreements among the different researchers are presented and require further experimental and theoretical investigations although some common characteristics exhibited in small tubes have been recognized by various researchers. The first stage of the project aims at collecting sufficient and accurate experimental data. In this chapter, the experimental facility design, construction, commissioning and modifications, the selection of the experimental parameters and the developed programs to control the rig, collect and analyse the experimental data are introduced and discussed.

3.1 Experiment system introduction

The proposed experiments focus on collecting adequate and accurate experimental data related to adiabatic flow patterns in small diameter tubes. An experimental facility was designed and constructed. The present author joined the research team when the facility was under construction for a parallel experimental study on flow boiling heat transfer, Huo (2005). The facility was designed to allow for heat transfer, pressure drop and flow visualization experiments. The contribution of the present candidate includes:

(1) Completion of the facility.
(2) Check and modify the previous design to fit the new requirements for flow pattern experiments.
(3) Complete the measurement and control system.
(4) Design and build four test sections for both flow pattern and heat transfer studies.
(5) Contribute to the calibration of the experimental instruments and the single-phase experiments used to validate the rig.
(6) Improve the purposely-developed program for experimental observation and data collection.
(7) Develop new program for data analysis.
(8) Contribute to the commissioning and testing.

The single-phase test results indicated that the facility could provide steady and precise experimental data which satisfies the current research requirements.

The investigation of two-phase flow patterns in small channels is difficult in both experimental and theoretical terms. The methodology used in such studies is very important for obtaining reasonable results. The existing facility meets the designed experimental range. It can be divided into three parts according to their functions, i.e. R134a experimental system, R22 cooling system and control and data acquisition system.

3.1.1 R134a experimental system

A schematic diagram and a photograph of the R134a experimental system are presented in Figures 3.1 and 3.2 respectively. The system is composed of (1) R134a tank; (2) R134a circulating pump; (3) filter dryer; (4) sight glass; (5) small Coriolis mass flow meter; (6) big Coriolis mass flow meter; (7) chiller; (8) preheater; test section which can be subdivided to (9) a calming section, (10) a heating section and (11) an observation section; (12) separator and (13) R134a condenser. The pipes and the test sections are actually insulated (not shown in Figure 3.2). Besides the above experimental facilities, a flow meter calibration pipe was installed beside the test section which is not shown in the diagram. The whole rig was designed to cover a wide range from subcooling to superheat with different mass flux and heat flux.

The tank consists of a cylinder; a sleeve heater; a small condenser tube, two liquid level glasses, a safety valve and a thermocouple (T6). The cylinder receives the returning fluid and contains most of the R134a in the system. The vapour volume in the tank also assists to calm pressure fluctuations in the system. The system pressure is controlled by the tank heater through a PID controller. The heater is positioned at the same level as the low level sight glass in order to protect the heater from burning out when the refrigerant in the tank drops below this level. The small condenser in the tank is activated when the system operates at low heating load, because the big condenser before the tank will cause system pressure instability in this case. The safety valve protects the tank from excessive pressure and the thermocouple T6 indicates superheated conditions in the tank. The signal from T6 switches off the heater automatically via the PID controller when the vapour temperature in the tank exceeds the preset safety value (55°C). A gear pump located after the tank circulates continuously the refrigerant to the filter dryer, the sight glass and the flow meters. The filter dryer removes water and particles in the refrigerant and the sight glass allows visual observation of the flow status. A thermocouple and a pressure transducer (T1, P1) are set before the flow meters to confirm single-phase liquid flow before the mass flow maters. The flow meters offer highly accurate measurement at low or high flow rates. Flow rate is subtly controlled by two precision metering valves located behind the meters (V4, V5). After the control valves, the refrigerant flows down to a tube-in-tube heat exchanger - chiller. R134a is cooled here by R22 from the cooling system to reach a certain degree of subcooling. A thermocouple and a pressure transducer (T2, P2) are installed to record the fluid state at the entry of the preheater. There are six heaters in the preheater which can be switch on or off individually. Also the power of the first heater can be adjusted through a variac. R134a is heated here to obtain the desired subcooled temperature or quality. In the flow pattern experiments, the PID controller automatically adjusts the fluid temperature at the inlet of the test sections to 3 K subcooling.

The current project uses four test sections with the inside diameters of 1.10, 2.01, 2.88 and 4.26 mm. Each test section is made up of three main parts: calming section, heating section and observation section. Single-phase flow is developed in the calming section. Then the liquid is heated to two-phase flow with the desired quality in the heating section. Finally the flow patterns were observed and recorded in the observation section, see Section 3.3 for more details. After the test section, the two-phase refrigerant is separated into liquid and vapour in the separator in order to reduce the pressure drop in the condenser. The liquid refrigerant flows directly into the tank and the vapour is first condensed. In the condenser, the latent heat of R134a is absorbed by the R22 cooling system. A 6 mm diameter pressure balance tube connects the inlet of the condenser and the tank to reduce the pressure fluctuation in the system. There is also a bypass loop after the pump to return extra refrigerant to the tank. The returned flow rate is adjusted by a needle valve (V14). Valve 14 combines with the two control valves in the main loop (V4, V5) to control the flow distribution in the system.

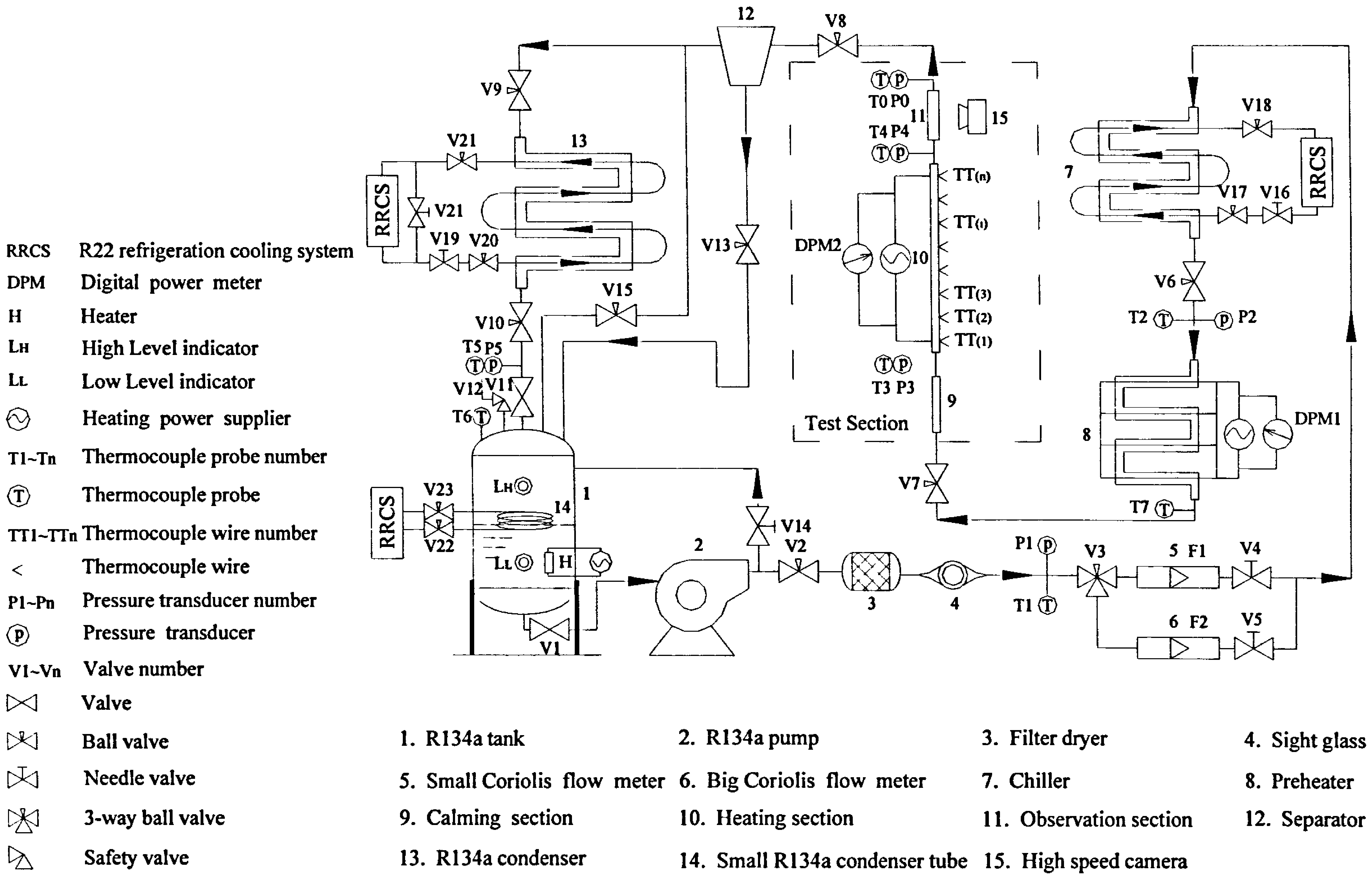

Figure 3.1 Schematic diagram of the flow patterns experimental system (Huo 2005).

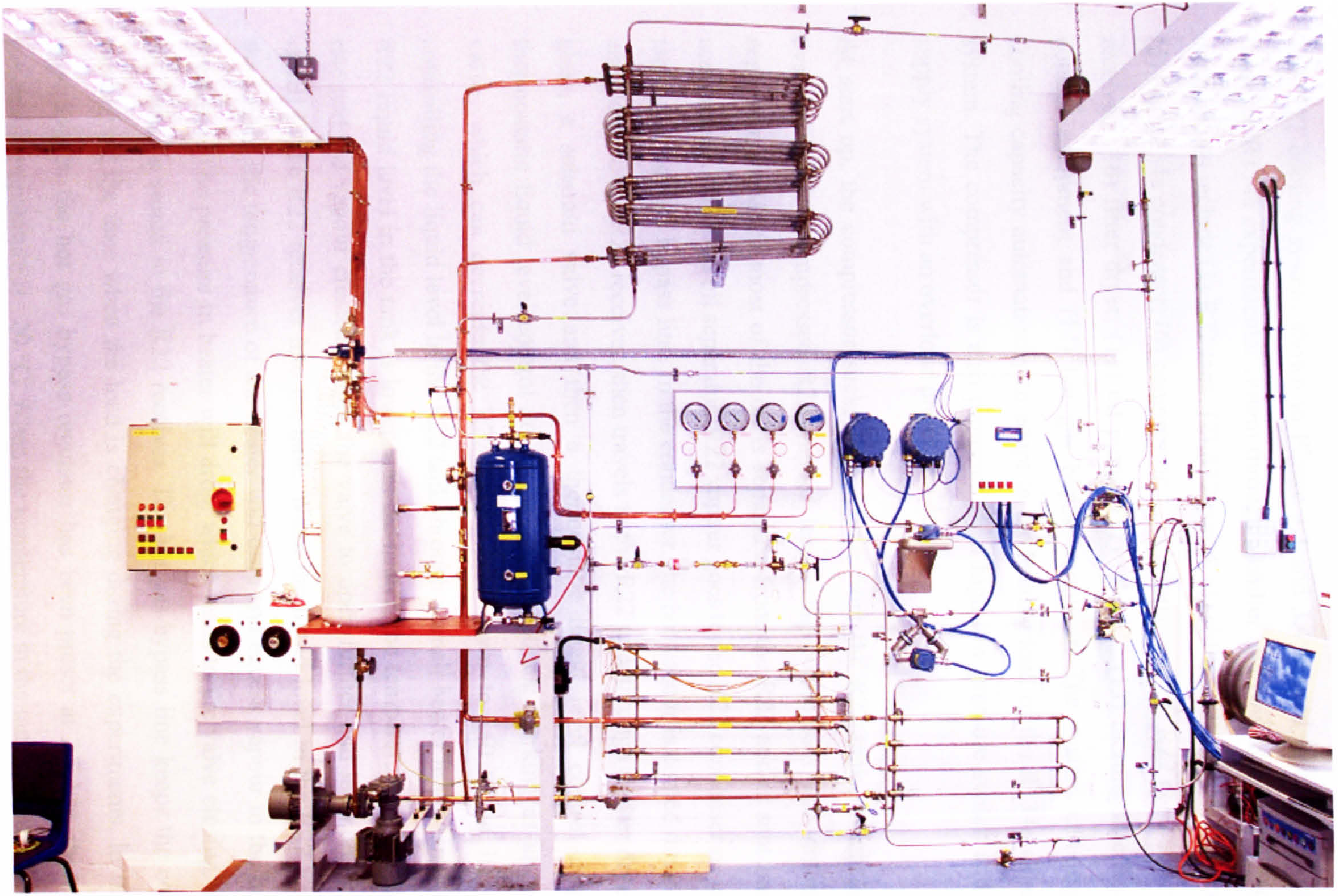

Figure 3.2 Photograph of the experimental facility.

3.1.2 R22 cooling system

The R22 cooling system shown in Figure 3.3 and 3.4 is used to carry the heat away from the R134a experimental system through a chiller and two condensers. The system components include (1) R22 tank; (2) R22 pump; (3) chiller; (4) small R134a condenser; (5) big R134a condenser; (6) compressor; (7) oil separator; (8) R22 condenser; (9) R22 receiver; (10) filter dryer; (11) oil pump; (12) oil tank; (13) thermostatic liquid level control equipment and (14) hot gas bypass regulator. The system can regulate its cooling capacity automatically to adapt to the heating load of the R134a experimental system. The compressor is also protected by a high-low pressure switch and a power supply system with an overload protection device.

At start up, the compressor sucks R22 vapour from the R22 tank, which acts as an evaporator. Hot compressed R22 vapour leaves the compressor and enters the oil separator, in which most of the oil is separated from the R22 and is sent back to the compressor. After the oil separator, R22 vapour goes to the R22 condenser or to the R22 tank via a hot gas bypass line. In the condenser, the hot vapour is cooled down to liquid and flows to the R22 receiver, then travels to the R22 tank through a filter dryer, a sight glass, a solenoid valve and then a thermostatic liquid level control device. The thermostatic liquid level control device has two functions: working as an expanding valve, which can decrease the R22 temperature down to -40 °C at its exit, and controlling the liquid level in the R22 tank through a small heater in the tank. When the R22 liquid level in the tank is lower than the heater, the temperature of the heater will rise and the vapour created pushes the valve to open further and let more R22 liquid stored in the R22 receiver into the tank. When the liquid level in the R22 tank covers the heater, the temperature of the heater will drop and excess vapour in the heater will condense. The pressure in heater will drop, which leads to the valve closing. The extra R22 will be stored in the R22 receiver. The hot gas bypass line keeps the compressor running all the time when the load is changing during the experiments. In the current experiments, the hot gas bypass regulator has been preset at 2.5 bar, the equivalent saturated temperature is –20 °C. When the temperature in the tank is lower than –20 °C, the pressure difference between the evaporation pressure in the tank and the preset pressure is high enough to push the regulator open and let more hot gas into the tank to prevent the temperature in the tank from dropping further. The regulator closes when the temperature in the tank is higher than the set value. In this loop, the solenoid valves and the liquid level control equipment operate together with the compressor, i.e. they can be opened only after the compressor is running. The cold liquid in the R22 tank is pumped to the big R134a condenser (or the small R134a condenser) and the R134a chiller by a circulating pump to cool the R134a in the experimental system. The flow rates, i.e. the cooling capacities, are controlled by three needle valves (V7, V10, V2) located before the big R134a condenser, the R134a chiller and in the bypass line. The pump was selected for the maximum load, so a needle valve is installed in the bypass line to let the extra R22 flow back to the tank. The small R134a condenser does not need a control valve because the heater capacity in the R134a tank is big enough to compensate for its cooling capacity. The oil from the R22 compressor will deposit in the R22 tank gradually since the efficiency of the oil separator is less than 100% and the return vapour can only carry very limited oil back to the compressor. This was a problem encountered during the commissioning of the system. Therefore, an oil return system was designed and built for separating the oil from R22 and re-injecting it to the compressor. The compressor oil (Bitzer B5.2) used is compatible with R22 even at very low temperature. This is a significant characteristic which is different from normal refrigerant oils. So the oil/R22 mixture can be pumped to an oil tank where it is heated by an oil pump or the R22 pump. The evaporated R22 flows to the compressor suction and the retained oil flows back to the compressor oil pool by gravity.

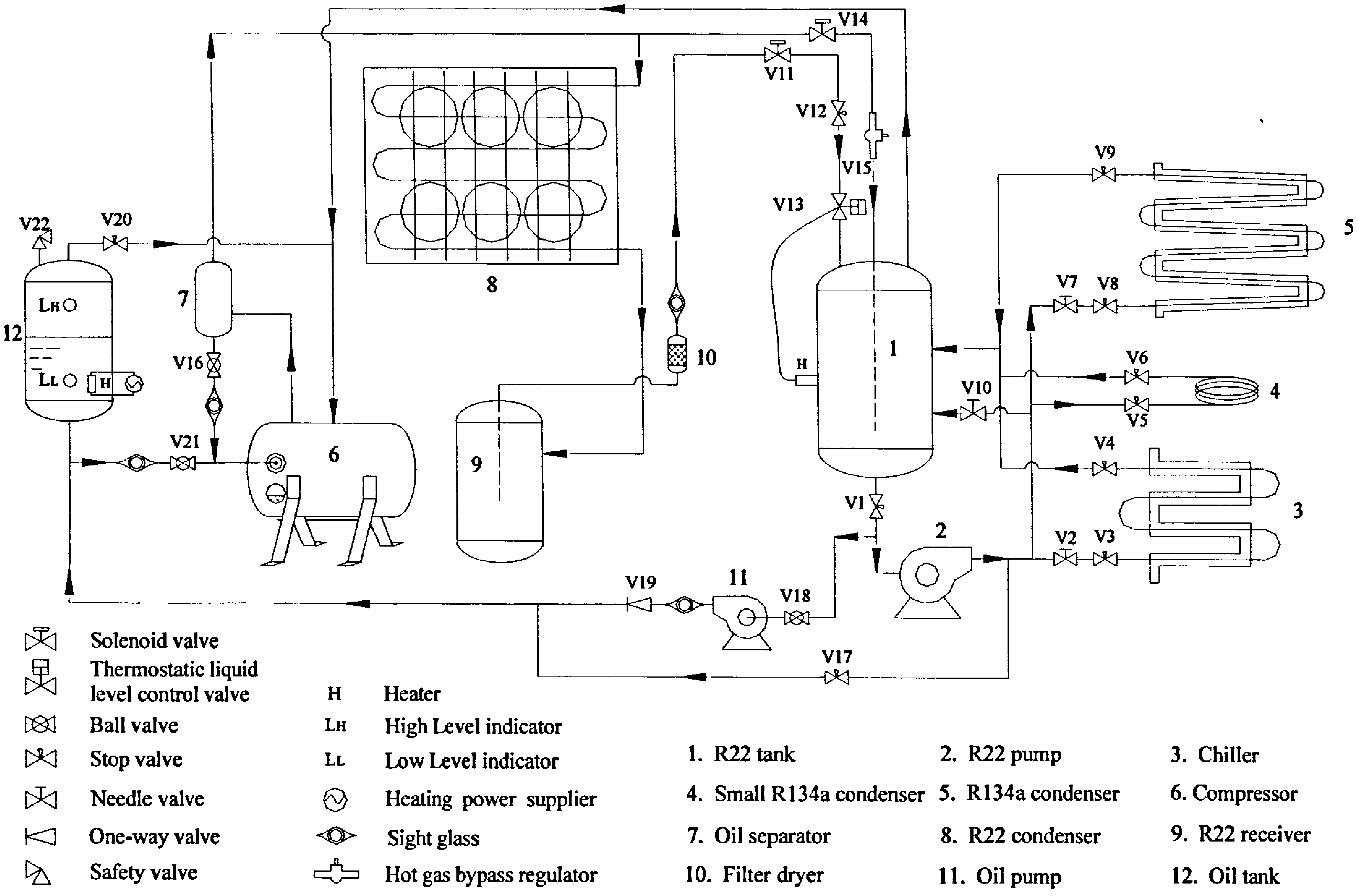

Figure 3.3 Schematic diagram of the R22 cooling system.

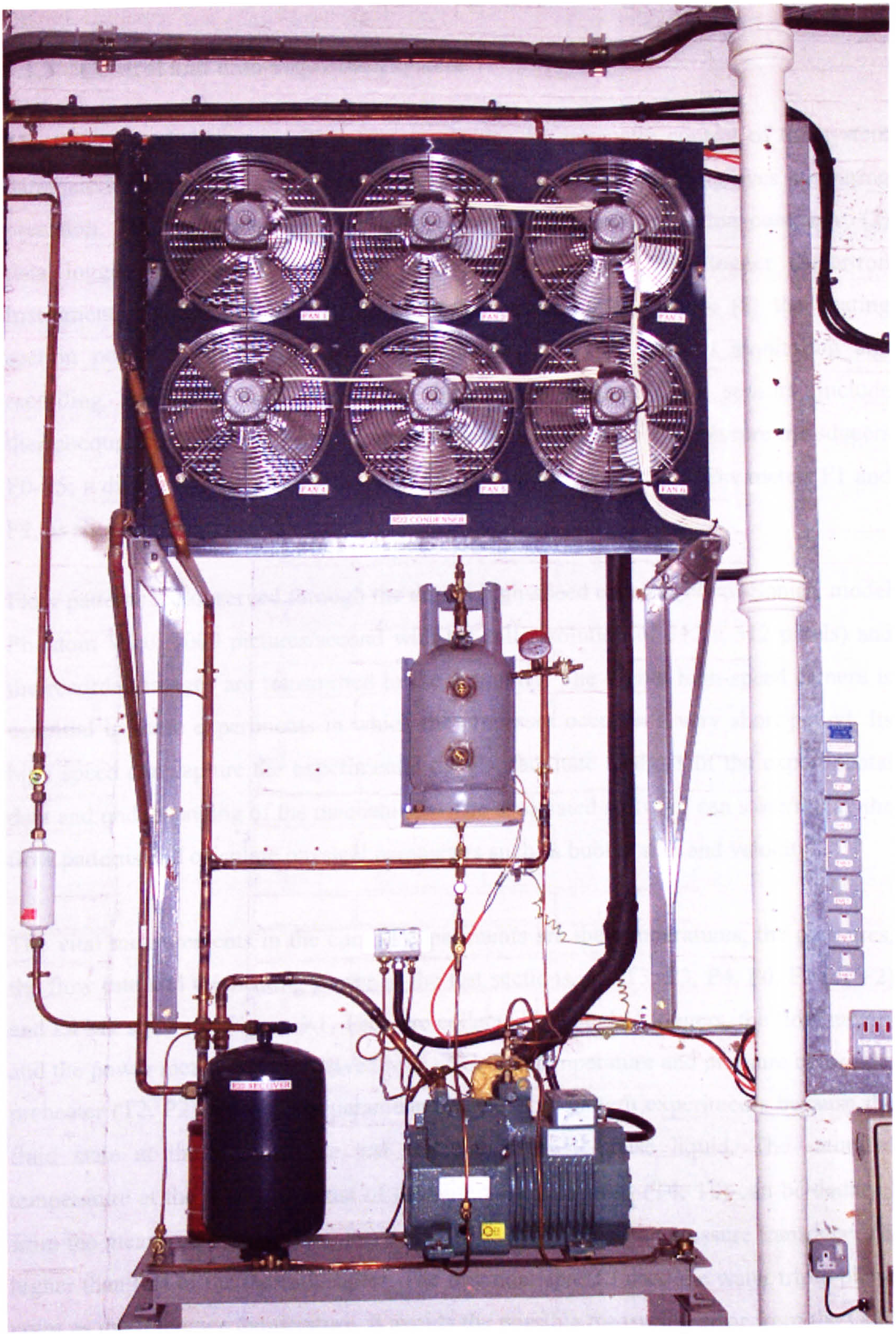

Figure 3.4 Photograph of the R22 cooling system (excluding the R22 tank, pump, chiller, condensers and oil pump, these are seen in Figures 3.1 and 3.3).

3.1.3 Control and data acquisition system

The control and data acquisition system enables an automatic control of the system parameters and the data collection, reduces manual operation and improves measuring precision. The main measuring equipment include: (1) data collection computer; (2) data logger (Solartron Instruments, model SI3535F); (3) data logger (Solartron Instruments, model SI35951E); (4) preheater power meter DPM1; (5) the heating section power meter DPM2; (6) PID controller; (7) flow pattern monitoring and recording computer and (8) digital high-speed camera. The sensors include thermocouple probes T0-T7 and thermocouple wires TT(0)-TT(n); pressure transducers P0-P5; a differential pressure transducer DP and two Coriolis mass flow meters F1 and F2, as shown in Figures 3.5 - 3.7.

Flow patterns are observed through the digital high-speed camera (Photo-Sonics, model Phantom V4.0, 1000 pictures/second with the full resolution of 512 x 512 pixels) and the recorded images are transmitted to the computer. The digital high-speed camera is essential in these experiments in which the processes occur in a very short period. Its high speed can capture the experimental details, facilitate analysis of the experimental data and understanding of the mechanisms. The associated software can store/replay the flow patterns and calculate physical parameters such as bubble size and velocity.

The vital measurements in the current experiments are the temperatures, the pressures, the flow rate and the heating power in the test sections, i.e. T3, P3, P4, P0, F1 (or F2) and DPM2 shown in Figure 3.1. They are collected by the data loggers, the flow meters and the power meter, and then saved in the PC. The temperature and pressure before the preheater (T2, P2) are not key parameters in the flow pattern experiments because the fluid state at the inlet of the test sections is single-phase liquid. The saturated temperature at the inlet and outlet of the observation sections (T4, T0) can be deduced from the measured pressure (P4, P0) because the accuracy of the pressure transducers is higher than that of the thermocouples. The thermocouple T3 used the water triple-phase point as the reference temperature. It avoids the possible measuring error from the Cold Junction Compensation (CJC), therefore improves the measuring accuracy. All thermocouple probes (except the needle probes T3, T4, T0) are ungrounded type to insulate the noise from the system. The whole test section floats above ground so that the probes (T3, T4, T0) and wires ($TT_{(1)}$-$TT_{(15)}$) exclusively use the data logger SI35951E, which has an allowed maximum voltage of 500V to the ground. The other thermocouples, pressure transducers, flow meters and differential pressure transducer connect to the data logger SI3535F with an allowed voltage of 14V. All power supplies, control circuits, measuring instruments and data acquisition devices share the same ground to avoid the case of different grounds having different potentials which will cause measuring error. The data logger SI3535F equips two analogue output ports and the equipped module has five output channels. The signals from T6, P0 and T7 are exported to the PID controller to control the R134a tank heater and the No.1 heater in the preheater. The signal from T6 can cut the power supply of the tank heater when it overheats. The P0 signal automatically adjusts the heating power in the tank to stabilize the system at a preset pressure. The T7 signal controls the No.1 heater in the preheater to get the desired degree of subcooling at the inlet of the test section. All experimental parameters, including temperatures, pressures, fluid state, flow rate, power, thermal loss, quality and superficial velocities, are monitored via a program developed by the researchers (X. Huo and L. Chen). The key parameters are also plotted with time history to ensure the system reaches a stable state. Group data, with the same diameter and pressure, can be converted to a flow pattern map using another purposely-developed program by the author. The different flow maps can be overlaid to find the shift of transition boundaries. In addition, the program can evaluate the existing correlations, the proposed coordinate groups, newly developed models and correlations. The experimental uncertainty can also be estimated.

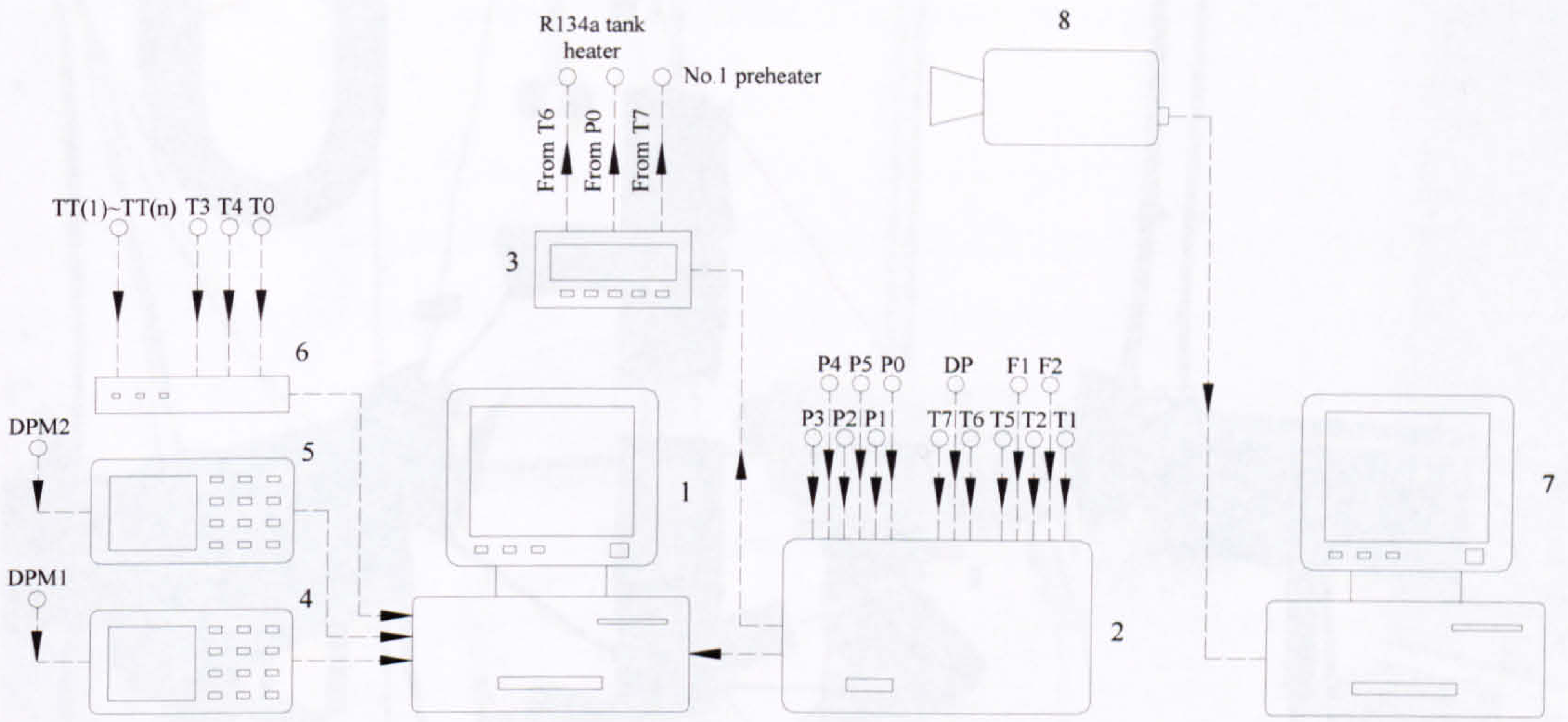

1. Data collecting computer
2. SI3535F data logger
3. PID controller
4. Power meter DPM1
5. Power meter DPM2
6. SI35951E data logger
7. Flow pattern monitoring and recording computer
8. Digital high-speed camera

Figure 3.5 Schematic diagram of the control and data acquisition system.

Figure 3.6 Photograph of the control and data acquisition system.

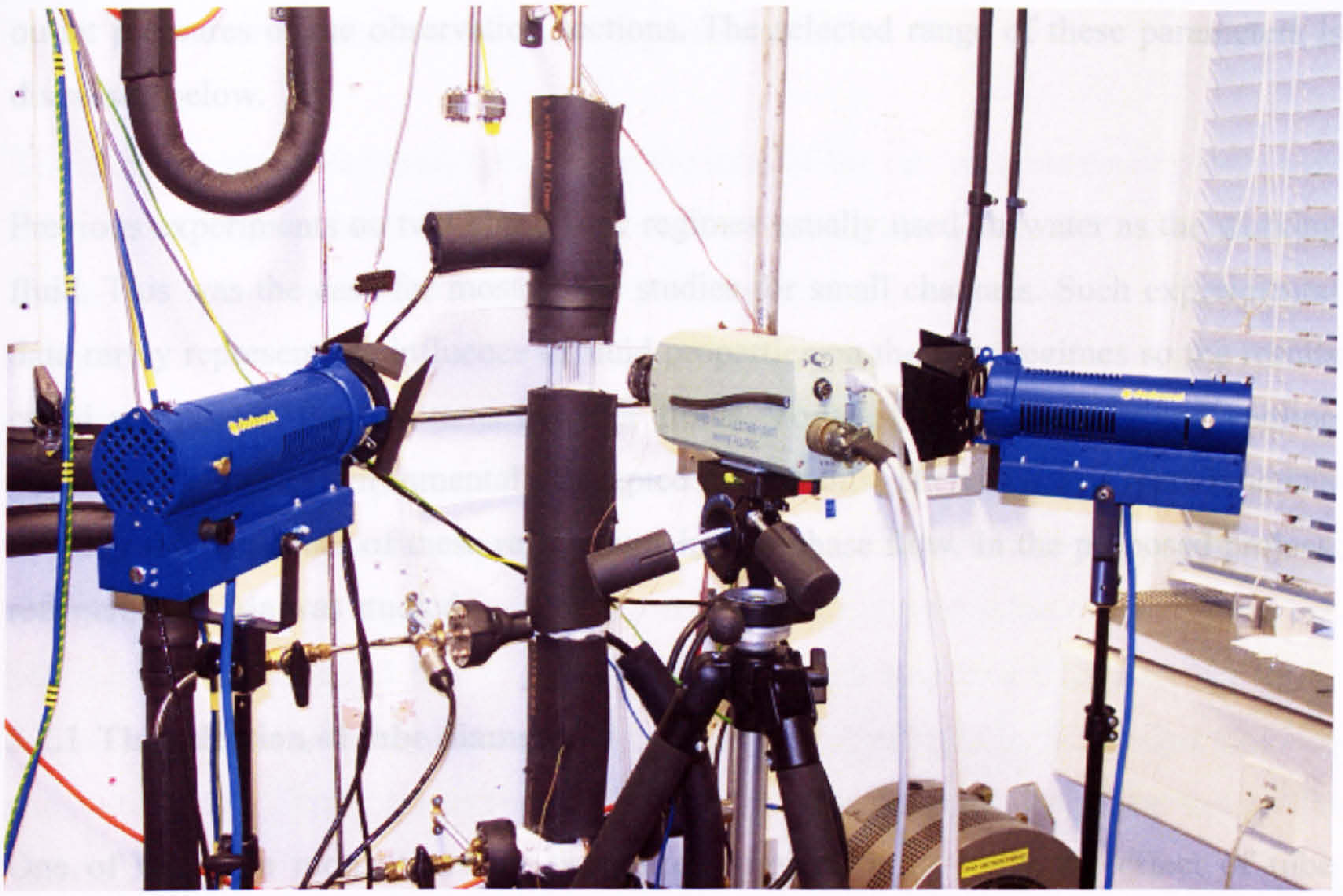

Figure 3.7 Photograph of the camera and lighting set up.

3.2 The selection of experimental parameters

The experimental data should include the key parameters affecting flow patterns. These will be useful in the theoretical study to reveal the effect of channel dimension and fluid parameters on flow patterns, and study further the transition mechanisms of flow patterns, pressure loss and heat transfer. Based on the dynamic analysis in Chapter 2, the necessary data in the current study include tube diameter D, liquid and gas superficial velocities (u_{ls}, u_{gs}), liquid and gas densities (ρ_l, ρ_g), liquid and gas viscosity (μ_l, μ_g), and surface tension σ. Clearly, density, viscosity and surface tension are not independent parameters in vapour-liquid flow and they are functions of the saturated pressure. Therefore, the most important and controlling parameters can be further reduced to tube diameter, liquid and gas superficial velocities and pressure. However, the measurable and controllable parameters are tube diameter D, mass flow rate m, heating power Q, temperature T and pressure P. Liquid and gas superficial velocities can be calculated accordingly. In the present experiments, the following parameters were measured and recorded: tube diameter, mass flow rate, the heating power of the test sections, the inlet temperature and pressure of the test sections and the inlet and outlet pressures of the observation sections. The selected range of these parameters is discussed below.

Previous experiments on two-phase flow regimes usually used air-water as the working fluid. This was the case for most of the studies for small channels. Such experimental data rarely represent the influence of fluid properties on the flow regimes so the results could not predict flow patterns in other fluids. Today, heat exchangers and cooling devices widely use environmentally accepted refrigerants. Therefore, it is more practical to study the behaviour of these refrigerants in two-phase flow. In the proposed project, refrigerant R134a was studied.

3.2.1 The selection of tube diameter

One of the main motivations for the current project, is to study the effect of tube diameter on flow patterns in small size tubes. The criteria needed to estimate the size for which we can define tubes as small are given in Table 2.1. In the current experimental conditions, the range could be between 0.20 to 5.3 mm. However, not all criteria are suitable to the proposed experiments, for example, the criterion of Eö=100 presented by Triplett et al. (1999) was based on the emergence of stratified flow which only appears in horizontal tubes. Another criterion, Bo=0.3, was put forward by Akbar et al. in 2003 when the design and construction of the current experimental facility have already been completed. The proposed tube diameters in the present study are 1.10, 2.01, 2.88 and 4.26 mm respectively. In this study the confinement number, proposed by Kew and Cornwell (1997), was used as the criterion that separates normal and small size tubes. Based on this, the range of diameter chosen would allow the study of flow patterns for both normal and small size tubes and allow a direct comparison. The existing experimental system and devices were therefore designed and selected based on this range. The experimental accuracy and flexibility will be worse if the tube size was decreased further. However, it can be improved by changing the control valves, the current transformer variac for the test sections and reducing the measuring span of the mass flow meters.

3.2.2 The selection of pressure and temperature

The experimental parameters recorded at the inlet of the test sections can be controlled automatically by the immersion heater in the R134a tank through the PID controller, see Figure 3.1. The experimental pressures were set to 6, 10 and 14 bar in the proposed experiments; the corresponding saturated temperatures were 21.6, 39.4 and 52.5 °C, respectively. The designed pressures and temperatures are listed in Table 3.1. Normally R134a is used at lower pressure and temperature in practical applications. However, the current experiments cannot operate at such parameters due to the limitation of the existing experimental rig. The main reason is that the considerable thermal exchange between the ambient and R134a after the chiller, which may heat R134a to two-phase before it reaches the test sections. The effect is more significant in the smaller tubes or at low flow rate. This problem could be solved by adding a small chiller just before the test sections.

Table 3.1 Experimental pressures and temperatures in the experiments.

Experimental pressure (bar)	6.0	10.0	14.0
Critical pressure ratio*	0.15	0.25	0.34
Experimental temperature (°C)	21.56	39.40	52.45

* The critical pressure of R134a is 40.65 bar.

3.2.3 The selection of gas and liquid superficial velocities

Logarithm of gas and liquid superficial velocities are used as the main coordinate groups in the flow maps. The experimental data should cover all possible flow patterns, i.e. dispersed bubble, bubbly, slug, churn and annular flow. The maximum liquid and gas superficial velocities should at least cover the transition boundaries of dispersed bubble flow and annular flow. More experiments were carried out near the transition boundaries.

Based on the existing models and correlations in Appendix B, the required liquid superficial velocity can be found at the boundary of dispersed bubble flow and the required vapour superficial velocity should be at the boundary of annular flow, see Figure 3.8. The required liquid and gas superficial velocities are 1.5 and 31 m/s respectively for vertical upward air-water flow in a 25 mm diameter tube.

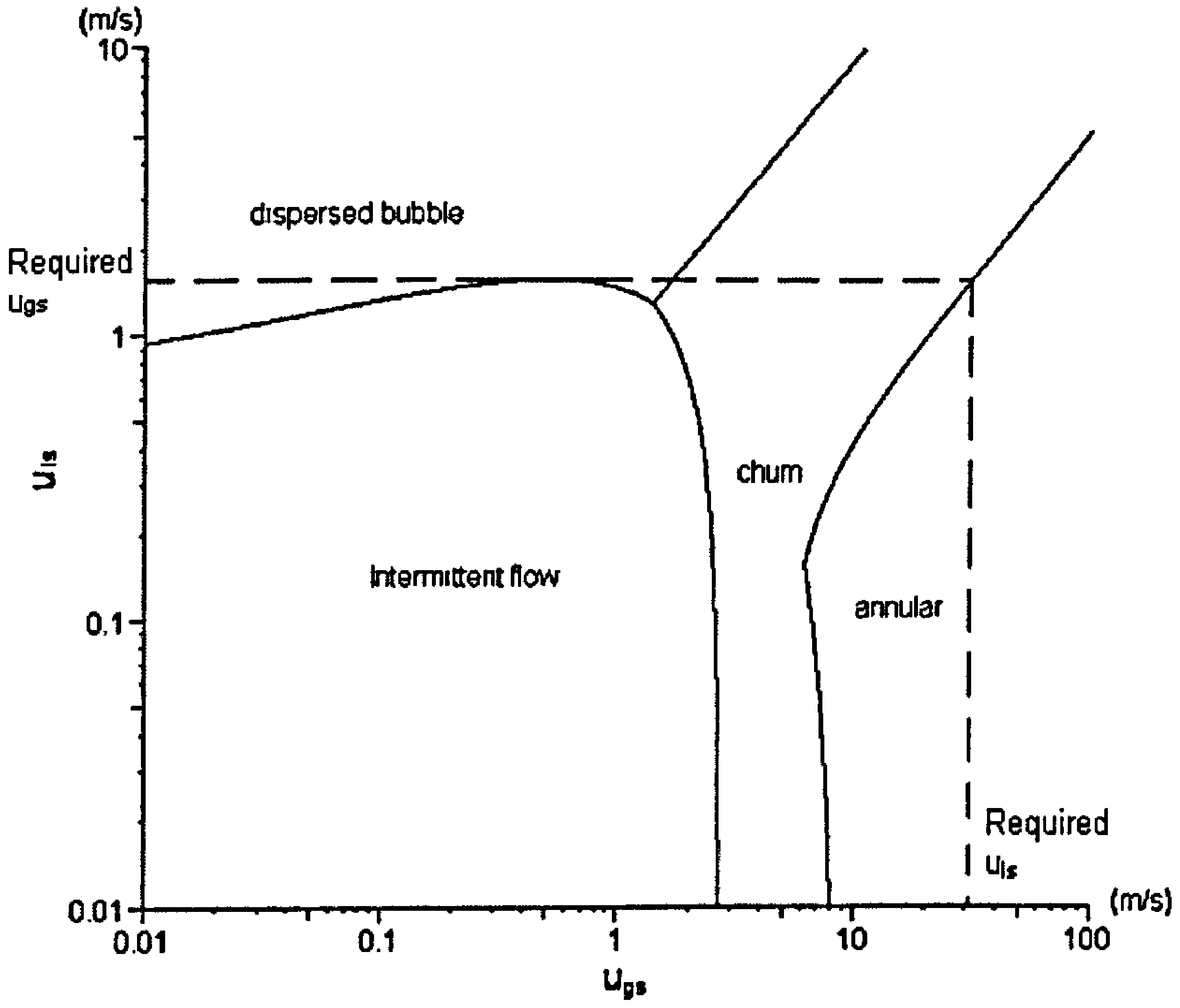

Figure 3.8 Air-water flow map in vertical upward 25 mm tube using the unified model summarized by Taitel et al. (1990).

Table 3.2 lists the calculation results for R134a at the proposed experimental pressures (6 –14 bar) based on the existing models.

Table 3.2 The required gas and liquid superficial velocities.

Models	1.10 mm tube				4.26 mm tube			
	6.0 bar		14.0 bar		6.0 bar		14.0 bar	
	u_{ls}	u_{gs}	u_{ls}	u_{gs}	u_{ls}	u_{gs}	u_{ls}	u_{gs}
Taitel et al. (1980)	1.6	1.7	0.90	0.96	1.7	1.8	1.1	0.96
Mishima and Ishii (1984)	3.4	1.9	1.9	1.1	3.5	2.0	1.9	1.1
Mcquillan and Whalley (1985)	1.2	0.65	1.1	0.45	1.4	1.3	1.3	0.77
Taitel (1990)	0.55	2.7	0.52	1.5	1.0	4.5	0.94	2.7

The maps from Mishima and Hibiki (1996) were also considered to ensure that the range required is covered. Eventually, the velocities ranges chosen are: liquid superficial velocity 0.04 – 5.0 m/s and vapour superficial velocity 0.01 – 10.0 m/s. The actual velocities may be smaller in the 1.10 mm tube due to the extremely large pressure loss in high velocity.

The liquid superficial velocity was initially kept at a pre-determined constant by adjusting control valve continually during the experiments. The gas superficial velocity was increased step by step by increasing the heating power on the heating section until annular flow and possibly mist flow, eventually appeared. All fluid parameters and flow patterns were recorded once steady state was reached, which can be confirmed by the parameters-time history curves plotted by the monitoring program. Then, the liquid superficial velocity was increased in step and the experiments were repeated at different gas superficial velocities. The selected velocities can distribute the data on the logarithm u_{gs}-u_{ls} flow maps at least in the grid of 10x10. However, the actual density distribution of data points depended on the position of the transition zones and the resolution of the variac for the heating section, as shown in Table 3.3.

Table 3.3 Selection of liquid and gas superficial velocities.

<table>
<tr><td colspan="14">Liquid superficial velocities (m/s)</td></tr>
<tr><td>0.04</td><td>0.07</td><td>0.11</td><td>0.18</td><td>0.28</td><td>0.45</td><td>0.72</td><td>(0.92)</td><td>1.17</td><td>(1.49)</td><td>1.90</td><td>(2.42)</td><td>3.09</td><td>5.00</td></tr>
<tr><td colspan="14">Vapour superficial velocities (m/s)</td></tr>
<tr><td colspan="14">0.01 to 10.0 m/s uniformly distributed and more in the transition zones</td></tr>
</table>

* The liquid superficial velocities in brackets are the optional velocities, depending on the transition boundary of dispersed bubble to bubbly flow.

3.2.4 The range of mass flow rate

The two mass flow meters can give highly accurate measurement in a wide range after careful setting and verification. The flow rate passing the test sections was adjusted by using the needle valves V4 (or V5) and V14, see Figure 3.1. The required mass flow rate can be calculated by the following equation.

$$m = \frac{\pi D^2 \left(\rho_g u_{gs} + \rho_l u_{ls}\right)}{4} \tag{3.1}$$

Table 3.4 lists the possible minimum/maximum mass flow rates in the present experiments, are 0.15 kg/hr and 327.4 kg/hr respectively. The corresponding experimental conditions are the 1.10 mm tube at 14 bar pressure and the 4.26 mm tube at 6 bar pressure.

Table 3.4 Selection of mass flow rates (kg/hr).

Diameter (mm)	1.10	1.10	4.26	4.26
Pressure (bar)	6	14	6	14
	Vapour superficial velocity (m/s)			
Liquid superficial velocity (m/s)	0.01	0.01	10.00	10.00
0.04	0.17	0.15	17.40	38.51
5.00	20.84	18.65	327.43	315.97

3.2.5 The selection of input power

The heating power of the test sections cannot be controlled automatically to get the desired quality because no quality signal could be exported at the current experimental conditions. Therefore, the power has to be regulated manually by watching the calculated superficial velocities in the monitoring program. The required input power can be estimated by the following equations:

$$Q - \Delta Q = m\Delta h_l + xmh_{fg} \qquad (3.2)$$

and

$$x = \frac{\rho_g u_{gs}}{\rho_l u_{ls} + \rho_g u_{gs}} \qquad (3.3)$$

The heating power was recorded by a digital power meter. The heat loss ΔQ was estimated in the single-phase flow experiments. Considering 2% thermal loss in the test sections and 5 K subcooling degree at the inlet of the test sections, the input power can be calculated based on Equations 3.2 and 3.3 and is 0.4 – 2297 W, see Table 3.5.

Table 3.5 Selection of heating power.

Diameter (mm)	1.10	1.10	4.26	4.26
Pressure (bar)	6	14	6	14
Vapour superficial velocity (m/s)	0.01	0.01	10.0	10.0
Liquid superficial velocity (m/s)	0.04	0.04	5.0	5.0
Quantity	0.59%	1.60%	4.55%	11.48%
Mass flow rate (kg/hr)	0.17	0.15	327.43	315.97
Thermal loss	5.0%	5.0%	5.0%	5.0%
Requested power (W)	0.40	0.45	1459.21	2296.76

Overall, four different diameter tubes, three experimental pressures, altogether twelve groups of experiments and therefore twelve flow maps were possible. Considering the fact that more experiments were done at the transition zones, about 2400 data points and images were recorded in the present experiments. The range of the parameters are summarised below:

Liquid	R134a
Orientation	Vertical upward
Diameter (mm)	1.10, 2.01, 2.88, 4.26
Pressure (bar)	6.0, 10.0, 14.0
Temperature (°C)	21.56, 39.40, 52.45
Gas superficial velocities (m/s)	0.01 - 10.0
Liquid superficial velocities (m/s)	0.04 - 5.0
Quality	0.0 – 1.0

The devices which were selected based on the designed parameters are discussed in Appendix C.

3.3 Test sections

Four test sections, with the inner diameters of 1.10, 2.01, 2.88 and 4.26 mm, were designed for both heat transfer experiments and flow pattern experiments. The test sections connect with the experimental rig through a pair of flanges. The main components include three parts namely calming section (steel tube before the upstream electrode), heating section (steel tube between the pair of electrodes) and observation section (glass tube), shown in Figures 3.9 and 3.10 and the details are given in Table 3.6 and Section C.1 (6) in Appendix C. The integrated functions include fluid heater, flow observation and experimental data collection. The test sections were wrapped by ID54x13 mm insulation tubes except the visualization section (25-30 mm length) in the observation section. The space between the test sections and the insulation tubes was filled with fibreglass to improve insulation efficiency.

A well-developed single-phase flow is achieved in the calming section. The length must be long enough to eliminate the inlet effect and get a uniform flow at its outlet, whilst the pressure drop is within a reasonable range. Generally a minimum length of 50 times hydraulic diameter is required in the calming section. In this project, the designed L/D ratios are between 55 and 91 as presented in Table 3.6.

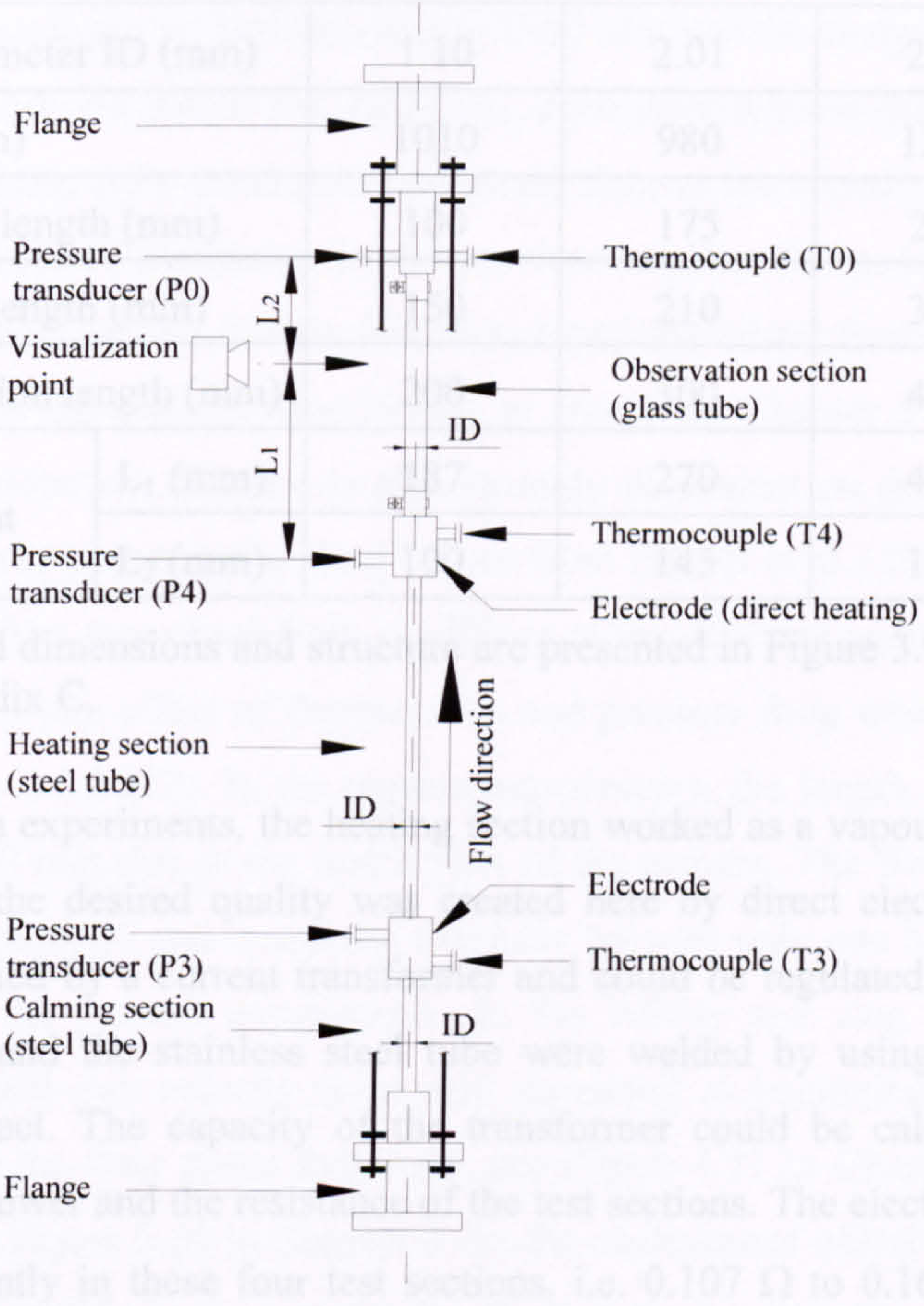

Figure 3.9 Schematic diagram of the test sections.

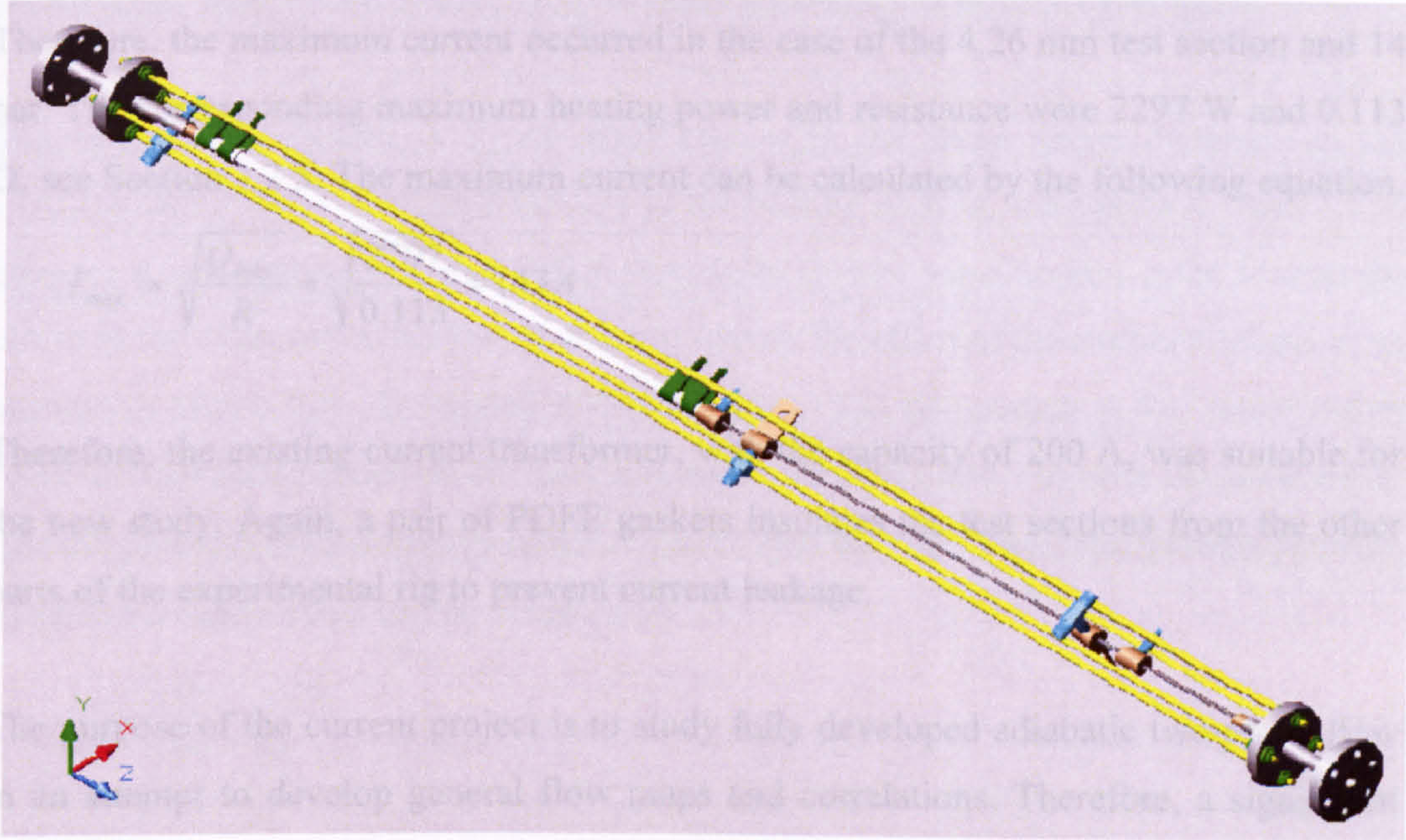

Figure 3.10 3-D model of the test sections.

Table 3.6 The dimensions of the test sections.

Tube insider diameter ID (mm)		1.10	2.01	2.88	4.26
Total length (mm)		1010	980	1260	1350
Calming section length (mm)		100	175	225	235
Heating section length (mm)		150	210	300	500
Observation section length (mm)		200	300	450	450
Observation point	L_1 (mm)	187	270	440	425
	L_2 (mm)	100	145	125	140

Note: The detailed dimensions and structure are presented in Figure 3.9 and Figures C.1 and C.2 in Appendix C.

In the flow pattern experiments, the heating section worked as a vapour producer. Two-phase flow with the desired quality was created here by direct electric heating. The current was supplied by a current transformer and could be regulated by a variac. The copper electrode and the stainless steel tube were welded by using silver solder to ensure good contact. The capacity of the transformer could be calculated from the required heating power and the resistance of the test sections. The electric resistance did not vary significantly in these four test sections, i.e. 0.107 Ω to 0.164 Ω, and is less affected by the temperature; increased about 5% from 10 °C to 60 °C (Huo 1999). Therefore, the maximum current occurred in the case of the 4.26 mm test section and 14 bar. The corresponding maximum heating power and resistance were 2297 W and 0.113 Ω, see Section 3.2.5. The maximum current can be calculated by the following equation.

$$I_{\max} = \sqrt{\frac{Q_{\max}}{R}} = \sqrt{\frac{2297}{0.113}} = 143A$$

Therefore, the existing current transformer, with the capacity of 200 A, was suitable for the new study. Again, a pair of PDFE gaskets insulates the test sections from the other parts of the experimental rig to prevent current leakage.

The purpose of the current project is to study fully developed adiabatic two-phase flow in an attempt to develop general flow maps and correlations. Therefore, a significant tube length, upstream of the observation section, allowed (within the limits of space and pressure drop) in order to eliminate the effect of upstream conditions in the heating section and obtain fully or near fully developed flow at the visualization point. The total length of the test sections are between 980 to 1350 mm and the designed L_l/D ratios are between 100 to 170, see Table 3.6. However, such development distance may not be long enough to obtain fully developed two-phase flow at the visualization point and in fact it is still a topic of discussion in the previous studies. For example, Taitel et al. (1980) did not predict bubbly flow in fully developed two-phase flow in small tubes but it was observed in the present experiments as shown in Chapter 5 Section 5.1.2. In addition, the development distance is also strongly dependent on the fluid parameters and the flow patterns based on the observations from Prasser et al. (2002), see Chapter 2 Section 2.3.3 (3). The two-phase flow conditions at the different positions could not be strictly same due to the effect of thermal loss and pressure drop which is discussed in Chapter 4 Section 4.1.3 (12). In the present experiments, the length of the observable part is about 25-30 mm due to the restrictions of the camera. The flow patterns within this range were examined and compared carefully because only one high-speed camera was available in the present experiments. In the bubbly and slug flow, the bubble diameter, length and rise velocity were also measured at beginning and end of this length to examine the flow status indirectly, see Figure 4.11 in Chapter 4 for the slug bubble length and Figure 5.49 in Chapter 5 for the coalescence of bubbles. However, it is difficult to give solid conclusions on the flow status because the difference within such a short observation distance (25-30 mm) is possibly difficult to distinguish.

The observation section, a Pyrex glass tube with the same inside diameter as the stainless steel tube is connected directly to the heating section, see Tables 4.1 and 4.2 in Chapter 4 and Figures C.1 and C.2 in Appendix C. The visualization point is near the outlet of the observation section in order to reduce the effect of the connection and in an attempt to obtain fully developed two-phase flow. The parameters at the visualization point are calculated based on the inlet and outlet pressures (P4, P0) with the assumption that the pressure drop along the observation section is linear. The experimental pressure at the observation point can be obtained as:

$$p = \frac{L_1 p_0 + L_2 p_4}{L_1 + L_2} \tag{3.4}$$

The pressure at the outlet of the observation section (p_0) is controlled automatically in the current experiments. The signal from the pressure transducer (P0) is exported to the PID controller to control the R134a tank heater. The preset pressure p_0 was slightly lower than the desired experimental pressure and was adjusted constantly depending on the pressure drop in the observation section to get constant experimental pressure (p).

The local gas and liquid superficial velocities at the visualization point were calculated as follows:

$$u_{gs} = \frac{mx}{A\rho_g} \tag{3.5}$$

$$u_{ls} = \frac{m(1-x)}{A\rho_l} \tag{3.6}$$

where,

$$x = \frac{m(h_{in} - h_l) + (Q - \Delta Q)}{m(h_g - h_l)} \tag{3.7}$$

The mass flow rate (m) and power (Q) were measured by the Coriolis mass flow meters (F1 or F2) and the power meter (DPM2), respectively. The inlet enthalpy (h_{in}) was calculated based on the temperature and pressure at the inlet of the heating section (T3, P3) and the saturated parameters at the visualization point (ρ_g, ρ_l, h_g, h_l) were calculated based on the local saturated pressure, which was deduced from the pressure at the inlet and outlet of the observation section (P4, P0) – the pressure drop was assumed linear. The thermal loss at the test section (ΔQ) was obtained using the temperature difference ($\Delta\overline{T}$) across the insulation and the thermal loss coefficient (K), which was estimated in the single-phase experiments and is summarized in the below.

Table 3.7 The thermal loss coefficient in the test sections.

Test section diameter (mm)	Thermal loss coefficient (W/K)
1.10	0.048
2.01	0.040
2.88	0.044
4.26	0.068

3.4 The control programs

Three control systems were used in the current project. The Phantom Camera Control supplied with the digital high-speed camera and two purposely developed programs. The Phantom Camera Control can objectively record the experimental process, which is useful in analysing the data and understanding the mechanisms. The available functions include capturing, recording and playing back flow patterns whilst measuring bubble sizes and velocity. The programs developed in this study were constructed and modified according to the practical needs of the research. Both programs integrate a lot of functions in order to reduce manual interference during the data treatment. The first program focuses on monitoring the fluid parameters and recording the experimental data. The second is used to process the collected data and develop new models and correlations. They are described in Appendix D while the source codes are saved in a CD available with the thesis.

3.5 Summary

The designed facility is composed of three independent systems: the R134a experimental system, the R22 cooling system and the control and data acquisition system. Their operation and functions are introduced in detail in this Chapter. All key components in the system were designed based on the experimental range and conditions and discussed in Appendix C, see the summary below:

Liquid	R134a
Orientation	Vertical upward
Diameter (mm)	1.10, 2.01, 2.88, 4.26
Pressure (bar)	6.0, 10.0, 14.0
Temperature (°C)	21.56, 39.40, 52.45
Vapour superficial velocities (m/s)	0.01 - 10.0
Liquid superficial velocities (m/s)	0.04 - 5.0
Quality	0.0 – 1.0

Four test sections with the inner diameters of 1.10, 2.01, 2.88 and 4.26 mm, were designed for both the heat transfer and the flow pattern experiments. They is composed of three main parts namely the calming section, the heating section and the observation section. Their design was such that they could be assembled easily whilst satisfying the required measurement accuracy.

A commercial software and two purposely developed programs are used in the current study, see the introduction in Appendix D. The entire experimental process and all experimental parameters were controlled, monitored and recorded automatically with these control facilities. The obtained data can be analysed in real time, which greatly accelerated the experimental progress. The experimental accuracy was improved also due to limited manual interference.

Chapter 4 Validation of the Experimental Facility

In all heat transfer and fluid flow experiments the experimental facility must be validated. The experimental error must be within an acceptable range and the whole system and its separate components must be shown to work properly at all experimental conditions. In these experiments the accuracy was verified in single-phase experiments.

4.1 Calibration and uncertainty analysis

All instruments used in this study were calibrated carefully before installation, either in the laboratory or by the manufacturer. Their contribution to the experimental accuracy was obtained by error analysis. This is very important in the experiment design and in the selection of instruments. The overall experimental accuracy is estimated and presented in this section.

4.1.1 General theory

The total experimental error should consider all potential factors that influence the experimental accuracy. It is the sum of systemic error (bias) and random errors (precision). The systemic error is the fixed or constant component of the total error. It is sometimes grouped into calibration error, data acquisition error, data reduction error and conceptual error. The combined systematic uncertainty is calculated as the root-sum-square (RSS) combination of the above elemental systematic errors. Calibration reduces the part "static" systematic errors to the level of the standard used in the calibration procedure. However, other systematic errors such as the stability should be additionally considered. If the calibration cannot be carried out properly in the laboratory, the systemic uncertainty data provided by the manufacturer are used. The random error follows the Gaussian distribution and can be reduced by increasing measurement times or collecting more data. The Chauvenet criterion is adopted to reject outliers (or wild points) in the current study. The quantification of uncertainty is determined at 95% confidence level in the current study. The overall uncertainty of a measured variable (U) can be calculated according to the ISO Guide (1993) (Coleman and Steele, 1999):

$$U_{95} = t_{95} u_c \tag{4.1}$$

t_{95} is the distribution coefficient with 95% confidence level and u_c is given by:

$$u_c = \sqrt{S_{B_X}^2 + S_X^2} \tag{4.2}$$

S_{B_X} and S_X in Equation 4.2 are calculated from:

$$S_{B_X} = \frac{B_X}{2} \tag{4.3}$$

$$S_X = \sqrt{\frac{1}{N-1}\sum_{i=1}^{N}\left(X_i - \overline{X}\right)^2} \tag{4.4}$$

Considering a general case, an experimental result, r, is a function of the measured variables Y (Coleman and Steele, 1999)

$$r = r(Y_1, Y_2, \cdots, Y_J) \tag{4.5}$$

Then the uncertainty of r can be obtained from the following equations.

$$U_r^2 = \left(\frac{\partial r}{\partial Y_1}\right)^2 U_{Y_1}^2 + \left(\frac{\partial r}{\partial Y_2}\right)^2 U_{Y_2}^2 + \cdots + \left(\frac{\partial r}{\partial Y_J}\right)^2 U_{Y_J}^2 \tag{4.6}$$

or given as a ratio

$$\frac{U_r^2}{r^2} = \left(\frac{Y_1}{r}\frac{\partial r}{\partial Y_1}\right)^2 \left(\frac{U_{Y_1}}{Y_1}\right)^2 + \left(\frac{Y_2}{r}\frac{\partial r}{\partial Y_2}\right)^2 \left(\frac{U_{Y_2}}{Y_2}\right)^2 + \cdots + \left(\frac{Y_J}{r}\frac{\partial r}{\partial Y_J}\right)^2 \left(\frac{U_{Y_J}}{Y_J}\right)^2 \tag{4.7}$$

4.1.2 Experimental range, conditions and assumptions

The current experiments require numerous measurements which include a number of parameters. The corresponding error analysis is also very diverse and complex. The experimental conditions are specified below with assumptions for the data analysis:

(1) Experimental range

• Tube inside diameter	1.10, 2.01, 2.88, 4.26 mm
• Experimental pressure	6.0, 10.0, 14.0 bar
• Max. liquid superficial velocity	5.0 m/s
• Max. gas superficial velocity	10.0 m/s
• Min. mass flow rate	0.5 kg/hr
• Max. mass flow rate	21.83 kg/hr (1.10 mm tube)

72.89 kg/hr	(2.01 mm tube)
149.65 kg/hr	(2.88 mm tube)
327.43 kg/hr	(4.26 mm tube)

(2) Conditions and assumptions:

- The heating section is of constant diameter and the tube wall thickness is the same, i.e. the section area and heat flux are constant along the tube.
- The observation section has uniform inside diameter and is same as the connected heating section.
- The maximum degree of subcooling at the outlet of the preheater is –5 K.
- The maximum temperature difference between the tube wall and the fluid temperature is 5 K, except at the condition of critical heat flux.
- The default ambient temperature is 20 °C.
- The maximum variation of the ambient temperature between summer and winter is ± 5 K.
- The error caused by the fitted equation is equal to the maximum deviation between the equation and the calibration data.
- The pressure drop along the observation section is linear.
- The heating section and the observation section have same thermal loss coefficient.
- For the non-measured parameters, such as the density of glass and stainless steel and properties of R134a, the errors are negligible.

4.1.3 Calibration process and error analysis

(1) Tube inside diameter

The inside diameter of the tubes was measured before the test sections were manufactured. The mean inside diameter of the stainless steel tube can be calculated by measuring its weight, length and outside diameter, i.e.

$$D_{in} = \sqrt{D_{out}^2 - \frac{4W}{\pi \rho L}} \tag{4.8}$$

The uncertainty can be obtained from

$$U_{D_{in}} = \frac{1}{2}\left(D_{out}^2 - \frac{4W}{\pi\rho L}\right)^{-1/2}\left[\left(2D_{out}U_{D_{out}}\right)^2 + \left(\frac{4U_W}{\pi\rho L}\right)^2 + \left(\frac{4WU_L}{\pi\rho L^2}\right)^2\right]^{1/2} \qquad (4.9)$$

However, the inside diameter of the glass tubes cannot be measured by using the above method because their outside diameters are much bigger than the inside diameters, and this will cause significant error. The appropriate method is to weigh the dry glass tube and the wet glass tube filled with water. The difference is the water weight in the tube. The inside diameter of the tube can be calculated by the water weight and the tube length, see the equations below.

$$D_{in} = \sqrt{\frac{4W}{\pi\rho L}} \qquad (4.10)$$

$$\frac{U_{D_{in}}}{D_{in}} = \frac{1}{2}\sqrt{\left(\frac{U_W}{W}\right)^2 + \left(\frac{U_L}{L}\right)^2} \qquad (4.11)$$

These will of course be compared with the diameters supplied by the manufacturer. The measured tubes should be cleaned carefully. The weights were recorded using an electronic scale with the accuracy of 1/1000 gram. The outside diameters were measured by a micrometer with the accuracy of 1/100 mm at several different sections and each section was measured twice at different directions. The lengths were measured by a tape meter with the accuracy of 1 mm. The density was available from the manufacturer. The measured results show that the manufacturing precision of the stainless steel tubes is much better than that of the glass tubes. For example, the measured diameters for the 2.01 mm steel tubes are 2.014 to 2.015 mm but for the glass tubes, the measured diameters are 2.01 to 2.04 mm even though they were cut from the same tube. In order to find the right glass tube for the observation section, several glass tubes with the same diameter were ordered and measured. Only the glass tube which inside diameter matches with the steel tube was selected and installed on the test section. The measured diameters and the uncertainty of the stainless steel tubes and the glass tubes are summarized in Tables 4.1 and 4.2 respectively.

Table 4.1 Diameter of the stainless steel tubes and the uncertainty.

Parameters	Tube 1	Tube 2	Tube 3	Tube 4
Outside diameter given by manufacturer (mm)	1.59	2.38	3.18	4.76
Inside diameter given by manufacturer (mm)	1.09	1.98	2.87	4.25
Measured outside diameter (mm)	1.60	2.39	3.18	4.75
Calculated inside diameter (mm)	1.10	2.01	2.88	4.26
Error of the inside diameter (mm)	0.014	0.012	0.011	0.011
Uncertainty of the inside diameter	1.31%	0.59%	0.38%	0.26%

Table 4.2 Diameter of the glass tubes and the uncertainty.

Parameters	Tube 1	Tube 2	Tube 3	Tube 4
Inside diameter given by manufacturer (mm)	1.10	2.01	2.88	4.26
Calculated inside diameter (mm)	1.10	2.01	2.88	4.26
Error of the inside diameter (mm)	0.004	0.004	0.002	0.005
Uncertainty of inside diameter (mm)	0.36%	0.17%	0.06%	0.11%

(2) Pressure sensor

The pressure sensors convert pressure into analogue electronic signal which is acceptable by the data logger (mV for pressure transducers and mA for pressure transmitters). The voltage signal can be measured by the data logger directly but the current signal must be converted to voltage signal first using a 500 Ω resistor. The data logger exports digital signals to a computer, in which the pressures are monitored and recorded by a purposely-developed program. Table 4.3 lists all pressure sensors used in the present experiments.

All pressure sensors were calibrated by a dead weight tester (Barnet Instrument Ltd, Series No 310/62, accuracy 0.1%). The test range (0-300 psi, i.e. 0-20.68 bar) covers the experimental range (6.0-14.0 bar). The output signals were compared with the actual applied pressures and a best-fit linear equation was produced for each sensor. The equations were then incorporated into the monitoring program, converting the mV or mA signals to pressure in bar.

Table 4.3 Pressure sensors in the experimental rig.

No.	Sensor	Manufacturer	Range	Output signal	Power supply
P1	GP series	RS	0-40 bar g	4-20 mA	12V
P2	PDCR 4010	Druck	0-10 bar a*	0-100 mV	12V
P3	PDCR 4010	Druck	0-20 bar a	0-100 mV	12V
P4	PDCR 910-0826	Druck	0-10 bar a*	0-100 mV	12V
P0	PDCR 910-0826	Druck	0-10 bar a*	0-100 mV	12V
P5	GP series	RS	0-40 bar g	4-20 mA	12V

*: Pressure transducers PDCR 4010 and 910-0826 allow 400% overpressure, i.e. the maximum allowed measuring range is 40 bar.

The following factors affect the accuracy of the pressure measurements:

- Accuracy of the calibration instrument, 0.1%.
- The power supply (12V) hardly affects the pressure transmitters (P1 and P5). However, the output signals of the pressure transducers, P2, P3, P4 and P0, are linear to the voltage of the power supply in the range of 1V to 12V. Therefore, the supplied voltage was measured and the measured pressures were compensated in the program to eliminate the effect of the voltage fluctuation.
- The output signals from the GP pressure transmitters (P1 and P5) are 4-20 mA current signals, which cannot be measured by the existing data logger. Therefore, a 500 Ω-wire wound pure resistor was used to convert the current signal into 2-10 V voltage signal for each sensor. The selected resistor has the characteristics of high accuracy (0.10%) and very low temperature-resistance coefficient in which the temperature effect can be neglected.
- The "dynamic" systematic error of the pressure sensor is given in Appendix E Table E.1.
- The "dynamic" systematic error of the data logger is given in Appendix E Table E.2.
- The calibration data and the produced best-fit equations are summarized in Appendix F Section F.1.

The combined uncertainty of the pressures is calculated as the root-sum-square (RSS) combination of the above elemental systematic errors, see Table 4.4.

Table 4.4 Combined uncertainty of the pressure measurement.

Elements	Systematic error						Experimental pressure
Pressure transducer	P1	P2	P3	P4	P0	P5	
Calibration standard	0.10%	0.10%	0.10%	0.10%	0.10%	0.10%	
Calibration equation	0.08%	0.12%	0.20%	0.18%	0.17%	0.27%	
12V power supply	0.00%	0.00%	0.00%	0.00%	0.00%	0.00%	
Pressure sensor	*	0.17%	0.35%	0.16%	0.16%	*	
Data logger	0.02%	0.04%	0.07%	0.04%	0.04%	0.02%	
Resistor	0.10%					0.10%	
Combined uncertainty	~0.16%	0.24%	0.42%	0.26%	0.26%	~0.31%	0.26%

*: The manufacturer did not provide the information on this error in the technical specification.

The uncertainty of sensors P1 and P5 is an estimated value because of the absence of the information on stability and temperature effect. They are actually not used in any calculations. The pressures measured by P3, P4 and P0 are the collected experimental data in the flow pattern visualization experiments. The experimental pressure at the visualization position is deduced from the pressures at the inlet and the outlet of the observation section, i.e.

$$p = Cp_4 + (1-C)p_0 \tag{4.12}$$

C is a ratio that represents the position of the visualization, which equates to L1/L in Figure 4.1. The uncertainty of the experimental pressure can be calculated by:

$$U_p^2 = C^2 U_{p_4}^2 + (1-C)^2 U_{p_0}^2 \tag{4.13}$$

In the current experiments, the pressure drop in the observation section was much smaller than the experimental pressure, i.e. $p \approx p_4 \approx p_0$. The uncertainty of p_4 and p_0 are the same, see Table 4.4. Therefore Equation 4.13 can be simplified as:

$$\left(\frac{U_p}{p}\right)^2 \approx \left[C^2 + (1-C)^2\right]\left(\frac{U_{p_4}}{p_4}\right)^2 \tag{4.14}$$

In the above equation, the coefficient $C^2 + (1-C)^2$ is bigger than 0.5 but smaller than 1 because the ratio C is between 0 and 1. Therefore, the uncertainty of the deduced experimental pressure at the visualization point is equal to or smaller than that of p_4 (or p_0).

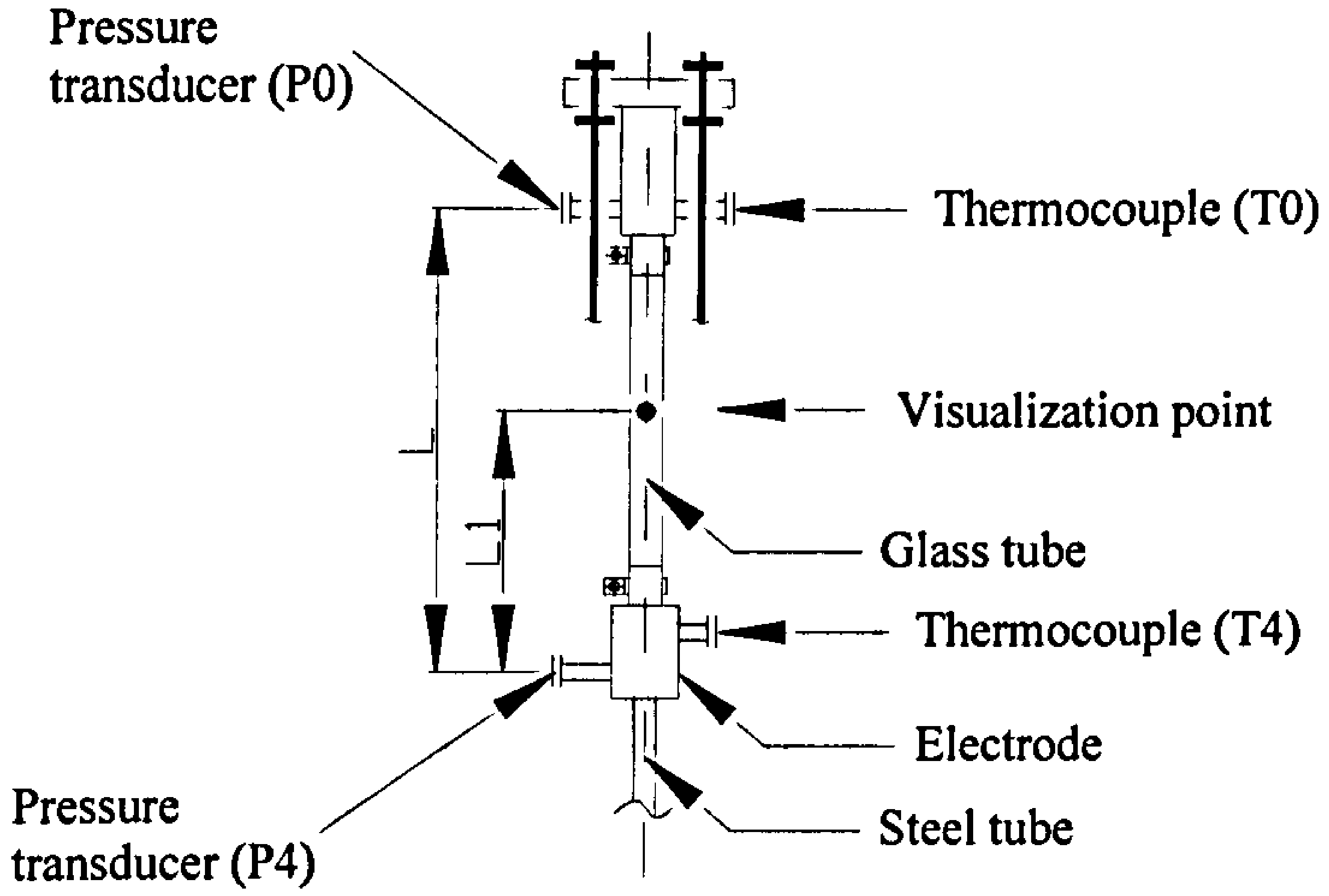

Figure 4.1 Sketch showing of the position of the visualization point.

(3) Thermocouples

Thermocouples convert temperature difference into voltage difference. The accuracy depends on the measurement of the reference temperature and the voltage signal. The measurement of the voltage signal has been introduced in the previous section. The reference temperature can be obtained in two ways, i.e. an external reference point or the use of the data logger input connection as the reference junction, called the cold junction compensation (CJC), through a thermal resistor. In the first case the water triple point (0.01 °C) is the most generally used reference temperature. It needs an additional ice/water box but provides higher precision. In the latter case the reference temperature is monitored and any change is compensated by the data logger into the measured temperature automatically. This inevitably introduces an extra error though it is a simpler method. Therefore, all the temperatures used as the experimental data employed the first method and the others, not actually needed in this study, used the second method, see Table 4.5. The readings from thermocouples T1, T5 and T6, which used the second method, were converted by the data logger into temperature. The readings from thermocouples T2, T3, T4, T0 and TT1-15, which used the first method, were voltage and this was converted into temperature in the PC using the best-fit equations. In order to insure a constant triple-phase point, the cold junctions were put in individual glass tubes filled with transformer oil. The tubes were immersed in the ice-water mixture stored in an insulated box. The temperature of the mixture was observed by a high accuracy National Physical Laboratory mercury-in-glass thermometer.

Table 4.5 Thermocouples in the experimental rig.

No.	Type	Calibration Range (°C)	Experiment Range (°C)	Data logger	Reference
T1	K type ungrounded probe	-18 - 66	20 - 55	SI 3535F	CJC
T2	K type ungrounded probe	-18 - 66	20 - 55	SI 3535F	triple point
T3	T type grounded needle probe	-20 - 80	20 - 55	SI 35951E	triple point
T4	T type grounded needle probe	-20 - 80	20 - 55	SI 35951E	triple point
T0	T type grounded needle probe	-20 - 80	20 - 55	SI 35951E	triple point
T5	K type ungrounded probe	-18 - 66	20 - 55	SI 3535F	CJC
T6	K type ungrounded probe	-18 - 66	20 - 55	SI 3535F	CJC
TT_{1-15}	K type thermocouple wires	-20 - 80	> 20	SI 35951E	triple point

Two types of thermocouples, K and T, were used in the experiments. Three T-type grounded thermocouples were installed in the test sections since only this type thermocouple was available as needle probe. Fifteen K-type thermocouple wires were equally spaced and welded on the outside wall of the heating section to measure the temperature distribution. Other thermocouples were K-type ungrounded probes to reduce electronic noise. Two data loggers were used in the experiments, i.e. SI 3535F and SI 35951E. The maximum allowed input voltage to ground in SI 3535F is ± 14 V because of the limitation of the analog input module 35301J. The test section floats above earth and its voltage to ground was higher than 14 V. Therefore, all the thermocouples in the test section, including T3, T4, T0 and TT1-15, connected to SI 35951E data logger for which the maximum allowed voltage to ground is 500 V. The calibrated temperature range covered the experimental range. However, the tube wall of the heating section could reach very high temperature when critical heat flux occurred. The standard temperature-voltage correlation for K-type thermocouple supplied by the manufactory replaced the user-defined equations when the measured temperature was above 80 °C.

All the thermocouples were calibrated in a temperature calibration equipment which was available in the Department of Engineering of Queen Mary, University of London. The unit is composed of a bath, a stirrer, a heater, a cooling system, a temperature controller and a high accuracy platinum resistance thermometer (R100 014), as presented in Figure 4.2. The working fluid is antifreeze TYFOXIT 1.18 which has a freezing point of –35 °C. The thermometer measures the liquid temperature with ±0.02 Ω (equivalent to ±0.05 K) uncertainty in the range of –80 to 300 °C. In the middle of the bath is a constant temperature zone namely the calibration zone. The thermometer and the thermocouples to be calibrated are put together in that zone. In a similar manner to the pressure sensors, the output signals from the thermocouples are compared with the reading of the thermometer and a three-order polynomial equation is produced for each thermocouple. The equations are integrated in the monitoring program to convert the mV signals to the temperatures. The calibration data for the thermocouples are shown in Appendix F Section F.2.

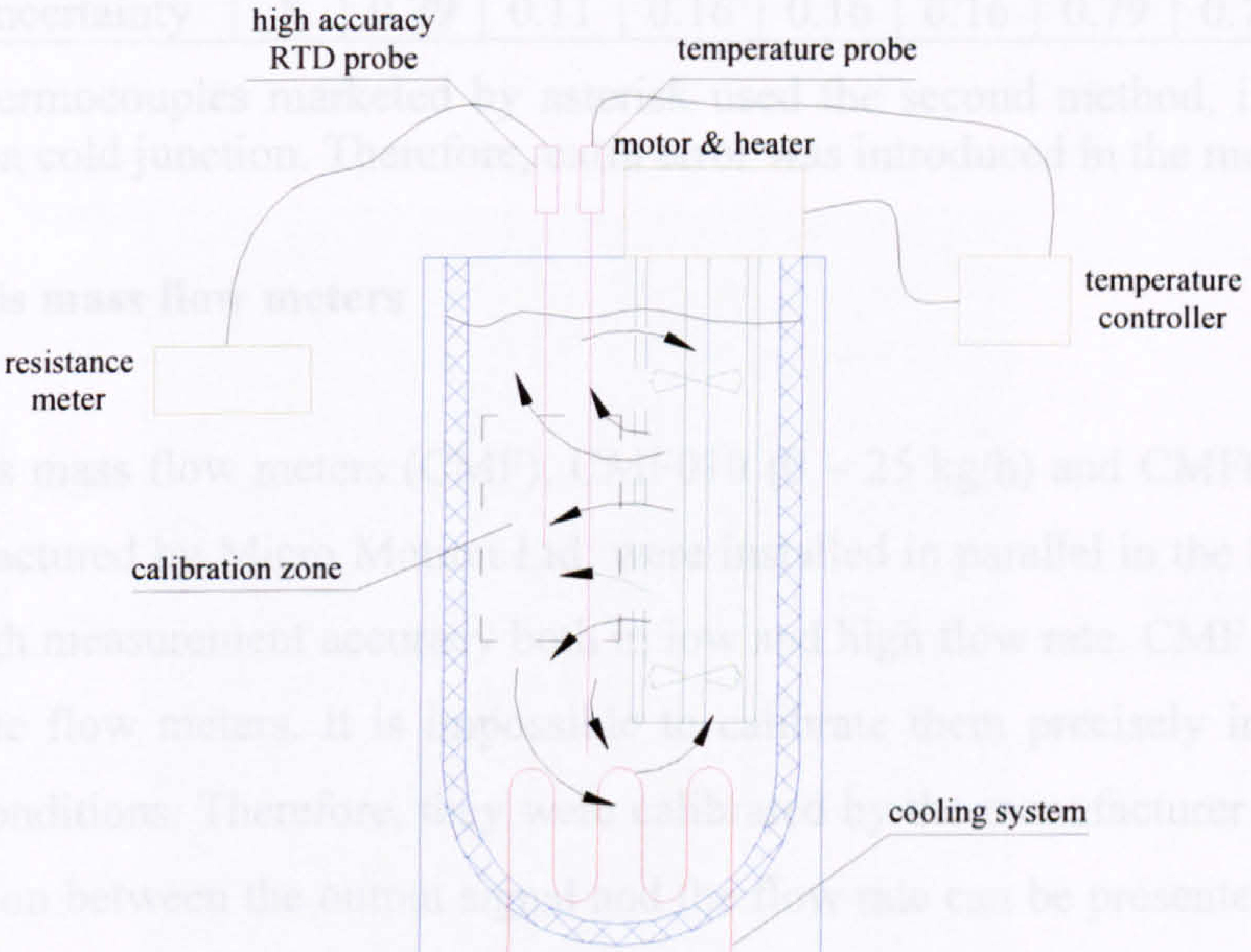

Figure 4.2 Sketch of the temperature calibration equipment.

According to the calibration process and the signal transmitted, in assessing the measuring error, the following must be considered:

- The measuring error of the calibration machine are analyzed and presented in Appendix F Section F.2 Tables F.8-F.10 and Figure F.7. The error includes systematic error and random error.
- The produced best-fit equations, which are summarized in Appendix F Section F.2 Tables F.11-F.19 and Figures F.8-F.15.
- The systematic error caused by the data logger is given in Appendix E Section E.2 Table E.3.

The combined uncertainty on the temperature measurement is calculated as the root-sum-square (RSS) combination of the above elemental systematic errors, which is summarized in Table 4.6.

Table 4.6 Combined uncertainty of the temperature measurement.

Instruments	Unit	Error							
Thermocouple		T1*	T2	T3	T4	T0	T5*	T6*	$TT_{1\text{-}15}$
Calibration equipment	K	0.07	0.07	0.07	0.07	0.07	0.07	0.07	0.07
Calibration equation	K	0.03	0.02	0.04	0.04	0.04	0.03	0.04	0.02
Data logger	K	0.79	0.08	0.14	0.14	0.14	0.79	0.79	0.14
Combined uncertainty	K	0.79	0.11	0.16	0.16	0.16	0.79	0.79	0.16

Note: the thermocouples marketed by asterisk used the second method, i.e. automatic compensation cold junction. Therefore, extra error was introduced in the measurement.

(4) Coriolis mass flow meters

Two Coriolis mass flow meters (CMF), CMF010 (0 – 25 kg/h) and CMF025 (0 – 500 kg/h) manufactured by Micro Motion Ltd, were installed in parallel in the loop in order to ensure high measurement accuracy both in low and high flow rate. CMF is one of the most accurate flow meters. It is impossible to calibrate them precisely in the current laboratory conditions. Therefore, they were calibrated by the manufacturer with R134a. The correlation between the output signal and the flow rate can be presented by a linear equation for each meter, see Appendix F Section F.3. The errors caused by the date logger and the 500 Ω-wire wound pure resistor should be considered properly. The systematic error of the date logger is given in Appendix E Table E.4. The combined uncertainty is the root-sum-square (RSS) combination of the above elements and a function of flow rate. The calculation results is summarized in Appendix E Table E.5 and presented in Figure 4.3.

As stated above, the CMF accuracy provided by the manufacturer is so high that they cannot be validated accurately in the laboratory. However, a verification test was carried out to ascertain "near enough" measured values and that the meters were correctly installed. The calibration system includes a stainless steel tube which is parallel with the test section and a differential pressure transmitter to measure the liquid level lift in a certain time interval.

$$\Delta h = \Delta p / \rho g \tag{4.15}$$

The mass flow rate can then be calculated from the mass obtained during this specified interval of time.

$$m = \frac{\pi D^2 \Delta p}{4 g \Delta t} \tag{4.16}$$

The difference between the reading of the CMFs and the flow rate deduced from the above equation was between 0.9% to 4.9% for the mass flow rate of 4.9 to 243.7 kg/hr, see Table 4.7. Considering the liquid level fluctuation, the result is reasonable. Therefore, we can conclude that the CMFs were installed correctly and work properly.

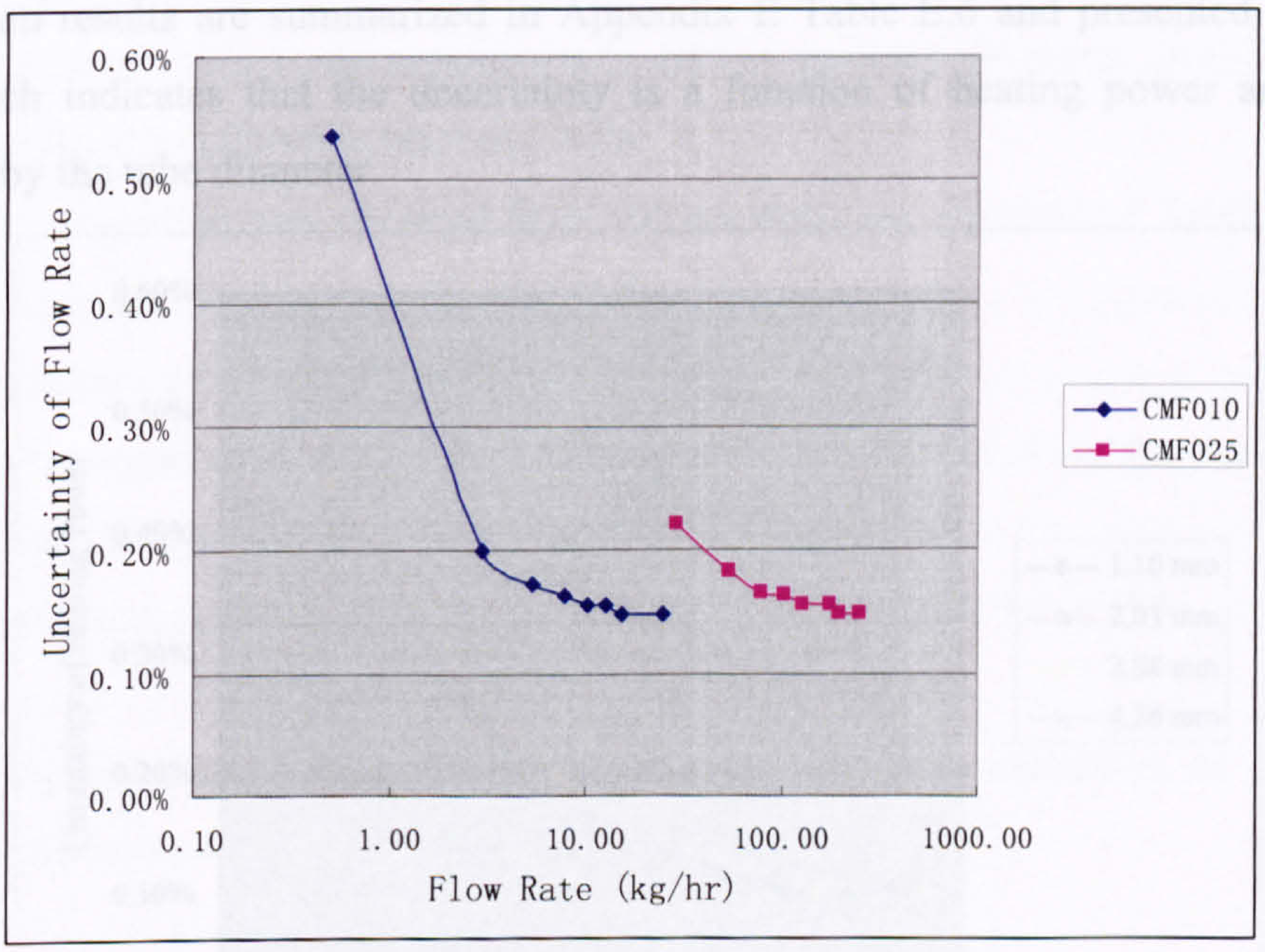

Figure 4.3 Combined uncertainty of the flow rate measurement.

Table 4.7 Verification of the Coriolis mass flow meters.

Items	Unit	CMF010				CMF025					
Diameter	mm	24.0	24.0	24.0	24.0	72.9	72.9	72.9	72.9	72.9	72.9
Different Pressure	Pa	8489	12679	9800	14500	6280	6100	8220	11700	15230	18950
Time interval	s	300	450	249	119	125	126	122	110	123	123
Calculated flow rate	kg/hr	4.70	4.68	6.54	20.24	76.98	74.18	103.2	163.0	189.7	236.1
Measured flow rate	kg/hr	4.94	4.91	6.83	20.58	78.35	76.84	107.5	164.5	199.2	243.7
Deviation		-4.9%	-4.8%	-4.2%	-1.7%	-1.7%	-3.5%	-4.0%	-0.9%	-4.8%	-3.1%

(5) Power meters

Two instruments are involved in the measurement of the heating power supplied to the test sections; the digital power meter, WT110 manufactured by Yokogawa Electric Corporation and the current transformer, produced by D.K. Moriarty Ltd. The current passing through the heating section can reach a very high value (up to 200 A) due to the low resistance coefficient of stainless steel. This is beyond the range of the power meter. Therefore, a current transformer was used to scale down the current to an acceptable range for the power meter, and the combined uncertainty includes the uncertainty of the current transformer and the power meter. Similar to the mass flow meters, the accuracy of the power meter and the current transformer was provided by the manufacturers. The calculation results are summarized in Appendix E Table E.6 and presented in Figure 4.4, which indicates that the uncertainty is a function of heating power and hardly affected by the tube diameter.

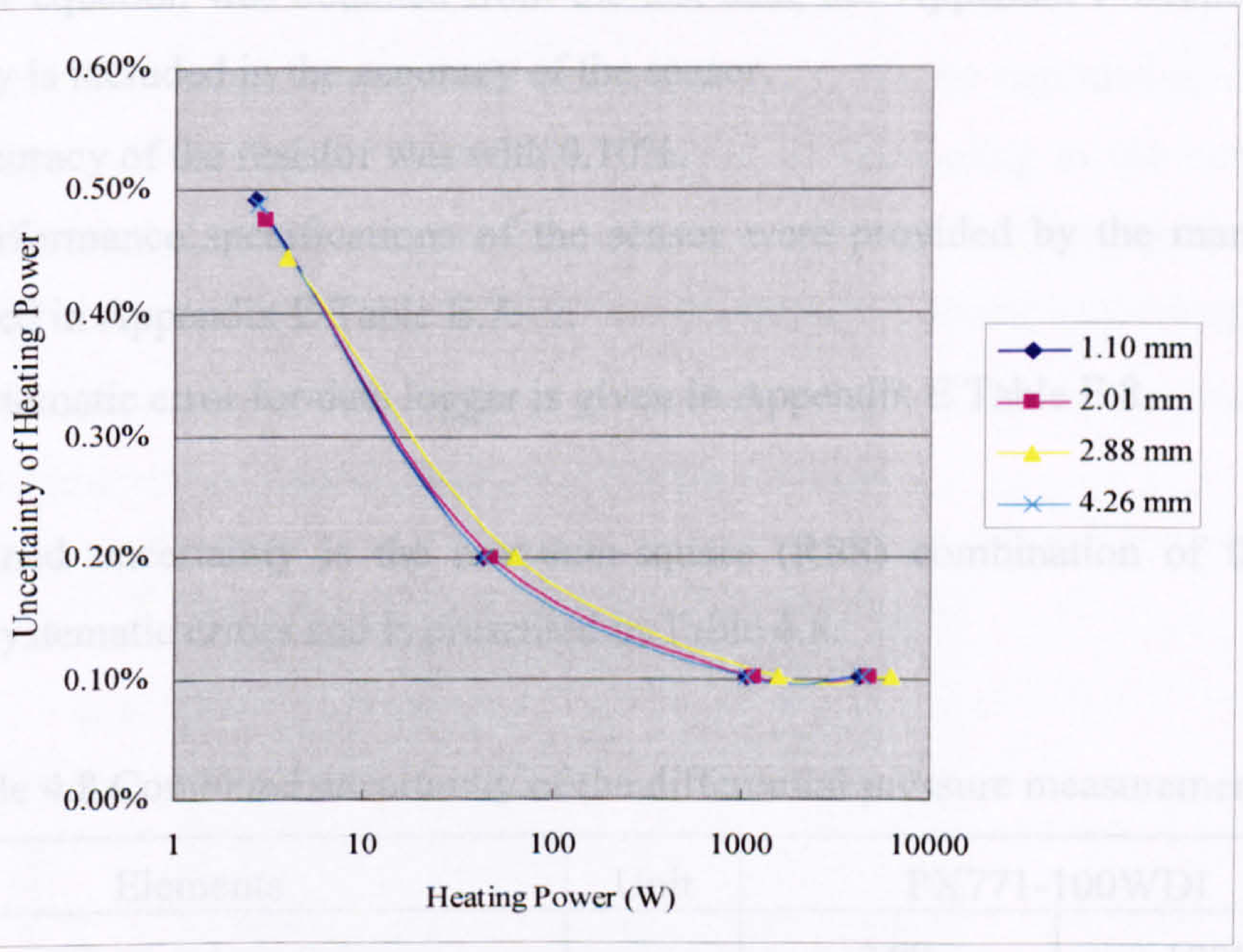

Figure 4.4 Combined uncertainty of the heating power on the test sections.

(6) Differential pressure transmitter

The entire experimental facility was validated in single-phase experiments by measuring the pressure drop at the test sections and comparing it with the Blasius's or Haaland's correlations, see Section 4.3. The pressure drop was measured by a differential pressure transmitter. The operation is the same as for the pressure transmitters, using a 500 Ω resistor to convert 4-20 mA current to 2-10V voltage signal then received by the data logger. The measuring uncertainty was analyzed as follows:

- The differential pressure transmitter was calibrated through measuring the water level difference at both sides of the transmitter. The measuring results are summarized in Appendix F Section F.4.

  The calibration uncertainty can be estimated as following:

  $$\Delta p = \rho g \Delta h \tag{4.17}$$

  The error in the water density, ρ and gravitational acceleration, g can be neglected. Hence, the uncertainty of Δp is:

  $$U_{\Delta p} = \rho g U_{\Delta h} \tag{4.18}$$

  A tape meter with 1 mm accuracy was used to measure the water level difference. Therefore, the calibration error is 9.8 Pa.
- A linear equation was obtained from the test data, see Appendix F Section F.4. Its linearity is included in the accuracy of the sensor.
- The accuracy of the resistor was with 0.10%.
- The performance specifications of the sensor were provided by the manufacturer and listed in Appendix E Table E.7.
- The systematic error for data logger is given in Appendix E Table E.8.

The combined uncertainty is the root-sum-square (RSS) combination of the above elemental systematic errors and is presented in Table 4.8.

Table 4.8 Combined uncertainty of the differential pressure measurement.

Elements	Unit	PX771-100WDI	
Full scale		24%	100%
	bar	0.0608	0.2491
Calibration method	Pa	9.8	9.8
Differential pressure transmitter	Pa	17.7	72.6
Data logger	Pa	0.6	2.2
Resistance		0.10%	0.10%
Measurement error caused by resistance	Pa	6.1	24.9
Combined uncertainty	Pa	21.2	77.4

(7) The inlet temperature at the heating section

The liquid temperature after the preheater can be adjusted to a certain degree of subcooling through controlling the power supply of the preheater. Therefore, the liquid temperature at the inlet of the test sections can be calculated if we know the thermal loss between the preheater and the test sections. The equation for the above calculation is as follows:

$$dQ = \frac{K}{L}(T - T_a)dl = -c_p m dT \tag{4.19}$$

Therefore,

$$\int_0^L \frac{-K}{Lc_p m} dl = \int_{T_7}^{T_3} \frac{1}{T - T_a} dT \tag{4.20}$$

$$T_3 = T_a + (T_7 - T_a)e^{\frac{-K}{c_p m}} \tag{4.21}$$

In the experimental range, the specific heat capacity, c_p can be regarded as a constant, approximately 1.48 kJ/(kg K). The default degree of subcooling at the outlet of the preheater is 0 to –5 K. The measured thermal loss coefficient K of the pipe between the preheater and the test section is 0.30 W/K and the default ambient temperature T_a is 20 °C. Figure 4.5 summarizes the deduced temperature at the inlet of the test sections based on different experimental pressure and mass flow rate.

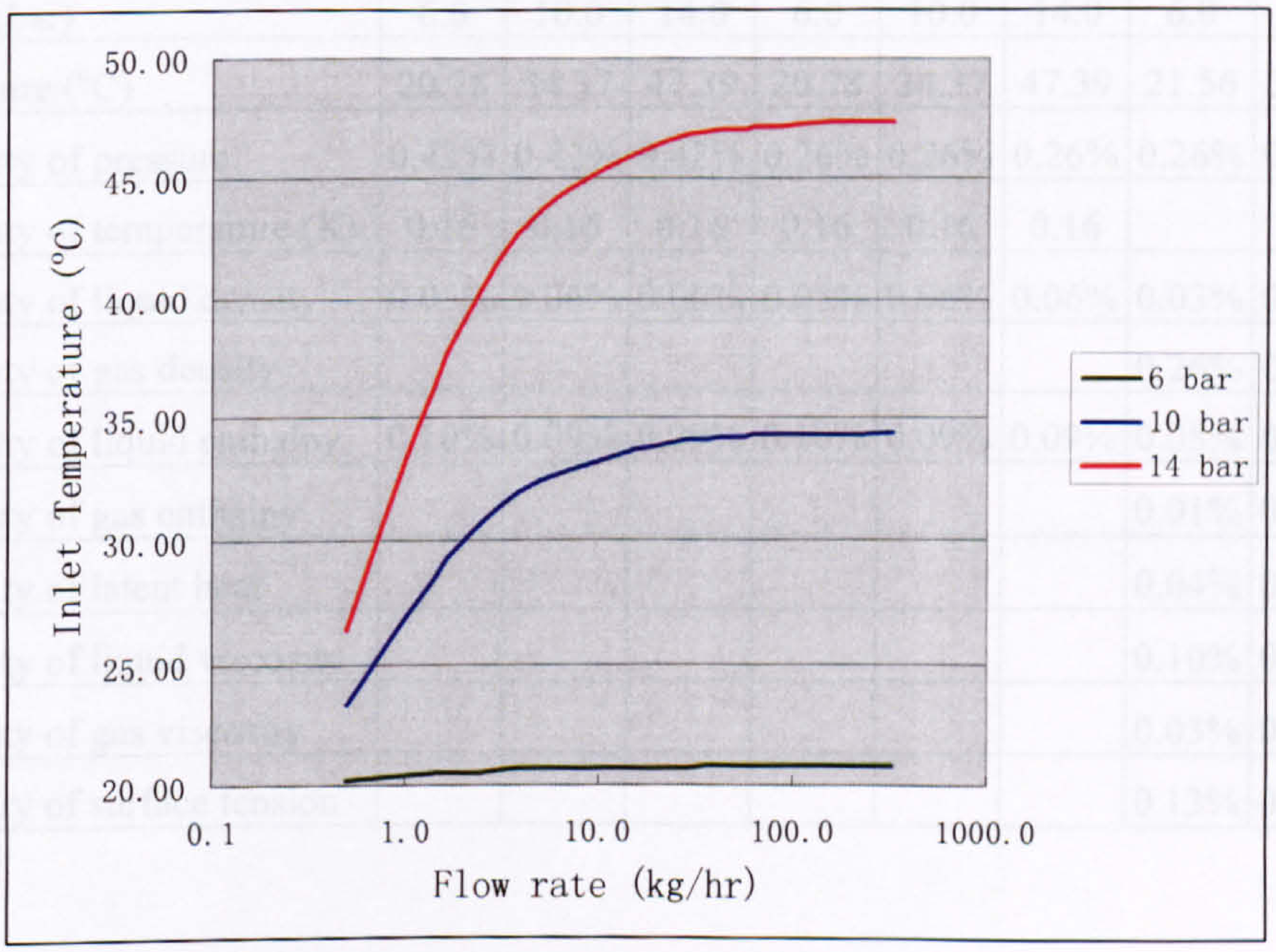

Figure 4.5 Temperature at the inlet of the test section.

(8) Fluid properties and associated uncertainty

Fluid properties, such as density, enthalpy, viscosity and surface tension, are functions of the temperature and pressure. At saturated state, the above parameters only depend on either pressure or temperature. Considering the accuracy of the pressure transducers is better than that of the thermocouples, the two-phase fluid parameters are obtained from the pressure sensors only.

However, it is very difficult to obtain the differential function directly because of the complexity of the property functions. Therefore, a numerical method presented in Equation 4.22 was proposed to estimate the uncertainty of fluid properties. This function has been integrated in the data analysis program. The calculation results at the different conditions are summarized in Table 4.9.

$$U_r^2 = \left[\frac{r_{(T+\Delta T,P)} - r_{(T,P)}}{\Delta T}\right]^2 U_T^2 + \left[\frac{r_{(T,P+\Delta P)} - r_{(T,P)}}{\Delta P}\right]^2 U_P^2 \qquad (4.22)$$

Table 4.9 Combined uncertainty of the fluid parameters.

Items	Heating section inlet			Observation section inlet and outlet			Observation section		
Fluid state	Single - phase fluid						Two - phase fluid		
Pressure (bar)	6.0	10.0	14.0	6.0	10.0	14.0	6.0	10.0	14.0
Temperature (°C)	20.78	34.37	47.39	20.78	34.37	47.39	21.56	39.40	52.45
Uncertainty of pressure	0.42%	0.42%	0.42%	0.26%	0.26%	0.26%	0.26%	0.26%	0.26%
Uncertainty of temperature (K)	0.16	0.16	0.16	0.16	0.16	0.16			
Uncertainty of liquid density	0.05%	0.06%	0.06%	0.05%	0.06%	0.06%	0.03%	0.04%	0.05%
Uncertainty of gas density							0.26%	0.27%	0.29%
Uncertainty of liquid enthalpy	0.10%	0.09%	0.09%	0.10%	0.09%	0.09%	0.05%	0.06%	0.06%
Uncertainty of gas enthalpy							0.01%	0.01%	0.01%
Uncertainty of latent heat							0.04%	0.06%	0.09%
Uncertainty of liquid viscosity							0.10%	0.11%	0.12%
Uncertainty of gas viscosity							0.03%	0.04%	0.05%
Uncertainty of surface tension							0.13%	0.19%	0.26%

(9) Thermal loss and associated uncertainty

The thermal loss at the test section can be calculated by the following equation:

$$\Delta Q = K\Delta\overline{T} \tag{4.23}$$

Here, K is the thermal loss coefficient of the test section and $\Delta\overline{T}$ is the average temperature difference at both sides of the insulation layer. The uncertainty is given by

$$U_{\Delta Q}^2 = \left(\Delta\overline{T}U_K\right)^2 + \left(KU_{\Delta\overline{T}}\right)^2 \tag{4.24}$$

The thermal loss at the heating section is discussed first. The average temperature at the inner side of the insulation can be obtained approximately from the fifteen thermocouple wires which are welded on the tube wall of the heating section. The outer temperature (T_{out}) is sampled by a K-type thermocouple placed at the middle of the heating section since there is negligible temperature difference for the ambient temperature along the heating section. Therefore, $\Delta\overline{T}$ can be estimated by

$$\Delta\overline{T} = \frac{1}{15}\sum_{i=1}^{15}\left(T_{in}\right)_i - T_{out} \tag{4.25}$$

The uncertainty of $\Delta\overline{T}$ can be calculated from:

$$U_{\Delta\overline{T}}^2 = \frac{1}{15^2}\sum_{i=1}^{15}\left(U_{T_{in}}^2\right)_i + U_{T_{out}}^2 \tag{4.26}$$

$U_{T_{in}}$ and $U_{T_{out}}$ have been given in Table 4.6, are 0.16 K. Therefore, the uncertainty of $\Delta\overline{T}$ is 0.165 K.

The thermal loss coefficient is assumed to be a constant and was obtained from the single-phase experiments. In single-phase flow, the thermal loss at the heating section can be calculated from:

$$\Delta Q = m(h_3 - h_4) \tag{4.27}$$

Combining with Equation 4.23, we can get the thermal loss coefficient at the heating section and its uncertainty as follows:

$$K = \frac{m(h_3 - h_4)}{\Delta\overline{T}} \tag{4.28}$$

$$U_K^2 = \left(\frac{h_3 - h_4}{\Delta\overline{T}}\right)^2 U_m^2 + \left(\frac{m}{\Delta\overline{T}}\right)^2\left(U_{h_3}^2 + U_{h_4}^2\right) + \left[\frac{m\left(h_3 - h_4\right)}{\Delta\overline{T}^2}\right]^2 U_{\Delta\overline{T}}^2 \tag{4.29}$$

$$\left(\frac{U_K}{K}\right)^2=\left(\frac{U_m}{m}\right)^2+\frac{\left(U_{h_3}^2+U_{h_4}^2\right)}{(h_3-h_4)^2}+\left(\frac{U_{\Delta\overline{T}}}{\Delta\overline{T}}\right)^2 \tag{4.30}$$

Obviously, the temperature difference $\Delta\overline{T}$ and the enthalpy difference h_3-h_4 should be big enough to allow accurate assessment of U_K. Therefore, the single-phase experiments for thermal loss test were run at low mass flow rate and high inlet temperature. For example, in one of the thermal loss experiments where the tube diameter was 4.26 mm, the flow rate was 2.03 kg/hr, the experimental pressure was 14 bar, the inlet and outlet liquid temperatures were 39.1 °C and 37.6 °C respectively, the average inside and outside temperatures of the insulation were 38.4 °C and 19.8 °C, the deduced thermal loss coefficient calculated using equation 4.28 of the heating section was 0.068. The uncertainty of the thermal loss coefficient is

$$\frac{U_K}{K}=\left[(0.54\%)^2+\frac{(255196\times 0.094\%)^2+(252959\times 0.094\%)^2}{(255196-252959)^2}+\left(\frac{0.165}{38.4-19.8}\right)^2\right]^{1/2}$$
$$=15.11\%$$

During the thermal loss tests, the experimental rig was warmed up at least for three hours whilst a program was developed to monitor the thermal loss coefficient continually to ensure the system had reached thermal balance and could obtain a constant thermal loss coefficient, see also the introduction in Appendix D Section D.2 (5). The experimental results and the uncertainty analysis, associated with the mass flow rate, the temperature difference between the pipe wall and ambient, the fluid enthalpy at the inlet and outlet of the test sections and their uncertainty, are calculated based on Equations 4.28 and 4.30 and summarized in Appendix E Table E.9.

Considering the fact that the observation section and the heating section use the same insulation material and thickness, we can assume that their thermal loss per unit length is the same. Therefore, the thermal loss between the inlet of the heating section and the visualization point can be deduced from the thermal loss at the heating section by multiplying by a length ratio. The thermal loss of the test sections and their uncertainty are calculated and summarized in Appendix E Table E.10 and presented in the Figure 4.6.

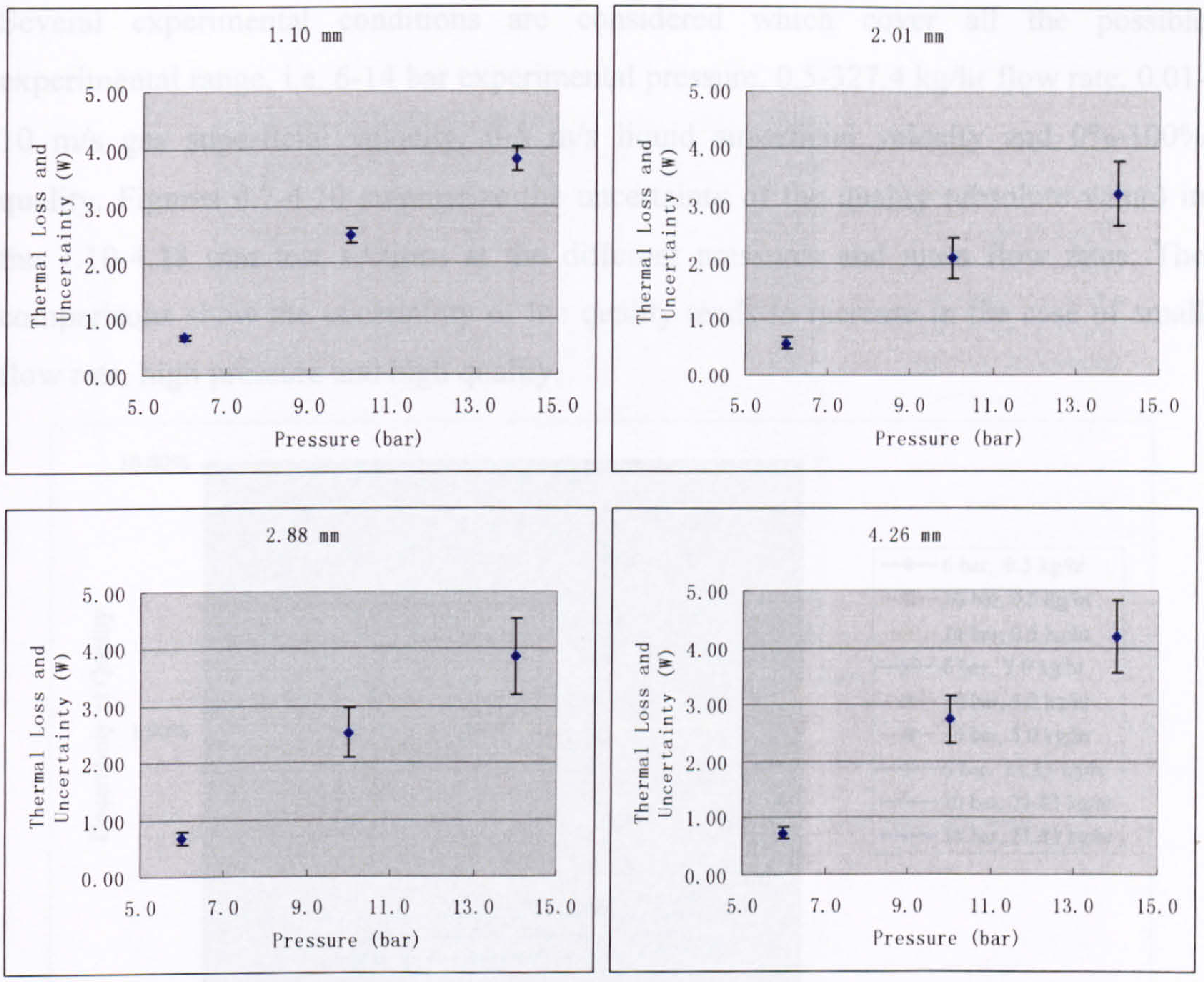

Figure 4.6 Thermal loss and the uncertainty in the four tubes.

(10) Quality and associated uncertainty

The quality is calculated based on the equation below, i.e.

$$x = \frac{h - h_l}{h_{fg}} \tag{4.31}$$

Here, h is the enthalpy of the two-phase mixture,

$$h = h_3 + \frac{Q - \Delta Q}{m} \tag{4.32}$$

The uncertainty of the enthalpy and the quality can be obtained from:

$$U_h^2 = \left(U_{h_3}\right)^2 + \left(\frac{U_Q}{m}\right)^2 + \left(\frac{U_{\Delta Q}}{m}\right)^2 + \left(\frac{Q - \Delta Q}{m^2} U_m\right)^2 \tag{4.33}$$

$$U_x^2 = \left(\frac{U_h}{h_{fg}}\right)^2 + \left(\frac{U_{h_l}}{h_{fg}}\right)^2 + \left(\frac{h - h_l}{h_{fg}^2} U_{h_{fg}}\right)^2 \tag{4.34}$$

Several experimental conditions are considered which cover all the possible experimental range, i.e. 6-14 bar experimental pressure, 0.5-327.4 kg/hr flow rate, 0.01-10 m/s gas superficial velocity, 0-5 m/s liquid superficial velocity and 0%-100% quality. Figures 4.7-4.10 summarize the uncertainty of the quality (absolute value) in the 1.10-4.28 mm test sections at the different pressures and mass flow rates. The comparisons show the uncertainty of the quality tends to increase in the case of small flow rate, high pressure and high quality.

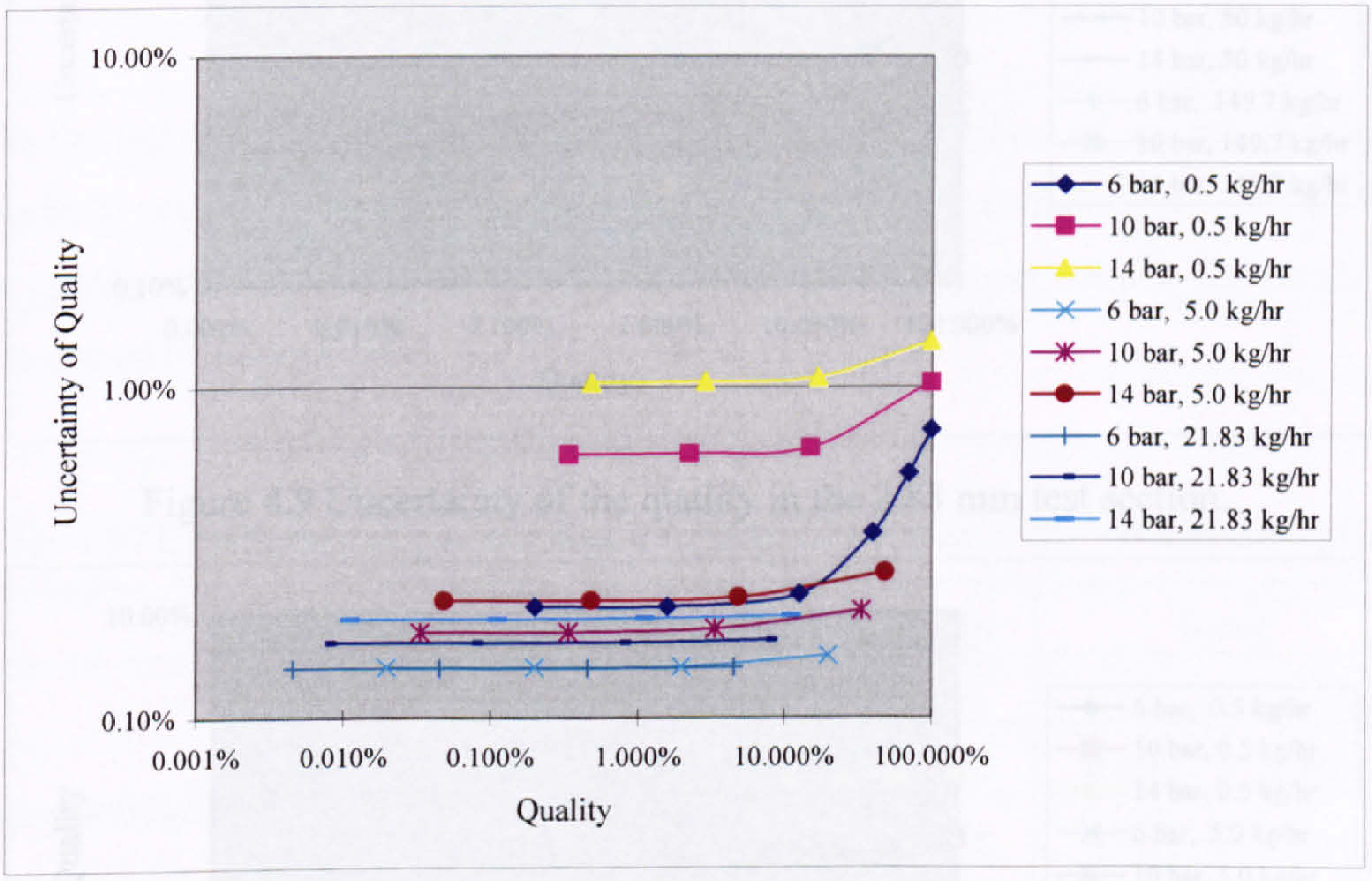

Figure 4.7 Uncertainty of the quality in the 1.10 mm test section.

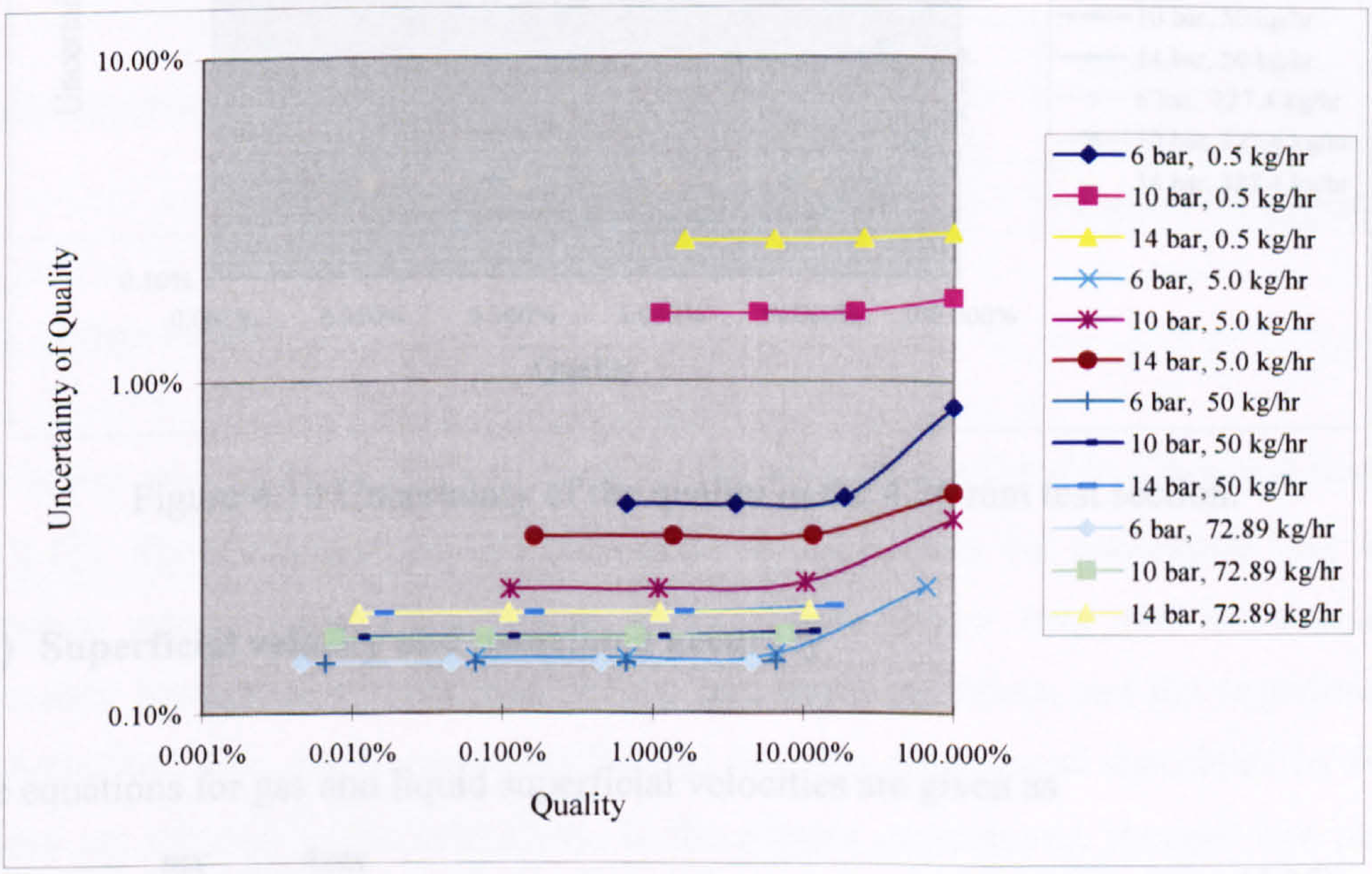

Figure 4.8 Uncertainty of the quality in the 2.01 mm test section.

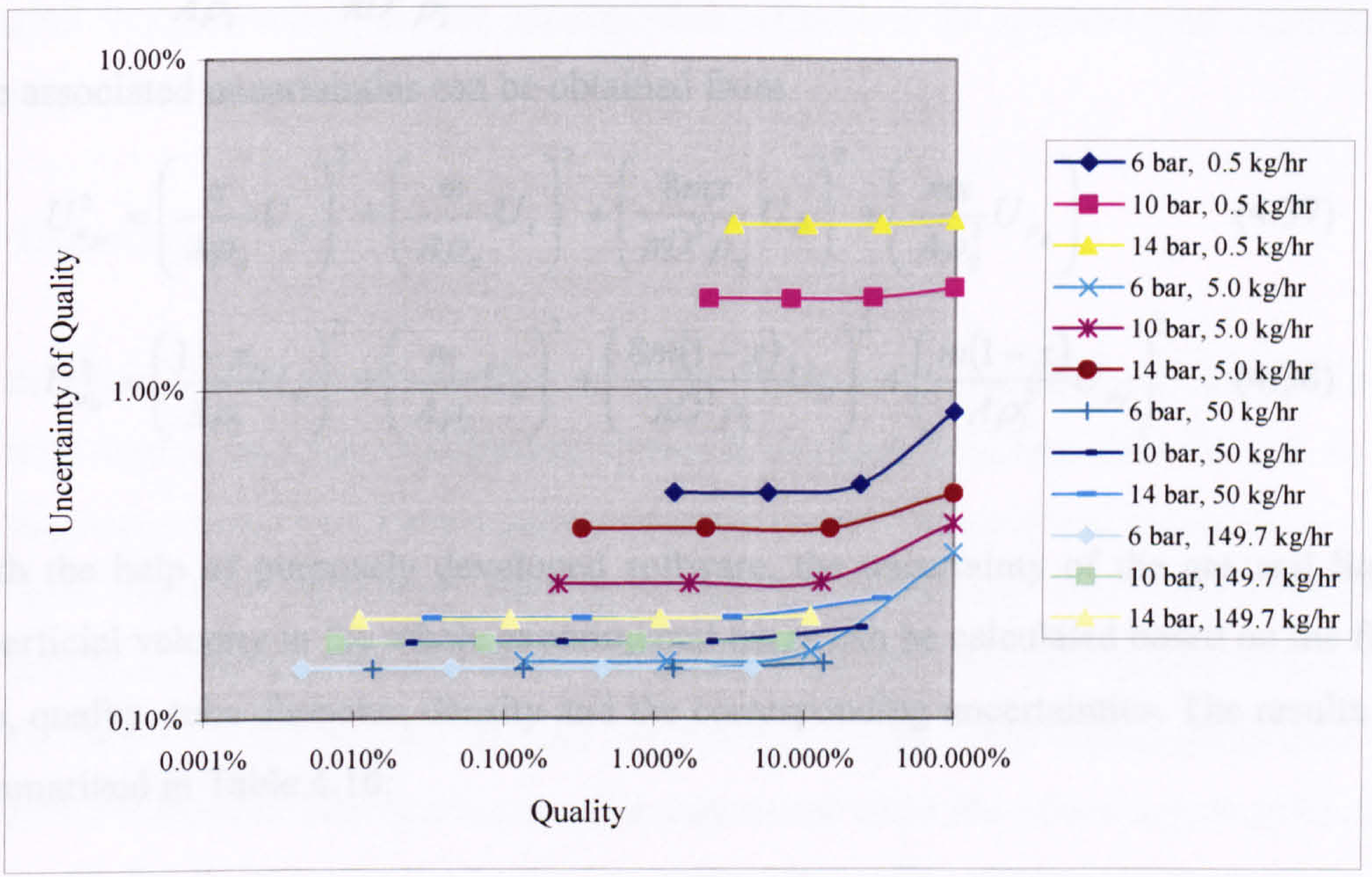

Figure 4.9 Uncertainty of the quality in the 2.88 mm test section.

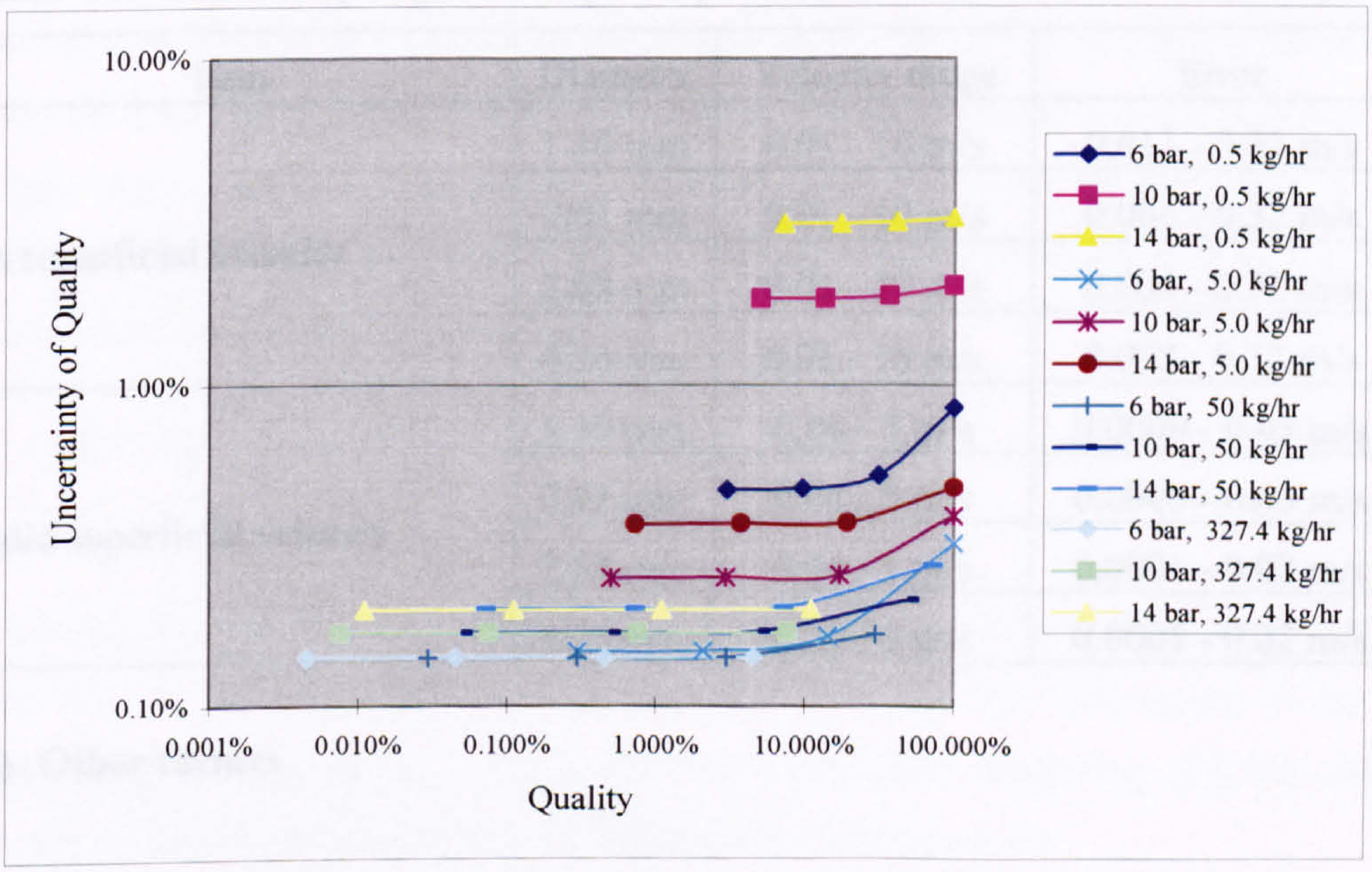

Figure 4.10 Uncertainty of the quality in the 4.26 mm test section.

(11) Superficial velocity and associated accuracy

The equations for gas and liquid superficial velocities are given as

$$u_{gs} = \frac{mx}{A\rho_g} = \frac{4mx}{\pi D^2 \rho_g} \tag{4.35}$$

$$u_{ls} = \frac{m(1-x)}{A\rho_l} = \frac{4m(1-x)}{\pi D^2 \rho_l} \tag{4.36}$$

The associated uncertainties can be obtained from

$$U_{u_{gs}}^2 = \left(\frac{x}{A\rho_g}U_m\right)^2 + \left(\frac{m}{A\rho_g}U_x\right)^2 + \left(\frac{8mx}{\pi D^3 \rho_g}U_D\right)^2 + \left(\frac{mx}{A\rho_g^2}U_{\rho_g}\right)^2 \tag{4.37}$$

$$U_{u_{ls}}^2 = \left(\frac{1-x}{A\rho_l}U_m\right)^2 + \left(\frac{m}{A\rho_l}U_x\right)^2 + \left(\frac{8m(1-x)}{\pi D^3 \rho_l}U_D\right)^2 + \left(\frac{m(1-x)}{A\rho_l^2}U_{\rho_l}\right)^2 \tag{4.38}$$

With the help of purposely developed software, the uncertainty of the gas and liquid superficial velocity in the whole experimental range can be calculated based on the flow rate, quality, tube diameter, density and the corresponding uncertainties. The results are summarized in Table 4.10:

Table 4.10 Uncertainty of gas and liquid superficial velocity at the visualization point.

Item	Diameter	Velocity range	Error
Gas superficial velocity	1.10 mm	0.01 - 10 m/s	0.011 - 0.32 m/s
	2.01 mm	0.01 - 10 m/s	0.006 - 0.32 m/s
	2.88 mm	0.01 - 10 m/s	0.004 - 0.32 m/s
	4.26 mm	0.01 - 10 m/s	0.002 - 0.32 m/s
Liquid superficial velocity	1.10 mm	0.04 - 5 m/s	0.0009 - 0.05 m/s
	2.01 mm	0.04 - 5 m/s	0.0003 - 0.03 m/s
	2.88 mm	0.04 - 5 m/s	0.0001 - 0.02 m/s
	4.26 mm	0.04 - 5 m/s	0.0001 - 0.02 m/s

(12) Other factors

The above uncertainty analysis is based on the assumptions listed in Chapter 4 Section 4.1.2 (2). These assumptions are reasonable in most cases but sometimes they may introduce considerable experimental errors. These errors may not be evaluated accurately because of the limitation of the laboratory conditions and the experimental methodology. As a result some experimental data that are affected significant by these factors are rejected in the later study. In the present experiments, thermal loss in the observation section and the pressure at the visualization point are estimated based on a series of assumptions. Their effect on two-phase flow state has been discussed in Chapter 3 Section 3.3. In this section, their effect on the experimental accuracy is discussed further.

A. Thermal loss

As mentioned in Chapter 4 Section 4.1.2 (2), the thermal loss between the inlet of the heating section and the visualization point is deduced from the thermal loss in the heating section based on the assumption that the thermal loss per unit length is the same for both sections. However, the above calculation method may overestimate or underestimate the thermal loss in the observation section. The overestimation may due to the fact that the heating section always has higher wall temperature than the observation section. The underestimation may occur when the experimental pressure is 10 or 14 bar because about 25-30 mm long glass tube (observable section) at the visualization point is exposed to lower ambient temperature. The thermal loss in the observable section is difficult to be calculated accurately in the present experiments. However, it can be expected that its influence on the measurement results is increasing in higher temperature, smaller diameter tube and lower flow velocity. The magnitude of the thermal loss in the observable section is estimated below to investigate its effect on the experimental results, see Equation 4.39.

$$\Delta Q = \frac{T_f - T_a}{\sum R} + \varepsilon A \sigma \left(T_w^4 - T_a^4\right) \tag{4.39}$$

The overall thermal resistance ΣR includes the resistances from forced convection of the liquid film in the tube, conduction of the glass tube and free convection of the air surrounding. The resistance of the liquid film is negligible comparing with the others. The overall thermal resistance can be calculated by Equation 4.40:

$$\sum R = R_p + R_a \tag{4.40}$$

The resistance of the Pyrex glass tube can be obtained by:

$$R_p = \frac{\ln \dfrac{D_{out}}{D_{in}}}{2\pi k_p L} \tag{4.41}$$

The worst case can be expected in the experiment for the 1.10 mm tube at 14 bar, in which case the effect of thermal loss was most significant as shown in Figure 4.11.

Therefore, the parameters in the above equation can be given as: D_{out}=7.8 mm, D_{in}=1.10 mm, L=30 mm and k_p=1.4 W/m.K. Then the thermal resistant of the glass tube can be calculated as:

$$R_p = \frac{\ln(7.8/1.1)}{2\pi \times 1.4 \times 0.03} = 7.42 \ K/W$$

If the free convection of surrounding air is the main thermal resistance in Equation 4.40, the temperature of the tube wall is approximate to the saturated temperature of 14 bar, i.e. T_W = 325.65 K (52.5 °C). If we also assume that the room temperature is T_a = 293.15 K (20 °C), the referent temperature of air can be given as: T_{ref} = (325.65+293.15)/2 = 309.04 K. Then the fluid properties can be obtained based on the reference temperature, i.e. $\beta = 1/T_{ref} = 1/309.04 = 0.00323$ 1/K, $\nu = 16.85\text{x}10^{-6}$ m^2/s, k = 0.027 W/m.K and Pr = 0.706.

$$\begin{aligned} Gr\Pr &= \frac{g\beta(T_w - T_a)L^3 \Pr}{\nu^2} \\ &= \frac{9.81 \times 0.00323 \times (325.65 - 293.15) \times 0.03^3 \times 0.706}{(16.85 \times 10^{-6})^2} \\ &= 6.91 \times 10^4 \end{aligned}$$

Therefore, the free convection is at laminar state because the calculated GrPr is smaller than the critical value for the differentiation of laminar and turbulence flow, i.e. $1\text{x}10^9$ (Incropera and DeWitt, 1996). The convection heat transfer coefficient h can be calculated based on the semi-empirical correlation for free convection at laminar state, see Equation 4.42.

$$Nu = \frac{hL}{k} = 0.59(Gr\Pr)^{1/4} \tag{4.42}$$

i.e.

$$h = \frac{0.027 \times 0.59 \times 69100^{1/4}}{0.03} = 8.61 \ W/m^2.K$$

The thermal resistance of surrounding air can be obtained by:

$$\begin{aligned} R_a &= \frac{1}{\pi D_{out} L h} \\ &= \frac{1}{\pi \times 0.0078 \times 0.03 \times 8.61} \\ &= 158 \ K/W \end{aligned}$$

The calculation results indicate that the above assumption is correct, i.e. $R_a >> R_p$. Therefore, it is not necessary to revise the above calculations.

The emissivity of Pyrex glass is about 0.9, the overall thermal loss in the observable section can be estimated based on Equation 4.39.

$$\begin{aligned}\Delta Q &= \frac{52.5-20}{7.42+158} + \pi \times 0.0078 \times 0.03 \times 0.9 \times 5.67 \times 10^{-8} \times \left(325.65^4 - 293.15^4\right) \\ &= 0.20 + 0.14 \ W \\ &= 0.34 \ W\end{aligned}$$

The above calculations indicate that the thermal loss in the observable section is negligible comparing with the thermal loss between the inlet of the heating section and the visualization point, which is about 3.8 W in the 1.10 mm tube at 14 bar as shown in Figure 4.6. The observations in the present experiments show that the flow regimes at the inlet of the observable section are quite similar to those downstream, which indicates that the thermal loss in the observable section has little effect on the flow patterns. Therefore, the flow maps are still accurate and reliable when the thermal loss in the observable section is neglected.

The thermal loss in the observable section leads that the bubbles downstream are shorter than those upstream. The above calculations show that the thermal loss on a 30 mm long glass tube is about 0.34 W in the 1.10 mm tube at 14 bar. In Figure 4.11 (iii) and (iii'), the average bubble length L = (4.04+3.54) = 3.79 mm, the time interval between the figure (iii) and (iii') is 0.085 s from the movie. Therefore, the total energy change for the bubble in the circle can be calculated when it travels from position (iii) to (iii'):

$$\Delta E = \frac{0.34 \times 3.79 \times 0.085}{30} = 0.00365 \ J$$

The condensed vapour can be estimated based on the vapour density and the latent heat of vaporization at 14 bar.

$$\begin{aligned}\Delta V_{cal} &= \frac{\Delta E}{h_{fg}\rho_g} \\ &= \frac{0.00365}{149210 \times 70.7} \\ &= 3.46 \times 10^{-10} \ m^3\end{aligned}$$

If the bubble diameter is 1.0 mm, the bubble length changed can be estimated from::

$$\Delta L = \frac{\Delta V_{cal}}{A} = \frac{4 \times 3.46 \times 10^{-10}}{\pi \times 0.001^2} = 4.4 \times 10^{-4} \ m = 0.44 \ mm$$

The measurement shows that this average 3.79 mm long bubble is shortened about 0.5 mm, i.e. 13.2%, after flowing up 15 mm as shown in Figure 4.11 (iii) and (iii'). It is in good agreement with the calculated result. Therefore, the thermal loss in the observable section is the main reason of bubble shrinkage. Such effect is significant in the smaller tube, higher pressure (temperature) and lower velocity. For example, bubble length decreased by about 0.25, 0.33 and 0.5 mm after flowing up 12-15 mm in the 2.01 mm tube at 14 bar (the length decreases about 3.1%), the 1.10 mm tube at 10 bar (the length decreases about 8.5%) and 14 bar (the length decreases about 13.2%), respectively. For bigger tubes, the effect of thermal loss on the bubble length can also be detected at low flow velocity, see the comparisons in Figure 4.11 (viii) and (ix) for the 2.88 mm tube.

The experimental data also indicate that the slopes of u_r/u_h decreased slightly in the 1.10 mm tube at 14 bar and the decrease may not be negligible in the 2.01 mm tube at 14 bar and the 1.10 mm tube at 10 bar, see Figures in Appendix I and comparisons in Table 7.1 Chapter 7. The above phenomenon can also be attributed to the effect of thermal loss because the measurements show that bubbles condense faster in the smaller tubes, higher pressure and lower flow velocity, see the measurements in Figure 4.11. It can be expected that the effect of thermal loss on bubble rise velocity is the same magnitude of that on bubble length, i.e. the measurement accuracy is sensitivity to the thermal loss in the smaller tubes, higher pressure and lower flow velocity. However, the decrease of bubble rise velocity is difficult to be estimated accurately because the measurements is only based on the velocity at the front of bubbles due to its regular shape, where the velocity change may be different from that at the bottom. In addition, the observable section is not long enough (about 25-30 mm) to compare the rise velocity upstream with that downstream. Therefore, the experimental data used to deduce the distribution parameter C_0 and drift velocity u_d do not include those for the 1.10 and 2.01 mm tubes at 14 bar and the 2.88 and 4.26 mm tubes at 14 bar at low velocity, see Chapter 7 Section 7.2.1. Further discussion on this is also presented in Chapter 5 Section 5.1.4 (2) and Chapter 7 Section 7.1.

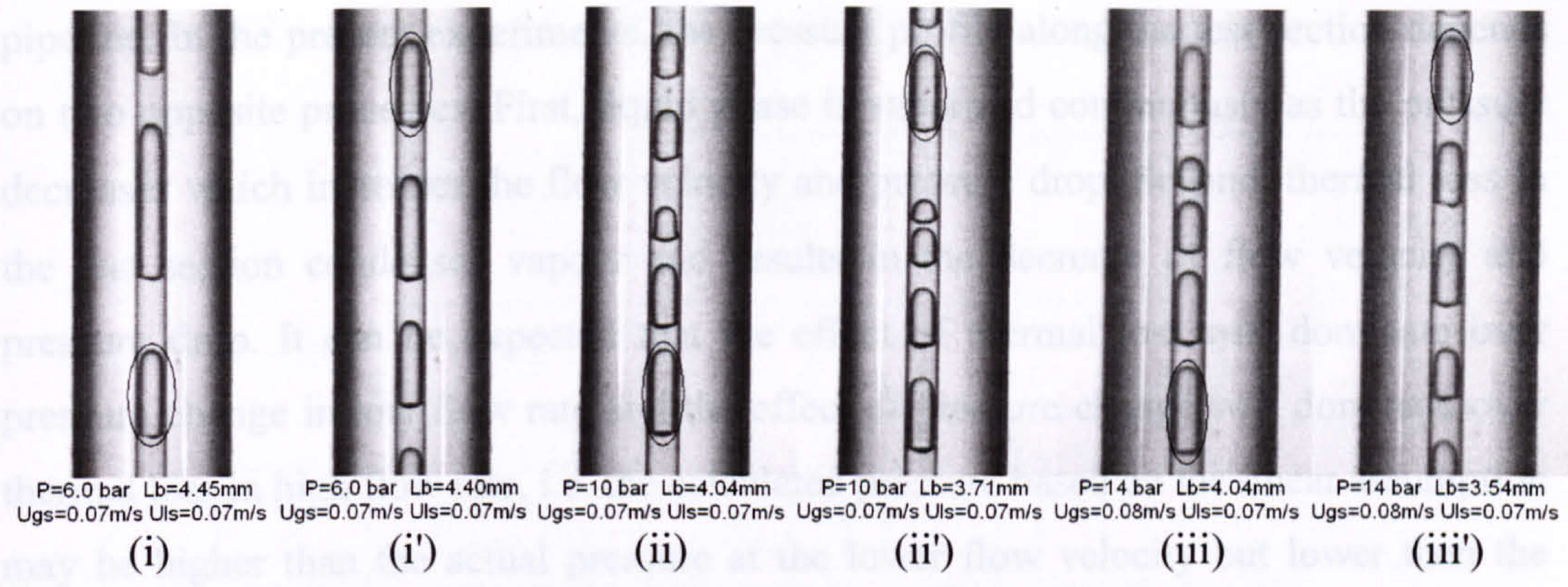

(a): 1.10 mm test section.

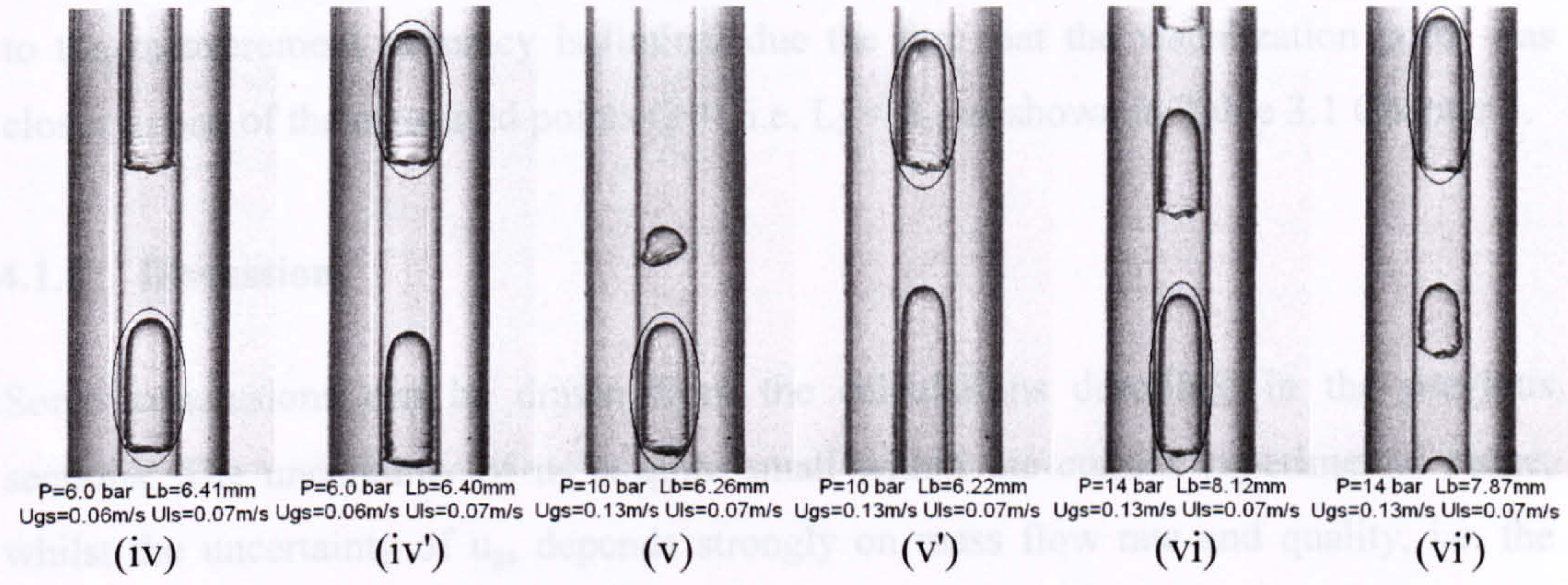

(b): the 2.01 mm test section.

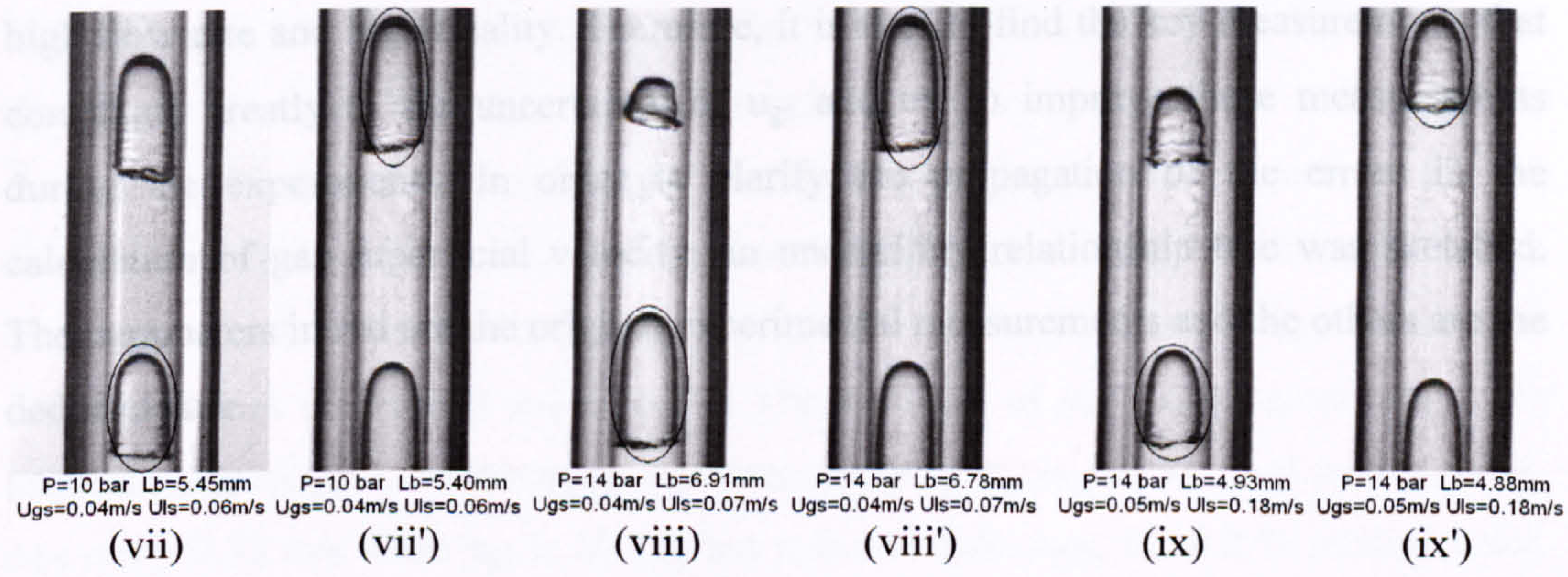

(c): the 2.88 mm test section.

Figure 4.11 The effect of thermal loss on bubble length.

B. Pressure drop

The parameters at the visualization point are deduced from the inlet and outlet pressures (P4, P0) with the assumption that the pressure drop along the observation section is linear. In fact, the fluid pressure in two-phase flow may not linearly decrease along the pipeline. In the present experiments, the pressure profile along the test section depends on two opposite processes. First, liquid phase is vaporized continuously as the pressure decreases which increases the flow velocity and pressure drop. Second, thermal loss in the test section condenses vapour and results in the decrease of flow velocity and pressure drop. It can be expected that the effect of thermal loss will dominate over pressure change in low flow rate and the effect of pressure change will dominate over thermal loss in high flow rate, i.e. the calculated pressure based on the linear assumption may be higher than the actual pressure at the lower flow velocity but lower than the actual pressure at the higher flow velocity. However, the effect of the linear assumption to the measurement accuracy is limited due the fact that the visualization point was closer to one of the measured points (P0), i.e. $L_2 < L_1$ as shown in Table 3.1 Chapter 3.

4.1.4 Discussions

Some conclusions can be drawn from the calculations described in the previous sections. The uncertainty of u_{ls} is quite small within the current experimental range, whilst the uncertainty of u_{gs} depends strongly on mass flow rate and quality, i.e. the accuracy of measuring of u_{gs} is excellent at low flow rate and low quality but is poor at high flow rate and high quality. Therefore, it is vital to find the key measurements that contribute greatly to the uncertainty of u_{gs} and try to improve these measurements during the experiments. In order to clarify the propagation of the errors in the calculation of gas superficial velocity, an uncertainty relationship tree was sketched. The parameters in red are the original experimental measurements and the others are the deduced data.

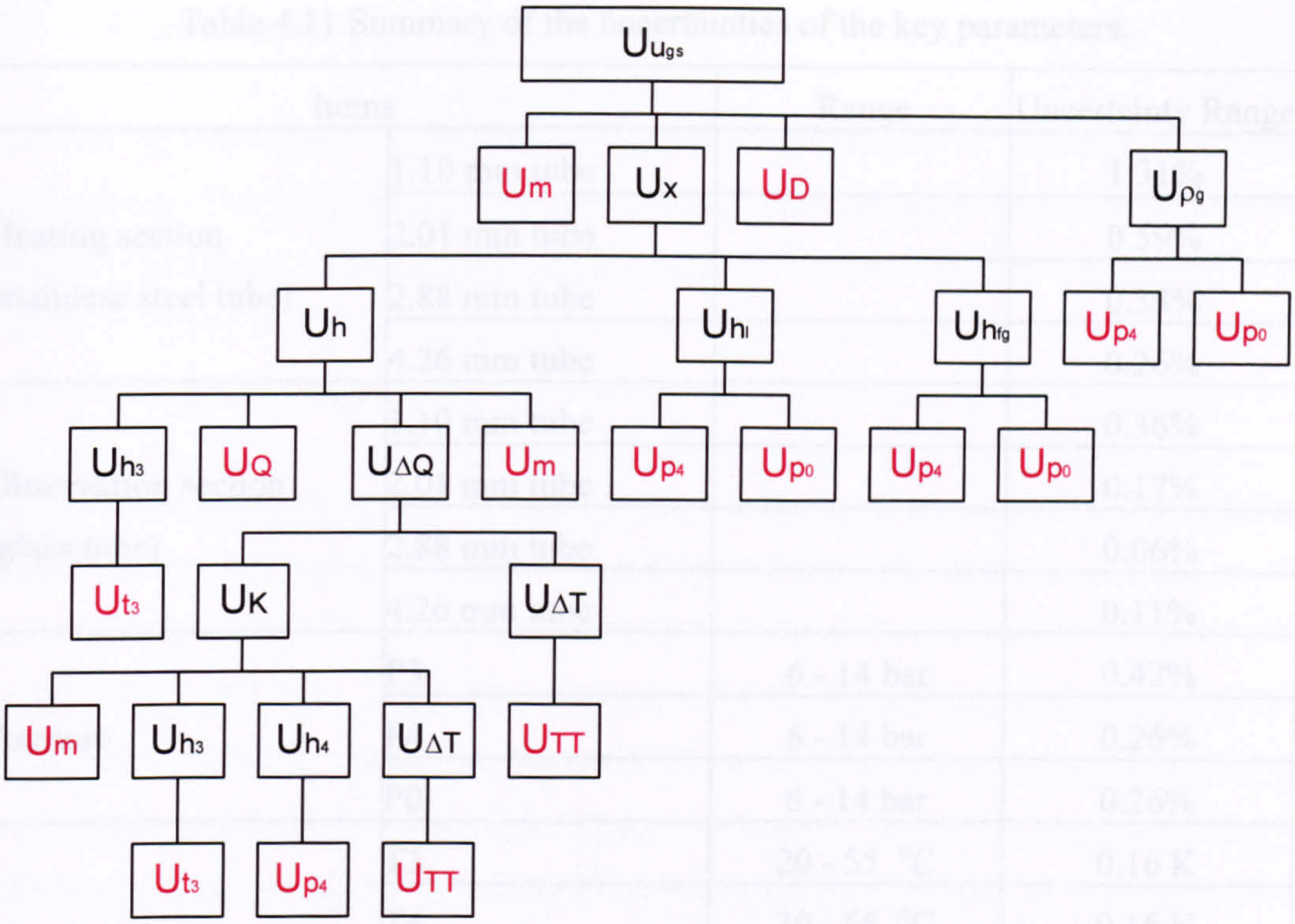

Figure 4.12 The factors affecting vapour superficial velocity measurement.

The experimental data analysis program can evaluate the importance of these measurements, see introduction in Appendix D Section D.3 (4). It is not difficult to find that the temperature T3, the pressures P4 and P0, the flow rate and the heating power are the most important measurements. Comparatively the pressure transducer P3, the thermocouple probes T4 and T0 and the thermocouple wires TT have a little effect on to the accuracy of gas superficial velocity. Table 4.11 summarizes the key parameters uncertainties in the current experiments. The accuracy of u_{ls} is quite good within the experimental range. Comparatively the uncertainty of u_{gs} is not so good as that of u_{ls}, can reach 0.32 m/s when u_{gs} is 10 m/s but it is still quite low, i.e. 3.2 % relative error. Therefore, the collected data can produce accurate flow maps.

Table 4.11 Summary of the uncertainties of the key parameters.

Items		Range	Uncertainty Range
Heating section (stainless steel tube)	1.10 mm tube		1.31%
	2.01 mm tube		0.59%
	2.88 mm tube		0.38%
	4.26 mm tube		0.26%
Observation section (glass tube)	1.10 mm tube		0.36%
	2.01 mm tube		0.17%
	2.88 mm tube		0.06%
	4.26 mm tube		0.11%
Pressure	P3	6 - 14 bar	0.42%
	P4	6 - 14 bar	0.26%
	P0	6 - 14 bar	0.26%
Temperature	T3	20 - 55 °C	0.16 K
	T4	20 - 55 °C	0.16 K
	T0	20 - 55 °C	0.16 K
	TT1-TT15	> 20 °C	0.16 K
Flow rate	Small meter CMF010	0.5 - 25 kg/hr	0.15 - 0.54%
	Big meter CMF025	25 - 500 kg/hr	0.15 - 0.22%
Heating power	Test section	2.68 - 1640 W	0.10 - 0.49 %
Differential pressure	24% full scale	0 - 0.0608 bar	21.16 Pa
	100% full scale	0.0608 - 0.2491 bar	77.43 Pa
Quality (absolute error)	1.10 mm test section	0 - 100%	0.14 - 1.37%
	2.01 mm test section	0 - 100%	0.14 - 2.88%
	2.88 mm test section	0 - 100%	0.14 - 3.33%
	4.26 mm test section	0 - 100%	0.14 - 3.21%
Gas superficial velocity (observation section)	1.10 mm	0.01 - 10 m/s	0.011 - 0.32 m/s
	2.01 mm	0.01 - 10 m/s	0.006 - 0.32 m/s
	2.88 mm	0.01 - 10 m/s	0.004 - 0.32 m/s
	4.26 mm	0.01 - 10 m/s	0.002 - 0.32 m/s
Liquid superficial velocity (observation section)	1.10 mm	0.04 - 5 m/s	0.0009 - 0.05 m/s
	2.01 mm	0.04 - 5 m/s	0.0003 - 0.03 m/s
	2.88 mm	0.04 - 5 m/s	0.0001 - 0.02 m/s
	4.26 mm	0.04 - 5 m/s	0.0001 - 0.02 m/s

4.2 Commissioning of the test facility

The test rig was commissioned step by step and finally validated by single-phase flow experiments. The problems encountered and the solutions are reviewed in this section and provide a better understanding of the system.

4.2.1 Compressor failure

The original compressor UA K750CS was manufactured by DORIN. The installed protection devices included a high-low pressure switch and three 32 A fuses in the power supply circuit. To the surprise of the research team the compressor burnt out after running for a few days. The main reason was that the lubricating oil escaped from the compressor whilst the protection system failed to cut off power on time. The oil in the compressor was carried by the high velocity refrigerant, flowed to an oil separator in which of course not all of the oil could be separated and returned to the compressor. Some oil inevitably escaped to the R22 tank. However, the vapour refrigerant back to the compressor could only carry a very small amount of oil due to the low vapour velocity in the tank. Over time the oil deposited in the tank. The compressor and the R22 tank were located in different rooms, which were always at a certain temperature difference, day and night. The refrigerant condensed in the compressor continually because of its lower room temperature, and indicated a false oil level in the oil pool. Therefore, the compressor operated with less oil than required and this caused a high working load. The big fuses (32 A) could not protect the compressor properly. The excess current overheated the motor until it burnt out.

The new compressor installed was a BITZER / 4CC-6.2 Y. The original 32 A fuses were replaced by an overload relay and three circuit breakers and the capacity was reduced to 20 A. A crankcase heater was installed in the oil pool to prevent the refrigerant condensing in the compressor. A new oil return system was designed and installed to separate the oil from R22 and reinject it to the compressor continually, as shown in Chapter 3 Figure 3.3.

4.2.2 Condenser cooling capacity

The cooling capacity of the R134a condenser designed based on the possible maximum heating load, is 8.5 KW according to the original calculations of Huo (2005). However, in most cases, the actual heating load in the test sections was much less than that. In this event, the heater in the R134a tank could not compensate for the extra cooling load. The needle valve used to control the R22 flow rate and the corresponding cooling capacity proved impractical because of its poor regulating performance. It usually resulted in an unexpected fluctuation in the system, which was extremely serious in the smaller tube or at low flow rate and quality.

Based on the above analysis, a new condenser with a smaller heat exchanging area was installed in the R134a tank, see Figure 3.3 component 4. The refrigerant flows through it without control. The cooling capacity is very limited but stable. Therefore, the system parameters can be kept at a desired value stably using the tank heater.

4.2.3 Measuring noise

All thermocouple probes were initially of the grounded type whilst the experimental system and the data acquisition system were connected to different earth points. The potential difference between the different earth wires caused huge measuring error, sometimes up to 10 °C. After changing to ungrounded probes, the error reduced but was still not acceptable. Finally, reasonable results were obtained by connecting the experimental system and the data acquisition system at a common earth point.

4.2.4 Test section clearance

In the beginning, neither Blasius's formula nor Moody's diagram could predict the pressure drop in the single-phase experiments. The possible reasons included: the effect of diameter or fluid properties much different than the expected for Blasius's formula and Moody's diagram or some local pressure loss. Therefore, a thick wall tube with similar inside diameter (4 mm) was tested. The measured results agreed well with Blasius's formula, which indicated the local pressure loss was the only reason to cause the discrepancy. Careful examination of the test tube revealed some distortion and some sediment. The results improved and agreed well with those predicted by Blasius's formula after the above were corrected.

4.2.5 Small preheater

The high degree of subcooling may cause unstable boiling flow. This phenomenon frequently happened in the small test sections at high experimental pressures. The origin of the problem was that the thermal loss between the preheater and the test section caused the low temperature at the inlet of the test sections, see Figure 4.5. Therefore, a small adjustable preheater was installed just before the test sections to heat the liquid to the desired temperature.

Besides the aforementioned amendments, the flow control valves, V4, V5 shown in Chapter 3 Figure 3.1 and V2, V7 in Figure 3.3, were changed to smaller valves in order to improve their regulating performance especially during small flow rate experiments.

4.3 Single-phase experiments

Single-phase experiments, which are easier to verify and validate, were performed before commissioning two-phase experiments. Although every device and instrument had been tested and calibrated carefully, the whole experimental system still needs to be verified. In detail, pressure drop in single-phase flow was measured and compared with the widely applicable correlations to validate the performance of the entire experimental facility. Then, the thermal loss coefficient in the test section was assessed and is presented in Section 4.1.3 (9). In this chapter, only the pressure drop experiments and the measurement uncertainty are calculated and discussed.

4.3.1 Methodology

Every test section and the general system performance must be validated by single-phase pressure drop experiments before proceeding with two-phase experiments because the existing correlations on pressure drop in single-phase flow have been proved and accepted widely. The experimental results, after considering the measuring uncertainty, should be in reasonable agreement with these correlations. The Blasius's and Haaland's formulae, which have been proved well in smooth and rough tubes, are used as the reference (Massey and Ward-Smith, 1998).

The Blasius's formulae used for smooth tube can be presented as:

$$f = 0.079\,\mathrm{Re}^{-1/4} \tag{4.43}$$

The Haaland's formulae used for rough tube can be presented as:

$$\frac{1}{\sqrt{f}} = -3.6\log_{10}\left\{\frac{6.9}{\mathrm{Re}} + \left(\frac{\varepsilon}{3.71D}\right)^{1.11}\right\} \tag{4.44}$$

The roughness of the tubes has been measured by Taylor Hobson Limited (Leicester, UK). Measurement was made in an axial direction within the bore of each tube, start at a position 10 mm in from on end face, and at 4 positions, A, B, C and D, normally 90 degrees apart, see Figure 4.13. The roughness profiles measured in the 4.26 mm steel and glass tubes are presented in Figures 4.14 and 4.15 and the complete results are summarized in Table 4.12. The average roughness used in the Haalan formulae is 1.28, 1.82, 1.54 and 1.75 μm for the 1.10, 2.01, 2.88 and 4.26 mm steel tubes respectively.

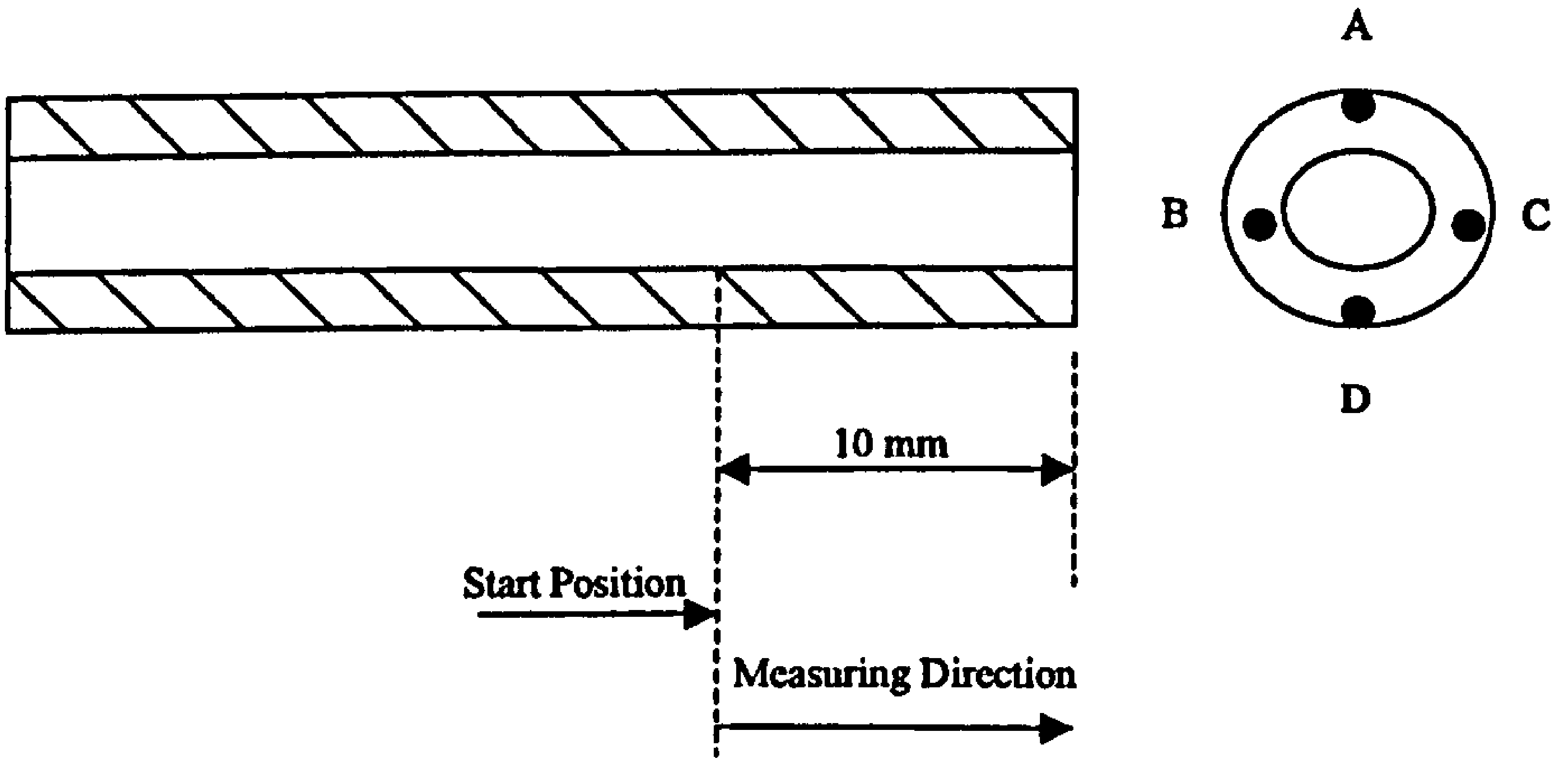

Figure 4.13 The position of the roughness measurement.

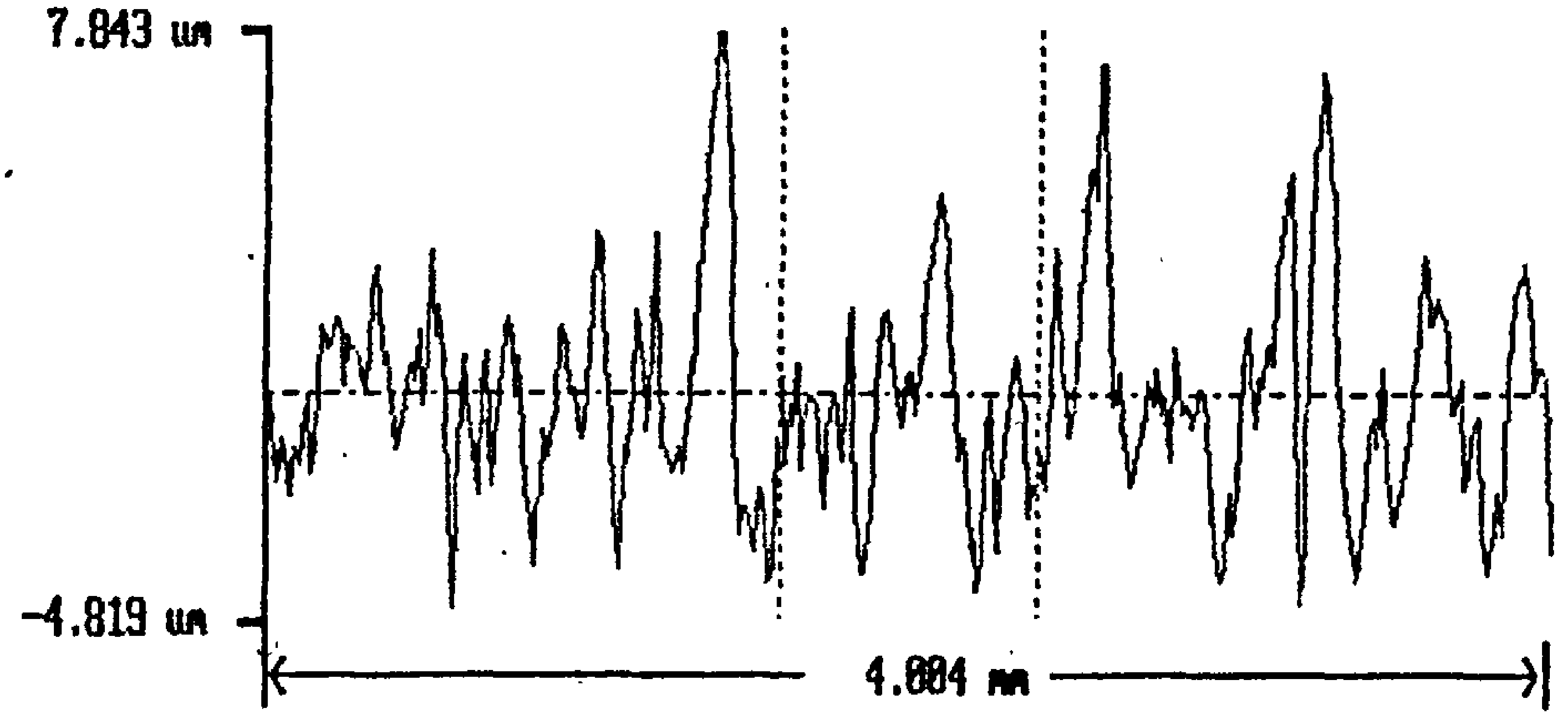

Figure 4.14 The roughness profile in the 4.28 steel tube.

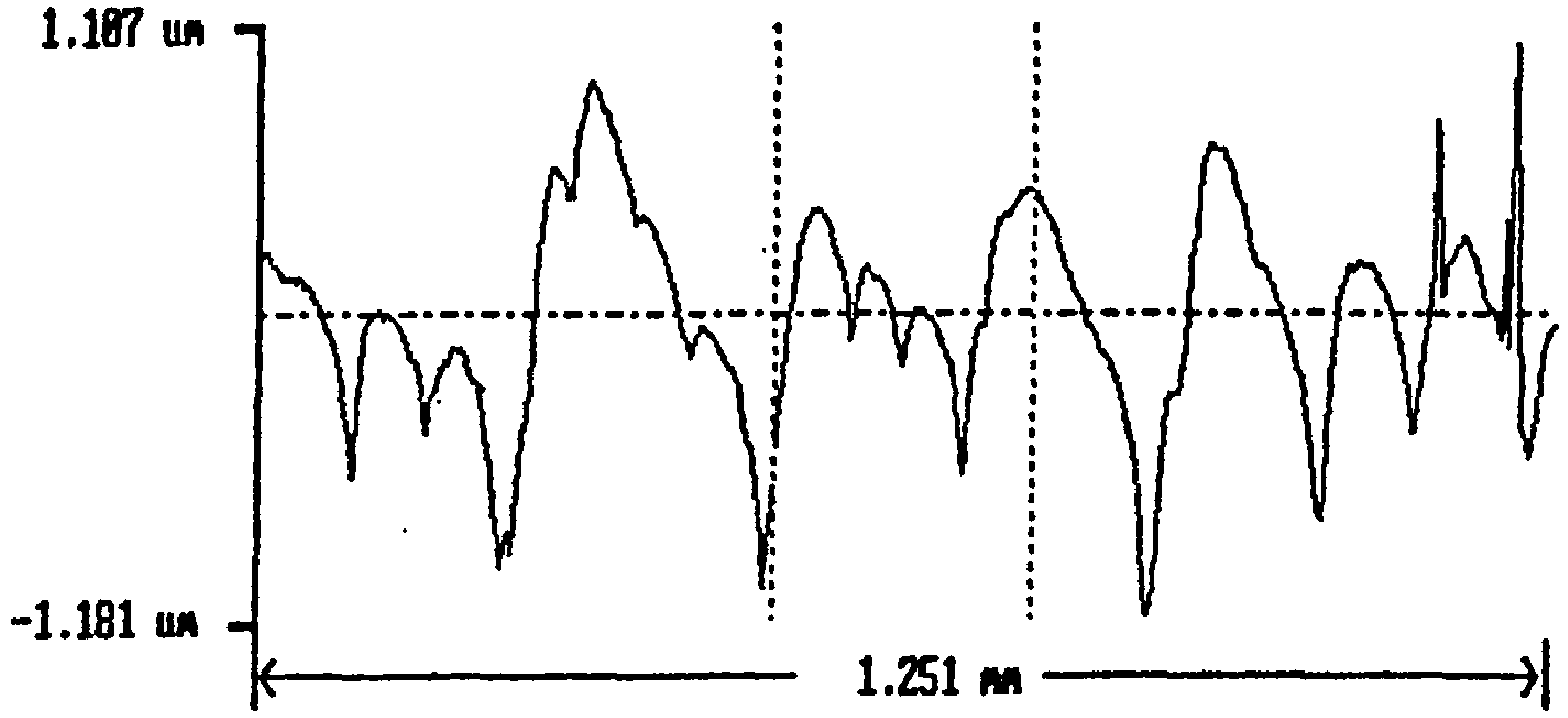

Figure 4.15 The roughness profile in the 4.28 glass tube.

Table 4.12 Summary of the measured roughness of the tubes.

Tubes	Steel Tubes (μm)		Glass Tubes (μm)	
	Peak to Valley	Average	Peak to Valley	Average
1.10 mm tube	12.94	1.27	3.60	0.47
2.01 mm tube	18.40	1.82	1.28	0.15
2.88 mm tube	10.70	1.54	N/A	N/A
4.26 mm tube	13.14	1.75	1.63	0.23

The measured friction factor can be obtained from:

$$f = \frac{\Delta p_f D}{2L\rho u^2} = \frac{\pi^2 \rho}{32} \frac{\Delta p_f D^5}{Lm^2} \tag{4.45}$$

The equation for the uncertainty of the measured friction factor is

$$\left(\frac{U_f}{f}\right)^2 = \left(\frac{U_\rho}{\rho}\right)^2 + \left(\frac{U_{\Delta p_f}}{\Delta p_f}\right)^2 + 25\left(\frac{U_D}{D}\right)^2 + \left(\frac{U_L}{L}\right)^2 + 4\left(\frac{U_m}{m}\right)^2 \tag{4.46}$$

The uncertainty analysis of fluid density ρ, test section diameter D and length L, and mass flow rate was presented in Section 4.1.3. Therefore, the uncertainty of the friction factor can be deduced form Equation 4.46 if the pressure drop and the corresponding uncertainty are known. In detail, the total pressure drop Δp is measured by a differential pressure transmitter. It consists of two parts: friction pressure drop (Δp_f) and pressure difference due to different density (Δp_{dc}). Δp_{dc} is used to compensate the measuring bias caused by the liquid density difference due to the fact that the liquid temperature in the test section could be different from that in the connecting tube leading to the differential pressure transmitter. The corresponding equations and the uncertainties are given below:

$$\Delta p_f = \Delta p - \Delta p_{dc} \tag{4.47}$$

$$U_{\Delta p_f}^2 = U_{\Delta p}^2 + U_{\Delta p_{dc}}^2 \tag{4.48}$$

where $U_{\Delta p}$ is the uncertainty of the measurement of the differential pressure, see Section 4.1.3 (6).

$$\Delta p_{dc} = \left(\rho_{lt} - \rho_{lp}\right) g L \tag{4.49}$$

$$U_{\Delta p_{dc}}^2 = g^2 L^2 \left(U_{\rho_{lt}}^2 + U_{\rho_{lp}}^2\right) + \left(\rho_{lt} - \rho_{lp}\right)^2 g^2 U_L^2 \tag{4.50}$$

Finally, the uncertainty of friction coefficient can be calculated by Equation 4.46.

4.3.2 Experimental results

According to the Equations 4.46, 4.48 and 4.50, the uncertainty of the friction factor depends on the measurement of the diameter, length, flow rate and the fluid parameters. Among these measurements, the accuracy of the differential pressure transmitter is the most important factor. Figure 4.16 summarizes the deduced uncertainty of the friction factor for all the test sections. The data indicates that the uncertainty of the friction factor tends to be smaller as the pressure drop increases. In other words, the maximum uncertainty occurs at the minimum flow rate or the minimum Reynolds number. The pressure drop measured in the single-phase experiments was 79 to 25321 Pa.

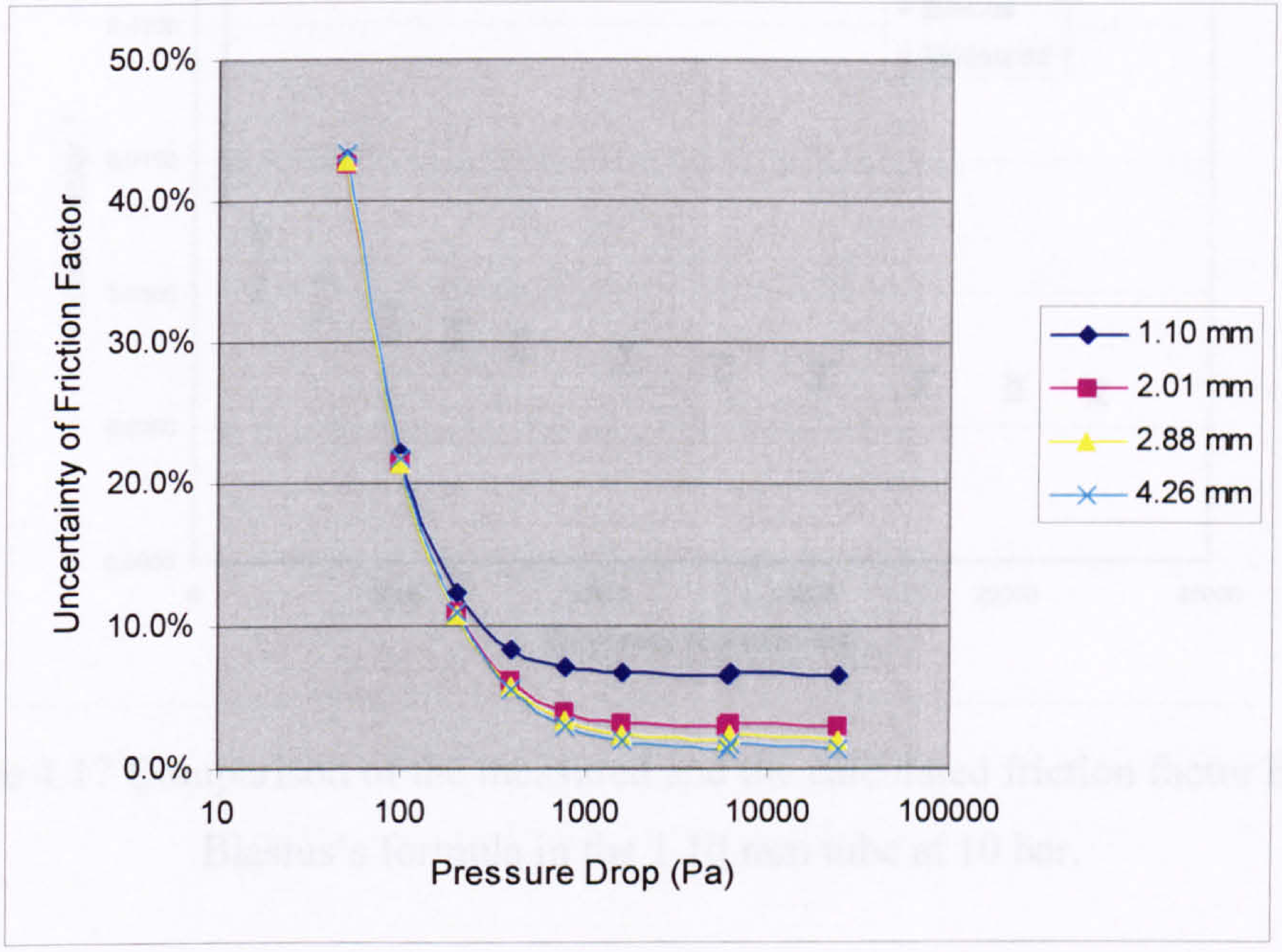

Figure 4.16 Pressure drop and the uncertainty of the friction factor.

Figures 4.17-4.21 depict the graphical comparisons of the experimental results and the predictions from the Blasius's or Haaland's formula. As seen in the figures, the agreement is excellent if the measuring error is considered. The bigger deviations happen at the lower mass flow rates where the expected error is large. The probable reasons are (i) the accuracy of Blasius's and Haaland's formula (ii) the test section is not a strictly smooth tube or the roughness changed after the test sections were built (iii) zero offset existing in the transmitter, which is a vital factor in the lower flow rate.

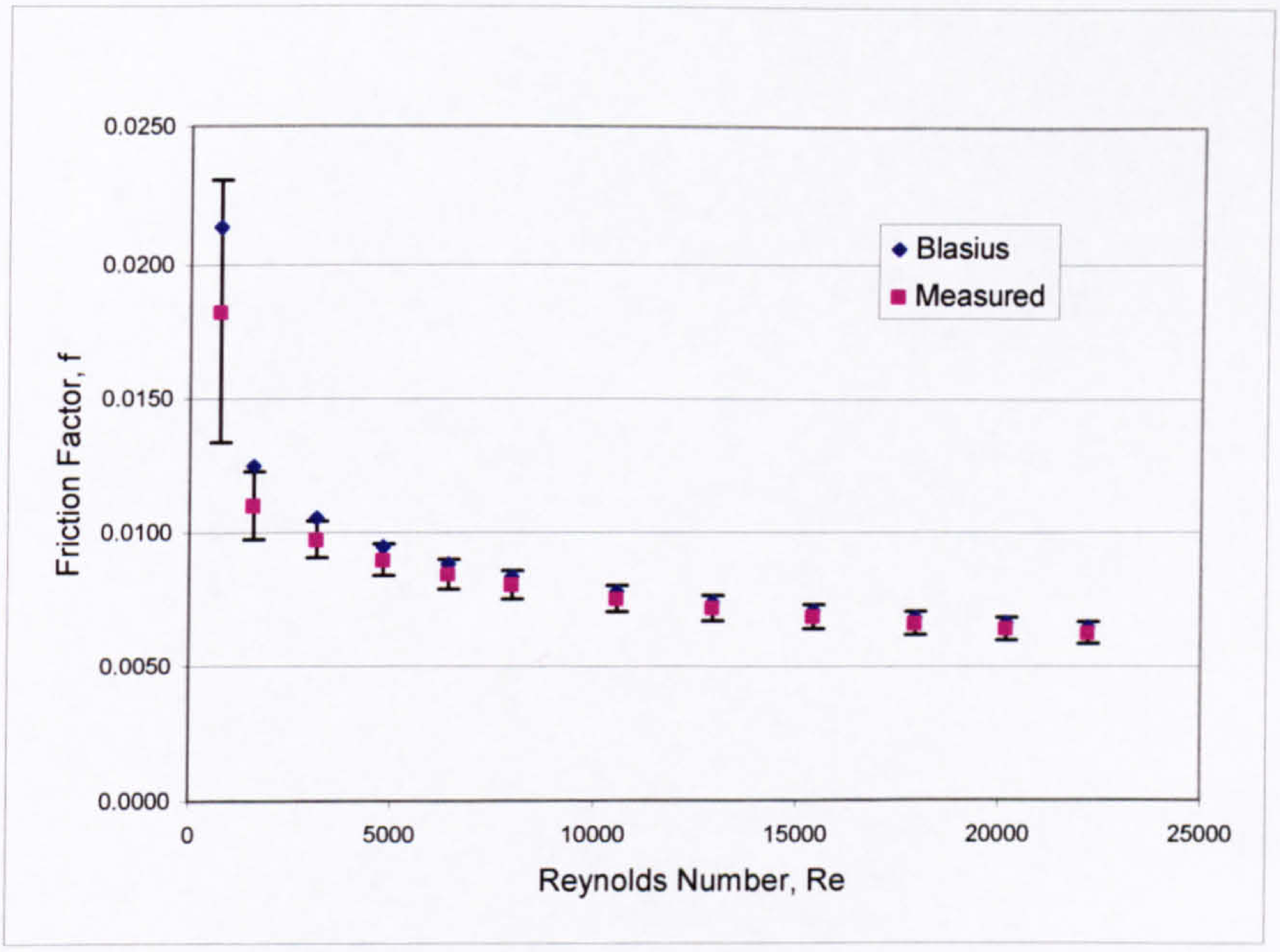

Figure 4.17 Comparison of the measured and the calculated friction factor by the Blasius's formula in the 1.10 mm tube at 10 bar.

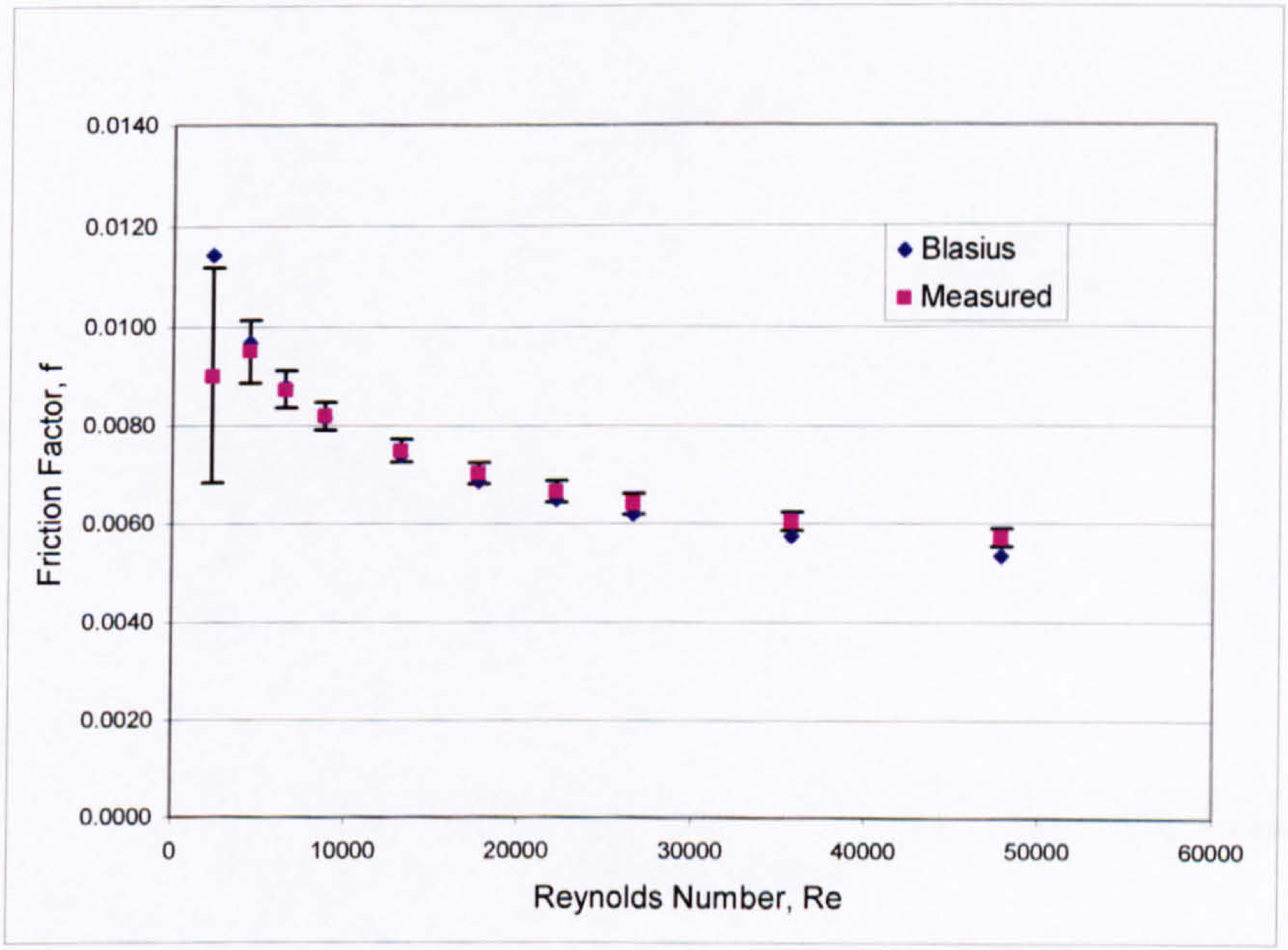

Figure 4.18 Comparison of the measured and the calculated friction factor by the Blasius's formula in the 2.01 mm tube at 7.5 bar.

The measured results for the 2.01 mm test section at 7.5 bar were also compared with Haaland's formula showing also better agreement in the higher flow rate, as seen in Figure 4.19.

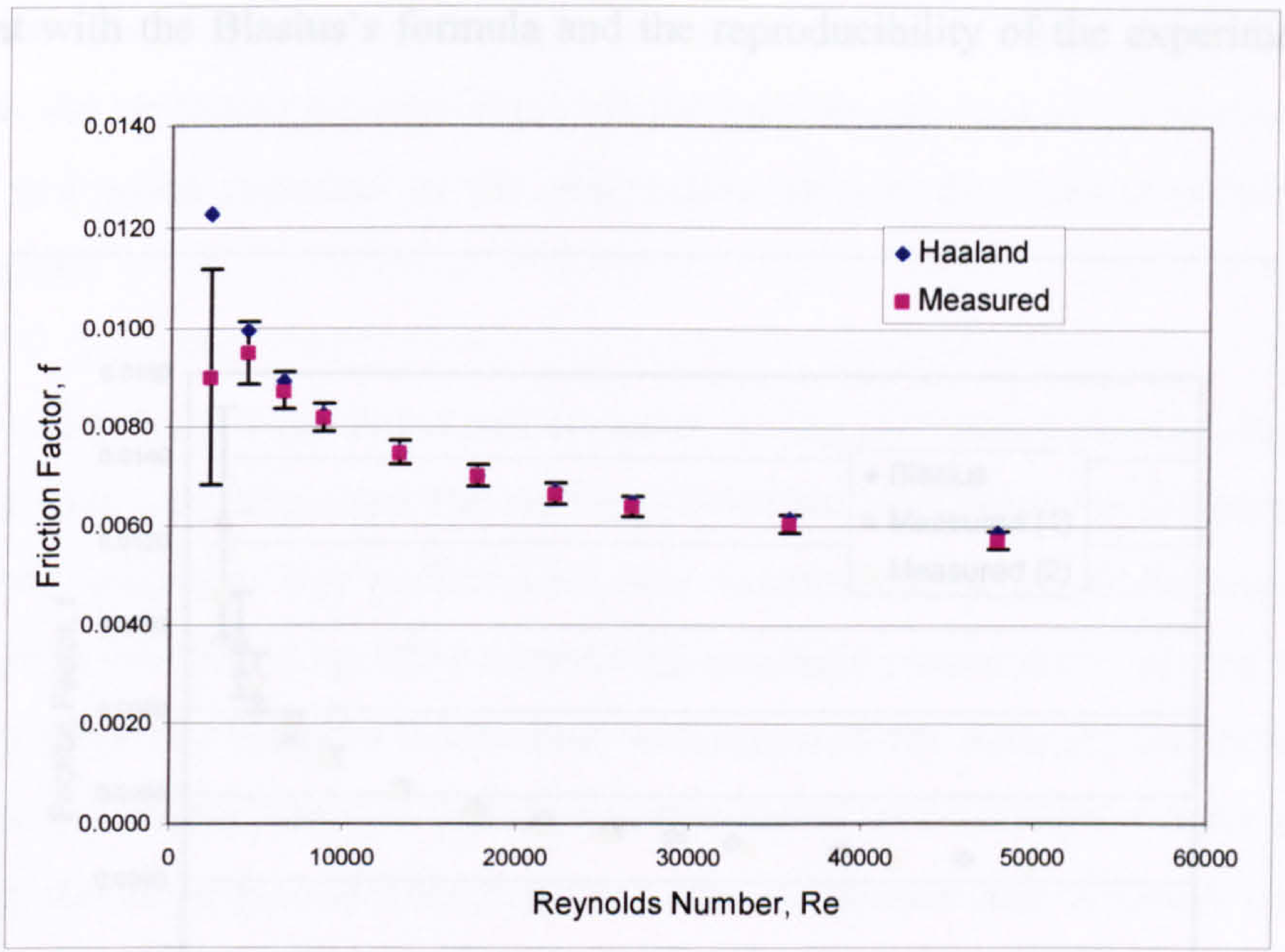

Figure 4.19 Comparison of the measured and the calculated friction factor by the Haaland's formula in the 2.01 mm tube at 7.5 bar.

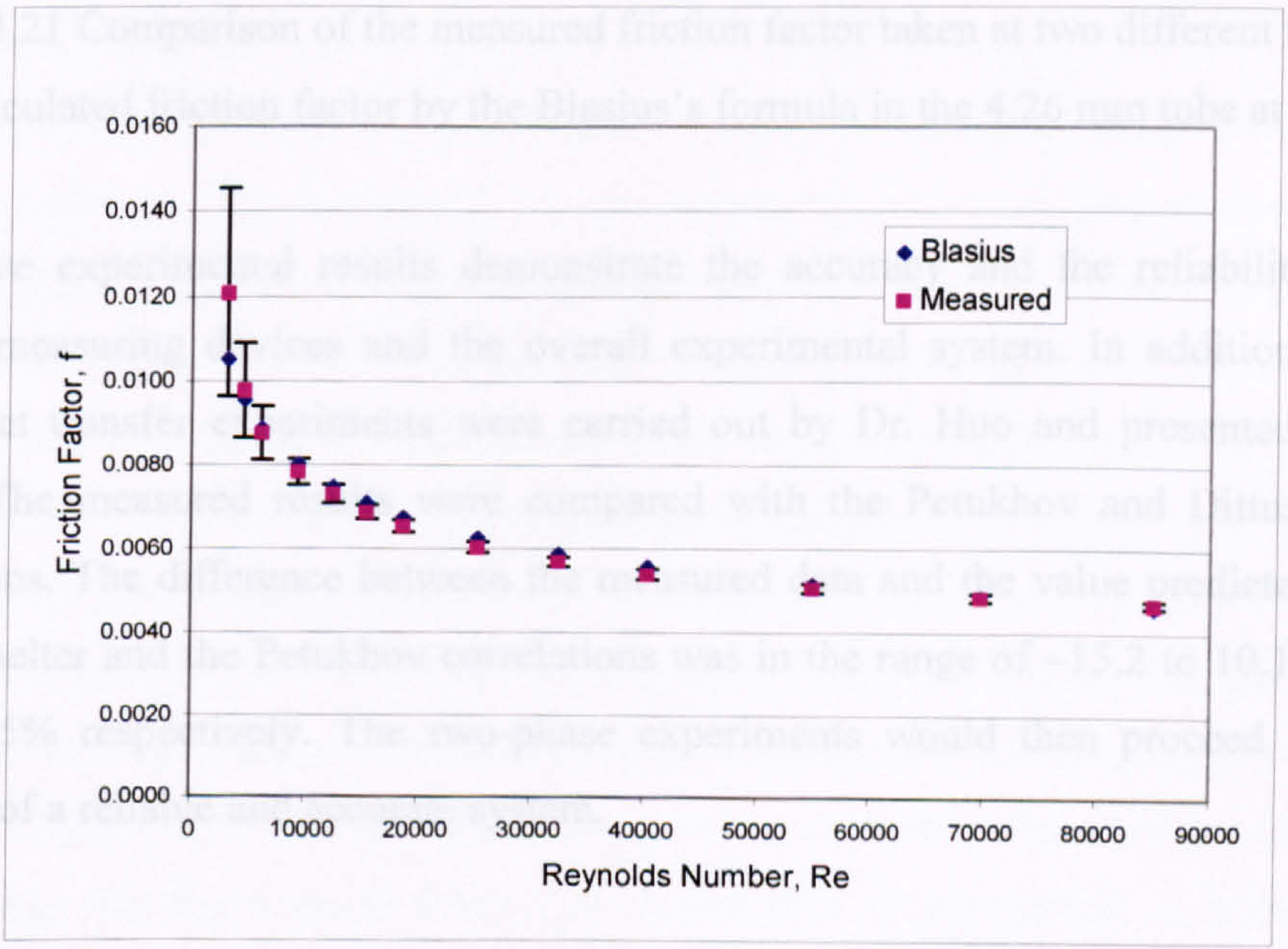

Figure 4.20 Comparison of the measured and the calculated friction factor by the Blasius's formula in the 2.88 mm tube at 10 bar.

The reproducibility of the system was also checked by repeating the same experiment at 7.5 bar on a different day, the results are shown in Figure 4.21. As seen in the figure, the agreement with the Blasius's formula and the reproducibility of the experiments were excellent.

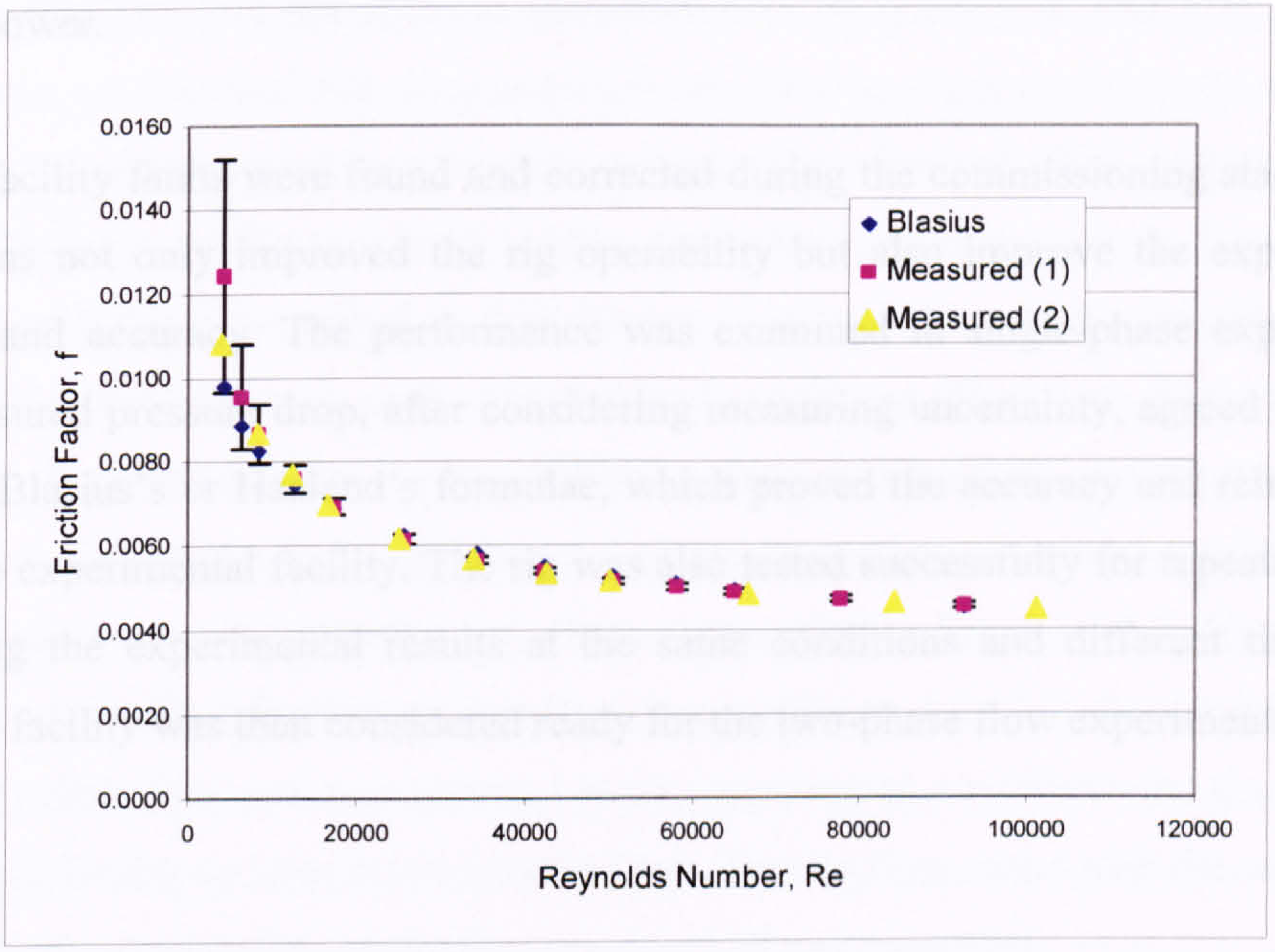

Figure 4.21 Comparison of the measured friction factor taken at two different times and the calculated friction factor by the Blasius's formula in the 4.26 mm tube at 7.5 bar.

The above experimental results demonstrate the accuracy and the reliability of the existing measuring devices and the overall experimental system. In addition, single-phase heat transfer experiments were carried out by Dr. Huo and presented in Huo (2005). The measured results were compared with the Petukhov and Dittus-Boelter correlations. The difference between the measured data and the value predicted by the Dittus-Boelter and the Petukhov correlations was in the range of –15.2 to 10.1% and –8.9 to 0.5% respectively. The two-phase experiments would then proceed with the certainty of a reliable and accurate system.

4.4 Summary

The current experiments involve various measurements, which include tube diameter, pressure, temperature, flow rate, power and differential pressure. All instruments used to measure these parameters were calibrated carefully and the corresponding uncertainties were given. In addition, the uncertainty in deduced parameters, thermal loss, quality and liquid/gas superficial velocities, were also calculated and the values were reasonable. All calculation results are summarized in Table 4.11. The results reveal that the important measurements are the inlet temperature of the heating section, the inlet and outlet pressures of the observation section, the mass flow rate and the heating power.

Several facility faults were found and corrected during the commissioning stage. These corrections not only improved the rig operability but also improve the experimental stability and accuracy. The performance was examined in single-phase experiments. The measured pressure drop, after considering measuring uncertainty, agreed very well with the Blasius's or Haaland's formulae, which proved the accuracy and reliability of the entire experimental facility. The rig was also tested successfully for repeatability by comparing the experimental results at the same conditions and different times. The validated facility was then considered ready for the two-phase flow experiments.

Chapter 5 Flow Pattern Experiments

Four test sections with the internal diameters of 1.10, 2.01, 2.88 and 4.26 mm were tested at the pressures of 6.0, 10.0 and 14.0 bar. Twelve group experiments, total 2392 experiments, were carried out in this project. The observed flow patterns include dispersed bubble, bubbly, confined bubble, slug, churn, annular and mist flow. Pictures are summarized and presented in this chapter. Five typical transition boundaries were recognized within the range of the experimental conditions. They were dispersed bubble – bubbly, dispersed bubble - churn, bubbly – slug, slug – churn and churn – annular boundaries. Considering mist flow was not observed at all experimental conditions, mist flow and mist – annular boundary are discussed together in Section 5.1.7. The transition boundary of confined bubble to slug flow is not discussed in this chapter because the confined bubble flow was not observed at all experimental conditions and the transition of confined bubble to slug is not very explicit. Twelve flow maps with the coordinates of liquid and gas superficial velocities are sketched and compared.

The picture resolution was set to 256 pixels (width) x 512 pixels (height) to get clear images as well as fast snap speed. In most cases, the exposure time used the fastest speed – 10 microseconds to reduce tail track and get a clear profile. The number of pictures recorded in one experiment was between 50 to 2048 frames and the sample rate was from 200 to 1900 pps (pictures per second), depending on the flow patterns and the fluid velocity. For example, the dispersed bubble, bubbly, short slug and fully developed annular flow normally needed fewer pictures to validate their flow state whilst more pictures were examined in long slug, churn, developing annular flow and the regions near the transition boundaries. High sample rate is required to show the flow details and process in the region of high u_{gs} or u_{ls}, including dispersed bubble, churn, annular flow and the associated transition boundaries. Comparatively, a lower sample rate allows recording for longer times and more bubbles in slug flow or slug-churn boundary using the same memory.

The measurements made in the current study included bubble diameter, slug length and rise velocity. In most cases 3 to 5 bubbles were measured for every data point depending on the bubble length. The average value was used in the study presented in

Section 5.1.4, 5.2.3 and Chapter 7 Section 7.1. Theoretically, the above measurement accuracy could reach 2 pixels resolution, i.e. 0.4% in the present experiments. However, the actual measurement error may be larger than the above assessment because it strongly depends on experimental stability and sample number rather than the image resolution. The measured bubble diameter was used to identify dispersed bubble, bubbly and slug flow. The criterion used to distinguish dispersed bubble and bubbly is based on the critical diameters presented in Table 5.3 whilst the tube diameter is the critical diameter used to differentiate bubbly and slug flow. Bubble diameter, slug length and rise velocity were used to validate flow state because they are constant in fully developed flow or changed slightly after considering measurement error. On the other hand, churn and annular flow could only be described qualitatively. As a result, the subjectivity, which can greatly depend on the observer, was inevitably introduced into the identification of these flow patterns. The classifications used in this study may be questioned by other researchers. In the current study, the transition of slug to churn flow was recognized when some (about 50%) slug bubbles distorted whilst the annular flow was obtained once gas core was continued in all frames verified. However, the above identifications are restricted by the length of the observation region.

All movies were examined frame by frame to identify the flow regimes in the current study. Comparatively the identifications based on movies are much reliable and accurate than those based on pictures. However, it is difficult to demonstrate movies in the thesis. Therefore, a few typical pictures are presented in this chapter to depict the characteristics of the flow patterns. If the pictures in the hard copy thesis cannot be identified clearly, the electronic version thesis in the attached disc can provide clearer images.

5.1 The observed flow patterns

All flow patterns can be categorized into four main classes: stratified flow, intermittent flow, annular flow and bubble flow. Their common characteristics have been described in Chapter 2 Section 2.2. Each main class could be subdivided into several subclasses. In the present experiments, dispersed bubble, bubbly, slug, churn and annular flow were observed in all test sections. Occasionally mist flow was observed in the bigger tubes at very high gas velocity whilst confined bubble flow was observed in the smaller tubes at low velocity. The above-mentioned seven flow patterns are defined as follows briefly.

(1) Dispersed bubble: numerous small bubbles float in continuous liquid phase.

(2) Bubbly: bubble size is comparable to but not as large as the tube diameter. The criterion used to distinguish dispersed bubble and bubbly flow will be discussed further in Section 5.2.1.

(3) Confined bubble: bubble size reaches the tube diameter and the length is greater than tube diameter. The bubbles have smooth gas-liquid interface and extrusive bottom.

(4) Slug: bubble size reaches the tube diameter and the length is greater than tube diameter. The difference between slug flow and confined bubble is that the slug bubbles have flat bottom with sharp edge whilst confined bubble have smooth extrusive bottom. Sometimes slug bubbles are followed by a stream of small bubbles creating a trail.

(5) Churn: bullet bubbles start to distort and small bubbles in liquid slug coalesce into gas clump with gas velocity increases. It is a highly oscillatory flow with chaotic interface.

(6) Annular: gas phase becomes a continuous flow in the core of tube.

(7) Mist: liquid film is blown away from tube wall and numerous liquid droplets float in high-speed gas stream.

Overall the flow patterns in the 1.10, 2.01, 2.88 and 4.26 mm tubes at 6-14 bar pressure are similar and could be grouped into the above seven typical patterns. However, on close observation, there are some differences among these tubes and pressures. In the following sections the flow patterns recorded in the present experiments are presented and compared to reveal the effect of gas/liquid velocities, tube diameter and pressure.

5.1.1 Dispersed bubble flow

Figure 5.1 shows dispersed bubble flow for the 4.26 mm tube at the different pressures and gas/liquid velocities. As seen in Figure 5.1 (a) (iii) and (iv), (b) (ii) and (iv) and (c) (ii) and (iv), bubbles tend to be smaller, regular and round as the liquid superficial velocity increases. The same argument can be put forward for the 2.88 mm tube and the 2.01 mm tube, see Figure 5.2 (c) (i) and (iv) and Figure 5.3 (c) (iii) and (v). However, this tendency was not observed clearly in the 1.10 mm tube possibly because the bubbles are very small at all conditions, see Figure 5.4.

On the other hand, increasing the gas superficial velocity may increase the probability of collision and facilitates bubble coalescent and growth. This phenomenon was observed in all four test sections, see for example Figure 5.1 (a) (ii) and (iii). Figure 5.2 (c) (iii), (iv) and (v), Figure 5.3 (c) (ii) and (iii) and Figure 5.4 (c) (iii) and (iv).

The effect of pressure on the dispersed bubble is also important in the tested tubes. Bubbles could not be produced until a high degree of superheat was reached at lower pressure. In addition, the bubble number and volume are obviously larger at higher pressure than those at lower pressure at the same superficial velocities, see for example Figure 5.1 (b) (i) and (c) (i), Figure 5.2 (a) (i) and (c) (ii), Figure 5.3 (b) (i) and (c) (ii), Figure 5.4 (a) (ii) and (c) (ii). One reasonable explanation is that small bubbles may collapse easily at lower pressure to become superheated liquid because of the higher surface tension. Equation 5.1 gives the minimum diameter (d_{min}) that bubbles can survive in superheated liquid. p_{sat} is the saturated pressure corresponding to the fluid temperature.

$$d_{min} = \frac{4\sigma}{p_b - p_{sat}} \qquad (5.1)$$

The effect of tube diameter on the dispersed bubble flow is obvious because the criterion used to distinguish dispersed bubble and bubbly depends on the tube diameter, i.e. a group of same size bubbles be reported as dispersed bubble in large tubes whilst they could be classed as bubbly in smaller tubes. For example, the biggest dispersed bubbles in the 4.26 mm tube can reach 1.5 mm diameter, see Figure 5.1 (a) (iii). However, such a big bubble will be identified as slug or confined bubble in the 1.10 mm tube.

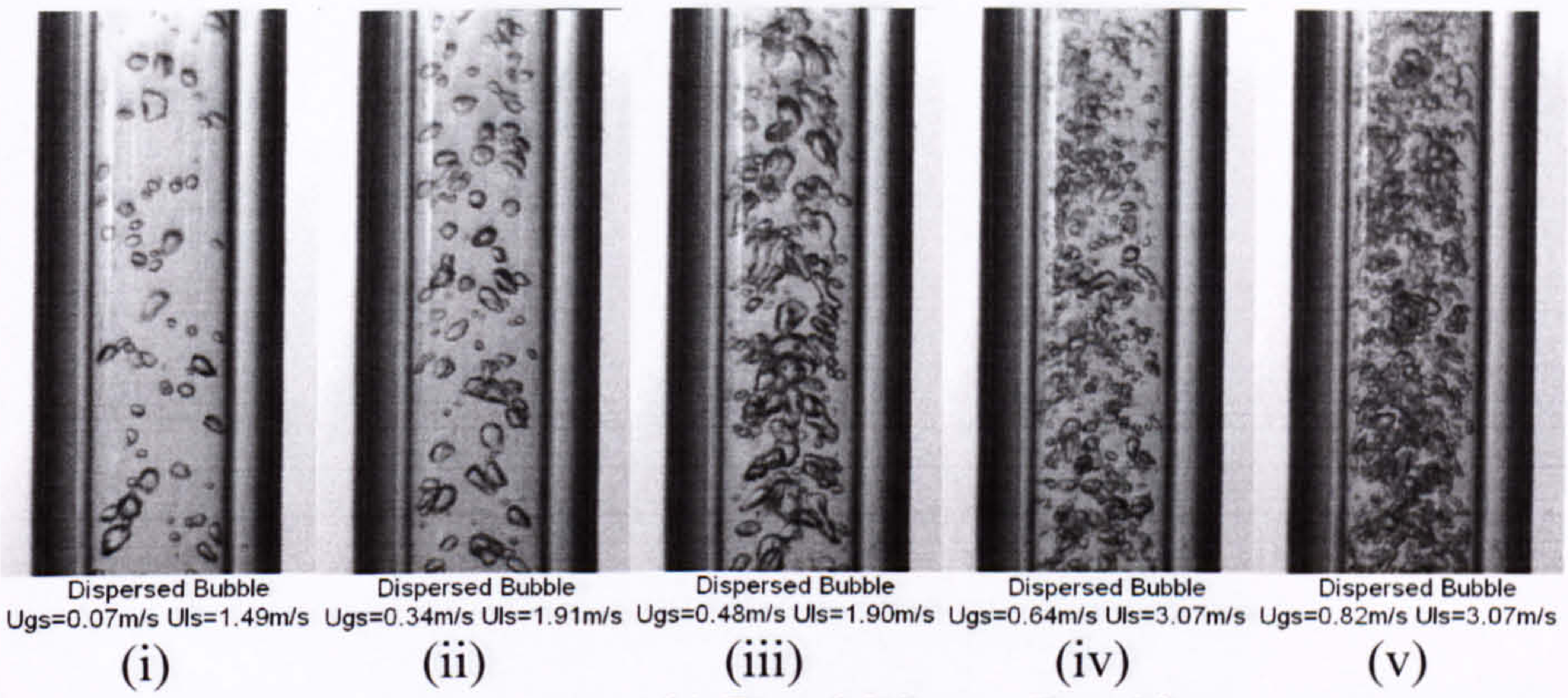

(a) D = 4.26 mm, P = 6 bar

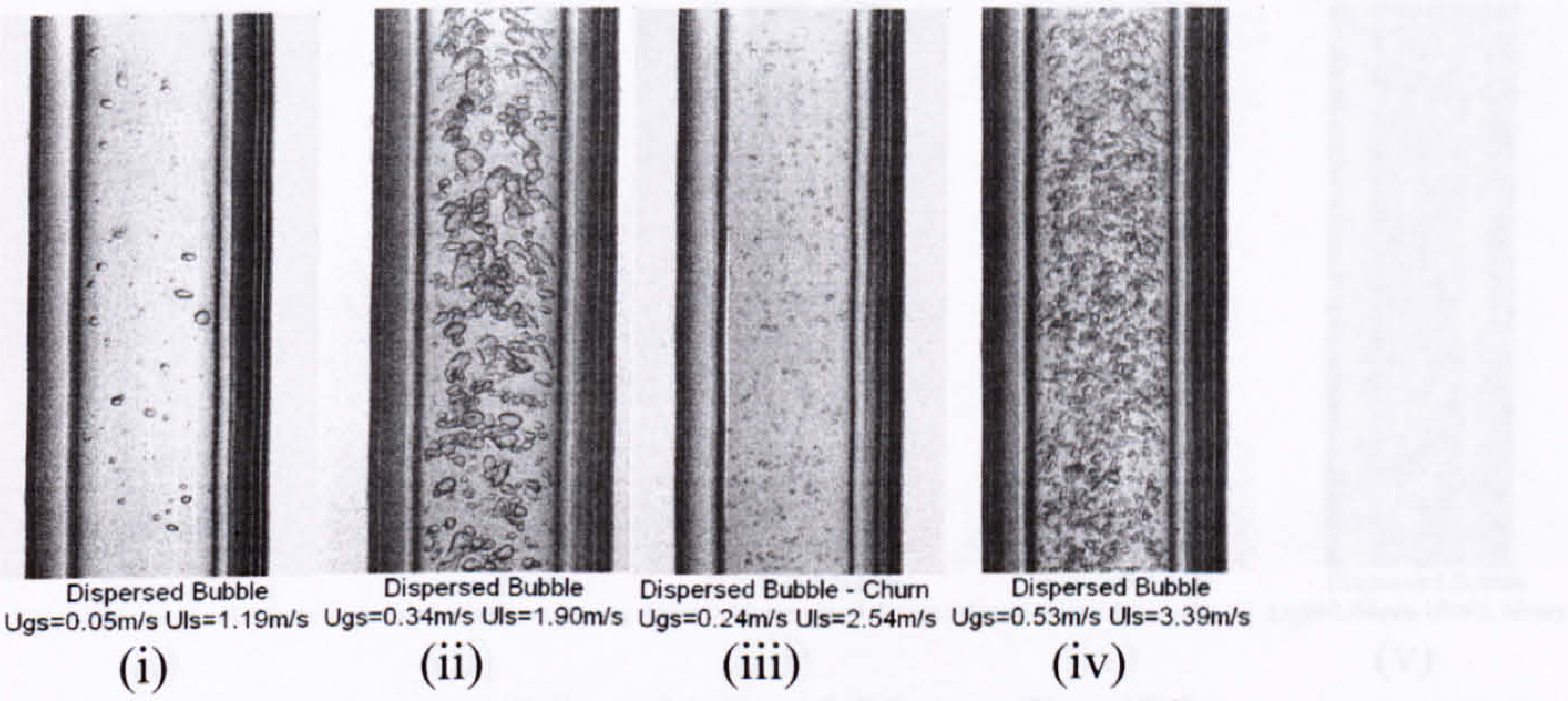

(b) D = 4.26 mm, P = 10 bar

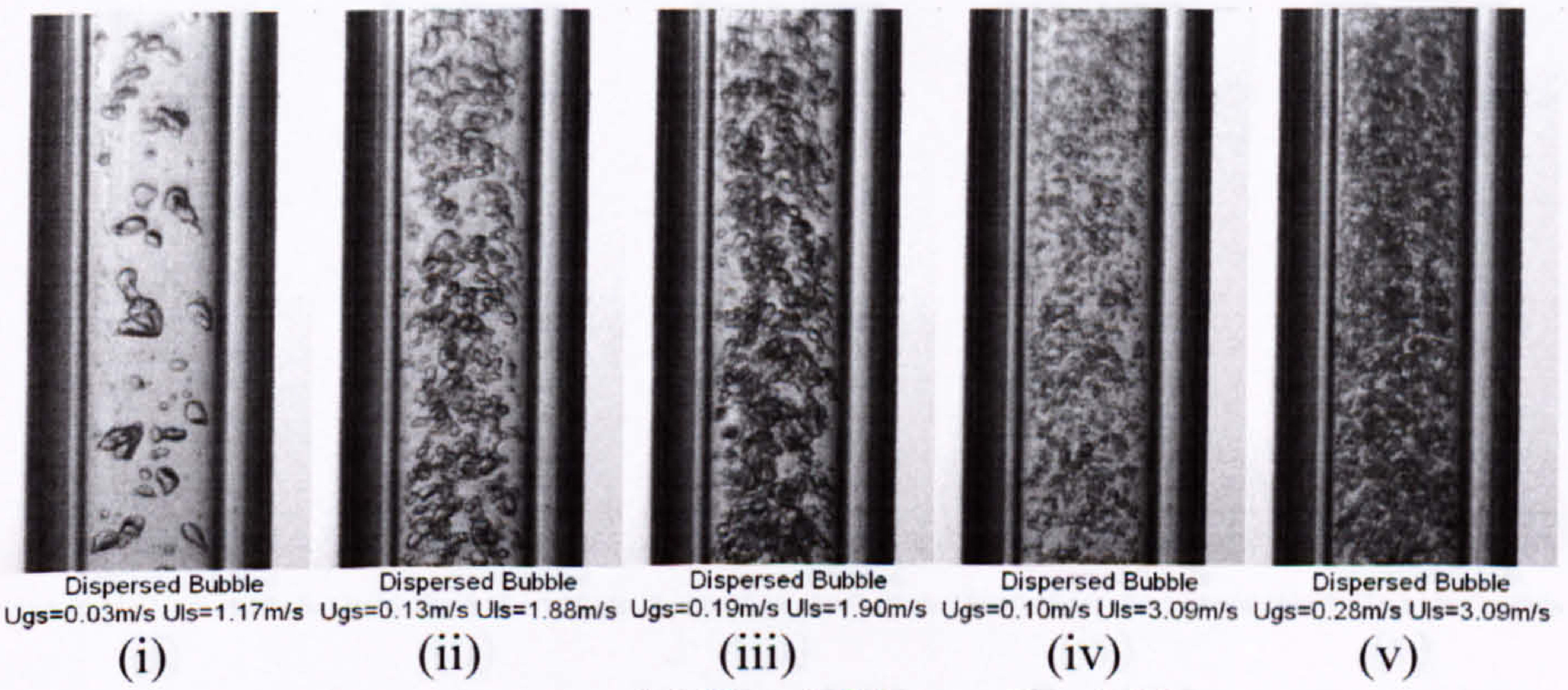

(c) D = 4.26 mm, P = 14 bar

Figure 5.1 Dispersed bubble flow observed in the 4.26 mm tube at different pressures. (a) 6 bar, (b) 10 bar and (c) 14 bar.

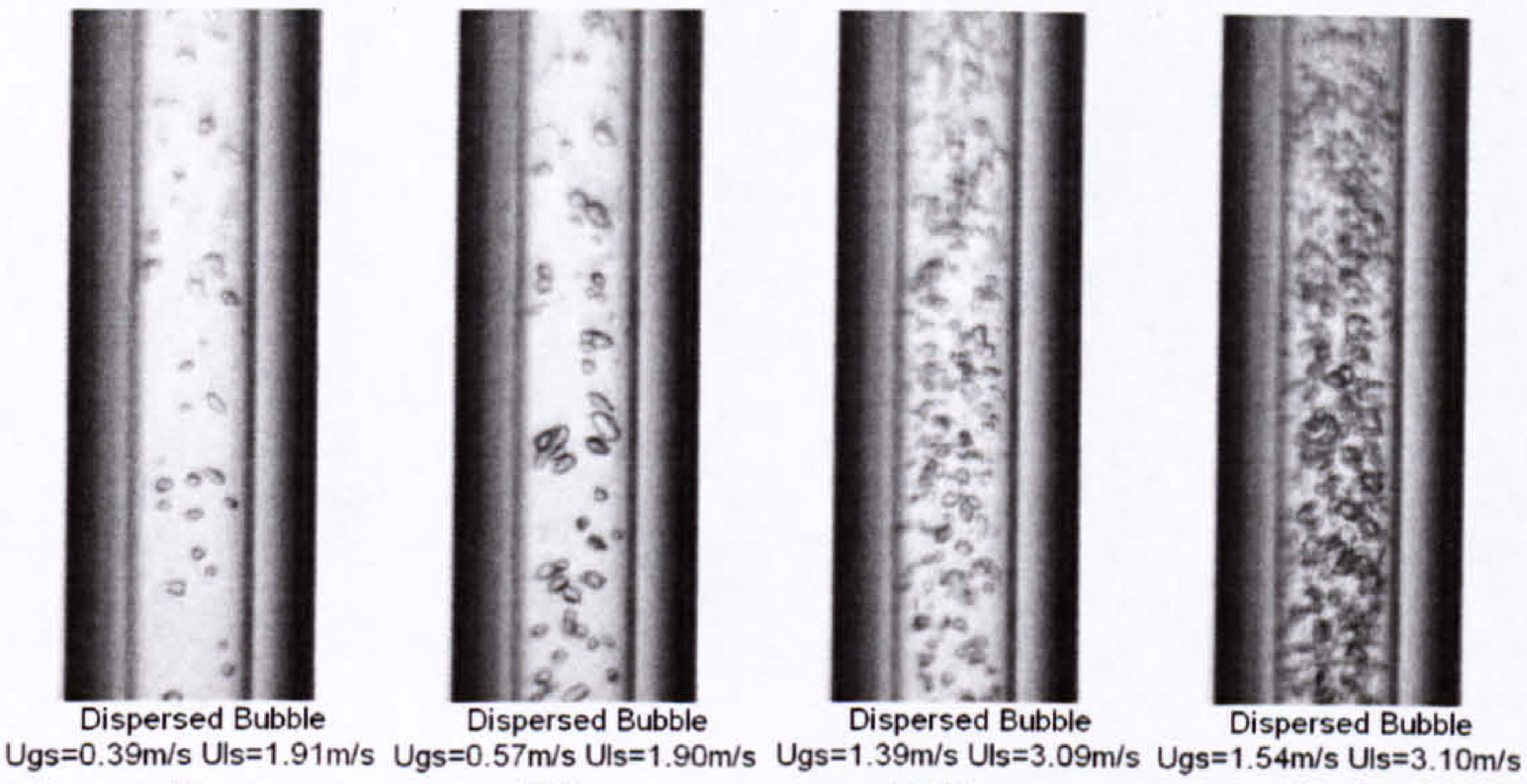

(i) (ii) (iii) (iv)

(a) D = 2.88 mm, P = 6 bar

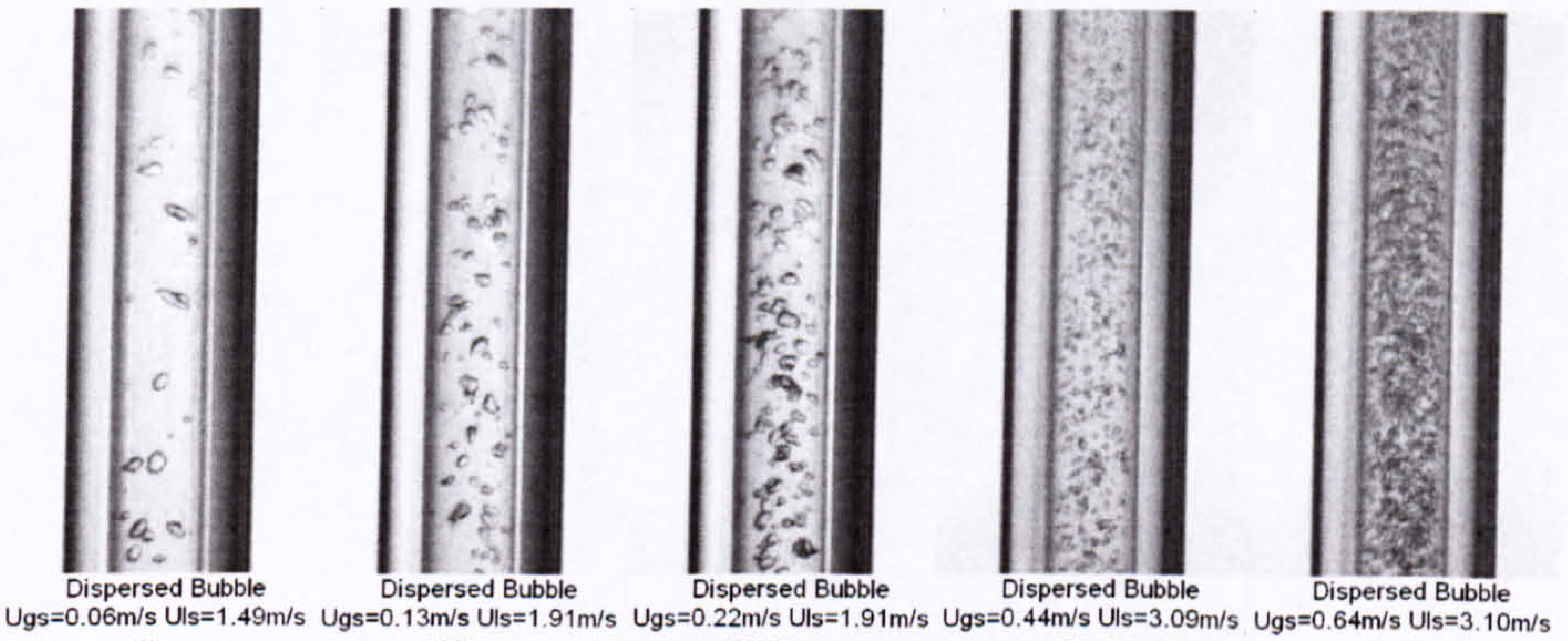

(i) (ii) (iii) (iv) (v)

(b) D = 2.88 mm, P = 10 bar

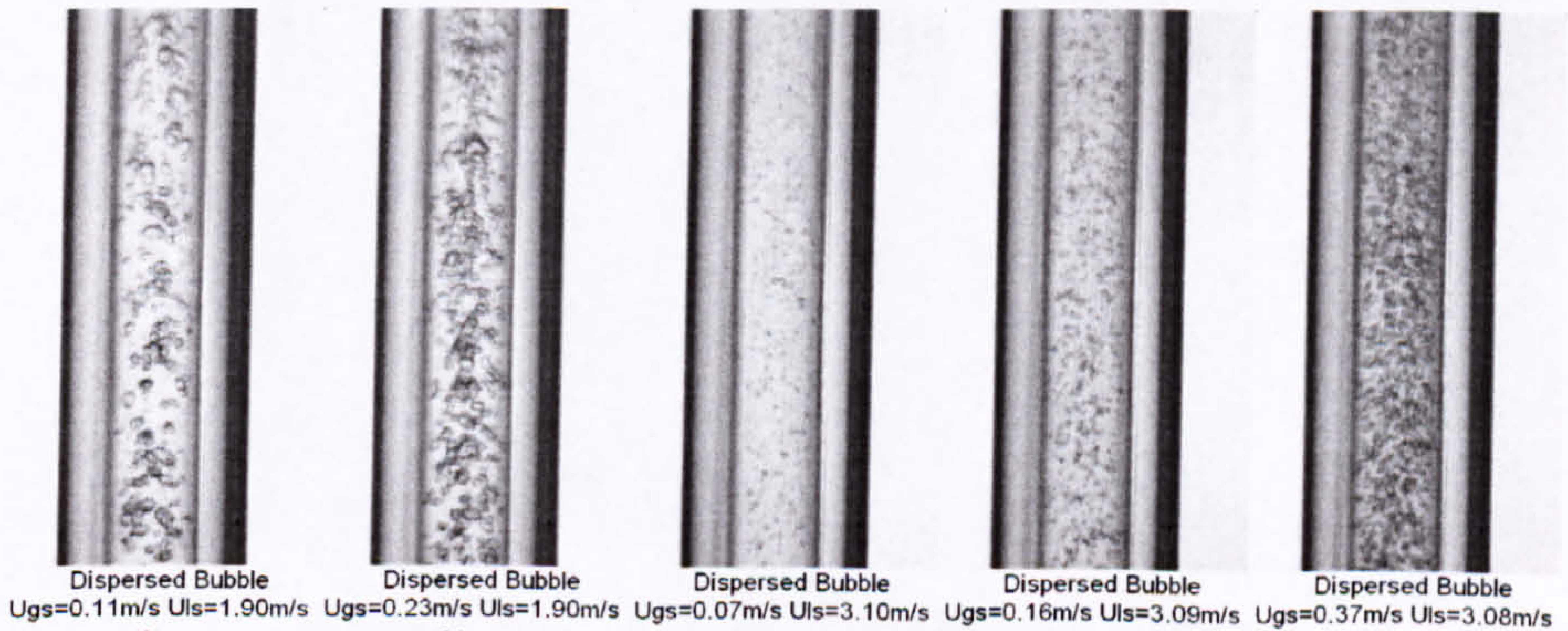

(i) (ii) (iii) (iv) (v)

(c) D = 2.88 mm, P = 14 bar

Figure 5.2 Dispersed bubble flow observed in the 2.88 mm tube at different pressures. (a) 6 bar, (b) 10 bar and (c) 14 bar.

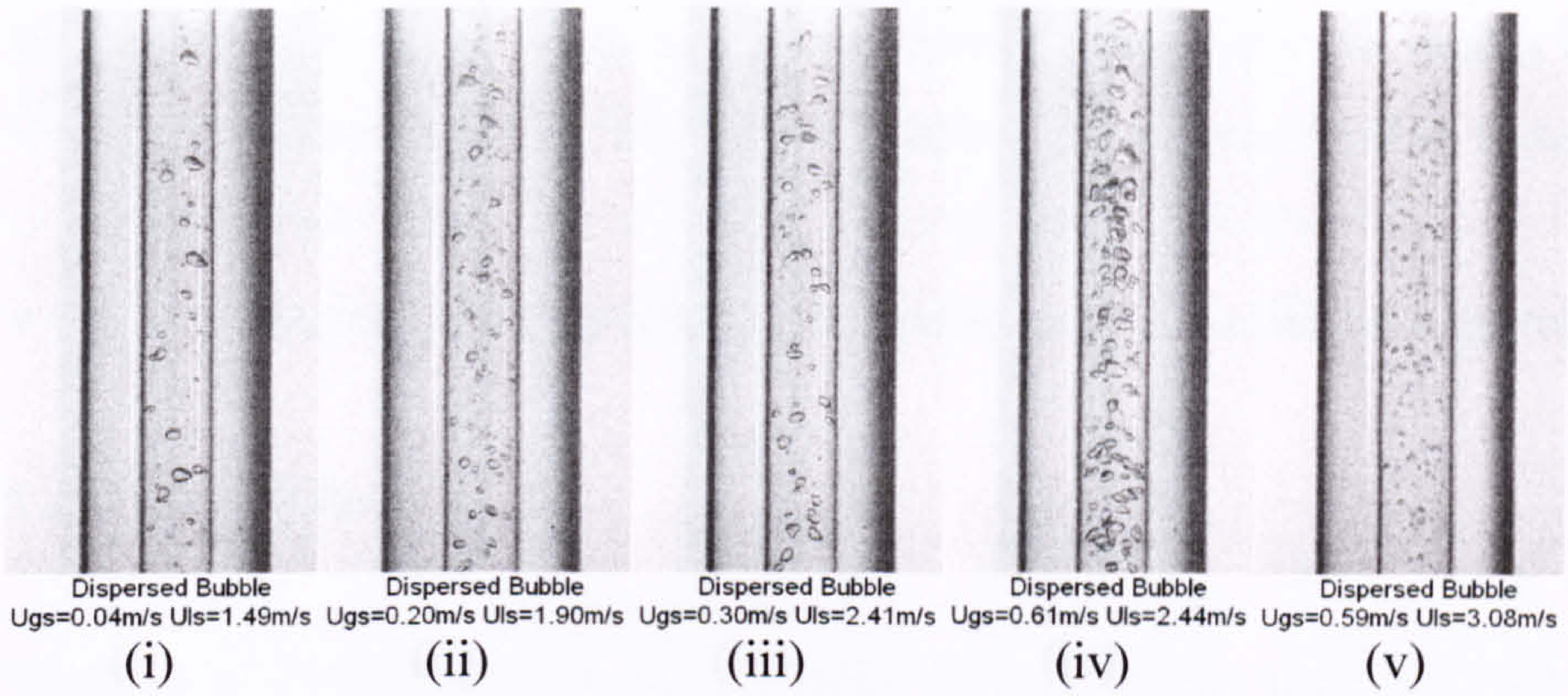

(a) D = 2.01 mm, P = 6 bar

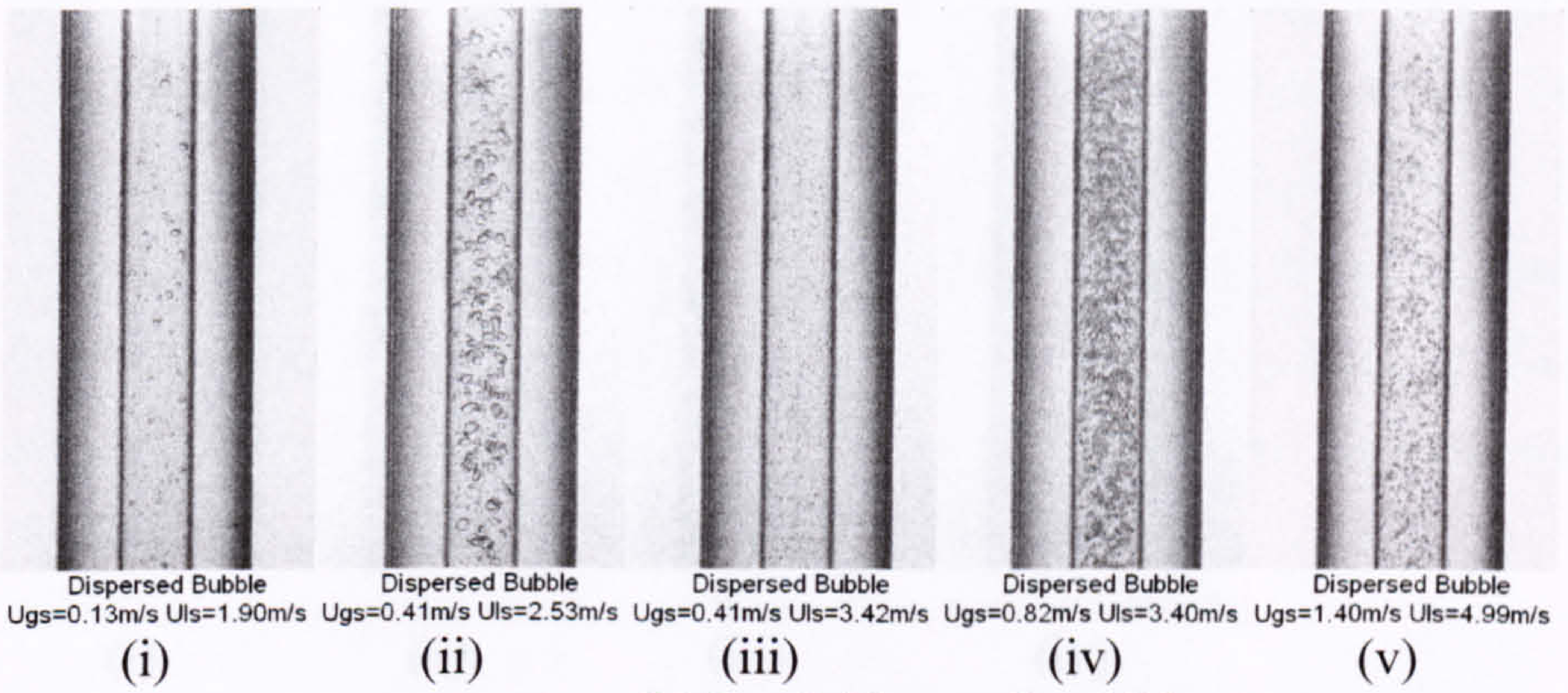

(b) D = 2.01 mm, P = 10 bar

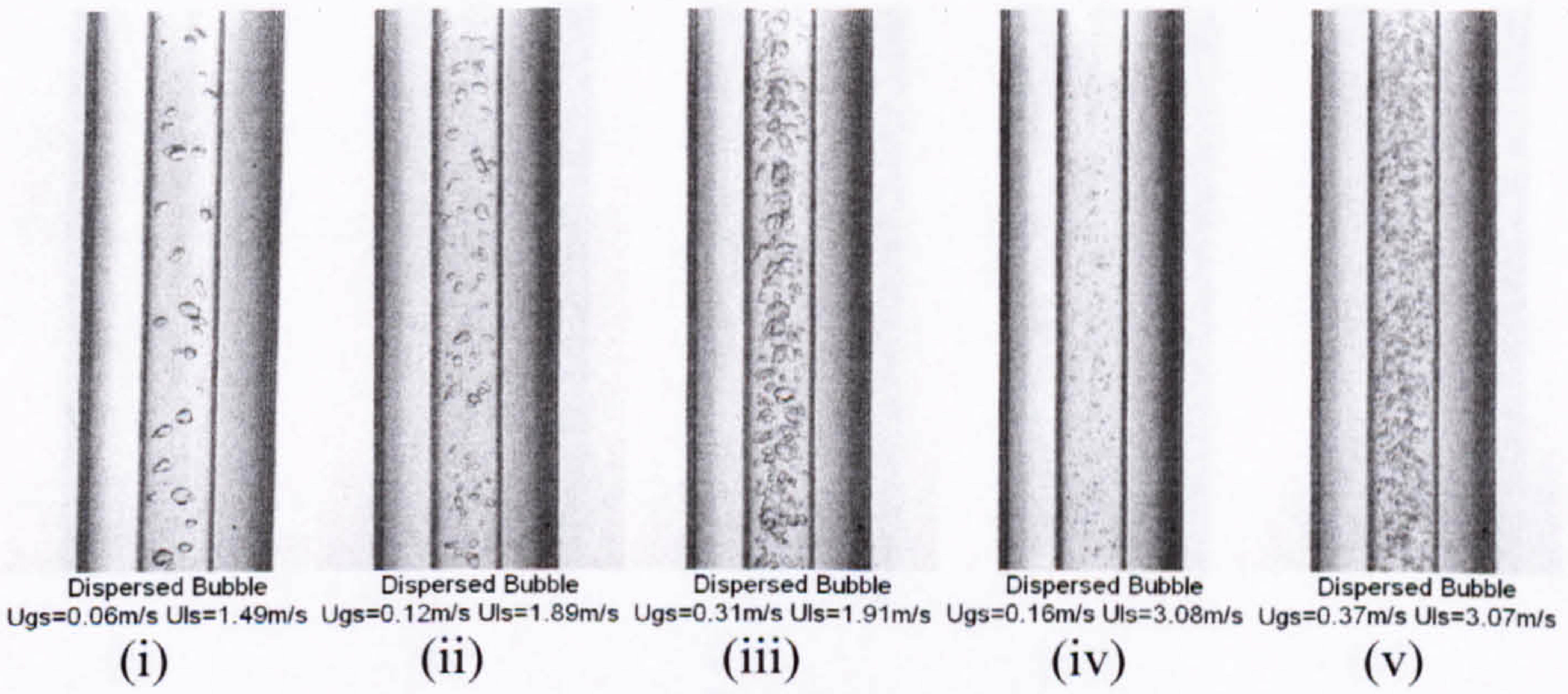

(c) D = 2.01 mm, P = 14 bar

Figure 5.3 Dispersed bubble flow observed in the 2.01 mm tube at different pressures. (a) 6 bar, (b) 10 bar and (c) 14 bar.

In summary, the following concluding statements can be made:

- Dispersed bubbles [illegible] [illegible], smaller and round as the liquid superficial velocity increases.
- Higher gas superficial velocities [illegible] bubble coalescence and growth.

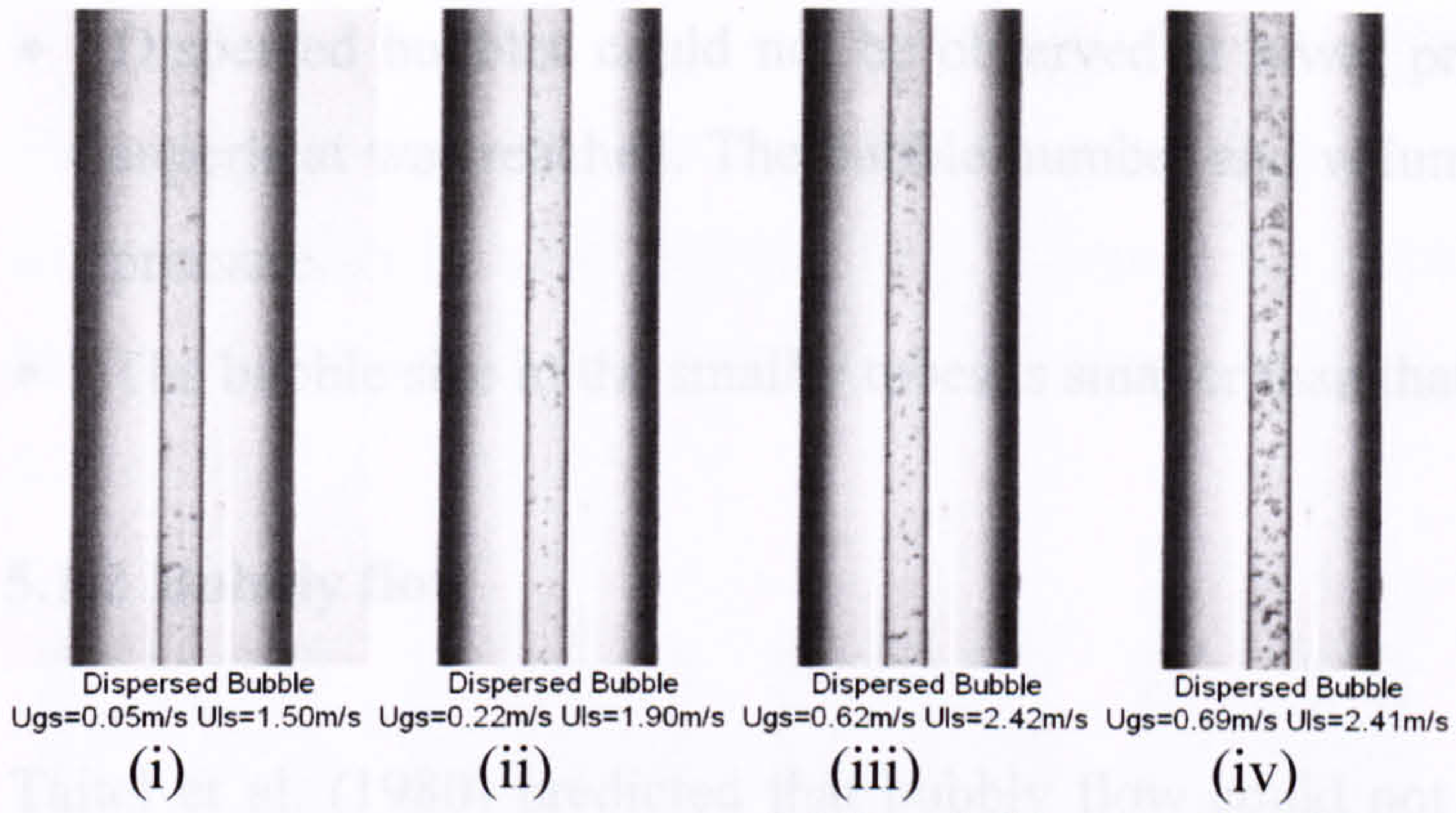

(a) D = 1.10 mm, P = 6 bar

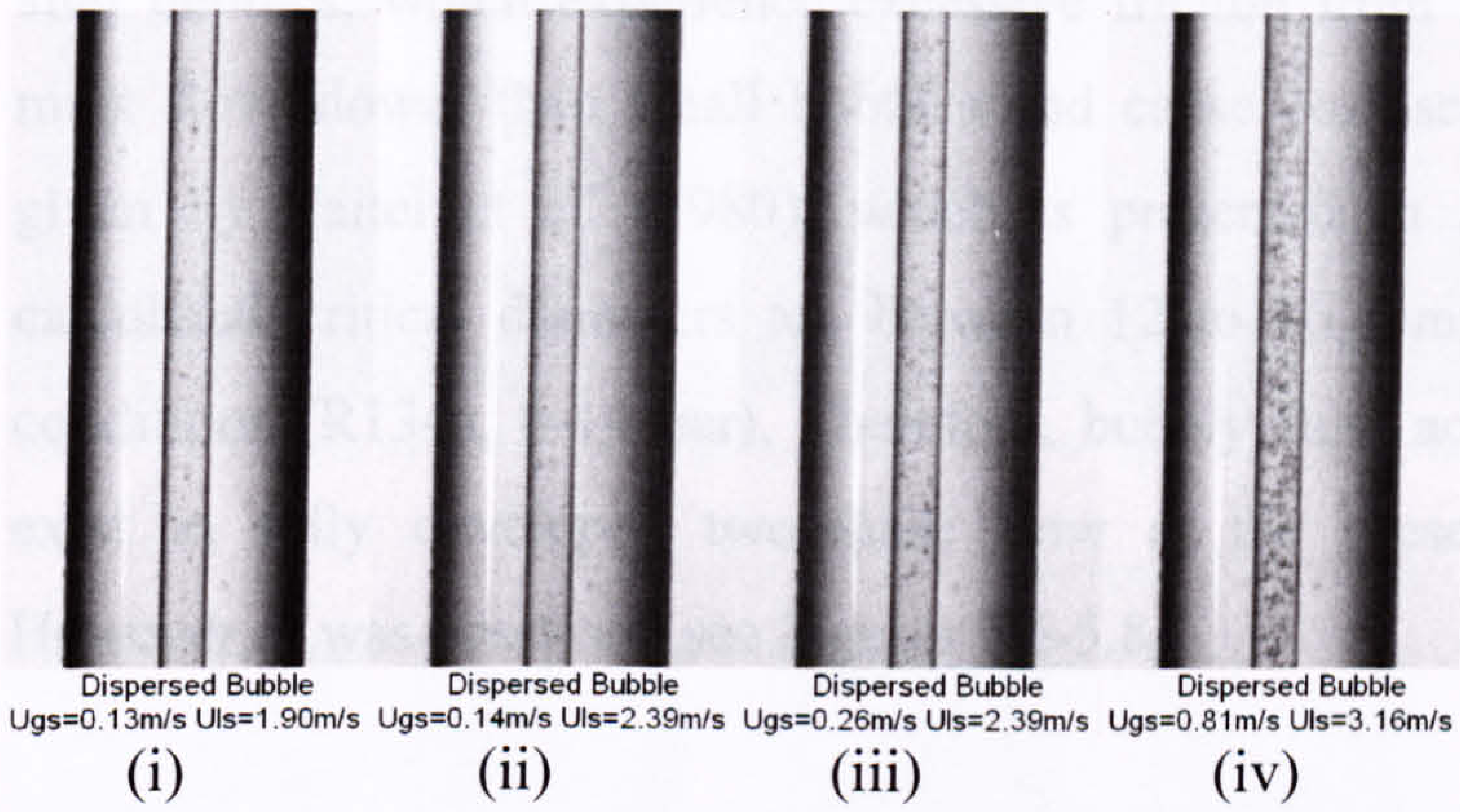

(b) D = 1.10 mm, P = 10 bar

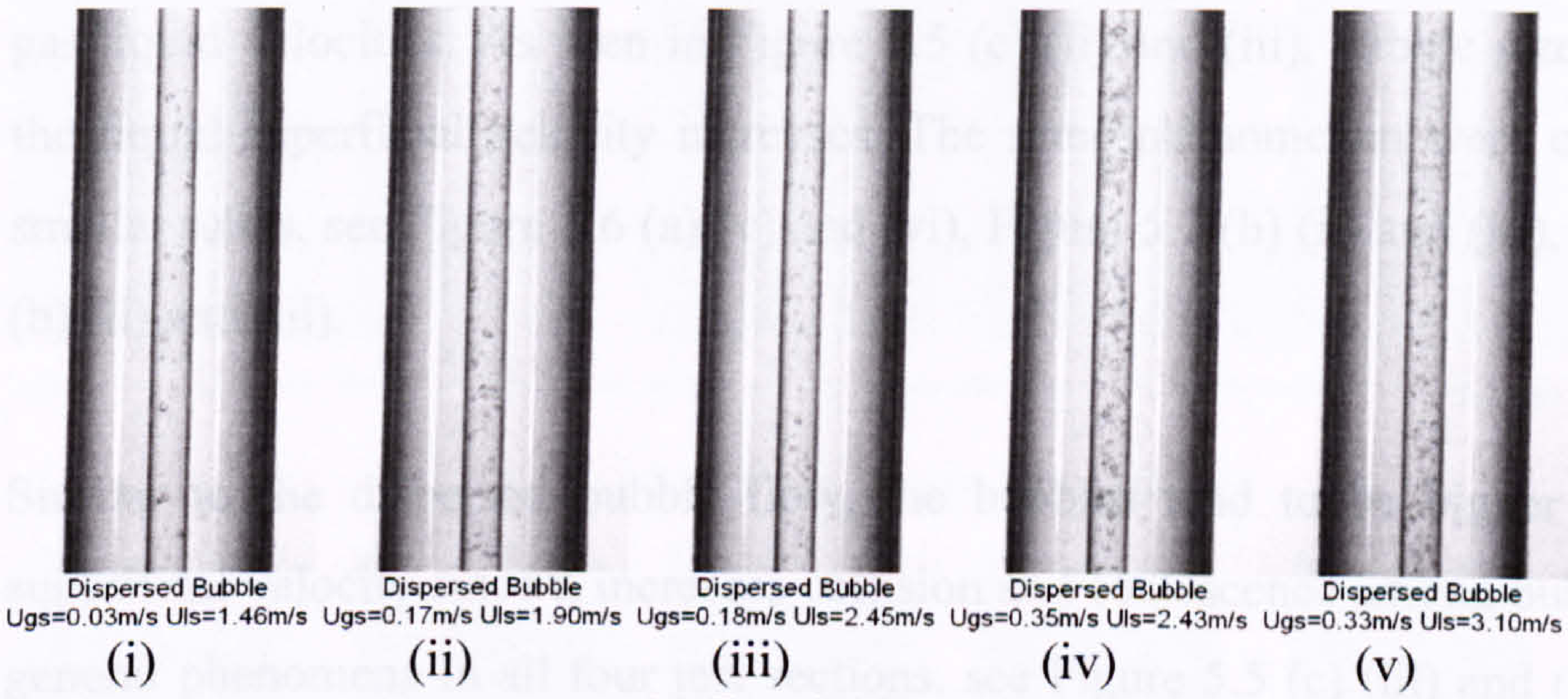

(c) D = 1.10 mm, P = 14 bar

Figure 5.4 Dispersed bubble flow observed in the 1.10 mm tube at different pressures. (a) 6 bar, (b) 10 bar and (c) 14 bar.

In summary, the following concluding observations can be made:

- Dispersed bubbles tend to be smaller, regular and round as the liquid superficial velocity increases.
- Higher gas superficial velocity facilitates bubble coalescence and growth.

- Dispersed bubbles could not be observed at lower pressure until a high degree of superheat was reached. The bubble number and volume tend to be smaller at lower pressure.
- The bubble size in the smaller tubes is smaller than that in the larger tubes.

5.1.2 Bubbly flow

Taitel et al. (1980) predicted that bubbly flow could not exist in small tubes because slug bubbles, which experience excessive friction from liquid film on the tube wall, must flow slower than small bubbles and cause coalescence. Based on the equation given by Taitel et al. (1980), which is presented in Appendix B Table B.1, the calculated critical diameters are between 12 to 16 mm at the current experimental conditions (R134a, 6-14 bar). Therefore, bubbly flow according to Taitel should not exist in fully developed two-phase flow at the present experimetnal conditions. However, it was observed, see Figures 5.5-5.8.

Figure 5.5 shows bubbly flow for the 4.26 mm tube at the different pressures and gas/liquid velocities. As seen in Figure 5.5 (c) (ii) and (iii), bubble size diminishes as the liquid superficial velocity increases. The same phenomenon were observed in the smaller tubes, see Figure 5.6 (a) (v) and (vi), Figure 5.7 (b) (ii) and (iii), and Figure 5.8 (b) (ii) and (iii).

Similar to the dispersed bubble flow, the bubbles tend to be bigger at higher gas superficial velocity since it increases collision and coalescence among bubbles. This is a general phenomena in all four test sections, see Figure 5.5 (c) (iii) and (iv), Figure 5.6 (a) (iv) and (v), Figure 5.7 (b) (iv) and (v), and Figure 5.8 (b) (iii) and (v).

It seems that pressure has little effect on the bubble's configuration at lower flow rate; for example, compare Figure 5.5 (a) (i) and (b) (i), Figure 5.6 (a) (ii), (b) (iii) and (c) (i), Figure 5.7 (a) (ii), (b) (ii) and (c) (iii), Figure 5.8 (a) (iii), (b) (ii) and (c) (ii). With increasing flow rate, numerous small bubbles were produced at the higher pressure in the 4.26 and 2.88 mm tubes, see Figure 5.5 (a) (vi) and (c) (vi), Figure 5.6 (b) (vi) and (c) (vi). However, the above tendency is not very obvious in the 1.10 and 2.01 mm tubes.

Bubbles tend to be regular and round in smaller tubes due to the enhanced effect of surface tension in small bubbles, e.g. compare the bubbles in Figure 5.5 (a) (i) and Figure 5.7 (a) (i), Figure 5.5 (b) (ii) and Figure 5.7 (b) (ii), Figure 5.5 (c) (iv) and Figure 5.7 (c) (iv).

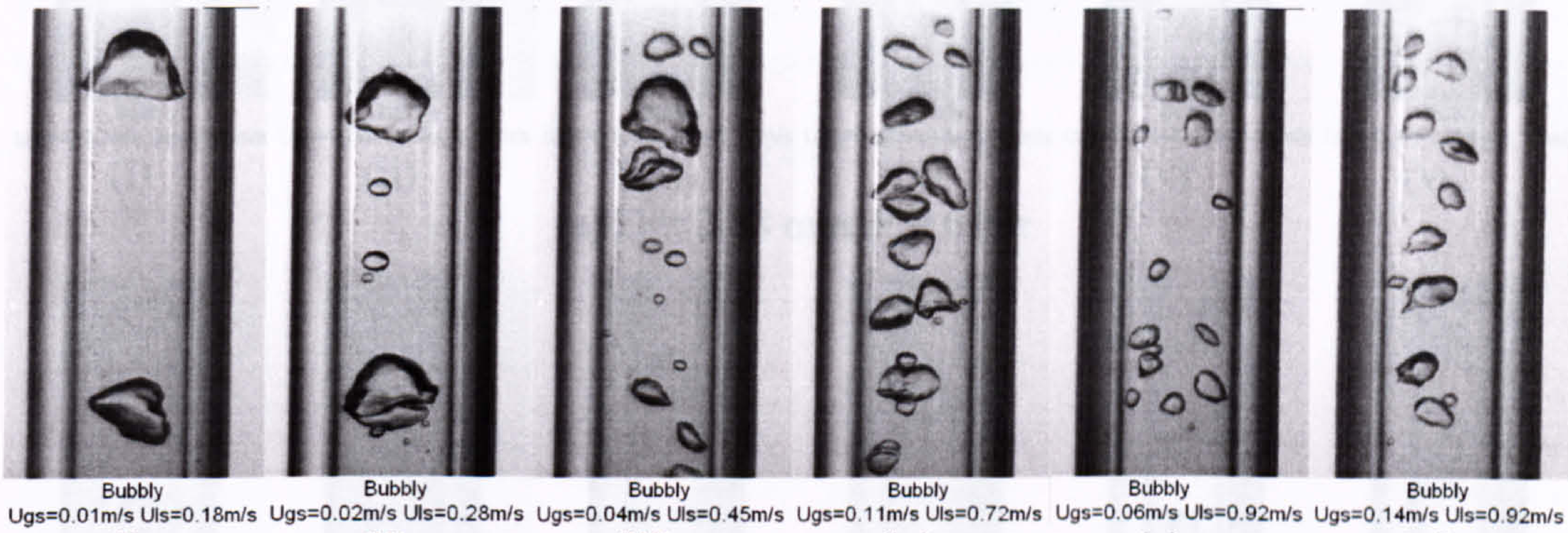

(i) (ii) (iii) (iv) (v) (vi)

(a) D = 4.26 mm, P = 6 bar

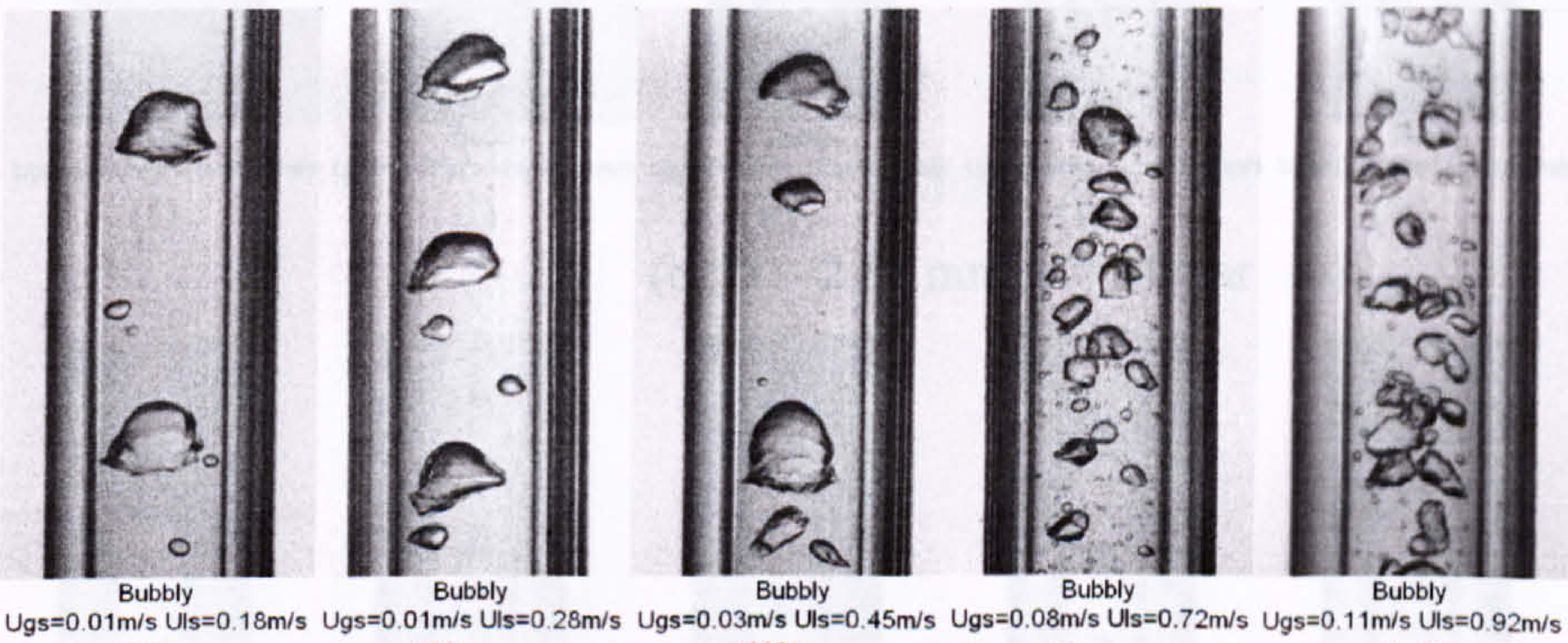

(i) (ii) (iii) (iv) (vi)

(b) D = 4.26 mm, P = 10 bar

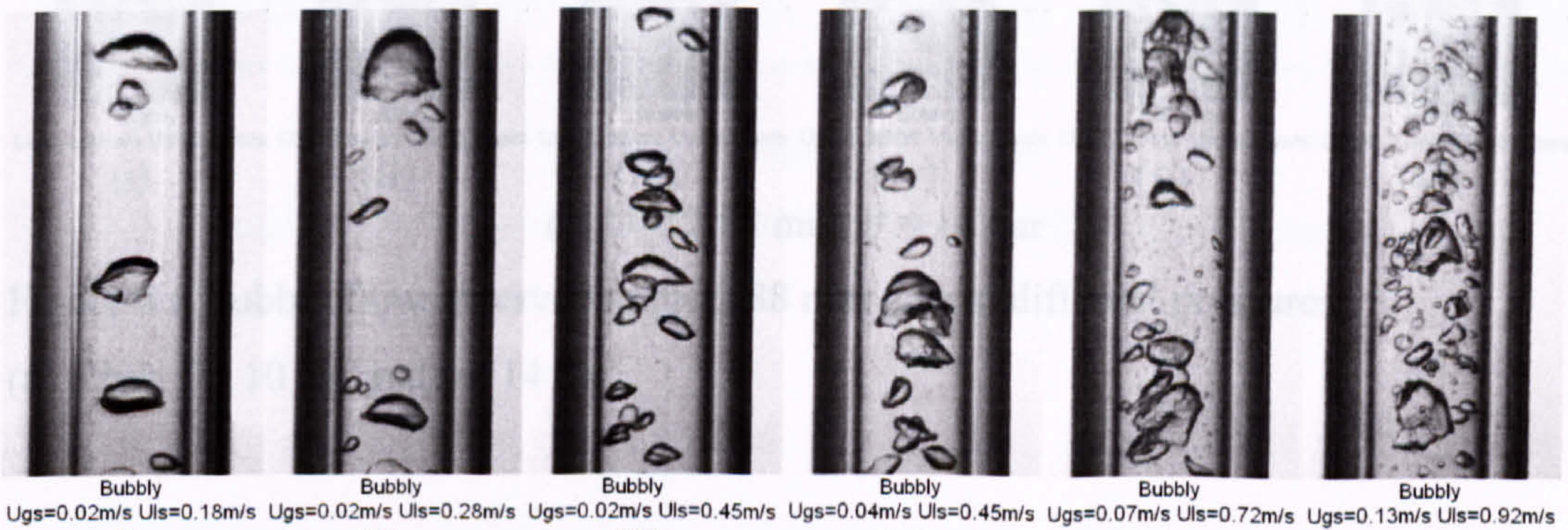

(i) (ii) (iii) (iv) (v) (vi)

(c) D = 4.26 mm, P = 14 bar

Figure 5.5 Bubbly flow observed in the 4.26 mm tube at different pressures. (a) 6 bar, (b) 10 bar and (c) 14 bar.

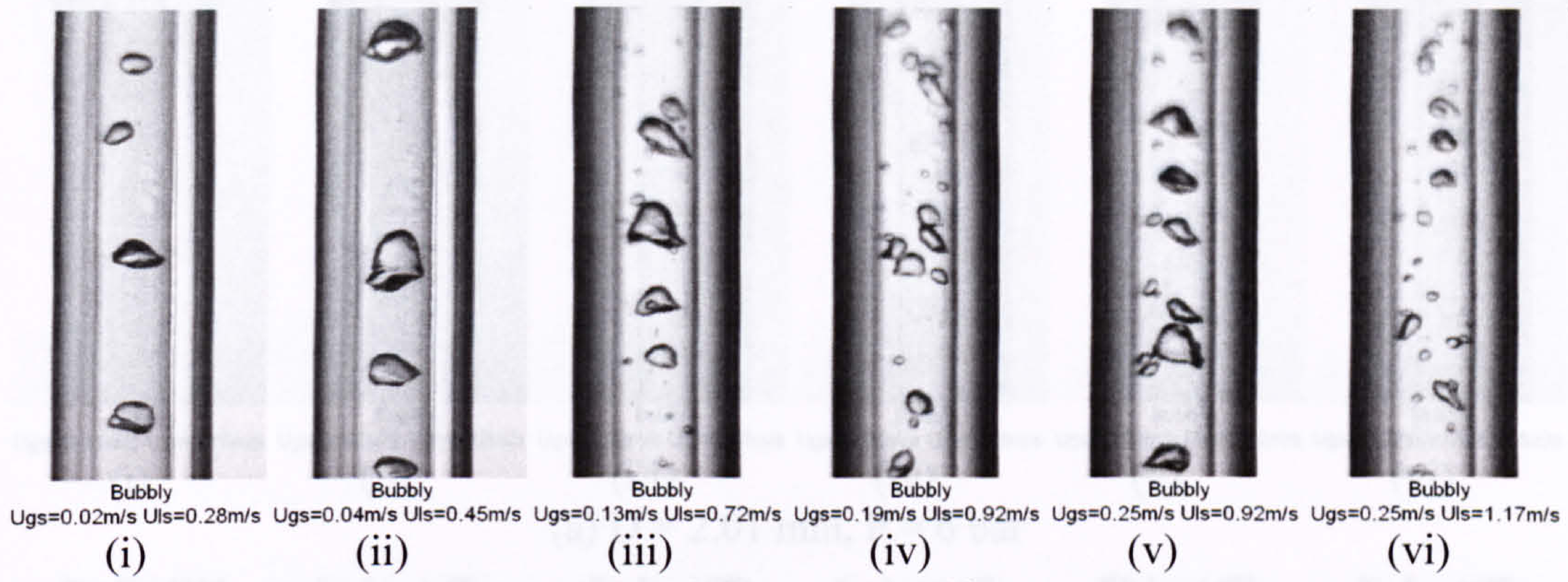

(a) D = 2.88 mm, P = 6 bar

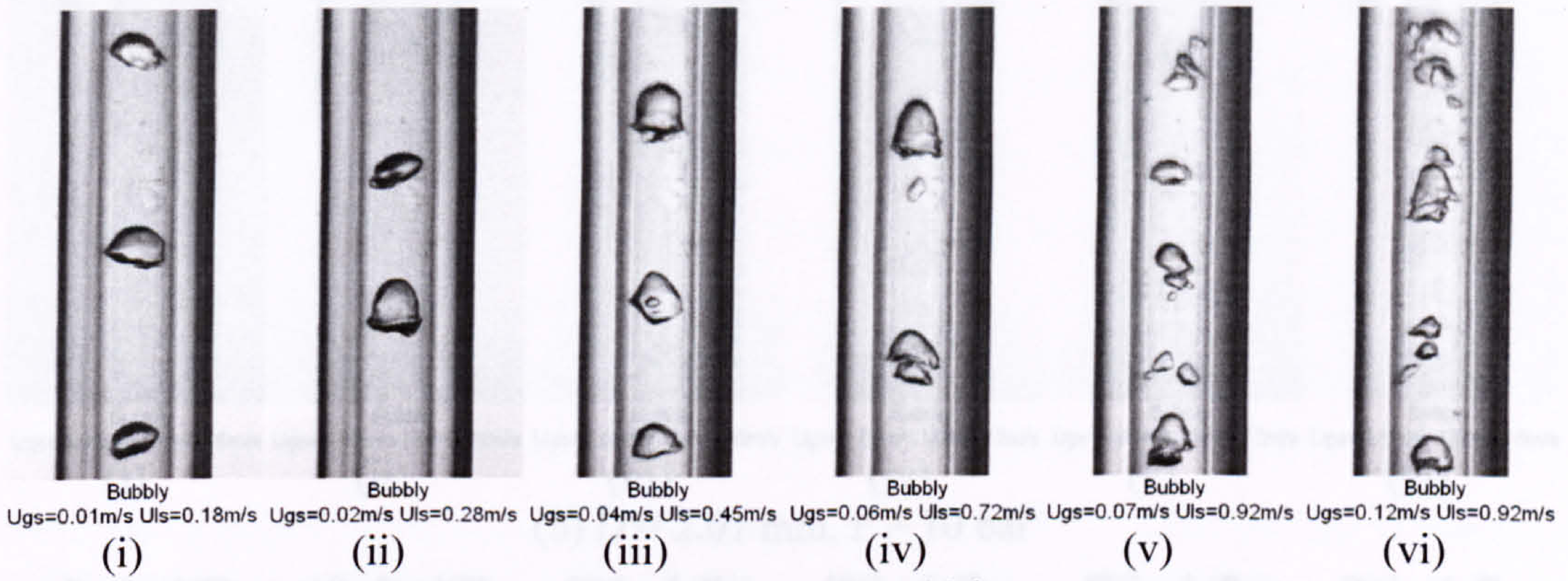

(b) D = 2.88 mm, P = 10 bar

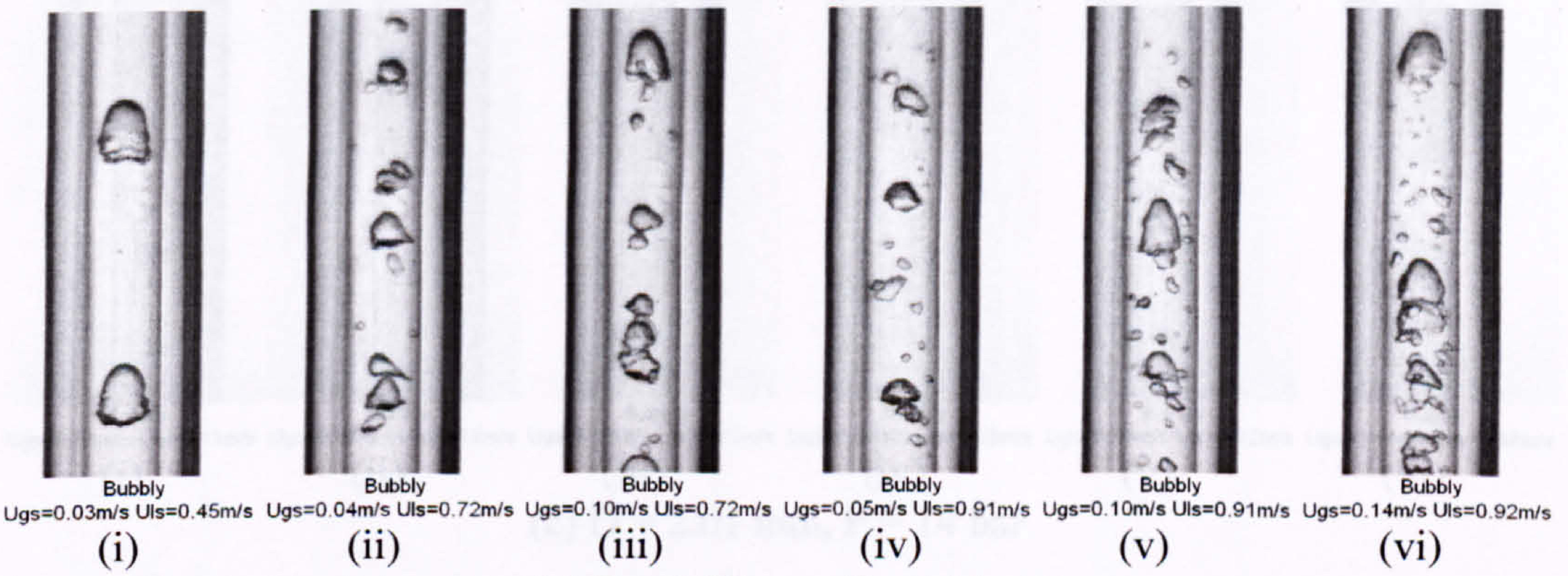

(c) D = 2.88 mm, P = 14 bar

Figure 5.6 Bubbly flow observed in the 2.88 mm tube at different pressures. (a) 6 bar, (b) 10 bar and (c) 14 bar.

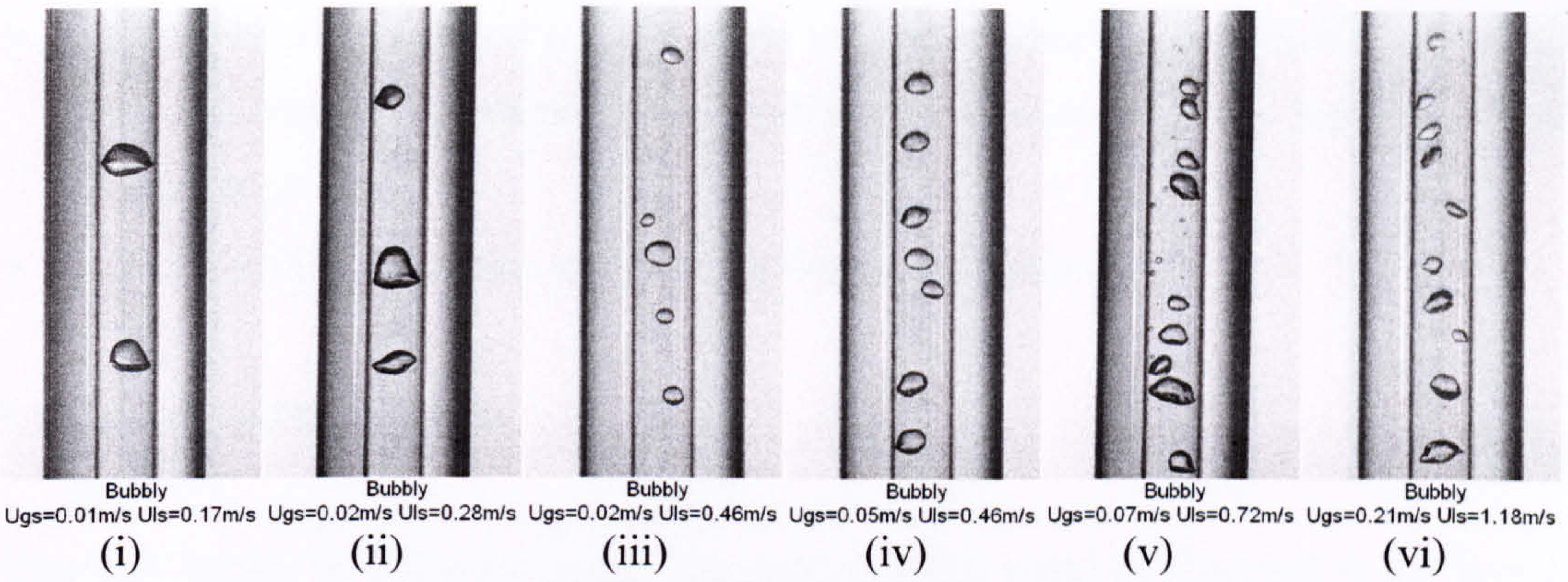

(a) D = 2.01 mm, P = 6 bar

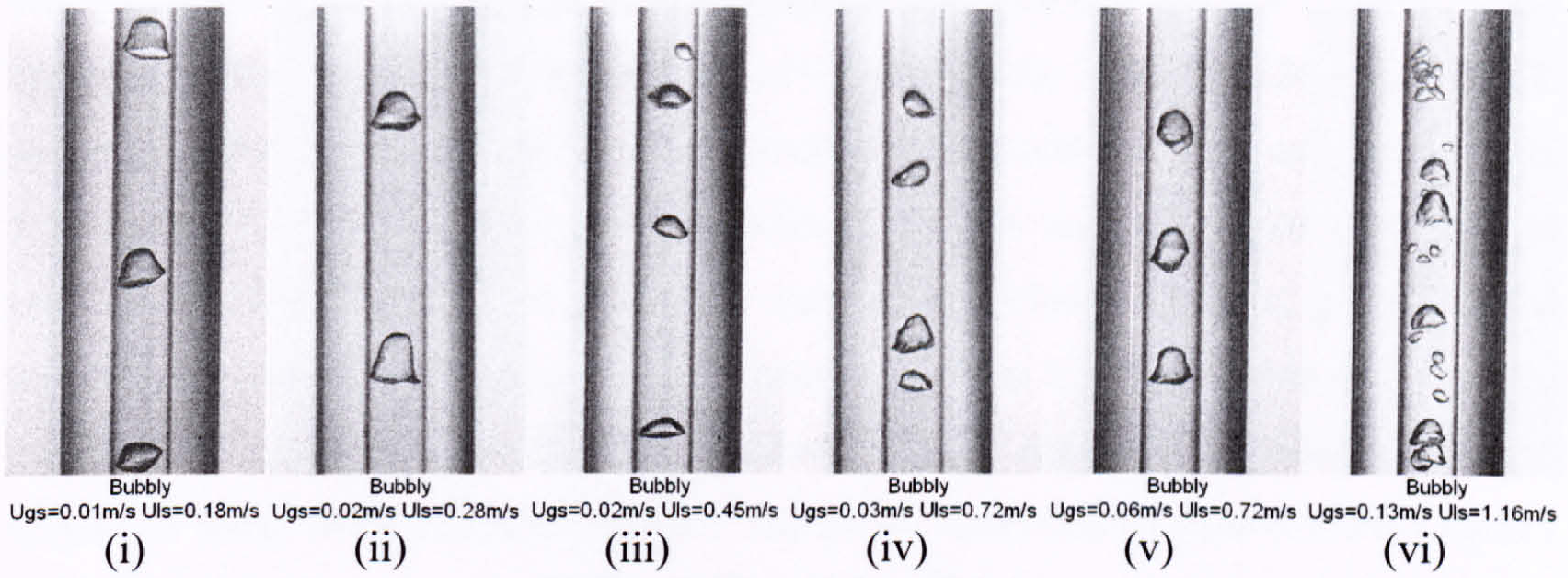

(b) D = 2.01 mm, P = 10 bar

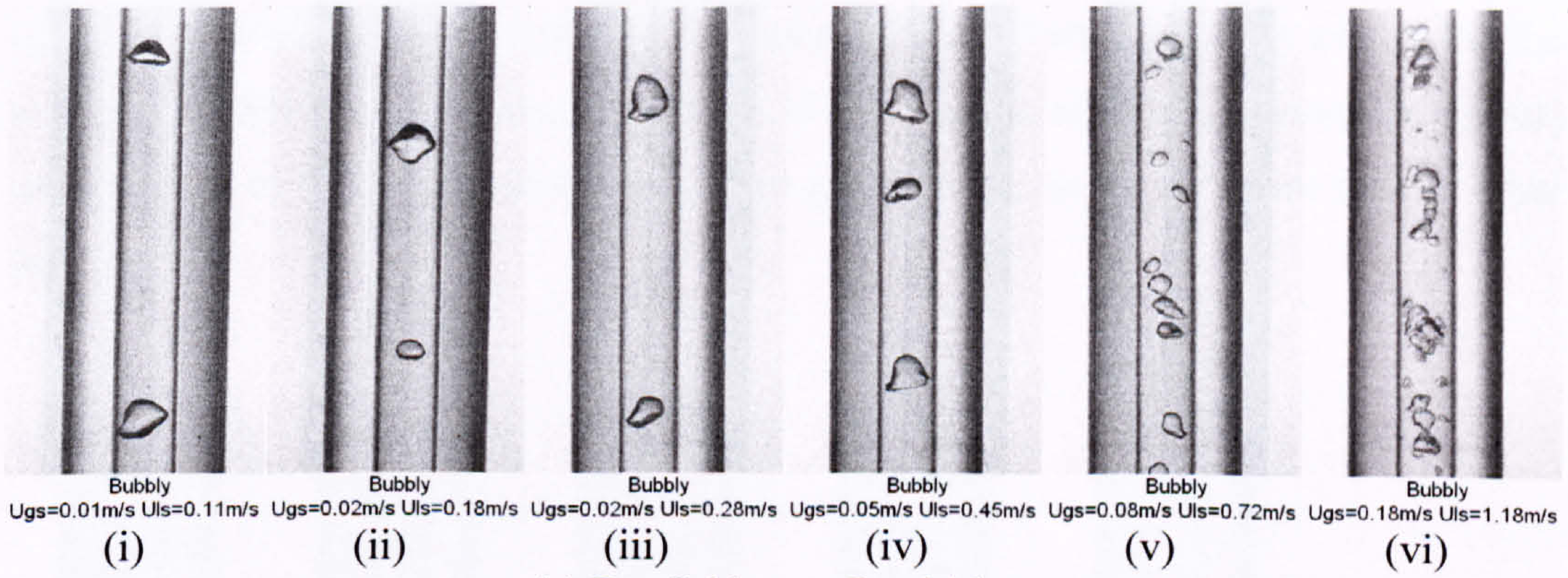

(c) D = 2.01 mm, P = 14 bar

Figure 5.7 Bubbly flow observed in the 2.01 mm tube at different pressures. (a) 6 bar, (b) 10 bar and (c) 14 bar.

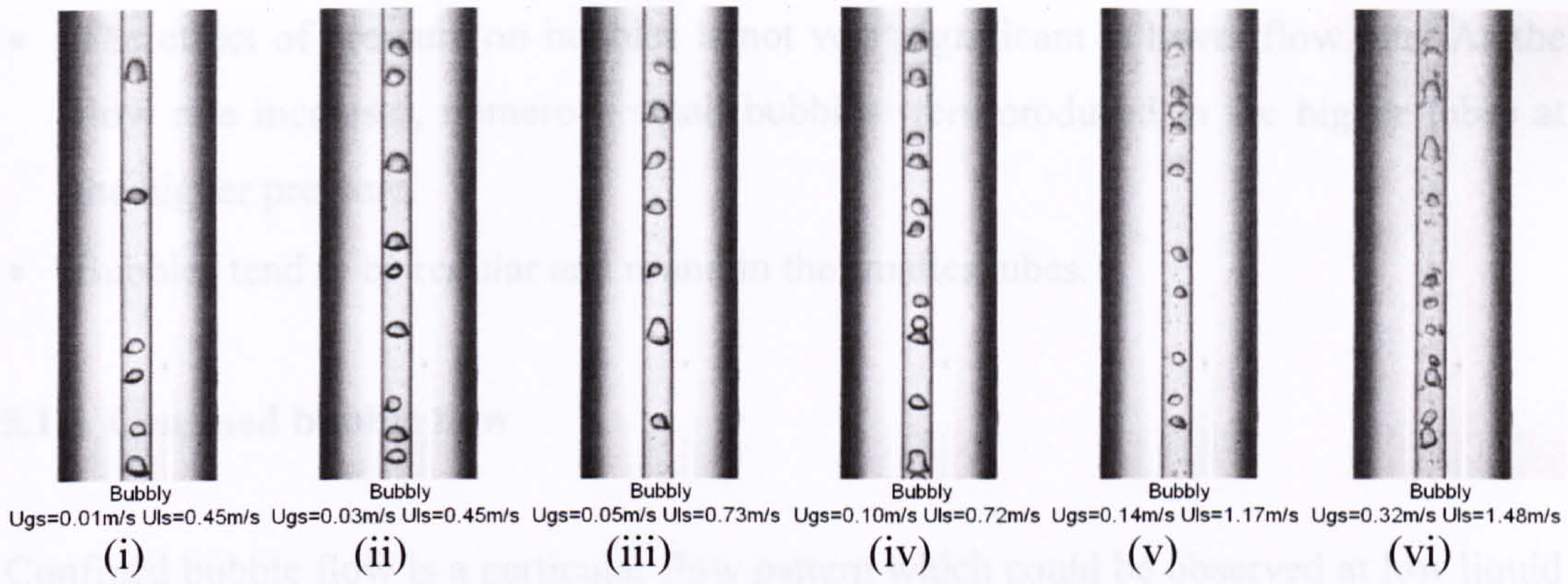

(a) D = 1.10 mm, P = 6 bar

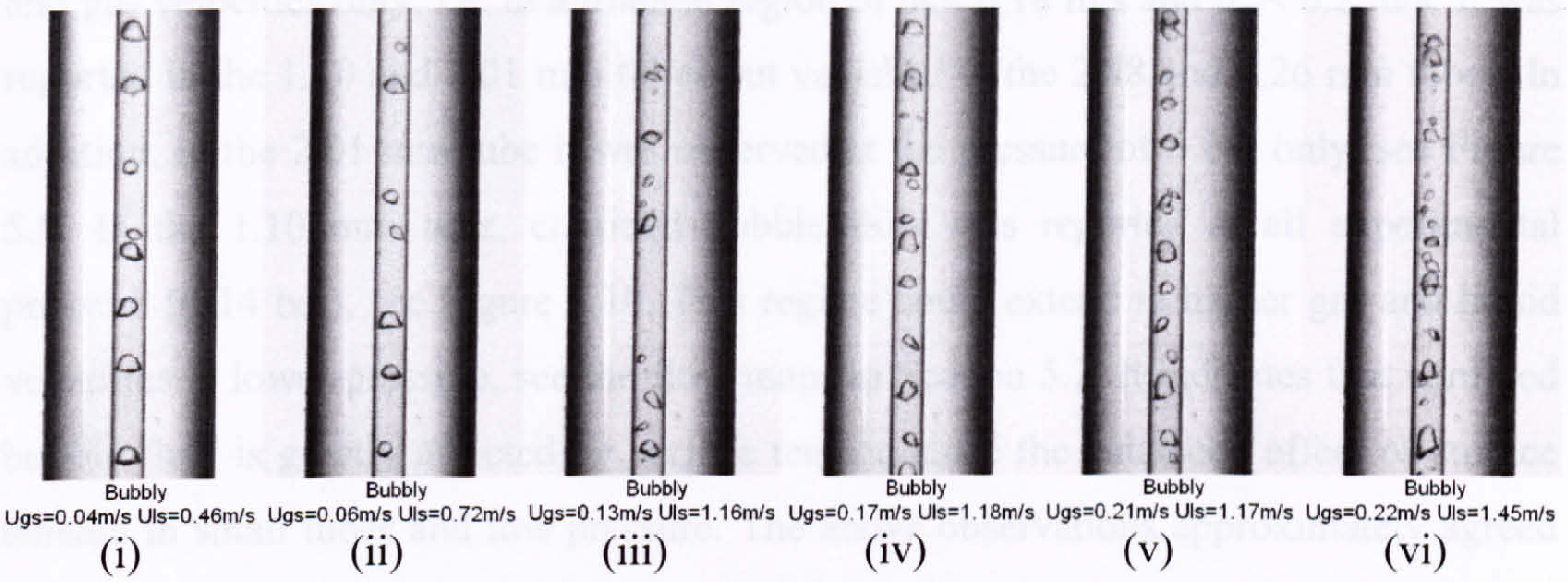

(b) D = 1.10 mm, P = 10 bar

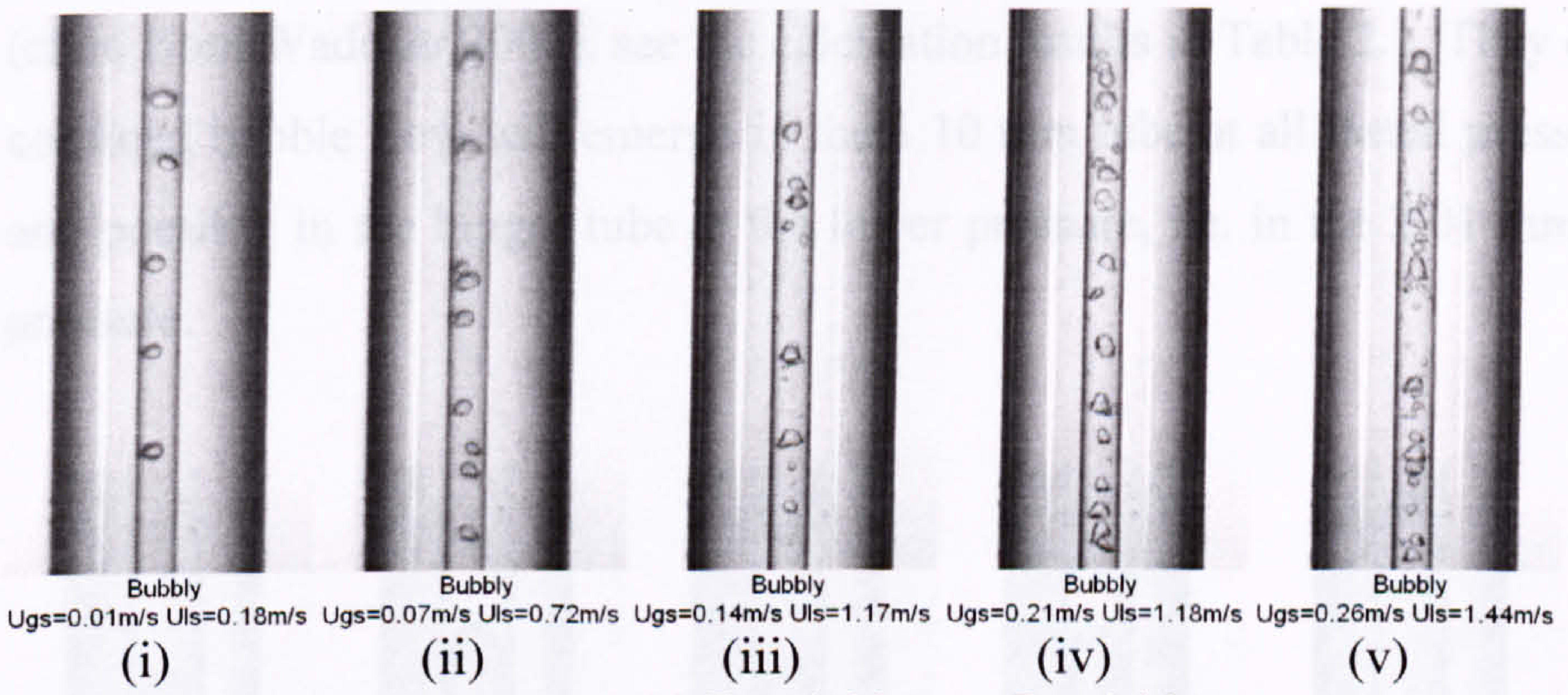

(c) D = 1.10 mm, P = 14 bar

Figure 5.8 Bubbly flow observed in the 1.10 mm tube at different pressures. (a) 6 bar, (b) 10 bar and (c) 14 bar.

In summary, the following concluding observations can be made:

- Bubbles tend to be smaller at higher liquid superficial velocity.
- Bubbles tend to be bigger at higher gas superficial velocity.

- The effect of pressure on bubbles is not very significant at lower flow rate. As the flow rate increases, numerous small bubbles were produced in the bigger tubes at the higher pressure.
- Bubbles tend to be regular and round in the smaller tubes.

5.1.3 Confined bubble flow

Confined bubble flow is a particular flow pattern which could be observed at low liquid and gas velocities only, i.e. in a triangle region of $u_{ls} < 0.18$ m/s and $u_{gs} < 0.2$ m/s. It was reported in the 1.10 and 2.01 mm tubes but vanished in the 2.88 and 4.26 mm tubes. In addition, in the 2.01 mm tube it was observed at the pressure of 6 bar only, see Figure 5.9. In the 1.10 mm tube, confined bubble flow was reported at all experimental pressure (6-14 bar), see Figure 5.10. This regime could extend to higher gas and liquid velocities at lower pressure, see the flow maps in Section 5.2. It indicates that confined bubble flow is greatly affected by surface tension since the enhanced effect of surface tension in small tubes and low pressure. The above observations approximately agreed with the criteria recommended by Kew and Cornwell (1997) or Hatori and Bretherton (cited from Wadekar 2002), see the calculation results in Table 2.1. They expect that the confined bubble flow will emerge in the 1.10 mm tube at all tested pressure (6-10 bar) and possibly in the bigger tube at the lower pressure, i.e. in the 2.01 mm tube at 6 bar pressure.

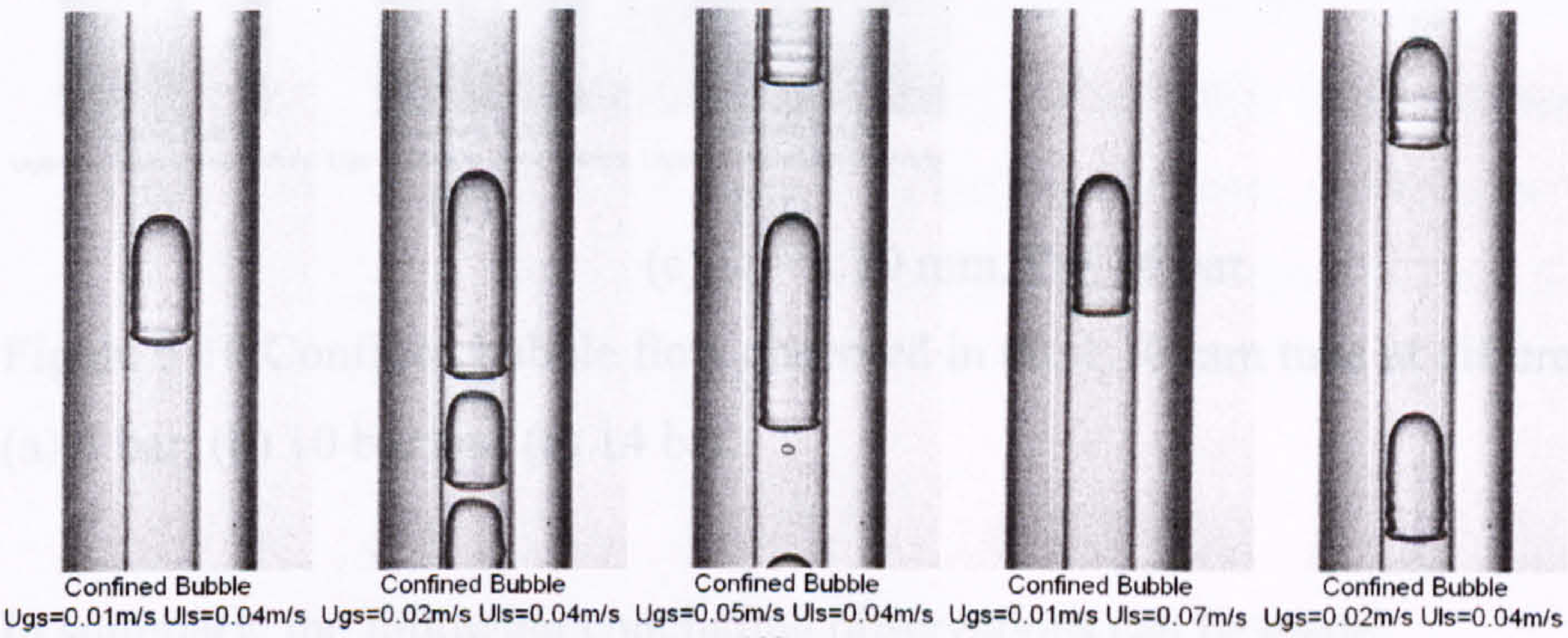

(i) (ii) (iii) (iv) (v)

Figure 5.9 Confined bubble flow observed in the 2.01 mm tube at 6 bar.

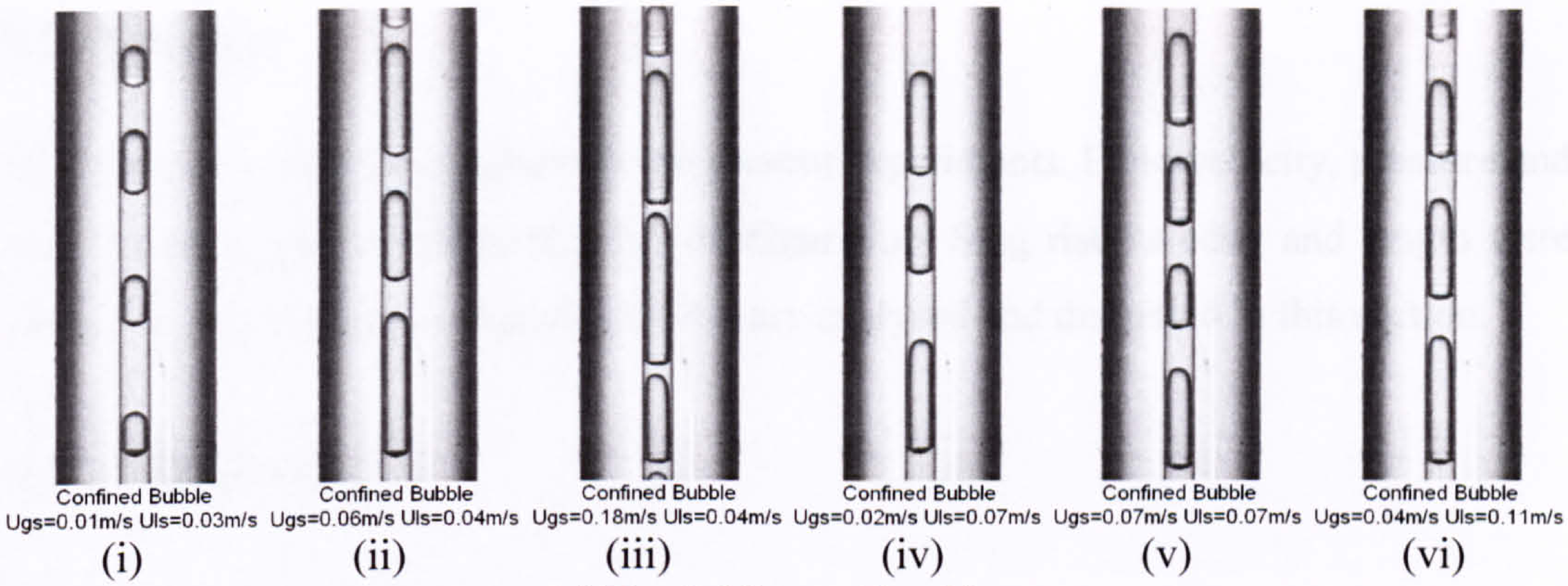

(a) D = 1.10 mm, P = 6 bar

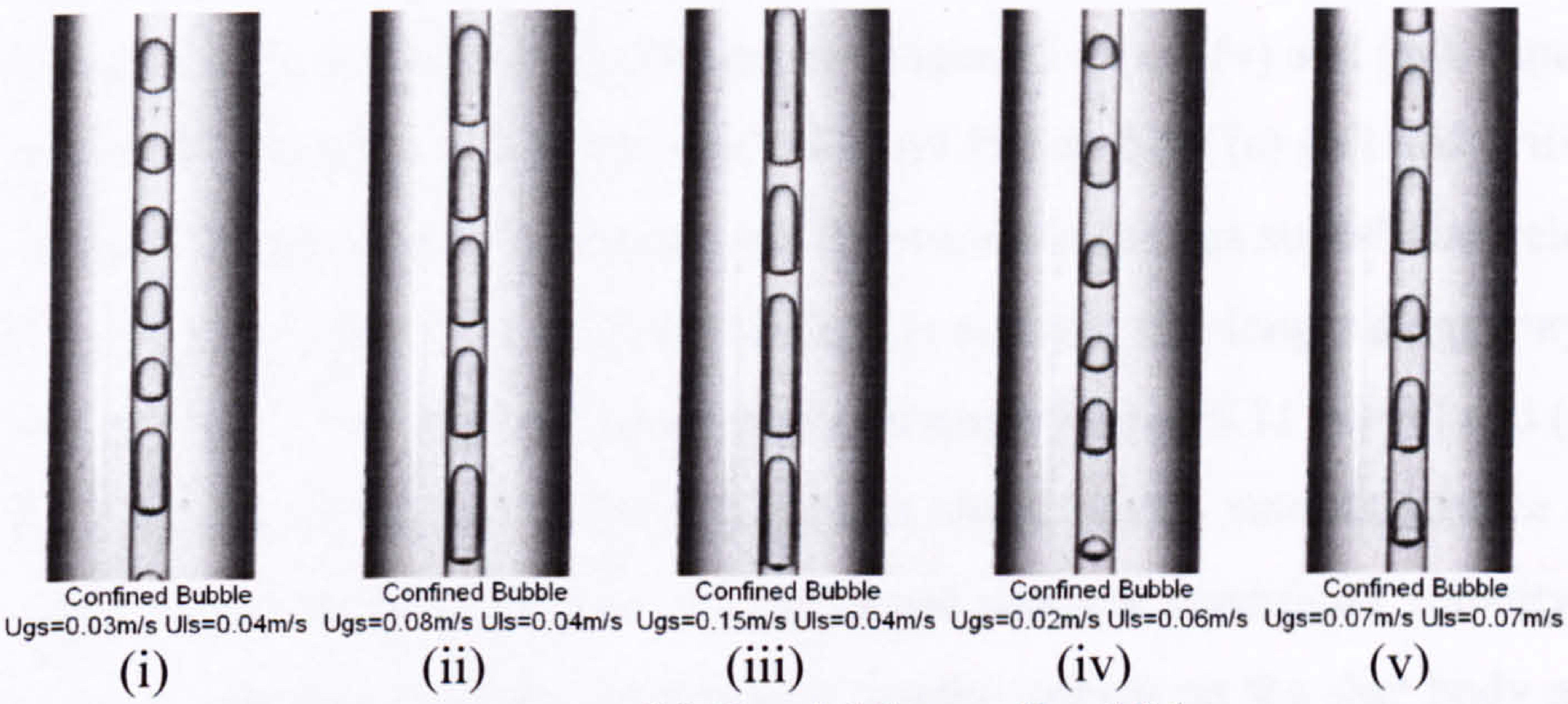

(b) D = 1.10 mm, P = 10 bar

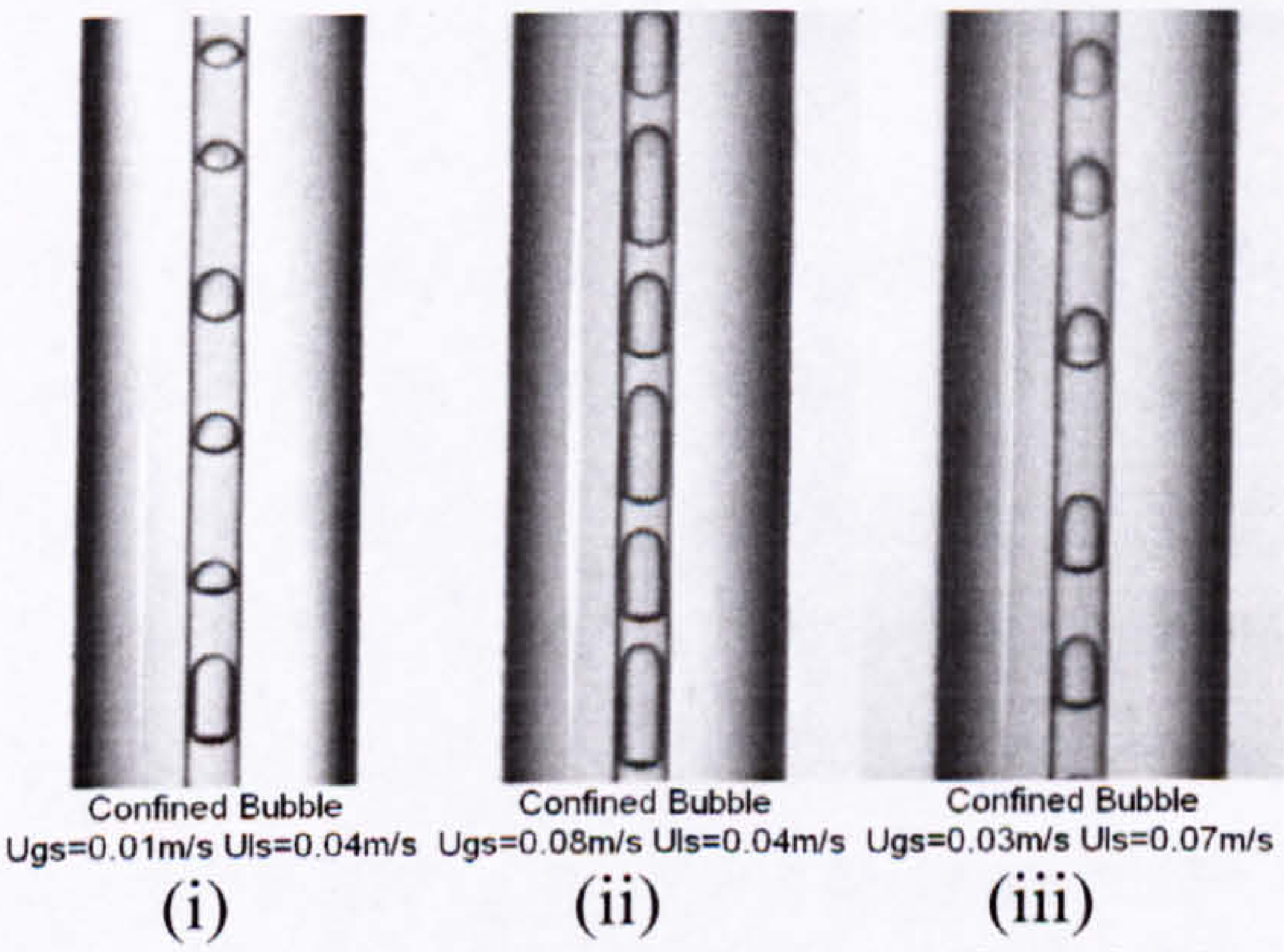

(c) D = 1.10 mm, P = 14 bar

Figure 5.10 Confined bubble flow observed in the 1.10 mm tube at different pressures. (a) 6 bar, (b) 10 bar and (c) 14 bar.

In summary, the following concluding observations can be made:

- Confined bubble flow is a particular flow pattern of low liquid and gas velocities.
- Small tubes and low pressure facilitate the formation of confined bubble flow because of the enhanced effect of surface tension.

5.1.4 Slug flow

Slug flow is a main flow pattern in the present experiments. Fluid velocity, pressure and tube diameter greatly affect the slug configuration. Slug rise velocity and length were measured and the factors that affect them are analysed and discussed in this section.

(1) Configuration

Slug bubbles receive a higher impact force, which results in a severe distortion as the liquid superficial velocity increases, see Figure 5.11 (a) (v) and (xi), Figure 5.12 (c) (vi) and (viii), Figure 5.13 (a) (iv) and (vi), and Figure 5.14 (c) (iv) and (viii). On the other hand, the slugs tend to be longer and deformed as the gas superficial velocity increases, as shown in Figure 5.11 (a) (vii), (viii), (ix) and (x). The longer slugs may deform easily even under the same conditions, see for example Figure 5.11 (a) (v) and (vi). Summarily the slug bubbles are in streamlined bullet shape with a smooth surface at lower liquid and gas superficial velocities. As the liquid and gas superficial velocity increased, the slug head becomes sharp and irregular, ripples appear on the slug body and the slug tail is chaotic and is followed by numerous small bubbles.

The higher fluid pressure results in smaller surface tension and weakening the rigidity of slug bubbles, which in turn facilitates the bubbles distortion in the 2.88 and 4.26 mm tubes, see the images in Figure 5.11 (a) (xi), (b) (vi) and (c) (vi), Figure 5.12 (b) (vii) and (c) (vii). However, the above tendency is not so distinct in the 1.10 and 2.01 mm tubes. Similarly the slug bubbles distort easily in the bigger tubes because the rigidity of bubbles is weakened as the increase of the bubble diameter, see Figures 5.11 (a) (x) and 5.14 (a) (iv), Figures 5.11 (b) (iii), 5.12 (b) (iii), 5.13 (b) (iii) and 5.14 (b) (i), and Figures 5.12 (c) (vii) and 5.13 (c) (vii).

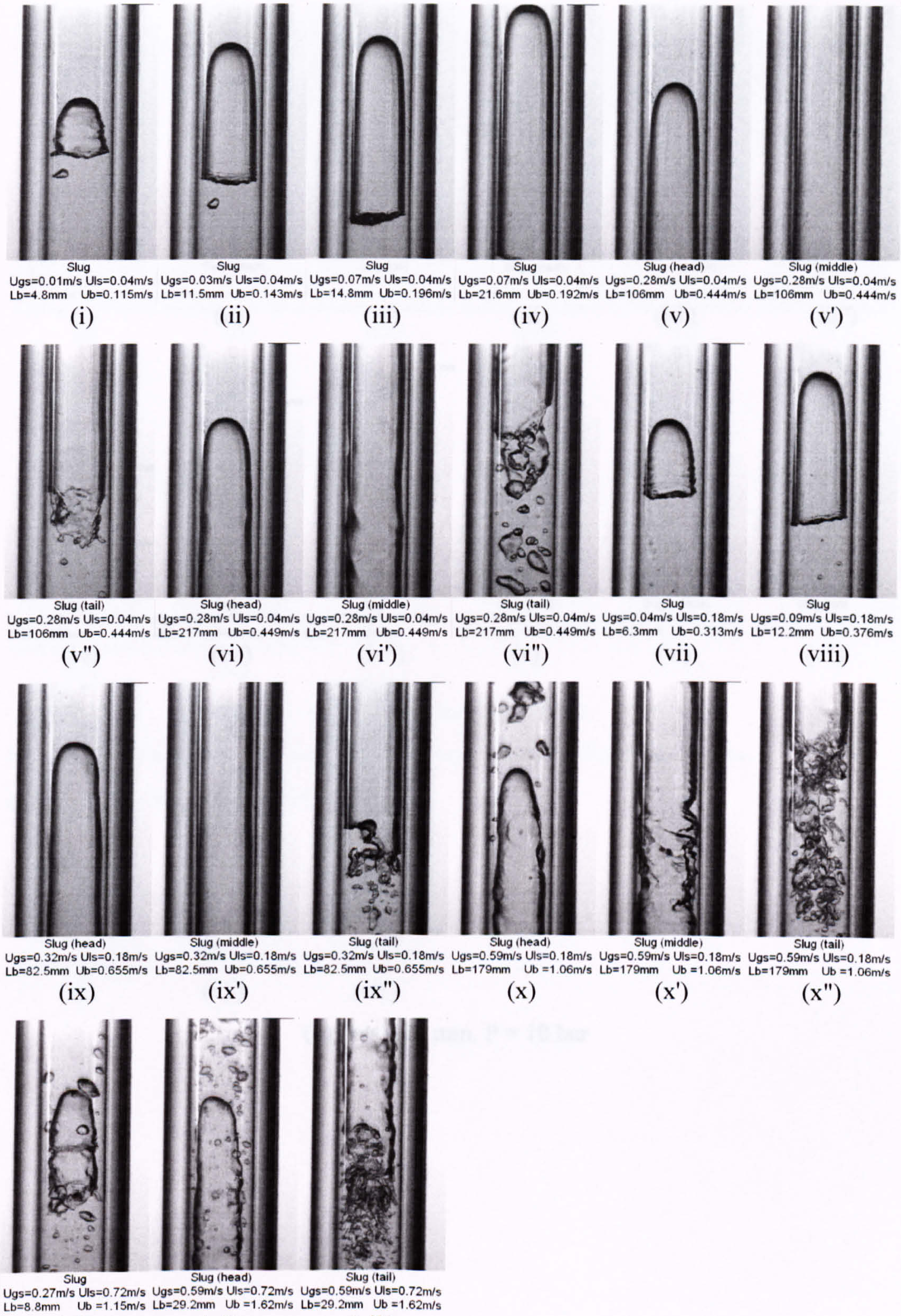

Slug
Ugs=0.01m/s Uls=0.04m/s
Lb=4.8mm Ub=0.115m/s
(i)

Slug
Ugs=0.03m/s Uls=0.04m/s
Lb=11.5mm Ub=0.143m/s
(ii)

Slug
Ugs=0.07m/s Uls=0.04m/s
Lb=14.8mm Ub=0.196m/s
(iii)

Slug
Ugs=0.07m/s Uls=0.04m/s
Lb=21.6mm Ub=0.192m/s
(iv)

Slug (head)
Ugs=0.28m/s Uls=0.04m/s
Lb=106mm Ub=0.444m/s
(v)

Slug (middle)
Ugs=0.28m/s Uls=0.04m/s
Lb=106mm Ub=0.444m/s
(v')

Slug (tail)
Ugs=0.28m/s Uls=0.04m/s
Lb=106mm Ub=0.444m/s
(v")

Slug (head)
Ugs=0.28m/s Uls=0.04m/s
Lb=217mm Ub=0.449m/s
(vi)

Slug (middle)
Ugs=0.28m/s Uls=0.04m/s
Lb=217mm Ub=0.449m/s
(vi')

Slug (tail)
Ugs=0.28m/s Uls=0.04m/s
Lb=217mm Ub=0.449m/s
(vi")

Slug
Ugs=0.04m/s Uls=0.18m/s
Lb=6.3mm Ub=0.313m/s
(vii)

Slug
Ugs=0.09m/s Uls=0.18m/s
Lb=12.2mm Ub=0.376m/s
(viii)

Slug (head)
Ugs=0.32m/s Uls=0.18m/s
Lb=82.5mm Ub=0.655m/s
(ix)

Slug (middle)
Ugs=0.32m/s Uls=0.18m/s
Lb=82.5mm Ub=0.655m/s
(ix')

Slug (tail)
Ugs=0.32m/s Uls=0.18m/s
Lb=82.5mm Ub=0.655m/s
(ix")

Slug (head)
Ugs=0.59m/s Uls=0.18m/s
Lb=179mm Ub =1.06m/s
(x)

Slug (middle)
Ugs=0.59m/s Uls=0.18m/s
Lb=179mm Ub =1.06m/s
(x')

Slug (tail)
Ugs=0.59m/s Uls=0.18m/s
Lb=179mm Ub =1.06m/s
(x")

Slug
Ugs=0.27m/s Uls=0.72m/s
Lb=8.8mm Ub =1.15m/s
(xi)

Slug (head)
Ugs=0.59m/s Uls=0.72m/s
Lb=29.2mm Ub =1.62m/s
(xii)

Slug (tail)
Ugs=0.59m/s Uls=0.72m/s
Lb=29.2mm Ub =1.62m/s
(xii')

(a) D = 4.26 mm, P = 6 bar

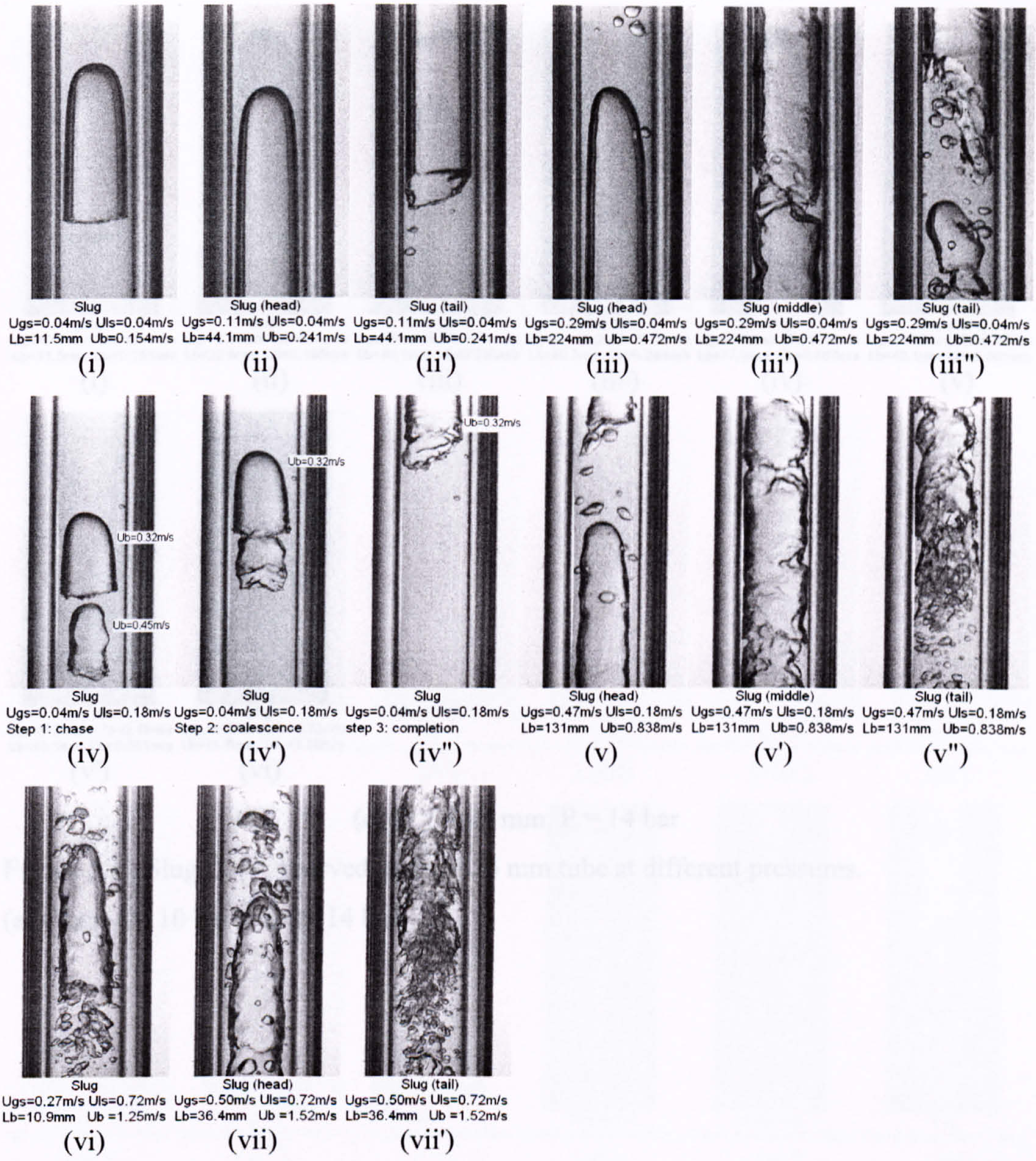

(b) D = 4.26 mm, P = 10 bar

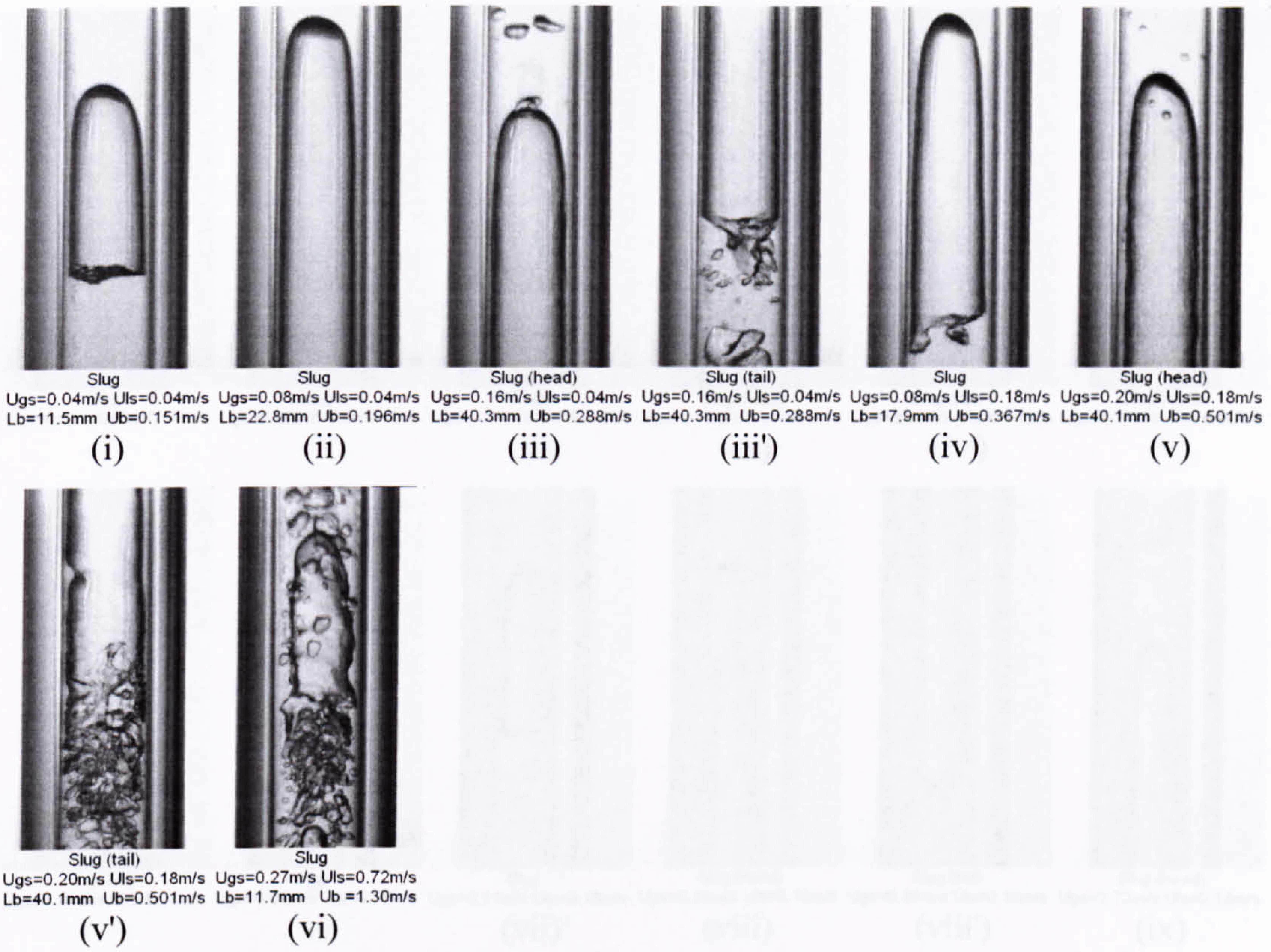

(c) D = 4.26 mm, P = 14 bar

Figure 5.11 Slug flow observed in the 4.26 mm tube at different pressures. (a) 6 bar, (b) 10 bar and (c) 14 bar.

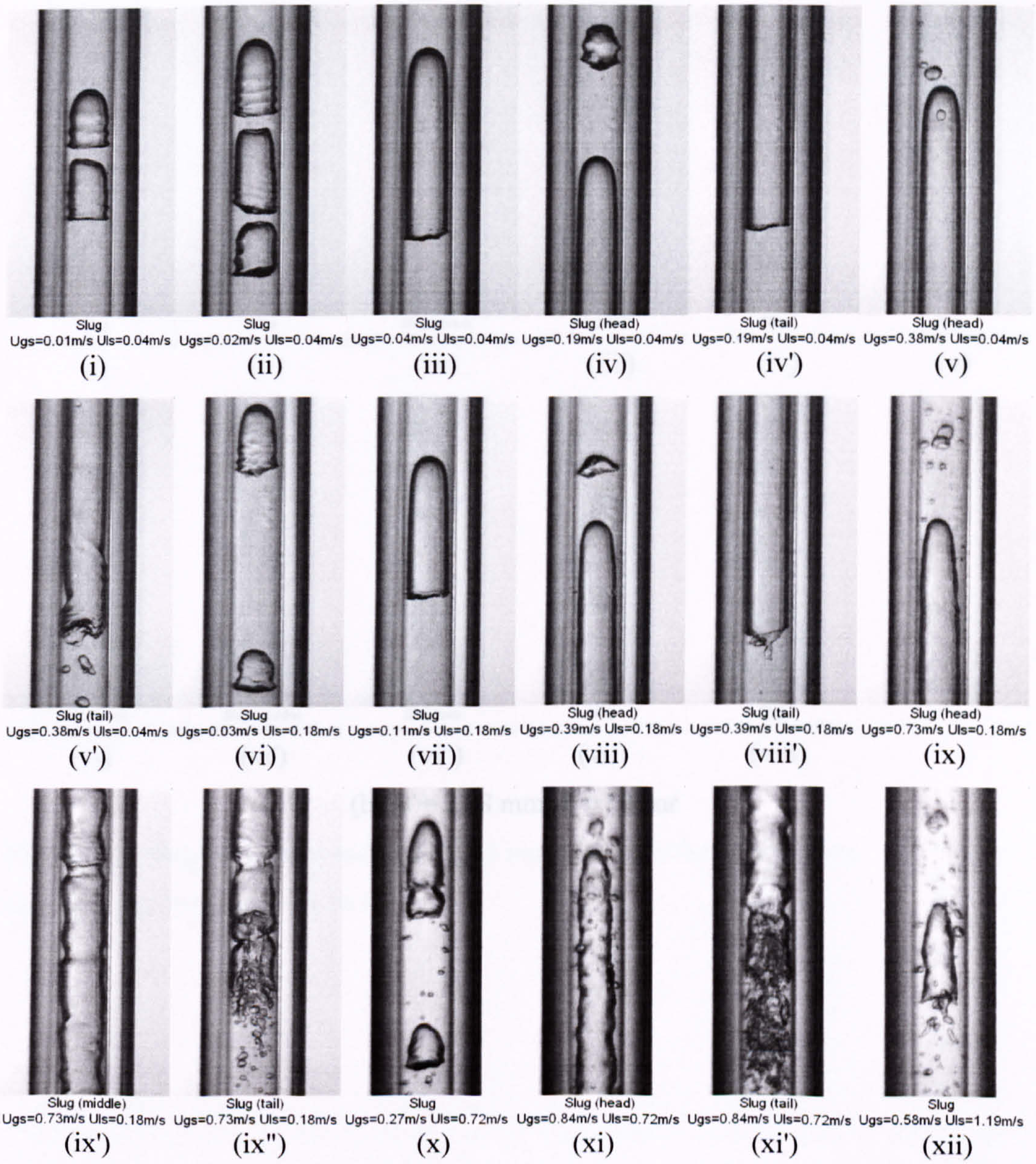

Slug Ugs=0.01m/s Uls=0.04m/s (i)
Slug Ugs=0.02m/s Uls=0.04m/s (ii)
Slug Ugs=0.04m/s Uls=0.04m/s (iii)
Slug (head) Ugs=0.19m/s Uls=0.04m/s (iv)
Slug (tail) Ugs=0.19m/s Uls=0.04m/s (iv')
Slug (head) Ugs=0.38m/s Uls=0.04m/s (v)

Slug (tail) Ugs=0.38m/s Uls=0.04m/s (v')
Slug Ugs=0.03m/s Uls=0.18m/s (vi)
Slug Ugs=0.11m/s Uls=0.18m/s (vii)
Slug (head) Ugs=0.39m/s Uls=0.18m/s (viii)
Slug (tail) Ugs=0.39m/s Uls=0.18m/s (viii')
Slug (head) Ugs=0.73m/s Uls=0.18m/s (ix)

Slug (middle) Ugs=0.73m/s Uls=0.18m/s (ix')
Slug (tail) Ugs=0.73m/s Uls=0.18m/s (ix")
Slug Ugs=0.27m/s Uls=0.72m/s (x)
Slug (head) Ugs=0.84m/s Uls=0.72m/s (xi)
Slug (tail) Ugs=0.84m/s Uls=0.72m/s (xi')
Slug Ugs=0.58m/s Uls=1.19m/s (xii)

(a) D = 2.88 mm, P = 6 bar

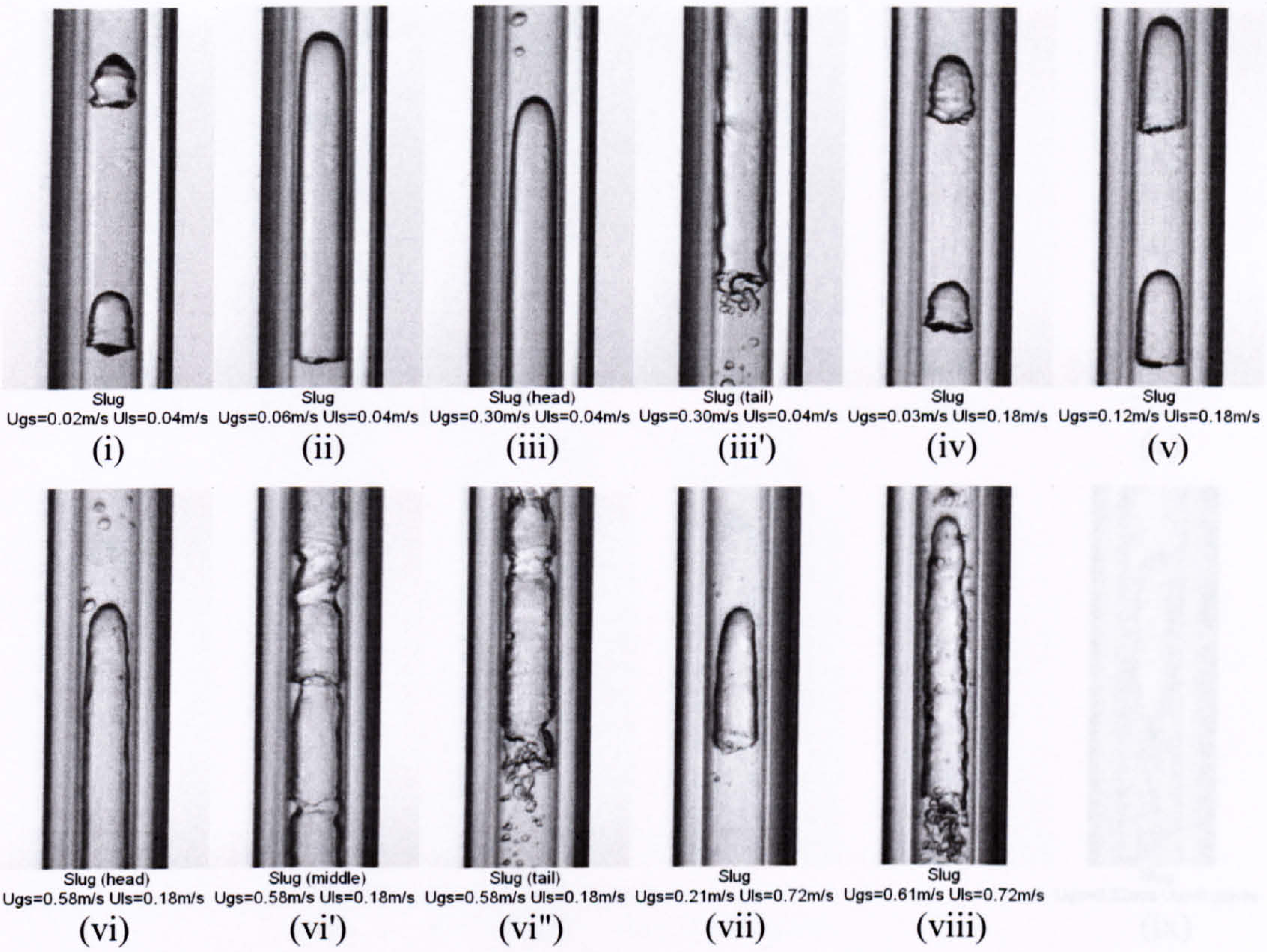

Slug Ugs=0.02m/s Uls=0.04m/s (i)

Slug Ugs=0.06m/s Uls=0.04m/s (ii)

Slug (head) Ugs=0.30m/s Uls=0.04m/s (iii)

Slug (tail) Ugs=0.30m/s Uls=0.04m/s (iii')

Slug Ugs=0.03m/s Uls=0.18m/s (iv)

Slug Ugs=0.12m/s Uls=0.18m/s (v)

Slug (head) Ugs=0.58m/s Uls=0.18m/s (vi)

Slug (middle) Ugs=0.58m/s Uls=0.18m/s (vi')

Slug (tail) Ugs=0.58m/s Uls=0.18m/s (vi")

Slug Ugs=0.21m/s Uls=0.72m/s (vii)

Slug Ugs=0.61m/s Uls=0.72m/s (viii)

(b) D = 2.88 mm, P = 10 bar

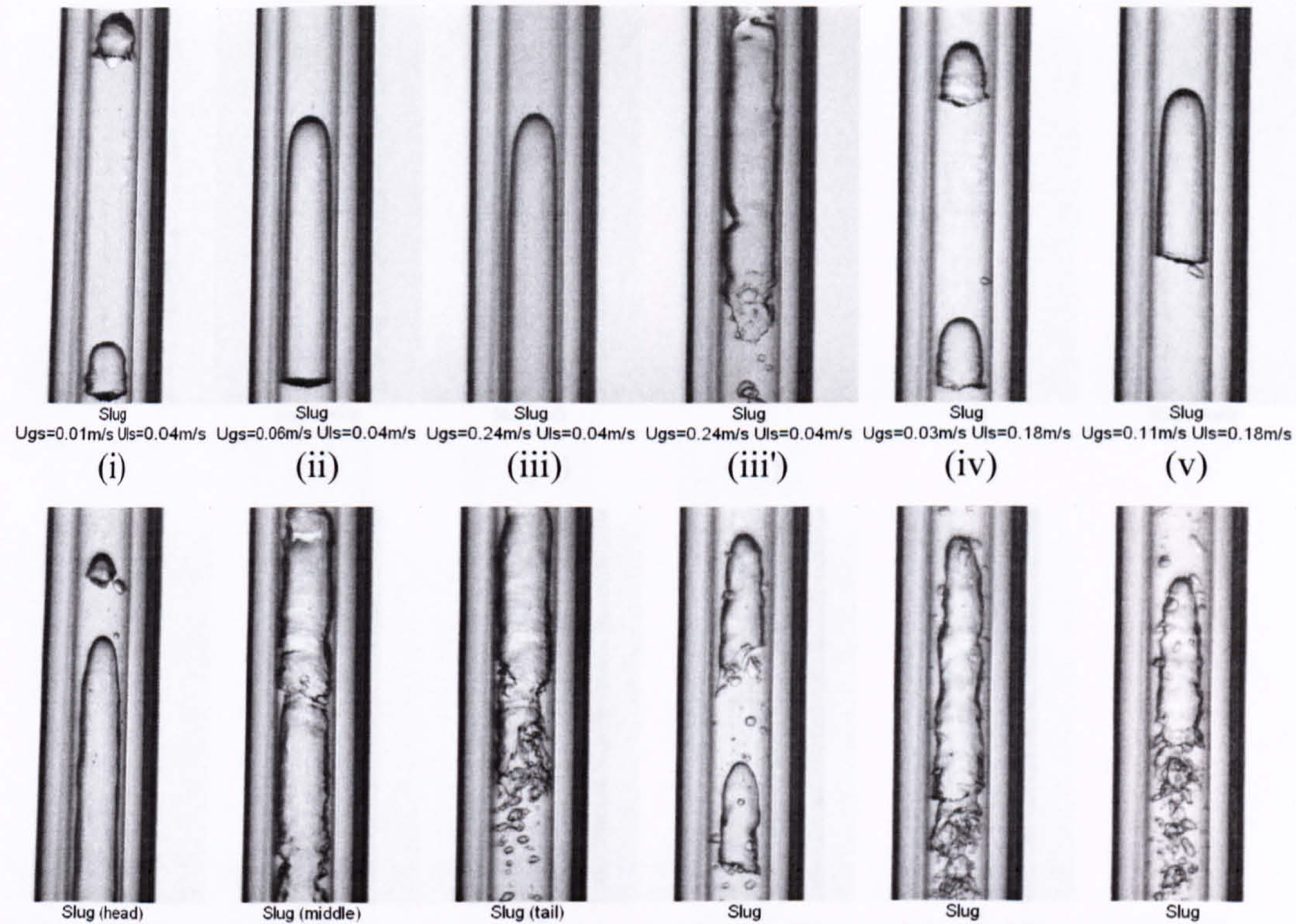

(i) (ii) (iii) (iii') (iv) (v)

(vi) (vi') (vi'') (vii) (viii) (ix)

(c) D = 2.88 mm, P = 14 bar

Figure 5.12 Slug flow observed in the 2.88 mm tube at different pressures. (a) 6 bar, (b) 10 bar and (c) 14 bar.

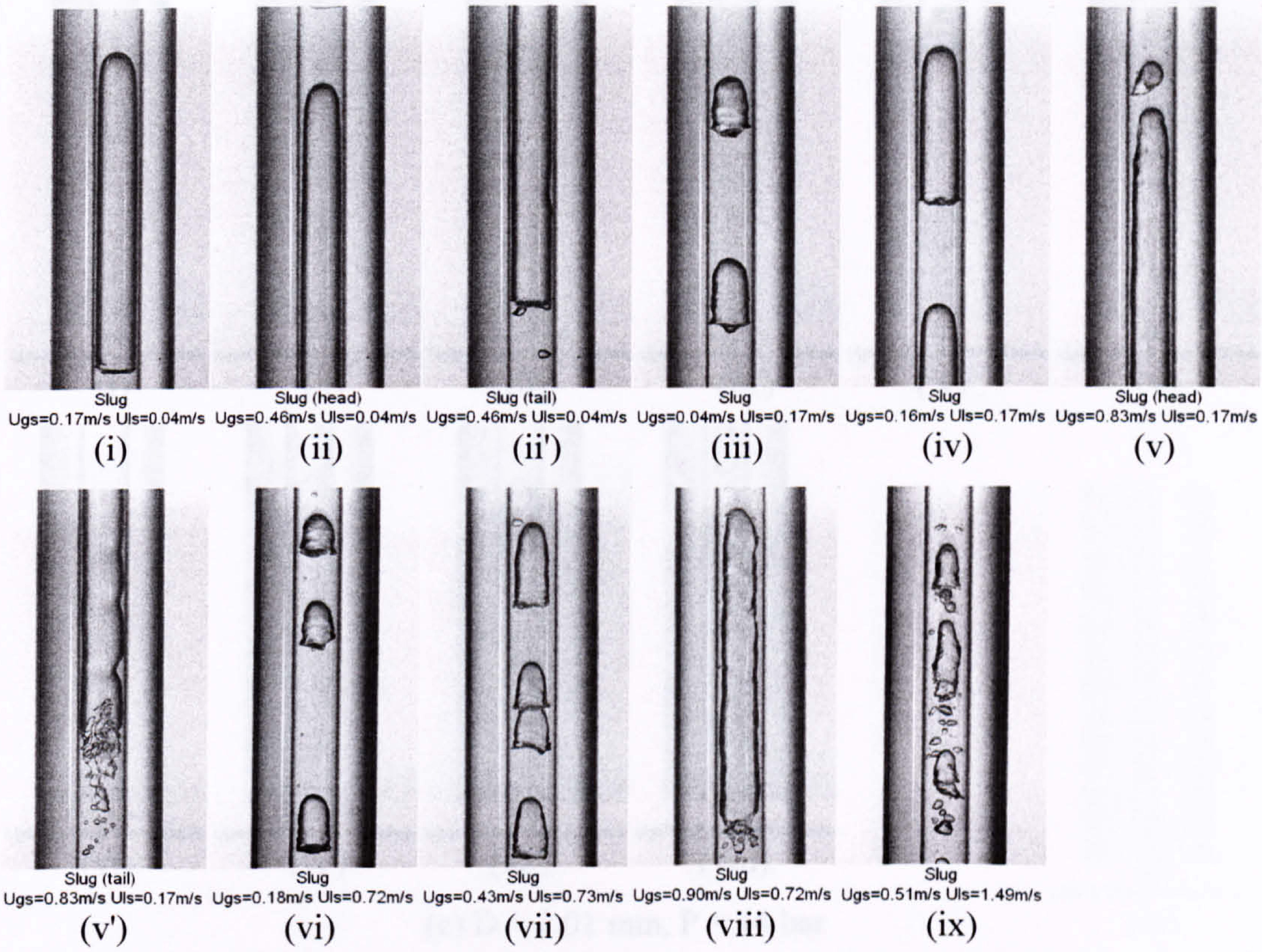

(a) D = 2.01 mm, P = 6 bar

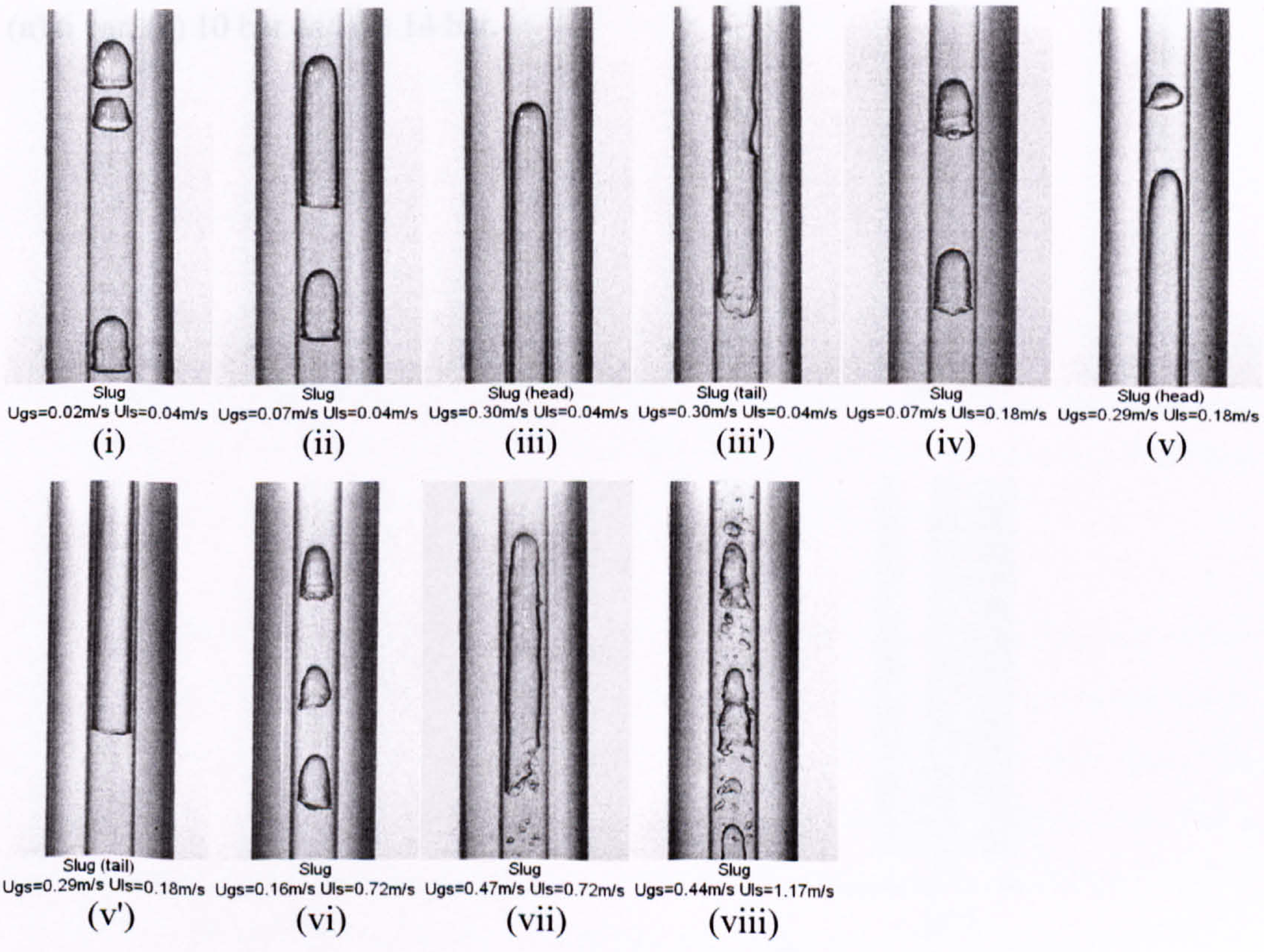

(b) D = 2.01 mm, P = 10 bar

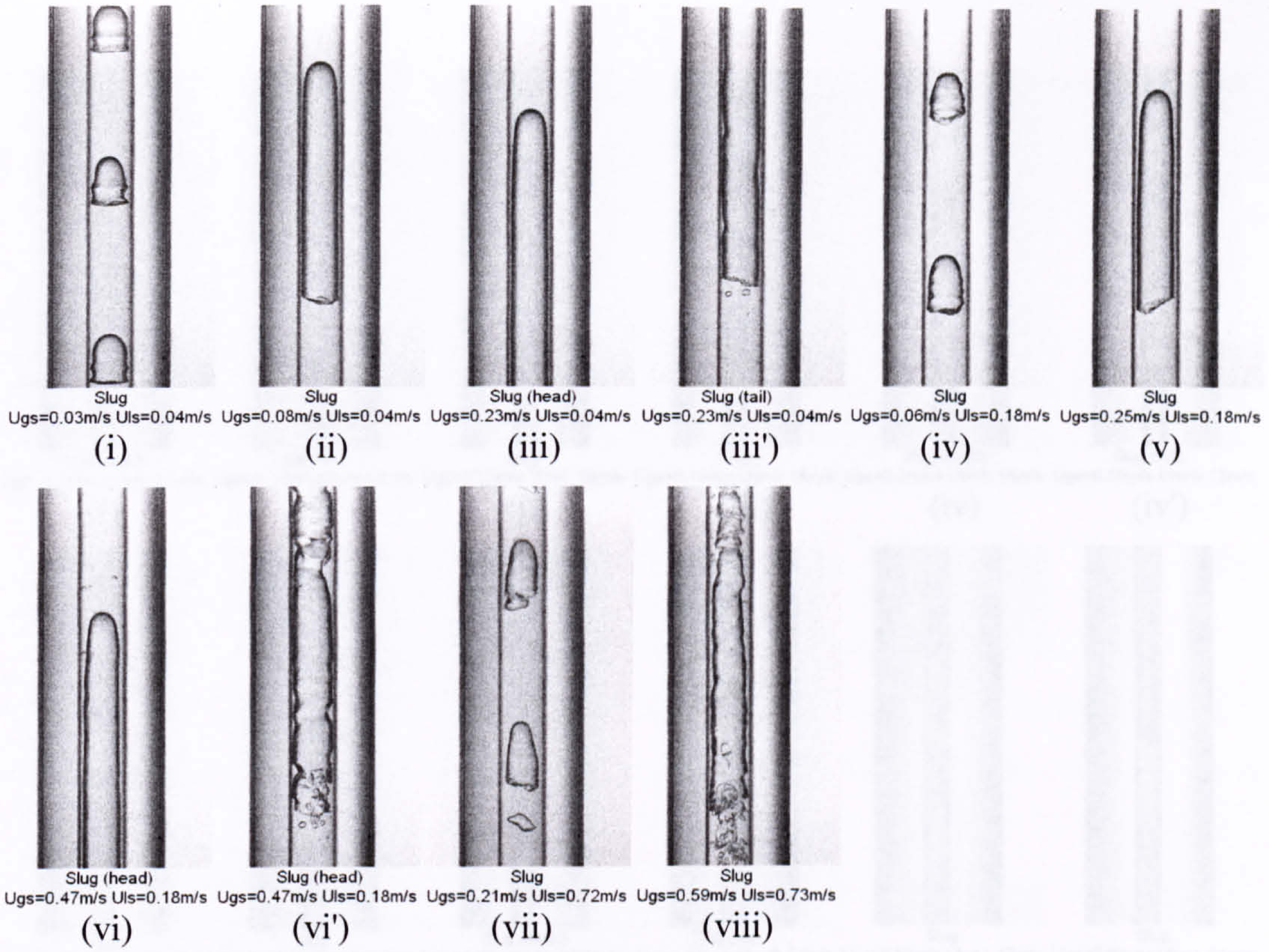

(c) D = 2.01 mm, P = 14 bar

Figure 5.13 Slug flow observed in the 2.01 mm tube at different pressures. (a) 6 bar, (b) 10 bar and (c) 14 bar.

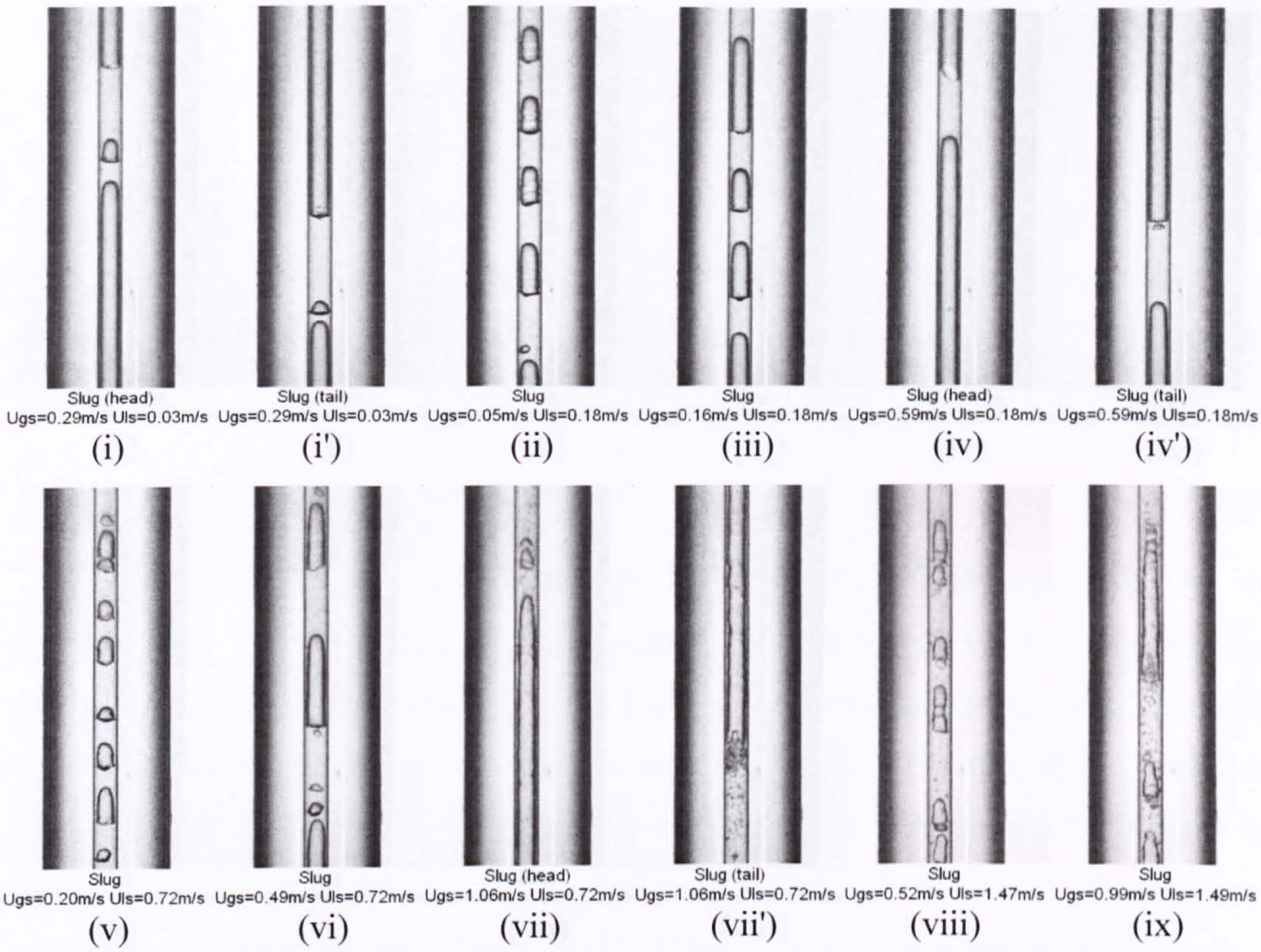

(a) D = 1.10 mm, P = 6 bar

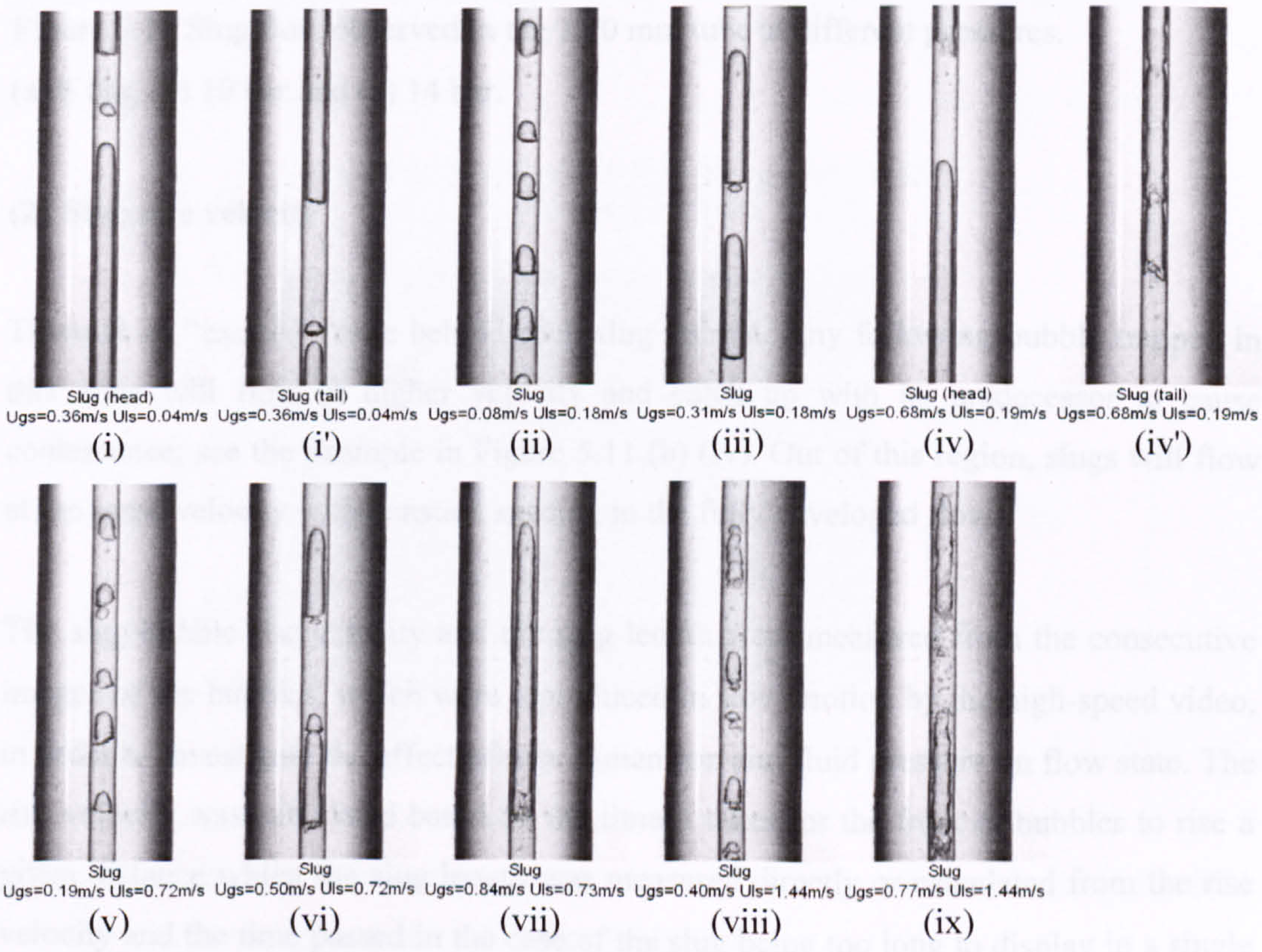

(b) D = 1.10 mm, P = 10 bar

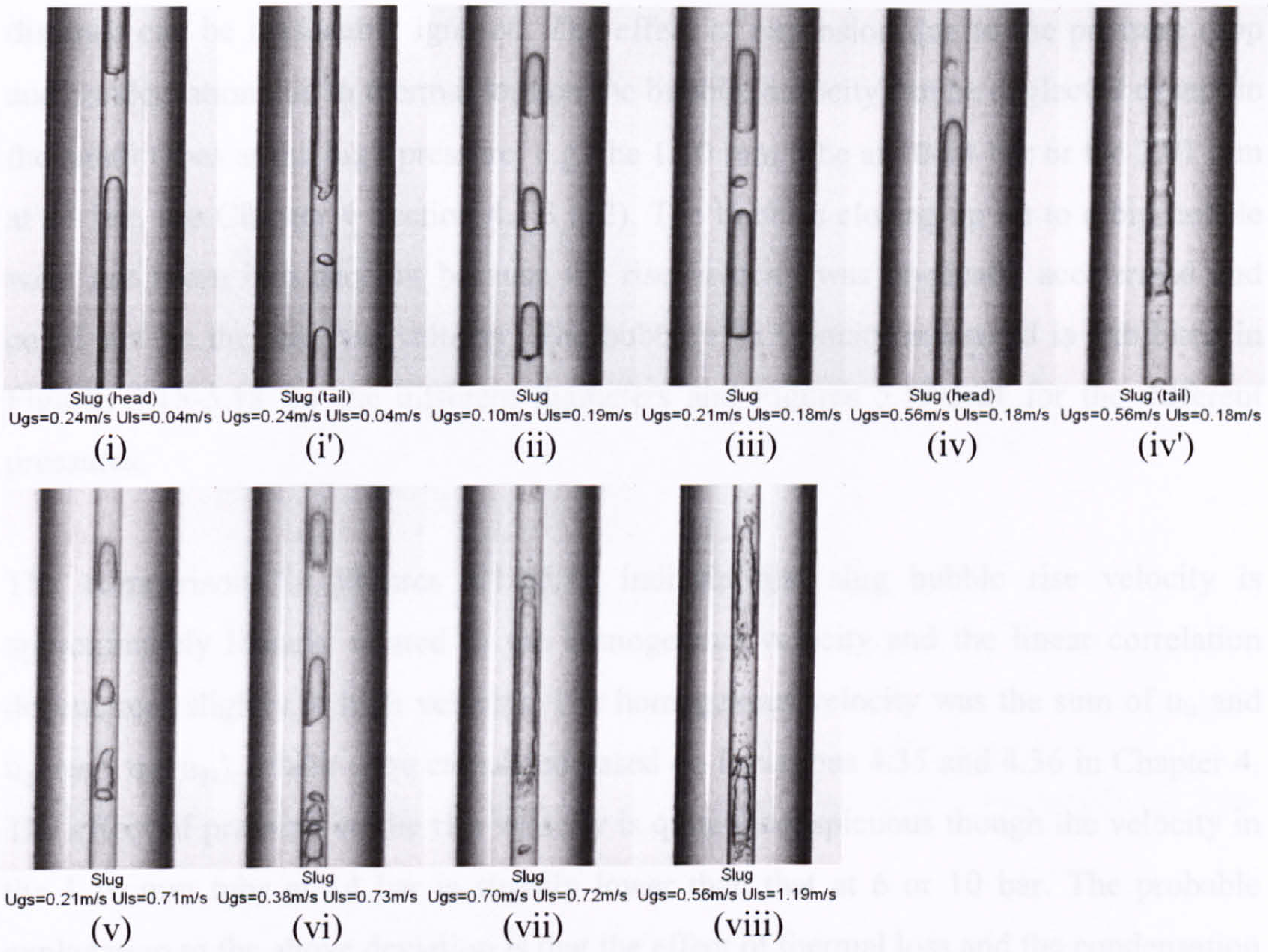

(c) D = 1.10 mm, P = 14 bar

Figure 5.14 Slug flow observed in the 1.10 mm tube at different pressures. (a) 6 bar, (b) 10 bar and (c) 14 bar.

(2) Slug rise velocity

There is an "excited" zone behind each slug bubble. Any following bubble trapped in this zone will flow at higher velocity and catch up with its predecessor to cause coalescence, see the example in Figure 5.11 (b) (iv). Out of this region, slugs will flow at the same velocity with constant spacing in the fully developed flow.

The slug bubble rise velocity and the slug length were measured from the consecutive images of the bubbles, which were reproduced in slow motion by the high-speed video, in order to investigate the effect of tube dimension and fluid pressure on flow state. The rise velocity was calculated based on the time it takes for the front of bubbles to rise a given distance whilst the slug length was measured directly or calculated from the rise velocity and the time passed in the case of the slug being too long to display in a single frame. The measured distance was so short that the pressure drop across the measuring distance can be reasonably ignored. The effect of expansion due to the pressure drop and condensation due to thermal loss on the bubbles velocity can be neglected except in the small tubes at the high pressure, e.g. the 1.10 mm tube at 10-14 bar or the 2.01 mm at 14 bar, see Chapter 4 Section 4.1.3 (12). The bubbles closing up on to a big bubble were not taken into account because the rise velocity was atypically accelerated and could not be the real rise velocity. The bubble rise velocity measured is exhibited in Figures 5.15-5.18 for the different diameters and Figures 5.19-5.21 for the different pressures.

The comparisons in Figures 5.15-5.18 indicate that slug bubble rise velocity is approximately linearly related to the homogenous velocity and the linear correlation degenerates slightly at high velocity. The homogenous velocity was the sum of u_{ls} and u_{gs} ($u_h = u_{ls} + u_{gs}$), which were calculated based on Equations 4.35 and 4.36 in Chapter 4. The effect of pressure on the rise velocity is quite inconspicuous though the velocity in the 1.10 mm tube at 14 bar is slightly lower than that at 6 or 10 bar. The probable explanation to the above deviation is that the effect of thermal loss and the condensation caused cannot be neglected completely in the 1.10 mm tube at 14 bar (T_{sat}= 52.5 °C).

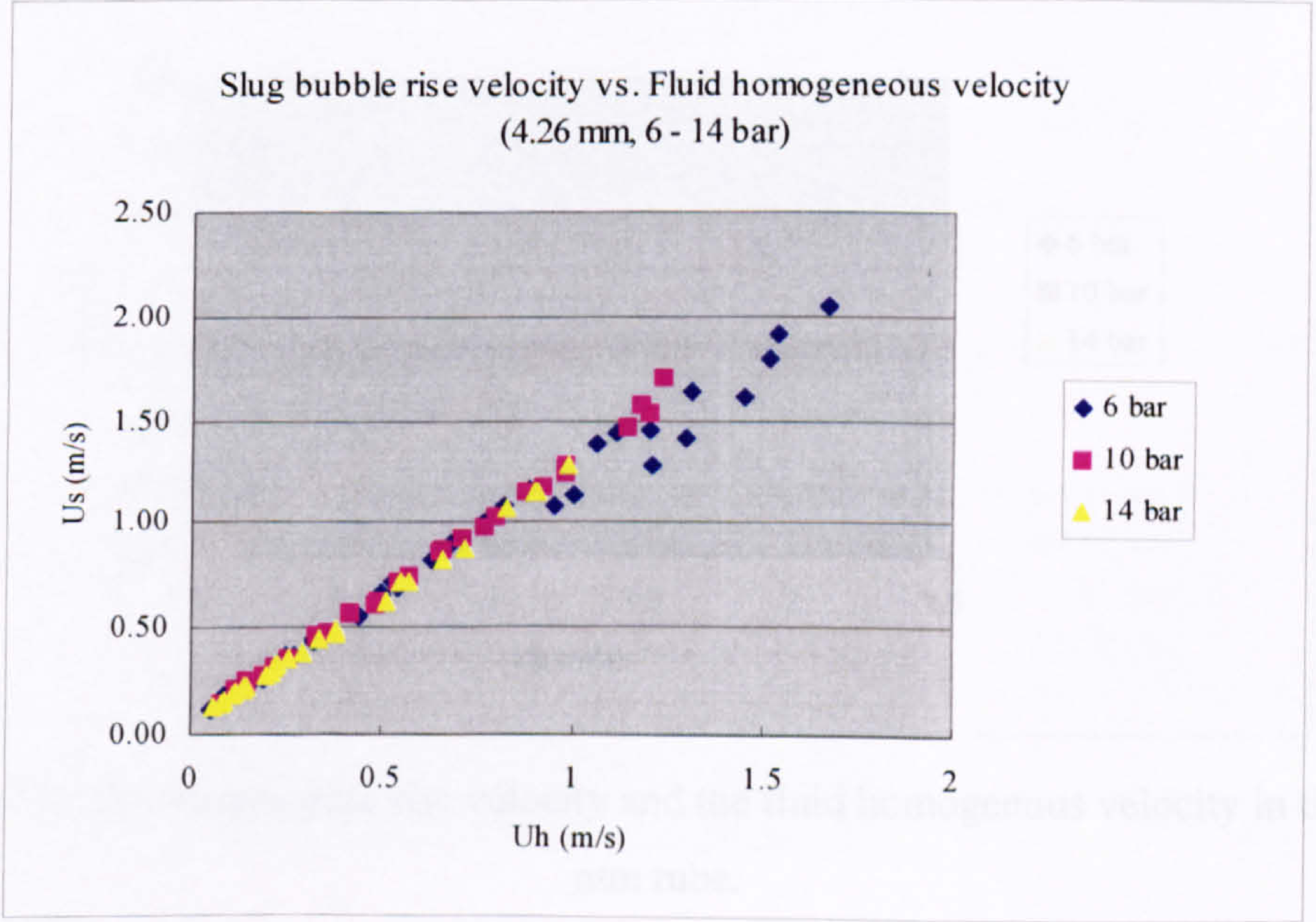

Figure 5.15 The slug bubble rise velocity and the fluid homogenous velocity in the 4.26 mm tube.

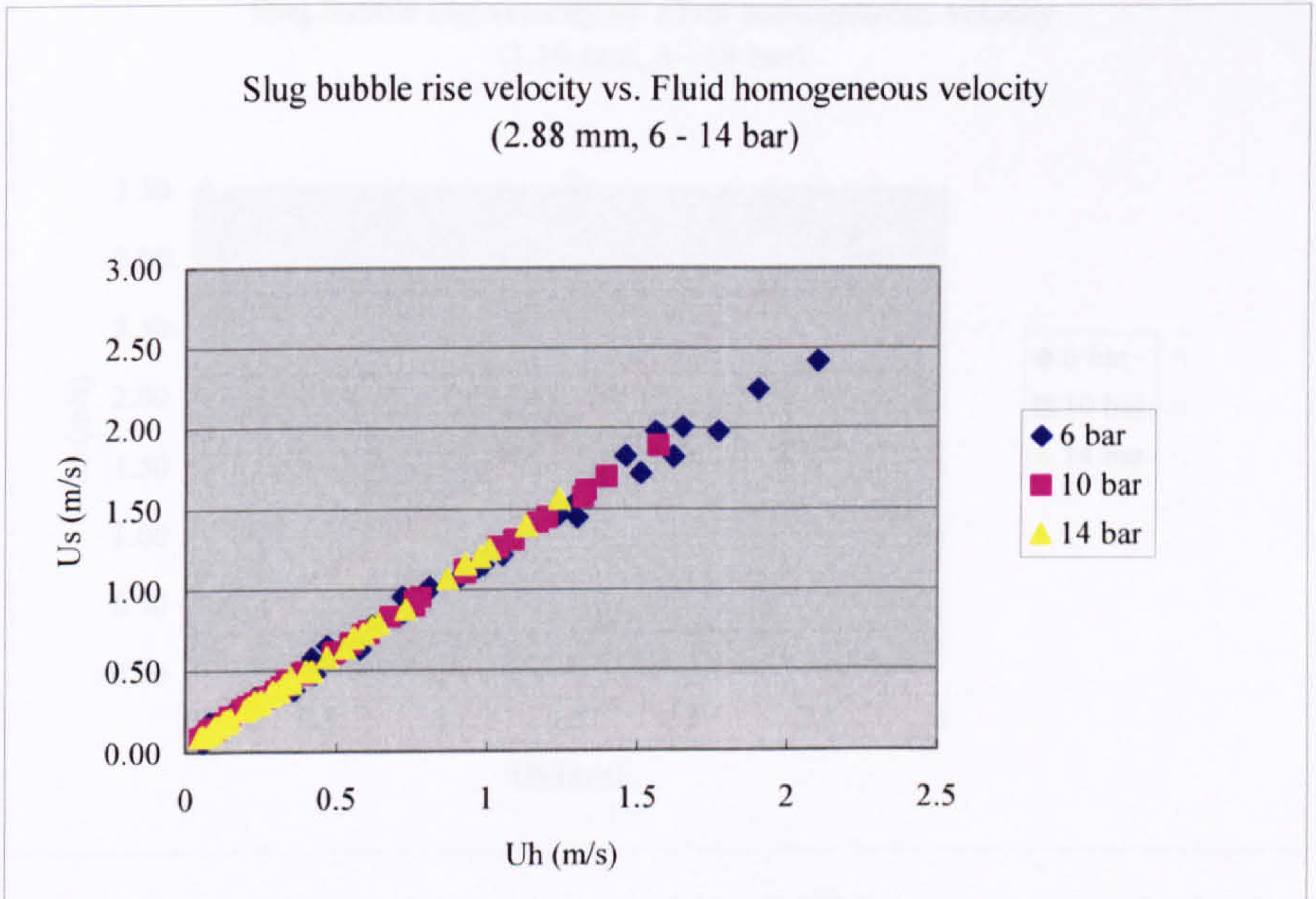

Figure 5.16 The slug bubble rise velocity and the fluid homogenous velocity in the 2.88 mm tube.

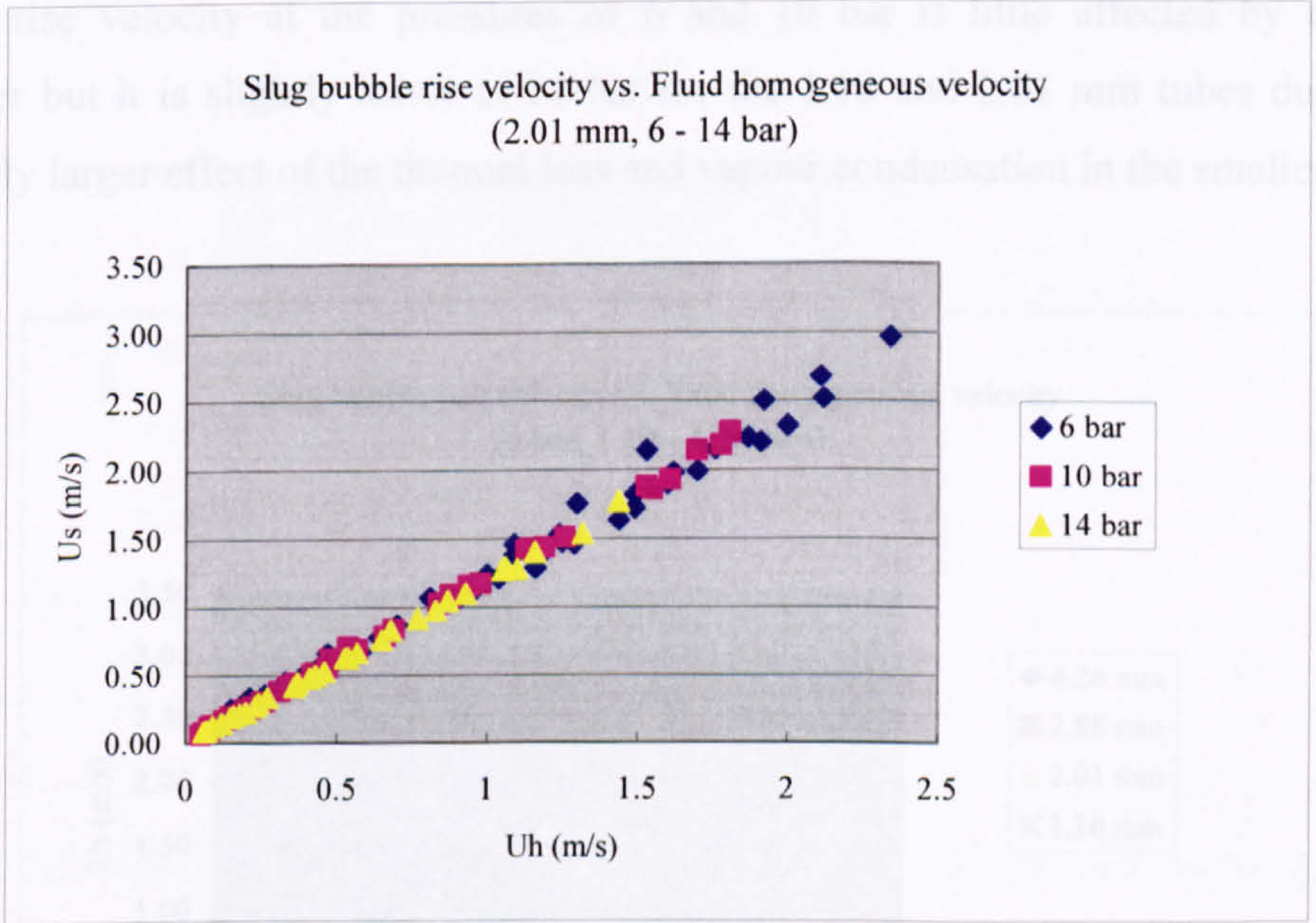

Figure 5.17 The slug bubble rise velocity and the fluid homogenous velocity in the 2.01 mm tube.

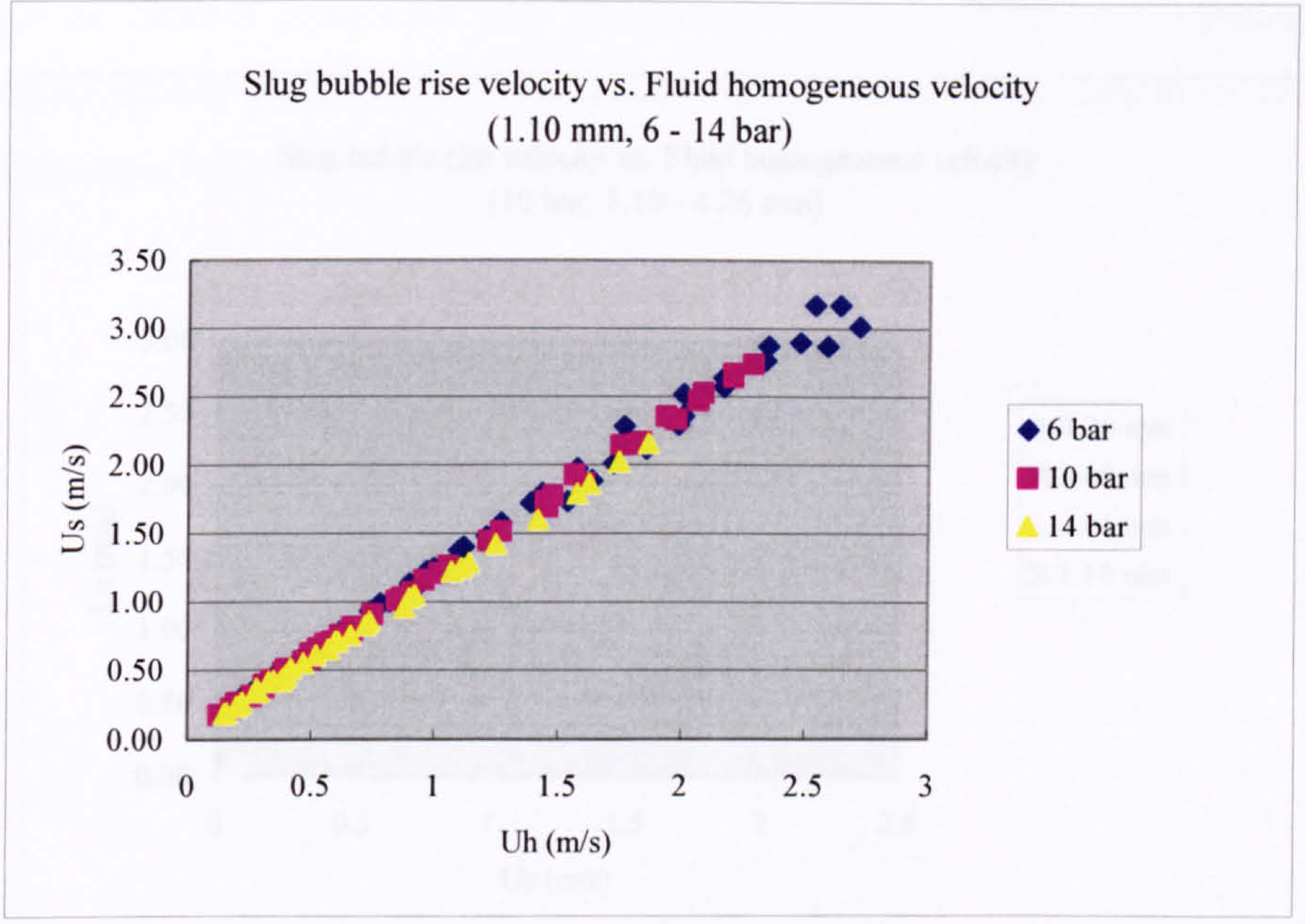

Figure 5.18 The slug bubble rise velocity and the fluid homogenous velocity in the 1.10 mm tube.

The effect of tube diameter on the rise velocity is shown in Figures 5.19-5.21. Slug bubble rise velocity at the pressures of 6 and 10 bar is little affected by the tube diameter but it is slightly lower at 14 bar for the 1.10 and 2.01 mm tubes due to the relatively larger effect of the thermal loss and vapour condensation in the smaller tubes.

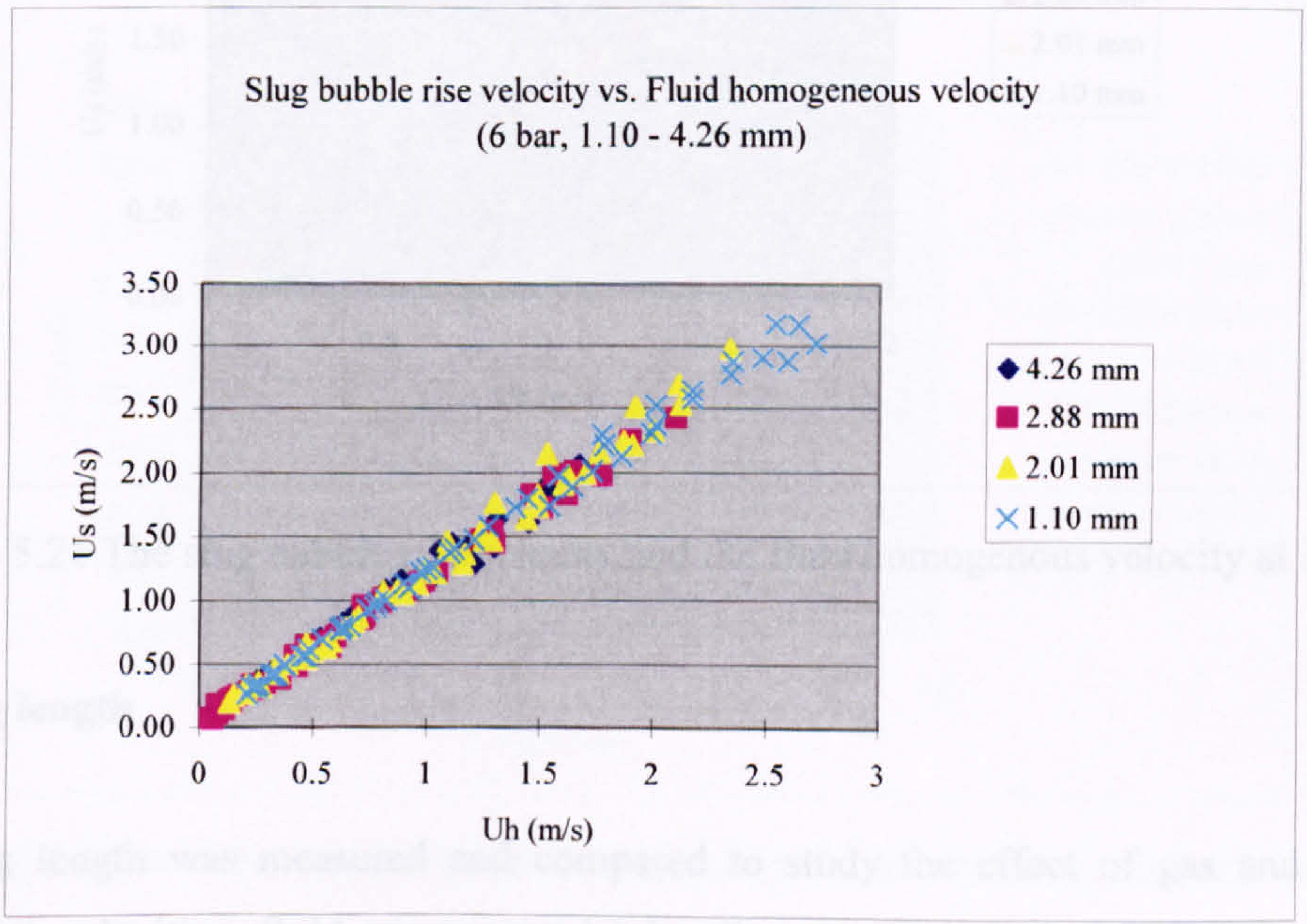

Figure 5.19 The slug bubble rise velocity and the fluid homogenous velocity at 6 bar.

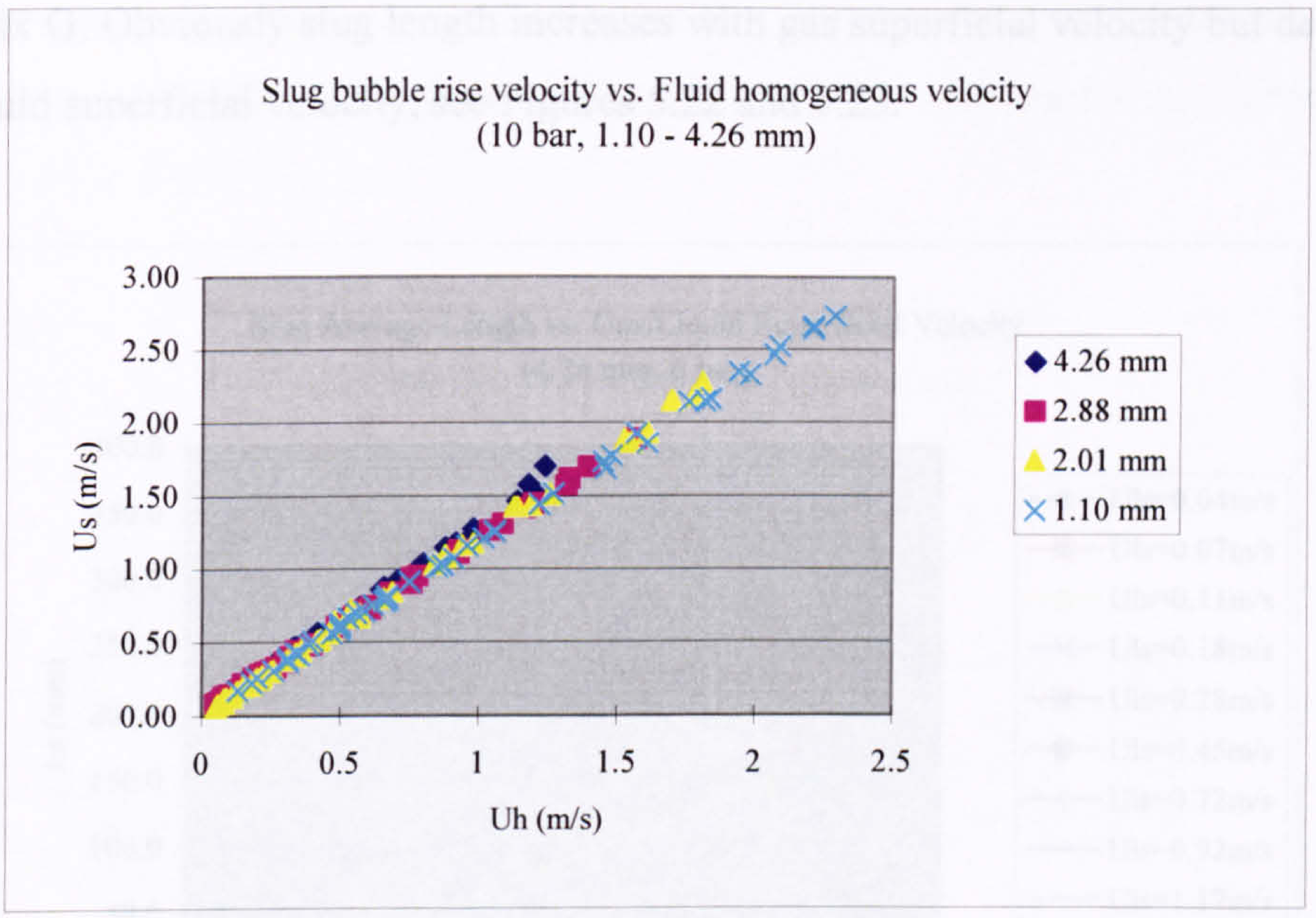

Figure 5.20 The slug bubble rise velocity and the fluid homogenous velocity at 10 bar.

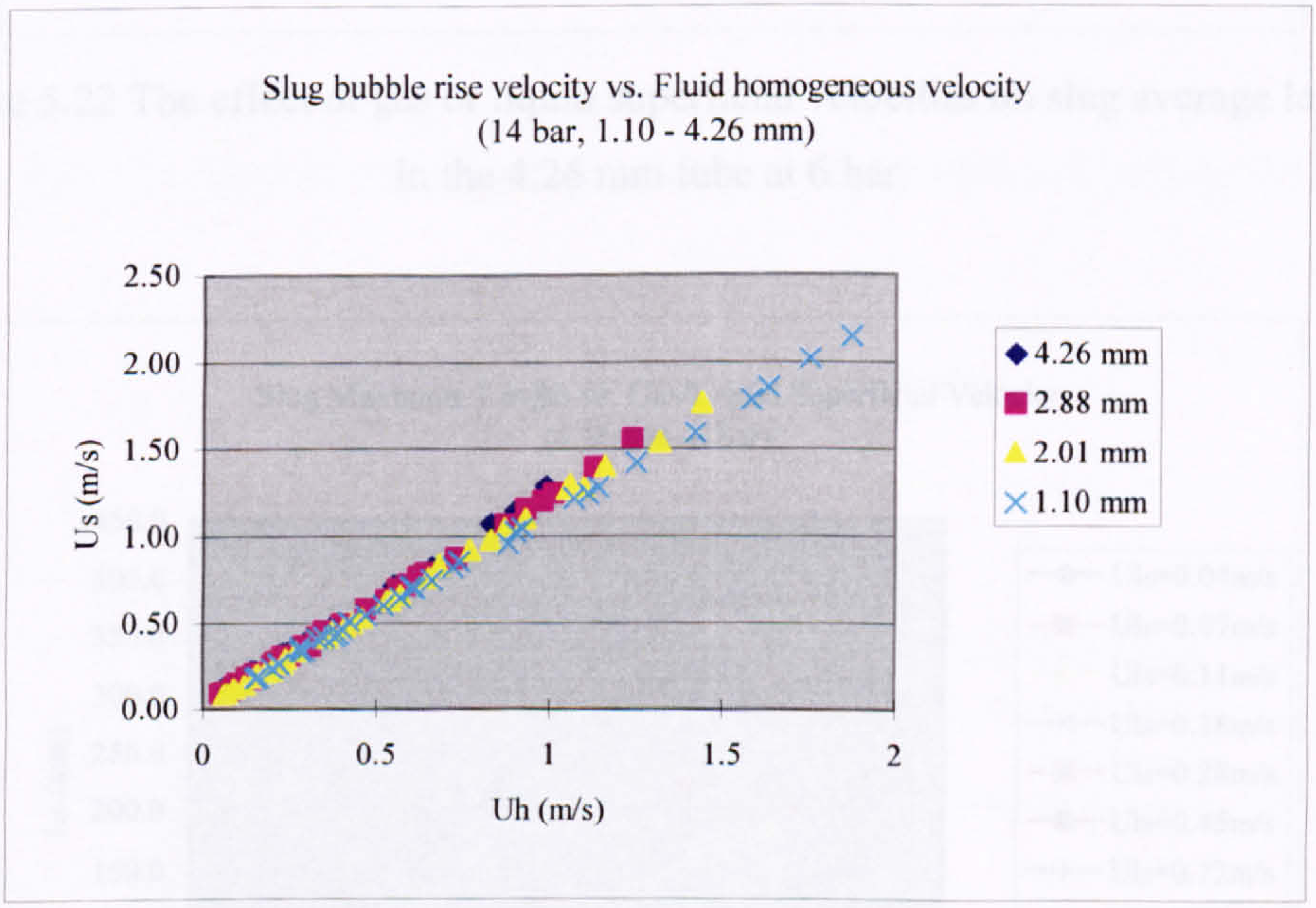

Figure 5.21 The slug bubble rise velocity and the fluid homogenous velocity at 14 bar.

(3) Slug length

The slug length was measured and compared to study the effect of gas and liquid superficial velocities, fluid pressure and tube diameter. The typical comparisons are presented in Figures 5.22-5.26. The complete experimental data are summarized in Appendix G. Obviously slug length increases with gas superficial velocity but decreases with liquid superficial velocity, see Figures 5.22 and 5.23.

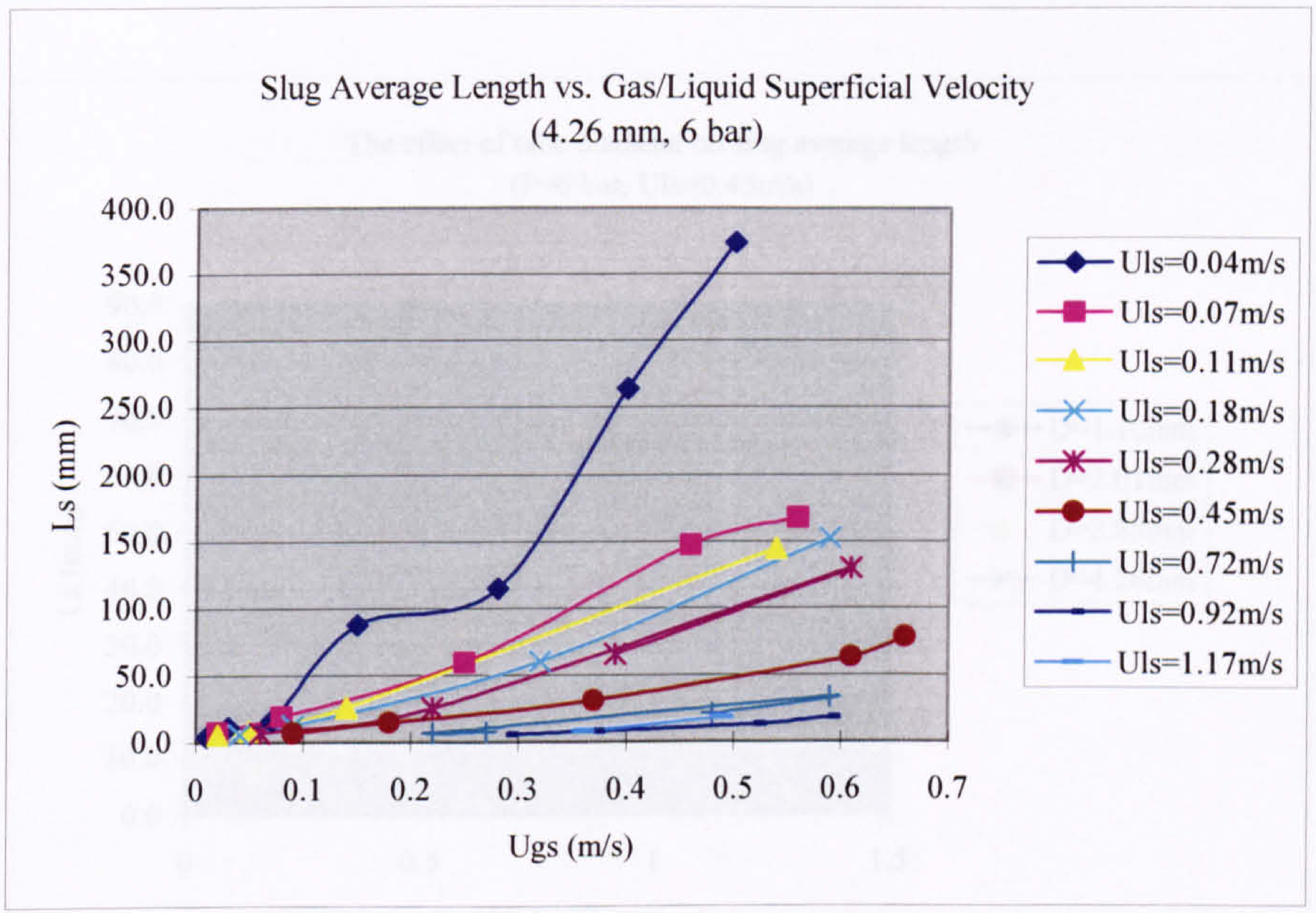

Figure 5.22 The effect of gas or liquid superficial velocities on slug average length in the 4.26 mm tube at 6 bar.

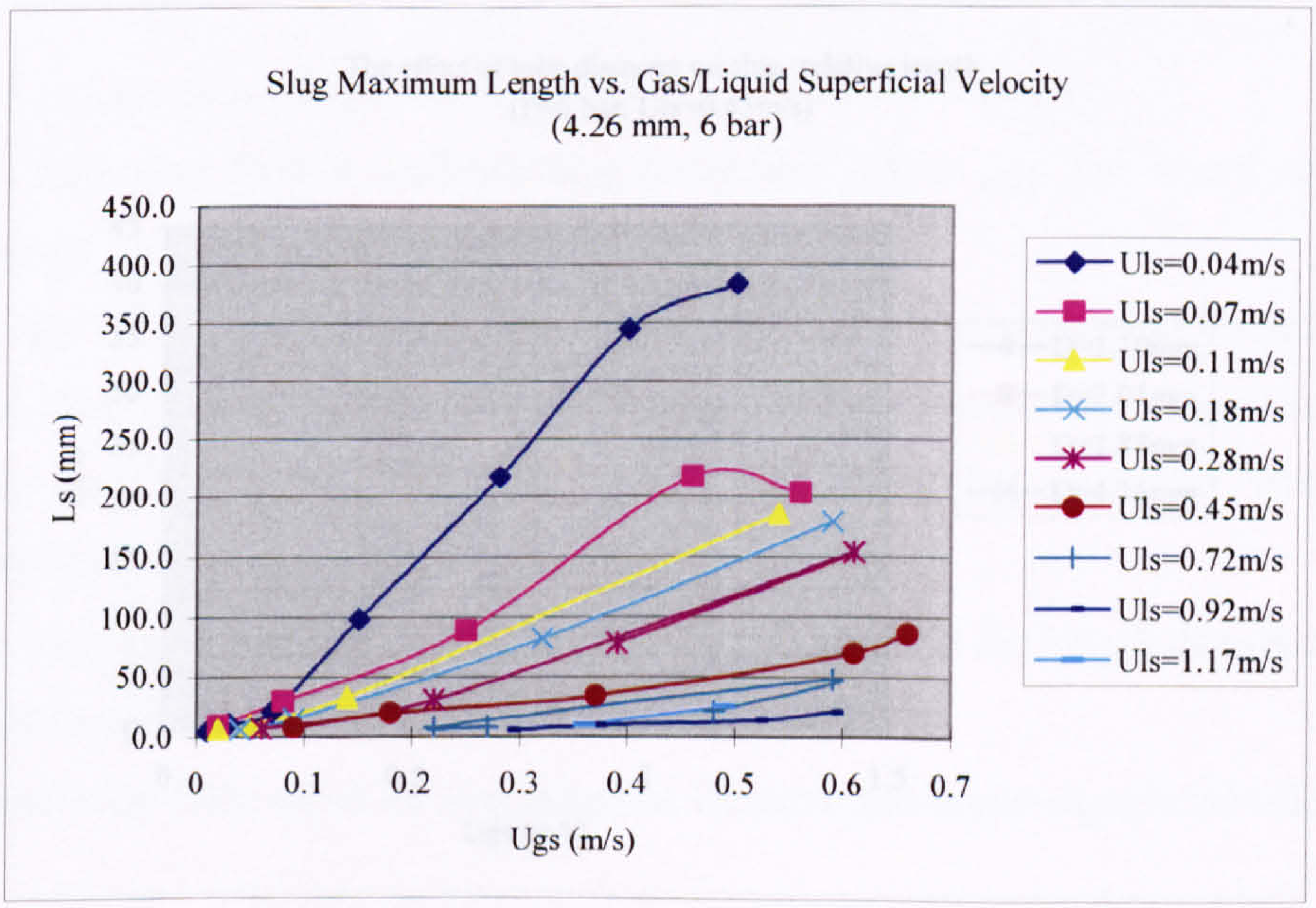

Figure 5.23 The effect of gas or liquid superficial velocities on slug maximum length in the 4.26 mm tube at 6 bar.

The absolute length of slug is longer in the bigger tubes at the same conditions, i.e. the same pressure and gas/liquid superficial velocities. However, the relative length, ratio of the bubble length to the tube diameter, is apparently less affected by the diameter, see Figures 5.24 and 5.25.

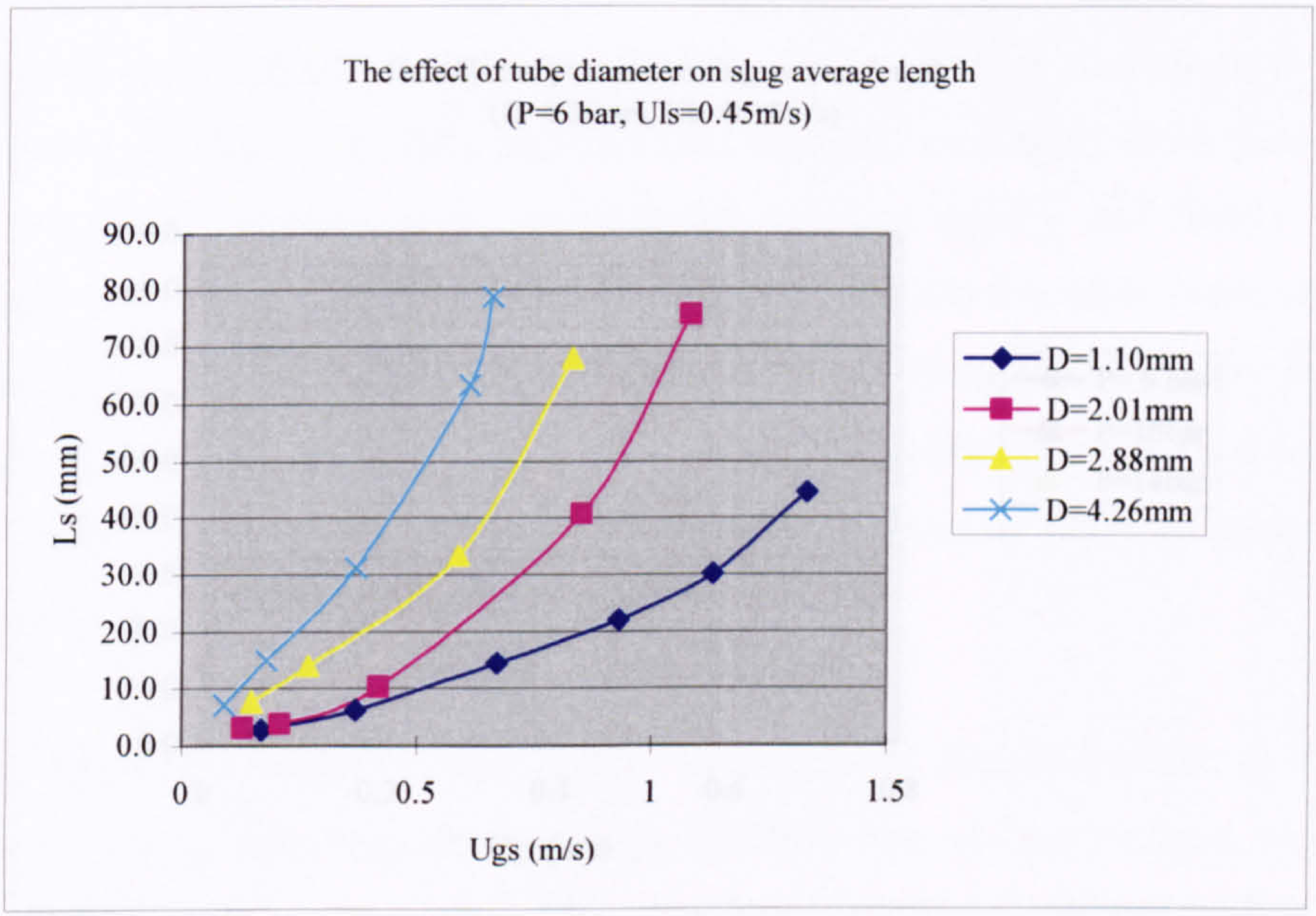

Figure 5.24 The effect of tube diameter on slug average length at 6 bar (u_{ls}=0.45m/s).

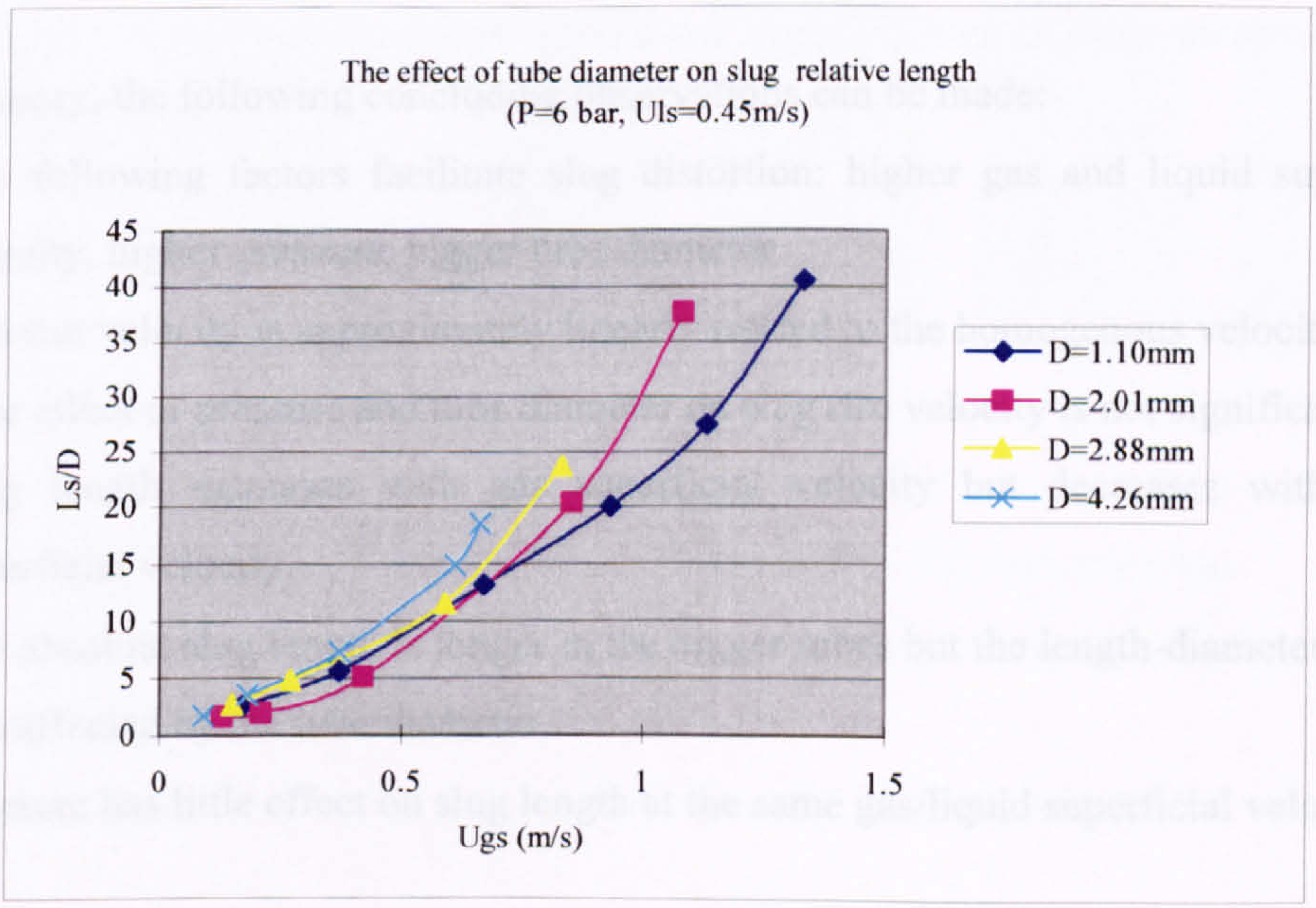

Figure 5.25 The effect of tube diameter on slug length-diameter ratio at 6 bar (u_{ls}=0.45m/s).

Overall pressure has little effect on slug length though the possible maximum length could be longer at lower pressures due to the fact that the slug-churn boundary shifts to higher gas superficial velocity, see Figure 5.26.

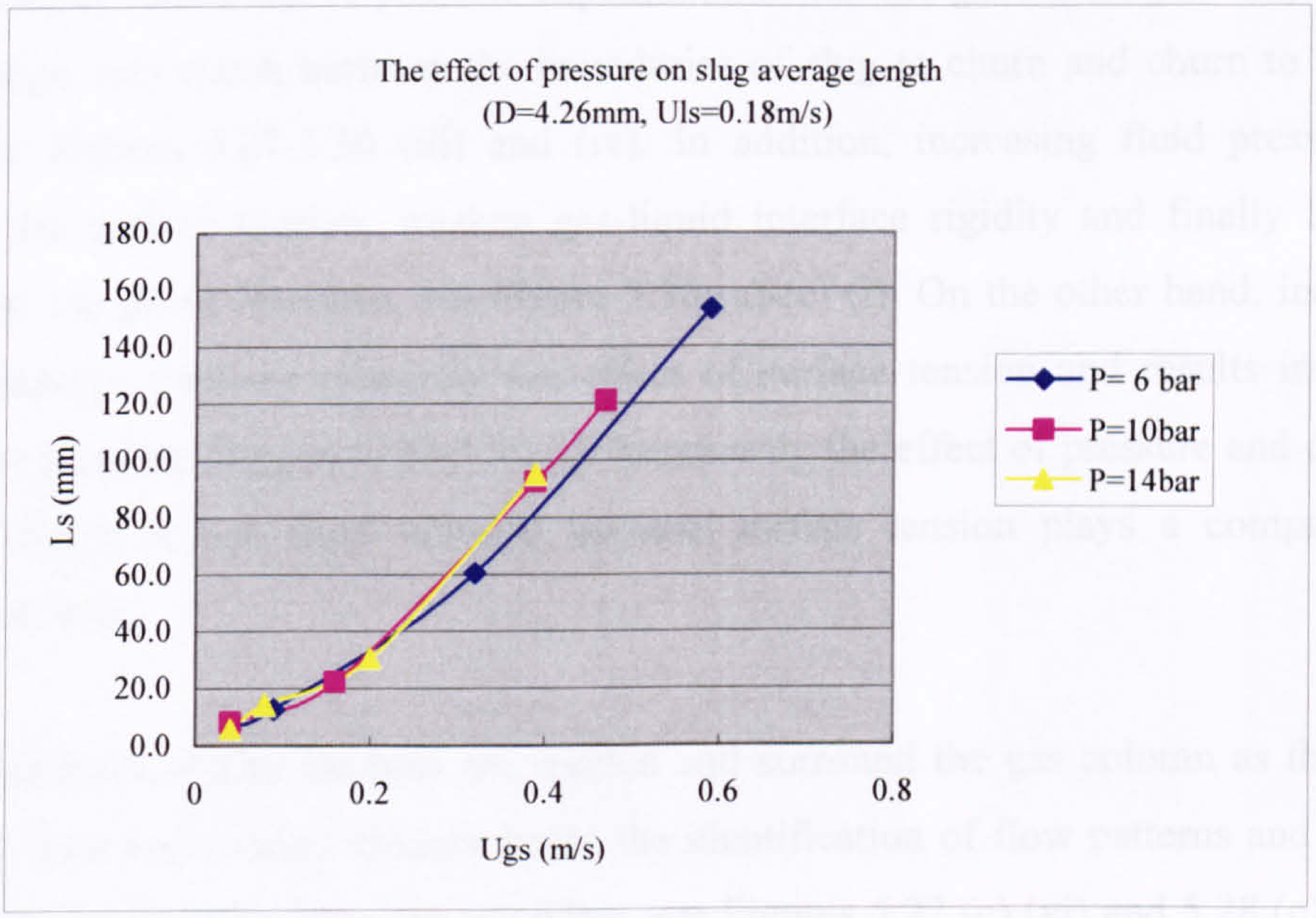

Figure 5.26 The effect of pressure on slug average length in the 4.26 mm tube (u_{ls}=0.18m/s).

In summary, the following concluding observations can be made:

- The following factors facilitate slug distortion: higher gas and liquid superficial velocity, higher pressure, bigger tube diameter.
- The rise velocity is approximately linearly related to the homogenous velocity.
- The effect of pressure and tube diameter on slug rise velocity is not significant.
- Slug length increases with gas superficial velocity but decreases with liquid superficial velocity.
- The absolute slug length is longer in the bigger tubes but the length-diameter ratio is less affected by the tube diameter.
- Pressure has little effect on slug length at the same gas/liquid superficial velocities.

5.1.5 Churn flow

The gas-liquid interface becomes chaotic as the liquid superficial velocity increases due to the severe impact from the liquid phase, see Figures 5.27-5.30. However, the effect of gas superficial velocity on the flow pattern is not very significant under the current experimental conditions. A possible explanation is that the gas superficial velocity does not change very much between the boundaries of slug to churn and churn to annular, compare Figures 5.27-5.30 (iii) and (iv). In addition, increasing fluid pressure can reduce the surface tension, weaken gas-liquid interface rigidity and finally intensify chaos on the phase interface, see Figure 5.30 (a)-(c) (i). On the other hand, increasing tube diameter weakens relatively the effect of surface tension and results in chaotic interface also, see Figures 5.27-5.30 (i). Summarily the effect of pressure and diameter is significant at low fluid velocity because surface tension plays a comparatively important role.

Large numbers of fine bubbles are created and surround the gas column as the liquid velocity increases, which disturbs badly the identification of flow patterns and is more serious in the high pressure and big tubes, see Figures 5.27 (c) (vi) and 5.28 (c) (vi). In fact, all flow patterns are identified based on the movies. The movies, including the electronic pictures in the attached disc, are much clearer than the pictures in the hard copy thesis. Therefore, the identifications and classifications in these pictures are still accurate and reliable.

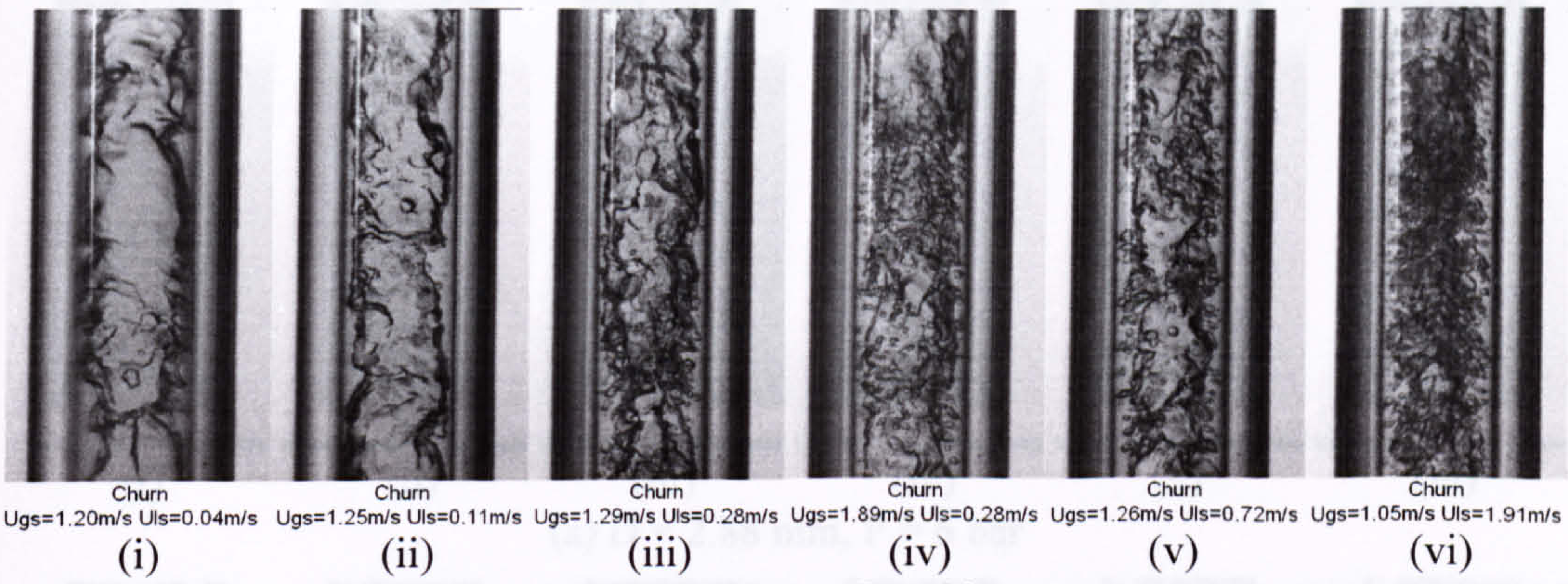

(a) D = 4.26 mm, P = 6 bar

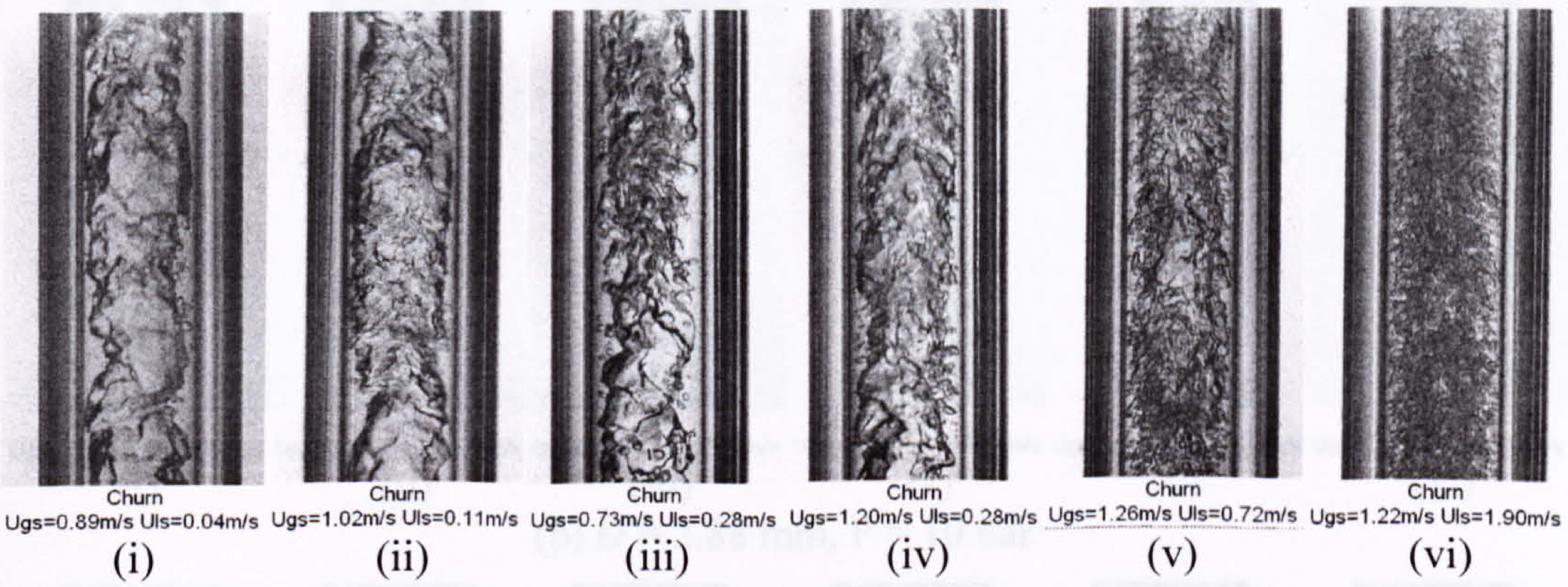

(b) D = 4.26 mm, P = 10 bar

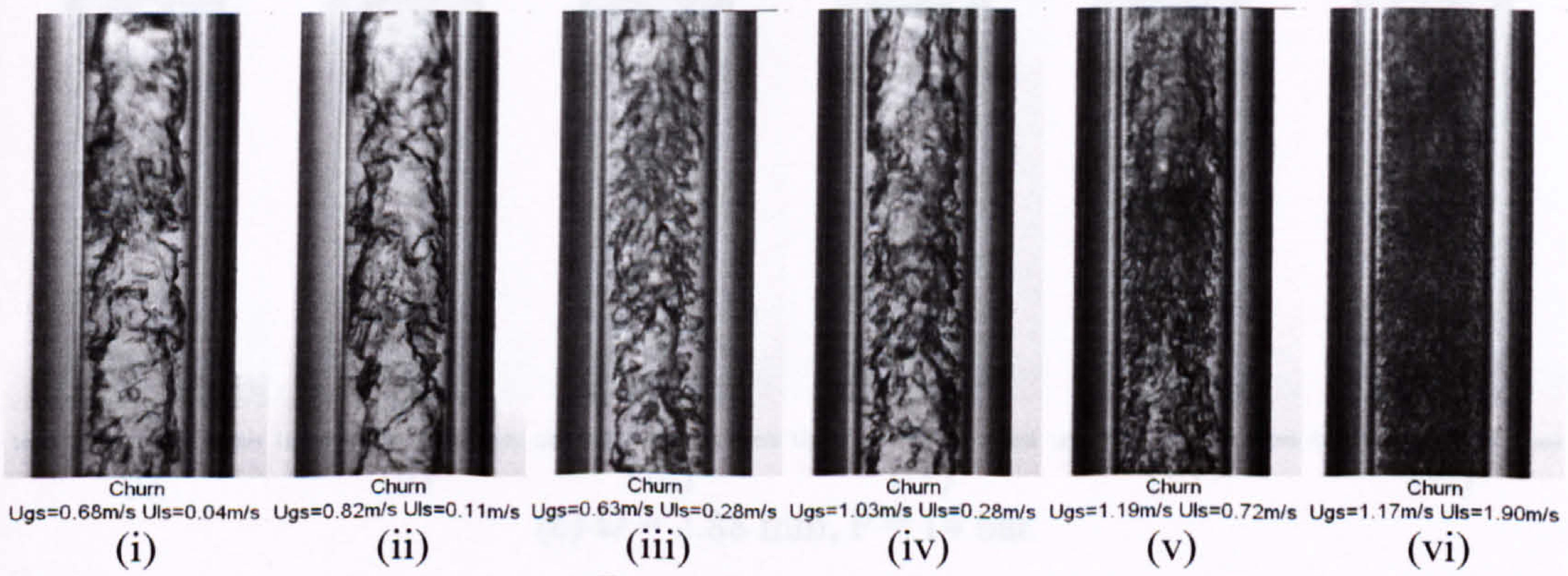

(c) D = 4.26 mm, P = 14 bar

Figure 5.27 Churn flow observed in the 4.26 mm tube at different pressures. (a) 6 bar, (b) 10 bar and (c) 14 bar.

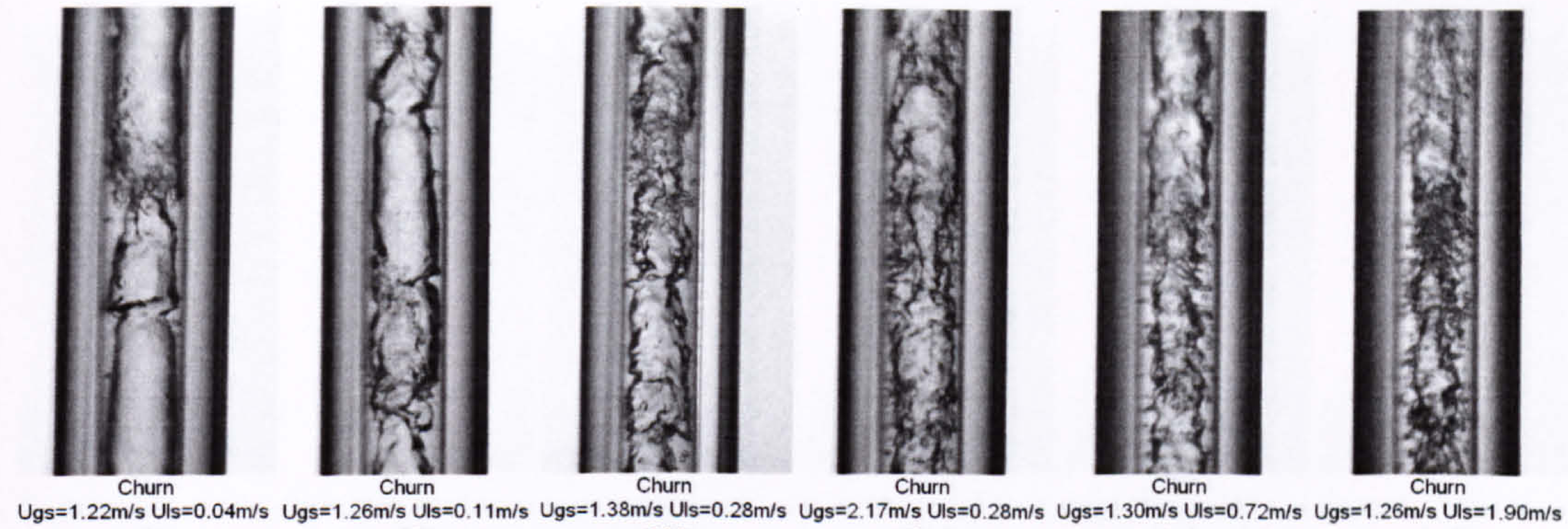

(i) (ii) (iii) (iv) (v) (vi)

(a) D = 2.88 mm, P = 6 bar

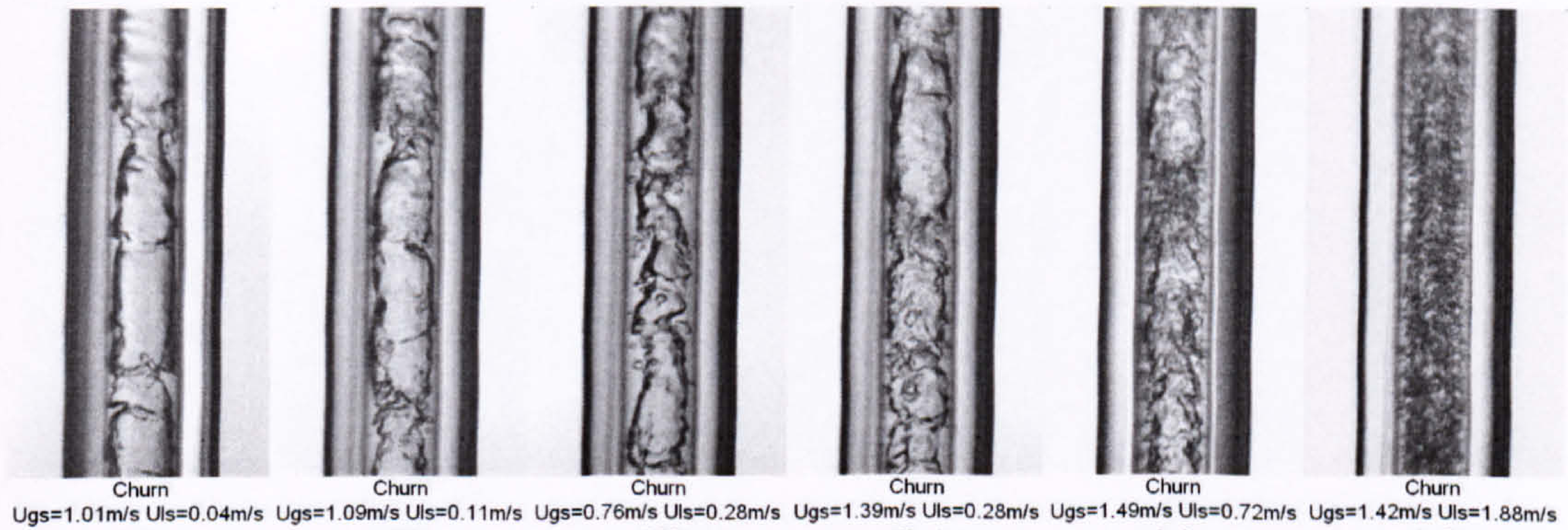

(i) (ii) (iii) (iv) (v) (vi)

(b) D = 2.88 mm, P = 10 bar

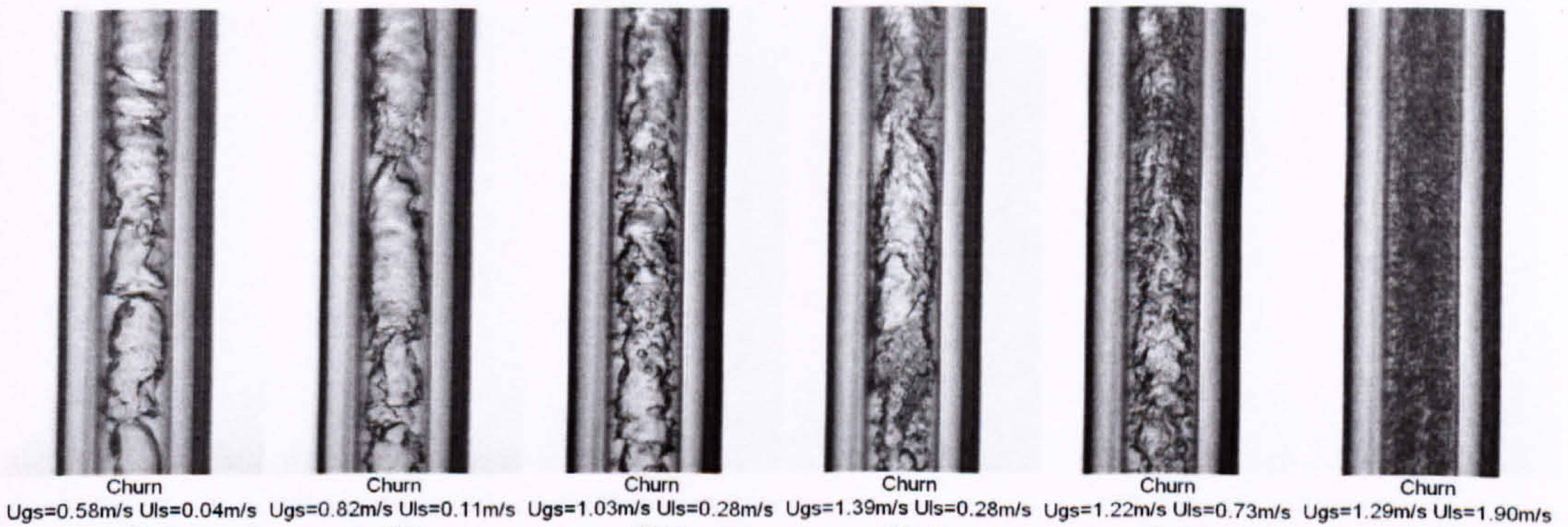

(i) (ii) (iii) (iv) (v) (vi)

(c) D = 2.88 mm, P = 14 bar

Figure 5.28 Churn flow observed in the 2.88 mm tube at different pressures.
(a) 6 bar, (b) 10 bar and (c) 14 bar.

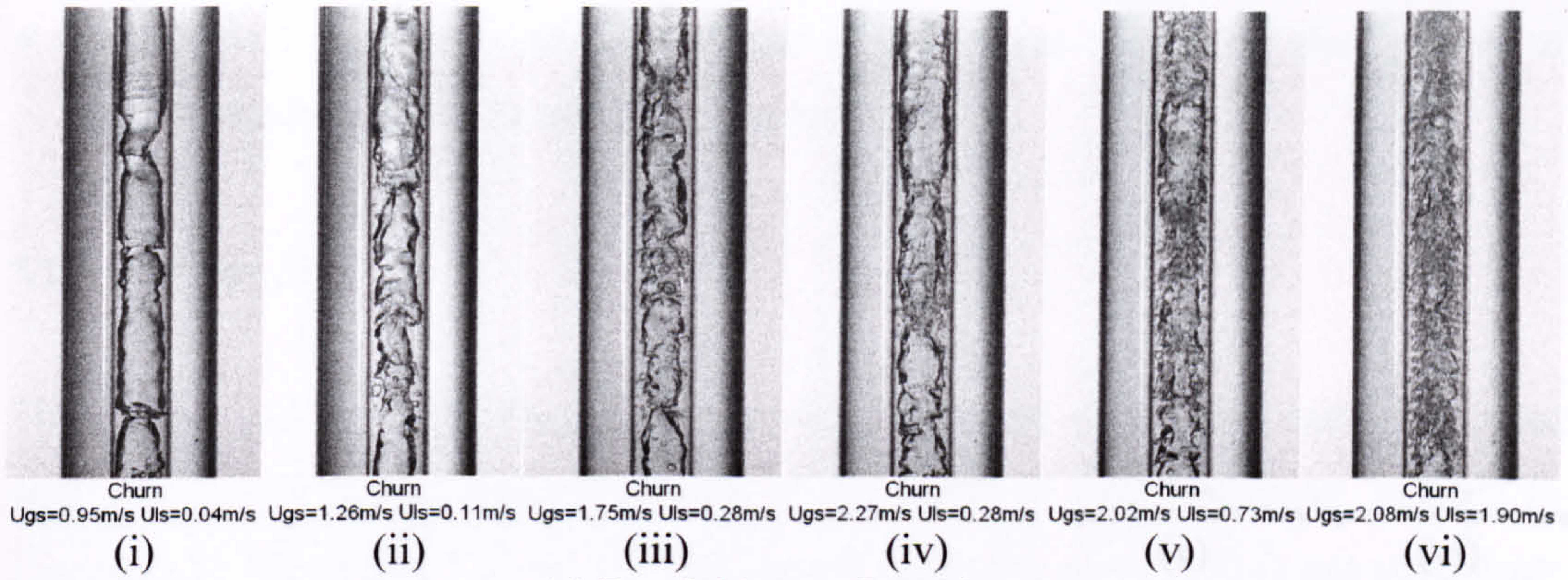

(a) D = 2.01 mm, P = 6 bar

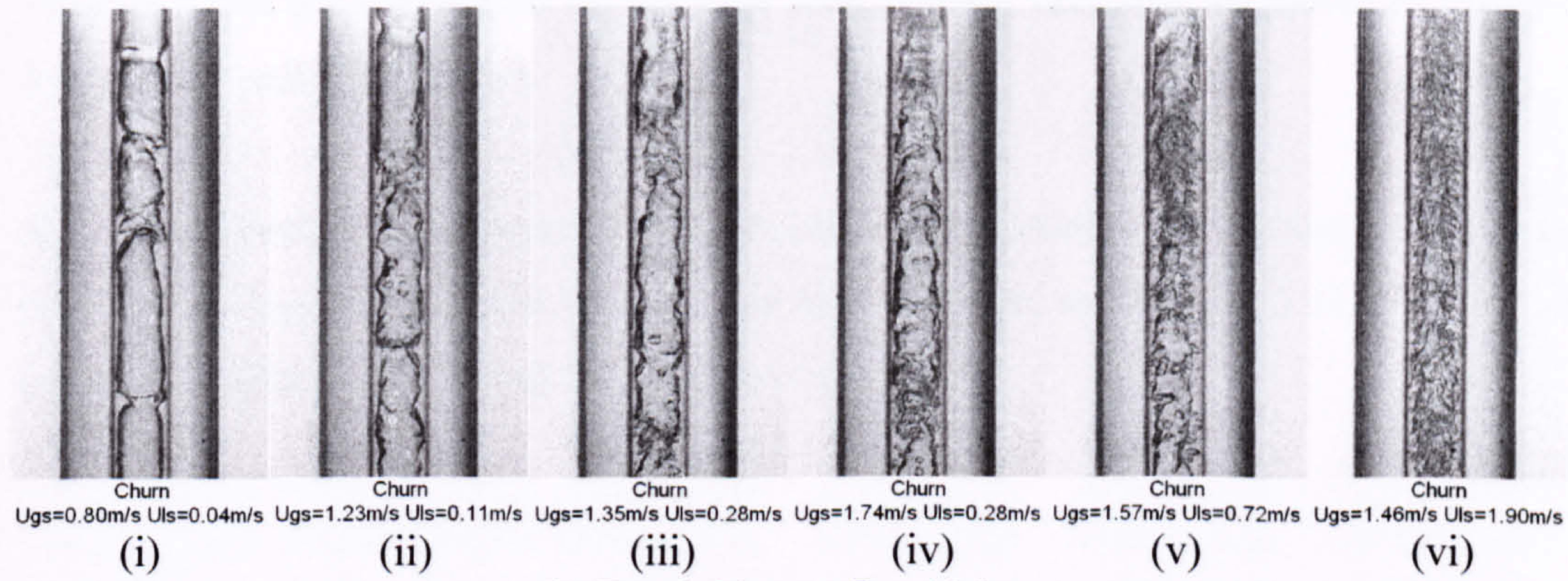

(b) D = 2.01 mm, P = 10 bar

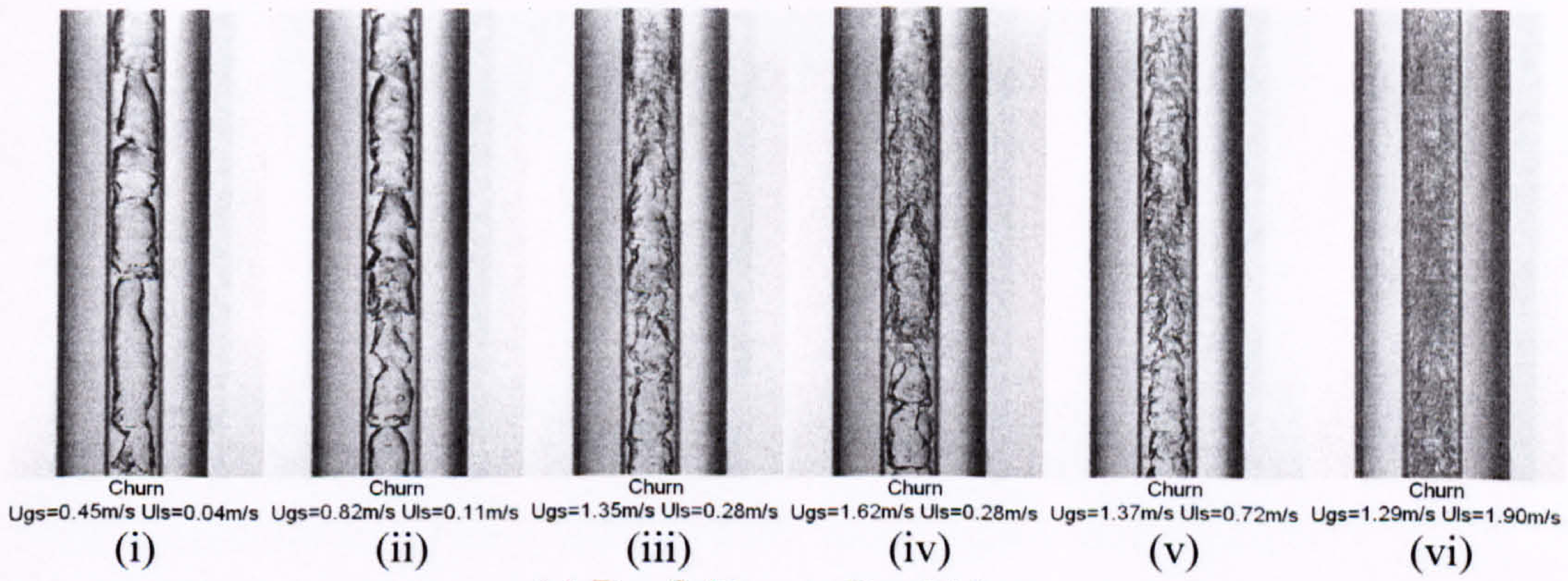

(c) D = 2.01 mm, P = 14 bar

Figure 5.29 Churn flow observed in the 2.01 mm tube at different pressures. (a) 6 bar, (b) 10 bar and (c) 14 bar.

In summary, the following concluding observations can be made:

- High liquid superficial velocity, high pressure and large tube diameter intensify chaos in churn flow. The effect of gas superficial velocity on the flow configuration is not quite distinct in the present experiments.

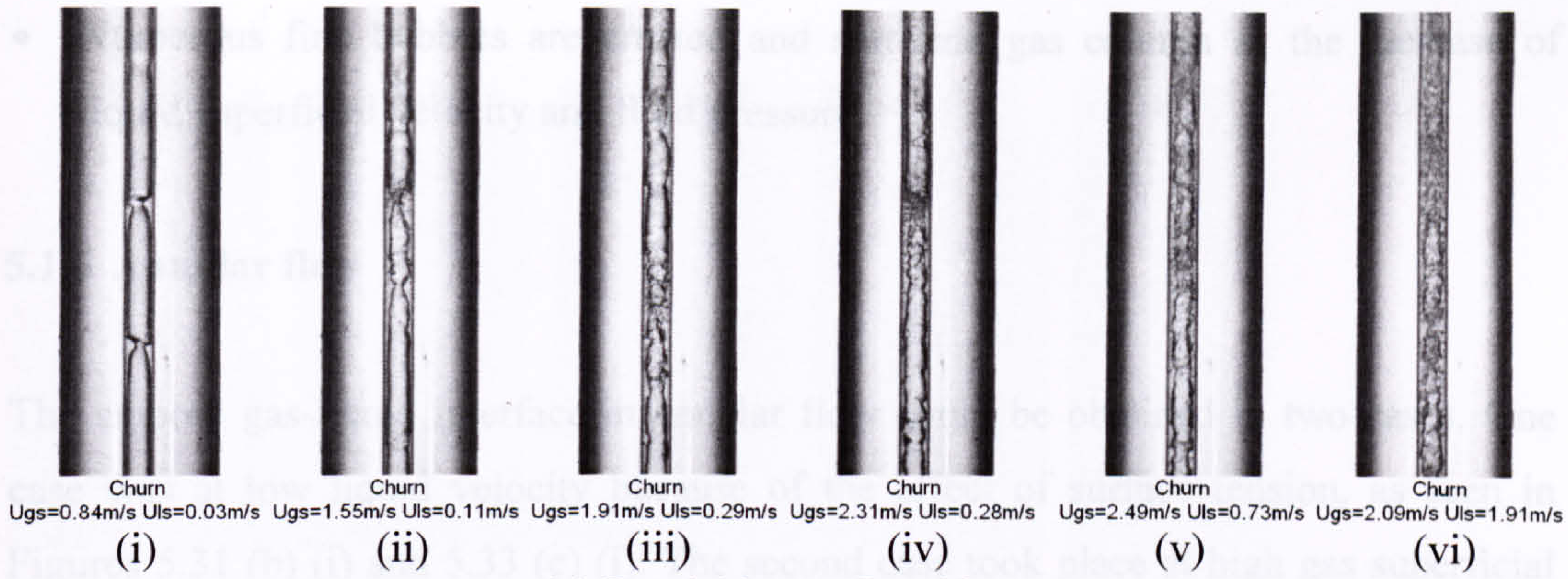

(a) D = 1.10 mm, P = 6 bar

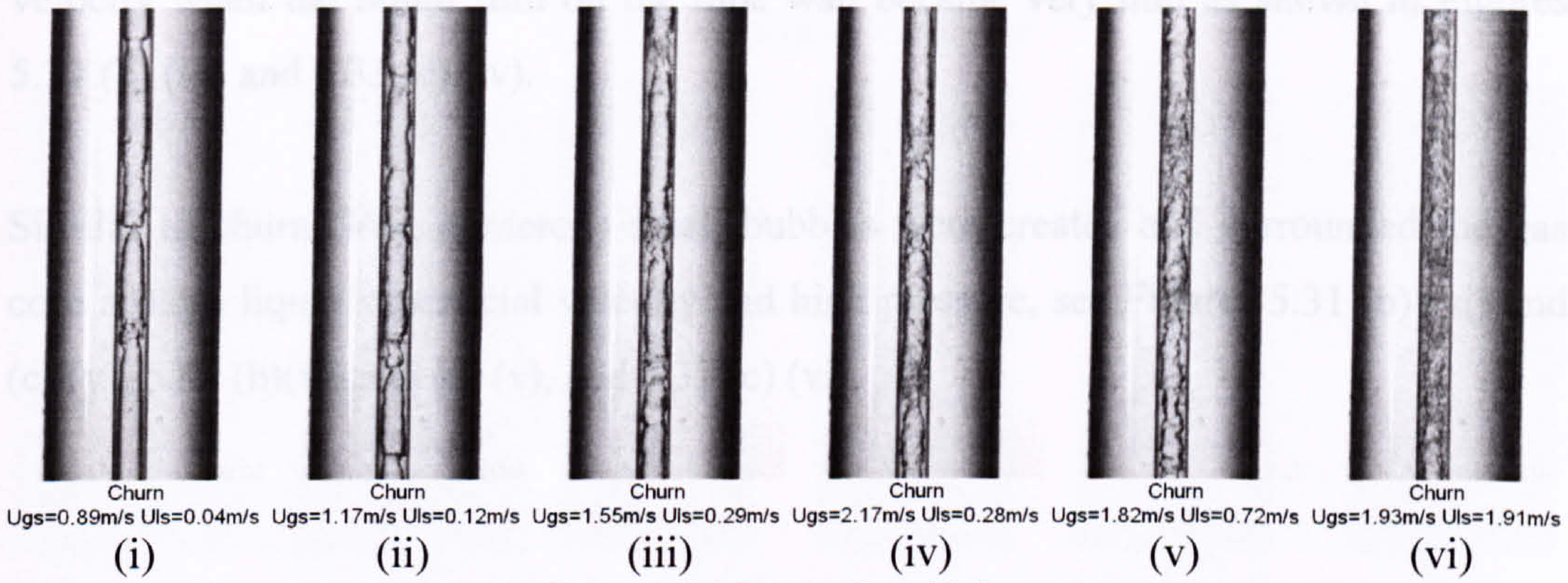

(b) D = 1.10 mm, P = 10 bar

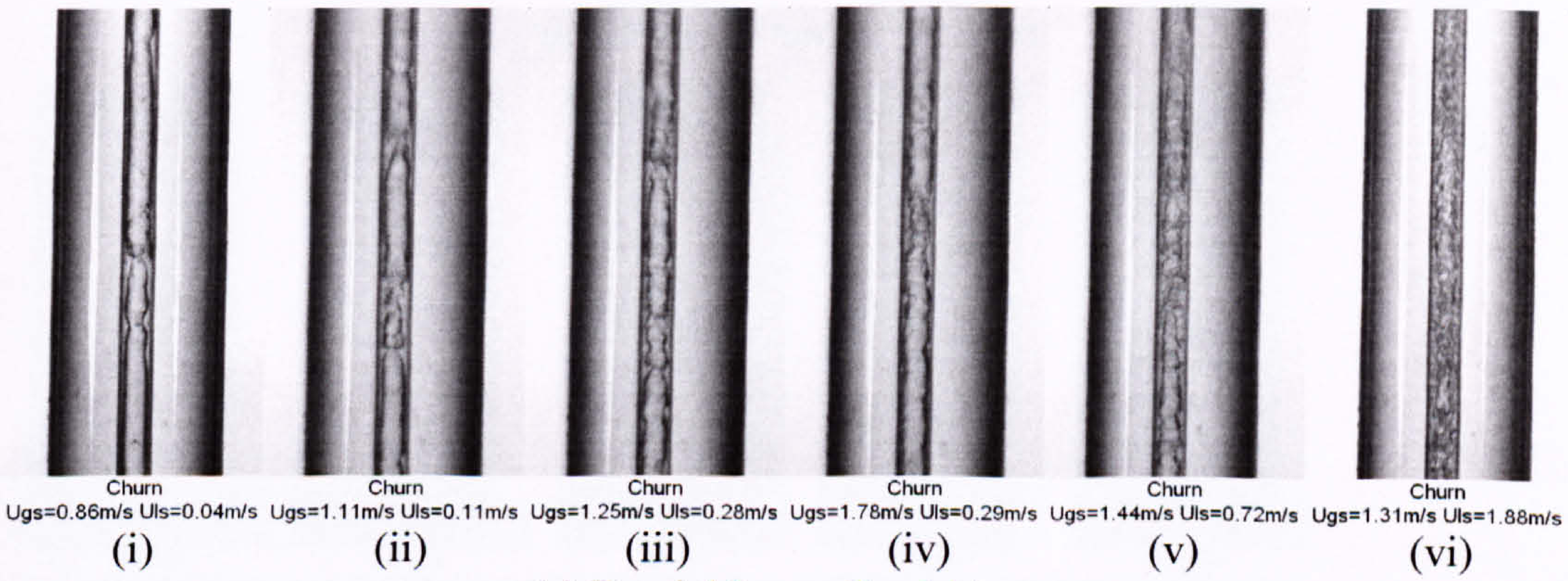

(c) D = 1.10 mm, P = 14 bar

Figure 5.30 Churn flow observed in the 1.10 mm tube at different pressures.
(a) 6 bar, (b) 10 bar and (c) 14 bar.

In summary, the following concluding observations can be made:

- High liquid superficial velocity, high pressure and large tube diameter intensify chaos in churn flow. The effect of gas superficial velocity on the flow configuration is not quite distinct in the present experiments.

- Numerous fine bubbles are created and surround gas column as the increase of liquid superficial velocity and fluid pressure.

5.1.6 Annular flow

The smooth gas-liquid interface in annular flow could be obtained in two cases. One case was at low liquid velocity because of the effect of surface tension, as seen in Figures 5.31 (b) (i) and 5.33 (c) (i). The second case took place at high gas superficial velocity when the liquid film on the tube wall became very thin as shown in Figures 5.31 (b) (iv) and 5.33 (c) (iv).

Similar to churn flow, numerous small bubbles were created and surrounded the gas core at high liquid superficial velocity and high pressure, see Figures 5.31 (b) (vi) and (c) (v), 5.32 (b)(vi) and (c) (v), and 5.33 (c) (vi).

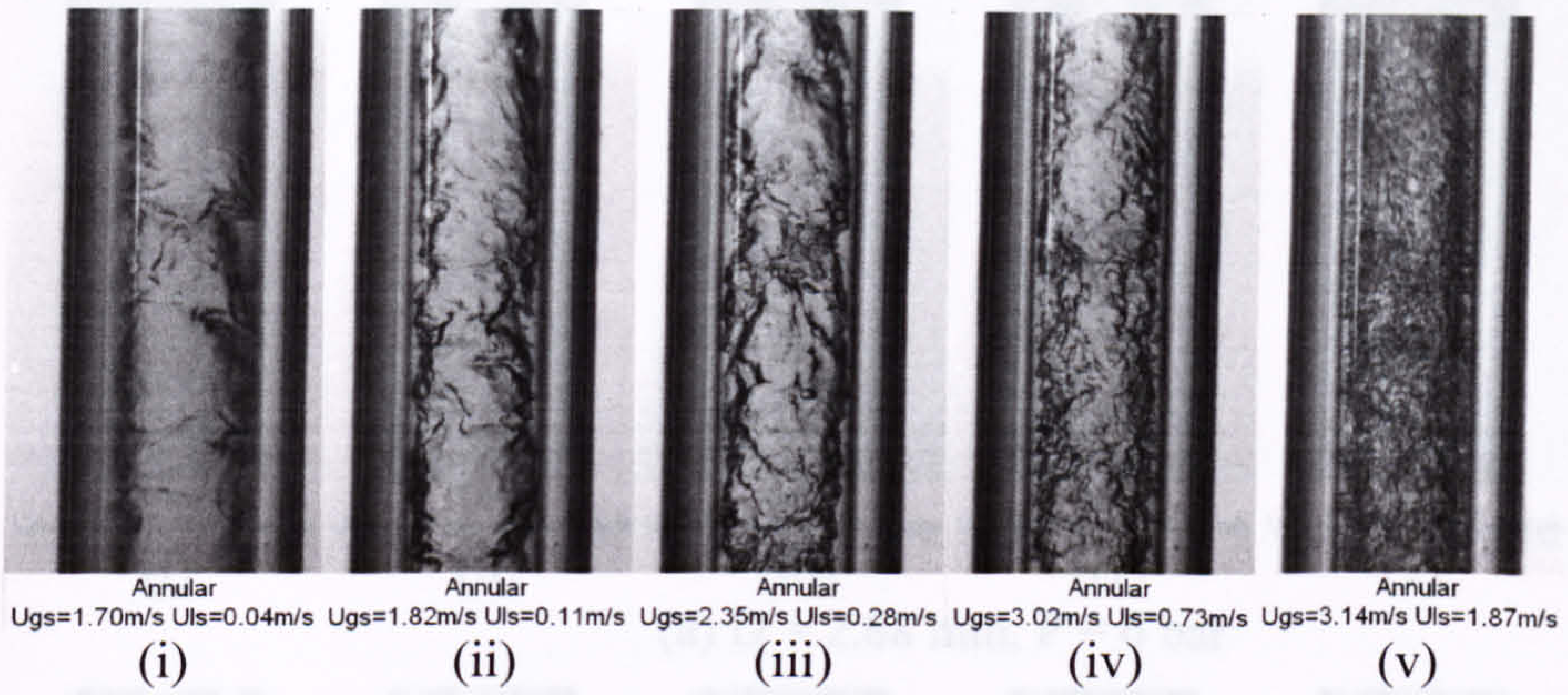

(a) D = 4.26 mm, P = 6 bar

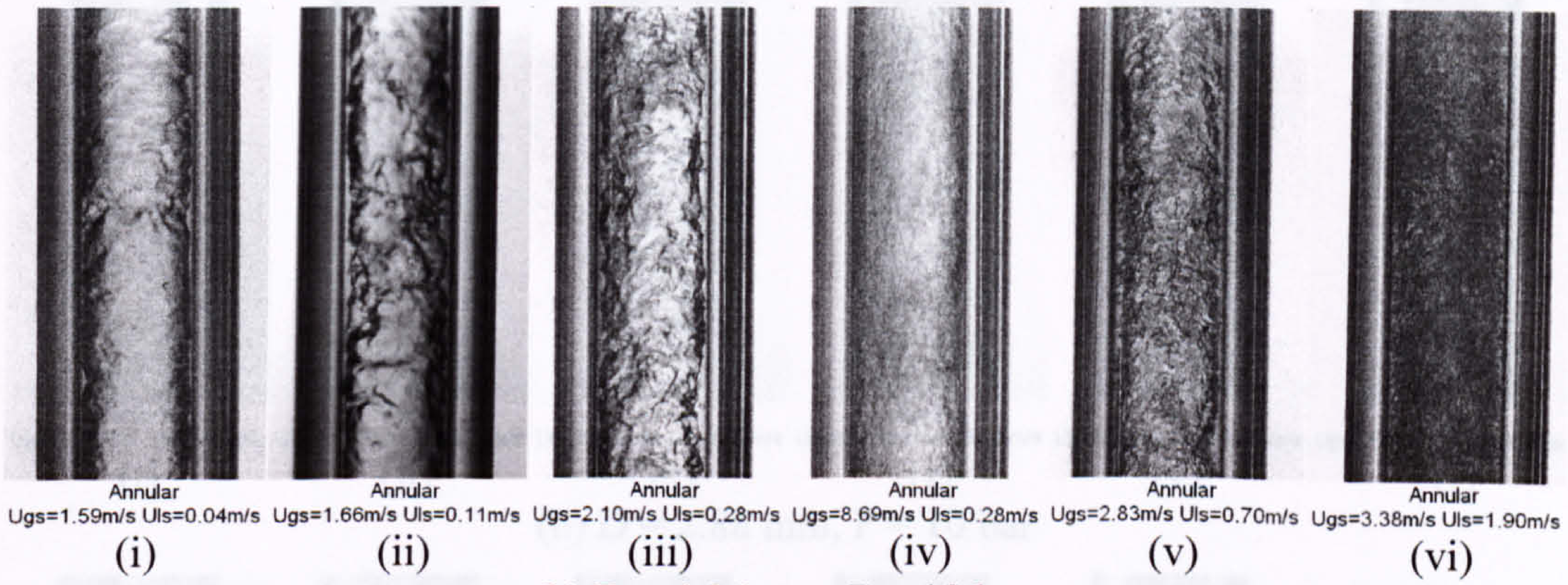

(b) D = 4.26 mm, P = 10 bar

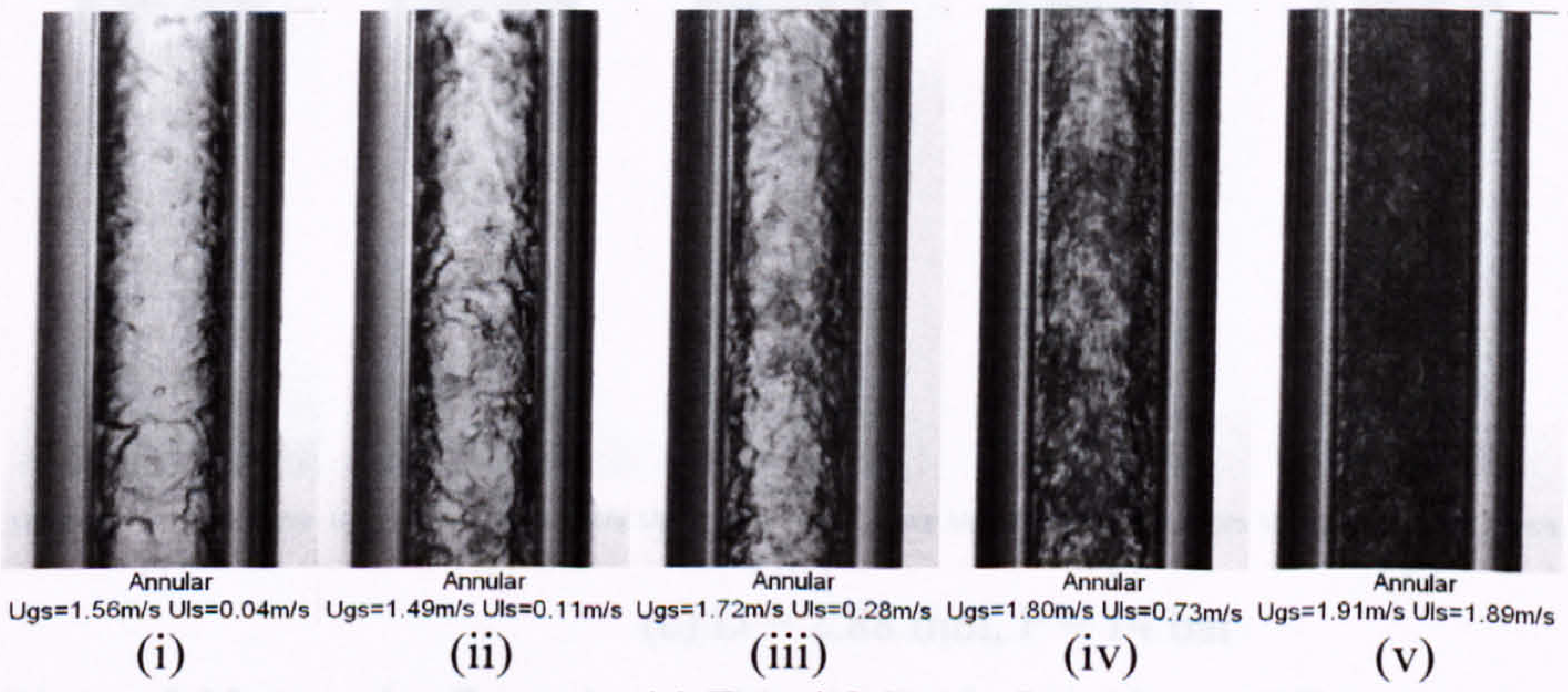

(c) D = 4.26 mm, P = 14 bar

Figure 5.31 Annular flow observed in the 4.26 mm tube at different pressures. (a) 6 bar, (b) 10 bar and (c) 14 bar.

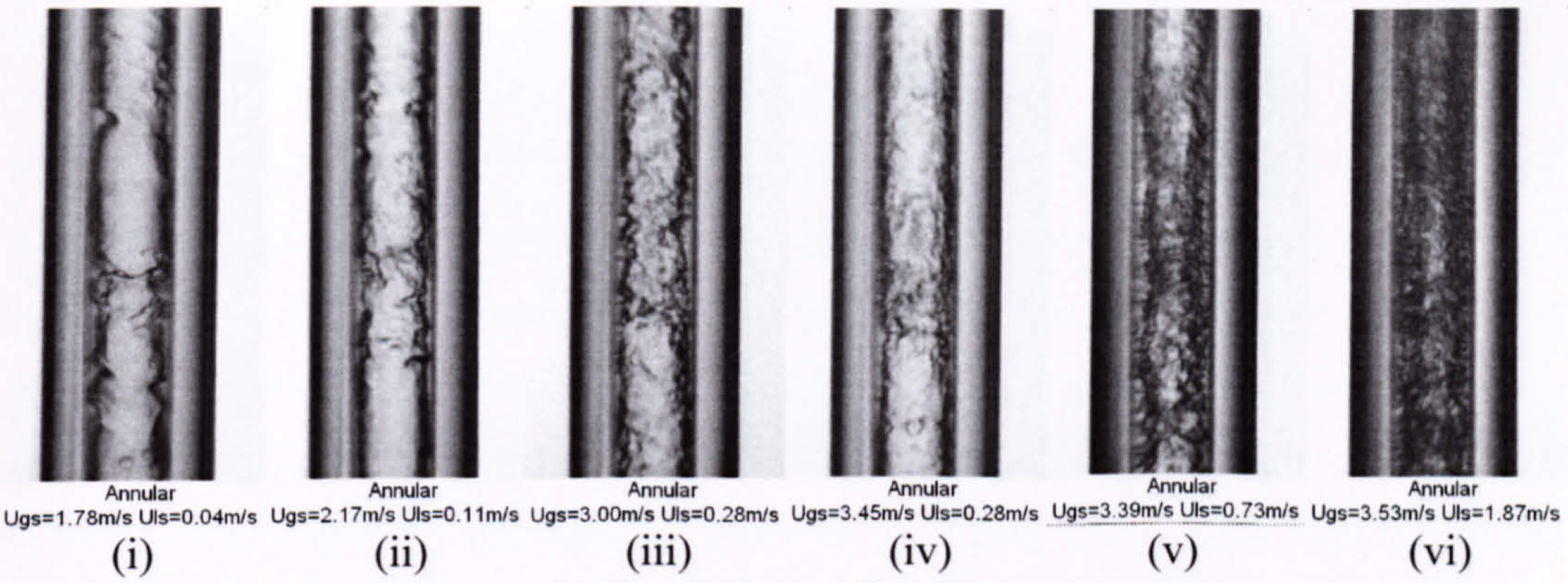

(a) D = 2.88 mm, P = 6 bar

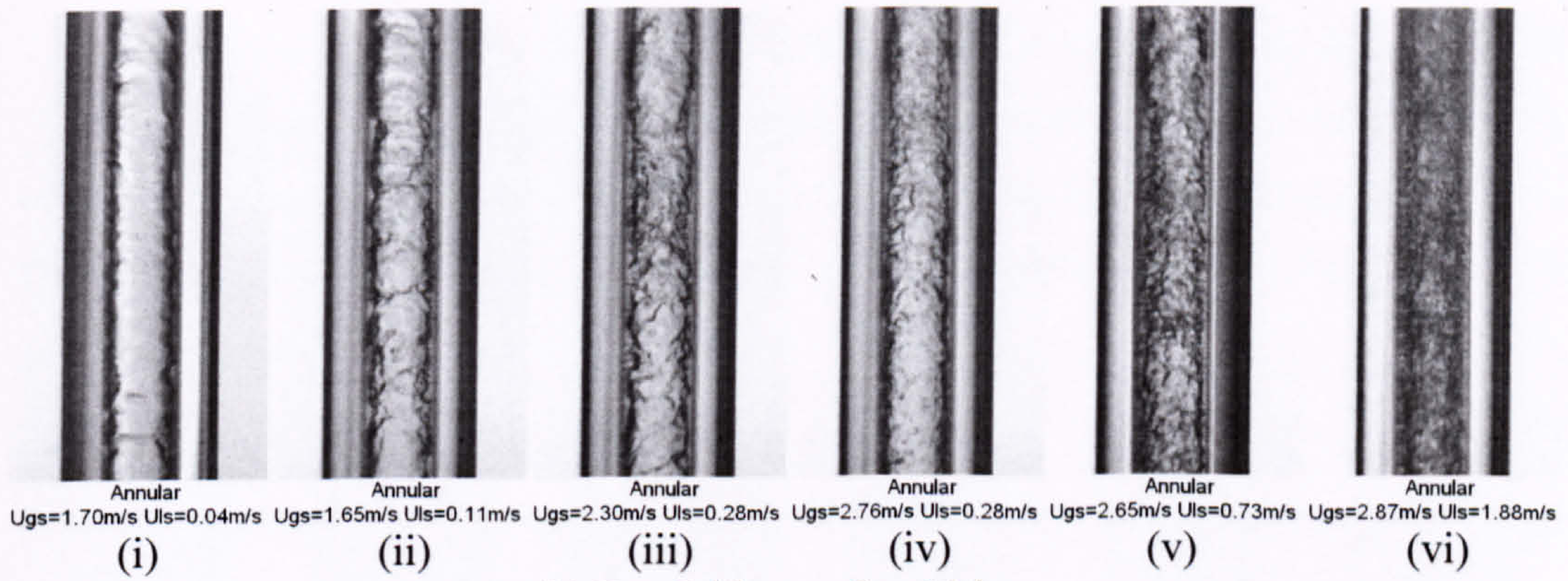

(b) D = 2.88 mm, P = 10 bar

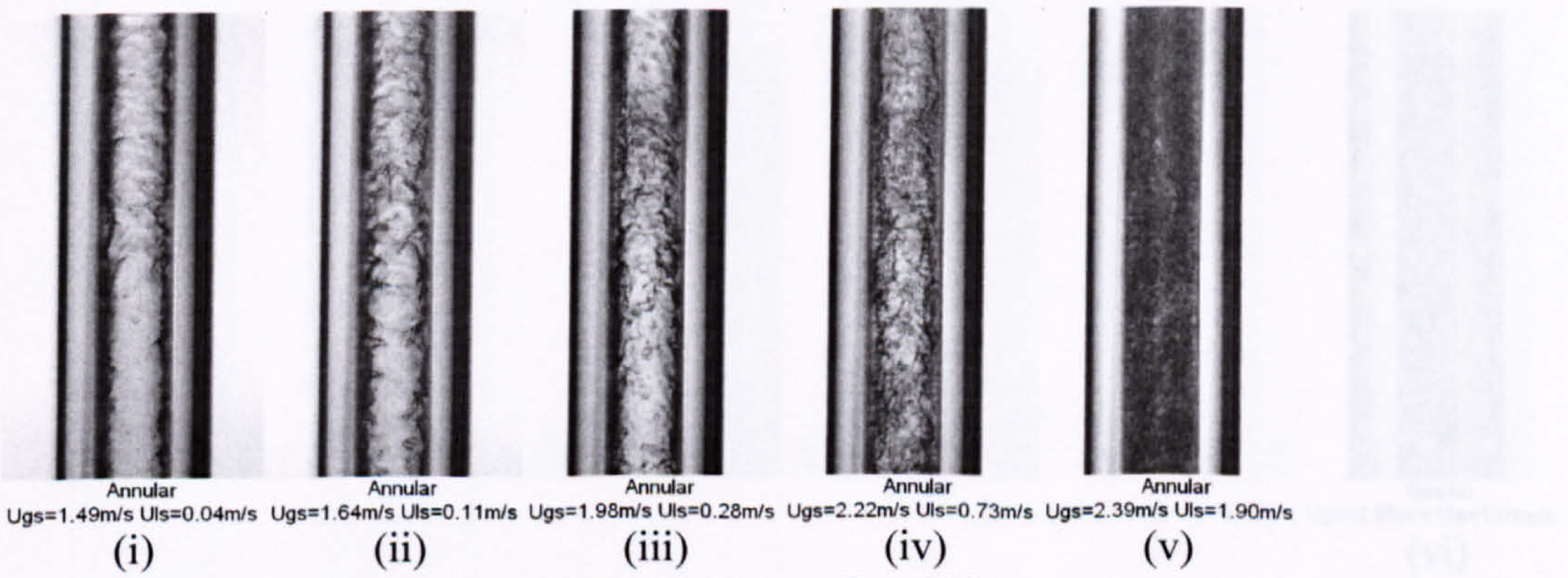

(c) D = 2.88 mm, P = 14 bar

Figure 5.32 Annular flow observed in the 2.88 mm tube at different pressures.
(a) 6 bar, (b) 10 bar and (c) 14 bar.

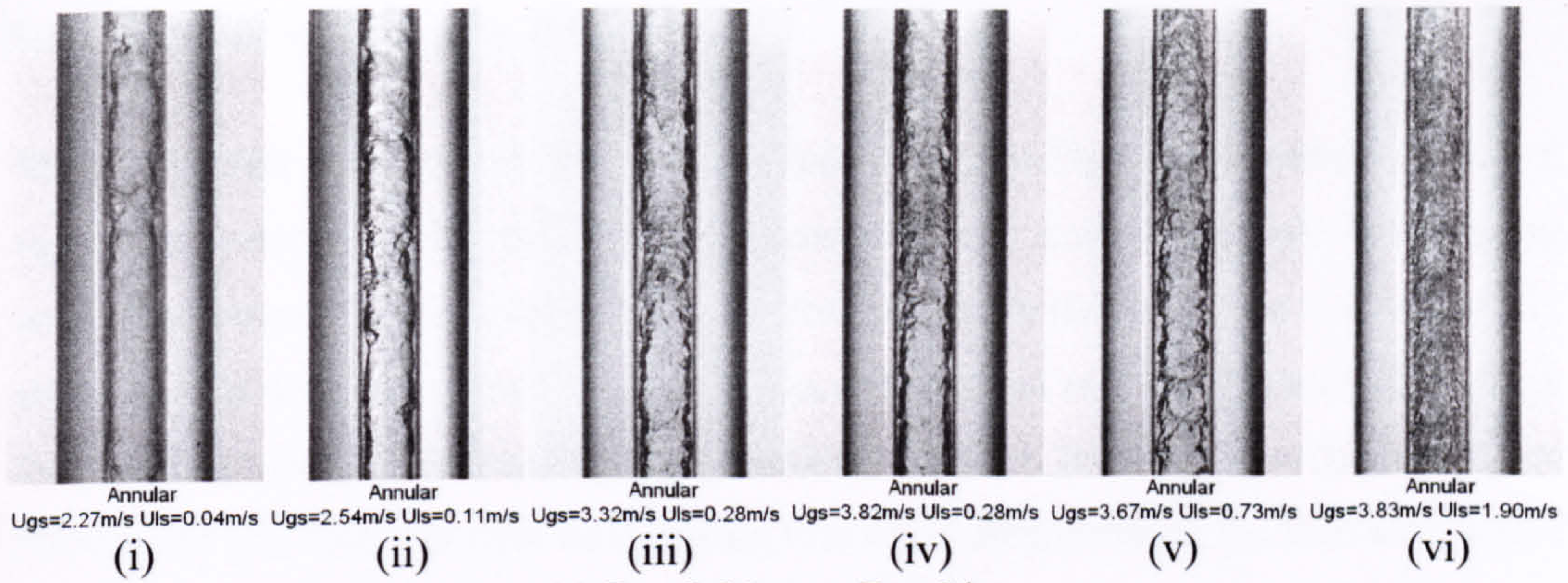

(a) D = 2.01 mm, P = 6 bar

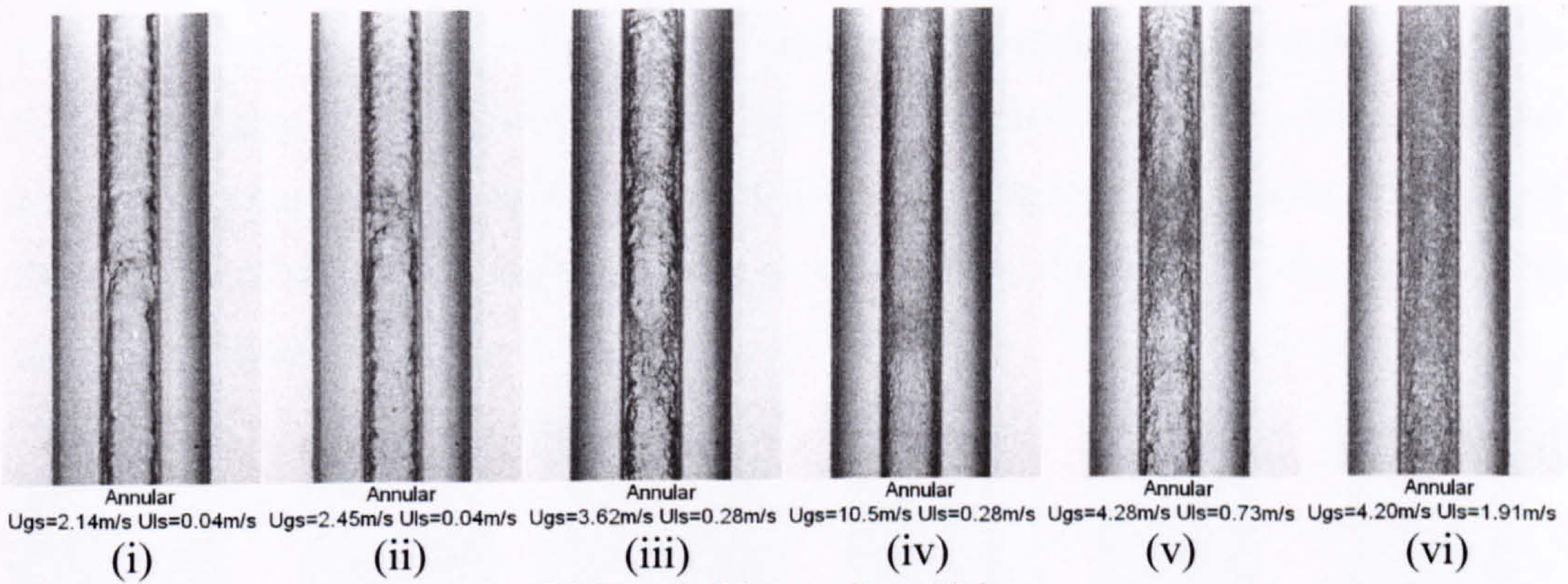

(b) D = 2.01 mm, P = 10 bar

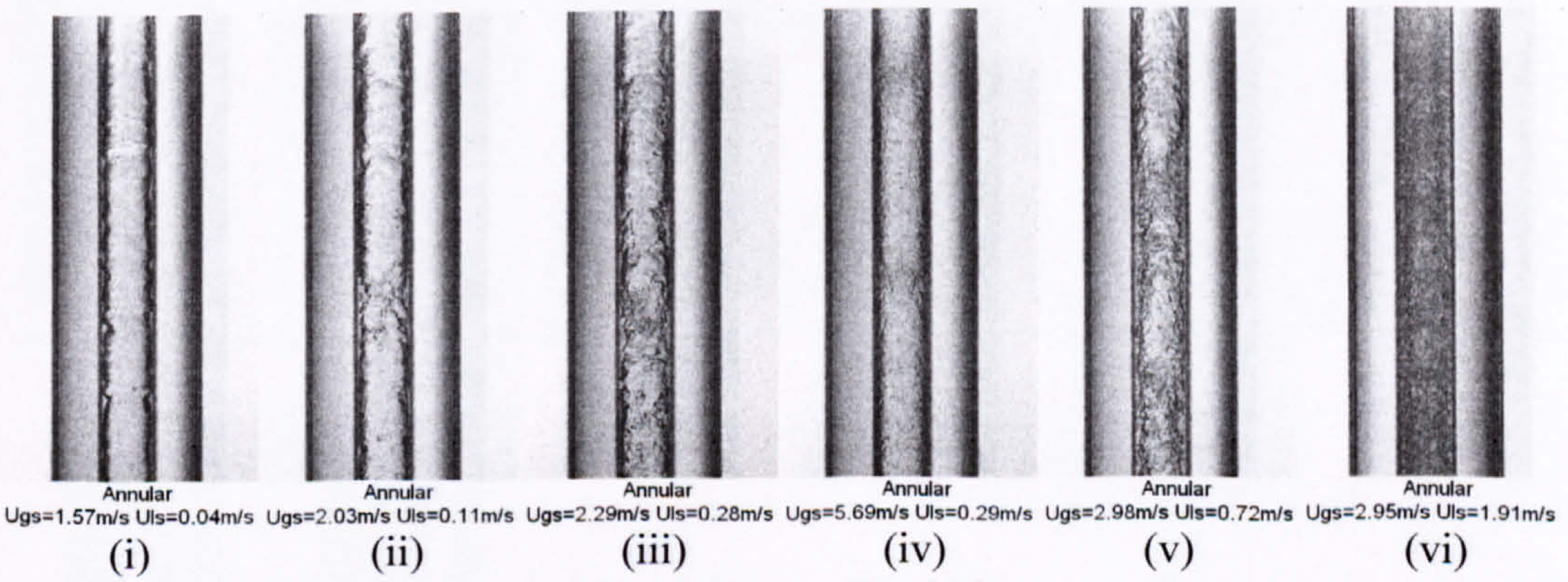

(c) D = 2.01 mm, P = 14 bar

Figure 5.33 Annular flow observed in the 2.01 mm tube at different pressures. (a) 6 bar, (b) 10 bar and (c) 14 bar.

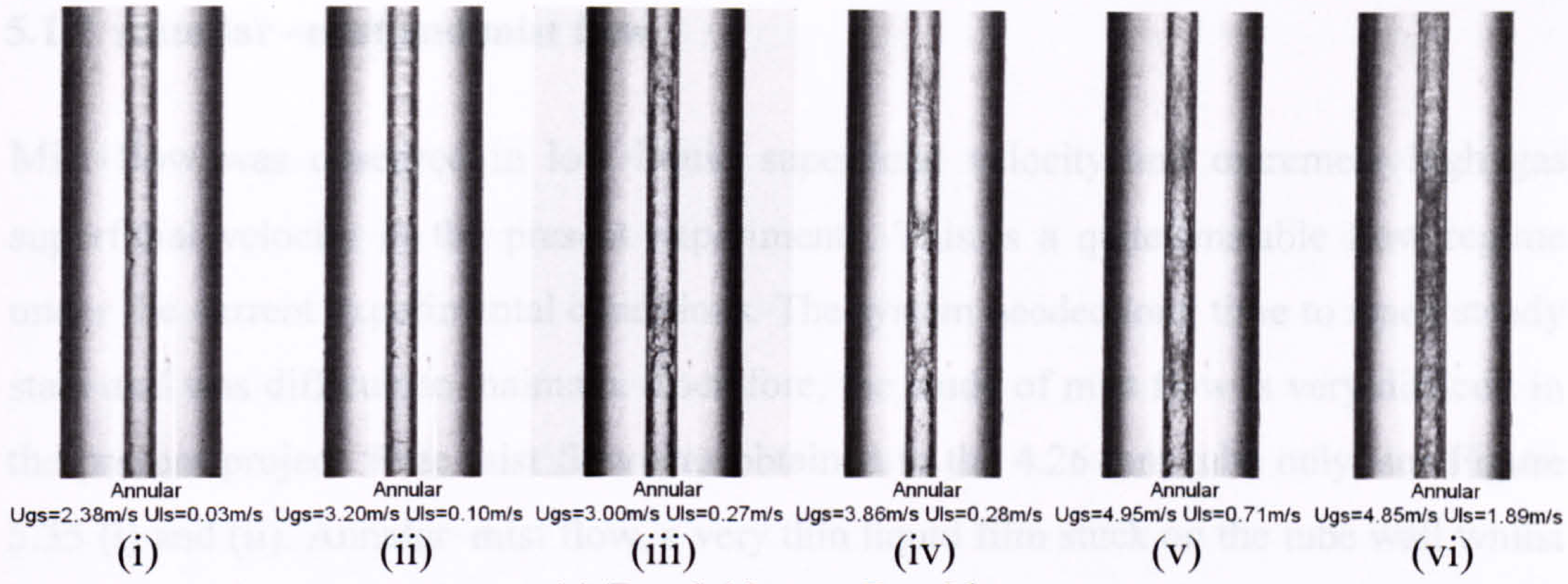

(a) D = 1.10 mm, P = 6 bar

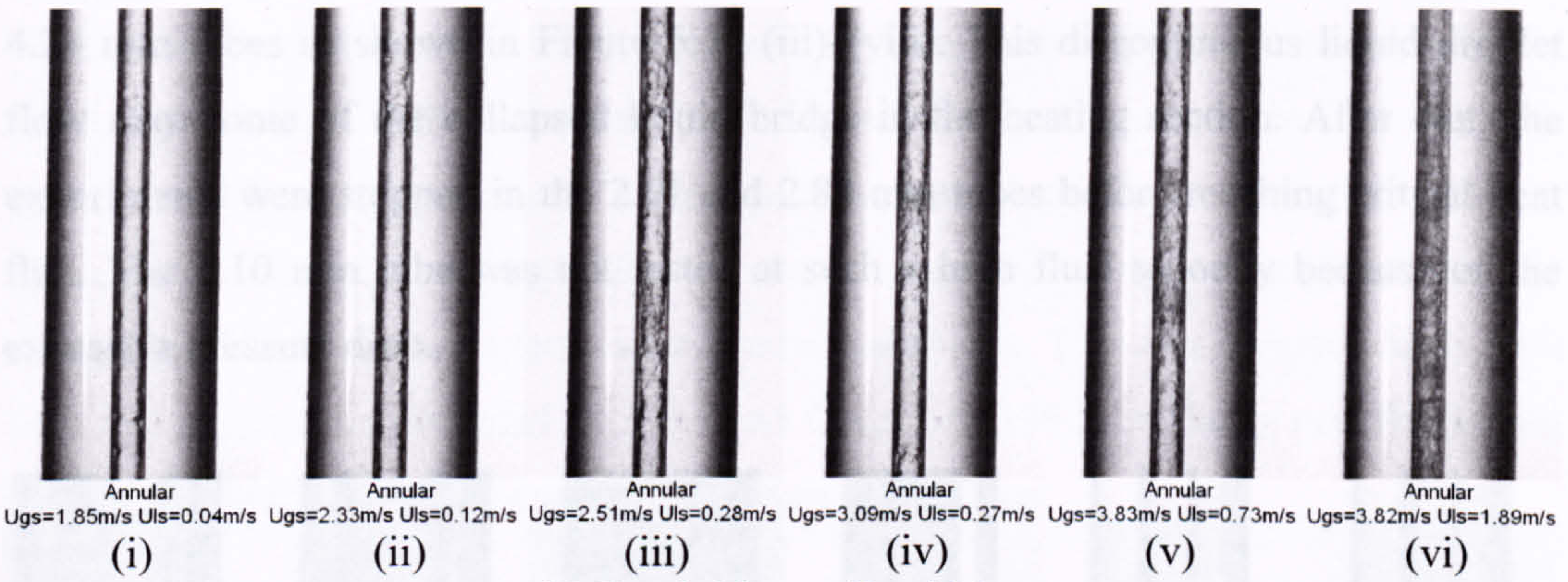

(b) D = 1.10 mm, P = 10 bar

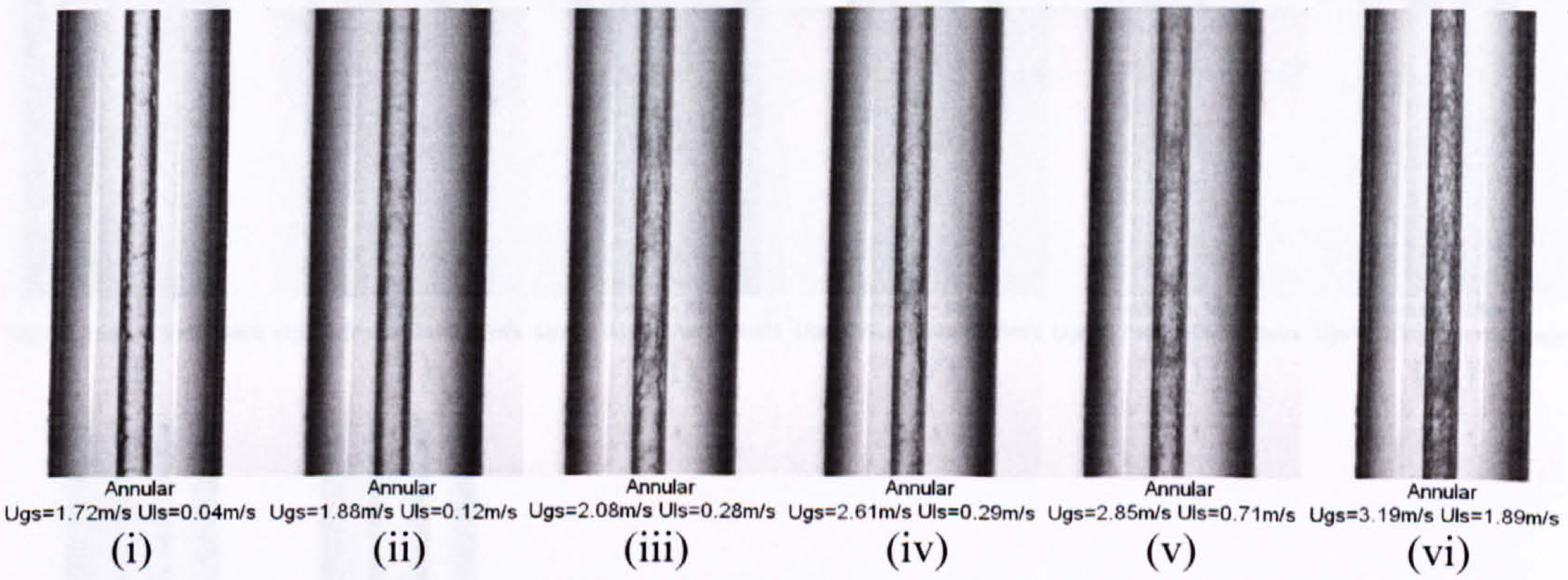

(c) D = 1.10 mm, P = 14 bar

Figure 5.34 Annular flow observed in the 1.10 mm tube at different pressures. (a) 6 bar, (b) 10 bar and (c) 14 bar.

In summary, the following concluding observations can be made:

- The gas-liquid interface is smoother at high quality or high void fraction.
- Numerous small bubbles were created and surrounded gas core at higher liquid superficial velocity and higher pressure.

5.1.7 Annular –mist and mist flow

Mist flow was observed in low liquid superficial velocity and extremely high gas superficial velocity in the present experiments. This is a quite unstable flow regime under the current experimental conditions. The system needed long time to reach steady state and was difficult to maintain. Therefore, the study of mist flow is very difficult in the present project. Pure mist flow was obtained in the 4.26 mm tube only, see Figure 5.35 (i) and (ii). Annular–mist flow, a very thin liquid film stuck on the tube wall whilst the liquid droplets passed through intermittently, was observed in the 2.01, 2.88 and 4.26 mm tubes as shown in Figure 5.35 (iii)–(viii). This discontinuous liquid droplet flow may come of the collapsed liquid bridge in the heating section. After that, the experiments were stopped in the 2.01 and 2.88 mm tubes before reaching critical heat flux. The 1.10 mm tube was not tested at such a high fluid velocity because of the excessive pressure drop.

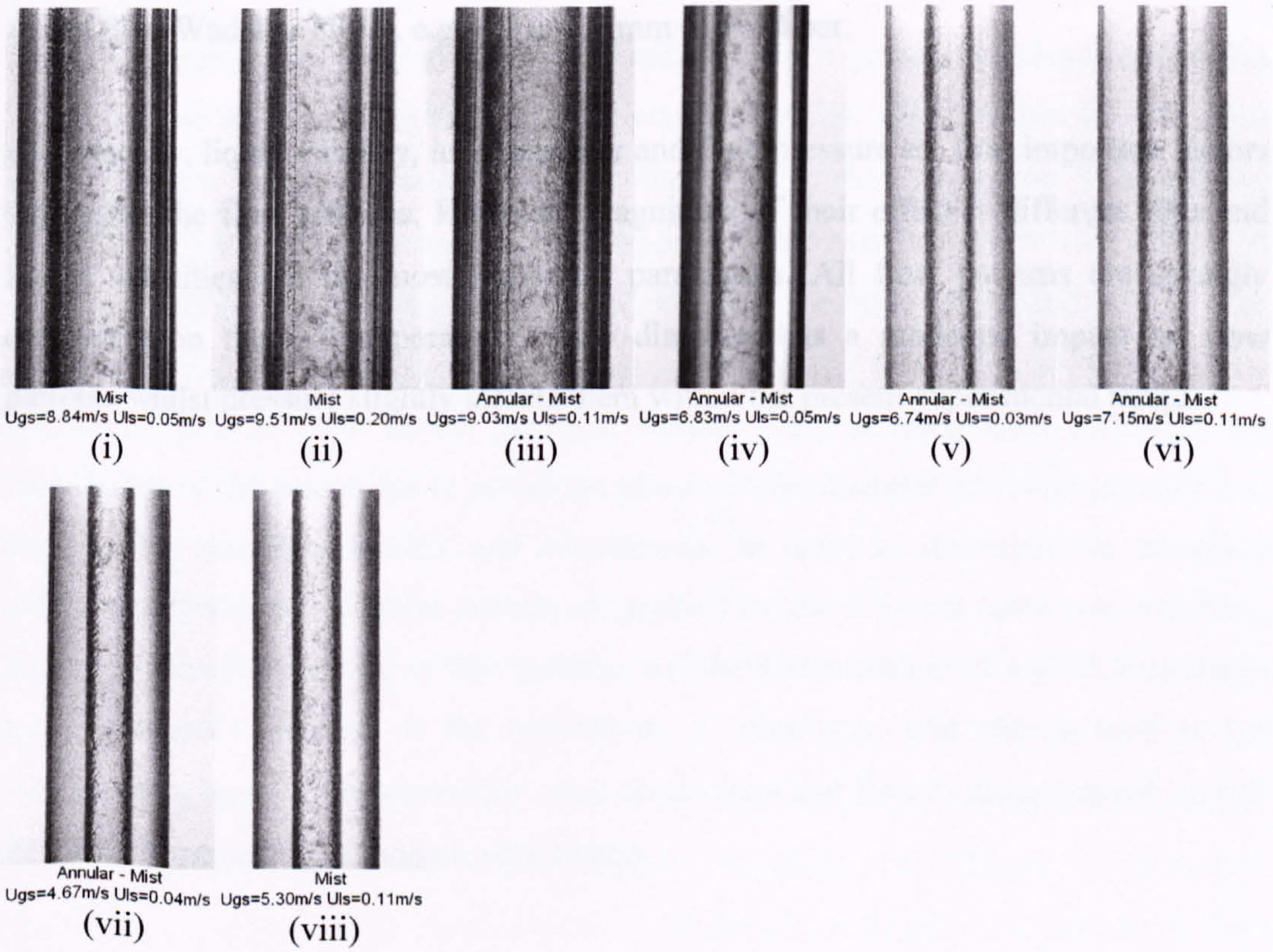

Figure 5.35 Annular –mist and mist flow observed in the present experiments.
(i) - (iii): 4.26 mm tube at 10 bar, (iv): 2.88 mm tube at 10 bar, (v) - (vi): 2.01 mm tube at 10 bar, (vii) - (viii): 2.01 mm tube at 14 bar.

5.1.8 Discussions

The flow patterns in the 2.88 and 4.26 mm tubes do not exhibit common characteristics of the flow patterns in small tubes. Comparatively, the flow patterns in the 2.01 mm tube show some "small tube characteristics", which indicates the increasing action of surface tension and tube confinement, e.g. the appearance of the confined bubble flow, the slimmer vapour slug, the thinner liquid film around the gas slug, and the less chaotic gas-liquid interface in churn flow. When the tube diameter decreases to 1.10 mm, the full small tube characteristics, as also described in the previous studies (Oya 1971, Damianides and Westwater 1988, Fukano and Kariyasaki 1993, Mishima and Hibiki 1996, Triplett et al. 1999, Lin et al. 1998), are exhibited. Therefore, the 2.01 mm tube possesses both characteristics of normal size and small size tube. From this point of view, a tube diameter around 2.0 mm can be regarded as the critical diameter for refrigerant R134a at the current experimental conditions. This result agrees fairly well with the criterion commended by Kew and Cornwell (1997) or Hatori and Bretherton (cited from Wadekar 2002), e.g. 1.2 to 1.7 mm at 6 -14 bar.

Gas velocity, liquid velocity, tube diameter and fluid pressure are four important factors that affect the flow patterns. However, magnitude of their effect is different. Gas and liquid velocities are the most important parameters. All flow patterns are strongly dependent on them. Comparatively tube diameter has a moderate impact on flow patterns whilst pressure slightly affects them within the present experimental range.

5.2 The observed transition boundaries

Five typical transition boundaries were reported in the present experiments. They were dispersed bubble – bubbly, dispersed bubble - churn, bubbly – slug, slug – churn and churn – annular boundaries. The characteristics of the above five transition boundaries are described as follows briefly.

(1) Dispersed bubble – bubbly: a few bubbles reach the critical diameter given in Table 5.3.
(2) Dispersed bubble – churn: numerous dispersed bubbles start to coalesce to large, chaotic gas clumps.
(3) Bubbly – slug: a few bubbles reach the size of the tube diameter.
(4) Slug – churn: the transition occurs when some slug bubbles distort.
(5) Churn – annular: liquid bridge is penetrated to become continual gas core.

Overall the transition at the above five boundaries was a gradual development process in which case the transition boundary became a transition zone. Within the transition zones the flow patterns possess characteristics of more than one of the flow patterns described in the previous section. For example, the flow pattern near the intersection of dispersed bubble, slug and churn can be considered as a mixture of the above three flow patterns. In the current study the transition zones are still simplified as the transition boundaries just as done in the previous studies. Such simplification facilitates the comparison of the flow maps to reveal the effect of tube diameter and fluid pressure and develop the transition models and correlations. In order to represent the transition processes objectively, uniform criteria are applied for the different tubes and pressures. However, the identification of flow patterns and the determination of regime boundaries are significantly affected by the subjectivity of observers. The criteria used in the current study may be questioned by other researchers and lead to disagreement. It was therefore important to state them very clearly.

As discussed in Chapter 3 Section 3.2.3, more experimental data were collected near the transition zones in an attempt to obtain the accurate transition boundaries. However, it is difficult to control u_{gs} at low u_{gs} for the smaller tubes because of the resolution of the heating variac. In addition, extremely dense data near transition boundaries cannot improve the experimental accuracy because of the effect of the following factors: (a) subjectivity in the identification and classification of flow regimes, (b) experiment stability, (c) measurement uncertainty. Therefore, the resolution of u_{ls} at the boundary of dispersed bubble to bubbly, i.e. u_{ls}=0.72, 0.92, 1.17, 1.49, 1.90 m/s as shown in Table 3.3, is 0.2, 0.25, 0.32, 0.41 m/s respectively. The resolution of u_{gs} at the boundary of slug to churn, i.e. u_{gs}=0.3-1.5 m/s, was about 0.05-0.2 m/s at all the experimental conditions. The resolution of u_{gs} at the boundary of churn to annular, i.e. u_{gs}=0.8-3.5 m/s, was about 0.1-0.3 m/s in most experiments. The above-mentioned transition boundaries and the corresponding resolutions are presented in the flow maps in Figures 5.62-5.73 and the experimental data file in the CD attached. Although the shift tendency of the transition boundaries may not be so explicit for the similar size tubes or pressures at the above resolutions, their effect on the flow patterns gradually emerged and recognized as the difference of tube diameter or fluid pressure increases. For example, Table 5.1 summarizes the effect of tube diameter on the flow patterns near the slug-churn boundary at 10 bar pressure by verifying the recorded movies frame by frame.

Table 5.1 The effect of tube diameter on the slug-churn boundary at 10 bar pressure.

Flow state	pure slug	transition zone			pure churn
Number of distorted slug bubbles (distortion degree)	none	few (slight)	some (middle)	most (serious)	all
u_{ls} (m/s)	0.11				
u_{gs} (m/s) for the 1.10 mm tube	0.56		0.69 *	0.78	0.92
u_{gs} (m/s) for the 2.01 mm tube	0.43		0.59 *	0.70	0.95
u_{gs} (m/s) for the 2.88 mm tube	0.39	0.50	0.59 *	0.67	0.76
u_{gs} (m/s) for the 4.26 mm tube	0.25	0.38	0.52 *	0.63	0.74

Note: the data marked with asterisk in the above table are identified as the slug-churn boundary in the current study.

The middle of the transition zone, i.e. when some (about 50%) slug bubbles distort, is plotted out as the slug-churn boundary in the current study. It is difficult to give a solid conclusion on the effect of tube diameter on the transition boundary based on the data for the 2.01 and 2.88 mm tubes only. However, the effect of tube diameter on the slug-churn boundary is still significant in the present experiments because the boundary shifts about 0.17 m/s u_{gs} (u_{ls} = 0.11 m/s) whilst the corresponding resolution is 0.08 – 0.14 m/s when the tube diameter changes from 1.10 to 4.26 mm. In addition, the distorted bubbles were observed in the 2.88 mm tube when $u_{gs} \geq 0.50$ m/s whilst all bubbles still had smooth gas-liquid interface in the 1.10 mm tube when u_{gs}=0.56 m/s, which indicates that the effect of tube diameter on the slug-churn boundary can be confidently concluded at the current experimental range and data density. The same conclusion can be given for the effect of fluid pressure on the slug-churn boundary, see Table 5.2. The effect of tube diameter and fluid pressure on other transition boundaries can be concluded in the similar method.

Table 5.2 The effect of pressure on the slug-churn boundary in the 2.01 mm tube.

Flow state	pure slug	transition zone			pure churn
Number of distorted slug bubbles (distortion degree)	none	few (slight)	some (middle)	most (serious)	all
u_{ls} (m/s)	0.11				
u_{gs} (m/s) for the 6 bar	0.70		0.88 *	1.06	1.26
u_{gs} (m/s) for the 10 bar	0.43		0.59 *	0.70	0.95
u_{gs} (m/s) for the 14 bar	0.35	0.42		0.47 *	0.63

Note: the data marked with asterisk in the above table are identified as the slug-churn boundary in the current study.

If a transition zone is represented by a transition boundary, the uncertainty in the determination of this transition boundary needs to be evaluated so that the data from the present experiments can be used by other researchers credibly. The transition zone of churn to annular flow occupies a narrow range of u_{gs} because the annular flow was identified once continued gas core was verified in all the frames of the movie. The non-annular regime at the highest u_{gs} was regarded as the churn-annular boundary. Therefore, the transition zone, or the uncertainty of the churn-annular boundary, is between the transition boundary and the annular flow at the lowest u_{gs}. However, other transition zones such as slug to churn flow may span a wider u_{gs} region because the transitions are gradual processes. As a result, the uncertainty of these transition boundaries is large accordingly. For example, the transition zone of slug to churn flow in the 2.01 mm tube at 10 bars is between 0.43 to 0.95 m/s u_{gs} when u_{ls} is constant 0.11 m/s, i.e. pure slug to pure churn flow as shown in Table 5.1. If the flow regime at u_{gs}= 0.59 m/s is identified as the slug-churn boundary when some (about 50%) slug bubbles distorted, the uncertainty of u_{gs} on the slug-churn boundary (2.01 mm, 10 bar, 0.11 m/s u_{ls}) is 0.16 m/s (0.43 to 0.59 m/s) and 0.36 m/s (0.59 to 0.95 m/s) for the upstream and downstream of the boundary respectively. The upper and lower bounds for other transition zones is described as following:

Dispersed bubble-bubbly transition zone: the upper bound is that most bubbles are smaller than the critical diameter given in Table 5.3 and the lower bound is that most bubbles are bigger than the critical diameter.

Bubbly-slug transition zone: the upper bound is that most bubbles are longer than the tube diameter and the lower bound is that most bubbles are smaller than the tube diameter.

Dispersed bubble-churn transition zone: the upper bound is that most bubbles coalesce into large gas clumps and the lower bound is that few bubbles are bigger than the critical diameter given in Table 5.3.

Figure 5.36 presents the transition zones in the flow map for the 2.01 mm tube at 10 bar. The uncertainty of the transition boundaries can be deduced. The bubbly-slug transition zone apparently covers wide range in the flow map because the transition occurs at low u_{gs} whilst the flow maps are sketched in logarithmic coordinate group. In fact, the bubbly-slug transition zone crosses three data points at the current data resolution. Similarly dispersed bubble-bubbly, dispersed bubble-churn and slug-churn transition zones span three data points in most cases and churn-annular transition zone is between two data points. Figure 5.36 shows that the transition zone of slug to churn flow at u_{ls}=0.11 m/s is apparently wider than others. With a close observation, most of the slug bubbles at the data point of u_{ls}=0.11 m/s and u_{gs}=0.70 m/s distorted badly. Therefore, although the flow pattern at u_{ls}=0.11 m/s and u_{gs}=0.70 m/s is reported as a middle point in the slug-churn transition zone, it can be expected that "pure churn" will be obtained when the u_{gs} is slightly higher than 0.70 m/s at u_{ls}=0.11 m/s.

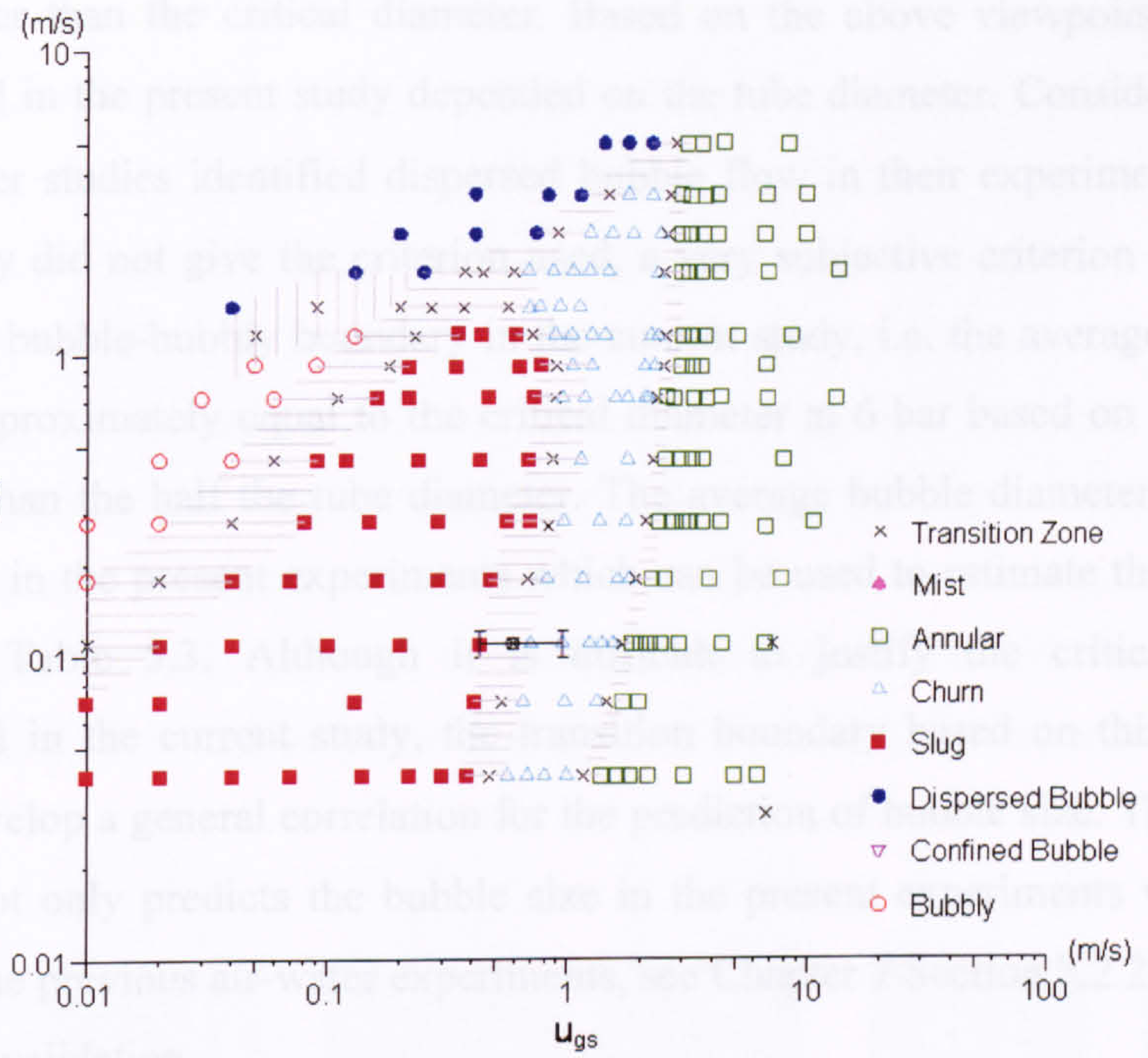

Figure 5.36 The flow map in the 2.01 mm diameter tube at 6 bar pressure with the transition zones (in shadow).

5.2.1 Dispersed bubble – bubbly transition boundary

The dispersed bubble and bubbly flow regimes have been widely recognized in earlier studies, see Barnea et al. (1985), Damianides and Westwater (1988), and Zhao and Bi (2001). The obvious difference between dispersed bubble and bubbly flow is that the bubble size in dispersed bubble flow is much smaller than that in bubbly flow. However, the critical size, used to distinguish the above two flows, was not clearly illuminated in the earlier studies. In fact, the critical size cannot be a definite value. Otherwise it may lead to a conflicting result when pipe size is smaller than the critical size. For example, the recommended critical bubble size by "Unified Model" (Taitel 1990) is:

$$d_c = 2\left[\frac{0.4\sigma}{(\rho_l - \rho_g)g}\right]^{1/2} \tag{5.2}$$

Therefore, the calculated critical diameter is 3.4 mm for air-water flow at 25 ºC and 1 bar. If a tube diameter were 2.0 mm whilst the equivalent diameter of bubbles were 2.5 mm, this practical slug flow could be identified as dispersed bubble flow since the slug size is smaller than the critical diameter. Based on the above viewpoint, the critical diameter used in the present study depended on the tube diameter. Considering the fact that the earlier studies identified dispersed bubble flow in their experiments for small tubes but they did not give the criterion used, a very subjective criterion was used for the dispersed bubble-bubbly boundary in the current study, i.e. the average diameter of bubbles is approximately equal to the critical diameter at 6 bar based on Equation 5.2 and smaller than the half the tube diameter. The average bubble diameter and number are estimated in the present experiments which can be used to estimate the actual void faction, see Table 5.3. Although it is difficult to justify the critical diameters recommended in the current study, the transition boundary based on this criterion is helpful to develop a general correlation for the prediction of bubble size. The developed correlation not only predicts the bubble size in the present experiments well but also agrees with the previous air-water experiments, see Chapter 7 Section 7.2.2. However, it needs further validation.

Table 5.3 The critical bubble diameter used in the present study for the dispersed bubble – bubbly boundary.

Parameters		R-134a		
Fluid pressure (bar)		6.0	10.0	14.0
Critical diameter based on Equation 5.2 (mm)		1.07	0.53	0.43
1.10 mm tube	The average diameter (mm)	0.4 ~ 0.5		
	The critical diameter (mm)	0.46	0.43	0.45
2.01 mm tube	The average diameter (mm)	0.9 ~ 1.1		
	The critical diameter (mm)	0.95	1.00	0.92
2.88 mm tube	The average diameter (mm)	0.8 ~ 1.1		
	The critical diameter (mm)	0.87	0.98	1.03
4.26 mm tube	The average diameter (mm)	0.8 ~ 1.2		
	The critical diameter (mm)	1.05	1.10	1.18

In air-water two-phase flow, the void fraction at the boundaries of dispersed bubble – bubbly flow can be calculated approximately based on the following equation:

$$\alpha = \frac{u_{gs}}{u_{gs} + u_{ls}} \tag{5.3}$$

However, the above equation may lead to considerable error in the present experiments. Figures 5.37-5.40 are the results of the transition boundary, dispersed bubble-bubbly, observed at the three pressures and four diameter tubes studied. Normally the observed void fraction was smaller than the calculated void fraction based on Equation 5.3 and difference increases in smaller tube or at lower pressure. As seen in Figure 5.37 (i) and (vi), and Figure 5.40 (ii) and (vi), the number and size of the bubbles at 6 bar are obviously smaller than that at 14 bar though their gas and liquid superficial velocities are similar.

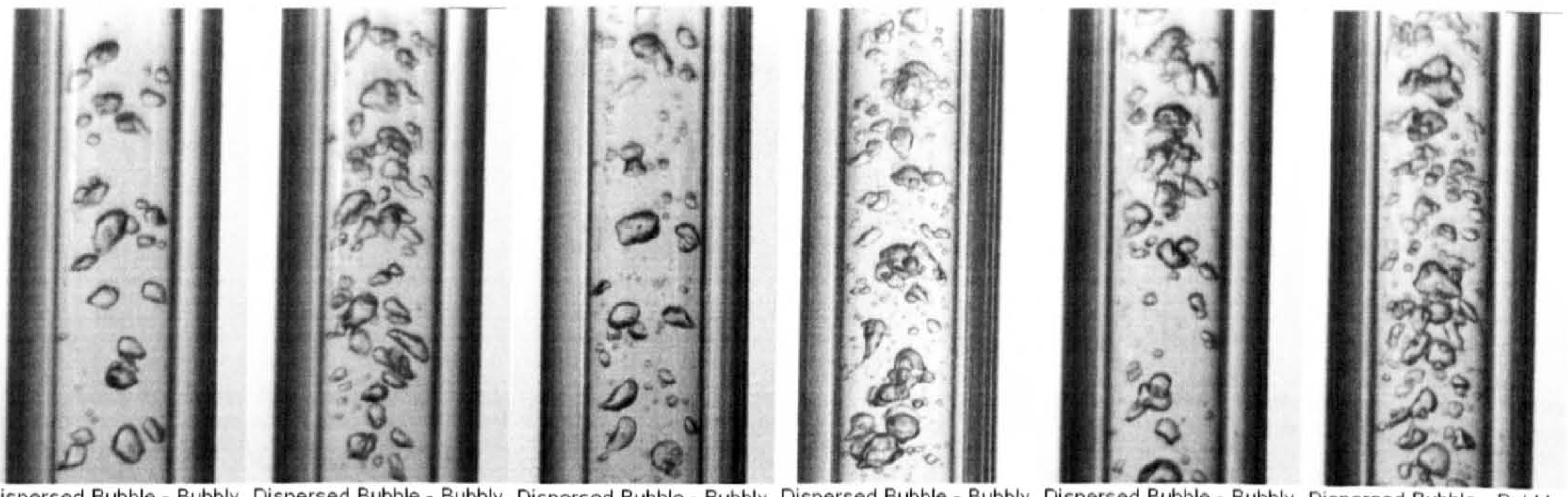

Dispersed Bubble - Bubbly Ugs=0.13m/s Uls=1.18m/s (i)
Dispersed Bubble - Bubbly Ugs=0.24m/s Uls=1.49m/s (ii)
Dispersed Bubble - Bubbly Ugs=0.06m/s Uls=0.92m/s (iii)
Dispersed Bubble - Bubbly Ugs=0.19m/s Uls=1.19m/s (iv)
Dispersed Bubble - Bubbly Ugs=0.08m/s Uls=0.92m/s (v)
Dispersed Bubble - Bubbly Ugs=0.12m/s Uls=1.17m/s (vi)

Figure 5.37 Bubbly – dispersed bubble transition boundary observed in the 4.26 mm tube. (i) and (ii) at 6 bar, (iii) and (iv) at 10 bar, (v) and (vi) at 14 bar.

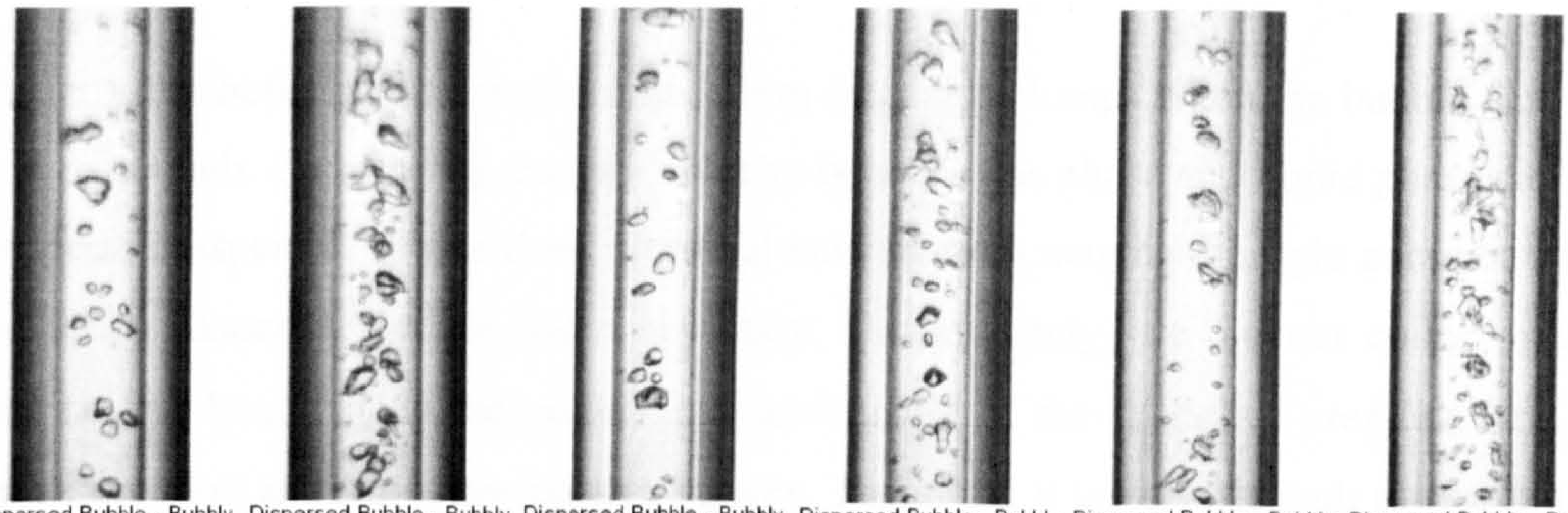

Dispersed Bubble - Bubbly Ugs=0.15m/s Uls=1.17m/s (i)
Dispersed Bubble - Bubbly Ugs=0.35m/s Uls=1.49m/s (ii)
Dispersed Bubble - Bubbly Ugs=0.06m/s Uls=1.19m/s (iii)
Dispersed Bubble - Bubbly Ugs=0.14m/s Uls=1.49m/s (iv)
Dispersed Bubble - Bubbly Ugs=0.03m/s Uls=1.18m/s (v)
Dispersed Bubble - Bubbly Ugs=0.10m/s Uls=1.49m/s (vi)

Figure 5.38 Bubbly – dispersed bubble transition boundary observed in the 2.88 mm tube. (i) and (ii) at 6 bar, (iii) and (iv) at 10 bar, (v) and (vi) at 14 bar.

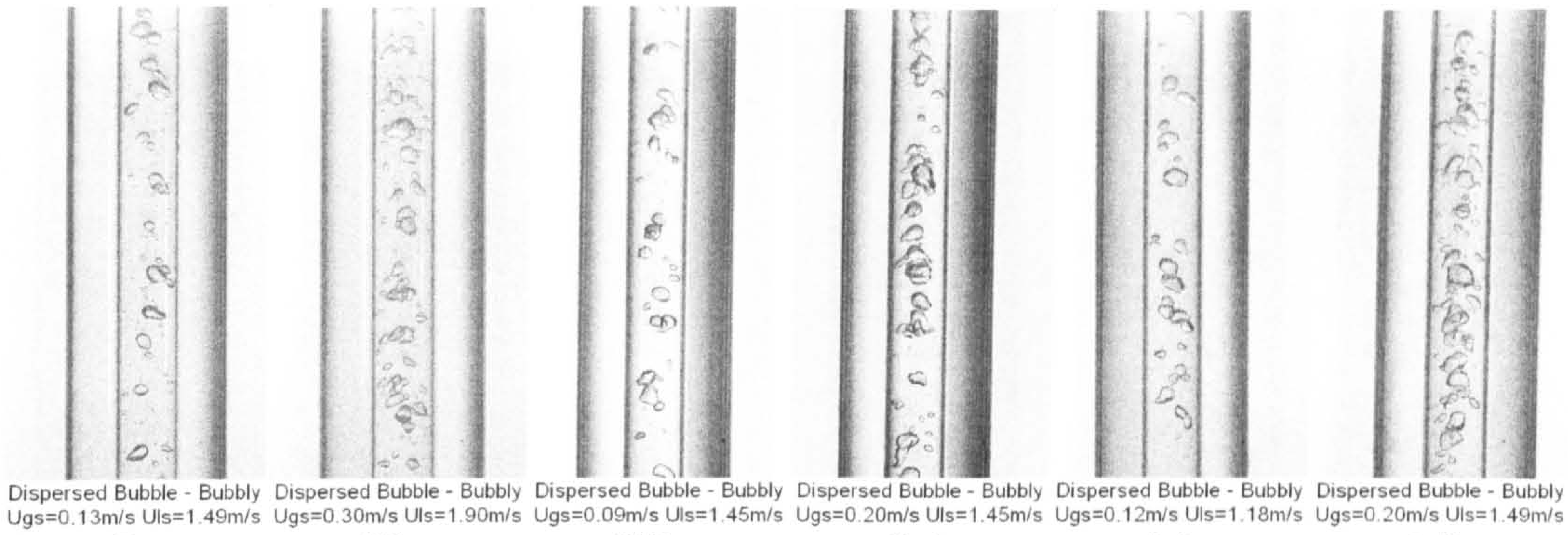

(i) (ii) (iii) (iv) (v) (vi)

Figure 5.39 Bubbly – dispersed bubble transition boundary observed in the 2.01 mm tube. (i) and (ii) at 6 bar, (iii) and (iv) at 10 bar, (v) and (vi) at 14 bar.

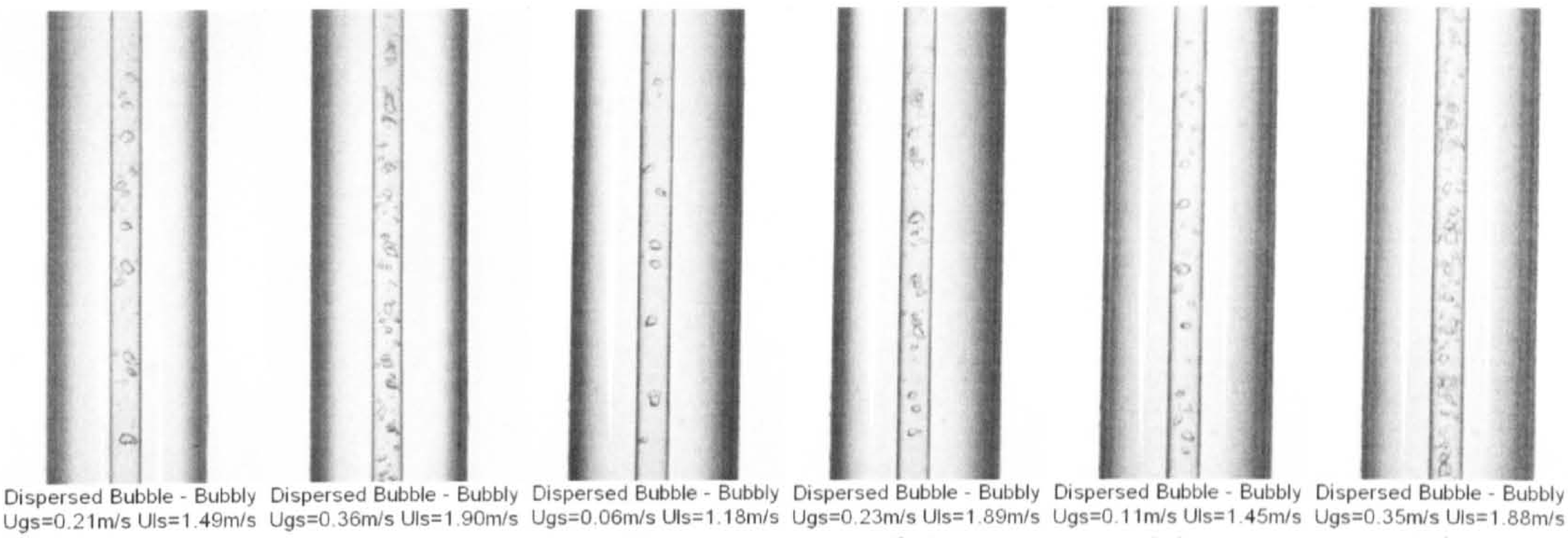

(i) (ii) (iii) (iv) (v) (vi)

Figure 5.40 Bubbly – dispersed bubble transition boundary observed in the 1.10 mm tube. (i) and (ii) at 6 bar, (iii) and (iv) at 10 bar, (v) and (vi) at 14 bar.

5.2.2 Dispersed bubble – churn transition boundary

Dispersed bubbles start to coalesce and form large gas clumps when the bubble density is high enough. Considering the slip velocity between gas phase and liquid phase can be ignored in dispersed bubble flow, a critical void fraction may be the right parameter for predicting dispersed bubble-churn boundary. Unfortunately, we did not collect much data on this boundary in the present project because of the excessive pressure drop in the test section and poor flow pattern images. Therefore, it is very difficult to sketch the accurate dispersed bubble-churn boundary in the current study. Figures 5.41-5.44 show the dispersed bubble – churn transition boundary observed in the current experiments.

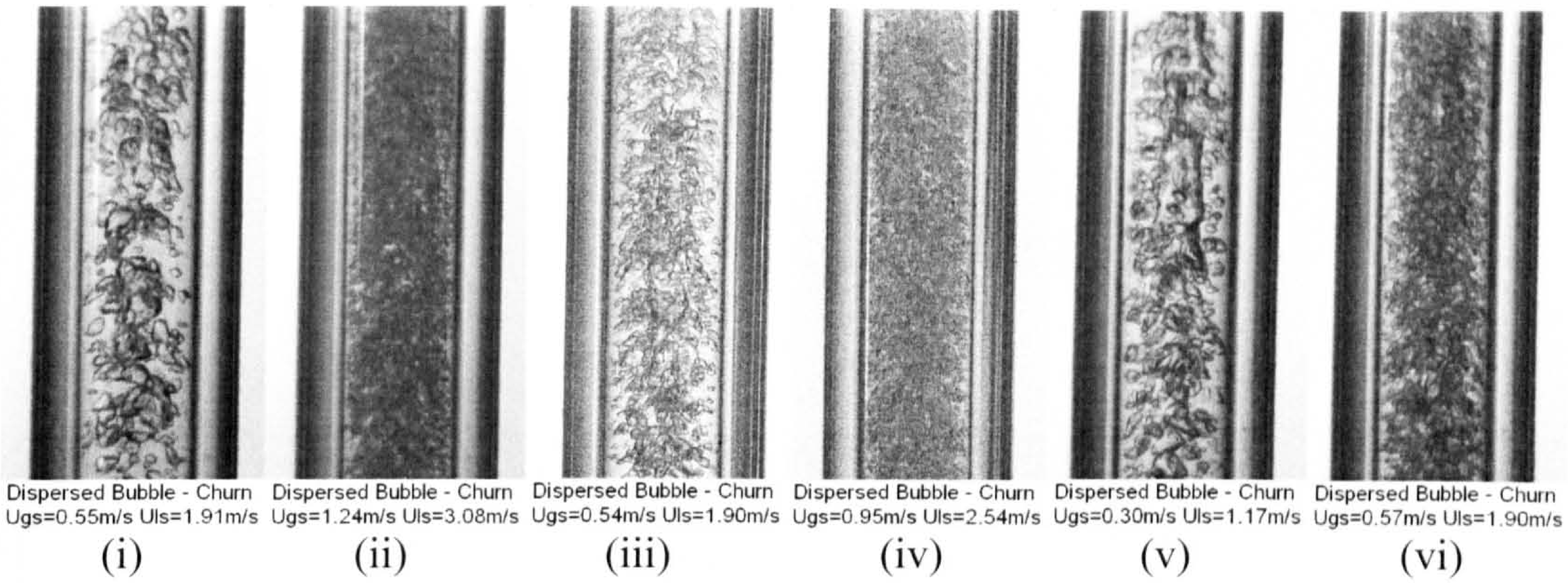

Figure 5.41 Dispersed bubble – churn transition boundary observed in the 4.26 mm tube. (i) and (ii) at 6 bar, (iii) and (iv) at 10 bar, (v) and (vi) at 14 bar.

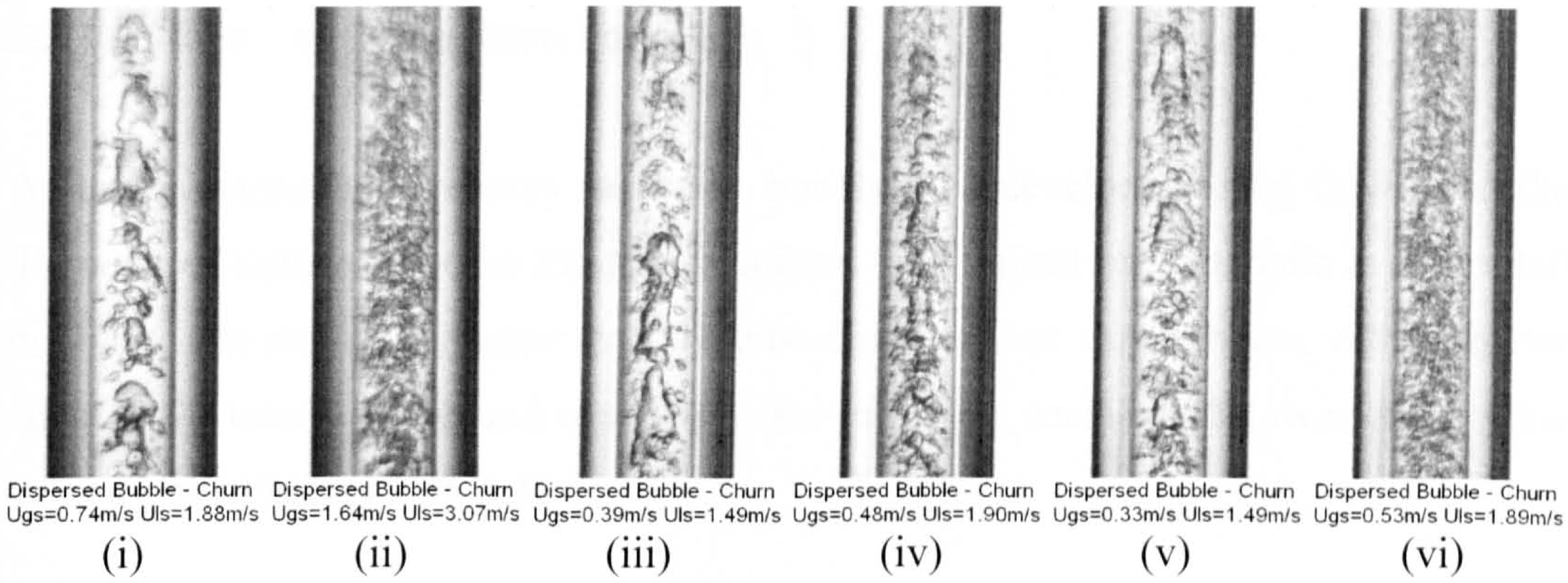

Figure 5.42 Dispersed bubble – churn transition boundary observed in the 2.88 mm tube. (i) and (ii) at 6 bar, (iii) and (iv) at 10 bar, (v) and (vi) at 14 bar.

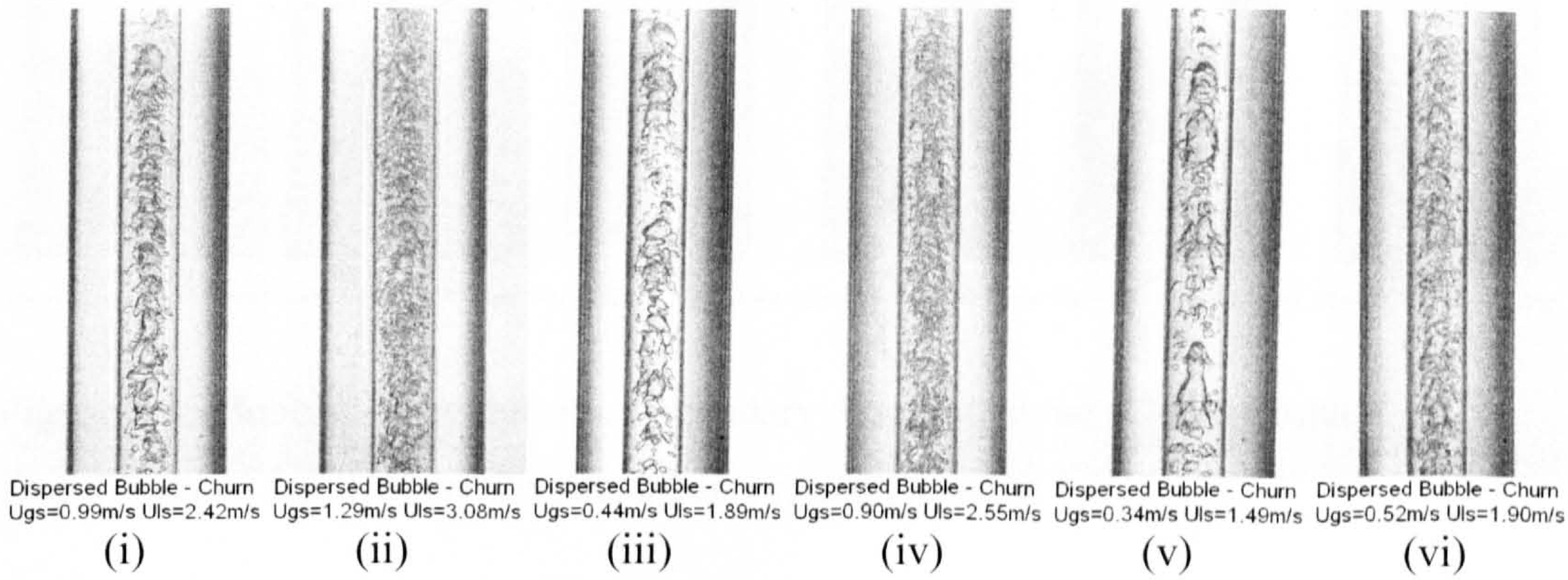

Figure 5.43 Dispersed bubble – churn transition boundary observed in the 2.01 mm tube. (i) and (ii) at 6 bar, (iii) and (iv) at 10 bar, (v) and (vi) at 14 bar.

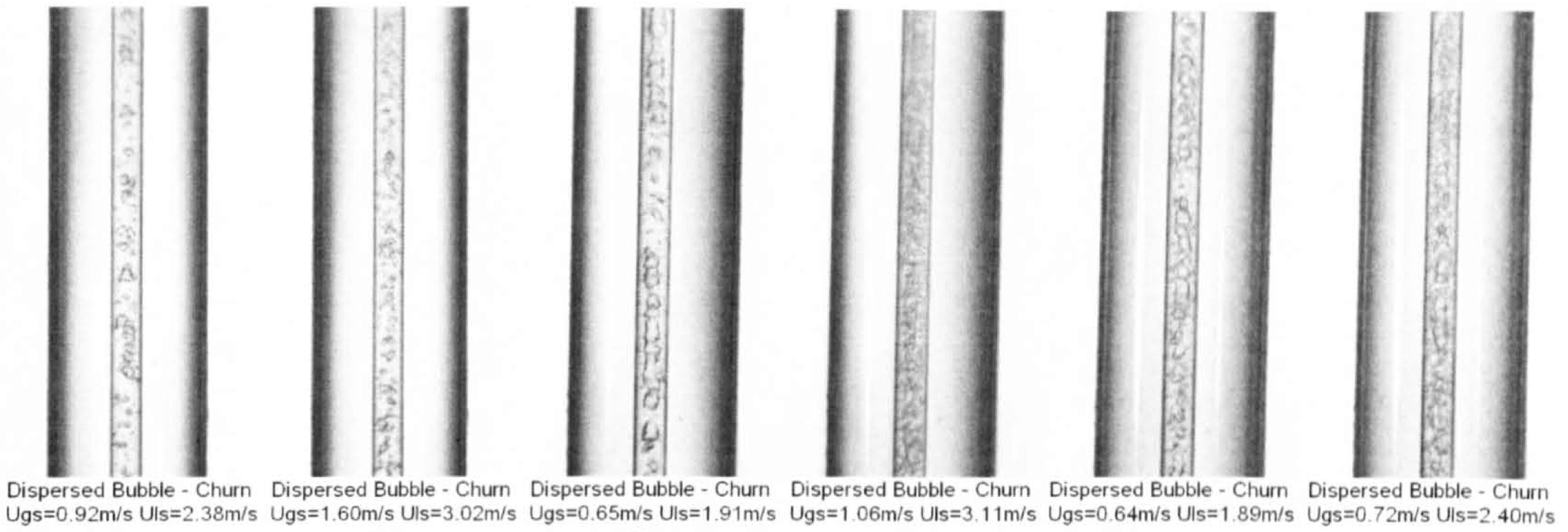

(i) (ii) (iii) (iv) (v) (vi)

Figure 5.44 Dispersed bubble – churn transition boundary observed in the 1.10 mm tube. (i) and (ii) at 6 bar, (iii) and (iv) at 10 bar, (v) and (vi) at 14 bar.

5.2.3 Bubbly – slug transition boundary

As the gas superficial velocity increases, bubbly flow develops to slug flow when the diameter of bubbles reaches the tube diameter. The typical characteristic is that small bubbles, with diameter smaller than the tube diameter, and slug bubbles, with diameter equal to the tube diameter and confined by the tube well, coexist and flow with the same velocity, see Figures 5.45-5.48.

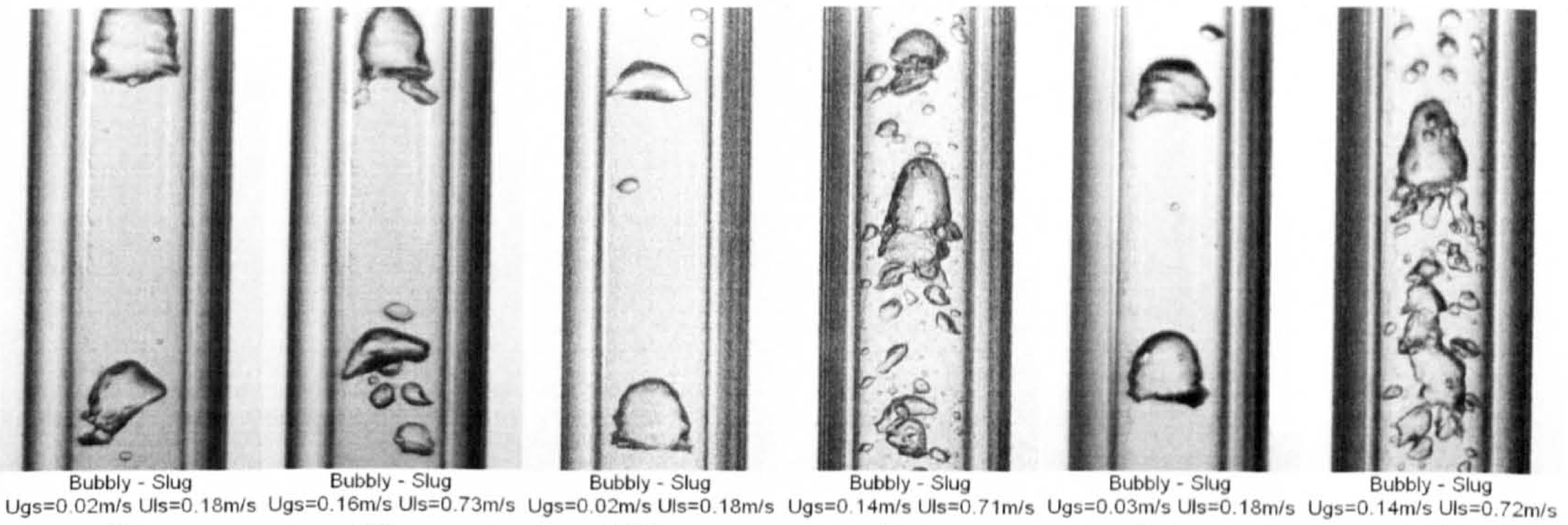

(i) (ii) (iii) (iv) (v) (vi)

Figure 5.45 Bubbly – slug transition boundary observed in the 4.26 mm tube. (i) and (ii) at 6 bar, (iii) and (iv) at 10 bar, (v) and (vi) at 14 bar.

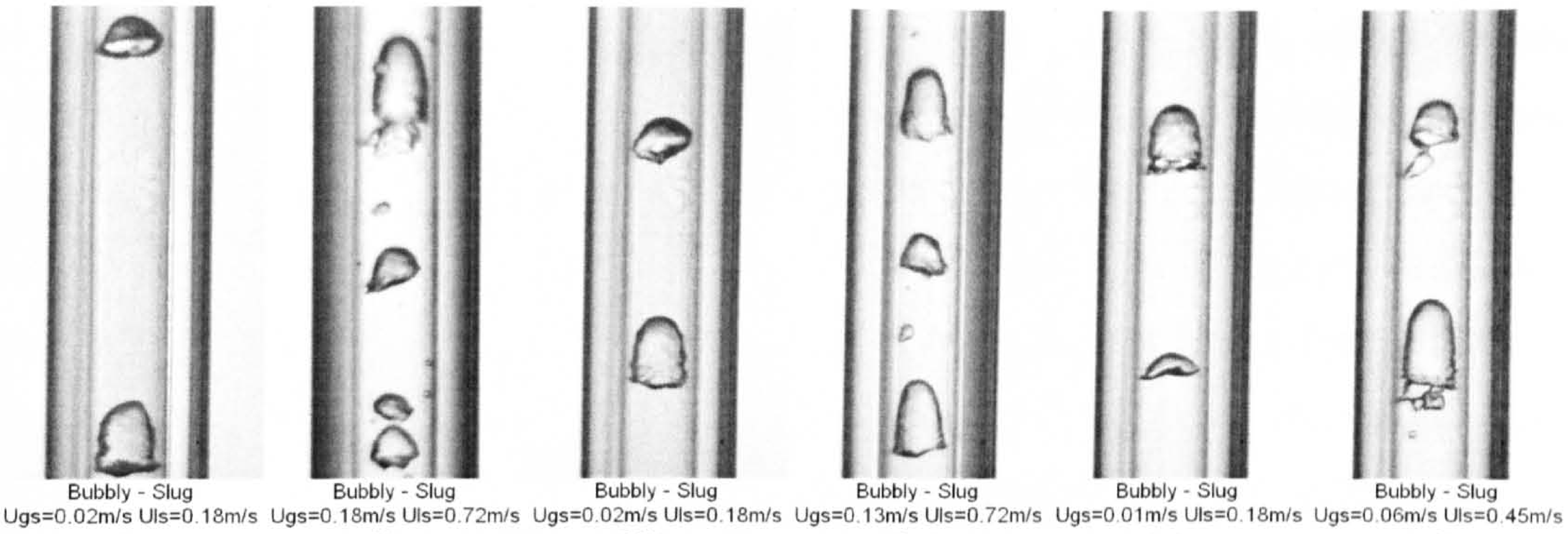

(i) (ii) (iii) (iv) (v) (vi)

Figure 5.46 Bubbly – slug transition boundary observed in the 2.88 mm tube.
(i) and (ii) at 6 bar, (iii) and (iv) at 10 bar, (v) and (vi) at 14 bar.

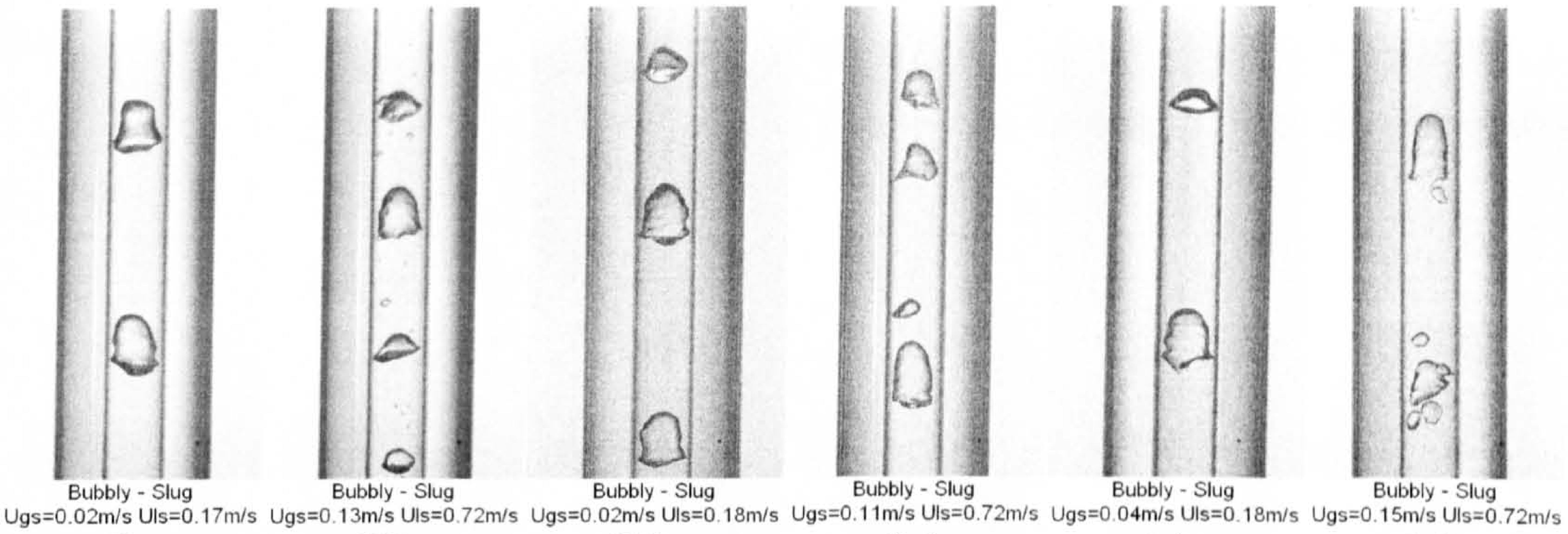

(i) (ii) (iii) (iv) (v) (vi)

Figure 5.47 Bubbly – slug transition boundary observed in the 2.01 mm tube.
(i) and (ii) at 6 bar, (iii) and (iv) at 10 bar, (v) and (vi) at 14 bar.

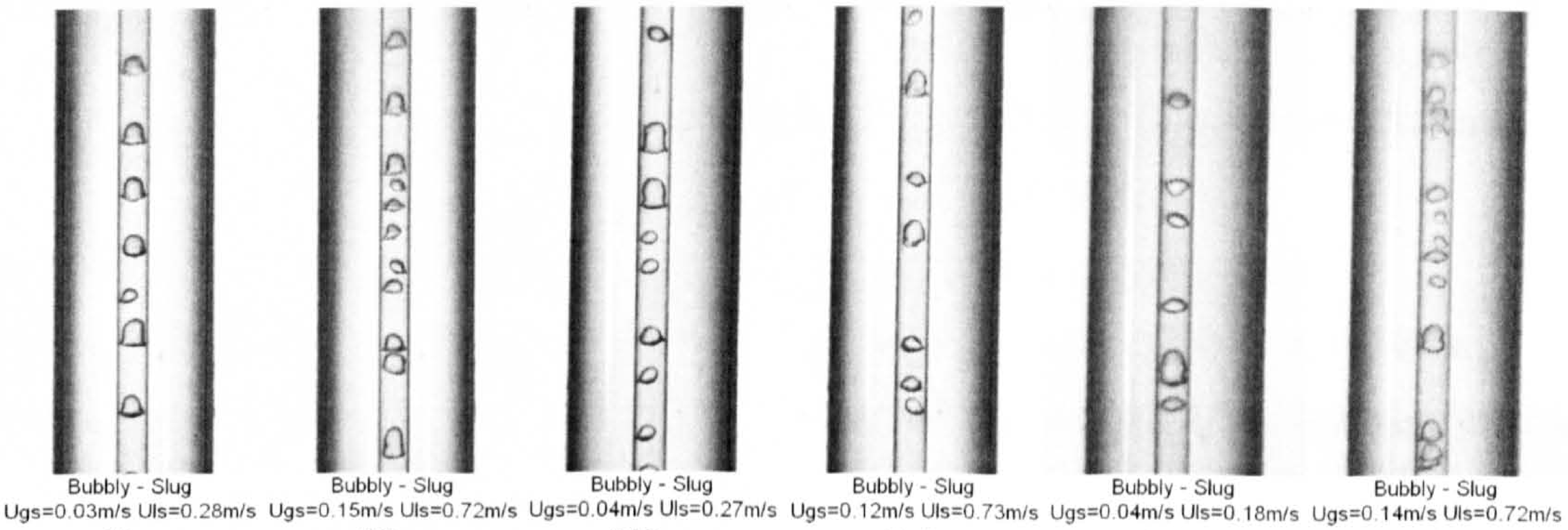

(i) (ii) (iii) (iv) (v) (vi)

Figure 5.48 Bubbly – slug transition boundary observed in the 1.10 mm tube.
(i) and (ii) at 6 bar, (iii) and (iv) at 10 bar, (v) and (vi) at 14 bar.

Unlike other typical flow patterns, bubbly and slug flows are generally affected by the observation position. For example, Barnea and Taitel (1993) reported that the required minimum distance for fully developed air-water two-phase flow was about 10-15 m in the 50 mm tube in their experiments, i.e. 200-300 times tube diameter. Within that distance bubbles and slugs flow at different velocity and coalesce ceaselessly. It can be expected that some bubbly flow, not all, may finally develop to slug flow after a long journey. This may be the reason that some earlier researchers, such as the model of Taitel et al. (1980) do not distinguish bubbly flow and slug flow when the tube diameter is smaller than the critical diameter, see Appendix B. In the present experiments, because of the limitation of the laboratory conditions, the visulaization points are located downstream of the heating sections about 100-170 times tube diameter. Two-phase flow might not reach fully developed state at that point. One indirect evidence of this is that coalescence among bubbles was observed occasionally within the observable section, see the pictures in Figure 5.49.

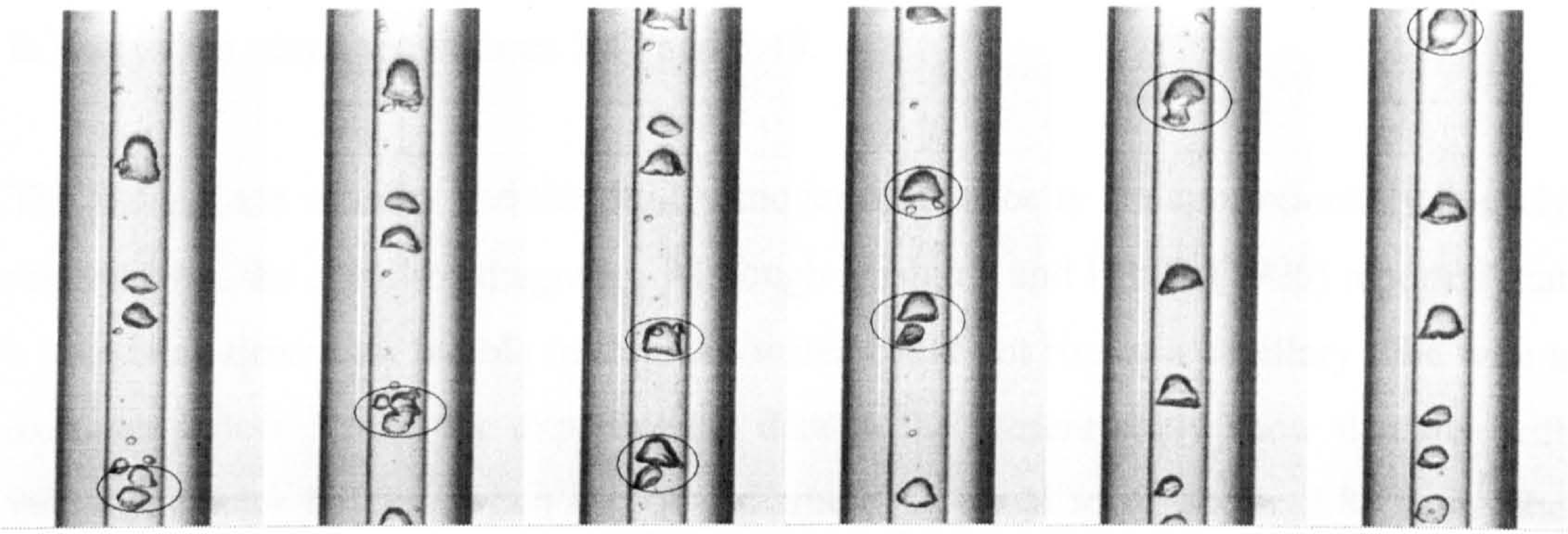
(i) (ii) (iii) (iv) (v) (vi)

Figure 5.49 Bubble coalescence process occurred at bubbly – slug transition boundary (2.01 mm, 10 bar, u_{gs}=0.13m/s, u_{ls}=0.72m/s).

Picture (i): two separate bubbles.	Picture (ii): coalescent starts.
Picture (iii): creation of a new big bubble.	Picture (iv): second group of bubbles.
Picture (v): coalescent starts.	Picture (vi): creation of another new bubble.

On the other hand, Figures 5.50-5.53 show that the coalescence likely finished because the small bubbles and slug bubbles almost flowed at the same velocity, which indicates that the two-phase flow at the observation point has reached or approached fully developed state under the present experimental conditions. Another interesting phenomenon as shown in Figures 5.50 and 5.51 is that the bubble rise velocity is higher at the higher pressures in the 2.88 and 4.26 mm tubes. In the smaller tubes, i.e. the 1.10 or 2.01 mm tubes, the rise velocity is less affected by the fluid pressure, see Figures 5.52 and 5.53. With a close observation it can be found that the bubbles at the tube centerline flow faster than those near the tube wall. Following Bankoff's development (cited from Chisholm, 1983), two-phase fluid will flow at maximum velocity along the pipe centerline and the velocity profile across the pipe section can be described by Equation 5.4 with the assumption that both phases have the same local velocity.

$$\frac{u}{u_{\max}} = \left(\frac{y}{R}\right)^{1/m} \tag{5.4}$$

The diameter of slugs is slightly smaller at the higher pressure in the 4.26 and 2.88 mm tubes because of the weaker surface tension, see Figures 5.45 and 5.46. The average velocity, according to the equation 5.4, should be slightly higher than the bigger slug bubblers at the lower pressure. However, the slug bubbles at the different pressures almost have the same diameter in the 1.10 and 2.01 mm tubes so that their rise velocity is almost the same, see Figures 5.47 and 5.48.

The bubble rise velocity and the fluid homogeneous velocity are approximately linearly related from the sketched diagrams. Although Mishima and Hibiki (1996) reported that a buoyancy-driven air bubble in stagnant water could not rise in a capillary tube with a diameter below 5 mm, the experimental data in the present study show that the drift velocity cannot be zero when the tube diameter is equal to or above 2.88 mm. The difference of fluid properties, especially the difference of viscosity and surface tension, might cause the discrepancy.

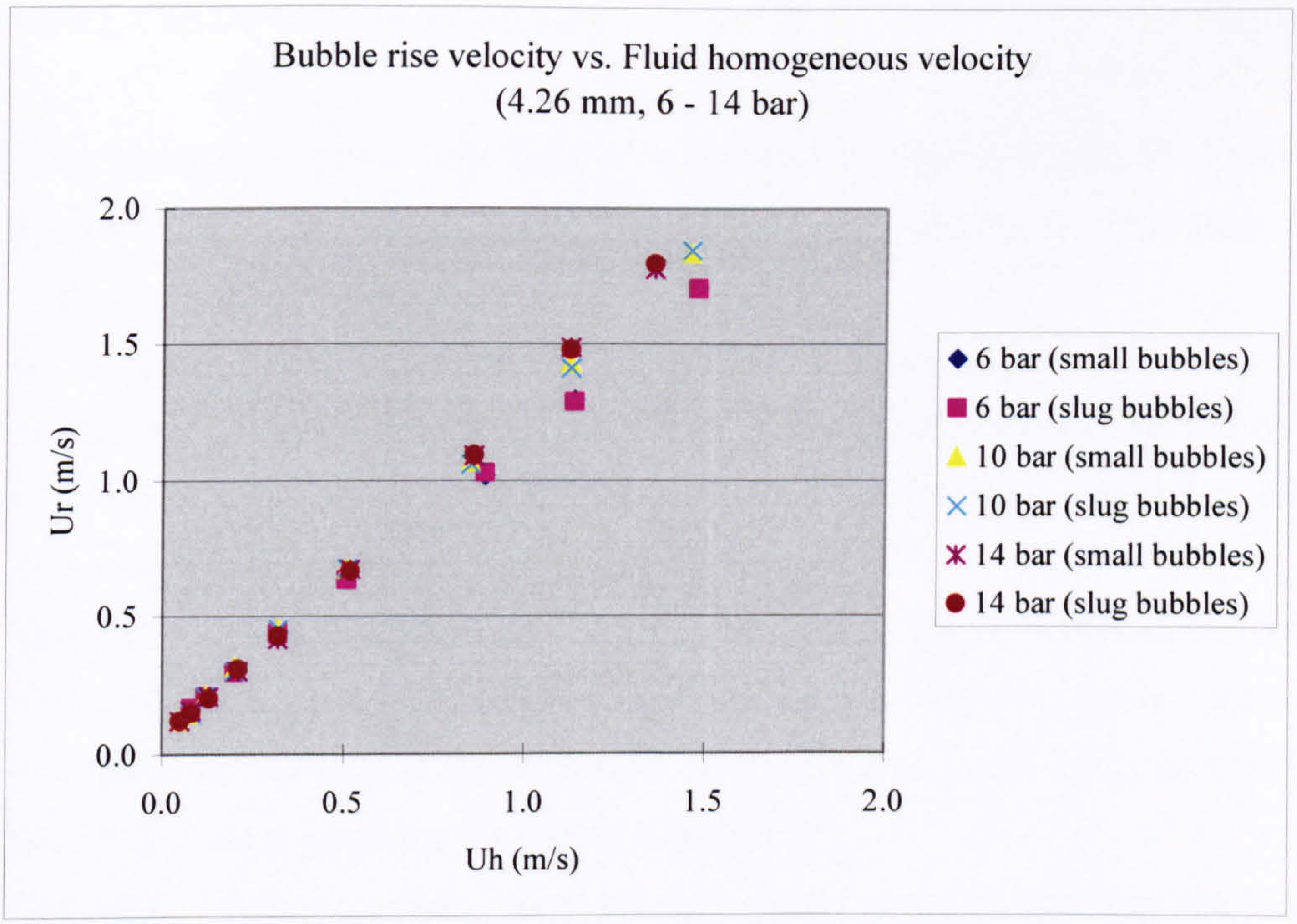

Figure 5.50 The bubble rise velocity and the fluid homogenous velocity in the 4.26 mm tube.

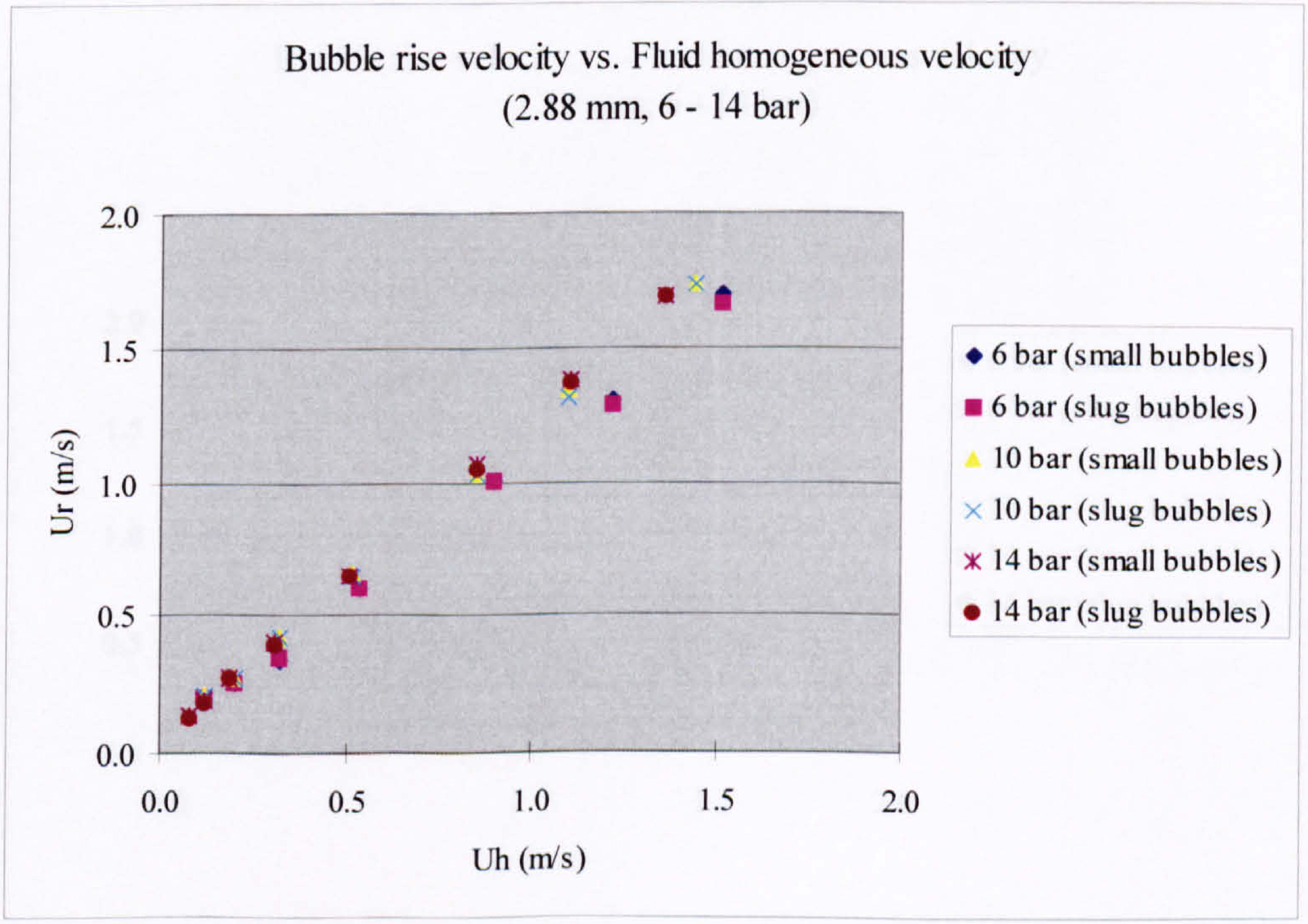

Figure 5.51 The bubble rise velocity and the fluid homogenous velocity in the 2.88 mm tube.

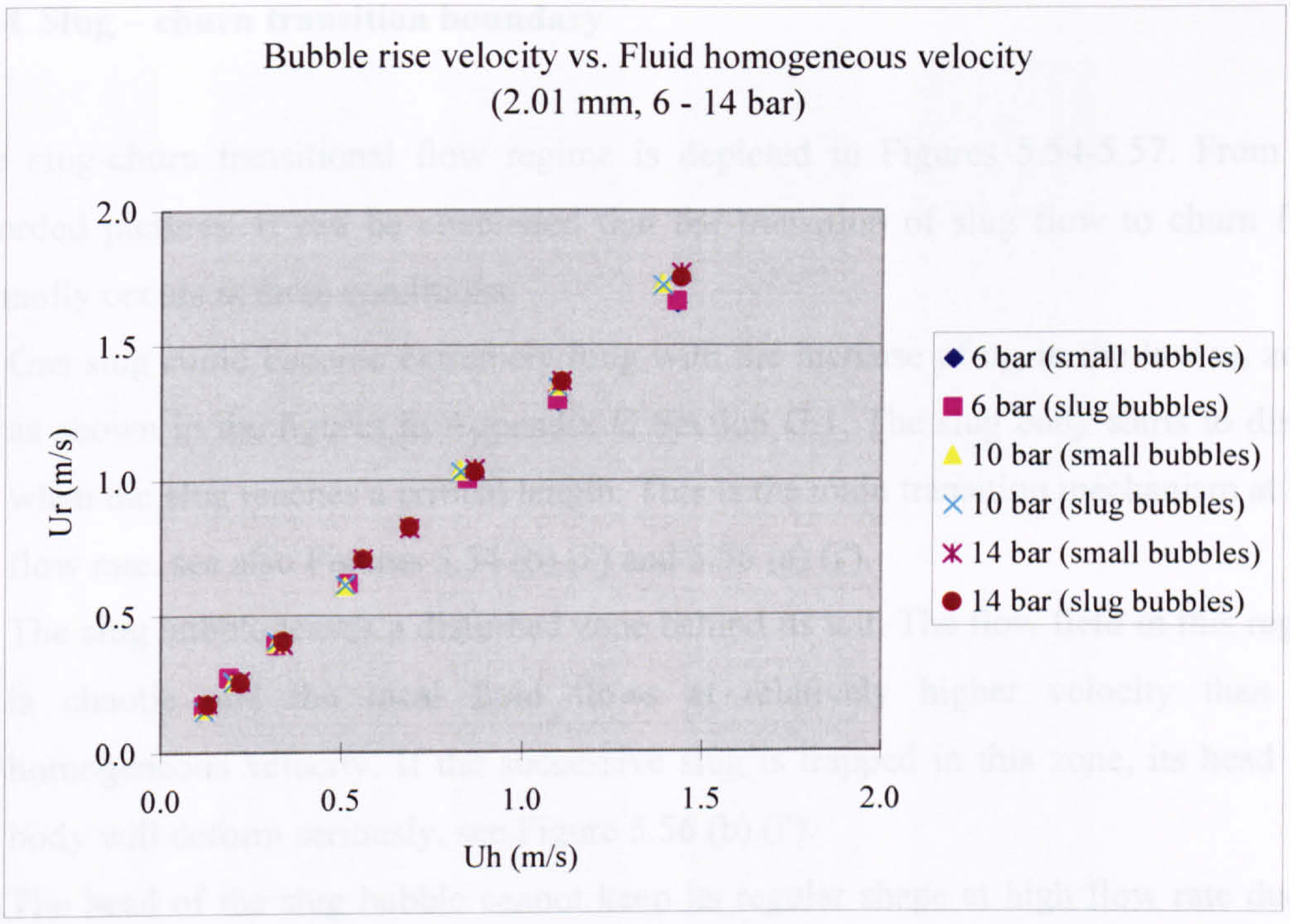

Figure 5.52 The bubble rise velocity and the fluid homogenous velocity in the 2.01 mm tube.

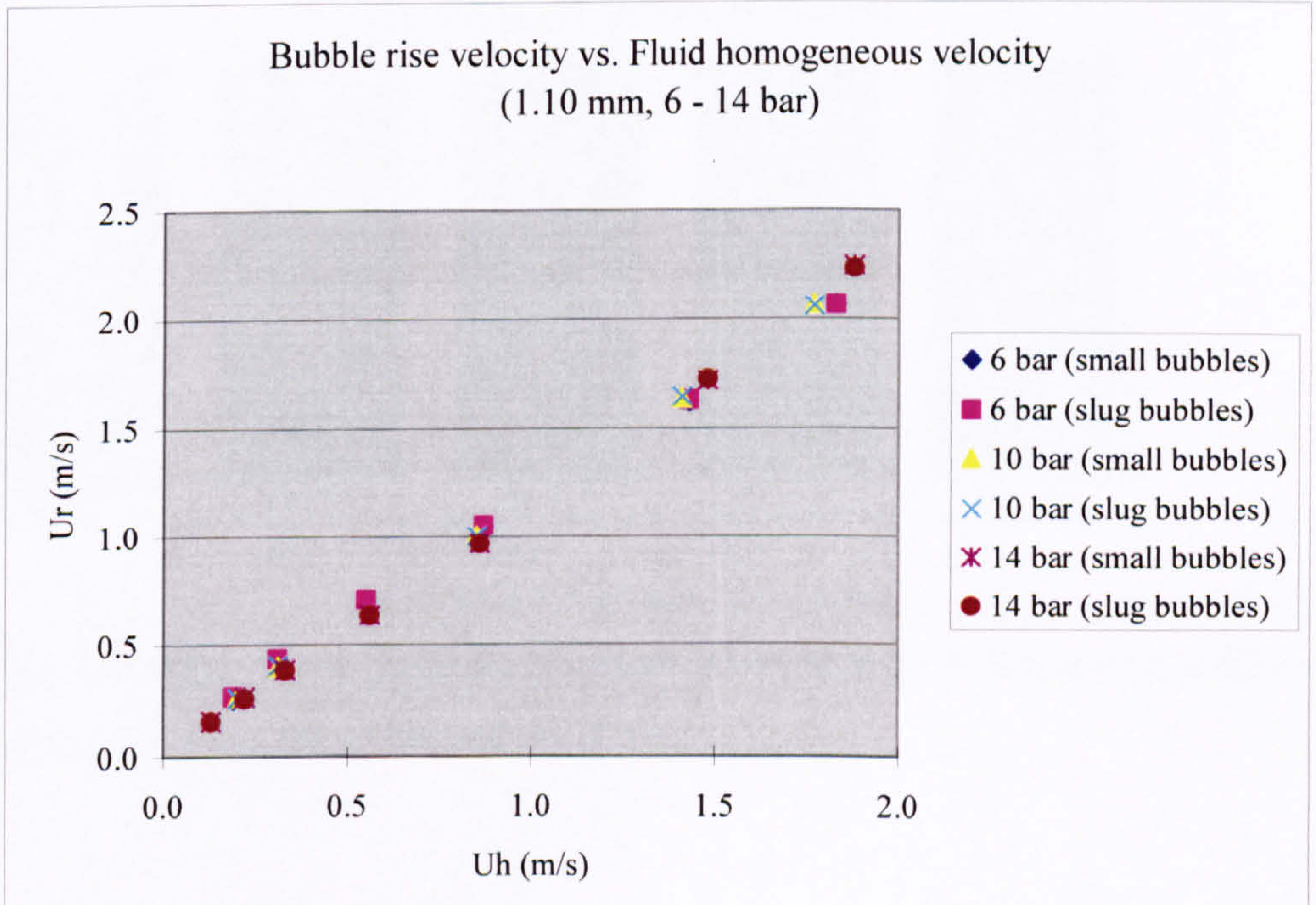

Figure 5.53 The bubble rise velocity and the fluid homogenous velocity in the 1.10 mm tube.

5.2.4 Slug – churn transition boundary

The slug-churn transitional flow regime is depicted in Figures 5.54-5.57. From the recorded pictures, it can be concluded that the transition of slug flow to churn flow normally occurs at three conditions:

(1) Gas slug could become extremely long with the increase of u_{gs} in the low u_{ls} zone, as shown in the figures in Appendix G Section G.1. The slug body starts to distort when the slug reaches a critical length. This is the main transition mechanism at low flow rate, see also Figures 5.54 (b) (i') and 5.56 (a) (i').

(2) The slug bubble leaves a disturbed zone behind its tail. The flow field in this region is chaotic and the local fluid flows at relatively higher velocity than the homogeneous velocity. If the successive slug is trapped in this zone, its head and body will deform seriously, see Figure 5.56 (b) (i').

(3) The head of the slug bubble cannot keep its regular shape at high flow rate due to the great impact force from the surrounding liquid and bubbles. This is the dominant transition mechanism of slug flow to churn flow at high flow rate, see Figures 5.55 (a) (iii), 5.56 (b) (iii) and 5.57 (c) (iii).

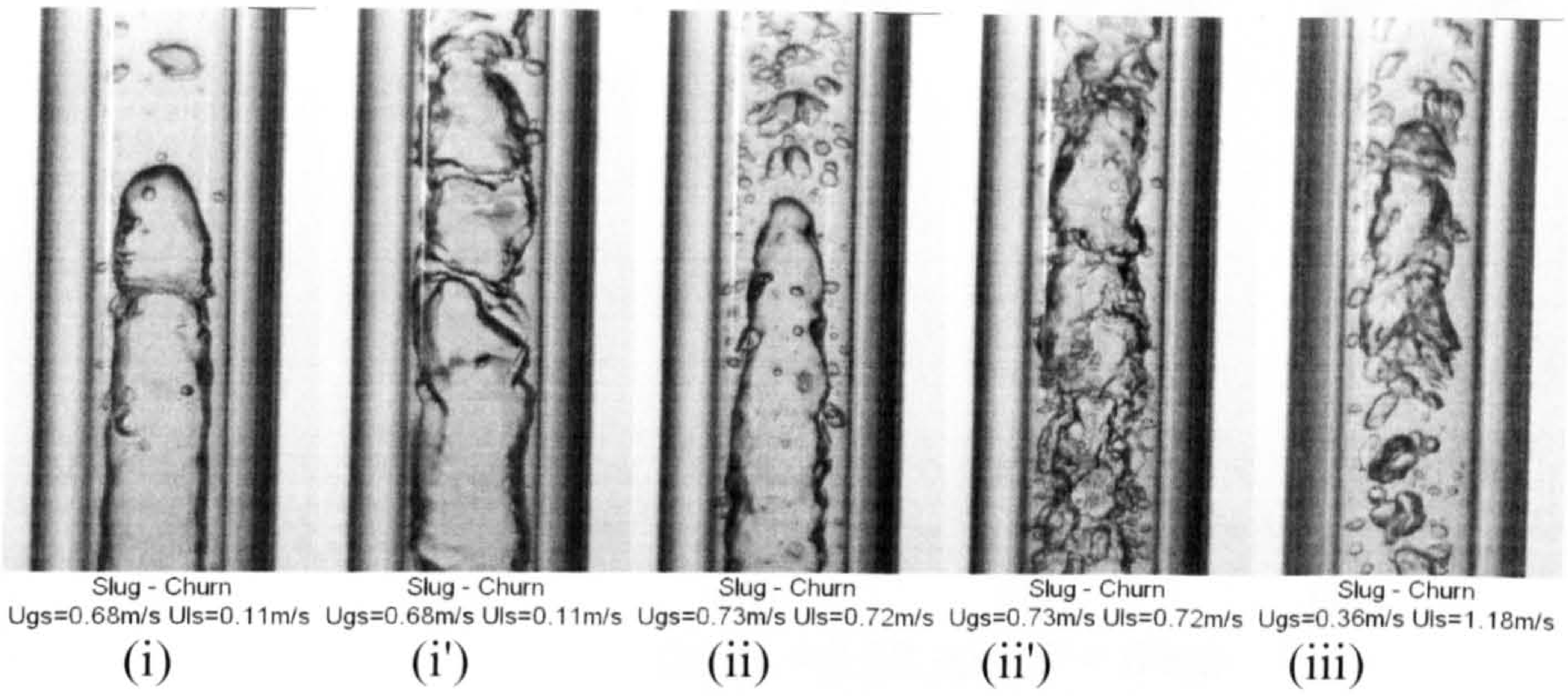

(a) D = 4.26 mm, P = 6 bar

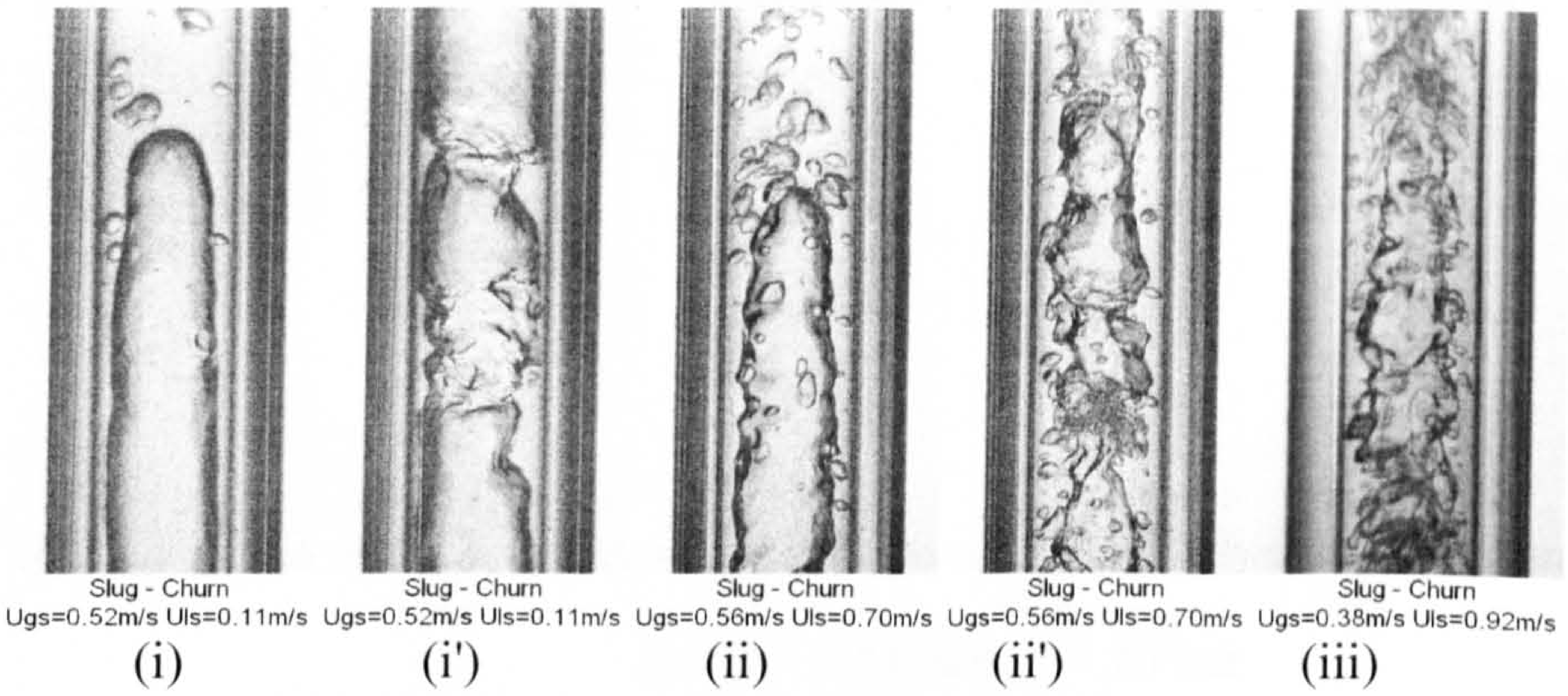

(b) D = 4.26 mm, P = 10 bar

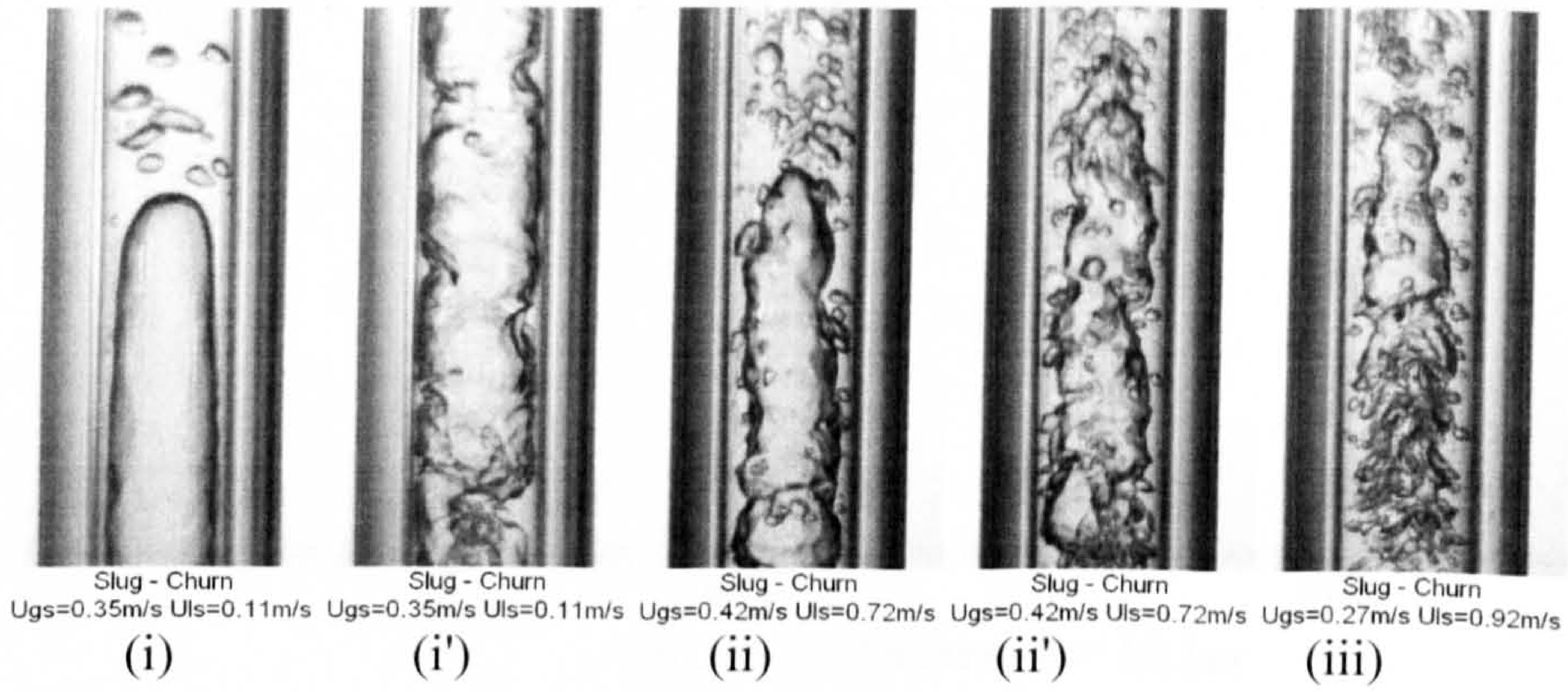

(c) D = 4.26 mm, P = 14 bar

Figure 5.54 Slug – churn transition boundary observed in the 4.26 mm tube at different pressures. (a) 6 bar, (b) 10 bar and (c) 14 bar.

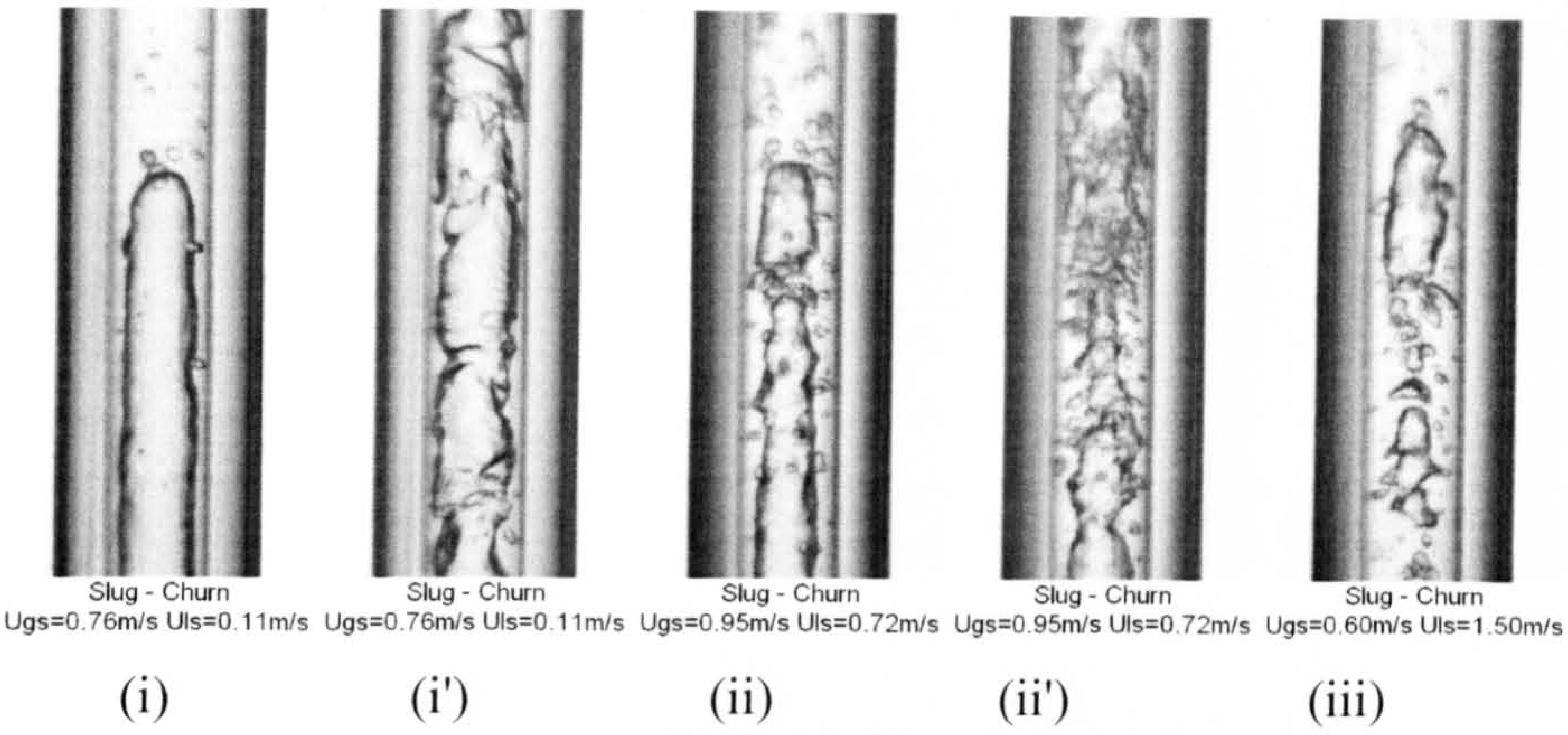

(a) $D = 2.88$ mm, $P = 6$ bar

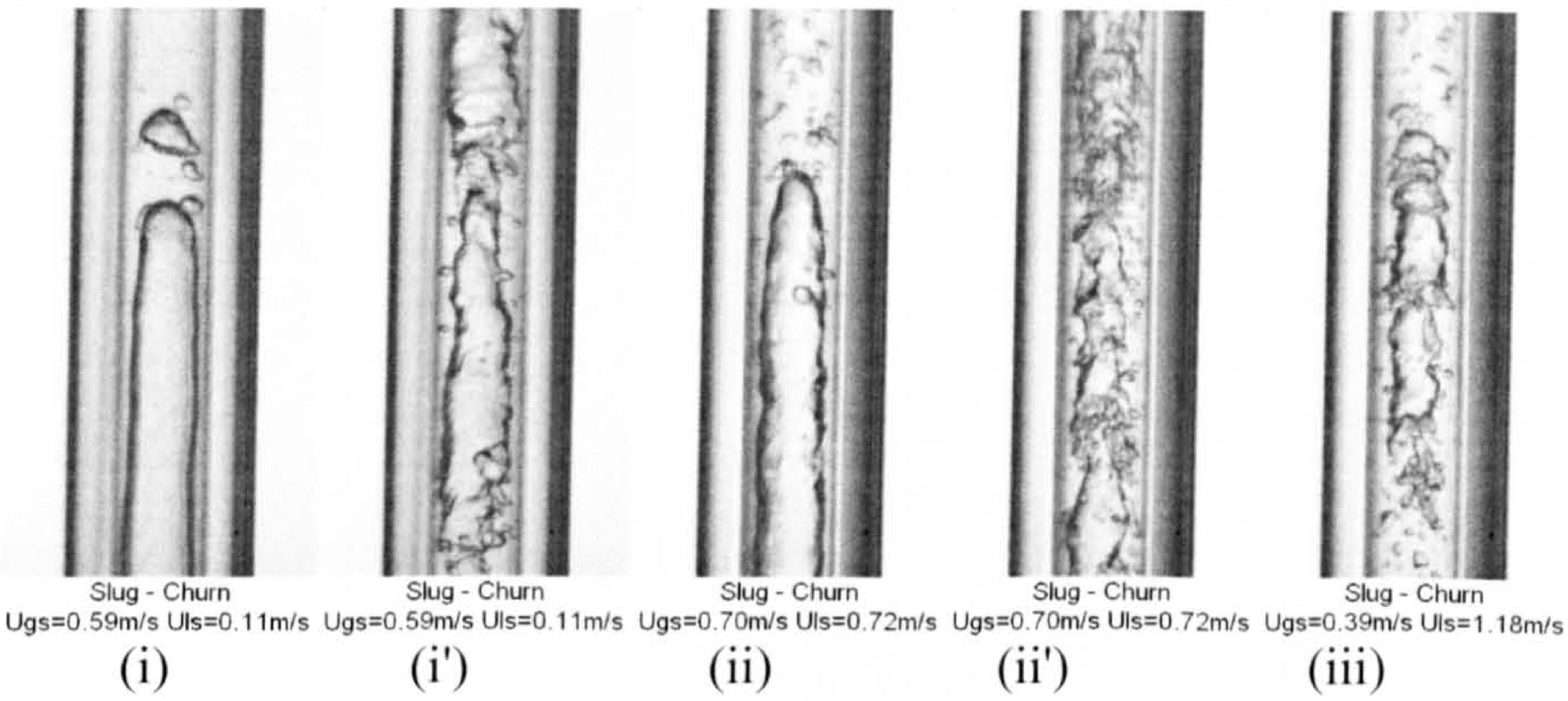

(b) $D = 2.88$ mm, $P = 10$ bar

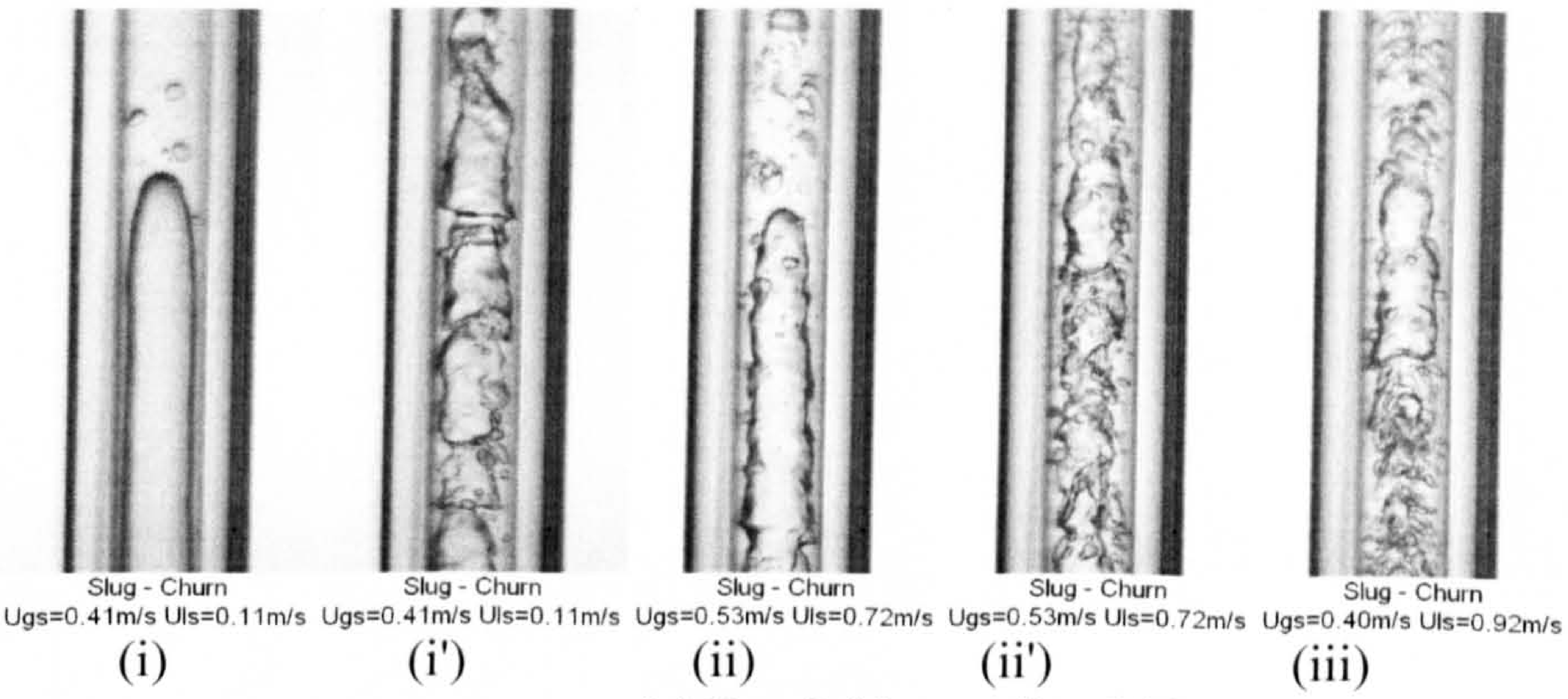

(c) $D = 2.88$ mm, $P = 14$ bar

Figure 5.55 Slug – churn transition boundary observed in the 2.88 mm tube at different pressures. (a) 6 bar, (b) 10 bar and (c) 14 bar.

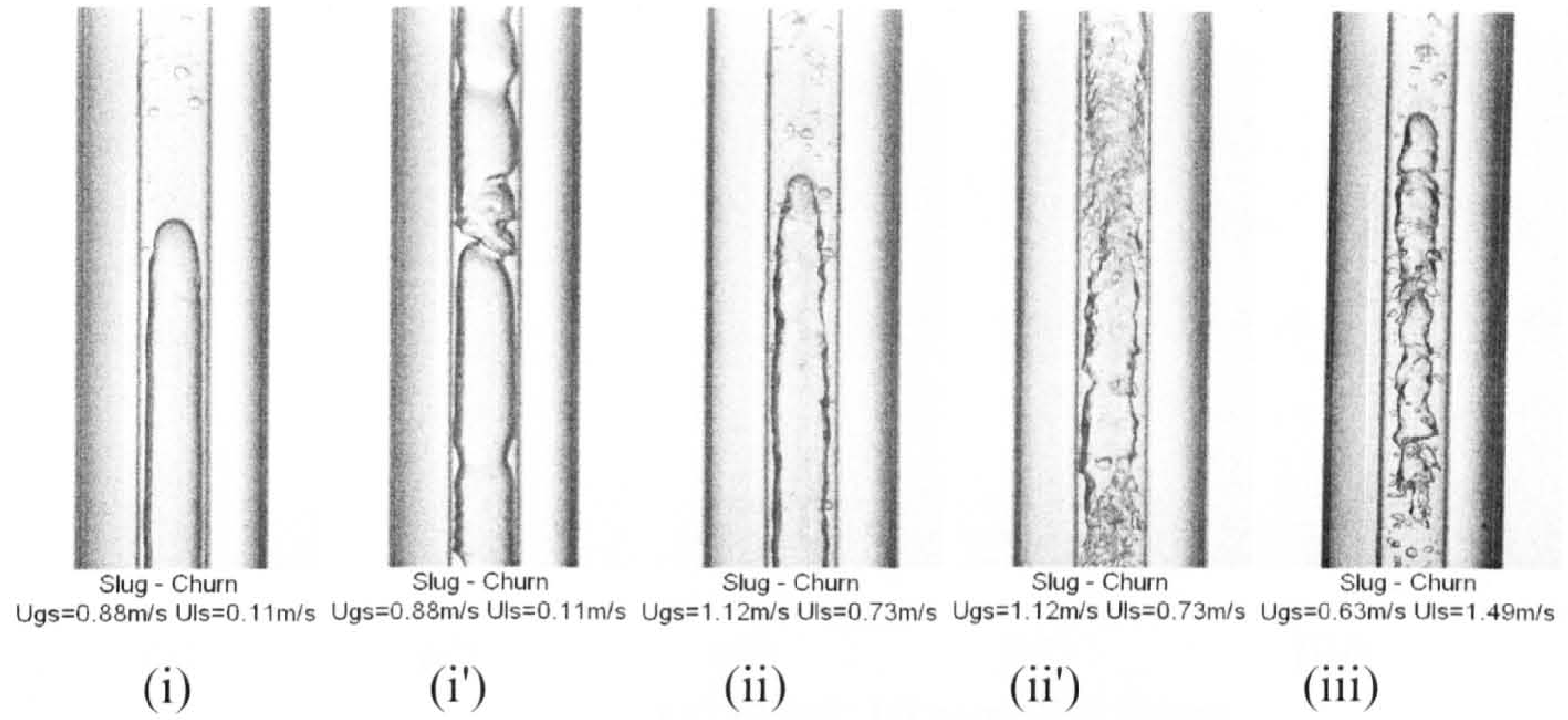

(a) D = 2.01 mm, P = 6 bar

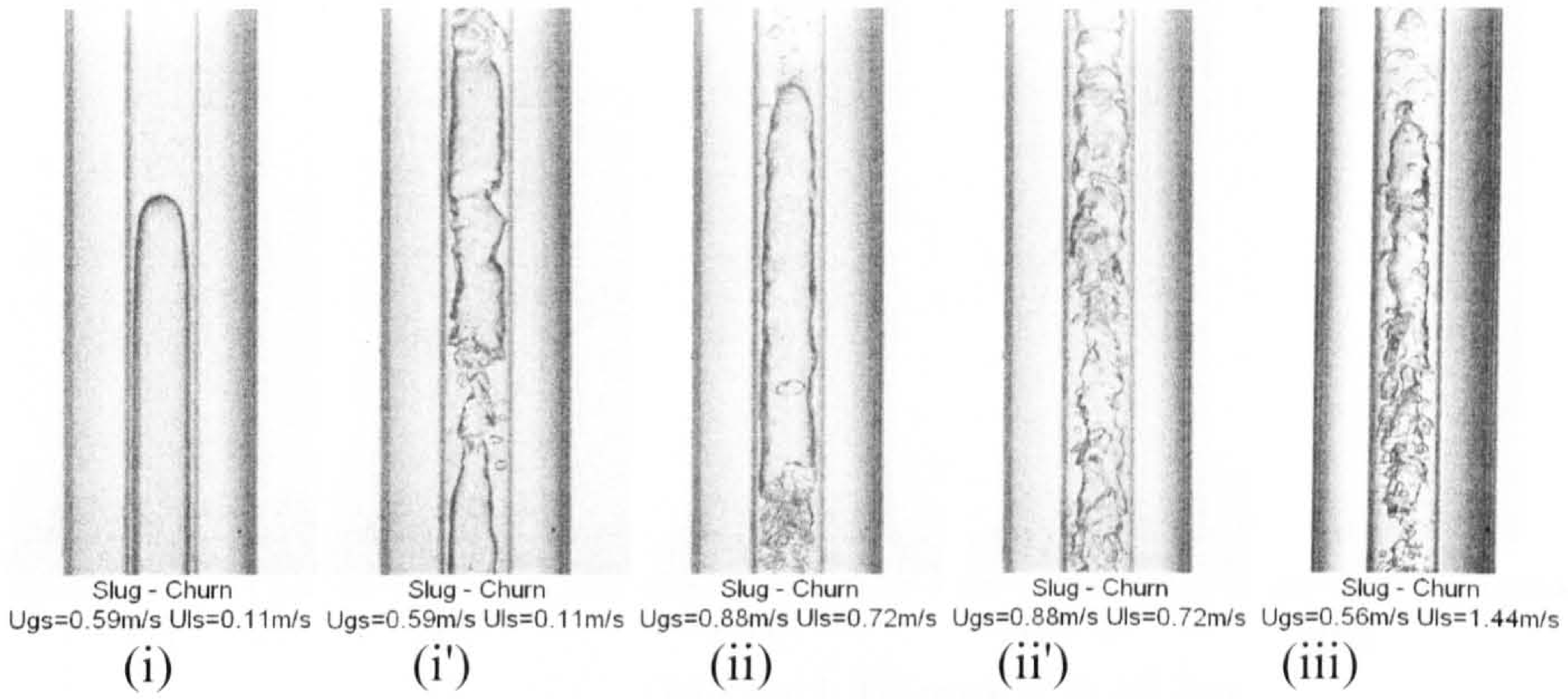

(b) D = 2.01 mm, P = 10 bar

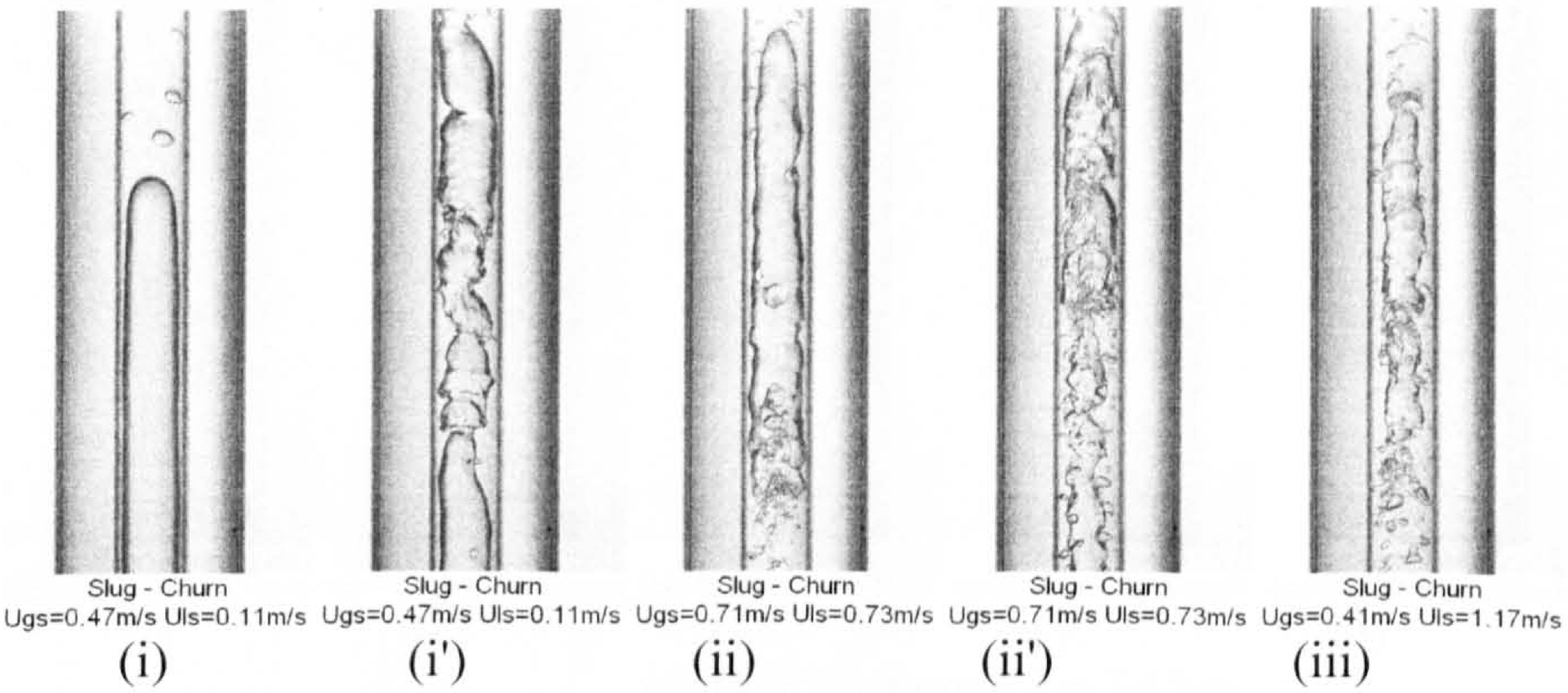

(c) D = 2.01 mm, P = 14 bar

Figure 5.56 Slug – churn transition boundary observed in the 2.01 mm tube at different pressures. (a) 6 bar, (b) 10 bar and (c) 14 bar.

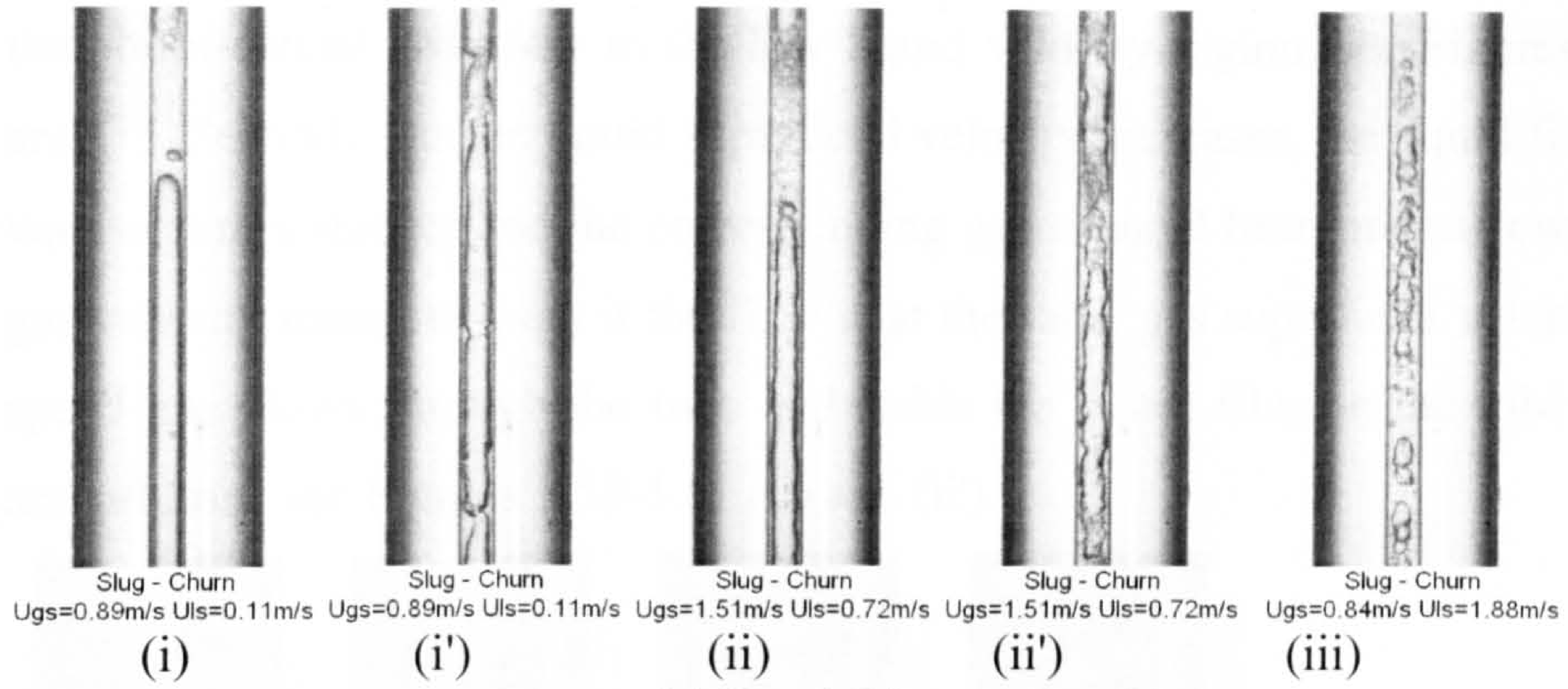

(a) D = 1.10 mm, P = 6 bar

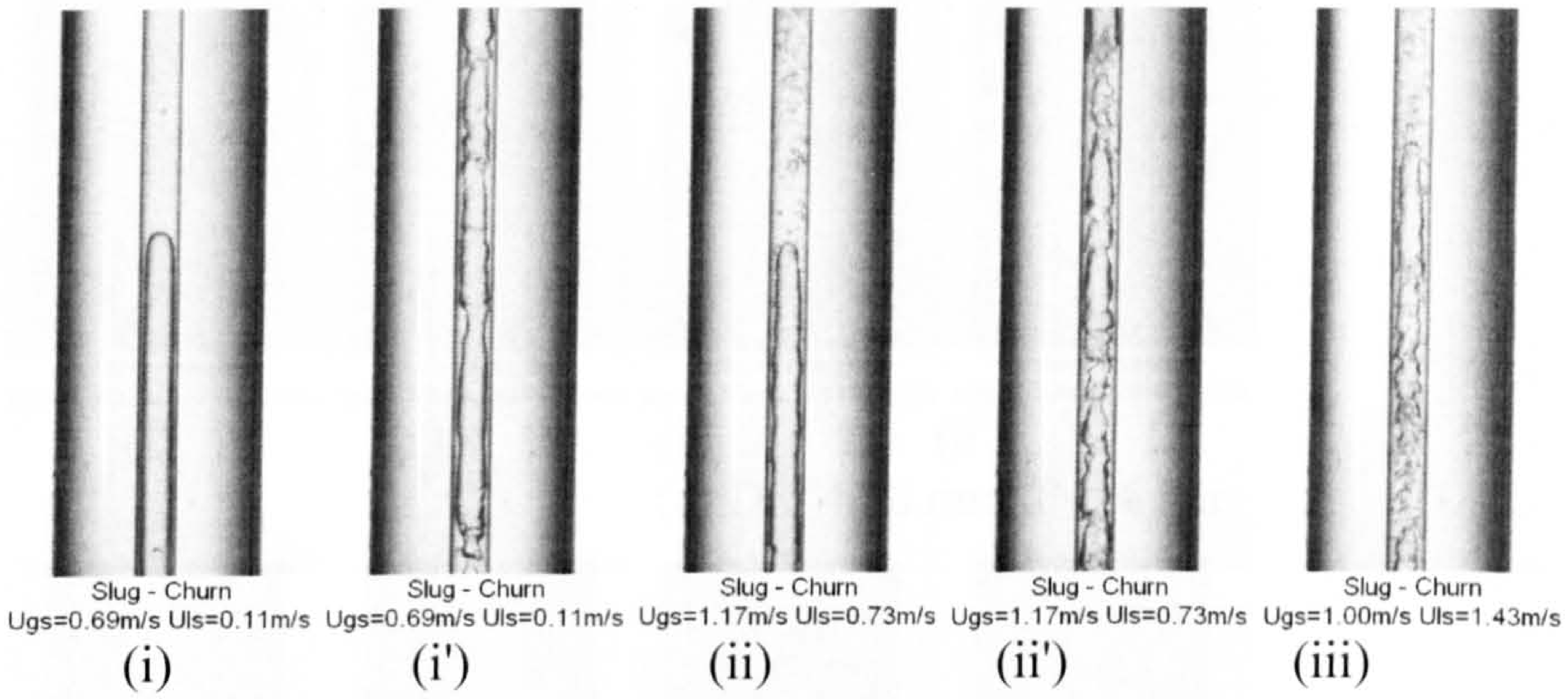

(b) D = 1.10 mm, P = 10 bar

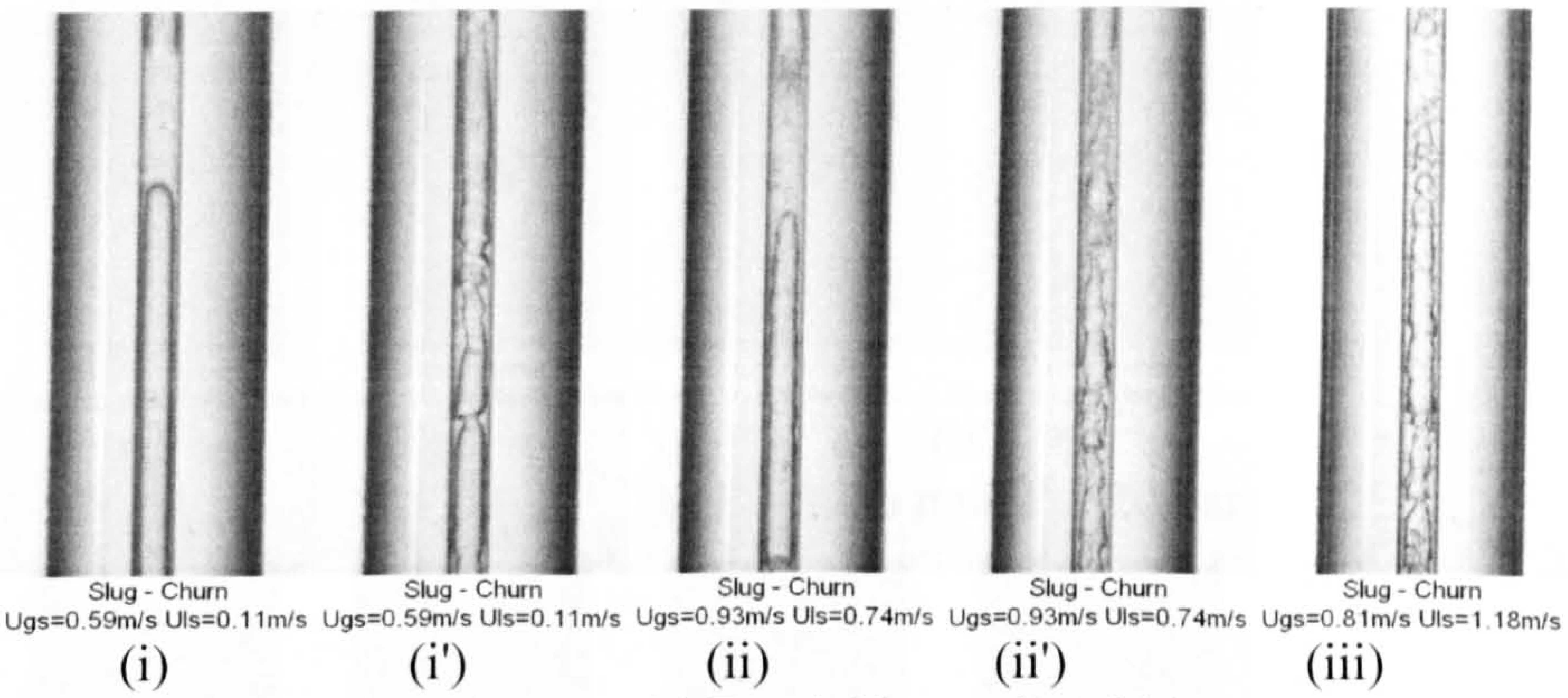

(c) D = 1.10 mm, P = 14 bar

Figure 5.57 Slug – churn transition boundary observed in the 1.10 mm tube at different pressures. (a) 6 bar, (b) 10 bar and (c) 14 bar.

5.2.5 Churn – annular transition boundary

The churn-annular transitional flow regime is depicted in Figures 5.58-5.61. Churn flow developed to annular flow at two situations from the observations in the present experiments. Firstly, gas slug can penetrate the liquid bridge to be a continual core when the average void fraction is high enough. This is main transition mechanism for the churn-annual boundary in the low liquid velocity region, see Figures 5.58-5.61 (i) and (i'). Secondly, as the liquid superficial velocity increases, the liquid film on the tube wall becomes thicker and the corresponding gas channel becomes narrower. The actual gas velocity increases even if the flow is at the same gas superficial velocity. The high-speed gas blows through the tube and holds the liquid film on the tube wall to form annual flow, see Figures 5.58-5.61 (ii) and (ii').

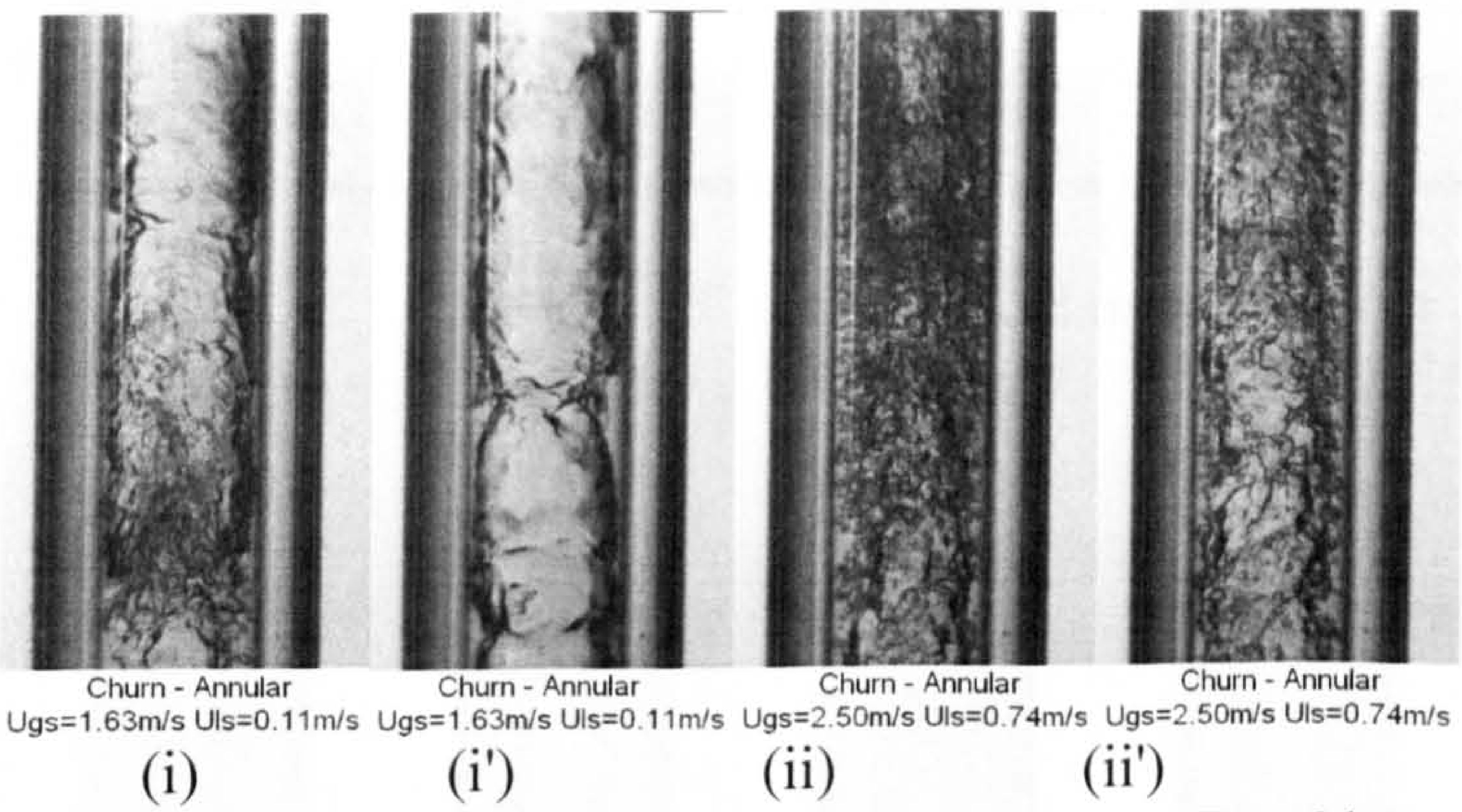

(a) D = 4.26 mm, P = 6 bar

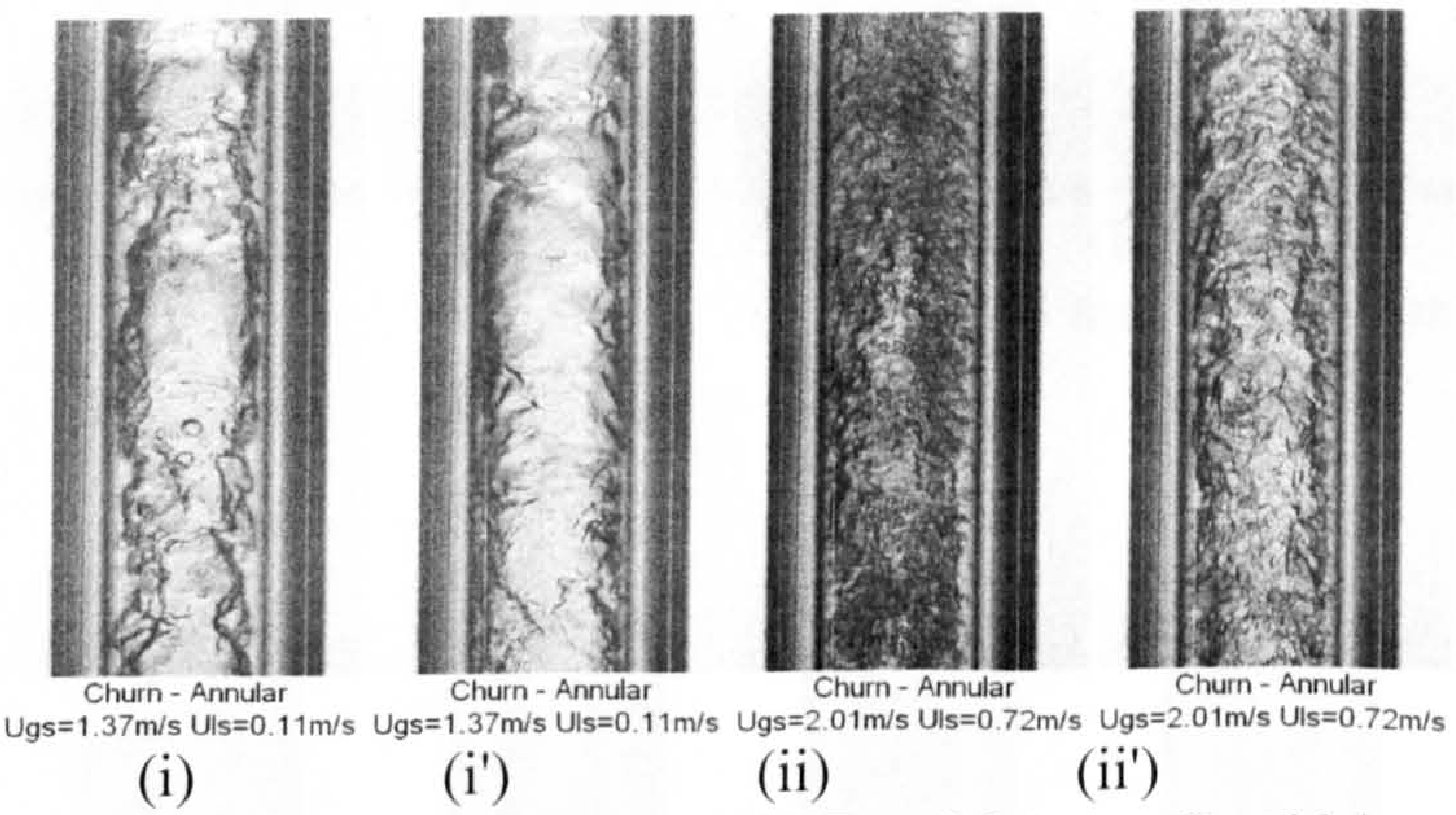

(b) D = 4.26 mm, P = 10 bar

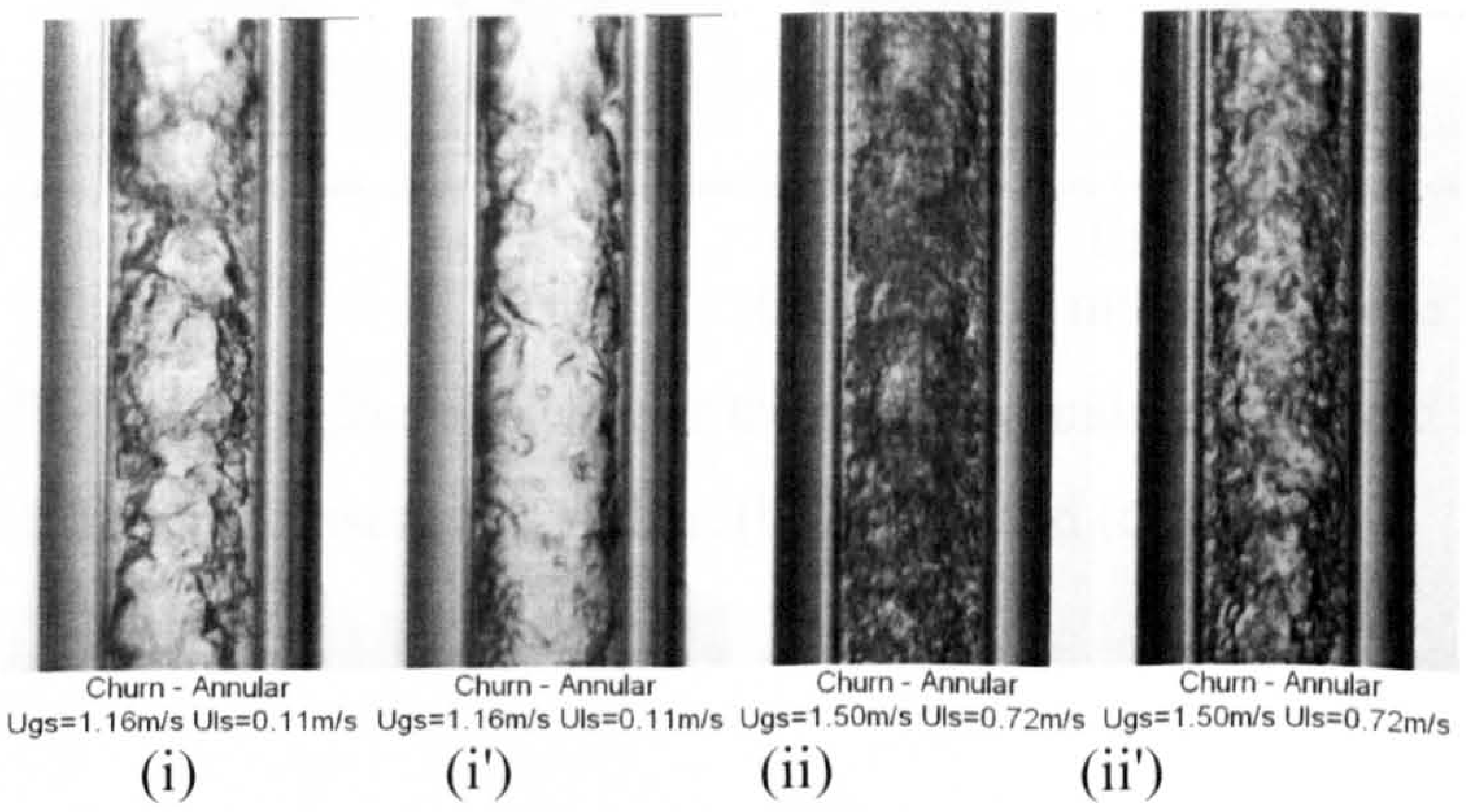

(c) D = 4.26 mm, P = 14 bar

Figure 5.58 Churn – annular transition boundary observed in the 4.26 mm tube at different pressures. (a) 6 bar, (b) 10 bar and (c) 14 bar.

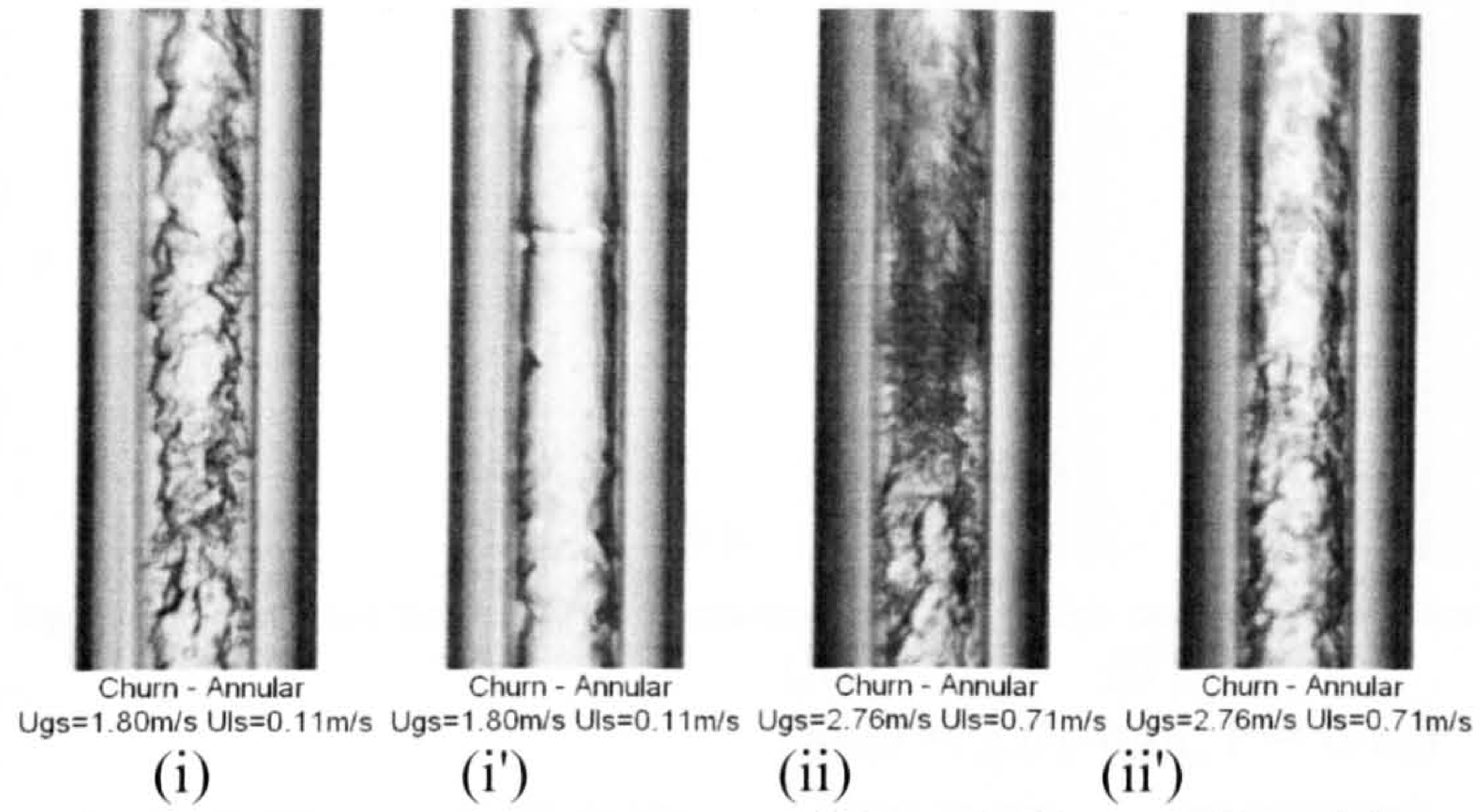

(a) D = 2.88 mm, P = 6 bar

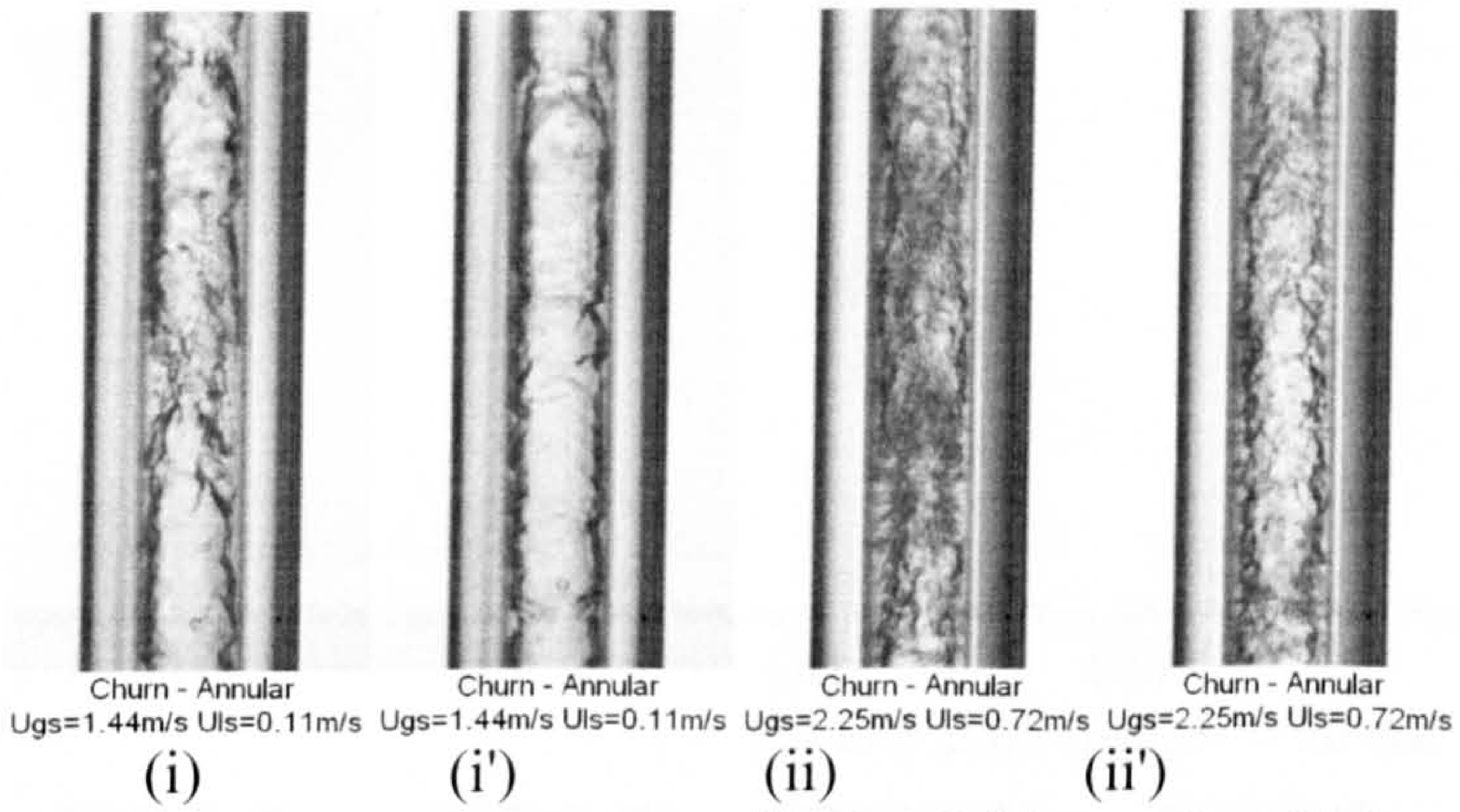

(b) D = 2.88 mm, P = 10 bar

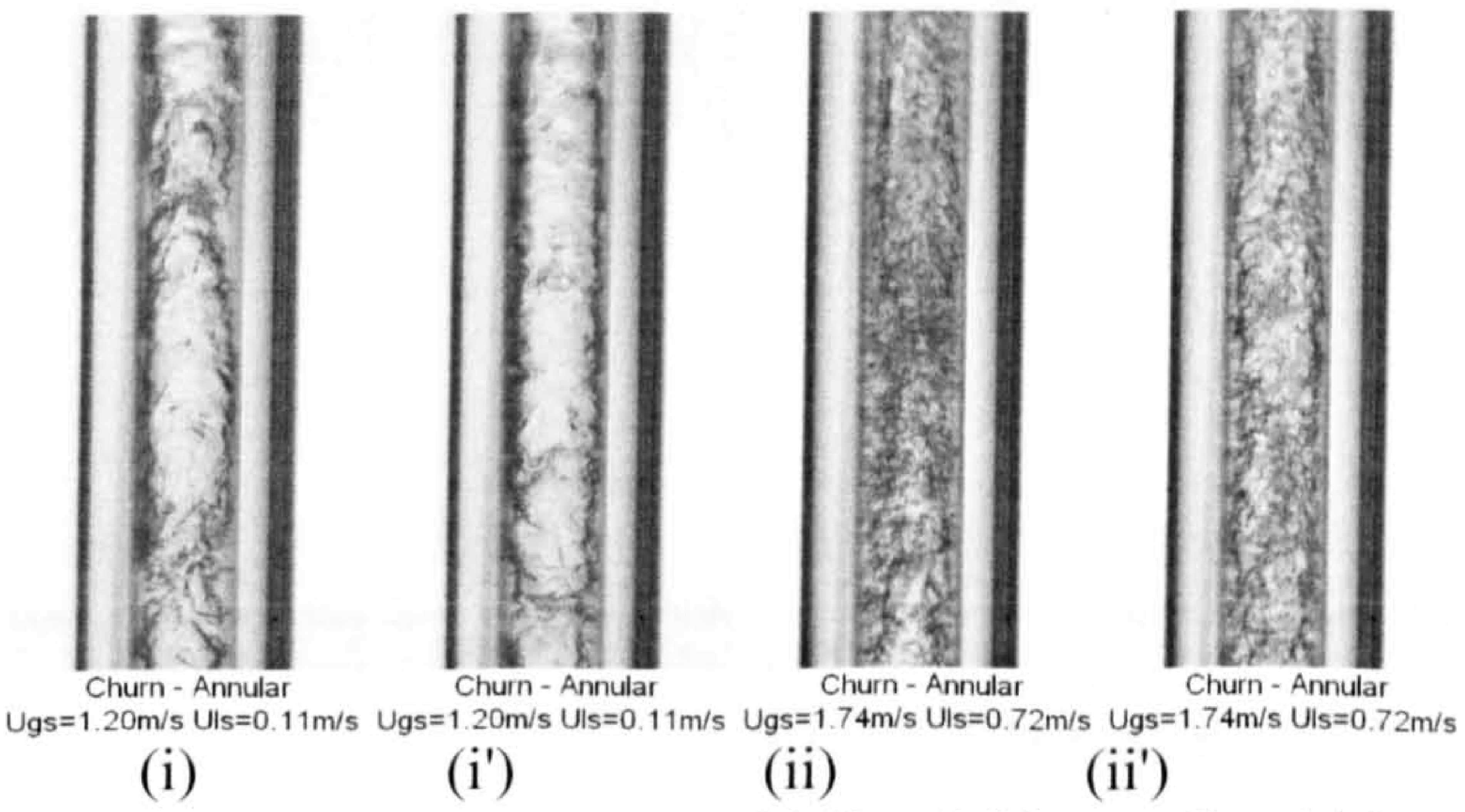

(c) D = 2.88 mm, P = 14 bar

Figure 5.59 Churn – annular transition boundary observed in the 2.88 mm tube at different pressures. (a) 6 bar, (b) 10 bar and (c) 14 bar.

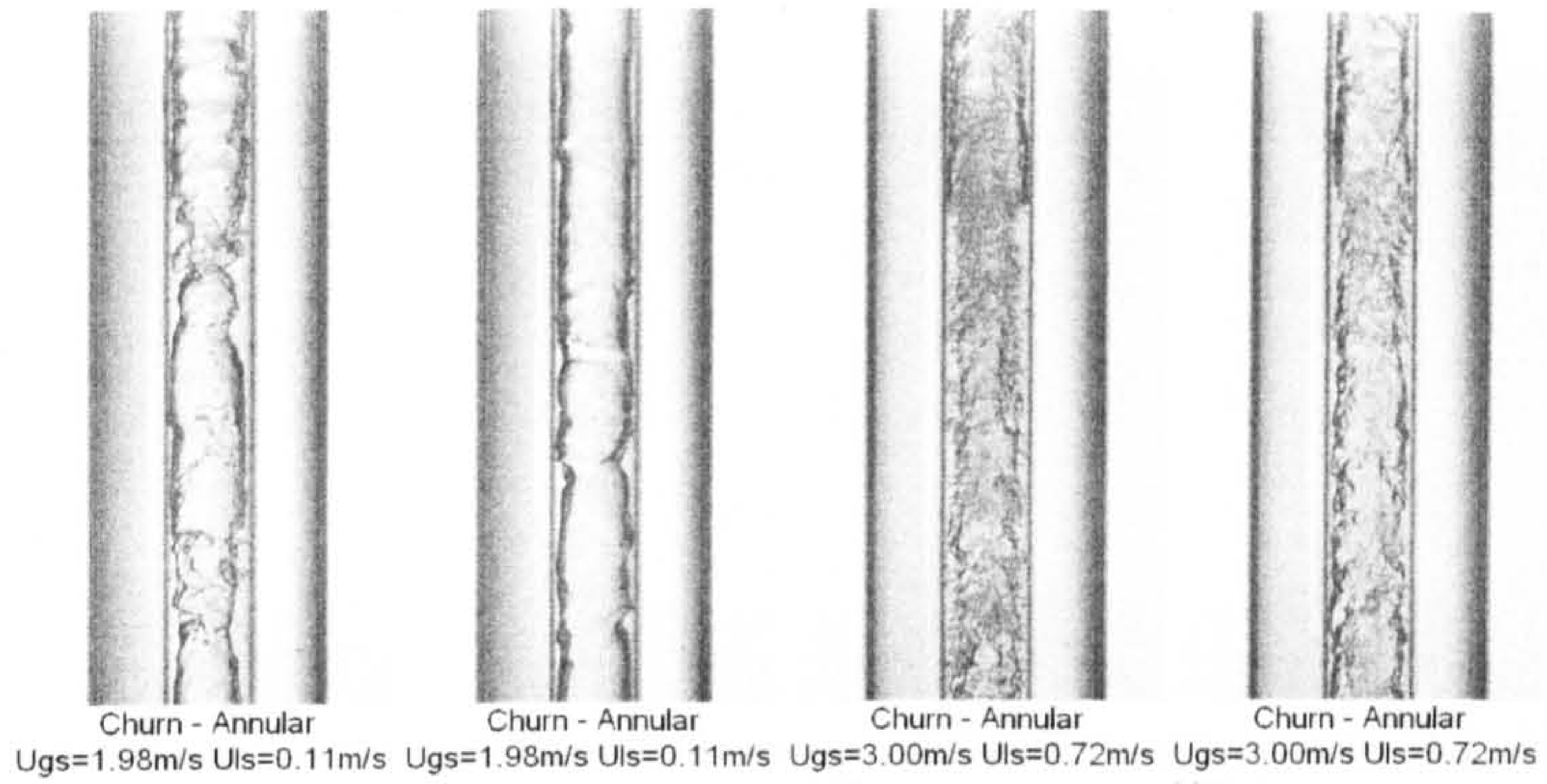

(i) (i') (ii) (ii')

(a) D = 2.01 mm, P = 6 bar

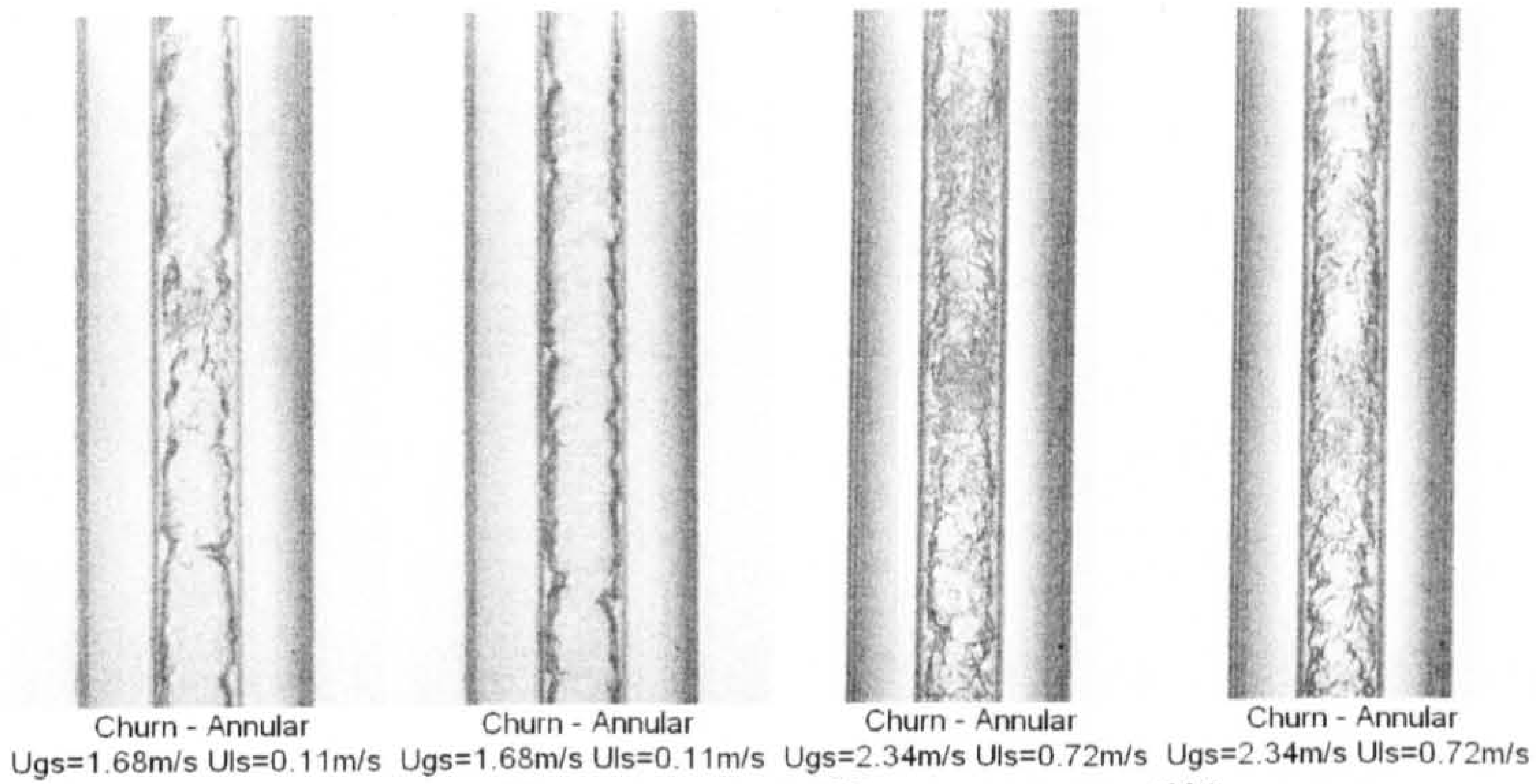

(i) (i') (ii) (ii')

(b) D = 2.01 mm, P = 10 bar

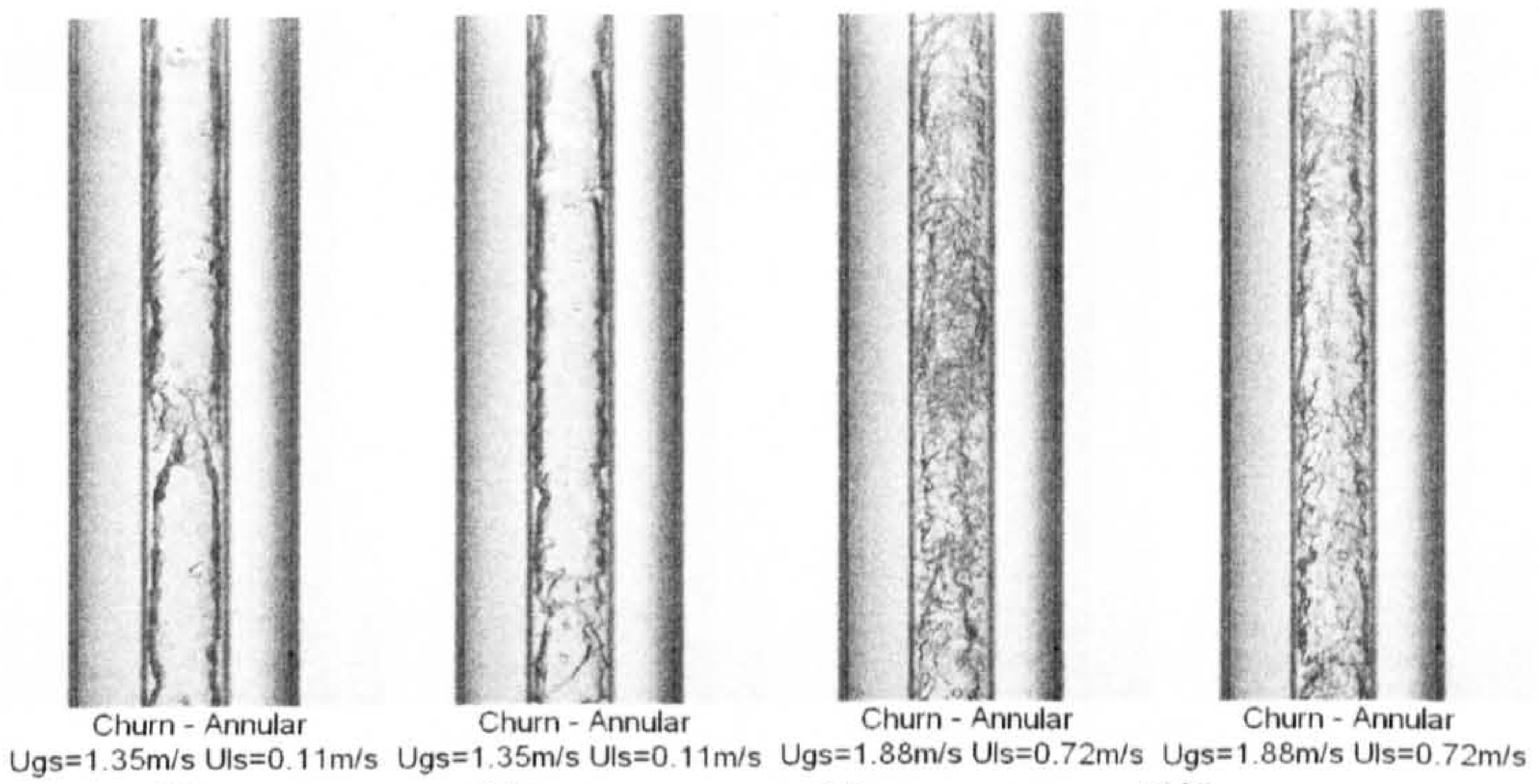

(i) (i') (ii) (ii')

(c) D = 2.01 mm, P = 14 bar

Figure 5.60 Churn – annular transition boundary observed in the 2.01 mm tube at different pressures. (a) 6 bar, (b) 10 bar and (c) 14 bar.

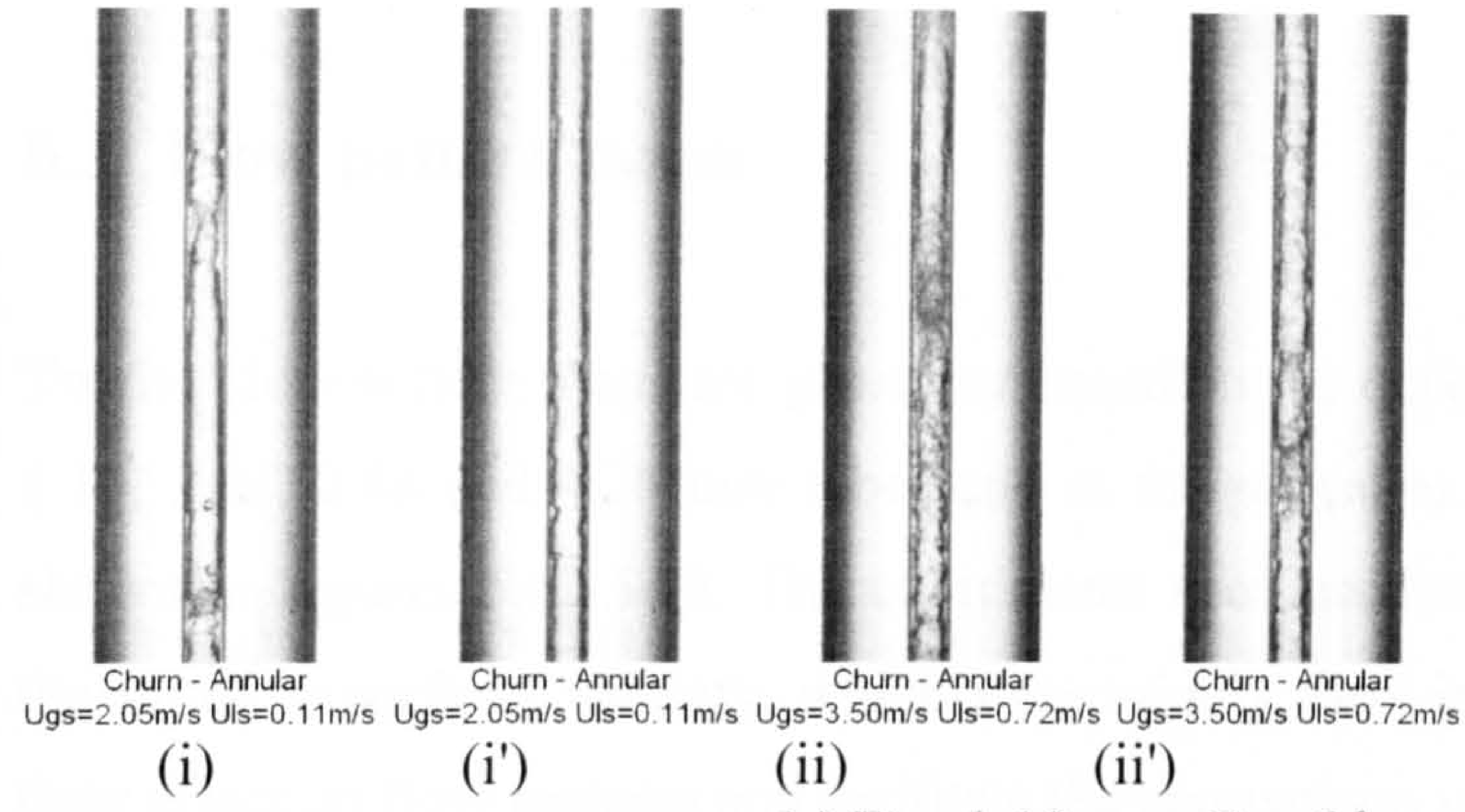

(a) D = 1.10 mm, P = 6 bar

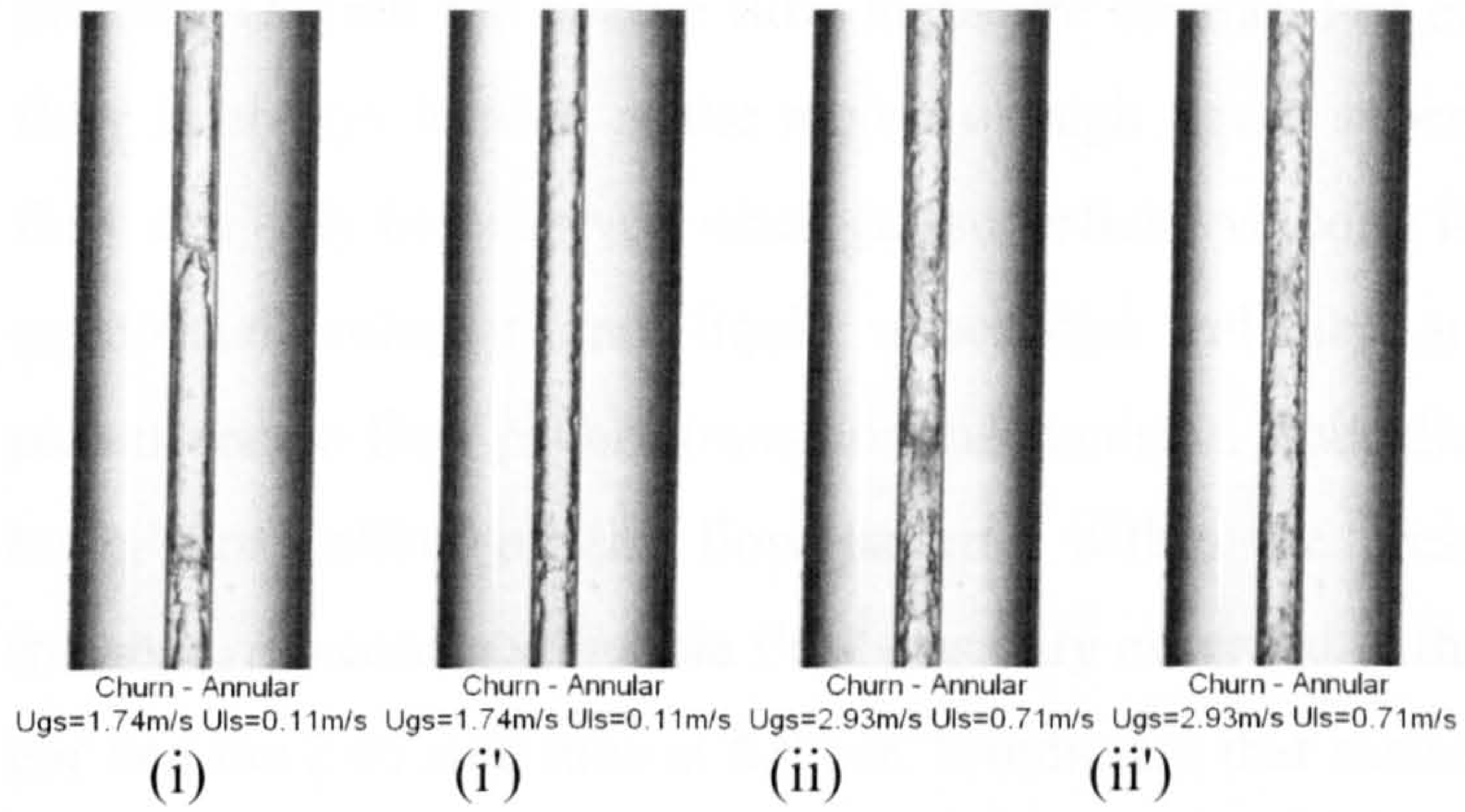

(b) D = 1.10 mm, P = 10 bar

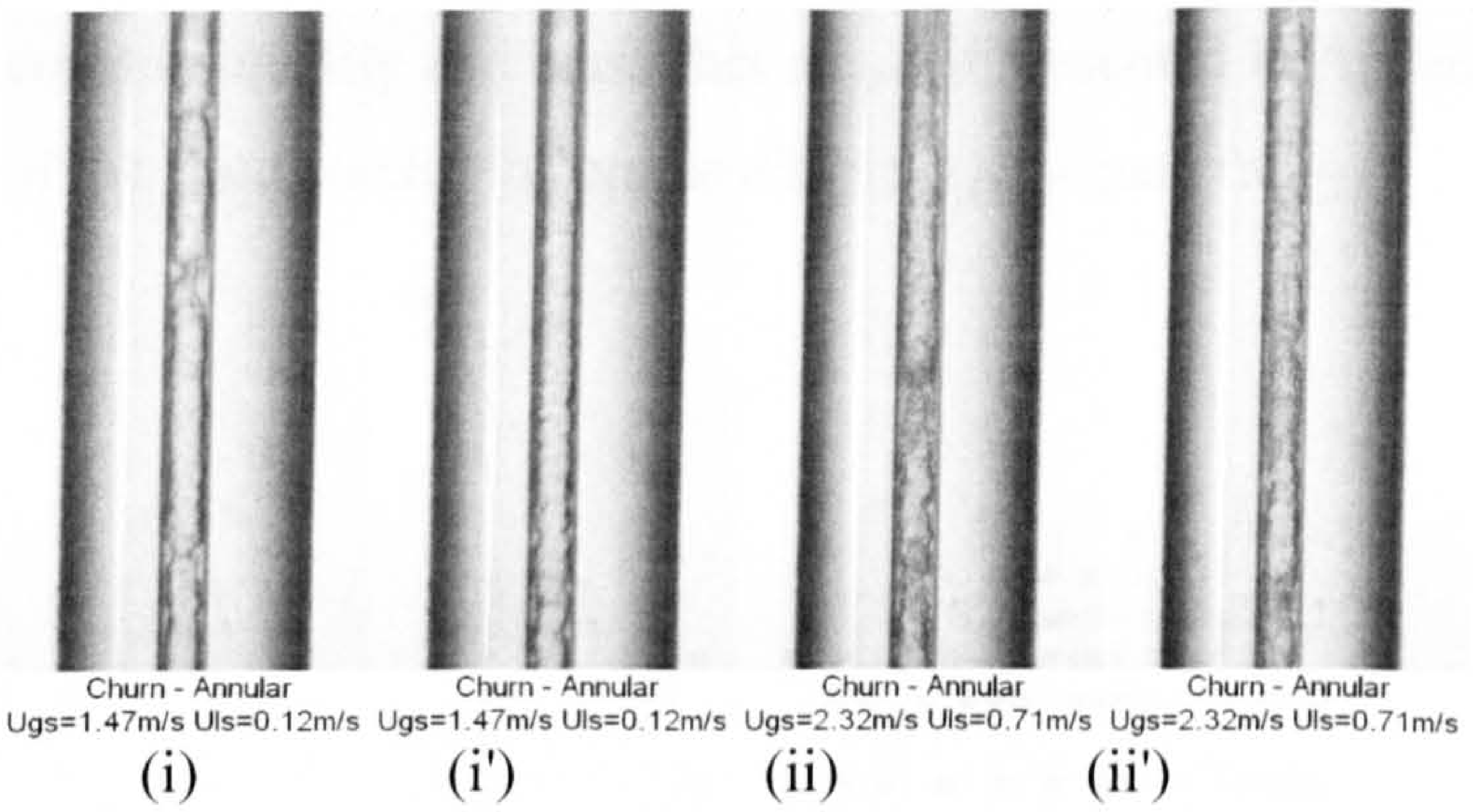

(c) D = 1.10 mm, P = 14 bar

Figure 5.61 Churn – annular transition boundary observed in the 1.10 mm tube at different pressures. (a) 6 bar, (b) 10 bar and (c) 14 bar.

5.3 Flow pattern maps

Twelve flow pattern maps are generated based on the experimental data collected in the 1.10, 2.01, 2.88 and 4.26 mm tubes and at the pressures of 6, 10 and 14 bar and are shown in Figures 5.62-5.73. The coordinates used are the gas superficial velocity and the liquid superficial velocity, which were widely used in the earlier studies to reveal their effect on flow patterns and facilitate the comparison with the existing flow maps or models. Overall the twelve flow maps are similar. For example, the dispersed bubble flow is always located at the region of high liquid superficial velocity whilst annular flow can only be observed when gas superficial velocity is high enough. Therefore, gas superficial velocity and liquid superficial velocity are the two most important parameters in flow pattern transition mechanisms. Tube diameter and fluid pressure also have some effect on the flow patterns within the present experimental range. For instance, the confined bubble flow was only observed in the 1.10 mm tube at 6.0 to 14.0 bar and the 2.01 mm tube at 6.0 bar. It indicates that surface tension is growing into the dominant force in the smaller tubes at low flow velocity. The flow maps with the grid of constant quality and mass flux are also presented in Appendix H to illuminate the effect of the fluid conditions on the different flow patterns.

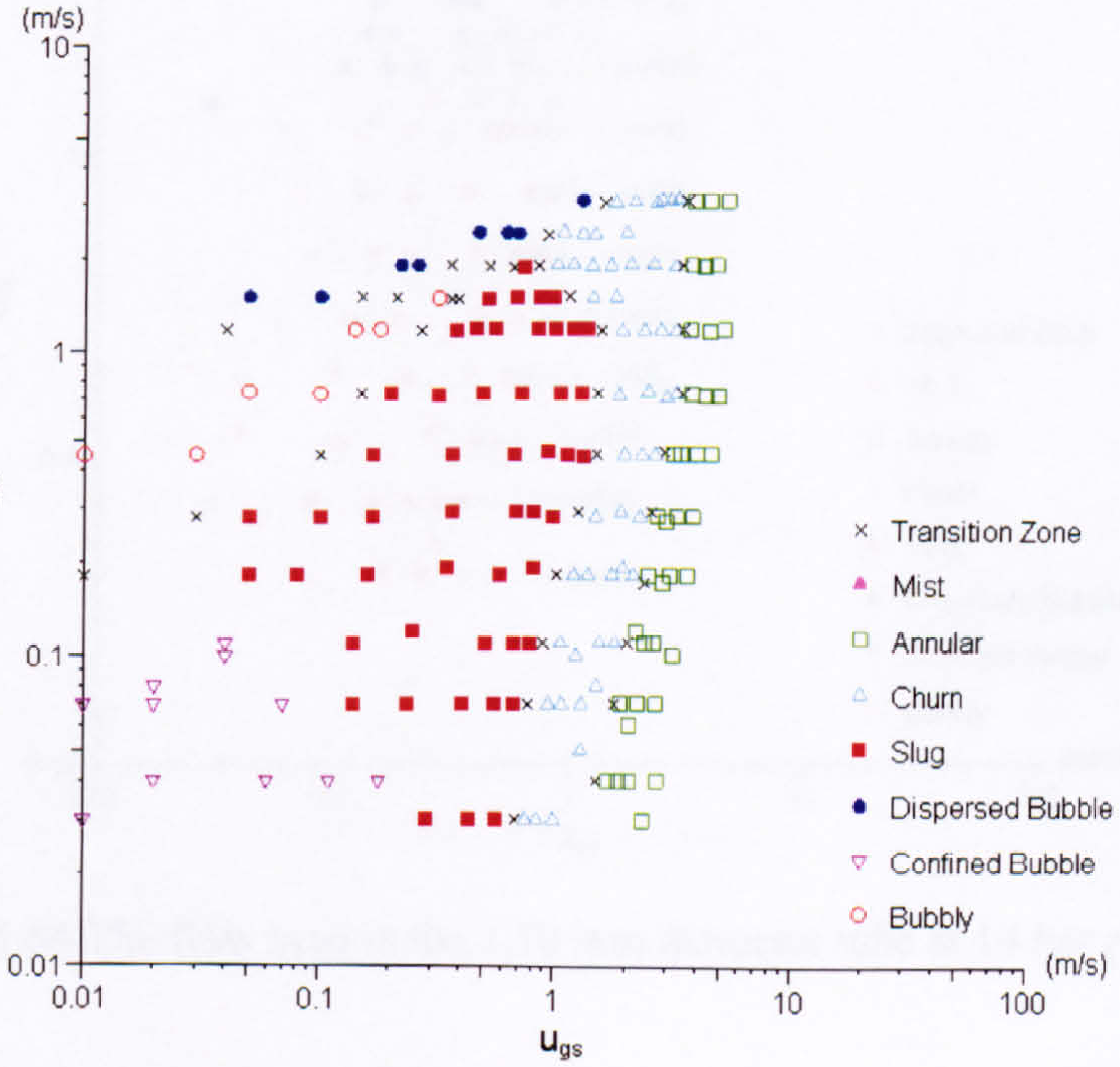

Figure 5.62 The flow map in the 1.10 mm diameter tube at 6 bar pressure.

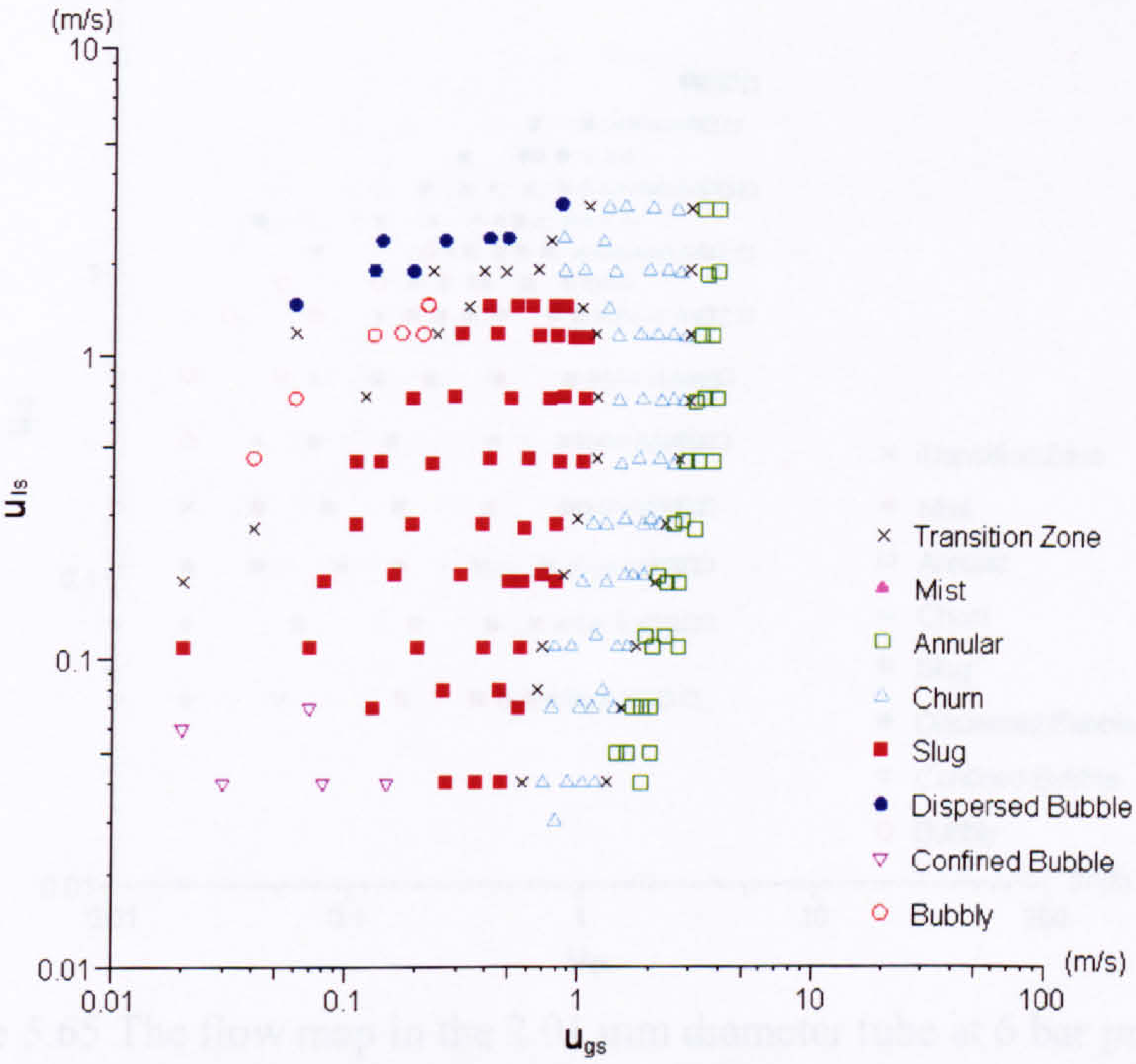

Figure 5.63 The flow map in the 1.10 mm diameter tube at 10 bar pressure.

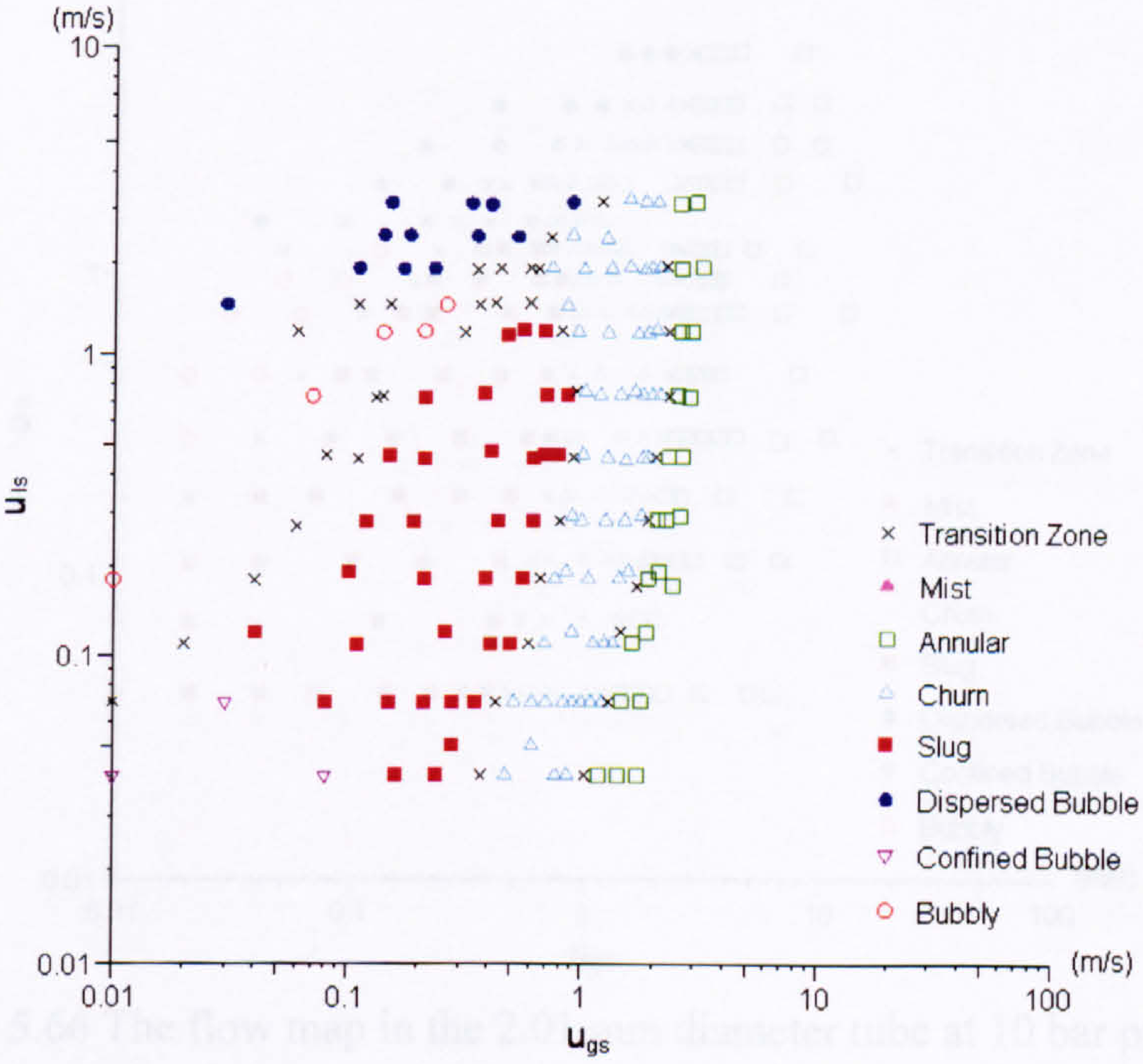

Figure 5.64 The flow map in the 1.10 mm diameter tube at 14 bar pressure.

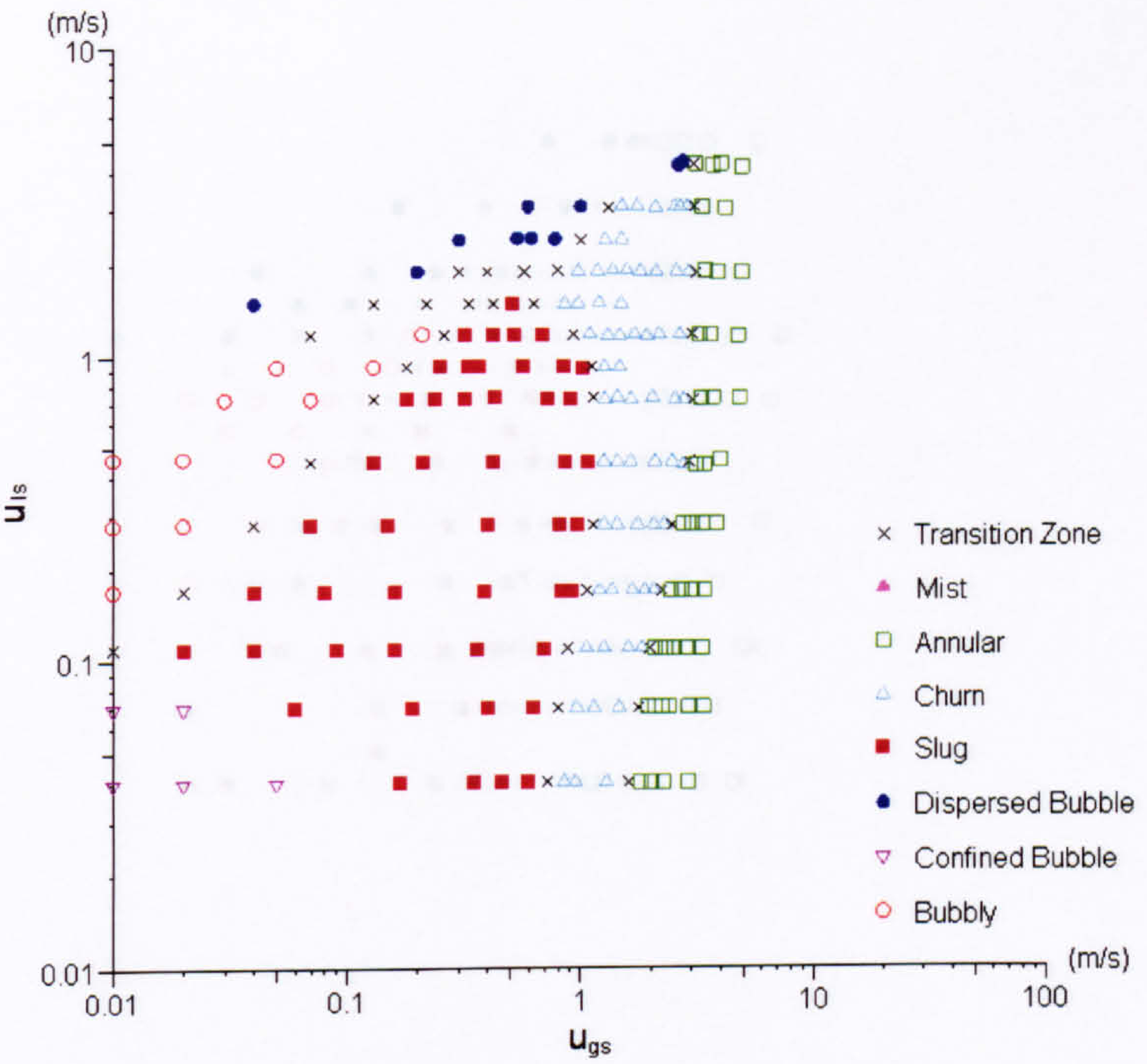

Figure 5.65 The flow map in the 2.01 mm diameter tube at 6 bar pressure.

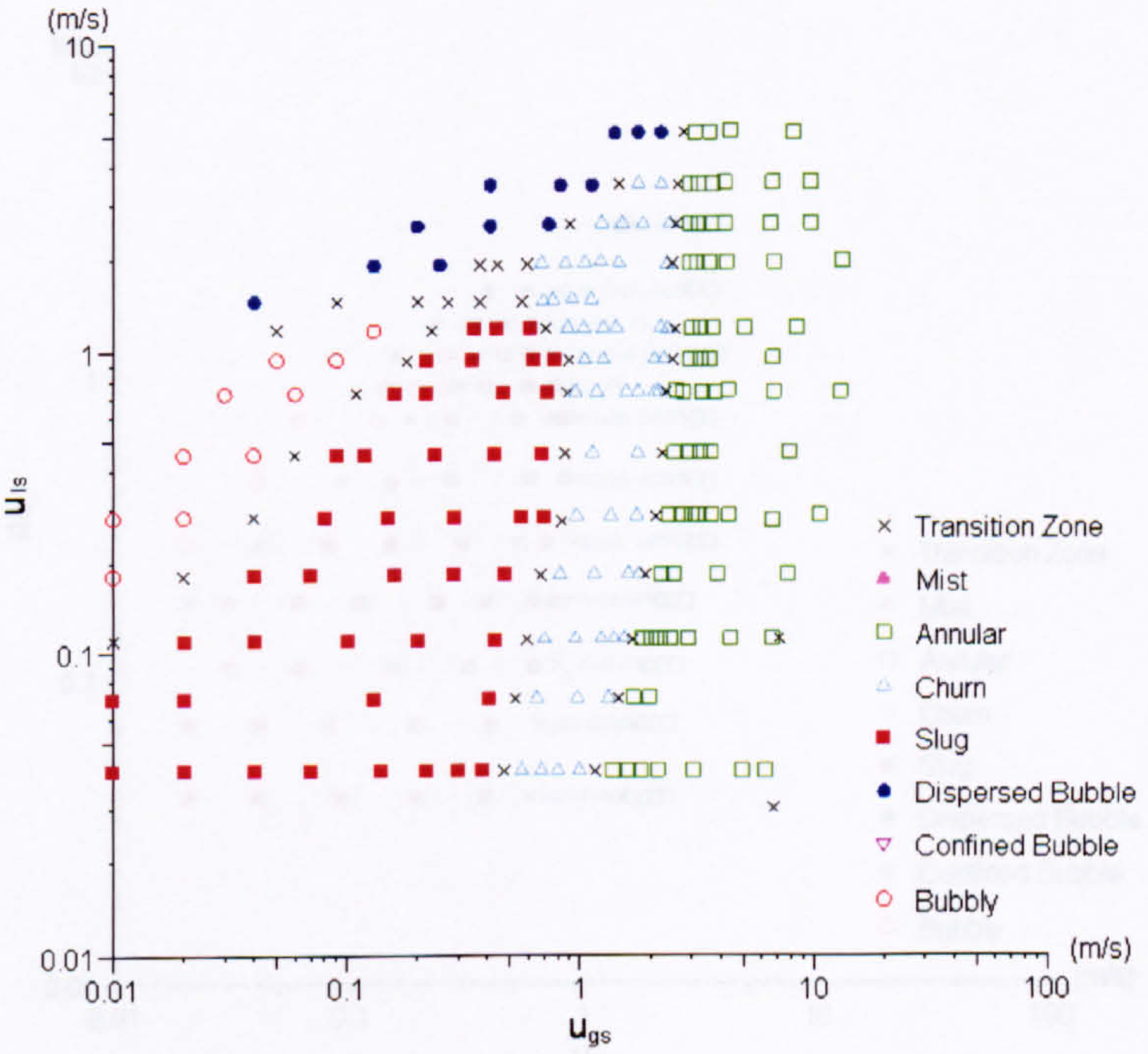

Figure 5.66 The flow map in the 2.01 mm diameter tube at 10 bar pressure.

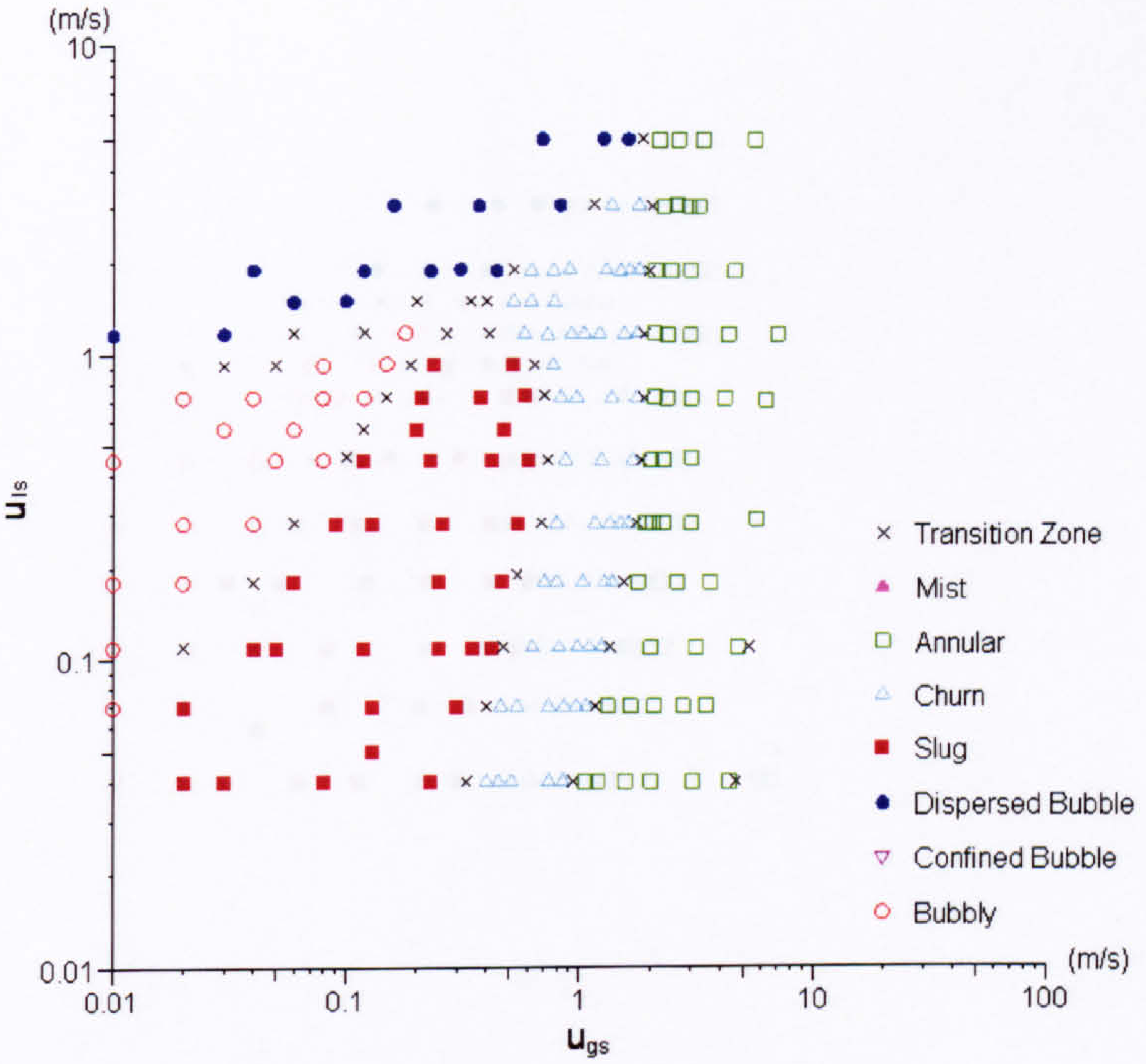

Figure 5.67 The flow map in the 2.01 mm diameter tube at 14 bar pressure.

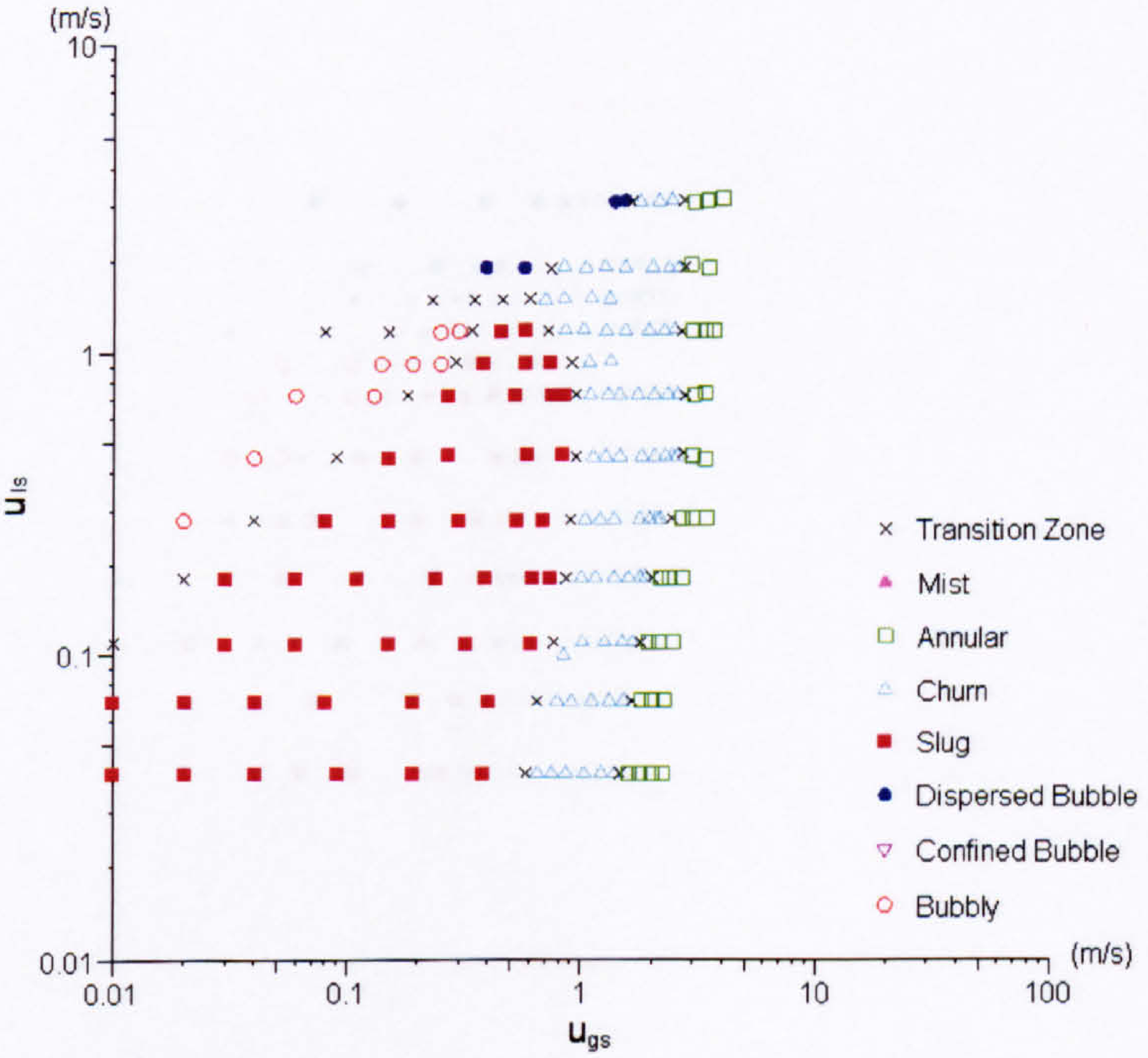

Figure 5.68 The flow map in the 2.88 mm diameter tube at 6 bar pressure.

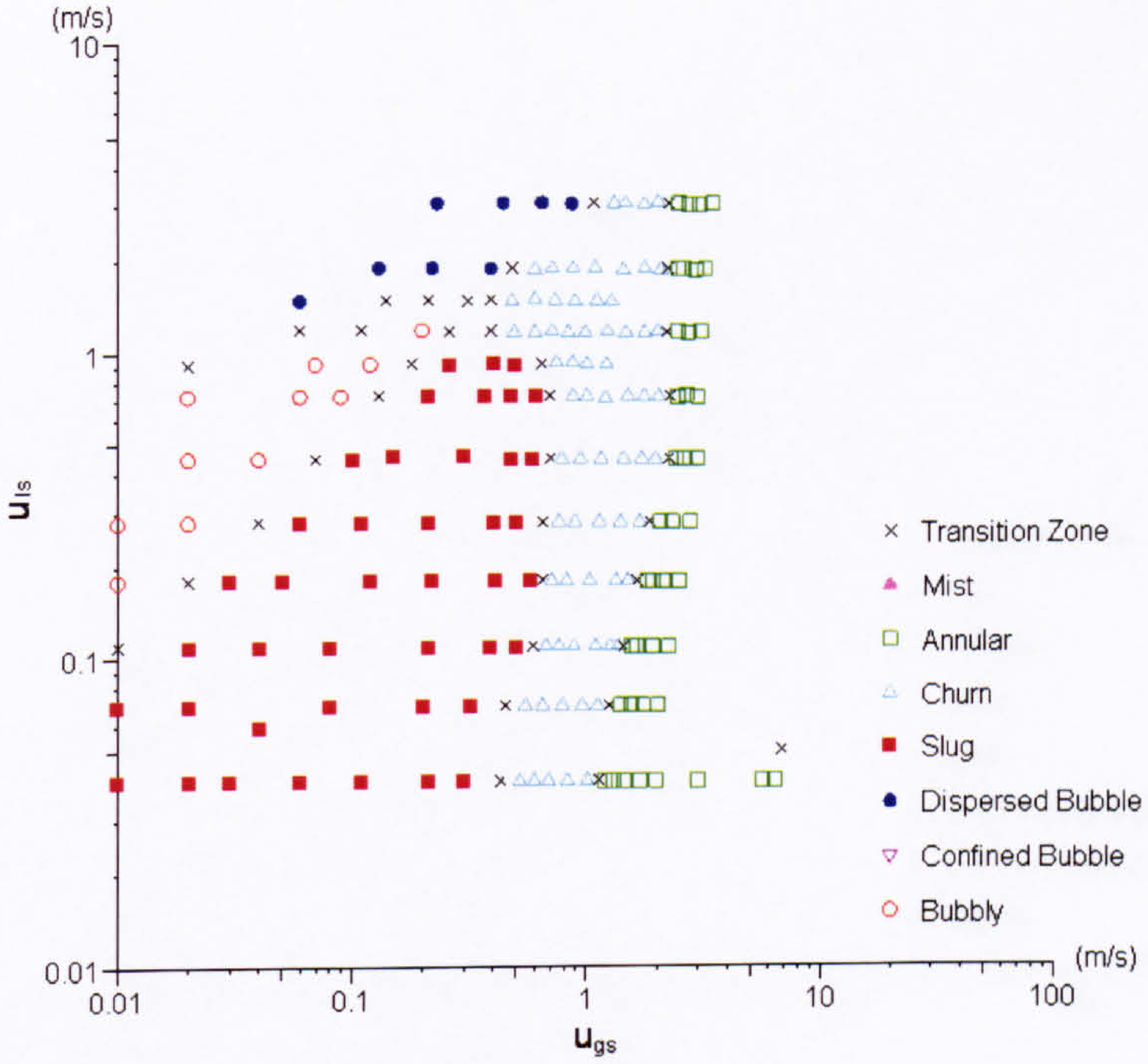

Figure 5.69 The flow map in the 2.88 mm diameter tube at 10 bar pressure.

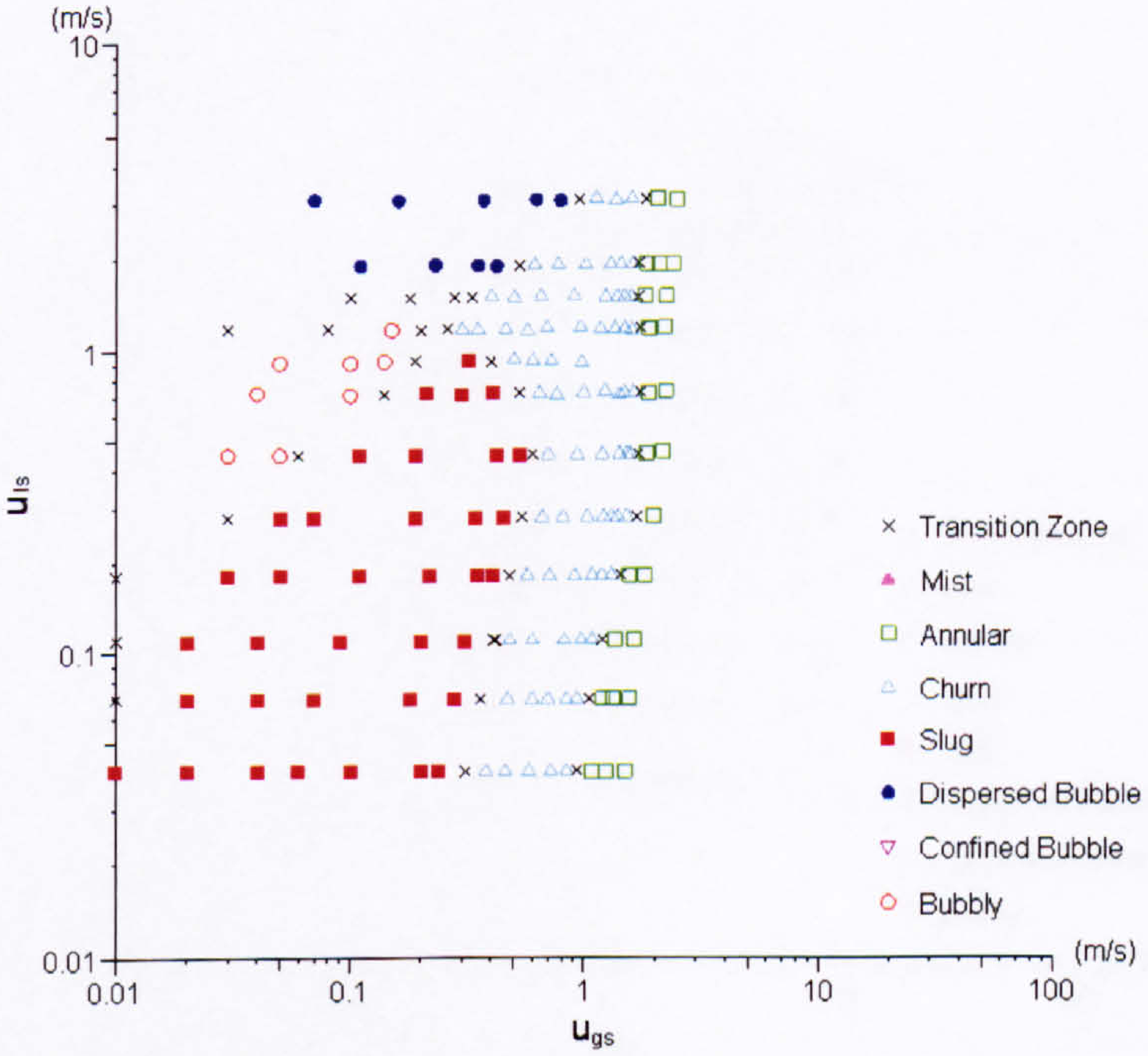

Figure 5.70 The flow map in the 2.88 mm diameter tube at 14 bar pressure.

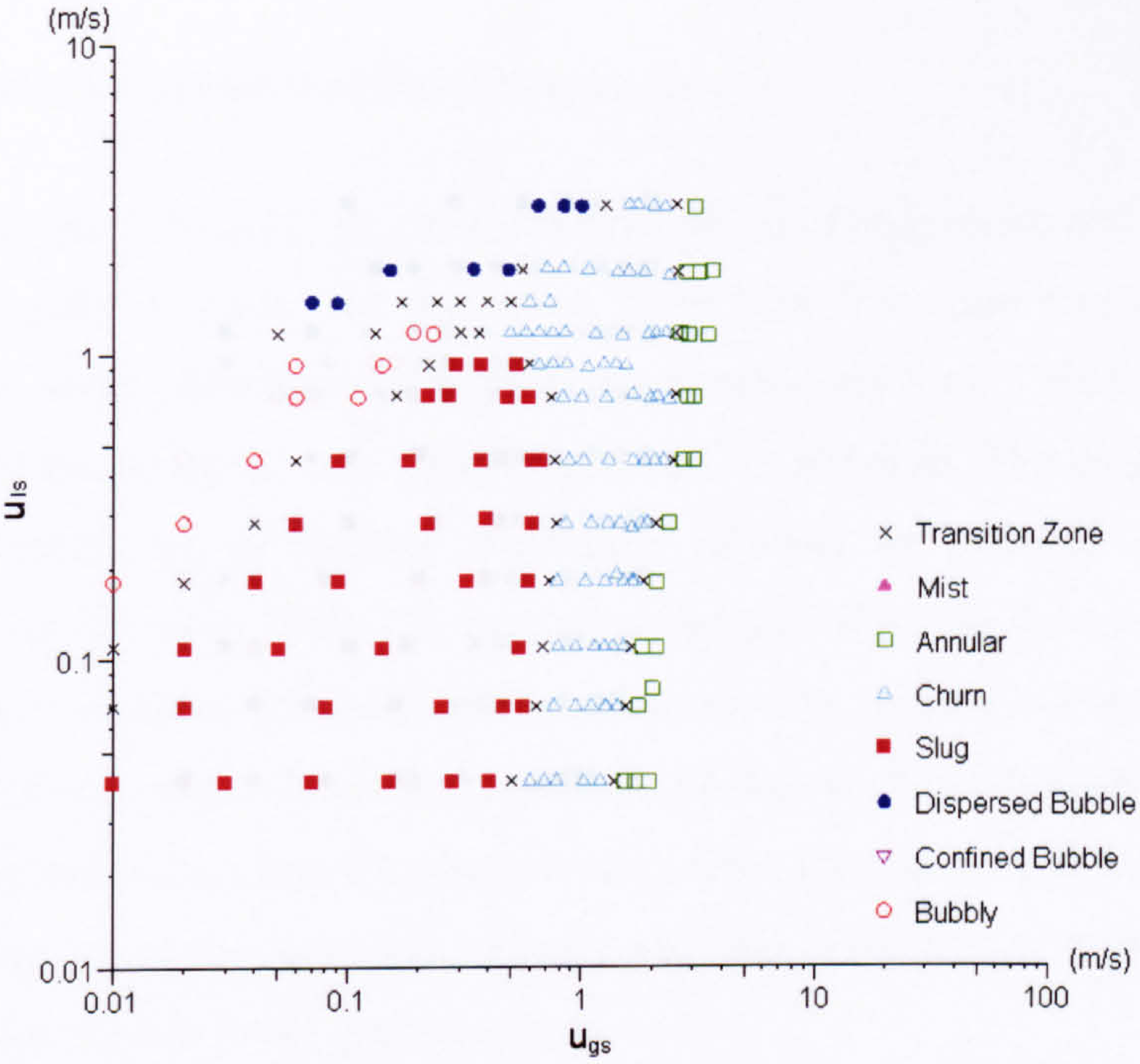

Figure 5.71 The flow map in the 4.26 mm diameter tube at 6 bar pressure.

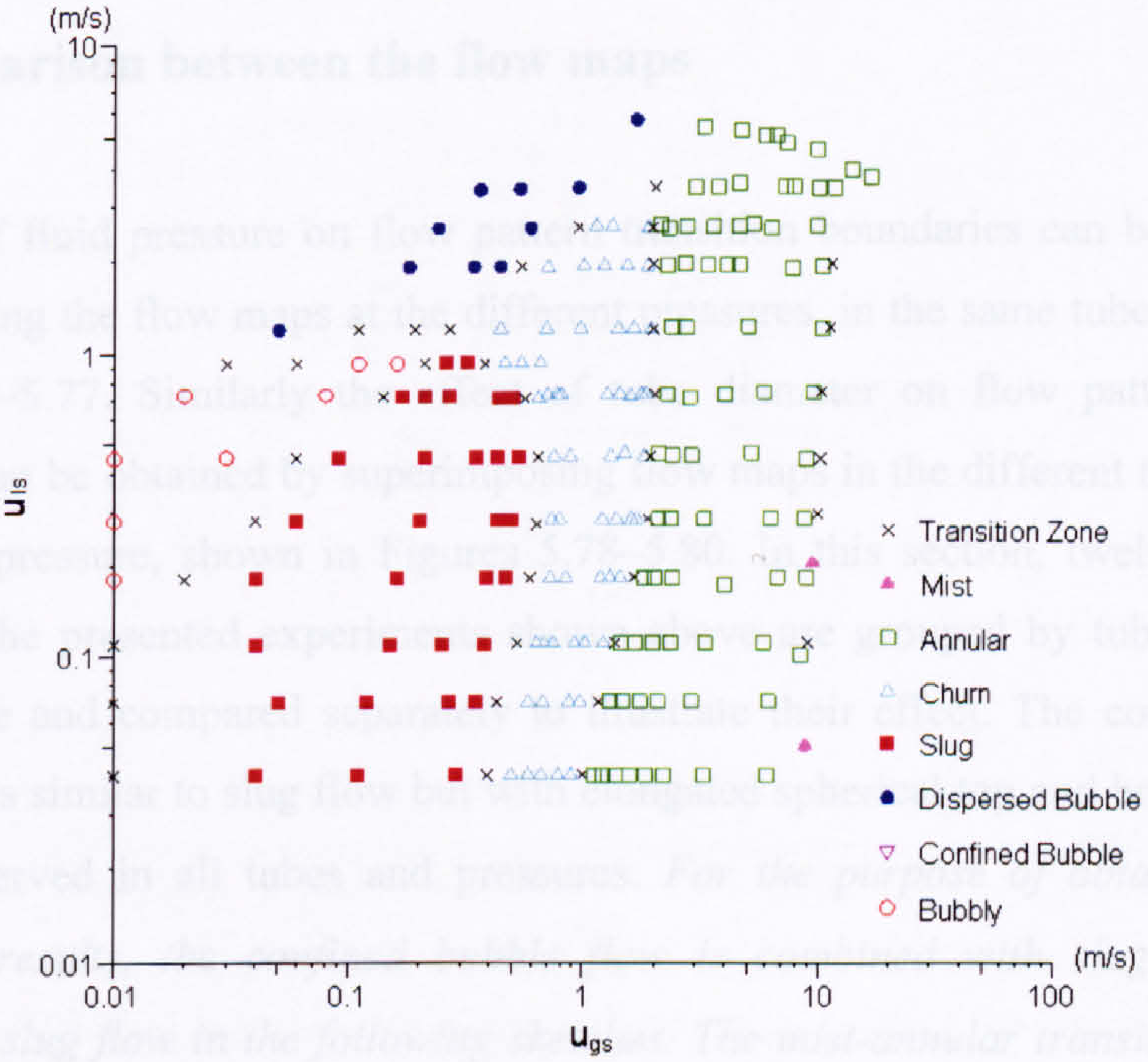

Figure 5.72 The flow map in the 4.26 mm diameter tube at 10 bar pressure.

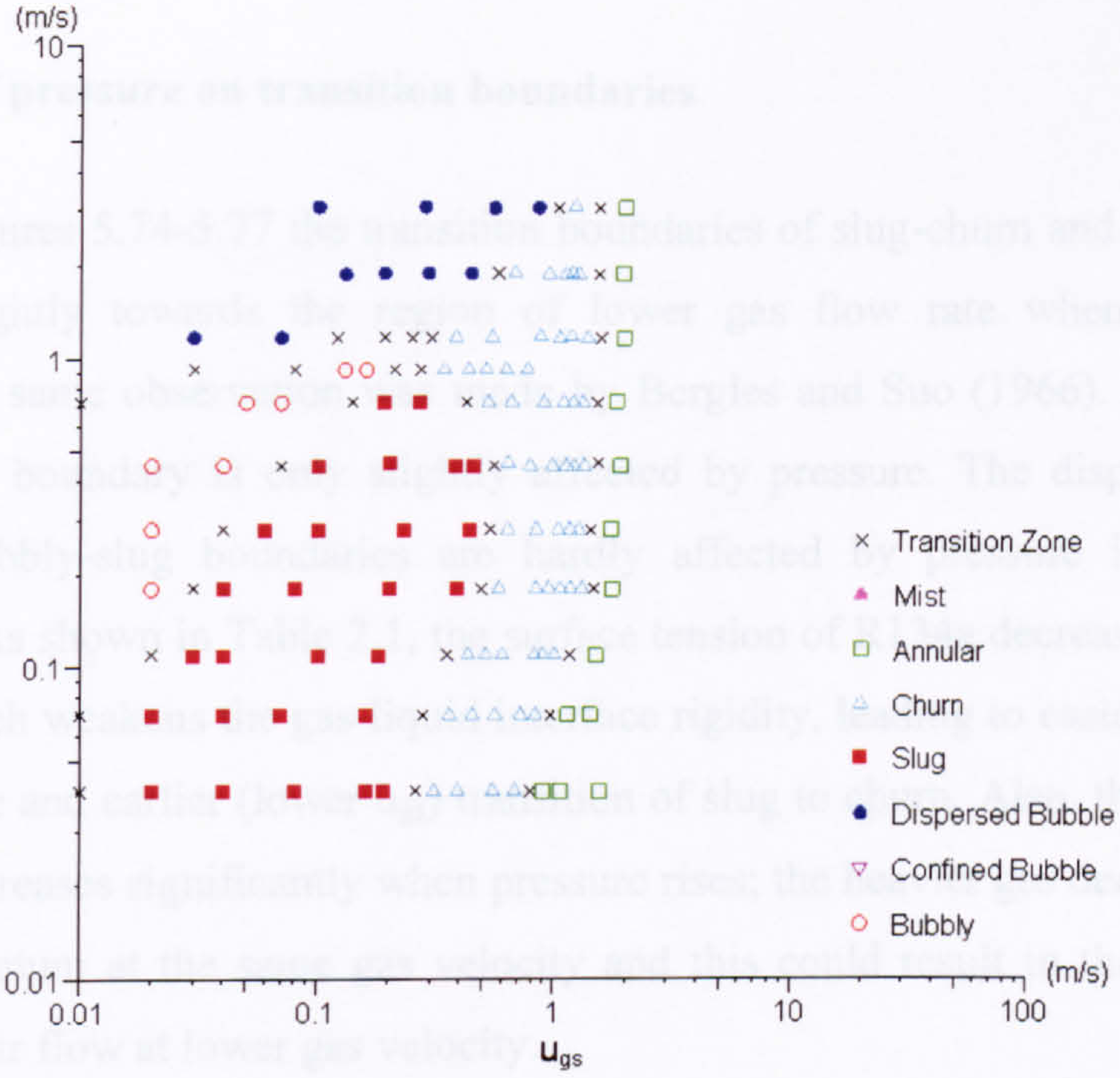

Figure 5.73 The flow map in the 4.26 mm diameter tube at 14 bar pressure.

5.4 Comparison between the flow maps

The effect of fluid pressure on flow pattern transition boundaries can be clearly seen with comparing the flow maps at the different pressures, in the same tube diameter, see Figures 5.74–5.77. Similarly the effect of tube diameter on flow pattern transition boundaries can be obtained by superimposing flow maps in the different tube diameters at the same pressure, shown in Figures 5.78–5.80. In this section, twelve flow maps obtained in the presented experiments shown above are grouped by tube diameter or fluid pressure and compared separately to illustrate their effect. The confined bubble flow, which is similar to slug flow but with elongated spherical top and bottom bubbles, was not observed in all tubes and pressures. *For the purpose of obtaining general comparison results, the confined bubble flow is combined with slug flow and is presented as slug flow in the following sketches. The mist-annular transition boundary is not included either for the same reason, i.e. it did not appear for all tube diameters and experimental pressures.*

5.4.1 Effect of pressure on transition boundaries

As seen in Figures 5.74-5.77 the transition boundaries of slug-churn and churn-annular flow shift slightly towards the region of lower gas flow rate when the pressure increases. The same observation was made by Bergles and Suo (1966). The dispersed bubble-bubbly boundary is only slightly affected by pressure. The dispersed bubble-churn and bubbly-slug boundaries are hardly affected by pressure in the current experiments. As shown in Table 2.1, the surface tension of R134a decreases as pressure increases, which weakens the gas-liquid interface rigidity, leading to easier deformation of the interface and earlier (lower u_{gs}) transition of slug to churn. Also, the value of the gas density increases significantly when pressure rises; the heavier gas density increases the gas momentum at the same gas velocity and this could result in the transition of churn to annular flow at lower gas velocity.

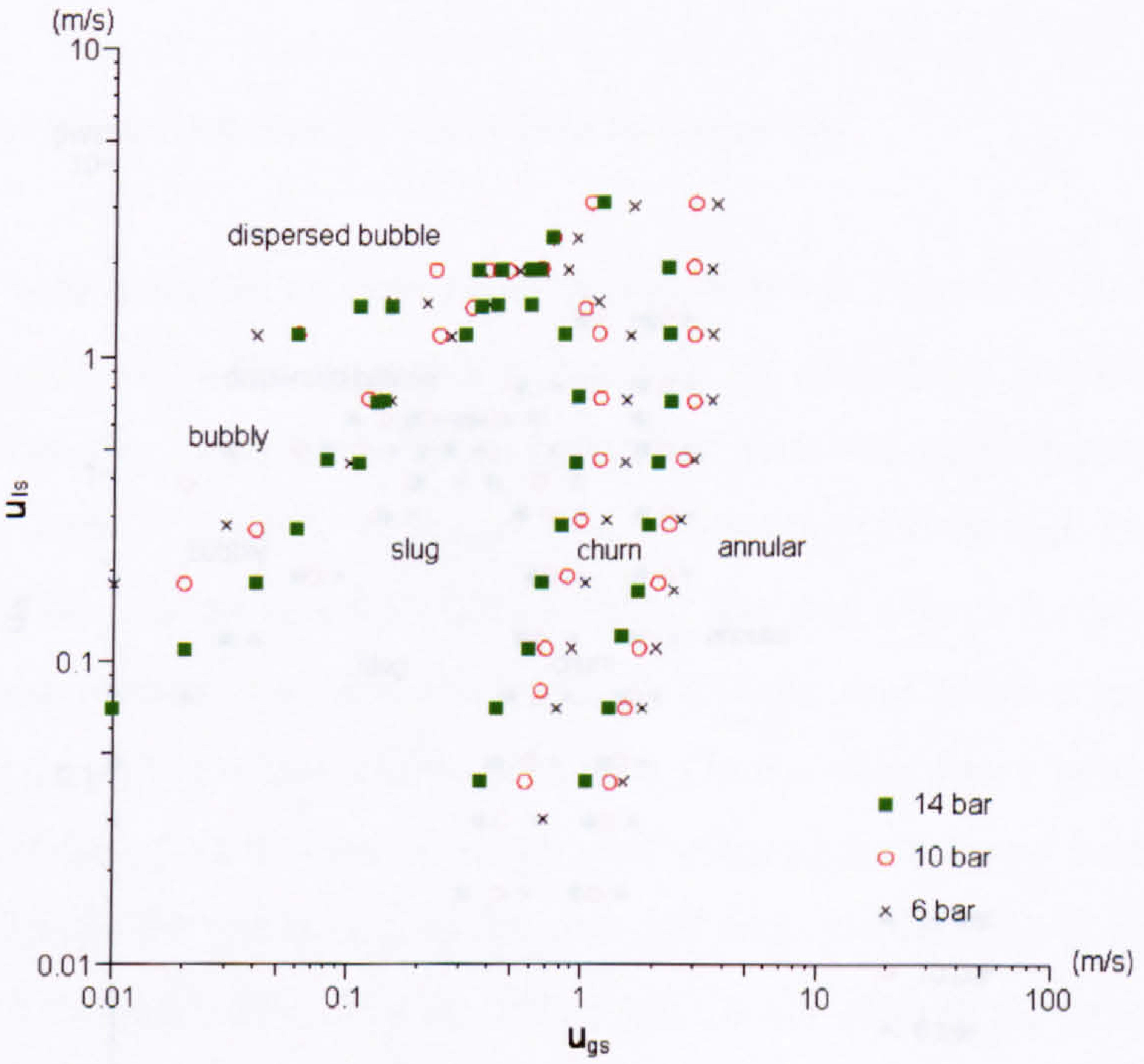

Figure 5.74 Effect of pressure on transition boundaries in the 1.10 mm diameter tube.

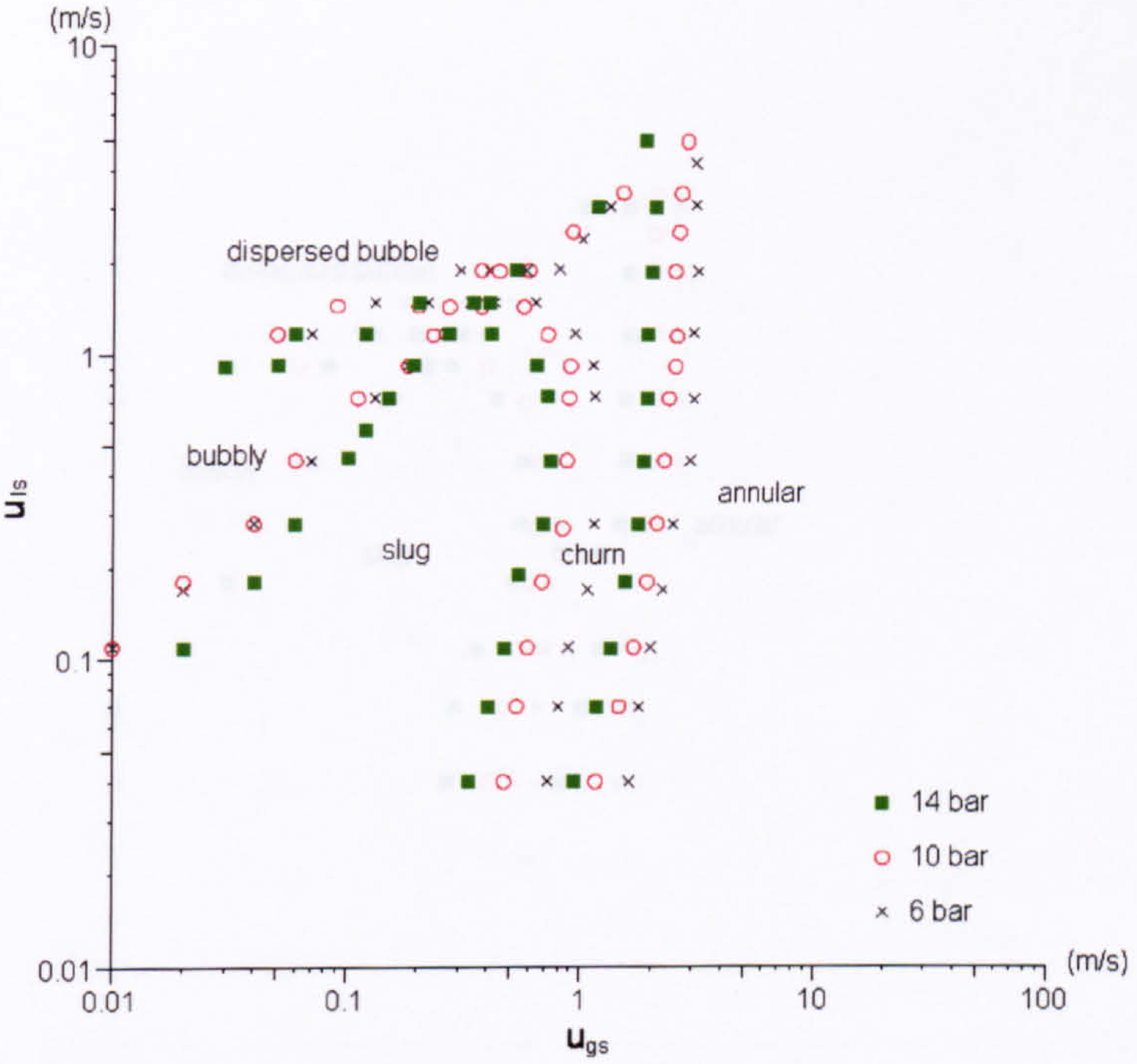

Figure 5.75 Effect of pressure on transition boundaries in the 2.01 mm diameter tube.

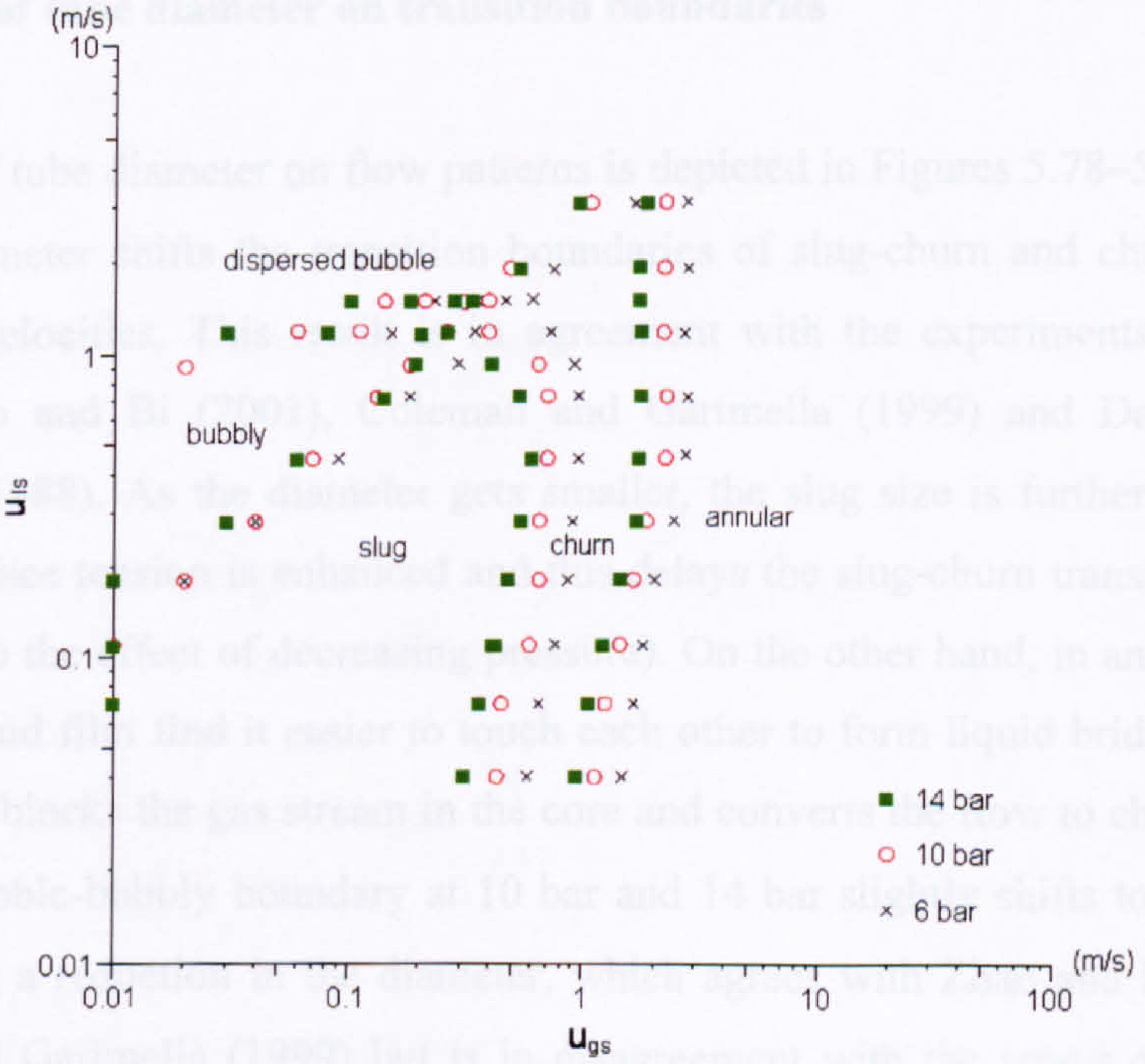

Figure 5.76 Effect of pressure on transition boundaries in the 2.88 mm diameter tube.

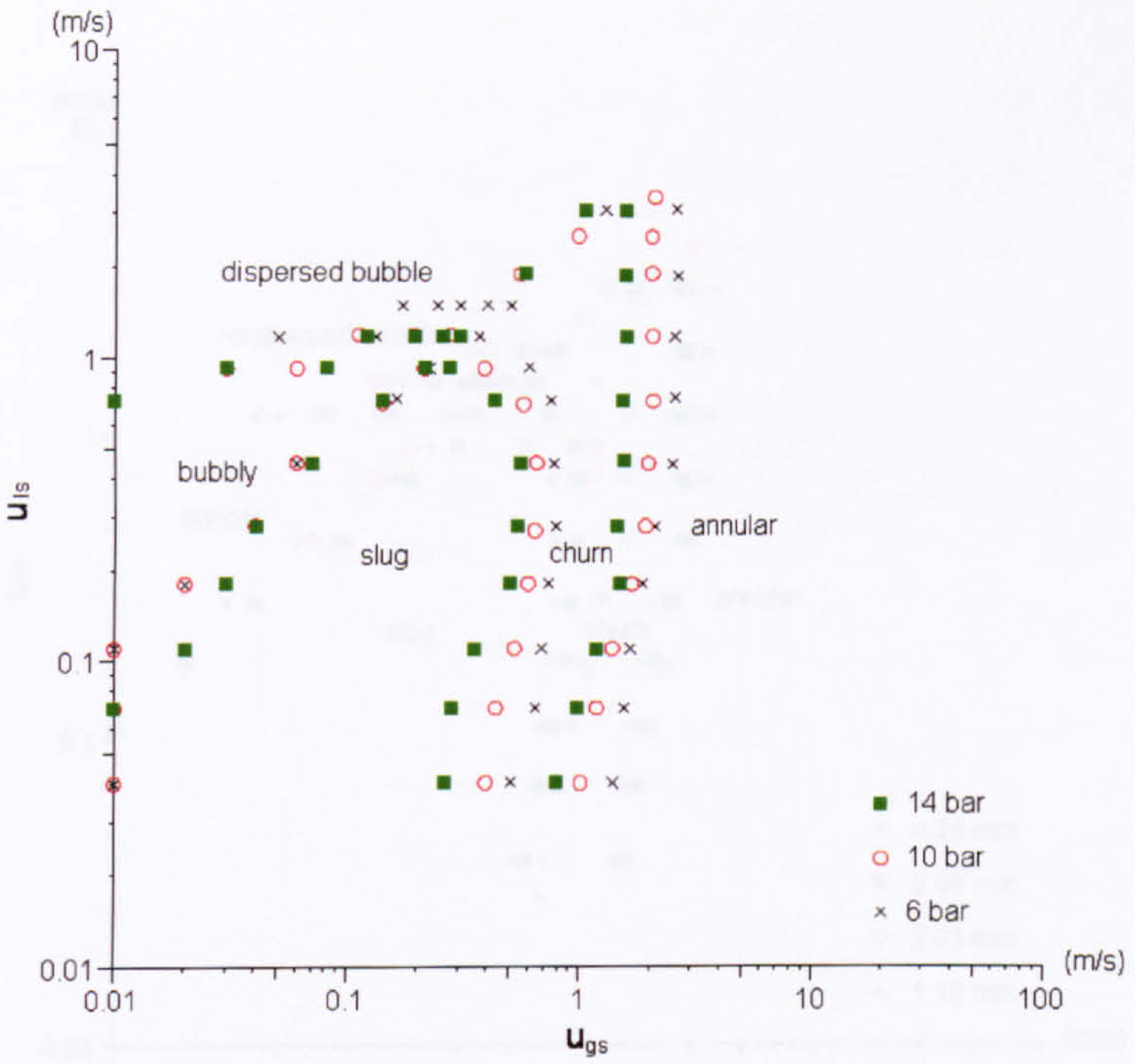

Figure 5.77 Effect of pressure on transition boundaries in the 4.26 mm diameter tube.

5.4.2 Effect of tube diameter on transition boundaries

The effect of tube diameter on flow patterns is depicted in Figures 5.78–5.80. Reducing the tube diameter shifts the transition boundaries of slug-churn and churn-annular to higher gas velocities. This result is in agreement with the experiments of Lin et al. (1998), Zhao and Bi (2001), Coleman and Garimella (1999) and Damianides and Westwater (1988). As the diameter gets smaller, the slug size is further confined; the effect of surface tension is enhanced and this delays the slug-churn transition to higher u_{gs} (similar to the effect of decreasing pressure). On the other hand, in annular flow the waves of liquid film find it easier to touch each other to form liquid bridges in smaller tubes, which blocks the gas stream in the core and converts the flow to churn flow. The dispersed bubble-bubbly boundary at 10 bar and 14 bar slightly shifts to higher liquid velocity with a reduction in the diameter, which agrees with Zhao and Bi (2001) and Coleman and Garimella (1999) but is in disagreement with the report of Damianides and Westwater (1988), see Table 2.8. However, tube diameter apparently has less influence on the dispersed bubble-bubbly boundary at 6 bar than that at 10 and 14 bar pressure. There seems to be no change for these four diameters at the boundaries of dispersed bubble-churn and bubbly-slug flow.

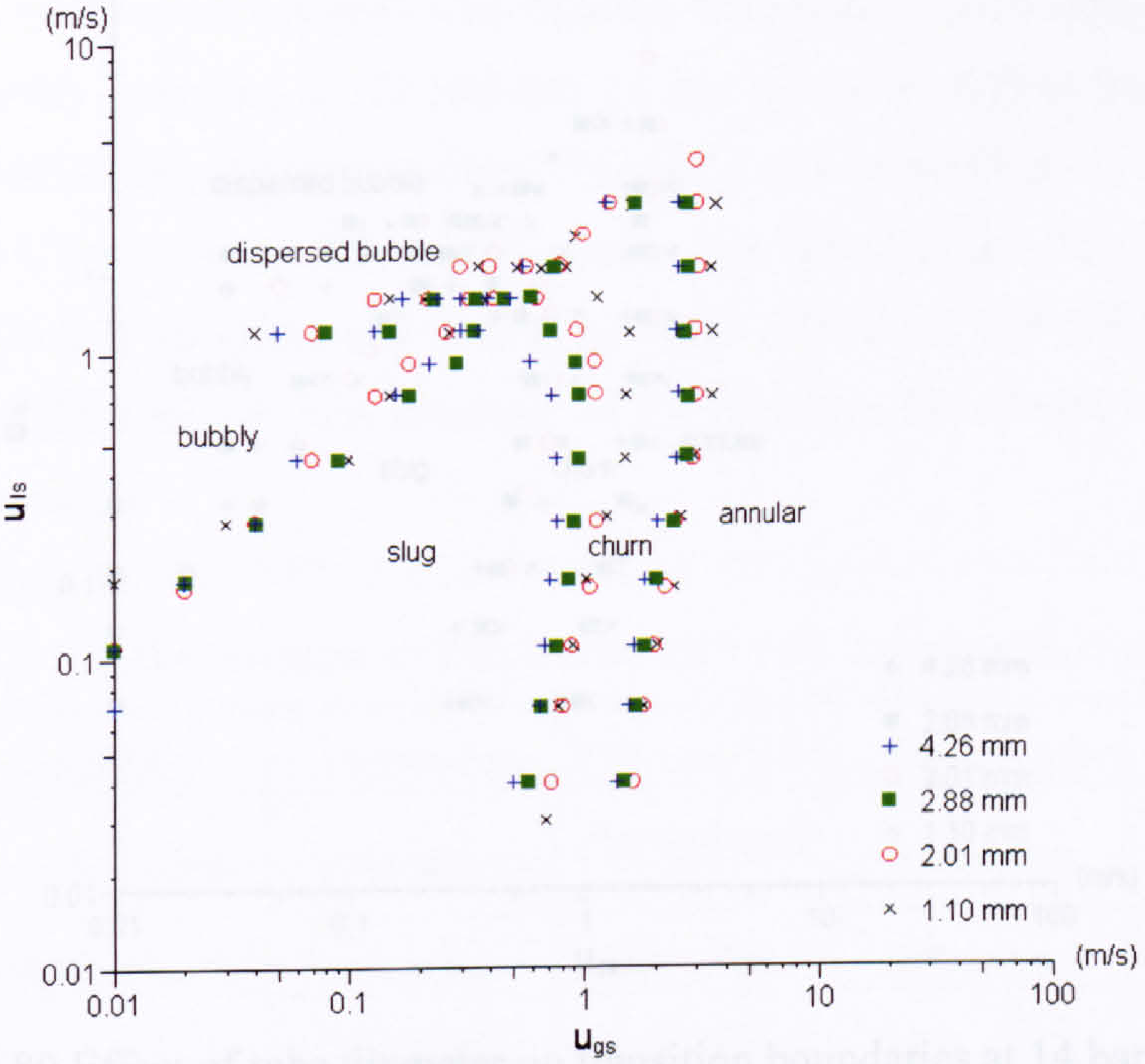

Figure 5.78 Effect of tube diameter on transition boundaries at 6 bar pressure.

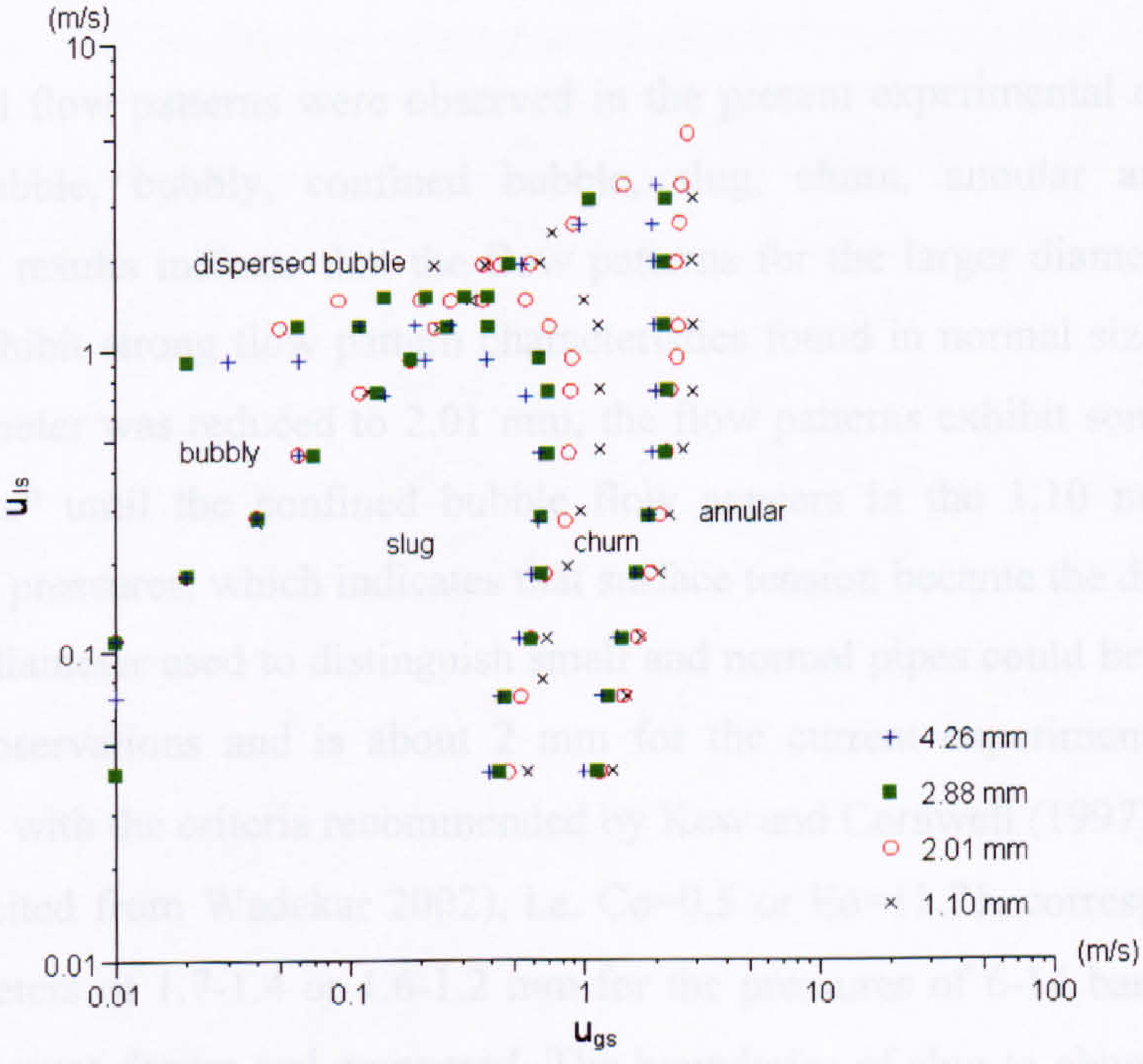

Figure 5.79 Effect of tube diameter on transition boundaries at 10 bar pressure.

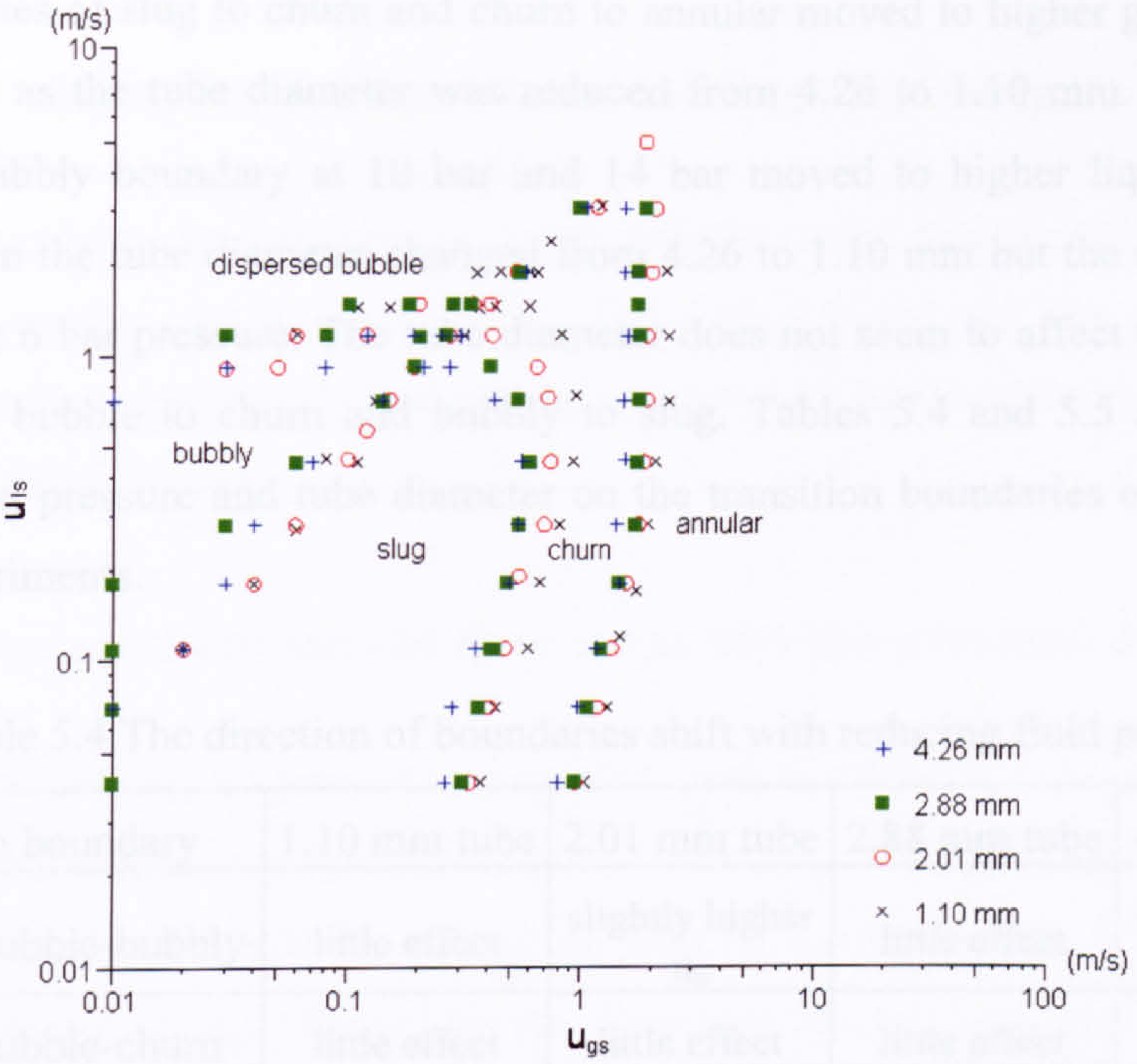

Figure 5.80 Effect of tube diameter on transition boundaries at 14 bar pressure.

5.5 Summary

Seven typical flow patterns were observed in the present experimental conditions, i.e. dispersed bubble, bubbly, confined bubble, slug, churn, annular and mist. The experimental results indicate that the flow patterns for the larger diameters (2.88 and 4.26 mm) exhibit strong flow pattern characteristics found in normal size tubes. When the tube diameter was reduced to 2.01 mm, the flow patterns exhibit some "small tube characteristics" until the confined bubble flow appears in the 1.10 mm tube at all experimental pressures, which indicates that surface tension became the dominant force. The critical diameter used to distinguish small and normal pipes could be deduced from the above observations and is about 2 mm for the current experimental conditions, which agrees with the criteria recommended by Kew and Cornwell (1997) or Hatori and Bretherton (cited from Wadekar 2002), i.e. Co=0.5 or Eö=11.71, corresponding to the critical diameters of 1.7-1.4 or 1.6-1.2 mm for the pressures of 6-14 bar. Twelve flow pattern maps were drawn and compared. The boundaries of slug to churn and churn to annular moved to lower gas velocity when the pressure increases from 6 bar to 14 bar. No or little effect was observed on the dispersed bubble to bubbly, dispersed bubble to churn and bubbly to slug boundaries with pressure changes in the current experiments.

The boundaries of slug to churn and churn to annular moved to higher gas velocity for all pressures as the tube diameter was reduced from 4.26 to 1.10 mm. The dispersed bubble to bubbly boundary at 10 bar and 14 bar moved to higher liquid superficial velocity when the tube diameter changed from 4.26 to 1.10 mm but the effect is not so significant at 6 bar pressure. The tube diameter does not seem to affect the boundaries of dispersed bubble to churn and bubbly to slug. Tables 5.4 and 5.5 summarise the effect of fluid pressure and tube diameter on the transition boundaries observed in the present experiments.

Table 5.4 The direction of boundaries shift with reducing fluid pressure.

Transition boundary	1.10 mm tube	2.01 mm tube	2.88 mm tube	4.26mm tube
Dispersed bubble-bubbly	little effect	slightly higher u_{ls}	little effect	slightly higher u_{ls}
Dispersed bubble-churn	little effect	little effect	little effect	little effect
Bubbly-slug	little effect	little effect	little effect	little effect
Slug-churn	higher u_{gs}	higher u_{gs}	higher u_{gs}	higher u_{gs}
Churn-annular	higher u_{gs}	higher u_{gs}	higher u_{gs}	higher u_{gs}

Table 5.5 The direction of boundaries shift with reducing tube diameter.

Transition boundary	6 bar pressure	10 bar pressure	14 bar pressure
Dispersed bubble-bubbly	slightly higher u_{ls}	higher u_{ls}	higher u_{ls}
Dispersed bubble-churn	little effect	little effect	little effect
Bubbly-slug	little effect	little effect	little effect
Slug-churn	higher u_{gs}	higher u_{gs}	higher u_{gs}
Churn-annular	higher u_{gs}	higher u_{gs}	higher u_{gs}

Chapter 6 Experimental Result Analysis

The current experimental data are compared with the earlier results such as flow maps, models and correlations in this Chapter. The data obtained are also mapped using different coordinate systems to find the right parameters to evaluate the effect of tube diameter and fluid pressure.

6.1 Comparison between the flow maps and the previous data

Flow maps are not only a common tool for flow pattern studies but also the first step to develop general correlations for flow regime prediction. It is significant and necessary to validate the present results by comparing with the earlier studies. It is well known that flow maps are greatly affected by the experimental conditions such as fluid type, flow parameters and tube diameter. Therefore, all compared flow maps should be based on the same or similar conditions. However, most of the earlier studies used air-water and worked at atmospheric conditions. In fact, to the best of the author's knowledge, none of the existing flow maps match entirely the present experimental conditions. As a result, it is not surprising that great discrepancies are shown in the comparisons. In addition, the subjectivity in flow pattern observation will inevitably affect the compared results.

Yang and Shieh (2001) sketched R134a flow maps based on their experiments in 2.0 and 3.0 mm horizontal tubes. The experimental pressure and temperature were 7.7 bar and 30 °C respectively. Yang and Shieh followed the traditional classifications used in small horizontal tubes and reported five flow regimes: bubble, dispersed, plug, slug and annular flow. What they call bubble corresponds to the dispersed bubble flow in the current study, see Figure 2.2 in Chapter 2. Overall the agreement between the maps obtained in the present experiments and those from Yang and Shieh (2001) is poor due to the different flow orientation and classifications, see the comparisons in Figures 6.1-6.4. For example, the dispersed flow in the Yang and Shieh's flow maps does not have an equivalent flow pattern in the current flow maps. However, on close observation the dispersed bubble and bubbly/slug flow observed in the present experiments corresponds to the bubble and plug flow reported by Yang and Shieh (2001) respectively. The boundary of dispersed bubble to bubbly flow obtained in the present experiments roughly matches with the boundary of bubble to plug flow in the Yang and Shieh's flow map. Also for the boundary of intermittent flow (include the slug/churn flow in the current study or the plug/slug flow in Yang and Shieh's study) to annular flow, is in good agreement considering the difference of experimental parameters and the effect of subjectivity. Theoretically, the effect of gravity is not so important in these two transition boundaries. Therefore, the transition boundaries at dispersed bubble and annular flow are not so sensitive to the flow orientation.

The present experimental data are also compared with the air-water upward vertical flow for the 4.0 mm tube from Barnea et al. (1983), the 2.05 mm tube from Mishima and Hibiki (1996) and the 1.0 mm tube from Fukano and Kariyasaki (1992). The disagreement is quite obvious except for the dispersed bubble-intermittent transition boundary, see Figures 6.5-6.7. The above conclusion can be predicted by the "Unified Model" (Taitel 1990). The transition boundary of dispersed bubble and intermittent is less affected by fluid properties as demonstrated in Figure 6.8, which is plotted using the "Unified Model".

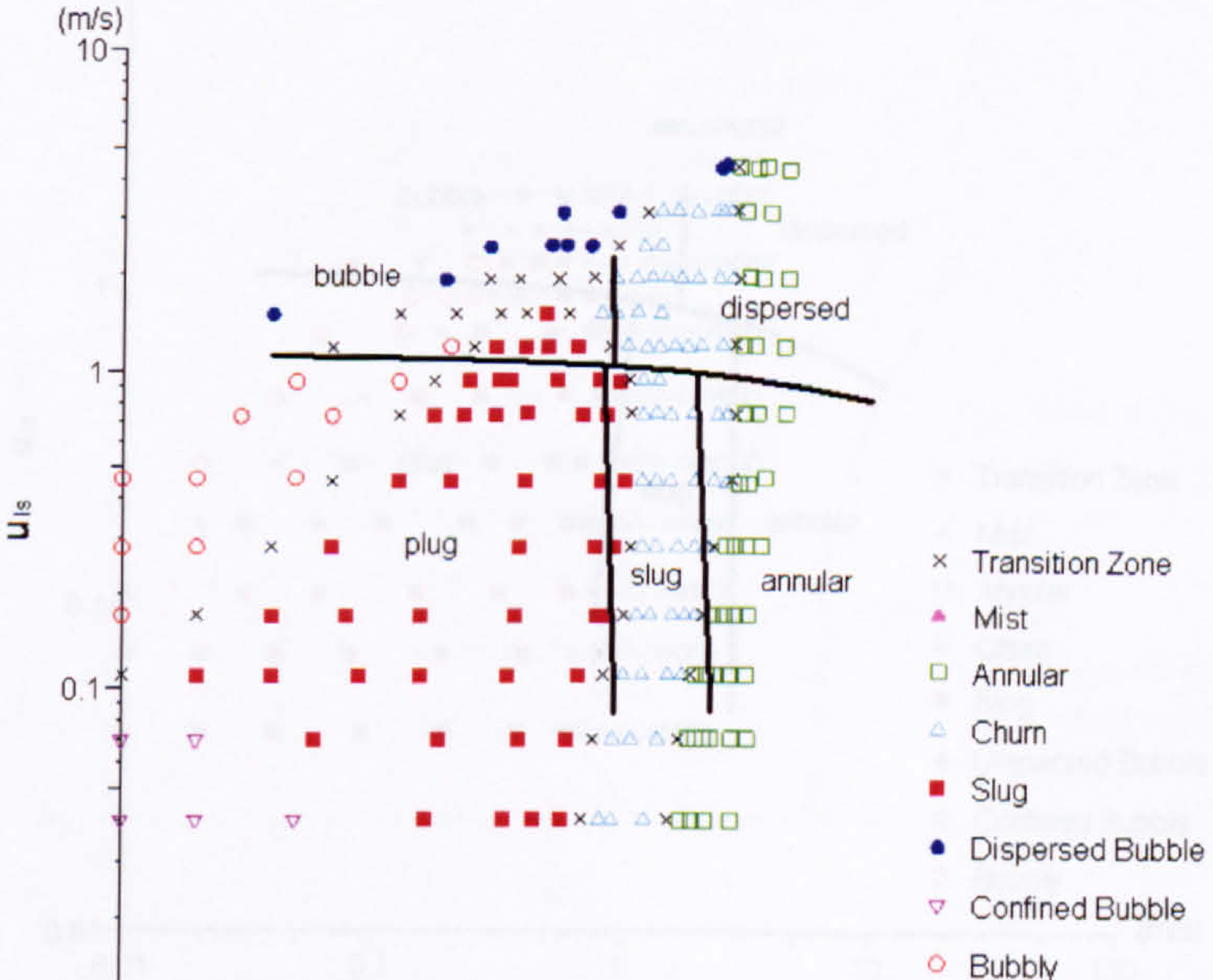

Figure 6.1 Comparison of R134a flow maps for the 2.01 mm vertical tube at 6 bar with Yang and Shieh (2001) for the 2.0 mm horizontal tube at 7.7 bar (in solid line).

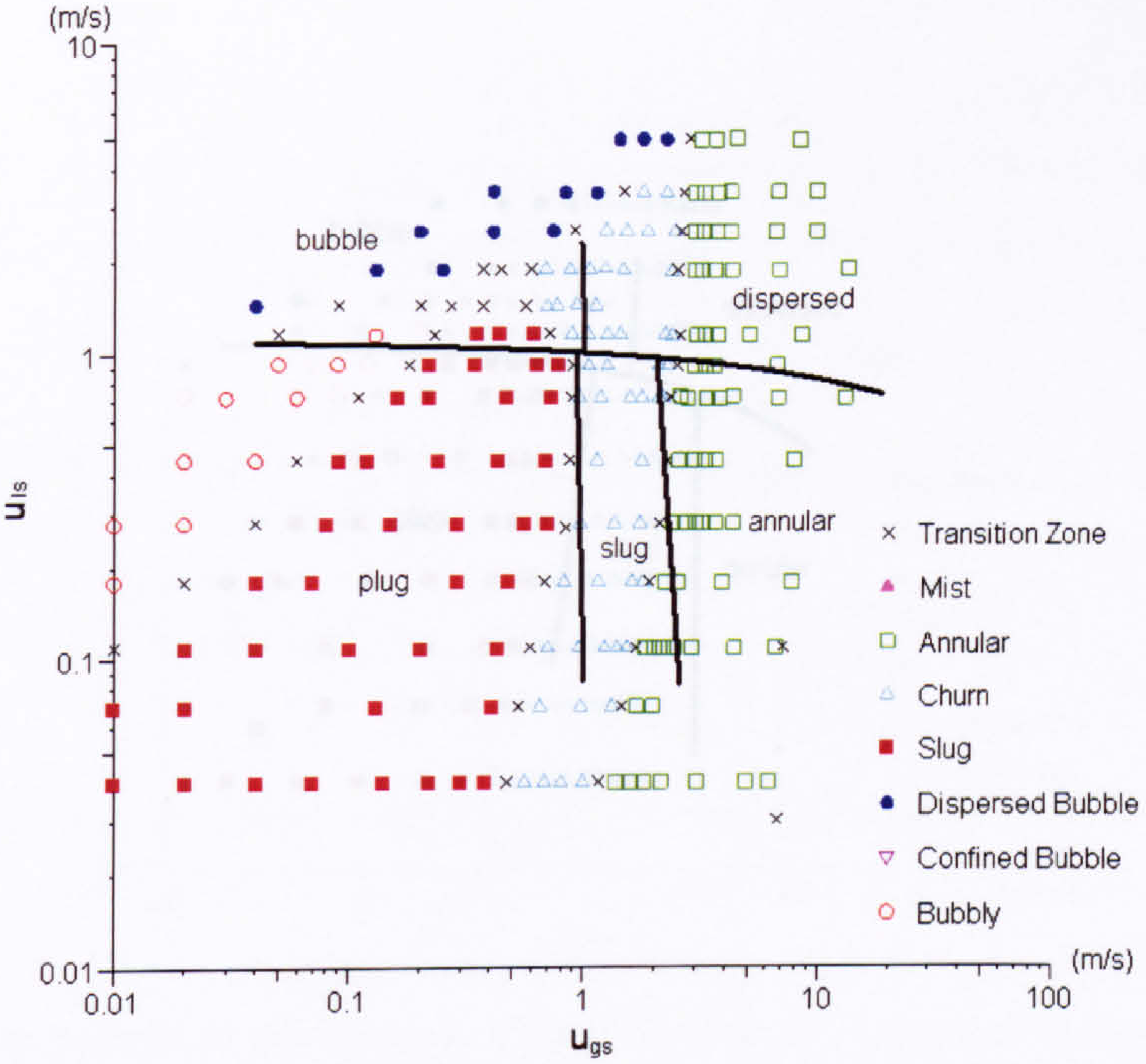

Figure 6.2 Comparison of R134a flow maps for the 2.01 mm vertical tube at 10 bar with Yang and Shieh (2001) for the 2.0 mm horizontal tube at 7.7 bar (in solid line).

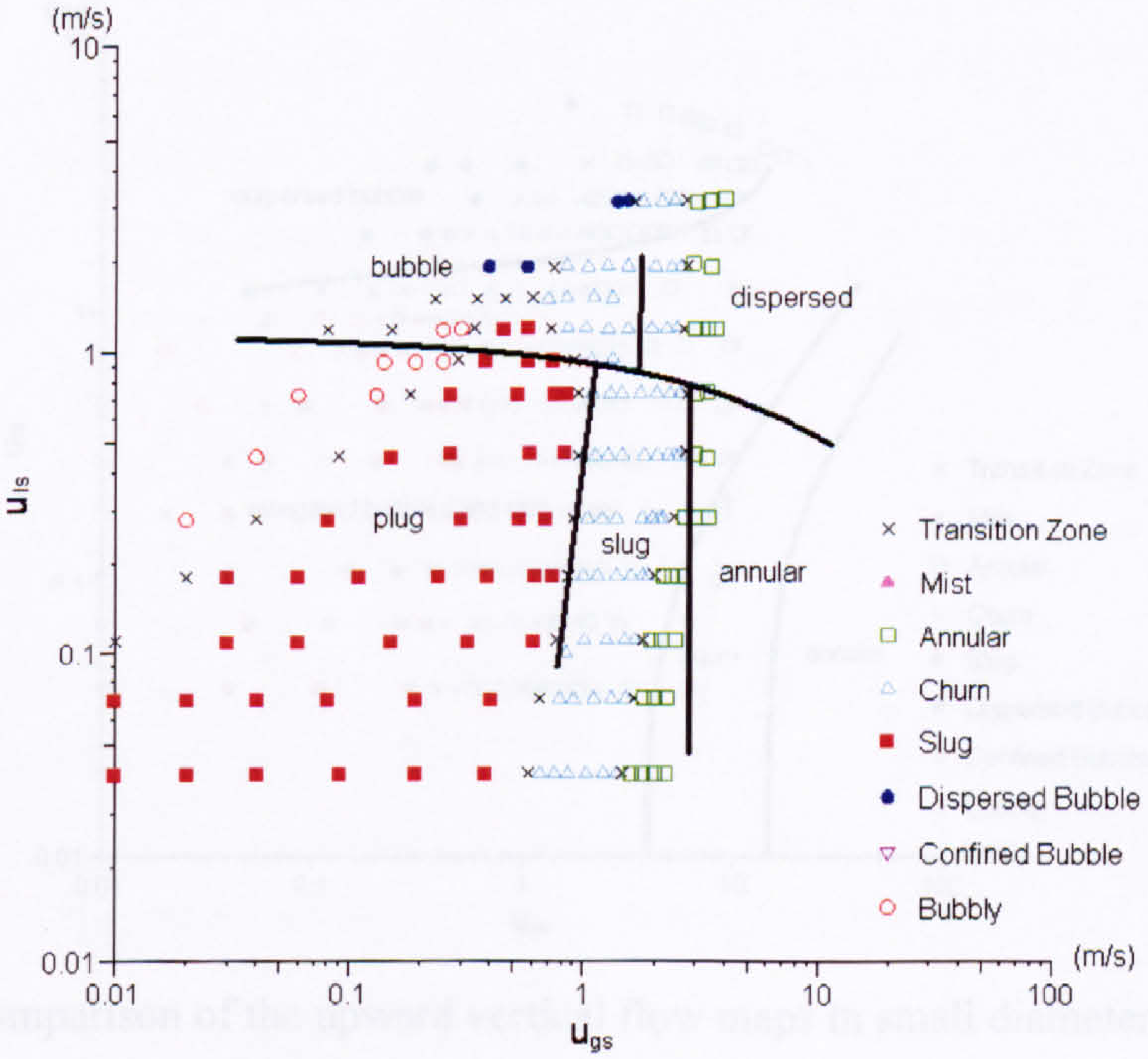

Figure 6.3 Comparison of R134a flow maps for the 2.88 mm vertical tube at 6 bar with Yang and Shieh (2001) for the 3.0 mm horizontal tube at 7.7 bar (in solid line).

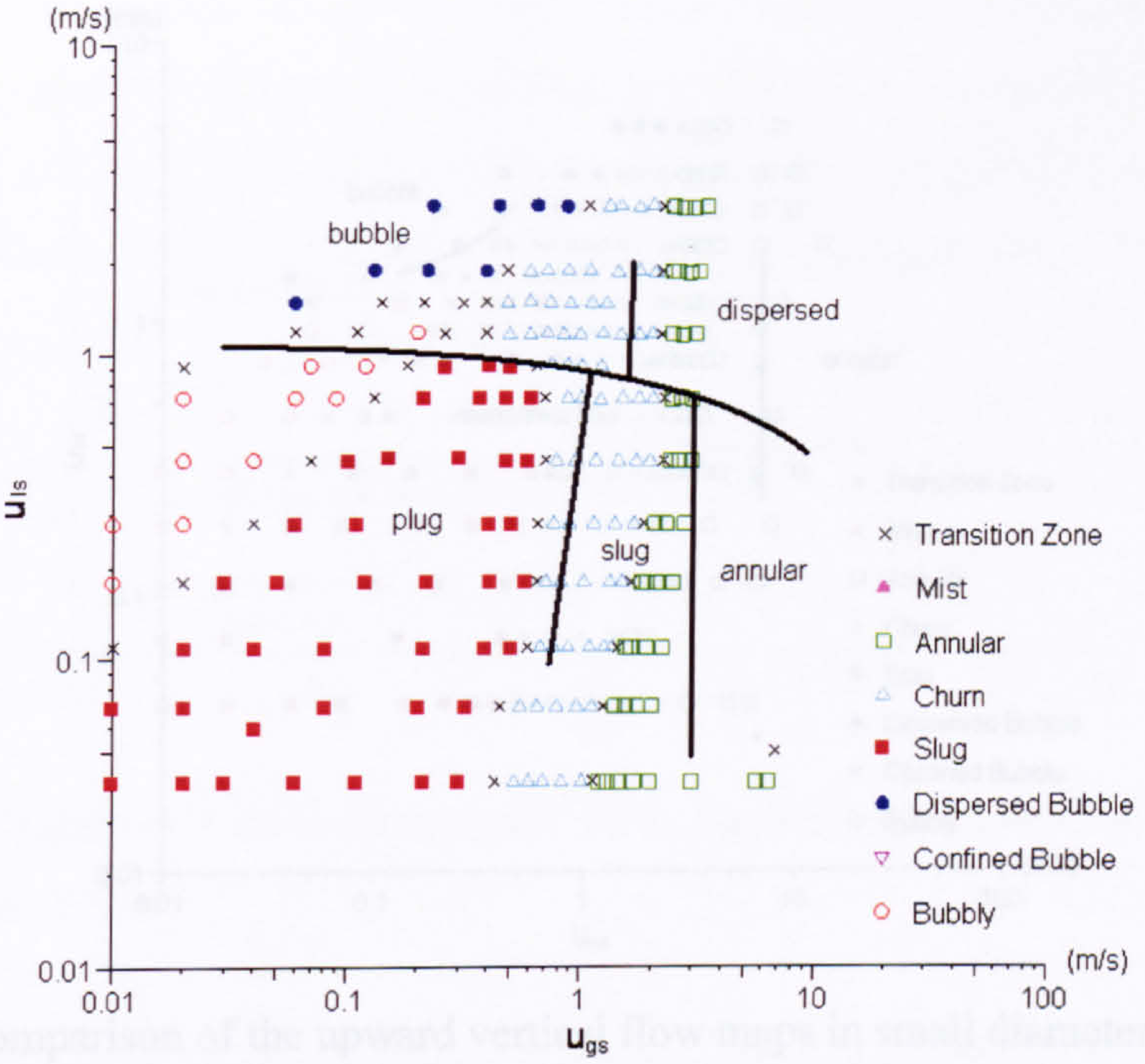

Figure 6.4 Comparison of R134a flow maps for the 2.88 mm vertical tube at 10 bar with Yang and Shieh (2001) for the 3.0 mm horizontal tube at 7.7 bar (in solid line).

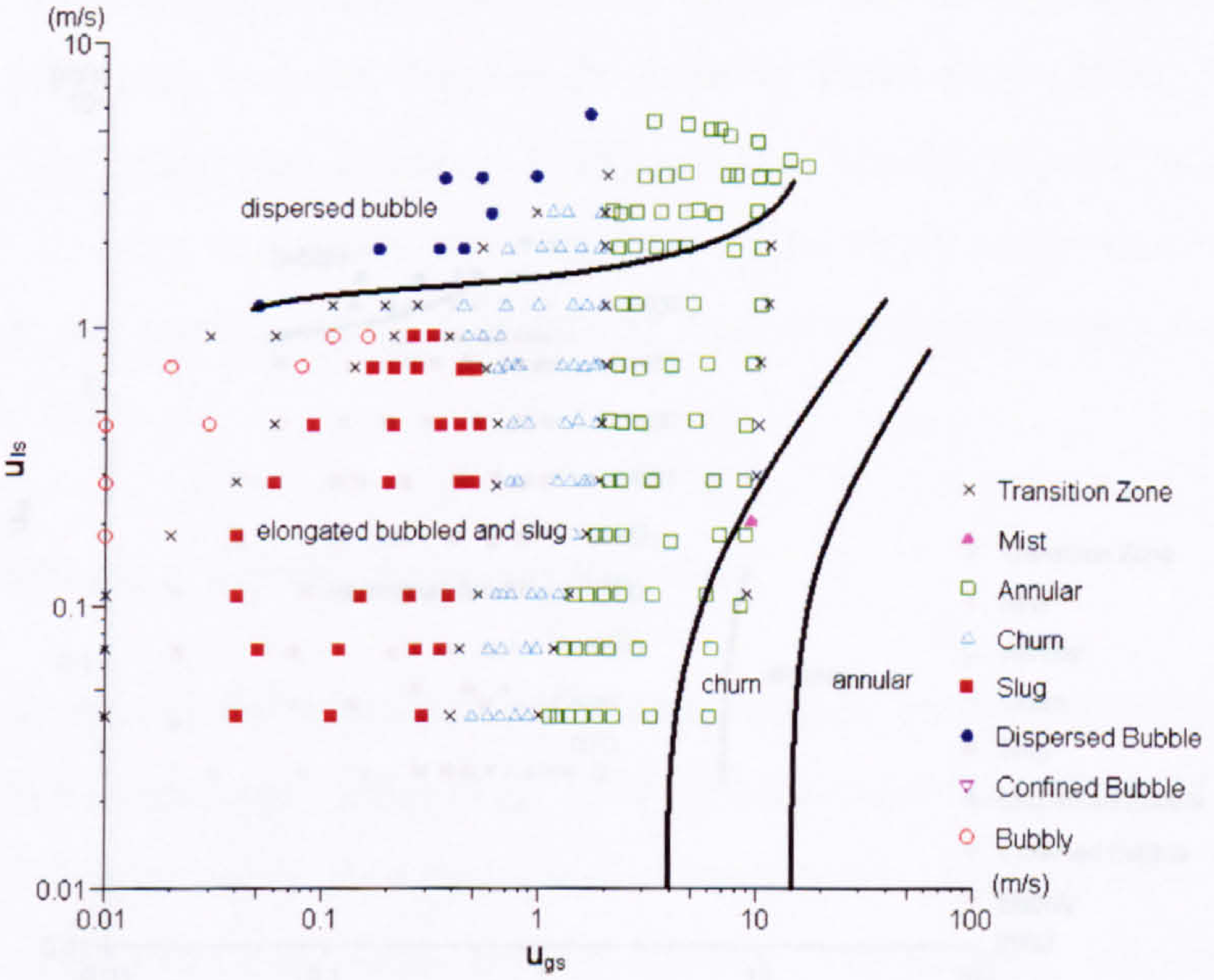

Figure 6.5 Comparison of the upward vertical flow maps in small diameter tubes (1). Symbols: R134a flow in the 4.26 mm tube at 10 bar from the present experiments. Solid lines: air-water flow in the 4.0 mm tube at 1 bar 25 ºC from Barnea et al. (1983).

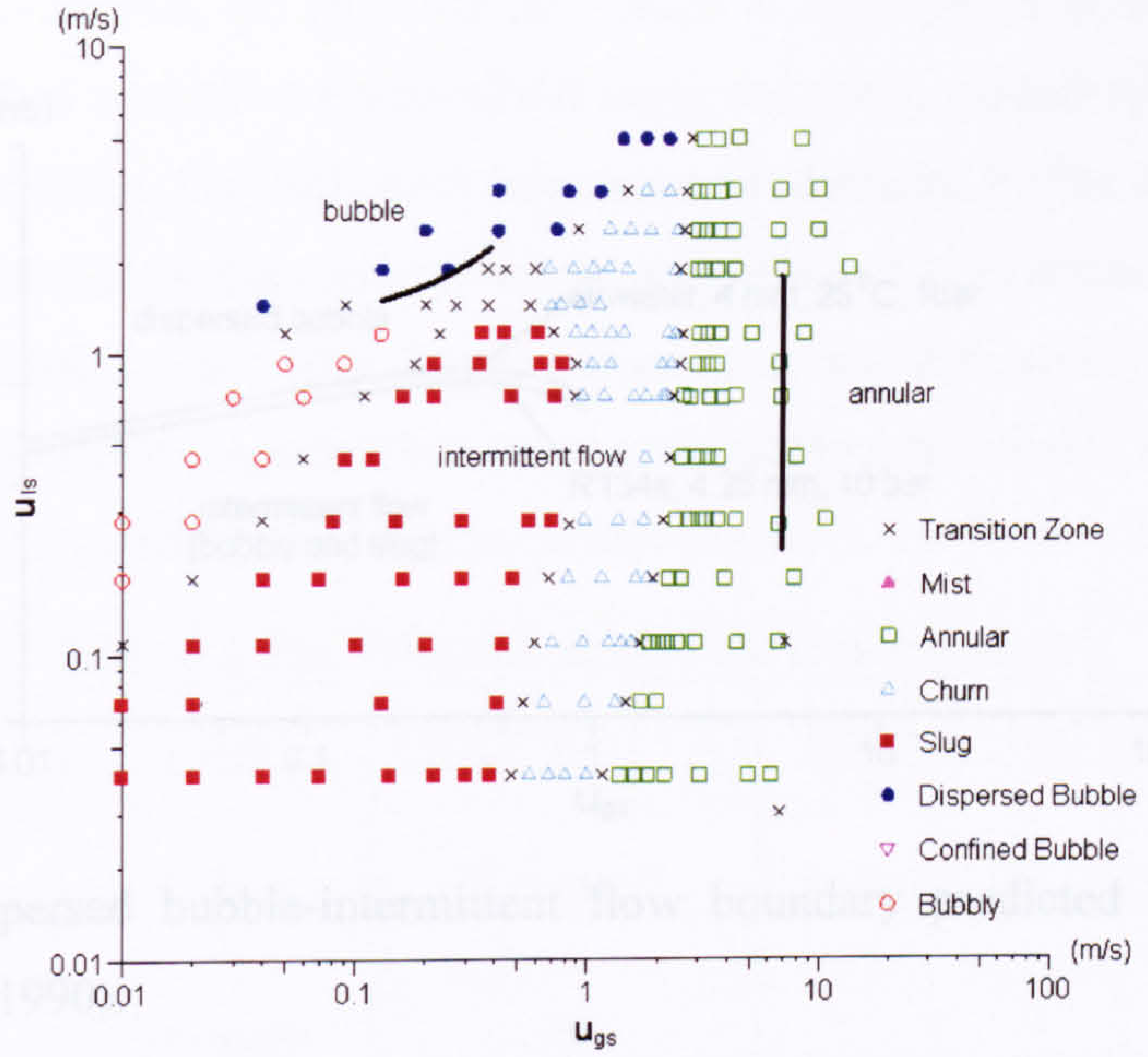

Figure 6.6 Comparison of the upward vertical flow maps in small diameter tubes (2). Symbols: R134a flow in the 2.01 mm tube at 10 bar from the present experiments. Solid lines: air-water flow in the 2.05 mm tube at atmospheric conditions from Mishima and Hibiki (1996).

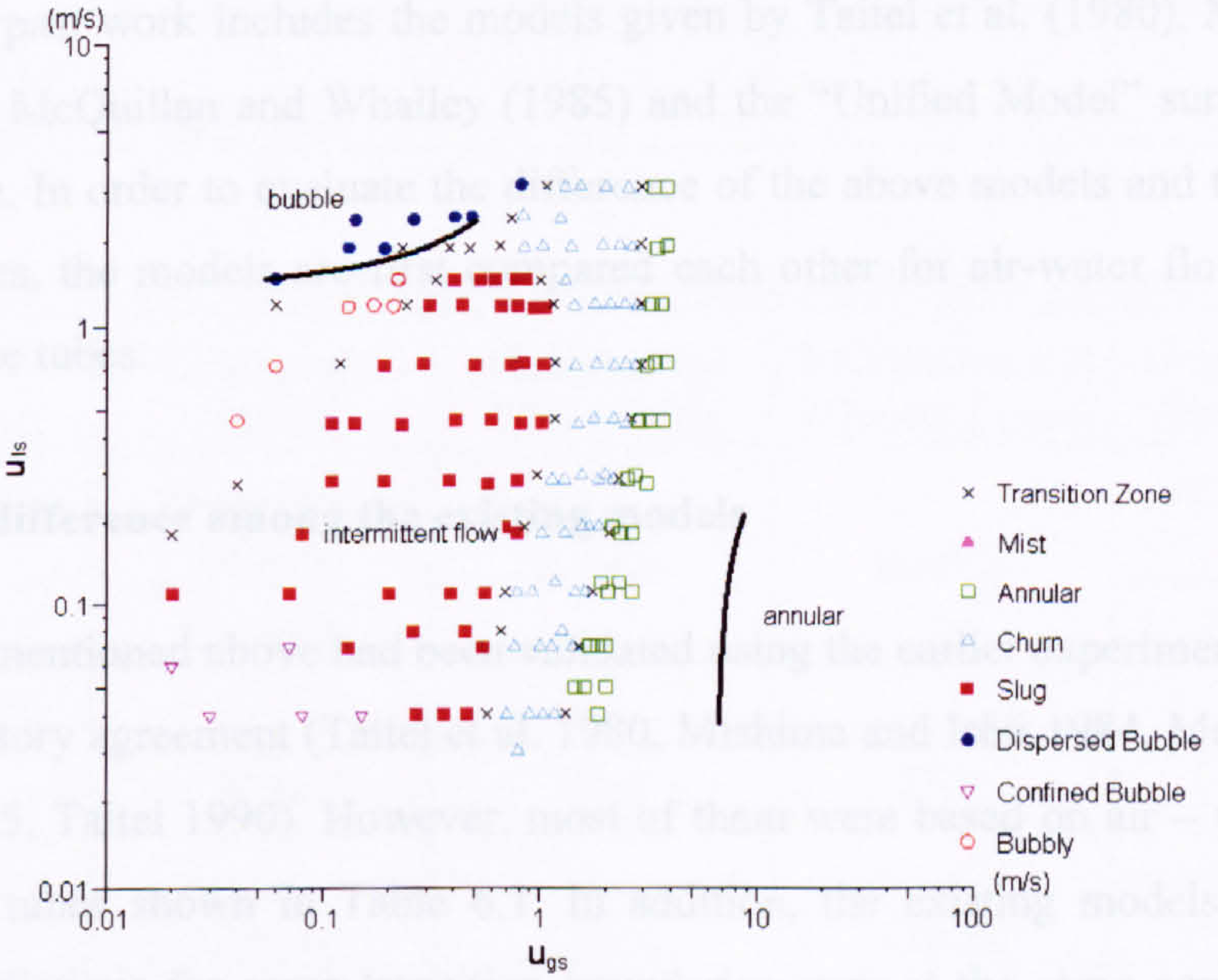

Figure 6.7 Comparison of the upward vertical flow maps in small diameter tubes (3). Symbols: R134a flow in the 1.10 mm tube at 10 bar from the present experiments. Solid lines: air-water flow in the 1.0 mm tube at atmospheric conditions from Fukano and Kariyasaki (1993).

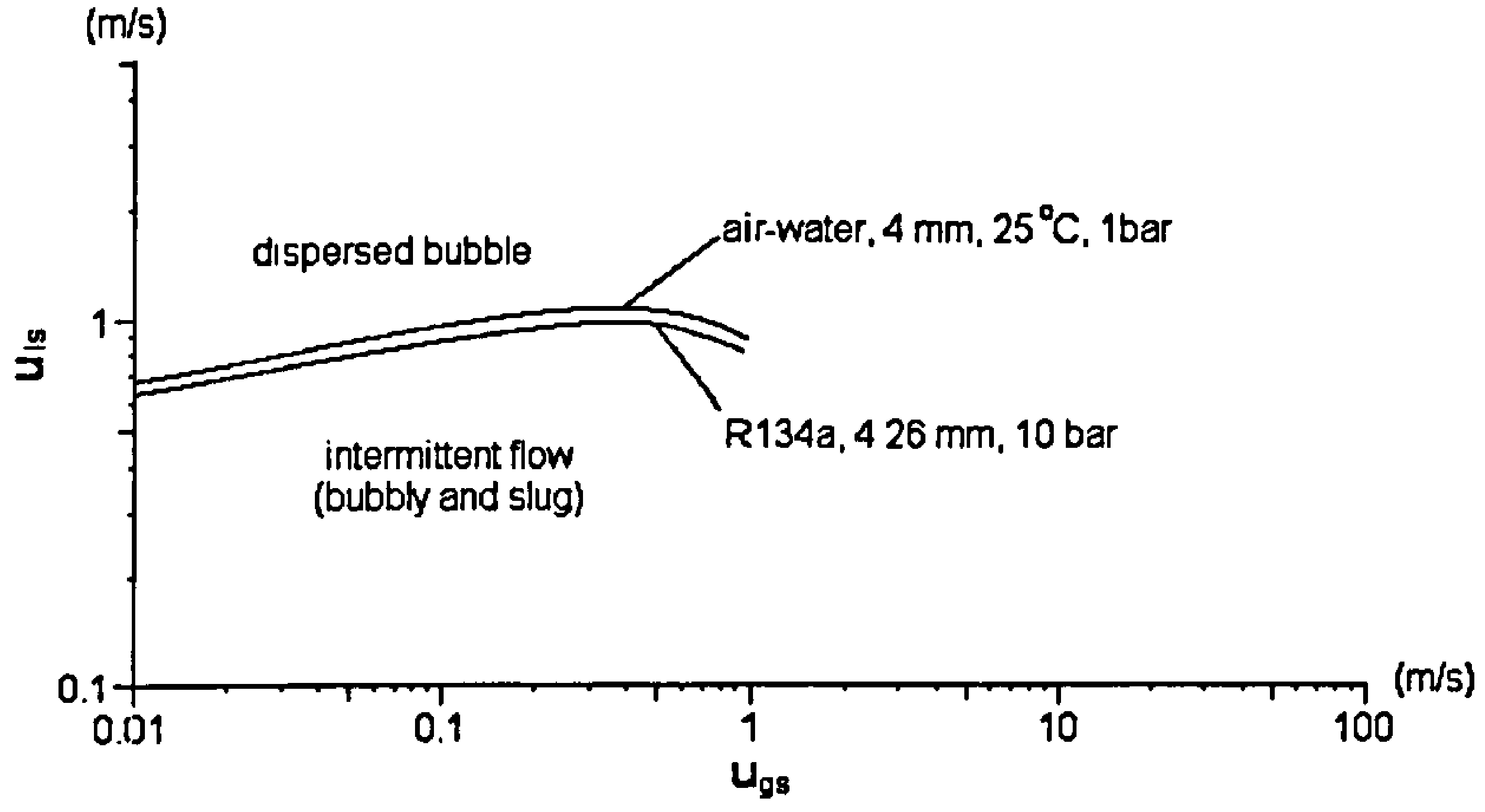

Figure 6.8 Dispersed bubble-intermittent flow boundary predicted by the "Unified Model" (Taitel 1990).

6.2 Applicability of the existing models and correlations

Twelve flow pattern maps were generated based on all the results obtained for the 1.10, 2.01, 2.88 and 4.26 mm tubes at 6, 10 and 14 bar pressures. The flow pattern maps are compared with the existing models for vertical upward flow in normal size tubes in this section. The past work includes the models given by Taitel et al. (1980), Mishima and Ishii (1984), McQuillan and Whalley (1985) and the "Unified Model" summarized by Taitel (1990). In order to evaluate the difference of the above models and their validity in small tubes, the models are first compared each other for air-water flow in normal and small size tubes.

6.2.1 The difference among the existing models

The models mentioned above had been validated using the earlier experimental data and gave satisfactory agreement (Taitel et al. 1980, Mishima and Ishii 1984, McQuillan and Whalley 1985, Taitel 1990). However, most of them were based on air – water and in normal size tubes shown in Table 6.1. In addition, the existing models might give different predictions for some transition boundaries even at the same conditions. The discrepancies are partially due to the subjectivities of the observations, such as the identifications and classifications of the flow patterns. However, the major discrepancies are attributed to the difference of the transition mechanisms on which they are based. In this section, the air-water flow maps at atmospheric conditions in the 1.0, 5.0, 25.4 and 101.6 mm tubes are predicted using the above models and compared with each other. In addition, the equivalent flow patterns identified by the above researchers are listed in Table 6.2 for the convenience of comparison. For example, the bubbly flow in the study of Mishima and Ishii (1984) is equivalent to the bubble flow in McQuillan and Whalley (1985), the dispersed bubble and bubble flow in Taitel et al. (1980) and the dispersed bubble and bubbly flow in the current study.

Table 6.1 The validated rang of the existing models.

Model	Fluid	Temperature (°C)	Pressure (bar)	Diameter (mm)
Present Experiments	R134a	Saturated	6, 10, 14	1.10, 2.01, 2.88, 4.26
Taitel et al. (1980)	Air-water	25	1	25, 51
Mishima and Ishii (1984)	Air-water	25	1	25, 51
	Steam-water	Saturated	34, 69	10, 13
McQuillan and Whalley (1985)	Air-water	25	1	51, 92
	Steam-water	Saturated	34.5, 69	10
	R11	Saturated	6.5	18
	R113	Saturated	4	25
Unified Model (Taitel, 1990)	Air-water	25	1	51

Table 6.2 The equivalent flow patterns from the different researchers.

Present Experiments	Taitel et al. (1980)	Mishima and Ishii (1984)	McQuillan and Whalley (1985)	Unified Model (Taitel, 1990)
Dispersed bubble	Dispersed bubble	Bubbly	Bubble	Dispersed bubble
Bubbly	Bubble*			Bubble*
Confined bubble	Slug	Slug	Plug	Slug
Slug				
Churn	Churn	Churn	Churn	Churn
Annular	Annular	Annular	Annular	Annular
Mist				

*Note: bubble flow in the models of Taitel et al. (1980) and "Unified Model" (Taitel, 1990) will develop to slug flow finally when the tube diameter is smaller than 51 mm for air-water at atmospheric conditions (1 bar, 25 °C).

Four separate flow pattern maps predicted by the existing models from Taitel et al. (1980), Mishima and Ishii (1984), McQuillan and Whalley (1985) and the "Unified Model" summarized by Taitel (1990) are depicted in Figure 6.9 in order to show the transition boundaries clearly. Their comparisons are sketched in Figures 6.10-6.14 to illustrate the agreement and divergence at the different conditions. As expected the models mentioned above can reach agreement on some boundaries but not for all. For example, the bubbly-slug boundary given by Mishima and Ishii (1984) is quite close to the bubble-plug boundary predicted by McQuillan and Whalley (1985) at all considered conditions, i.e. air-water or R134a flow and in normal or small tubes. Sometimes the different models can give similar transition boundary only at a particular condition, see the churn-annular boundaries in figure 6.11 for the air-water flow in the 25.4 mm tube at atmospheric conditions. However, the disagreement on many boundaries is obvious. For instant, there is always disagreement on the location of boundary of slug (or plug) to churn. In addition, the models based on air-water flow in normal size tubes may produce a self-contradicting prediction when applied to a new condition. The typical case is that the "Unified Model" creates a region where the slug-churn boundary crosses with the churn-annular boundary when it is used in air-water flow in small tubes or R134a flow in normal tubes, i.e. the shaded zone in Figures 6.13 and 6.14. Therefore, there are very serious limitations on the application of these models.

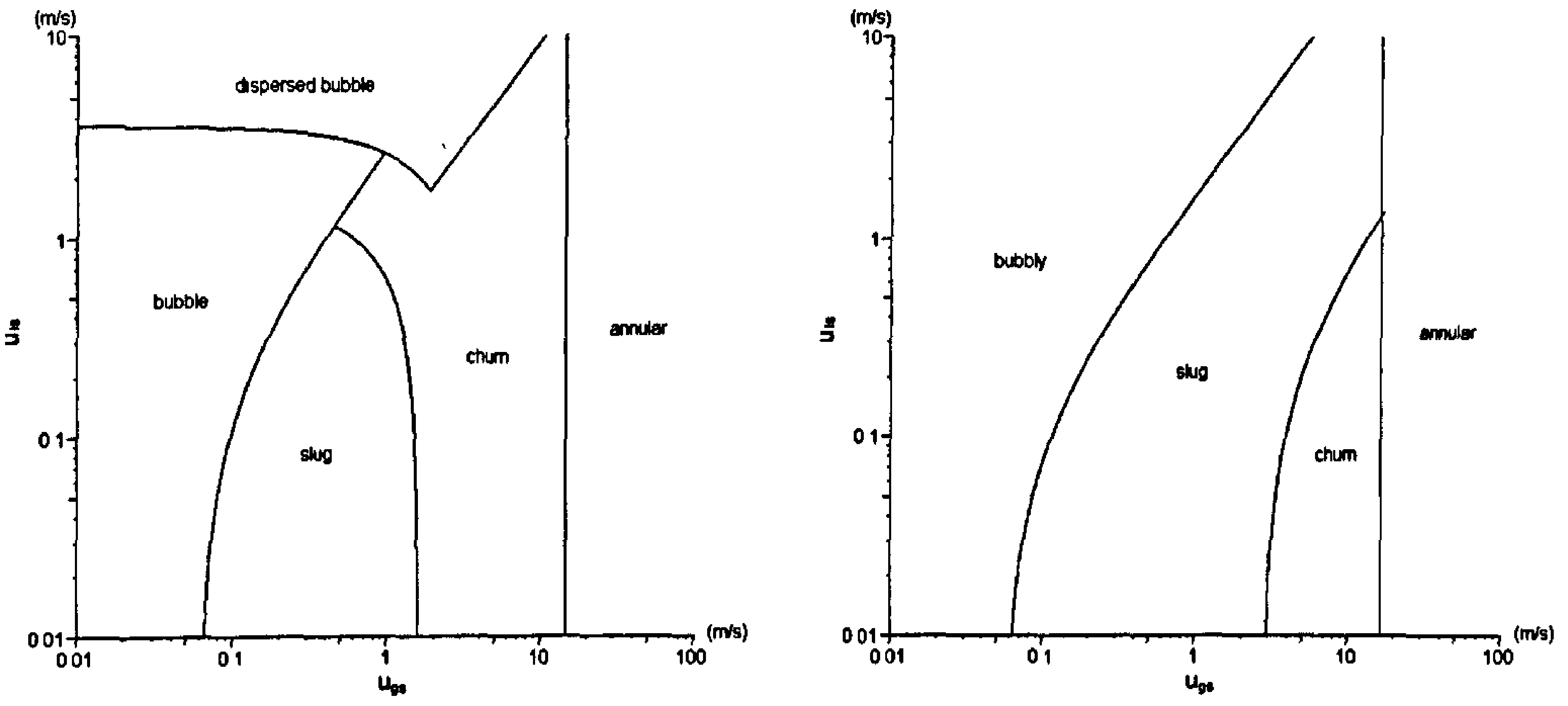

(a) Taitel et al. (1980) (b) Mishima and Ishii (1984)

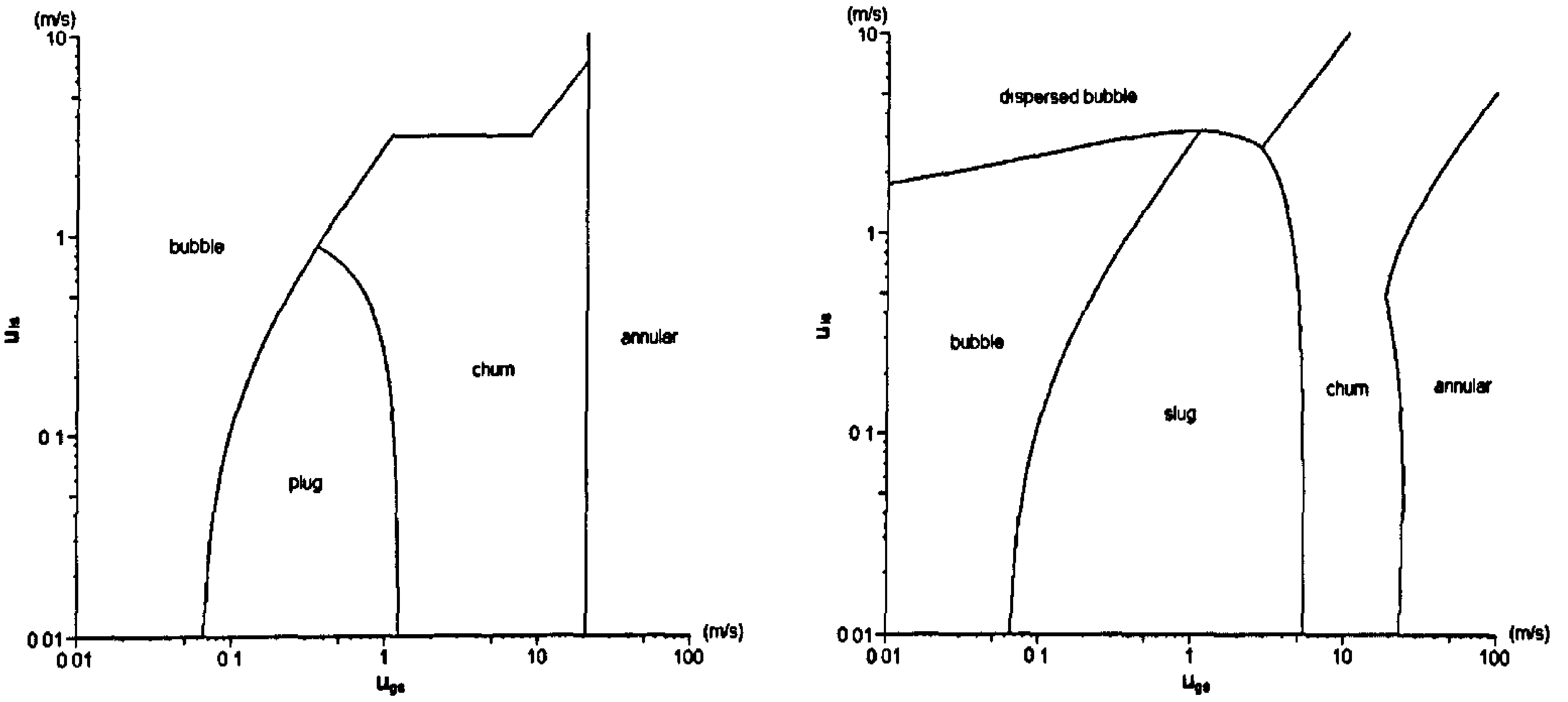

(c) McQuillan and Whalley (1985) (d) Unified Model, Taitel (1990)

Figure 6.9 Flow pattern maps predicted by the exiting models for air-water flow in the 51 mm tube at atmospheric conditions (1 bar, 25 °C).

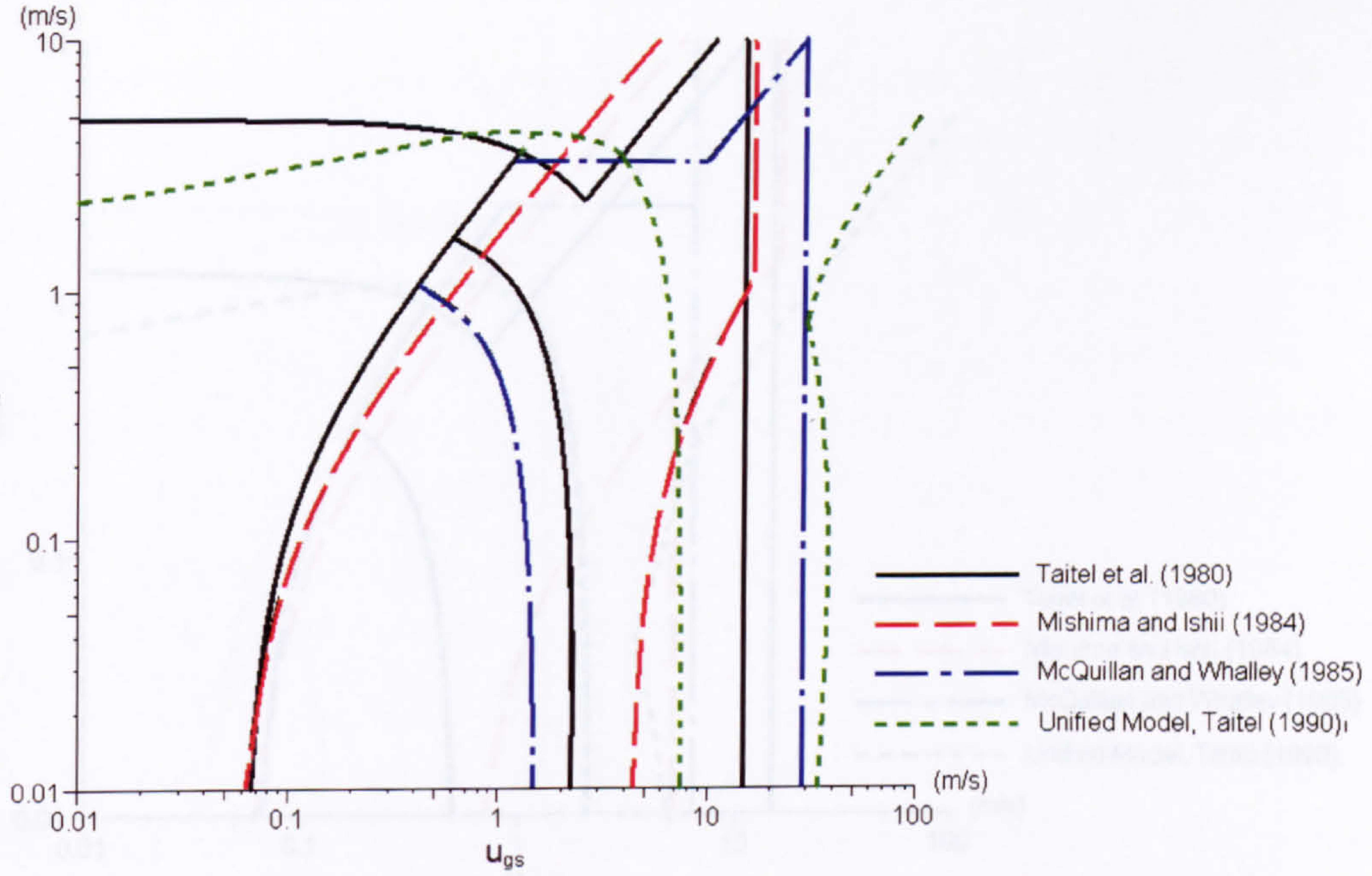

Figure 6.10 Comparison of the different models for the air-water flow maps in the 101.6 mm tube at atmospheric conditions (1 bar, 25 ºC).

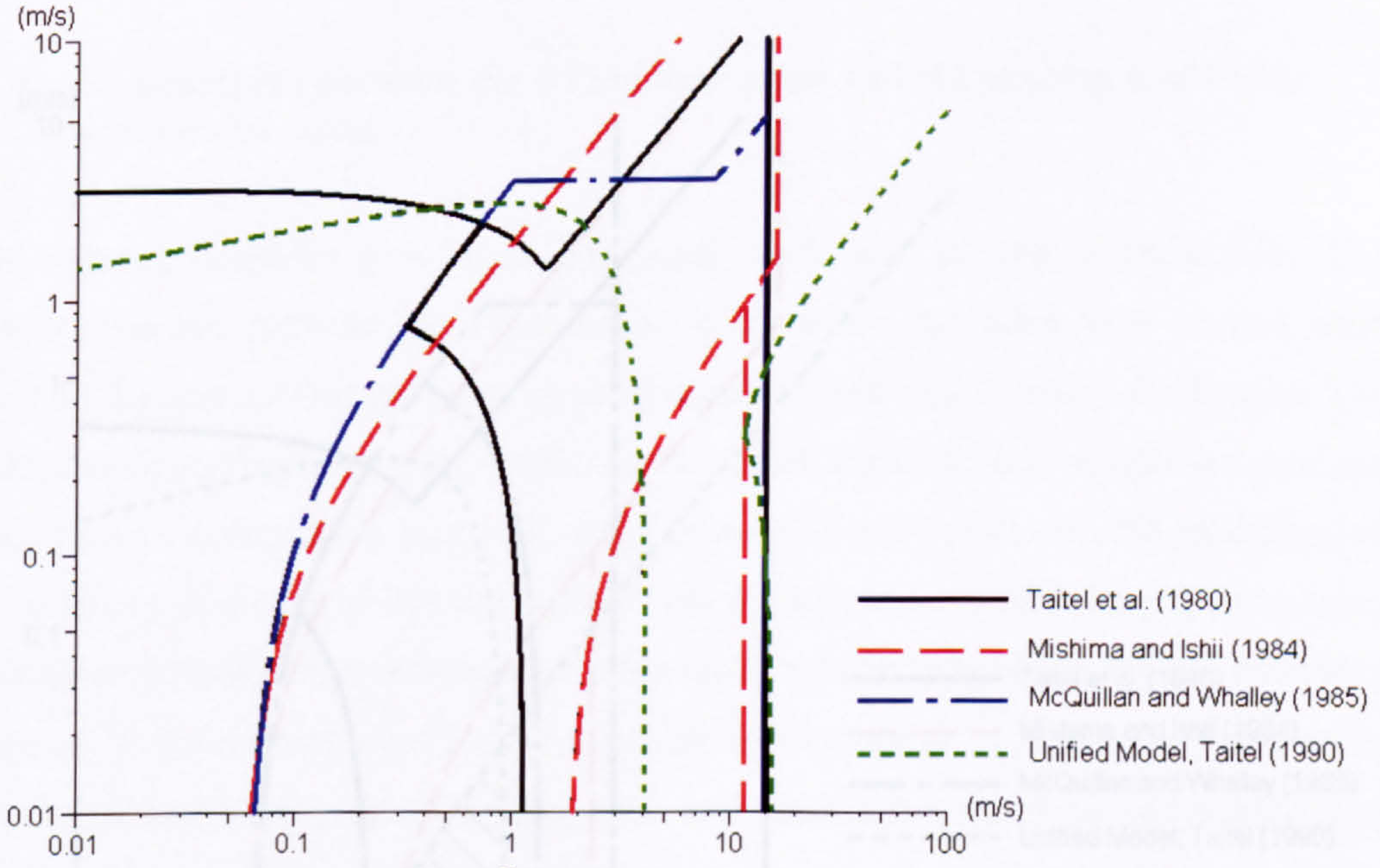

Figure 6.11 Comparison of the different models for the air-water flow maps in the 25.4 mm tube at atmospheric conditions (1 bar, 25 ºC).

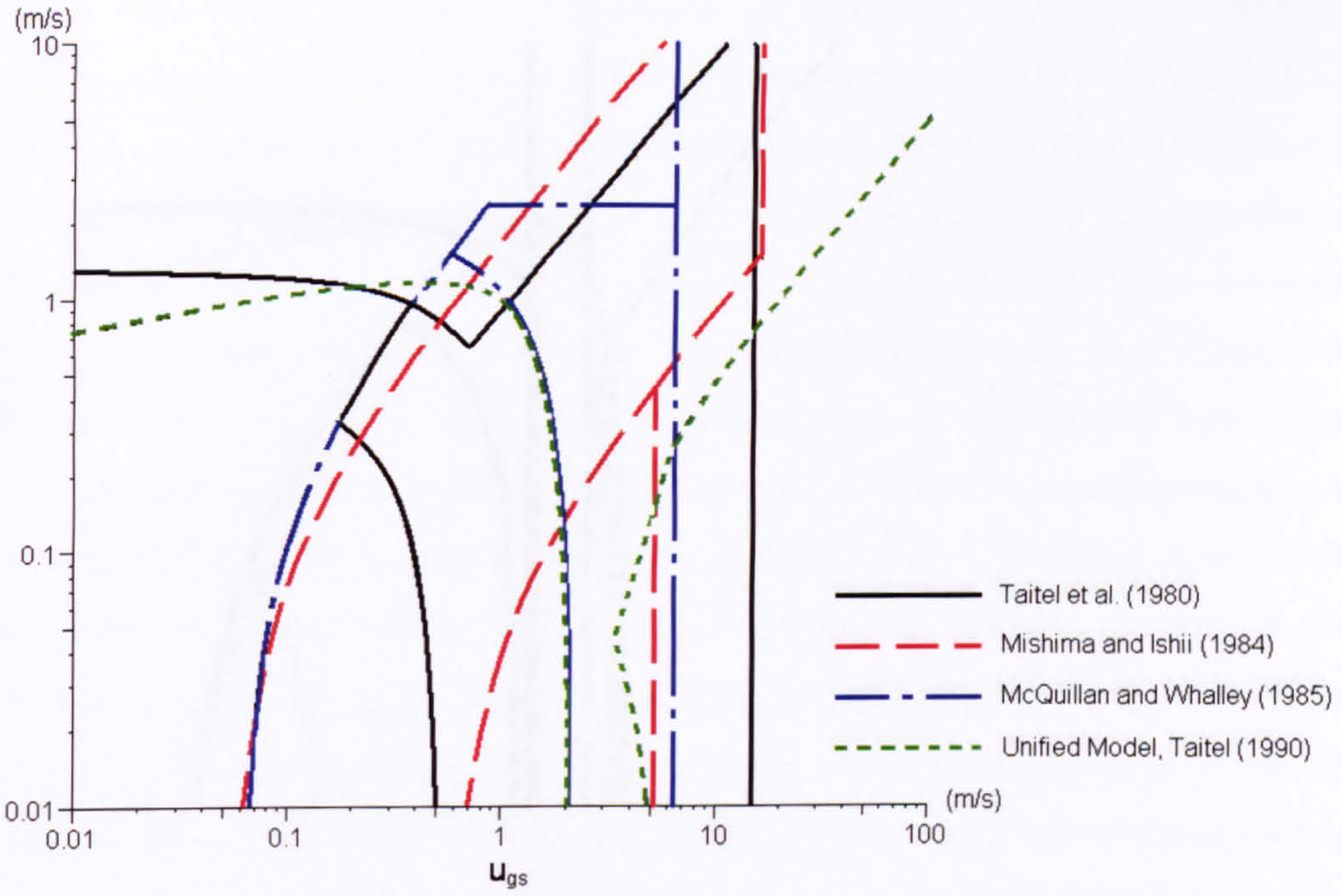

Figure 6.12 Comparison of the different models for the air-water flow maps in the 5.0 mm tube at atmospheric conditions (1 bar, 25 ºC).

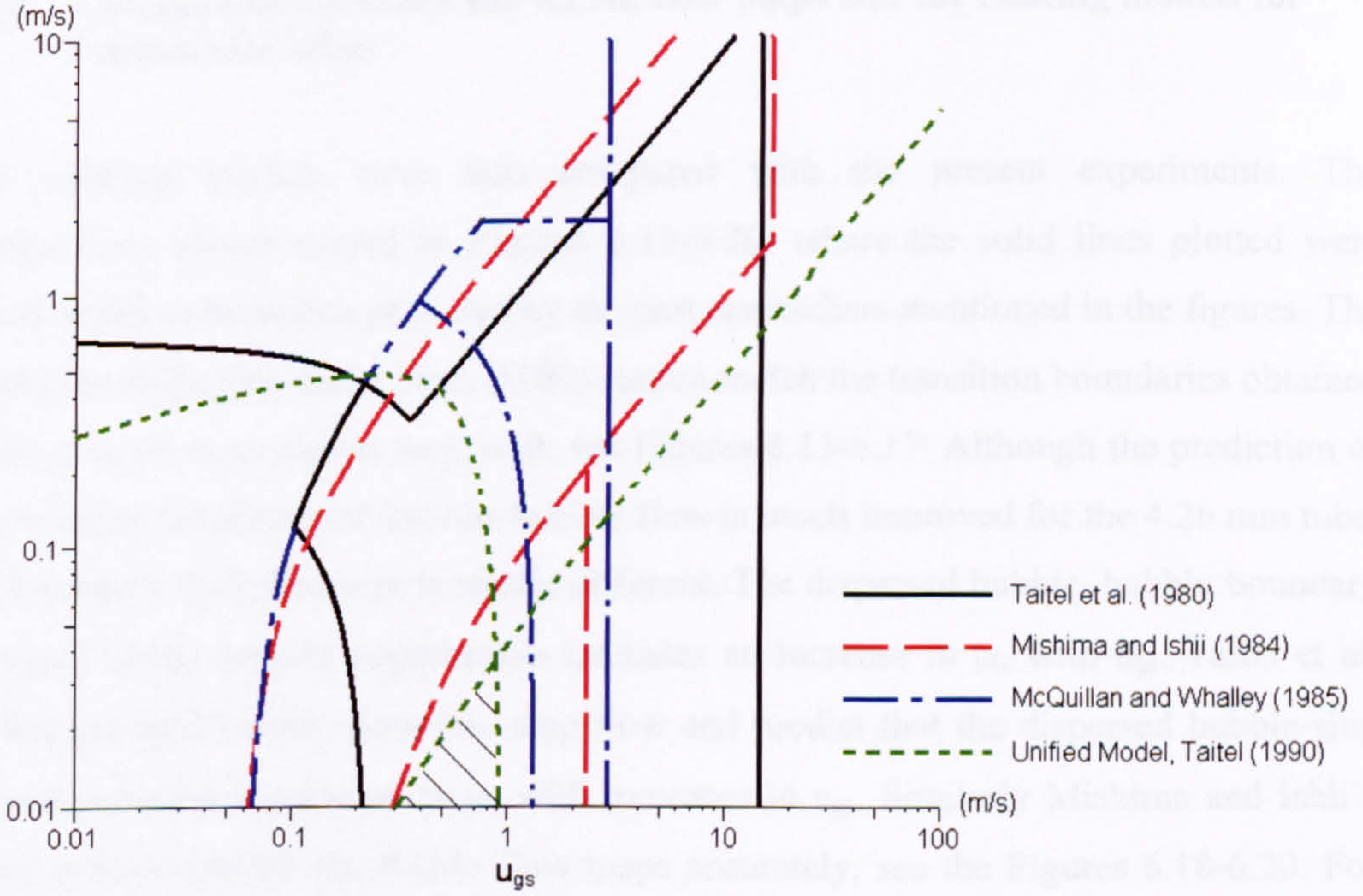

Figure 6.13 Comparison of the different models for the air-water flow maps in the 1.0 mm tube at atmospheric conditions (1 bar, 25 ºC).

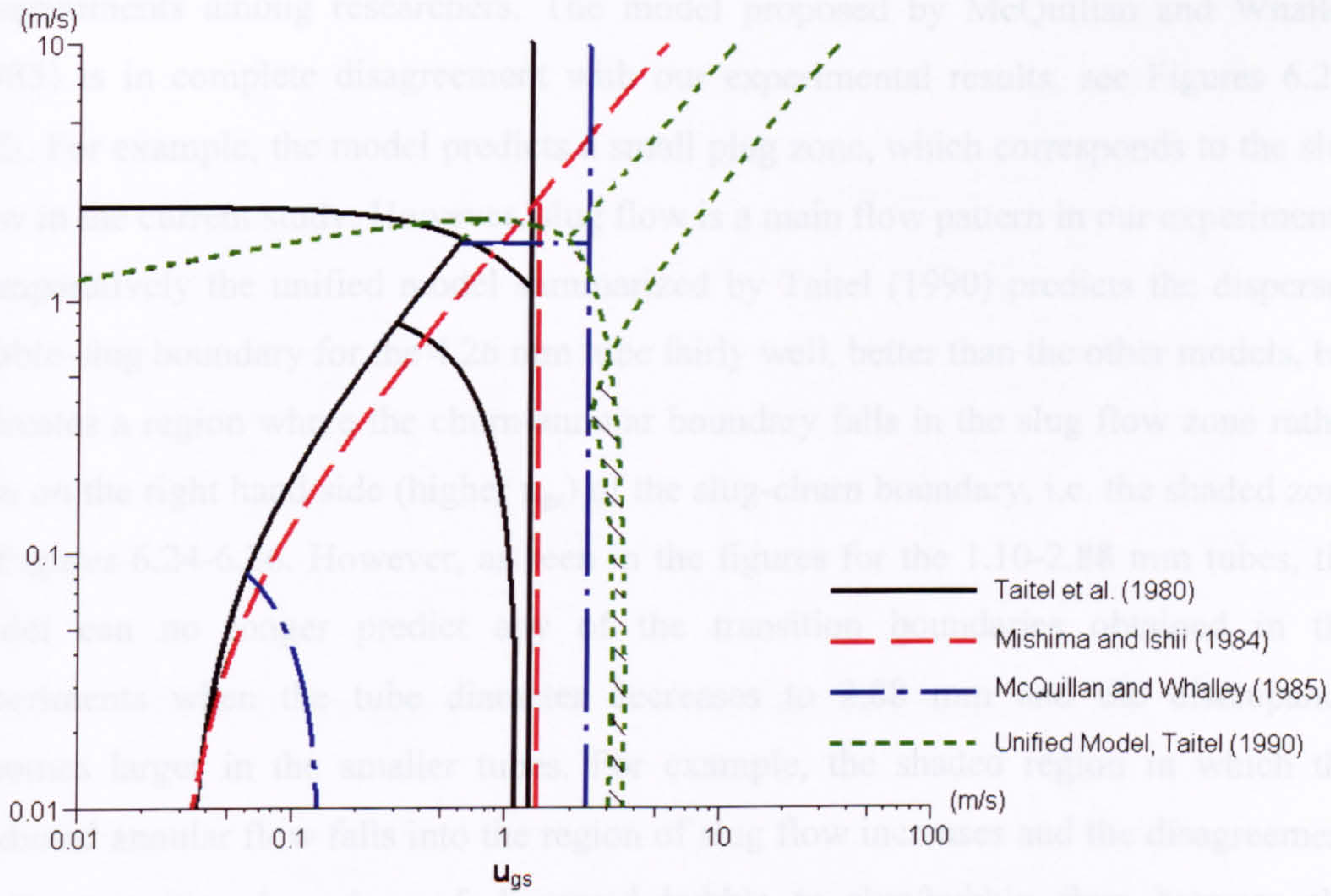

Figure 6.14 Comparison of the different models for the R134a flow maps in the 25.4 mm tube at 10 bar.

6.2.2 Comparisons between the R134a flow maps and the existing models for normal size tubes

The existing models were also compared with the present experiments. The comparisons are presented in Figures 6.15-6.26, where the solid lines plotted were based on the correlations provided by the past researchers mentioned in the figures. The model developed by Taitel et al. (1980) cannot match the transition boundaries obtained in the present experiments very well, see Figures 6.15-6.17. Although the prediction of the boundary of dispersed bubble–bubbly flow is much improved for the 4.26 mm tube, the boundary shift direction is totally different. The dispersed bubble–bubbly boundary obtained in the present experiments indicates an increase in u_{ls} with u_{gs}. Taitel et al. (1980) grouped bubbly flow into slug flow and predict that the dispersed bubble-slug boundary shows a decrease in u_{ls} with increases in u_{gs}. Similarly Mishima and Ishii's model cannot predict the R134a flow maps accurately, see the Figures 6.18-6.20. For example, the model expects an extremely small churn zone, which vanishes completely when the experimental pressure increased to 14 bar. However, churn flow is a main flow pattern at all experimental pressures in our experiments. This has a lot of disagreements among researchers. The model proposed by McQuillan and Whalley (1985) is in complete disagreement with our experimental results, see Figures 6.21-6.23. For example, the model predicts a small plug zone, which corresponds to the slug flow in the current study. However, slug flow is a main flow pattern in our experiments. Comparatively the unified model summarized by Taitel (1990) predicts the dispersed bubble-slug boundary for the 4.26 mm tube fairly well, better than the other models, but it creates a region where the churn-annular boundary falls in the slug flow zone rather than on the right hand side (higher u_{gs}) of the slug-churn boundary, i.e. the shaded zone in Figures 6.24-6.26. However, as seen in the figures for the 1.10-2.88 mm tubes, the model can no longer predict any of the transition boundaries obtained in the experiments when the tube diameter decreases to 2.88 mm and the discrepancy becomes larger in the smaller tubes. For example, the shaded region in which the predicted annular flow falls into the region of slug flow increases and the disagreement on the transition boundary of dispersed bubble to slug/bubbly flow between the experimental data and the predictions increases as the diameter gets smaller. Therefore, the existing models for the air-water flow in normal size tubes cannot predict the R134a flow maps in the small tubes and the results of the models start to deviate further from the observations in the present experiments in the smaller tubes or at the higher pressure.

Although the flow patterns for R134a in the 2.88 and 4.26 mm tubes exhibit strong characteristics of the normal size tube, the agreement between the current maps and the existing models based on air-water flow in the normal tubes is still very poor. From the comparisons presented in Figures 6.15-6.26, it is difficult to find which is the main factor, diameter or fluid, which causes the discrepancies. However, the comparisons in Figures 6.13 and 6.14 reveal that the existing models cannot agree with each other when applied for air-water flow in small tubes or R134a flow in normal tubes. It indicates that the existing models have strict restrictions on their applicability. They cannot be extended to the small tubes or other fluids. Otherwise, they may give inaccurate predictions. The above conclusions are also supported by the earlier studies reviewed in Chapter 2. For example, Zhao and Bi (2001), as discussed in Section 2.3.2 (5). Their study revealed that the existing models by Taitel et al. (1980) and Mishima and Ishii (1984) could not predict flow patterns in small triangular channels used in their experiments.

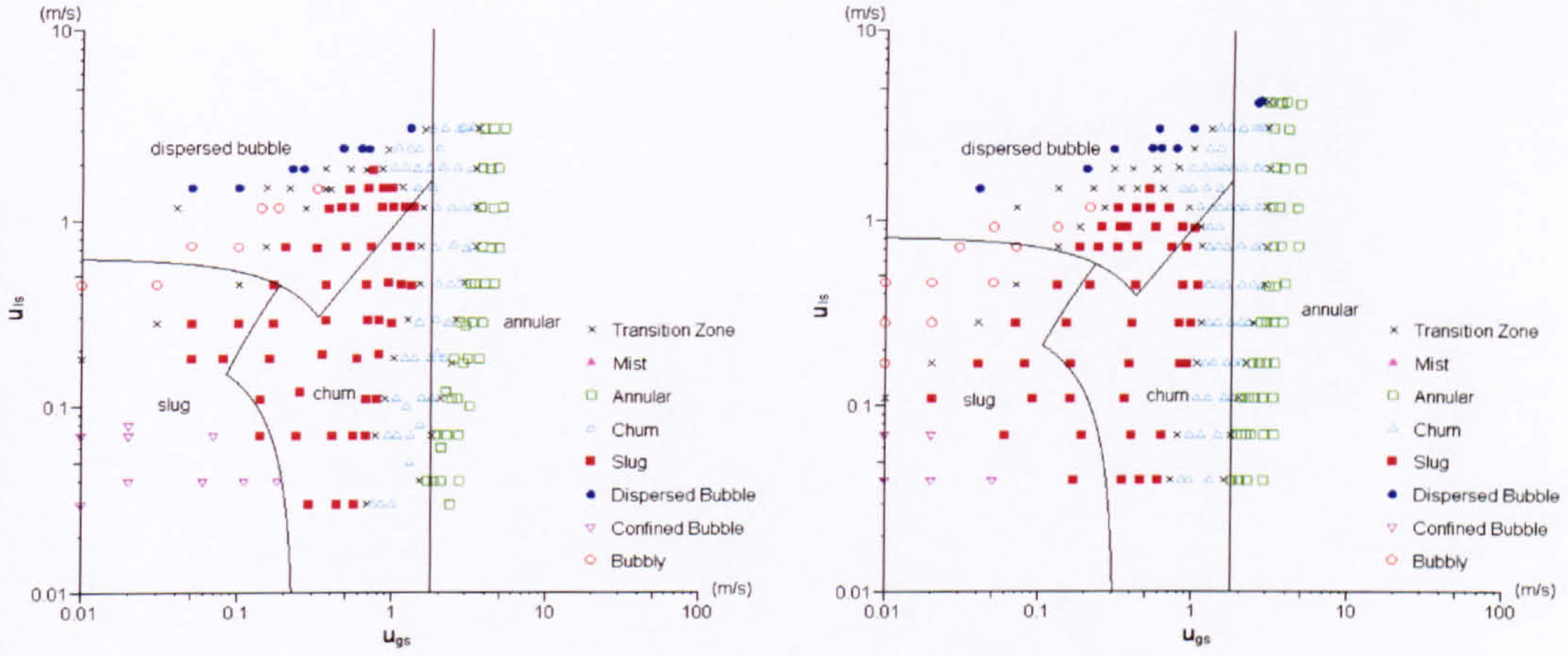

(a) 1.10 mm tube (b) 2.01 mm tube

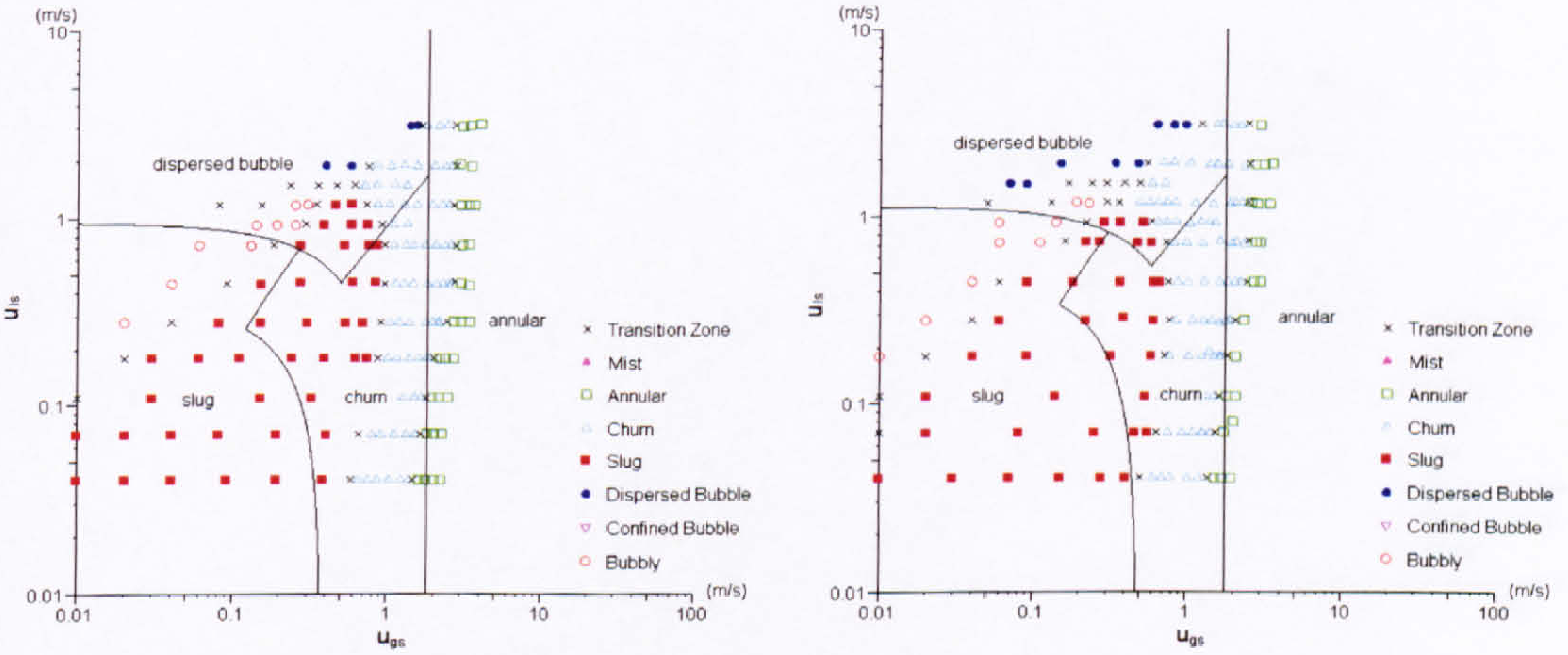

(c) 2.88 mm tube (d) 4.26 mm tube

Figure 6.15 Comparison of the R134a flow maps at 6 bar and the model of Taitel et al. (1980).

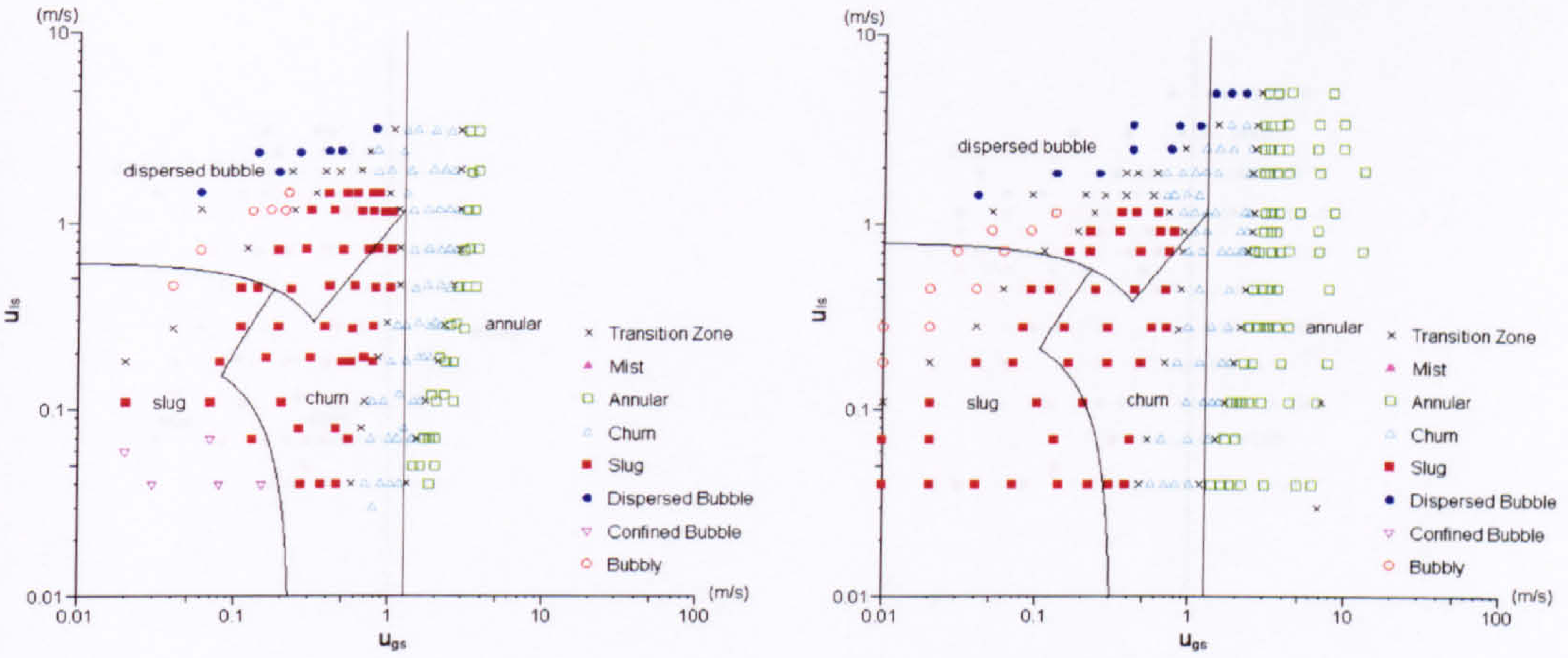

(a) 1.10 mm tube (b) 2.01 mm tube

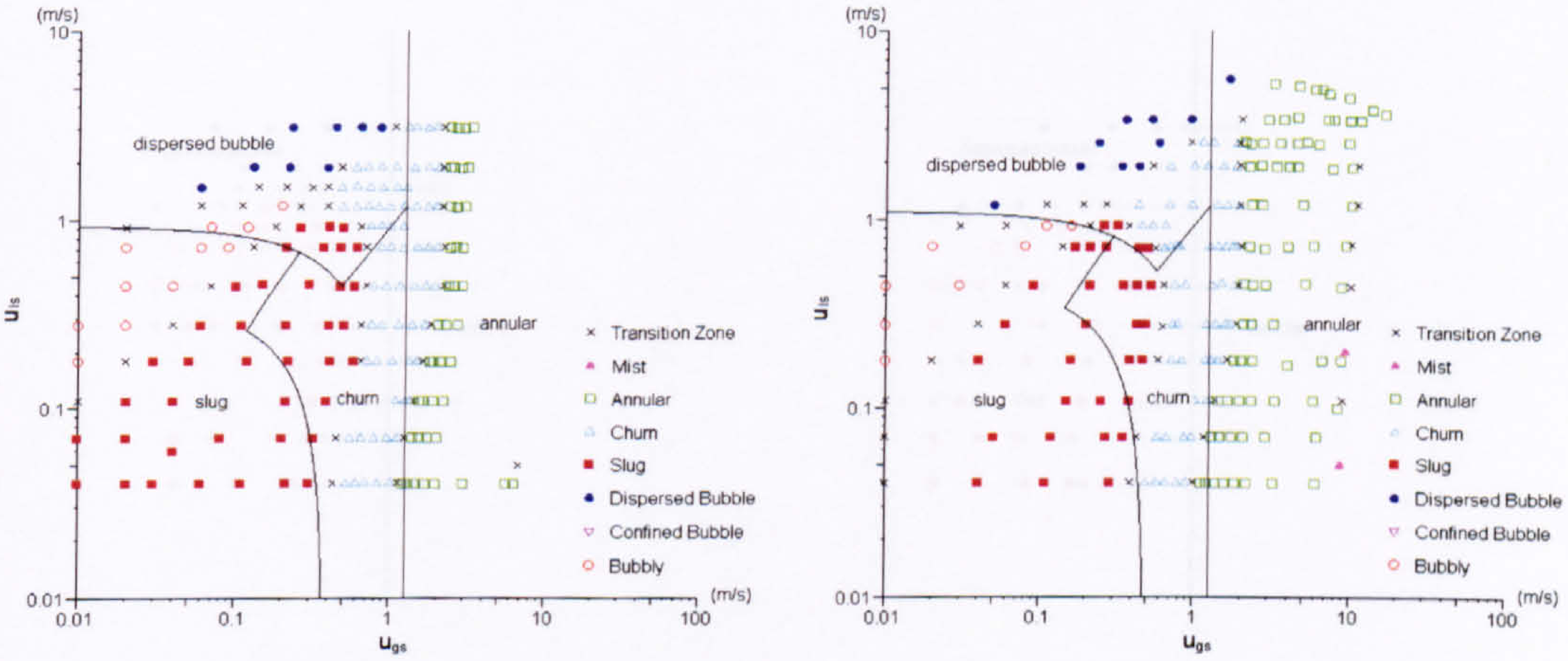

(c) 2.88 mm tube (d) 4.26 mm tube

Figure 6.16 Comparison of the R134a flow maps at 10 bar and the model of Taitel et al. (1980).

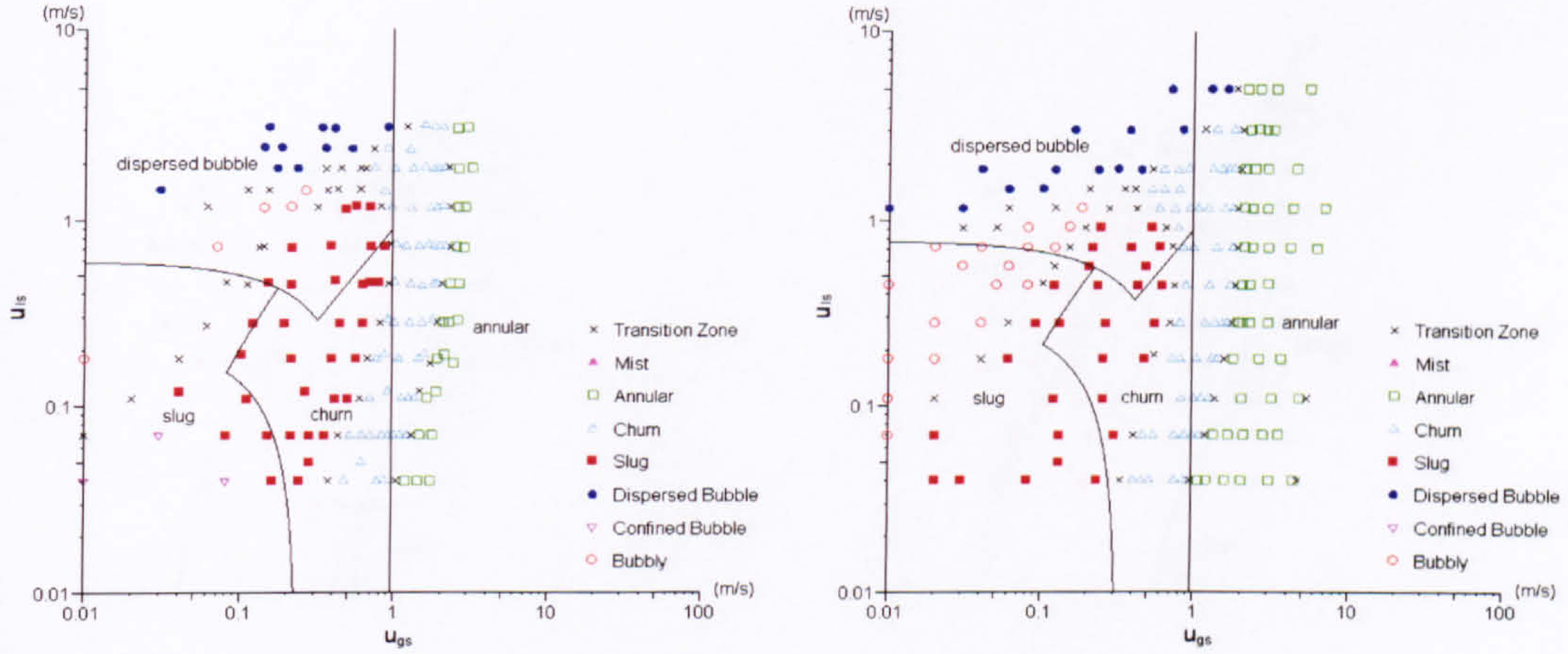

(a) 1.10 mm tube (b) 2.01 mm tube

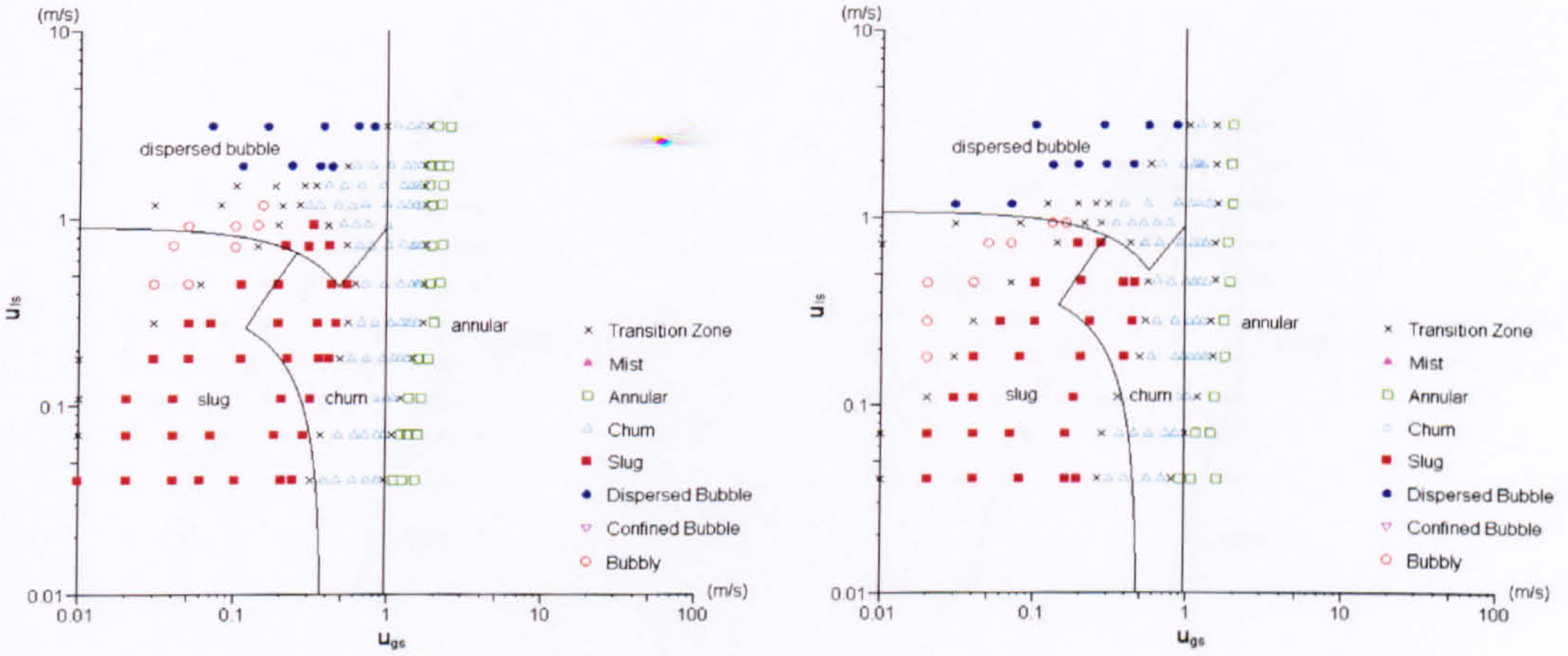

(c) 2.88 mm tube (d) 4.26 mm tube

Figure 6.17 Comparison of the R134a flow maps at 14 bar and the model of Taitel et al. (1980).

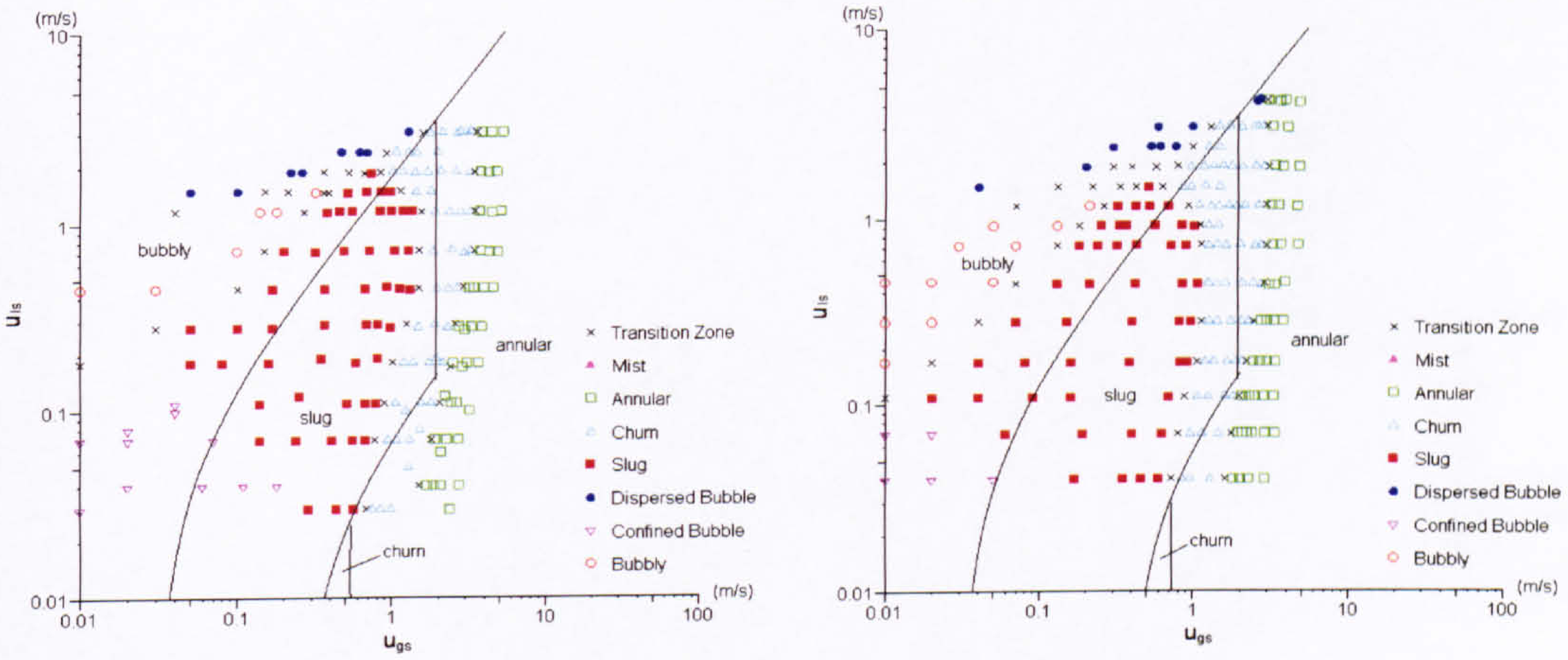

(a) 1.10 mm tube

(b) 2.01 mm tube

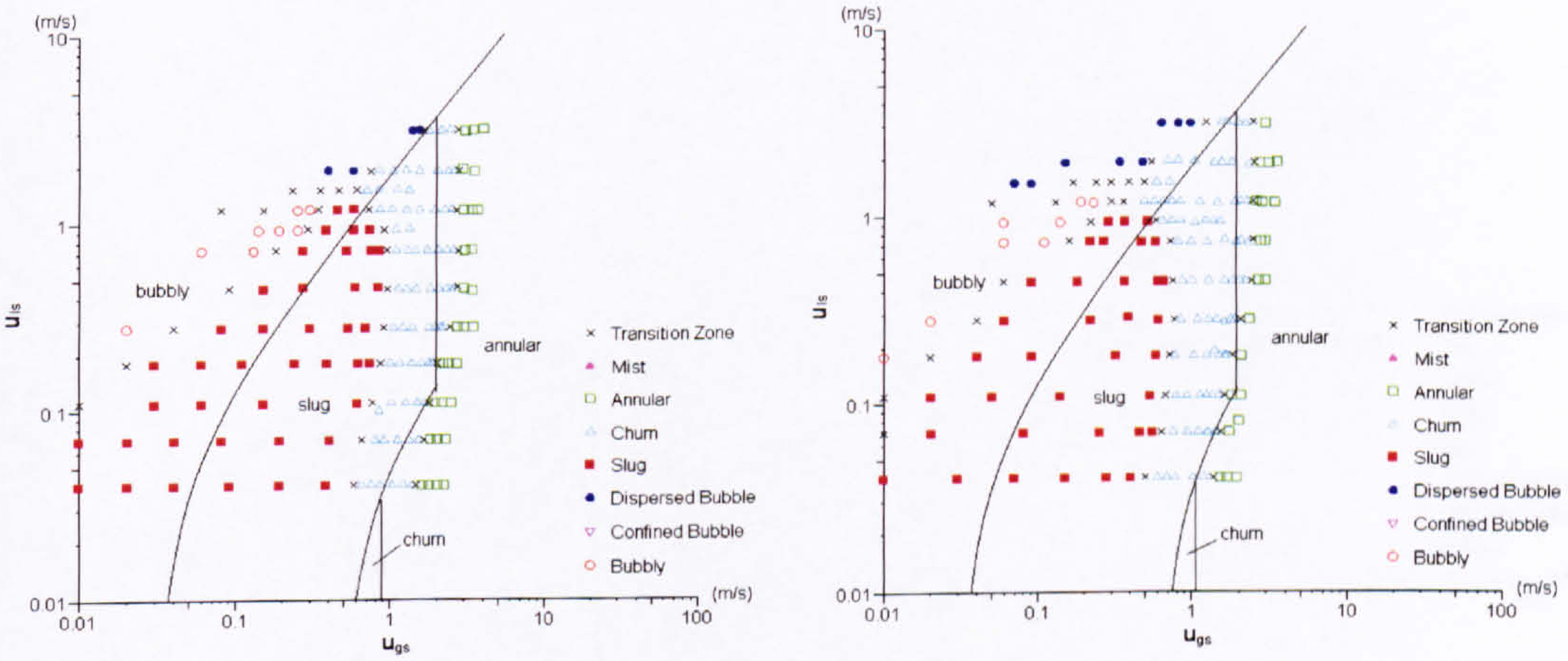

(c) 2.88 mm tube

(d) 4.26 mm tube

Figure 6.18 Comparison of the R134a flow maps at 6 bar and the model of Mishima and Ishii (1984).

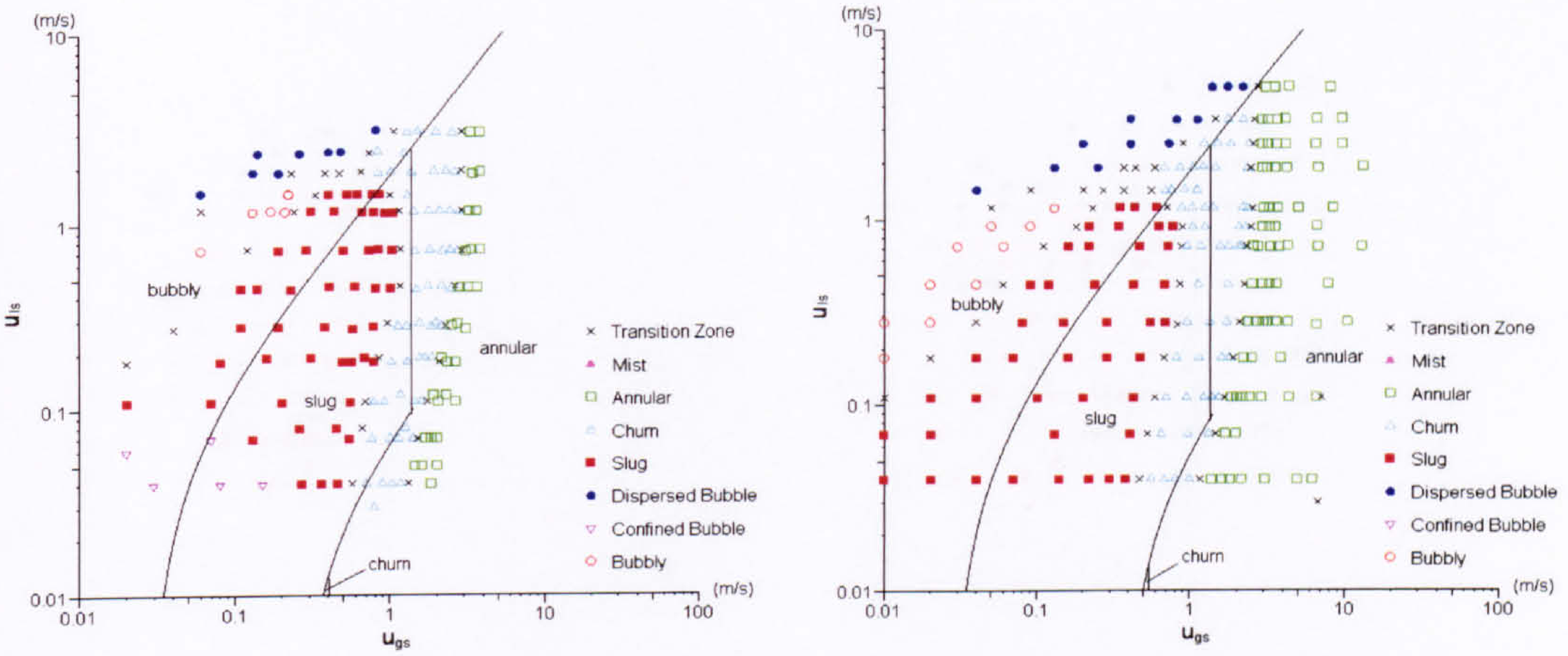

(a) 1.10 mm tube

(b) 2.01 mm tube

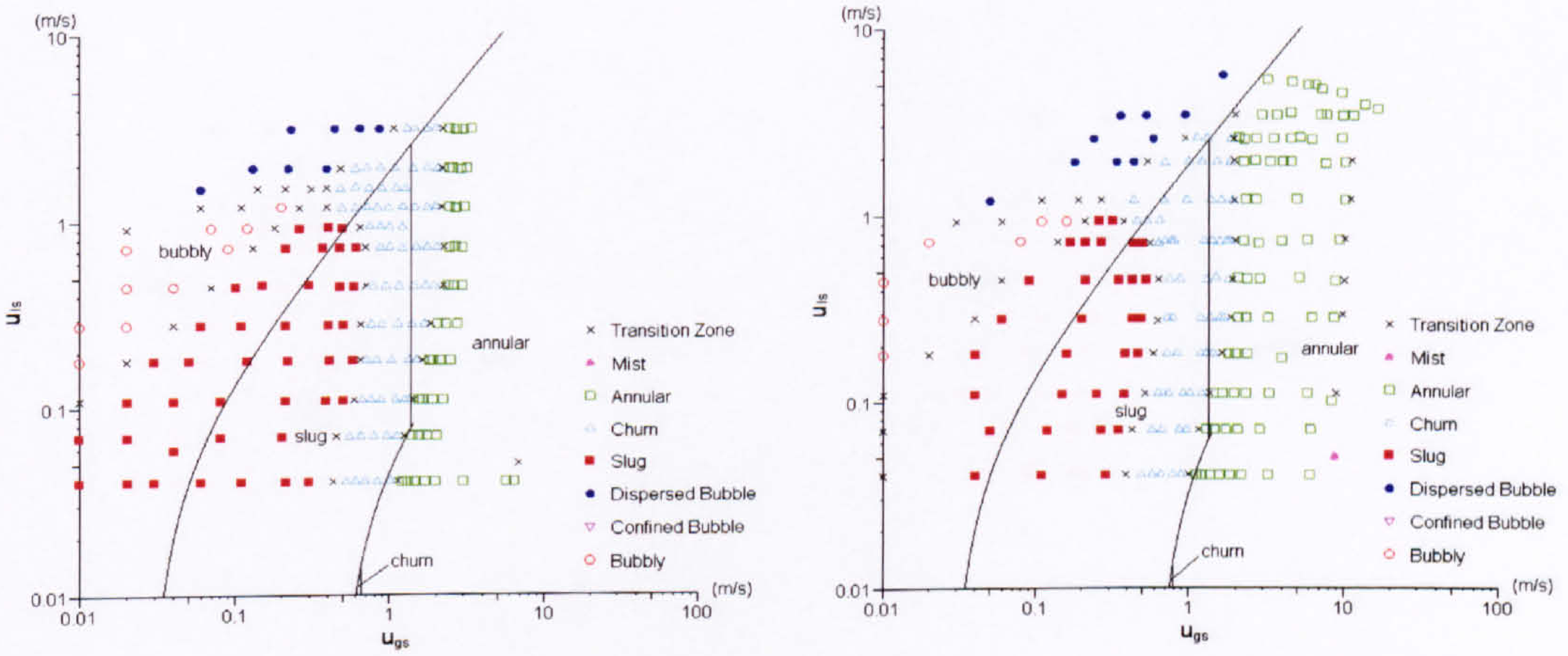

(c) 2.88 mm tube

(d) 4.26 mm tube

Figure 6.19 Comparison of the R134a flow maps at 10 bar and the model of Mishima and Ishii (1984).

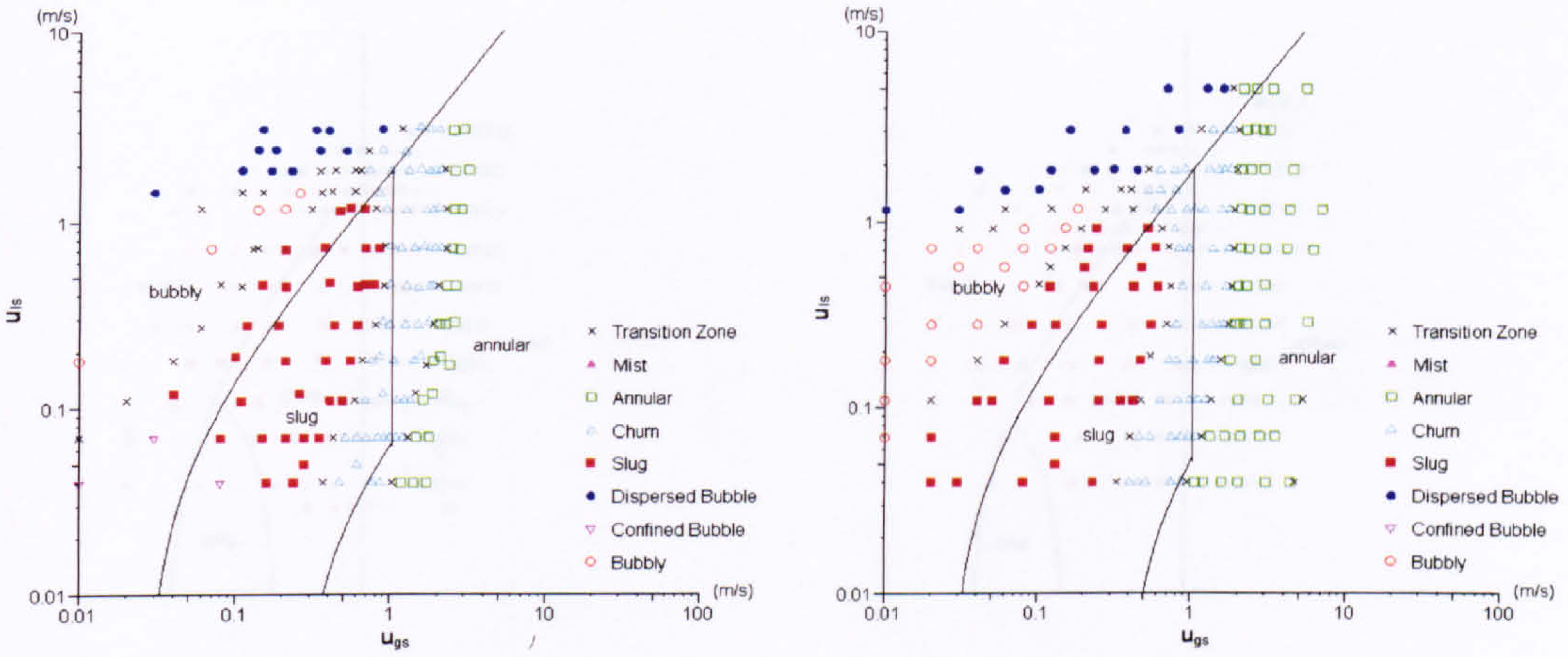

(a) 1.10 mm tube (b) 2.01 mm tube

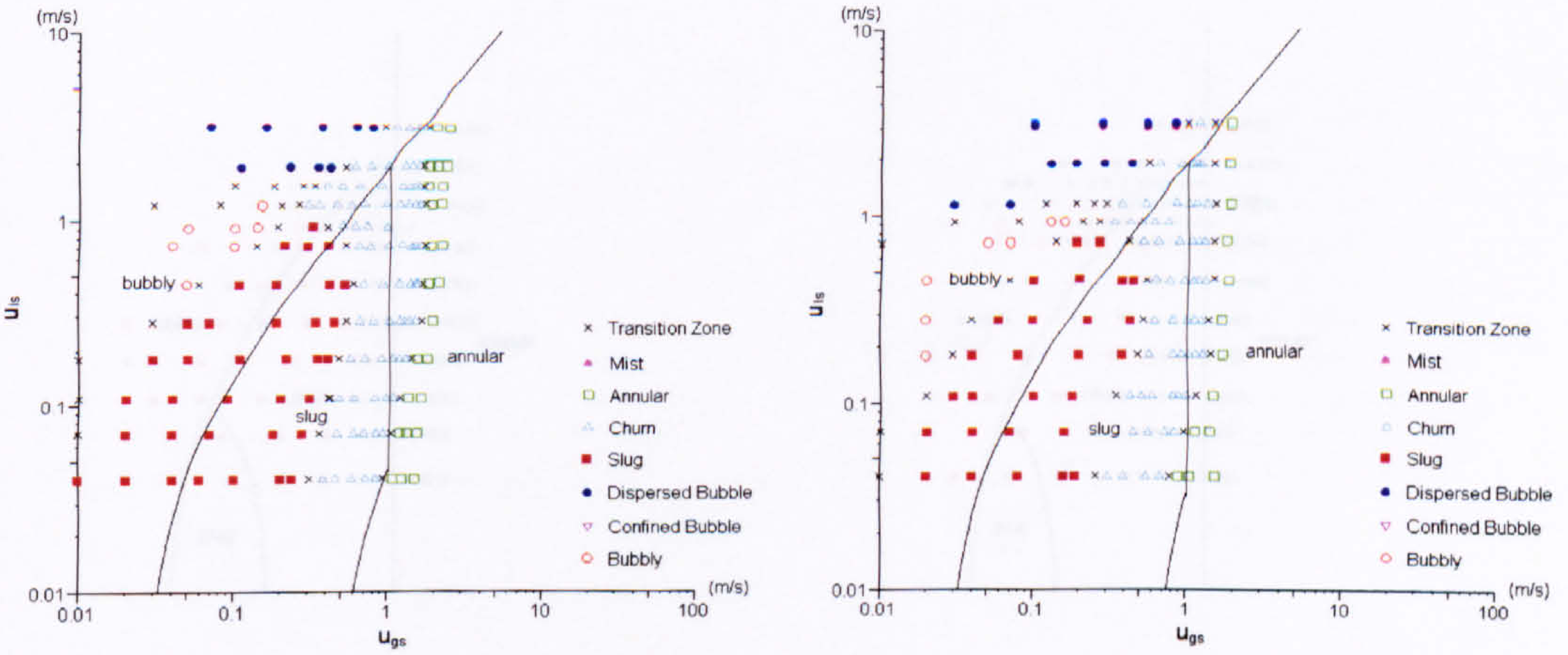

(c) 2.88 mm tube (d) 4.26 mm tube

Figure 6.20 Comparison of the R134a flow maps at 14 bar and the model of Mishima and Ishii (1984).

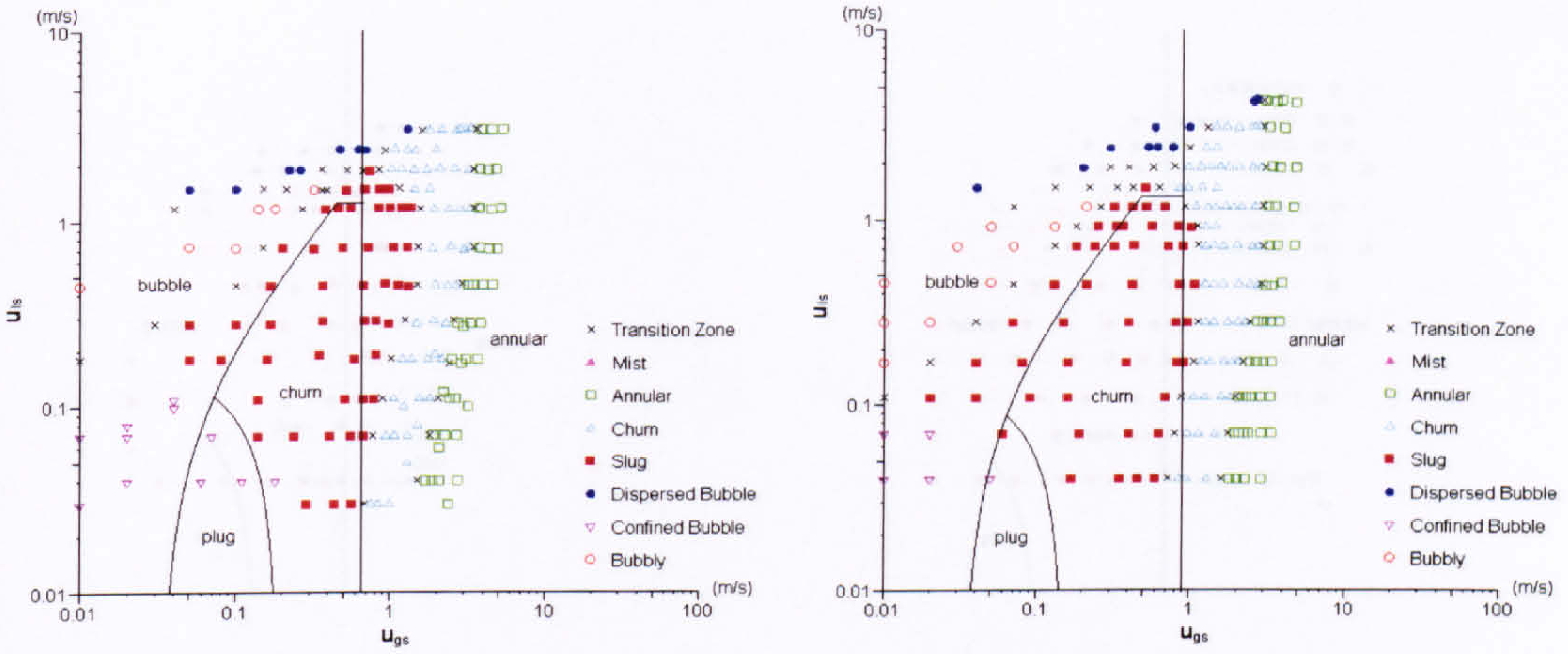

(a) 1.10 mm tube

(b) 2.01 mm tube

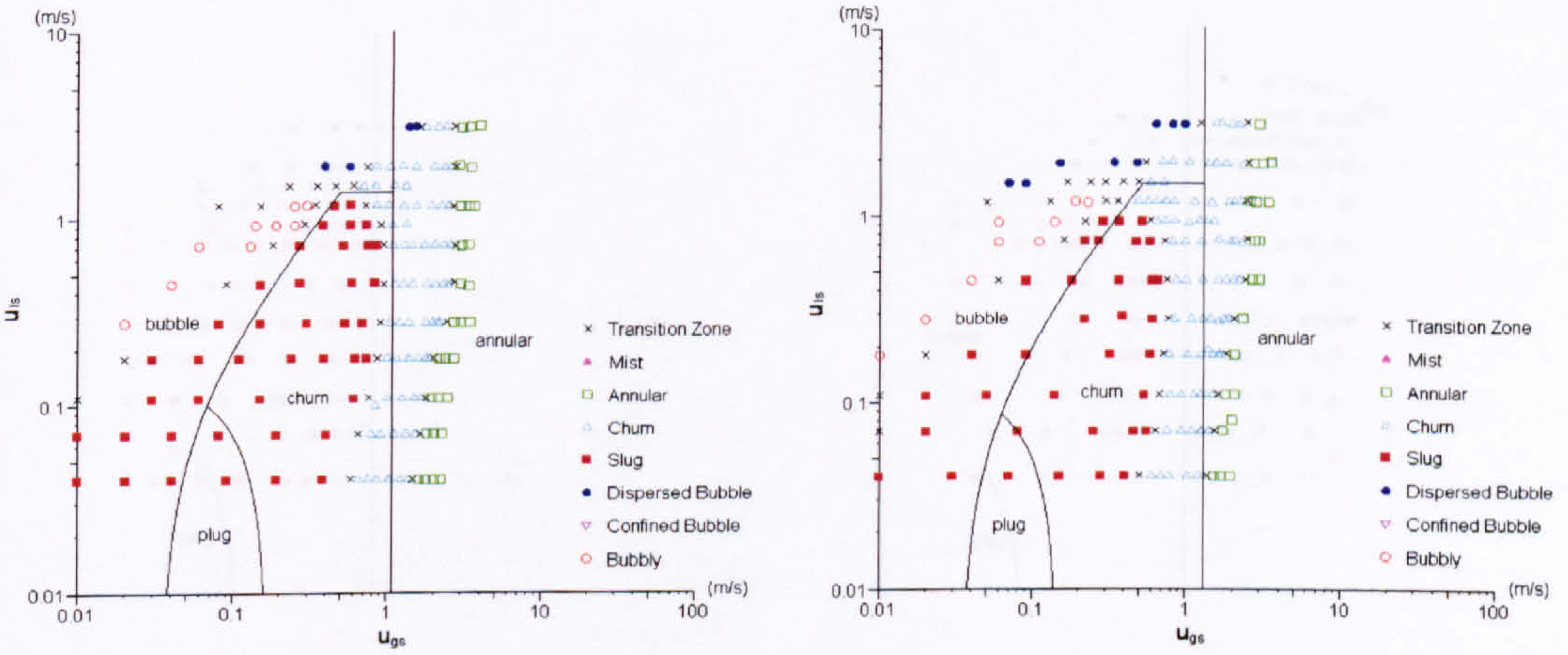

(c) 2.88 mm tube

(d) 4.26 mm tube

Figure 6.21 Comparison of the R134a flow maps at 6 bar and the model of McQuillan and Whalley (1985).

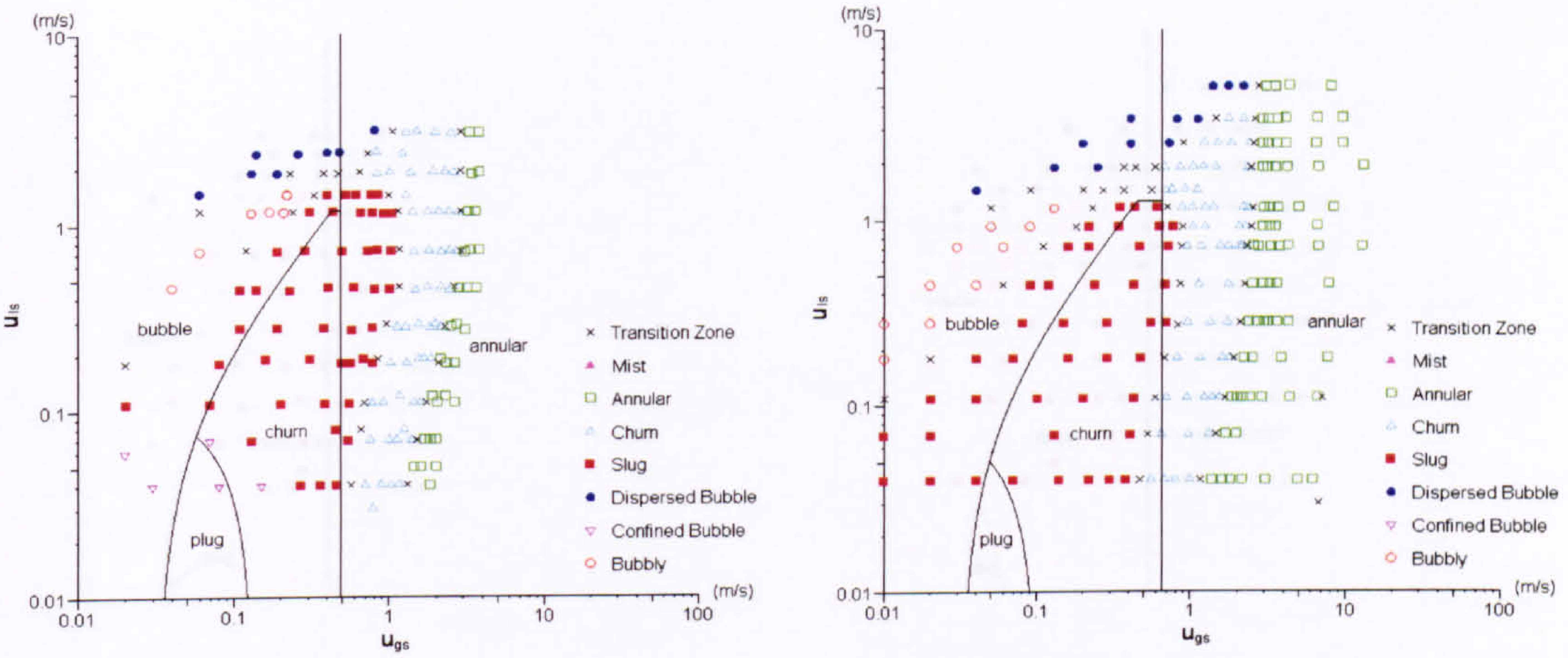

(a) 1.10 mm tube

(b) 2.01 mm tube

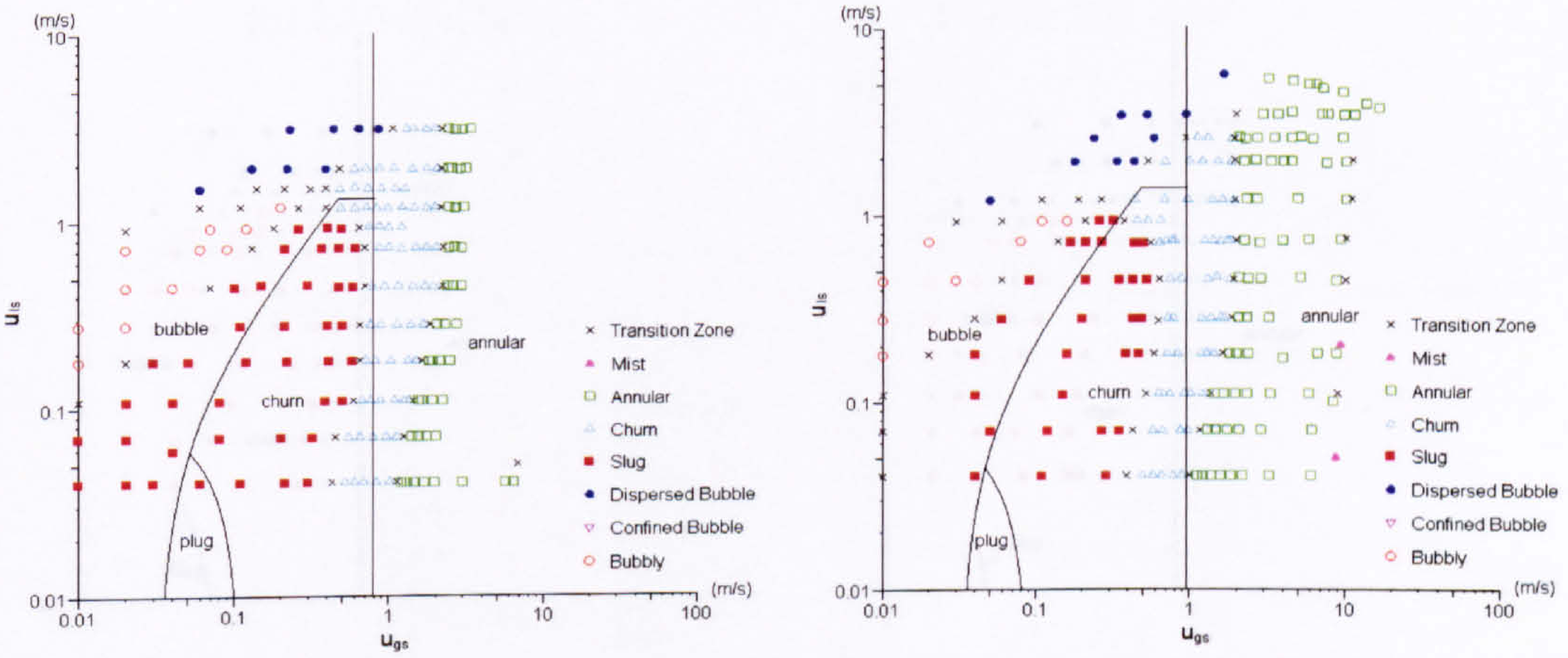

(c) 2.88 mm tube

(d) 4.26 mm tube

Figure 6.22 Comparison of the R134a flow maps at 10 bar and the model of McQuillan and Whalley (1985).

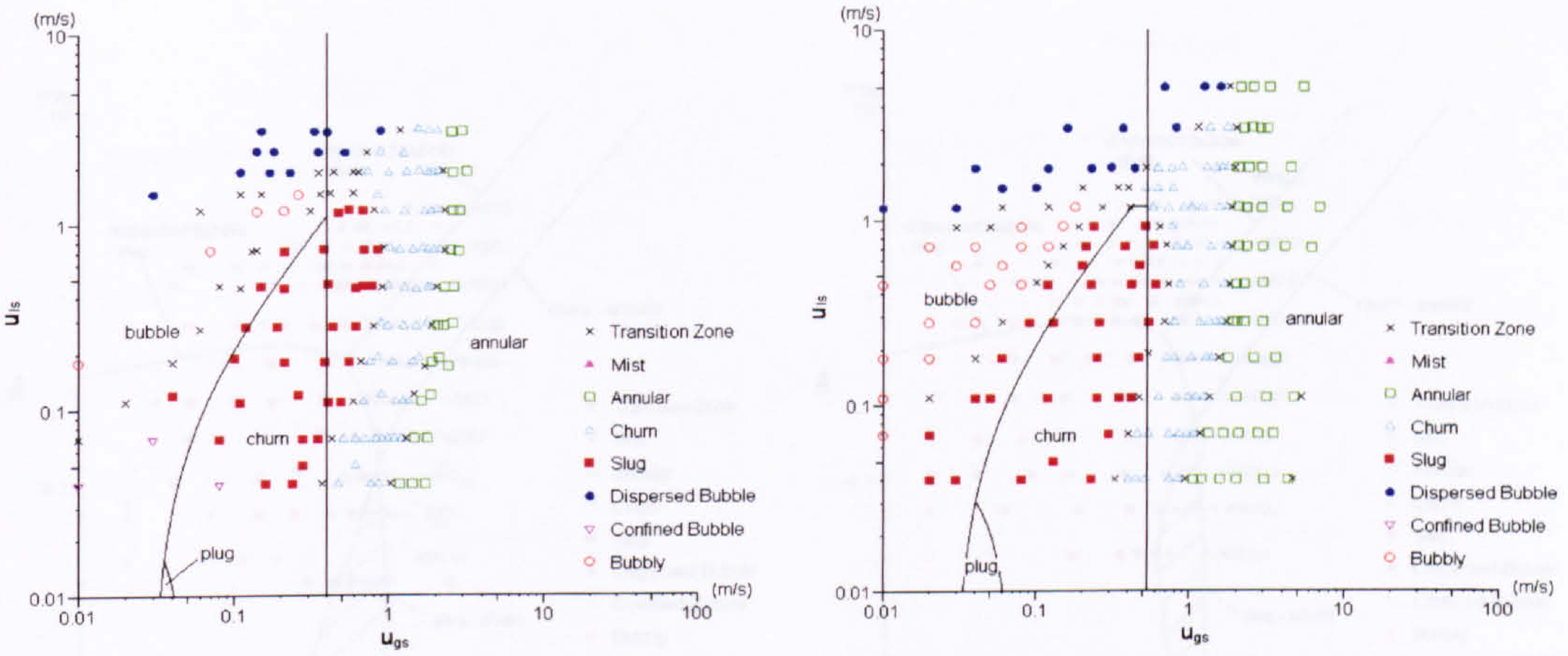

(a) 1.10 mm tube

(b) 2.01 mm tube

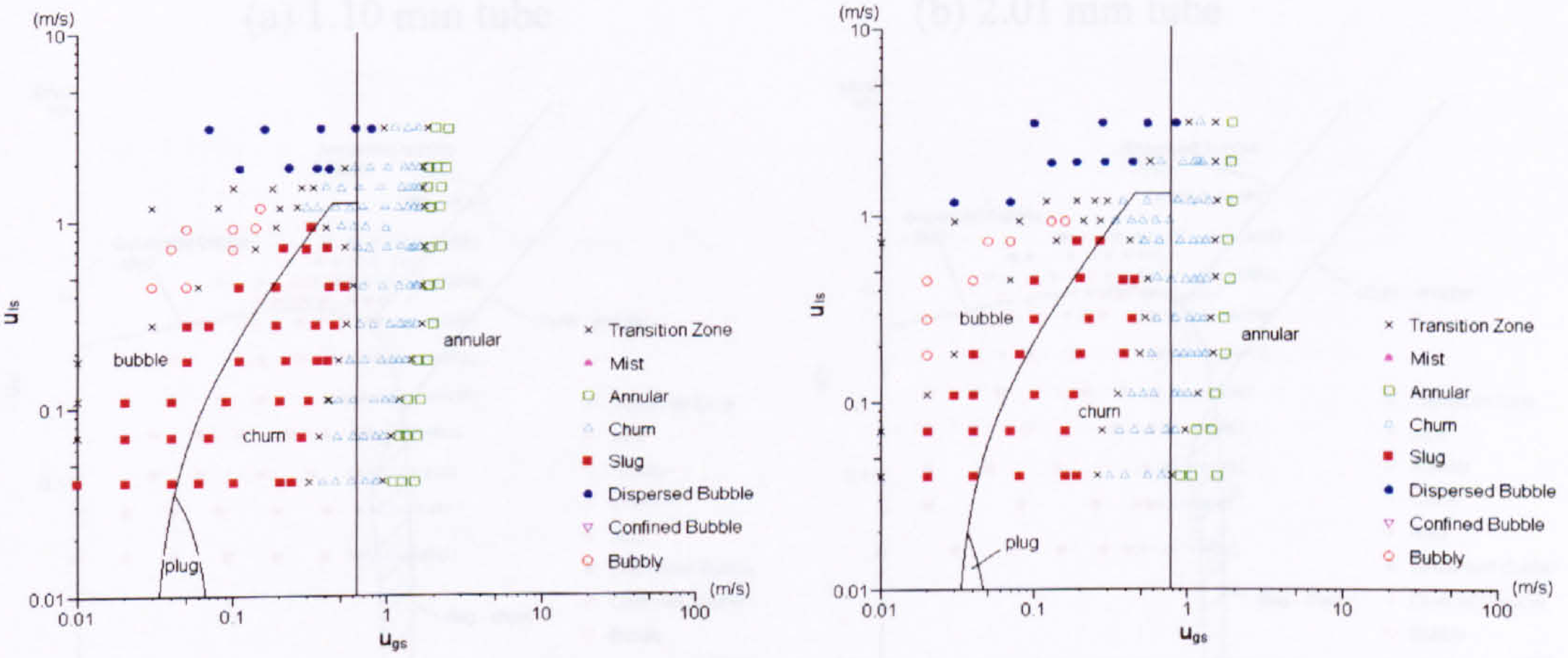

(c) 2.88 mm tube

(d) 4.26 mm tube

Figure 6.23 Comparison of the R134a flow maps at 14 bar and the model of McQuillan and Whalley (1985).

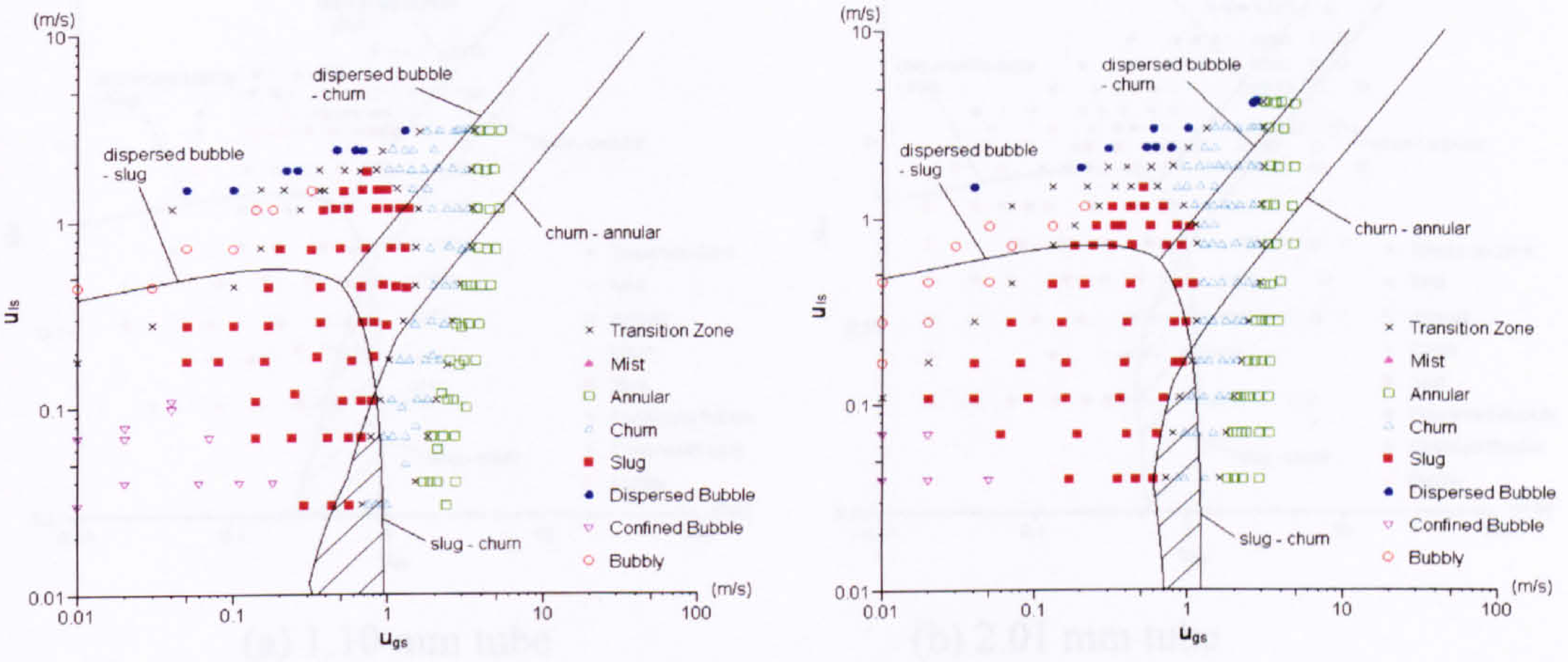

(a) 1.10 mm tube (b) 2.01 mm tube

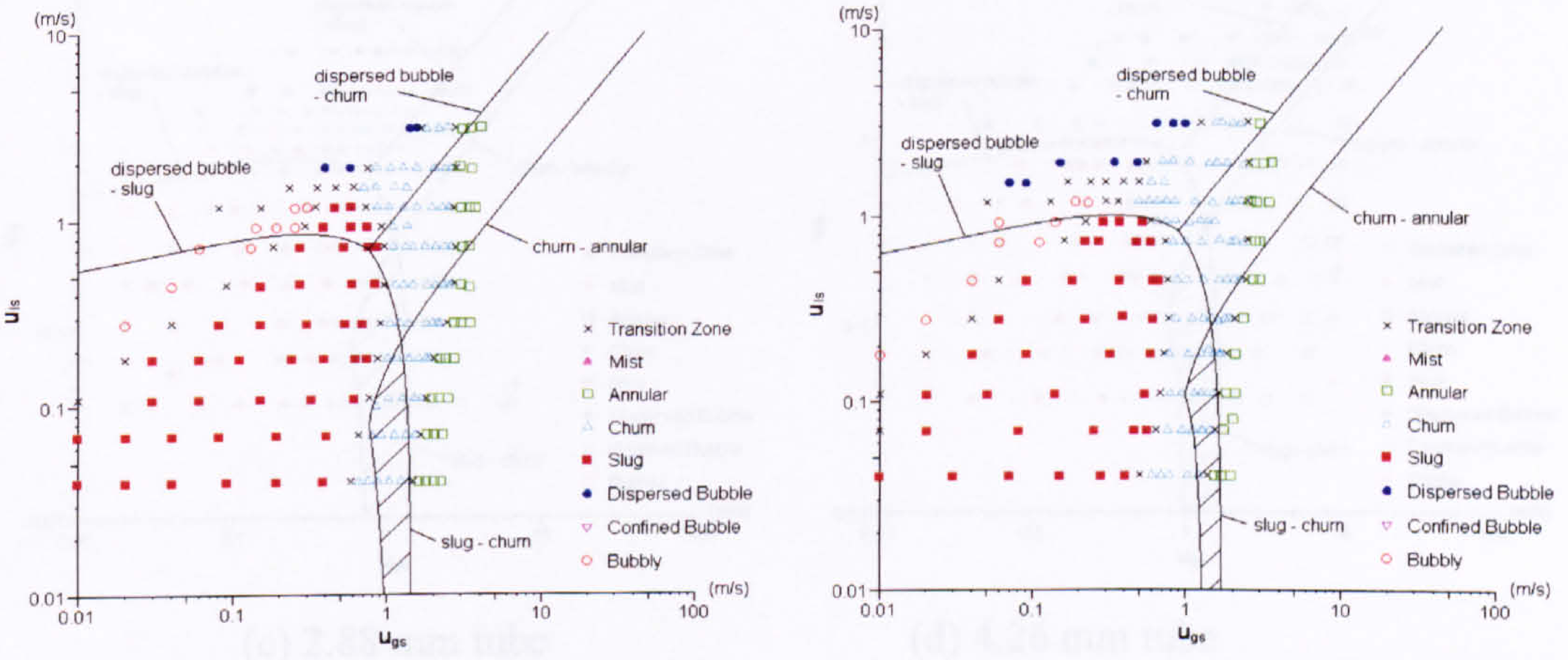

(c) 2.88 mm tube (d) 4.26 mm tube

Figure 6.24 Comparison of the R134a flow maps at 6 bar and the "Unified Model" summarized by Taitel (1990).

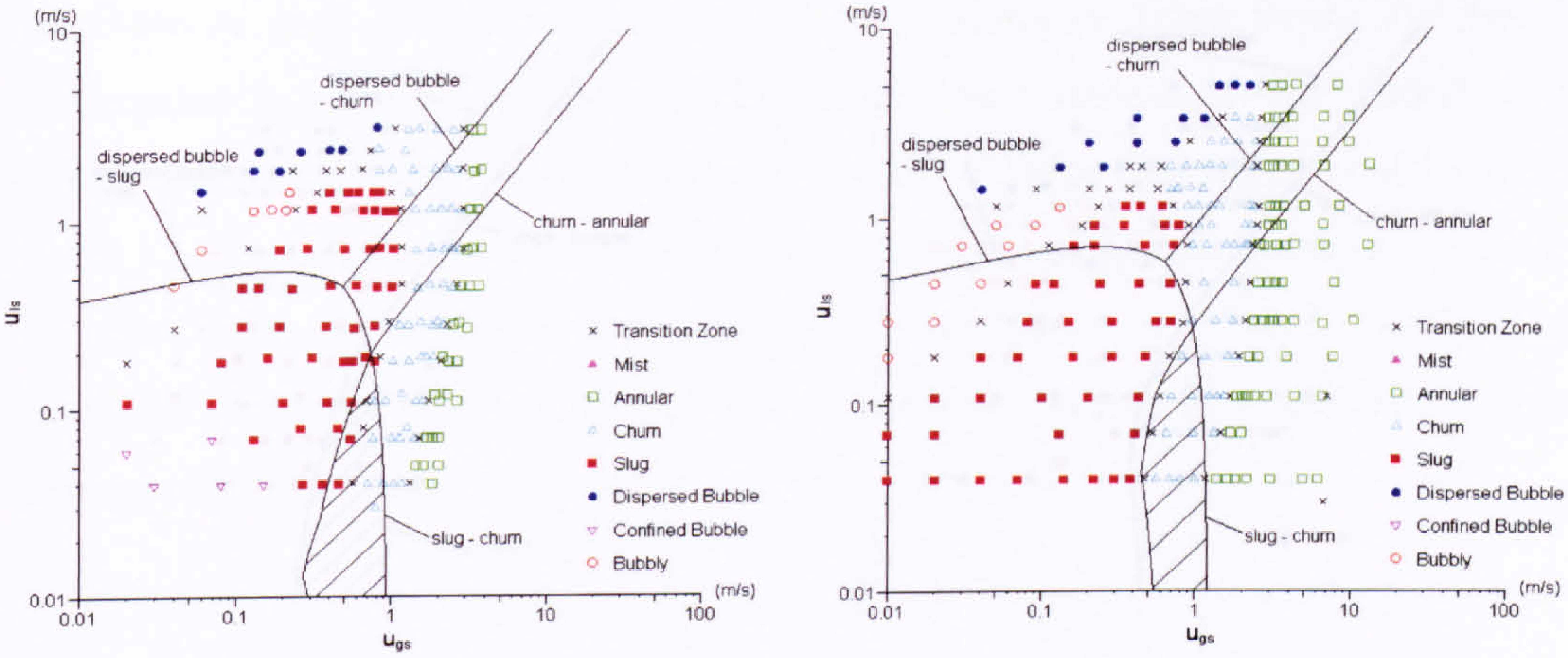

(a) 1.10 mm tube

(b) 2.01 mm tube

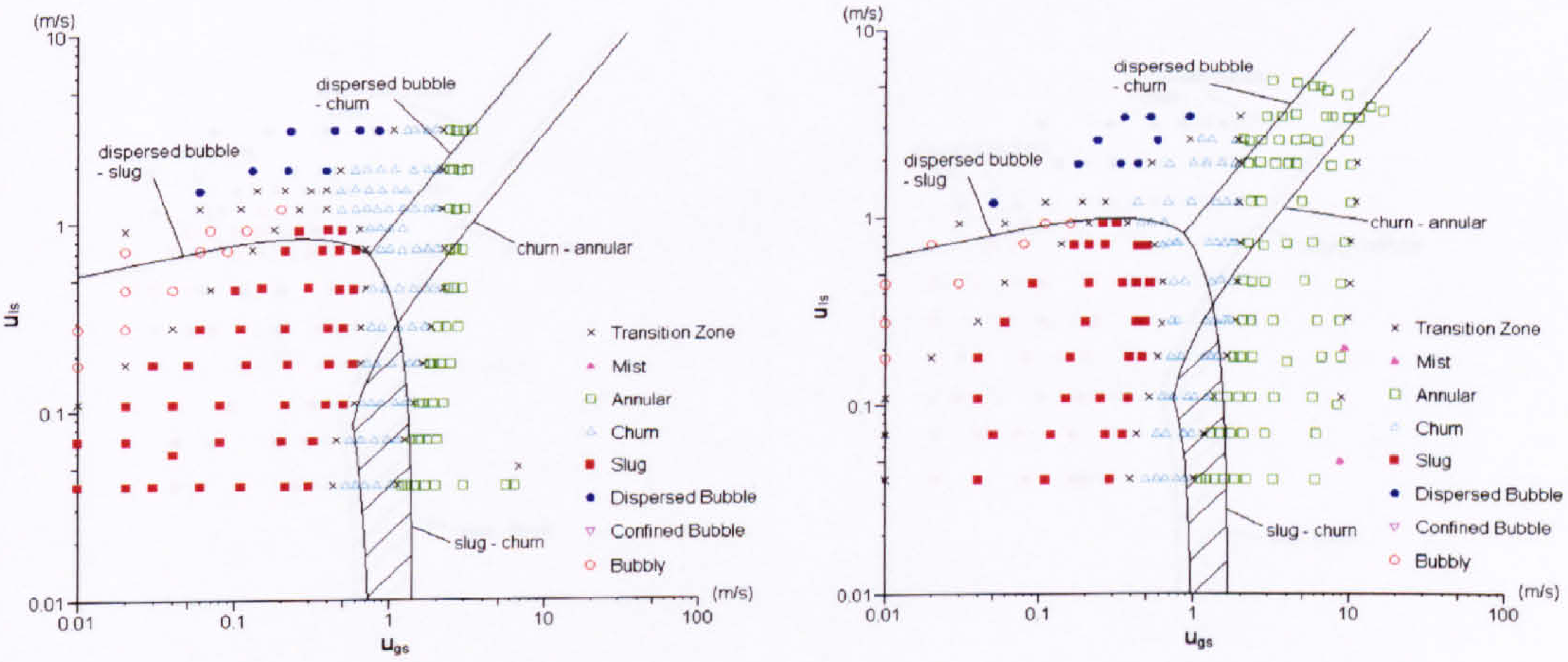

(c) 2.88 mm tube

(d) 4.26 mm tube

Figure 6.25 Comparison of the R134a flow maps at 10 bar and the “Unified Model” summarized by Taitel (1990).

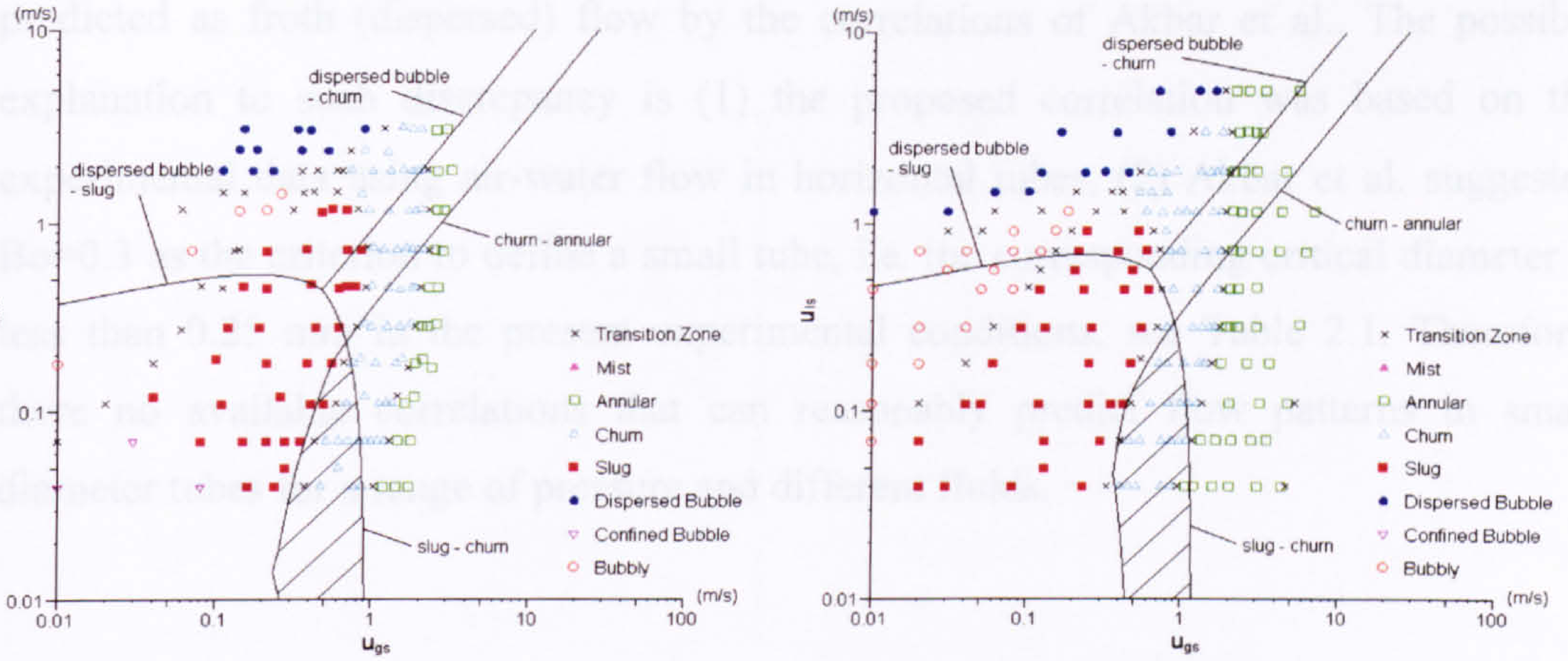

(a) 1.10 mm tube

(b) 2.01 mm tube

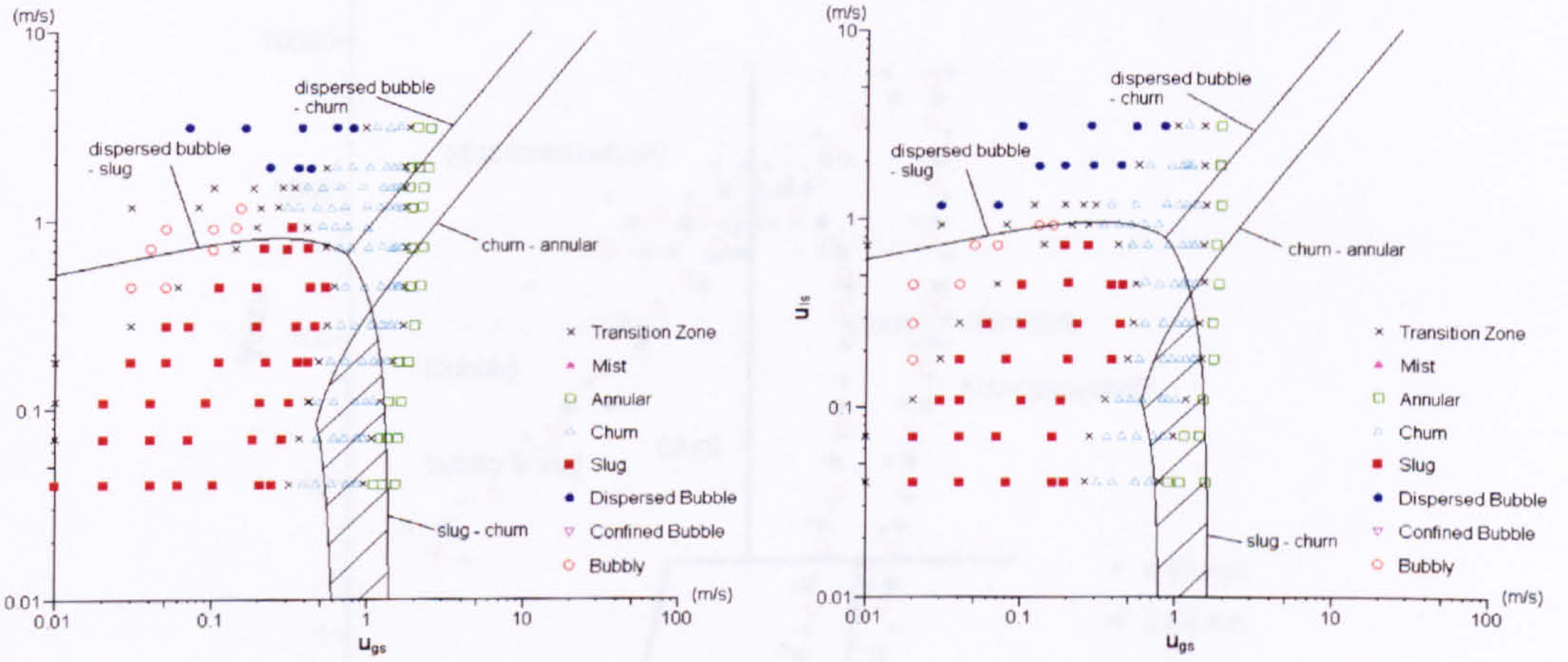

(c) 2.88 mm tube

(d) 4.26 mm tube

Figure 6.26 Comparison of the R134a flow maps at 14 bar and the "Unified Model" summarized by Taitel (1990).

6.2.3 Comparison between the R134a flow maps and the existing correlations for small tubes

Figures 6.27-6.29 compare the present experimental data and the semi-empirical correlations for small tubes proposed by Akbar et al. (2003). Obviously the comparisons show poor agreement though the correlations have been supported by the earlier data for air-water flow in the ~1 mm tubes, see Figure 2.24 in Chapter 2. The transition boundaries predicted by the correlations (see Table B.2 in Appendix B) are sketched in solid lines and the flow patterns observed in the current study are labelled in brackets. None of the flow patterns at the present experiments are predicted well. For example, in most cases slug, churn and annular flow observed in the present experiments are predicted as froth (dispersed) flow by the correlations of Akbar et al.. The possible explanation to such discrepancy is (1) the proposed correlation was based on the experimental data using air-water flow in horizontal tubes, (2) Akbar et al. suggested Bo=0.3 as the criterion to define a small tube, i.e. the corresponding critical diameter is less than 0.25 mm in the present experimental conditions, see Table 2.1. Therefore, there no available correlations that can reasonably predict flow patterns in small diameter tubes for a range of pressure and different fluids.

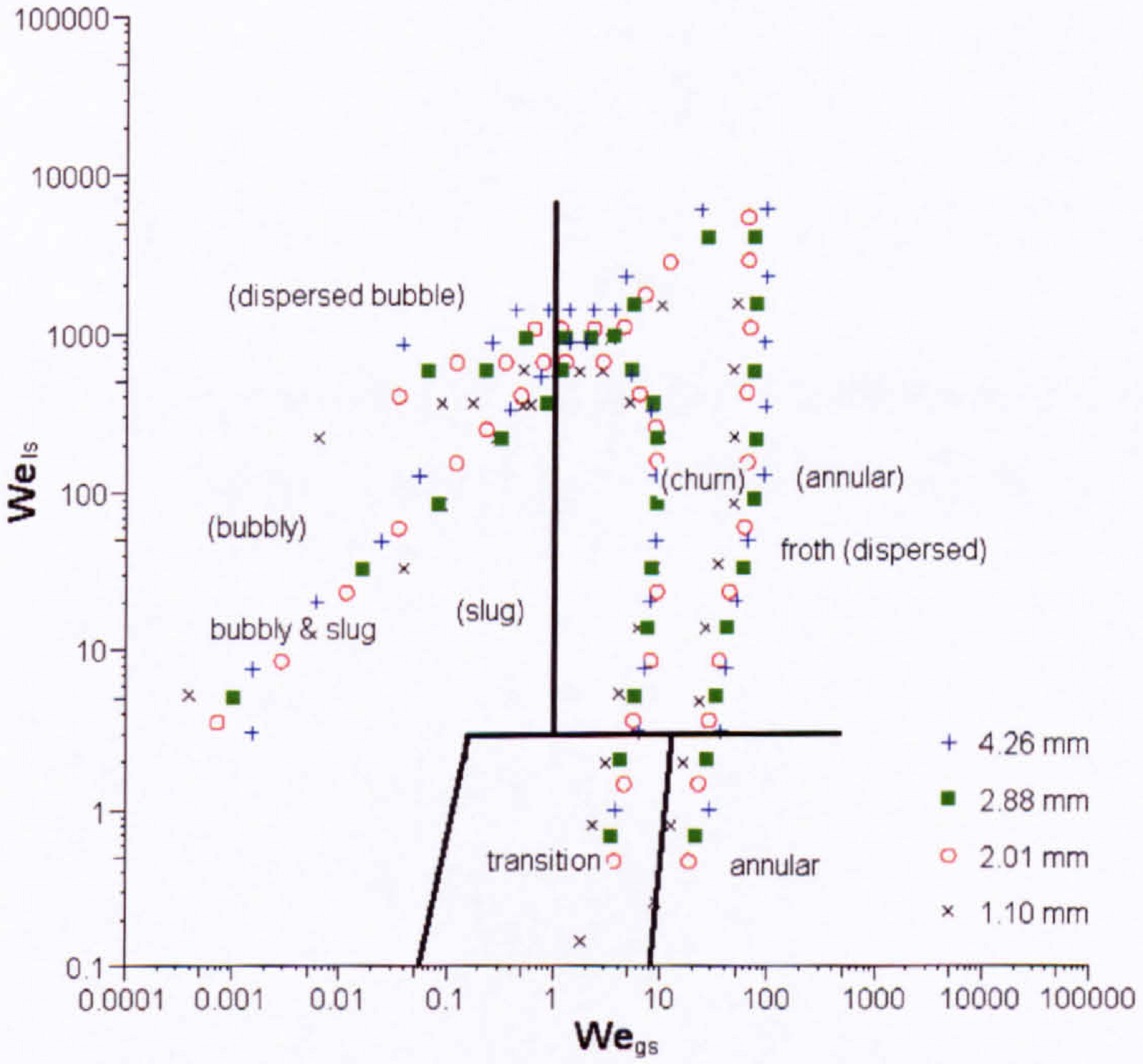

Figure 6.27 The comparison between the correlations proposed by Akbar et al. (2003) and the present experimental data at 6 bar.

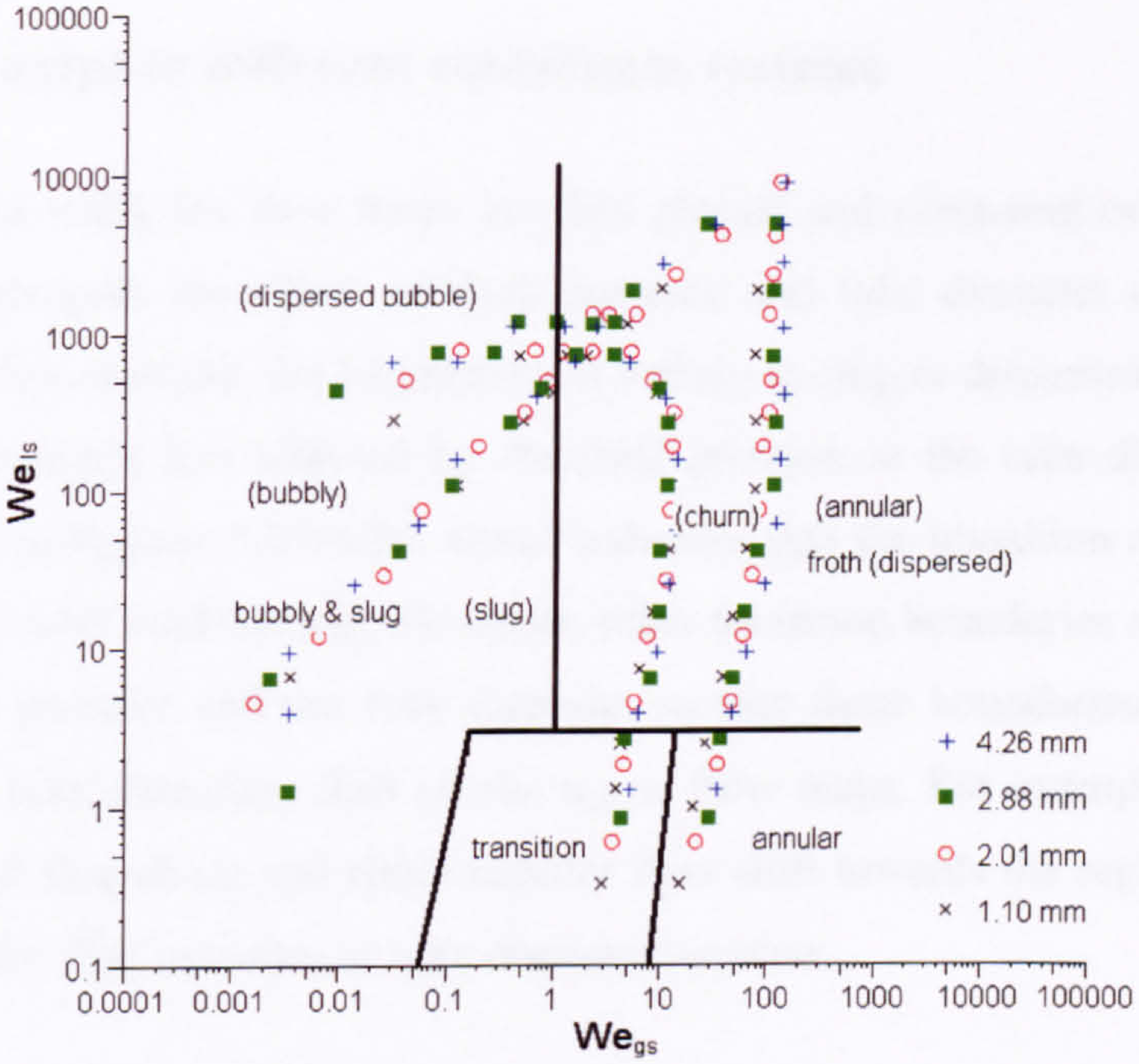

Figure 6.28 The comparison between the correlations proposed by Akbar et al. (2003) and the present experimental data at 10 bar.

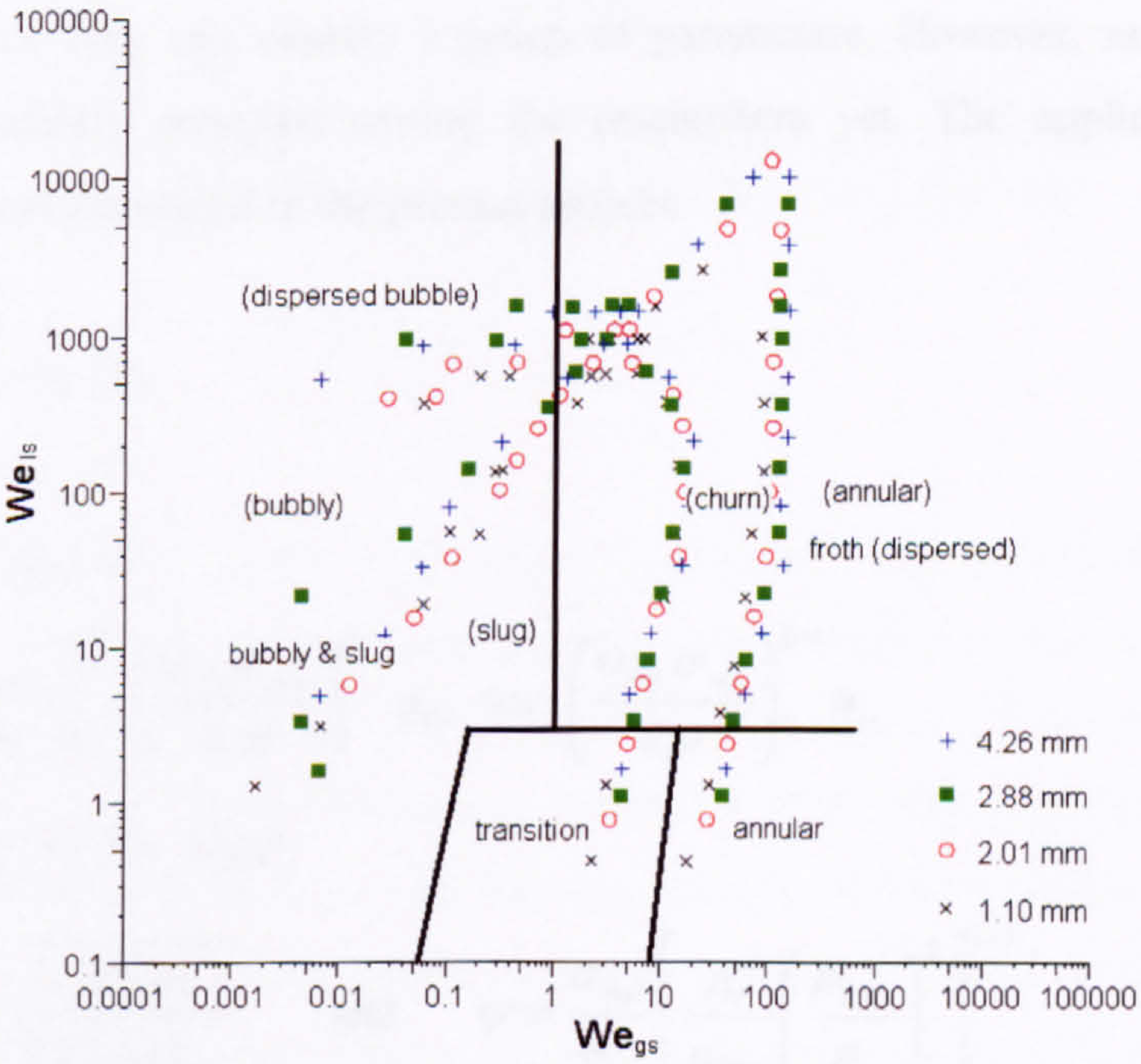

Figure 6.29 The comparison between the correlations proposed by Akbar et al. (2003) and the present experimental data at 14 bar.

6.3 Flow maps in different coordinate systems

In the current study the flow maps are first plotted and compared on the u_{gs}-u_{ls} flow maps to investigate the effect of fluid pressure and tube diameter on the transition boundaries. For example, the boundaries of bubbly to slug or dispersed bubble to churn flow are apparently less affected by the fluid pressure or the tube diameter from the comparisons in Figures 5.74-5.80, which indicates that the transition mechanisms may relate closely with void fraction. However, other transition boundaries are quite affected by the fluid pressure and the tube diameter so that these boundaries at the different pressures or tube diameters shift on the u_{gs}-u_{ls} flow maps. For example, the transition boundaries of slug-churn and churn-annular flow shift towards the region of lower gas flow rate as the fluid pressure or tube diameter increase.

The flow maps are also sketched on different coordinate systems in an attempt to obtain general and accurate prediction of the flow patterns in the flow regime studies, see the list below. The dimensionless coordinate groups were regarded to be more general and effective since they can contain a group of parameters. However, no one coordinate group was widely accepted among the researchers yet. The applicability of these parameters was examined in the present project.

(1) u_{gs} vs. u_{ls}

(2) x vs. G

(3) X vs. G

(4) $\left(\frac{\upsilon_{gref}}{\upsilon_g}\right)^{1/3}\left(\frac{\upsilon_{lref}\sigma_{ref}}{\upsilon_l\sigma}\right)^{1/4}u_{gs}$ vs. $\left(\frac{\upsilon_{lref}\sigma_{ref}}{\upsilon_l\sigma}\right)^{1/4}u_{ls}$

(5) G_{gs}/λ vs. $G_{ls}\psi$

$$\lambda=\sqrt{\frac{\rho_g\rho_l}{\rho_{gref}\rho_{lref}}} \quad \text{and} \quad \psi=\frac{\sigma_{ref}}{\sigma}\left[\frac{\mu_l}{\mu_{lref}}\left(\frac{\rho_{lref}}{\rho_l}\right)^2\right]^{1/3}$$

(6) $\frac{G_{ls}}{G_{gs}}\lambda\psi$ vs. $\frac{G_{gs}}{\lambda}$

(7) u_h vs. β

(8) G_{gs} vs. G_{ls}

(9) Fr_h vs. β

(10) $u_{gs}^2\rho_g$ vs. $u_{ls}^2\rho_l$

(11) $\frac{u_{gs}}{u_{ls}}$ vs. u_{ls}

(12) m_l vs. m_g

(13) Re_{gs} vs. Re_{ls}

(14) We_{gs} vs. We_{ls}

(15) X vs. Y

$$Y=\frac{(\rho_l-\rho_g)g}{\Delta P_g}$$

(16) $u_{gs}\sqrt{\frac{\rho_g}{gD(\rho_l-\rho_g)}}$ vs. $u_{ls}\sqrt{\frac{\rho_l}{gD(\rho_l-\rho_g)}}$

(17) $u_{gs}\sqrt{\frac{\rho_g}{\sqrt{g\sigma(\rho_l-\rho_g)}}}$ vs. $u_{ls}\sqrt{\frac{\rho_l}{\sqrt{g\sigma(\rho_l-\rho_g)}}}$

(18) $\frac{u_{gs}}{D}\sqrt{\frac{\rho_g}{\sqrt{g\sigma(\rho_l-\rho_g)}}}\sqrt{\frac{\sigma}{g(\rho_l-\rho_g)}}$ vs. $\frac{u_{ls}}{D}\sqrt{\frac{\rho_l}{\sqrt{g\sigma(\rho_l-\rho_g)}}}\sqrt{\frac{\sigma}{g(\rho_l-\rho_g)}}$

(19) $u_{gs}\left(\frac{\rho_g}{g\sigma}\right)^{0.25}$ vs. $u_{ls}\left(\frac{\rho_l}{g\sigma}\right)^{0.25}$

The flow maps based on the above groups seem disorderly without following a clear rule. For example, the flow maps using quality and mass flux as the coordinate group at the different pressures and diameters are compared in Figure 6.30 for the 1.10 mm tubes and Figure 6.31 for 10 bar pressure, in which the all transition boundaries obtained at the different fluid pressure and tube diameter can not match with each other. The same conclusions can be obtained for other tubes and pressures. Some groups may consider the effect of fluid properties or tube dimension. The flow maps using these coordinate systems can provide reasonable predictions at different conditions. Semi-empirical correlations may be developed based on these parameters.

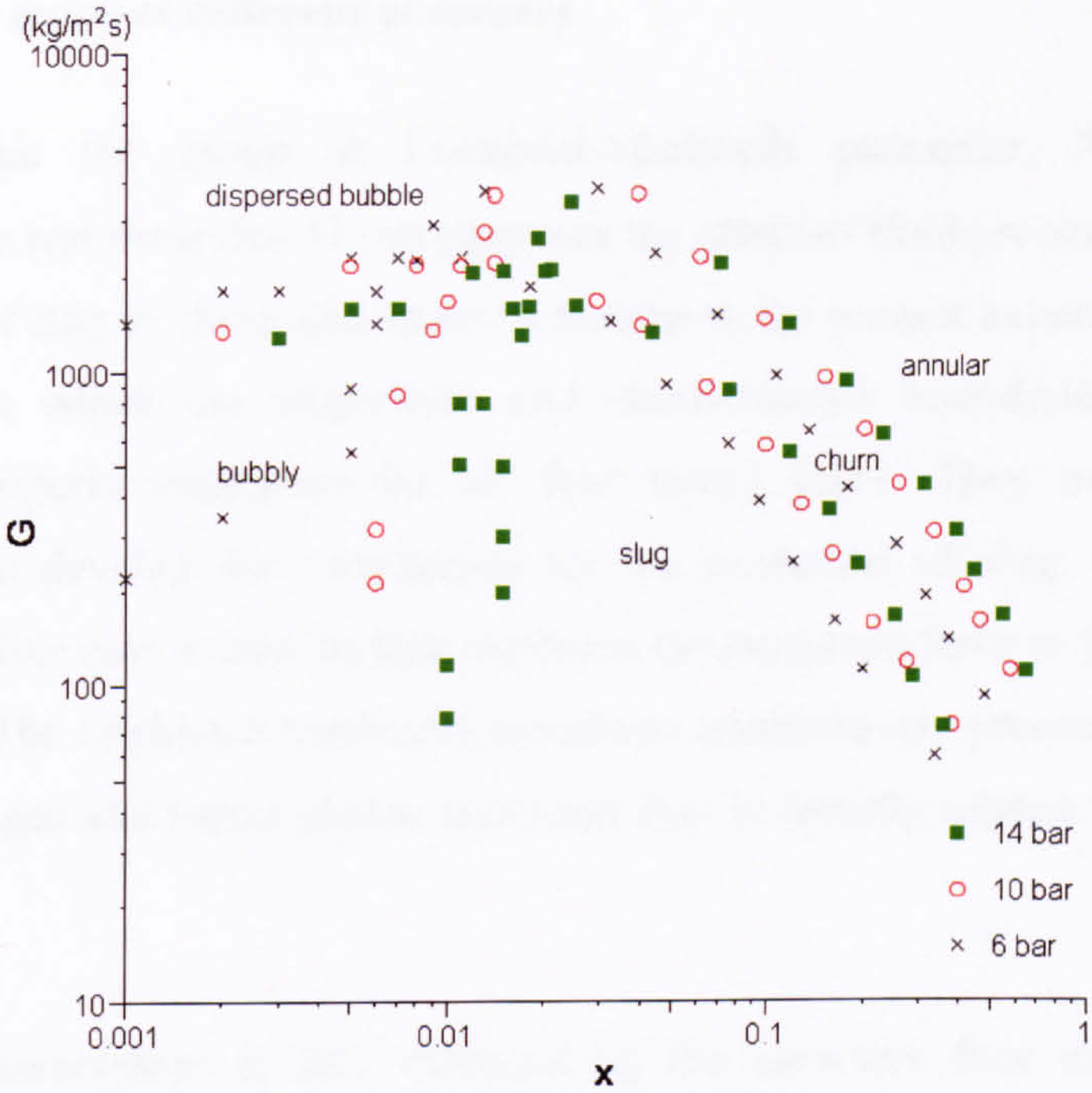

Figure 6.30 Comparison of the flow pattern transition boundaries using mass flux and quality for the 1.10 mm tube.

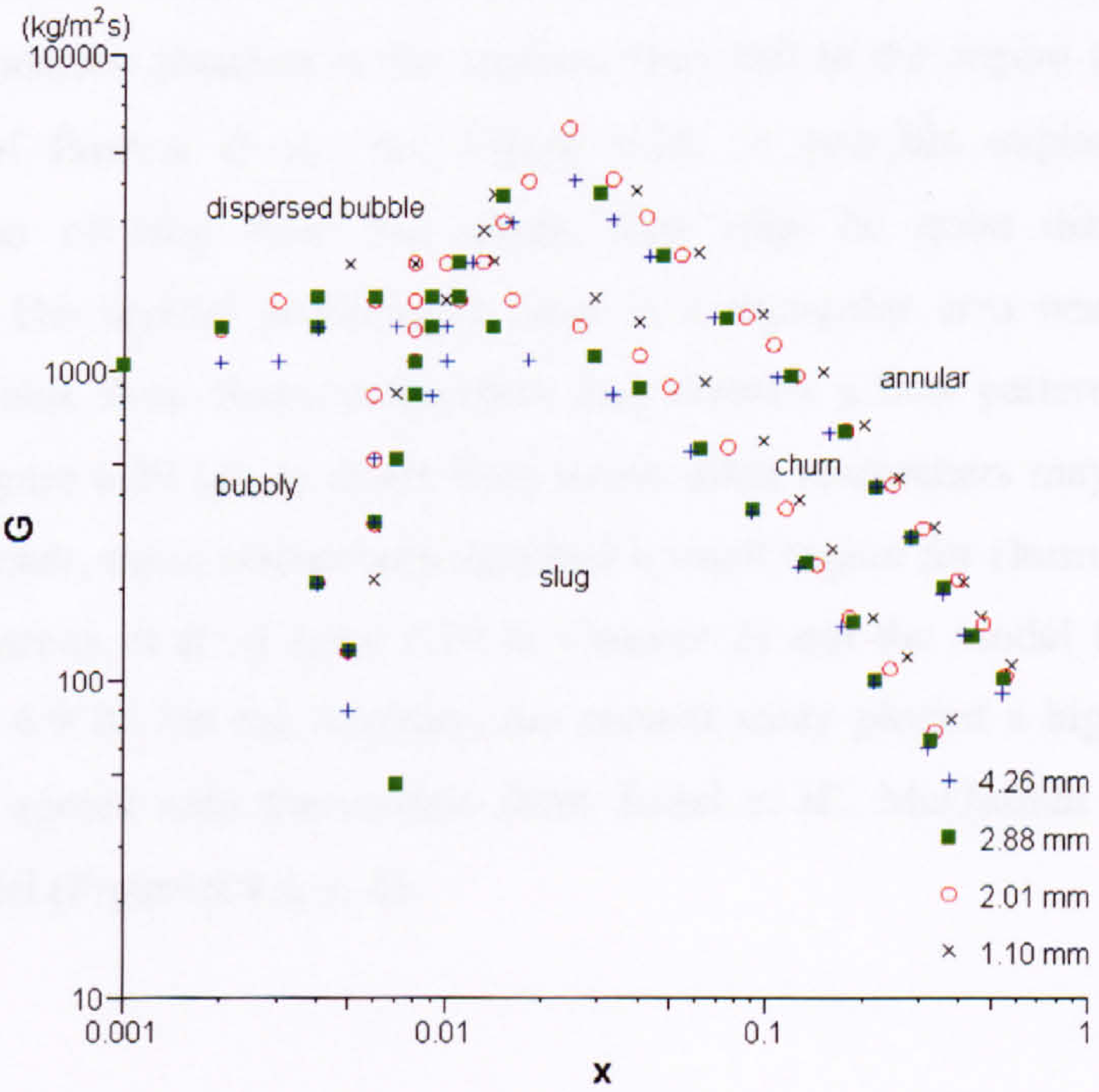

Figure 6.31 Comparison of the flow pattern transition boundaries using mass flux and quality at 10 bar.

6.3.1 Flow maps at different pressures

It seems that the group of Lockhard-Martinelli parameter, X defined in the nomenclature and mass flux G can represent the effect of fluid pressure on the transition boundaries of slug to churn and churn to annular in the present experiments, see Figures 6.32-6.35, in which the slug-churn and churn-annular boundaries at the different pressures properly superpose for all four tested tubes. They might be the right parameters to develop the correlations for the prediction of slug, churn and annular flow. A possible reason may be that friction is the dominant force in these two transition boundaries. The Lockhard-Martinelli parameter quantitatively presents the friction ratio between the gas and liquid phases and mass flux is directly related to the overall fluid friction.

The above assumption is also validated by the air-water flow maps for the small diameter tubes obtained in the earlier studies. For example, the transition boundaries indicated by solid lines on the current data agree with the Mishima and Hibiki (1996) experimental data on the boundary to slug flow, see Figures 6.36 and 6.37. However, there is significant distinction with Barnea et al. (1983). The slug-churn and churn-annular boundaries obtained in the current study fall in the region of slug flow in the flow map of Barnea et al., see Figure 6.38. A possible explanation is that the identifications of slug flow and churn flow may be quite different among the researchers. The typical problematic zone is a triangular area near slug, churn and dispersed bubble flow. Some researchers may identify a flow pattern, such as the flow regime in Figure 6.39 (a), as churn flow whilst other researchers may group it into slug flow. As a result, some researchers sketched a small region for churn flow, see the flow map from Barnea et al. (Figure 2.19 in Chapter 2) and the model from Mishima and Ishii (Figure 6.9 b). On the contrary, the present study plotted a bigger area for churn flow, which agrees with the models from Taitel et al., McQuillan and Whalley, and Unified Model (Figure 6.9 a, c, d).

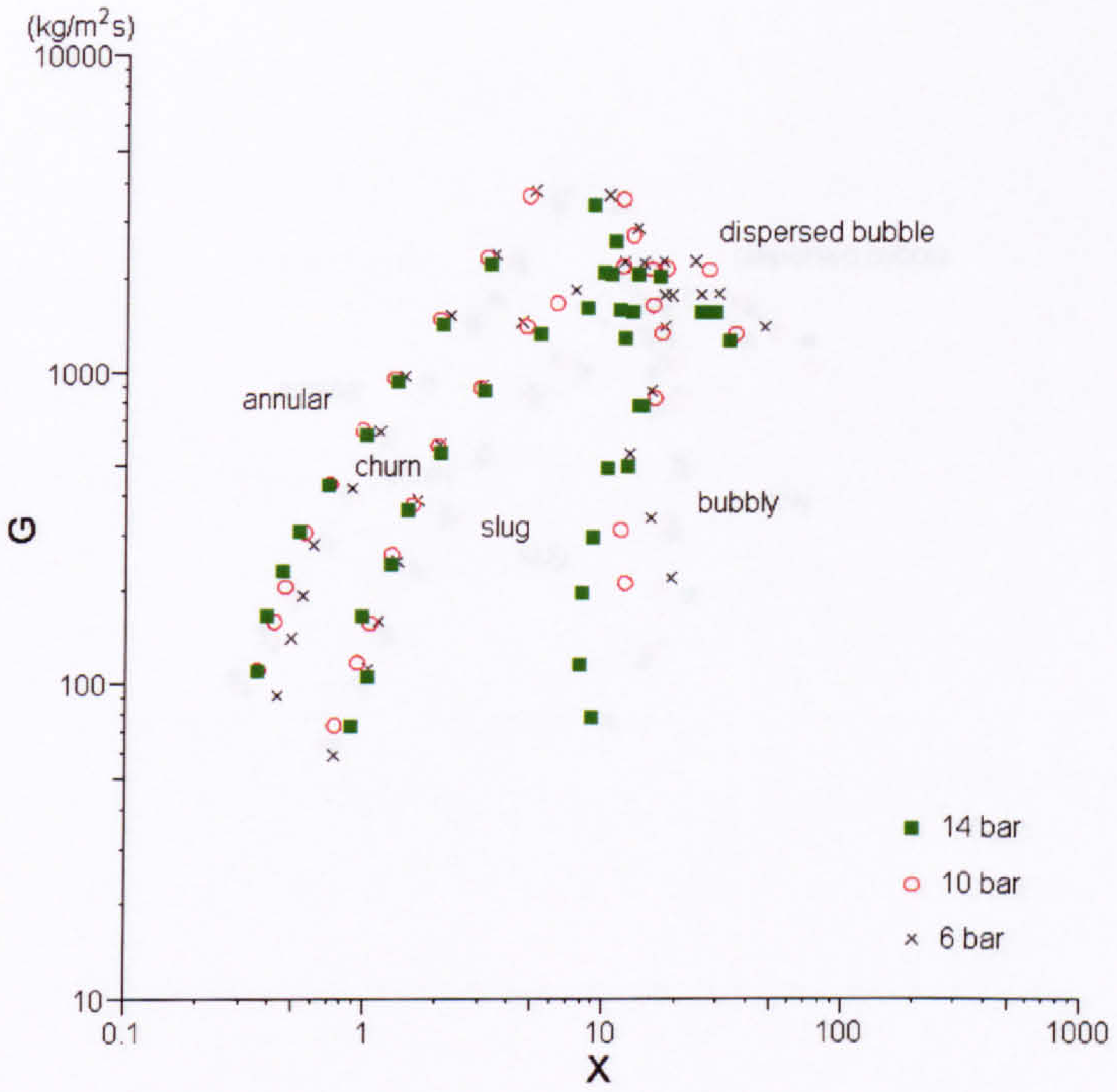

Figure 6.32 Comparison of the flow pattern transition boundaries using mass flux and Lockhard-Martinelli Parameter for the 1.10 mm tube.

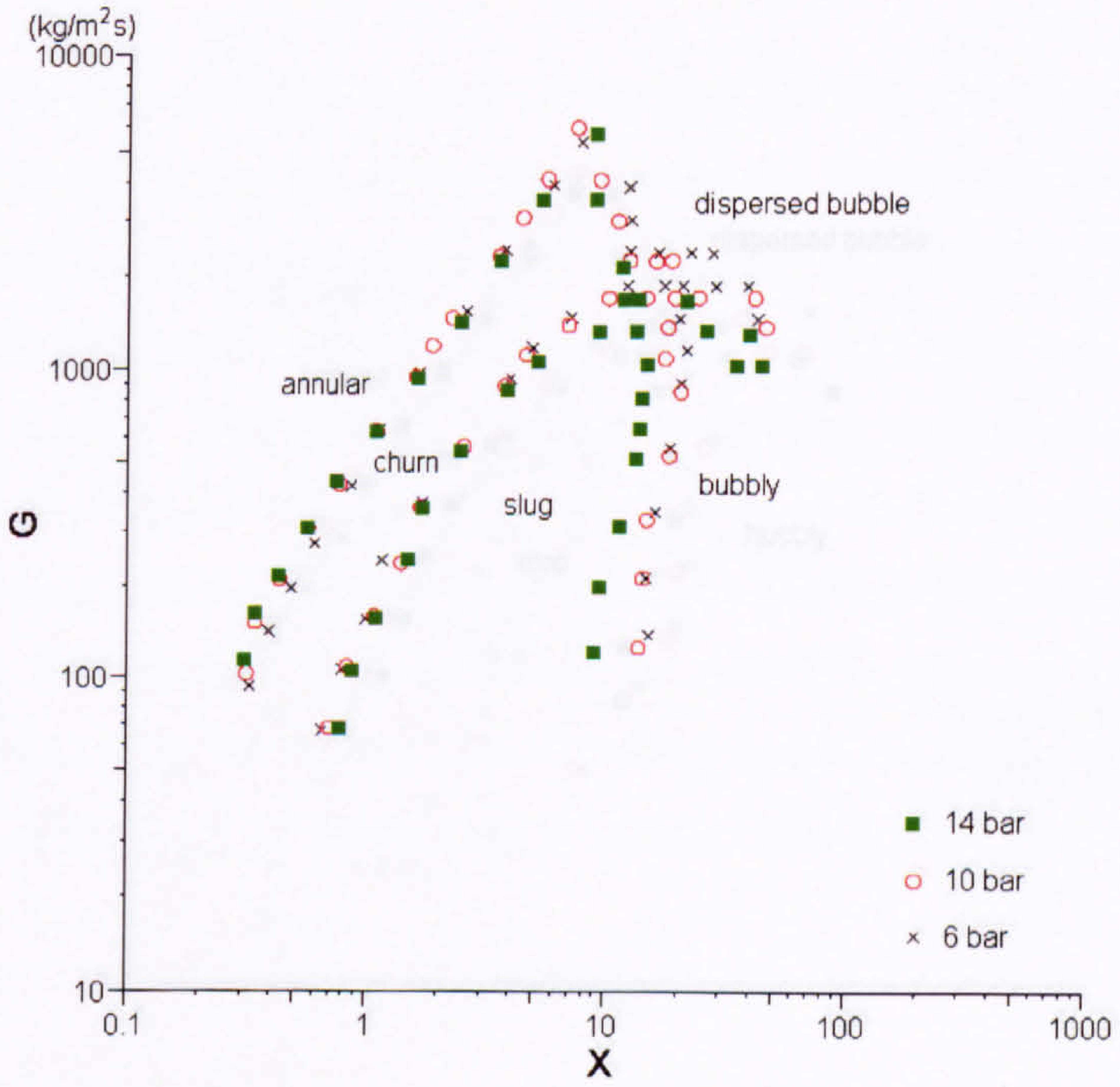

Figure 6.33 Comparison of the flow pattern transition boundaries using mass flux and Lockhard-Martinelli Parameter for the 2.01 mm tube.

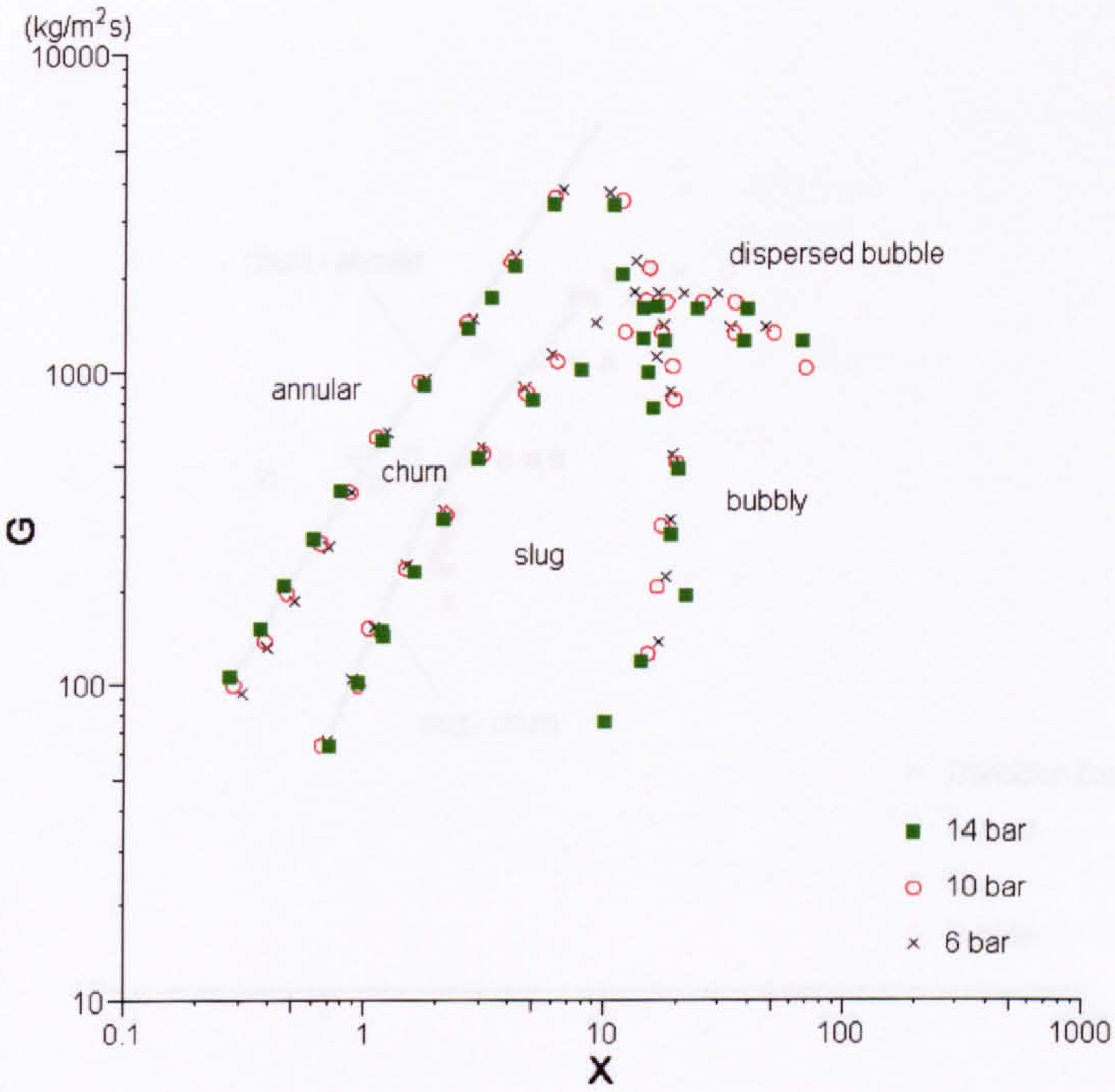

Figure 6.34 Comparison of the flow pattern transition boundaries using mass flux and Lockhard-Martinelli Parameter for the 2.88 mm tube.

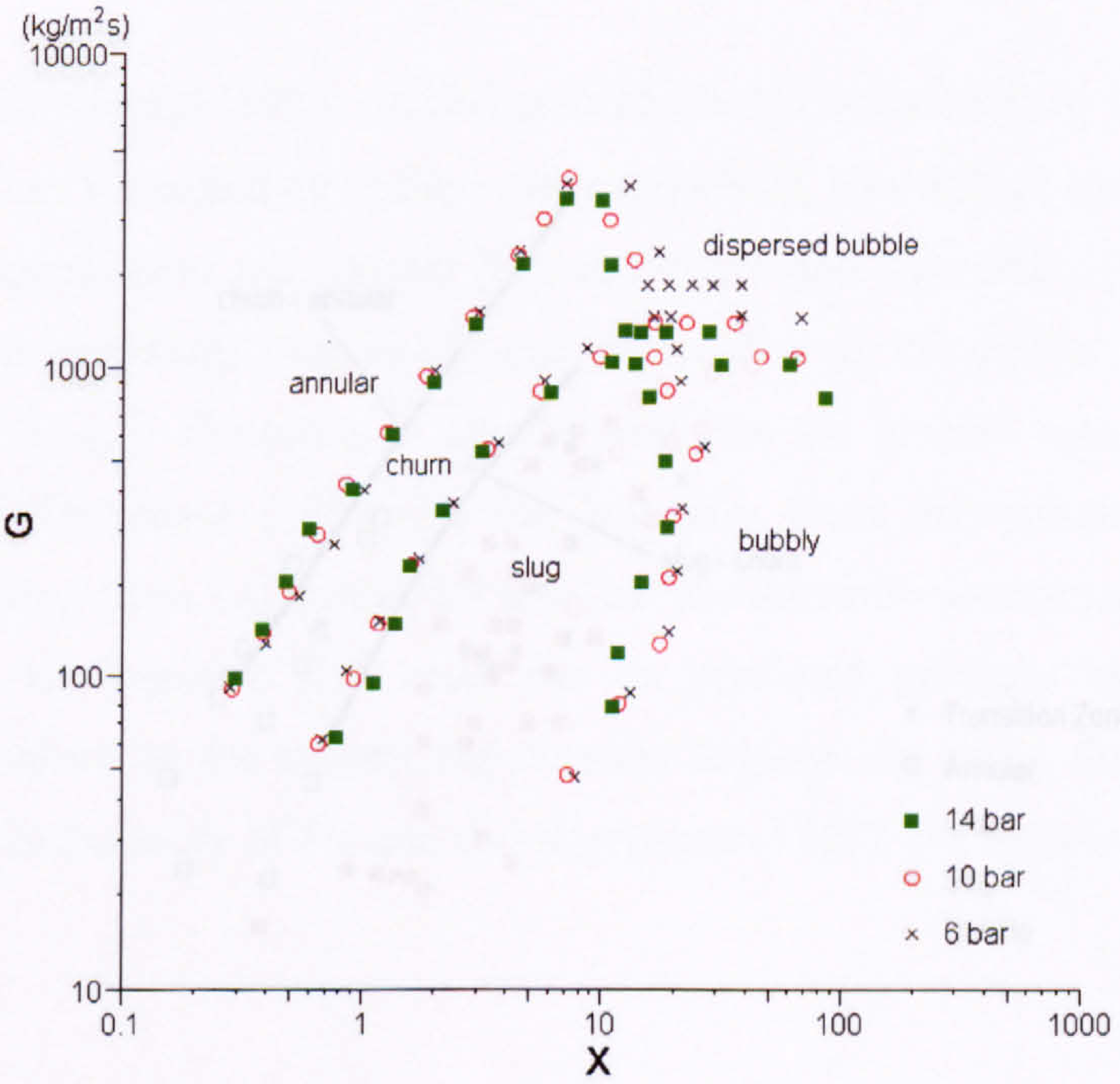

Figure 6.35 Comparison of the flow pattern transition boundaries using mass flux and Lockhard-Martinelli Parameter for the 4.26 mm tube.

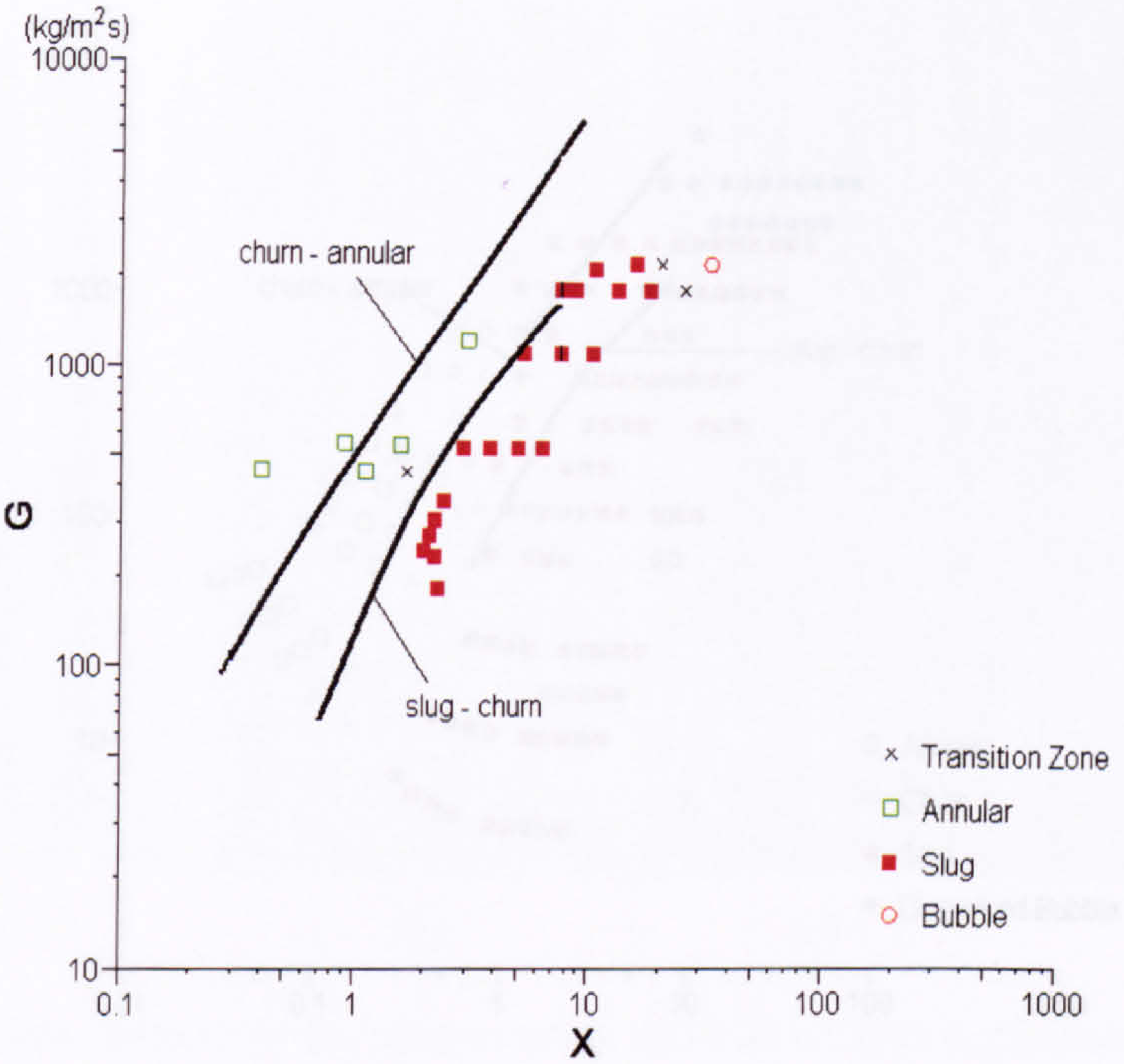

Figure 6.36 Comparison of the slug-churn and churn-annular boundaries in the 2.01 mm tube from the present experiments (solid lines) and the air-water flow map in the 2.05 mm tube from Mishima and Hibiki (1996).

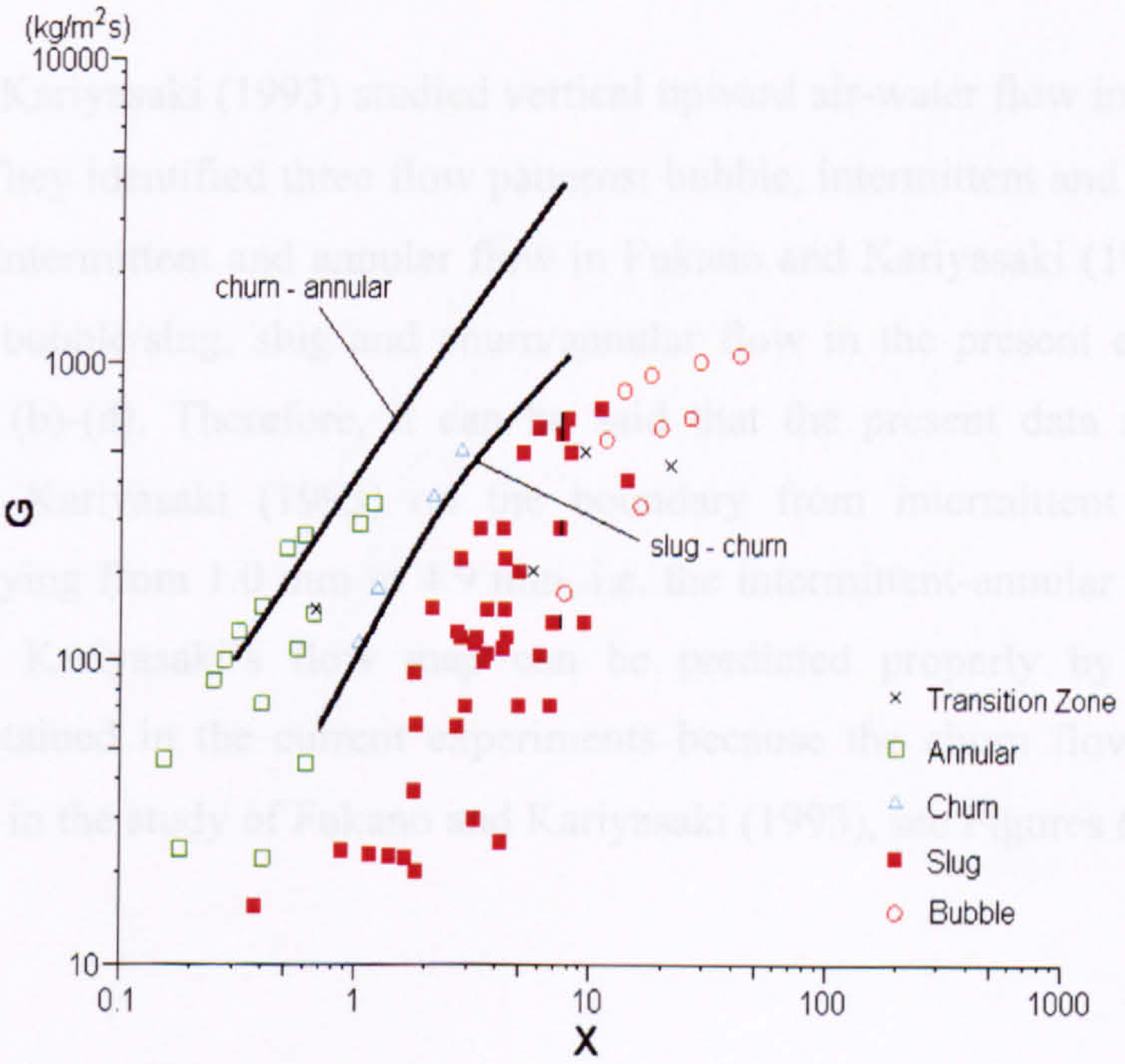

Figure 6.37 Comparison of the slug-churn and churn-annular boundaries in the 4.26 mm tube from the present experiments (solid lines) and the air-water flow map in the 4.08 mm tube from Mishima and Hibiki (1996).

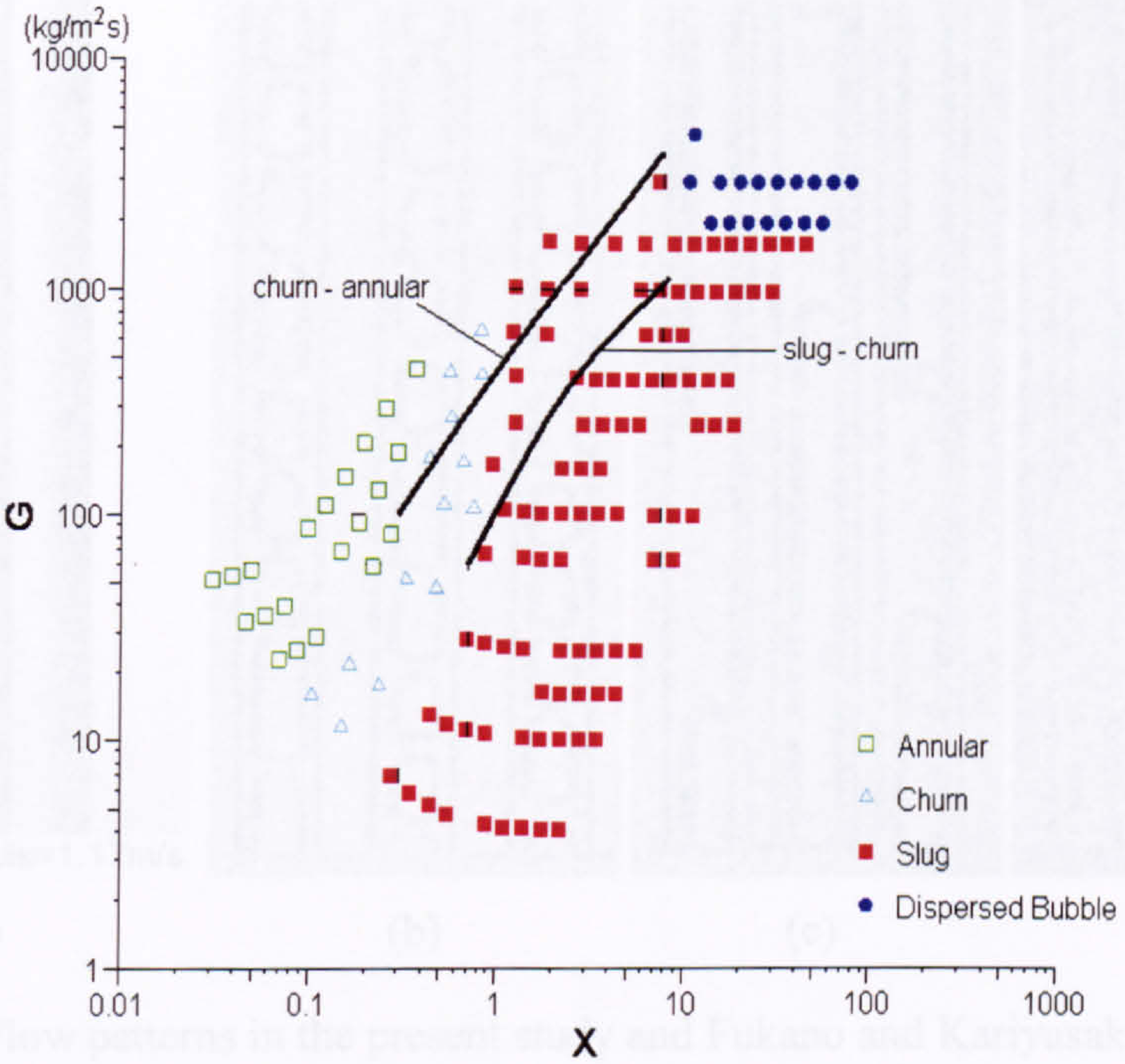

Figure 6.38 Comparison of the slug-churn and churn-annular boundaries in the 4.26 mm tube from the present experiments (solid lines) and the air-water flow map in the 4 mm tube from Barnea et al. (1983).

Fukano and Kariyasaki (1993) studied vertical upward air-water flow in 1.0, 2.4 and 4.9 mm tubes. They identified three flow patterns: bubble, intermittent and annular. In fact, the bubble, intermittent and annular flow in Fukano and Kariyasaki (1993) correspond to confined bubble/slug, slug and churn/annular flow in the present experiments, see Figure 6.39 (b)-(d). Therefore, it can be said that the present data agree well with Fukano and Kariyasaki (1993) on the boundary from intermittent to annular for diameter varying from 1.0 mm to 4.9 mm, i.e. the intermittent-annular boundary in the Fukano and Kariyasaki's flow map can be predicted properly by the slug-churn boundary obtained in the current experiments because the churn flow is included in annular flow in the study of Fukano and Kariyasaki (1993), see Figures 6.40-6.43.

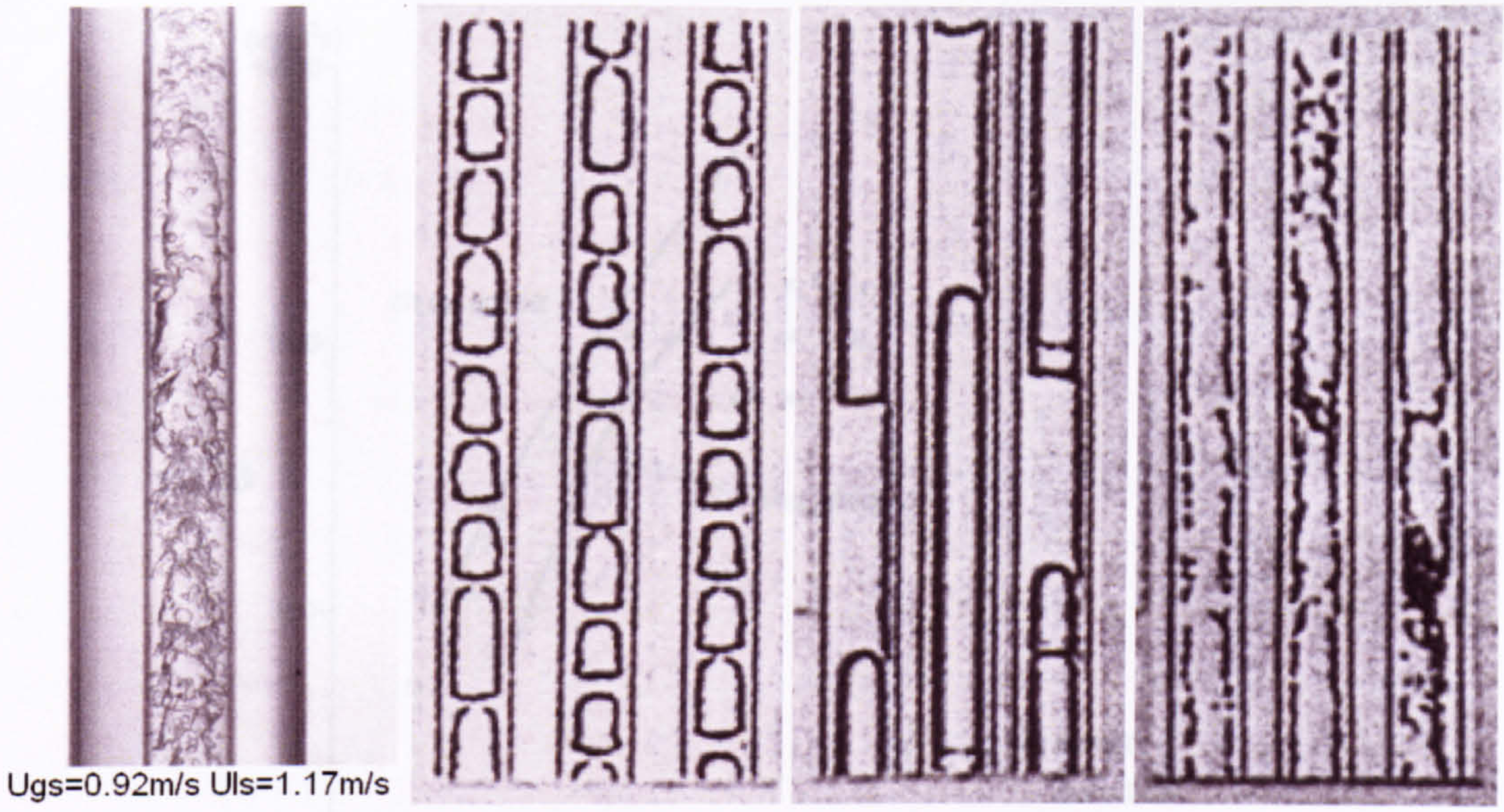

(a) (b) (c) (d)

Figure 6.39 Flow patterns in the present study and Fukano and Kariyasaki (1993).

(a) Churn flow in the present experiments.
(b) Bubble flow in the experiments of Fukano and Kariyasaki (1993).
(c) Intermittent flow in the experiments of Fukano and Kariyasaki (1993).
(d) Annular flow in the experiments of Fukano and Kariyasaki (1993).

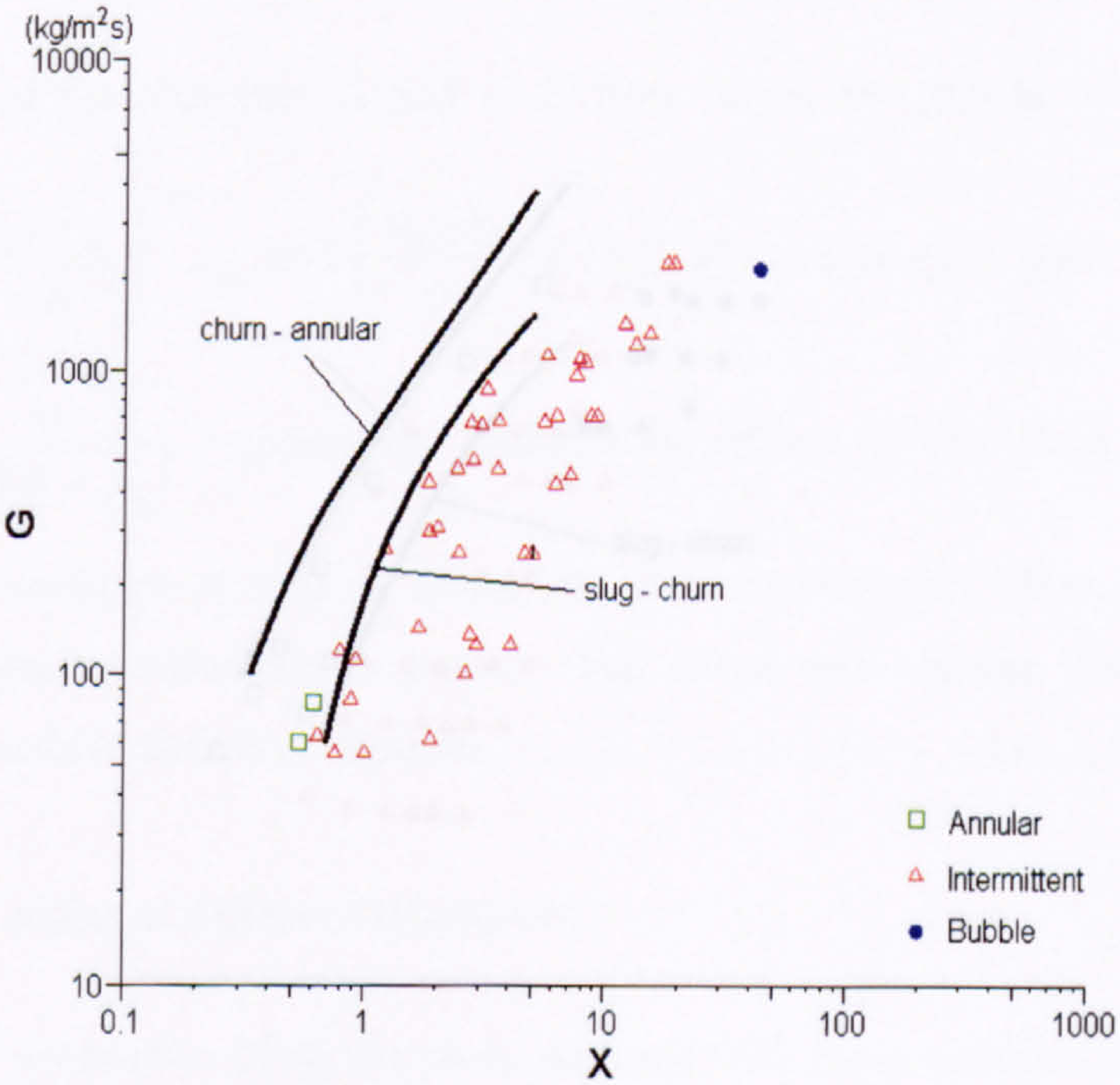

Figure 6.40 Comparison of the slug-churn and churn-annular boundaries in the 1.10 mm tube from the present experiments (solid lines) and the air-water flow map in the 1.0 mm tube from Fukano and Kariyasaki (1993).

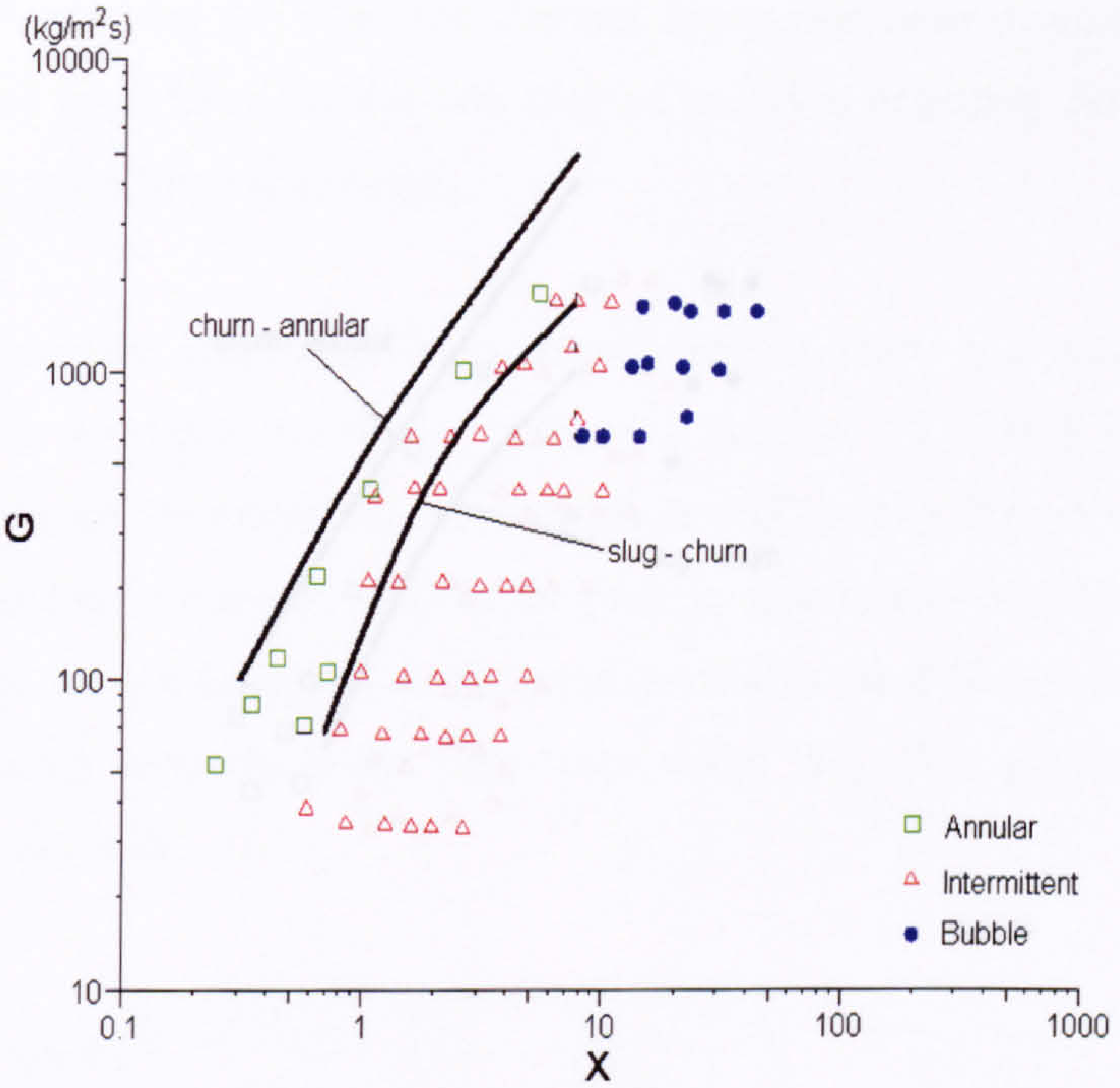

Figure 6.41 Comparison of the slug-churn and churn-annular boundaries in the 2.01 mm tube from the present experiments (solid lines) and the air-water flow map in the 2.4 mm tube from Fukano and Kariyasaki (1993).

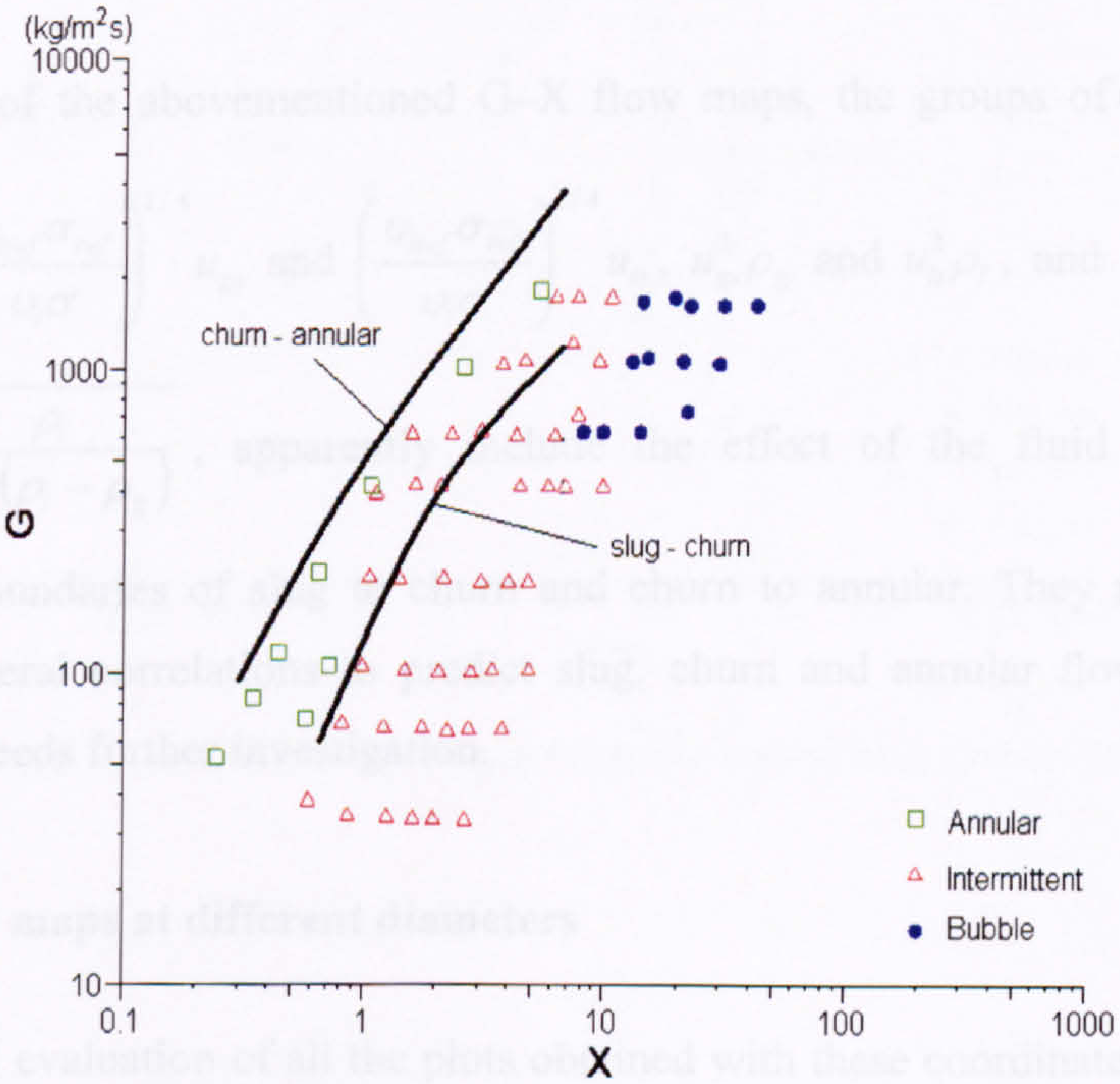

Figure 6.42 Comparison of the slug-churn and churn-annular boundaries in the 2.88 mm tube from the present experiments (solid lines) and the air-water flow map in the 2.4 mm tube from Fukano and Kariyasaki (1993).

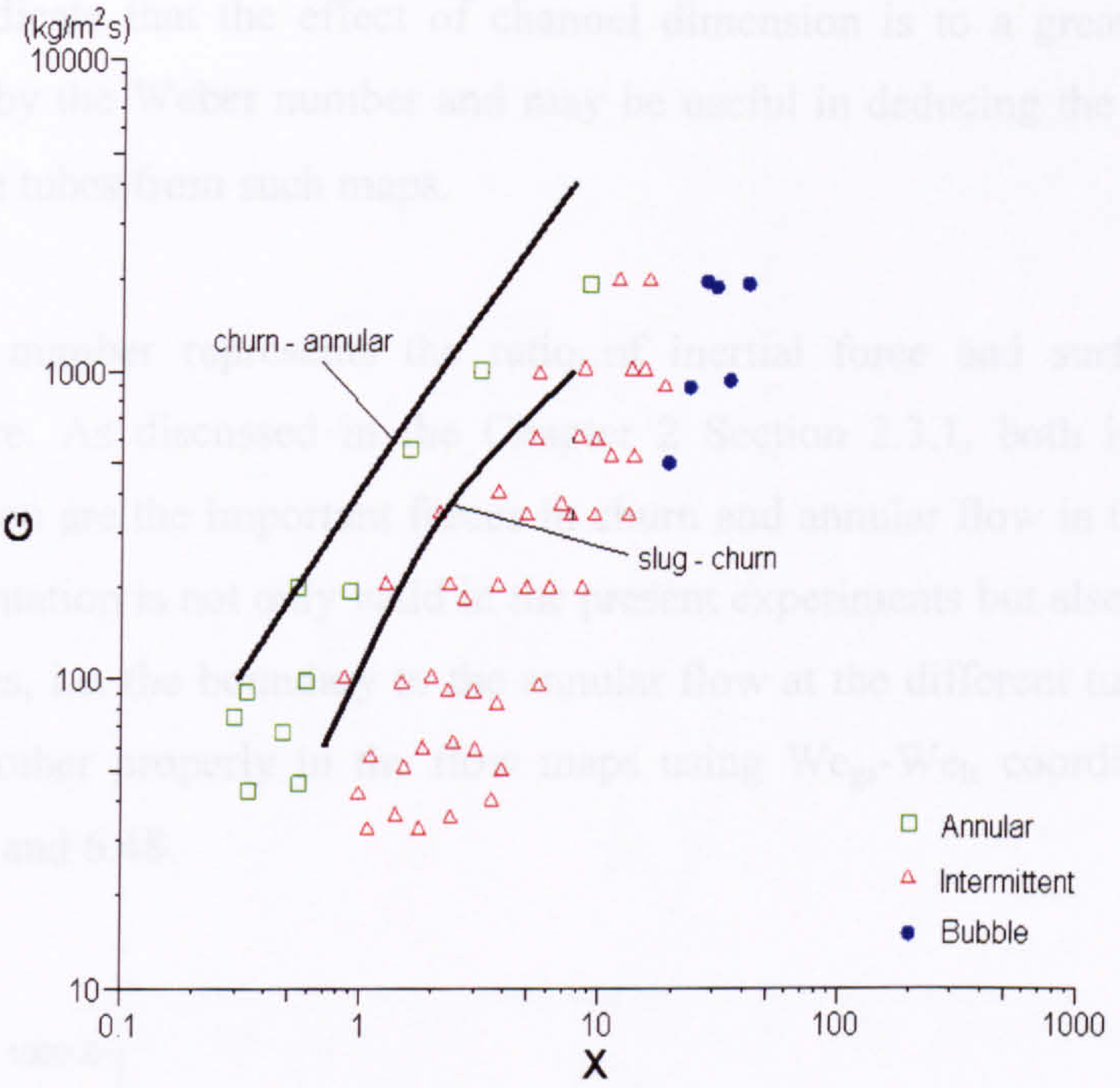

Figure 6.43 Comparison of the slug-churn and churn-annular boundaries in the 4.26 mm tube from the present experiments (solid lines) and the air-water flow map in the 4.9 mm tube from Fukano and Kariyasaki (1993).

In addition of the abovementioned G–X flow maps, the groups of G_{gs}/λ and $G_{ls}\psi$, $\left(\frac{\upsilon_{gref}}{\upsilon_g}\right)^{1/3}\left(\frac{\upsilon_{lref}\sigma_{ref}}{\upsilon_l\sigma}\right)^{1/4}u_{gs}$ and $\left(\frac{\upsilon_{lref}\sigma_{ref}}{\upsilon_l\sigma}\right)^{1/4}u_{ls}$, $u_{gs}^2\rho_g$ and $u_{ls}^2\rho_l$, and $u_{gs}\sqrt{\frac{\rho_g}{gD(\rho_l-\rho_g)}}$ and $u_{ls}\sqrt{\frac{\rho_l}{gD(\rho_l-\rho_g)}}$, apparently include the effect of the fluid pressure on the transition boundaries of slug to churn and churn to annular. They might be used to develop general correlations to predict slug, churn and annular flow. However, this possibility needs further investigation.

6.3.2 Flow maps at different diameters

After careful evaluation of all the plots obtained with these coordinate systems one can reach the conclusion that the use of the Weber number may be a good choice. As seen in Figures 6.44-6.46, the transition boundaries of slug-churn and churn-annular for the four different diameter tubes are superimposed at all the experimental pressures. It seems to indicate that the effect of channel dimension is to a great extent correctly represented by the Weber number and may be useful in deducing the flow regimes for different size tubes from such maps.

The Weber number represents the ratio of inertial force and surface tension, see Nomenclature. As discussed in the Chapter 2 Section 2.3.1, both inertial force and surface tension are the important forces in churn and annular flow in the smaller tubes. This representation is not only valid in the present experiments but also holds true in the earlier studies, i.e. the boundary to the annular flow at the different tube diameters can match each other properly in the flow maps using We_{gs}-We_{ls} coordinate system, see Figures 6.47 and 6.48.

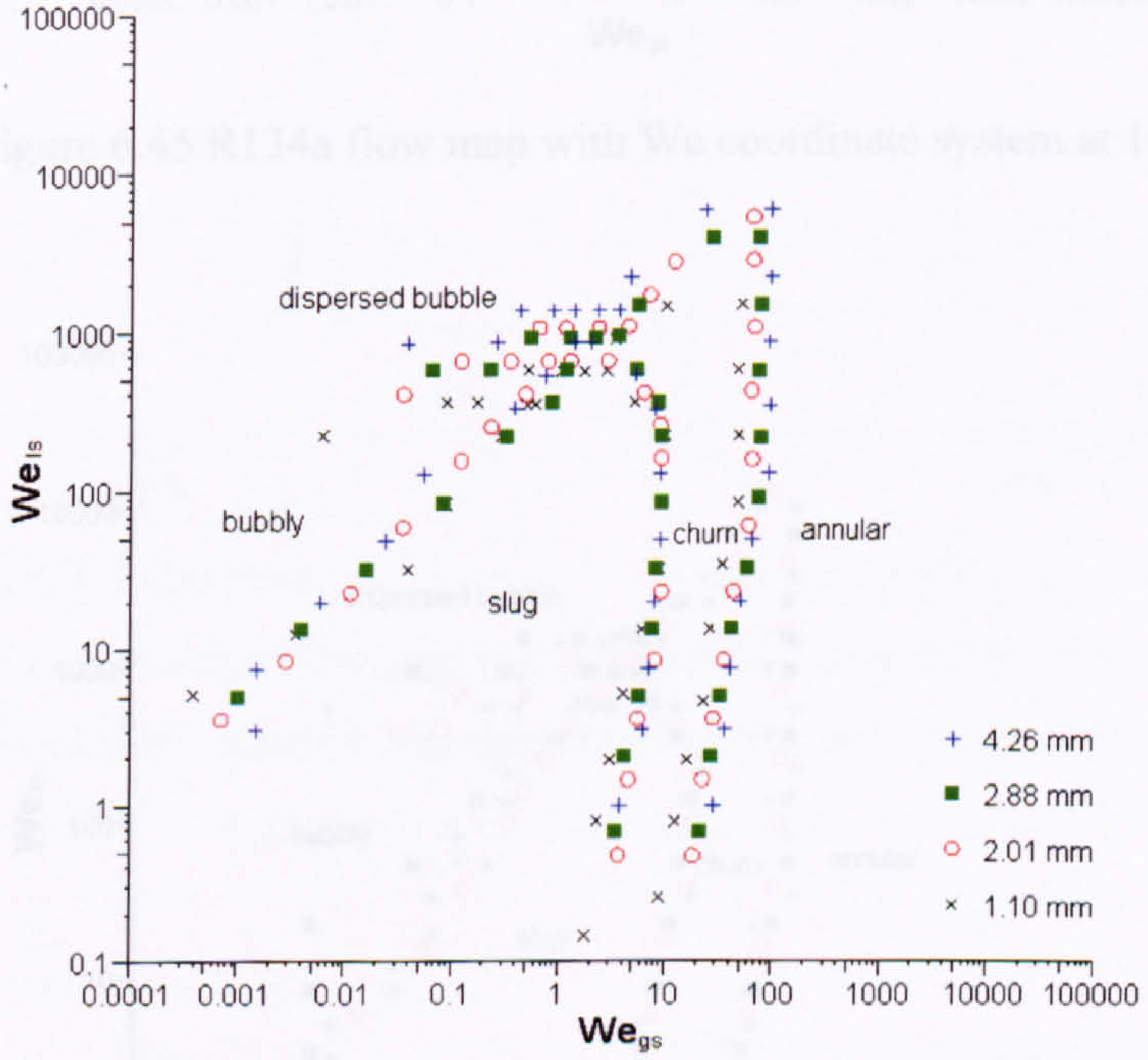

Figure 6.44 R134a flow map with We coordinate system at 6 bar.

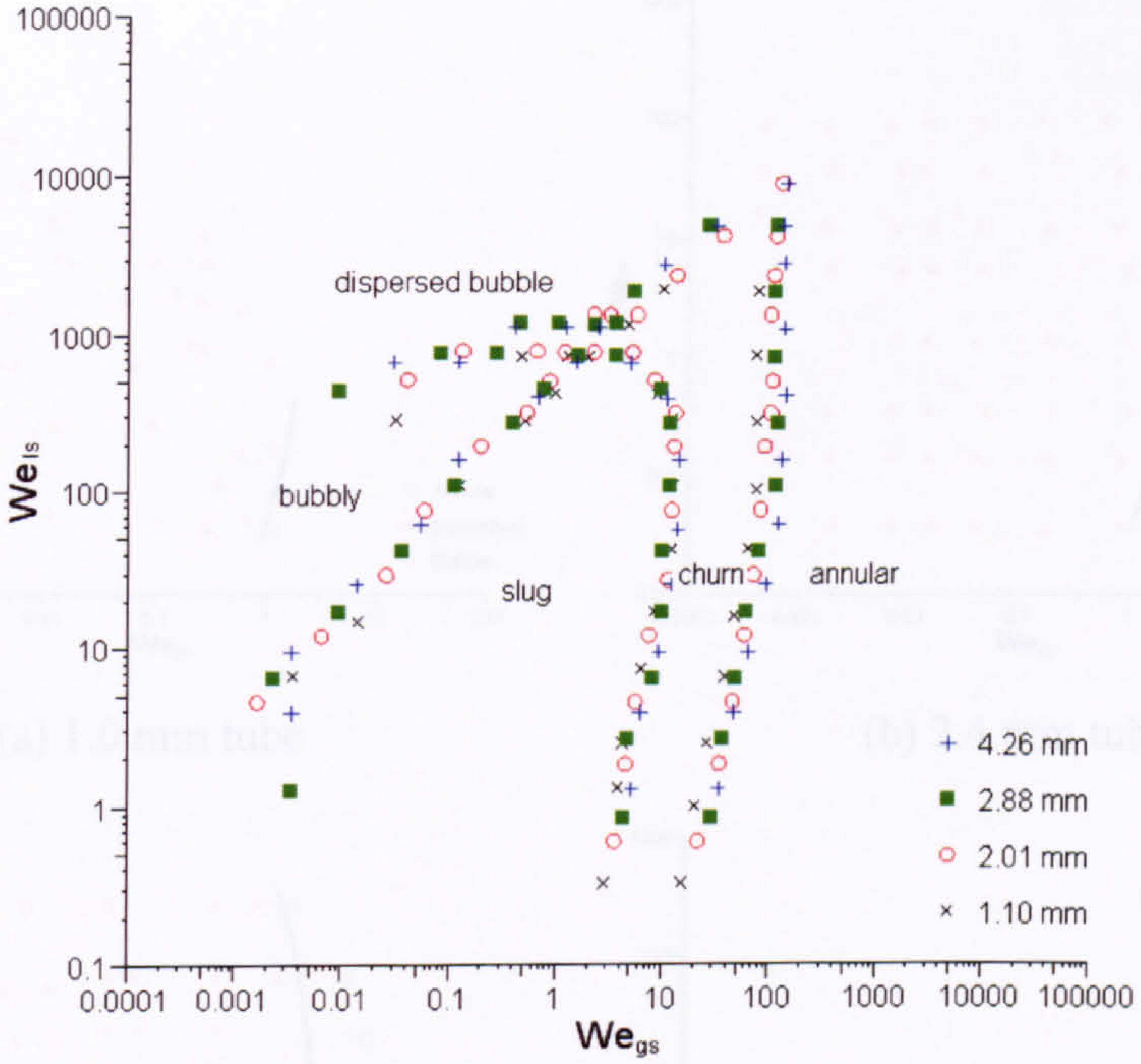

Figure 6.45 R134a flow map with We coordinate system at 10 bar.

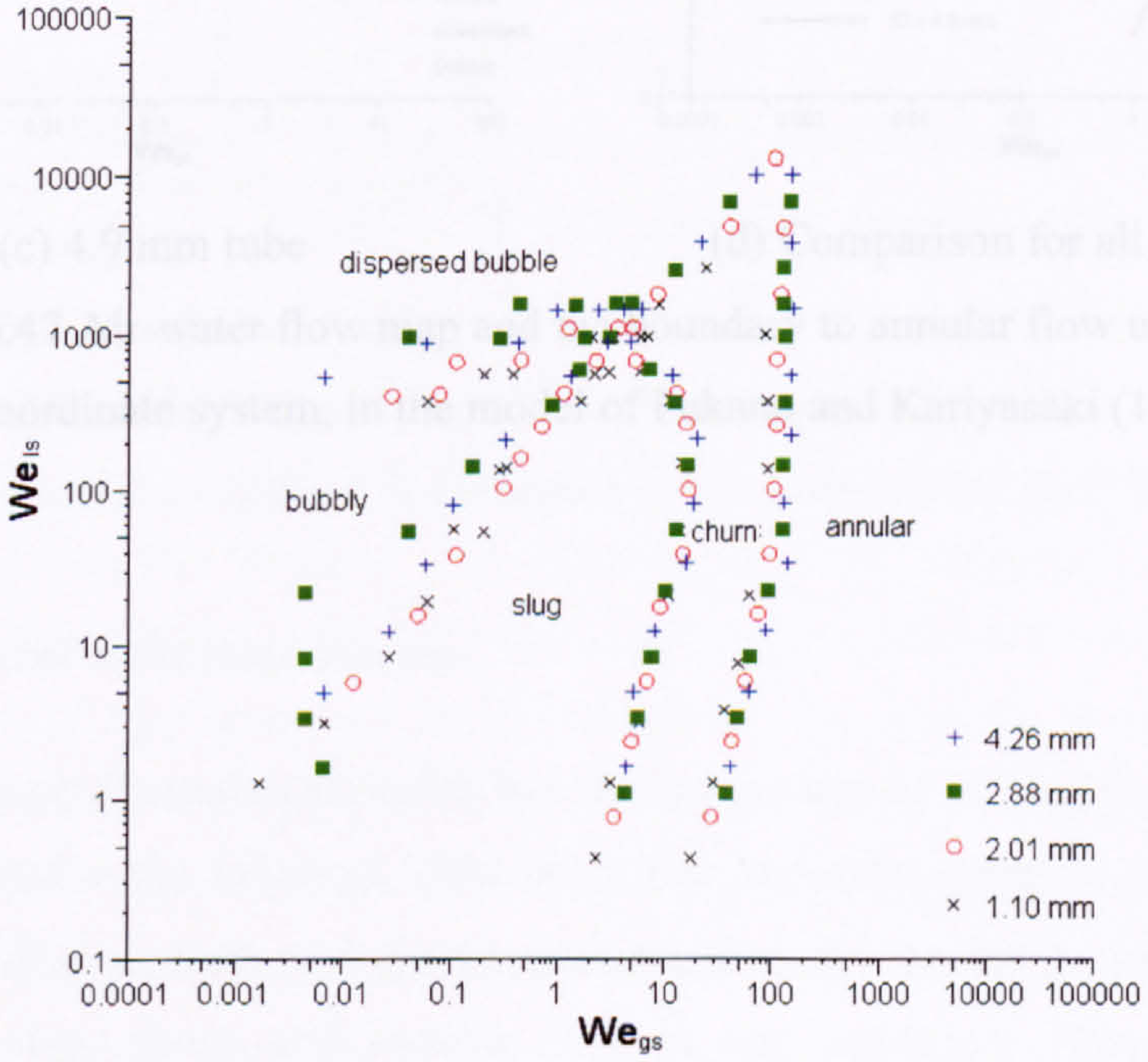

Figure 6.46 R134a flow map with We coordinate system at 14 bar.

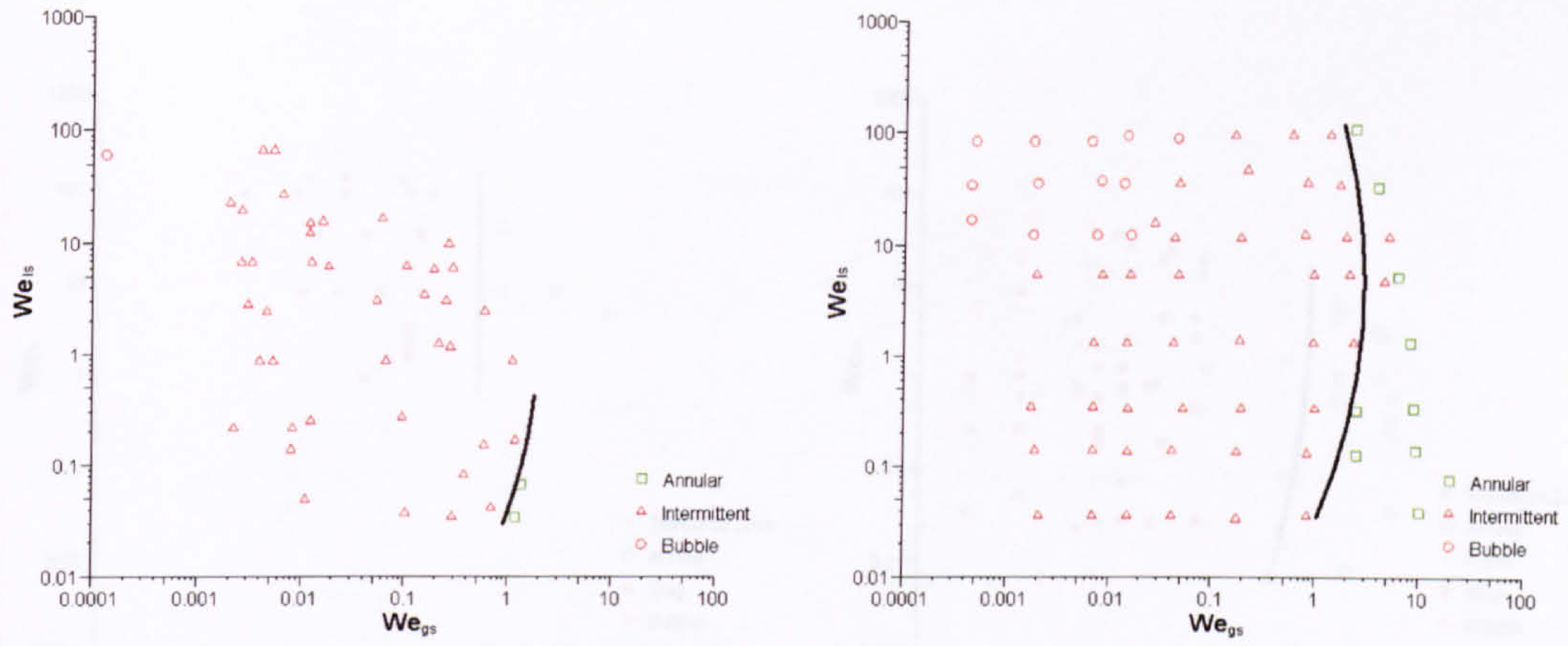

(a) 1.0 mm tube

(b) 2.4 mm tube

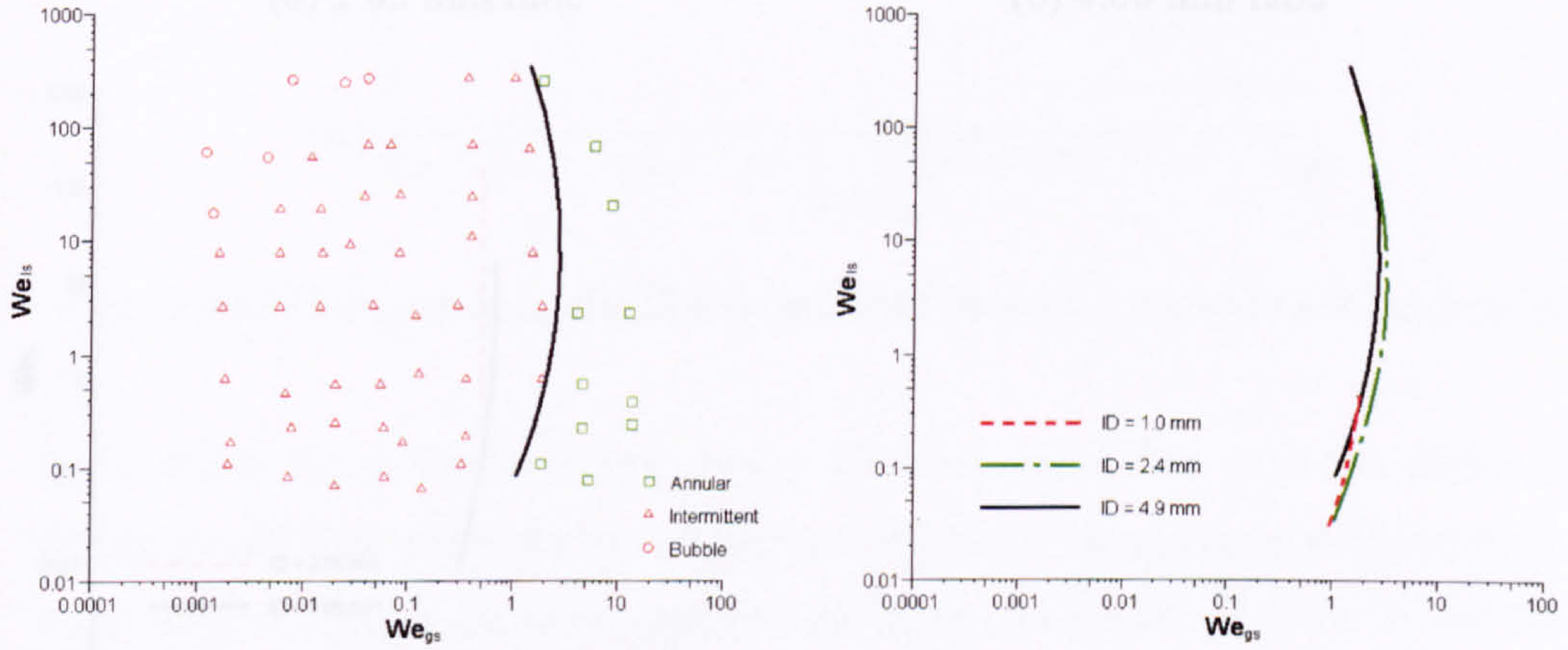

(c) 4.9 mm tube

(d) Comparison for all diameters

Figure 6.47 Air-water flow map and the boundary to annular flow using the We coordinate system, in the model of Fukano and Kariyasaki (1993).

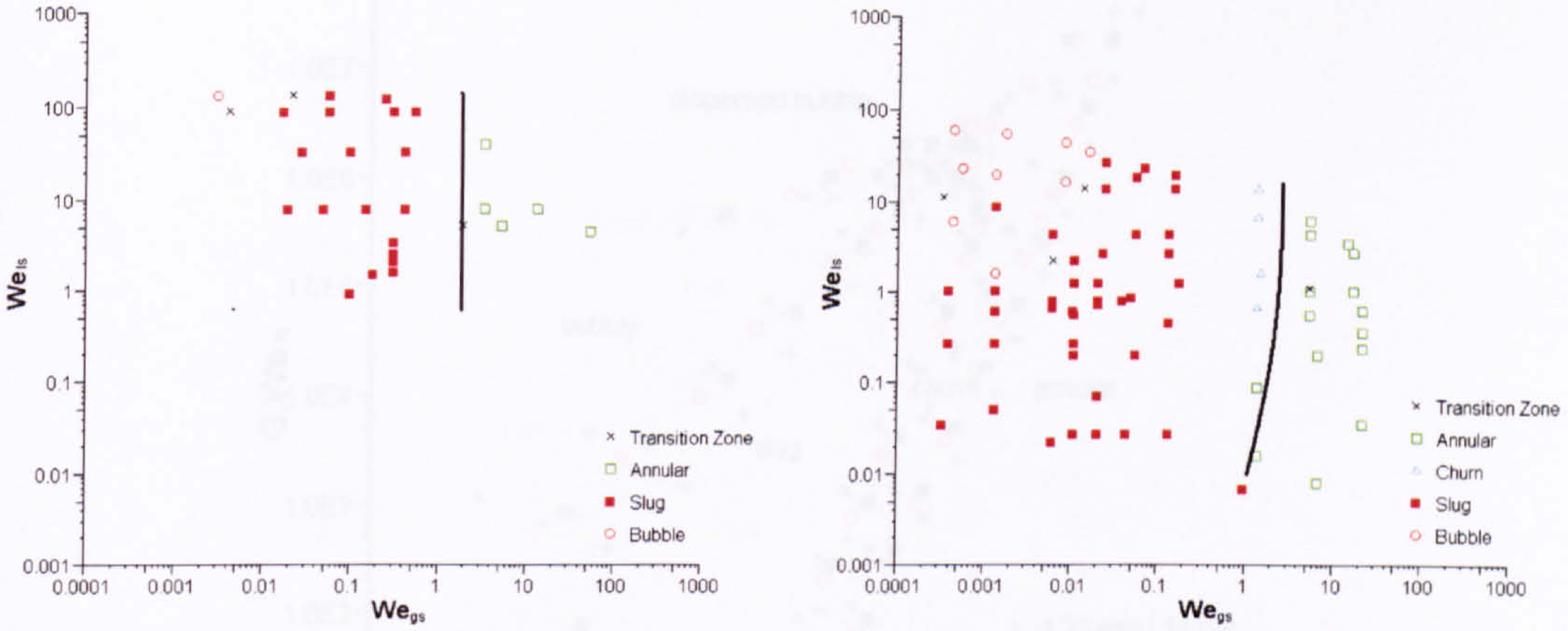

(a) 2.05 mm tube (b) 4.08 mm tube

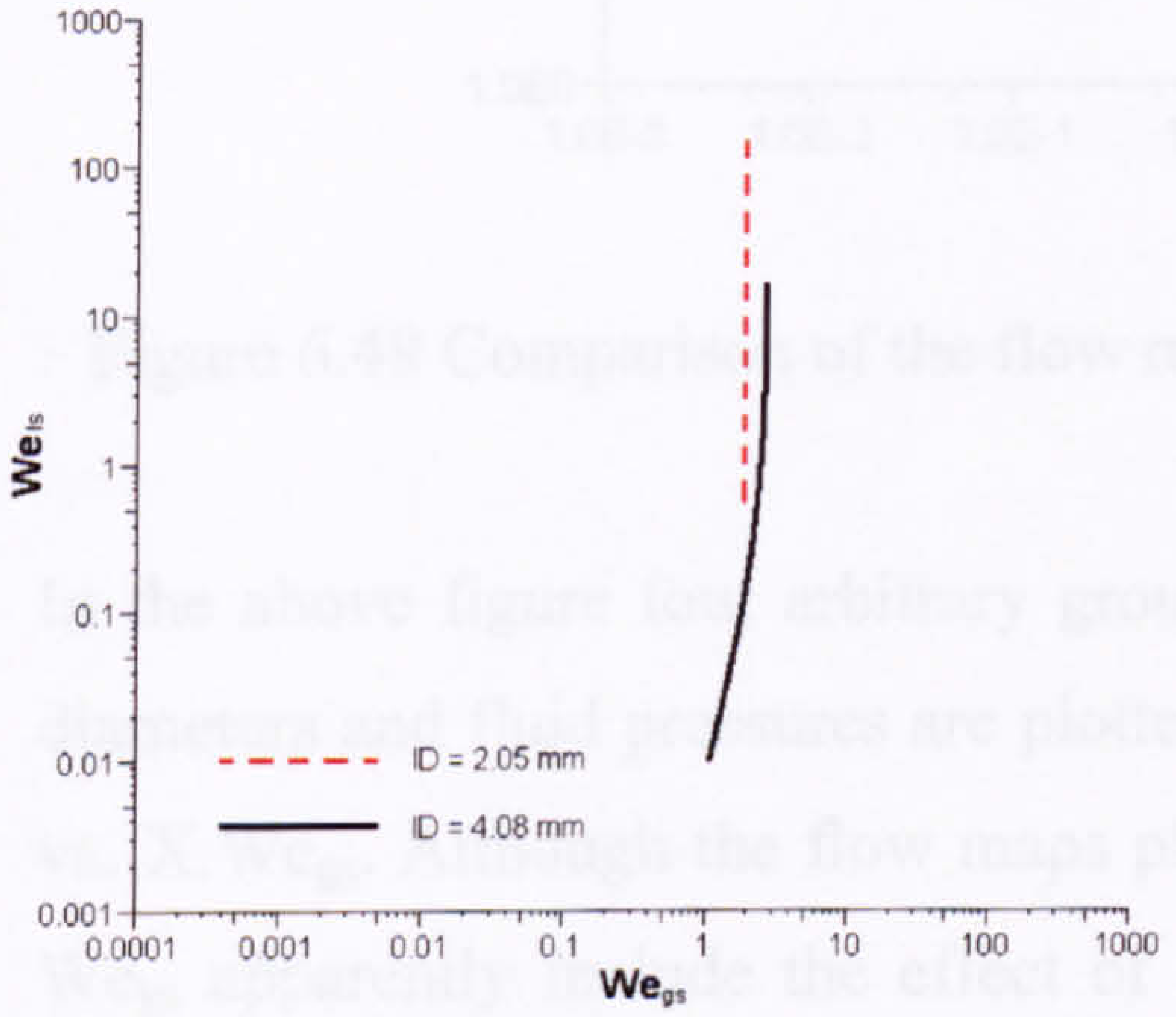

(c) Comparison for both diameters

Figure 6.48 Air-water flow map and the boundary to annular flow using the We coordinate system, in the model of Mishima and Hibiki (1996).

6.3.3 General coordinate systems

From the above discussion it seems that the parameters of X, G, We_{gs} and We_{ls} may properly consider the effect of fluid properties and tube diameter on the transition boundaries of slug-churn and churn-annular and might be the proper parameters to predict the slug, churn and annular flow in any condition. However, the above assumption cannot be supported by the comparisons depicted in Figure 6.49.

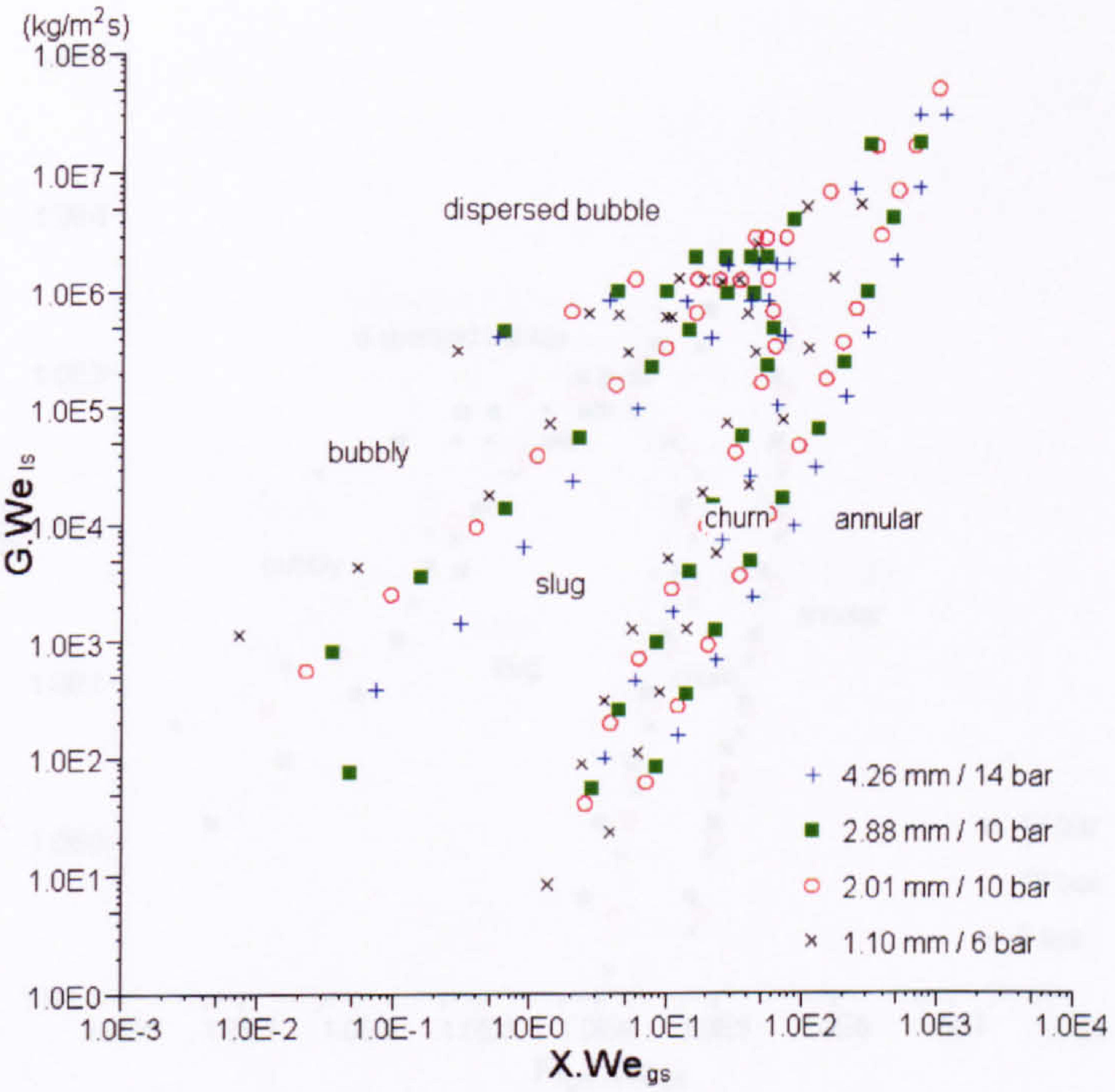

Figure 6.49 Comparison of the flow maps with the coordinates of G.We$_{ls}$ vs. X.We$_{gs}$.

In the above figure four arbitrary groups of experimental data from the different tube diameters and fluid pressures are plotted and compared using the coordinates of G.We$_{ls}$ vs. X.We$_{gs}$. Although the flow maps plotted using coordinates of G vs. X and We$_{ls}$ vs. We$_{gs}$ apparently include the effect of fluid properties and tube diameter respectively, their combination cannot predict well any flow pattern when both tube diameter and pressure change. The reason is that parameters G and X may consider the effect of fluid properties but cannot include the effect of tube diameter whereas parameters We$_{ls}$ and We$_{gs}$ cannot consider properly the influence of fluid properties on the transient boundaries. Therefore, it is urgent to find a pair of new parameters which can account for both effect of fluid properties and tube diameter. For example, inertia force, friction, gravity and surface tension are the dominant forces in the transition mechanism of churn to annular flow based on the force analysis, a semi-empirical correlation for the boundary of churn to annular flow could include Froude number Fr, Reynold number Re and Weber number We. In the current study the churn-annular boundary is consistent perfectly in the flow maps using We$_{ls}$ vs. Fr$_{gs}$We$_{gs}$ coordinate system at all different tube diameters and fluid pressures, see Figures 6.50-6.56. A comparison at different diameters and pressures also exhibits perfect consistency on the boundary of churn to annular as shown in Figure 6.57.

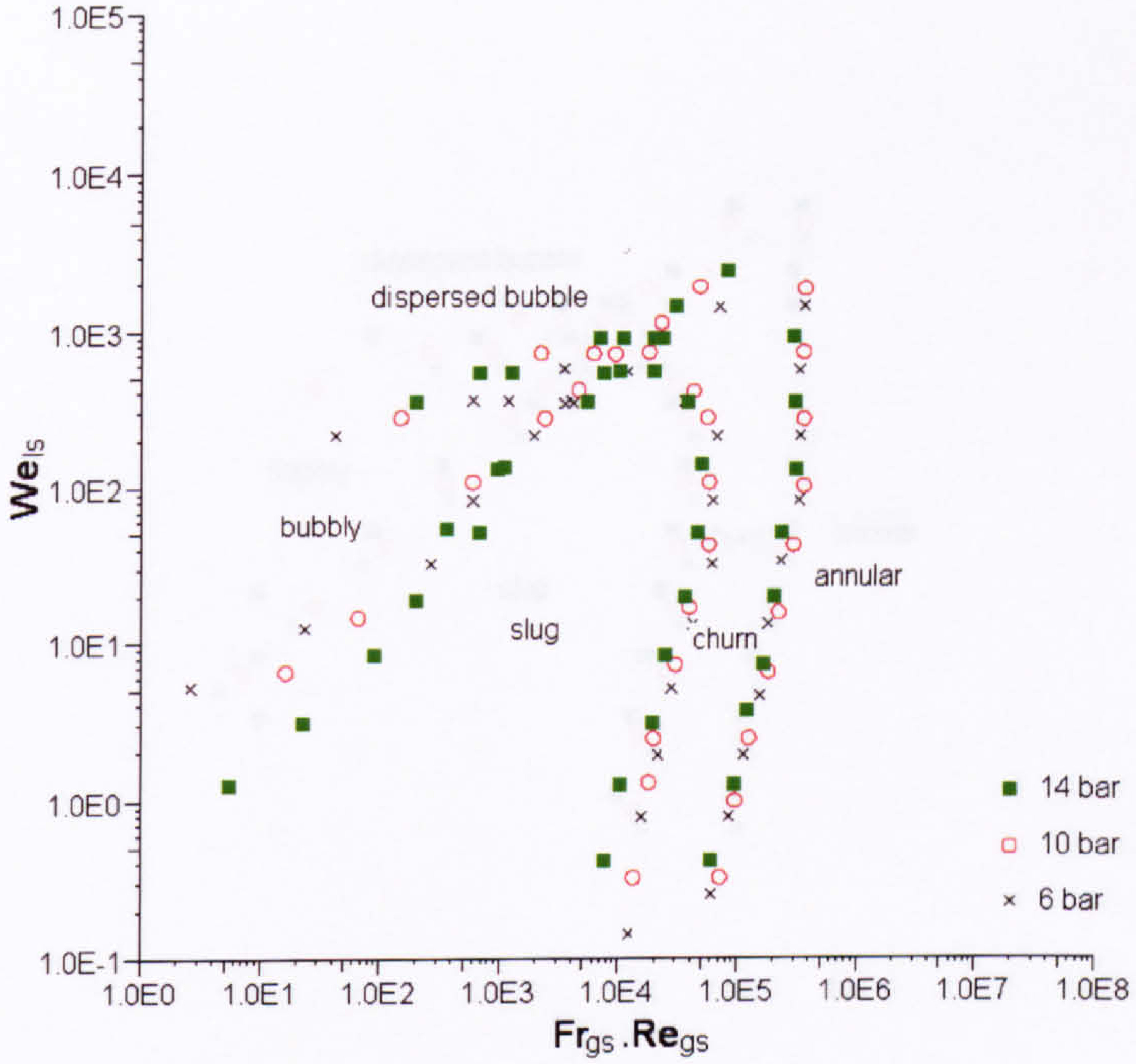

Figure 6.50 R134a flow map with We_{ls} vs. $Fr_{gs}Re_{gs}$ coordinate system in the 1.10 mm tube.

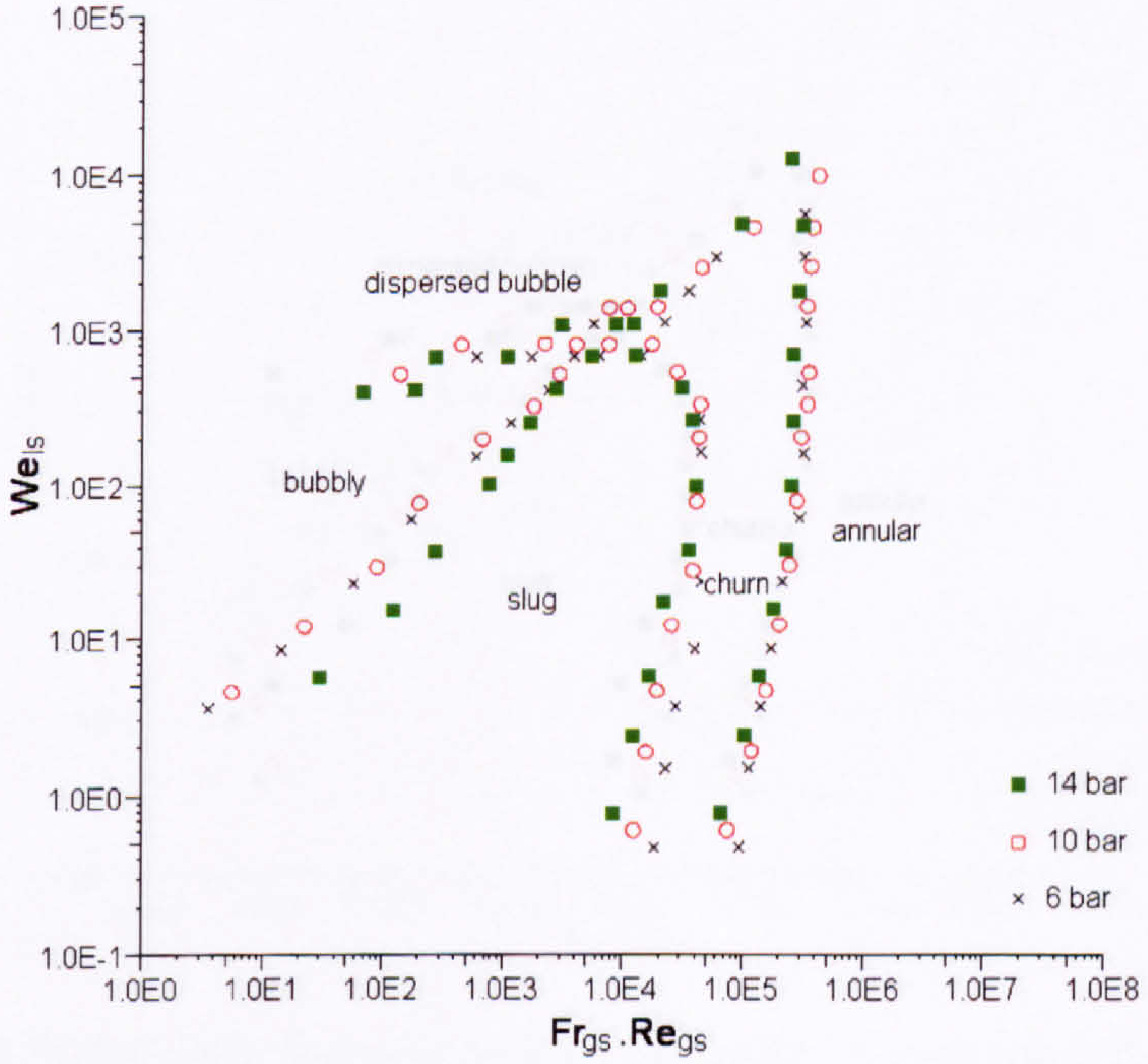

Figure 6.51 R134a flow map with We_{ls} vs. $Fr_{gs}Re_{gs}$ coordinate system in the 2.01 mm tube.

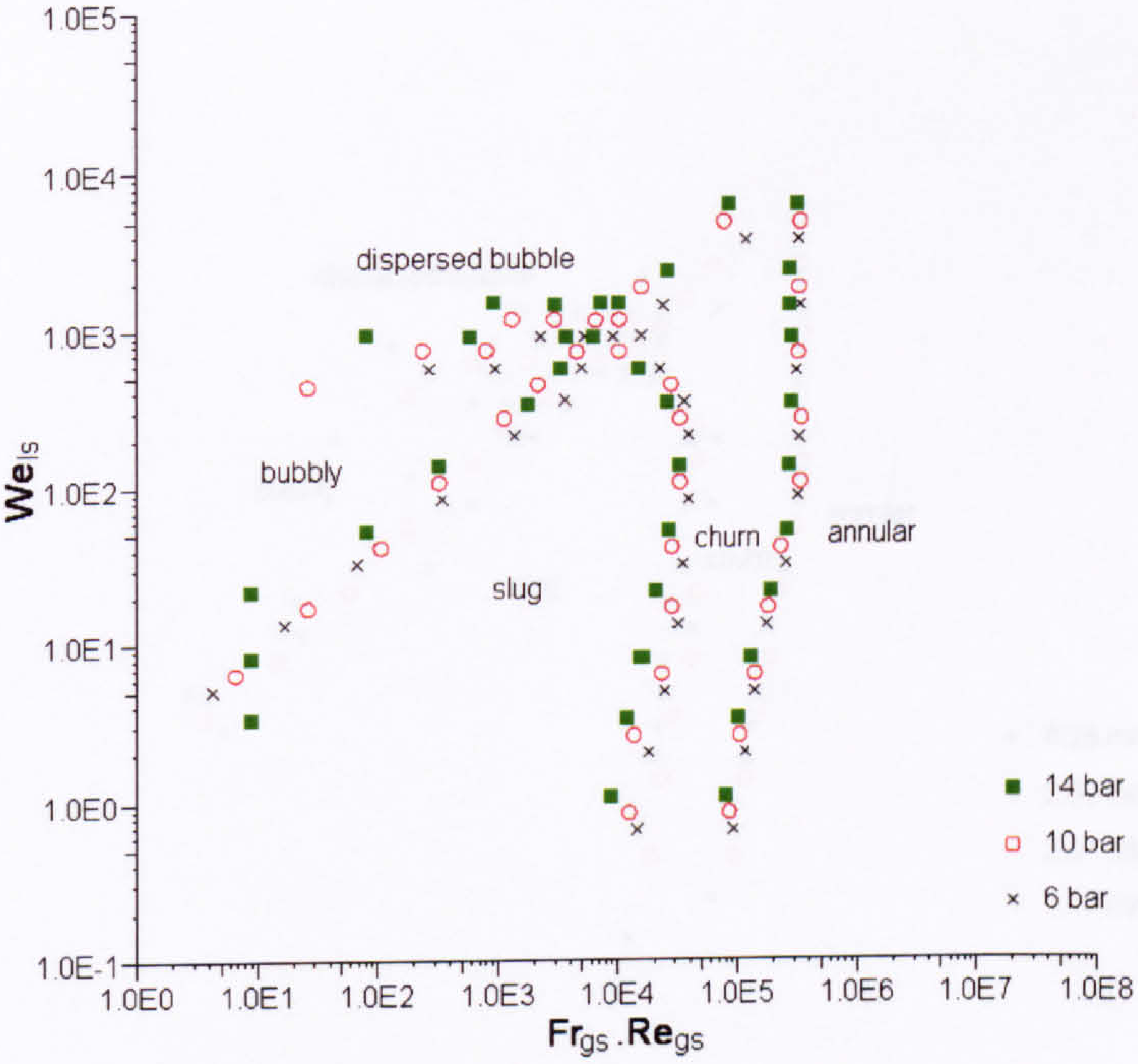

Figure 6.52 R134a flow map with We_{ls} vs. $Fr_{gs}Re_{gs}$ coordinate system in the 2.88 mm tube.

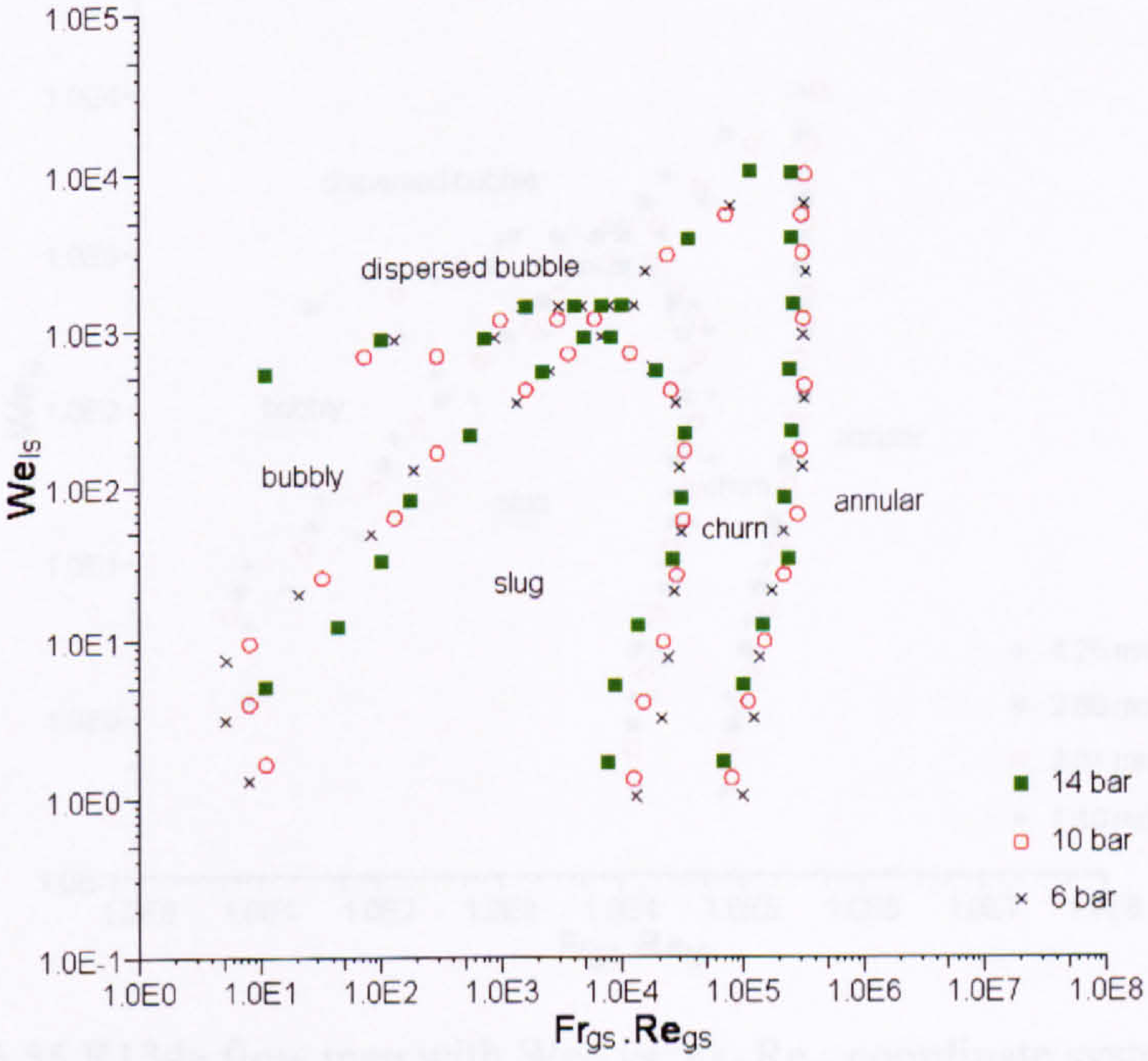

Figure 6.53 R134a flow map with We_{ls} vs. $Fr_{gs}Re_{gs}$ coordinate system in the 4.26 mm tube.

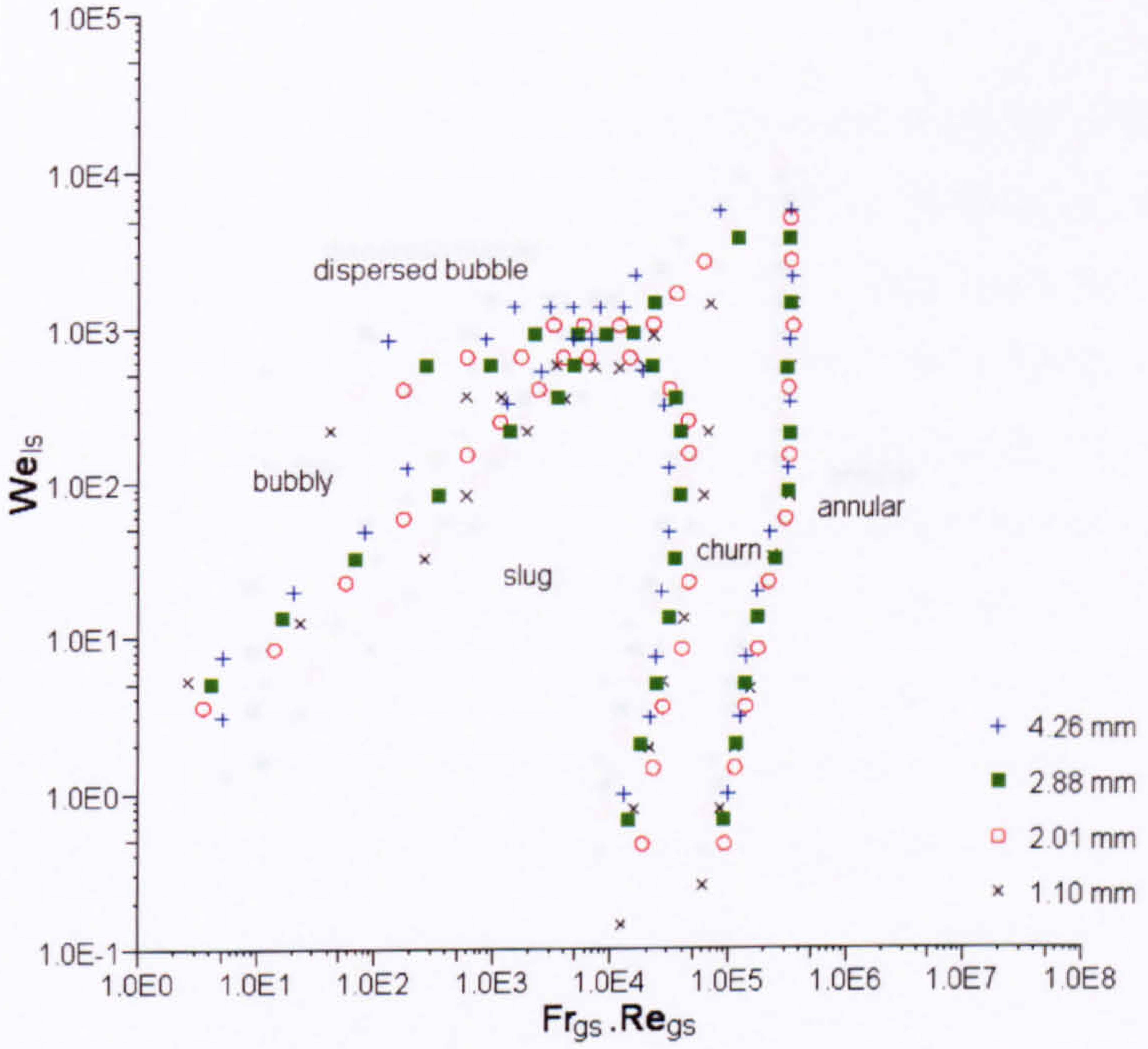

Figure 6.54 R134a flow map with We_{ls} vs. $Fr_{gs}Re_{gs}$ coordinate system at 6 bar.

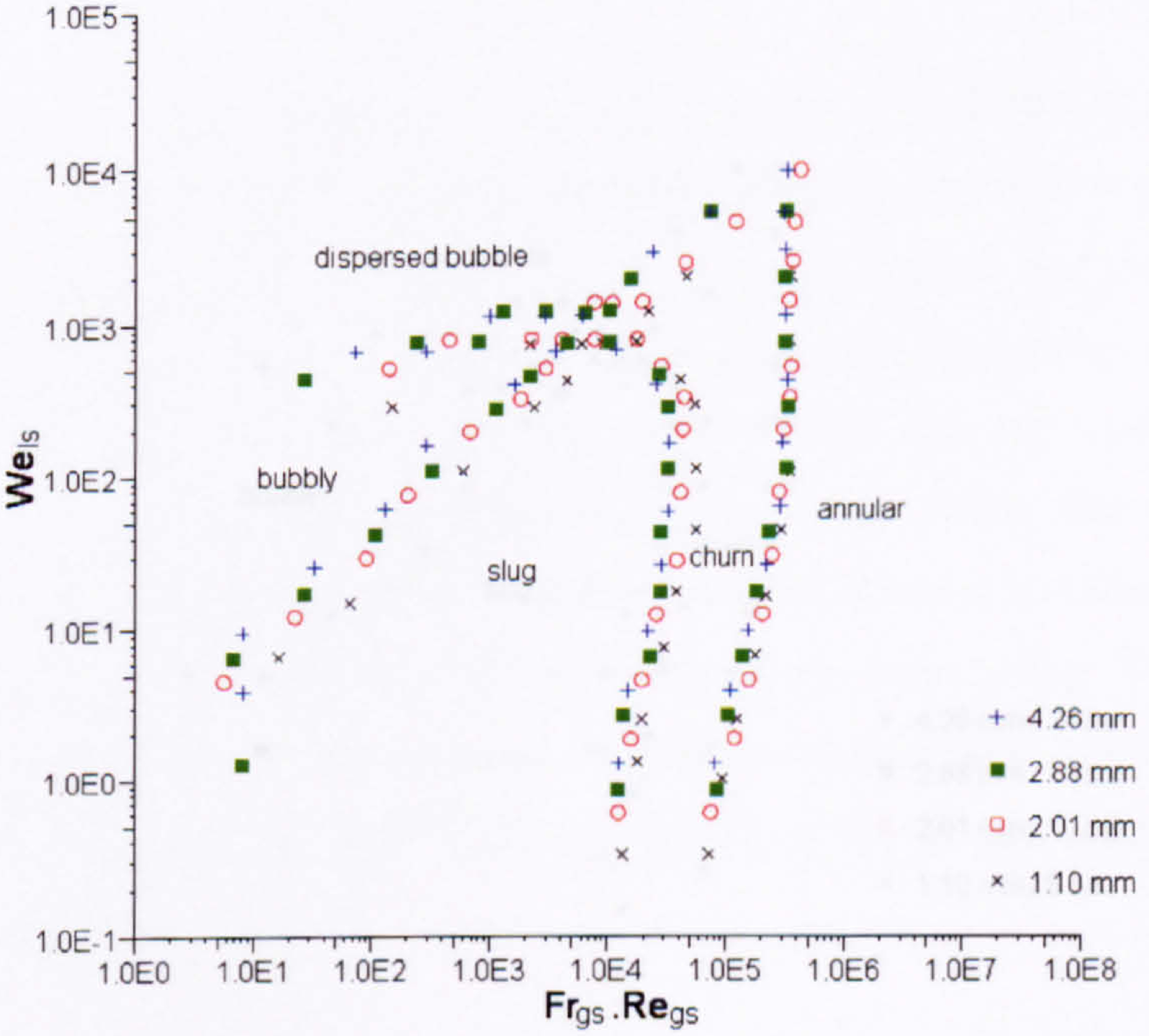

Figure 6.55 R134a flow map with We_{ls} vs. $Fr_{gs}Re_{gs}$ coordinate system at 10 bar.

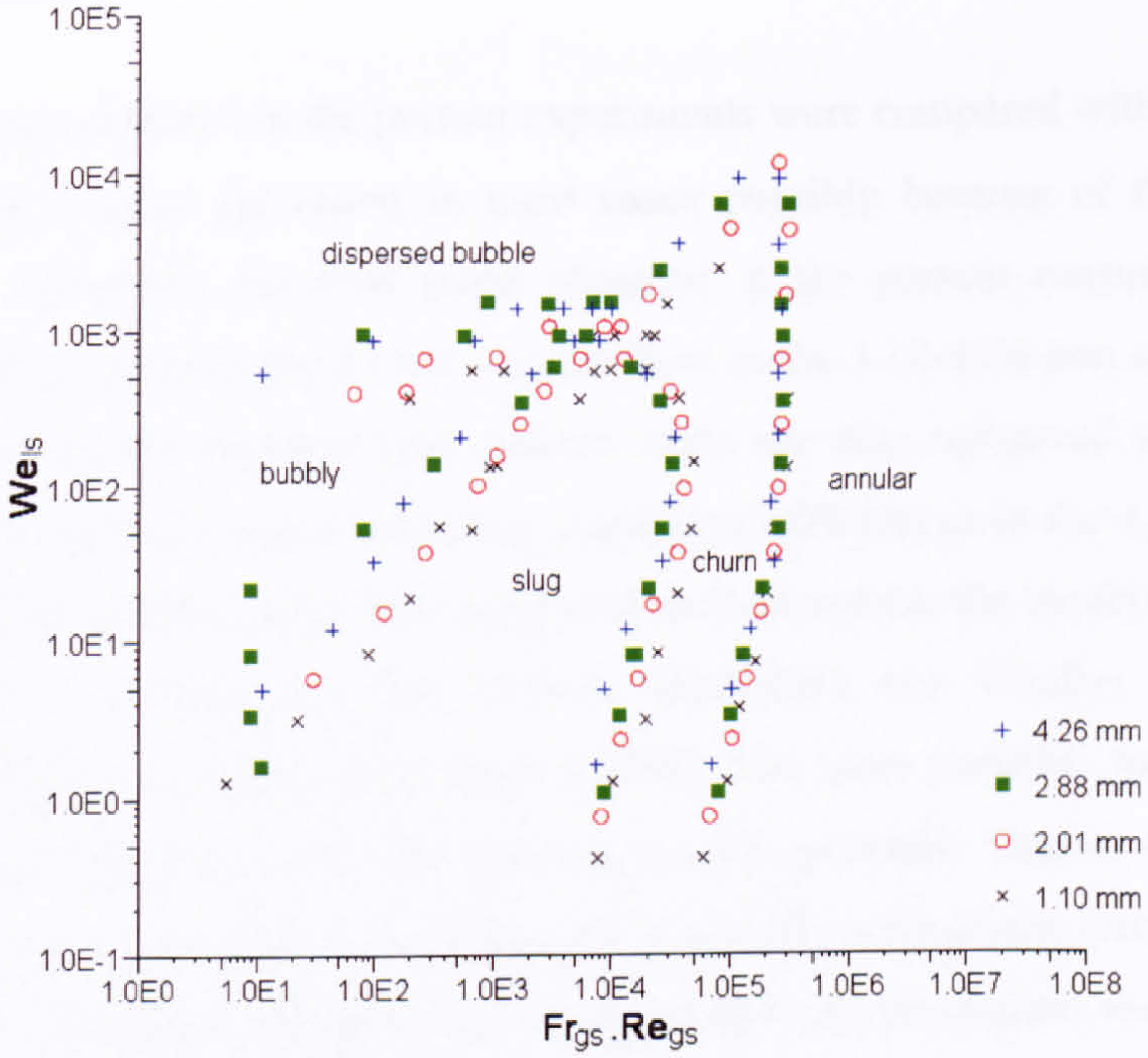

Figure 6.56 R134a flow map with We_{ls} vs. $Fr_{gs}Re_{gs}$ coordinate system at 14 bar.

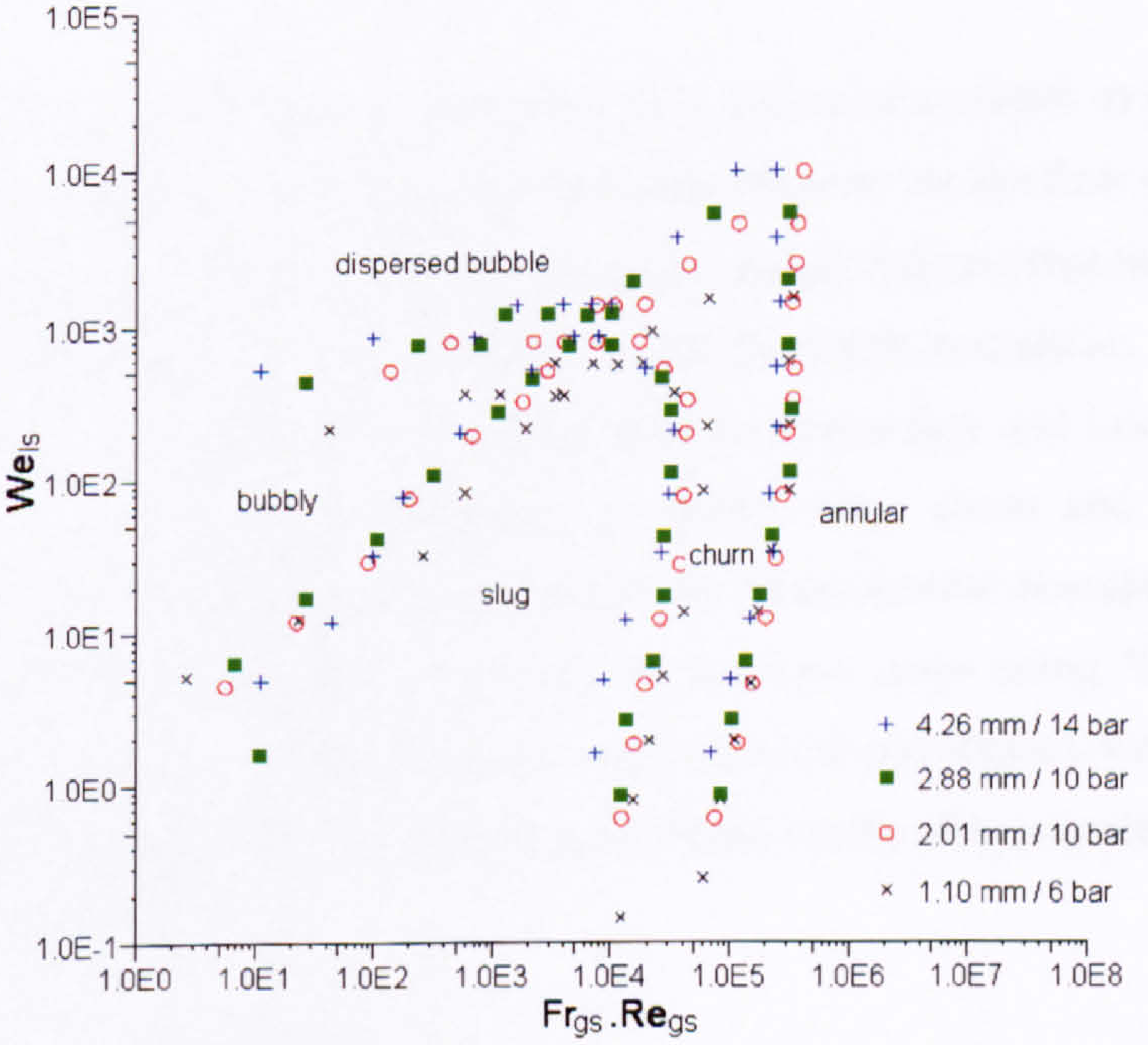

Figure 6.57 R134a flow map with We_{ls} vs. $Fr_{gs}Re_{gs}$ coordinate system in the different tube diameters and at the different pressures.

6.4 Summary

The flow maps obtained in the present experiments were compared with the earlier flow maps but show poor agreement in most cases possibly because of the different test conditions. Therefore, the flow maps obtained in the present experiments can only predict the flow patterns for R134a vertical flow in the 1.10-4.26 mm tubes and at 6-14 bar. In addition, the sketched flow pattern maps are also compared with the existing models for normal size tubes indicating significant differences in the 4.26 mm tube and more so for the smaller tubes. The compared models include the models given by Taitel et al. (1980), Mishima and Ishii (1984), McQuillan and Whalley (1985) and the "Unified Model" summarized by Taitel (1990). The most probable reason that causes the above discrepancy is that the existing models generally neglect the influence of surface tension on the flow patterns but this is actually a dominant force in small tubes. Akbar et al. (2003) put forward a set of semi-empirical correlations for small tubes but the flow maps in the present study still cannot be predicted properly because (1) the proposed correlations are based on air-water flow in horizontal tubes and (2) the tubes used in the present experiments are not small enough.

The experimental data obtained were plotted in various coordinate systems in order to investigate the effect of fluid properties and tube diameter on the flow patterns and help to develop general correlations. The comparison results indicate that the Weber number may include the effect of tube diameter on the transition boundaries of slug to churn flow and churn to annular flow whilst the group of mass flux and Lockhard-Martinelli Parameter may be the right parameter to predict slug, churn and annular flow at different pressures. Further study reveals that the churn-annular boundaries under all the test conditions were consistent perfectly in the flow maps using We_{ls} vs. $Fr_{gs}We_{gs}$ coordinate system. As a result the new semi-empirical correlations were developed for the transition boundary of churn to annular based on the dimensionless parameters of Fr_{gs}, We_{gs} and We_{ls}.

Chapter 7 Theoretical Study

The general transition boundaries observed in all the present experiments, which include bubbly to slug, dispersed bubble to bubbly, dispersed bubble to churn, slug to churn and churn to annular, are analyzed in this Chapter. New semi-empirical models and curve-fitting correlations were developed based on all the data points chosen as the regime boundaries. Some models and correlations are compared with the existing data for the air-water flow in small or normal size tubes and demonstrate good agreement.

7.1 Bubble rise velocity in slug flow

Void fraction is a very useful parameter in two-phase flow study. For example, the existing models suppose bubbly flow will change to slug flow when the void fraction exceeds a critical value, see Appendix B. However, the void fraction in small tubes is very difficult to measure accurately. A few traditional methods, like using quick-closing valves, will introduce considerable measurement error because of the great volume in the valve chamber and the frequently stagnant bubbles along the tube. On the other hand, some new measurement instruments, such as neutron radiography (Hibiki et al. 1993), are not available in most laboratories. Despite these problems, the void faction in slug flow could be calculated properly by measuring the rise velocity of slug bubbles. According to the drift flux model, the relationship between the gas velocity and the homogeneous velocity can be expressed by the following equation (Mishima and Hibiki, 1996):

$$u_g = \frac{u_{gs}}{\alpha} = C_0 u_h + u_d \tag{7.1}$$

In well developed slug flow, all bubbles should flow at the same rise velocity except those small bubbles just behind the slug bubbles. In fact, the total volume of these small bubbles make only a very small proportion of the gross gas volume in slug flow. Therefore, the gas velocity, u_g, should be approximately the same as the measured rise velocity, u_r. Equation 7.1 can then be rewritten as:

$$u_g = u_r = C_0 u_h + u_d \tag{7.2}$$

The distribution parameter C_0 and the drift velocity u_d in Equation 7.2 may be the functions of tube diameter and fluid properties. Ishii introduced the following equations for slug flow in round tubes in 1977 (cited from Mishima and Hibiki 1996):

$$C_0 = 1.2 - 0.2\sqrt{\frac{\rho_g}{\rho_l}} \tag{7.3}$$

$$u_d = 0.35\sqrt{\frac{gD(\rho_l - \rho_g)}{\rho_l}} \tag{7.4}$$

Overall the bubble rise velocity and the homogeneous velocity exhibit excellent linear relationship in the present data. The measured rise velocity, including the curve-fitting equations, are given in Appendix I and summarised in Table 7.1. The effect of diameter and pressure on the rise velocity has been analysed qualitatively in Chapter 5 Section 5.1.4, i.e. the rise velocity is not affected significantly by the tube diameter and fluid pressure in most cases except for the 2.01 mm tube at 14 bar and the 1.10 mm tube at 10 and 14 bar because of the thermal loss. The experimental data indicate that the slopes of u_r/u_h are slightly lower in the small tubes at the high pressures and low velocity, see the discussions in Chapter 4 Section 4.1.3 (12) and Figures 5.20 and 5.21 in Chapter 5. In general the bubble rise velocity became slightly lower when the fluid temperature was higher than the ambient temperature due to the thermal loss at the exposed part of the observation section. In most cases, such as when the fluid pressure was 6 bar or the tube diameters were 4.26 or 2.88 mm, the effect of the thermal loss on the bubble rise velocity was not so significant. However, with the decrease of tube diameter and the increase of fluid pressure, the measured rise velocity may be slightly slower than the expected velocity because of the increased effect of condensation. The qualitative analysis and the relative calculations are given in Chapter 4 Section 4.1.3 (12). Considering that the magnitude of these measurement errors is very difficult to estimate, the measured velocity for the 2.01 mm tube at 14 bar and the 1.10 mm tube at 10 and 14 bar will not be considered in the later analysis, see Table 7.2 and Figures 7.1 and 7.2.

Table 7.1 The summarized curve-fitting equations for the bubble rise velocity.

Diameter (mm)	Pressure (bar)	Bubble rise velocity (u_g) vs. Homogeneous velocity (u_h)
4.26	6.0	$u_g = 1.193u_h + 0.059$
	10.0	$u_g = 1.240u_h + 0.044$
	14.0	$u_g = 1.218u_h + 0.041$
2.88	6.0	$u_g = 1.194u_h + 0.025$
	10.0	$u_g = 1.178u_h + 0.030$
	14.0	$u_g = 1.208u_h + 0.019$
2.01	6.0	$u_g = 1.230u_h + 0.019$
	10.0	$u_g = 1.221u_h + 0.005$
	14.0	$u_g = 1.194u_h + 0.001$
1.10	6.0	$u_g = 1.244u_h + 0.006$
	10.0	$u_g = 1.186u_h + 0.013$
	14.0	$u_g = 1.129u_h + 0.014$

Table 7.2 The comparison of the experimental data and the Ishii's equation.

Diameter (mm)	Pressure (bar)	Present experiments			Ishii (1977)	
		Best-fit equation	C_0	u_d	C_0	u_d
4.26	6.0	$u_g = 1.193u_h + 0.059$	1.193	0.059	1.17	0.07
	10.0	$u_g = 1.240u_h + 0.044$	1.240	0.044	1.16	0.07
	14.0	$u_g = 1.218u_h + 0.041$	1.218	0.041	1.15	0.07
	Avg.	$u_g = 1.220u_h + 0.050$	1.220	0.048	1.16	0.07
2.88	6.0	$u_g = 1.194u_h + 0.025$	1.194	0.025	1.17	0.06
	10.0	$u_g = 1.178u_h + 0.030$	1.178	0.030	1.16	0.06
	14.0	$u_g = 1.208u_h + 0.019$	1.208	0.019	1.15	0.06
	Avg.	$u_g = 1.190u_h + 0.020$	1.190	0.025	1.16	0.06
2.01	6.0	$u_g = 1.230u_h + 0.019$	1.230	0.019	1.17	0.05
	10.0	$u_g = 1.221u_h + 0.005$	1.221	0.005	1.16	0.05
	14.0					
	Avg.	$u_g = 1.230u_h + 0.010$	1.230	0.012	1.16	0.05
1.10	6.0	$u_g = 1.244u_h + 0.006$	1.244	0.006	1.17	0.04
	10.0					
	14.0					
	Avg.	$y = 1.24x + 0.01$	1.24	0.006	1.17	0.04

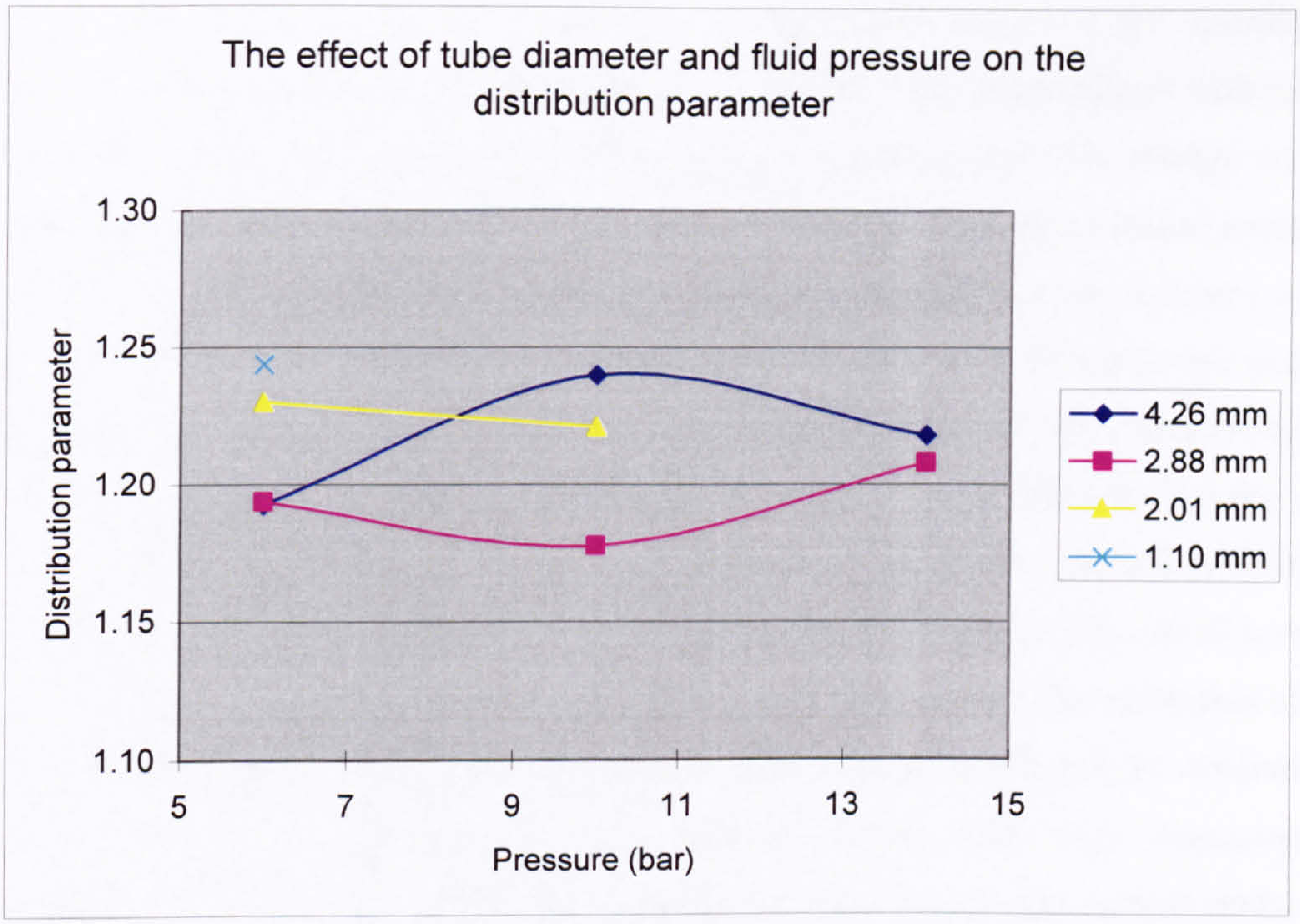

Figure 7.1 The effect of tube diameter and fluid pressure on the distribution parameter.

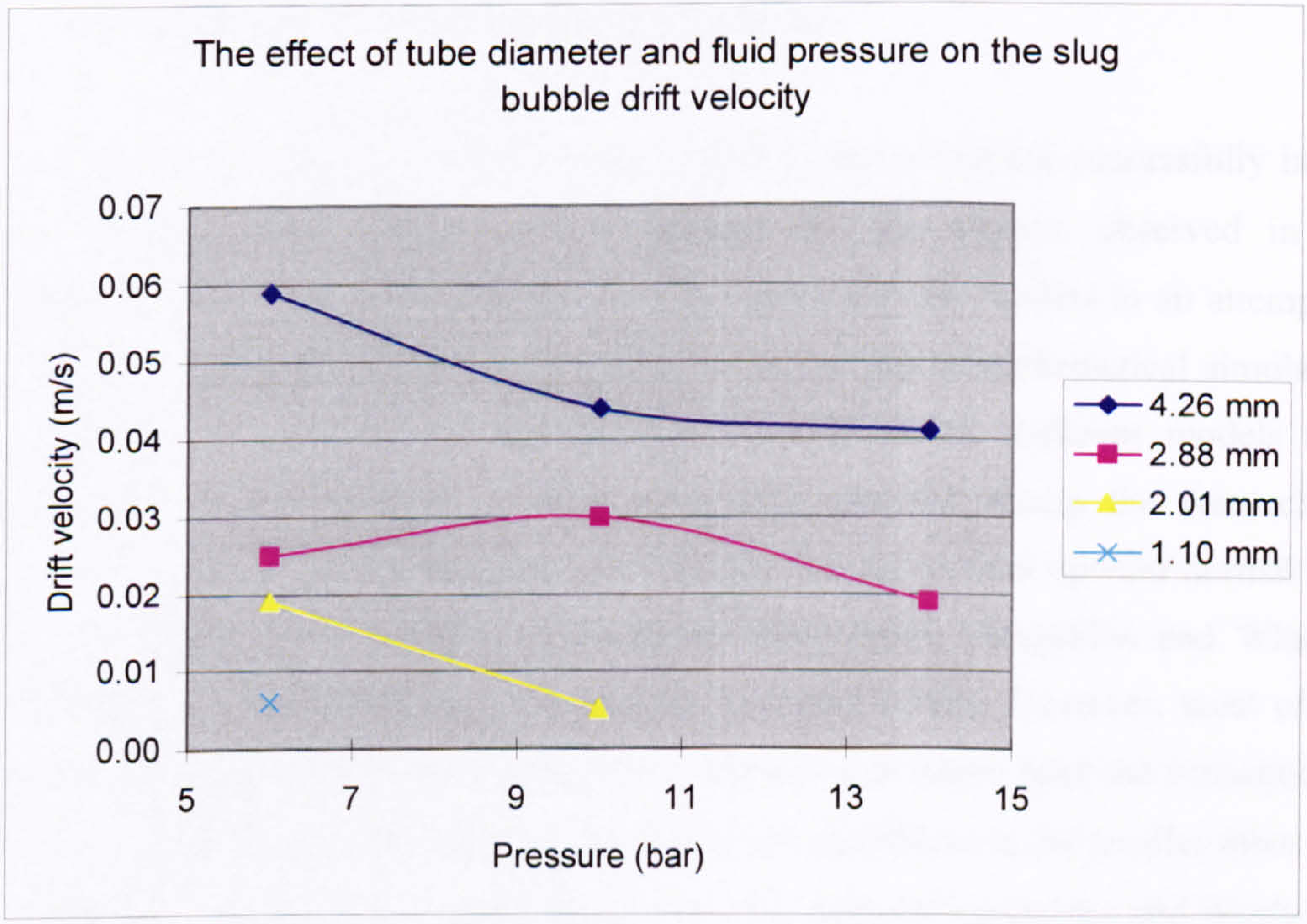

Figure 7.2 The effect of tube diameter and fluid pressure on the slug bubble drift velocity.

It seems that fluid pressure does not have a significant effect on the distribution parameter and the drift velocity, see Figures 7.1 and 7.2. This result agrees with Ishii's equations in principle because the Ishii's equation predicts only 2% change on the distribution parameter and almost a constant drift velocity when the pressure increases from 6 to 14 bar. The distribution parameter is slightly changed but the tendency is not very clear when the tube diameters decrease from 4.26 mm to 1.10 mm in the present experiments, which makes it very difficult to consider the effect of tube diameter on the distribution parameter correlation. Although the effect of tube diameter on the drift velocity is quite significant, it is still very difficult to propose a general correlation depending on the experimental data from the current study because (i) the small number of previous studies related to the rise velocity in small tubes makes the validation of the proposed correlation very difficult, (ii) accurate drift velocity could only be obtained in stagnant fluid instead of deducing from flowing system, (iii) large measurement uncertainty at low flow rate affects the correlation's accuracy. In the current study, the measured rise velocity will be used directly.

7.2 New developed models and correlations

Several transition models were put forward and had been validated successfully in the earlier studies. These models try to represent the true physics observed in the experiments. Some less important factors were ignored in the models in an attempt to simplify the description of the physical phenomena so that a mathematical simulation was possible. In addition, the transition mechanisms in the different models may disagree due to the variance of observation and analysis among the researchers. Appendix B reviews the existing transition models for the vertical upward normal size tubes from Taitel et al. (1980), Mishima and Ishii (1984), McQuillan and Whalley (1985) and the "Unified Model" summarized by Taitel (1990). However, most of the earlier works were based on air-water flow in normal size tubes, with the consequence that some of the factors that were ignored, which are significant in the smaller tubes can invalidate the models in these applications. The later works (Damianides and Westwater 1988, Lin et al. 1998, and Coleman and Garimella 1999) indicated that the existing models could not predict satisfactorily the transition boundaries in small tubes. The effect of surface tension must be considered in the transition models for the small diameter tubes. The above conclusion is also supported by the present work, see

Chapter 6 Section 6.2. In this section, the transition mechanisms are analysed and new models and correlations for small tubes are proposed based on the analysis and the present data.

7.2.1 Bubbly – slug boundary

According to the models of Taitel et al. (1980) and Barnea et al. (1982) a fully developed bubbly flow could not exist in small diameter tubes because small bubbles rise faster than slug bubbles and cause coalescence. The critical diameter for the upward vertical flow is given as:

$$D > 19.01\left[\frac{(\rho_l - \rho_g)\sigma}{g\rho_l^2}\right]^{1/2} \tag{7.5}$$

The calculated critical diameters are between 12 to 16 mm at the current experimental conditions (R134a, 6-14 bar). Therefore, bubbly flow should not exist in the present experiments. However, it was observed, see the figures in Chapter 5 Section 5.1.2. The possibilities lead to the above inconsistency include:

(1) The calming distance or in fact the test section itself is too short to reach fully developed flow in the present experiments. Barnea and Taitel (1993) reported that the required distance for fully developed two-phase flow is about 10-15 m in the 50 mm tube, i.e. 200-300 times tube diameter. The distance from the outlet of the heating section to the visualization point is about 100-170 times the inner diameter in the present experiments so that the observed bubbly flow might not be a fully developed flow. However, the measured rise velocity, depicted in Figures 5.50-5.53, indicates that the observed two-phase flow was already at fully developed state because the small bubbles and slug bubbles flowed at the same velocity. This needs further investigation and direct evidence.

(2) When compared to air-water mixing methods usually used in the earlier studies, flow boiling might produce finer bubbles even at very low flow rate due to the smaller surface tension of R134a. This may delay or terminate altogether the coalescence of bubbles, so the transition of bubbly to slug flow is not affected by the tube diameter.

(3) Equation 7.5 was obtained from the experiments using air-water two-phase flow and is not suitable for other fluids.

The effect of the observation position on the bubbly-slug boundary was not part of the current study due to the limitation of the laboratory conditions. In fact, the effect of flow state on the transition boundaries was not recognized by all researchers. For example, Oya (1971) experimentally testified that the flow patterns were hardly affected by flow state.

The existing studies considered that void fraction was a vital parameter in the transition mechanism of bubbly to slug flow. For example, Taitel et al. (1980), Barnea et al. (1982), and McQuillan and Whalley (1985) considered that the transition takes place when the void fraction is 0.25, whilst Mishima and Ishii (1984) recommended 0.3 as the critical void fraction. The void fraction can be obtained from Equation 7.1 as follows:

$$\alpha = \frac{u_{gs}}{C_0\left(u_{gs} + u_{ls}\right) + u_d} \tag{7.6}$$

Although the distribution parameter C_0 and the drift velocity u_d in Table 7.2 are deduced from the data of slug flow, their applicability could be extended to the bubbly-slug boundary because the examined data covered a wide range from the bubbly-slug boundary to the slug-churn boundary and all showed excellent linear relationship. The above assumption agrees with Ishii, who proposed the same C_0 correlation for all bubbly flow, slug flow and churn flow, see Mishima and Hibiki (1996). Therefore, the critical void fraction at the bubbly-slug boundary in the present experiments can be estimated by Equation 7.6. As discussed in Chapter 4 Section 4.1.3 (12), the data analyzed do not include the 1.10 and 2.01 mm tubes at 14 bar and the 2.88 and 4.26 mm tubes at 14 bar at low velocity, i.e. $u_{ls}<0.11$ m/s for the 2.88 mm tube and $u_{ls}<0.07$ m/s for the 4.26 mm tube because of the measurement error caused by the thermal loss.

Unlike the existing models for normal size tubes, the critical void fraction at the bubbly-slug boundary is not a constant in the present experiments. It is a function of homogeneous velocity and apparently is not affected significantly by fluid pressure and tube diameter. The transition of bubbly to slug flow starts at a lower void fraction at lower homogeneous velocity and shifts to the higher void fraction with increasing homogeneous velocity, see Figures 7.3 and 7.4.

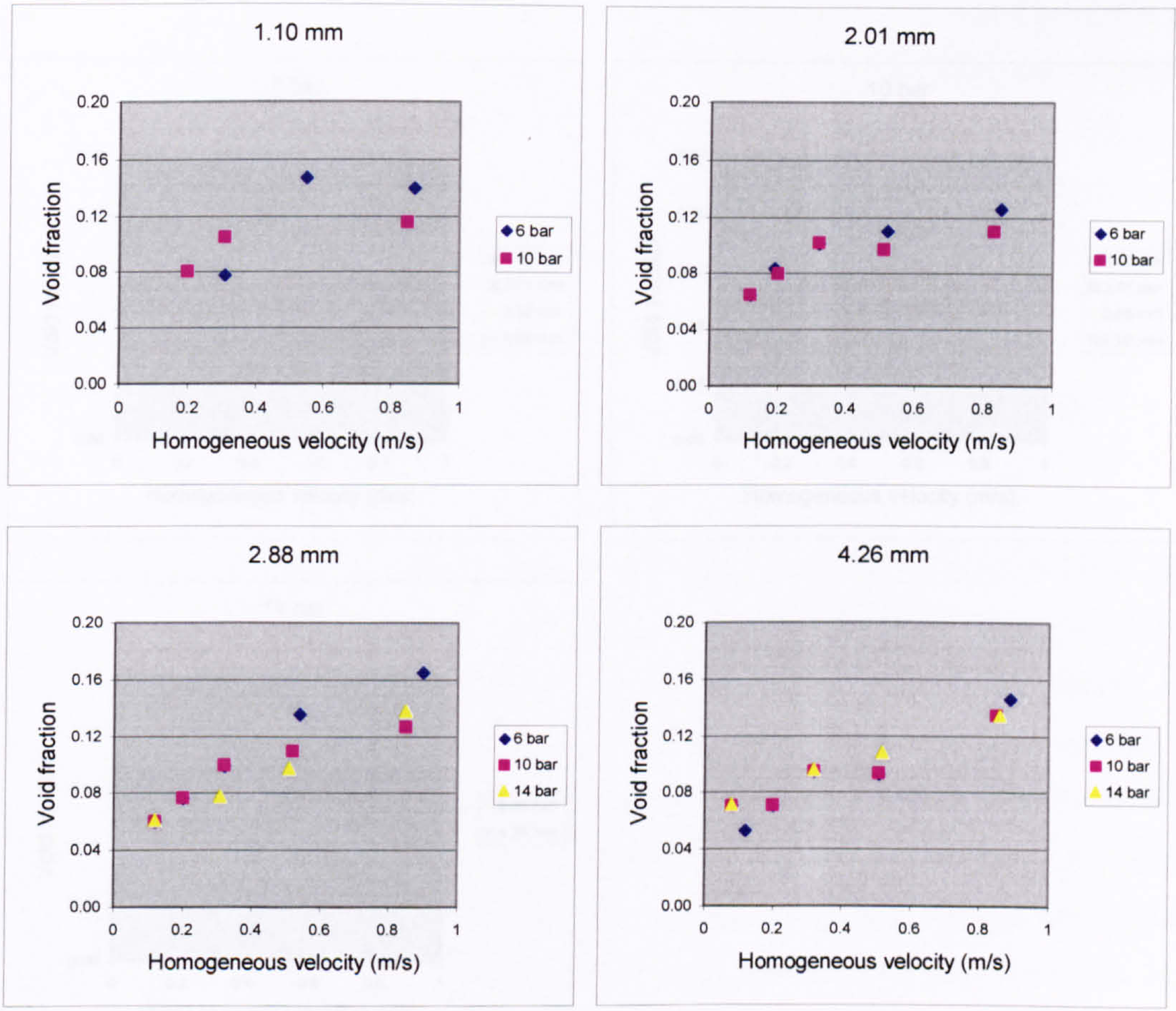

Figure 7.3 The variation of the critical void fraction with homogeneous velocity at different fluid pressures.

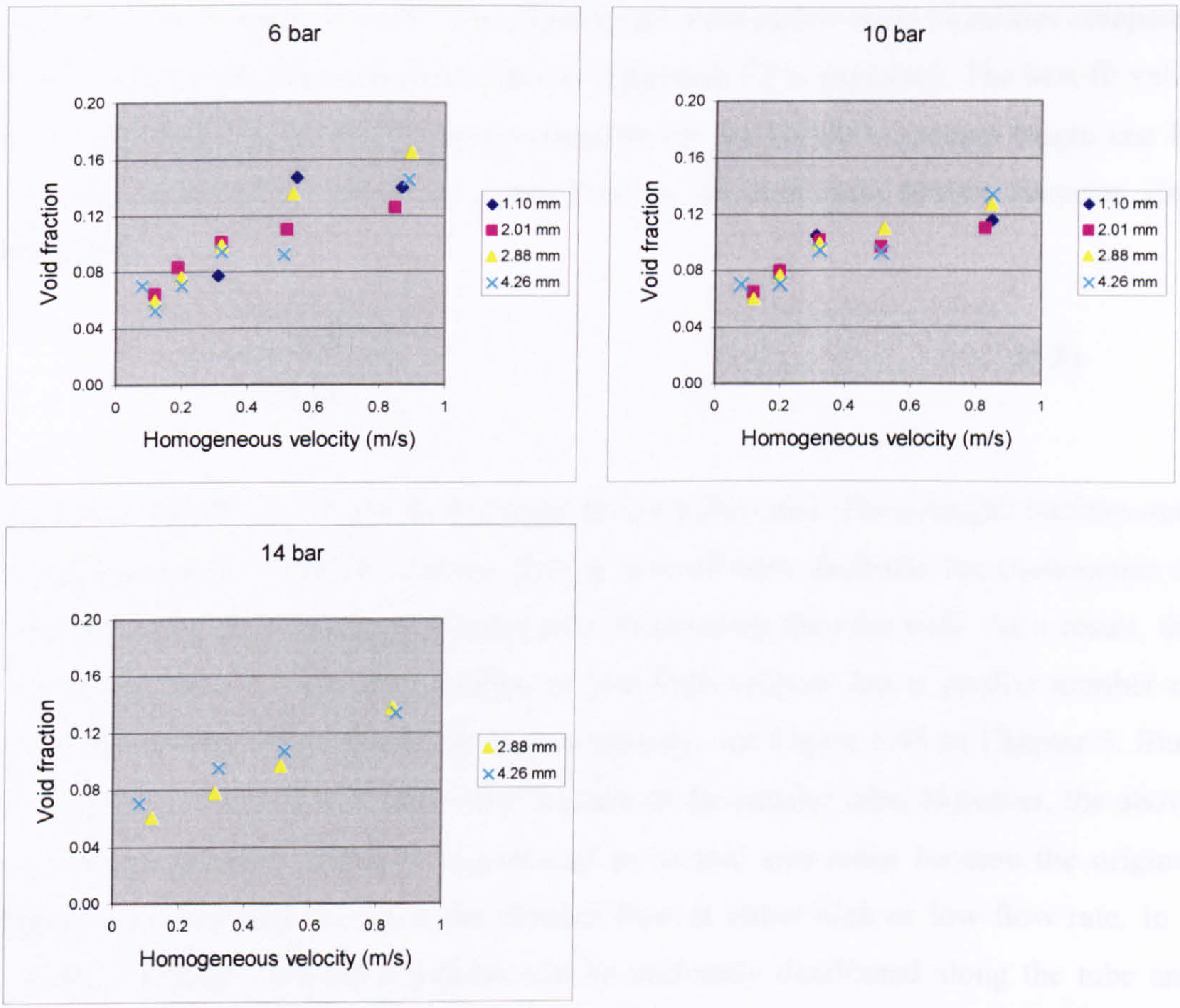

Figure 7.4 The variation of the critical void fraction with homogeneous velocity at different tube diameters.

The above transition tendency can be explained as follows. When a bubble leaves the heating wall, its original size relates closely to the mass flux, fluid properties and tube inner surface roughness. Levy (1967) gave a semi-empirical correlation about the average distance from the wall to the tip of the bubble, Y_B, as

$$Y_B = C\left[\frac{\sigma D}{\tau_w}\right]^{\frac{1}{2}}\left[1 + C'\left(\frac{g(\rho_l - \rho_g)D}{\tau_w}\right)\right]^{-\frac{1}{2}} \tag{7.7}$$

where

$$\tau_w = \frac{f_l G^2}{2\rho_l}$$

Levy evaluated the constants C and C' from experimental data. It was found that the buoyancy force appears to play a negligible part even at low mass velocities compared to the shear stress. Thus the second part of Equation 7.7 is neglected. The best-fit value of C was found to be 0.015, i.e. the equation for the bubble's average height can be rewritten as Equation 7.8. It is proportional to the maximum bubble diameter after departure.

$$Y_B = 0.015\left[\frac{\sigma D}{\tau_w}\right]^{\frac{1}{2}} \tag{7.8}$$

Therefore, bubble size tends to be bigger at lower flow rate. These longer bubbles may be big enough to block the channel flow in a small tube, facilitate the coalescence of bubbles in the fluid and those "embryonic" bubbles on the tube wall. As a result, the liquid slug between two slug bubbles at low fluid velocity has a smaller number of small size bubbles than that at the higher velocity, see Figure 5.45 in Chapter 5. Slug flow could be formed at a lower void fraction in the smaller tube. However, the above coalescence process cannot be reproduced in normal size tubes because the original bubbles are too small to block the channel flow at either high or low flow rate. In a normal size tube, numerous bubbles will be uniformly distributed along the tube and many bubbles can coexist in the same section until the void fraction reaches the critical value when the bubbles collide and coalesce frequently so that the bubbly flow changes to slug flow. This critical void fraction is less affected by the fluid velocity and was considered as a constant for normal size tubes in the earlier studies. In a recent seminar (Transient Multiphase Flows, 2nd Feb 2006, Imperial College London), B. J. Azzopardi stated that the critical void fraction at the bubbly-slug boundary is not a constant but a function of tube diameter. Generally the required void fraction is smaller in the small tube when the transition happened. For example, the critical void fractions are 0.68, 0.40 and 0.25 for the 189, 70 and 50 mm tubes, respectively. Based on the above analysis and the present data, a curve-fitting equation is proposed for the critical void fraction in small tubes, as,

$$\alpha_c = c_1\left(u_{gs} + u_{ls}\right)^{c_2} \tag{7.9}$$

Here the factors c_1 and c_2 are experimental coefficients and may relate with tube diameter, fluid properties and bubble original size, i.e. the method of bubble generation.

At the present experimental conditions, the coefficients c_1 and c_2 appear to be less affected by tube diameter and fluid properties. The experimental relation is given in Equation 7.10 after fitting the data shown in Figure 7.5.

$$\alpha_c = 0.138 u_h^{0.344} = 0.138 (u_{gs} + u_{ls})^{0.344} \tag{7.10}$$

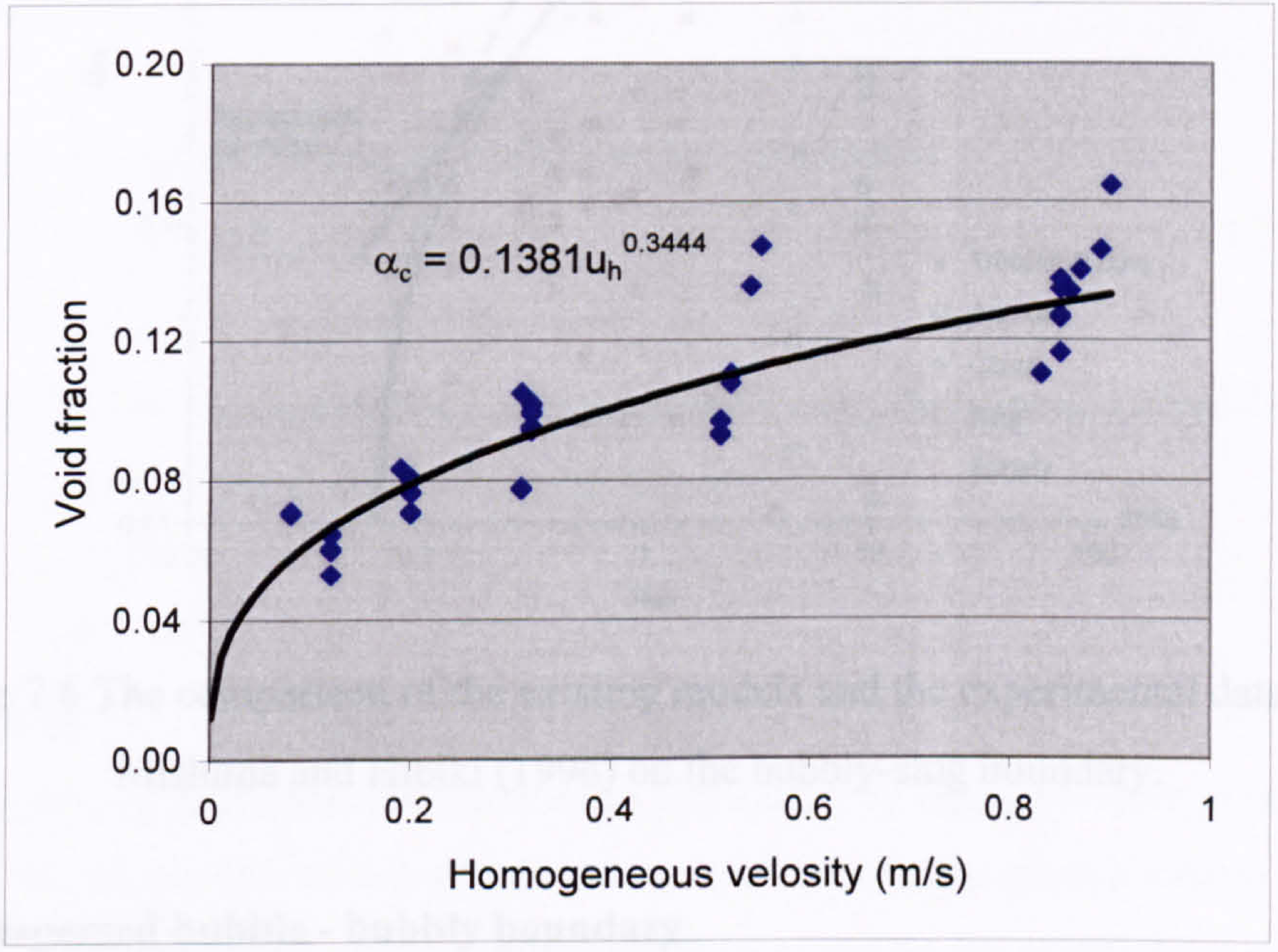

Figure 7.5 The relationship of the homogeneous velocity and the critical void fraction at the bubbly-slug boundary.

The above analysis indicates that the transition of bubbly to slug flow, especially at low flow rate, strongly depends on the experimental conditions. Therefore, Equation 7.10, which was obtained from the present experiments, might not be applicable to other conditions. However, it may explain why the constant critical void fraction cannot predict the bubbly-slug boundary well in small tubes and the actual transition starts at lower void fraction in lower homogeneous velocity in some experiments, see Figure 7.6. The figure shows the models of Mishima and Ishii (1984) and McQuillan and Whalley (1985), which using constant void fraction as the criterion, can predict the bubbly-slug boundary properly in the region of high homogeneous velocity. The experimental transition boundary, which is presented in solid line, shifts to low void fraction as the homogeneous velocity decreases.

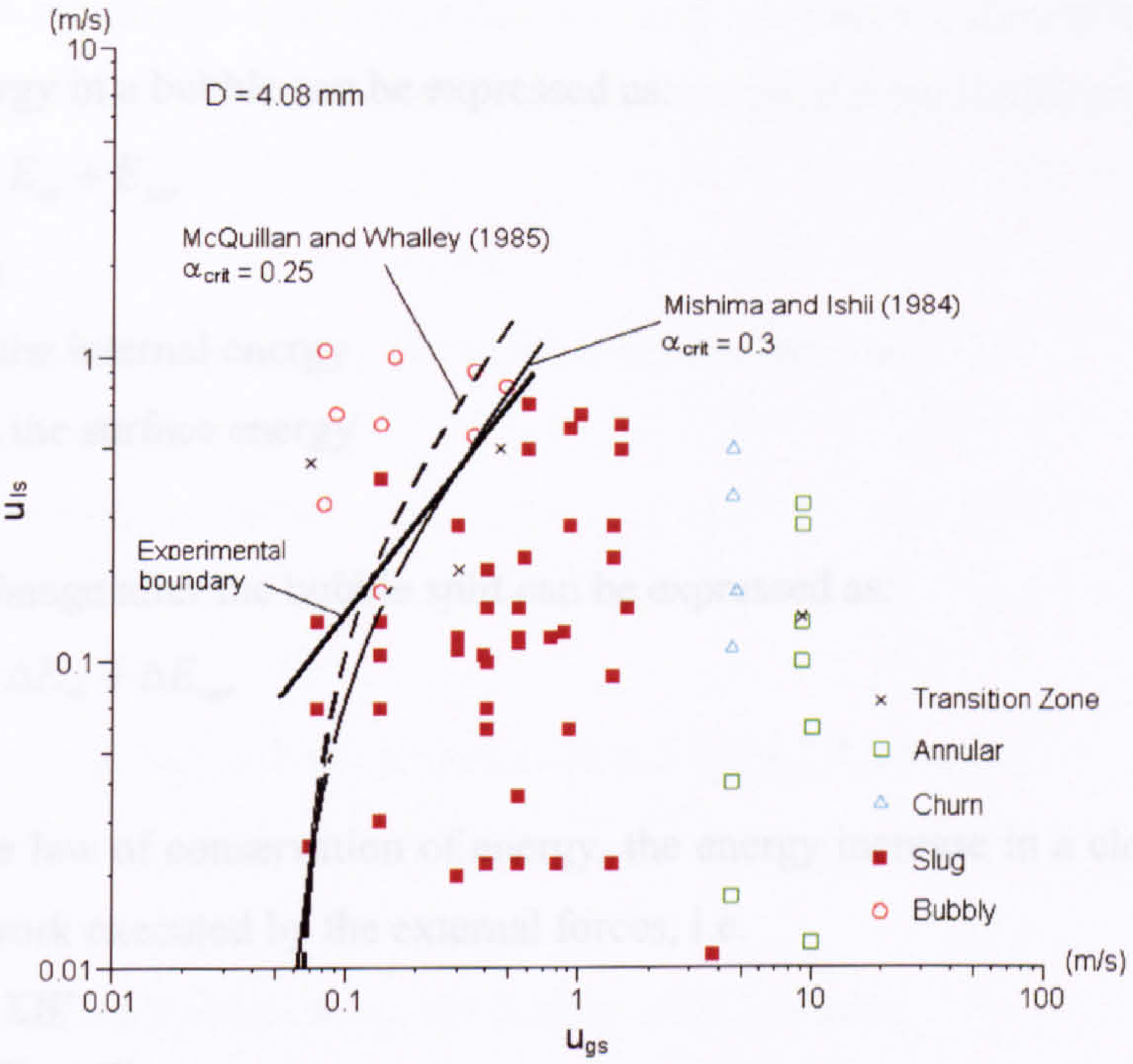

Figure 7.6 The comparison of the existing models and the experimental data from Mishima and Hibiki (1996) on the bubbly-slug boundary.

7.2.2 Dispersed bubble - bubbly boundary

It is assumed that a big bubble separates into two small bubbles in an adiabatic process with no mass exchange between liquid phase and gas phase. The bubbles in question are round and the two small bubbles have the same diameter. Ignoring the pressure change in the bubbles, the total volume of the two small bubbles is equal to the volume of the big bubble, i.e. $d_1 = \sqrt[3]{0.5}d$, see Figure 7.7, where Δp is the pressure difference of the vapour pressure in bubbles and the saturated pressure of the liquid temperature.

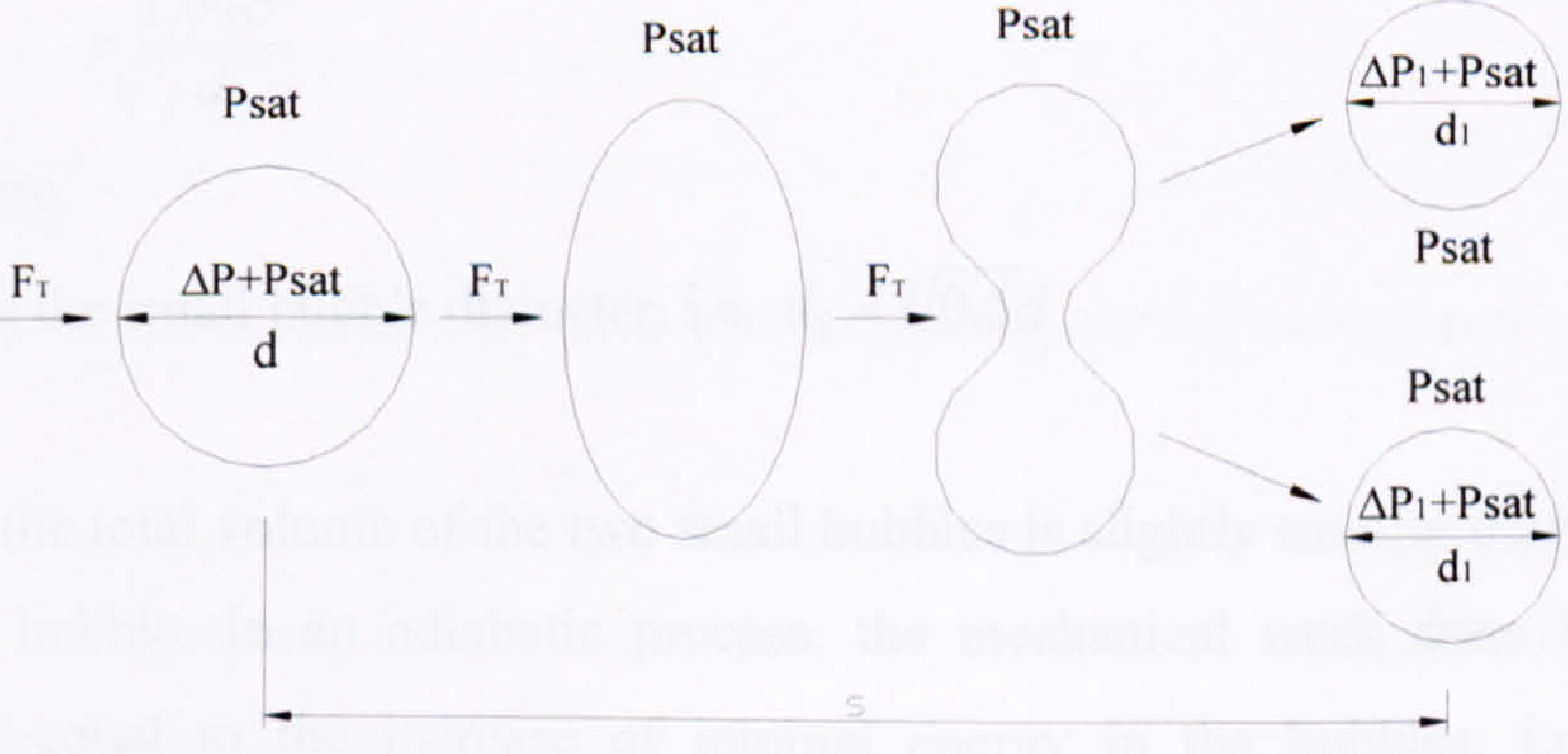

Figure 7.7 One big bubble separates into two small bubbles.

The total energy in a bubble can be expressed as:

$$\Sigma E = E_{in} + E_{sur} \tag{7.11}$$

where

E_{in} is the internal energy

E_{sur} is the surface energy

The energy change after the bubble split can be expressed as:

$$\Delta E = \Delta E_{in} + \Delta E_{sur} \tag{7.12}$$

According the law of conservation of energy, the energy increase in a closed volume is equal to the work executed by the external forces, i.e.

$$\begin{aligned} \Delta E &= \Sigma W \\ &= W_P + W_F \end{aligned} \tag{7.13}$$

where

W_p can be defined as the mechanical work done by liquid pressure, which equals to the product of liquid pressure and volume change when a bubble splits.

W_F can be defined as the mechanical work done by the external force from the liquid, which equals to the product of the turbulent force and the drift distance when a bubble splits into two.

In the above example, the bubble pressure change when it splits can be calculated as

$$\begin{aligned} p_1 - p &= (\Delta p_1 + p_{sat}) - (\Delta p + p_{sat}) \\ &= \frac{4\sigma}{d_1} - \frac{4\sigma}{d} \\ &= \frac{1.04\sigma}{d} \end{aligned} \tag{7.14}$$

where

d_1 is the small bubble diameter, i.e. $d_1 = \sqrt[3]{0.5}d$

Therefore, the total volume of the two small bubbles is slightly smaller than the volume of the big bubble. In an adiabatic process, the mechanical work done by the fluid pressure is equal to the increase of internal energy in the bubbles, i.e. $\Delta E_{in} = W_P$.

Combining this equation with Equations 7.12 and 7.13, the increase of surface energy is equal to the mechanical work done by the turbulent force from liquid, say,

$$\Delta E_{sur} = W_F \tag{7.15}$$

The change of surface energy of the bubbles can be given as:

$$\begin{aligned}\Delta E_{sur} &= \Delta A_b \sigma \\ &= 2\pi d_1^2 \sigma - \pi d^2 \sigma \\ &= 0.26\pi d^2 \sigma\end{aligned} \tag{7.16}$$

The work by the turbulent force is presented in Figure 7.7, given by:

$$W_F = F_T s \tag{7.17}$$

where

s is the drift distance when the bubble splits into two.

According to the analysis in Chapter 2 Section 2.3.1, the turbulent force can be expressed as (Levich 1962):

$$F_T \propto d^2 f_l \rho_l u_l^2 \tag{7.18}$$

Here the distance s is assumed to be proportional to the bubble diameter and therefore the work done by the turbulent force can be expressed as:

$$W_F \propto f_l \rho_l u_l^2 d^3 \tag{7.19}$$

Combining Equations 7.15, 7.16 and 7.19, we can obtain the critical liquid velocity at the transition boundary of dispersed bubble to bubbly flow:

$$u_l = C\sqrt{\frac{\sigma}{f_l \rho_l d_c}} \tag{7.20}$$

where

d_c is the critical diameter used to distinguish dispersed bubble and bubbly flow.

The above analysis only explores the bubble splitting process and the required minimum homogeneous velocity. On the other hand, small bubbles may collide and coalesce into big bubbles. Therefore, the effect of void fraction and Weber number should be considered properly because they directly correlate with the probability of collision and possibility of coalescence respectively. In other words, high void fraction leads to frequent collisions and high Weber number facilitates bubble coalescence. As a result, the required fluid velocity at the transition boundary of dispersed bubble to bubbly flow increases correspondingly. Therefore, the coefficient C in Equation 7.20 may include a constant and an enhanced coefficient which relates to void fraction and Weber number, i.e. $C = C_0 + f(\alpha, We)$. Several equation forms were proposed for the coefficient C and finally a semi-empirical equation is recommended because it is in good agreement with the present experimental data and the previous results for air-water flow, see Equation 7.21:

$$u_l = 0.45\left[1 + 4.0\left(\alpha_{act} We_b^{1/2}\right)^{1/3}\right]\left(\frac{\sigma}{f_l \rho_l d_c}\right)^{1/2} \tag{7.21}$$

where:

α_{act}: actual void fraction

$$We_b = \frac{\rho_g d_c u_h^2}{\sigma}$$

$$f_l = \frac{C_l}{\mathrm{Re}_h^n}$$

$$\mathrm{Re}_h = \frac{\rho_l D u_h}{\mu_l}$$

As mentioned above, d_c is the critical diameter used to distinguish dispersed bubble and bubbly flow. In the previous air-water two-phase flow studies, the recommended critical diameter was given in Chapter 5 Equation 5.2 and was taken to be less than the tube inside diameter. In the present study, the critical diameters used were listed in Chapter 5 Table 5.3.

In air-water flow, the liquid velocity at the dispersed bubble-bubbly boundary is equal to the homogeneous velocity, i.e. $u_l = u_h = u_{gs} + u_{ls}$. However, in the present experiments the actual liquid velocity is lower than the sum of u_{gs} and u_{ls} because the actual void fraction is smaller than the calculated void fraction, see Table 7.3. Therefore, the actual liquid velocity u_l must consider the effect of the void fraction correction coefficient k and can be deduced by combining the following equations:

$$\rho_g u_{gs} + \rho_l u_{ls} = \rho_g u'_{gs} + \rho_l u'_{ls}$$

$$\alpha_{act} = k \alpha_{cal}$$

where

$$\alpha_{act} = \frac{u'_{gs}}{u'_{gs} + u'_{ls}}$$

$$\alpha_{cal} = \frac{u_{gs}}{u_{gs} + u_{ls}}$$

The actual liquid velocity can be given by:

$$u_l = u'_{gs} + u'_{ls} = \frac{(\rho_g u_{gs} + \rho_l u_{ls})(u_{gs} + u_{ls})}{k(\rho_g u_{gs} - \rho_l u_{gs}) + \rho_l (u_{gs} + u_{ls})} \qquad (7.22)$$

k is a correction coefficient used to correct the calculated void fraction. As mentioned in Chapter 5 Sections 5.1.1 and 5.2.1, the actual void fraction at the higher pressure is obviously higher than that at the lower pressure even at the same u_{gs} and u_{ls}. In detail, the actual void fraction, α_{act}, was smaller than the calculated void fraction α_{cal} and the void fraction at the lower pressure was smaller. However, the above phenomenon will not occur in air-water two-phase flow because of their incompatible characteristics. The α_{cal} can be calculated based on u_{gs} and u_{ls}. The α_{act} is the percentage of the total volume of bubbles in the inside vôlume of the tube. The total volume of bubbles can be estimated based on the number and average diameter of bubbles. The k factors measured in the current study are listed in Table 7.3.

Table 7.3 The correction coefficient for the void fraction in the present study.

Fluid	Diameter (mm)	Pressure (bar)	k factor
R134a	1.10	6.0	0.212
		10.0	0.240
		14.0	0.296
	2.01	6.0	0.400
		10.0	0.604
		14.0	0.625
	2.88	6.0	0.181
		10.0	0.371
		14.0	0.624
	4.26	6.0	0.299
		10.0	0.391
		14.0	0.562
air-water	-	-	1.00

The proposed dispersed bubble–bubbly semi-empirical model is validated by the present R134a flow maps and the existing air-water flow maps, including Taitel et al. (1980), Barnea et al (1983), Barnea (1987), Fukano and Kariyasaki (1993) and Mishima and Hibiki (1996). Taitel et al. (1980), Barnea et al. (1983) and Barnea (1987) did not distinguish bubbly and slug flow when the tube diameter was smaller than 51 mm in air-water flow at atmospheric conditions because they thought bubbly flow would develop to slug flow in fully developed two-phase flow. Therefore, the compared results show that the proposed model agrees well with the air-water flow maps in the range of 1.0 to 51.0 mm inner diameter tubes except a few data, see Figures 7.8-7.14. For example, the proposed model agrees with Taitel et al. (1980) on the dispersed bubble-bubbly boundary in the 51 mm tube except for one data point for bubbly flow, as shown in Figure 7.8. In the 25 mm tubes, the proposed model predicts that the transition occurs at a slightly higher u_{ls} than the experimental data from Barnea (1987), which is shown in Figure 7.9. However, it agrees well with Taitel (1980) under the same conditions, see Figure 7.10. In addition, the proposed model and the "Unified Model" predict the same boundary when the tube diameter is 25 mm. In the 12.3 mm or smaller tubes the prediction by the proposed model is better than the existing models, see Figures 7.11-7.14. The comparisons of the model with the present R134a results are presented later in Section 7.3.

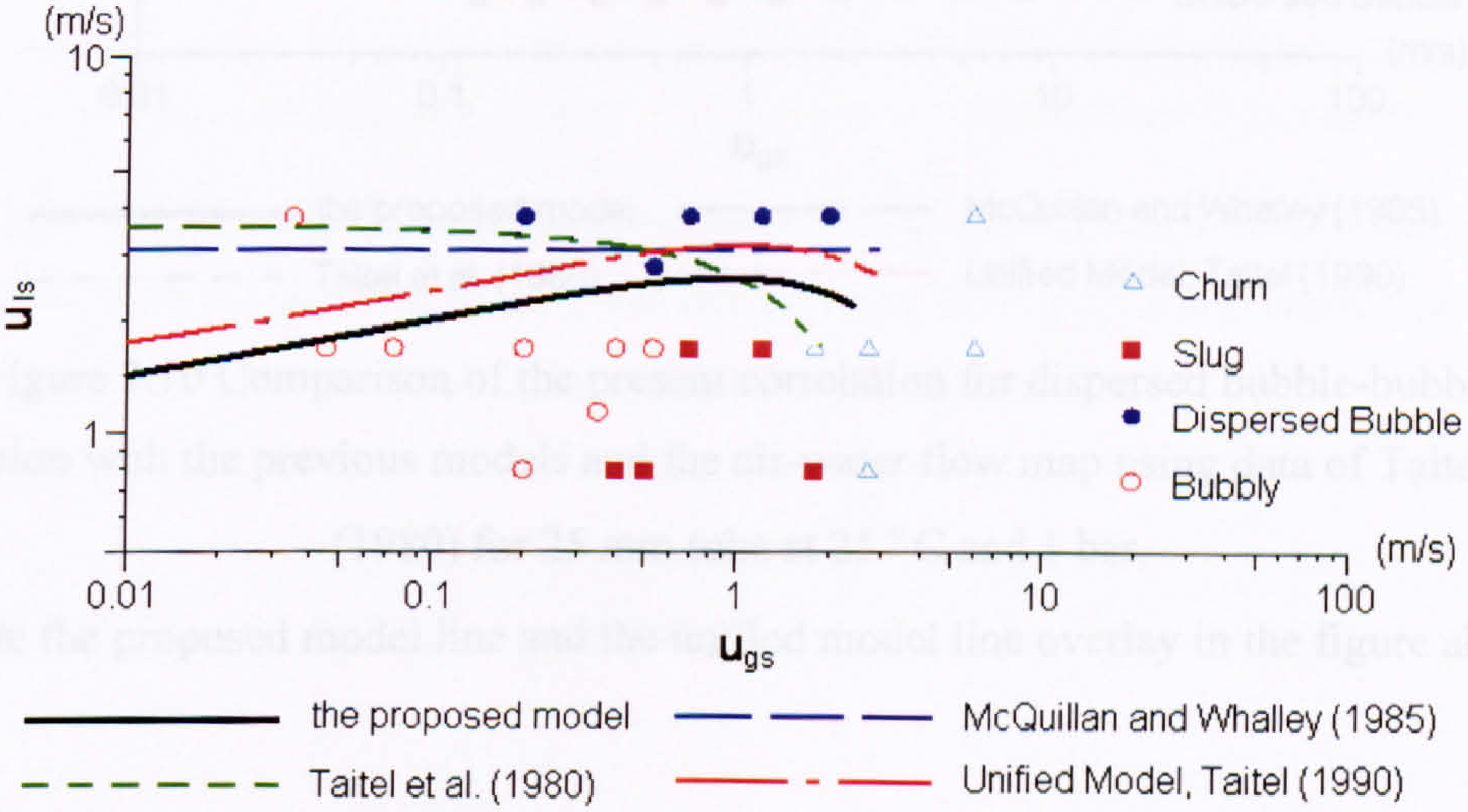

Figure 7.8 Comparison of the present correlation for dispersed bubble-bubbly transition with the previous models and the air-water flow map using data of Taitel et al (1980) for 51 mm tube at 25 °C and 1 bar.

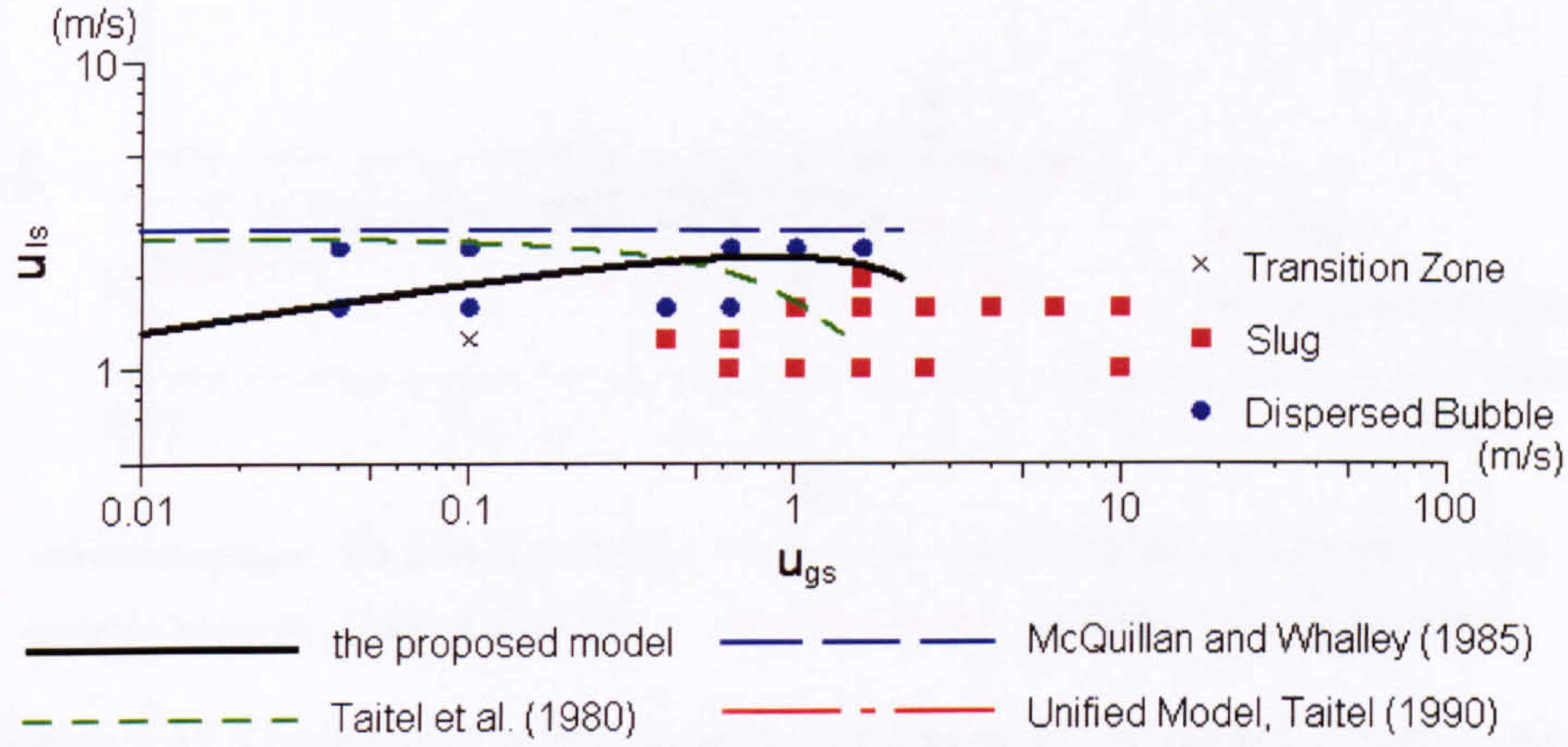

Figure 7.9 Comparison of the present correlation for dispersed bubble-bubbly transition with the previous models and the air-water flow map using data of Barnea (1987) for 25.4 mm tube at 25 °C and 1 bar.

(Note the proposed model line and the unified model line overlay in the figure above)

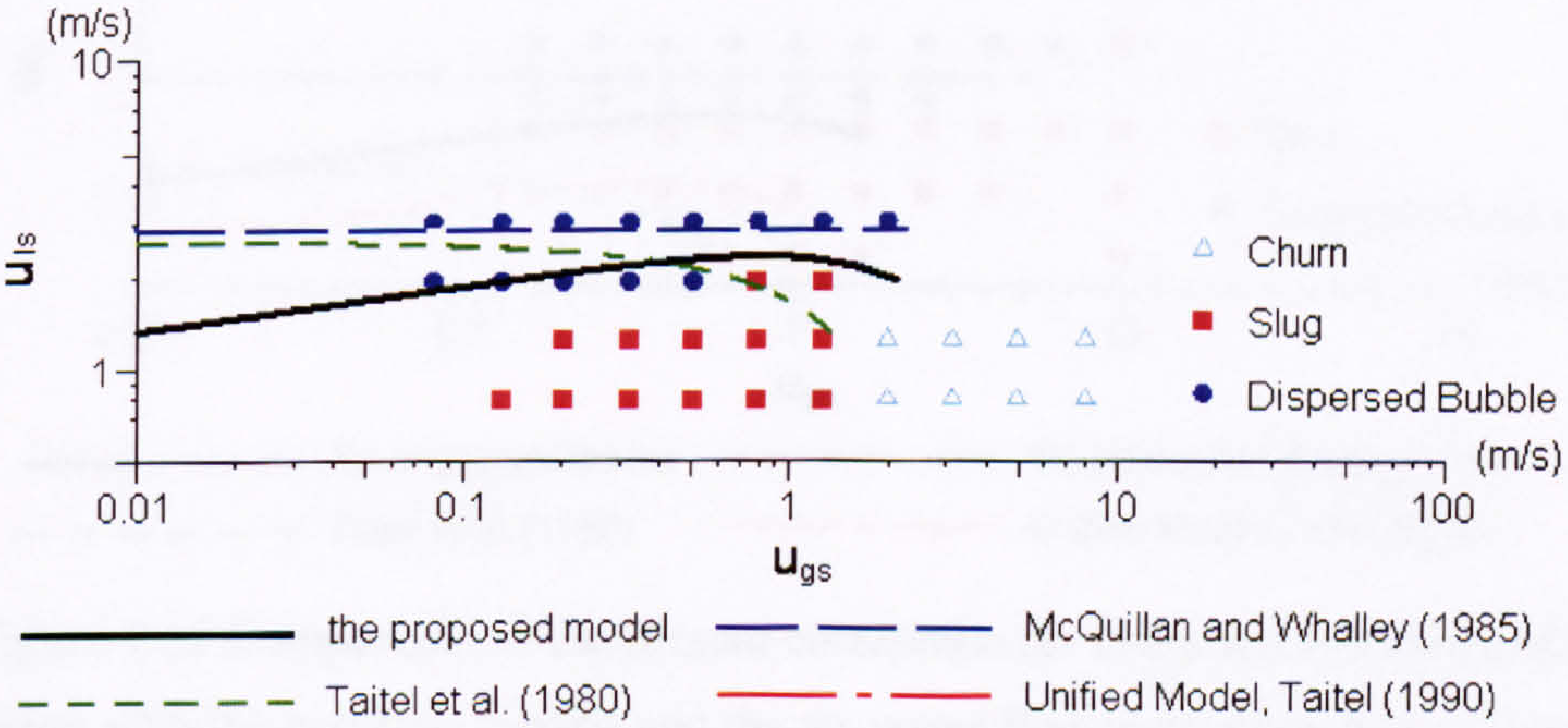

Figure 7.10 Comparison of the present correlation for dispersed bubble-bubbly transition with the previous models and the air-water flow map using data of Taitel et al. (1980) for 25 mm tube at 25 °C and 1 bar.

(Note the proposed model line and the unified model line overlay in the figure above)

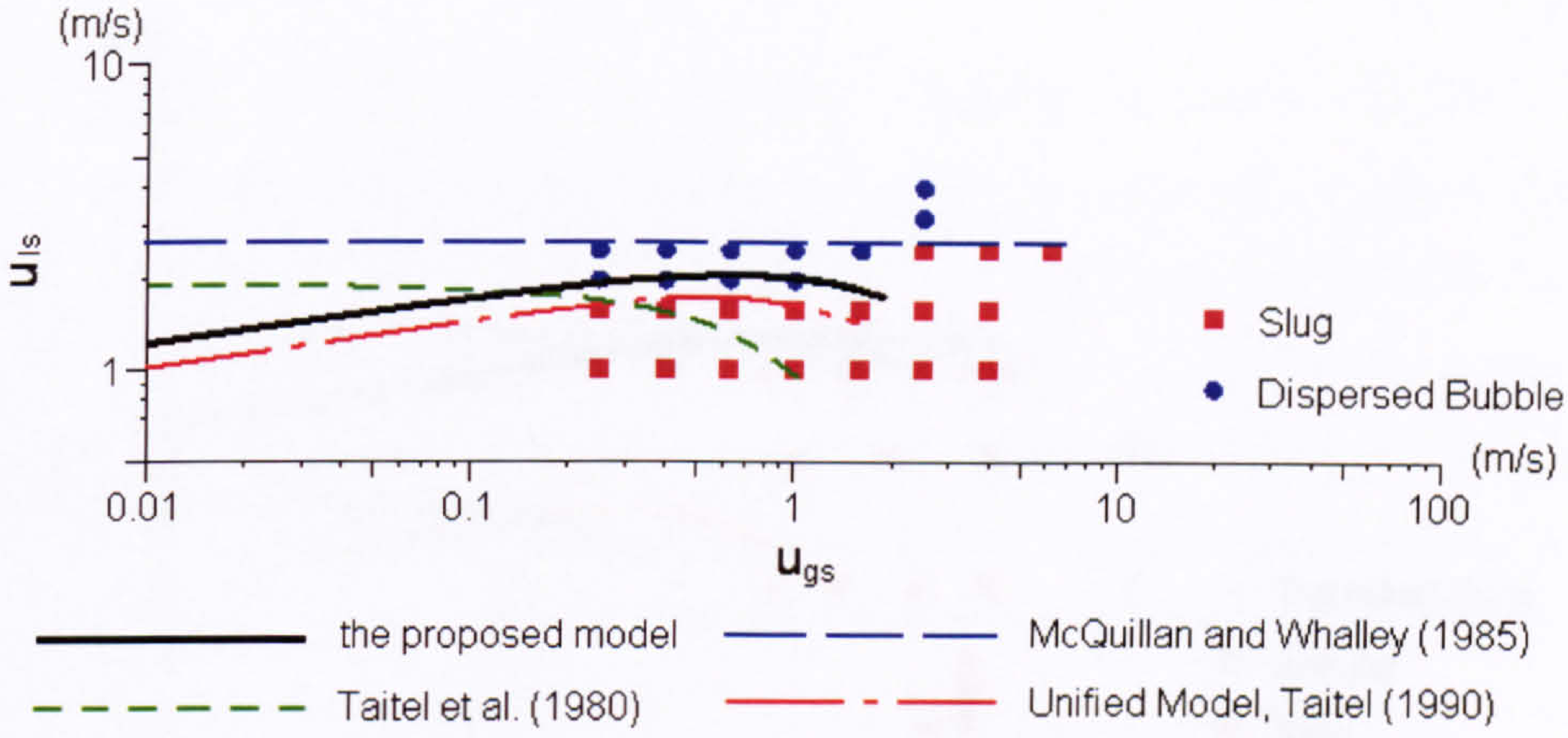

Figure 7.11 Comparison of the present correlation for dispersed bubble-bubbly transition with the previous models and the air-water flow map using data of Barnea et al. (1983) for 12.3 mm tube at 25 ° C and 1 bar.

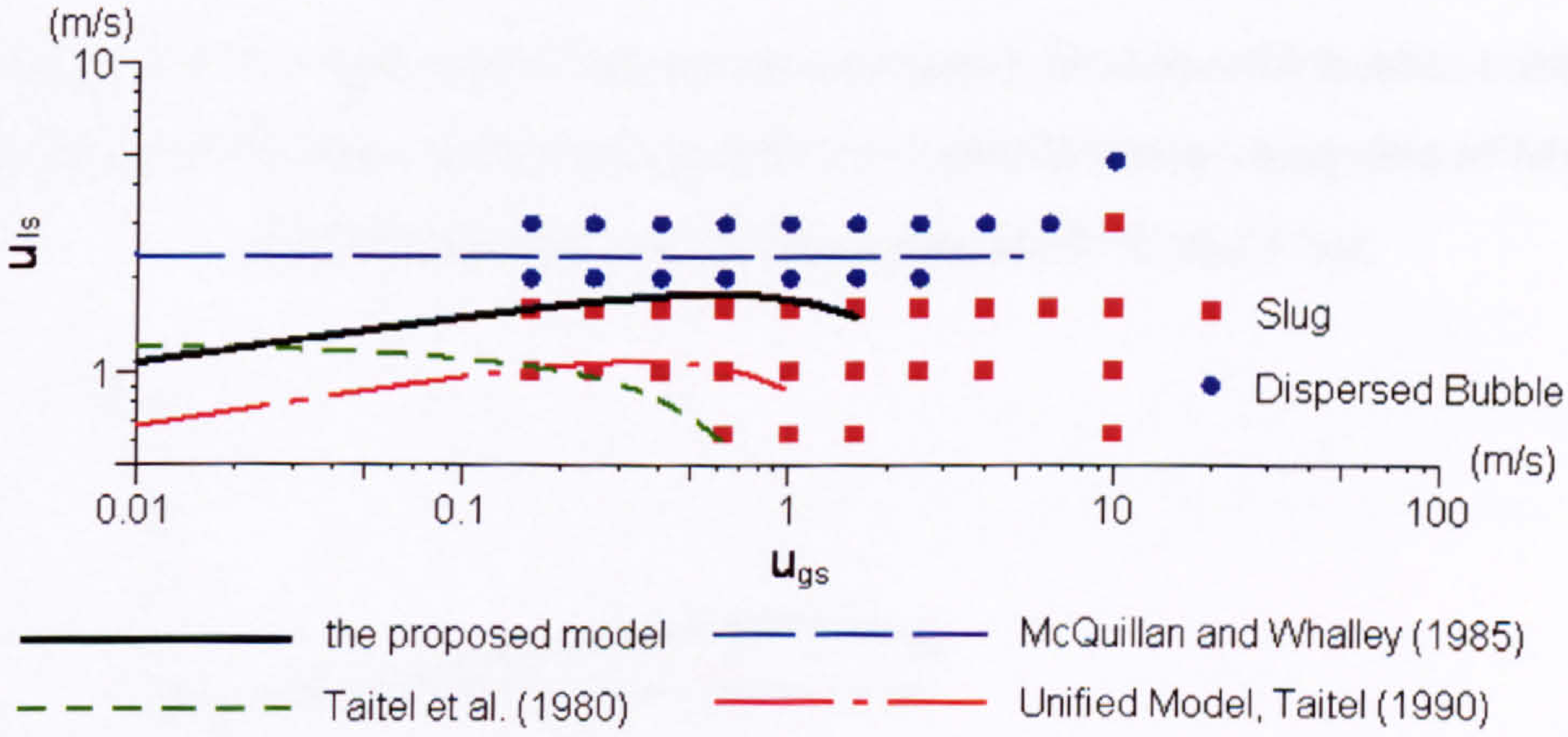

Figure 7.12 Comparison of the present correlation for dispersed bubble-bubbly transition with the previous models and the air-water flow map using data of Barnea et al. (1983) for 4 mm tube at 25 ° C and 1 bar.

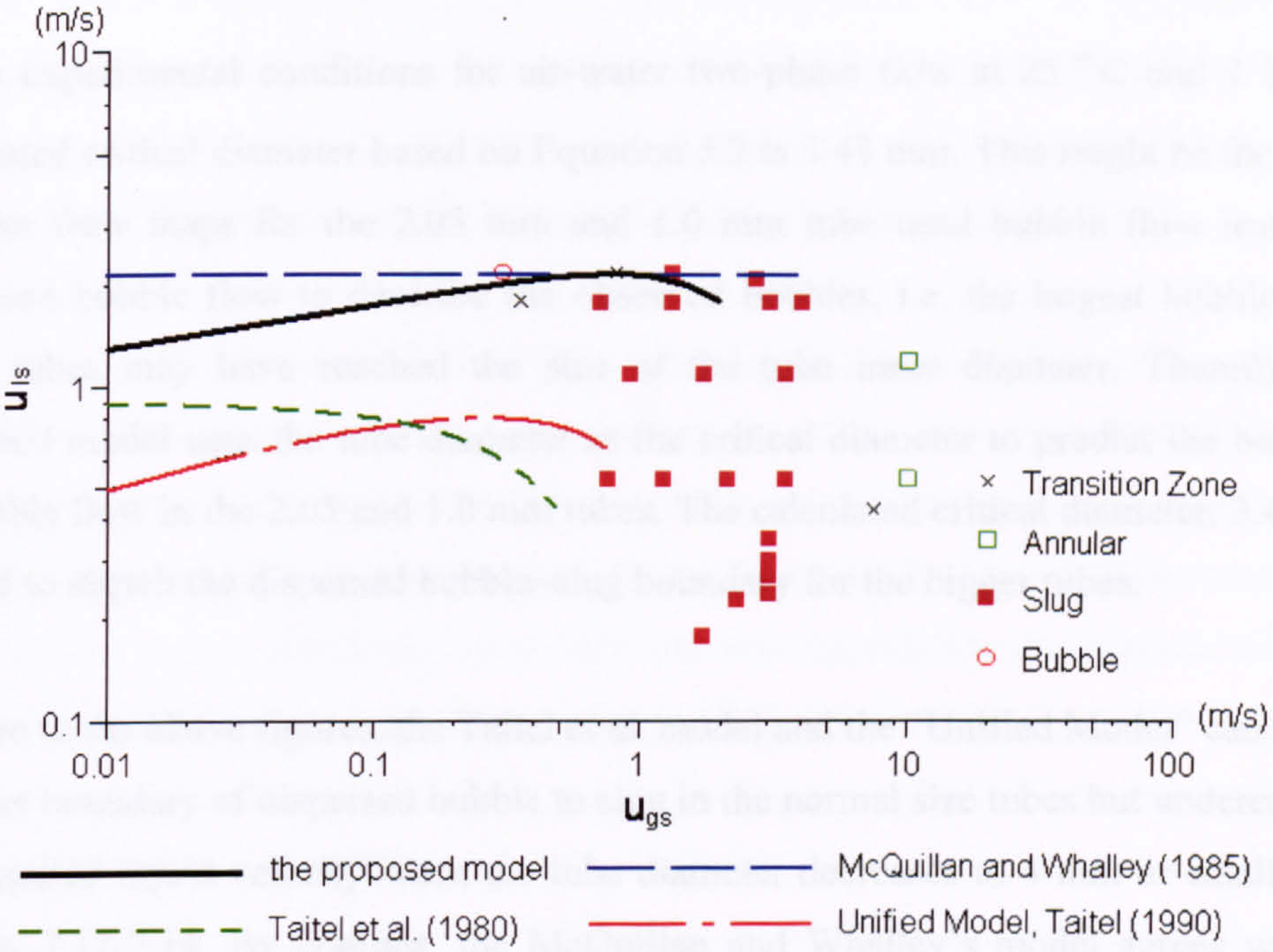

Figure 7.13 Comparison of the present correlation for dispersed bubble-bubbly transition with the previous models and the air-water flow map using data of Mishima and Hibiki (1996) for 2.05 mm tube at 25 °C and 1 bar.

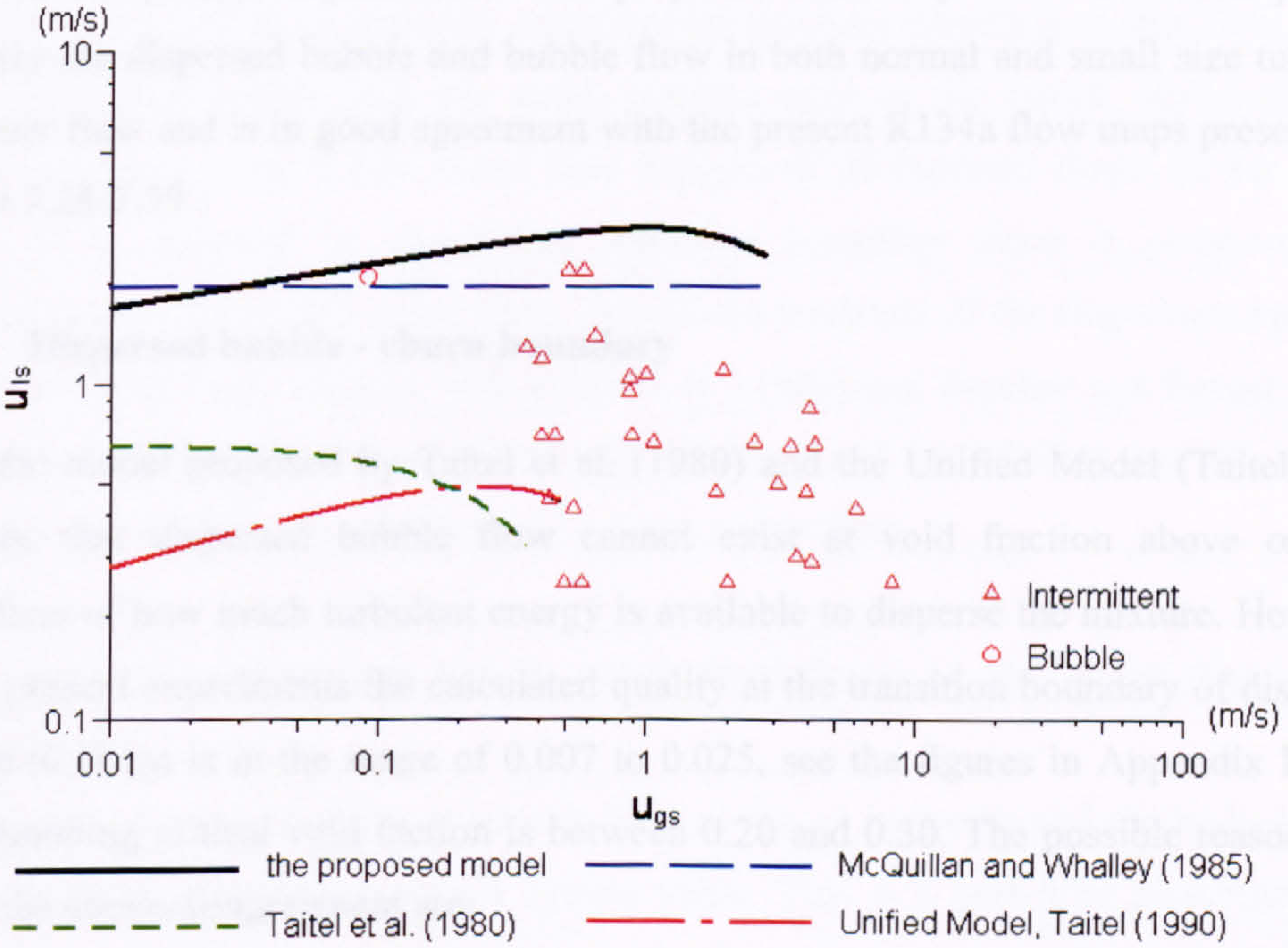

Figure 7.14 Comparison of the present correlation for dispersed bubble-bubbly transition with the previous models and the air-water flow map using data of Fukano and Kariyasaki (1993) for 1.0 mm tube at 25 °C and 1 bar.

In the experimental conditions for air-water two-phase flow at 25 °C and 1 bar, the calculated critical diameter based on Equation 5.2 is 3.43 mm. This might be the reason that the flow maps for the 2.05 mm and 1.0 mm tube used bubble flow instead of dispersed bubble flow to describe the observed bubbles, i.e. the largest bubble in the small tubes may have reached the size of the tube inner diameter. Therefore, the proposed model uses the tube diameter as the critical diameter to predict the boundary of bubble flow in the 2.05 and 1.0 mm tubes. The calculated critical diameter, 3.43 mm, is used to sketch the dispersed bubble–slug boundary for the bigger tubes.

As seen in the above figures, the Taitel et al. model and the "Unified Model" can predict well the boundary of dispersed bubble to slug in the normal size tubes but underestimate the required liquid velocity when the tube diameter decreases to 4 mm or smaller, see Figures 7.12-7.14. By contrast, the McQuillan and Whalley's model agrees with the experimental data for the small tubes well but generally overestimates the necessary liquid velocity in normal size tubes. In addition, the comparisons presented earlier in Chapter 6 Section 6.2 show that the existing models cannot predict well the R134a flow maps in the present experiments. The proposed semi-empirical correlation predicts properly the dispersed bubble and bubble flow in both normal and small size tubes for air-water flow and is in good agreement with the present R134a flow maps presented in Figure 7.28-7.39 .

7.2.3 Dispersed bubble - churn boundary

Both the model proposed by Taitel et al. (1980) and the Unified Model (Taitel 1990) suppose that dispersed bubble flow cannot exist at void fraction above α_c=0.52 regardless of how much turbulent energy is available to disperse the mixture. However, in the present experiments the calculated quality at the transition boundary of dispersed bubble to churn is in the range of 0.007 to 0.025, see the figures in Appendix H. The corresponding critical void faction is between 0.20 and 0.30. The possible reasons that cause the above disagreement are:

(1) Dispersed bubbles in two-phase flow tend to gather at the pipe centre and such asymmetric distribution becomes more severe in small tubes. As a result the critical void fraction in small tubes is smaller than that in normal size tubes.

(2) The Taitel et al. model and the Unified Model were based on the experimental results for air-water flow, i.e. the surface tension is much higher than R134a used in the present experiments. Therefore, the coalescence of bubbles might be easier in two-phase R134a flow so that the required critical void fraction is lower.

The present data is not enough to deduce a precise dispersed bubble-churn correlation. In addition, the existing experimental results rarely relate to the boundary of dispersed bubble to churn flow in small tubes. However, the obtained experimental correlation for bubbly to slug boundary apparently predicts the transition boundary of dispersed bubble to churn flow well, which indicates that the two boundaries may follow the same transition mechanism but requires more work and further investigation.

7.2.4 Slug - churn boundary

Although all researchers gave a similar description or definition for churn flow, like chaotic gas-liquid interface and foaming liquid slug, there was no general agreement on the criteria to distinguish slug and churn flow. The typically problematic region is the triangular area near slug, churn and dispersed bubble flow. Take the flow pattern in Figure 5.56 (a) (iii) as an example; some researchers may classify it as slug flow since it is a single slug bubble and few small bubbles exist in the liquid. However, other researchers may group it into churn flow because of its distorted shape. In the current study, it is regarded as slug-churn transition boundary since it possesses both characteristics of slug and churn flow. Overall the tendency of the slug-churn boundary obtained in this study accords with Taitel et al. (1980) and Brauner and Barnea (1986) approximately but distinctly conflicts with Mishima and Ishii (1984) and this may be attributed to the different criteria used by these researchers.

Three transition mechanisms can be summarized based on the observations in the present study:

Mechanism A: slug could be extremely long as the u_{gs} increases and the body starts to distort when the length exceeds a certain value. This is a particular phenomenon in small tubes and is the main transition mechanism at low u_{ls}, see Figure 5.56 (a) (i'). However, some researchers may not agree with the above criterion because the slug head is still regular bullet shape at this moment, see Figure 5.56 (a) (i).

Mechanism B: a slug will leave chaotic flow field behind its tail. If any successive slug is trapped in this field, its head and body will deform seriously, see Figure 5.56 (a) (ii'). This is the dominant mechanism in the middle range of u_{ls}.

Mechanism C: slug cannot keep its regular shape and change into churn flow at high homogeneous velocity due to the great impact force from the surrounding liquid and small bubbles. This is the prevailing transition mechanism at high u_{ls}, see Figure 5.56 (a) (iii).

A dimensionless correlation is proposed for Mechanism A based on the present experimental data using a data analysis tool, i.e. "linest" function in Microsoft Excel, to analyse the relativity of the parameters and obtain the best-fit correlation. This tool calculates the statistics for a line by using the "least squares" method to calculate a straight line that best fits the data. Unlike the "trendline" function in the Chart utility, the "linest" function can analyse the relativity of three or more parameters and propose a multi-variables correlation. All the semi-empirical correlations, including Equations 7.23, 7.24, 7.28 and 7.29 are obtained by this method. The detailed procedure is explained below:

1. Save the analysed data in Excel sheet. For example, the data at the low u_{ls} region of slug-churn boundary is chosen for Mechanism A.
2. Analyse the transition mechanism and propose an exponent format correlation, e.g. $Re=C*We^{m}Fr^{n}$
3. Calculate all the parameters appearing in the correlation, e.g. Re, We and Fr in the equation above.
4. Linearize the proposed correlation, i.e. convert the exponent format correlation into a linear equation, e.g. $\ln(Re)=\ln(C)+m*\ln(We)+n*\ln(Fr)$.
5. Evaluate the proposed linear equation to seek the constant C, m and n by the function "linest", the syntax see the help file in Excel.
6. Modify the proposed correlation and repeat steps (2)-(5) until an idea correlation is achieved, i.e. the coefficient of determination is close to 1.

The deduced correlation for Mechanism A is unlikely to be applicable for normal size pipe since the distorted long slug bubble is a particular phenomenon in small tubes. In addition, the applicability to other fluids needs further validation because the available experimental data is scarce.

Mechanism A:

$$\mathrm{Re}_{ls} = 81.08 We_{gs}^{1.626} Fr_{gs}^{*\,-0.267} \tag{7.23}$$

where

$$\mathrm{Re}_{ls} = \frac{\rho_l D u_{ls}}{\mu_l}$$

$$We_{gs} = \frac{\rho_g D u_{gs}^2}{\sigma}$$

$$Fr_{gs}^* = \sqrt{\frac{\rho_g}{(\rho_l - \rho_g) g D}} u_{gs}$$

As the liquid velocity increases, slug bubbles tend to be shorter so that Mechanism B displaces Mechanism A and becomes the prevailing transition mechanism. In the region dominated by Mechanism B, an obvious characteristic is that the sketched slug-churn boundary is approximately a vertical line in the u_{gs}-u_{ls} flow maps. It indicates that the deduced correlation might not include the parameter of liquid velocity or that the reference liquid velocity is a constant at the transition boundary. Finally a curve-fitting correlation is developed in Microsoft Excel based on the data points at the slug-churn boundary, see Equation 7.24.

Mechanism B:

$$\mathrm{Re}^* = C_1 We_{gs}^{C_2} \tag{7.24}$$

where

$$\mathrm{Re}^* = \frac{\rho_g D^2 u_{gs}^2}{\mu_l D u_l^*} = \frac{\rho_g D u_{gs}^2}{\mu_l u_l^*}$$

$$We_{gs} = \frac{\rho_g D u_{gs}^2}{\sigma}$$

Re^* is a newly introduced dimensionless parameter which presents the ratio of the inertia force related to gas velocity and the friction based on a reference liquid velocity. u^*_l is the reference liquid velocity which is a critical constant at the boundary of slug to churn flow. Therefore, Equation 7.24 can be rewritten as:

$$\frac{\rho_g D u_{gs}^2}{\mu_l} = u_l^* C_1 \left(\frac{\rho_g D u_{gs}^2}{\sigma} \right)^{C_2} = C^* \left(\frac{\rho_g D u_{gs}^2}{\sigma} \right)^{C_2} \tag{7.25}$$

In the above equation C^* is a dimensional coefficient which includes the unknown critical reference velocity u_l^*. The coefficients C^* and C_2 can be obtained from the data point at the slug-churn boundary, see Equation 7.26 below:

$$\frac{\rho_g D u_{gs}^2}{\mu_l} = 84.53 \left(\frac{\rho_g D u_{gs}^2}{\sigma} \right)^{0.6523} \tag{7.26}$$

In the high u_{ls} region the distortion of the slug can be attributed to the great impact force from the surrounding liquid and small bubbles. In other words, the slug-churn transition boundary in this region is the balance resulting between turbulent force and surface tension. The required homogeneous velocity can be given by combining Equations 2.7 and 2.8, see Equation 7.27 below.

Mechanism C:

$$u_h = C \sqrt{\frac{\sigma}{f_l \rho_l D}} \tag{7.27}$$

where

$$u_h = u_{gs} + u_{ls}$$

$$f_l = \frac{C_l}{\mathrm{Re}_h^n}$$

$$\mathrm{Re}_h = \frac{\rho_l D u_h}{\mu_l}$$

The coefficient C is an experimental factor and can be obtained by the developed data analysis program after several tests. A value of 2.75 can give good results at the current experimental conditions.

Intermittent flow is subdivided into slug and churn in the present study based on the above three relevant mechanisms (A, B, C). Slug flow takes place at lower gas velocity whilst churn flow dominates the higher gas velocity region as shown in Figures 7.26 and 7.27.

Churn flow is not always considered as a typical flow pattern in the previous studies for small tubes. Sometimes it is grouped into intermittent flow but in other cases it might be integrated with annular flow. Therefore, the proposed correlations are only compared with the air-water flow maps in which churn flow was identified and presented, see Figures 7.15-7.19. The compared results show that the proposed correlations accord with the earlier studies when the tube diameter is 25 mm or less, see Figures 7.15-7.18. However, a few experimental data at the region of high u_{ls}, which were reported as slug flow by Barnea et al. (1983) and should be at the left hand of the slug-churn boundary, are actually located at the right hand of the boundary predicted by the proposed model, see Figures 7.16 and 7.17. The above disagreement may be attributable to the differences in the definition of churn flow in the region of high u_{ls}, i.e. the triangular area near slug, churn and dispersed bubble flow. Obviously the proposed model underestimates the required u_{gs} at the transition boundary when compared with the flow map for the 51 mm tube reported by Taitel et al. (1980), i.e. the predicted boundary is at the left side of the experimental boundary, see Figure 7.19. The following comparisons include the existing models except that proposed by Taitel et al. (1980) since they considered that the slug-churn boundary was a function of the observation position which is an unknown parameter in some flow maps. However, the applicability of the developed correlations needs further validation because (1) all the comparisons are based on air-water flow maps;. (2) the available flow maps are for 4 mm tube or above; (3) the data points near the slug-churn boundary are too sparse to prove the validity of correlation, see Figures 7.15 and 7.16; (4) the criteria used in the earlier studies for the slug-churn boundary may differ from those in the current study because only a small number of pictures are available in the existing papers. The typically problematic region is the triangular area near slug, churn and dispersed bubble flow as shown in Figure 7.16 and 7.17.

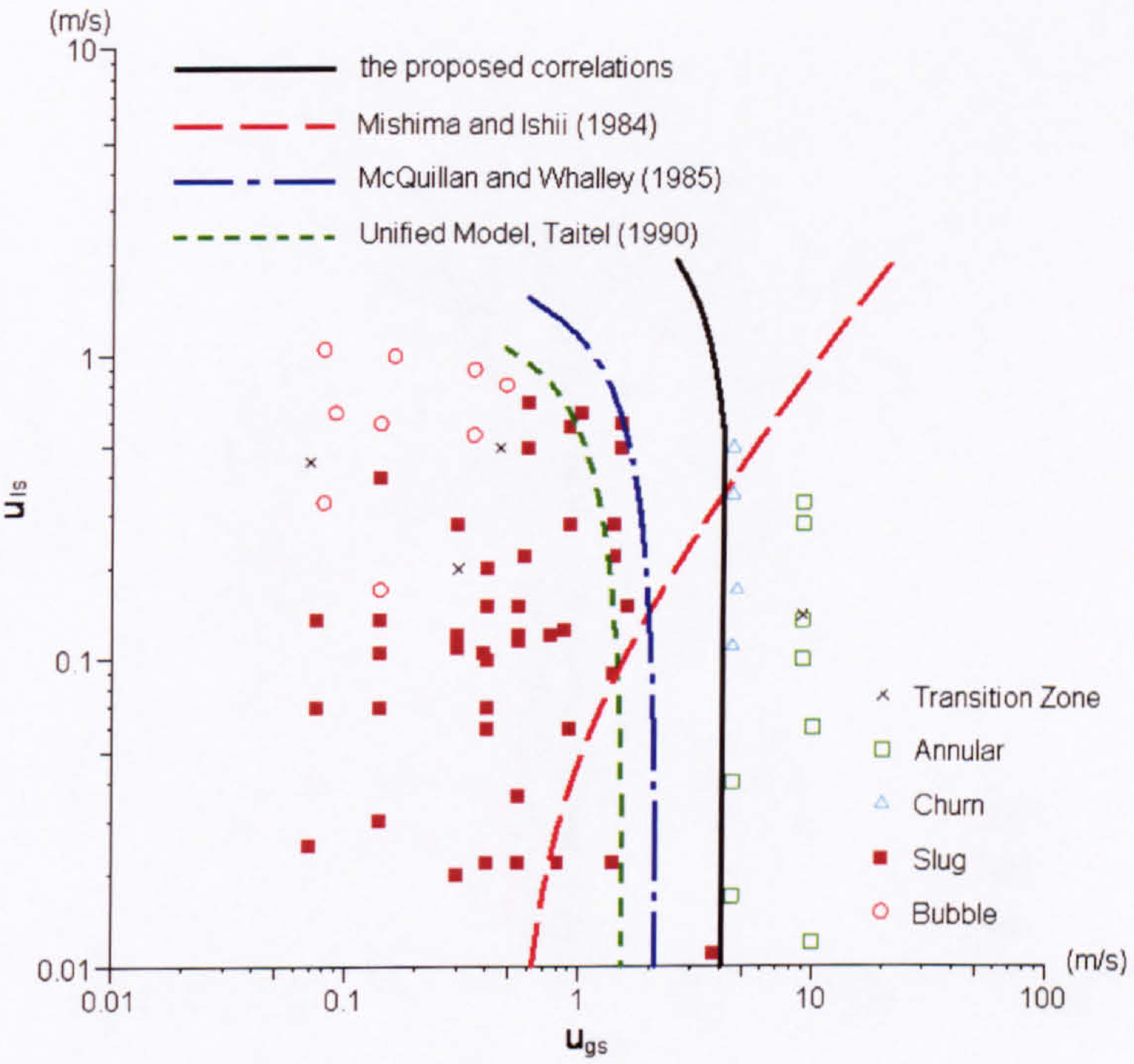

Figure 7.15 Comparison of the present correlation for slug-churn transition with the previous models and the air-water flow map using data of Mishima and Hibiki (1996) for 4.08 mm tube at 25 ° C and 1 bar.

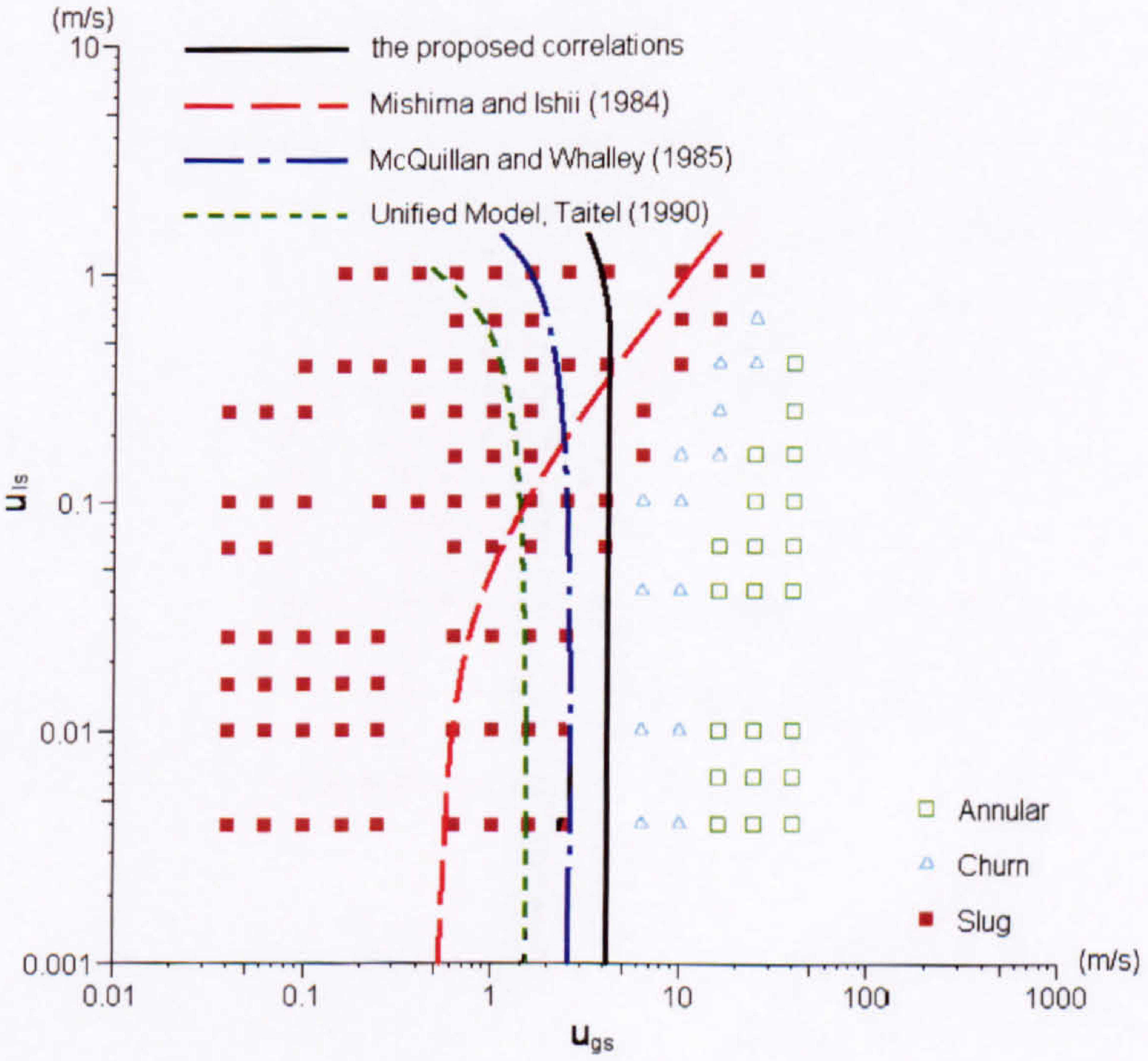

Figure 7.16 Comparison of the present correlation for slug-churn transition with the previous models and the air-water flow map using data of Barnea et al. (1983) for 4 mm tube at 25 ° C and 1 bar.

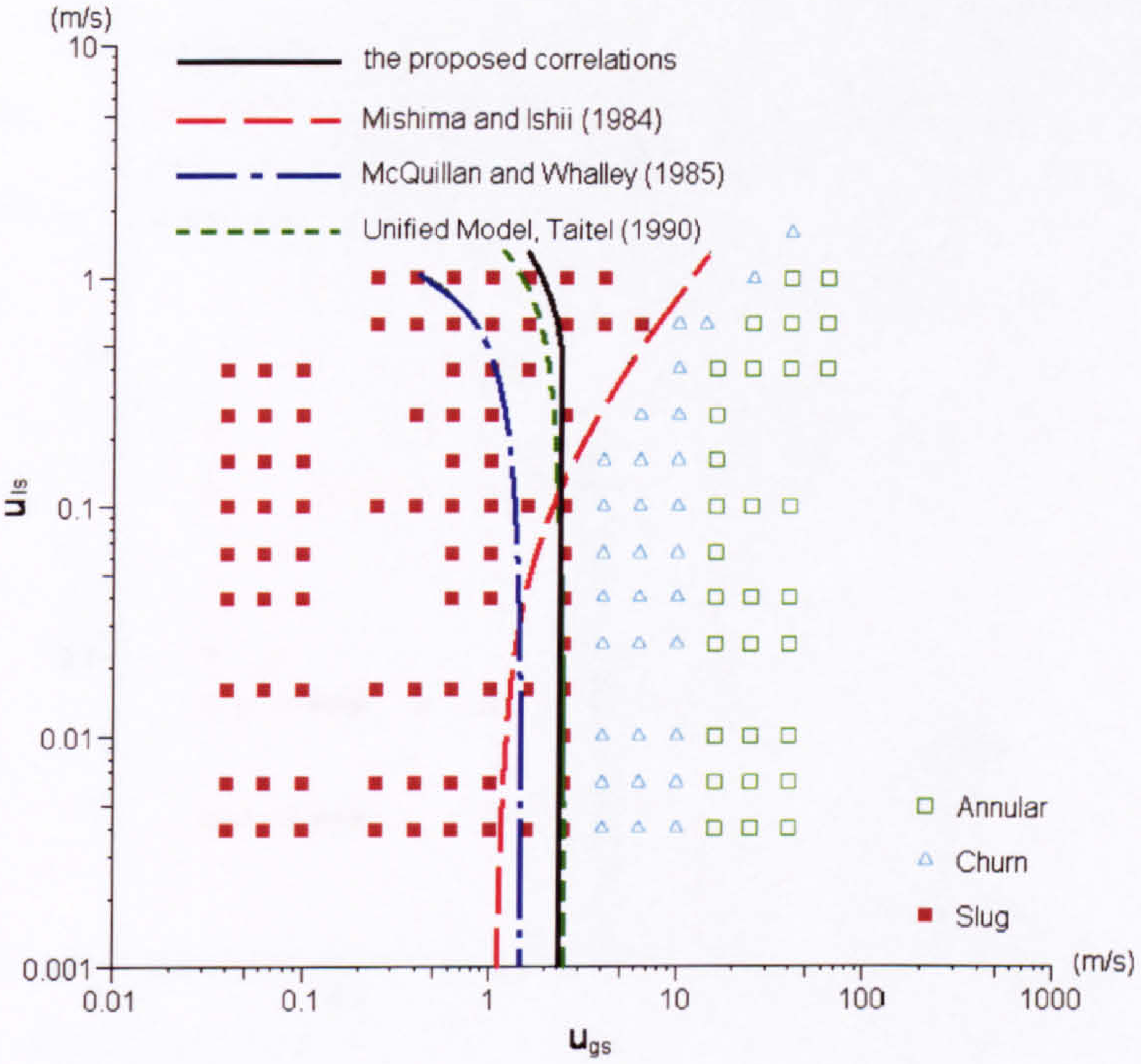

Figure 7.17 Comparison of the present correlation for slug-churn transition with the previous models and the air-water flow map using data of Barnea et al. (1983) for 12.3 mm tube at 25 °C and 1 bar.

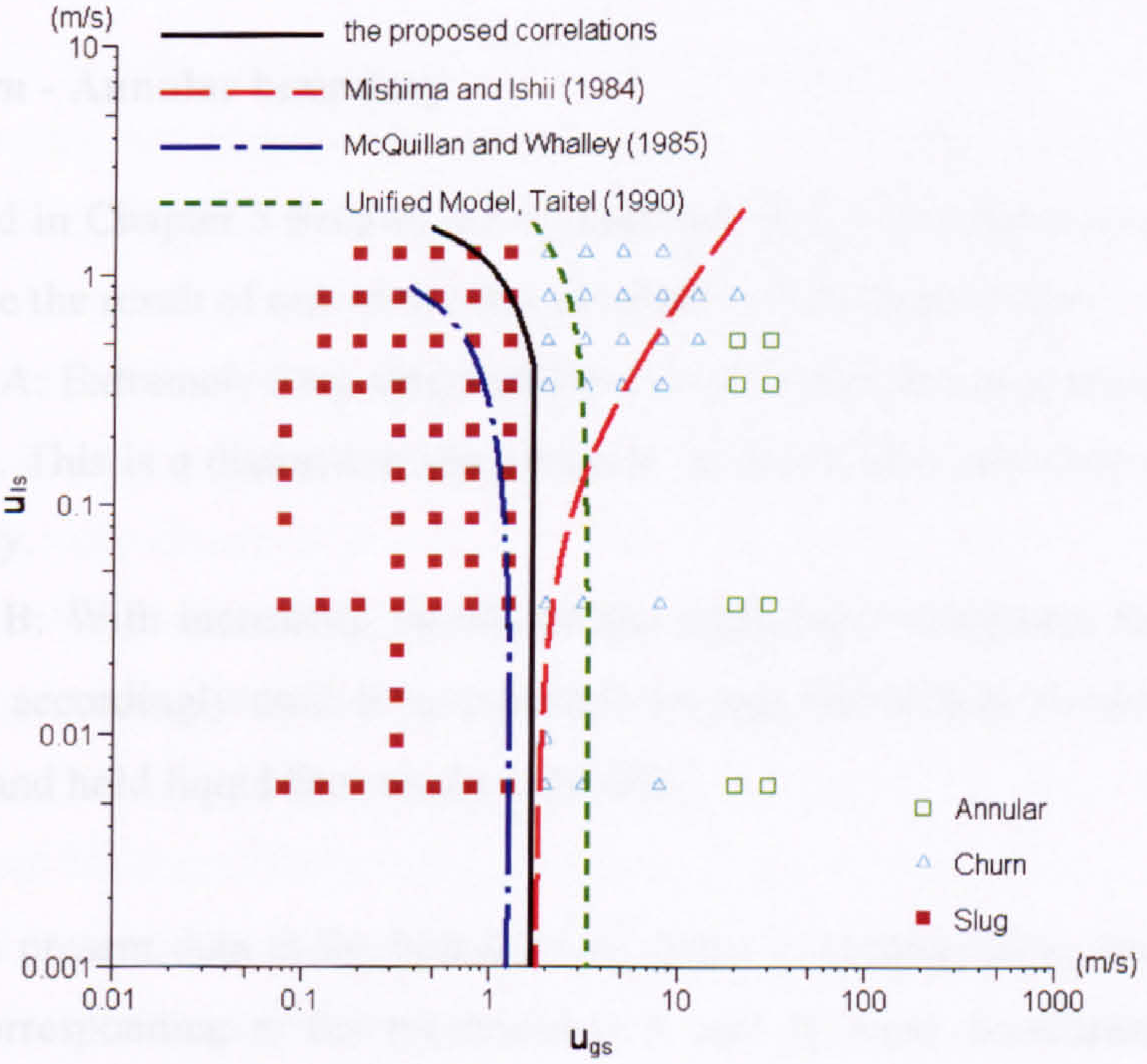

Figure 7.18 Comparison of the present correlation for slug-churn transition with the previous models and the air-water flow map using data of Taitel et al. (1980) for 25 mm tube at 25 °C and 1 bar.

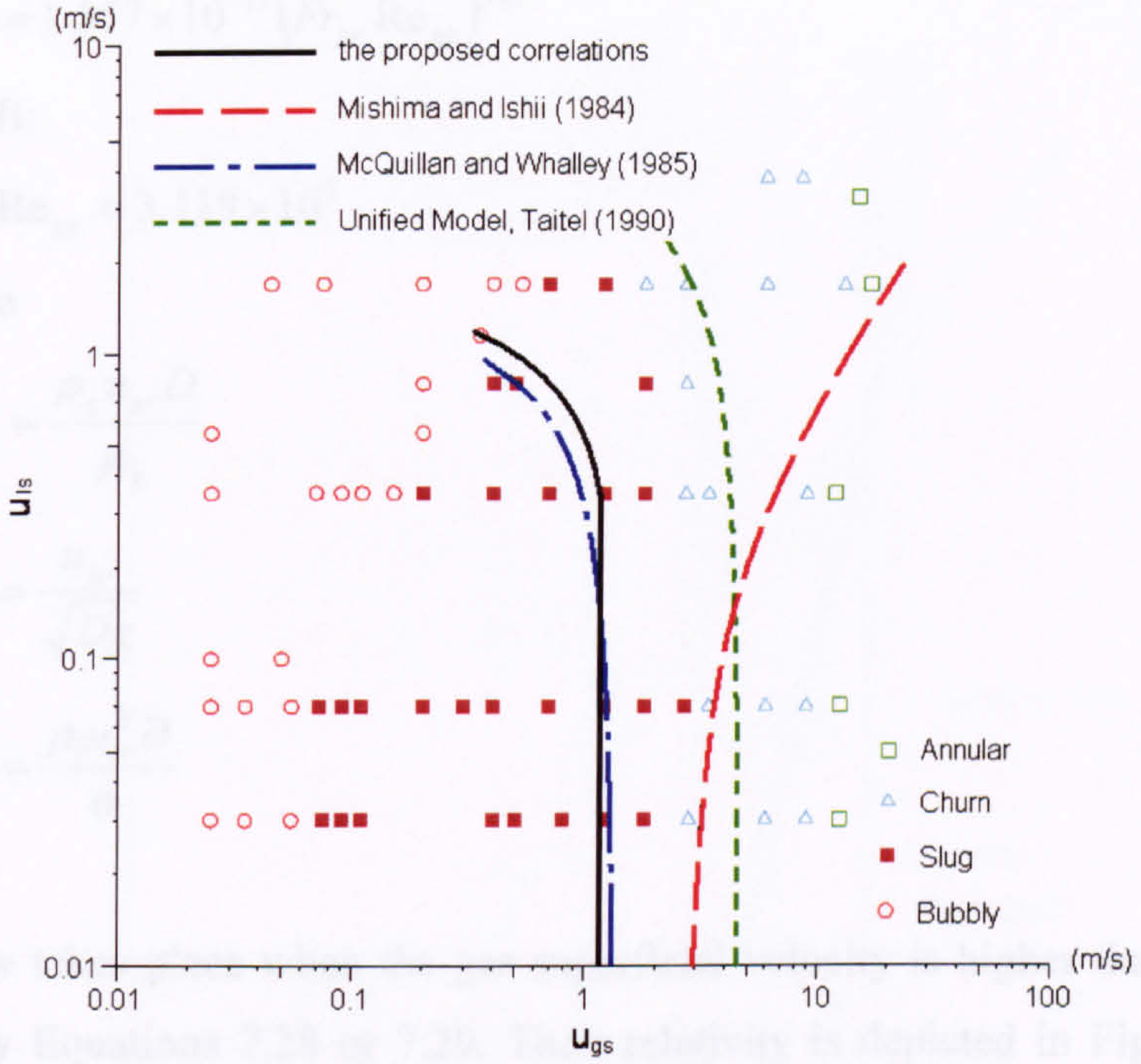

Figure 7.19 Comparison of the present correlation for slug-churn transition with the previous models and the air-water flow map using data of Taitel et al. (1980) for 51 mm tube at 25 °C and 1 bar.

7.2.5 Churn - Annular boundary

As mentioned in Chapter 5 Section 5.2.5, transition from churn flow to annular flow is assumed to be the result of one of the two mechanisms discussed below.

Mechanism A: Extremely long slug bubbles evolve to continuous gas core due to high void fraction. This is a distinctive phenomenon in small tubes and only appears at low liquid velocity.

Mechanism B: With increasing liquid and gas superficial velocities, the gas velocity will increase accordingly until it accumulates enough momentum to blow through the liquid block and hold liquid film on the tube wall.

Based on the present data at the boundary of churn to annular flow, two curve-fitting equations, corresponding to the mechanisms A and B, were developed in Microsoft Excel, see Equations 7.28 and 7.29.

Mechanism A:

$$We_{ls} = 1.567 \times 10^{-17} \left(Fr_{gs} \, \mathrm{Re}_{gs} \right)^{3.41} \tag{7.28}$$

Mechanism B:

$$Fr_{gs} \, \mathrm{Re}_{gs} = 3.119 \times 10^{5} \tag{7.29}$$

where

$$\mathrm{Re}_{gs} = \frac{\rho_g u_{gs} D}{\mu_g}$$

$$Fr_{gs} = \frac{u_{gs}}{\sqrt{Dg}}$$

$$We_{ls} = \frac{\rho_l u_{ls}^2 D}{\sigma}$$

Annular flow takes place when the gas superficial velocity is higher than the velocity calculated by Equations 7.28 or 7.29. Their relativity is depicted in Figures 7.26 and 7.27.

The proposed correlations apparently agree with the flow maps for air-water flow maps in both small and normal size tubes, see Figures 7.20-7.25. Here, the correlation from Mechanism A is only used for the tubes with a diameter smaller than 5 mm. For example, the proposed correlations coincide with the 1 mm tube flow map from Fukano and Kariyasaki (1993). By contrast, the existing models show poor agreement, see Figure 7.20. Comparing with the flow maps for the 2.4 and 4.08 mm tubes from Mishima and Hibiki (1996) shown in Figures 7.21 and 7.22, the newly developed correlations properly predict the annular flow except for a few data in the high u_{ls} region, which were observed as annular flow in the experiments but are predicted as churn flow by the proposed correlations. In the 12.3 and 25 mm tubes, the proposed correlations agree with both the experimental data from Barnea et al. (1983) and Taitel et al. (1980) and the existing models from Taitel et al. (1980), Mishima and Ishii (1984), McQuillan and Whalley (1985) and the "Unified Model" summarized by Taitel (1990), see Figures 7.23 and 7.24. When the tube diameter increases to 51 mm, e.g. the flow map from Taitel et al. (1980) shown in Figure 7.25, the proposed correlation slightly underestimates the required u_{gs} at the churn-annular boundary when compared with the experimental data. By contrast, the past models generally overestimate the required u_{gs}. However, the difference is within a reasonable range.

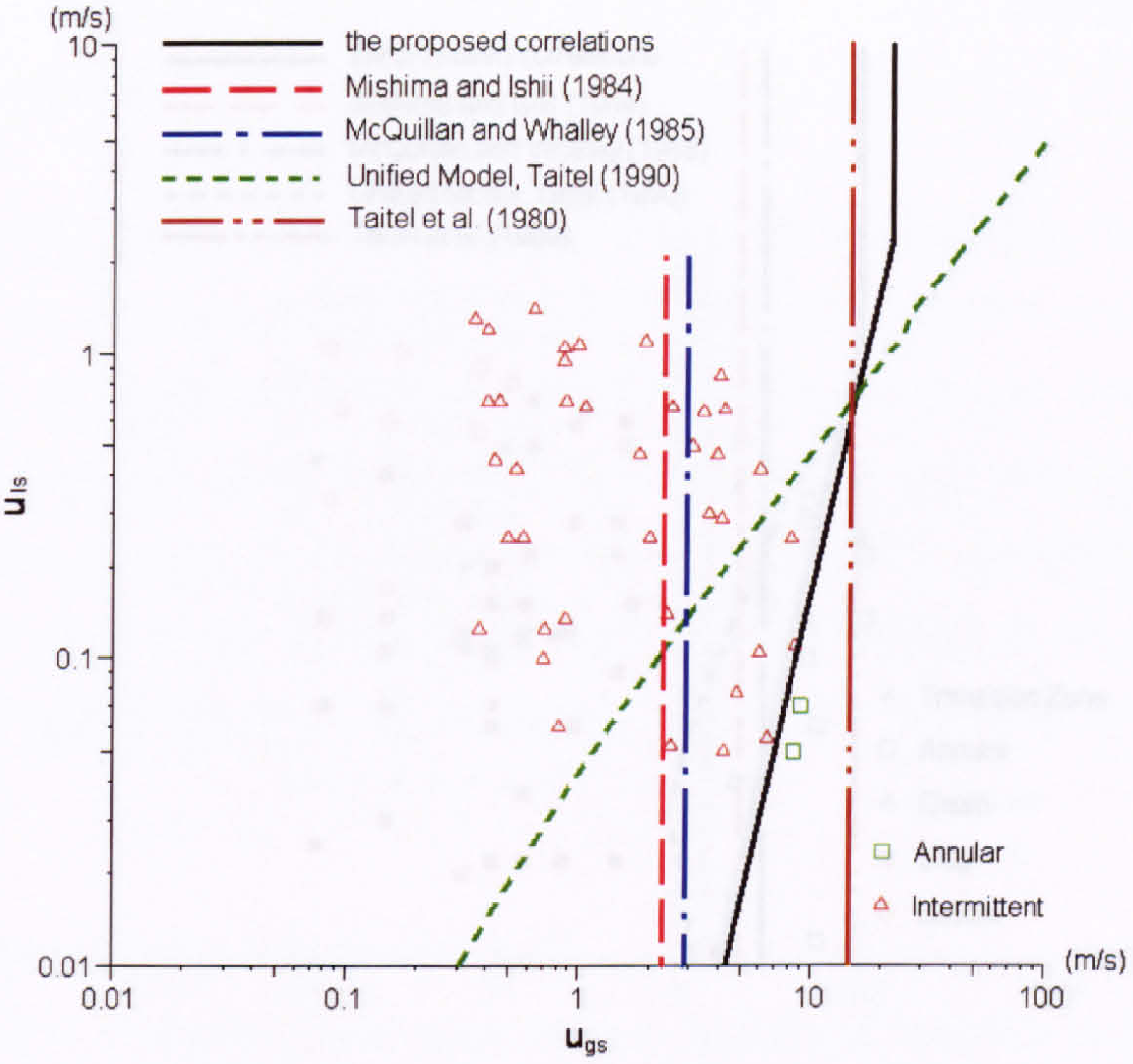

Figure 7.20 Comparison of the present correlation for churn-annular transition with the previous models and the air-water flow map using data of Fukano and Kariyasaki (1993) for 1 mm tube at 25 ^{o} C and 1 bar.

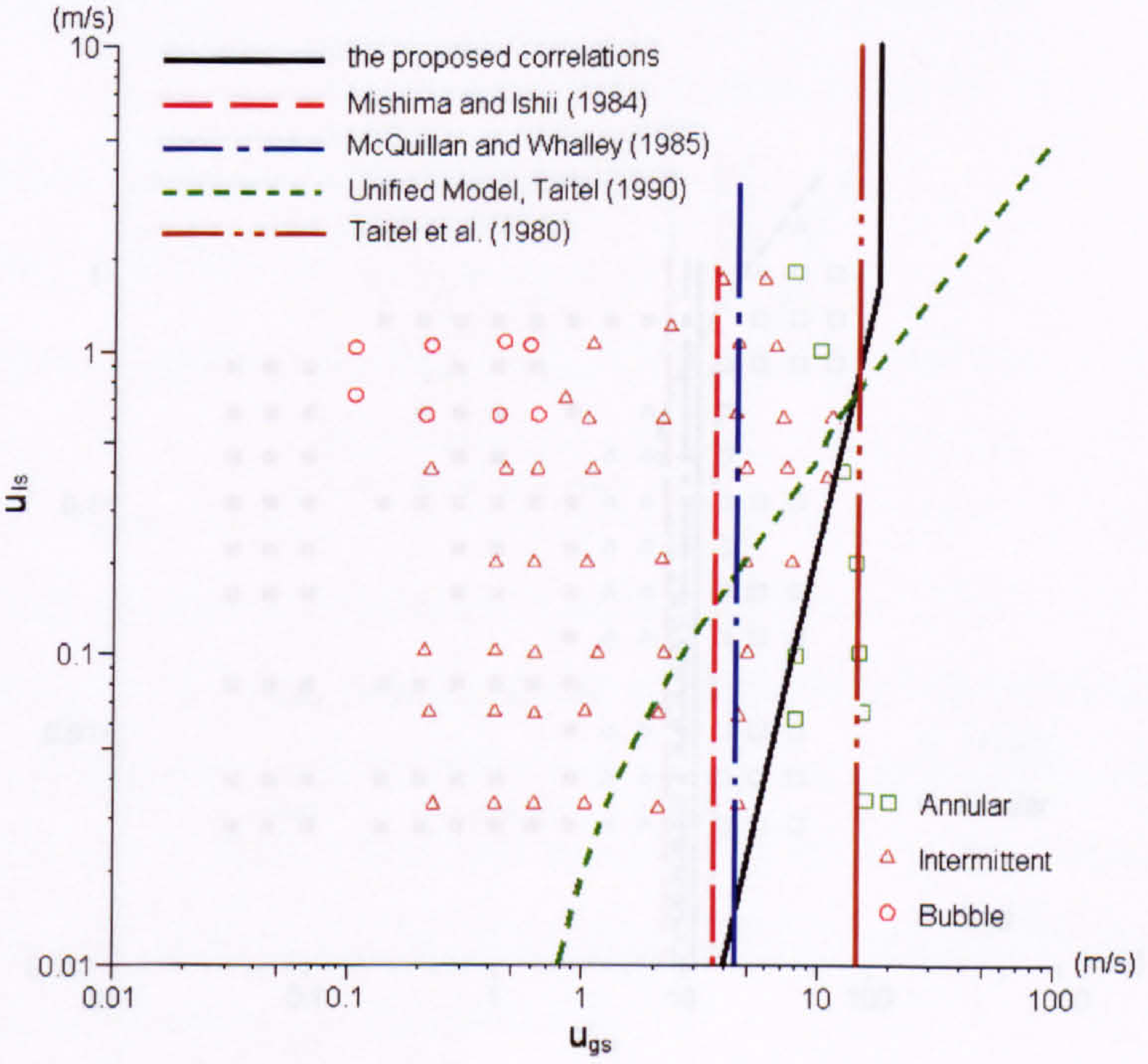

Figure 7.21 Comparison of the present correlation for churn-annular transition with the previous models and the air-water flow map using data of Fukano and Kariyasaki (1993) for 2.4 mm tube at 25 ^{o} C and 1 bar.

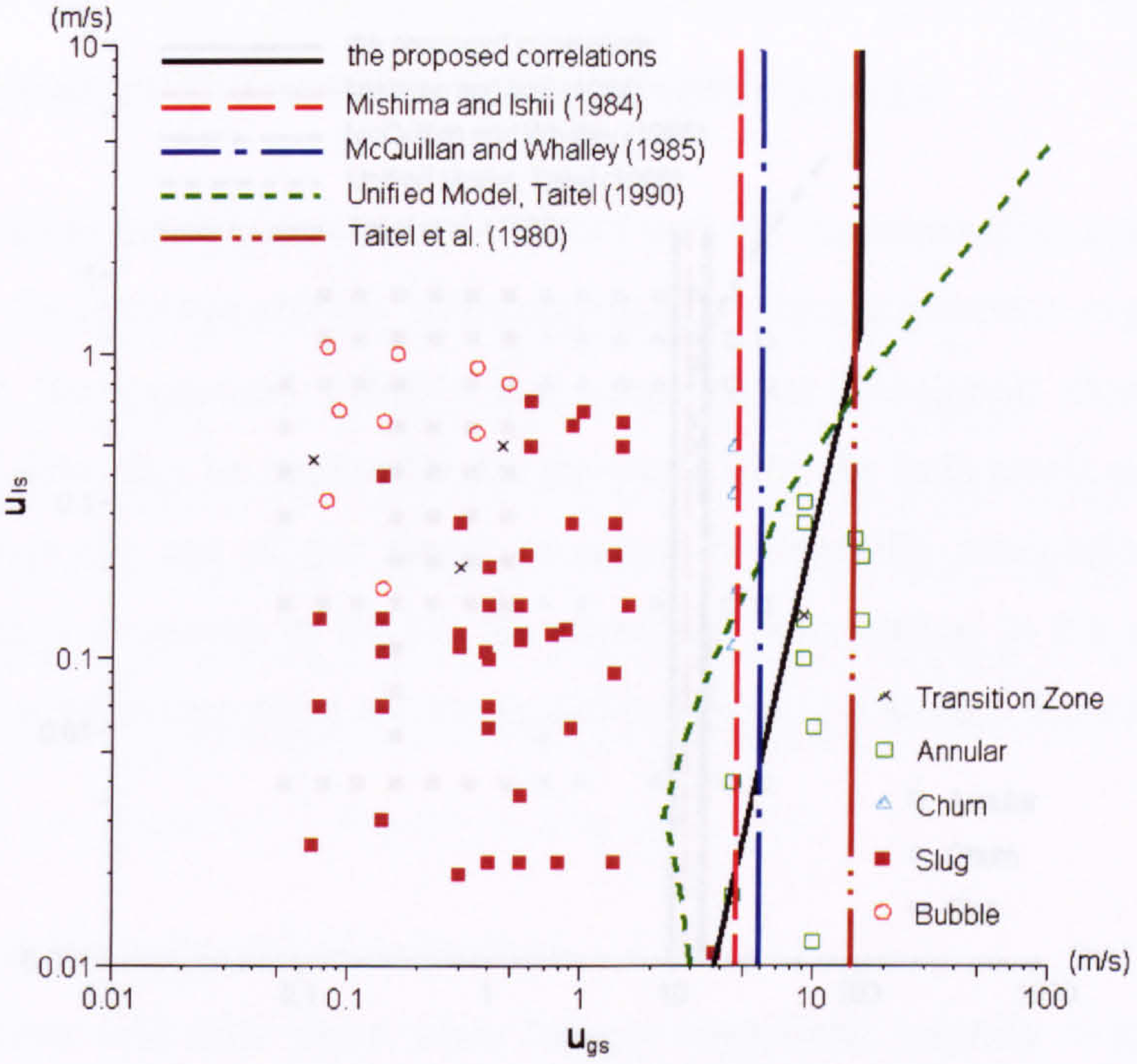

Figure 7.22 Comparison of the present correlation for churn-annular transition with the previous models and the air-water flow map using data of Mishima and Hibiki (1996) for 4.08 mm tube at 25 ° C and 1 bar.

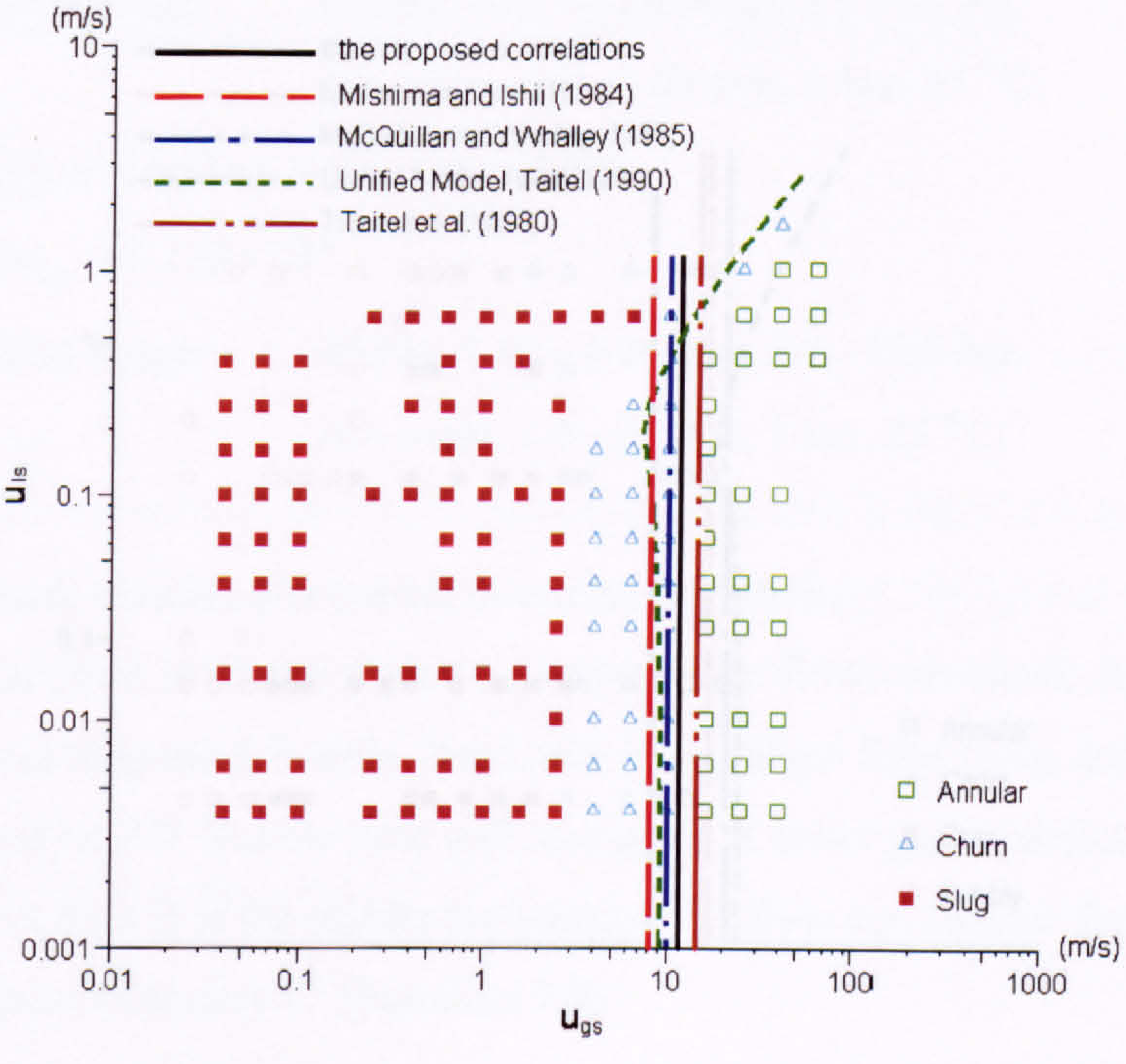

Figure 7.23 Comparison of the present correlation for churn-annular transition with the previous models and the air-water flow map using data of Barnea et al (1983) for 12.3 mm tube at 25 ° C and 1 bar.

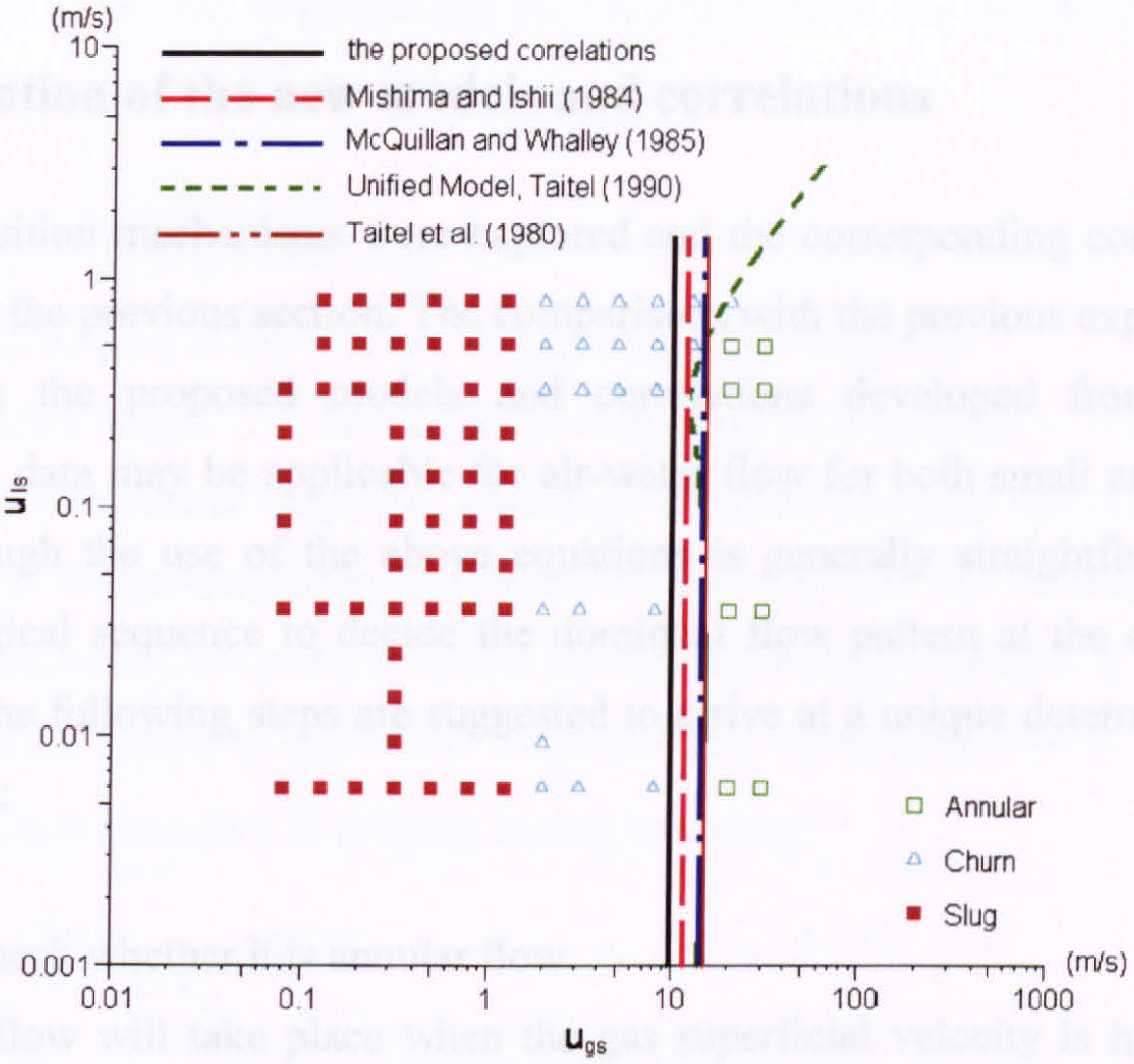

Figure 7.24 Comparison of the present correlation for churn-annular transition with the previous models and the air-water flow map using data of Taitel et al (1980) for 25 mm tube at 25 °C and 1 bar.

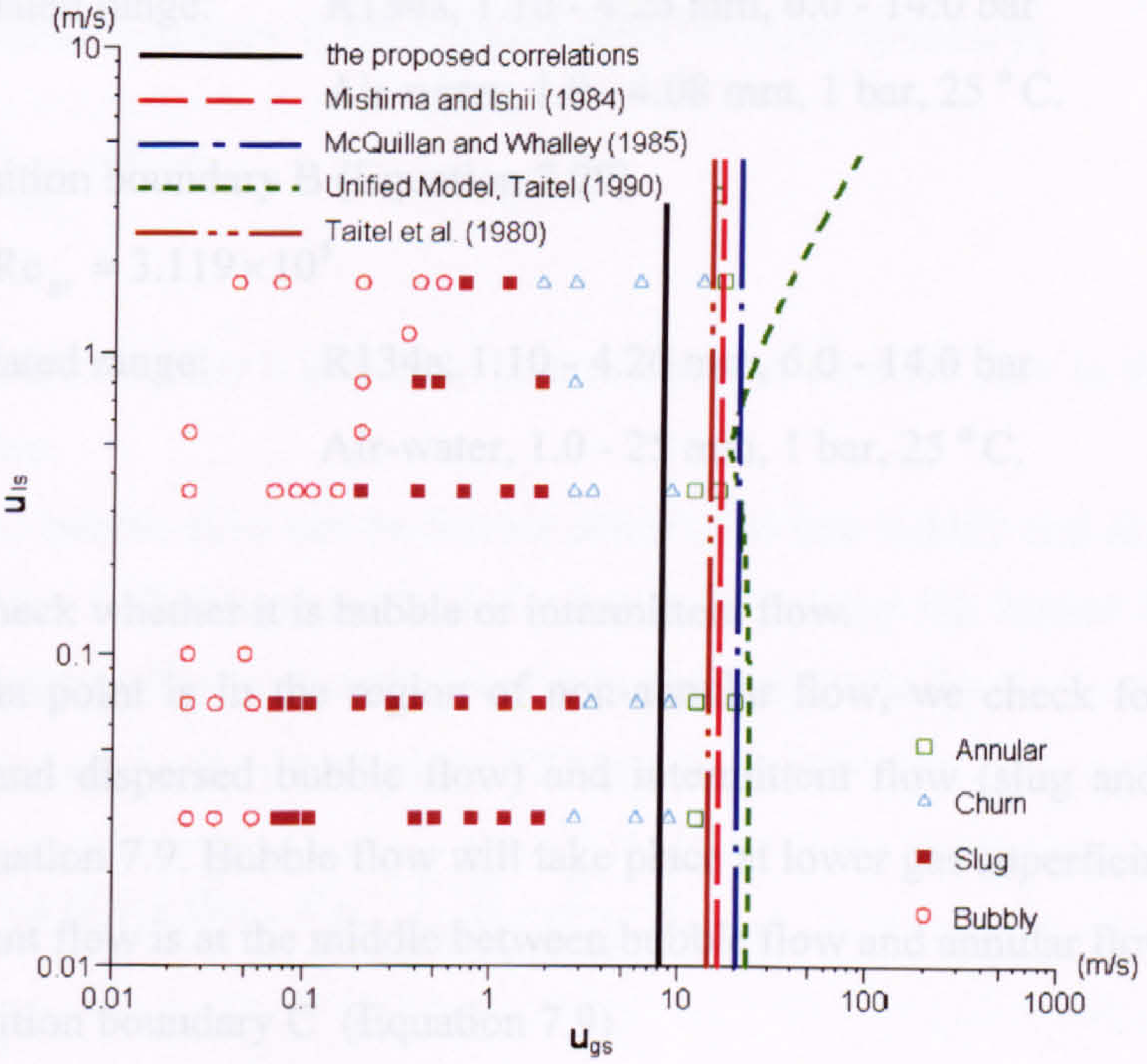

Figure 7.25 Comparison of the present correlation for churn-annular transition with the previous models and the air-water flow map using data of Taitel et al (1980) for 51 mm tube at 25 °C and 1 bar.

7.3 Validation of the new models and correlations

Various transition mechanisms were explored and the corresponding correlations were developed in the previous section. The comparisons with the previous experimental data indicate that the proposed models and correlations developed from the current experimental data may be applicable for air-water flow for both small and normal size tubes. Although the use of the above equations is generally straightforward, it does require a logical sequence to decide the dominant flow pattern at the cross sectional area. Thus, the following steps are suggested to arrive at a unique determination of the flow patterns:

(1) Step 1: check whether it is annular flow.

Annular flow will take place when the gas superficial velocity is higher than the velocity calculated by Equations 7.28 or 7.29.

- Transition boundary A (Equation 7.28)

  $$We_{ls} = 1.567\times10^{-17}\left(Fr_{gs}\,\mathrm{Re}_{gs}\right)^{3.41}$$

  Validated range: R134a, 1.10 - 4.26 mm, 6.0 - 14.0 bar
  Air-water, 1.0 - 4.08 mm, 1 bar, 25 °C.

- Transition boundary B (Equation 7.29)

  $$Fr_{gs}\,\mathrm{Re}_{gs} = 3.119\times10^{5}$$

  Validated range: R134a, 1.10 - 4.26 mm, 6.0 - 14.0 bar
  Air-water, 1.0 - 25 mm, 1 bar, 25 °C.

(2) Step 2: check whether it is bubble or intermittent flow.

If the data point is in the region of non-annular flow, we check for bubble flow (bubbly and dispersed bubble flow) and intermittent flow (slug and churn flow), using Equation 7.9. Bubble flow will take place at lower gas superficial velocity and intermittent flow is at the middle between bubble flow and annular flow.

- Transition boundary C (Equation 7.9)

  $$\alpha_c = c_1\left(u_{gs} + u_{ls}\right)^{c_2}$$

  where:

c_1 and c_2 are the experimental coefficients, which are 0.138 and 0.344 in the present experimental conditions, respectively.

$$\alpha_c = \frac{u_{gs}}{C_0\left(u_{gs}+u_{ls}\right)+u_d}$$

C_0 and u_d used in the current study are listed in Table 7.2.

Validated range: R134a, 1.10 - 4.26 mm, 6.0 - 14.0 bar

The author considers that this boundary depends strongly on the experimental conditions. Therefore, the critical void fractions used in the existing correlations, e.g. 0.25 and 0.52, are recommended for the transition boundaries of bubbly to slug and dispersed bubble to churn flow in normal size tubes, respectively.

- Transition boundary D (bubbly to slug boundary)

$$\frac{u_{gs}}{C_0\left(u_{gs}+u_{ls}\right)+u_d} = 0.25$$

The following equations can be used to calculate C_0 and u_d for air-water flow in normal size tubes (Mishima and Hibiki 1996).

$$C_0 = 1.2 - 0.2\sqrt{\frac{\rho_g}{\rho_l}} \quad \text{and} \quad u_d = 0.35\sqrt{\frac{gD\left(\rho_l-\rho_g\right)}{\rho_l}}$$

- Transition boundary E (dispersed bubble to churn boundary)

$$\frac{u_{gs}}{u_{gs}+u_{ls}} = 0.52$$

(3) Step 3: check whether it is bubbly flow or dispersed bubble flow in the subregion of bubble flow.

The above bubble flow can be further subdivided into bubbly and dispersed bubble by Equation 7.21. Dispersed bubble flow will occupy the higher liquid velocity region whilst bubbly flow will appear at lower liquid velocity.

- Transition boundary F (Equation 7.21)

$$u_t = 0.45\left[1+4.0\left(\alpha_{acl}We_b^{1/2}\right)^{1/3}\right]\left(\frac{\sigma}{f_l\rho_l d_c}\right)^{1/2}$$

where

$u_t = u_{gs} + u_{ls}$ (for air-water two-phase flow)

$$u_t = \frac{\left(\rho_g u_{gs}+\rho_l u_{ls}\right)\left(u_{gs}+u_{ls}\right)}{k\left(\rho_g u_{gs}-\rho_l u_{gs}\right)+\rho_l\left(u_{gs}+u_{ls}\right)} \quad \text{(in the present R134a experiments)}$$

Validated range: R134a, 1.10 - 4.26 mm, 6.0 - 14.0 bar
Air-water, 1.0 - 51 mm, 1 bar, 25 °C.

(4) Step 4: check whether it is slug flow or churn flow in the subregion of intermittent flow.

The intermittent flow can be subdivided into slug and churn by Equations 7.23, 7.26 and 7.27. Slug flow will take place at lower gas velocity whilst churn flow will dominate the higher gas velocity region.

- Transition boundary G (Equation 7.23)

$$\mathrm{Re}_{ls} = 81.08 We_{gs}^{\ 1.626} Fr_{gs}^{*\ -0.267}$$

Validated range: R134a, 1.10 - 4.26 mm, 6.0 - 14.0 bar
Air-water, <5 mm, 1 bar, 25 °C.

- Transition boundary H (Equation 7.26)

$$\frac{\rho_g D u_{gs}^2}{\mu_l} = 84.53 \left(\frac{\rho_g D u_{gs}^2}{\sigma} \right)^{0.6523}$$

Validated range: R134a, 1.10 - 4.26 mm, 6.0 - 14.0 bar
Air-water, <51 mm, 1 bar, 25 °C.

- Transition boundary I (Equation 7.27)

$$u_h = 2.75 \sqrt{\frac{\sigma}{f_l \rho_l D}}$$

Validated range: R134a, 1.10 - 4.26 mm, 6.0 - 14.0 bar

Following the above sequence a unique flow pattern will be predicted at any condition. Figures 7.26 and 7.27 take the small and normal size tubes as the examples to show the predicted transition boundaries by the above correlations. The developed correlations have been compared with the air-water flow maps individually in the previous sections and show good agreement in some conditions. The comprehensive comparisons with the present flow maps are summarized in Figures 7.28-7.39 and show excellent agreement. In addition, the comparisons in Figures 7.40-7.42 indicate that some models and correlations (boundaries A, B, F, G, H, I) developed from the present experimental data may be used for air-water flow in both small and normal size tubes. However, further investigation is needed.

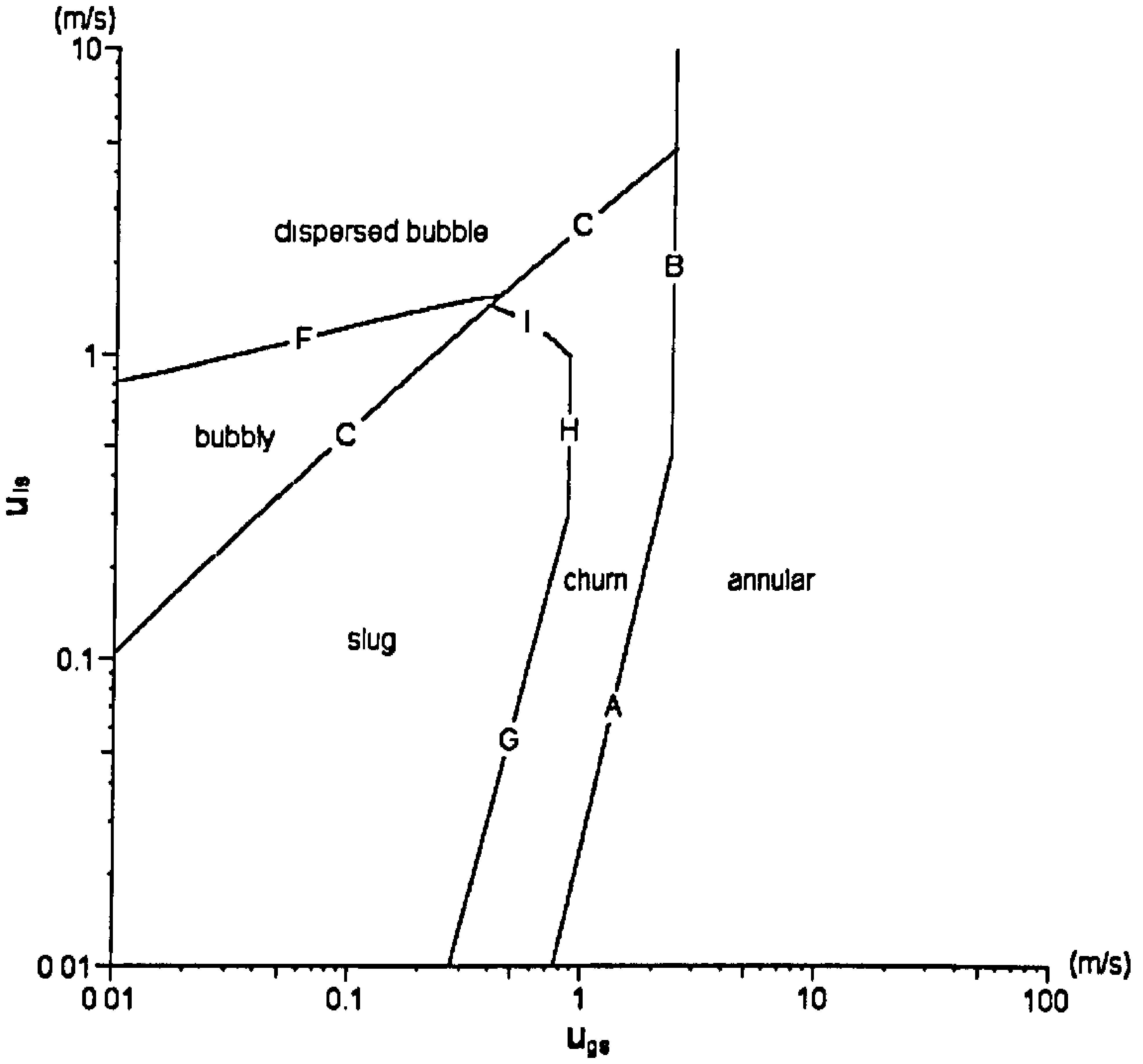

Figure 7.26 The predicted transition boundary by the new correlations (A, B, C, F, G, H, I) based on the R134a two-phase flow in the 2.01 mm tube at10 bar pressure.

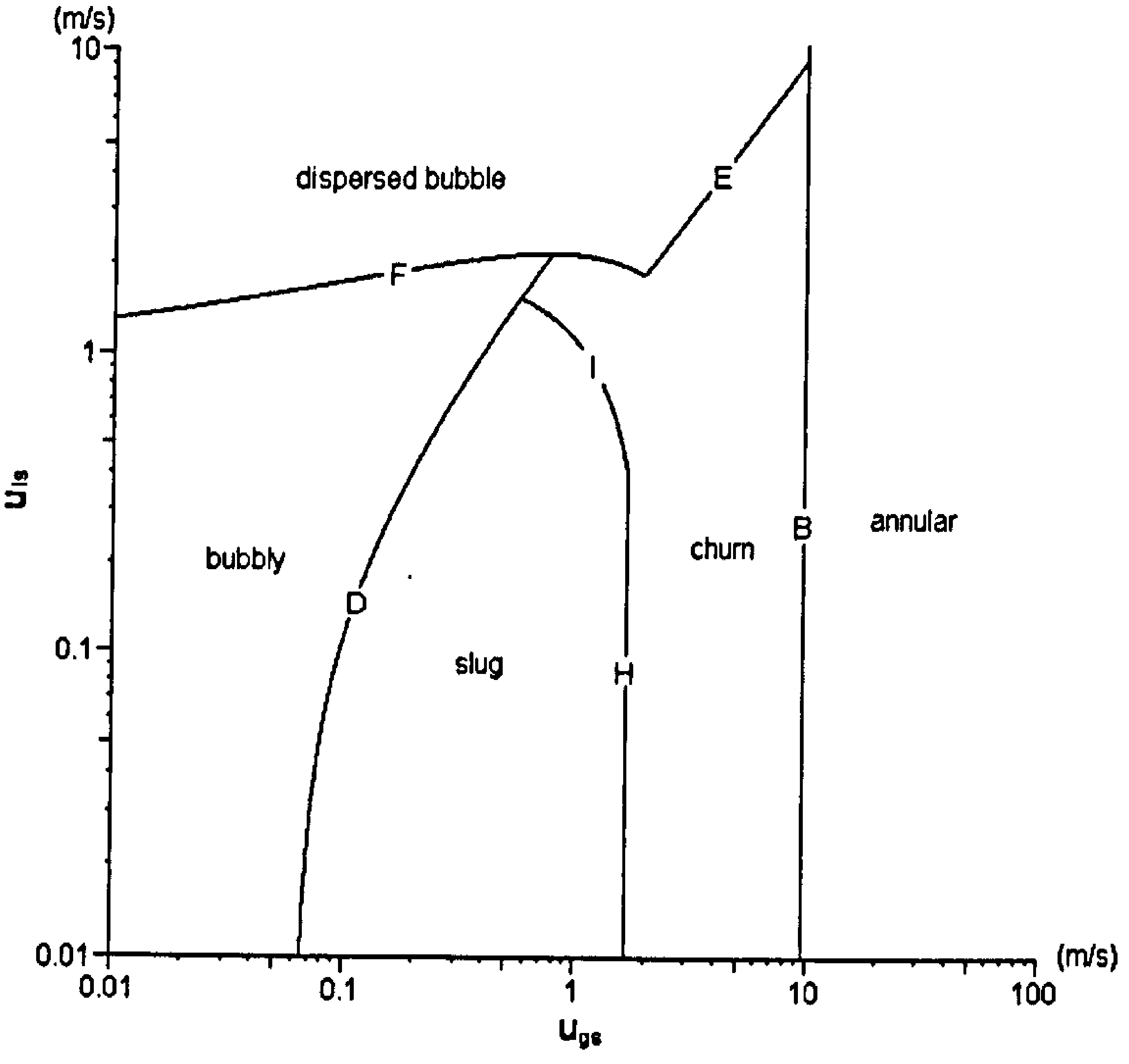

Figure 7.27 The predicted transition boundary by the new correlations (B, F, H, I) and the existing correlations (D, E) for air-water flow in the 25 mm tube at 1 bar, 25 ° C.

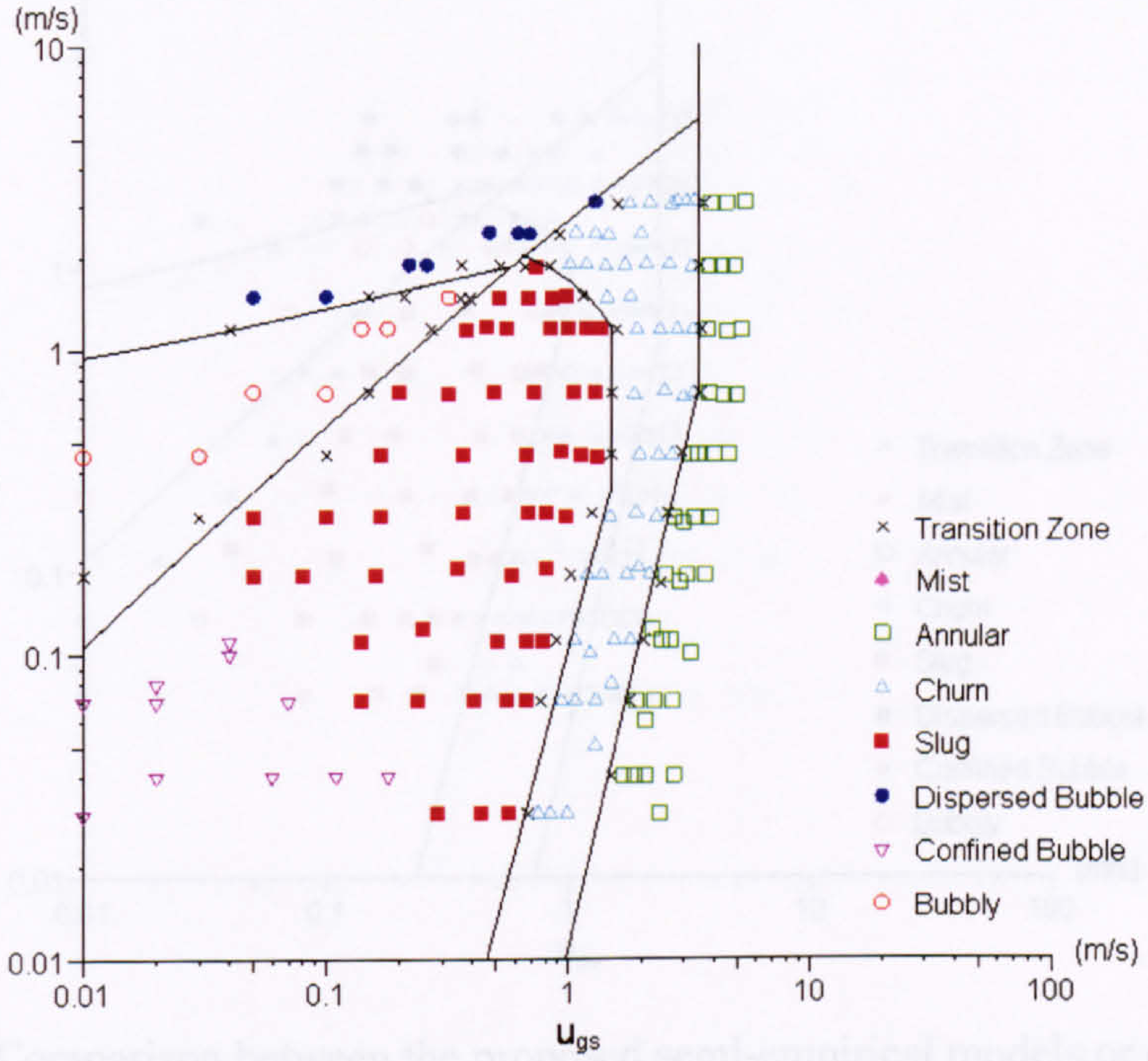

Figure 7.28 Comparison between the proposed semi-empirical models or correlations and the R134a flow map in the 1.10 mm diameter tube at 6 bar.

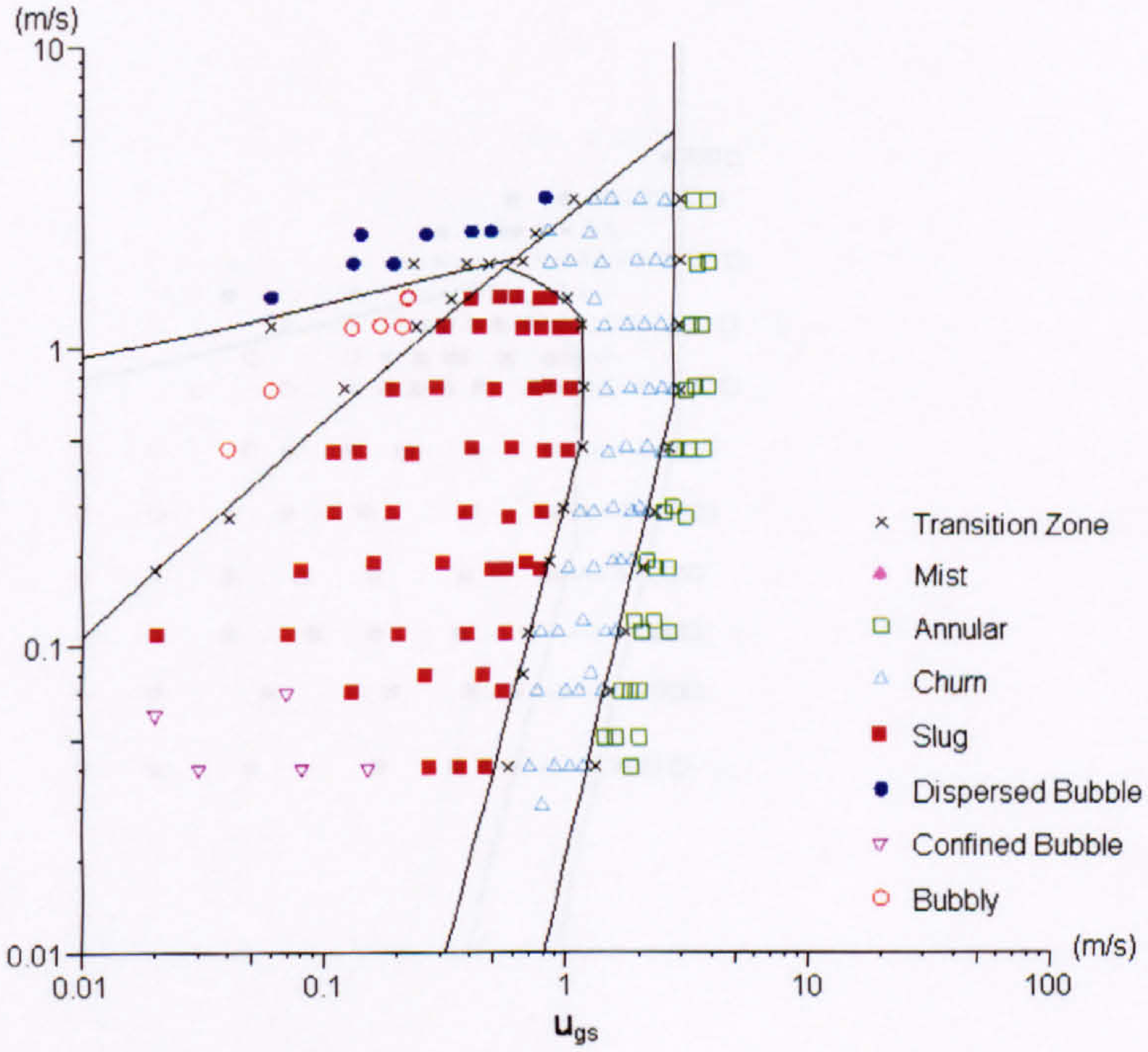

Figure 7.29 Comparison between the proposed semi-empirical models or correlations and the R134a flow map in the 1.10 mm diameter tube at 10 bar.

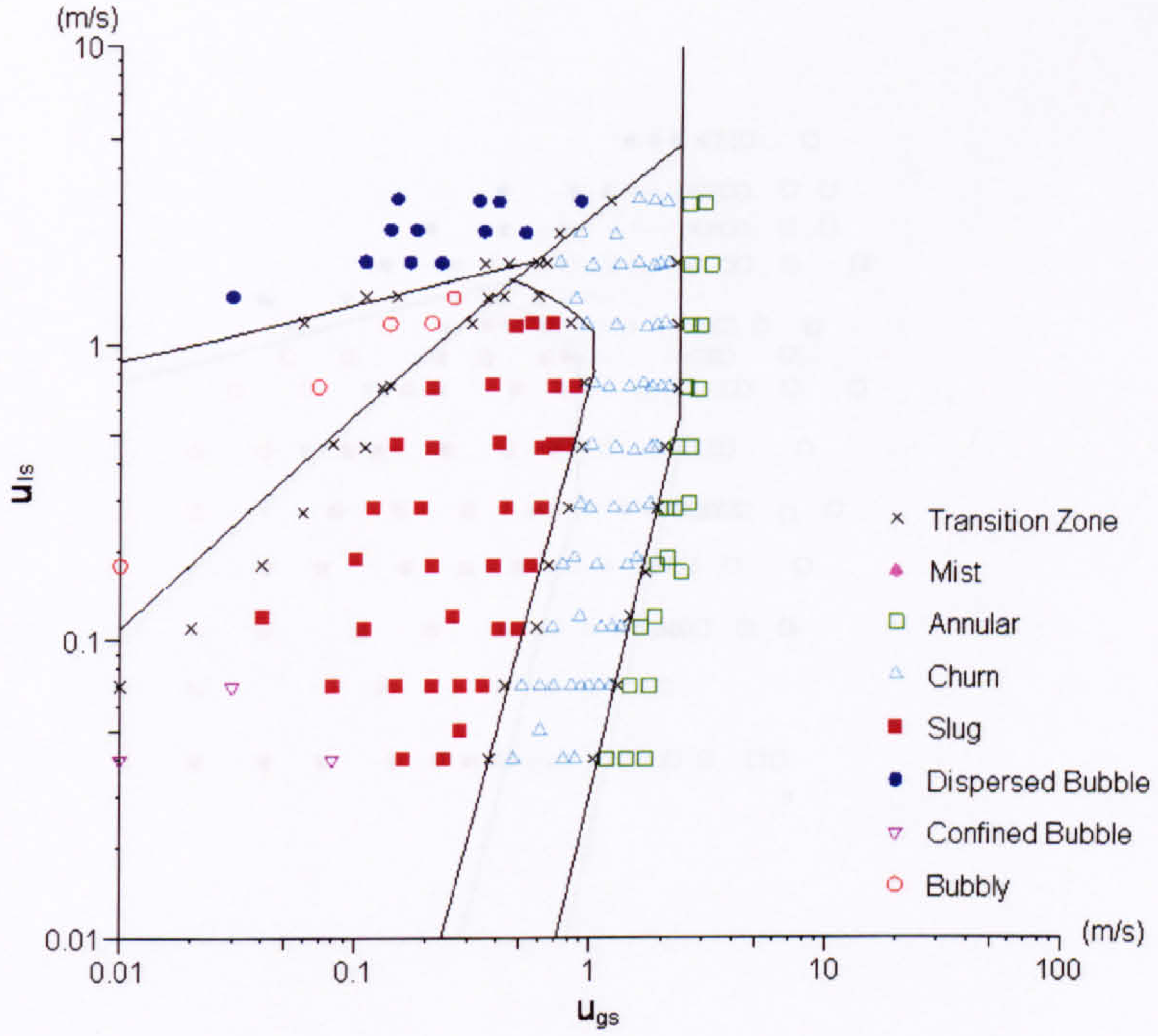

Figure 7.30 Comparison between the proposed semi-empirical models or correlations and the R134a flow map in the 1.10 mm diameter tube at 14 bar.

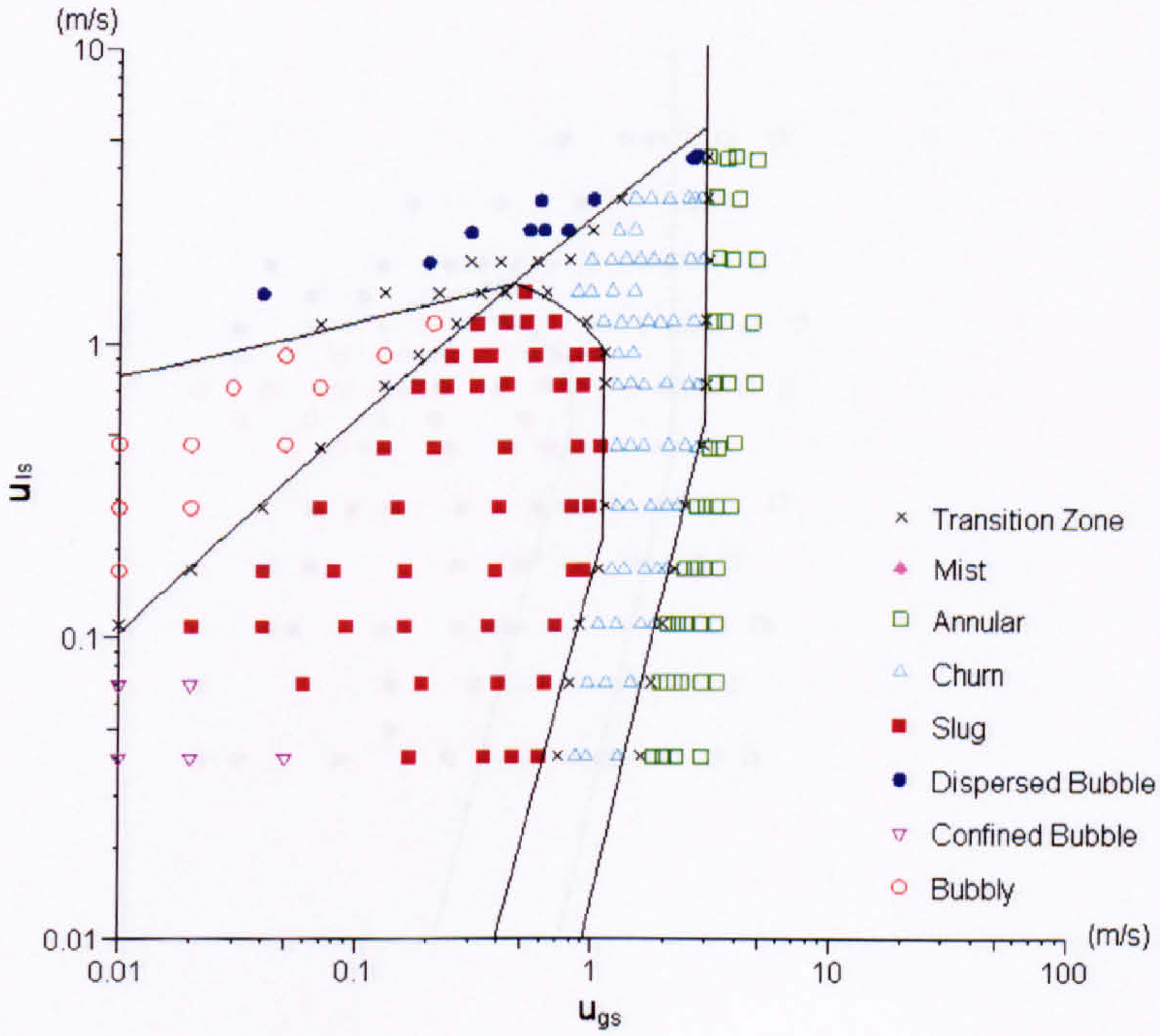

Figure 7.31 Comparison between the proposed semi-empirical models or correlations and the R134a flow map in the 2.01 mm diameter tube at 6 bar.

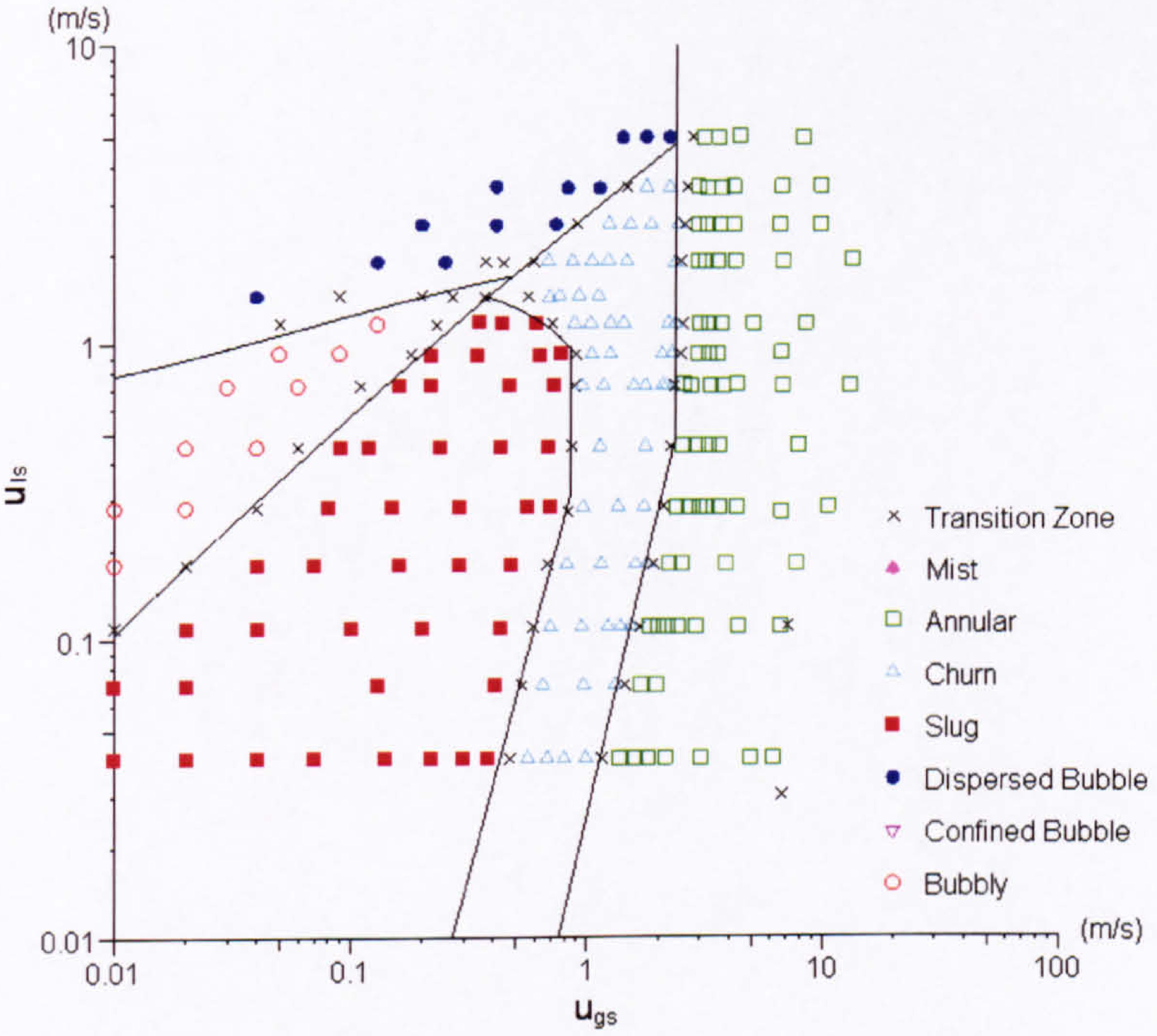

Figure 7.32 Comparison between the proposed semi-empirical models or correlations and the R134a flow map in the 2.01 mm diameter tube at 10 bar.

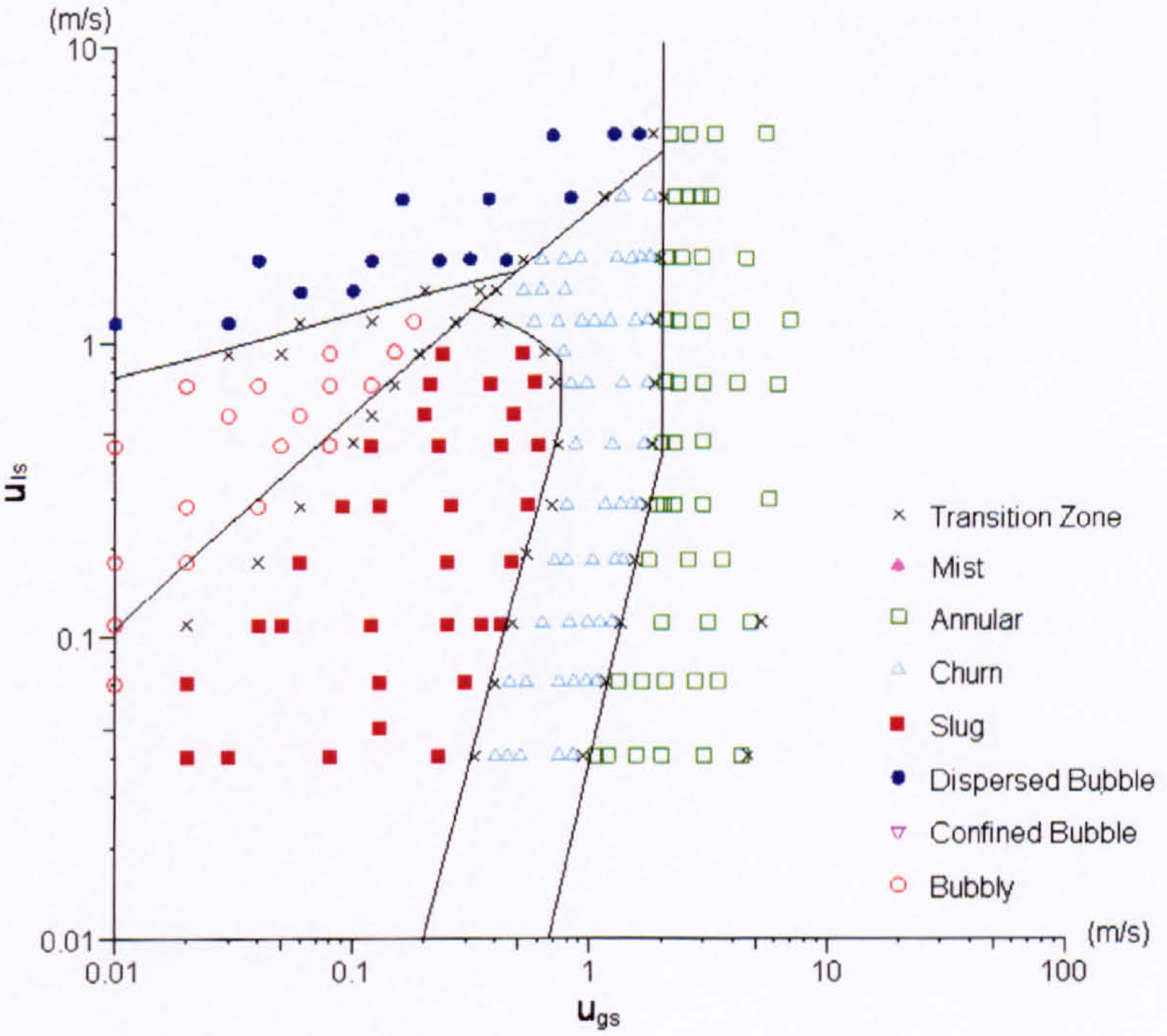

Figure 7.33 Comparison between the proposed semi-empirical models or correlations and the R134a flow map in the 2.01 mm diameter tube at 14 bar.

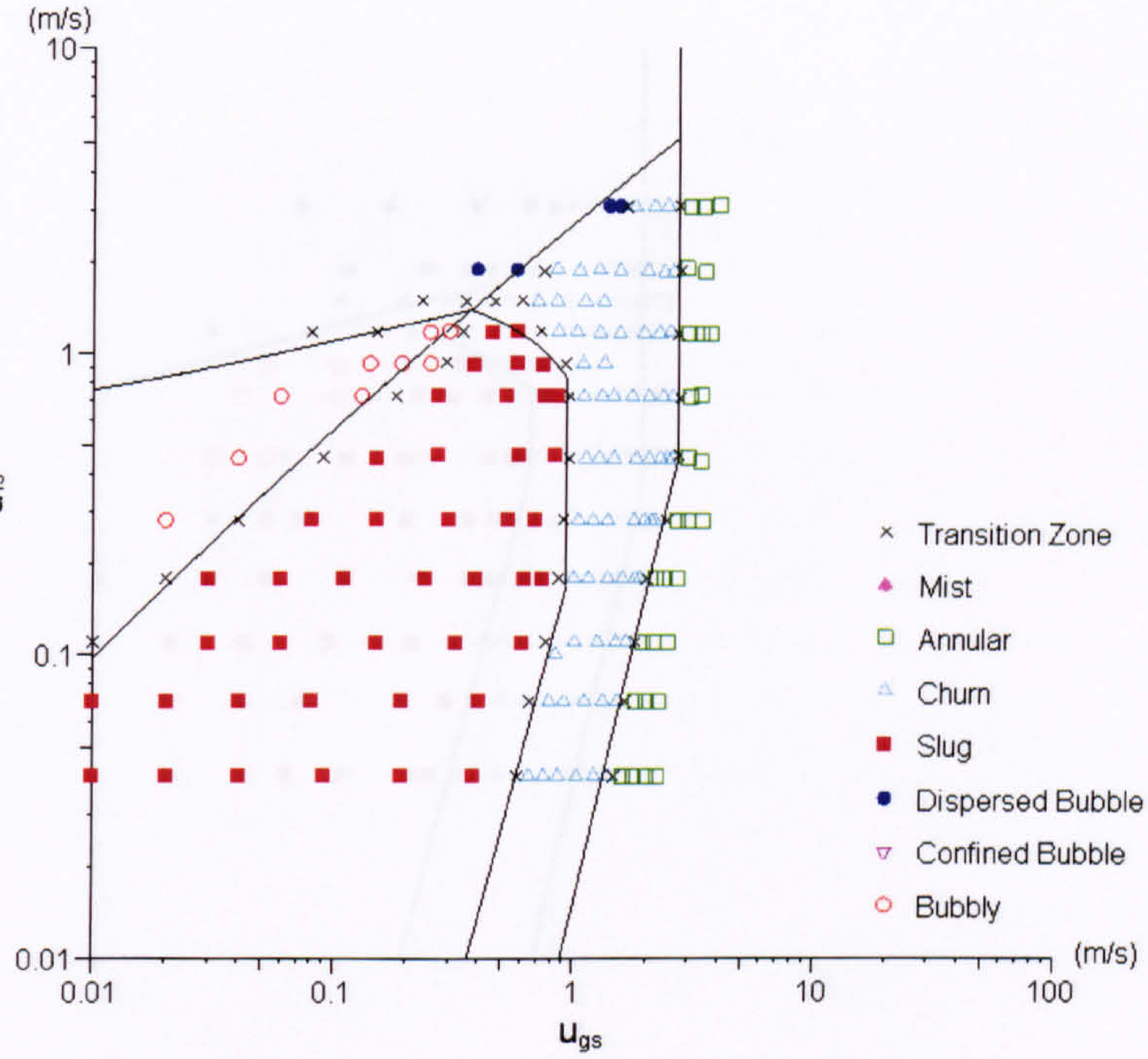

Figure 7.34 Comparison between the proposed semi-empirical models or correlations and the R134a flow map in the 2.88 mm diameter tube at 6 bar.

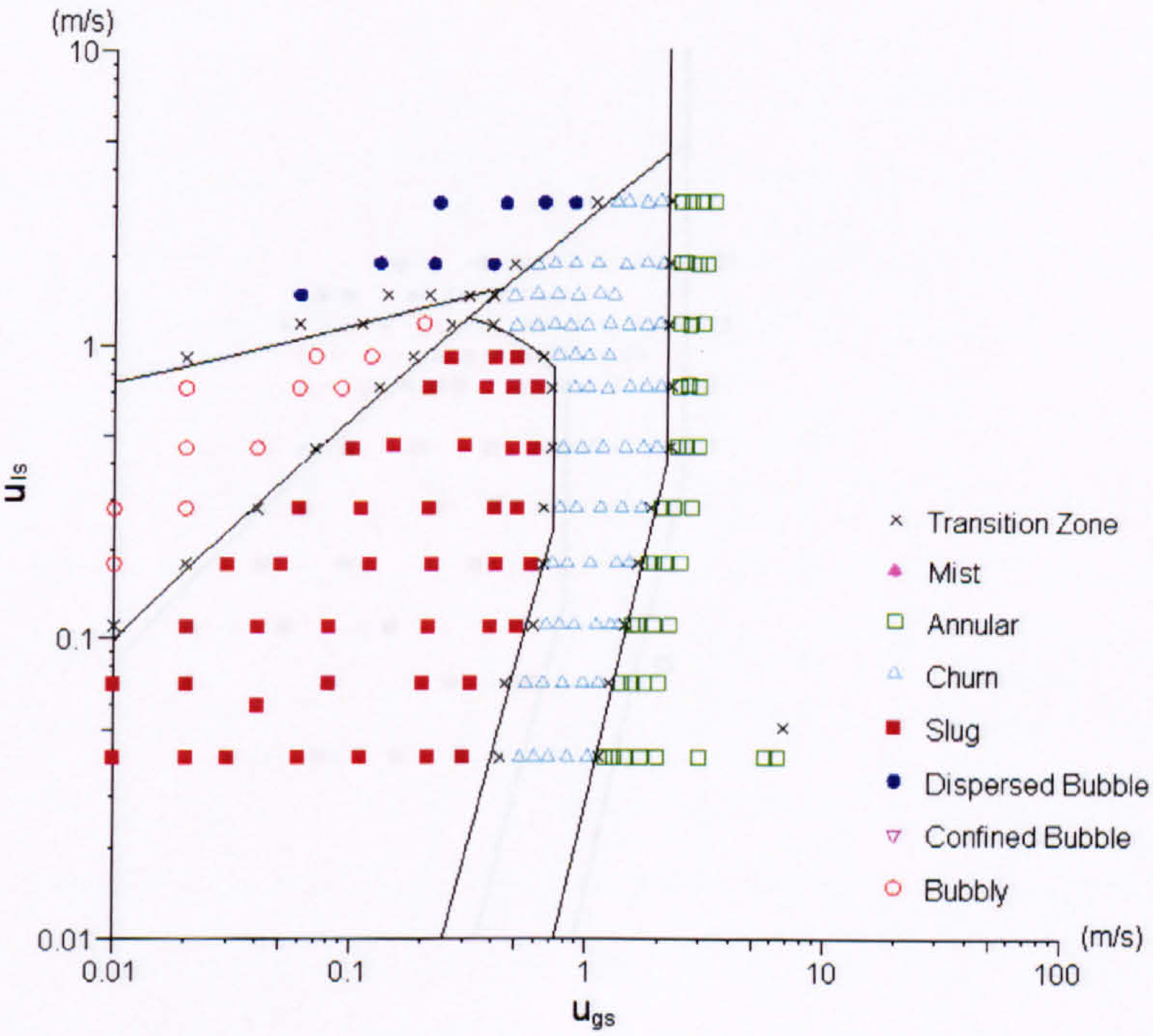

Figure 7.35 Comparison between the proposed semi-empirical models or correlations and the R134a flow map in the 2.88 mm diameter tube at 10 bar.

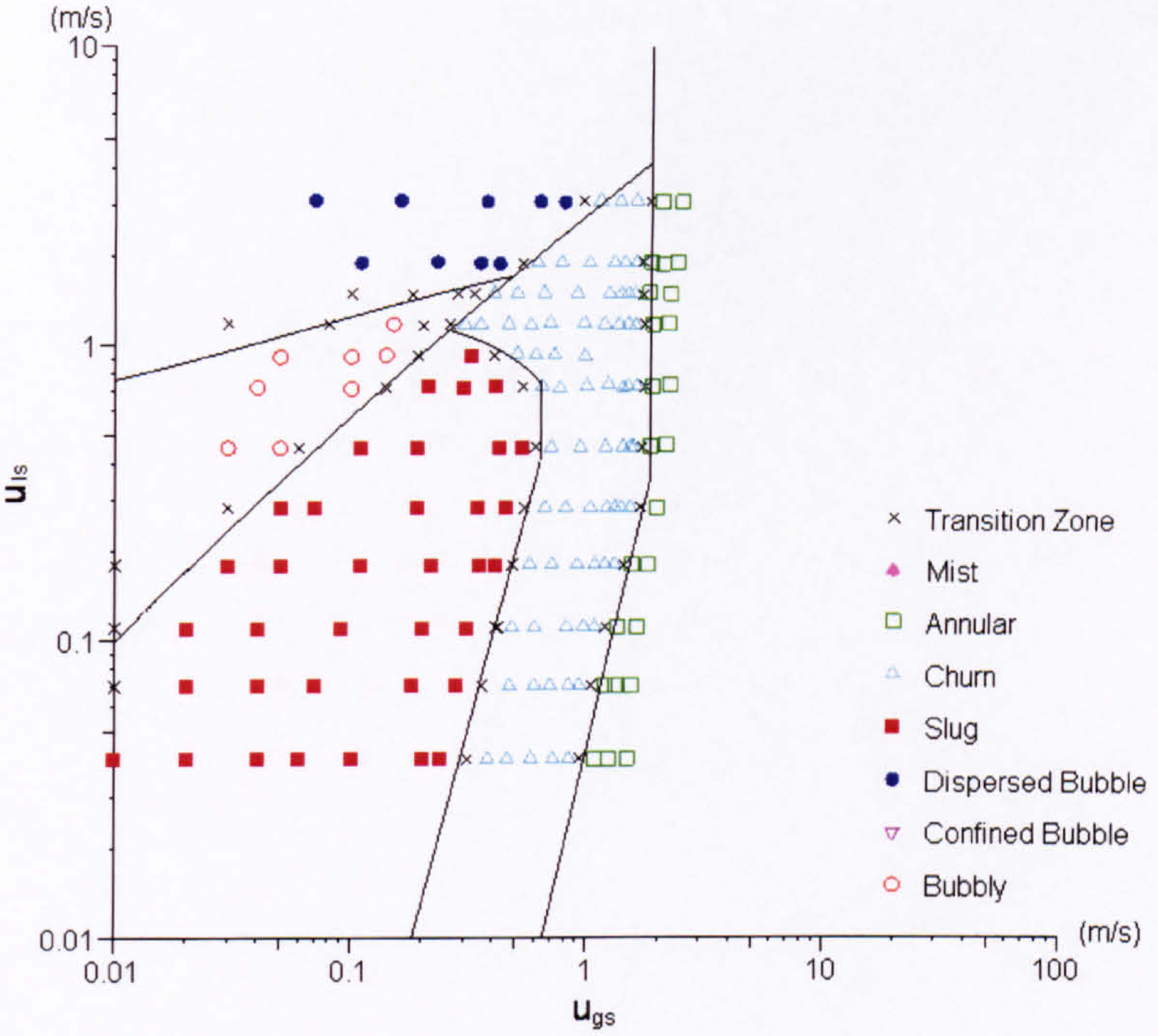

Figure 7.36 Comparison between the proposed semi-empirical models or correlations and the R134a flow map in the 2.88 mm diameter tube at 14 bar.

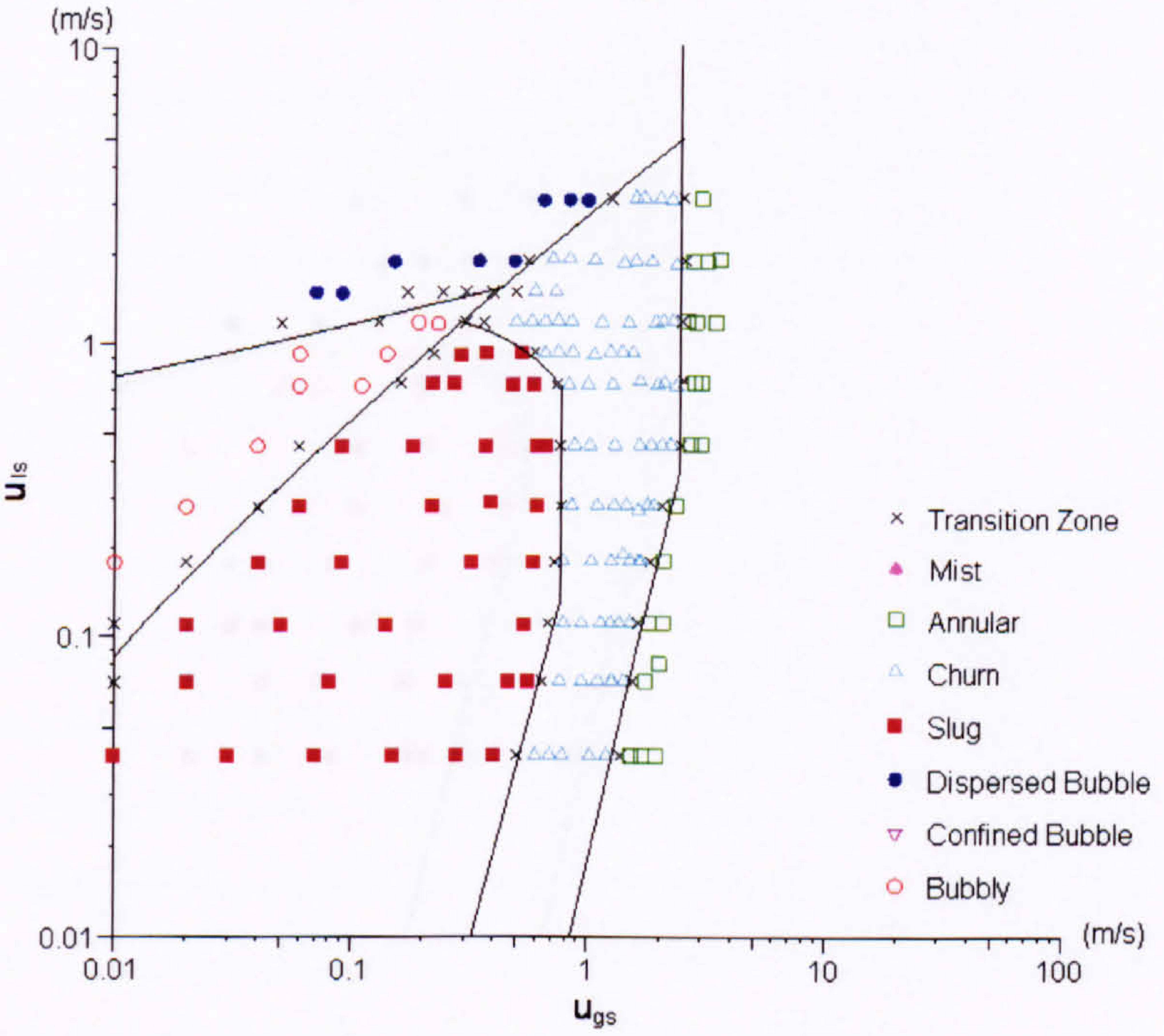

Figure 7.37 Comparison between the proposed semi-empirical models or correlations and the R134a flow map in the 4.26 mm diameter tube at 6 bar.

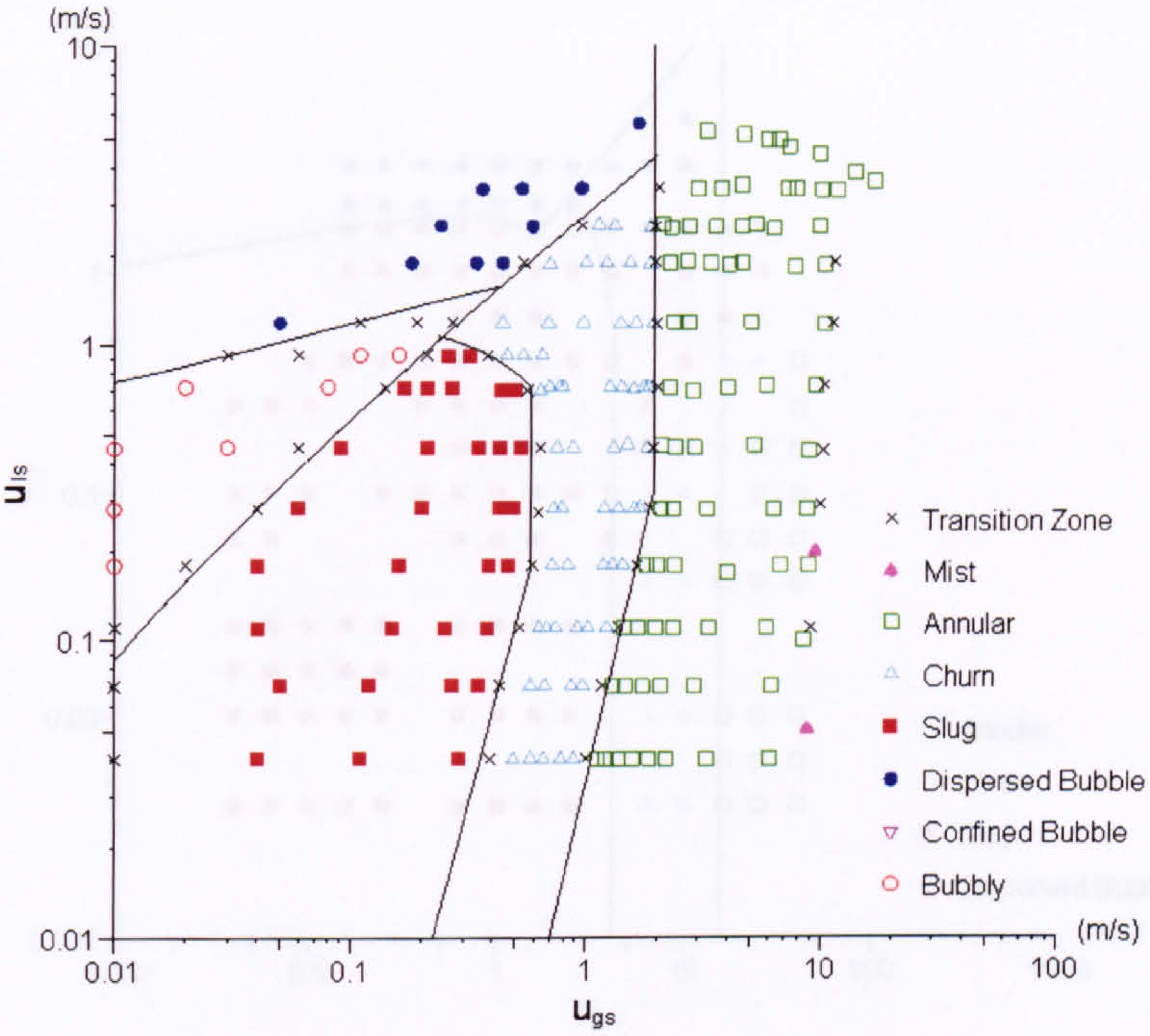

Figure 7.38 Comparison between the proposed semi-empirical models or correlations and the R134a flow map in the 4.26 mm diameter tube at 10 bar.

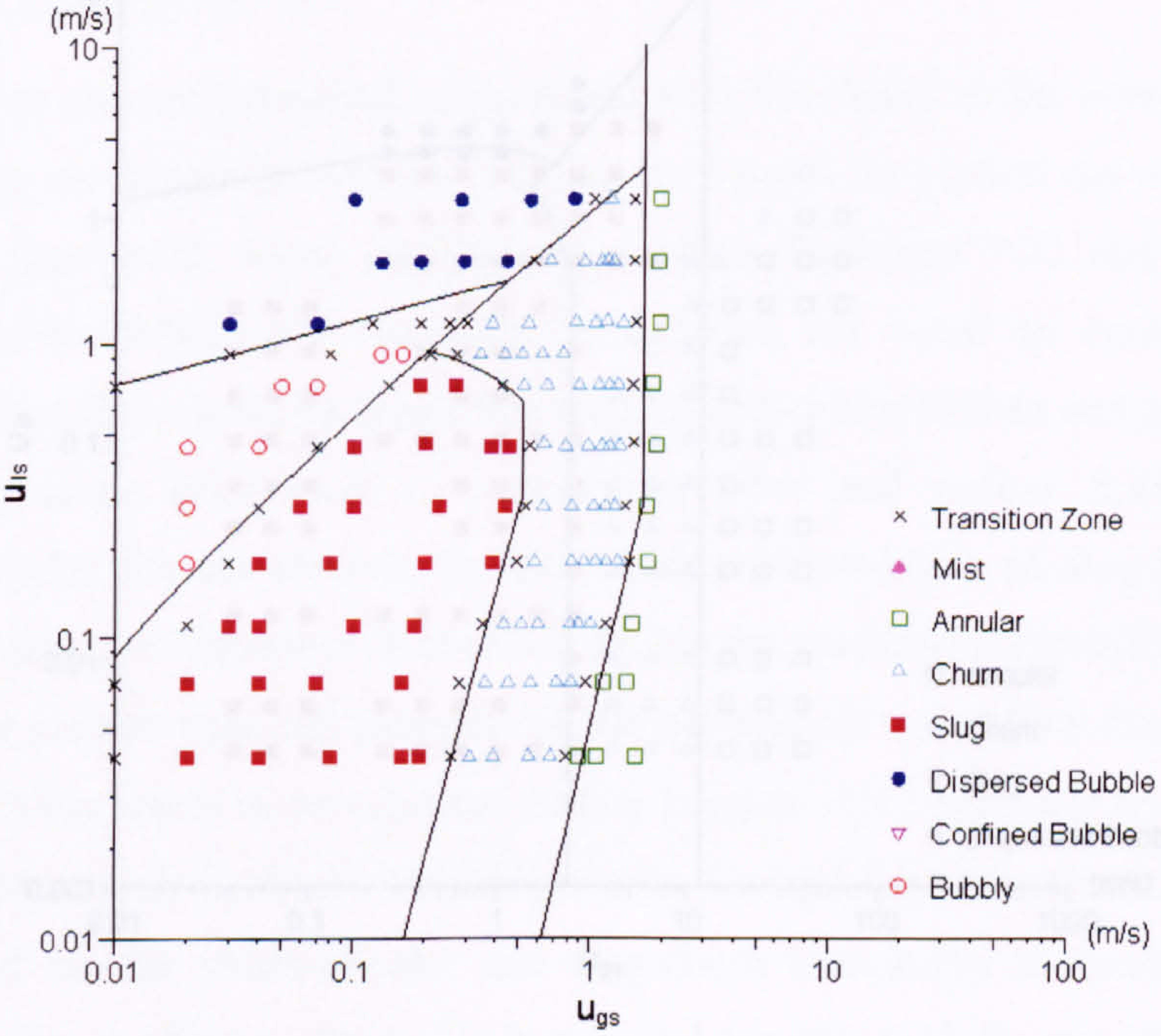

Figure 7.39 Comparison between the proposed semi-empirical models or correlations and the R134a flow map in the 4.26 mm diameter tube at 14 bar.

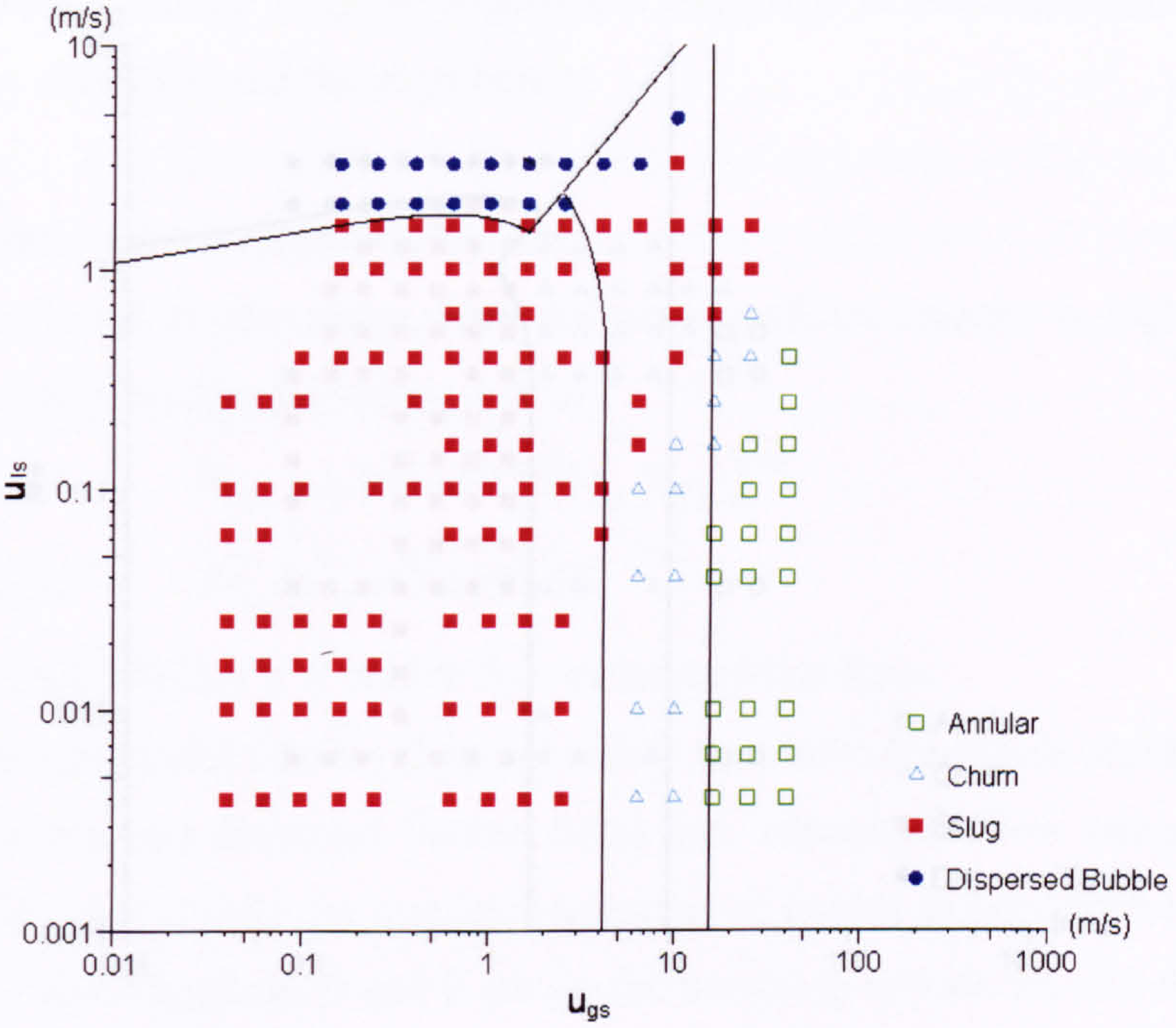

Figure 7.40 Comparison between the proposed semi-empirical models or correlations and the air-water flow map in the 4 mm tube (Barnea et al 1983).

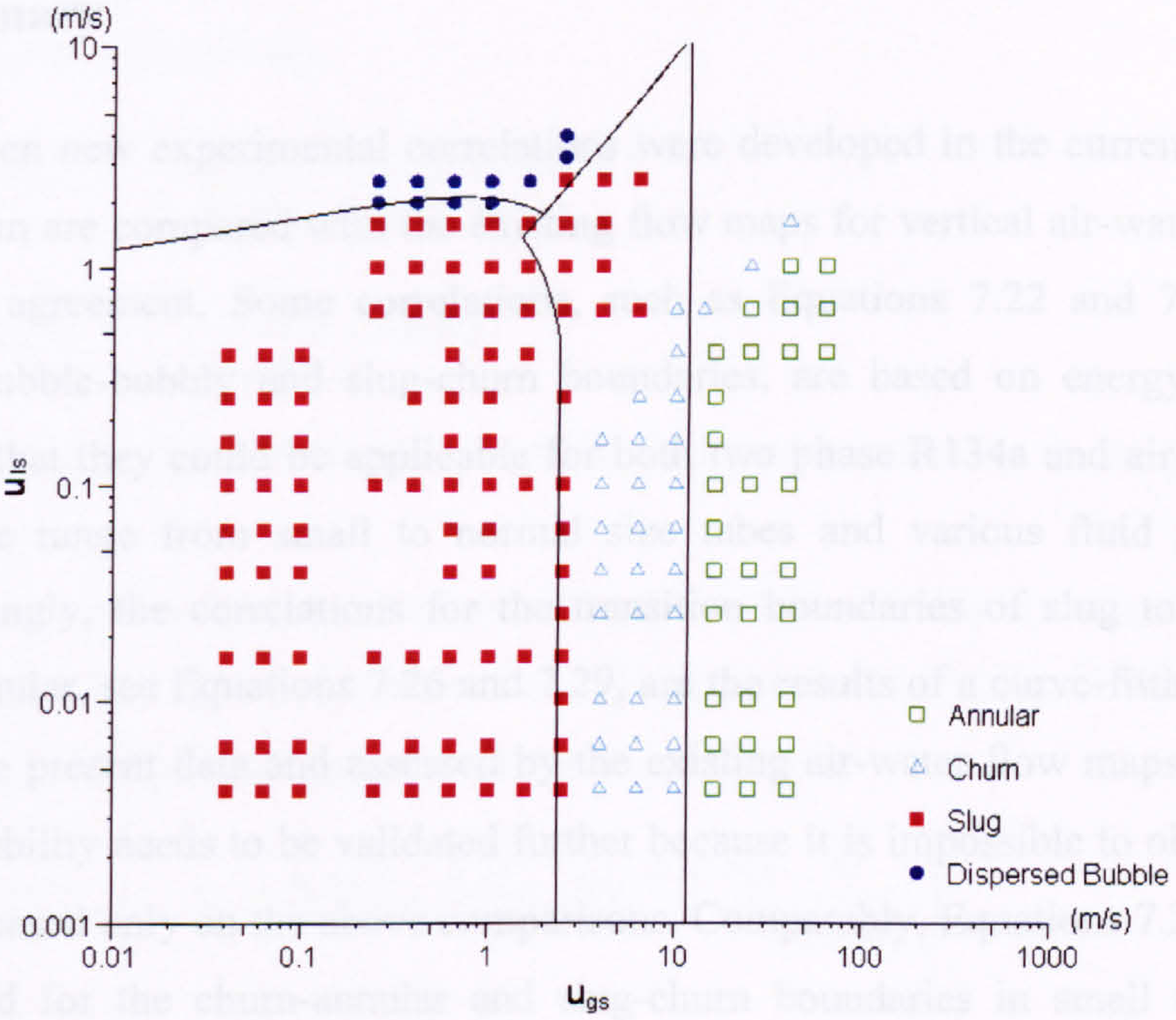

Figure 7.41 Comparison between the proposed semi-empirical models or correlations and the air-water flow map in the 12.3 mm tube (Barnea et al 1983).

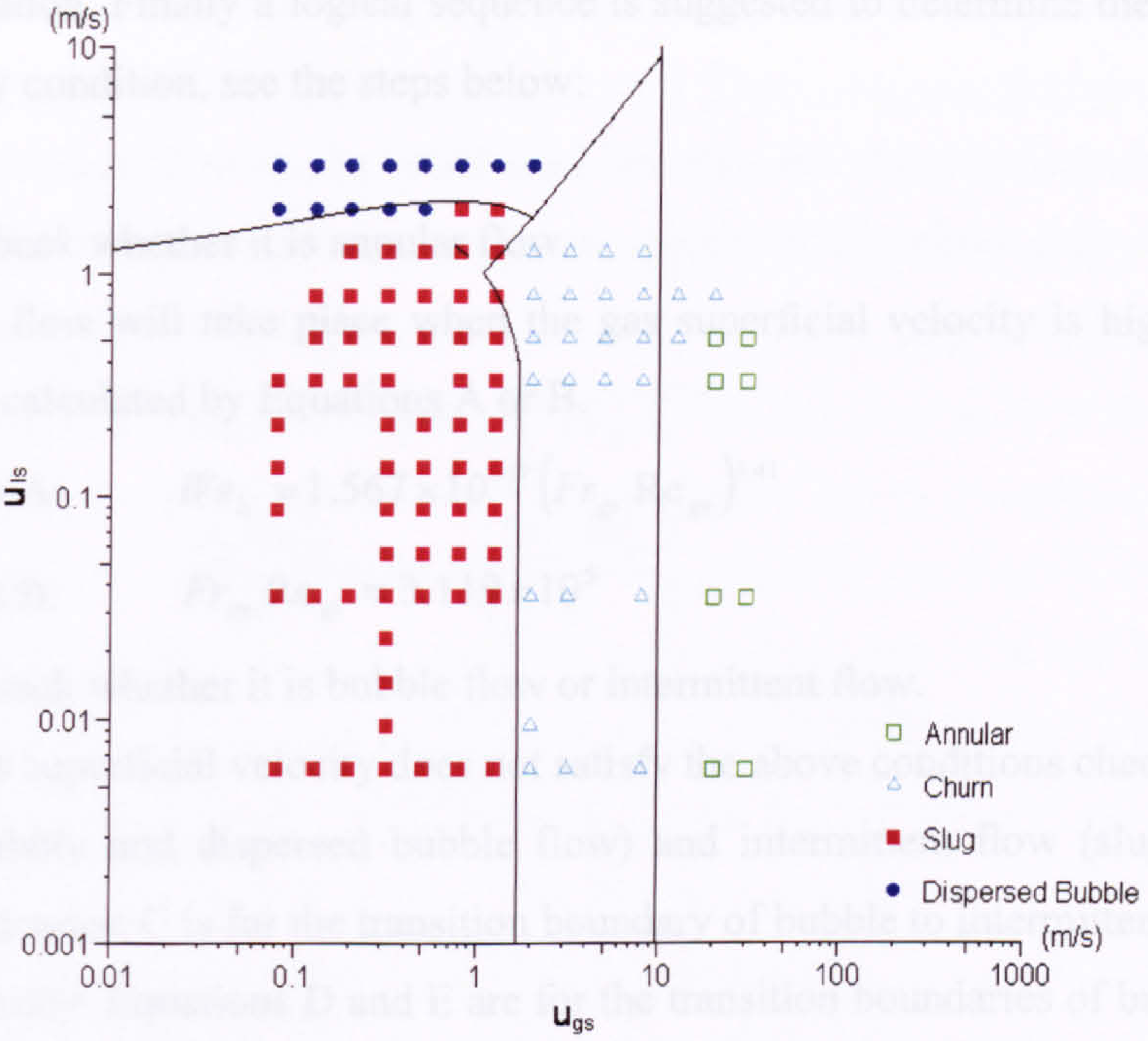

Figure 7.42 Comparison between the proposed semi-empirical models or correlations and the air-water flow map in the 25 mm tube (Taitel 1980).

7.4 Summary

In total, seven new experimental correlations were developed in the current study and some of them are compared with the existing flow maps for vertical air-water flow and show good agreement. Some correlations, such as Equations 7.22 and 7.27 for the dispersed bubble-bubbly and slug-churn boundaries, are based on energy and force analysis so that they could be applicable for both two phase R134a and air-water flow with a wide range from small to normal size tubes and various fluid parameters. Correspondingly, the correlations for the transition boundaries of slug to churn and churn to annular, see Equations 7.26 and 7.29, are the results of a curve-fitting program based on the present data and assessed by the existing air-water flow maps. However, their applicability needs to be validated further because it is impossible to obtain a firm conclusion based only on the above comparisons. Comparably, Equations 7.23 and 7.28 are proposed for the churn-annular and slug-churn boundaries in small tubes only. Considering the significant effect of experimental conditions to the transition boundary of bubbly to slug, Equation 7.9 is restricted to the current conditions. The new developed correlations might have much more extensive application but they need further validation. Finally a logical sequence is suggested to determine the unique flow pattern at any condition, see the steps below:

(1) Step 1: check whether it is annular flow.

Annular flow will take place when the gas superficial velocity is higher than the velocity calculated by Equations A or B.

Equation A: $$We_{ls} = 1.567 \times 10^{-17} \left(Fr_{gs} \, \mathrm{Re}_{gs} \right)^{3.41}$$

Equation B: $$Fr_{gs} \, \mathrm{Re}_{gs} = 3.119 \times 10^{5}$$

(2) Step 2: check whether it is bubble flow or intermittent flow.

If the gas superficial velocity does not satisfy the above conditions check for bubble flow (bubbly and dispersed bubble flow) and intermittent flow (slug and churn flow). Equation C is for the transition boundary of bubble to intermittent flow in the current study. Equations D and E are for the transition boundaries of bubbly to slug and dispersed bubble to churn flow in normal size tubes respectively.

Equation C: $$\alpha_c = c_1 \left(u_{gs} + u_{ls} \right)^{c_2}$$

c_1 and c_2 are the experimental coefficients, which are 0.138 and 0.344 in the present experiments respectively.

Equation D: $$\frac{u_{gs}}{C_0 \left(u_{gs} + u_{ls} \right) + u_d} = 0.25$$

Equation E: $$\frac{u_{gs}}{u_{gs} + u_{ls}} = 0.52$$

(3) Step 3: check whether it is bubbly flow or dispersed bubble flow in the subregion of bubble flow.

The above bubble flow can be further subdivided into bubbly and dispersed bubble by Equation F. Dispersed bubble flow will occupy the higher liquid velocity region whilst bubbly flow will appear at lower liquid velocity.

Equation F: $$u_l = 0.45 \left[1 + 4.0 \left(\alpha_{act} We_b^{1/2} \right)^{1/3} \right] \left(\frac{\sigma}{f_l \rho_l d_c} \right)^{1/2}$$

where

$u_l = u_{gs} + u_{ls}$ (for air-water two-phase flow)

$$u_l = \frac{\left(\rho_g u_{gs} + \rho_l u_{ls} \right)\left(u_{gs} + u_{ls} \right)}{k \left(\rho_g u_{gs} - \rho_l u_{gs} \right) + \rho_l \left(u_{gs} + u_{ls} \right)}$$ (in the present R134a experiments)

(4) Step 4: check whether it is slug flow or churn flow in the subregion of intermittent flow.

The intermittent flow can be subdivided into slug and churn by Equations G, H and I. Slug flow will take place at lower gas velocity whilst churn flow will dominate the higher gas velocity region.

Equation G: $$\mathrm{Re}_{ls} = 81.08 We_{gs}^{\;1.626} Fr_{gs}^{*\;-0.267}$$

Equation H: $$\frac{\rho_g D u_{gs}^2}{\mu_l} = 84.53\left(\frac{\rho_g D u_{gs}^2}{\sigma}\right)^{0.6523}$$

Equation I: $$u_h = 2.75\sqrt{\frac{\sigma}{f_l \rho_l D}}$$

Chapter 8 Conclusions and Recommendations

The rapid developments of micro-devices and systems require accurate prediction of two-phase flow patterns in small channels but this has not been accomplished yet. The present project used R134a as the working fluid. Four test sections with the diameters of 1.10-4.26 mm were tested at a pressure range of 6-14 bar to investigate the effect of channel dimension and fluid parameters on flow patterns in small tubes. In total, twelve flow maps were plotted based on the 2392 experimental data collected in the present experiments. Seven typical flow patterns, i.e. dispersed bubble, bubbly, confined bubble, slug, churn, annular and mist, were observed. Seven new correlations are developed in the current study for the prediction of the transition boundaries of dispersed bubble-bubbly, dispersed bubble-churn, bubbly-slug, slug-churn and churn-annular. Some correlations are compared with the existing flow maps for the vertical air-water flow from small to normal size tubes and show good agreement.

8.1 Conclusions

The following conclusions can be obtained based on the observations and analysis in the current study.

(1) The experimental facility covered a wide experimental range with high measurement accuracy.

(2) Seven typical flow patterns were observed in the present experiments, including dispersed bubble, bubbly, confined bubble, slug, churn, annular and mist.

(3) Confined bubble flow was observed in the 1.10 and 2.01 mm tubes only so that a tube diameter around 2.0 mm can be regarded as the critical diameter between small and normal size tubes at the current experimental conditions.

(4) Slug bubble rise velocity is approximately linear to the homogeneous velocity. The effect of fluid pressure and tube diameter on the rise velocity is small.

(5) Slug bubble relative length, i.e. length-diameter ratio, is little affected by the tube diameter and fluid pressure.

(6) Slug-churn and churn-annular boundaries shift towards the region of lower gas superficial velocity as the pressure increases, whilst little effect was observed on the dispersed bubble-bubbly, dispersed bubble-churn and bubbly-slug boundaries.

(7) Slug-churn and churn-annular boundaries moved to higher gas superficial velocity, whilst dispersed bubble-bubbly boundary shifted to higher liquid superficial velocity when the tube diameters decreased from 4.26 to 1.10 mm. The diameter has little effect on the boundaries of dispersed bubble to churn and bubbly to slug flow.

(8) The existing models or correlations cannot predict R134 flow patterns in small tubes well.

(9) Seven new semi-empirical models and correlations were developed for the prediction of the transition boundaries of dispersed bubble-bubbly, dispersed bubble-churn, bubbly-slug, slug-churn and churn-annular based on the present data.

(10) The correlations for the transition boundaries of dispersed bubble-bubbly, slug-churn and churn-annular may be used to predict the flow maps for the vertical air-water flow from small to normal size tubes but their applicability needs further investigation.

8.2 Recommendations

Based on the current experimental facilities, the following tasks are strongly recommended for further research.

(1) Smaller diameters need to be tested to confirm further the effect of diameter on the flow patterns.

(2) Lower experimental pressure is suggested to achieve fluid properties which may be closer to the practical range of R134a used in systems.

(3) The experimental facility, except the R134a tank, is made of stainless steel. The capacity of the pump, heaters, flow meters and other devices is big enough to cover a wide range. Therefore, a new two-phase flow, such as steam-water, carbon-dioxide can be tested in the future to reveal the effect of fluid properties further.

(4) It is recommended to build new test sections for the measurement of void fraction because it is a vital parameter in the transition mechanism of flow regimes.

(5) The experiments for R134a two-phase flow in horizontal and inclined small tubes can be integrated with the present study and may generate more general models and correlations.

(6) Experiments on parallel channels, which are possible with this facility, can be more useful for practical applications in compact/mini heat exchangers.

References

Andreussi, P., Paglianti, A. and Silva, F.S. (1999) Dispersed bubble flow in horizontal pipes, Chemical Engineering Science, Vol. 72, No. 3, pp. 1101-1107.

Agostini, B. and Bontemps, A. (2004) Vertical flow boiling of refrigerant R134a in small channels, International Journal Heat and Fluid Flow, accepted.

Akbar, M.K., Plummer, D.A. and Ghiaasiaan, S.M. (2003) On gas-liquid two-phase flow regimes in microchannels, International Journal of Multiphase Flow, Vol. 29, pp. 855-865.

Bang, I.C., Chang, S.H. and Baek, W.P. (2004) Visualization of the cubcooled flow boiling of R-134a in a vertical rectangular channel with an electrically heated wall, International Journal of Heat and Mass Transfer. Vol. 47, pp. 4349-4363.

Barajas, A.M. and Panton, R.L. (1993) The effects of contact angle on two-phase flow in capillary tubes, International Journal of Multiphase Flow, Vol. 19, No. 2, pp. 337-346.

Barnea, D., Shoham, O. and Taitel, Y. (1982) Flow pattern transition for downward inclined two-phase flow, horizontal to vertical, Chemical Engineering Science, Vol. 37, pp. 735-740.

Barnea, D., Shoham, O. and Taitel, Y. (1982) Flow pattern transition for vertical downward two-phase flow, Chemical Engineering Science, Vol. 37, pp. 741-746.

Barnea, D., Luninski, Y. and Taitel, Y. (1983) Flow pattern in horizontal and vertical two phase flow in small diameter pipes, The Canadian Journal of Chemical Engineering, Vol. 61, No. 5, pp. 617-620.

Barnea, D. and Brauner, N. (1985) Hold-up of the liquid slug in two phase intermittent flow, International Journal of Multiphase Flow, Vol. 11, No. 1, pp. 43-49.

Barnea, D., Shoham, O., Taitel, Y. and Dukler, A.E. (1985) Gas-liquid flow in inclined tubes: Flow pattern transition for upward flow, Chemical Engineering Science, Vol. 40, No. 1, pp. 131-136.

Barnea, D. (1986) Transition from annular flow and from dispersed bubble flow-Unified models for the whole range of pipe inclinations, International Journal of Multiphase Flow, Vol. 12, No. 5, pp. 733-744.

Barnea, D. (1987) An unified model for predicting flow-pattern transitions for the whole range of pipe inclinations, International Journal of Multiphase Flow, Vol. 13, No. 1, pp. 1-12.

Barnea, D. and Taitel, Y. (1993) A model for slug length distribution in gas-liquid slug flow, International Journal of Multiphase Flow, Vol. 19, No. 5, pp. 829-838.

Bergles, A.E. and Suo, M. (1966) Investigation of boiling water flow regimes at high pressure, Dynatech Corporation, Report No. 3304-8 (unpublished).

Biswas, J. and Greenfield, P.F. (1985) Two phase flow through vertical capillaries – existence of a stratified flow pattern, International Journal of Multiphase Flow, Vol. 11, pp. 553-563.

Bousman, W. S., McQuillen, J. B. and Witte, L. C. (1996) Gas-liquid flow patterns in microgravity: effects of tube diameter, liquid viscosity and surface tension, International Journal of Multiphase Flow, Vol.22, No.6, pp.1035-1053.

Brauner, N. and Barnea, D. (1986) Slug/churn transition in upward gas-liquid flow, Chemical Engineering Science, Vol.41, No.1, pp.159-163.

Brauner, N. and Moalem-Maron, D. (1992) Identification of the range of small diameter conduits, regarding two-phase flow pattern transitions, International Community Heat Mass Transfer, Vol. 19, pp. 29-39.

Cheng, T.W. and Lin, T.L. (2001) Characteristics of gas-liquid two-phase flow in small diameter inclined tubes, Chemical Engineering Science, Vol. 56, pp. 6393-6398.

Chisholm, D. (1983) Two-phase flow in pipelines and heat exchangers, New York, Longman Inc.

Chung, P.M.-Y. and Kawaji, M. (2004) The effect of channel diameter on adiabatic two-phase flow characteristics in microchannels, International Journal of Multiphase Flow, Vol.30, pp.735-761.

Coleman, H.W. and Steele W.G. (1999) Experimentation and uncertainty analysis for engineers, Second edition, New York, John Wiley & Sons, INC.

Coleman, J.W. and Garimella S. (1999) Characterization of two-phase flow patterns in small diameter round and rectangular tubes, International Journal of Heat and Mass Transfer, Vol. 42, pp. 2869-2881.

Damianides, D.A. and Westwater, J.W. (1988) Two-phase flow patterns in a compact heat exchanger and in small tubes, Second UK National Conference on Heat Transfer, Volume II Sessions 4A-6C, pp. 1257-1268.

Dukler, A.E., Fabre, J.A., MuQuillen, J.B. and Vernon, R. (1988) Flow at microgavity conditions: flow patterns and their transitions, International Journal of Multiphase Flow, Vol. 14, pp. 389.

Dukler, A.E. and Taitel, Y. (1991) Two-phase gas-liquid flow: a short course on principles of modelling gas-liquid flow and on modern measuring methods, Chap. 3, 5 and 7, University of Houston, Houston.

Feng, Z.P. and Serizawa, A. (1999) Visualization of two-phase flow patterns in an ultra-small tube, Proceeding of the 18th Multiphase Flow Symposium of Japan, 15-16 July, Osaka, Japan, pp. 33-36.

Frankum, D.P., Wadekar, V.V. and Azzopardi, B.J. (1997) Two-phase flow patterns for evaporating flow, Experimental Thermal and Fluid Science, Vol. 15, pp. 183-192.

Fukano, T. and Kariyasaki, A. (1993) Characteristics of gas-liquid two-phase flow in a capillary tube, Nuclear Engineering and Design, Vol. 141, pp. 59-68.

Furukawa, T. and Fukano, T. (2001) Effects of liquid viscosity on flow patterns in vertical upward gas-liquid two-phase flow, International Journal of Multiphase Flow, Vol. 27, pp. 1109-1126.

Galbiati, L. and Andreini, P. (1992) Flow pattern transition for vertical downward two-phase flow in capillary tubes, inlet mixing effects, International Communications in Heat and Mass Transfer, Vol. 19, 791-799.

Galbiati, L. and Andreini, P. (1994) Flow pattern transition for horizontal air-water flow in capillary tubes, a microgravity "equivalent system" simulation, International Communications in Heat and Mass Transfer, Vol. 21, No.4, 461-468.

Graska, M.L. (1986) Effects of fluid surface tension and tube diameter in horizontal two-phase flow in small diameter tubes, M.S. Thesis, University of Illinois at Urbana-Champaign, IL.

Hibiki, T., Mishima, K., Nishihara, H. and Motomura, T. (1993) Study on air-water two-phase flow in a small diameter tube, Annu. Rep. Res. Reactor Inst., Vol. 26, pp. 33-44.

Hout, R.V., Shemer, L. and Barnea, D. (1992) Spatial distribution of void fraction within a liquid slug and some other related slug parameters, International Journal of Multiphase Flow, Vol. 18, No. 6, pp. 831-845.

Huo, X. (1999) Experimental study of flow boiling heat transfer in small diameter tubes, Ten Month Report, London South Bank University.

Huo, X. (2005) Experimental study of flow boiling heat transfer in small diameter tubes, PhD Thesis, London South Bank University.

Hosain, A. and Weisman, J. (1978) Applicability of the homogeneous flow model to two phase pressure drop in straight pipe and across area changes, AIChE Symp. Ser., Vol. 74, No. 174, pp. 205-214.

Incropera, F. P. and DeWitt, D. P. (1996) Fundamentals of Heat and Mass Transfer, Fourth Edition, John Wiley & Sons.

International Organization for Standardization (1993), Guide to the expression of uncertainty in measurement, ISO, Geneva

Kadambi, V. (1982) Stability of annular flow in horizontal tubes, International Journal of Multiphase Flow, Vol. 8, pp.311-328.

Kandlikar, S.G. (2002) Fundamental issues related to flow boiling in minichannels and microchannels, Experimental Thermal and Fluid Science, Vol. 26, pp.389-407.

Kawahara, A., Chung, P.M.-Y. and Kawaji, M. (2002) Investigation of two-phase flow pattern, void fraction and pressure drop in a microchannel, International Journal of Multiphase Flow, Vol. 28, pp.1411-1435.

Kew, P.A. and Cornwell, K. (1997) Correlations for the prediction of boiling heat transfer in small-diameter channels, Applied Thermal Engineering, Vol.17, Nos.8-10, pp.705-715.

Kokal, S. L. and Stanislav, J. F. (1989) An experimental study of two-phase flow in slightly inclined pipes, 1. Flow patterns, Chemical engineering science, Vol. 44, No. 3, pp. 665-679.

Laborie, S., Cabassud, C., Durand-Bourlier, L. and Lainé, J.M. (1999) Characterisation of gas-liquid two-phase flow inside capillaries, Chemical Engineering Science, Vol. 54, pp. 5723-5735.

Lee. D., Best, F.R. and McGraw, N. (1987) Microgravity two-phase flow pattern modelling, in Proceedings of the America Nuclear Society Winter Meeting, Los Angeles, pp. 94-100.

Levich. V.G. (1962) Physicochemical hydrodynamics, Prentice Hall, Englewood Cliffs, NJ.

Levy, S. (1967) Forced convection subcooled boiling prediction of vapour volumetric fraction,., International Journal of Heat Mass Transfer, Vol.10, pp.951-965.

Lin, P.Y. and Hanratty, T.J. (1986) Prediction of the initiation of slugs with linear stability theory, International Journal of Multiphase Flow, Vol. 12, pp.79-98.

Lin, S., Kew, P.A. and Cornwell, K. (1998) Two-phase flow regimes and heat transfer in small tubes and channels, Heat Transfer1998, Proceedings of 11th IHTC, Vol. 2, August 23-28, Kyongju, Korea, pp. 45-50.

Lin, S., Kew, P.A. and Cornwell, K. (1999) Characteristics of air/water flow in small tubes, Heat and Technology, Vol. 17, No. 2, pp. 63-70.

Lowe, D.C. and Rezkallah, K.S. (1999) Flow regime identification in microgravity two-phase flow using void fraction signals, International Journal of Multiphase Flow, Vol. 25, pp. 433-457.

Mao, Z. and Dukler, A.E. (1989) An experimental study of gas-liquid slug flow, Experiments in Fluids, Vol. 8, pp.169-182.

Massey, B. and Ward-Smith, J. (1998) Mechanics of Fluids, seventh edition, Stanley Thornes (Publishers) Ltd.

McQuillan, K. W. and Whalley, P. B. (1985) Flow patterns in vertical two-phase flow, International Journal of Multiphase Flow, Vol. 11, No. 2, pp. 161-175.

Mishima, K. and Ishii, M. (1984) Flow regime transition criteria for upward two-phase flow in vertical tubes, International Journal of Heat Mass Transfer, Vol. 27, No. 5, pp. 723-737.

Mishima, K., Hibiki, T. and Nishihara, H. (1995) Some characteristics of air-water two-phase flow in small diameter tubes, Proc 2nd International Conference Multiphase Flow, Vol. 4, April 3-7, Tokyo, Japan, pp. 39-46.

Mishima, K. and Hibiki, T. (1996) Some characteristics of air-water two-phase flow in small diameter vertical tubes, International Journal of Multiphase Flow, Vol. 22, No. 4, pp. 703-712.

Nagano, H. (1990) Thermophysical properties of environmentally acceptable fluorocarbons: HFC-134a and HCFC-123, Japanese Association of Refrigeration.

Nash, C.A., McCreery, G.E. and Stoots, C.M. (1992) Two-phase pressure losses and flow regimes in a horizontal annular heat exchanger tube, Heat Transfer, Vol. 88, No. 288, pp. 64-78.

Nicholson, M.K., Aziz, K. and Gregory, G.A. (1978) Intermittent two phase flow in horizontal pipes: predictive models, Can. J. Chem. Eng., Vol. 56, pp. 653-663.

Oya, T. (1971) Upward liquid Flow in small tube into which air streams (1st Report, Experimental apparatus and flow patterns), Vol. 14, No. 78, pp. 1320-1329.

Prasser, H.M., Krepper, E. and Lucas, D. (2002) Evolution of the two-phase flow in a vertical tube-decomposition of gas fraction profiles according to bubble size classed using wire-mesh sensors, International Journal of Thermal Sciences, Vol. 41, pp. 17-28.

Reinarts, T.R. (1993) Adiabatic two-phase flow regime data and modelling for zero and reduced (horizontal flow) acceleration field, Ph.D. Dissertation, Texas A&M University, USA.

Rezkallah, K.S. (1996) Weber number based flow-pattern maps for liquid-gas flows at microgravity, International Journal of Multiphase Flow, Vol. 22, pp. 1265-1270.

Rogers, G.F.C. and Mayhew, Y.R. (1988) Thermodynamic and transport properties of fluids, SI Units, Basil Blackwell Ltd.

Serizawa, A. and Feng, Z.P. (2001) Two-phase flow in micro-channels, Proceeding of the 4th International Conference on Multiphase Flow, May 17-June 1, 2001, New Orleans, LA, USA.

Serizawa, A., Feng, Z.P. and Kawara, Z. (2002) Two-phase flow in microchannels, Exp. Therm. Fluid Sci., Vol. 26, pp. 703-714.

Schmidt, E. and Grigull, U. (1981) Properties of water and steam in SI-Units, 0-800C, 0-1000bar.

Suo, M. and Griffith, T. (1964) Two-phase flow in capillary tubes, J. Basic Engineering, Vol. 86, pp. 576-582.

Taitel, Y. and Dukler, A. E. (1976) A model for predicting flow regime transitions in horizontal and near-horizontal flow, AIChE, Vol. 22, pp. 47-55.

Taitel, Y., Barnea, D. and Dukler, A. E. (1980) Modelling flow pattern transitions for steady upward gas-liquid flow in vertical tubes, AIChE, Vol. 26, pp. 345-354.

Taitel, Y. (1990) Flow pattern transition in two phase flow, Keynote lecture, 9th International Heat Transfer Conference, Jerusalem, Israel, 19-24 Aug., pp. 237-254.

Taitel, Y., Sarica, C. and Brill, J.P. (2000) Slug flow modelling for downward inclined pipe flow: theoretical considerations, International Journal of Multiphase Flow, Vol. 26, pp. 833-844.

Takamasa, T., Goto, T., Hibiki, T. and Ishii, M. (2003) Experimental study of interfacial area transport of bubbly flow in small-diameter tube, International Journal of Multiphase Flow, Vol. 29, pp. 395-409.

Tong, L.S. and Tang, Y.S. (1997) Boiling heat transfer and two-phase flow, Second edition, Taylor & Francis Ltd.

Triplett, K.A., Ghiaasiaan, S.M., Abdel-Khalik, S.I. and Sadowski, D.L. (1999) Gas-liquid two-phase flow in microchannels, Part I: Two-phase flow patterns, International Journal of Multiphase Flow, Vol. 25, Elsevier Science Ltd., pp. 377-394.

Troniewski, L. and Ulbrich, R. (1984) The analysis of flow regime maps of two-phase gas-liquid flow in pipes, Chemical Engineering Science, Vol. 39, pp. 1213-1224.

Wadekar, V. (2002) Compact heat exchangers for phase change, International Journal of Heat Exchangers, Vol. 3, pp. 169-200.

Watel, B. (2003) Review of saturated flow boiling in small passages of compact heat-exchangers, International Journal of Thermal Sciences, Vol. 42, pp. 107-140.

Weisman, J., Duncan, D., Gibson, J. and Crawford, T. (1979) Effects of fluid droperties and pipe diameter on two-phase flow patterns in horizontal lines, International Journal of Multiphase Flow, Vol. 5, pp. 437-462.

Wölk, G., Dreyer, M. and Rath, H.J. (2000) Flow patterns in small diameter vertical non-circular channels, International Journal of Multiphase Flow, Vol. 26, pp. 1037-1061.

Wongwises, S., Disawas, S., Kaewon, J. and Onurai, C. (2000) Two-phase evaporative heat transfer coefficients of refrigerant HFC-134a under forced flow conditions in a small horizontal tube, International Community Heat Mass Transfer, Vol. 27, No. 1, pp. 35-48.

Yang, C.Y. and Shieh C.C. (2001) Flow pattern of air-water and two-phase R-134a in small circular tubes, International Journal of Multiphase Flow, Vol.27, pp.1163-1177.

Yu, M.H., Lin T.K., and Tseng C.C. (2002) Heat transfer and flow pattern during two-phase flow boiling of R-134a in horizontal smooth and microfin tubes, International Journal of Refrigeration, Vol.25, pp.789-798.

Zhao, J.F., Xie, J.C., Lin, H., Hu, W.R., Ivanov, A.V. and Belyaev, A.Yu. (2001) Experimental studies on two-phase flow patterns aboard the Mir space station, International Journal of Multiphase Flow, Vol. 27, pp. 1931-1944.

Zhao, L. and Rezkallah, K.S. (1993) Gas-liquid flow patterns at microgravity conditions, International Journal of Multiphase Flow, Vol. 19, pp. 751-763.

Zhao, T.S. and Bi, Q.C. (2001) Co-current air-water two-phase flow patterns invertical triangular microchannels, International Journal of Multiphase Flow, Vol. 27, pp. 765-782.

Zietlow, D.C. and Pedersen, C.O. (1998) Flow regime mapping and analysis of R-134a in a small-channel cross-flow condenser, ASHRAE Transactions, Vol. 104, No. 2, pp. 540-547.

Appendix A

The Previous Two-Phase Flow Pattern Studies in Small Tubes and Narrow Channels

Appendix A summarizes the previous two-phase flow regime studies in small diameter tubes and narrow channels since 1960 to 2004 based on the statistic of Lin et al. (1998, 1999) and the literature review in the present study. Table A.1 gives the details of the experimental conditions. Figures A.1-A.3 classify them based on tube geometry, flow orientation, heating method, fluid type and publication year.

Table A.1 Past two-phase flow pattern studies in small tubes and narrow channels.

Investigator	Date	Geometry	Diameter/ Hydraulic diameter (mm)	Orientation	Fluid/Mixture	Test mode	Pressure/ Temperature (MPa / °C)	Mass flux (kg/m^2 s)	Superficial velocity (gas/liquid) m/s	Heat flux kW/m^2
Marchessault and Mason	1960	circular tube	1-3	I	air/water, air/glycerine	adiabatic				
Taylor	1961	circular tube	1.5-3	H	air/glycerine	adiabatic				
Suo and Griffith	1964	circular tube	1-2	H	air/water, He,N2/heptane	adiabatic	0.1/	0.001-0.1		
Hosler	1968	rectangular channel	3.4x25.4	V	steam/water	heated	1-13.8/	136-5424		5678 (max.)
Oya	1971	circular tube	2,3,6	V	air/water, air/gasoline	adiabatic	0.1/10-40			
Bamea et al.	1983	circular tube	4,6,8.15, 9.85,12.3	V, H	air/water	adiabatic	0.1/25	1.01-10100		
Yao and Chang	1983	annular tube	0.6375, 1.585,5.013	V	R113, acetone, steam/water	heated	0.1/			0.8-300
Biwsas and Greenfield	1985	circular tube	0.5-7.1	V	air/water	adiabatic				

Table A.1 Past two-phase flow pattern studies in small tubes and narrow channels (Cont.).

Investigator	Date	Geometry	Diameter/ Hydraulic diameter (mm)	Orientation	Fluid/Mixture	Test mode	Pressure/ Temperature (MPa / °C)	Mass flux (kg/m^2 s)	Gas/liquid superficial velocity (m/s)	Heat flux (kW/m^2)
Damianides and Westwater	1988	maze style/ circular tube	1.74/1,2,3,4,5	H	air/water	adiabatic	0.5/10-21	1.01-10100	1.05-101.2/0.0084-8.62, 0.015-125.3/0.0024-5.72	
Lowry and Kawaji	1988	rectangular channel	80x0.5, 80x1, 80x2	V, H	air/water	adiabatic	0.1/	9.97-7990		
Mishima et al.	1991	narrow channel	δ=1.07, 2.4, 5.0		air/water	adiabatic			0.02-30/0.07-4	
Wambsganss et al.	1991	rectangular channel	3.18x19.05	H	air/water	adiabatic	0.1/	50-2000		
Galbiati and Andreini	1992	circular tube	0.5, 1.1, 2.0	V	air/water	adiabatic	/25			
Moriyama and Inoue	1992	narrow channel	δ=0.035-0.11		R113	heated		200-1000		4-30
Nash et al.	1992	annular tube	D=10.23/ δ=1.35	H	N2/water	adiabatic			0-4/0.03-3	
Wambasganss et al.	1992	rectangular channel	9.52X1.59	H	air/water	adiabatic		50-2000		
Ali et al.	1993	rectangular channel	1.54,2.88	V, H, I	air/water	adiabatic	0.2/	190-6010		
Barajas and Panton	1993	circular tube	1.6	H	air/water	adiabatic	0.15/20	2.1-2100		
Cornwell and Kew	1993	rectangular channel	1.03,1.64	V	R113	heated	0.1-0.2/	100-650		3-30
Fukano and Kariyasaki	1993	circular tube	1.0,2.4,4.9,9.0	V, H	air/water	adiabatic	0.1/20			
Hibiki et al.	1993	circular tube	4.08	V	air/water	adiabatic				
Mishima et al.	1993	rectangular channel	1.95,4.53, 8.89	V	air/water	adiabatic	0.1/	79.8-8060		

Table A.1 Past two-phase flow pattern studies in small tubes and narrow channels (Cont.).

Investigator	Date	Geometry	Diameter/ Hydraulic diameter (mm)	Orientation	Fluid/Mixture	Test mode	Pressure/ Temperature (MPa / °C)	Mass flux (kg/m^2 s)	Gas/liquid superficial velocity (m/s)	Heat flux (kW/m^2)
Galbiati and Andreini	1994	circular tube	1	H	air/water	adiabatic	1.0-5.0/20		0.2-10/0.1-1.2	
Wilmarth and Ishii	1994	rectangular channel	1x20, 2x15	H, V	air/water	adiabatic	0.1/	19-5010		
Mishima et al.	1995	circular tube	1.05	V	air/water	adiabatic	0.1/~20		1-80/0.5-20	
Aligoodarz and Kenning	1995	rectangular channel	1.33	V	steam/water	heated	0.1/	~85		~61
Bar-Cohen et al.	1995	rectangular channel	1.01	V	N2, vapour/FC-72	adiabatic heated	0.1-0.142/	2.7-287		9.1-37.9
Fourar and Bories	1995	rectangular channel	δ=1,0.54, 0.4,0.18	H	air/water	adiabatic				
Fujita et al.	1995	rectangular channel	0.2x10, 1.2x10, 2x10	H	N2/ethanol solution	adiabatic				
Kew	1995	rectangular channel	2.0,2.22, 2.94,3.0	V	R141b, Flutec PP1	heated	0.1-0.15/	10-565		5-95
Solbreken and Bar-Cohen	1995	rectangular channel	1.01	V	air, steam/water	adiabatic, heated	1.5/	0.65-430		116-1160
Bonjour et al.	1996	rectangular channel	0.6,0.9, 1.2,2.0	V	R113	heated	0.1-0.3/			1-200
Mertz et al.	1996	rectangular channel	1.0-3.0		steam/water, R141b	heated		50-300		3-227
Mishima and Hibiki	1996	circular tube	1.0-4.0	V	air/water	adiabatic	0.1/20	0.1-900		
Kasza et al.	1997	rectangular channel	2.5x6.0		steam/water	heated		21		110
Thulasides et al.	1997	circular tube/ rectangular channel	2.0/2x2	V	air/water, silicone oil	adiabatic				

Table A.1 Past two-phase flow pattern studies in small tubes and narrow channels (Cont.).

Investigator	Date	Geometry	Diameter/ Hydraulic diameter (mm)	Orientation	Fluid/Mixture	Test mode	Pressure/ Temperature (MPa / °C)	Mass flux ($kg/m^2 s$)	Gas/liquid superficial velocity (m/s)	Heat flux (kW/m^2)
Bonjour and Lallemand	1998	rectangular channel	δ=0.5-2.0	V	R113	heated				0-200
Zietlow and Pedersen	1998	parabolic cross section	0.74	H	R134a	heated			0-4.06/0-0.48	0-11.7
Coleman and Garimella	1999	circular tube/ rectangular channel	1.3,1.75,2.6, 5.5/5.36	H	air/water	adiabatic			0.1-100/0.01-10	
Ekberg et al.	1999	annular tube	ID6.6/OD8.6, ID33.2/OD35.2	H	air/water	adiabatic	0.1/		0.02-57/0.1-6.1	0.8-300
Kuznetsov and Shamirzaev	1999	annular tube	δ=0.9	H	R318c	heated		200-900		2-110
Laborie et al.	1999	circular tube	1, 2, 3, 4	V	air/water, glyceril, ethyl alcohol	adiabatic	0.1/5-25		0.1-1.0/0.08-0.9	
Lin, Kew and Cornwell	1999	circular tube	0.5-4.0	V	air/water	adiabatic	0.1/20			
Triplett et al.	1999	circular tube/ semi-triangular	1.1,1.45/ 1.09,1.49	H	air/water	adiabatic	0.1/20		0.02-80/0.02-8	
Xu et al.	1999	rectangular channel	12x0.3, 12x0.6, 12x1.0	V	air/water	adiabatic				
Bao et al.	2000	circular tube	1.95		air/water	heated			0.1-50/0.08-0.5	3-58
Kuwahara et al.	2000	circular tube	1.2	H	R134a	heated				
Wolk et al.	2000	circular tube/rectangular/ rhombic/equilateral triangular	6	V	air/water	adiabatic	0.3/20		0.15-5.0/0.36-4.0	
Cheng and Lin	2001	circular tube	2, 4, 6, 8	I	air/ dextran aqueous solution	adiabatic			0.04-0.32/0.168-0.672	
Kim and Bang	2001	rectangular channel	1.32x1.78		R22	heated		384-570		2-10

Table A.1 Past two-phase flow pattern studies in small tubes and narrow channels (Cont.).

Investigator	Date	Geometry	Diameter/ Hydraulic diameter (mm)	Orientation	Fluid/Mixture	Test mode	Pressure/ Temperature (MPa / °C)	Mass flux (kg/m^2 s)	Gas/liquid superficial velocity (m/s)	Heat flux (kW/m^2)
Yang and Shieh	2001	circular tube	1	H	air/water	adiabatic	0.1/~20		0.21-75/0.014-1.34	
Yang and Shieh	2001	circular tube	3		R134a	heated		300-1600		
Zhao and Bi	2001	triangular channel	0.866, 1.443, 2.886	V	air/water	adiabatic	0.1/22		0.1-100/0.08-10	
Pettersen	2002	circular tube	0.98	H	CO_2	heated	3.5, 5.7/	93-584		0, 13
Yang et al.	2002	circular tube	3	H	R125, R407C	heated	/5, 20	300-1000		
Coleman and Garimella	2003	circular tube/ rectangular channel	4.91/4x4, 4x6, 6x4, 2x4, 4x2	H	R134a	heated	1.38-1.72/	150-750		
Satitchaicharoen and Wongwises	2004	narrow channel	δ=1, 2, 3	V	air/water, glycerol solution	adiabatic			0.05-25/0.075-2.5	
Yun and Kim	2004	rectangular channel	2x16	H	CO_2	heated	4.0/	217-868		0-250

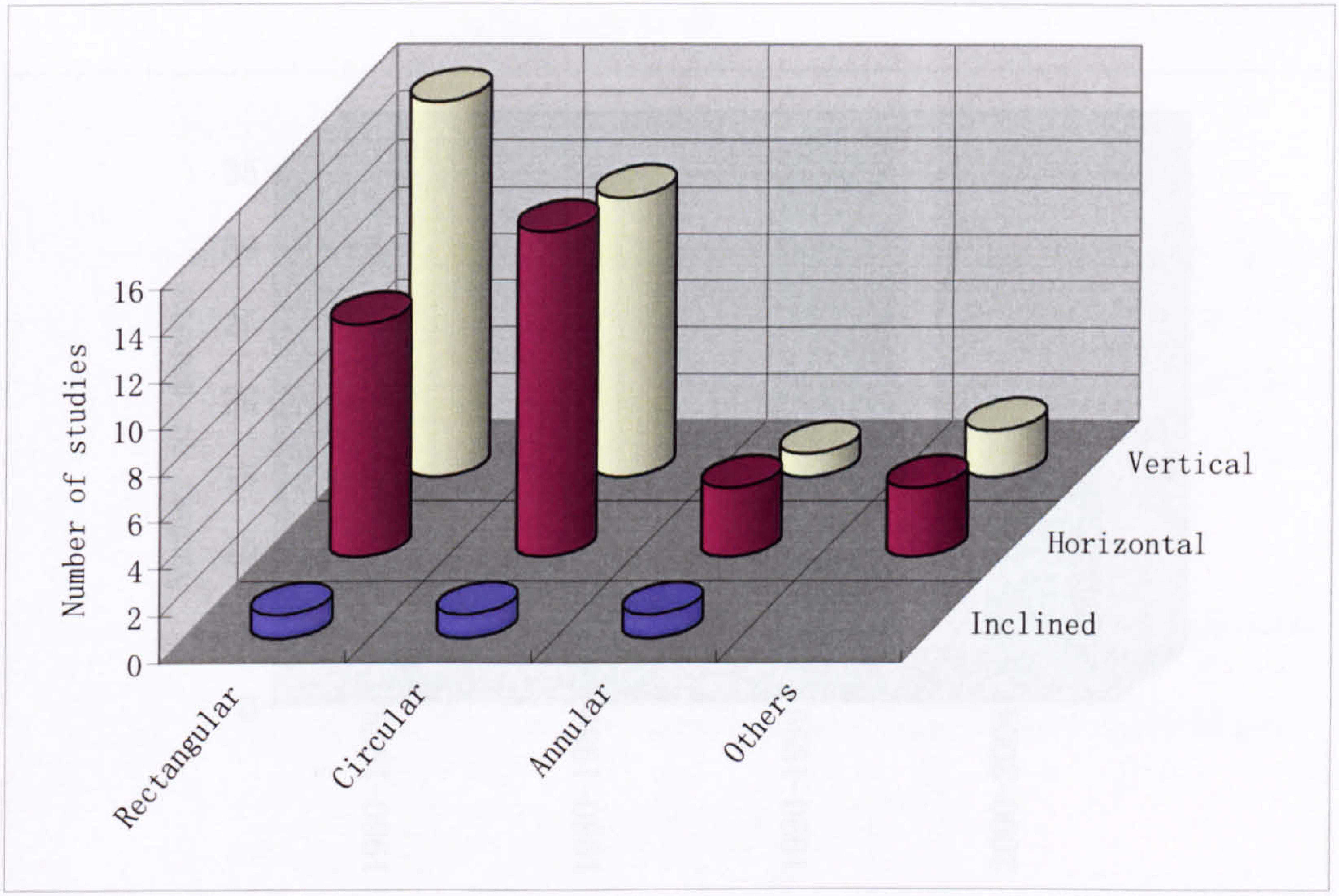

Figure A.1 Tube geometries and flow orientations used in studies reported in the literature (1960-2004) for small channels.

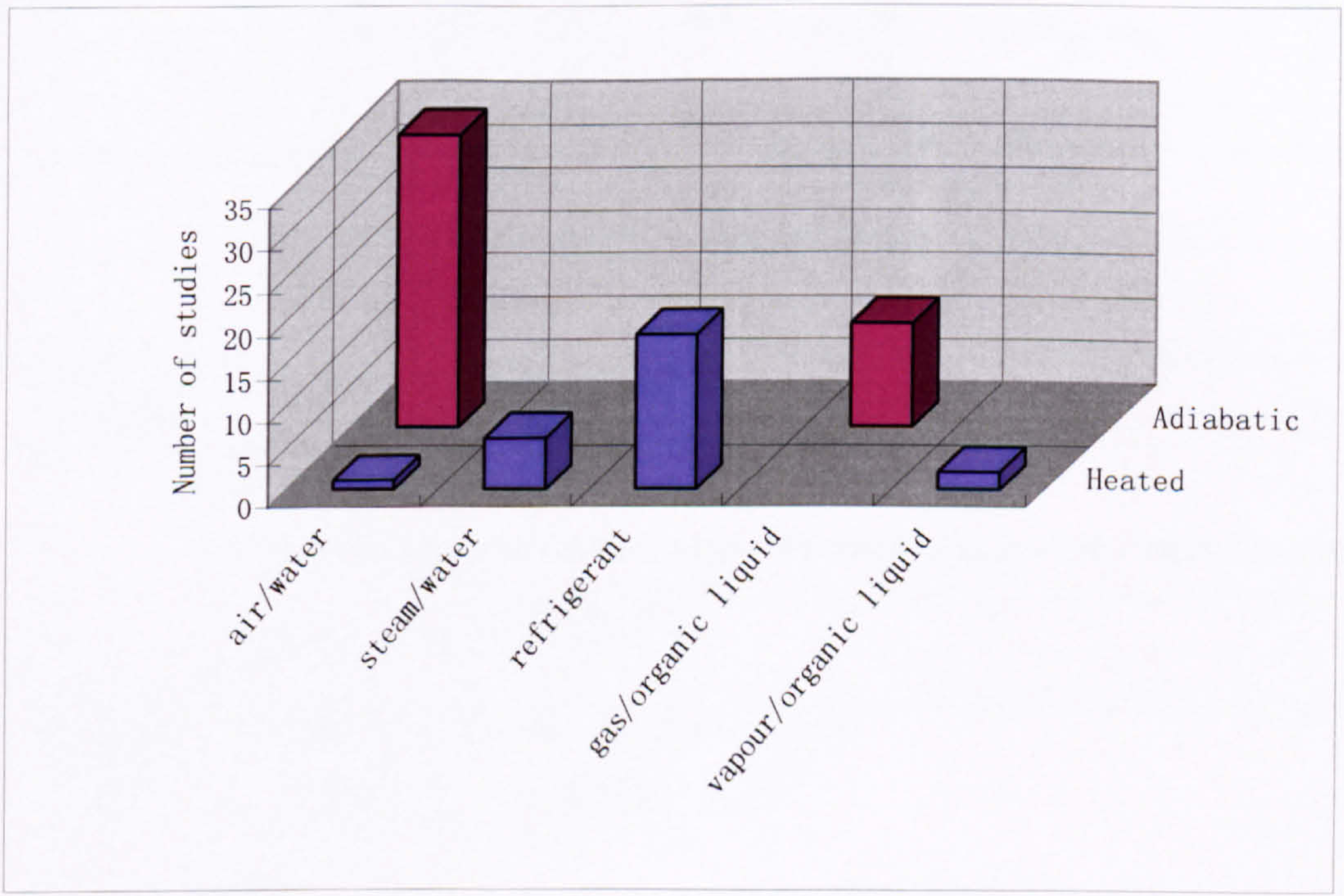

Figure A.2 Fluids and test modes used in studies reported in the literature (1960-2004) for small channels.

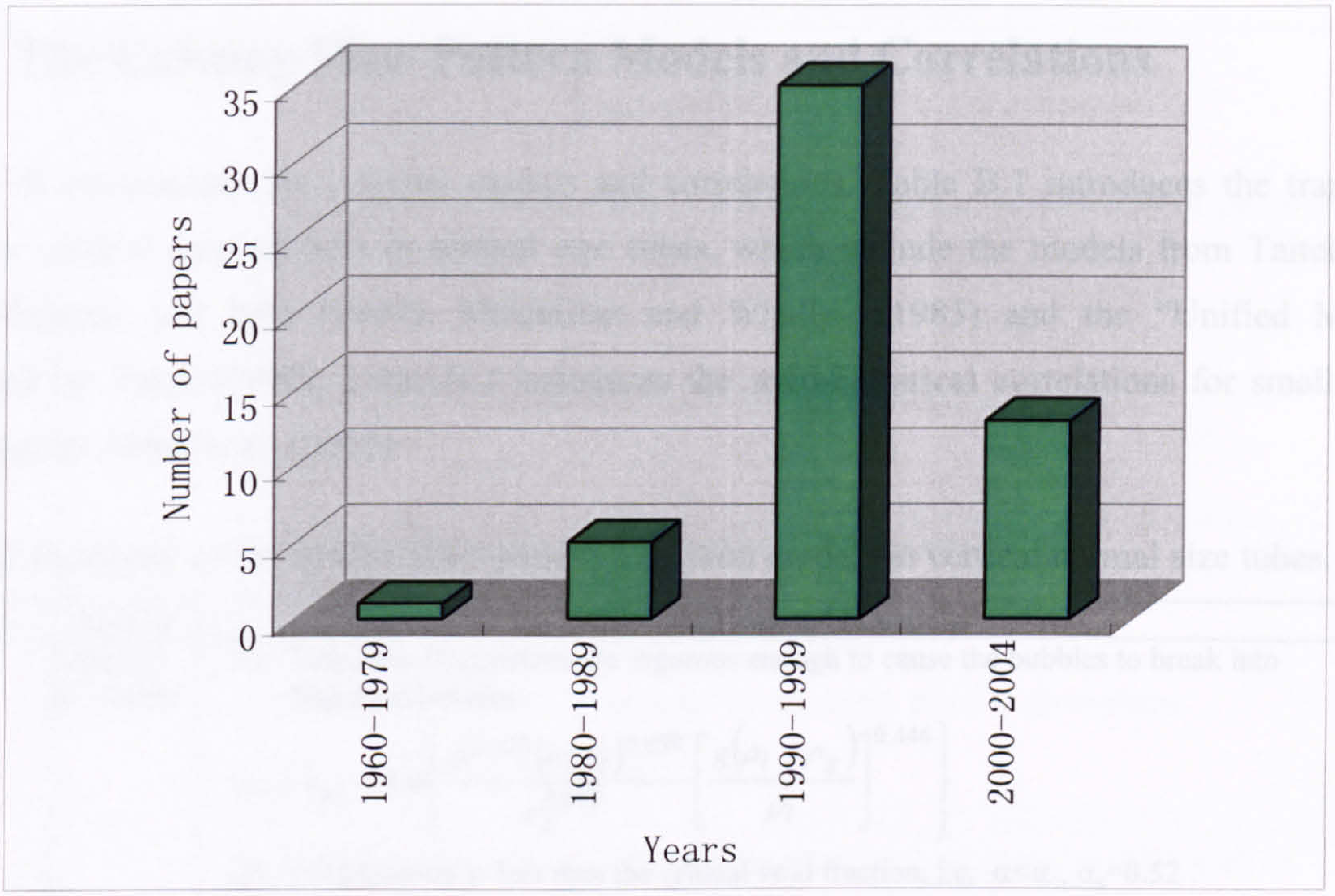

Figure A.3 Number of papers on two-phase flow in small channels published between 1960 and 2004.

Appendix B

The Existing Flow Pattern Models and Correlations

Appendix B summarizes the existing models and correlations. Table B.1 introduces the transition models for vertical upward flow in normal size tubes, which include the models from Taitel et al. (1980), Mishima and Ishii (1984), McQuillan and Whalley (1985) and the "Unified Model" summarized by Taitel (1990). Table B.2 introduces the semi-empirical correlations for small tubes summarized by Akbar et al. (2003).

Table B.1 Summary of the upward flow pattern transition models in vertical normal size tubes.

Boundary	Authors	Conditions and Equations
Dispersed bubble to intermittent flow	Taitel et al. (1980)	(1) Turbulent fluctuations are vigorous enough to cause the bubbles to break into dispersed bubbles $u_{ls}+u_{gs}=4.0\left\{\frac{D^{0.429}(\sigma/\rho_l)^{0.089}}{\nu_l^{0.072}}\left[\frac{g(\rho_l-\rho_g)}{\rho_l}\right]^{0.446}\right\}$ (2) Void fraction is less than the critical void fraction, i.e. $\alpha<\alpha_c$, $\alpha_c=0.52$. $\alpha\approx\frac{u_{gs}}{u_h}$ $u_h=u_{gs}+u_{ls}$
	Taitel (1990)	(1) Bubble size is small enough, i.e. $d_{st}<d_{cd}$ and $d_{st}<d_{cb}$ $d_{st}=\left(0.725+4.15\sqrt{\alpha}\right)\left(\frac{\sigma}{\rho_l}\right)^{3/5}\kappa^{-2/5}$ $\alpha\approx\frac{u_{gs}}{u_h}$ $u_h=u_{gs}+u_{ls}$ $\kappa=\frac{2f_h}{D}u_h^3$ $d_{cd}=2\left[\frac{0.4\sigma}{(\rho_l-\rho_g)g}\right]^{1/2}$ $d_{cb}=\frac{3}{8}\frac{\rho_l}{\rho_l-\rho_g}\frac{f_h u_h^2}{g\cos\theta}$ (2) Void fraction is less than the critical void fraction, i.e. $\alpha<\alpha_c$, $\alpha_c=0.52$. $\alpha\approx\frac{u_{gs}}{u_h}$ $u_h=u_{gs}+u_{ls}$
Bubble to slug	Taitel et al. (1980)	(1) The tube diameter is large enough. $D>19.01\left[\frac{(\rho_l-\rho_g)\sigma}{g\rho_l^2}\right]^{1/2}$ (2) Void fraction is less than the critical void fraction, i.e. $\alpha<0.25$, which deduced to $u_{ls}=3.0u_{gs}-1.15\left[\frac{g(\rho_l-\rho_g)\sigma}{\rho_l^2}\right]^{1/4}$
	Mishima and Ishii (1984)	Transition occurs at a void fraction of around 0.3. $u_{ls}=\left(\frac{3.33}{C_0}-1\right)u_{gs}-\frac{0.76}{C_0}\left[\frac{\sigma g(\rho_l-\rho_g)}{\rho_l^2}\right]^{1/4}$ where $C_0=1.2-0.2\sqrt{\frac{\rho_g}{\rho_l}}$ (for round tubes) or $C_0=1.35-0.35\sqrt{\frac{\rho_g}{\rho_l}}$ (for rectangular ducts)

Table B.1 Summary of the upward flow pattern transition models in vertical normal size tubes (Cont.).

Boundary	Authors	Conditions and Equations
Bubble to slug	McQuillan and Whalley (1985)	(1) Liquid flow rate is large enough. $u_{ls} = \frac{6.8}{\rho_l^{0.444}} \left[g\sigma(\rho_l - \rho_g) \right]^{0.278} \left(\frac{D}{\mu_l} \right)^{0.112}$ (2) The dispersion forces are not dominant to suppress the formation of gas plugs, i.e. $\alpha < 0.25$ $u_{ls} = 3.0 u_{gs} - 1.15 \left[\frac{g(\rho_l - \rho_g)\sigma}{\rho_l^2} \right]^{1/4}$ (3) Void fraction is bigger than the critical void fraction, α_c=0.74. $\alpha > \alpha_c$ where $\alpha \approx \frac{u_{gs}}{u_{gs} + u_{ls}}$
	Taitel (1990)	(1) The tube diameter is larger the critical diameter given by. $D_c = \frac{2.34 \sin^2 \theta}{(0.35 \sin\theta + 0.54 \cos\theta)^2} \left[\frac{(\rho_l - \rho_g)\sigma}{g \rho_l^2} \right]^{1/2}$ (2) The inclination angle is larger the critical angle, which is given below. $\frac{\cos\theta_c}{\sin^2\theta_c} = \frac{3}{4} \cos 45° \frac{u_r^2}{g} \left(\frac{C_{lt} \gamma^2}{d} \right)$ (3) The distance between bubbles becomes less than half the radius of the bubbles. $\alpha < 0.25$ (4) The flow is not annular flow.
Slug to churn	Taitel et al. (1980)	Taitel et al. considered churn flow to be an entry region phenomenon; the location of the slug-churn transition boundary depends on the point of observation along the pipe. $\frac{L_E}{D} = 40.6 \left(\frac{u_{gs} + u_{ls}}{\sqrt{gD}} + 0.22 \right)$
	Mishima and Ishii (1984)	It is assumed that the transition from slug to churn flow occurs when the mean void fraction over the entire region reaches the mean void fraction in the slug-bubble section. Combining $\alpha = 1 - 0.813 \left\{ \frac{(C_0 - 1)(u_{gs} + u_{ls}) + 0.35\sqrt{(\rho_l - \rho_g) gD/\rho_l}}{u_{gs} + u_{ls} + 0.75\sqrt{(\rho_l - \rho_g) gD/\rho_l} \left((\rho_l - \rho_g) gD^3/\rho_l \nu_l^2 \right)^{1/18}} \right\}^{0.75}$ with $\alpha = \frac{u_{gs}}{C_0 (u_{gs} + u_{ls}) + 0.35\sqrt{(\rho_l - \rho_g) gD/\rho_l}}$ where $C_0 = 1.2 - 0.2\sqrt{\frac{\rho_g}{\rho_l}}$ (for round tubes) or $C_0 = 1.35 - 0.35\sqrt{\frac{\rho_g}{\rho_l}}$ (for rectangular ducts)
	Taitel (1990)	There are a few or no bubbles in liquid slug. $\alpha_s > 0.52$ $\alpha_s = 0.058 \left[d_c \left(\frac{2 f_h u_h^3}{D} \right)^{2/5} \left(\frac{\rho_l}{\sigma} \right)^{3/5} - 0.725 \right]^2$ $d_c = \min(d_{cd}, d_{cb})$
Churn to annular	Taitel et al. (1980)	Gas velocity in the gas core is sufficient to lift the entrained droplets. $u_{gs} = 3.1 \left[\frac{\sigma g (\rho_l - \rho_g)}{\rho_g^2} \right]^{1/4}$

Table B.1 Summary of the upward flow pattern transition models in vertical normal size tubes (Cont.).

Boundary	Authors	Conditions and Equations
Churn to annular	McQuillan and Whalley (1985)	Inertia force dominates gravity. $u_{gs}=\sqrt{\frac{gD(\rho_l-\rho_g)}{\rho_g}}$
	Mishima and Ishii (1984)	(1) Flow reversal in the liquid film section along large bubbles. $u_{gs}=\sqrt{\frac{(\rho_l-\rho_g)gD}{\rho_g}(\alpha-0.11)}$ $\alpha=1-0.813\left\{\frac{(C_0-1)(u_{gs}+u_{ls})+0.35\sqrt{(\rho_l-\rho_g)gD/\rho_l}}{u_{gs}+u_{ls}+0.75\sqrt{(\rho_l-\rho_g)gD/\rho_l}\left((\rho_l-\rho_g)gD^3/\rho_l v_l^2\right)^{1/18}}\right\}^{0.75}$ (2) Destruction of liquid slugs or large waves by entrainment or deformation. $u_{gs}=\left[\frac{\sigma g(\rho_l-\rho_g)}{\rho_g^2}\right]^{1/4}N_{\mu l}^{-0.2}$ where $N_{\mu l}=\frac{\mu_l}{\left[\rho_l\sigma\sqrt{\sigma/g(\rho_l-\rho_g)}\right]^{1/2}}$
	Taitel (1990)	(1) The liquid film thickness is thin enough, i.e. the film thickness obtained from combining $\tau_i=\frac{1}{2}f_i\rho_g\frac{u_{gs}^2}{\left(1-2\delta/D\right)^4}$ with $\tau_i=g(\rho_l-\rho_g)D\sin\theta\left[\frac{\delta}{D}-\left(\frac{\delta}{D}\right)^2\right]\left[1-2\left(\frac{\delta}{D}\right)\right]+\frac{1}{32}C_l\rho_l\left(\frac{D}{v_l}\right)^{-n}u_{ls}^{2-n}\left[\frac{1-2\delta/D}{\left(\delta/D-(\delta/D)^2\right)^2}\right]$ is less than the solution from $g(\rho_l-\rho_g)D\sin\theta\left[\left(1-\frac{2\delta}{D}\right)^2-2\left(\frac{\delta}{D}-\left(\frac{\delta}{D}\right)^2\right)\right]-\frac{1}{16}C_l\rho_l\left(\frac{D}{v_l}\right)^{-n}u_{ls}^{2-n}\left[\frac{\left(\delta/D-(\delta/D)^2\right)+\left(1-2\delta/D\right)^2}{\left(\delta/D-(\delta/D)^2\right)^3}\right]=0$ (2) Lower liquid hold-up $\frac{\alpha_l}{\alpha_{sc}}=\frac{A_l}{A\alpha_{sc}}\geq 0.5$ Barnea and Brauner (1985) estimated the maximum stable liquid holdup α_{sc} to be 0.48.

Table B.2 The semi-empirical correlations for small tubes (Akbar et al. 2003).

Boundary	Conditions and Equations
Surface tension dominated zone	$We_{gs} \leq 0.11 We_{ls}^{0.315}$ for $We_{ls} \leq 3.0$ $We_{gs} \leq 1.0$ for $We_{ls} > 3.0$
Inertia dominated zone 1 (annular flow zone)	$We_{gs} \geq 11.0 We_{ls}^{0.14}$ $We_{ls} \leq 3.0$
Inertia dominated zone 2 (dispersed flow zone)	$We_{gs} > 1.0$ $We_{ls} > 3.0$

Appendix C
Validation of the Existing Experimental Facility

The existing test facility was designed for flow boiling heat transfer experiments instead of flow pattern experiments. Some parameters required in the flow pattern experiments exceed the original designed range. Therefore, it was necessary to re-evaluate the capacity of the existing experimental facility and the possible modifications that were required. A summary of the key equipments used is also included here.

C.1 R134a experimental system

(1) R134a Tank

Manufactory	ESK Schultze
Model	OSA - 40
Design pressure	25 bar
Volume	40 L
Heater	1.0 kW

(2) R134a Pump

Manufactory		Tuthill Pump Group
Model		1010/028 (gear pump)
Power supply		370 W, 1 PHASE, 220 - 240 V, 50 Hz
Fluid		R134a
Flow		6 lit/min
Head		5 bar
Design pressure	(suction)	15 barg
	(discharge)	20 barg
Design temperature		-30-100 °C
Viscosity		0.3 – 1.0 Cp

The maximum flow rate required in the flow pattern experiments was at the condition of 4.26 mm test section, 6.0 bar, maximum u_{ls} (5 m/s) and u_{gs} (10 m/s).

$$
\begin{aligned}
Q &= \frac{AG}{\rho_l} = \frac{\pi D^2\left(\rho_g u_{gs} + \rho_l u_{ls}\right)}{4\rho_l} \\
&= \frac{\pi \times 0.00426^2 \times (29.0 \times 10 + 1218.2 \times 5)}{4 \times 1218.2} \\
&= 7.16 \times 10^{-5} \quad m^3/s \\
&= 4.30 \quad lit/\min
\end{aligned}
$$

Therefore, the selected pump can provide the required flow rate.

The pump head should be checked by the total pressure loss in the loop. The formula developed by Mishima and Hibiki (1996) for small tubes was used here.

$$\varphi_l^2 = \frac{\Delta p}{\Delta p_l} = 1 + \frac{C}{X} + \frac{1}{X^2}$$

$$C = 21\left(1 - e^{-0.333D}\right)$$

The single liquid phase pressure gradient due to friction is given by Chisholm (1983):

$$\Delta p_l = f_l \frac{2\rho_l u_{ls}^2}{D}$$

where

$$f_l = C_l \operatorname{Re}_{ls}^{-n}$$

The calculation results are given in Table C.1.

Table C.1 Total pressure losses in experimental system.

Test section diameter	1.10		2.01		2.88		4.26		mm
Conduit diameter	10.0		10.0		10.0		10.0		mm
Test section length	0.54		0.83		1.10		1.40		m
Conduit length	48.00		48.00		48.00		48.00		m
Pressure	6	14	6	14	6	14	6	14	bar
Temperature	21.56	52.45	21.56	52.45	21.56	52.45	21.56	52.45	°C
Gas superficial velocity	10.0	10.0	10.0	10.0	10.0	10.0	10.0	10.0	m/s
Liquid superficial velocity	5.0	5.0	5.0	5.0	5.0	5.0	5.0	5.0	m/s
Pressure drop at test section	5.5	6.6	5.6	7.0	5.8	7.2	5.4	6.9	bar
Pressure drop at conduits	0.0	0.0	0.0	0.0	0.2	0.2	0.7	0.8	bar
Total pressure loss	5.5	6.6	5.6	7.0	6.0	7.4	6.1	7.7	bar

The maximum pressure loss happens in the 4.26 mm tube at 14 bar, is 7.7 bar, which seems beyond the lift range of the pump. However, the practical measurement indicated that the above equations overestimated the pressure loss in two-phase flow. For example, the measured pressure drop was about 1.9 bar when the vapour and liquid superficial velocities were 9.95 m/s and 4.42 m/s in one of the present experiments. The calculated pressure drop is 3.9 bar which is double of the measured value. Therefore, the existing pump could be suitable for the proposed flow pattern experiments.

(3) Mass flow meters

ELITE CMF010:	
Manufactory	Micro Motion Ltd
Type	Coriolis mass flow meter
Nominal flow range	0-82 kg/hr
Maximum flow rate	108 kg/hr
Applied flow range	0-25 kg/hr
Accuracy (at 0.5 kg/hr)	0.51 %
(at 25 kg/hr)	0.11 %

ELITE CMF025:	
Manufactory	Micro Motion Ltd
Type	Coriolis mass flow meter
Nominal flow range	0-1090 kg/hr
Maximum flow rate	2180 kg/hr
Applied flow range	25-500 kg/hr
Accuracy (at 25 kg/hr)	0.51 %
(at 500 kg/hr)	0.11 %

The maximum flow rate of the proposed experiments is 327.4 kg/hr. Therefore, the Coriolis mass flow meters are big enough in the flow pattern experiments. The practical measuring spans were decreased to 25 kg/hr and 500 kg/hr in order to improve their measuring accuracy.

(4) Chiller

Type	tube-in-tube exchanger
Heating exchange area	0.13 m^2
Design capacity	3.1 kW (at 55 K temperature difference)

The chiller was not used in the flow pattern experiments. The two valves used to isolate R22 cooling system were always closed.

(5) Preheaters

No.1 heater (regulable)	0 - 1350 W
No.2 - No.5 heaters (fixed)	5 x 1350 W
Small preheater (regulable)	0 - 300 W

The purpose of the preheaters is to obtain the desired temperature at the inlet of the test sections. Otherwise, the excessive subcooling degree may lead to an unstable experimental state. However, the designed preheater could not work well in the flow pattern experiments because of the excessively long conduit between the preheater and the test sections. In low flow rate experiments, it needed a very long time to reach steady state. Therefore, a smaller tape heater was wrapped on the conduit just before the test sections. The existing variac for the No.1 heater was used to control this 300 W preheater.

(6) Test sections

The test sections have been introduced in detail in Chapter 3 Section 3.3. The detailed dimensions and structure, take the 1.10 mm test section as an example, are presented in Figures C.1 and C.2.

Drawing No.	FP-T110-00

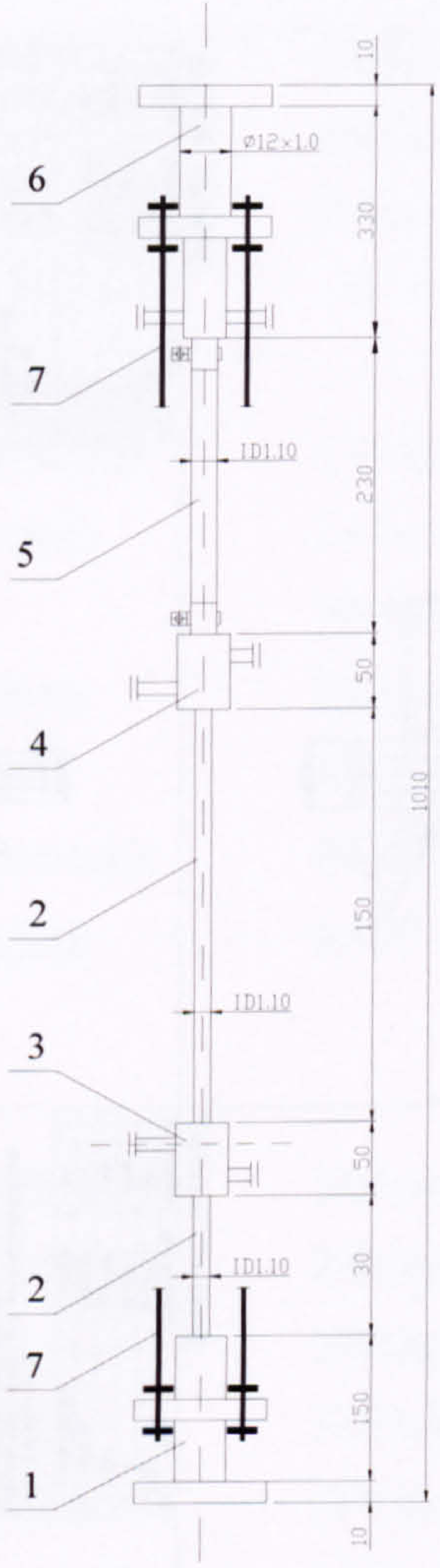

Notes:

1. The drawing is only available for the ID 1.10 mm test section.
2. All dimensions in figure are in mm.

No.	name	drawing & type	material	qt.	
7	studding	M5 L=650mm	steel	4	new
6	flange module	FP-T110-04	316L	1	new
5	glass tube	ID 1.10mm L=200mm	pyrex glass	1	new
4	electrode & connecter	FP-T110-03		1	new
3	electrode & connecter	FP-T110-02		1	new
2	tube	ID 1.10mm L=305mm	316L	1	new
1	flange module	FP-T110-01	316L	1	new

Figure C.1 Design drawing of the 1.10 mm test section (1).

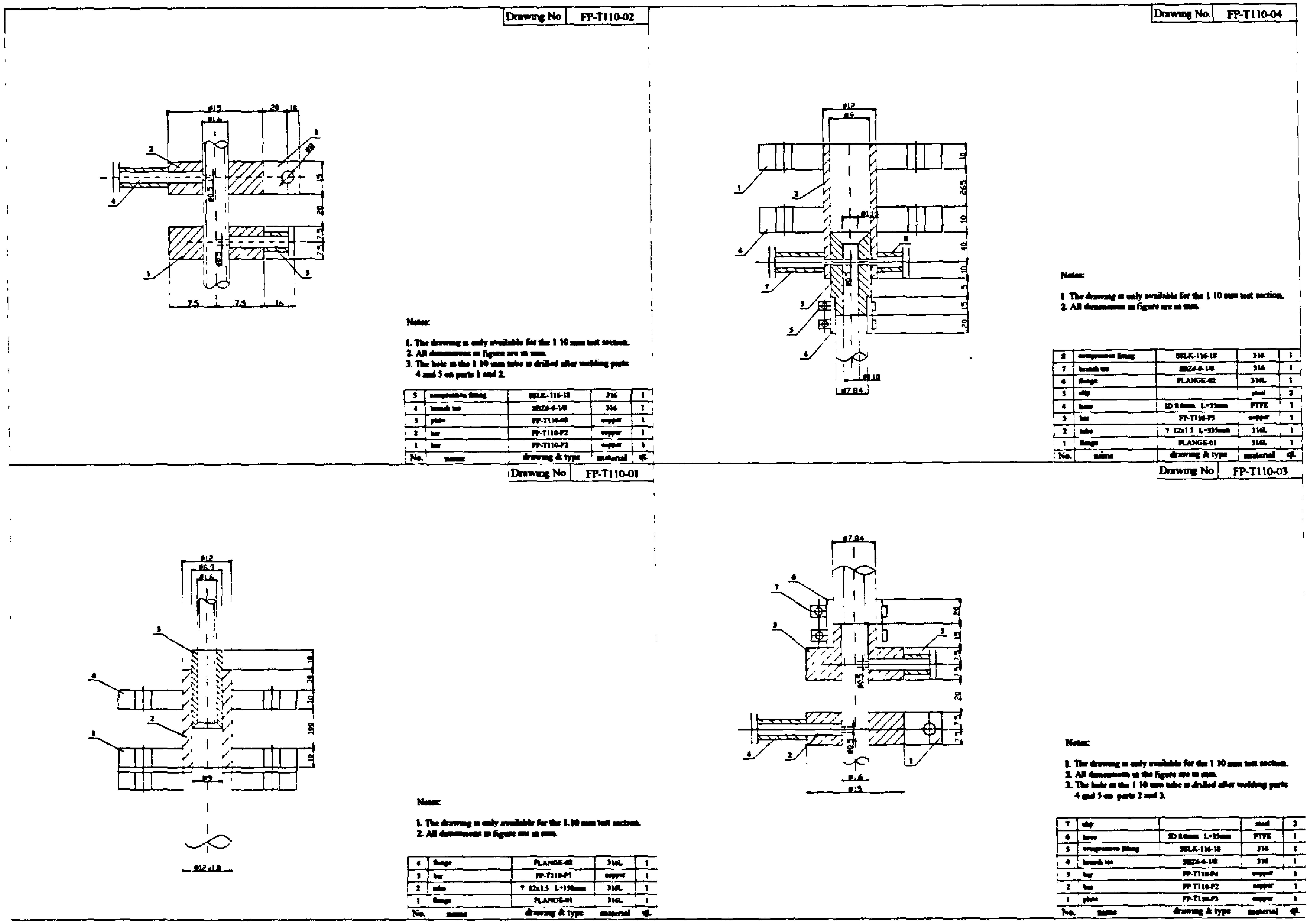

Drawing No | FP-T110-02

Notes:

1. The drawing is only available for the 1.10 mm test section.
2. All dimensions in figure are in mm.
3. The hole in the 1.10 mm tube is drilled after welding parts 4 and 5 on parts 1 and 2.

5	compression fitting	SSLK-116-18	316	1
4	branch tee	SBZ6-6-1/8	316	1
3	plate	FP-T110-P3	copper	1
2	bar	FP-T110-P2	copper	1
1	bar	FP-T110-P2	copper	1
No.	name	drawing & type	material	qt.

Drawing No | FP-T110-01

Drawing No. | FP-T110-04

Notes:

1. The drawing is only available for the 1.10 mm test section.
2. All dimensions in figure are in mm.

8	compression fitting	SSLK-116-18	316	1
7	branch tee	SBZ6-6-1/8	316	1
6	flange	FLANGE-02	316L	1
5	clip		steel	2
4	hose	ID 8.0mm L=35mm	PTFE	1
3	bar	FP-T110-P5	copper	1
2	tube	Φ 12x1.5 L=335mm	316L	1
1	flange	FLANGE-01	316L	1
No.	name	drawing & type	material	qt.

Drawing No | FP-T110-03

Notes:

1. The drawing is only available for the 1.10 mm test section.
2. All dimensions in figure are in mm.

4	flange	FLANGE-02	316L	1
3	bar	FP-T110-P1	copper	1
2	tube	Φ 12x1.5 L=150mm	316L	1
1	flange	FLANGE-01	316L	1
No.	name	drawing & type	material	qt.

Notes:

1. The drawing is only available for the 1.10 mm test section.
2. All dimensions in the figure are in mm.
3. The hole in the 1.10 mm tube is drilled after welding parts 4 and 5 on parts 2 and 3.

7	clip		steel	2
6	hose	ID 8.0mm L=35mm	PTFE	1
5	compression fitting	SSLK-116-18	316	1
4	branch tee	SBZ6-6-1/8	316	1
3	bar	FP-T110-P4	copper	1
2	bar	FP-T110-P2	copper	1
1	plate	FP-T110-P3	copper	1
No.	name	drawing & type	material	qt.

Figure C.2 Design drawing of the 1.10 mm test section (2).

The specifications of the all test sections are summarized below based on the above design drawings.

Material	(calming section):	stainless steel
	(heating section):	stainless steel
	(observation section):	Pyrex glass

1.10 mm test section:

Diameter	(stainless steel tube):	1.10 mm (ID) x 1.60 mm (OD)
	(Pyrex glass tube):	1.10 mm (ID) x 7.8 mm (OD)
Length	(total)	1010 mm
	(calming section):	100 mm
	(heating section):	150 mm
	(observation section):	200 mm
Resistance	(heating section):	0.107 - 0.112 Ω (10 - 60 ° C)

2.01 mm test section:

Diameter	(stainless steel tube):	2.01 mm (ID) x 2.39 mm (OD)
	(Pyrex glass tube):	2.01 mm (ID) x 7.6 mm (OD)
Length	(total)	980 mm
	(calming section):	175 mm
	(heating section):	210 mm
	(observation section):	300 mm
Resistance	(heating section):	0.119 - 0.125 Ω (10 - 60 ° C)

2.88 mm test section:

Diameter	(stainless steel tube):	2.88 mm (ID) x 3.18 mm (OD)
	(Pyrex glass tube):	2.88 mm (ID) x 7.8 mm (OD)
Length	(total)	1260 mm
	(calming section):	225 mm
	(heating section):	300 mm
	(observation section):	450 mm
Resistance	(heating section):	0.156 - 0.164 Ω (10 - 60 ° C)

4.26 mm test section:

Diameter	(stainless steel tube):	4.26 mm (ID) x 4.75 mm (OD)
	(Pyrex glass tube):	4.26 mm (ID) x 9.4 mm (OD)
Length	(total)	1350 mm
	(calming section):	235 mm
	(heating section):	500 mm
	(observation section):	450 mm
Resistance (heating section):		0.108 - 0.113 Ω (10 - 60 °C)

(7) Separator

Type	centrifugal
Diameter	50 mm
Volume	$0.0004\ m^3$

(8) Condensers

R134a condenser:

Type	tube-in-tube exchanger
Heating exchange area	$0.79\ m^2$
Design capacity	11.6 kW (at 10 K temperature difference)

Small condenser (in R134a tank):

Type	immersed tube exchanger
Heating exchange area	$0.016\ m^2$
Design capacity	500 W (at 40 K temperature difference)

The created vapour in the test sections is condensed in the condensers. In fact, the fluid temperature was always higher than the ambient temperature in the present experiments. Therefore, the surrounding air also contributed, i.e. heat loss to the ambient. In some experiments, the two condensers were not needed at all, see Table C.2.

Table C.2 The launch of the condensers.

Tube diameter (mm)	1.10			2.01			2.88			4.26		
Pressure (bar)	6.0	10.0	14.0	6.0	10.0	14.0	6.0	10.0	14.0	6.0	10.0	14.0
Small condenser	X			X	X		X	X	X	X	X	X
Big condenser							X			X	X	

The required capacity of the condensers can be calculated by the following equation, in which the energy dissipation to environment is neglected. Obviously, the maximum requirement happens at the conditions of 4.26 mm tube, 14 bar and 10 m/s u_{gs},.

$$\begin{aligned} Q &= \frac{\pi}{4} D^2 \rho_g u_{gs} h_{fg} \\ &= \frac{\pi}{4} \times 0.00426^2 \times 70.7 \times 10 \times (424879 - 275669) \\ &= 1504 \quad W \end{aligned}$$

Therefore, the existing condensers can condense all vapour generated in the flow pattern experiments.

(9) Current transformer

Manufactory	Todd Systems Inc.
Model	HC 56100B
Current range	0 - 100 / 0 - 200 A
Voltage range	0 - 56 / 0 - 28 V
Max. output	5600 VA

C.2 R22 cooling system

In the flow pattern experiments, the R22 cooling system should be capable of absorbing all heat created in the experimental system. The existing cooling capacity is 12 kW at an evaporating pressure of 2.5 bar (-20 ° C), which satisfies the requirement of the experimental system, i.e. 1504 W.

(1) Compressor

Manufactory	Bitzer
Model	4CC – 6.2 (semi-hermetic)
No. of cylinder	4
Power supply	380 - 420 V, Y 3 phase, 50 Hz
Displacement (1450 RPM 50Hz)	32480 m^3/h
Cooling capacity	12.0 Kw (30 ° C condensing temperature, -20 ° C evaporating temperature)
Max. pressure (LP/HP)	19 / 28 bar
Max operating current	15.9 A
Working Fluid	R22
Oil	Bitzer B 5.2
Crankcase heater	120 W

(2) Oil separator

Manufactory	Temprite (Europe) Ltd.
Model	903
Efficiency	99.97 % of all oil greater than 0.03 microns

(3) R22 condenser

The condenser and receiver are the components of the air conditioner unit K750CS. The compressor was broken during the commissioning. The capacity of the new compressor was only slightly smaller than the original unit. Therefore, the existing condenser and receiver are bigger enough for the new unit.

Manufactory	Dorin
Unit model	K750CS
Number of fans	6
Fan power	34 W
Total air volume	10400 m^3/hr

(4) R22 receiver

Manufactory	Dorin
Unit model	K750CS
Test pressure	20 bar
Volume	14 L

(5) R22 tank

Test pressure	20 bar
Volume	55 L
Heater	350 W

(6) R22 pump

Same as the R134a pump

(7) Oil pump

Supplier	Omega
Model	FPUGR 101 (gear)
Power supply	370 W, 1 PHASE, 230 V, 50 Hz
Flow	0.9 - 0.61 GPM (reference fluid: water)
Head	0 - 100 psi (reference fluid: water)

(8) Oil tank

Test pressure	20 bar
Volume	12.5 L

(9) Thermostatic liquid level control equipment

Manufactory	Danfoss
Model	TEVA 20-20
Temperature	-50 - 10 °C

Heater	10 W
Capacity	15.4 kW (R22, ΔP=8 bar)

(10) Hot gas bypass regulator

Manufactory	Parker
Model	A9
Maximum rated pressure	27.5 bar
Adjustment range	0.33 - 8.2 bar
Temperature range	- 45 - 93 °C

C.3 Control and data acquisition system

(1) Computers

Data collecting computer:

Manufactory	Dell
Model	Dimension V400C
Operating system	Windows 2000
CPU	Pentium Celeron 400 MHz
RAM	256 MB
Hard disk	6.4 GB
Monitor	15”

Flow pattern monitoring and recording computer:

Manufactory	Dell
Model	Dimension 8300
Operating system	Windows XP (Home Edition)
CPU	Pentium IV 2.4 GHz
RAM	512 MB
Hard disk	120 GB
Monitor	17” UltraScan

(2) Data loggers

Data logger 1:

Model	SI3535F
Input module	35301 J high speed solid state scanner
Number of input channels	20 per module (Max. 200 input channels)
Max. scan rate	500 / second
Max. measured voltage	13.7 V
Max. voltage to ground	14 V
Integration time	0.625 - 80 ms
Voltage range	0 - 10 VDC (in the current experiments)
stability	(0.005% rdg + 2 digits + 3μV)/year
temperature effect	(0.001% rdg + 0.1μV)/K
Output module	SI35301E analog
Number of output channels	5
Range (voltage)	0 - 10 V
(current)	4 - 20 mA

Data logger 2:

Model	SI35951E
Number of input channels	20
Max. measured voltage	12 V
Max. voltage to ground	500 V
Integration time	1.25 - 20 ms
Voltage range	0 - 20 mV (in the current experiments)
stability	(0.02% rdg + 5μV)/year
temperature effect	(0.0015% rdg + 0.2μV)/K

(3) Power meters

Manufactory	Yokogawa Electric Corporation
Model	WT110 (Digital)
Max. input current	20 A
Max. input voltage	600 V

Accuracy	0.25% rdg + 0.1% rng

(4) PID controller

Supplier	OMEGA
Model	CN1504TC-1
Channel number	4
Input type	J, K, T, E, R, S, B, thermistor, RTD 4 - 20 mA loop current 0 - 10 VDC 0 - 100 mv
Accuracy	Temperature: 1K/1° F, 0.1% full scale Voltage: 0.05% full scale Current: 0.05% full scale
Scan rate	2 channels per second
Proportional band	0 - 100%
Reset	0 - 50 repeats per minute
Rate	0 - 500 seconds

(5) Digital high-speed camera

Manufactory	Vision Research, Inc.
Model	Phantom V4 B/W
Resolution	512 x 512 pixel
Speed	1000 pictures/second with full resolution
Maximum speed	32000 pictures/second
Exposure time	Variable, Minimum 10 μs
Memory	256 MB

The digital high-speed camera can objectively record the experimental process and flow patterns. It will be useful in analysing the data and understanding the mechanisms. The cool light resource provides extremely high levels of illumination at very low ambient temperature. This characteristic is very useful in flow boiling experiments. The software available with the camera can capture, study the flow field and measure some parameters, like bubble size and velocity.

(6) Pressure transducers

The pressure transducers used in the current experiments are listed in Table C.3.

Table C.3 The summary of pressure transducers.

No.	Sensor	Supplier	Range	Output signal	Power supply	Error
P1	GP series	RS	0-40 bar g	4-20mA	12V	
P2	PDCR 4010	Druck	0-10 bar a	0-100mV	12V	0.17%
P3	PDCR 4010	Druck	0-20 bar a	0-100mV	12V	0.35%
P4	PDCR 910-0826	Druck	0-10 bar a	0-100mV	12V	0.16%
P0	PDCR 910-0826	Druck	0-10 bar a	0-100mV	12V	0.16%
P5	GP series	RS	0-40 bar g	4-20mA	12V	

(7) Thermocouples

The thermocouples used in the current experiments are listed in Table C.4.

Table C.4 The summary of thermocouples.

No.	Type	Calibration Range (°C)	Experiment Range (°C)	Reference	Error*
T1	K type ungrounded probe	-18 - 66	20 - 55	Ambient	0.08
T2	K type ungrounded probe	-18 - 66	20 - 55	Ice box	0.08
T3	T type grounded needle probe	-20 - 80	20 - 55	Ice box	0.08
T4	T type grounded needle probe	-20 - 80	20 - 55	Ice box	0.08
T0	T type grounded needle probe	-20 - 80	20 - 55	Ice box	0.08
T5	K type ungrounded probe	-18 - 66	20 - 55	Ambient	0.08
T6	K type ungrounded probe	-18 - 66	20 - 55	Ambient	0.08
TT_{1-15}	K type thermocouple wires	-20 - 80	> 20	Ice box	0.08

*: The error is the calibration error only, not include the measurement error caused by the data loggers.

(8) Differential pressure transducers

Supplier		Omega
Model		PX771-100WDI
Measurement range		100 inch water (0.2491 bar)
Accuracy	(at 24% full scale)	17.7 Pa
	(at 100% full scale)	72.6 Pa

Appendix D

Control Programs

Three programs were used in the present study. The phantom camera control program operates the digital high-speed camera. The data collecting program controls the data loggers and the instruments, collects the experimental data. Finally, the data analysing program is a useful tool for the post-analysis of the experimental data.

D.1 Phantom camera control

The phantom camera control program is installed in the host computer. It exhibits the flow scene on the monitor in real time and controls the operation of the digital high-speed camera. After recording a set of pictures, the software transmits them to the computer through a firewire cable. The data obtained can be replayed and edited there. Meanwhile, physical parameters, like bubble size and velocity, can be measured by the software. In summary, its main functions include:

(1) Operate the digital high-speed camera.
(2) Transfer the recorded films to the computer.
(3) Edit and save the films in the computer.
(4) Replay and display the films in detail.
(5) Measure the physical parameters.

The interface of the phantom camera control program is presented in Figure D.1. The resolution was set to 256 pixels (width) x 512 pixels (height) to get clear images as well as fast snap speed. The sample rate was from 200 pps (pictures per second) to 1900 pps depending on flow velocity. In most cases, the exposure time used the fastest speed – 10 microseconds to reduce tail track in the pictures and get clear profile. All the information about the camera state and the experiments was written in the description of each set of data collected.

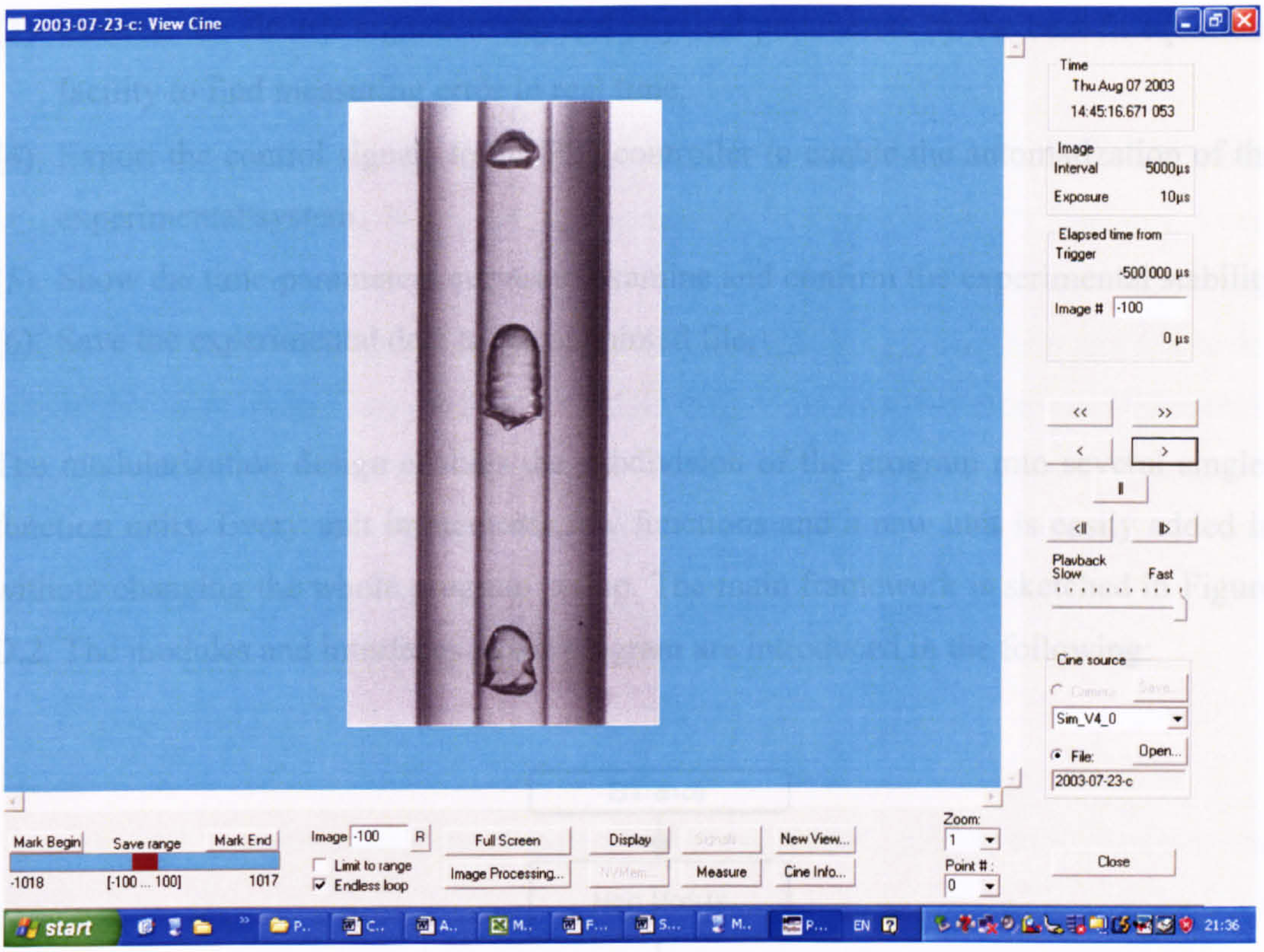

2003-07-23-c: View Cine

Time
Thu Aug 07 2003
14:45:16.671 053

Image Interval 5000µs

Exposure 10µs

Elapsed time from Trigger -500 000 µs

Image # -100

0 µs

Cine source
○ Camera
Sim_V4_0
● File: 2003-07-23-c

Zoom: 1

Point #: 0

Mark Begin -1018

Save range [-100 ... 100]

Mark End 1017

Image -100

☐ Limit to range

☑ Endless loop

Figure D.1 The interface of phantom camera control program.

D.2 Data collecting program

The data collecting program was developed in Visual Basic 6.0. This popular software is famous of its friendly interface and is easily managed. The most important point is that almost all the original communicating codes provided by the manufacturers are written in Basic or Visual Basic. These characteristics facilitate the quick development of an integrated, multi-function data collecting program. Visual Basic is a user-friendly language but hardly used to develop high performance codes. The average scan frequency in the present experiments was about 7 seconds. This speed affected only marginally the current study because the experiments were based on steady state. However, more attention must be paid when the experiments were close to critical heat flux (CHF). The overall functions built in the program are listed below:

(1) Monitor the measured parameters, which include pressure, temperature, pressure difference, heating power and flow rate.

(2) Calculate the experimental parameters in real time, such as flow status, quality, superficial velocities, thermal loss, heat flux and mass flux.

(3) Convert the electric signals to the real physical parameters by the best-fit equations facility to find measuring error in real time.

(4) Export the control signals to the PID controller to enable the automatization of the experimental system.

(5) Show the time-parameters curves to examine and confirm the experimental stability.

(6) Save the experimental data to the appointed file.

The modularization design enables the subdivision of the program into several single-function units. Every unit implements few functions and a new unit is easily added in without changing the whole program set-up. The main framework is sketched in Figure D.2. The modules and interfaces in the program are introduced in the following:

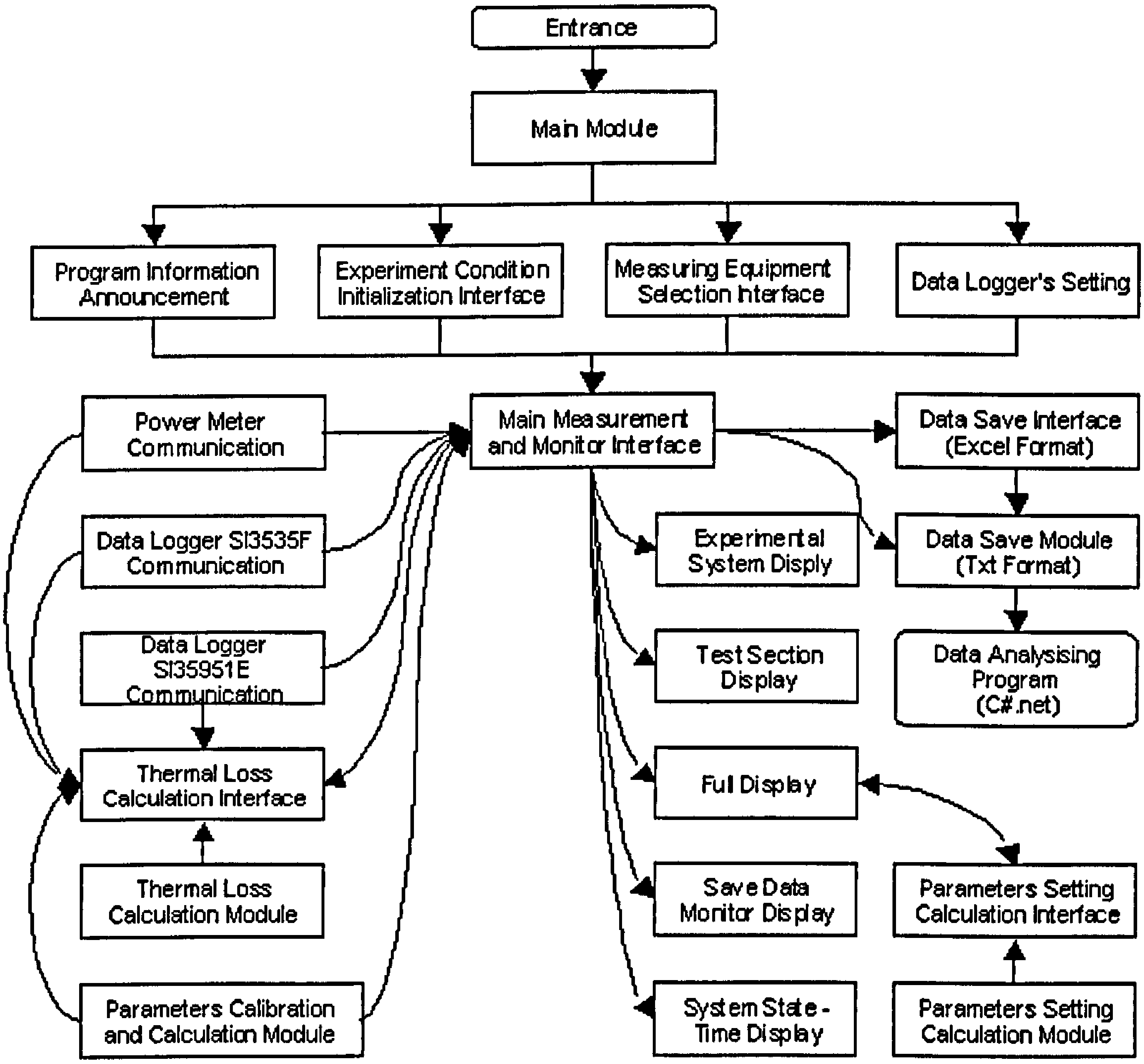

Figure D.2 Flow chart of the data collecting program.

(1) Main Module

The program starts with the Main Module. The Main Module defines all global variables and public functions, which include the R134a property equations. Every external module or interface can access these public variables and functions without any restrictions. The data loggers' settings, such as the measuring channels and the tasks, are defined here also. Then the Main Module triggers in turn the Program Information Announcement, Experiment Condition Initialization Interface, Measuring Equipment Selection Interface, Main Measurement and Monitor Interface. The program is then ready for measurement and recording.

(2) Experiment Condition Initialisation Interface

This interface initialises the current experimental conditions, such as tube diameter and length, flow direction, heat transfer or flow pattern experiment option, observation position, thermocouple quantity, differential pressure transducer type, atmospheric pressure and alarm setting, see Figures D.3 and D.4.

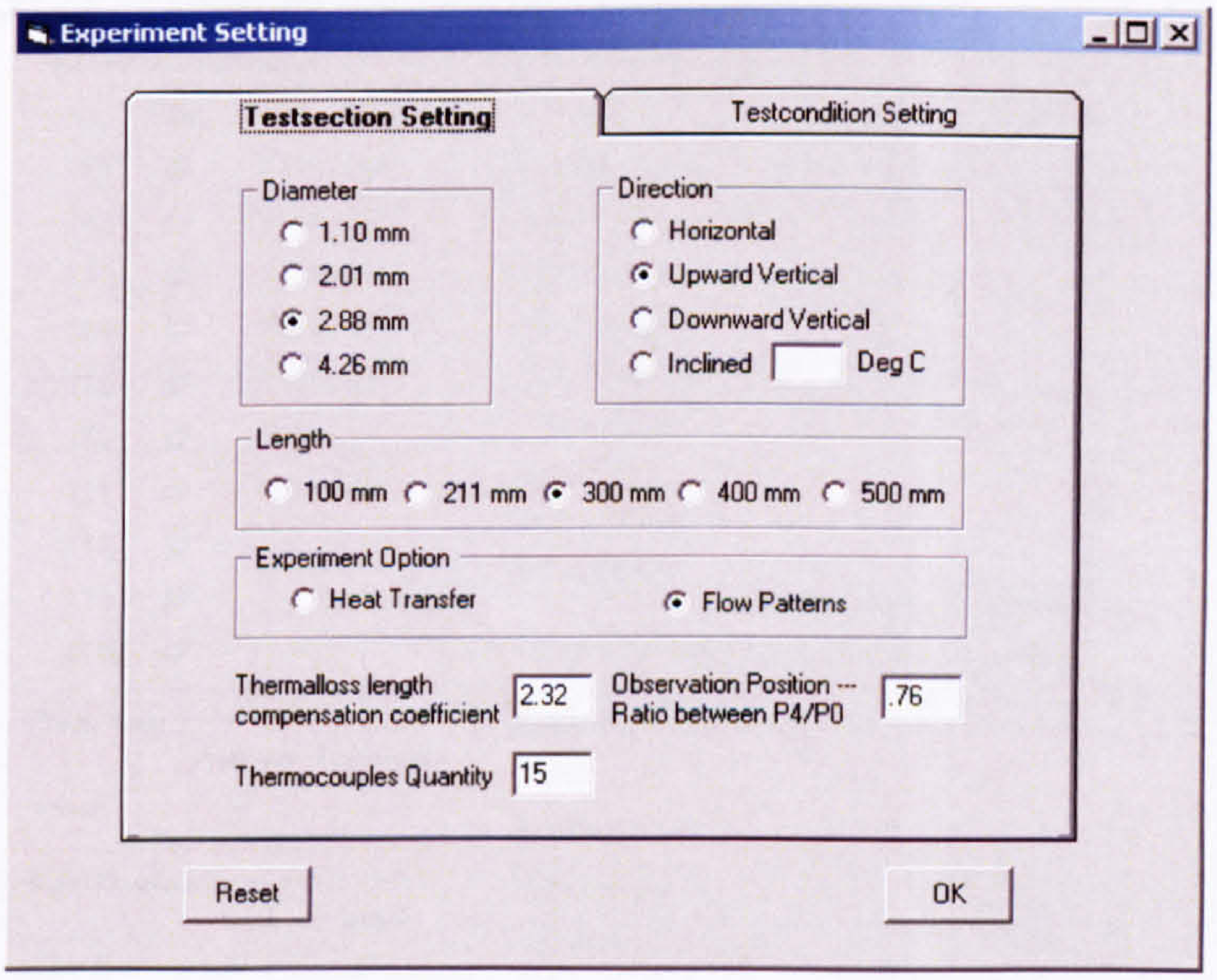

Diameter
○ 1.10 mm
○ 2.01 mm
● 2.88 mm
○ 4.26 mm

Direction
○ Horizontal
● Upward Vertical
○ Downward Vertical
○ Inclined ☐ Deg C

Length
○ 100 mm ○ 211 mm ● 300 mm ○ 400 mm ○ 500 mm

Experiment Option
○ Heat Transfer ● Flow Patterns

Thermalloss length compensation coefficient: 2.32
Observation Position --- Ratio between P4/P0: .76
Thermocouples Quantity: 15

Figure D.3 Experiment condition initialisation interface (1).

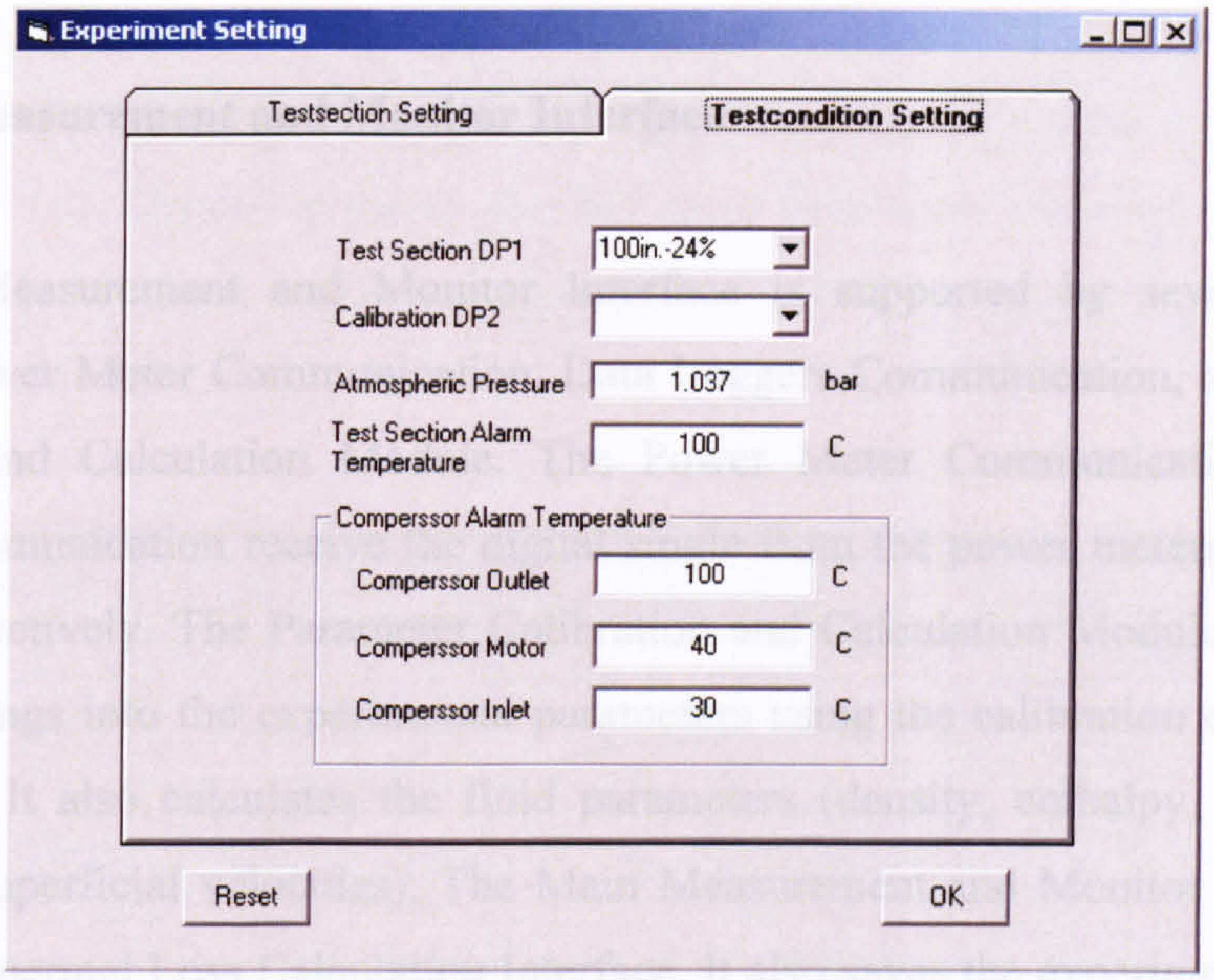

Test Section DP1: 100in.-24%

Calibration DP2:

Atmospheric Pressure: 1.037 bar

Test Section Alarm Temperature: 100 C

Compessor Alarm Temperature

Compessor Outlet: 100 C

Compessor Motor: 40 C

Compessor Inlet: 30 C

Figure D.4 Experiment condition initialisation interface (2).

(3) Measuring Equipment Selection Interface

The measuring equipments used in the experiments are selected in the interface shown in Figure D.5 according to the experimental requirements.

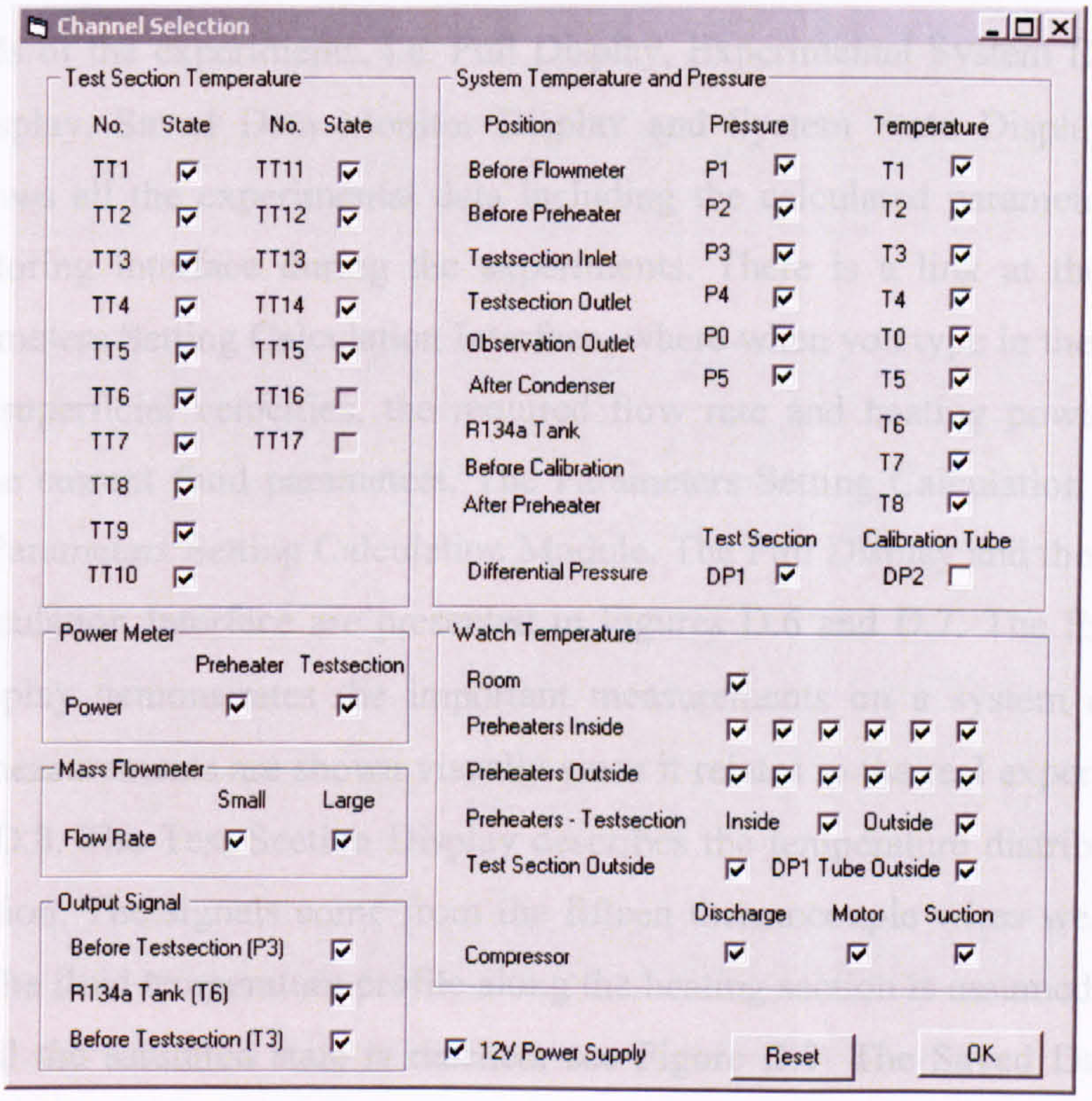

Test Section Temperature

No.	State	No.	State
TT1	☑	TT11	☑
TT2	☑	TT12	☑
TT3	☑	TT13	☑
TT4	☑	TT14	☑
TT5	☑	TT15	☑
TT6	☑	TT16	☐
TT7	☑	TT17	☐
TT8	☑		
TT9	☑		
TT10	☑		

System Temperature and Pressure

Position	Pressure	Temperature
Before Flowmeter	P1 ☑	T1 ☑
Before Preheater	P2 ☑	T2 ☑
Testsection Inlet	P3 ☑	T3 ☑
Testsection Outlet	P4 ☑	T4 ☑
Observation Outlet	P0 ☑	T0 ☑
After Condenser	P5 ☑	T5 ☑
R134a Tank		T6 ☑
Before Calibration		T7 ☑
After Preheater		T8 ☑
	Test Section	Calibration Tube
Differential Pressure	DP1 ☑	DP2 ☐

Power Meter

	Preheater	Testsection
Power	☑	☑

Mass Flowmeter

	Small	Large
Flow Rate	☑	☑

Output Signal

Before Testsection (P3) ☑

R134a Tank (T6) ☑

Before Testsection (T3) ☑

Watch Temperature

Room ☑

Preheaters Inside ☑ ☑ ☑ ☑ ☑ ☑

Preheaters Outside ☑ ☑ ☑ ☑ ☑ ☑

Preheaters - Testsection Inside ☑ Outside ☑

Test Section Outside ☑ DP1 Tube Outside ☑

	Discharge	Motor	Suction
Compressor	☑	☑	☑

☑ 12V Power Supply

Figure D.5 Measuring equipment selection interface.

(4) Main Measurement and Monitor Interface

The Main Measurement and Monitor Interface is supported by several modules, including Power Meter Communication, Data Loggers Communication, and Parameter Calibration and Calculation Module. The Power Meter Communication and Data Loggers Communication receive the digital single from the power meters and the data loggers, respectively. The Parameter Calibration and Calculation Module converts the original readings into the experimental parameters using the calibration equations, see Appendix F. It also calculates the fluid parameters (density, enthalpy, thermal loss, quality and superficial velocities). The Main Measurement and Monitor Interface can activate the Thermal Loss Calculation Interface. It also saves the experimental data into an Excel file and a Txt file. The Excel file is easily managed so that data processing can be done in a short time. The Txt file is a common format file and is accessible by other programs. In the current study, it is a bridge to the Data Analysing Program which is written in C# .net.

The Main Measurement and Monitor Interface includes five different interfaces based on the needs of the experiments, i.e. Full Display, Experimental System Display, Test Section Display, Saved Data Monitor Display and System State Display. The Full Display shows all the experimental data including the calculated parameters. It is the main monitoring interface during the experiments. There is a link at the bottom to access Parameters Setting Calculation Interface, where when you type in the desired gas and liquid superficial velocities, the required flow rate and heating power are given based on the current fluid parameters. The Parameters Setting Calculation Interface is backed by Parameters Setting Calculation Module. The Full Display and the Parameters Setting Calculation Interface are presented in Figures D.6 and D.7. The Experimental System Display demonstrates the important measurements on a system diagram, in which the measurements are shown visually since it relates to the real experimental rig, see Figure D.8. The Test Section Display describes the temperature distribution along the test section. The signals come from the fifteen thermocouple wires welded on the tube wall. The fluid temperature profile along the heating section is assumed to increase linearly until the saturated state is reached, see Figure D.9. The Saved Data Monitor Display is useful during saving the experimental data. It can exhibit twelve different group data on one screen. The saving process can be cancelled at any moment if one or a few data are different from the other readings for an obvious reason, see Figure D.10. The System State Display presents the key time dependent variation of the system parameters. It is helpful to ensure the system has reached steady state before saving the data, see Figure D.11.

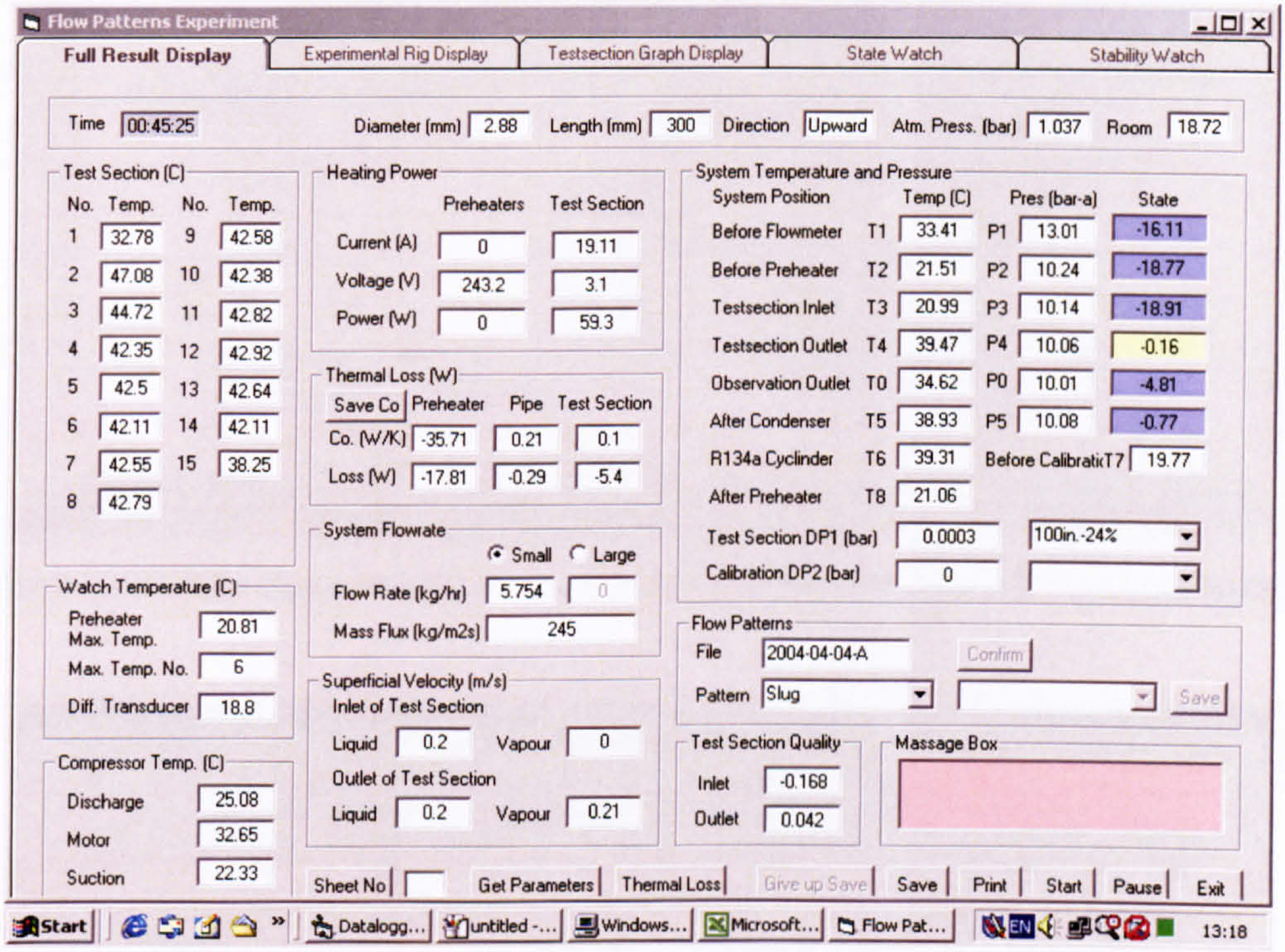

Time 00:45:25 Diameter (mm) 2.88 Length (mm) 300 Direction Upward Atm. Press. (bar) 1.037 Room 18.72

Test Section (C)

No.	Temp.	No.	Temp.
1	32.78	9	42.58
2	47.08	10	42.38
3	44.72	11	42.82
4	42.35	12	42.92
5	42.5	13	42.64
6	42.11	14	42.11
7	42.55	15	38.25
8	42.79		

Watch Temperature (C)

Preheater Max. Temp. 20.81
Max. Temp. No. 6
Diff. Transducer 18.8

Compressor Temp. (C)

Discharge 25.08
Motor 32.65
Suction 22.33

Heating Power

	Preheaters	Test Section
Current (A)	0	19.11
Voltage (V)	243.2	3.1
Power (W)	0	59.3

Thermal Loss (W)

	Preheater	Pipe	Test Section
Co. (W/K)	-35.71	0.21	0.1
Loss (W)	-17.81	-0.29	-5.4

System Flowrate

● Small ○ Large
Flow Rate (kg/hr) 5.754 0
Mass Flux (kg/m2s) 245

Superficial Velocity (m/s)

Inlet of Test Section
Liquid 0.2 Vapour 0
Outlet of Test Section
Liquid 0.2 Vapour 0.21

System Temperature and Pressure

System Position		Temp (C)		Pres (bar-a)	State
Before Flowmeter	T1	33.41	P1	13.01	-16.11
Before Preheater	T2	21.51	P2	10.24	-18.77
Testsection Inlet	T3	20.99	P3	10.14	-18.91
Testsection Outlet	T4	39.47	P4	10.06	-0.16
Observation Outlet	T0	34.62	P0	10.01	-4.81
After Condenser	T5	38.93	P5	10.08	-0.77
R134a Cyclinder	T6	39.31	Before CalibratiтT7	19.77	
After Preheater	T8	21.06			

Test Section DP1 (bar) 0.0003 100in.-24%
Calibration DP2 (bar) 0

Flow Patterns

File 2004-04-04-A
Pattern Slug

Test Section Quality

Inlet -0.168
Outlet 0.042

Massage Box

Figure D.6 Main measurement and monitor interface - full display.

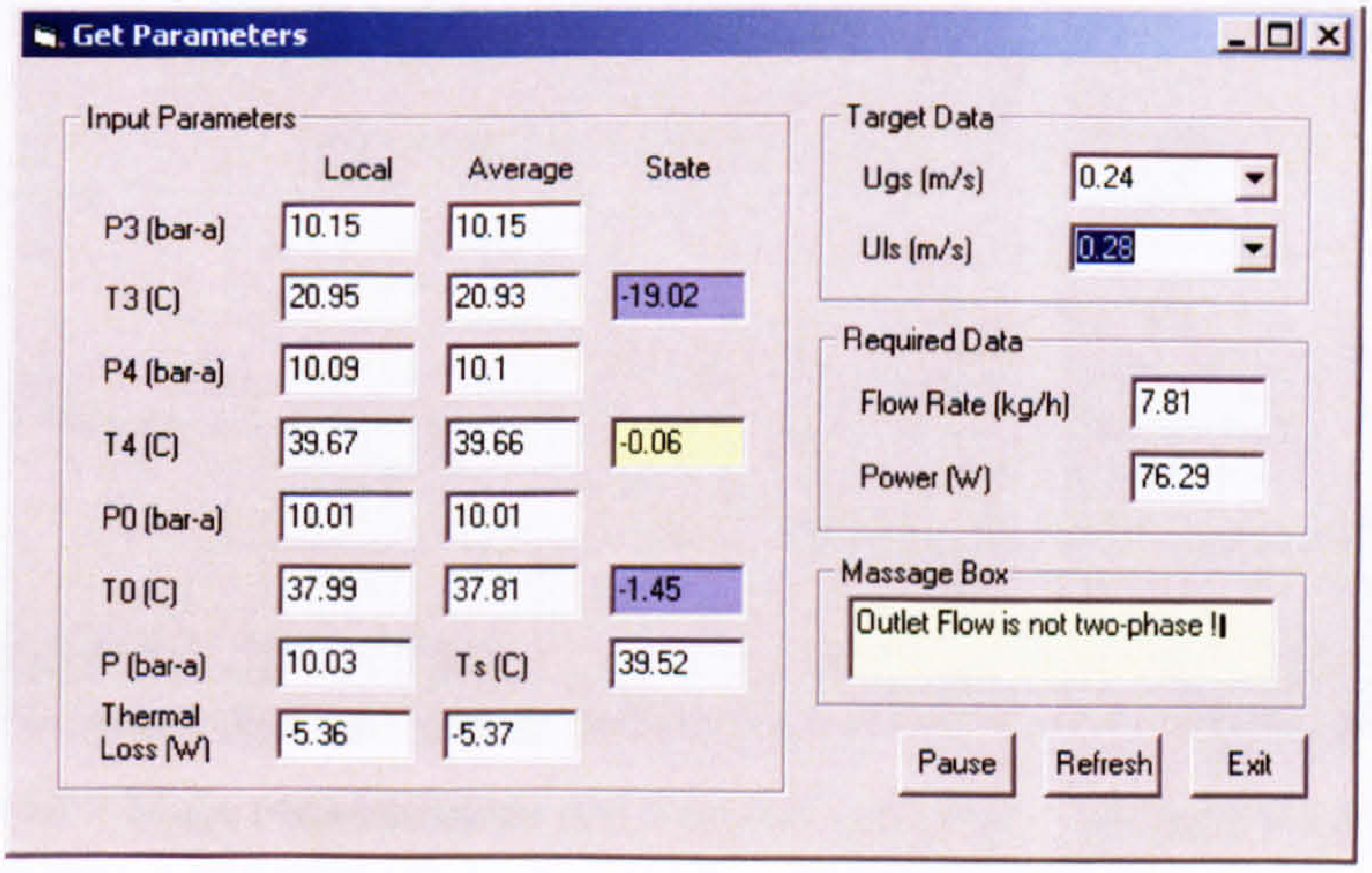

Input Parameters

	Local	Average	State
P3 (bar-a)	10.15	10.15	
T3 (C)	20.95	20.93	-19.02
P4 (bar-a)	10.09	10.1	
T4 (C)	39.67	39.66	-0.06
P0 (bar-a)	10.01	10.01	
T0 (C)	37.99	37.81	-1.45
P (bar-a)	10.03	Ts (C)	39.52
Thermal Loss (W)	-5.36	-5.37	

Target Data

Ugs (m/s) 0.24
Uls (m/s) 0.28

Required Data

Flow Rate (kg/h) 7.81
Power (W) 76.29

Massage Box

Outlet Flow is not two-phase !

Figure D.7 Parameters setting calculation interface.

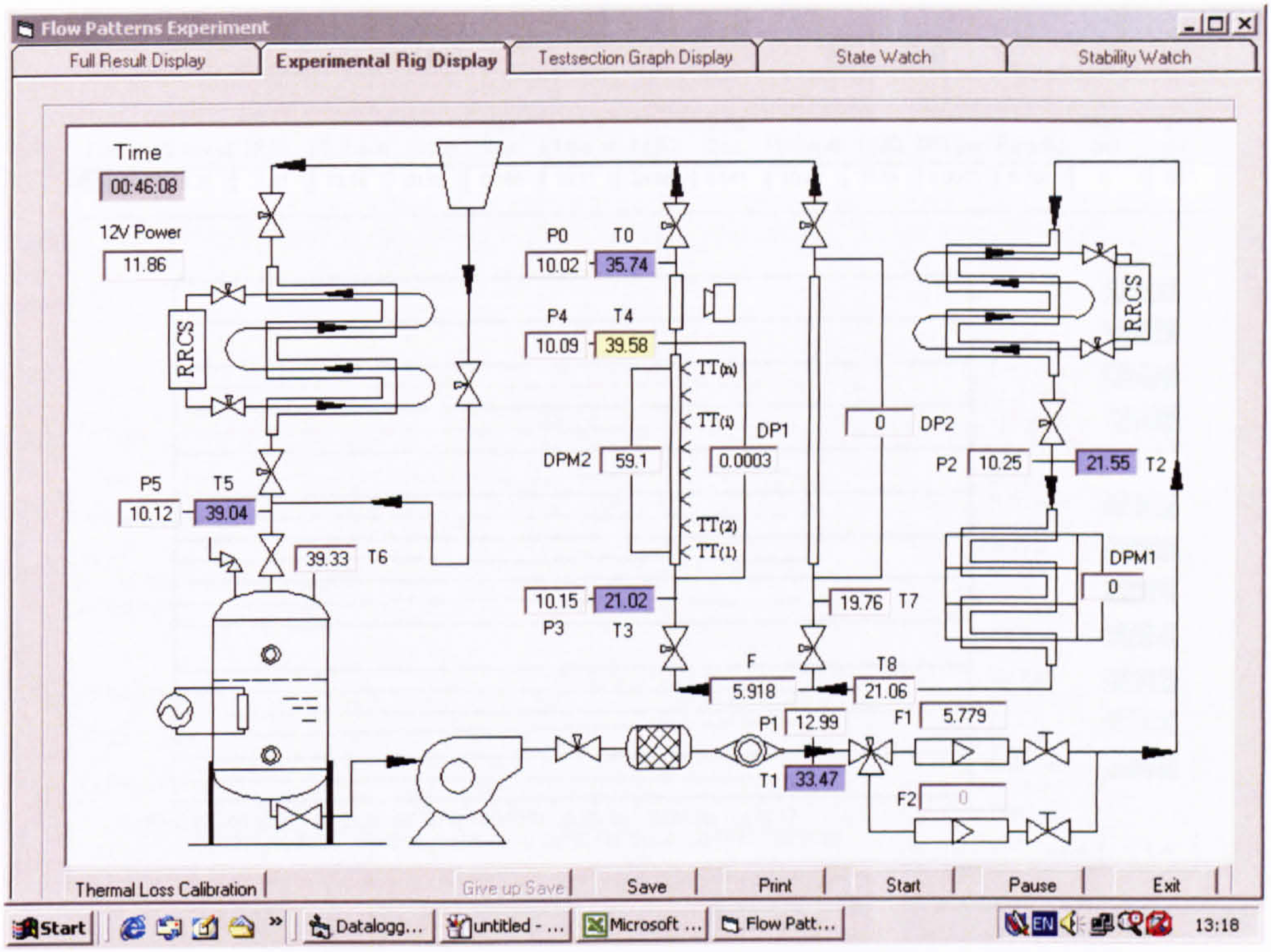

Time 00:46:08
12V Power 11.86
P0 10.02
T0 35.74
P4 10.09
T4 39.58
DPM2 59.1
DP1 0.0003
DP2 0
P2 10.25
T2 21.55
P5 10.12
T5 39.04
T6 39.33
P3 10.15
T3 21.02
T7 19.76
DPM1 0
F 5.918
T8 21.06
P1 12.99
F1 5.779
T1 33.47
F2 0

Figure D.8 Main measurement and monitor interface - experimental system display.

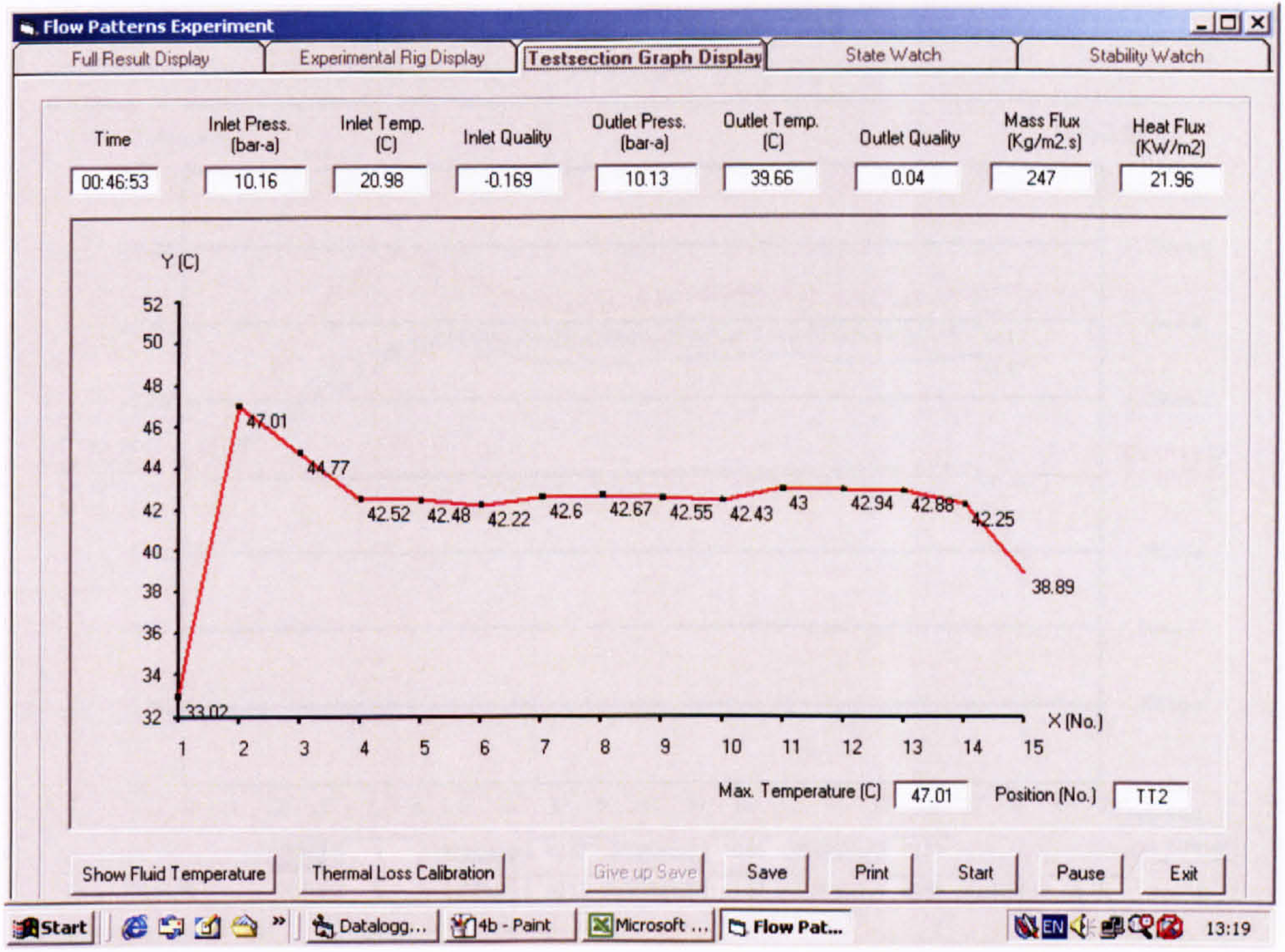

Time 00:46:53
Inlet Press. (bar-a) 10.16
Inlet Temp. (C) 20.98
Inlet Quality -0.169
Outlet Press. (bar-a) 10.13
Outlet Temp. (C) 39.66
Outlet Quality 0.04
Mass Flux (Kg/m2.s) 247
Heat Flux (KW/m2) 21.96

Max. Temperature (C) 47.01
Position (No.) TT2

Figure D.9 Main measurement and monitor interface - test section display.

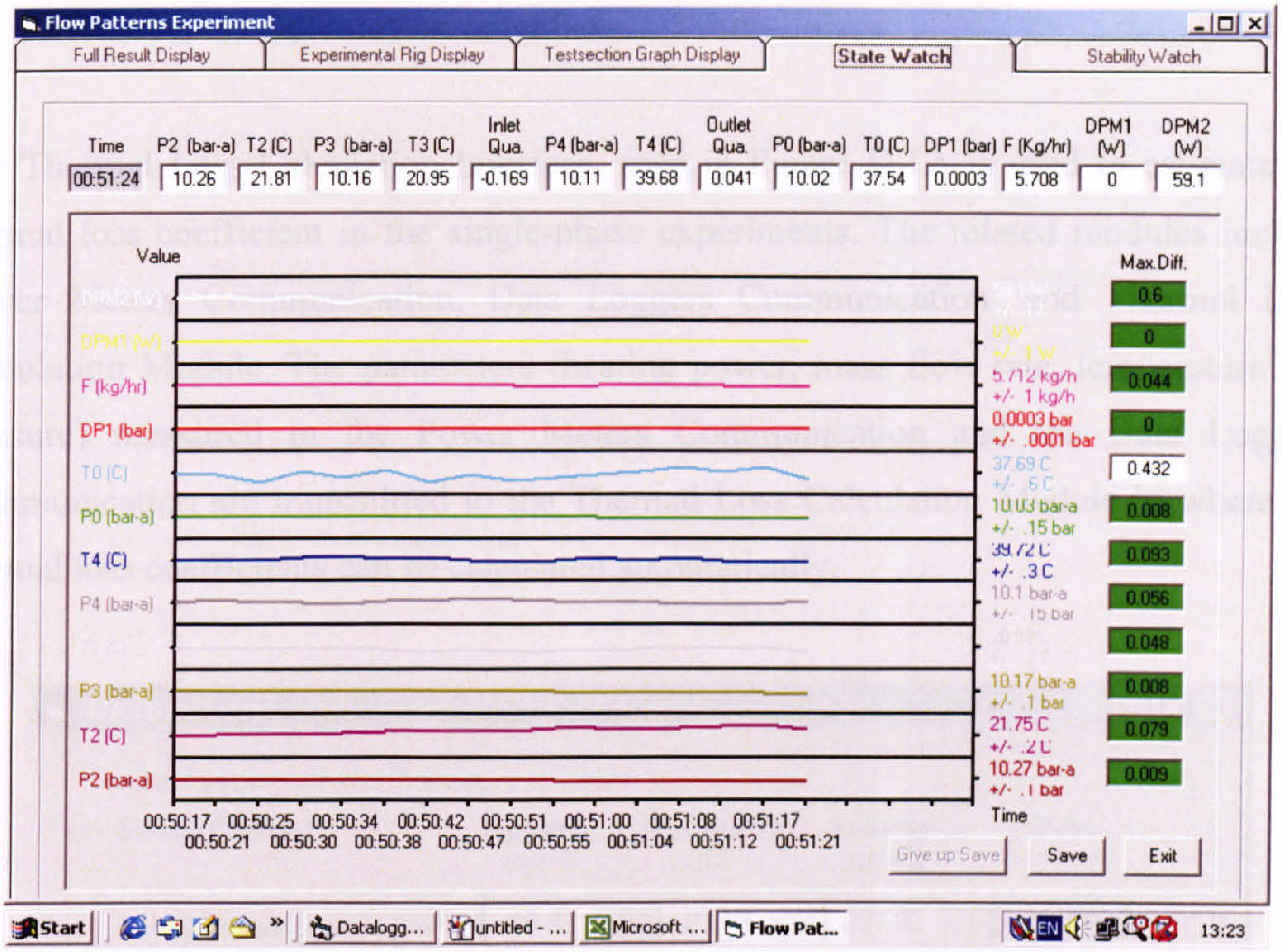

Time 00:51:24
P2 (bar-a) 10.26
T2 (C) 21.81
P3 (bar-a) 10.16
T3 (C) 20.95
Inlet Qua. -0.169
P4 (bar-a) 10.11
T4 (C) 39.68
Outlet Qua. 0.041
P0 (bar-a) 10.02
T0 (C) 37.54
DP1 (bar) 0.0003
F (Kg/hr) 5.708
DPM1 (W) 0
DPM2 (W) 59.1

Figure D.10 Main measurement and monitor interface – the saved data monitor display.

Time 00:44:05
DP 1
DT 5
P0 (bars-a) 10.57
P4 (bars-a) 10.66
P3 (bars-a) 10.72
T0 (C) 40.13
T4 (C) 41.57
T3 (C) 20.98
T2 (C) 25.12

Figure D.11 Main measurement and monitor interface – system state display.

(5) Thermal Loss Calculation Interface

The Thermal Loss Calculation Interface, seen in Figure D.12, is used to estimate the thermal loss coefficient in the single-phase experiments. The related modules include Power Meters Communication, Data Loggers Communication, and Thermal Loss Calculation Module. The parameters (heating power, mass flow rate, temperature and pressure) measured in the Power Meters Communication and the Data Loggers Communication are transmitted to the Thermal Loss Calculation Module in where the thermal loss coefficients can be calculated automatically.

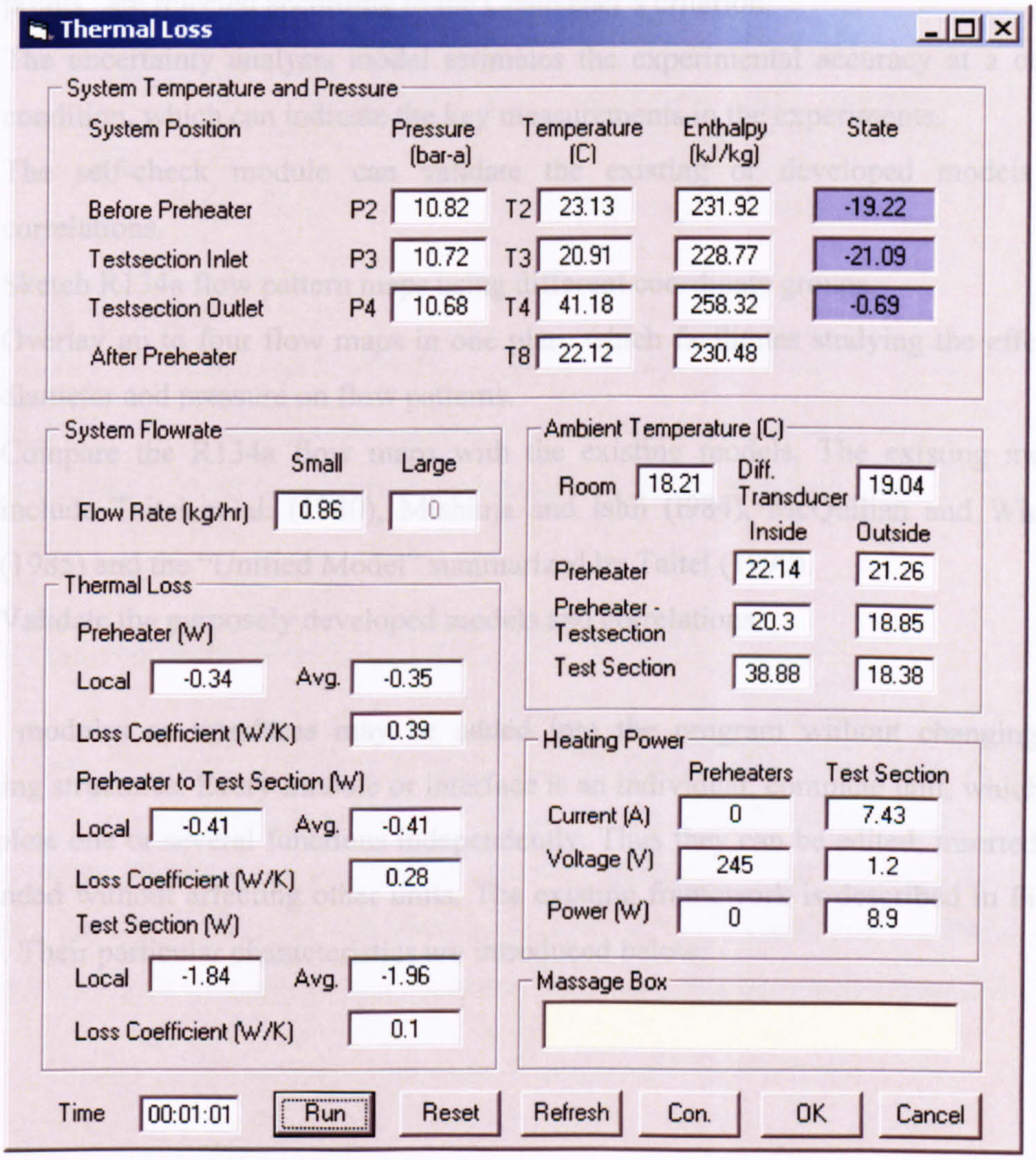

System Temperature and Pressure

System Position		Pressure (bar-a)		Temperature (C)	Enthalpy (kJ/kg)	State
Before Preheater	P2	10.82	T2	23.13	231.92	-19.22
Testsection Inlet	P3	10.72	T3	20.91	228.77	-21.09
Testsection Outlet	P4	10.68	T4	41.18	258.32	-0.69
After Preheater			T8	22.12	230.48	

System Flowrate

	Small	Large
Flow Rate (kg/hr)	0.86	0

Ambient Temperature (C)

Room 18.21

Diff. Transducer	Inside	Outside
		19.04
Preheater	22.14	21.26
Preheater - Testsection	20.3	18.85
Test Section	38.88	18.38

Thermal Loss

Preheater (W)

Local -0.34 Avg. -0.35

Loss Coefficient (W/K) 0.39

Preheater to Test Section (W)

Local -0.41 Avg. -0.41

Loss Coefficient (W/K) 0.28

Test Section (W)

Local -1.84 Avg. -1.96

Loss Coefficient (W/K) 0.1

Heating Power

	Preheaters	Test Section
Current (A)	0	7.43
Voltage (V)	245	1.2
Power (W)	0	8.9

Massage Box

Time 00:01:01

Figure D.12 Thermal loss calculation interface.

D.3 Data analysing program

The data analysing program was written in Visual C# on the platform of Visual Studio.net. It is a fully object oriented language. Comparing with Visual Basic 6.0, Visual C# is more effective, organizable and powerful. These advantages make for developing large, fast, complex and exigent commercial software. The existing developed functions in the data analysing program include:

(1) Calculation of R134a properties.
(2) Conversion of the original data into the experimental results, in which the "wild points" are rejected according to the Chauvenet's criterion.
(3) The uncertainty analysis model estimates the experimental accuracy at a certain condition, which can indicate the key measurements in the experiments.
(4) The self-check module can validate the existing or developed models and correlations.
(5) Sketch R134a flow pattern maps using different coordinate groups.
(6) Overlay up to four flow maps in one plan, which facilitates studying the effect of diameter and pressure on flow patterns.
(7) Compare the R134a flow maps with the existing models. The existing models include Taitel et al. (1980), Mishima and Ishii (1984), McQuilian and Whalley (1985) and the "Unified Model" summarized by Taitel (1990).
(8) Validate the purposely developed models and correlations.

New modules or interfaces may be added into the program without changing the existing structures. Every module or interface is an individual, complete unit, which can complete one or several functions independently. Thus they can be edited, inserted and expanded without affecting other units. The existing framework is described in Figure D.13. Their particular characteristics are introduced below:

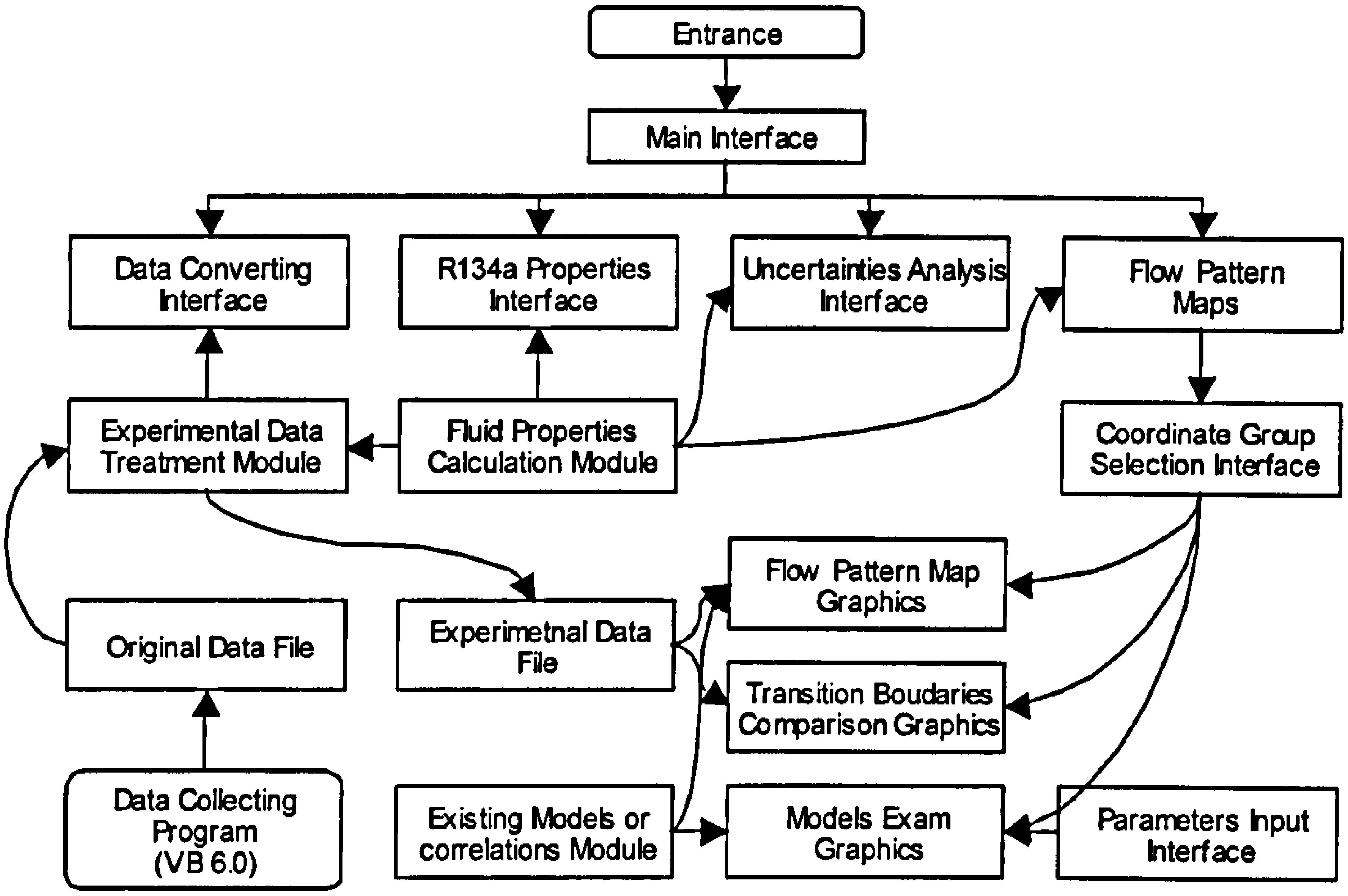

Figure D.13 Flow chart of the data analysing program.

(1) Main Interface

The Main Interface is the entrance of the program. Five menus lead to R134a Properties Interface, Data Converting Interface, Uncertainty Analysis Interface, Flow Pattern Map and Exit.

(2) R134a Properties Interface

The R134a Properties Interface is used for obtaining R134a properties. A second purpose is to check the correctness of Fluid Properties Calculation Module. In this interface, the R134a properties, i.e. the saturated temperature and pressure, fluid state, density, enthalpy, viscosity and surface tension, are calculated and exhibited after typing in the fluid temperature and pressure. This interface is shown in Figure D.14.

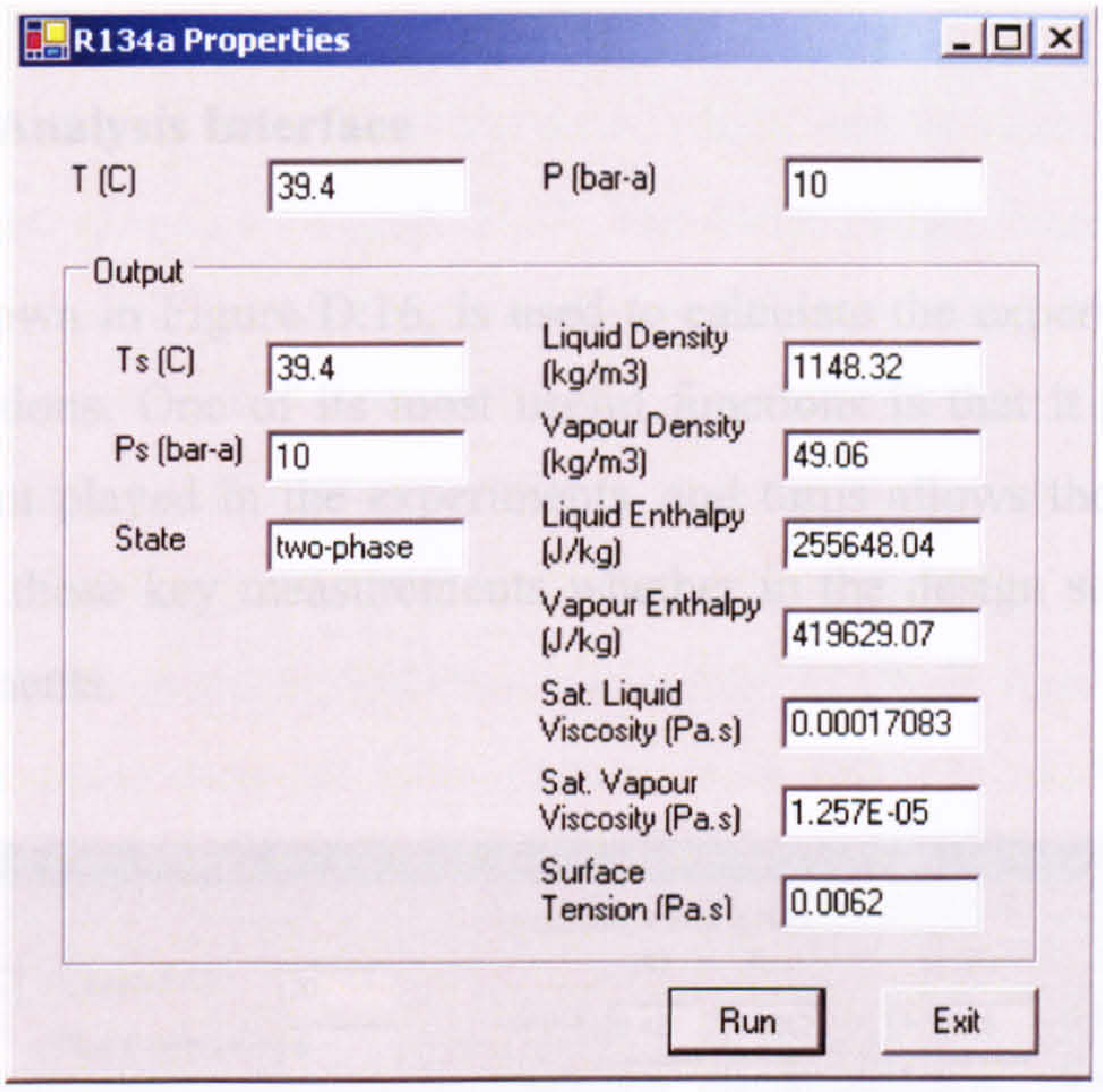

T (C) 39.4
P (bar-a) 10
Ts (C) 39.4
Ps (bar-a) 10
State two-phase
Liquid Density (kg/m3) 1148.32
Vapour Density (kg/m3) 49.06
Liquid Enthalpy (J/kg) 255648.04
Vapour Enthalpy (J/kg) 419629.07
Sat. Liquid Viscosity (Pa.s) 0.00017083
Sat. Vapour Viscosity (Pa.s) 1.257E-05
Surface Tension (Pa.s) 0.0062

Figure D.14 R134a properties interface.

(3) Data Converting Interface

The Data Converting Interface which is shown in Figure D.15 calls the Experimental Data Treatment Module to convert the original data into the experimental results. The original data and the calculated experimental results are presented here in order to inspect them in time.

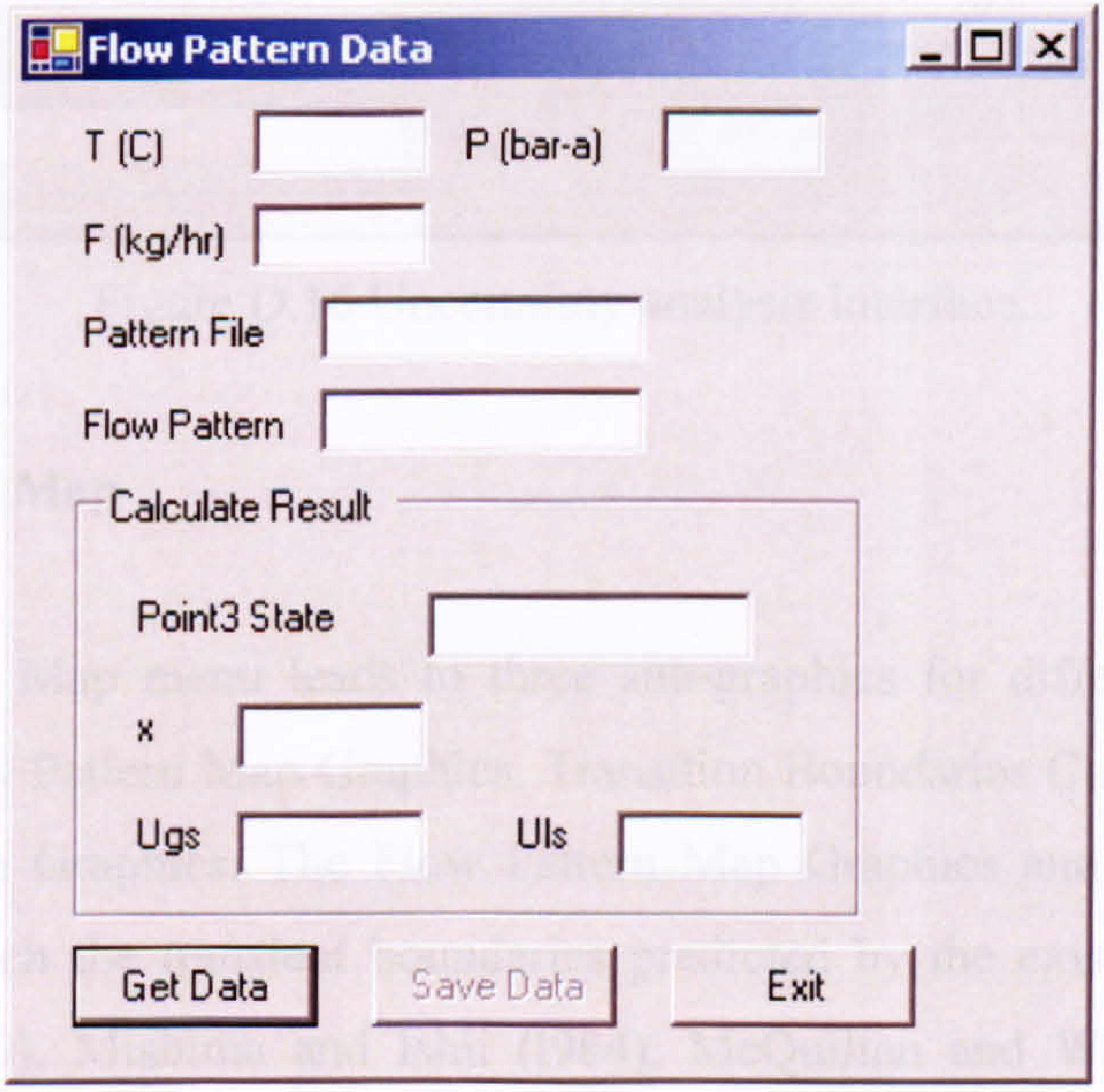

Figure D.15 Data converting interface.

(4) Uncertainty Analysis Interface

This interface, shown in Figure D.16, is used to calculate the experimental uncertainty at different conditions. One of its most useful functions is that it reveals the role of every measurement played in the experiments, and turns allows the researcher to pay more attention to those key measurements whether in the design stage, installation or during the experiments.

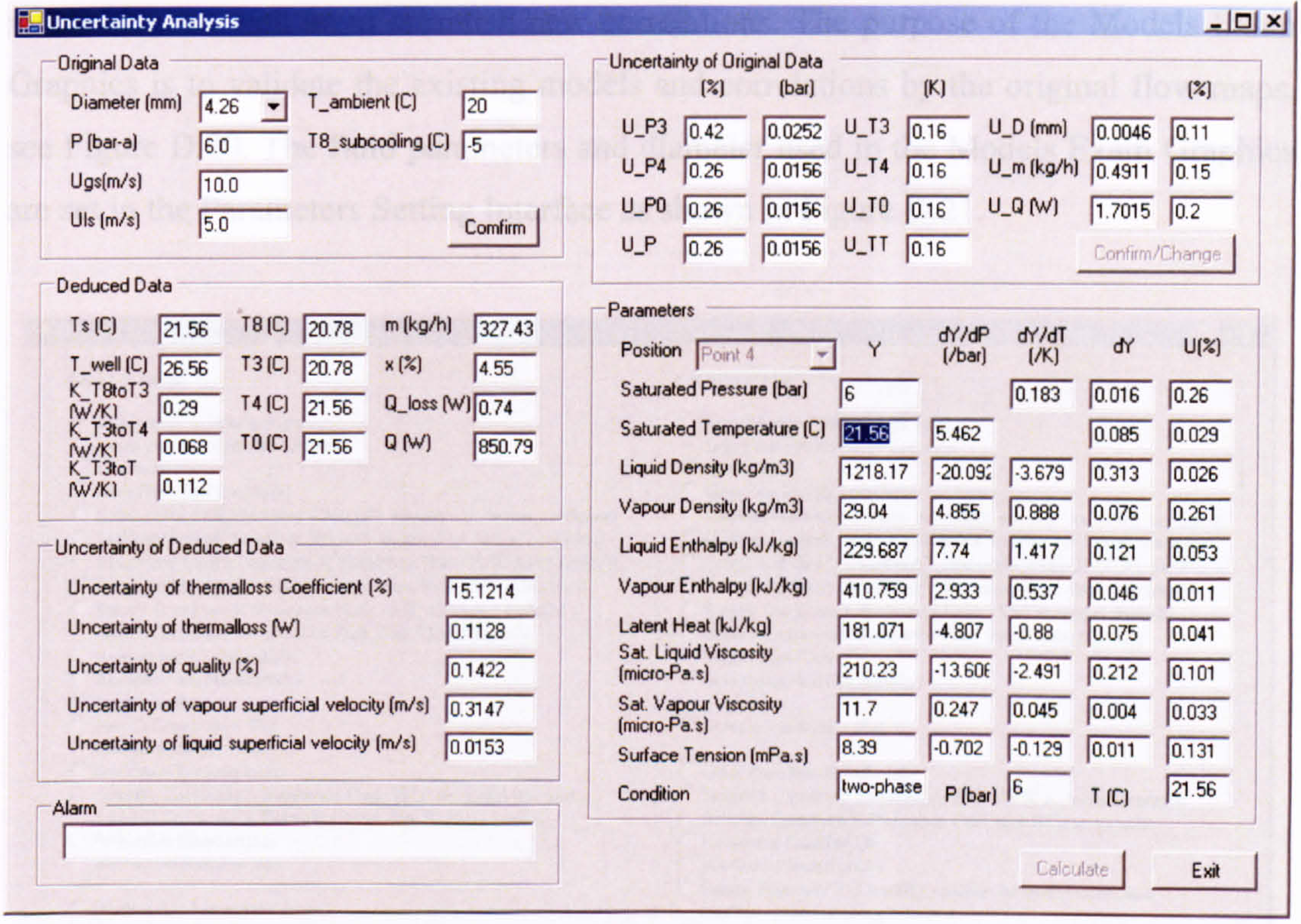

Original Data
Diameter (mm) 4.26
T_ambient (C) 20
P (bar-a) 6.0
T8_subcooling (C) -5
Ugs(m/s) 10.0
Uls (m/s) 5.0

Deduced Data

Ts (C)	21.56	T8 (C)	20.78	m (kg/h)	327.43
T_well (C)	26.56	T3 (C)	20.78	x (%)	4.55
K_T8toT3 (W/K)	0.29	T4 (C)	21.56	Q_loss (W)	0.74
K_T3toT4 (W/K)	0.068	T0 (C)	21.56	Q (W)	850.79
K_T3toT (W/K)	0.112				

Uncertainty of Deduced Data
Uncertainty of thermalloss Coefficient (%) 15.1214
Uncertainty of thermalloss (W) 0.1128
Uncertainty of quality (%) 0.1422
Uncertainty of vapour superficial velocity (m/s) 0.3147
Uncertainty of liquid superficial velocity (m/s) 0.0153

Uncertainty of Original Data

	(%)	(bar)		(K)			(%)
U_P3	0.42	0.0252	U_T3	0.16	U_D (mm)	0.0046	0.11
U_P4	0.26	0.0156	U_T4	0.16	U_m (kg/h)	0.4911	0.15
U_P0	0.26	0.0156	U_T0	0.16	U_Q (W)	1.7015	0.2
U_P	0.26	0.0156	U_TT	0.16			

Parameters

Position: Point 4	Y	dY/dP (/bar)	dY/dT (/K)	dY	U(%)
Saturated Pressure (bar)	6		0.183	0.016	0.26
Saturated Temperature (C)	21.56	5.462		0.085	0.029
Liquid Density (kg/m3)	1218.17	-20.092	-3.679	0.313	0.026
Vapour Density (kg/m3)	29.04	4.855	0.888	0.076	0.261
Liquid Enthalpy (kJ/kg)	229.687	7.74	1.417	0.121	0.053
Vapour Enthalpy (kJ/kg)	410.759	2.933	0.537	0.046	0.011
Latent Heat (kJ/kg)	181.071	-4.807	-0.88	0.075	0.041
Sat. Liquid Viscosity (micro-Pa.s)	210.23	-13.606	-2.491	0.212	0.101
Sat. Vapour Viscosity (micro-Pa.s)	11.7	0.247	0.045	0.004	0.033
Surface Tension (mPa.s)	8.39	-0.702	-0.129	0.011	0.131
Condition	two-phase	P (bar)	6	T (C)	21.56

Figure D.16 Uncertainty analysis interface.

(5) Flow Pattern Map

The Flow Pattern Map menu leads to three sub-graphics for different functions and purposes, i.e. Flow Pattern Map Graphics, Transition Boundaries Comparison Graphics and Models Exam Graphics. The Flow Pattern Map Graphics and the Models Exam Graphics can sketch the transient boundaries predicted by the existing modules from Taitel et al. (1980), Mishima and Ishii (1984), McQuilian and Whalley (1985), and Taitel (1990). The newly developed models and correlations can also be examined here.

The first step is to define the coordinate system, which includes the coordinate variables, coordinate scale and range, see Figure D.17. The Flow Pattern Map Graphics depicted in Figure D.18 draws a flow map based on the experimental data. The flow map can be sketched in different coordinate system. The most common coordinate group is the gas and liquid superficial velocities. The Transition Boundaries Comparison Graphics super imposes up to four flow maps in one map to show the shift of the transition boundaries at the different experimental conditions, see Figure D.19. It intuitively presents the effect of physical parameters on flow patterns and helps to analysis the transition mechanism as well as to establish new correlations. The purpose of the Models Exam Graphics is to validate the existing models and correlations by the original flow maps, see Figure D.20. The fluid parameters and diameter used in the Models Exam Graphics are set in the Parameters Setting Interface as shown in Figure D.21.

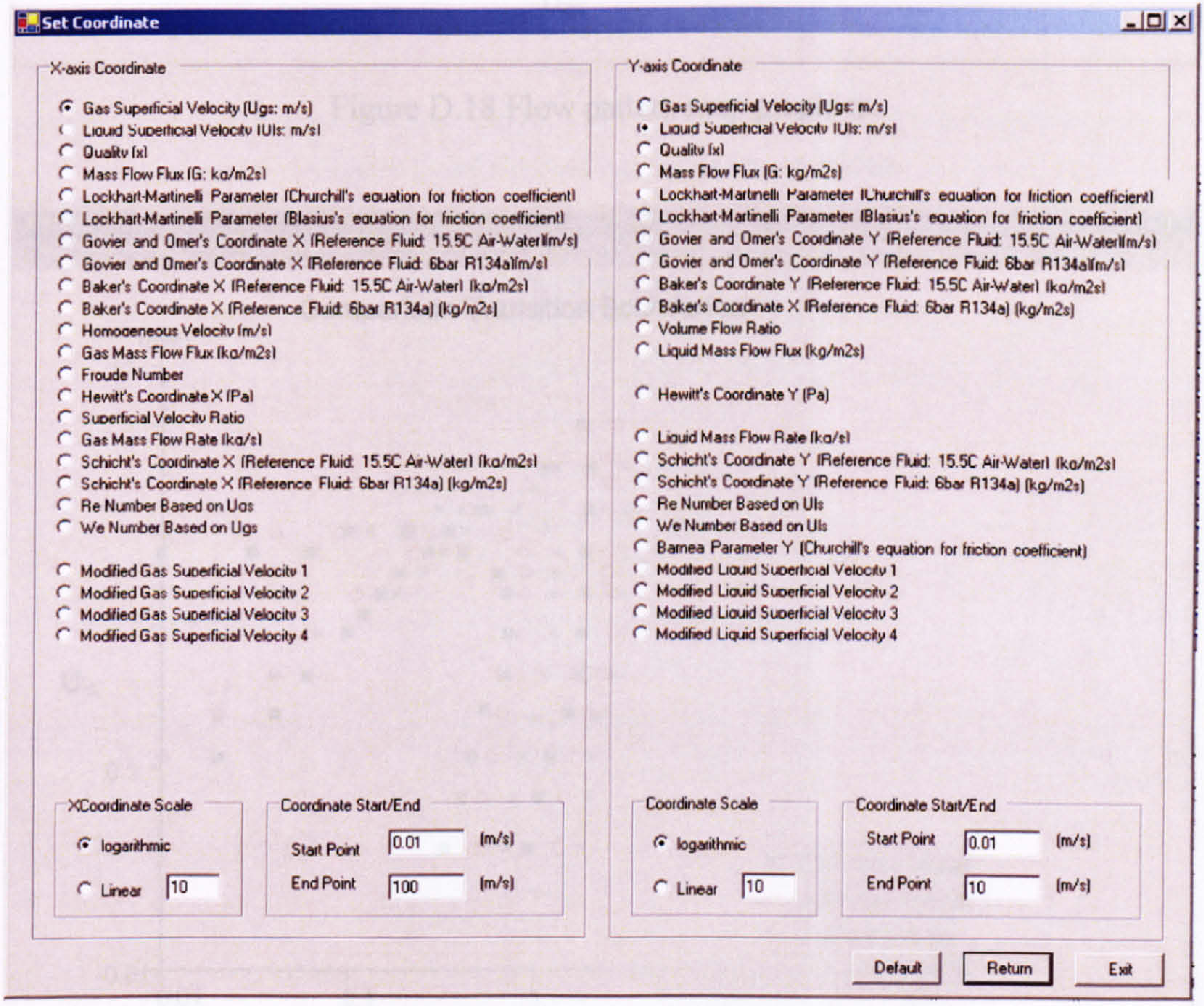

X-axis Coordinate

- ● Gas Superficial Velocity (Ugs: m/s)
- ○ Liquid Superficial Velocity (Uls: m/s)
- ○ Quality (x)
- ○ Mass Flow Flux (G: kg/m2s)
- ○ Lockhart-Martinelli Parameter (Churchill's equation for friction coefficient)
- ○ Lockhart-Martinelli Parameter (Blasius's equation for friction coefficient)
- ○ Govier and Omer's Coordinate X (Reference Fluid: 15.5C Air-Water)(m/s)
- ○ Govier and Omer's Coordinate X (Reference Fluid: 6bar R134a)(m/s)
- ○ Baker's Coordinate X (Reference Fluid: 15.5C Air-Water) (kg/m2s)
- ○ Baker's Coordinate X (Reference Fluid: 6bar R134a) (kg/m2s)
- ○ Homogeneous Velocity (m/s)
- ○ Gas Mass Flow Flux (kg/m2s)
- ○ Froude Number
- ○ Hewitt's Coordinate X (Pa)
- ○ Superficial Velocity Ratio
- ○ Gas Mass Flow Rate (kg/s)
- ○ Schicht's Coordinate X (Reference Fluid: 15.5C Air-Water) (kg/m2s)
- ○ Schicht's Coordinate X (Reference Fluid: 6bar R134a) (kg/m2s)
- ○ Re Number Based on Ugs
- ○ We Number Based on Ugs

- ○ Modified Gas Superficial Velocity 1
- ○ Modified Gas Superficial Velocity 2
- ○ Modified Gas Superficial Velocity 3
- ○ Modified Gas Superficial Velocity 4

XCoordinate Scale

● logarithmic

○ Linear 10

Coordinate Start/End

Start Point 0.01 (m/s)

End Point 100 (m/s)

Y-axis Coordinate

- ○ Gas Superficial Velocity (Ugs: m/s)
- ● Liquid Superficial Velocity (Uls: m/s)
- ○ Quality (x)
- ○ Mass Flow Flux (G: kg/m2s)
- ○ Lockhart-Martinelli Parameter (Churchill's equation for friction coefficient)
- ○ Lockhart-Martinelli Parameter (Blasius's equation for friction coefficient)
- ○ Govier and Omer's Coordinate Y (Reference Fluid: 15.5C Air-Water)(m/s)
- ○ Govier and Omer's Coordinate Y (Reference Fluid: 6bar R134a)(m/s)
- ○ Baker's Coordinate Y (Reference Fluid: 15.5C Air-Water) (kg/m2s)
- ○ Baker's Coordinate X (Reference Fluid: 6bar R134a) (kg/m2s)
- ○ Volume Flow Ratio
- ○ Liquid Mass Flow Flux (kg/m2s)

- ○ Hewitt's Coordinate Y (Pa)

- ○ Liquid Mass Flow Rate (kg/s)
- ○ Schicht's Coordinate Y (Reference Fluid: 15.5C Air-Water) (kg/m2s)
- ○ Schicht's Coordinate Y (Reference Fluid: 6bar R134a) (kg/m2s)
- ○ Re Number Based on Uls
- ○ We Number Based on Uls
- ○ Barnea Parameter Y (Churchill's equation for friction coefficient)
- ○ Modified Liquid Superficial Velocity 1
- ○ Modified Liquid Superficial Velocity 2
- ○ Modified Liquid Superficial Velocity 3
- ○ Modified Liquid Superficial Velocity 4

Coordinate Scale

● logarithmic

○ Linear 10

Coordinate Start/End

Start Point 0.01 (m/s)

End Point 10 (m/s)

Figure D.17 Coordinate system selection interface.

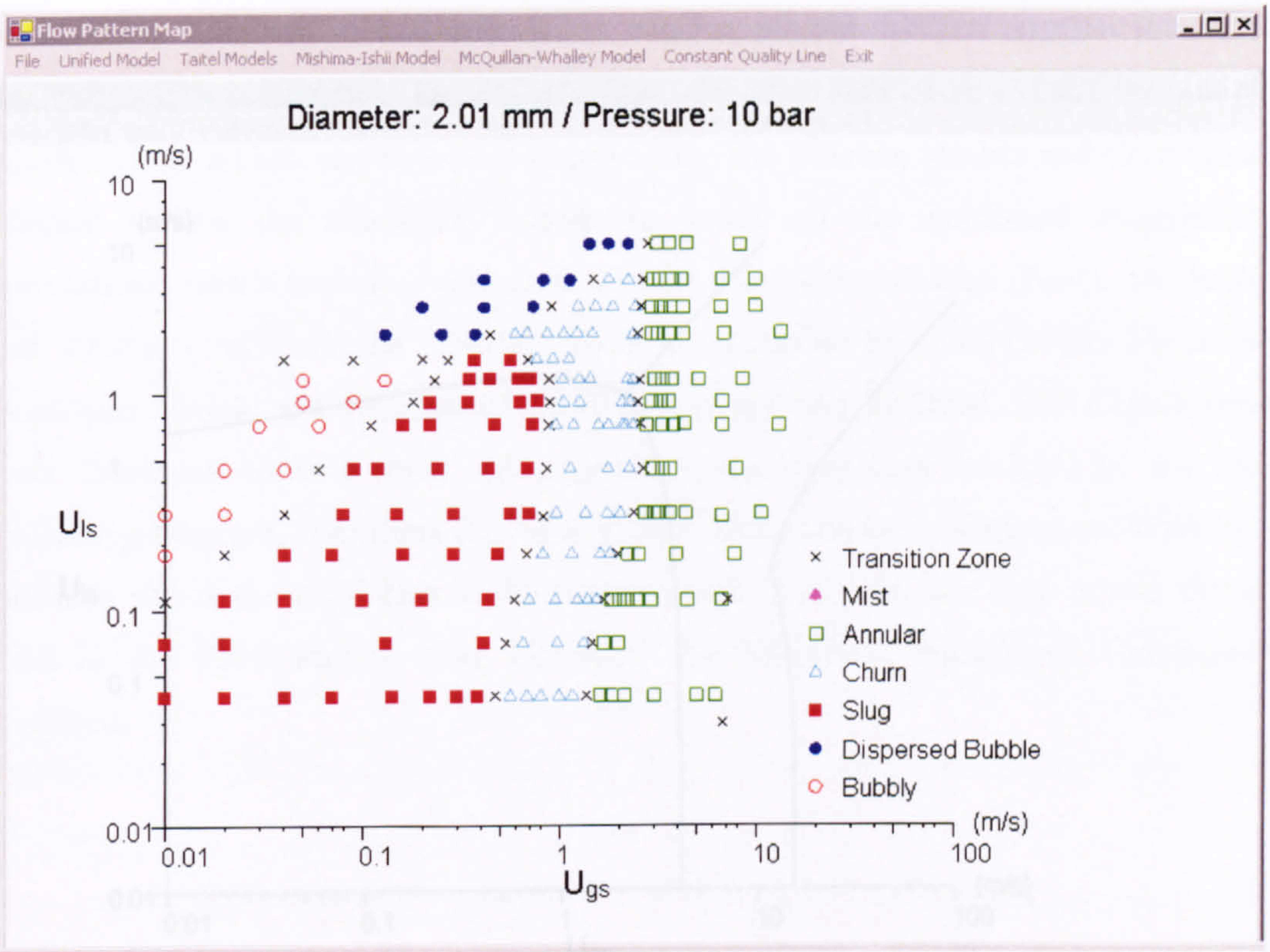

Figure D.18 Flow pattern map graphics.

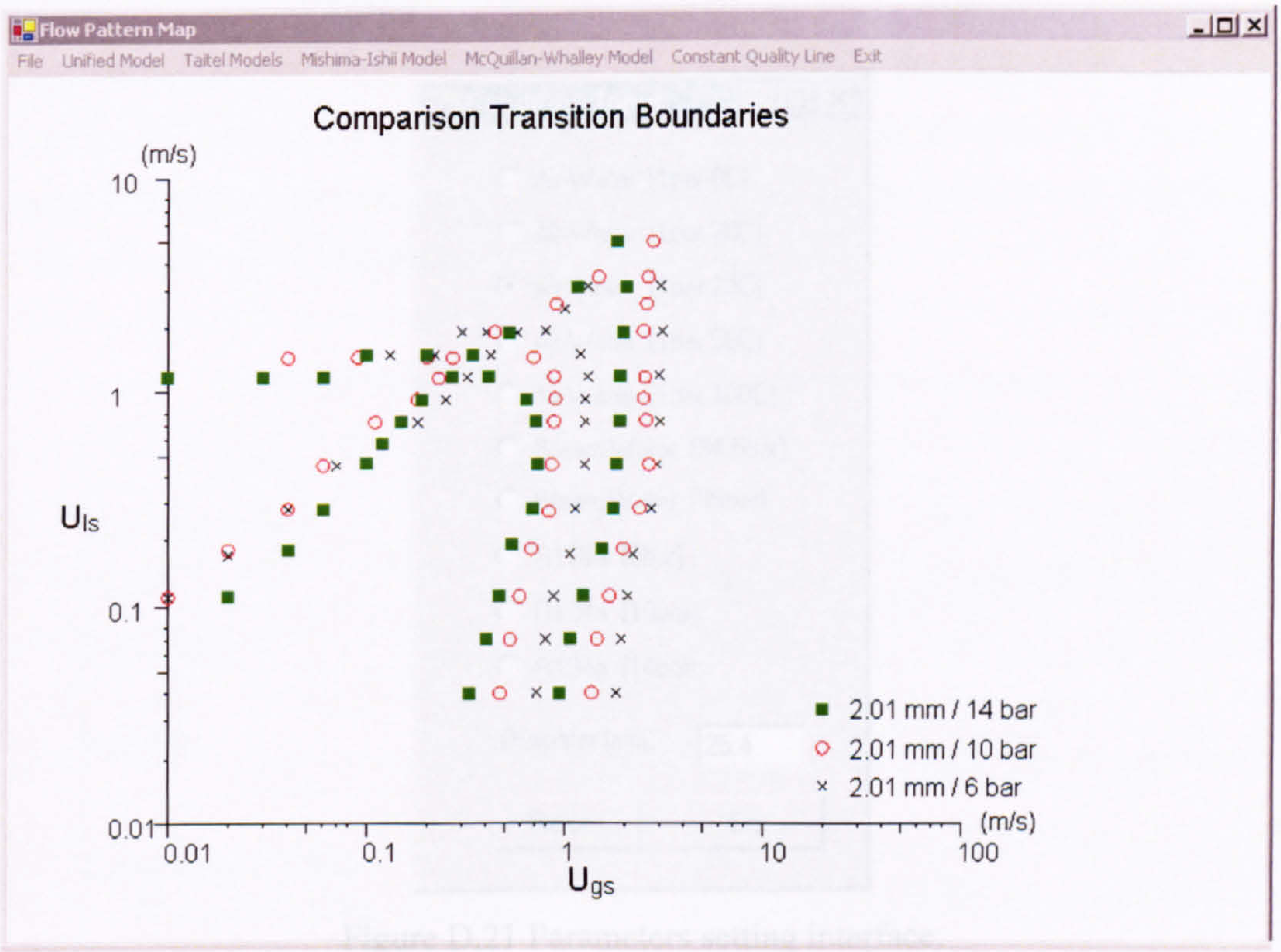

Figure D.19 Transition boundaries comparison graphics.

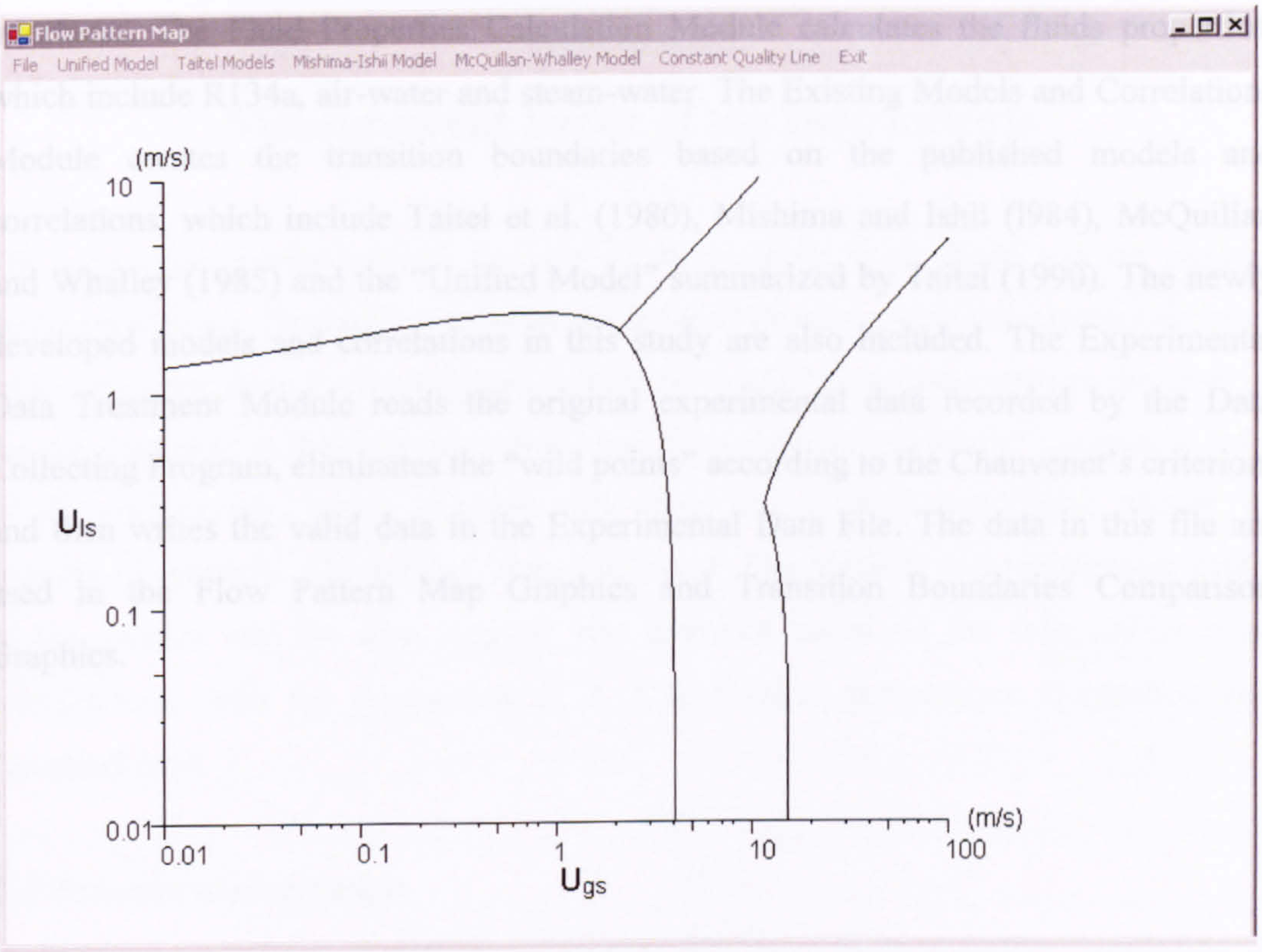

Figure D.20 Models examination graphics.

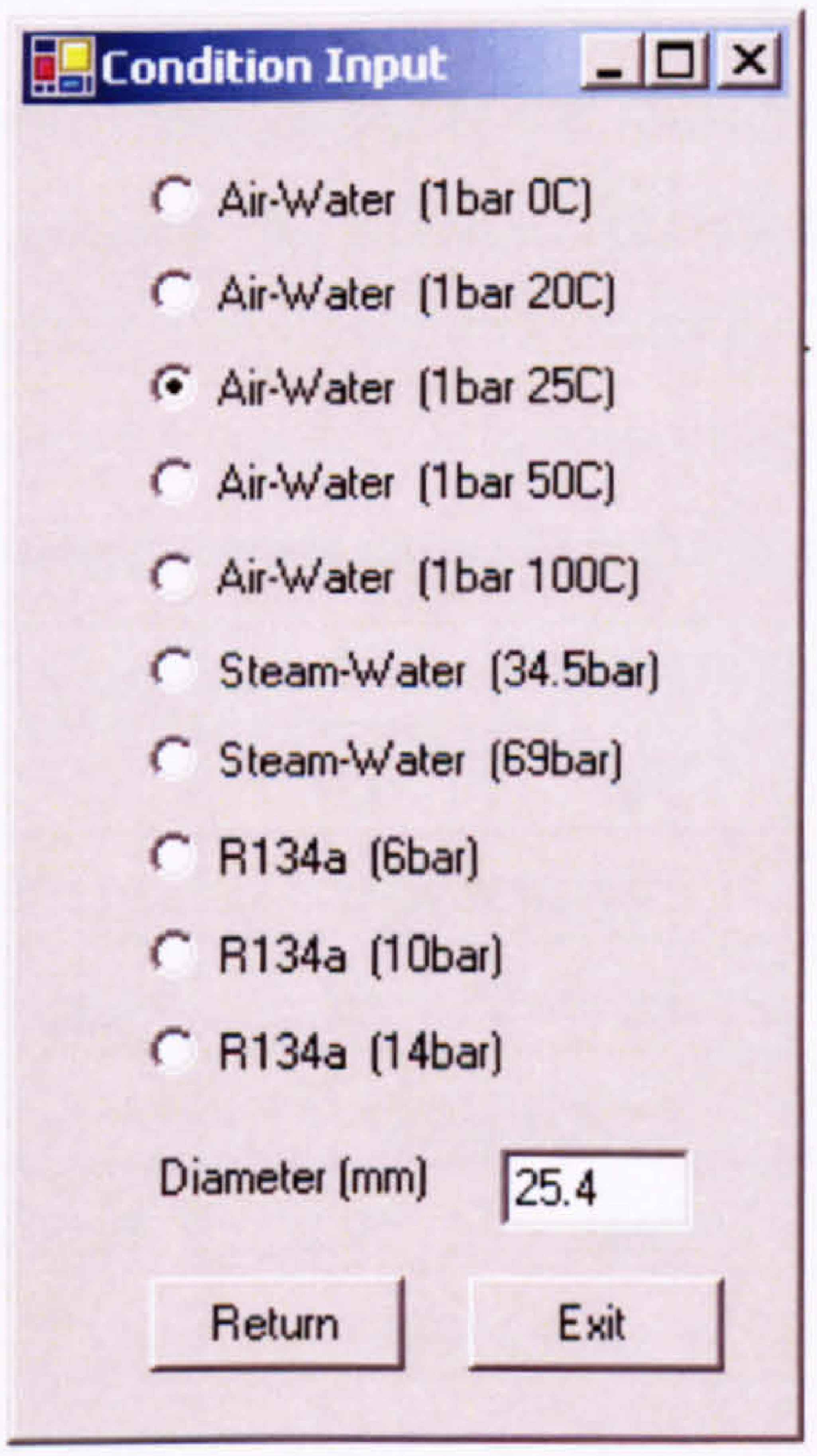

○ Air-Water (1bar 0C)
○ Air-Water (1bar 20C)
● Air-Water (1bar 25C)
○ Air-Water (1bar 50C)
○ Air-Water (1bar 100C)
○ Steam-Water (34.5bar)
○ Steam-Water (69bar)
○ R134a (6bar)
○ R134a (10bar)
○ R134a (14bar)

Diameter (mm) 25.4

Figure D.21 Parameters setting interface.

In addition, there are several calculation engines (or modules) to support the above interfaces. The Fluid Properties Calculation Module calculates the fluids properties, which include R134a, air-water and steam-water. The Existing Models and Correlations Module creates the transition boundaries based on the published models and correlations, which include Taitel et al. (1980), Mishima and Ishii (1984), McQuilian and Whalley (1985) and the "Unified Model" summarized by Taitel (1990). The newly developed models and correlations in this study are also included. The Experimental Data Treatment Module reads the original experimental data recorded by the Data Collecting Program, eliminates the "wild points" according to the Chauvenet's criterion, and then writes the valid data in the Experimental Data File. The data in this file are used in the Flow Pattern Map Graphics and Transition Boundaries Comparison Graphics.

Appendix E

Measurement Error of the Instruments

The total experimental error is the sum of the systemic error (bias) and the random errors (precision). The random error can be reduced by increasing measurement times or collecting more data. Calibration can reduce the "static" systematic error to the level of the standard used in the calibration procedure. However, the "dynamic" systematic error of the instruments, which changes with time and ambient conditions, should be considered properly. The typical "dynamic" error, like stability and temperature effect of the sensors and the data loggers, was analysed based on the information from manufactures with the assumption of ± 5 K ambient temperature fluctuation and discussed here.

E.1 Pressure measurement

Table E.1 analyses the stability and temperature effect of pressure sensors and the caused measurement error of pressure. The relative error is based on the minimum experimental pressure (6 bar), which produces the maximum relative error. P1 and P5 are not included in the table because the manufacturer did not provide such information in the technical specification.

Table E.1 Systematic error caused by the pressure sensors.

Item	Unit	Error			
Pressure sensor		P2	P3	P4	P0
Type		PDCR 4010		PDCR 910-0826	
Full scale	bar	10	20	10	10
Stability		0.1% F.S.		0.1 mV	
	bar	0.01	0.02	0.008	0.008
Temperature effect		0.03% F.S.		0.05% F.S.	
	bar	0.003	0.006	0.005	0.005
Systemic error	bar	0.010	0.021	0.009	0.009
Max. relative error		0.17%	0.35%	0.16%	0.16%

Table E.2 analyses the stability and temperature effect on the data logger and the resulting measurement error of pressure. The relative error is based on the minimum experimental pressure (6 bar), which produces the maximum relative error.

Table E.2 Systematic error caused by the data logger.

Item	Unit	Error					
Pressure sensor		P1	P2	P3	P4	P0	P5
Data logger		SI 3535F					
Scale	V	10	1	1	1	1	10
Stability		(0.005% rdg + 2 digits + 3 μV)/year					
		0.005% rdg + 203 μV	0.005% rdg + 23 μV				0.005% rdg + 203 μV
		0.02%	0.04%	0.07%	0.04%	0.04%	0.02%
Temperature effect		(0.001% rdg + 0.1 μV)/K					
		0.005% rdg + 0.5 μV					
		0.01%	0.01%	0.01%	0.01%	0.01%	0.01%
Systemic error		0.02%	0.04%	0.07%	0.04%	0.04%	0.02%

E.2 Thermocouples

Table E.3 analyses the stability and temperature effect on the data logger and the resulting error in temperature measurement. The relative error is based on the maximum experimental temperature of 52.5 °C, which produces the maximum absolute error. The more accurate results of T1, T5 and T6 cannot be given because the manufacturer does not provide the detailed information when using the CJC method. However, their error could be estimated by comparing the accuracy with a different reference method. For example, the measuring accuracy of the data logger is 0.50 K at the range of −30 – 110 °C for K-type thermocouple when using the water triple point as the reference temperature, while the accuracy at the CJC method is 0.93 K. Therefore, the extra error caused by the CJC method is about $\sqrt{0.93^2 - 0.5^2} = 0.78$ K. Considering the stability and the temperature effect of the data logger, about 0.08 K, the overall measuring error of T1, T5 and T6 caused by the data logger is 0.79 K.

Table E.3 Systematic error caused by the data logger.

Item	Unit	Error							
Data logger		SI 3535F				SI 35951E			
Thermocouple		T1	T2	T5	T6	T3	T4	T0	TT_{1-15}
Scale	mV		10			20	20	20	20
Stability			(0.005% rdg + 2 digits + 3μV)/year			(0.02% rdg + 5 μV)/year			
			0.005% rdg + 3.2 μV			0.02% rdg + 5 μV			
	K		0.083			0.136	0.136	0.136	0.136
Temperature effect			(0.001% rdg + 0.1 μV)/K			(0.0015% rdg + 0.2 μV)/K			
			0.005% rdg + 0.5 μV			0.0075% rdg + 1 μV			
	K		0.015			0.029	0.029	0.029	0.029
Systemic error	K	0.79	0.08	0.79	0.79	0.14	0.14	0.14	0.14

E.3 Coriolis mass flow meters

Table E.4 lists the stability and temperature effect on the data logger. The error is a function of the flow rate. The combined uncertainty at the different flow rate is summarized in Table E.5.

Table E.4 Systematic error caused by the data logger in the mass flow rate measurement.

Item	Unit	Error	
Mass flow meter		CMF010	CMF025
Measurement range	kg/hr	0-25	25-500
Data logger		SI 3535F	
Scale	V	10	10
Stability		(0.005% rdg + 2 digits + 3 μV)/year	(0.005% rdg + 2 digits + 3 μV)/year
	kg/hr	0.005% rdg + 0.0006343	0.005% rdg + 0.01269
Temperature effect		(0.001% rdg + 0.1 μV)/K	(0.001% rdg + 0.1 μV)/K
	kg/hr	0.005% rdg + 0.00000156	0.005% rdg + 0.00003125

Table E.5 Combined uncertainty of the flow rate measurement.

CMF010								
Flow rate (kg/hr)	0.50	2.95	5.40	7.85	10.30	12.75	15.20	25.00
Mass flow meter	0.51%	0.17%	0.14%	0.13%	0.12%	0.12%	0.11%	0.11%
Resistor	0.10%	0.10%	0.10%	0.10%	0.10%	0.10%	0.10%	0.10%
Data logger stability	0.005% rdg + 0.0006343 kg/hr							
	0.132%	0.027%	0.017%	0.013%	0.011%	0.010%	0.009%	0.008%
Data logger temperature effect	0.005% rdg + 0.00000156 kg/hr							
	0.005%	0.005%	0.005%	0.005%	0.005%	0.005%	0.005%	0.005%
Combined uncertainty	0.54%	0.20%	0.17%	0.16%	0.16%	0.16%	0.15%	0.15%
CMF025								
Flow rate (kg/hr)	29.5	54.0	78.5	103.0	127.5	176.5	201.0	>250
Mass flow meter	0.19%	0.15%	0.13%	0.13%	0.12%	0.12%	0.11%	0.11%
Resistor	0.10%	0.10%	0.10%	0.10%	0.10%	0.10%	0.10%	0.10%
Data logger stability	0.005% rdg + 0.01269 kg/hr							
	0.048%	0.029%	0.021%	0.017%	0.015%	0.012%	0.011%	0.010%
Data logger temperature effect	0.005% rdg + 0.00003125 kg/hr							
	0.005%	0.005%	0.005%	0.005%	0.005%	0.005%	0.005%	0.005%
Combined uncertainty	0.22%	0.18%	0.17%	0.17%	0.16%	0.16%	0.15%	0.15%

E.4 Power meters

Table E.6 gives the combined uncertainty considering the effect of the current transformer and the power meter, which covers widely experimental conditions, i.e. 0-6560 W heating power and the 1.10-4.26 mm tubes with the resistance of 0.107-0.164 Ω.

Table E.6 Combined uncertainty of the power measurement.

Items	Unit	Error					
Current via the heating section	A	5	5	20	20	200	200
Resistance of the heating section	Ω	0.107	0.164	0.107	0.164	0.107	0.164
Heating power	W	2.68	4.10	42.8	65.6	4280	6560
Current transformer convert ratio		2.5%	2.5%	2.5%	2.5%	2.5%	2.5%
Current transformer uncertainty		0.4%	0.4%	0.2%	0.2%	0.1%	0.1%
Range of the power meter	W	7.5	7.5	7.5	7.5	150.0	300.0
Reading of the power meter	W	0.067	0.103	1.070	1.640	107.0	164.0
Power meter uncertainty		0.25% rdg + 0.1% rng					
		0.29%	0.19%	0.02%	0.02%	0.01%	0.01%
Combined uncertainty		0.49%	0.44%	0.20%	0.20%	0.10%	0.10%

E.5 Differential pressure transmitter

The error associated with the sensor and the data logger includes the accuracy, stability, temperature effect and power supply effect. The calculation results are given in Table E.7 and E.8 for 24% and 100% scale, respectively.

Table E.7 Systematic error caused by the sensor.

Item	Unit	Error	
Type		PX771-100WDI	
Full scale		24%	100%
	bar	0.0608	0.2491
Accuracy (linearity, hysteresis and repeatability)		0.15% F.S.	0.15% F.S.
	Pa	9.1	37.4
Stability (regulated every six months)		0.25% F.S.	0.25% F.S.
	Pa	15.2	62.3
Temperature effect (based on +/- 5 K temperature fluctuation)		0.00135% F.S.	0.00135% F.S.
	Pa	0.1	0.3
Power supply effect (based on +/- 0.2V fluctuation)		0.001% F.S.	0.001% F.S.
	Pa	0.1	0.2
Systemic error	Pa	17.7	72.6

Table E.8 Systematic error caused by the data logger.

Item	Unit		
Type		PX771-100WDI	
Full scale		24%	100%
	bar	0.06082	0.24909
Data logger		SI 3535F	
Scale	V	10	
Stability		(0.005% rdg + 2 digits + 3 µV)/year	
		0.005% rdg + 203 µV	
	Pa	0.5	1.8
Temperature effect		(0.001% rdg + 0.1 µV)/K	
		0.005% rdg + 0.5 µV	
	Pa	0.3	1.2
Systemic error	Pa	0.6	2.2

E.6 Thermal loss and associated uncertainty

Thermal loss coefficients of the heating sections and their uncertainty are summarized in Table E.9. The Thermal loss of the test sections and their uncertainty are summarized in Table E.10.

Table E.9 Thermal loss coefficients and their uncertainty (the heating section part).

Item	Unit	Data			
Inside Diameter	mm	1.10	2.01	2.88	4.26
Test pressure	bar	14.0	14.0	14.0	14.0
Flow rate	kg/hr	0.52	0.97	1.30	2.03
Inlet temperature	°C	48.15	33.20	39.93	39.10
Outlet temperature	°C	43.82	31.9	38.6	37.6
Average steel well temperature	°C	42.82	32.55	37.32	38.35
Average ambient temperature	°C	23.16	19.6	20.97	19.8
Uncertainty of flow rate		0.54%	0.54%	0.54%	0.54%
Uncertainty of temperature difference	K	0.165	0.165	0.165	0.165
Thermal loss coefficient	W/K	0.048	0.040	0.044	0.068
Uncertainty of thermal loss coefficient		5.32%	17.46%	17.05%	15.11%

Table E.10 Thermal loss and the uncertainty.

Items	Unit	Data											
Inside Diameter	mm	1.10			2.01			2.88			4.26		
Test pressure	bar	6.0	10.0	14.0	6.0	10.0	14.0	6.0	10.0	14.0	6.0	10.0	14.0
Temperature difference at the insulation	$^{\circ}$C	6.56	24.40	37.45	6.56	24.40	37.45	6.56	24.40	37.45	6.56	24.40	37.45
Uncertainty of temperature difference	K	0.165	0.165	0.165	0.165	0.165	0.165	0.165	0.165	0.165	0.165	0.165	0.165
Uncertainty of thermal loss coefficient		5.3%	5.3%	5.3%	17.5%	17.5%	17.5%	17.1%	17.1%	17.1%	15.1%	15.1%	15.1%
Heating section													
Length	mm	150	150	150	211	211	211	300	300	300	500	500	500
Thermal loss coefficient	W/K	0.048	0.048	0.048	0.040	0.040	0.040	0.044	0.044	0.044	0.068	0.068	0.068
Thermal loss	W	0.31	1.17	1.80	0.26	0.98	1.50	0.29	1.07	1.65	0.45	1.66	2.55
Uncertainty of thermal loss	W	0.02	0.06	0.10	0.05	0.17	0.26	0.05	0.18	0.28	0.07	0.25	0.39
Heating section + part observation section													
Length	mm	319	319	319	454	454	454	705	705	705	825	825	825
Thermal loss coefficient	W/K	0.102	0.102	0.102	0.086	0.086	0.086	0.103	0.103	0.103	0.112	0.112	0.112
Thermal loss	W	0.67	2.49	3.82	0.56	2.10	3.22	0.68	2.52	3.87	0.74	2.74	4.20
Uncertainty of thermal loss	W	0.039	0.134	0.204	0.100	0.367	0.563	0.117	0.431	0.660	0.113	0.414	0.635

Appendix F

Instruments Calibration Results

Appendix F summarizes the calibration results of all the instruments of the experimental facility, including pressure transducers/transmitters, thermocouple probes/wires, mass flow meters and differential pressure transmitters. Based on the calibration results the best-fit equations were obtained and presented in this appendix for all instruments.

All pressure transducers and transmitters were calibrated by a dead weight tester (Barnet Instrument Ltd, Series No 310/62, accuracy 0.1%). The test range (0-300 psi, i.e. 0-20.68 bar) covers the proposed experimental pressures (6, 10 and 14 bar). Every instrument was tested twice at each test point. The first test was carried out with increasing pressure and the second test with decreasing pressure in order to reduce the effect of the dead zone of the tester. The average pressures were used as the final results. The calibration data and the best-fit equation for each pressure transducer/transmitter are presented in Tables F.1-F.6 and Figures F.1-F.6 respectively. The best-fit equations and its error for all pressure transducers/transmitters are summarized in Table F.7.

All the thermocouples were calibrated in a temperature calibration equipment with the range of –20 to 80 °C. Table F.8 and Figure F.7 show the calibration data and the deduced best-fit equation for the platinum resistance thermometer in the calibration equipment. The measurement error of the platinum resistance is analysed and presented in Tables F.9 and F.10. The thermocouples T1, T5 and T6 used the CJC method. The signal was converted into temperature in the data logger directly. The thermocouples T2, T3, T4, T0 and TT1-15 used the triple-phase point of water as the reference point. The output signal of the data logger was voltage and was converted into temperature using the best-fit equations. In order to improve the test accuracy, 3-5 groups of data were read at each test point. The average temperatures were used as the final results. The calibration data and the best-fit equation for each thermocouple are presented in Tables F.11-F.18 and Figures F.8-F.15 respectively. The best-fit equations and the error for all thermocouples are summarized in Table F.19.

The mass flow meters were calibrated by the manufacturer and tested and reset by the manufacturer on the site after installation. The best-fit equations were deduced based on the test data and the measurement error was provided by the manufacturer, see Table F.20.

The differential pressure transmitter was calibrated through measuring the water level difference at both sides of the transmitter. Two linear best-fit equations, corresponding to 24% and 100% scale range respectively, were obtained from the test results. The calibration data and the best-fit equations are presented in Tables F.21-F.22 and Figures F.16-F.17. The calibration results are summarized in Table F.23.

F.1 Pressure transducers/transmitters

Table F.1 The calibration data for the pressure transmitter P1.

Pressure		Meas. 1	Meas. 2	Ave. value	Pressure (best-fit equation, bar)			Error (bar / %)					
Psi	bar(g)	V	V	V	Meas. 1	Meas. 2	Ave. value	Meas. 1		Meas. 2		Ave. value	
0	0.00	2.0116	2.0093	2.0105	0.007	-0.005	0.001	0.0065		-0.0049		0.0008	
10	0.69	2.1503	2.1485	2.1494	0.695	0.686	0.691	0.0059	0.85%	-0.0031	-0.44%	0.0014	0.20%
20	1.38	2.2866	2.2865	2.2866	1.372	1.372	1.372	-0.0067	-0.48%	-0.0072	-0.52%	-0.0069	-0.50%
40	2.76	2.5650	2.5648	2.5649	2.755	2.754	2.754	-0.0030	-0.11%	-0.0040	-0.14%	-0.0035	-0.13%
60	4.14	2.8426	2.8426	2.8426	4.134	4.134	4.134	-0.0033	-0.08%	-0.0033	-0.08%	-0.0033	-0.08%
80	5.52	3.1204	3.1212	3.1208	5.513	5.517	5.515	-0.0026	-0.05%	0.0014	0.03%	-0.0006	-0.01%
100	6.89	3.3980	3.3989	3.3985	6.892	6.896	6.894	-0.0029	-0.04%	0.0016	0.02%	-0.0006	-0.01%
120	8.27	3.6759	3.6773	3.6766	8.272	8.279	8.276	-0.0017	-0.02%	0.0053	0.06%	0.0018	0.02%
140	9.65	3.9545	3.9553	3.9549	9.656	9.660	9.658	0.0030	0.03%	0.0070	0.07%	0.0050	0.05%
160	11.03	4.2327	4.2326	4.2327	11.037	11.037	11.037	0.0057	0.05%	0.0052	0.05%	0.0055	0.05%
180	12.41	4.5097	4.5106	4.5102	12.413	12.417	12.415	0.0024	0.02%	0.0069	0.06%	0.0047	0.04%
200	13.79	4.7868	4.7888	4.7878	13.789	13.799	13.794	-0.0003	0.00%	0.0096	0.07%	0.0046	0.03%
220	15.17	5.0641	5.0667	5.0654	15.166	15.179	15.173	-0.0021	-0.01%	0.0108	0.07%	0.0043	0.03%
240	16.55	5.3424	5.3429	5.3427	16.548	16.551	16.550	0.0011	0.01%	0.0036	0.02%	0.0023	0.01%
260	17.93	5.6191	5.6209	5.6200	17.923	17.932	17.927	-0.0037	-0.02%	0.0052	0.03%	0.0008	0.00%
280	19.31	5.8966	5.8975	5.8971	19.301	19.305	19.303	-0.0045	-0.02%	0.0000	0.00%	-0.0022	-0.01%
290	19.99	6.0335	6.0335	6.0335	19.981	19.981	19.981	-0.0141	-0.07%	-0.0141	-0.07%	-0.0141	-0.07%

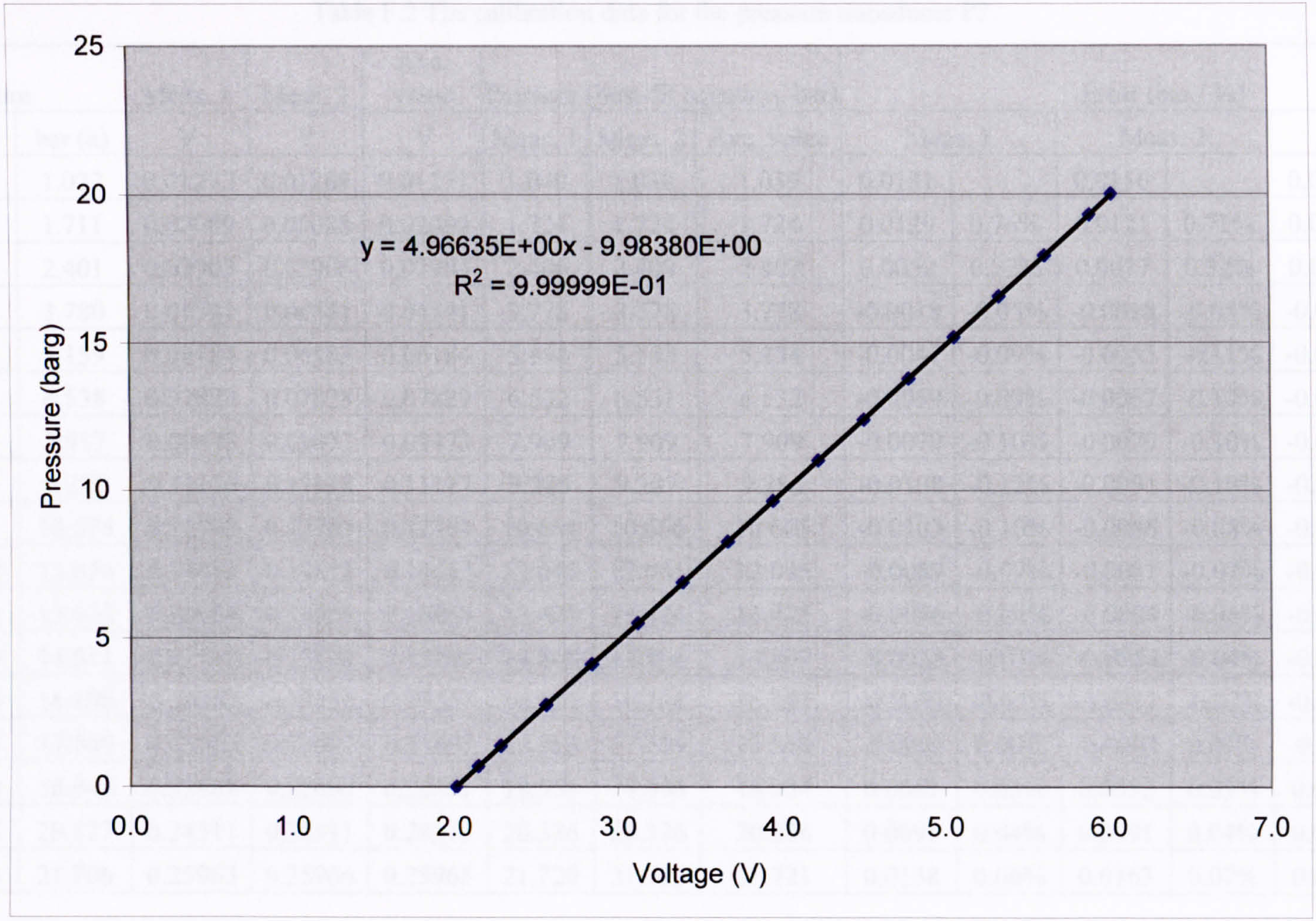

Figure F.1 The best-fit equation for the pressure transmitter P1.

Table F.2 The calibration data for the pressure transducer P2.

Pressure			Meas. 1	Meas. 2	Ave. value	Pressure (best-fit equation, bar)			Error (bar / %)					
Psi	bar (g)	bar (a)	V	V	V	Meas. 1	Meas. 2	Ave. value	Meas. 1		Meas. 2		Ave. value	
0	0.000	1.022	0.01272	0.01269	0.01271	1.040	1.038	1.039	0.0181		0.0156		0.0169	
10	0.689	1.711	0.02089	0.02088	0.02089	1.724	1.724	1.724	0.0129	0.76%	0.0121	0.71%	0.0125	0.73%
20	1.379	2.401	0.02903	0.02906	0.02905	2.406	2.409	2.407	0.0052	0.22%	0.0077	0.32%	0.0065	0.27%
40	2.758	3.780	0.04541	0.04541	0.04541	3.778	3.778	3.778	-0.0018	-0.05%	-0.0018	-0.05%	-0.0018	-0.05%
60	4.137	5.159	0.06184	0.06183	0.06184	5.154	5.153	5.154	-0.0047	-0.09%	-0.0055	-0.11%	-0.0051	-0.10%
80	5.516	6.538	0.07829	0.07828	0.07829	6.532	6.531	6.532	-0.0059	-0.09%	-0.0067	-0.10%	-0.0063	-0.10%
100	6.895	7.917	0.09473	0.09473	0.09473	7.909	7.909	7.909	-0.0079	-0.10%	-0.0079	-0.10%	-0.0079	-0.10%
120	8.274	9.296	0.11116	0.11118	0.11117	9.285	9.287	9.286	-0.0108	-0.12%	-0.0091	-0.10%	-0.0099	-0.11%
140	9.653	10.675	0.12763	0.12765	0.12764	10.664	10.666	10.665	-0.0103	-0.10%	-0.0086	-0.08%	-0.0094	-0.09%
160	11.032	12.054	0.14411	0.14412	0.14412	12.045	12.045	12.045	-0.0089	-0.07%	-0.0081	-0.07%	-0.0085	-0.07%
180	12.411	13.433	0.16059	0.16058	0.16059	13.425	13.424	13.425	-0.0076	-0.06%	-0.0084	-0.06%	-0.0080	-0.06%
200	13.789	14.811	0.17710	0.17708	0.17709	14.808	14.806	14.807	-0.0038	-0.03%	-0.0054	-0.04%	-0.0046	-0.03%
220	15.168	16.190	0.19357	0.19356	0.19357	16.187	16.186	16.187	-0.0033	-0.02%	-0.0041	-0.03%	-0.0037	-0.02%
240	16.547	17.569	0.21007	0.21007	0.21007	17.569	17.569	17.569	-0.0003	0.00%	-0.0003	0.00%	-0.0003	0.00%
260	17.926	18.948	0.22661	0.22660	0.22661	18.954	18.954	18.954	0.0061	0.03%	0.0052	0.03%	0.0057	0.03%
280	19.305	20.327	0.24311	0.24311	0.24311	20.336	20.336	20.336	0.0091	0.04%	0.0091	0.04%	0.0091	0.04%
300	20.684	21.706	0.25963	0.25966	0.25965	21.720	21.723	21.721	0.0138	0.06%	0.0163	0.07%	0.0150	0.07%

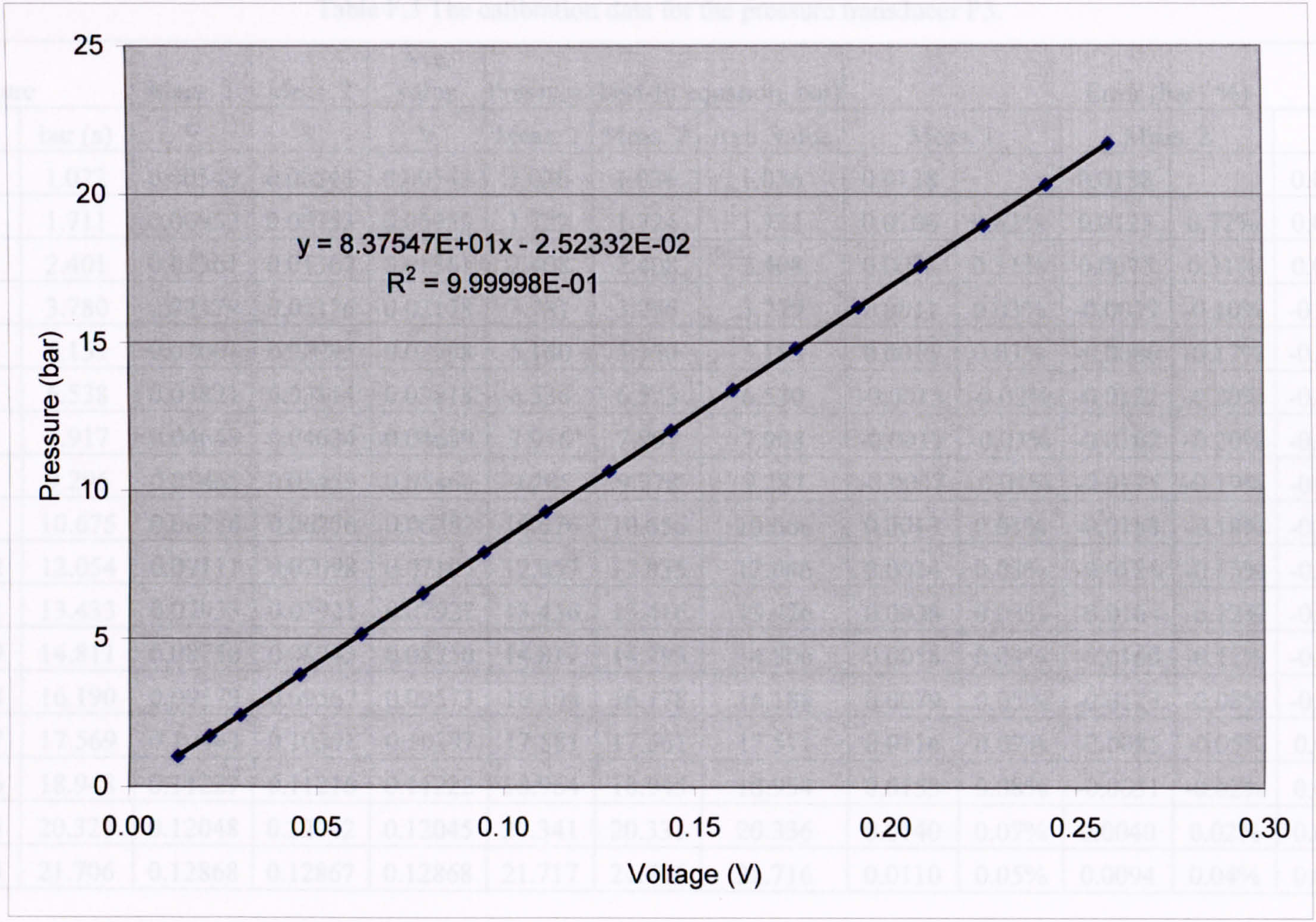

Figure F.2 The best-fit equation for the pressure transducer P2.

Table F.3 The calibration data for the pressure transducer P3.

Pressure			Meas. 1	Meas. 2	Ave. value	Pressure (best-fit equation, bar)			Error (bar / %)					
Psi	bar(g)	bar (a)	V	V	V	Meas. 1	Meas. 2	Ave. value	Meas. 1		Meas. 2		Ave. value	
0	0.000	1.022	0.00543	0.00543	0.00543	1.036	1.036	1.036	0.0138		0.0138		0.0138	
10	0.689	1.711	0.00952	0.00953	0.00953	1.722	1.724	1.723	0.0106	0.62%	0.0123	0.72%	0.0115	0.67%
20	1.379	2.401	0.01361	0.01361	0.01361	2.408	2.408	2.408	0.0075	0.31%	0.0075	0.31%	0.0075	0.31%
40	2.758	3.780	0.02179	0.02176	0.02178	3.781	3.776	3.779	0.0011	0.03%	-0.0039	-0.10%	-0.0014	-0.04%
60	4.137	5.159	0.03001	0.02995	0.02998	5.160	5.150	5.155	0.0015	0.03%	-0.0086	-0.17%	-0.0035	-0.07%
80	5.516	6.538	0.03821	0.03814	0.03818	6.536	6.525	6.530	-0.0015	-0.02%	-0.0132	-0.20%	-0.0074	-0.11%
100	6.895	7.917	0.04643	0.04634	0.04639	7.916	7.901	7.908	-0.0011	-0.01%	-0.0162	-0.20%	-0.0087	-0.11%
120	8.274	9.296	0.05465	0.05455	0.05460	9.295	9.278	9.287	-0.0007	-0.01%	-0.0175	-0.19%	-0.0091	-0.10%
140	9.653	10.675	0.06288	0.06276	0.06282	10.676	10.656	10.666	0.0013	0.01%	-0.0188	-0.18%	-0.0087	-0.08%
160	11.032	12.054	0.07111	0.07098	0.07105	12.057	12.035	12.046	0.0034	0.03%	-0.0184	-0.15%	-0.0075	-0.06%
180	12.411	13.433	0.07933	0.07921	0.07927	13.436	13.416	13.426	0.0038	0.03%	-0.0164	-0.12%	-0.0063	-0.05%
200	13.789	14.811	0.08756	0.08743	0.08750	14.817	14.795	14.806	0.0058	0.04%	-0.0160	-0.11%	-0.0051	-0.03%
220	15.168	16.190	0.09579	0.09567	0.09573	16.198	16.178	16.188	0.0079	0.05%	-0.0123	-0.08%	-0.0022	-0.01%
240	16.547	17.569	0.10403	0.10391	0.10397	17.581	17.561	17.571	0.0116	0.07%	-0.0085	-0.05%	0.0015	0.01%
260	17.926	18.948	0.11227	0.11216	0.11222	18.964	18.945	18.954	0.0153	0.08%	-0.0031	-0.02%	0.0061	0.03%
280	19.305	20.327	0.12048	0.12042	0.12045	20.341	20.331	20.336	0.0140	0.07%	0.0040	0.02%	0.0090	0.04%
300	20.684	21.706	0.12868	0.12867	0.12868	21.717	21.716	21.716	0.0110	0.05%	0.0094	0.04%	0.0102	0.05%

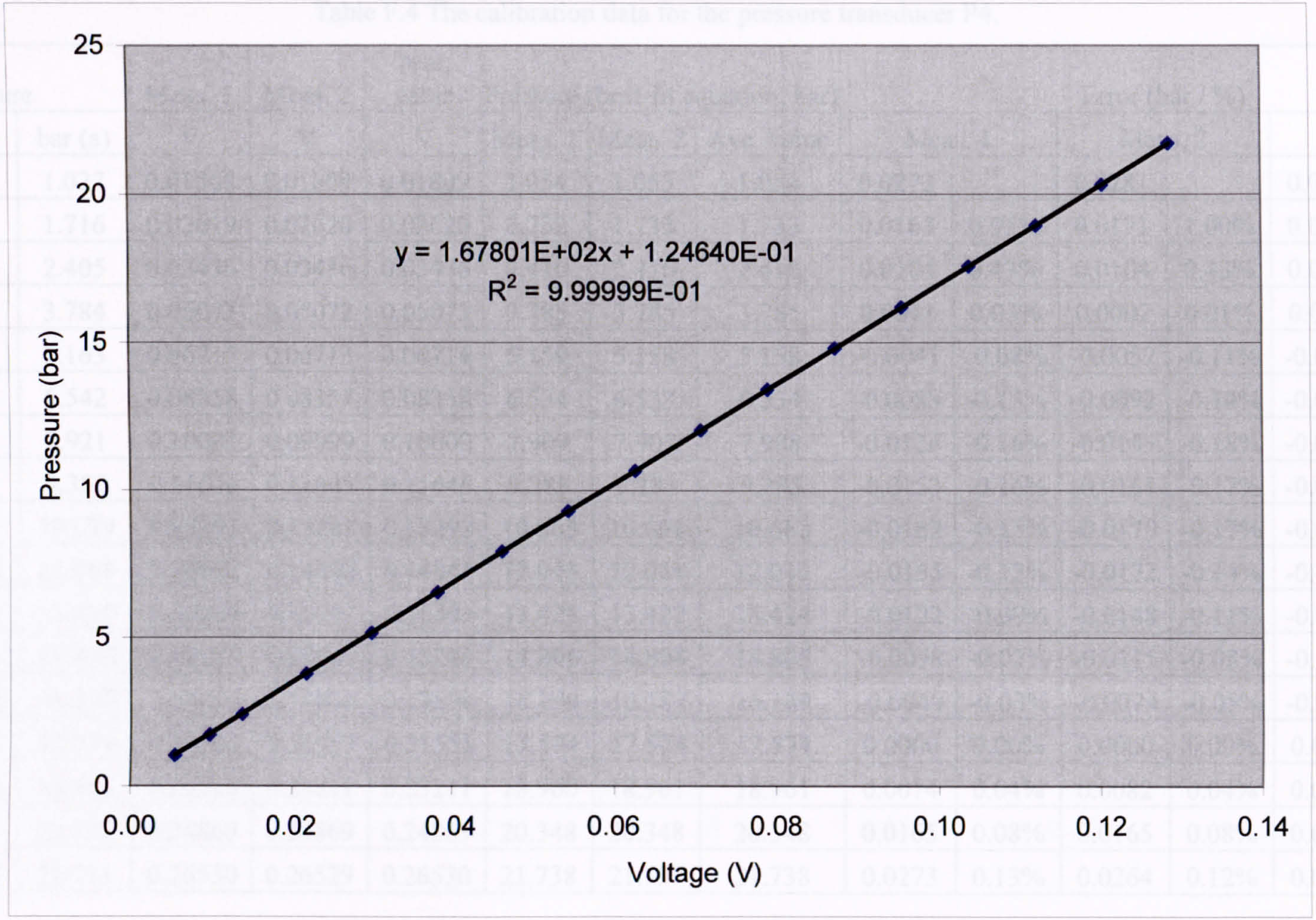

Figure F.3 The best-fit equation for the pressure transducer P3.

Table F.4 The calibration data for the pressure transducer P4.

Pressure			Meas. 1	Meas. 2	Ave. value	Pressure (best-fit equation, bar)			Error (bar / %)					
Psi	bar (g)	bar (a)	V	V	V	Meas. 1	Meas. 2	Ave. value	Meas. 1		Meas. 2		Ave. value	
0	0.000	1.027	0.01808	0.01809	0.01809	1.054	1.055	1.054	0.0272		0.0281		0.0277	
10	0.689	1.716	0.02619	0.02620	0.02620	1.732	1.733	1.733	0.0163	0.95%	0.0171	1.00%	0.0167	0.97%
20	1.379	2.405	0.03436	0.03436	0.03436	2.416	2.416	2.416	0.0104	0.43%	0.0104	0.43%	0.0104	0.43%
40	2.758	3.784	0.05073	0.05072	0.05073	3.785	3.785	3.785	0.0011	0.03%	0.0002	0.01%	0.0007	0.02%
60	4.137	5.163	0.06715	0.06713	0.06714	5.159	5.158	5.158	-0.0041	-0.08%	-0.0057	-0.11%	-0.0049	-0.09%
80	5.516	6.542	0.08358	0.08357	0.08358	6.534	6.533	6.534	-0.0083	-0.13%	-0.0092	-0.14%	-0.0088	-0.13%
100	6.895	7.921	0.10001	0.09999	0.10000	7.909	7.907	7.908	-0.0126	-0.16%	-0.0143	-0.18%	-0.0135	-0.17%
120	8.274	9.300	0.11646	0.11645	0.11646	9.285	9.284	9.285	-0.0153	-0.16%	-0.0161	-0.17%	-0.0157	-0.17%
140	9.653	10.679	0.13293	0.13291	0.13292	10.663	10.661	10.662	-0.0162	-0.15%	-0.0179	-0.17%	-0.0170	-0.16%
160	11.032	12.058	0.14942	0.14940	0.14941	12.043	12.041	12.042	-0.0155	-0.13%	-0.0172	-0.14%	-0.0163	-0.14%
180	12.411	13.437	0.16594	0.16591	0.16593	13.425	13.422	13.424	-0.0122	-0.09%	-0.0148	-0.11%	-0.0135	-0.10%
200	13.789	14.816	0.18245	0.18243	0.18244	14.806	14.804	14.805	-0.0098	-0.07%	-0.0115	-0.08%	-0.0107	-0.07%
220	15.168	16.195	0.19899	0.19896	0.19898	16.190	16.187	16.189	-0.0049	-0.03%	-0.0074	-0.05%	-0.0062	-0.04%
240	16.547	17.574	0.21553	0.21553	0.21553	17.574	17.574	17.574	0.0000	0.00%	0.0000	0.00%	0.0000	0.00%
260	17.926	18.953	0.23210	0.23211	0.23211	18.960	18.961	18.961	0.0074	0.04%	0.0082	0.04%	0.0078	0.04%
280	19.305	20.332	0.24869	0.24869	0.24869	20.348	20.348	20.348	0.0165	0.08%	0.0165	0.08%	0.0165	0.08%
300	20.684	21.711	0.26530	0.26529	0.26530	21.738	21.737	21.738	0.0273	0.13%	0.0264	0.12%	0.0268	0.12%

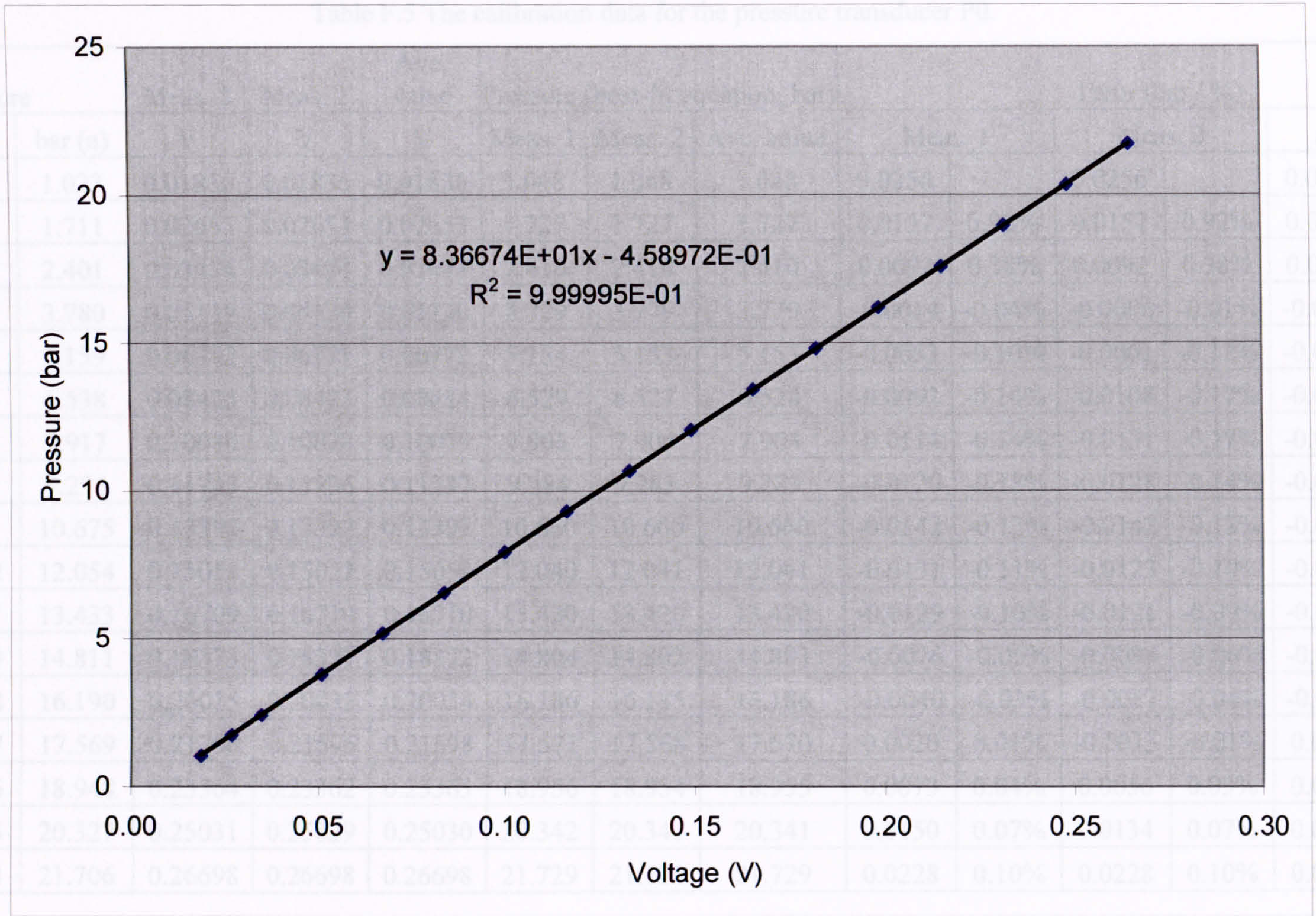

Figure F.4 The best-fit equation for the pressure transducer P4.

Table F.5 The calibration data for the pressure transducer P0.

Pressure			Meas. 1	Meas. 2	Ave. value	Pressure (best-fit equation, bar)			Error (bar / %)					
Psi	bar (g)	bar (a)	V	V	V	Meas. 1	Meas. 2	Ave. value	Meas. 1		Meas. 2		Ave. value	
0	0.000	1.022	0.01836	0.01836	0.01836	1.048	1.048	1.048	0.0256		0.0256		0.0256	
10	0.689	1.711	0.02653	0.02653	0.02653	1.727	1.727	1.727	0.0157	0.92%	0.0157	0.92%	0.0157	0.92%
20	1.379	2.401	0.03474	0.03474	0.03474	2.410	2.410	2.410	0.0092	0.38%	0.0092	0.38%	0.0092	0.38%
40	2.758	3.780	0.05119	0.05120	0.05120	3.779	3.779	3.779	-0.0014	-0.04%	-0.0006	-0.01%	-0.0010	-0.03%
60	4.137	5.159	0.06772	0.06771	0.06772	5.154	5.153	5.153	-0.0053	-0.10%	-0.0061	-0.12%	-0.0057	-0.11%
80	5.516	6.538	0.08425	0.08423	0.08424	6.529	6.527	6.528	-0.0092	-0.14%	-0.0108	-0.17%	-0.0100	-0.15%
100	6.895	7.917	0.10080	0.10078	0.10079	7.905	7.904	7.904	-0.0114	-0.14%	-0.0131	-0.17%	-0.0123	-0.15%
120	8.274	9.296	0.11737	0.11736	0.11737	9.284	9.283	9.283	-0.0120	-0.13%	-0.0128	-0.14%	-0.0124	-0.13%
140	9.653	10.675	0.13392	0.13392	0.13392	10.660	10.660	10.660	-0.0142	-0.13%	-0.0142	-0.13%	-0.0142	-0.13%
160	11.032	12.054	0.15051	0.15052	0.15052	12.040	12.041	12.041	-0.0131	-0.11%	-0.0123	-0.10%	-0.0127	-0.11%
180	12.411	13.433	0.16709	0.16710	0.16710	13.420	13.420	13.420	-0.0129	-0.10%	-0.0121	-0.09%	-0.0125	-0.09%
200	13.789	14.811	0.18373	0.18371	0.18372	14.804	14.802	14.803	-0.0076	-0.05%	-0.0093	-0.06%	-0.0085	-0.06%
220	15.168	16.190	0.20035	0.20033	0.20034	16.186	16.185	16.186	-0.0040	-0.03%	-0.0057	-0.04%	-0.0049	-0.03%
240	16.547	17.569	0.21700	0.21696	0.21698	17.571	17.568	17.570	0.0020	0.01%	-0.0013	-0.01%	0.0004	0.00%
260	17.926	18.948	0.23364	0.23362	0.23363	18.956	18.954	18.955	0.0073	0.04%	0.0056	0.03%	0.0064	0.03%
280	19.305	20.327	0.25031	0.25029	0.25030	20.342	20.341	20.341	0.0150	0.07%	0.0134	0.07%	0.0142	0.07%
300	20.684	21.706	0.26698	0.26698	0.26698	21.729	21.729	21.729	0.0228	0.10%	0.0228	0.10%	0.0228	0.10%

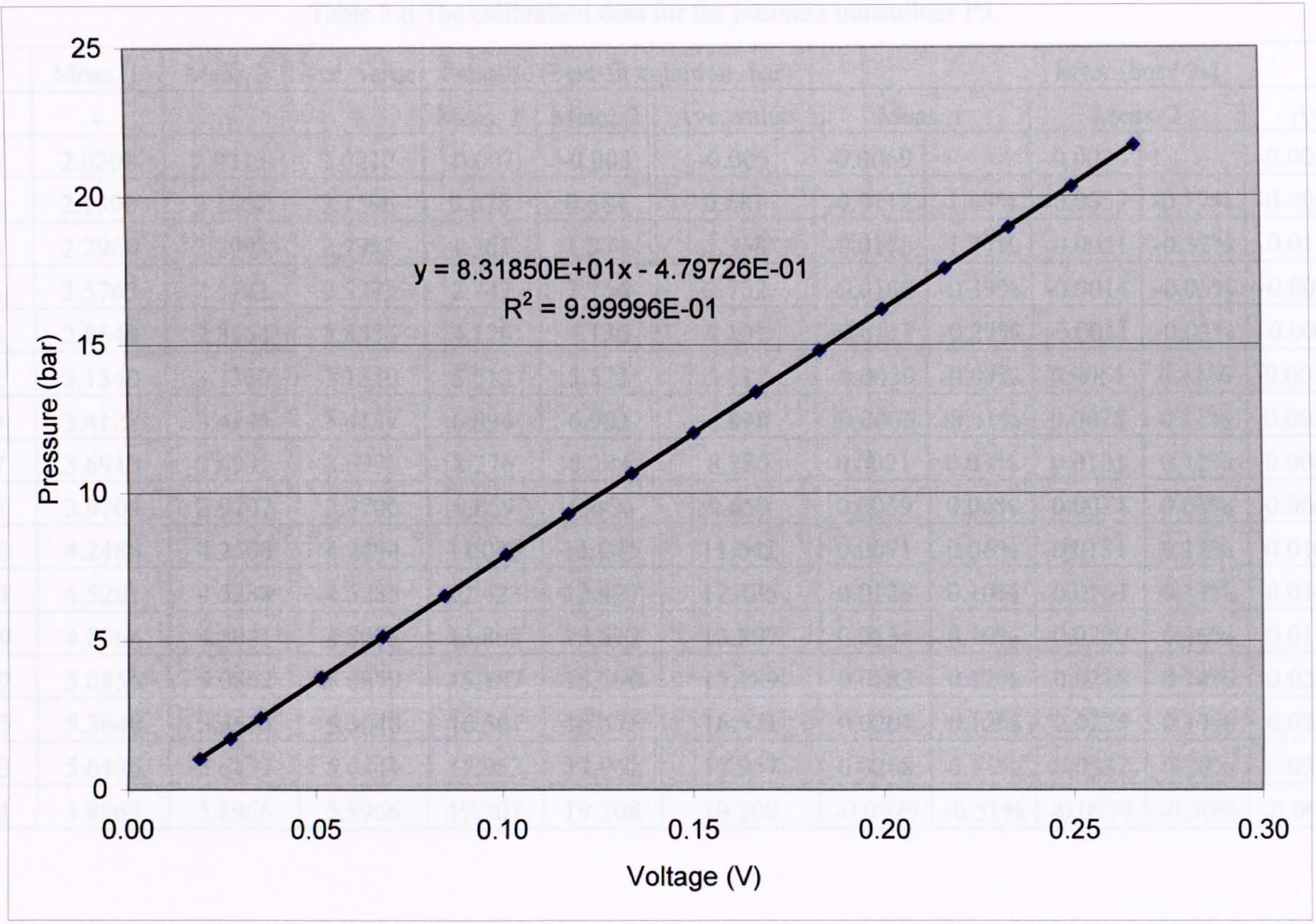

Figure F.5 The best-fit equation for the pressure transducer P0.

Table F.6 The calibration data for the pressure transmitter P5.

Pressure		Meas. 1	Meas. 2	Ave. value	Pressure (best-fit equation, bar)			Error (bar / %)					
Psi	bar	v	v	v	Meas. 1	Meas. 2	Ave. value	Meas. 1		Meas. 2		Ave. value	
0	0.00	2.0208	2.0215	2.0212	-0.007	-0.003	-0.005	-0.0069		-0.0034		-0.0052	
10	0.69	2.1590	2.1602	2.1596	0.678	0.684	0.681	-0.0112	-1.63%	-0.0053	-0.77%	-0.0083	-1.20%
20	1.38	2.2968	2.2993	2.2981	1.361	1.374	1.368	-0.0175	-1.27%	-0.0051	-0.37%	-0.0113	-0.82%
40	2.76	2.5763	2.5782	2.5773	2.747	2.756	2.752	-0.0108	-0.39%	-0.0014	-0.05%	-0.0061	-0.22%
60	4.14	2.8544	2.8564	2.8554	4.126	4.136	4.131	-0.0111	-0.27%	-0.0011	-0.03%	-0.0061	-0.15%
80	5.52	3.1340	3.1360	3.1350	5.512	5.522	5.517	-0.0039	-0.07%	0.0061	0.11%	0.0011	0.02%
100	6.89	3.4128	3.4145	3.4137	6.894	6.903	6.898	-0.0006	-0.01%	0.0078	0.11%	0.0036	0.05%
120	8.27	3.6915	3.6931	3.6923	8.276	8.284	8.280	0.0021	0.03%	0.0101	0.12%	0.0061	0.07%
140	9.65	3.9704	3.9707	3.9706	9.659	9.660	9.659	0.0059	0.06%	0.0074	0.08%	0.0066	0.07%
160	11.03	4.2488	4.2500	4.2494	11.039	11.045	11.042	0.0071	0.06%	0.0131	0.12%	0.0101	0.09%
180	12.41	4.5281	4.5288	4.5285	12.423	12.427	12.425	0.0128	0.10%	0.0163	0.13%	0.0146	0.12%
200	13.79	4.8064	4.8081	4.8073	13.803	13.812	13.807	0.0136	0.10%	0.0220	0.16%	0.0178	0.13%
220	15.17	5.0855	5.0862	5.0859	15.187	15.190	15.189	0.0183	0.12%	0.0218	0.14%	0.0201	0.13%
240	16.55	5.3640	5.3655	5.3648	16.567	16.575	16.571	0.0201	0.12%	0.0275	0.17%	0.0238	0.14%
260	17.93	5.6435	5.6452	5.6444	17.953	17.962	17.957	0.0268	0.15%	0.0352	0.20%	0.0310	0.17%
280	19.31	5.8965	5.8966	5.8966	19.207	19.208	19.208	-0.0979	-0.51%	-0.0974	-0.50%	-0.0976	-0.51%

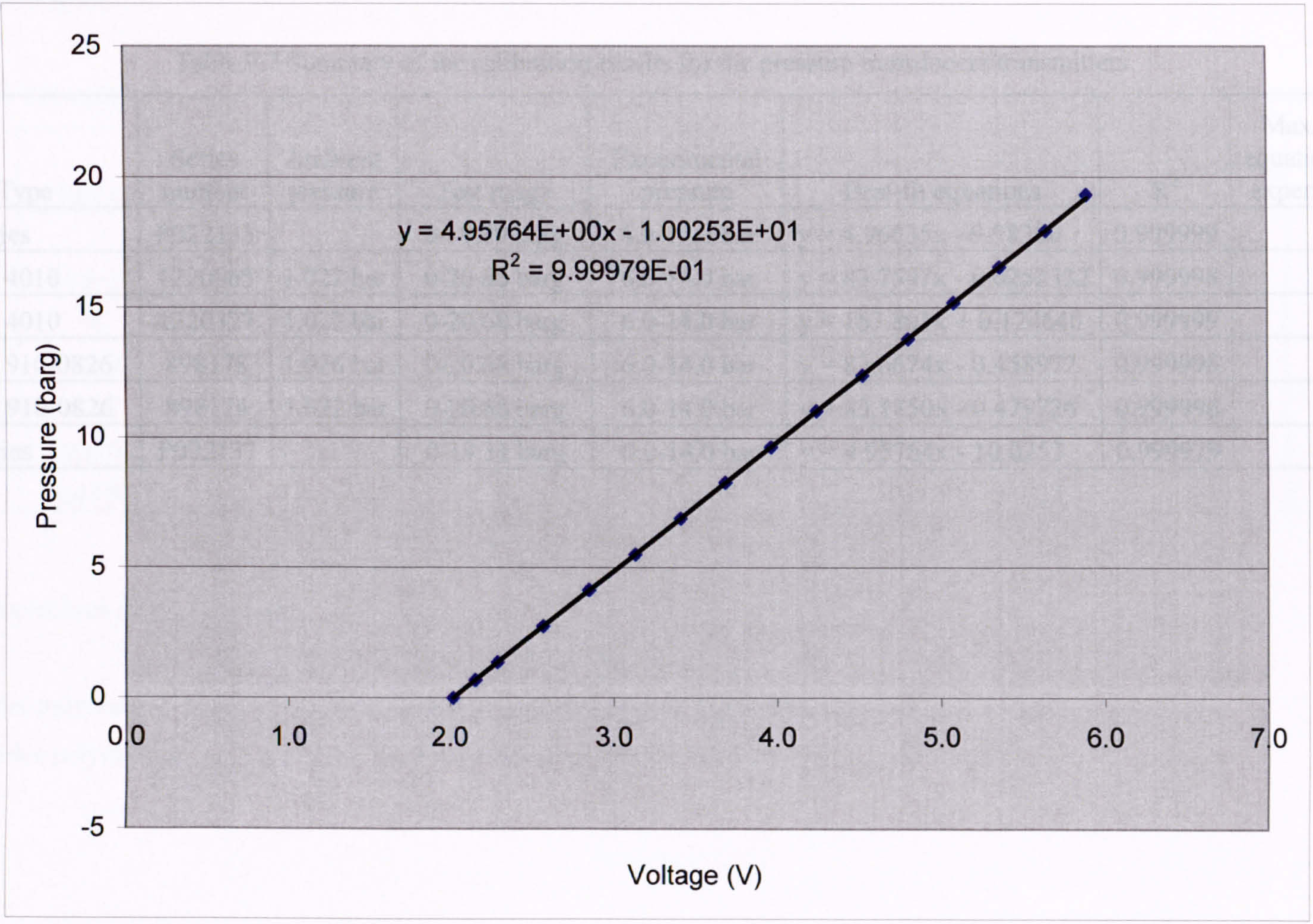

Figure F.6 The best-fit equation for the pressure transmitter P5.

Table F.7 Summary of the calibration results for the pressure transducers/transmitters.

No.	Type	Series number	Ambient pressure	Test range	Experimental pressure	Best-fit equations	R^2	Max. error of the equations within the experimental range
P1	GP series	P022133		0-19.99 barg	6.0-14.0 bar	$y = 4.96635x - 9.98380$	0.999999	0.08%
P2	PDCR 4010	1220065	1.022 bar	0-20.68 barg	6.0-14.0 bar	$y = 83.7547x - 0.0252332$	0.999998	0.12%
P3	PDCR 4010	1220327	1.022 bar	0-20.68 barg	6.0-14.0 bar	$y = 167.801x + 0.124640$	0.999999	0.20%
P4	PDCR 910-0826	898178	1.026 bar	0-20.68 barg	6.0-14.0 bar	$y = 83.6674x - 0.458972$	0.999995	0.18%
P0	PDCR 910-0826	898174	1.022 bar	0-20.68 barg	6.0-14.0 bar	$y = 83.1850x - 0.479726$	0.999996	0.17%
P5	GP series	P022137		0-19.31 barg	6.0-14.0 bar	$y = 4.95764x - 10.0253$	0.999979	0.27%

F.2 Thermocouples

Table F.8 The calibration data and the deduced best-fit equation for the platinum resistance thermometer in the calibration equipment.

	Test temperature		The calculated temperature from the best-fit equation			The difference between the test temperature and the best-fit equation			The error of the equation
Thermometer reading	ITS -90	Error	Linear	Two-order polynomial	Three-order polynomial	Linear	Two-order polynomial	Three-order polynomial	Three-order polynomial
Ω	°C	K	°C	°C	°C	K	K	K	K
72.262	-68.92	0.05	-70.73	-68.90	-68.92	-1.81	0.02	0.00	0.05
100.065	0.03	0.05	1.01	0.00	0.03	0.98	-0.03	0.00	0.05
139.342	100.03	0.05	102.35	100.06	100.04	2.32	0.03	0.01	0.05
195.991	249.97	0.05	248.51	249.97	249.98	-1.46	0.00	0.01	0.05

Notice:

The deduced best-fit equations are:

Linear: y = 2.5801E+00x - 2.5717E+02

Two-order polynomial: y = 1.0311E-03x2 + 2.3006E+00x - 2.4053E+02

Three-order polynomial: y = 5.3271E-07x3 + 8.1893E-04x2 + 2.3269E+00x - 2.4154E+02

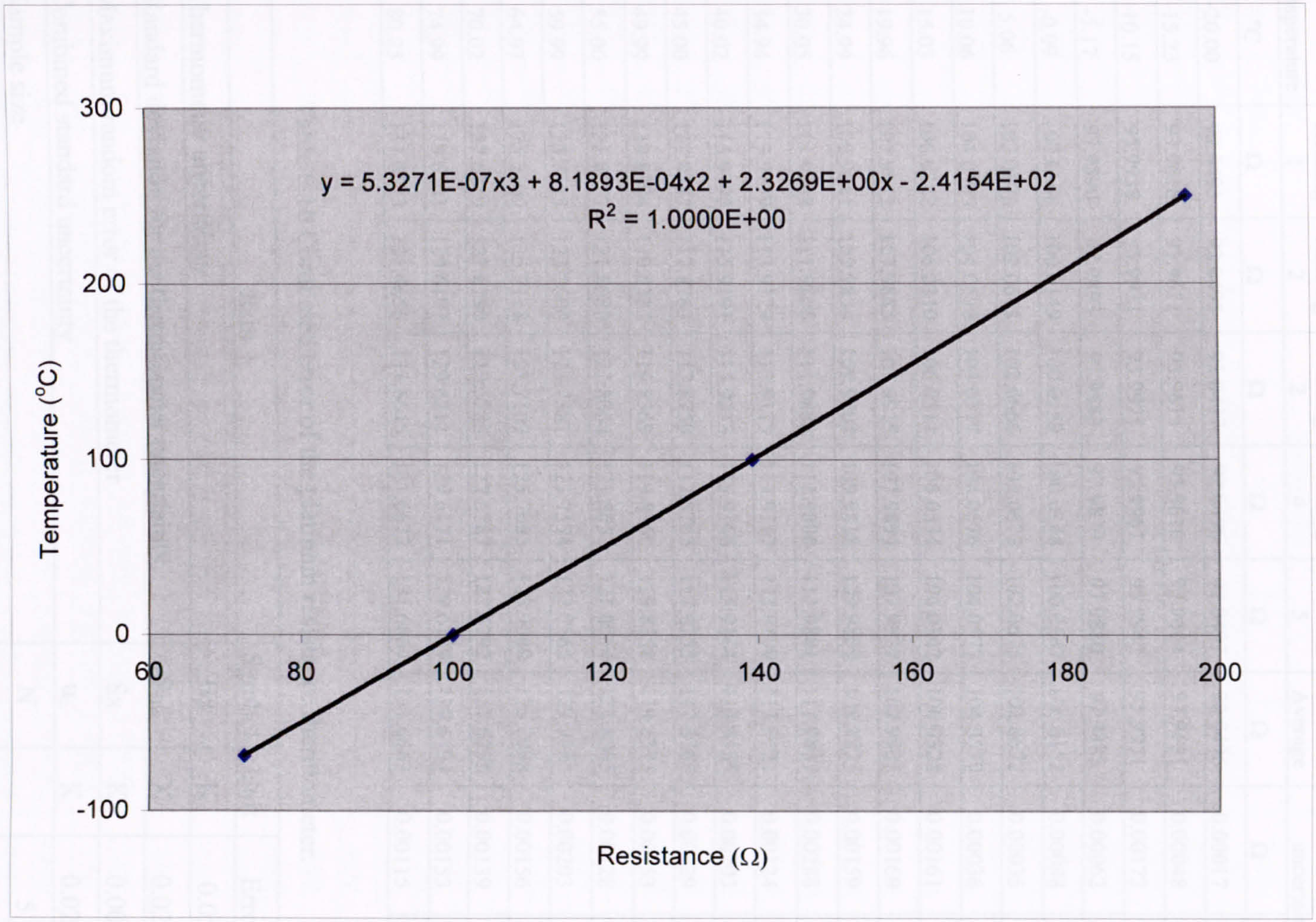

Figure F.7 The best-fit equation (three-order polynomial) for the platinum resistance thermometer in the calibration equipment.

Table F.9 Repeatability test of the platinum resistance thermometer.

Temperature	Reading 1	Reading 2	Reading 2	Reading 4	Reading 5	Average	Standard uncertainty	
°C	Ω	Ω	Ω	Ω	Ω	Ω	Ω	K
-20.00	92.0493	92.0495	92.0497	92.0496	92.0497	92.0496	0.00017	0.000
-15.23	93.9616	93.9611	93.9615	93.9610	93.9604	93.9611	0.00048	0.001
-10.15	95.9938	95.9933	95.9975	95.9961	95.9947	95.9951	0.00172	0.004
-5.17	97.9890	97.9893	97.9883	97.9879	97.9880	97.9885	0.00062	0.001
-0.09	100.0168	100.0149	100.0150	100.0148	100.0147	100.0152	0.00088	0.002
5.06	102.0673	102.0673	102.0666	102.0673	102.0675	102.0672	0.00035	0.001
10.06	104.0585	104.0578	104.0577	104.0576	104.0577	104.0579	0.00036	0.001
15.03	106.0342	106.0310	106.0311	106.0334	106.0342	106.0328	0.00161	0.004
19.96	107.9912	107.9885	107.9915	107.9894	107.9927	107.9907	0.00169	0.004
24.99	109.9841	109.9834	109.9804	109.9818	109.9809	109.9821	0.00159	0.004
30.05	111.9868	111.9805	111.9803	111.9806	111.9801	111.9817	0.00288	0.007
34.94	113.9139	113.9129	113.9113	113.9117	113.9109	113.9121	0.00124	0.003
40.02	115.9190	115.9191	115.9213	115.9166	115.9164	115.9185	0.00203	0.005
45.00	117.8787	117.8763	117.8759	117.8765	117.8753	117.8765	0.00129	0.003
49.99	119.8394	119.8382	119.8369	119.8360	119.8358	119.8373	0.00153	0.004
55.00	121.8077	121.8080	121.8064	121.8052	121.8054	121.8065	0.00128	0.003
59.99	123.7615	123.7600	123.7581	123.7574	123.7565	123.7587	0.00203	0.005
64.97	125.7100	125.7118	125.7107	125.7085	125.7080	125.7098	0.00156	0.004
70.02	127.6819	127.6790	127.6785	127.6787	127.6792	127.6795	0.00139	0.003
74.99	129.6203	129.6197	129.6211	129.6171	129.6189	129.6194	0.00153	0.004
80.25	131.6673	131.6658	131.6645	131.6672	131.6664	131.6662	0.00115	0.003

Table F.10 Combined error of the platinum resistance thermometer.

Item	Symbol	Unit	Error
Thermometer uncertainty	Bx	K	0.05
Standard deviation for the thermometer uncertainty	S_{Bx}	K	0.025
Maximum random error of the thermometer	Sx	K	0.007
Combined standard uncertainty	u_c	K	0.026
Sample size	N		5
Distribution coefficient	t_{95}		2.776
Combined error of the thermometer with 95% confidence	U_{95}	K	0.07

Table F.11 The calibration data and the best-fit equation for the thermocouple (K-type thermocouple wires TT_1 - TT_{15}).

Thermometer		Voltage (V)						Best-fit equation	
Reading (Ω)	Temp. (°C)	Sample 1	Sample 2	Sample 3	Sample 4	Sample 5	Average	Temp. (°C)	Error (K)
92.0493	-20.00	-0.000786	-0.000787	-0.000786	-0.000782	-0.000789	-0.000786	-20.00	0.00
92.0495	-20.00	-0.000786	-0.000786	-0.000786	-0.000782	-0.000790	-0.000786	-20.00	0.00
92.0497	-20.00	-0.000785	-0.000786	-0.000787	-0.000781	-0.000789	-0.000786	-19.99	0.01
92.0496	-20.00	-0.000787	-0.000787	-0.000787	-0.000782	-0.000790	-0.000787	-20.01	-0.02
92.0497	-20.00	-0.000786	-0.000787	-0.000786	-0.000782	-0.000790	-0.000786	-20.00	-0.01
93.9616	-15.23	-0.000603	-0.000604	-0.000603	-0.000599	-0.000606	-0.000603	-15.24	-0.01
93.9611	-15.23	-0.000602	-0.000603	-0.000603	-0.000599	-0.000606	-0.000603	-15.23	0.00
93.9615	-15.23	-0.000603	-0.000603	-0.000603	-0.000599	-0.000606	-0.000603	-15.23	0.00
93.9610	-15.23	-0.000603	-0.000603	-0.000603	-0.000599	-0.000606	-0.000603	-15.23	0.00
93.9604	-15.23	-0.000603	-0.000603	-0.000603	-0.000599	-0.000606	-0.000603	-15.23	0.00
95.9938	-10.15	-0.000406	-0.000407	-0.000407	-0.000402	-0.000409	-0.000406	-10.16	0.00
95.9933	-10.16	-0.000405	-0.000406	-0.000407	-0.000402	-0.000410	-0.000406	-10.15	0.00
95.9975	-10.15	-0.000406	-0.000407	-0.000406	-0.000402	-0.000409	-0.000406	-10.15	-0.01
95.9961	-10.15	-0.000406	-0.000406	-0.000406	-0.000402	-0.000409	-0.000406	-10.15	0.00
95.9947	-10.15	-0.000406	-0.000406	-0.000406	-0.000402	-0.000409	-0.000406	-10.15	0.00
97.9890	-5.16	-0.000210	-0.000212	-0.000211	-0.000207	-0.000214	-0.000211	-5.15	0.01
97.9893	-5.16	-0.000210	-0.000211	-0.000211	-0.000207	-0.000214	-0.000211	-5.15	0.02
97.9883	-5.17	-0.000211	-0.000211	-0.000210	-0.000207	-0.000214	-0.000211	-5.15	0.02
97.9879	-5.17	-0.000210	-0.000211	-0.000211	-0.000207	-0.000214	-0.000211	-5.15	0.02
97.9880	-5.17	-0.000210	-0.000212	-0.000211	-0.000207	-0.000215	-0.000211	-5.16	0.01
100.0168	-0.09	-0.000011	-0.000012	-0.000012	-0.000007	-0.000014	-0.000011	-0.08	0.01
100.0149	-0.09	-0.000012	-0.000013	-0.000012	-0.000008	-0.000015	-0.000012	-0.10	-0.01
100.0150	-0.09	-0.000011	-0.000012	-0.000012	-0.000008	-0.000015	-0.000012	-0.09	0.00
100.0148	-0.09	-0.000012	-0.000012	-0.000012	-0.000007	-0.000015	-0.000012	-0.09	0.00
100.0147	-0.09	-0.000012	-0.000012	-0.000011	-0.000008	-0.000015	-0.000012	-0.09	0.00
102.0673	5.06	0.000192	0.000192	0.000192	0.000196	0.000190	0.000192	5.06	0.00
102.0673	5.06	0.000193	0.000192	0.000193	0.000196	0.000189	0.000193	5.06	0.01
102.0666	5.06	0.000192	0.000192	0.000192	0.000197	0.000188	0.000192	5.05	0.00
102.0673	5.06	0.000193	0.000192	0.000192	0.000196	0.000189	0.000192	5.06	0.00
102.0675	5.06	0.000192	0.000192	0.000192	0.000196	0.000190	0.000192	5.06	0.00
104.0585	10.06	0.000392	0.000391	0.000392	0.000395	0.000389	0.000392	10.06	0.00
104.0578	10.06	0.000393	0.000391	0.000391	0.000396	0.000389	0.000392	10.07	0.01
104.0577	10.06	0.000391	0.000391	0.000392	0.000395	0.000389	0.000392	10.06	0.00
104.0576	10.06	0.000391	0.000392	0.000391	0.000396	0.000389	0.000392	10.06	0.00
104.0577	10.06	0.000393	0.000391	0.000391	0.000395	0.000389	0.000392	10.06	0.00

Table F.11 The calibration data and the best-fit equation for the thermocouple (Cont.) (K-type thermocouple wires TT_1 - TT_{15}).

Thermometer		Voltage (V)						Best-fit equation	
Reading (Ω)	Temp. (°C)	Sample 1	Sample 2	Sample 3	Sample 4	Sample 5	Average	Temp. (°C)	Error (K)
106.0342	15.03	0.000591	0.000590	0.000591	0.000594	0.000588	0.000591	15.02	-0.01
106.0310	15.03	0.000592	0.000590	0.000591	0.000595	0.000587	0.000591	15.02	0.00
106.0311	15.03	0.000591	0.000591	0.000591	0.000595	0.000588	0.000591	15.03	0.00
106.0334	15.03	0.000592	0.000590	0.000591	0.000594	0.000587	0.000591	15.02	-0.01
106.0342	15.03	0.000590	0.000591	0.000591	0.000595	0.000587	0.000591	15.02	-0.01
107.9912	19.97	0.000791	0.000790	0.000791	0.000794	0.000786	0.000790	19.97	0.00
107.9885	19.96	0.000789	0.000790	0.000791	0.000794	0.000786	0.000790	19.96	0.00
107.9915	19.97	0.000791	0.000790	0.000790	0.000794	0.000786	0.000790	19.96	-0.01
107.9894	19.96	0.000790	0.000790	0.000790	0.000795	0.000785	0.000790	19.96	0.00
107.9927	19.97	0.000790	0.000790	0.000791	0.000794	0.000786	0.000790	19.96	-0.01
109.9841	25.00	0.000994	0.000994	0.000995	0.000997	0.000991	0.000994	24.99	-0.01
109.9834	25.00	0.000994	0.000994	0.000995	0.000998	0.000992	0.000995	25.00	0.01
109.9804	24.99	0.000994	0.000994	0.000994	0.000997	0.000991	0.000994	24.99	0.00
109.9818	24.99	0.000994	0.000994	0.000994	0.000998	0.000991	0.000994	24.99	0.00
109.9809	24.99	0.000994	0.000993	0.000994	0.000997	0.000991	0.000994	24.98	-0.01
111.9868	30.06	0.001200	0.001200	0.001201	0.001204	0.001197	0.001200	30.05	-0.01
111.9805	30.04	0.001201	0.001201	0.001201	0.001205	0.001197	0.001201	30.06	0.02
111.9803	30.04	0.001202	0.001200	0.001201	0.001204	0.001197	0.001201	30.06	0.02
111.9806	30.04	0.001200	0.001200	0.001201	0.001204	0.001197	0.001200	30.05	0.01
111.9801	30.04	0.001202	0.001200	0.001201	0.001204	0.001198	0.001201	30.06	0.02
113.9139	34.94	0.001400	0.001399	0.001400	0.001404	0.001398	0.001400	34.93	-0.01
113.9129	34.94	0.001401	0.001399	0.001400	0.001403	0.001398	0.001400	34.93	-0.01
113.9113	34.93	0.001400	0.001400	0.001401	0.001404	0.001399	0.001401	34.95	0.01
113.9117	34.93	0.001401	0.001401	0.001401	0.001404	0.001398	0.001401	34.95	0.02
113.9109	34.93	0.001400	0.001399	0.001400	0.001404	0.001398	0.001400	34.93	0.00
115.9190	40.03	0.001610	0.001609	0.001609	0.001613	0.001606	0.001609	40.02	0.00
115.9191	40.03	0.001609	0.001609	0.001609	0.001612	0.001606	0.001609	40.01	-0.01
115.9213	40.03	0.001610	0.001609	0.001609	0.001612	0.001607	0.001609	40.02	-0.01
115.9166	40.02	0.001609	0.001609	0.001609	0.001612	0.001607	0.001609	40.02	0.00
115.9164	40.02	0.001609	0.001609	0.001609	0.001612	0.001607	0.001609	40.02	0.00
117.8787	45.00	0.001815	0.001814	0.001814	0.001817	0.001811	0.001814	44.99	-0.01
117.8763	45.00	0.001814	0.001814	0.001814	0.001817	0.001811	0.001814	44.99	-0.01
117.8759	45.00	0.001815	0.001814	0.001815	0.001818	0.001811	0.001815	45.00	0.00
117.8765	45.00	0.001814	0.001815	0.001814	0.001817	0.001812	0.001814	45.00	0.00
117.8753	45.00	0.001815	0.001813	0.001814	0.001818	0.001811	0.001814	44.99	0.00

Table F.11 The calibration data and the best-fit equation for the thermocouple (Cont.) (K-type thermocouple wires TT_1 - TT_{15}).

Thermometer		Voltage (V)						Best-fit equation	
Reading (Ω)	Temp. (°C)	Sample 1	Sample 2	Sample 3	Sample 4	Sample 5	Average	Temp. (°C)	Error (K)
119.8394	49.99	0.002021	0.002020	0.002021	0.002024	0.002018	0.002021	49.99	0.00
119.8382	49.99	0.002021	0.002021	0.002020	0.002024	0.002019	0.002021	49.99	0.00
119.8369	49.99	0.002021	0.002020	0.002021	0.002023	0.002018	0.002021	49.98	0.00
119.8360	49.98	0.002020	0.002020	0.002021	0.002023	0.002018	0.002020	49.98	-0.01
119.8358	49.98	0.002021	0.002020	0.002021	0.002024	0.002018	0.002021	49.99	0.00
121.8077	55.01	0.002228	0.002228	0.002228	0.002232	0.002226	0.002228	55.00	-0.01
121.8080	55.01	0.002228	0.002229	0.002229	0.002231	0.002226	0.002229	55.00	-0.01
121.8064	55.00	0.002229	0.002228	0.002229	0.002232	0.002226	0.002229	55.01	0.00
121.8052	55.00	0.002229	0.002228	0.002228	0.002232	0.002225	0.002228	55.00	0.00
121.8054	55.00	0.002228	0.002228	0.002229	0.002232	0.002226	0.002229	55.00	0.00
123.7615	59.99	0.002435	0.002435	0.002434	0.002438	0.002433	0.002435	59.98	-0.02
123.7600	59.99	0.002435	0.002434	0.002433	0.002439	0.002433	0.002435	59.97	-0.02
123.7581	59.99	0.002434	0.002436	0.002433	0.002439	0.002433	0.002435	59.98	-0.01
123.7574	59.98	0.002435	0.002434	0.002433	0.002439	0.002433	0.002435	59.97	-0.01
123.7565	59.98	0.002435	0.002436	0.002433	0.002438	0.002433	0.002435	59.98	-0.01
125.7100	64.97	0.002643	0.002643	0.002642	0.002647	0.002641	0.002643	64.99	0.01
125.7118	64.98	0.002643	0.002643	0.002642	0.002646	0.002641	0.002643	64.98	0.00
125.7107	64.98	0.002643	0.002643	0.002642	0.002647	0.002641	0.002643	64.99	0.01
125.7085	64.97	0.002643	0.002643	0.002641	0.002646	0.002641	0.002643	64.98	0.01
125.7080	64.97	0.002642	0.002643	0.002642	0.002647	0.002641	0.002643	64.98	0.01
127.6819	70.02	0.002853	0.002853	0.002851	0.002856	0.002850	0.002853	70.02	0.00
127.6790	70.02	0.002853	0.002852	0.002851	0.002857	0.002851	0.002853	70.03	0.01
127.6785	70.01	0.002854	0.002853	0.002851	0.002857	0.002851	0.002853	70.04	0.02
127.6787	70.01	0.002853	0.002854	0.002852	0.002856	0.002851	0.002853	70.04	0.02
127.6792	70.02	0.002854	0.002853	0.002851	0.002856	0.002850	0.002853	70.03	0.01
129.6203	74.99	0.003060	0.003061	0.003057	0.003064	0.003057	0.003060	75.01	0.01
129.6197	74.99	0.003060	0.003060	0.003058	0.003063	0.003058	0.003060	75.01	0.01
129.6211	74.99	0.003061	0.003061	0.003058	0.003064	0.003057	0.003060	75.02	0.02
129.6171	74.98	0.003060	0.003060	0.003058	0.003064	0.003057	0.003060	75.01	0.02
129.6189	74.99	0.003061	0.003061	0.003057	0.003064	0.003058	0.003060	75.02	0.03
131.6673	80.25	0.003279	0.003280	0.003275	0.003272	0.003277	0.003277	80.22	-0.03
131.6658	80.25	0.003280	0.003279	0.003274	0.003272	0.003277	0.003276	80.22	-0.03
131.6645	80.24	0.003279	0.003280	0.003276	0.003273	0.003277	0.003277	80.23	-0.01
131.6672	80.25	0.003279	0.003279	0.003274	0.003272	0.003277	0.003276	80.21	-0.04
131.6664	80.25	0.003281	0.003280	0.003275	0.003273	0.003277	0.003277	80.24	-0.01

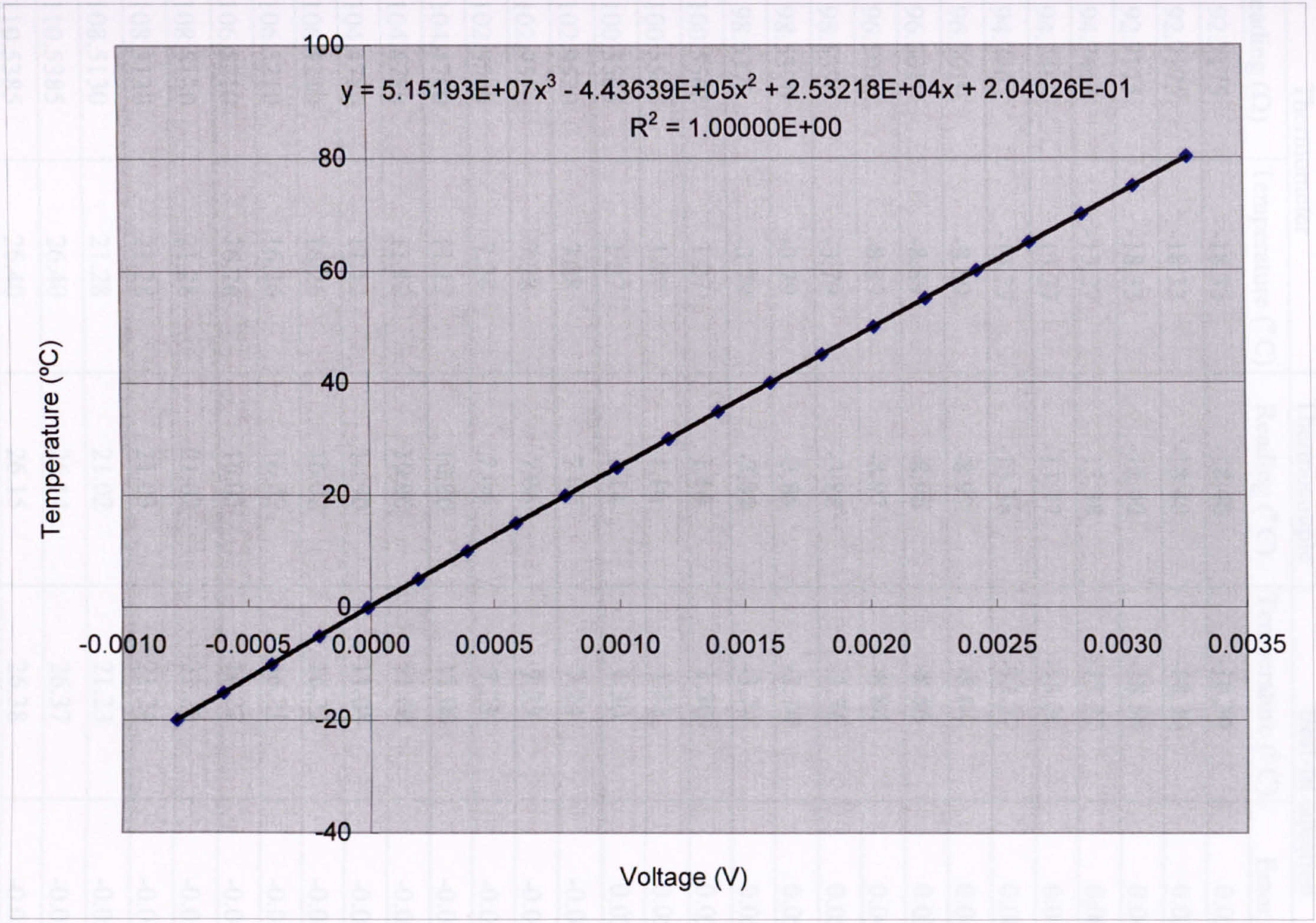

Figure F.8 The best-fit equation for the thermocouple wires TT_1 - TT_{15}.

Table F.12 The calibration data and the best-fit equation for the thermocouple (K-type thermocouple probe T1).

Thermometer		Thermocouple	Best-fit equation	
Reading (Ω)	Temperature (° C)	Reading (° C)	Temperature (° C)	Error (K)
92.7175	-18.33	-18.40	-18.30	0.03
92.7175	-18.33	-18.40	-18.30	0.03
92.7175	-18.33	-18.40	-18.30	0.04
94.7465	-13.27	-13.38	-13.27	0.00
94.7465	-13.27	-13.37	-13.26	0.01
94.7465	-13.27	-13.38	-13.27	0.00
96.5010	-8.89	-8.97	-8.84	0.04
96.5010	-8.89	-8.98	-8.86	0.03
96.5010	-8.89	-8.97	-8.84	0.04
98.5370	-3.79	-3.88	-3.74	0.05
98.5370	-3.79	-3.88	-3.74	0.05
98.5370	-3.79	-3.88	-3.74	0.05
100.5565	1.27	1.14	1.30	0.03
100.5565	1.27	1.16	1.32	0.05
100.5565	1.27	1.14	1.30	0.03
102.9520	7.28	7.07	7.24	-0.04
102.9520	7.28	7.06	7.23	-0.05
102.9520	7.28	7.06	7.23	-0.05
104.4780	11.12	10.90	11.08	-0.04
104.4780	11.12	10.90	11.08	-0.03
104.4780	11.12	10.90	11.08	-0.04
106.5210	16.26	16.02	16.22	-0.04
106.5210	16.26	16.02	16.21	-0.05
106.5210	16.26	16.03	16.22	-0.04
108.5130	21.28	21.02	21.23	-0.05
108.5130	21.28	21.03	21.24	-0.05
108.5130	21.28	21.02	21.23	-0.05
110.5385	26.40	26.14	26.37	-0.03
110.5385	26.40	26.15	26.38	-0.02
110.5385	26.40	26.16	26.39	-0.01
112.4626	31.26	30.98	31.22	-0.05

Table F.12 The calibration data and the best-fit equation for the thermocouple (Cont.) (K-type thermocouple probe T1).

Thermometer		Thermocouple	Best-fit equation	
Reading (Ω)	Temperature (° C)	Reading (° C)	Temperature (° C)	Error (K)
112.4626	31.26	30.99	31.23	-0.04
112.4626	31.26	30.98	31.22	-0.05
114.4926	36.41	36.10	36.36	-0.05
114.4926	36.41	36.10	36.35	-0.05
114.4926	36.41	36.11	36.36	-0.05
116.4071	41.26	40.98	41.25	-0.02
116.4071	41.26	40.98	41.25	-0.02
116.4071	41.26	40.98	41.25	-0.01
118.4382	46.43	46.16	46.44	0.02
118.4382	46.43	46.17	46.45	0.02
118.4382	46.43	46.16	46.44	0.02
120.1965	50.90	50.63	50.92	0.02
120.1965	50.90	50.64	50.93	0.03
120.1965	50.90	50.63	50.92	0.02
122.2254	56.07	55.79	56.10	0.03
122.2254	56.07	55.77	56.08	0.01
122.2254	56.07	55.77	56.08	0.01
124.1204	60.91	60.62	60.94	0.03
124.1204	60.91	60.62	60.94	0.03
124.1204	60.91	60.61	60.93	0.02
126.1486	66.10	65.82	66.15	0.06
126.1486	66.10	65.81	66.15	0.05
126.1486	66.10	65.81	66.15	0.05

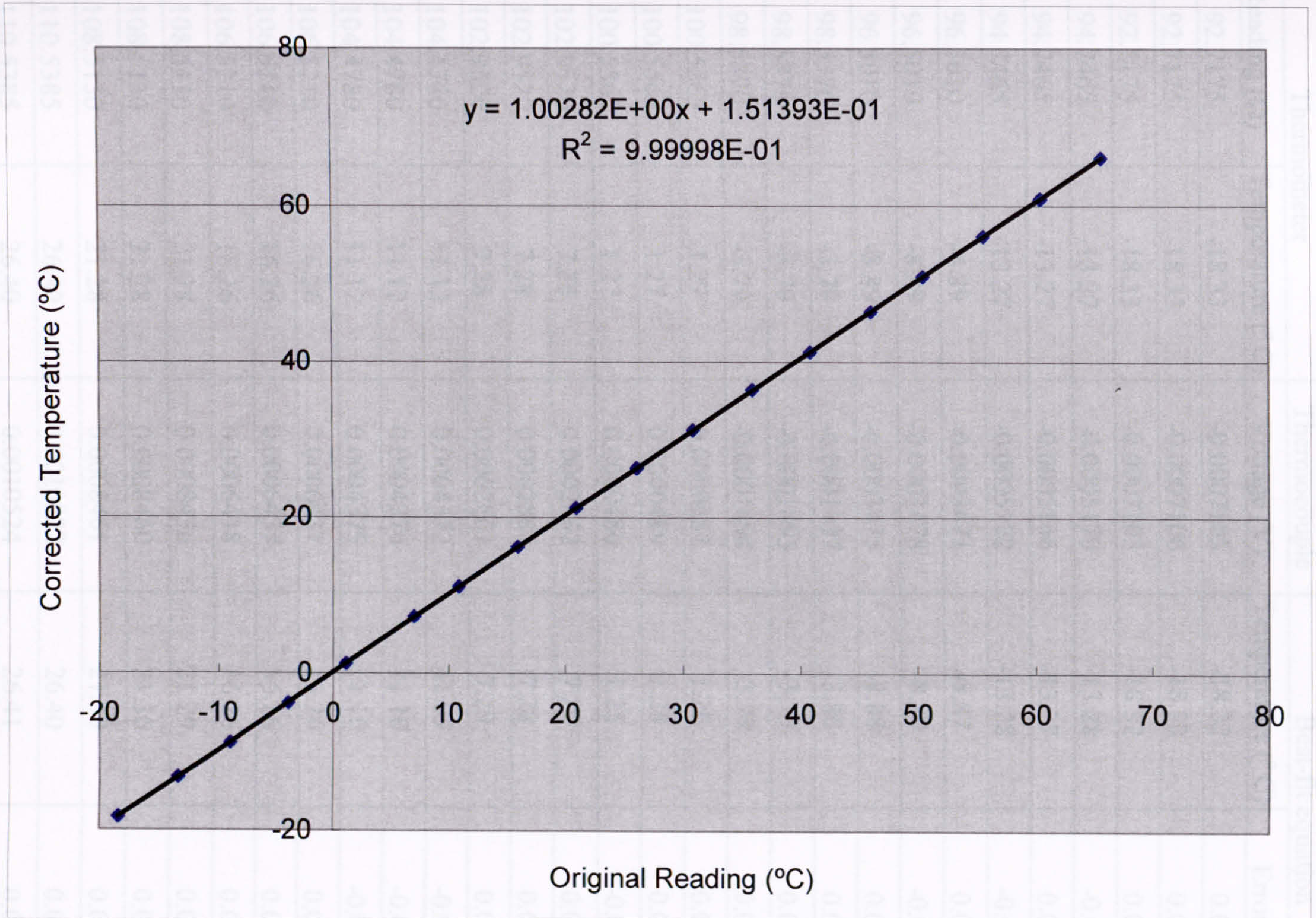

Figure F.9 The best-fit equation for the thermocouple probe T1.

Table F.13 The calibration data and the best-fit equation for the thermocouple (K-type thermocouple probe T2).

Thermometer		Thermocouple	Best-fit equation	
Reading (Ω)	Temperature (° C)	Voltage (V)	Temperature (° C)	Error (K)
92.7175	-18.33	-0.0007103	-18.32	0.01
92.7175	-18.33	-0.0007106	-18.33	0.00
92.7175	-18.33	-0.0007103	-18.32	0.01
94.7465	-13.27	-0.0005170	-13.28	-0.01
94.7465	-13.27	-0.0005166	-13.27	0.00
94.7465	-13.27	-0.0005172	-13.28	-0.01
96.5010	-8.89	-0.0003471	-8.87	0.01
96.5010	-8.89	-0.0003478	-8.89	-0.01
96.5010	-8.89	-0.0003475	-8.88	0.00
98.5370	-3.79	-0.0001497	-3.80	0.00
98.5370	-3.79	-0.0001495	-3.79	0.00
98.5370	-3.79	-0.0001494	-3.79	0.00
100.5565	1.27	0.0000484	1.26	0.00
100.5565	1.27	0.0000489	1.28	0.01
100.5565	1.27	0.0000480	1.25	-0.01
102.9520	7.28	0.0002862	7.29	0.01
102.9520	7.28	0.0002860	7.28	0.00
102.9520	7.28	0.0002861	7.29	0.01
104.4780	11.12	0.0004372	11.09	-0.03
104.4780	11.12	0.0004376	11.10	-0.02
104.4780	11.12	0.0004375	11.10	-0.02
106.5210	16.26	0.0006437	16.26	0.00
106.5210	16.26	0.0006437	16.26	0.00
106.5210	16.26	0.0006438	16.26	0.00
108.5130	21.28	0.0008456	21.29	0.00
108.5130	21.28	0.0008460	21.30	0.01
108.5130	21.28	0.0008461	21.30	0.02
110.5385	26.40	0.0010522	26.40	0.00
110.5385	26.40	0.0010524	26.41	0.01
110.5385	26.40	0.0010529	26.42	0.02
112.4626	31.26	0.0012496	31.26	0.00

Table F.13 The calibration data and the best-fit equation for the thermocouple (Cont.) (K-type thermocouple probe T2).

Thermometer		Thermocouple	Best-fit equation	
Reading (Ω)	Temperature (° C)	Voltage (V)	Temperature (° C)	Error (K)
112.4626	31.26	0.0012495	31.26	0.00
112.4626	31.26	0.0012493	31.26	-0.01
114.4926	36.41	0.0014587	36.39	-0.02
114.4926	36.41	0.0014591	36.40	-0.01
114.4926	36.41	0.0014594	36.41	0.00
116.4071	41.26	0.0016582	41.26	0.00
116.4071	41.26	0.0016582	41.26	0.00
116.4071	41.26	0.0016587	41.28	0.01
118.4382	46.43	0.0018700	46.42	-0.01
118.4382	46.43	0.0018702	46.42	0.00
118.4382	46.43	0.0018700	46.42	-0.01
120.1965	50.90	0.0020550	50.91	0.01
120.1965	50.90	0.0020557	50.92	0.02
120.1965	50.90	0.0020549	50.90	0.00
122.2254	56.07	0.0022684	56.07	0.00
122.2254	56.07	0.0022682	56.07	-0.01
122.2254	56.07	0.0022679	56.06	-0.01
124.1204	60.91	0.0024687	60.91	0.00
124.1204	60.91	0.0024687	60.91	0.00
124.1204	60.91	0.0024685	60.91	-0.01
126.1486	66.10	0.0026841	66.10	0.01
126.1486	66.10	0.0026839	66.10	0.00
126.1486	66.10	0.0026838	66.10	0.00

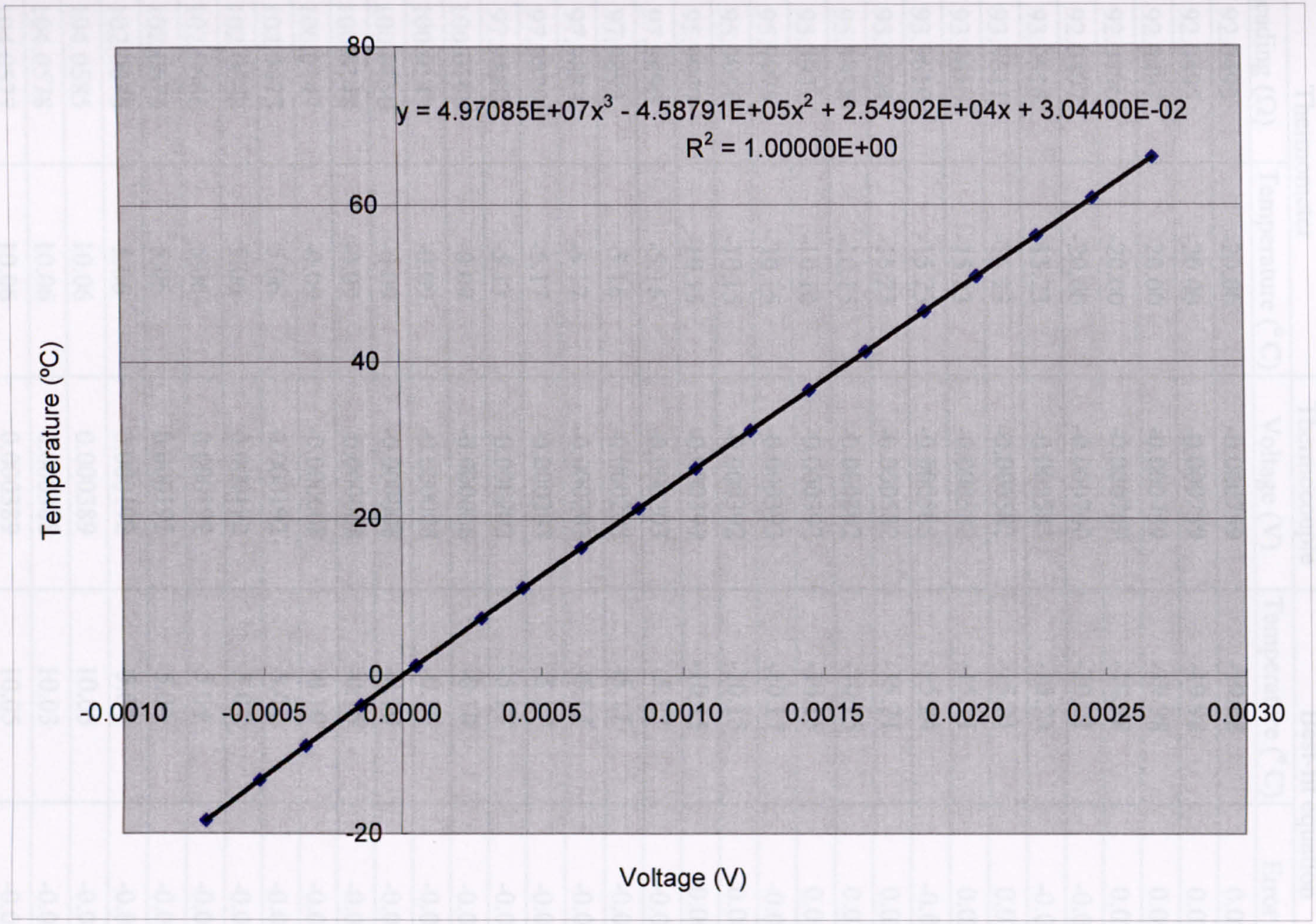

Figure F.10 The best-fit equation for the thermocouple probe T2.

Table F.14 The calibration data and the best-fit equation for the thermocouple (T-type thermocouple probe T3).

Thermometer		Thermocouple	Best-fit equation	
Reading (Ω)	Temperature (° C)	Voltage (V)	Temperature (° C)	Error (K)
92.0493	-20.00	-0.000759	-19.98	0.02
92.0495	-20.00	-0.000759	-19.98	0.02
92.0497	-20.00	-0.000759	-19.98	0.02
92.0496	-20.00	-0.000759	-19.98	0.02
92.0497	-20.00	-0.000760	-20.01	-0.01
93.9616	-15.23	-0.000583	-15.24	-0.01
93.9611	-15.23	-0.000582	-15.21	0.02
93.9615	-15.23	-0.000582	-15.21	0.02
93.9610	-15.23	-0.000583	-15.24	-0.01
93.9604	-15.23	-0.000582	-15.21	0.02
95.9938	-10.15	-0.000392	-10.15	0.01
95.9933	-10.16	-0.000392	-10.15	0.01
95.9975	-10.15	-0.000393	-10.17	-0.03
95.9961	-10.15	-0.000392	-10.15	0.00
95.9947	-10.15	-0.000392	-10.15	0.00
97.9890	-5.16	-0.000203	-5.17	-0.01
97.9893	-5.16	-0.000203	-5.17	-0.01
97.9883	-5.17	-0.000203	-5.17	-0.01
97.9879	-5.17	-0.000203	-5.17	-0.01
97.9880	-5.17	-0.000203	-5.17	-0.01
100.0168	-0.09	-0.000008	-0.10	-0.01
100.0149	-0.09	-0.000008	-0.10	-0.01
100.0150	-0.09	-0.000008	-0.10	-0.01
100.0148	-0.09	-0.000008	-0.10	-0.01
100.0147	-0.09	-0.000008	-0.10	-0.01
102.0673	5.06	0.000192	5.04	-0.01
102.0673	5.06	0.000192	5.04	-0.01
102.0666	5.06	0.000192	5.04	-0.01
102.0673	5.06	0.000192	5.04	-0.01
102.0675	5.06	0.000192	5.04	-0.01
104.0585	10.06	0.000389	10.05	-0.01
104.0578	10.06	0.000388	10.03	-0.03
104.0577	10.06	0.000389	10.05	-0.01
104.0576	10.06	0.000389	10.05	-0.01
104.0577	10.06	0.000388	10.03	-0.03

Table F.14 The calibration data and the best-fit equation for the thermocouple (Cont.) (T-type thermocouple probe T3).

Thermometer		Thermocouple	Best-fit equation	
Reading (Ω)	Temperature (° C)	Voltage (V)	Temperature (° C)	Error (K)
106.0342	15.03	0.000586	15.01	-0.03
106.0310	15.03	0.000587	15.03	0.01
106.0311	15.03	0.000586	15.01	-0.02
106.0334	15.03	0.000587	15.03	0.00
106.0342	15.03	0.000586	15.01	-0.03
107.9912	19.97	0.000785	19.96	-0.01
107.9885	19.96	0.000785	19.96	0.00
107.9915	19.97	0.000785	19.96	-0.01
107.9894	19.96	0.000785	19.96	-0.01
107.9927	19.97	0.000785	19.96	-0.01
109.9841	25.00	0.000989	24.97	-0.02
109.9834	25.00	0.000989	24.97	-0.02
109.9804	24.99	0.000990	25.00	0.01
109.9818	24.99	0.000990	25.00	0.01
109.9809	24.99	0.000989	24.97	-0.01
111.9868	30.06	0.001199	30.09	0.02
111.9805	30.04	0.001199	30.09	0.04
111.9803	30.04	0.001199	30.09	0.04
111.9806	30.04	0.001199	30.09	0.04
111.9801	30.04	0.001199	30.09	0.04
113.9139	34.94	0.001403	35.00	0.06
113.9129	34.94	0.001402	34.97	0.04
113.9113	34.93	0.001402	34.97	0.04
113.9117	34.93	0.001402	34.97	0.04
113.9109	34.93	0.001402	34.97	0.04
115.9190	40.03	0.001615	40.05	0.03
115.9191	40.03	0.001615	40.05	0.03
115.9213	40.03	0.001616	40.08	0.05
115.9166	40.02	0.001615	40.05	0.03
115.9164	40.02	0.001615	40.05	0.04
117.8787	45.00	0.001825	45.01	0.01
117.8763	45.00	0.001824	44.99	-0.01
117.8759	45.00	0.001824	44.99	-0.01
117.8765	45.00	0.001824	44.99	-0.01
117.8753	45.00	0.001825	45.01	0.02

Table F.14 The calibration data and the best-fit equation for the thermocouple (Cont.)

(T-type thermocouple probe T3).

Thermometer		Thermocouple	Best-fit equation	
Reading (Ω)	Temperature (° C)	Voltage (V)	Temperature (° C)	Error (K)
119.8394	49.99	0.002037	49.97	-0.02
119.8382	49.99	0.002036	49.95	-0.04
119.8369	49.99	0.002037	49.97	-0.01
119.8360	49.98	0.002037	49.97	-0.01
119.8358	49.98	0.002037	49.97	-0.01
121.8077	55.01	0.002253	54.98	-0.03
121.8080	55.01	0.002254	55.00	-0.01
121.8064	55.00	0.002254	55.00	0.00
121.8052	55.00	0.002254	55.00	0.00
121.8054	55.00	0.002253	54.98	-0.02
123.7615	59.99	0.002469	59.94	-0.05
123.7600	59.99	0.002469	59.94	-0.05
123.7581	59.99	0.002470	59.97	-0.02
123.7574	59.98	0.002470	59.97	-0.02
123.7565	59.98	0.002470	59.97	-0.02
125.7100	64.97	0.002688	64.93	-0.04
125.7118	64.98	0.002688	64.93	-0.05
125.7107	64.98	0.002689	64.96	-0.02
125.7085	64.97	0.002689	64.96	-0.01
125.7080	64.97	0.002689	64.96	-0.01
127.6819	70.02	0.002914	70.04	0.02
127.6790	70.02	0.002913	70.02	0.01
127.6785	70.01	0.002913	70.02	0.01
127.6787	70.01	0.002914	70.04	0.03
127.6792	70.02	0.002913	70.02	0.00
129.6203	74.99	0.003134	74.98	-0.01
129.6197	74.99	0.003135	75.00	0.01
129.6211	74.99	0.003135	75.00	0.01
129.6171	74.98	0.003134	74.98	-0.01
129.6189	74.99	0.003133	74.96	-0.03
131.6673	80.25	0.003371	80.26	0.01
131.6658	80.25	0.003372	80.28	0.04
131.6645	80.24	0.003372	80.28	0.04
131.6672	80.25	0.003371	80.26	0.01
131.6664	80.25	0.003371	80.26	0.01

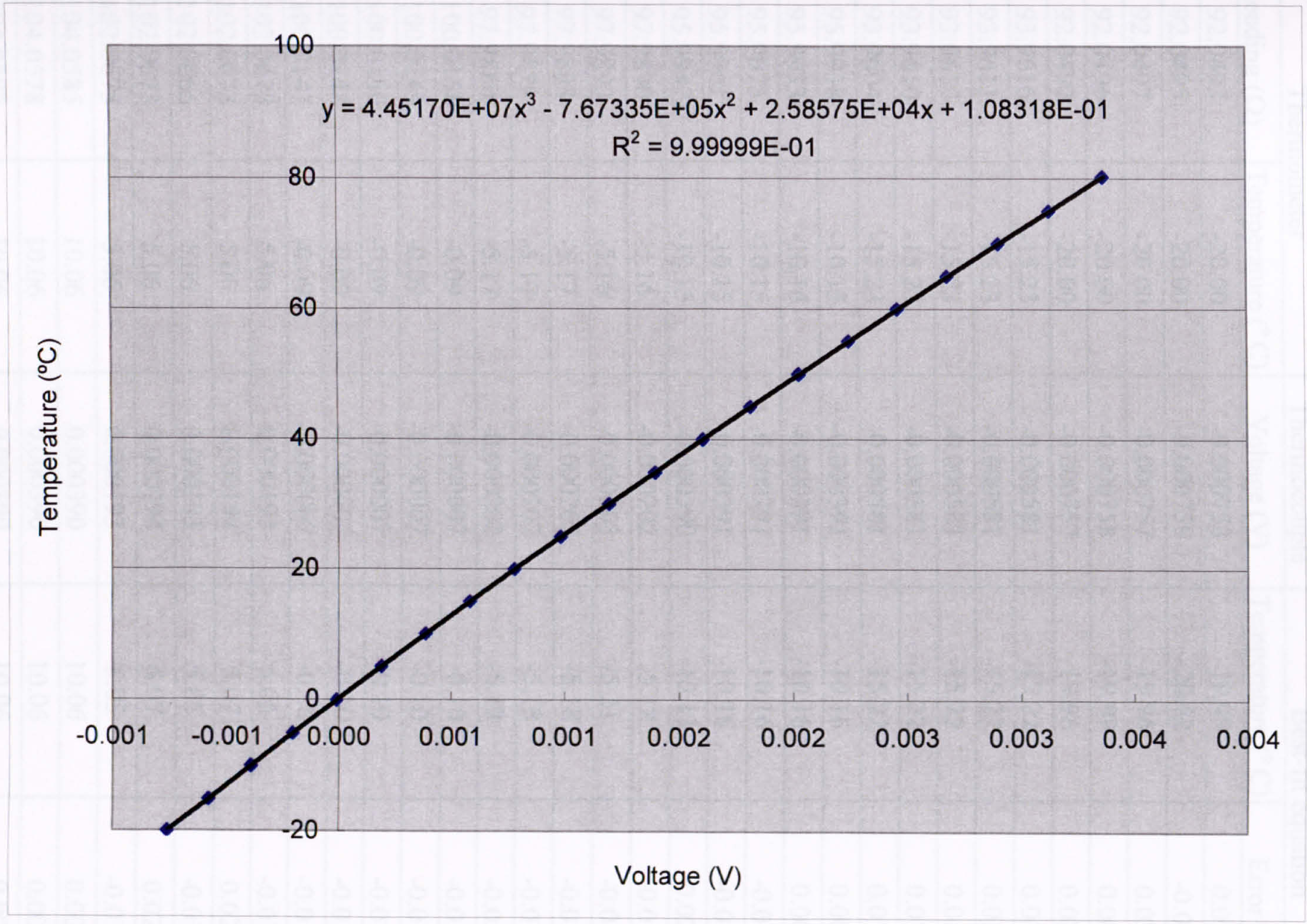

Figure F.11 The best-fit equation for the thermocouple probe T3.

Table F.15 The calibration data and the best-fit equation for the thermocouple (T-type thermocouple probe T4).

Thermometer		Thermocouple	Best-fit equation	
Reading (Ω)	Temperature (° C)	Voltage (V)	Temperature (° C)	Error (K)
92.0493	-20.00	-0.000758	-19.99	0.01
92.0495	-20.00	-0.000759	-20.02	-0.02
92.0497	-20.00	-0.000757	-19.96	0.03
92.0496	-20.00	-0.000758	-19.99	0.00
92.0497	-20.00	-0.000757	-19.96	0.03
93.9616	-15.23	-0.000581	-15.22	0.01
93.9611	-15.23	-0.000581	-15.22	0.01
93.9615	-15.23	-0.000581	-15.22	0.01
93.9610	-15.23	-0.000581	-15.22	0.01
93.9604	-15.23	-0.000581	-15.22	0.01
95.9938	-10.15	-0.000391	-10.16	0.00
95.9933	-10.16	-0.000391	-10.16	0.00
95.9975	-10.15	-0.000391	-10.16	-0.01
95.9961	-10.15	-0.000391	-10.16	-0.01
95.9947	-10.15	-0.000390	-10.13	0.02
97.9890	-5.16	-0.000202	-5.18	-0.01
97.9893	-5.16	-0.000203	-5.21	-0.04
97.9883	-5.17	-0.000202	-5.18	-0.01
97.9879	-5.17	-0.000202	-5.18	-0.01
97.9880	-5.17	-0.000202	-5.18	-0.01
100.0168	-0.09	-0.000007	-0.10	-0.01
100.0149	-0.09	-0.000007	-0.10	-0.01
100.0150	-0.09	-0.000007	-0.10	-0.01
100.0148	-0.09	-0.000007	-0.10	-0.01
100.0147	-0.09	-0.000007	-0.10	-0.01
102.0673	5.06	0.000193	5.05	-0.01
102.0673	5.06	0.000194	5.07	0.02
102.0666	5.06	0.000193	5.05	-0.01
102.0673	5.06	0.000194	5.07	0.02
102.0675	5.06	0.000193	5.05	-0.01
104.0585	10.06	0.000390	10.06	0.00
104.0578	10.06	0.000390	10.06	0.00
104.0577	10.06	0.000390	10.06	0.00
104.0576	10.06	0.000389	10.04	-0.02
104.0577	10.06	0.000390	10.06	0.00

Table F.15 The calibration data and the best-fit equation for the thermocouple (Cont.)

(T-type thermocouple probe T4).

Thermometer		Thermocouple	Best-fit equation	
Reading (Ω)	Temperature (° C)	Voltage (V)	Temperature (° C)	Error (K)
106.0342	15.03	0.000587	15.02	-0.01
106.0310	15.03	0.000587	15.02	-0.01
106.0311	15.03	0.000587	15.02	-0.01
106.0334	15.03	0.000587	15.02	-0.01
106.0342	15.03	0.000586	14.99	-0.04
107.9912	19.97	0.000785	19.95	-0.02
107.9885	19.96	0.000785	19.95	-0.01
107.9915	19.97	0.000786	19.97	0.01
107.9894	19.96	0.000786	19.97	0.01
107.9927	19.97	0.000785	19.95	-0.02
109.9841	25.00	0.000990	24.99	0.00
109.9834	25.00	0.000991	25.02	0.02
109.9804	24.99	0.000990	24.99	0.01
109.9818	24.99	0.000990	24.99	0.00
109.9809	24.99	0.000990	24.99	0.01
111.9868	30.06	0.001198	30.06	0.00
111.9805	30.04	0.001199	30.08	0.04
111.9803	30.04	0.001199	30.08	0.04
111.9806	30.04	0.001199	30.08	0.04
111.9801	30.04	0.001200	30.11	0.06
113.9139	34.94	0.001401	34.95	0.01
113.9129	34.94	0.001402	34.97	0.03
113.9113	34.93	0.001401	34.95	0.01
113.9117	34.93	0.001401	34.95	0.01
113.9109	34.93	0.001402	34.97	0.04
115.9190	40.03	0.001615	40.05	0.02
115.9191	40.03	0.001615	40.05	0.02
115.9213	40.03	0.001615	40.05	0.01
115.9166	40.02	0.001615	40.05	0.03
115.9164	40.02	0.001615	40.05	0.03
117.8787	45.00	0.001824	44.97	-0.03
117.8763	45.00	0.001824	44.97	-0.02
117.8759	45.00	0.001825	45.00	0.00
117.8765	45.00	0.001825	45.00	0.00
117.8753	45.00	0.001825	45.00	0.00

Table F.15 The calibration data and the best-fit equation for the thermocouple (Cont.) (T-type thermocouple probe T4).

Thermometer		Thermocouple	Best-fit equation	
Reading (Ω)	Temperature (° C)	Voltage (V)	Temperature (° C)	Error (K)
119.8394	49.99	0.002038	49.97	-0.03
119.8382	49.99	0.002038	49.97	-0.02
119.8369	49.99	0.002039	49.99	0.00
119.8360	49.98	0.002038	49.97	-0.02
119.8358	49.98	0.002039	49.99	0.01
121.8077	55.01	0.002255	54.98	-0.03
121.8080	55.01	0.002255	54.98	-0.03
121.8064	55.00	0.002256	55.00	0.00
121.8052	55.00	0.002255	54.98	-0.02
121.8054	55.00	0.002256	55.00	0.00
123.7615	59.99	0.002472	59.94	-0.06
123.7600	59.99	0.002472	59.94	-0.05
123.7581	59.99	0.002472	59.94	-0.05
123.7574	59.98	0.002472	59.94	-0.05
123.7565	59.98	0.002472	59.94	-0.04
125.7100	64.97	0.002695	64.99	0.01
125.7118	64.98	0.002696	65.01	0.03
125.7107	64.98	0.002695	64.99	0.01
125.7085	64.97	0.002696	65.01	0.04
125.7080	64.97	0.002695	64.99	0.02
127.6819	70.02	0.002921	70.05	0.03
127.6790	70.02	0.002920	70.03	0.02
127.6785	70.01	0.002920	70.03	0.02
127.6787	70.01	0.002920	70.03	0.02
127.6792	70.02	0.002920	70.03	0.02
129.6203	74.99	0.003143	74.98	-0.01
129.6197	74.99	0.003144	75.01	0.02
129.6211	74.99	0.003143	74.98	-0.01
129.6171	74.98	0.003143	74.98	0.00
129.6189	74.99	0.003144	75.01	0.02
131.6673	80.25	0.003383	80.27	0.02
131.6658	80.25	0.003382	80.25	0.00
131.6645	80.24	0.003382	80.25	0.00
131.6672	80.25	0.003381	80.22	-0.03
131.6664	80.25	0.003382	80.25	0.00

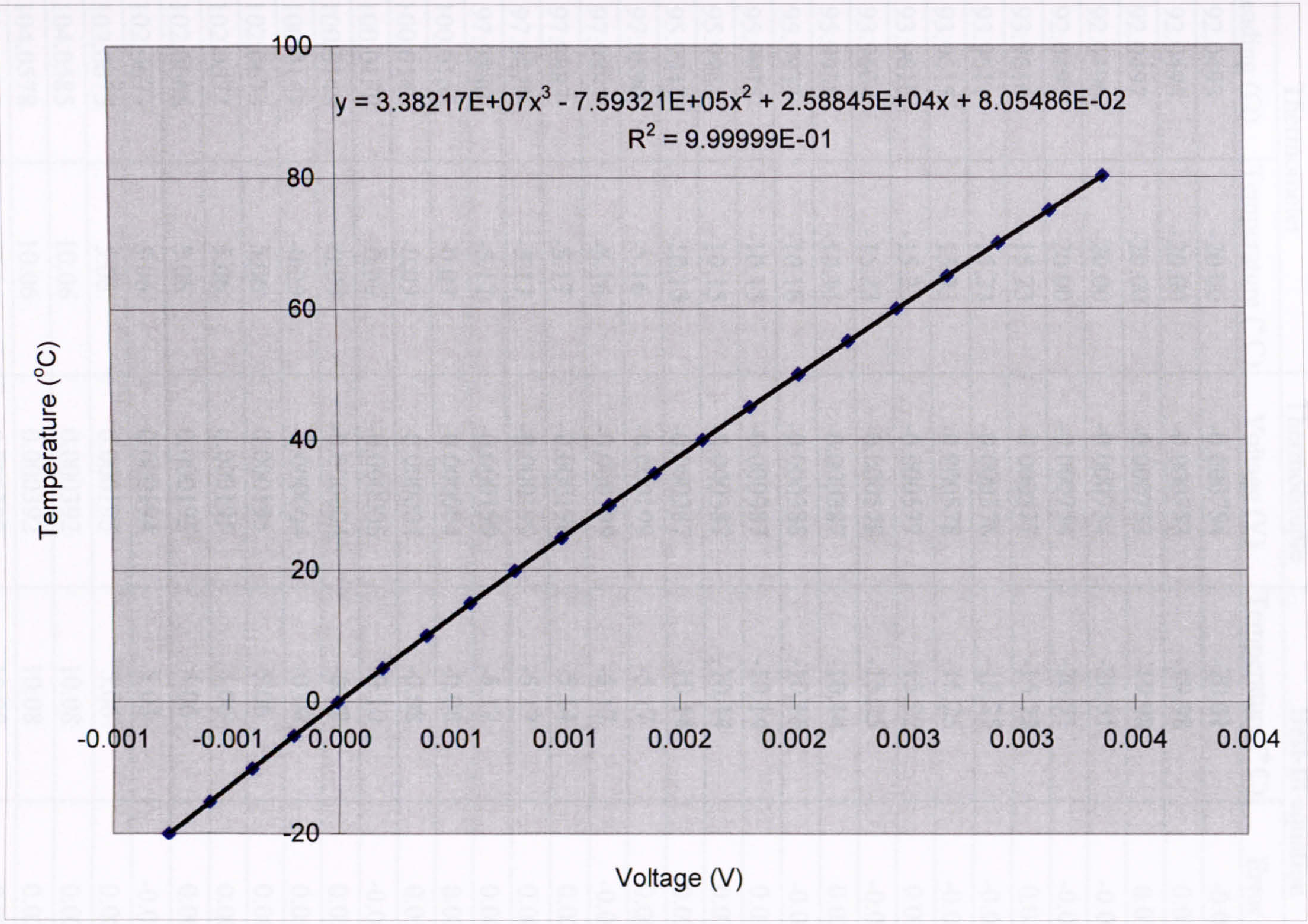

Figure F.12 The best-fit equation for the thermocouple probe T4.

Table F.16 The calibration data and the best-fit equation for the thermocouple (T-type thermocouple probe T0).

Thermometer		Thermocouple	Best-fit equation	
Reading (Ω)	Temperature (° C)	Voltage (V)	Temperature (° C)	Error (K)
92.0493	-20.00	-0.000754	-20.01	-0.01
92.0495	-20.00	-0.000753	-19.98	0.01
92.0497	-20.00	-0.000753	-19.98	0.01
92.0496	-20.00	-0.000754	-20.01	-0.01
92.0497	-20.00	-0.000754	-20.01	-0.01
93.9616	-15.23	-0.000577	-15.22	0.01
93.9611	-15.23	-0.000578	-15.25	-0.02
93.9615	-15.23	-0.000578	-15.25	-0.02
93.9610	-15.23	-0.000577	-15.22	0.01
93.9604	-15.23	-0.000578	-15.25	-0.01
95.9938	-10.15	-0.000387	-10.14	0.02
95.9933	-10.16	-0.000388	-10.16	-0.01
95.9975	-10.15	-0.000387	-10.14	0.01
95.9961	-10.15	-0.000387	-10.14	0.01
95.9947	-10.15	-0.000387	-10.14	0.02
97.9890	-5.16	-0.000199	-5.17	0.00
97.9893	-5.16	-0.000199	-5.17	-0.01
97.9883	-5.17	-0.000198	-5.14	0.02
97.9879	-5.17	-0.000199	-5.17	0.00
97.9880	-5.17	-0.000199	-5.17	0.00
100.0168	-0.09	-0.000004	-0.08	0.01
100.0149	-0.09	-0.000004	-0.08	0.01
100.0150	-0.09	-0.000005	-0.10	-0.01
100.0148	-0.09	-0.000004	-0.08	0.01
100.0147	-0.09	-0.000004	-0.08	0.01
102.0673	5.06	0.000195	5.06	0.00
102.0673	5.06	0.000195	5.06	0.00
102.0666	5.06	0.000195	5.06	0.00
102.0673	5.06	0.000194	5.03	-0.03
102.0675	5.06	0.000195	5.06	0.00
104.0585	10.06	0.000392	10.08	0.02
104.0578	10.06	0.000392	10.08	0.02
104.0577	10.06	0.000392	10.08	0.02
104.0576	10.06	0.000392	10.08	0.02
104.0577	10.06	0.000391	10.05	-0.01

Table F.16 The calibration data and the best-fit equation for the thermocouple (Cont.) (T-type thermocouple probe T0).

Thermometer		Thermocouple	Best-fit equation	
Reading (Ω)	Temperature (° C)	Voltage (V)	Temperature (° C)	Error (K)
106.0342	15.03	0.000588	15.02	-0.01
106.0310	15.03	0.000588	15.02	-0.01
106.0311	15.03	0.000589	15.04	0.02
106.0334	15.03	0.000588	15.02	-0.01
106.0342	15.03	0.000588	15.02	-0.01
107.9912	19.97	0.000786	19.96	-0.01
107.9885	19.96	0.000786	19.96	0.00
107.9915	19.97	0.000786	19.96	-0.01
107.9894	19.96	0.000785	19.93	-0.03
107.9927	19.97	0.000786	19.96	-0.01
109.9841	25.00	0.000990	24.99	-0.01
109.9834	25.00	0.000990	24.99	-0.01
109.9804	24.99	0.000990	24.99	0.00
109.9818	24.99	0.000990	24.99	-0.01
109.9809	24.99	0.000990	24.99	0.00
111.9868	30.06	0.001197	30.04	-0.03
111.9805	30.04	0.001197	30.04	-0.01
111.9803	30.04	0.001197	30.04	-0.01
111.9806	30.04	0.001197	30.04	-0.01
111.9801	30.04	0.001198	30.06	0.02
113.9139	34.94	0.001400	34.94	0.00
113.9129	34.94	0.001400	34.94	0.00
113.9113	34.93	0.001401	34.96	0.03
113.9117	34.93	0.001400	34.94	0.00
113.9109	34.93	0.001400	34.94	0.00
115.9190	40.03	0.001613	40.03	0.00
115.9191	40.03	0.001614	40.05	0.03
115.9213	40.03	0.001613	40.03	0.00
115.9166	40.02	0.001613	40.03	0.01
115.9164	40.02	0.001613	40.03	0.01
117.8787	45.00	0.001824	45.02	0.02
117.8763	45.00	0.001823	45.00	0.00
117.8759	45.00	0.001823	45.00	0.00
117.8765	45.00	0.001824	45.02	0.02
117.8753	45.00	0.001824	45.02	0.03

Table F.16 The calibration data and the best-fit equation for the thermocouple (Cont.) (T-type thermocouple probe T0).

Thermometer		Thermocouple	Best-fit equation	
Reading (Ω)	Temperature (° C)	Voltage (V)	Temperature (° C)	Error (K)
119.8394	49.99	0.002036	49.99	0.00
119.8382	49.99	0.002036	49.99	0.00
119.8369	49.99	0.002036	49.99	0.01
119.8360	49.98	0.002036	49.99	0.01
119.8358	49.98	0.002037	50.02	0.03
121.8077	55.01	0.002250	54.97	-0.04
121.8080	55.01	0.002251	54.99	-0.02
121.8064	55.00	0.002251	54.99	-0.01
121.8052	55.00	0.002251	54.99	-0.01
121.8054	55.00	0.002251	54.99	-0.01
123.7615	59.99	0.002468	59.99	0.00
123.7600	59.99	0.002467	59.97	-0.02
123.7581	59.99	0.002467	59.97	-0.02
123.7574	59.98	0.002467	59.97	-0.01
123.7565	59.98	0.002468	59.99	0.01
125.7100	64.97	0.002686	64.98	0.00
125.7118	64.98	0.002686	64.98	0.00
125.7107	64.98	0.002686	64.98	0.00
125.7085	64.97	0.002685	64.95	-0.02
125.7080	64.97	0.002686	64.98	0.01
127.6819	70.02	0.002908	70.01	-0.01
127.6790	70.02	0.002909	70.04	0.02
127.6785	70.01	0.002908	70.01	0.00
127.6787	70.01	0.002909	70.04	0.02
127.6792	70.02	0.002909	70.04	0.02
129.6203	74.99	0.003128	74.97	-0.02
129.6197	74.99	0.003128	74.97	-0.02
129.6211	74.99	0.003129	74.99	0.00
129.6171	74.98	0.003129	74.99	0.01
129.6189	74.99	0.003129	74.99	0.01
131.6673	80.25	0.003364	80.26	0.01
131.6658	80.25	0.003363	80.23	-0.01
131.6645	80.24	0.003364	80.26	0.01
131.6672	80.25	0.003363	80.23	-0.02
131.6664	80.25	0.003364	80.26	0.01

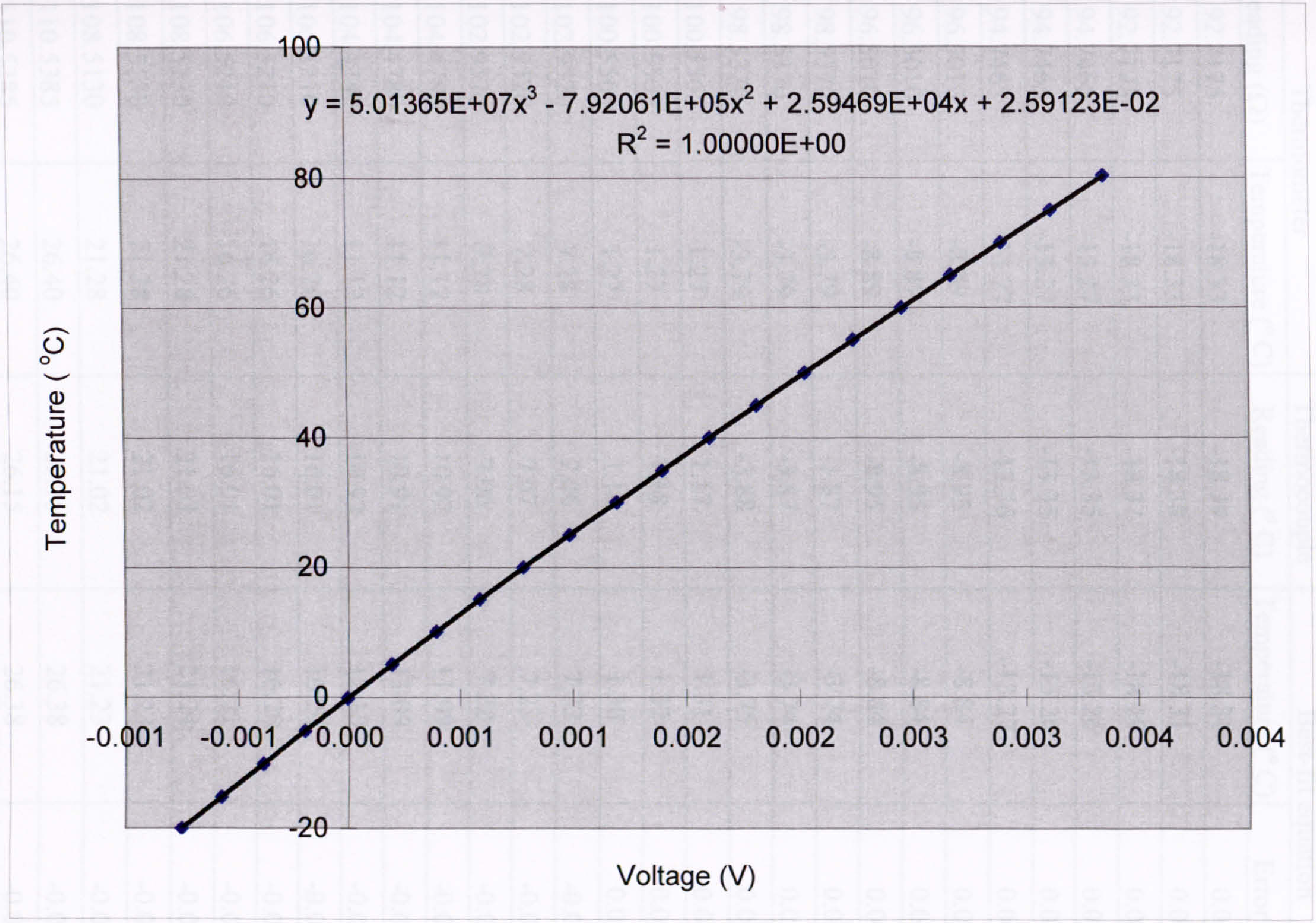

Figure F.13 The best-fit equation for the thermocouple probe T0.

Table F.17 The calibration data and the best-fit equation for the thermocouple (K-type thermocouple probe T5).

Thermometer		Thermocouple	Best-fit equation	
Reading (Ω)	Temperature (° C)	Reading (° C)	Temperature (° C)	Error (K)
92.7175	-18.33	-18.39	-18.31	0.02
92.7175	-18.33	-18.38	-18.31	0.02
92.7175	-18.33	-18.37	-18.29	0.04
94.7465	-13.27	-13.35	-13.26	0.01
94.7465	-13.27	-13.35	-13.26	0.01
94.7465	-13.27	-13.36	-13.27	0.00
96.5010	-8.89	-8.95	-8.84	0.04
96.5010	-8.89	-8.95	-8.84	0.05
96.5010	-8.89	-8.95	-8.84	0.04
98.5370	-3.79	-3.87	-3.74	0.05
98.5370	-3.79	-3.87	-3.74	0.05
98.5370	-3.79	-3.88	-3.75	0.04
100.5565	1.27	1.17	1.31	0.04
100.5565	1.27	1.18	1.32	0.06
100.5565	1.27	1.16	1.30	0.04
102.9520	7.28	7.06	7.22	-0.06
102.9520	7.28	7.07	7.23	-0.05
102.9520	7.28	7.06	7.22	-0.06
104.4780	11.12	10.92	11.09	-0.02
104.4780	11.12	10.91	11.09	-0.03
104.4780	11.12	10.92	11.10	-0.02
106.5210	16.26	16.01	16.20	-0.06
106.5210	16.26	16.01	16.20	-0.06
106.5210	16.26	16.01	16.21	-0.05
108.5130	21.28	21.03	21.24	-0.04
108.5130	21.28	21.02	21.23	-0.05
108.5130	21.28	21.02	21.23	-0.05
110.5385	26.40	26.15	26.38	-0.02
110.5385	26.40	26.15	26.38	-0.02
110.5385	26.40	26.16	26.39	-0.01
112.4626	31.26	30.97	31.22	-0.05

Table F.17 The calibration data and the best-fit equation for the thermocouple (Cont.) (K-type thermocouple probe T5).

Thermometer		Thermocouple	Best-fit equation	
Reading (Ω)	Temperature (° C)	Reading (° C)	Temperature (° C)	Error (K)
112.4626	31.26	30.97	31.22	-0.05
112.4626	31.26	30.97	31.22	-0.05
114.4926	36.41	36.09	36.36	-0.05
114.4926	36.41	36.10	36.36	-0.05
114.4926	36.41	36.10	36.36	-0.05
116.4071	41.26	40.96	41.24	-0.02
116.4071	41.26	40.98	41.26	-0.01
116.4071	41.26	40.98	41.26	-0.01
118.4382	46.43	46.15	46.45	0.02
118.4382	46.43	46.15	46.45	0.02
118.4382	46.43	46.15	46.45	0.02
120.1965	50.90	50.61	50.92	0.02
120.1965	50.90	50.61	50.92	0.02
120.1965	50.90	50.60	50.91	0.01
122.2254	56.07	55.76	56.09	0.02
122.2254	56.07	55.76	56.09	0.02
122.2254	56.07	55.75	56.08	0.01
124.1204	60.91	60.59	60.94	0.03
124.1204	60.91	60.59	60.94	0.03
124.1204	60.91	60.59	60.94	0.03
126.1486	66.10	65.79	66.15	0.06
126.1486	66.10	65.79	66.15	0.05
126.1486	66.10	65.78	66.15	0.05

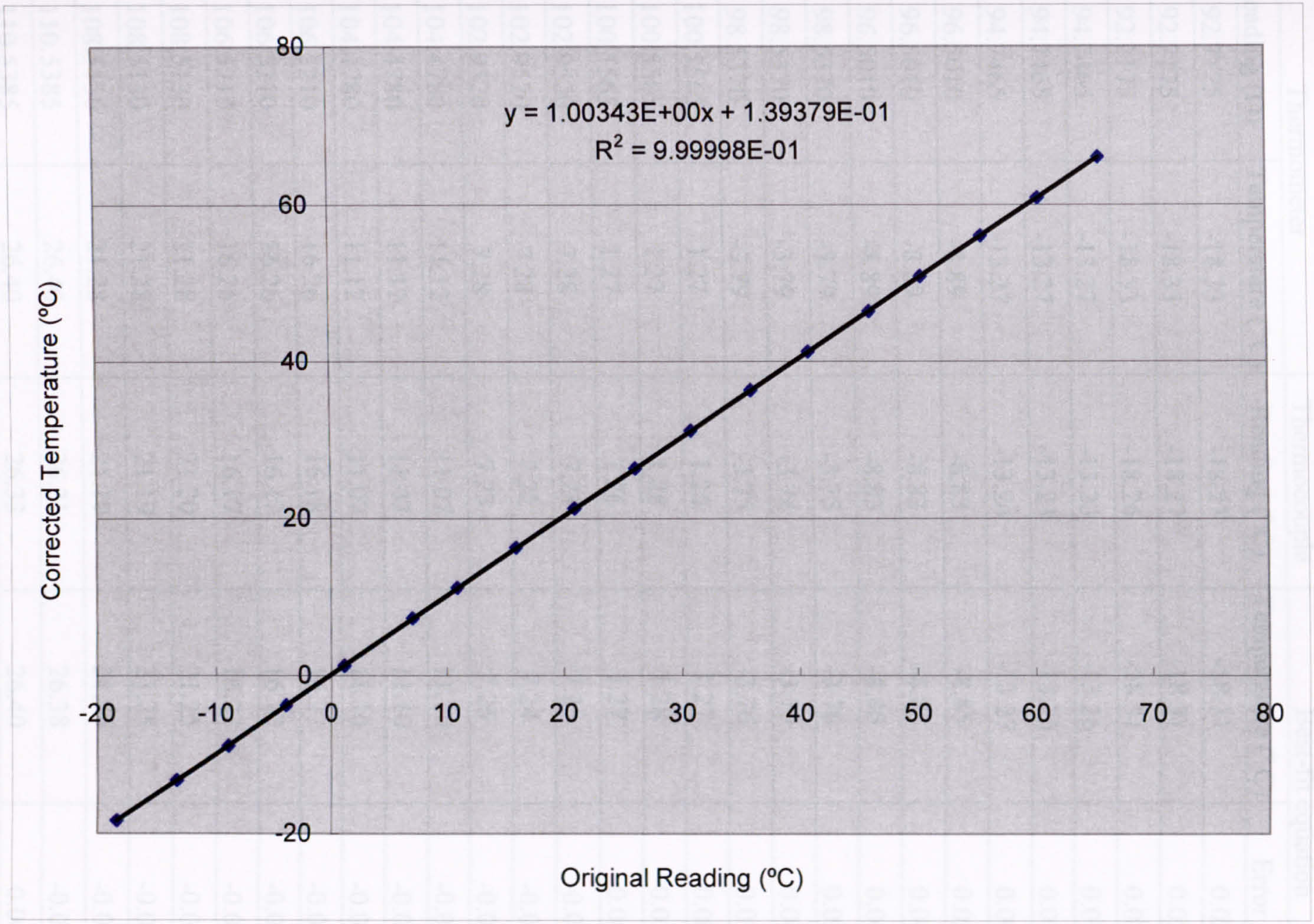

Figure F.14 The best-fit equation for the thermocouple probe T5.

Table F.18 The calibration data and the best-fit equation for the thermocouple (K-type thermocouple probe T6).

Thermometer		Thermocouple	Best-fit equation	
Reading (Ω)	Temperature (° C)	Reading (° C)	Temperature (° C)	Error (K)
92.7175	-18.33	-18.27	-18.31	0.02
92.7175	-18.33	-18.27	-18.31	0.02
92.7175	-18.33	-18.26	-18.31	0.03
94.7465	-13.27	-13.23	-13.26	0.01
94.7465	-13.27	-13.23	-13.26	0.01
94.7465	-13.27	-13.24	-13.27	0.00
96.5010	-8.89	-8.83	-8.85	0.03
96.5010	-8.89	-8.83	-8.85	0.04
96.5010	-8.89	-8.83	-8.85	0.04
98.5370	-3.79	-3.75	-3.76	0.03
98.5370	-3.79	-3.74	-3.75	0.04
98.5370	-3.79	-3.75	-3.76	0.03
100.5565	1.27	1.26	1.27	0.00
100.5565	1.27	1.28	1.28	0.02
100.5565	1.27	1.26	1.27	0.00
102.9520	7.28	7.23	7.25	-0.03
102.9520	7.28	7.22	7.24	-0.04
102.9520	7.28	7.23	7.25	-0.03
104.4780	11.12	11.07	11.10	-0.01
104.4780	11.12	11.07	11.10	-0.01
104.4780	11.12	11.07	11.10	-0.01
106.5210	16.26	16.18	16.22	-0.04
106.5210	16.26	16.17	16.22	-0.04
106.5210	16.26	16.17	16.22	-0.04
108.5130	21.28	21.20	21.25	-0.03
108.5130	21.28	21.19	21.25	-0.03
108.5130	21.28	21.19	21.25	-0.03
110.5385	26.40	26.31	26.38	-0.02
110.5385	26.40	26.33	26.40	0.00
110.5385	26.40	26.33	26.40	0.00
112.4626	31.26	31.15	31.23	-0.03

Table F.18 The calibration data and the best-fit equation for the thermocouple (Cont.) (K-type thermocouple probe T6).

Thermometer		Thermocouple	Best-fit equation	
Reading (Ω)	Temperature (° C)	Reading (° C)	Temperature (° C)	Error (K)
112.4626	31.26	31.15	31.23	-0.03
112.4626	31.26	31.15	31.23	-0.03
114.4926	36.41	36.27	36.37	-0.04
114.4926	36.41	36.27	36.37	-0.04
114.4926	36.41	36.28	36.37	-0.03
116.4071	41.26	41.15	41.26	-0.01
116.4071	41.26	41.15	41.26	0.00
116.4071	41.26	41.16	41.27	0.00
118.4382	46.43	46.33	46.45	0.03
118.4382	46.43	46.33	46.46	0.03
118.4382	46.43	46.33	46.46	0.03
120.1965	50.90	50.78	50.92	0.01
120.1965	50.90	50.79	50.93	0.02
120.1965	50.90	50.77	50.91	0.00
122.2254	56.07	55.94	56.09	0.02
122.2254	56.07	55.93	56.08	0.01
122.2254	56.07	55.93	56.08	0.01
124.1204	60.91	60.76	60.92	0.01
124.1204	60.91	60.76	60.92	0.01
124.1204	60.91	60.76	60.92	0.01
126.1486	66.10	65.95	66.12	0.03
126.1486	66.10	65.94	66.12	0.02
126.1486	66.10	65.95	66.12	0.03

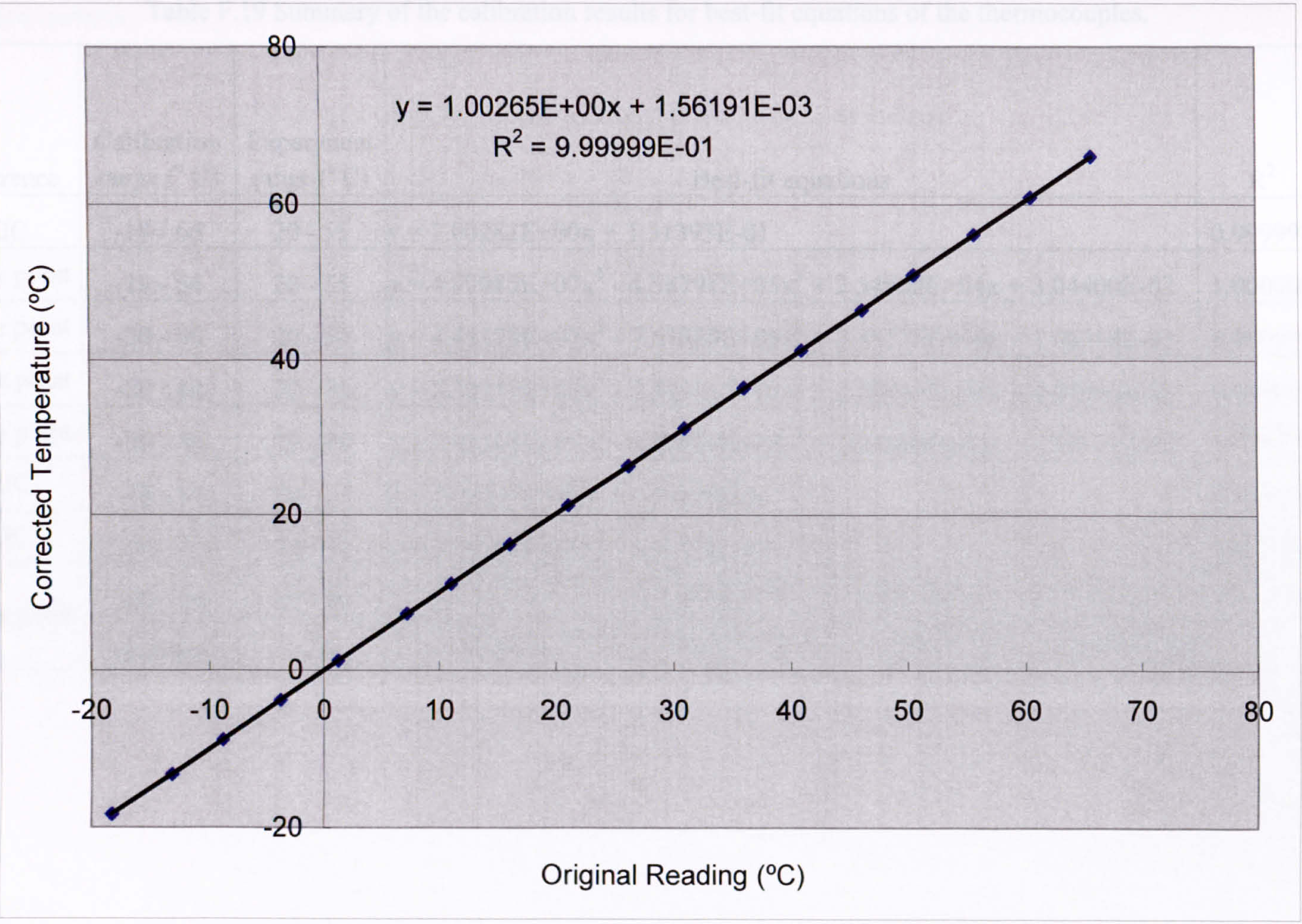

Figure F.15 The best-fit equation for the thermocouple probe T6.

Table F.19 Summary of the calibration results for best-fit equations of the thermocouples.

No.	Reference	Calibration range (°C)	Experiment range (°C)	Best-fit equations	R^2	Max. error within the experimental range (K)
T1	CJC	-18 - 66	20 - 55	$y = 1.00282E{+}00x + 1.51393E{-}01$	0.999998	0.03
T2	Triple point	-18 - 66	20 - 55	$y = 4.97085E{+}07x^3 - 4.58791E{+}05x^2 + 2.54902E{+}04x + 3.04400E{-}02$	1.000000	0.02
T3	Triple point	-20 - 80	20 - 55	$y = 4.45170E{+}07x^3 - 7.67335E{+}05x^2 + 2.58575E{+}04x + 1.08318E{-}01$	0.999999	0.04
T4	Triple point	-20 - 80	20 - 55	$y = 3.38217E{+}07x^3 - 7.59321E{+}05x^2 + 2.58845E{+}04x + 8.05486E{-}02$	0.999999	0.04
T0	Triple point	-20 - 80	20 - 55	$y = 5.01365E{+}07x^3 - 7.92061E{+}05x^2 + 2.59469E{+}04x + 2.59123E{-}02$	1.000000	0.04
T5	CJC	-18 - 66	20 - 55	$y = 1.00343E{+}00x + 1.39379E{-}01$	0.999998	0.03
T6	CJC	-18 - 66	20 - 55	$y = 1.00265E{+}00x + 1.56191E{-}03$	0.999999	0.04
TT_{1-15}	Triple point	-20 - 80	20 - 80	$y = 5.15193E{+}07x^3 - 4.43639E{+}05x^2 + 2.53218E{+}04x + 2.04026E{-}01$	1.000000	0.02
		Standard	> 80	$y = -2.03857E{+}07x^3 + 4.75514E{+}05x^2 + 2.12931E{+}04x + 6.14897E{+}00$		

F.3 Mass flow meters

Table F.20 The equations for the mass flow meters.

No.	Type	Maximum range (kg/hr)	Calibration range (kg/hr)	Equations	Error range
F1	CMF010M325NM	0 - 81.6	0 -25	y = 3.12500E+00x - 6.25000E+00	0.11% - 0.51%
F2	CMF025M319NM	0 - 1088.6	25 - 500	y = 3.12500E+01x - 6.25000E+01	0.11% - 0.19%

F.4 Differential pressure transmitters

Table F.21 The calibration data for the differential pressure transmitter DP1 (24% scale range).

Test No.	1	2	3	4	Unit
Water density (at 18.5 °C)	998.53	998.53	998.53	998.53	kg/m^3
Water level difference	0.0	323.0	477.5	621.2	mm
Measured pressure difference	0.00000	0.03163	0.04676	0.06082	bar
Signal output	2.0465	6.1745	8.1763	10.0000	V
Calculated pressure difference	0.00001	0.03156	0.04685	0.06079	bar
Difference between measurement and calculation	1	-7	10	-4	Pa
Relative error		0.23%	-0.20%	0.06%	

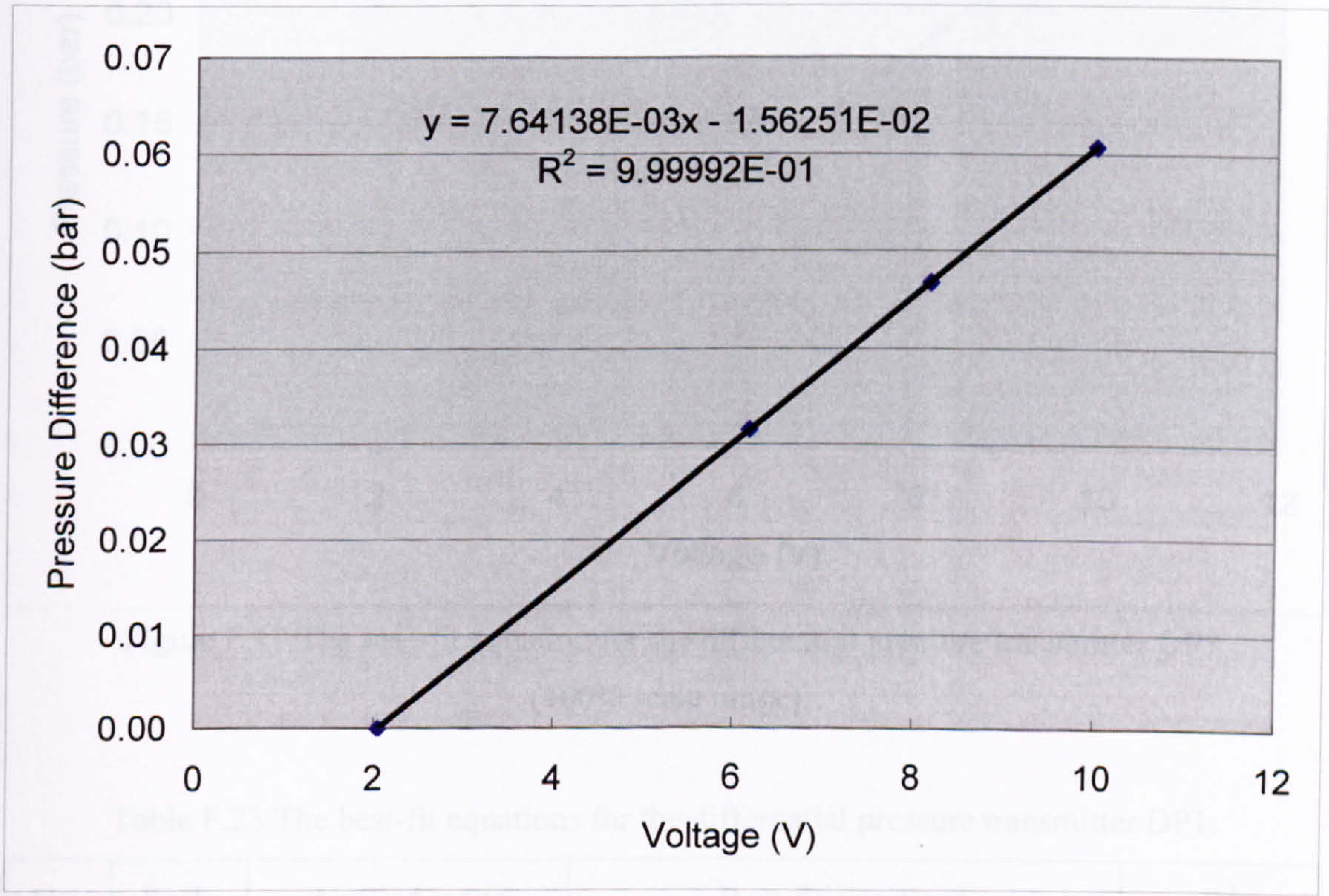

Figure F.16 The best-fit equation for the differential pressure transmitter DP1 (24% scale range).

Table F.22 The calibration data for the differential pressure transmitter DP1 (100% scale range).

Test No.	1	2	Unit
Water density	1000.0	1000.0	kg/m^3
Water level difference	0.0	100.0	in.
Measured pressure difference	0.0000	0.2491	bar
Signal output	2.0	10.0	v
Calculated pressure difference	0.0000	0.2491	bar
Difference between measurement and calculation	0	0	Pa

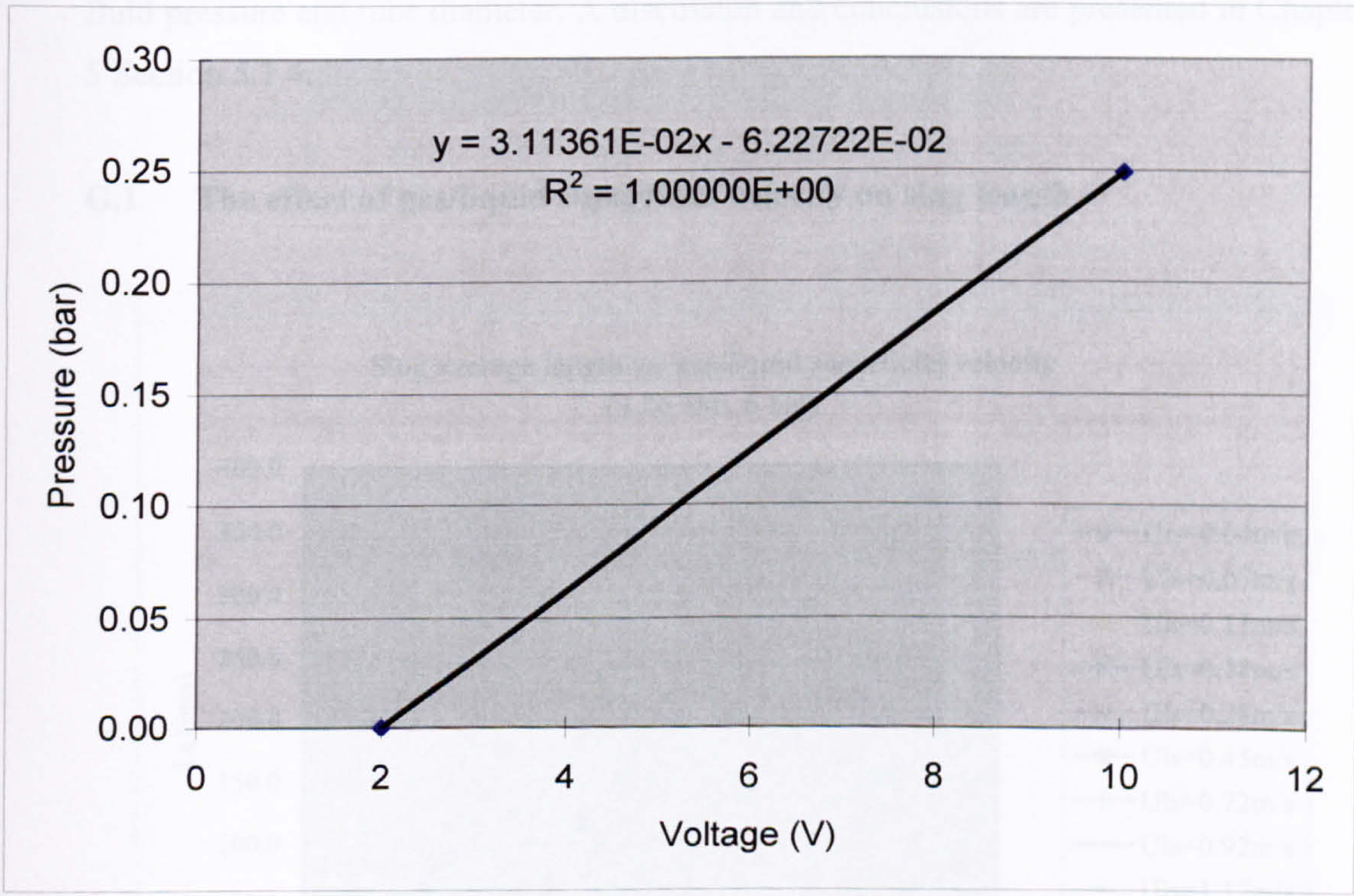

Figure F.17 The best-fit equation for the differential pressure transmitter DP1 (100% scale range).

Table F.23 The best-fit equations for the differential pressure transmitter DP1.

No.	Scale	Applied range	Best-fit equations	R^2
DP1	24%	0 - 24 in. water	y = 7.64138E-03x - 1.56251E-02	0.999992
	100%	24 - 100 in. water	y = 3.11361E-02x - 6.22722E-02	1.000000

Appendix G

Effect Factors on Slug Length

The present study indicates that slug length is an important factor affecting the slug configuration and may reveal the transition mechanism from slug flow to churn flow. The maximum and average slug length was measured in the present experiments and shows that various parameters affect it. The complete experimental results are presented and compared in this appendix to reveal the effect of gas/liquid superficial velocity, fluid pressure and tube diameter. A discussion and conclusions are presented in Chapter 5 Section 5.1.4.

G.1 The effect of gas/liquid superficial velocity on slug length

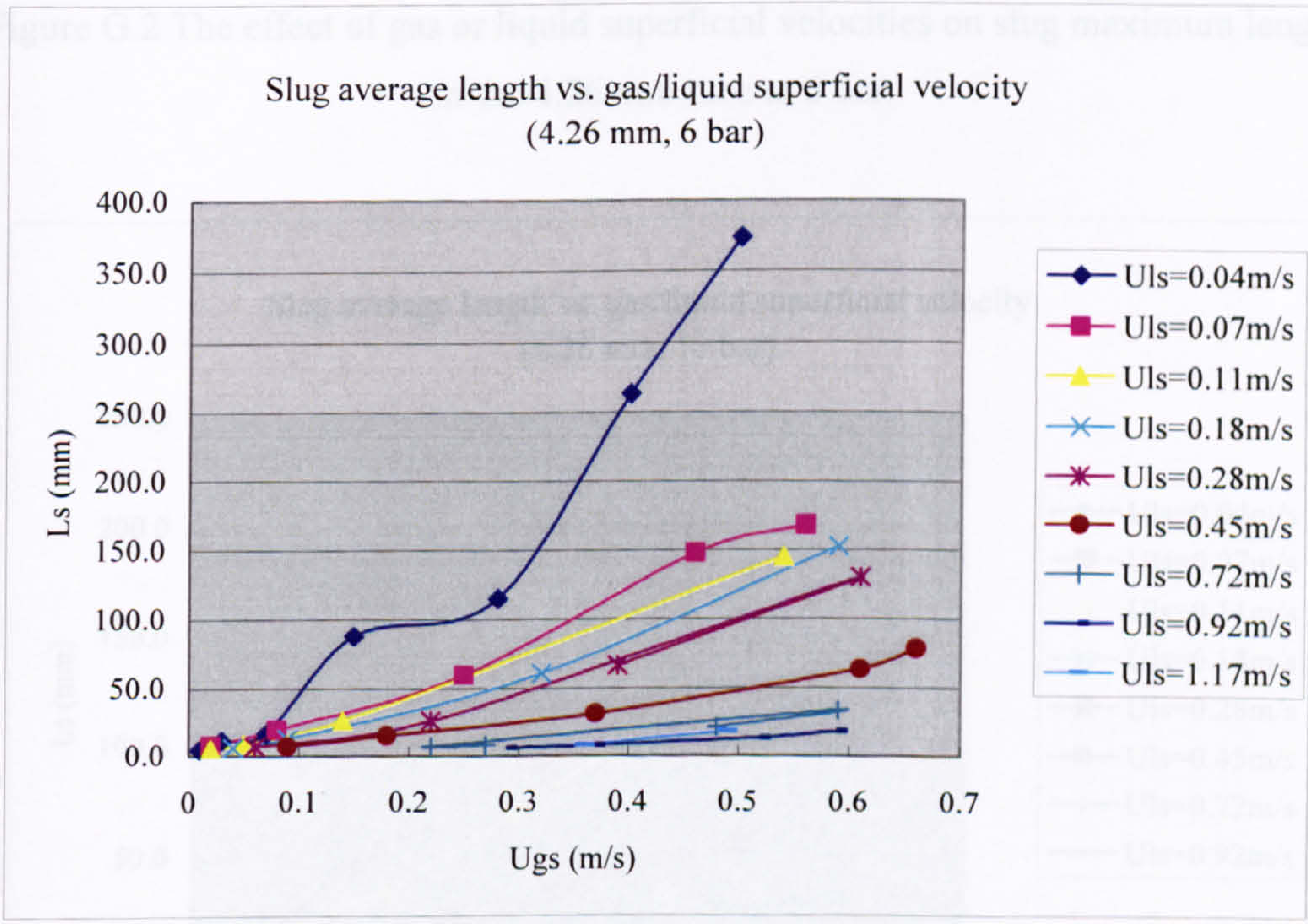

Figure G.1 The effect of gas or liquid superficial velocities on slug average length in the 4.26 mm tube at 6 bar.

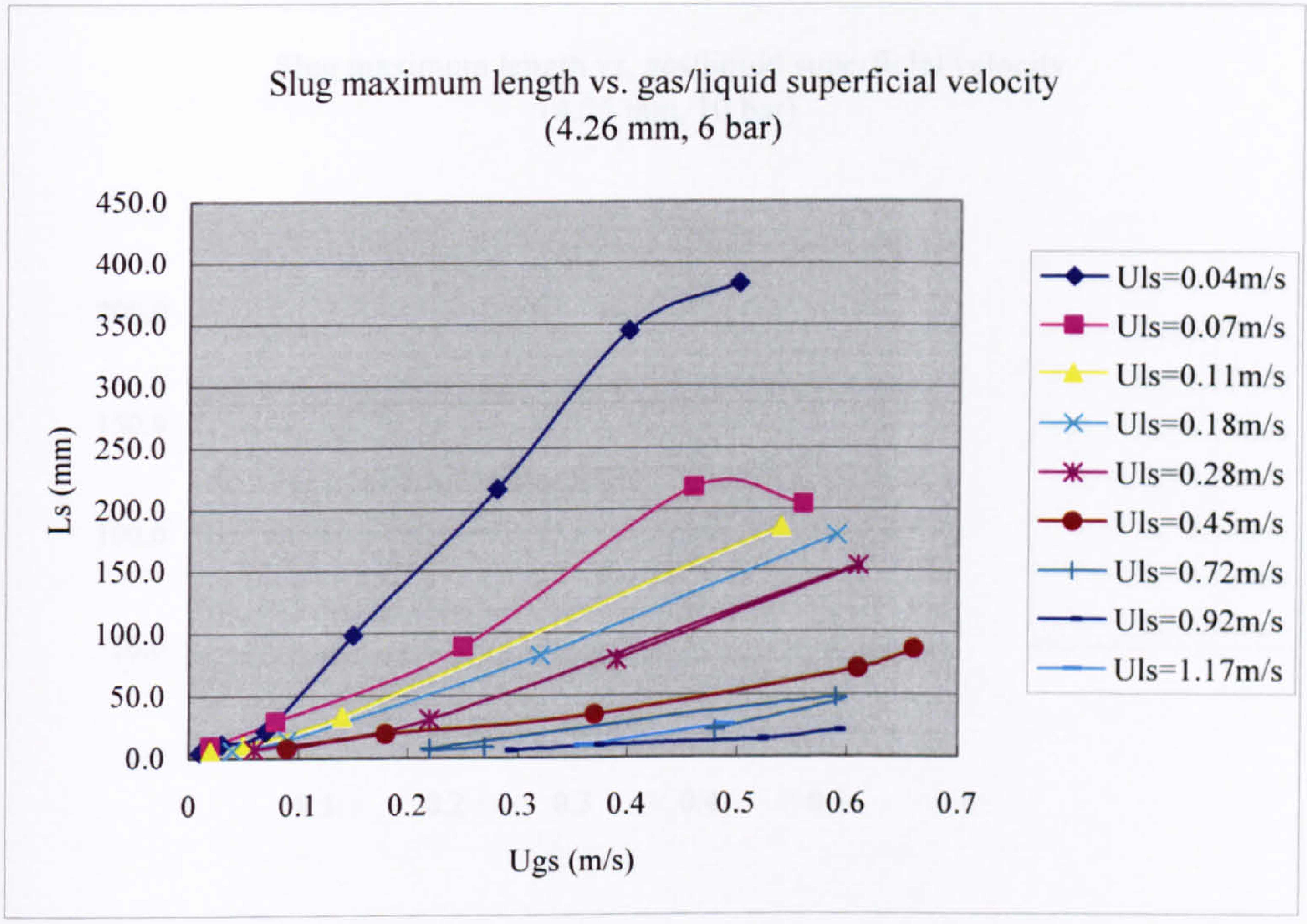

Figure G.2 The effect of gas or liquid superficial velocities on slug maximum length in the 4.26 mm tube at 6 bar.

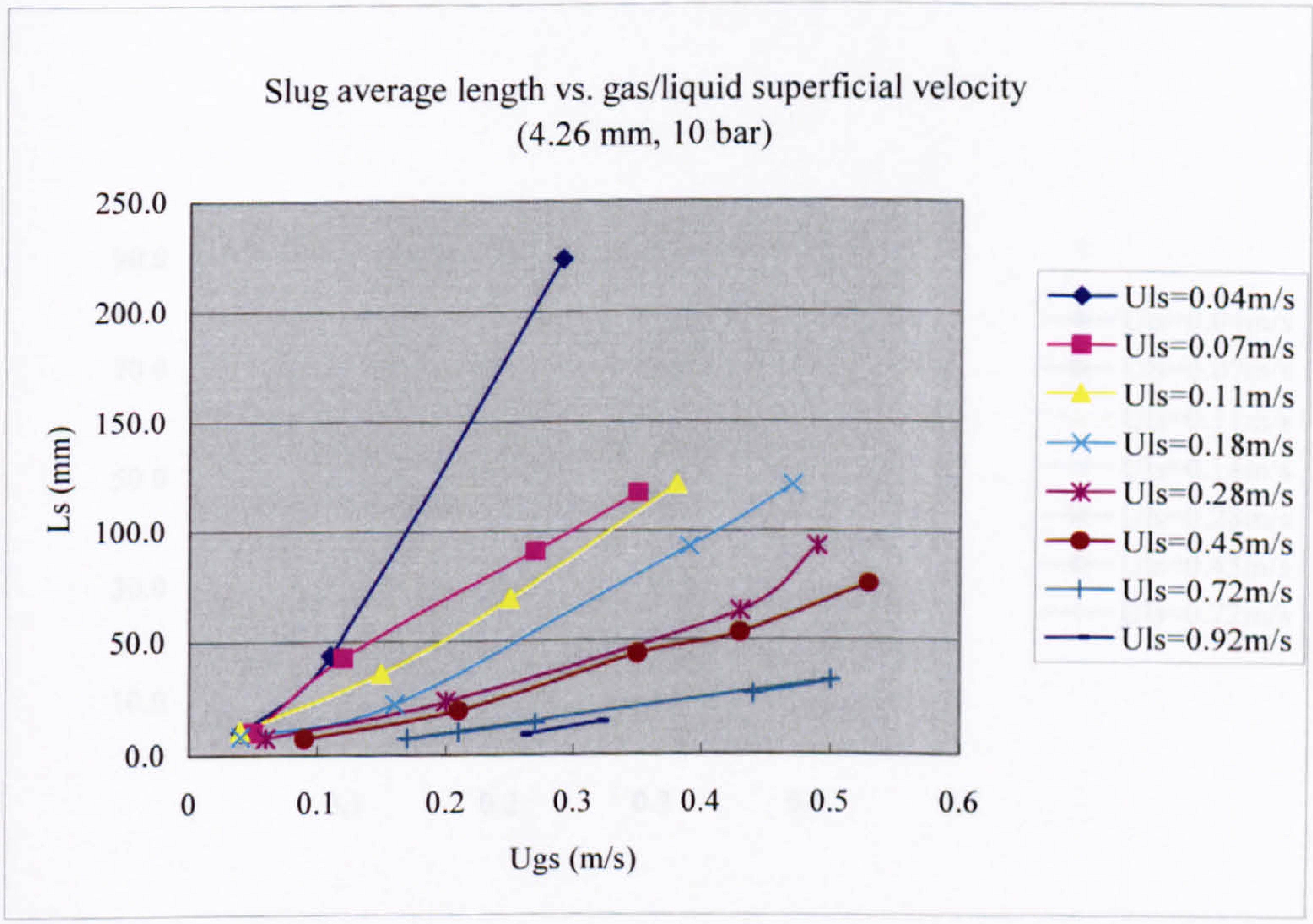

Figure G.3 The effect of gas or liquid superficial velocities on slug average length in the 4.26 mm tube at 10 bar.

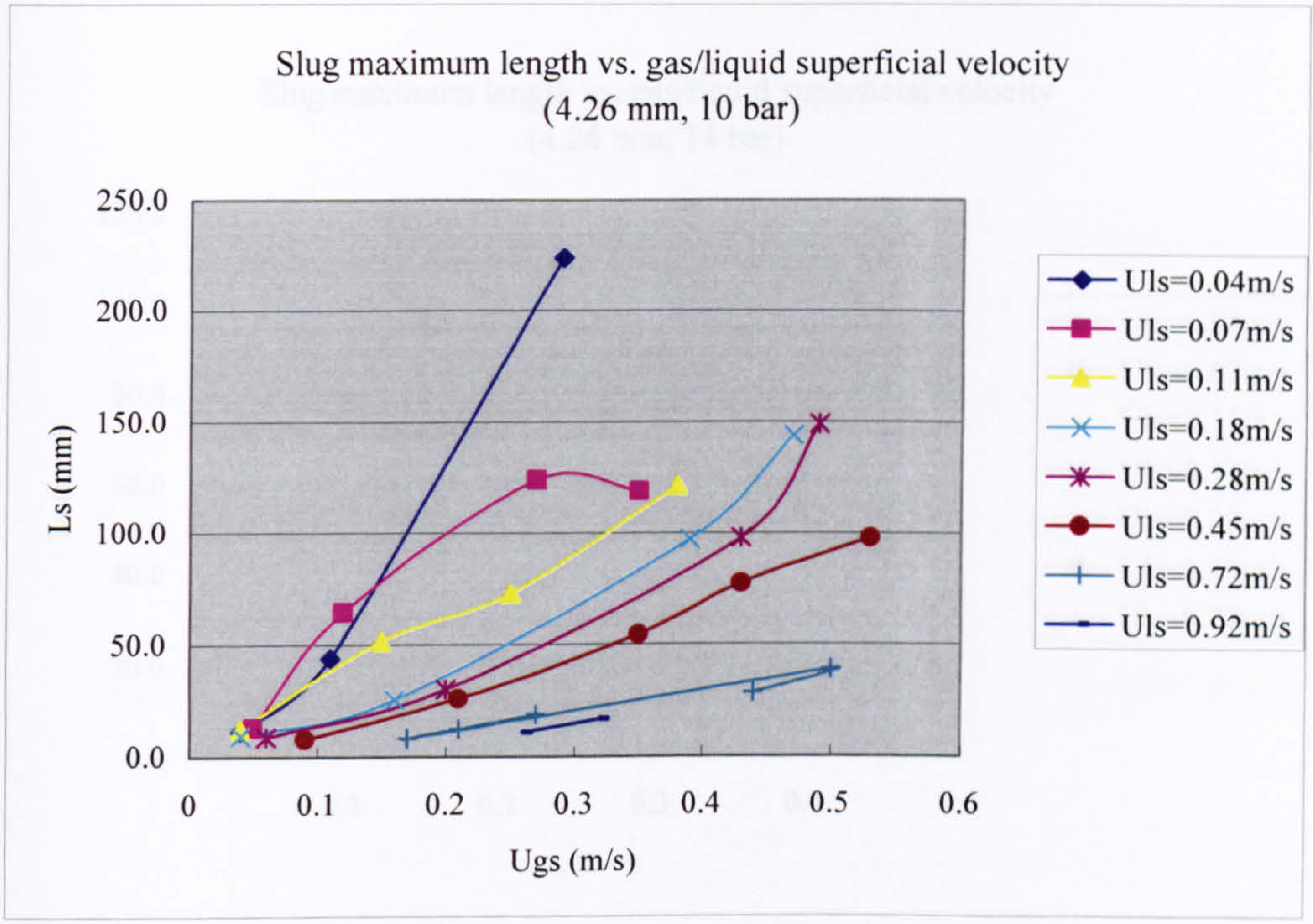

Figure G.4 The effect of gas or liquid superficial velocities on slug maximum length in the 4.26 mm tube at 10 bar.

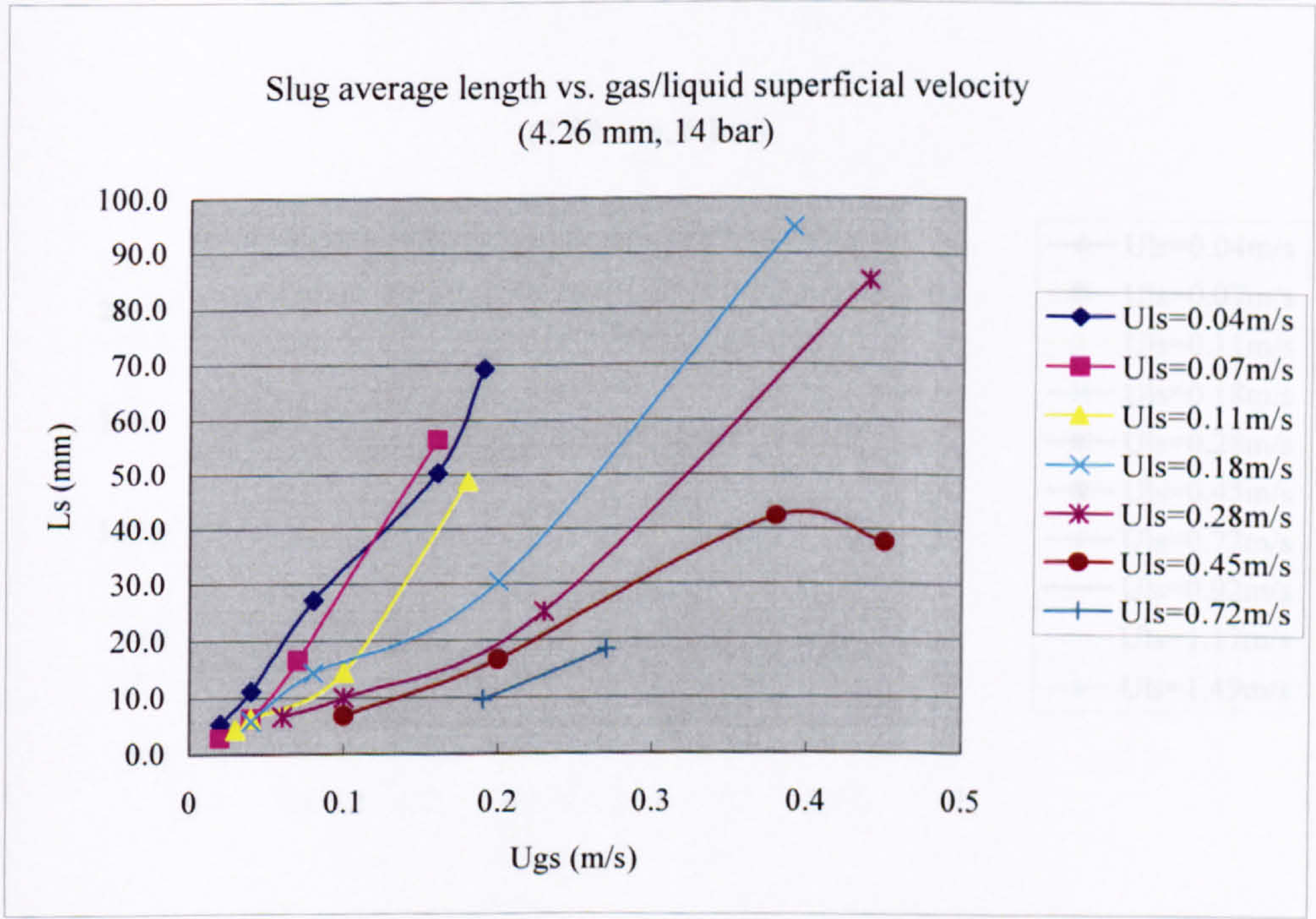

Figure G.5 The effect of gas or liquid superficial velocities on slug average length in the 4.26 mm tube at 14 bar.

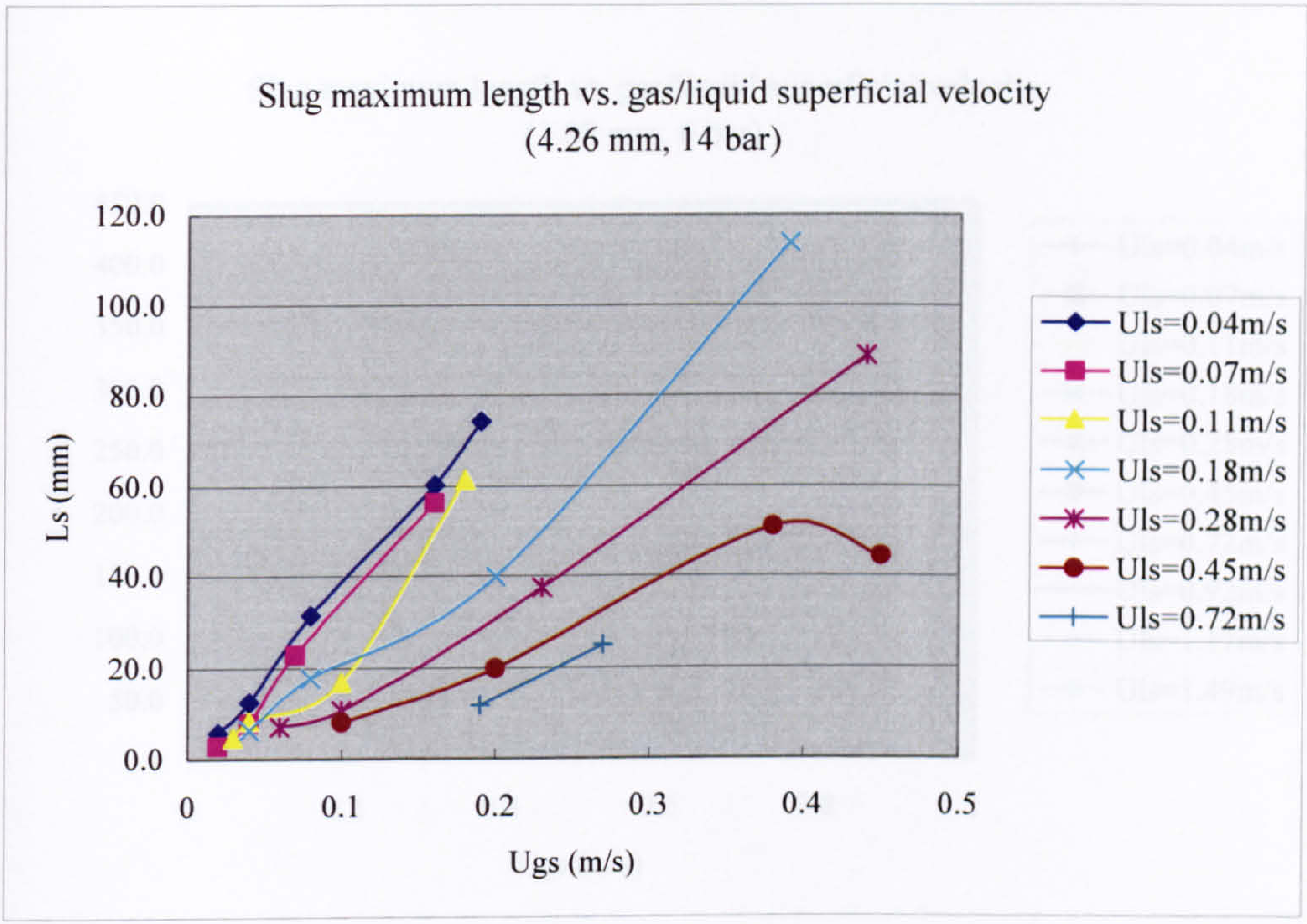

Figure G.6 The effect of gas or liquid superficial velocities on slug maximum length in the 4.26 mm tube at 14 bar.

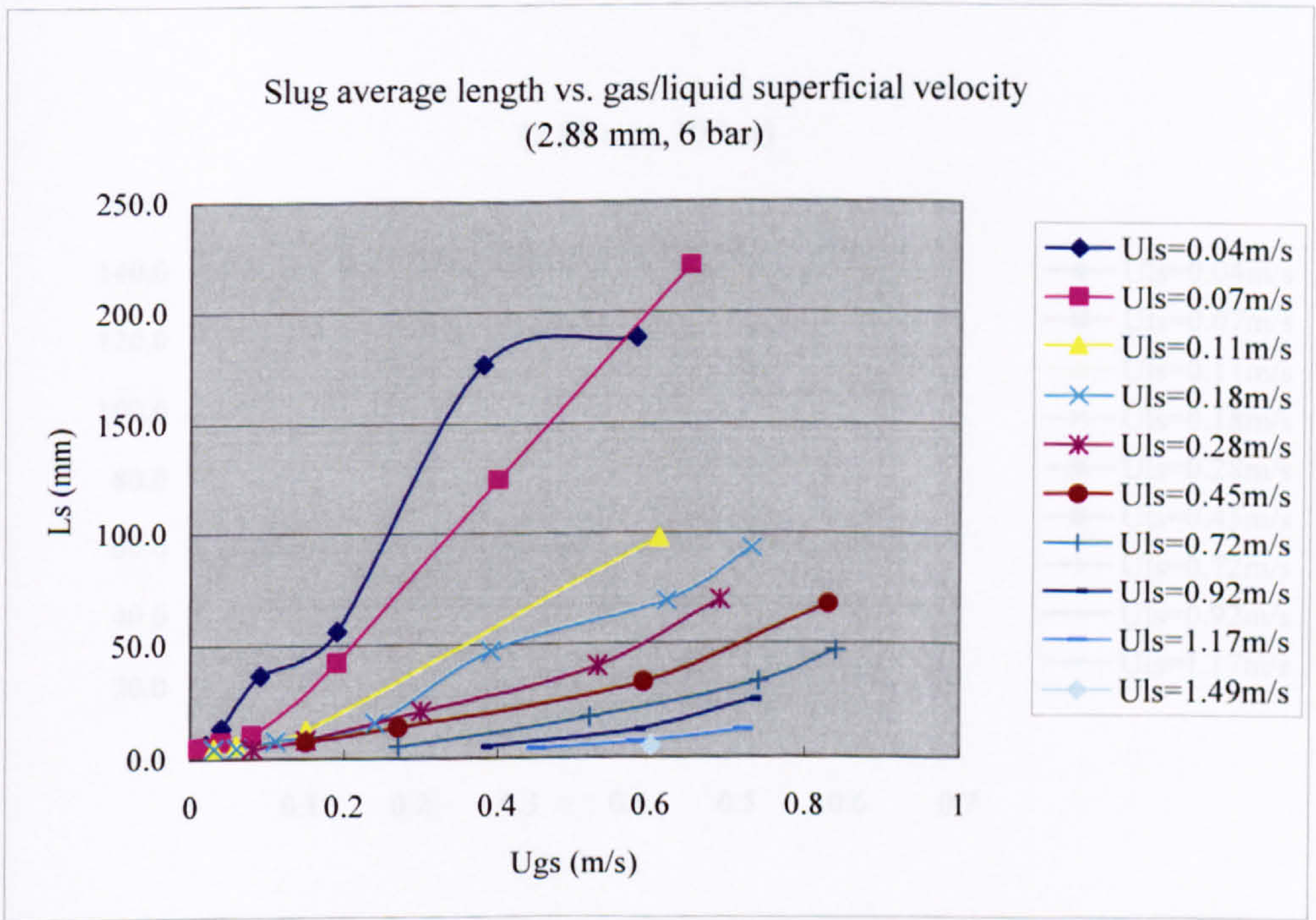

Figure G.7 The effect of gas or liquid superficial velocities on slug average length in the 2.88 mm tube at 6 bar.

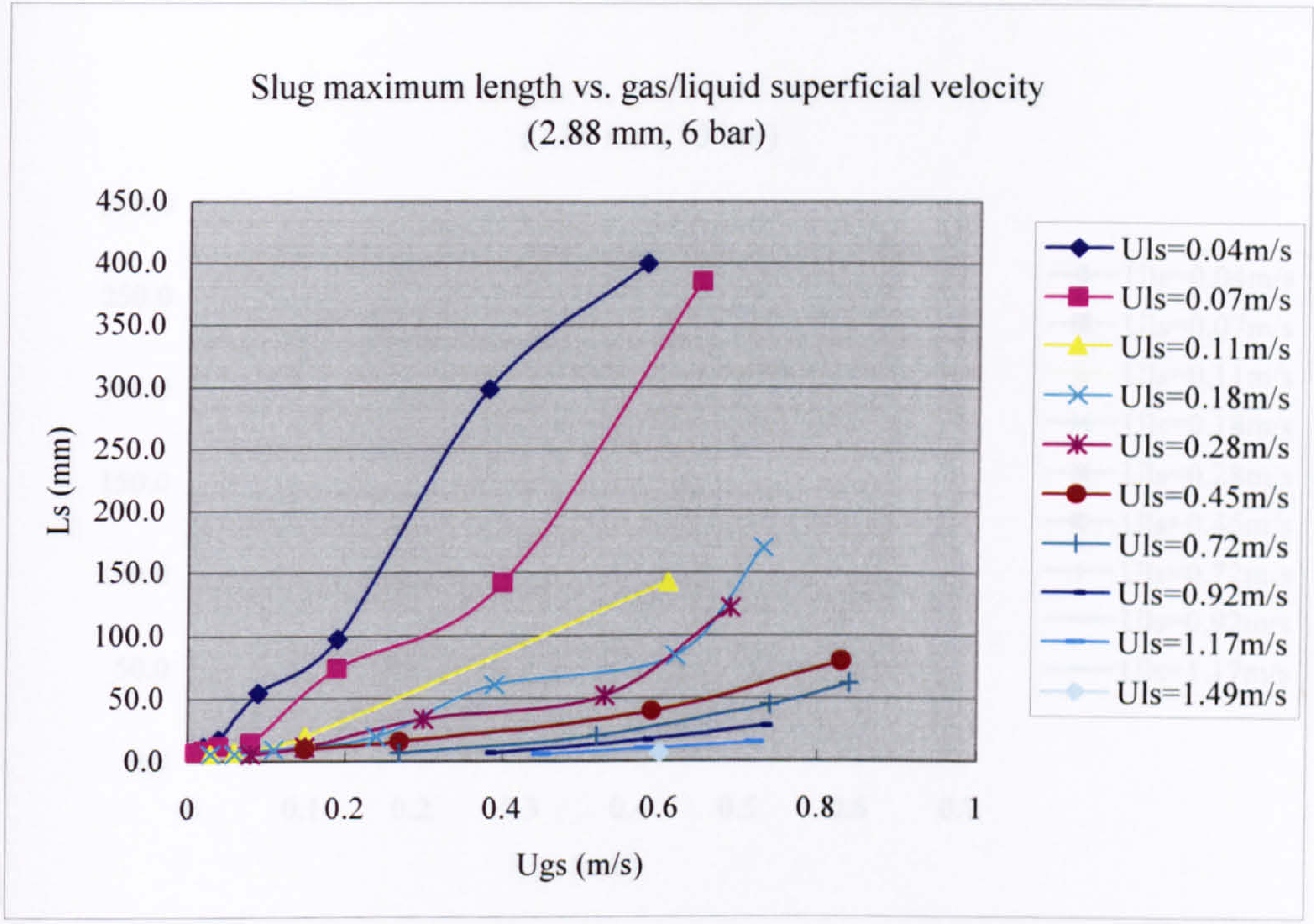

Figure G.8 The effect of gas or liquid superficial velocities on slug maximum length in the 2.88 mm tube at 6 bar.

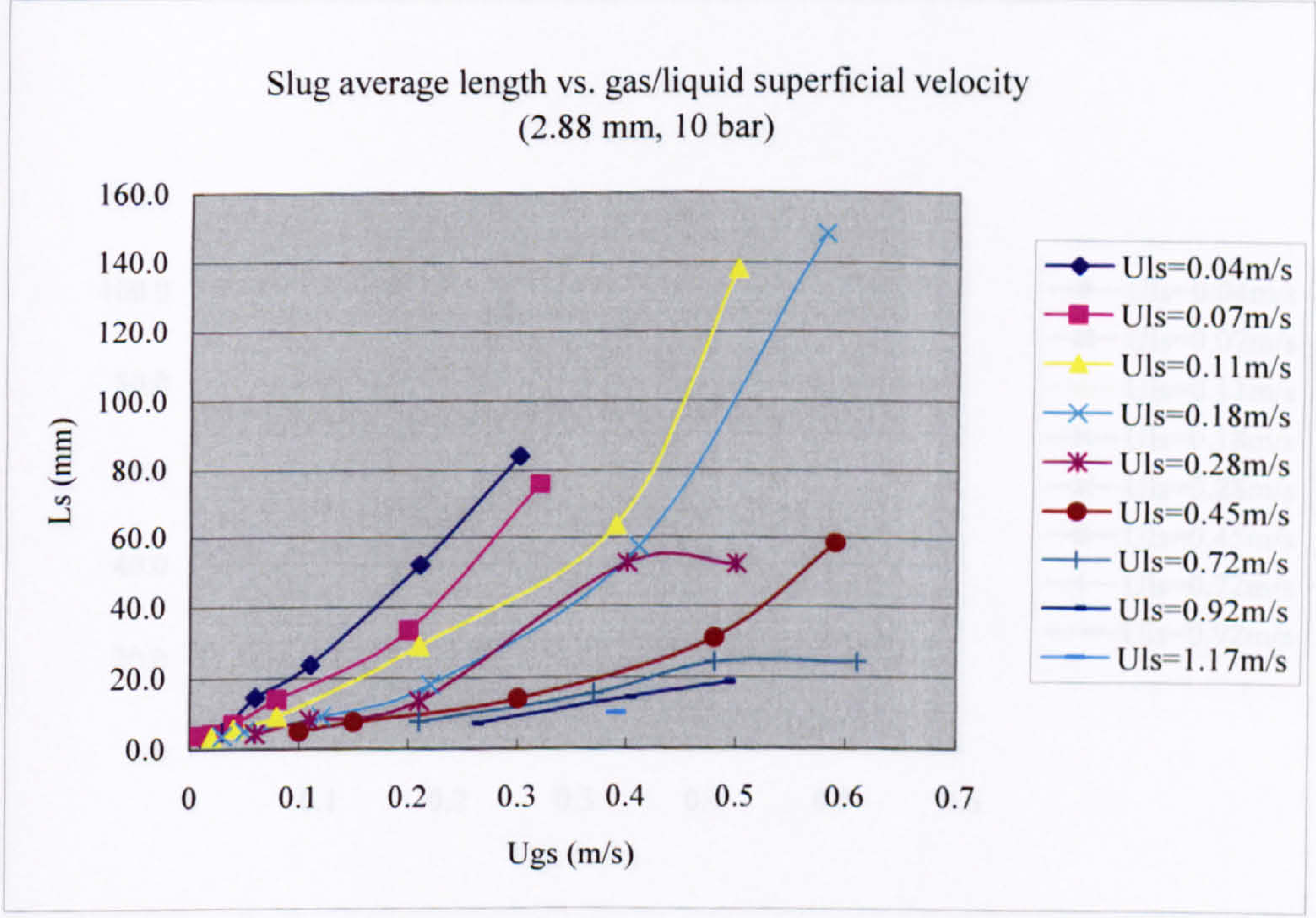

Figure G.9 The effect of gas or liquid superficial velocities on slug average length in the 2.88 mm tube at 10 bar.

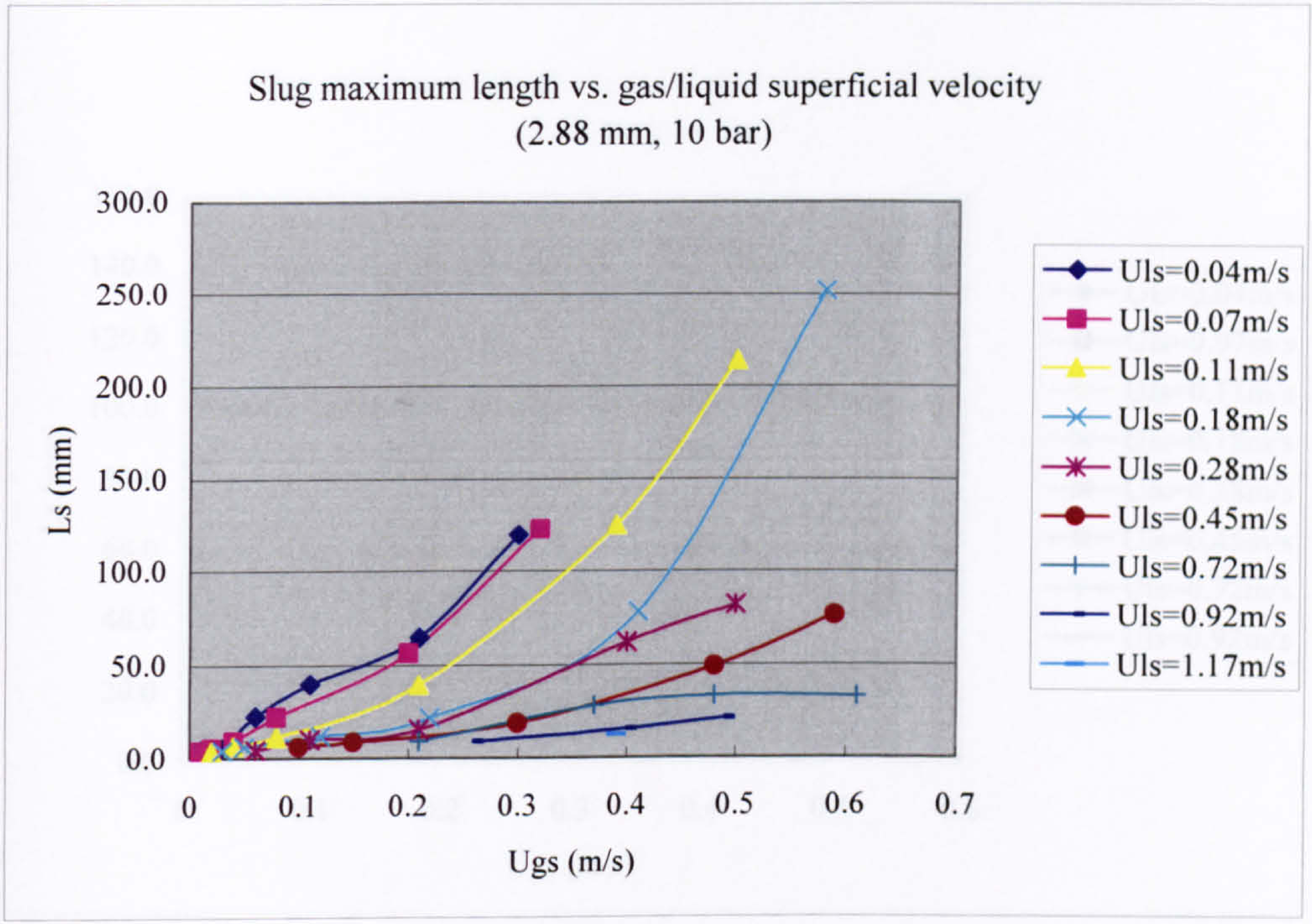

Figure G.10 The effect of gas or liquid superficial velocities on slug maximum length in the 2.88 mm tube at 10 bar.

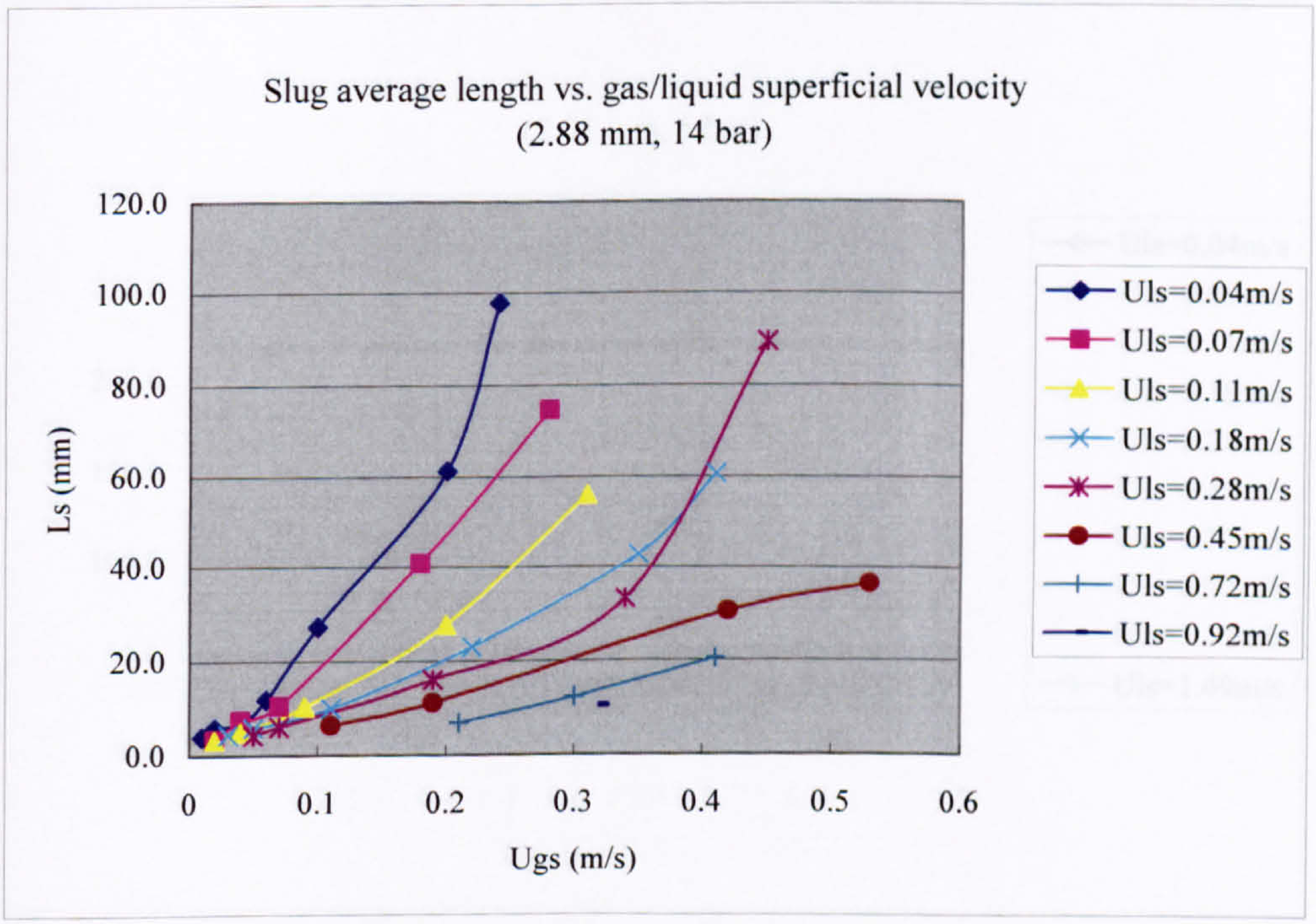

Figure G.11 The effect of gas or liquid superficial velocities on slug average length in the 2.88 mm tube at 14 bar.

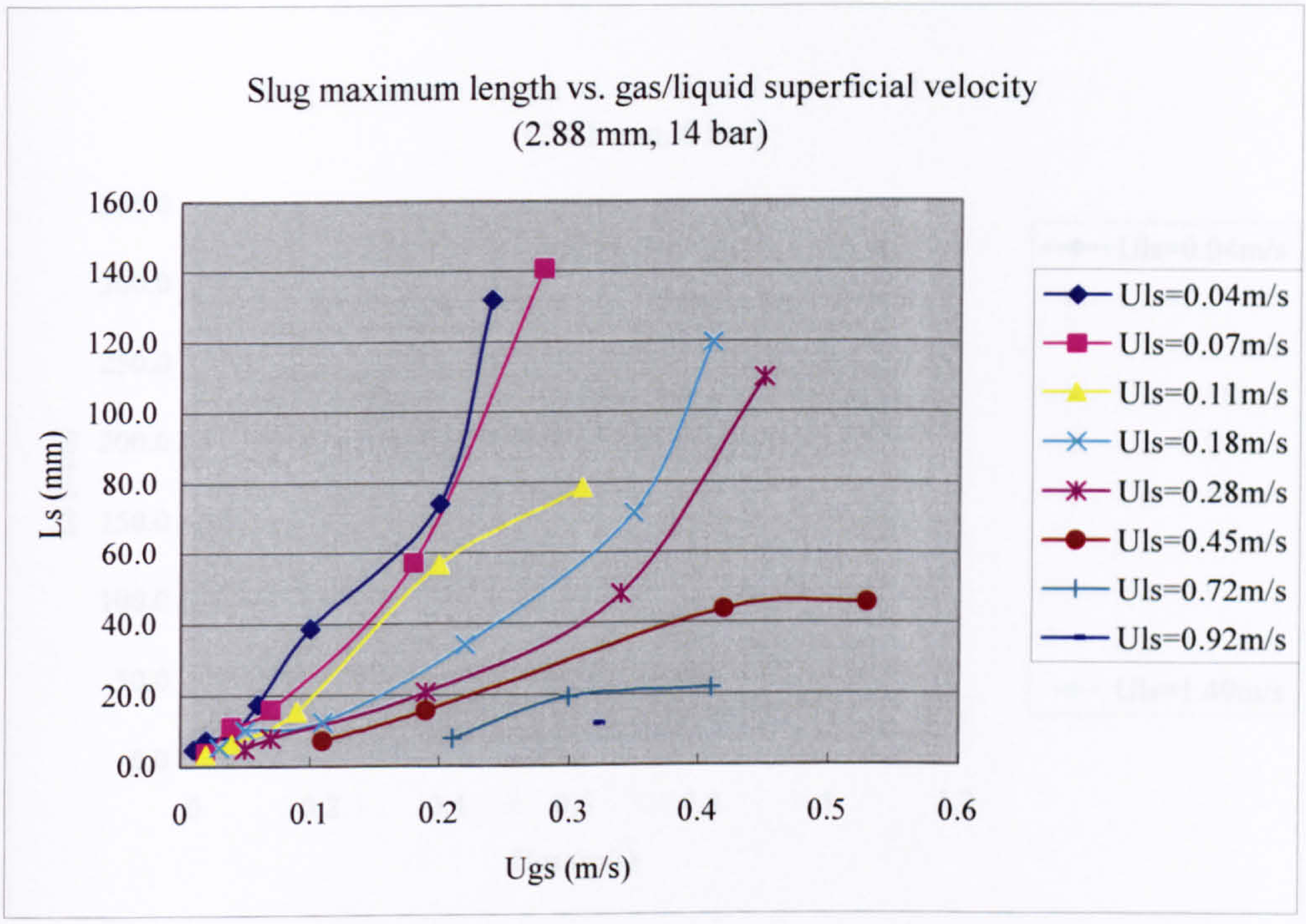

Figure G.12 The effect of gas or liquid superficial velocities on slug maximum length in the 2.88 mm tube at 14 bar.

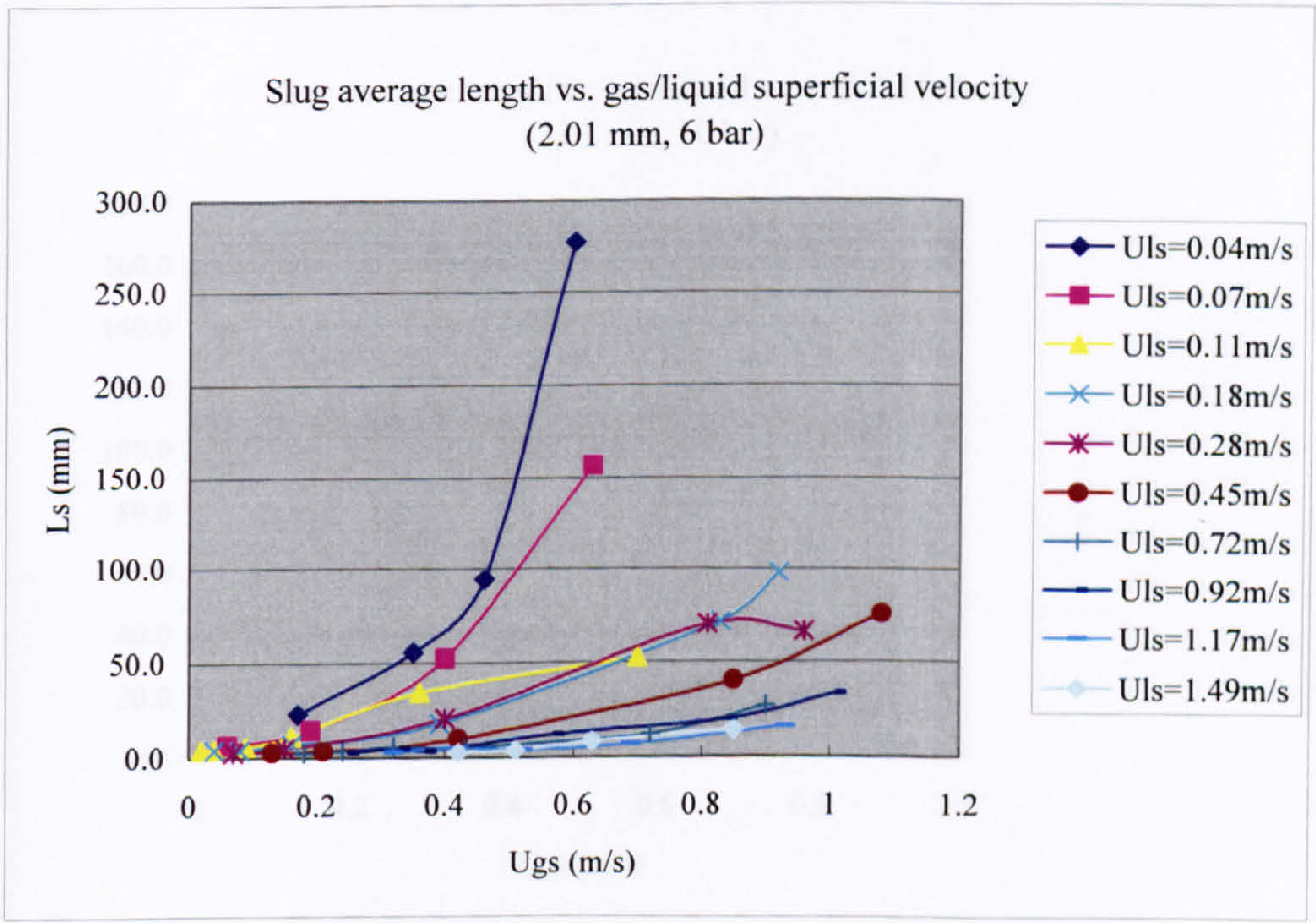

Figure G.13 The effect of gas or liquid superficial velocities on slug average length in the 2.01 mm tube at 6 bar.

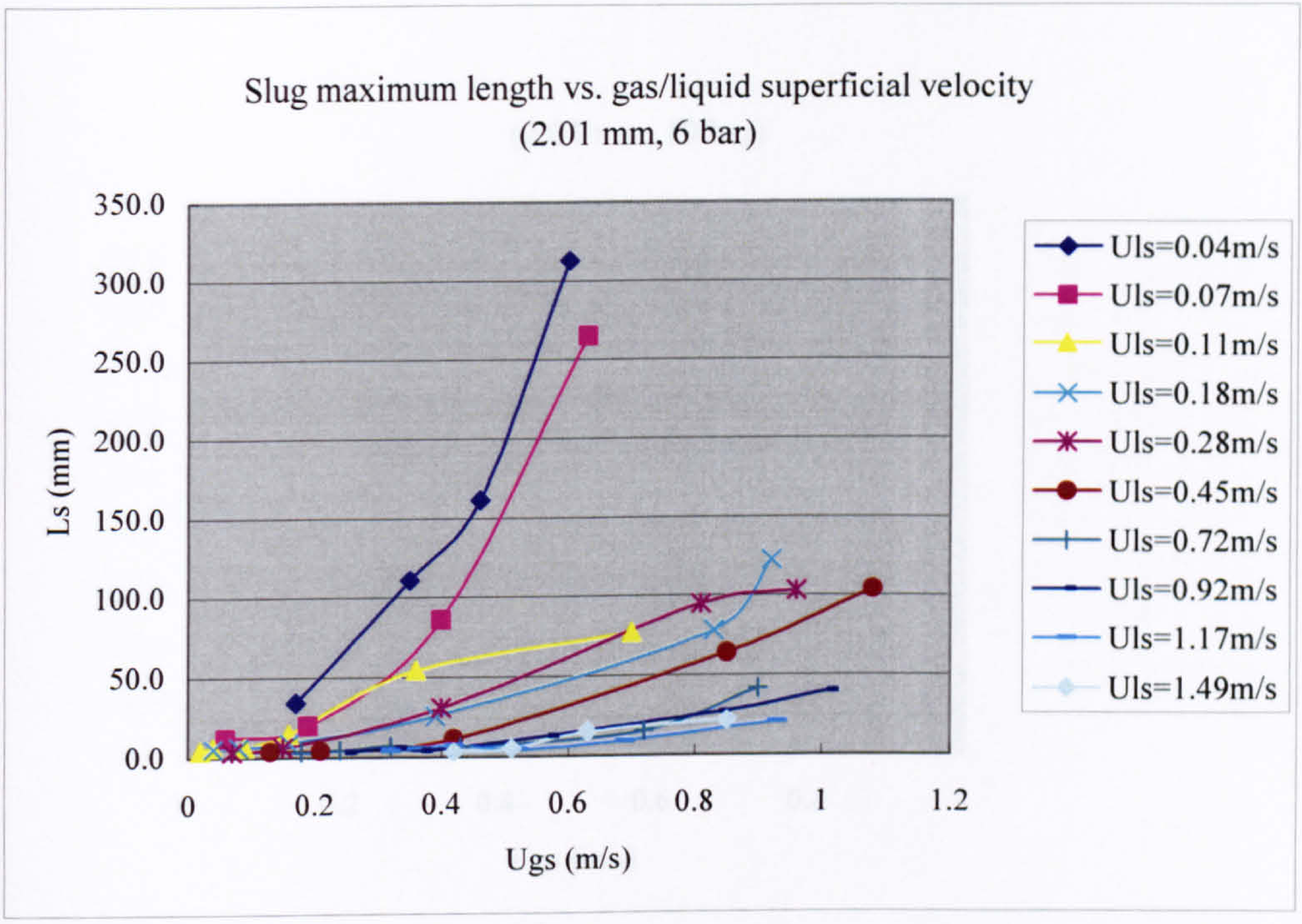

Figure G.14 The effect of gas or liquid superficial velocities on slug maximum length in the 2.01 mm tube at 6 bar.

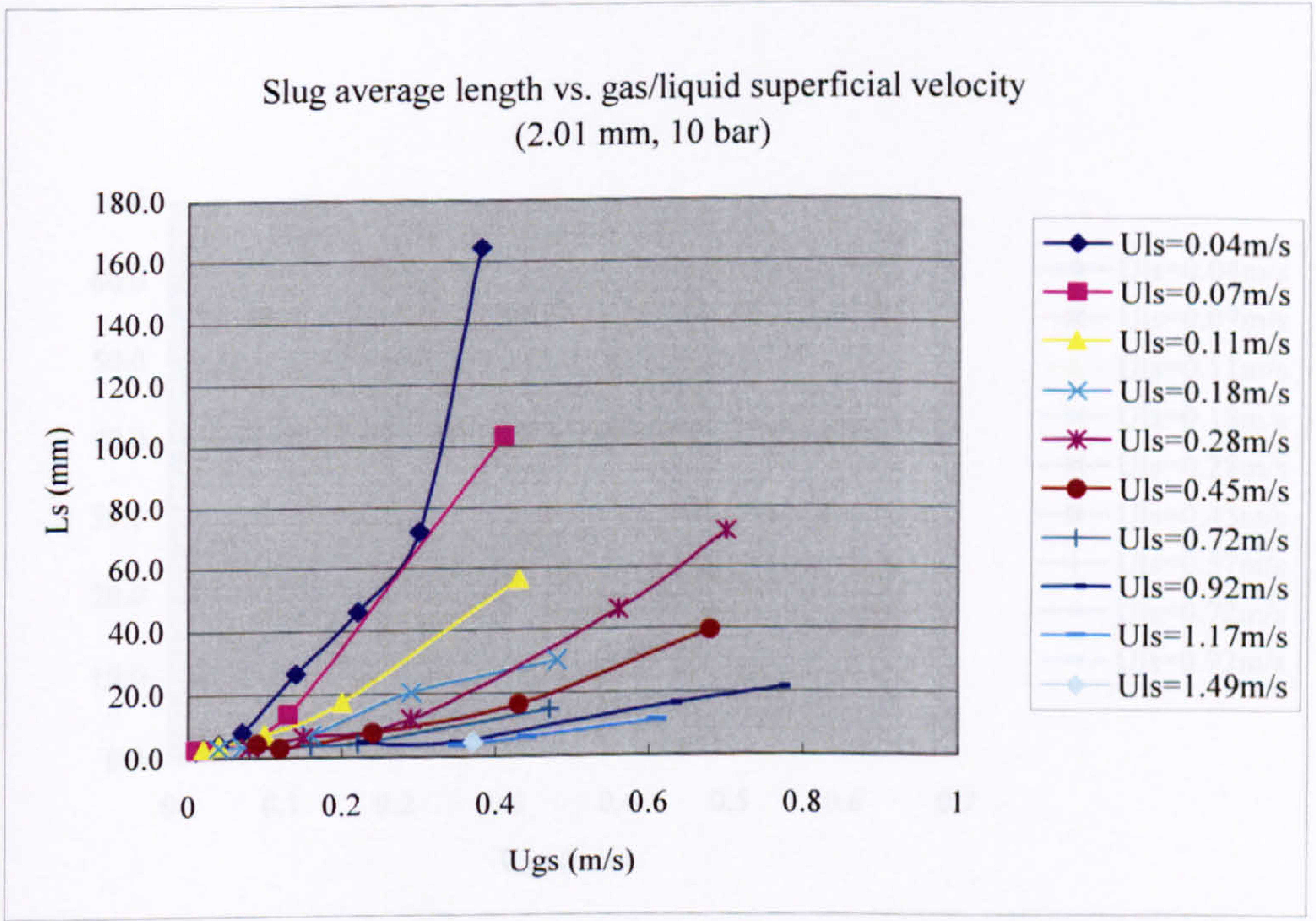

Figure G.15 The effect of gas or liquid superficial velocities on slug average length in the 2.01 mm tube at 10 bar.

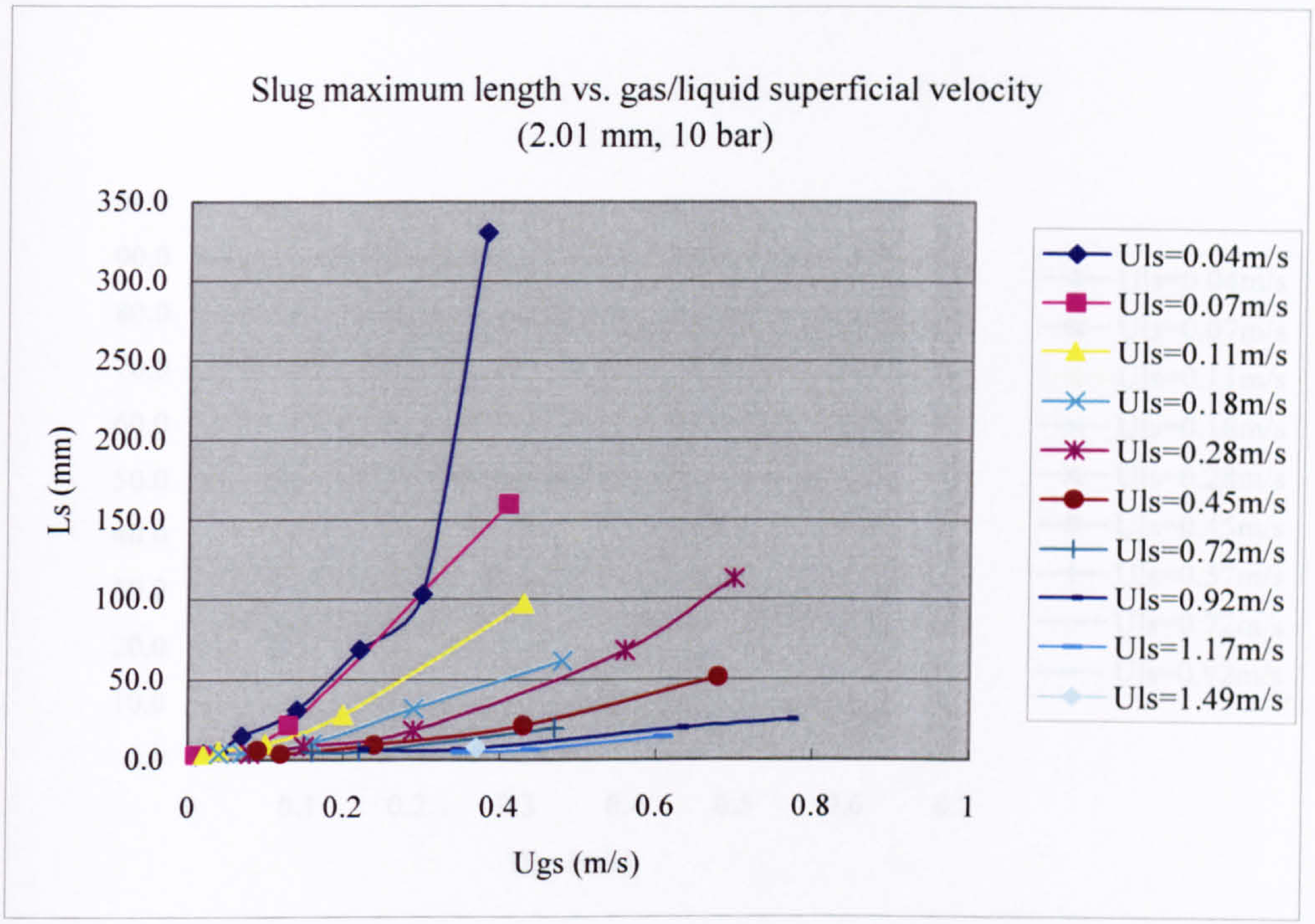

Figure G.16 The effect of gas or liquid superficial velocities on slug maximum length in the 2.01 mm tube at 10 bar.

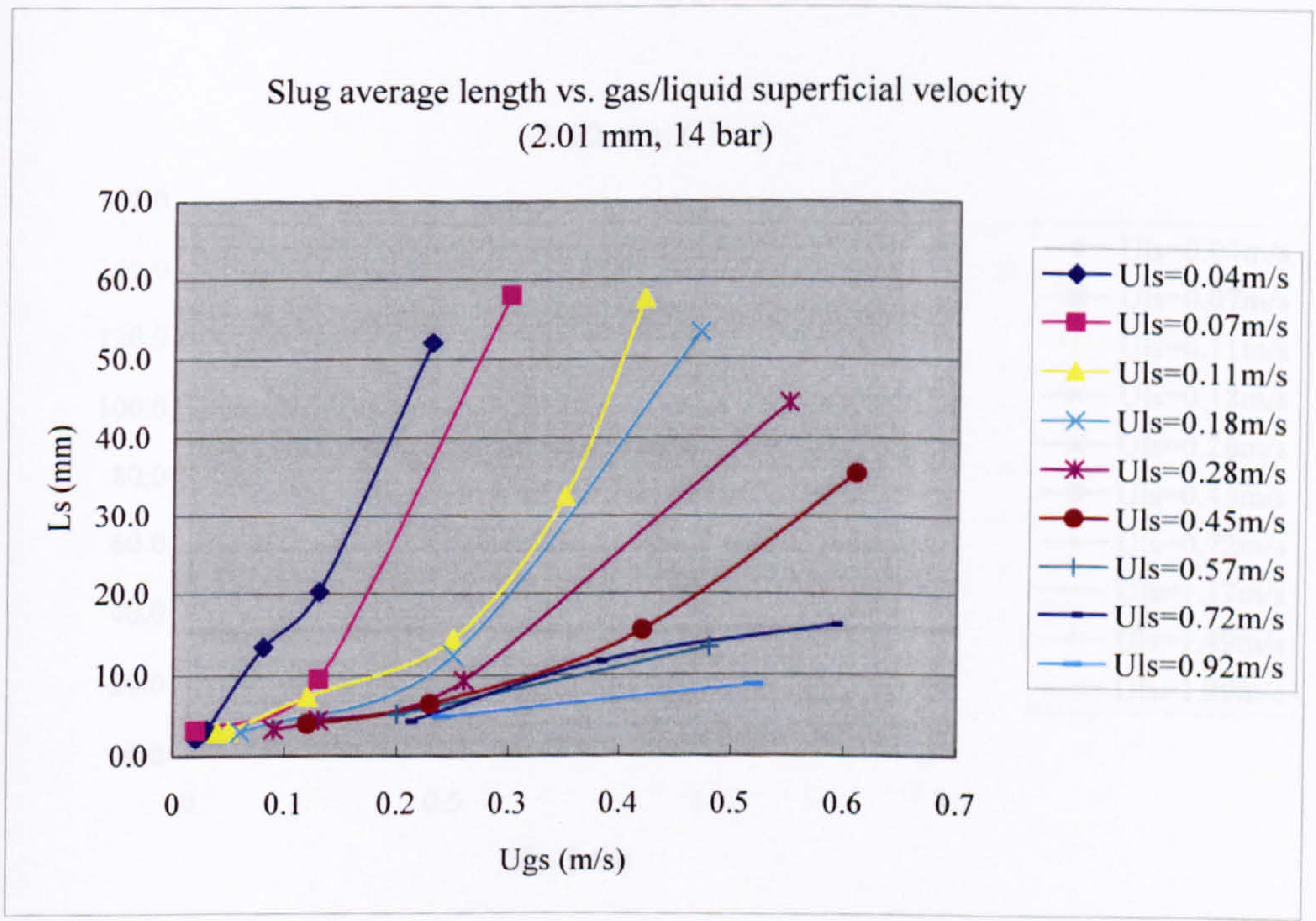

Figure G.17 The effect of gas or liquid superficial velocities on slug average length in the 2.01 mm tube at 14 bar.

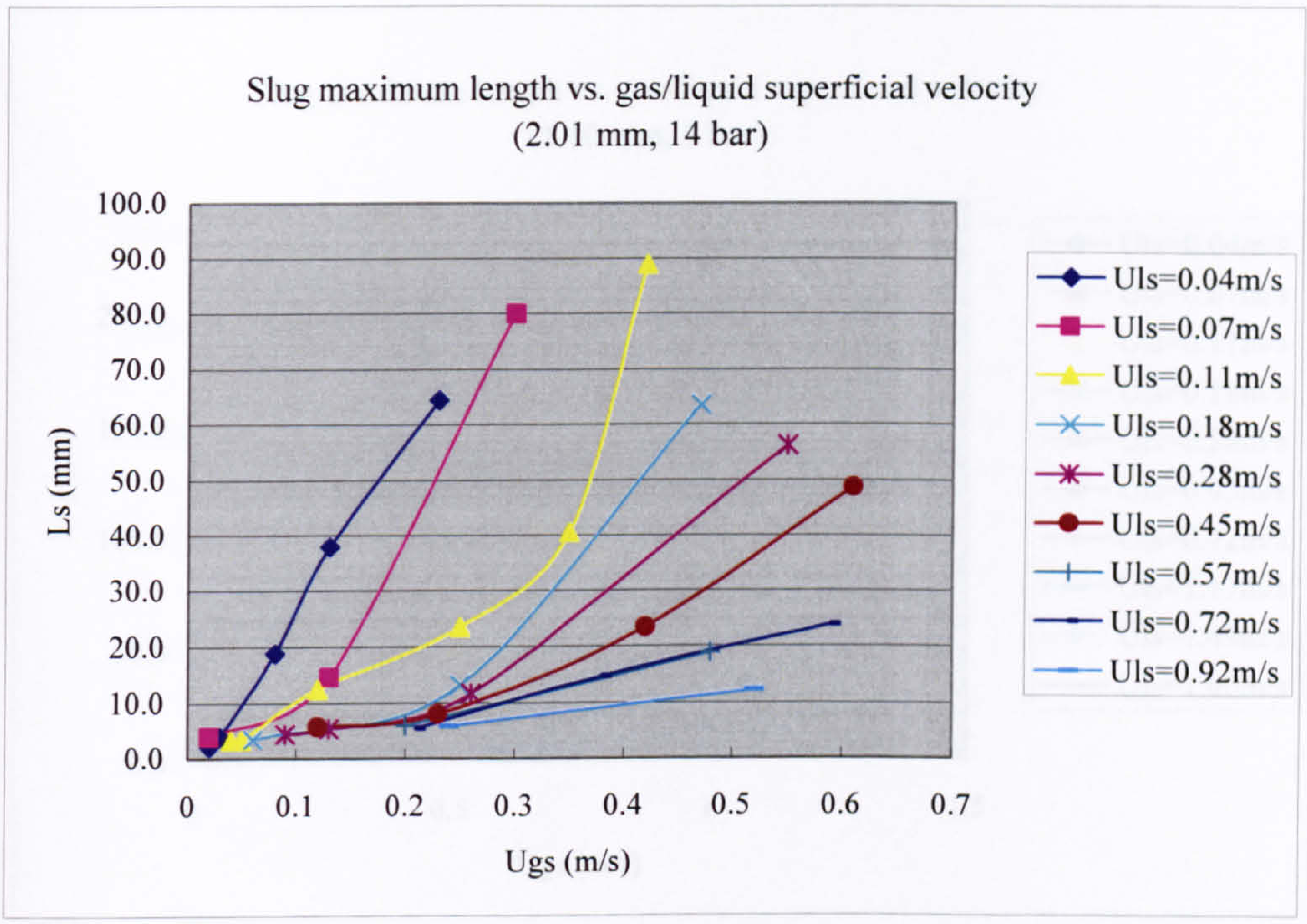

Figure G.18 The effect of gas or liquid superficial velocities on slug maximum length in the 2.01 mm tube at 14 bar.

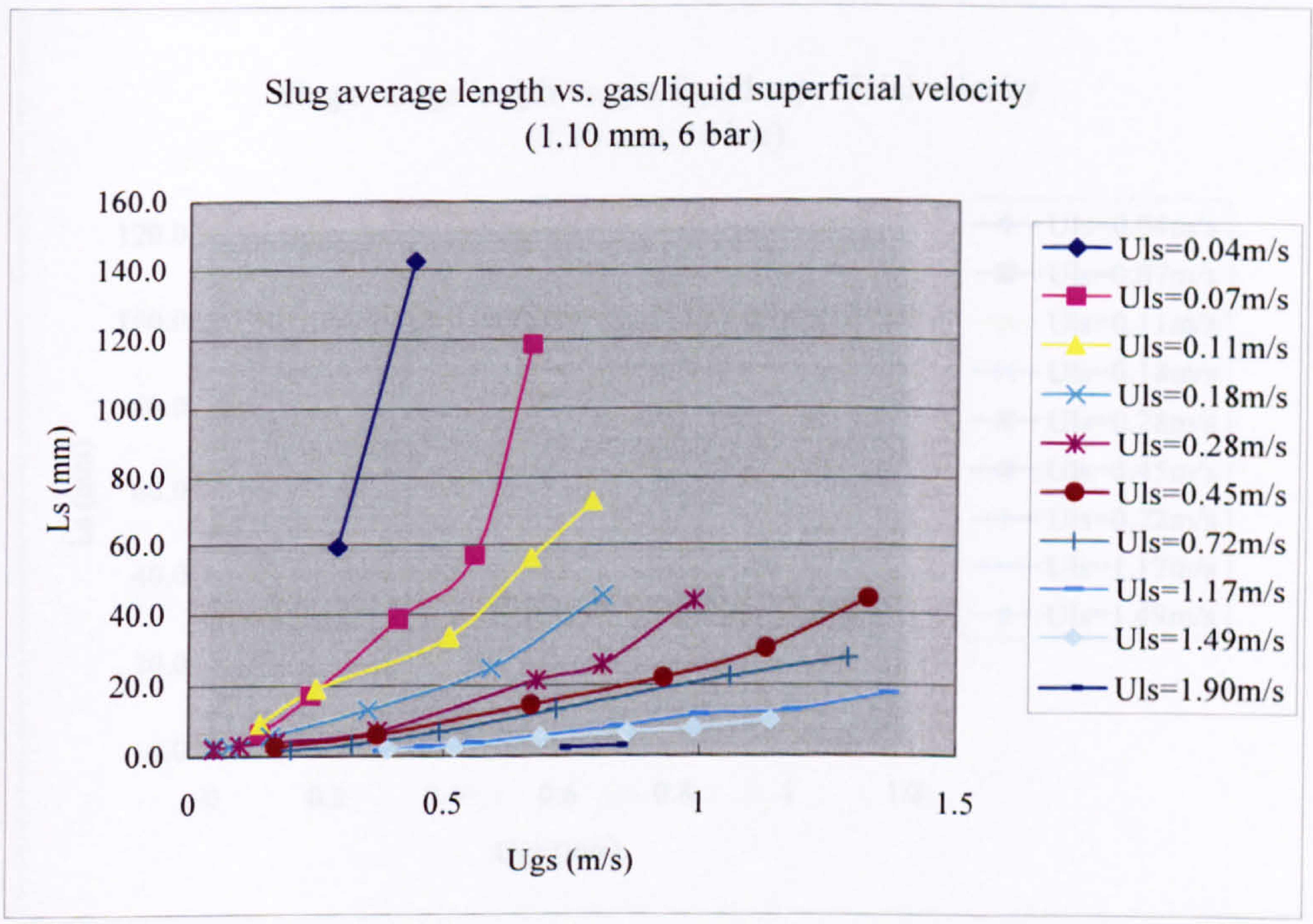

Figure G.19 The effect of gas or liquid superficial velocities on slug average length in the 1.10 mm tube at 6 bar.

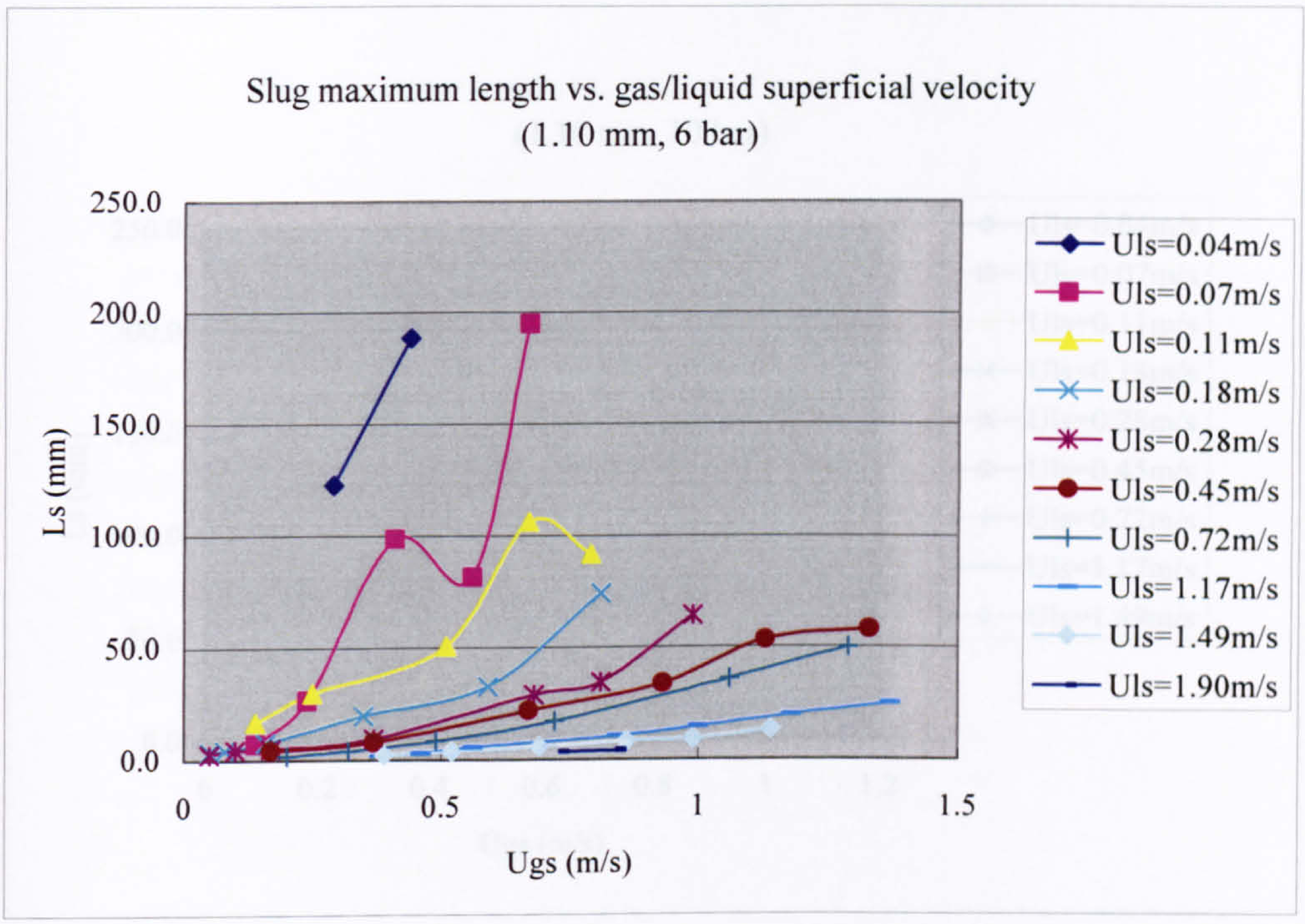

Figure G.20 The effect of gas or liquid superficial velocities on slug maximum length in the 1.10 mm tube at 6 bar.

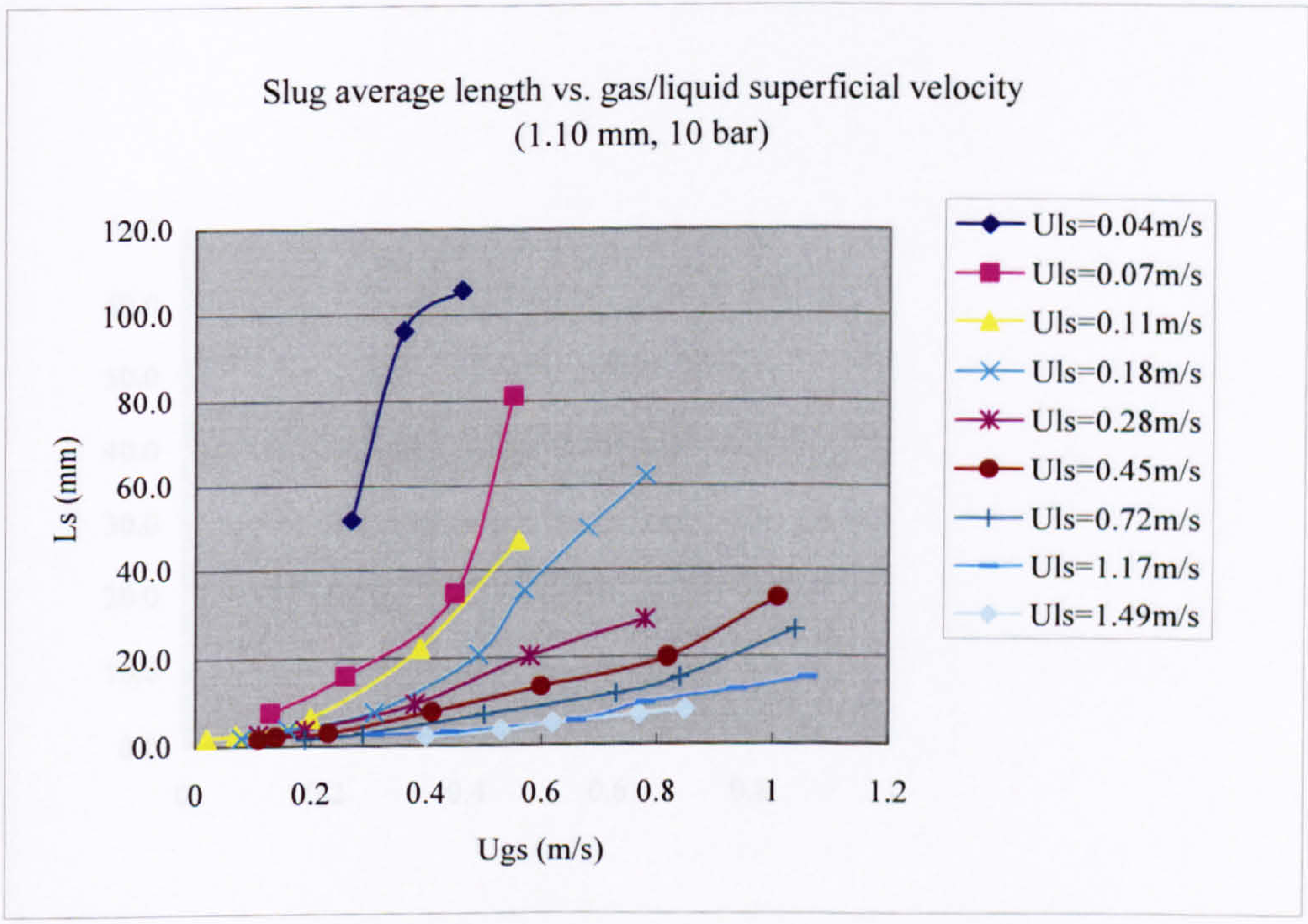

Figure G.21 The effect of gas or liquid superficial velocities on slug average length in the 1.10 mm tube at 10 bar.

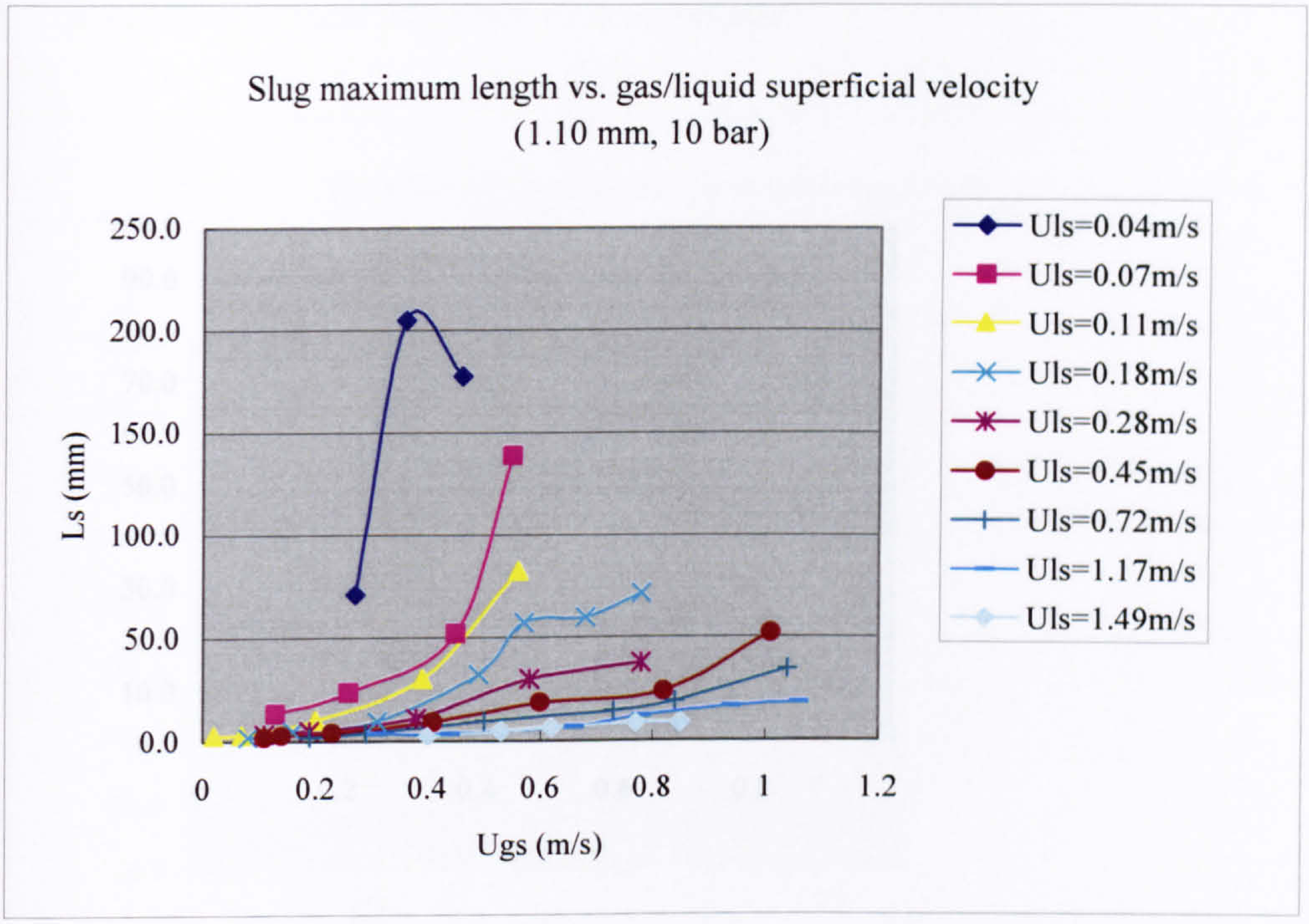

Figure G.22 The effect of gas or liquid superficial velocities on slug maximum length in the 1.10 mm tube at 10 bar.

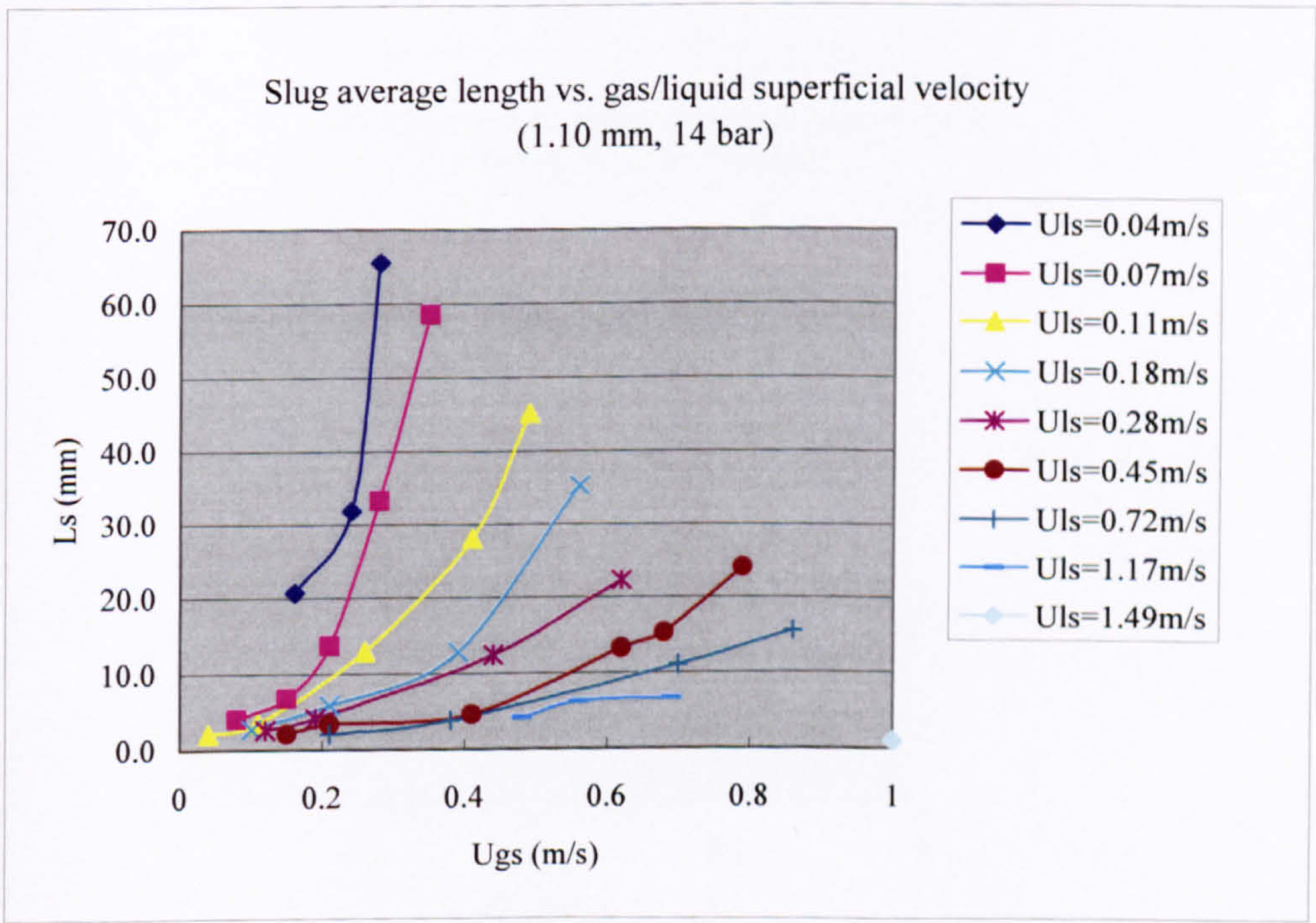

Figure G.23 The effect of gas or liquid superficial velocities on slug average length in the 1.10 mm tube at 14 bar.

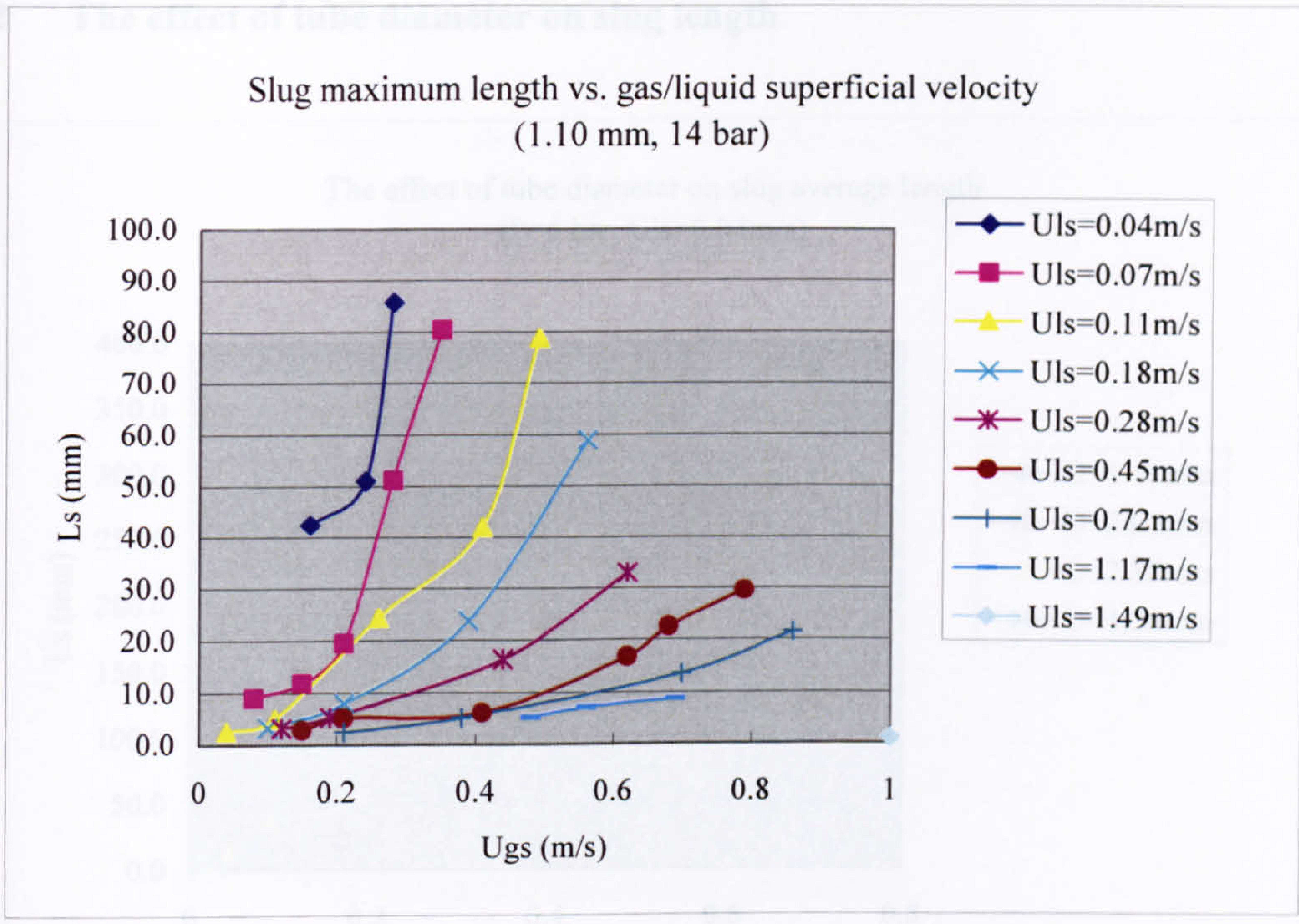

Figure G.24 The effect of gas or liquid superficial velocities on slug maximum length in the 1.10 mm tube at 14 bar.

G.2 The effect of tube diameter on slug length

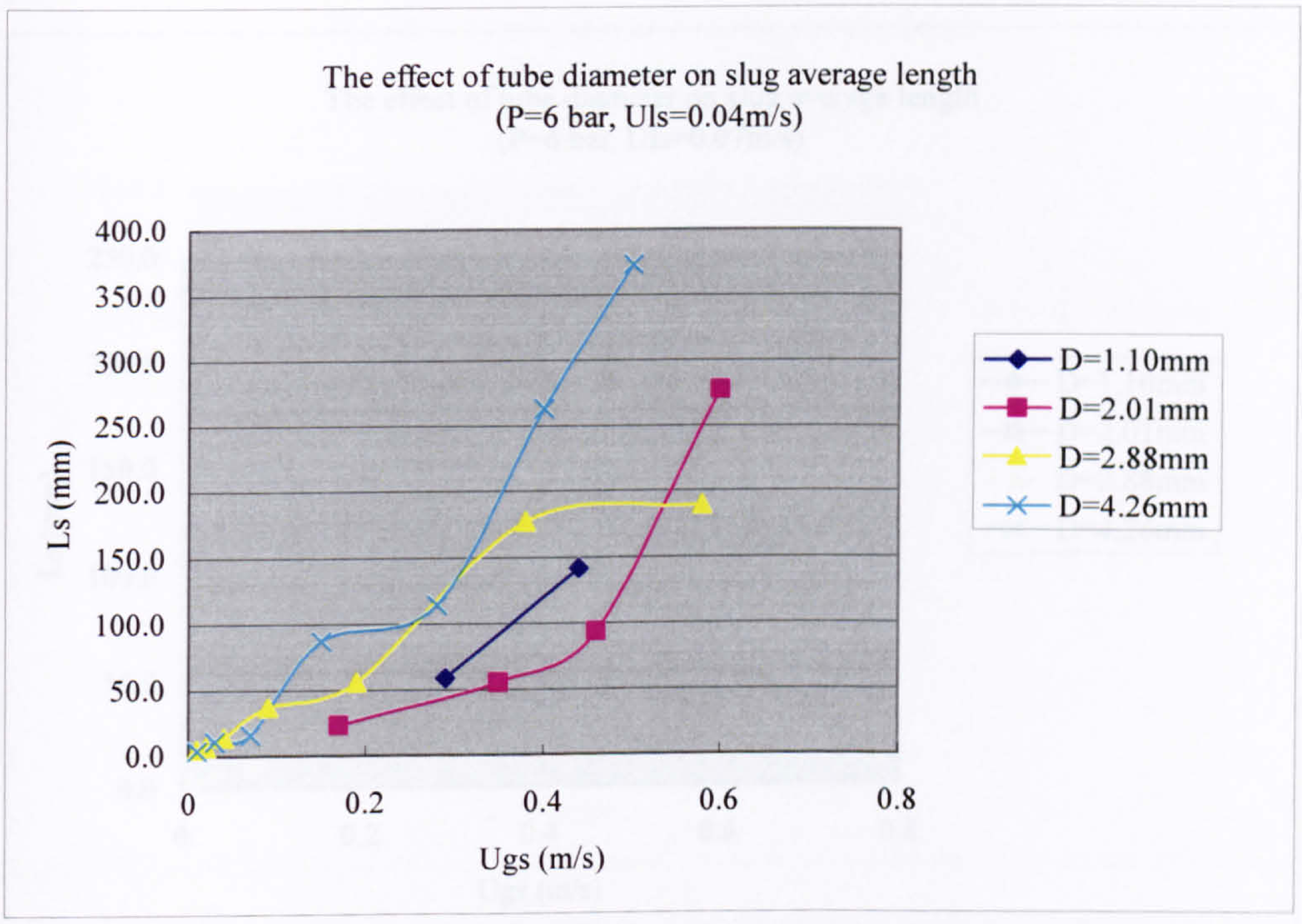

Figure G.25 The effect of tube diameter on slug average length at 6 bar (u_{ls}=0.04m/s).

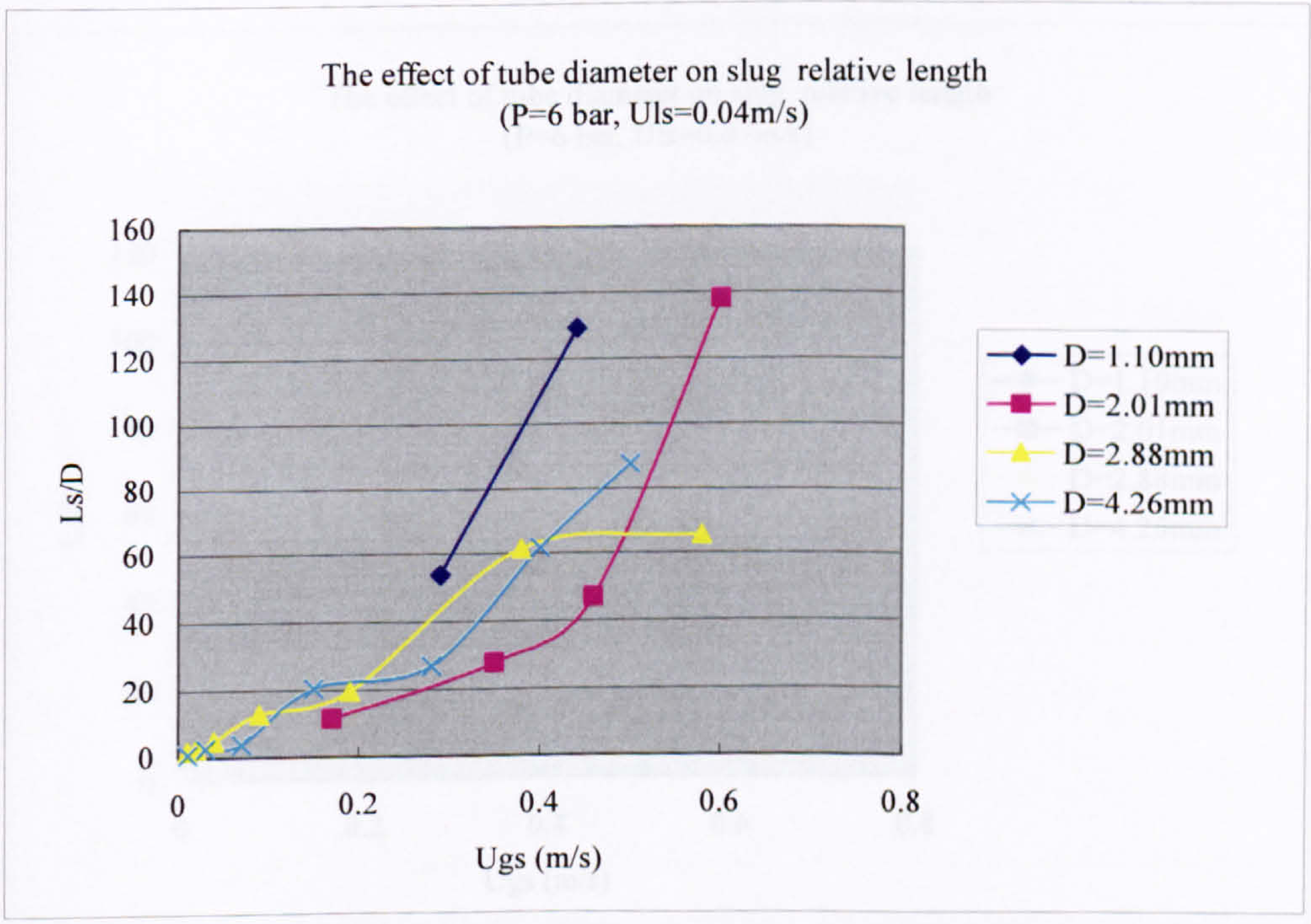

Figure G.26 The effect of tube diameter on slug length-diameter ratio at 6 bar (u_{ls}=0.04m/s).

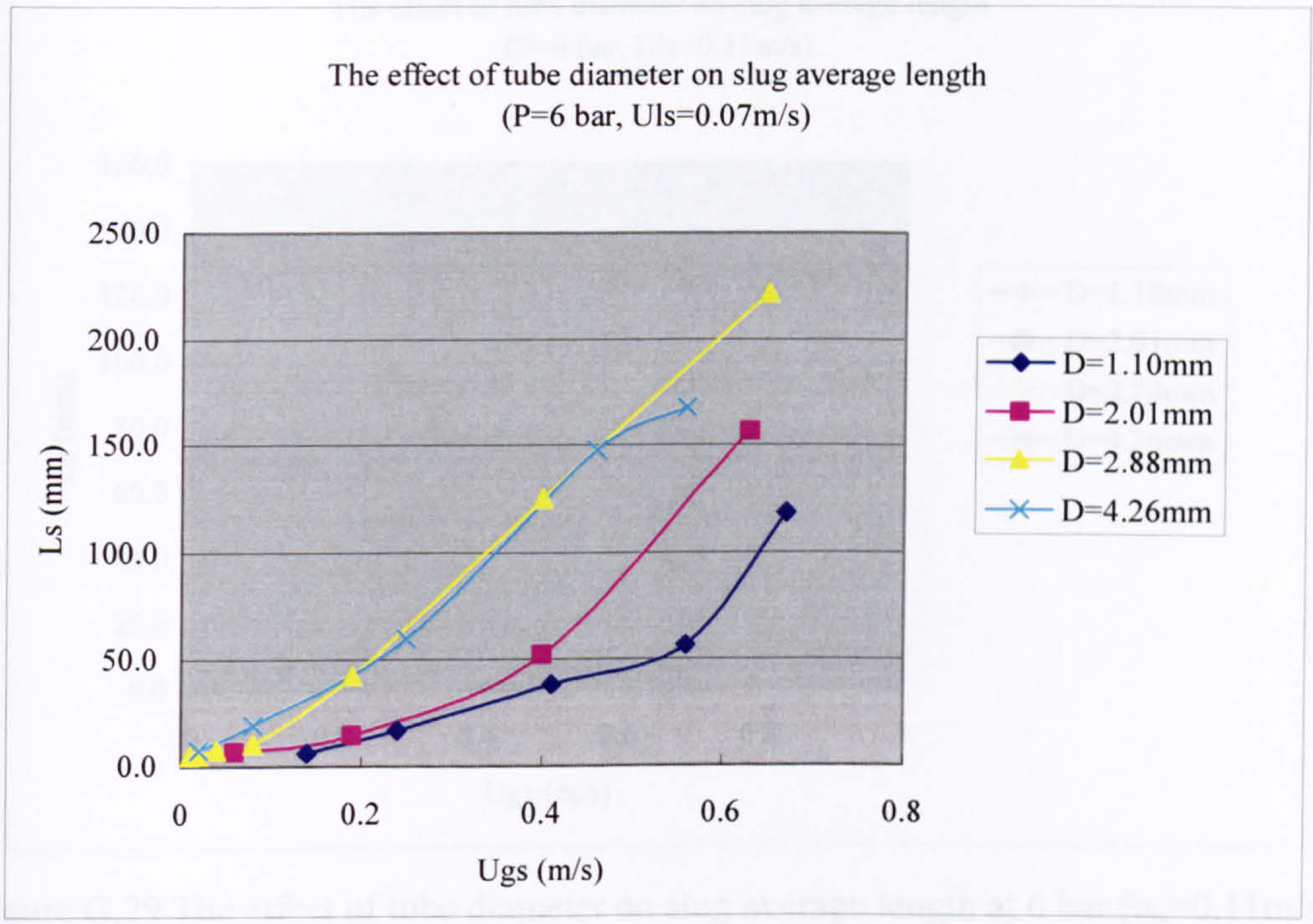

Figure G.27 The effect of tube diameter on slug average length at 6 bar (u_{ls}=0.07m/s).

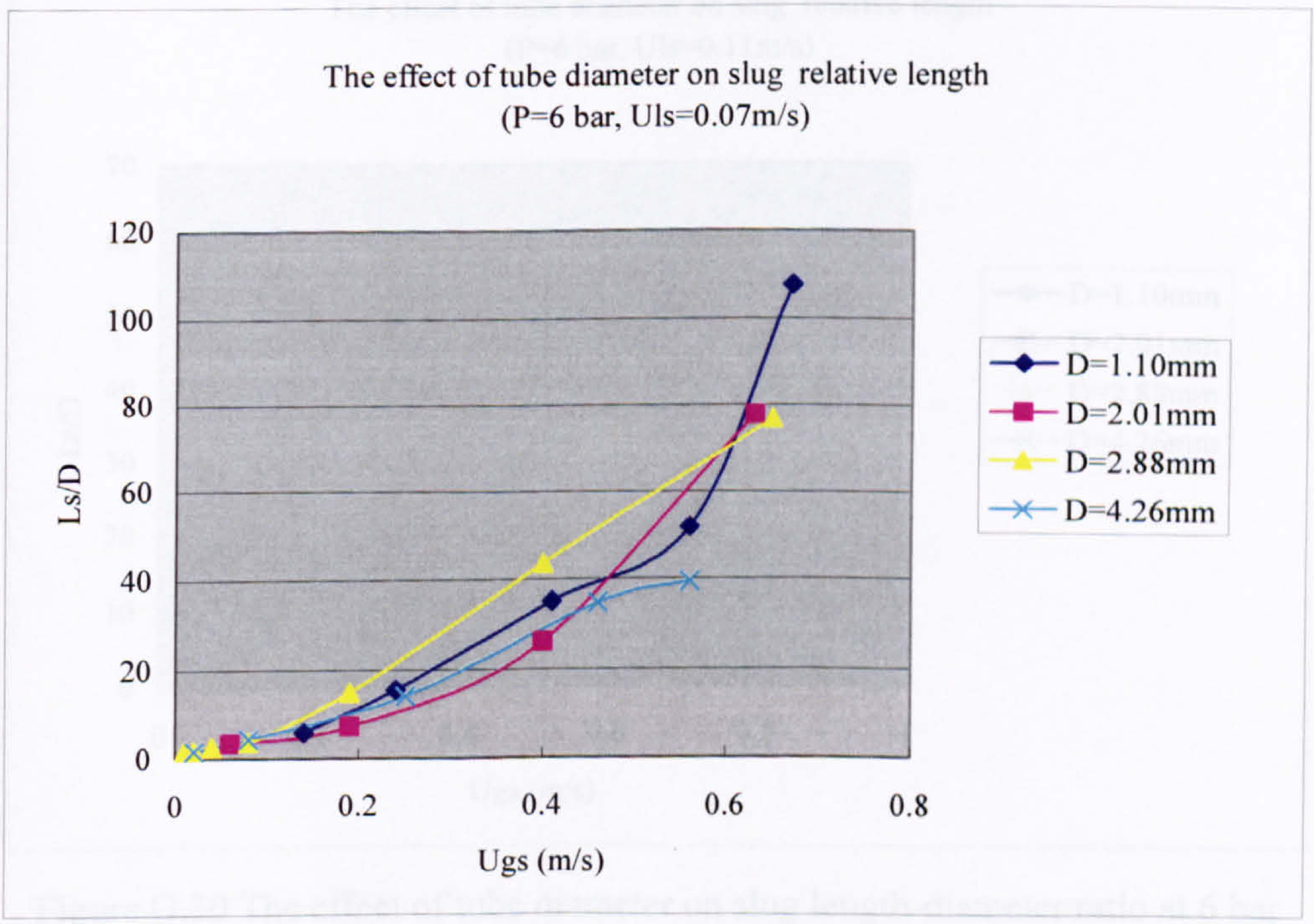

Figure G.28 The effect of tube diameter on slug length-diameter ratio at 6 bar (u_{ls}=0.07m/s).

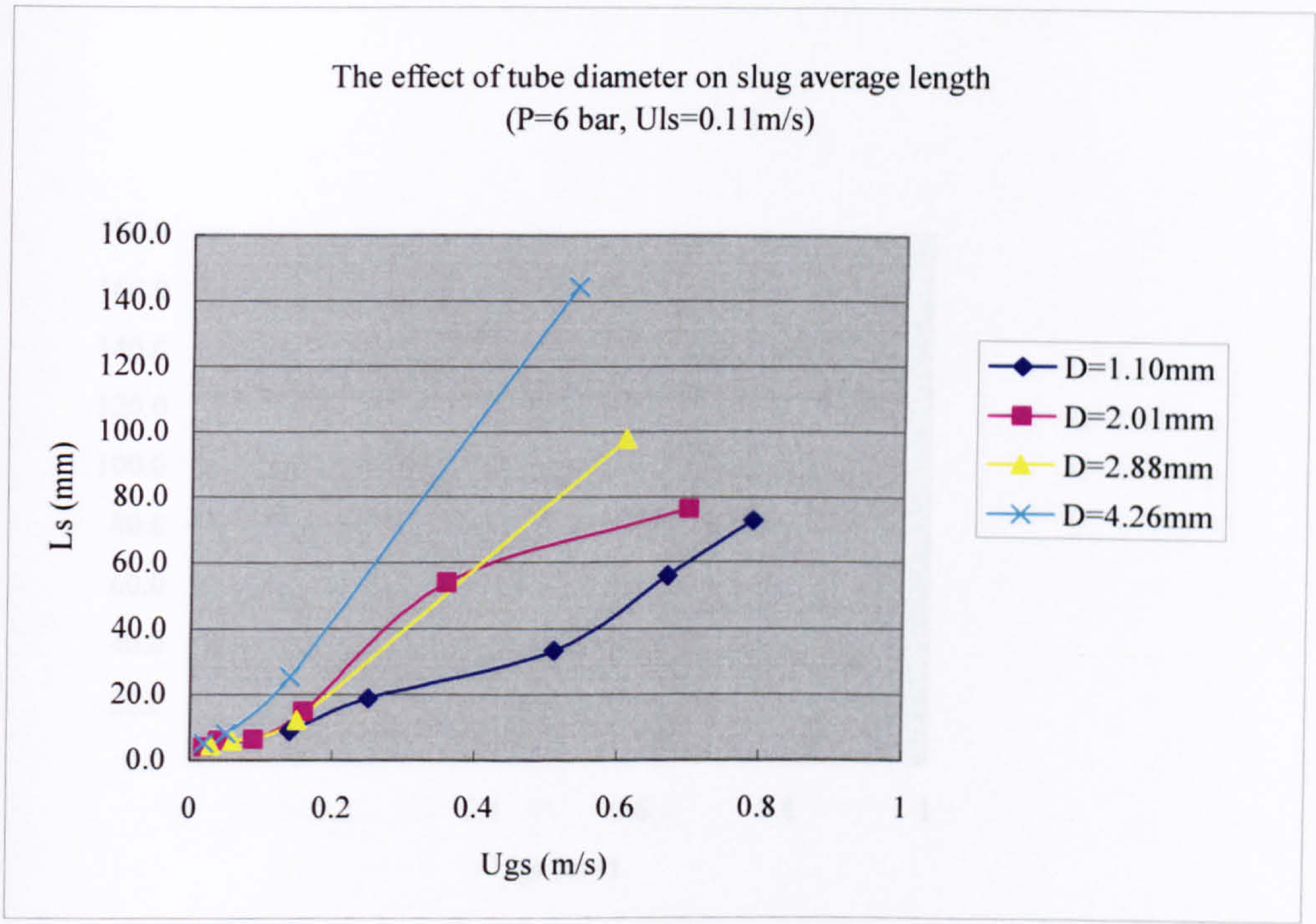

Figure G.29 The effect of tube diameter on slug average length at 6 bar (u_{ls}=0.11m/s).

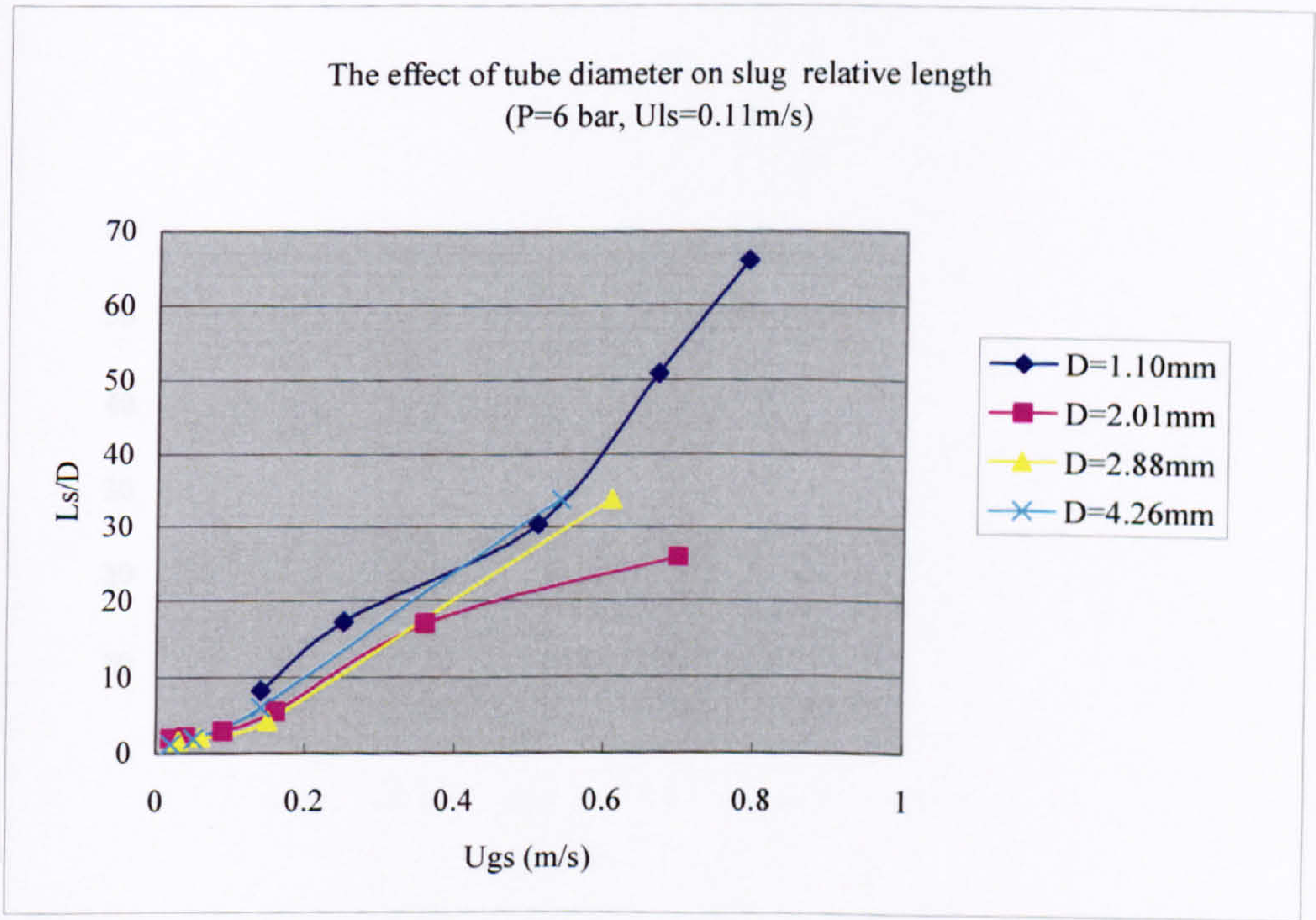

Figure G.30 The effect of tube diameter on slug length-diameter ratio at 6 bar (u_{ls}=0.11m/s).

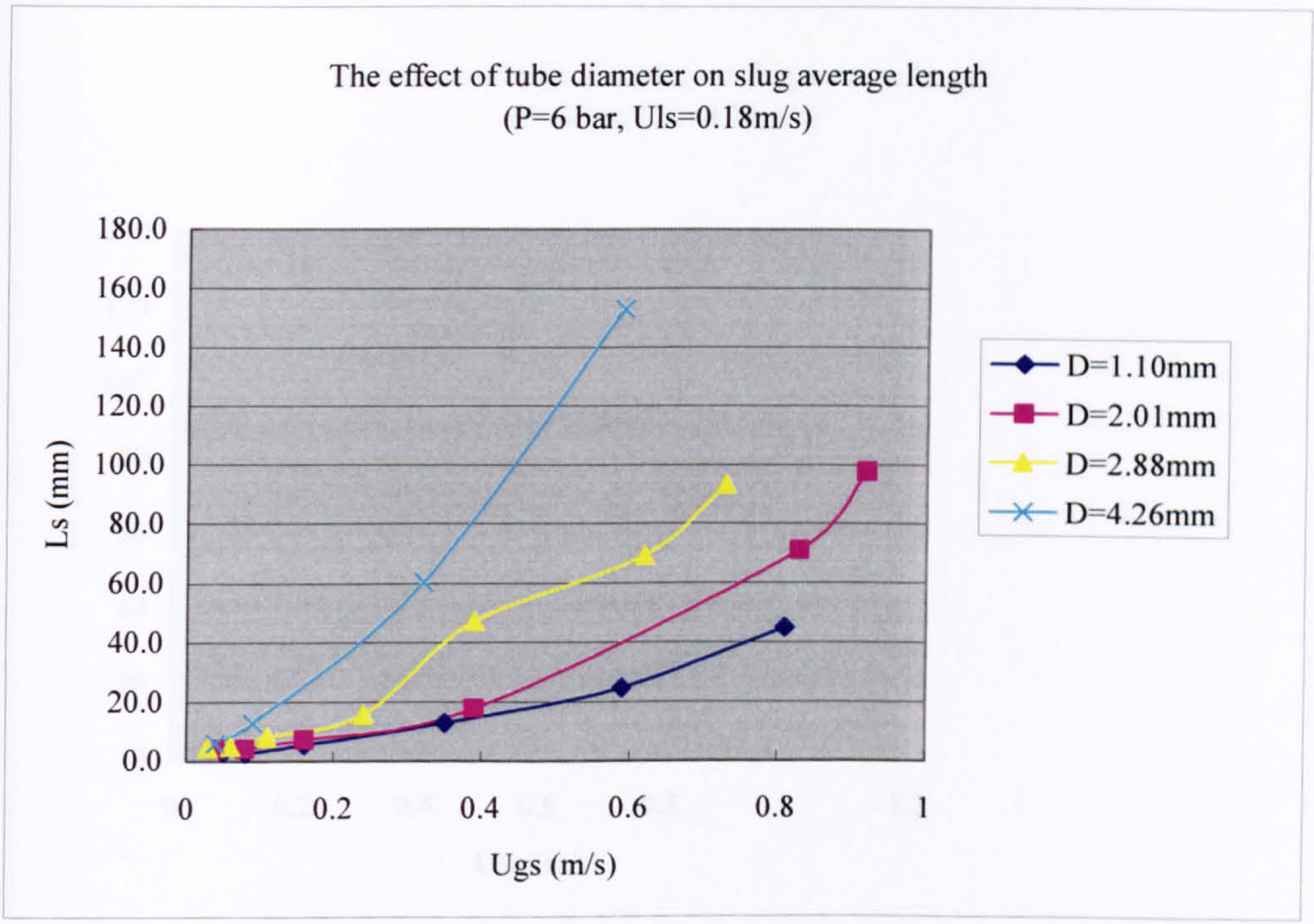

Figure G.31 The effect of tube diameter on slug average length at 6 bar (u_{ls}=0.18m/s).

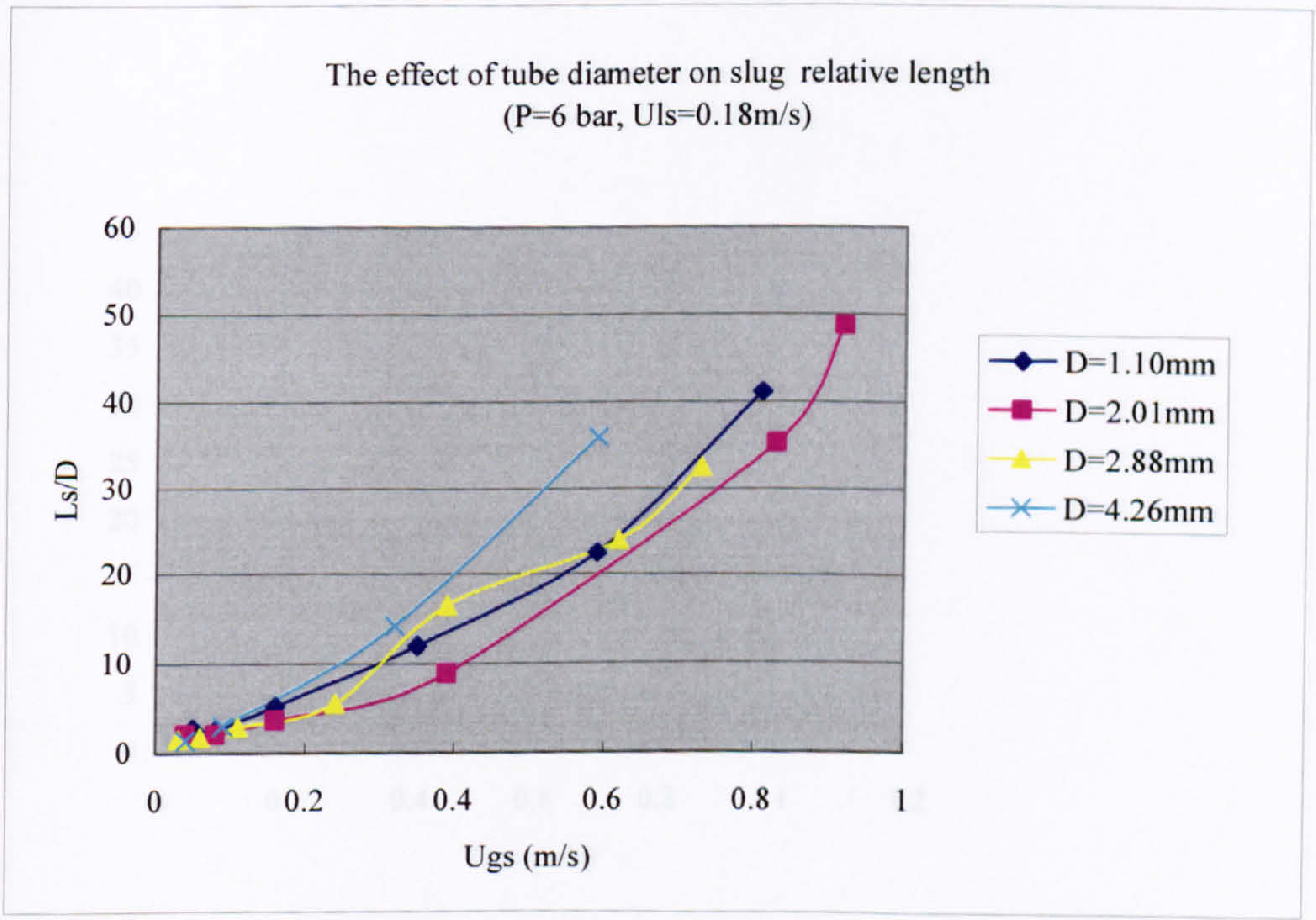

Figure G.32 The effect of tube diameter on slug length-diameter ratio at 6 bar (u_{ls}=0.18m/s).

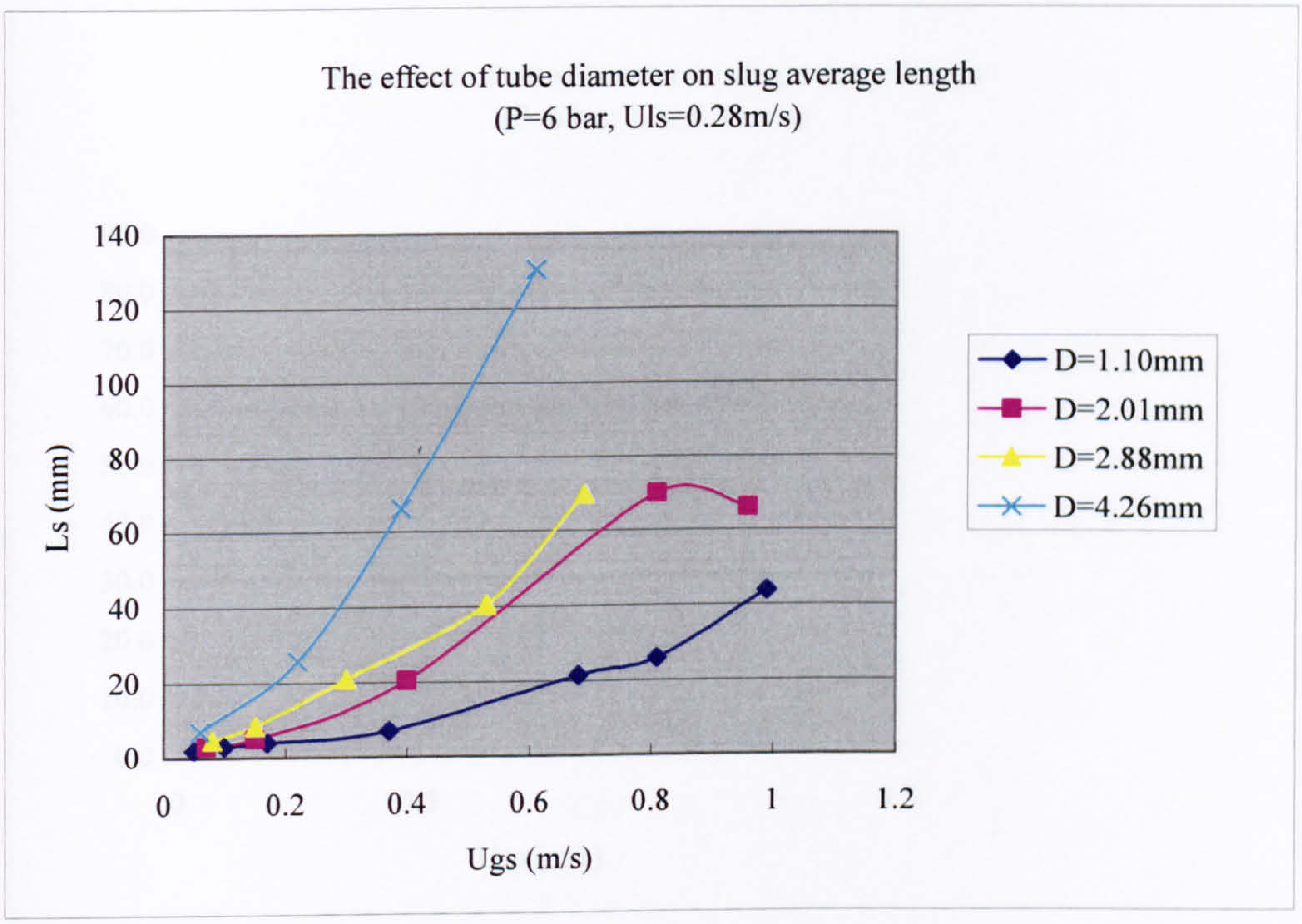

Figure G.33 The effect of tube diameter on slug average length at 6 bar (u_{ls}=0.28m/s).

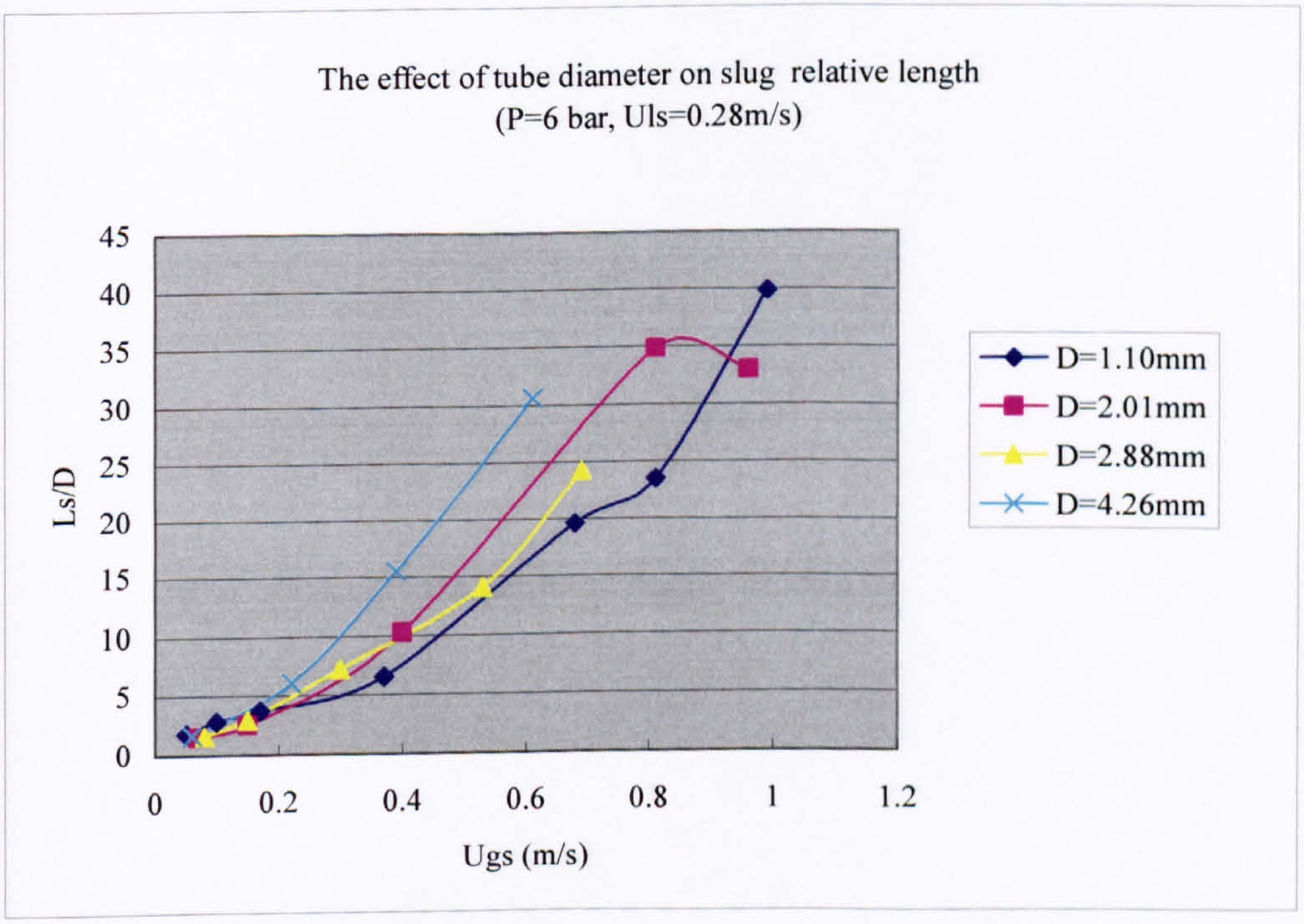

Figure G.34 The effect of tube diameter on slug length-diameter ratio at 6 bar (u_{ls}=0.28m/s).

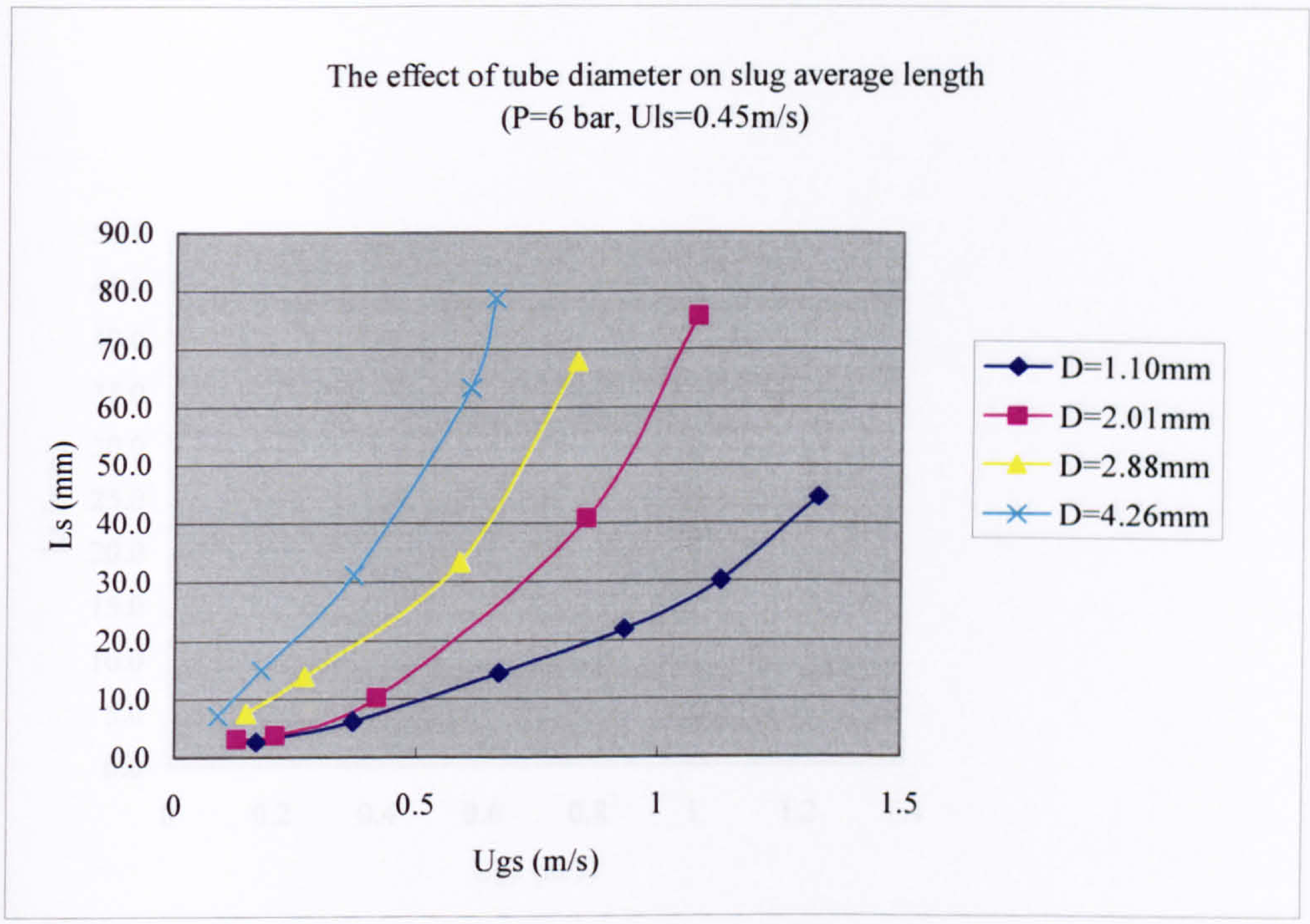

Figure G.35 The effect of tube diameter on slug average length at 6 bar (u_{ls}=0.45m/s).

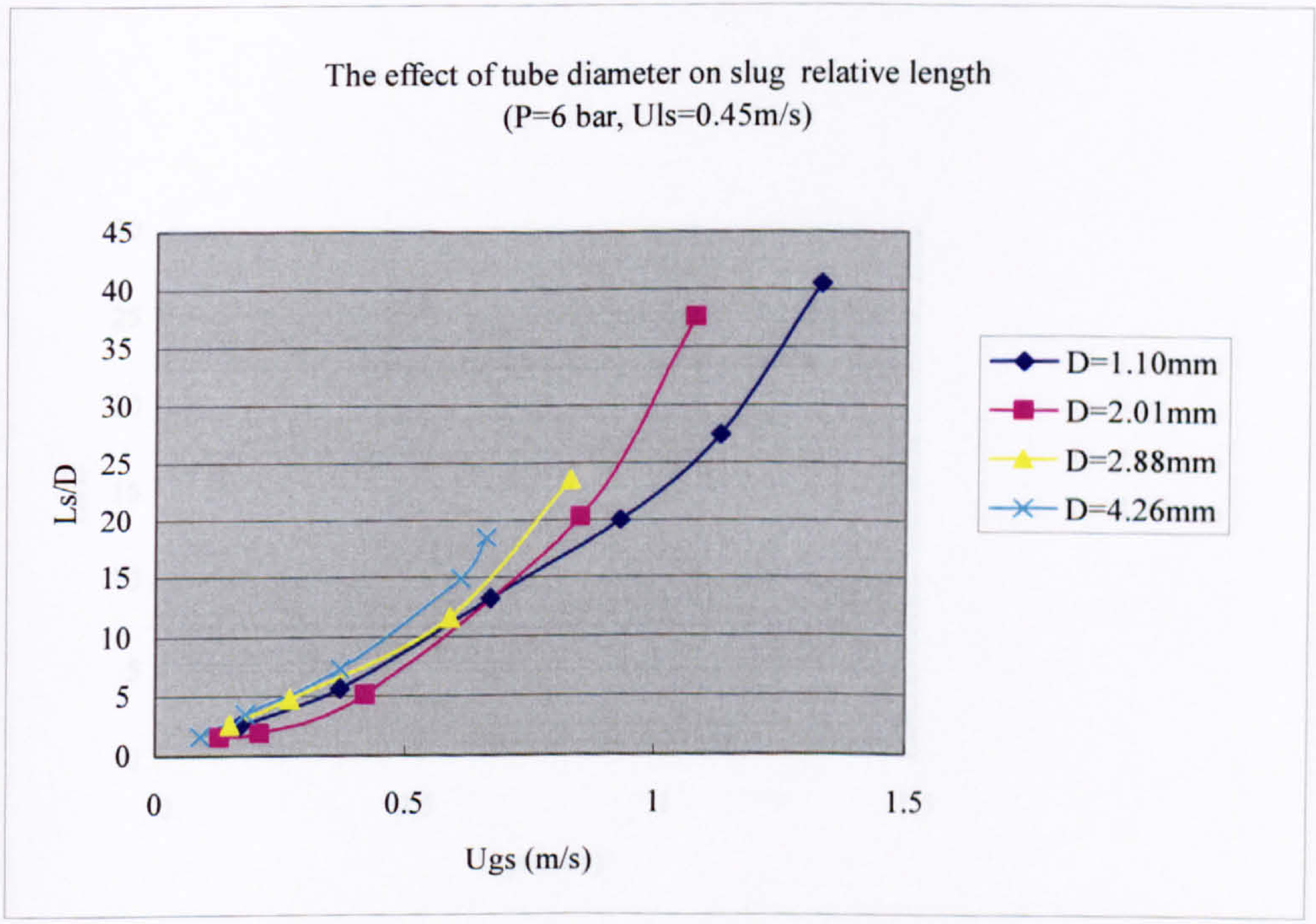

Figure G.36 The effect of tube diameter on slug length-diameter ratio at 6 bar (u_{ls}=0.45m/s).

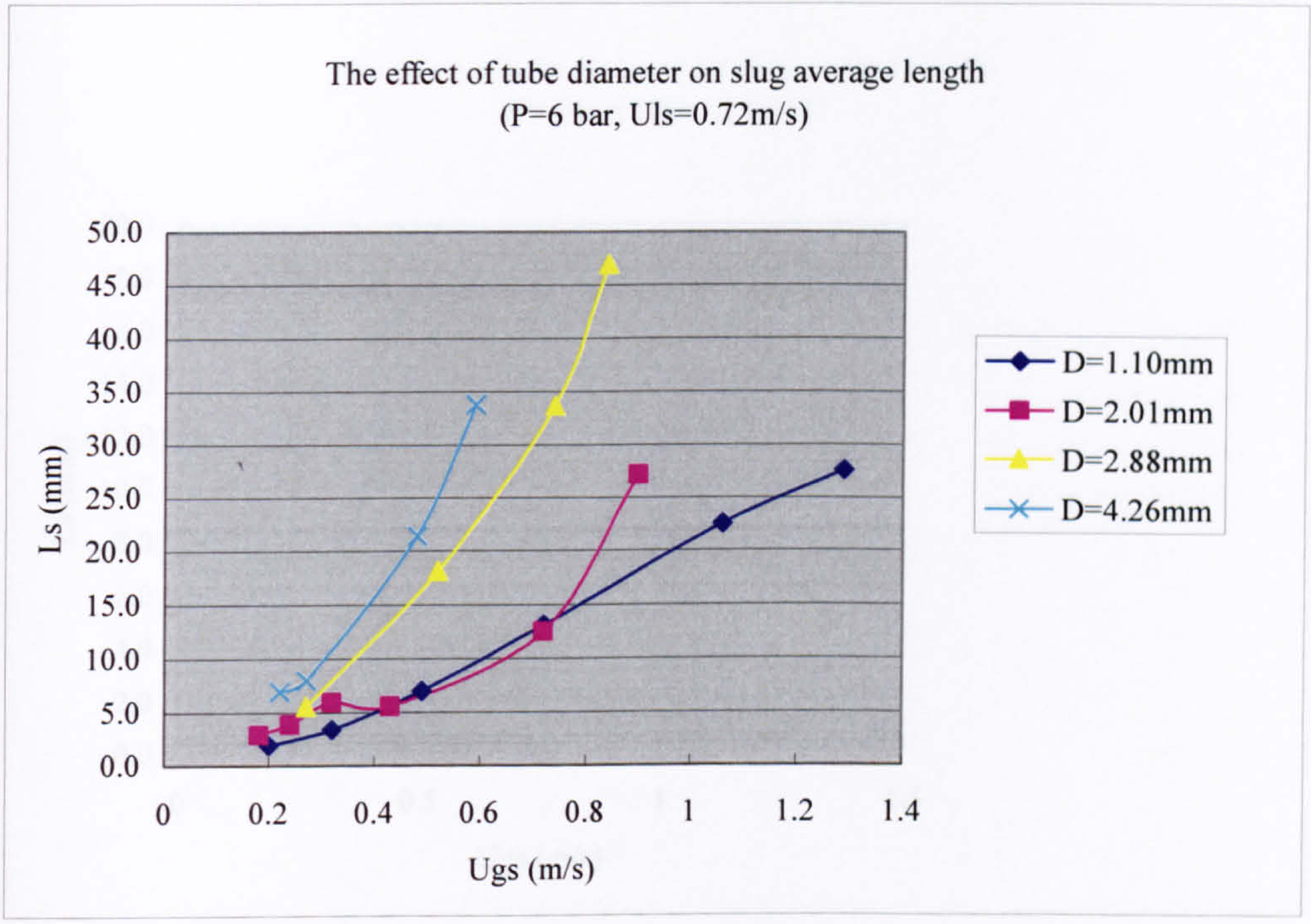

Figure G.37 The effect of tube diameter on slug average length at 6 bar (u_{ls}=0.72m/s).

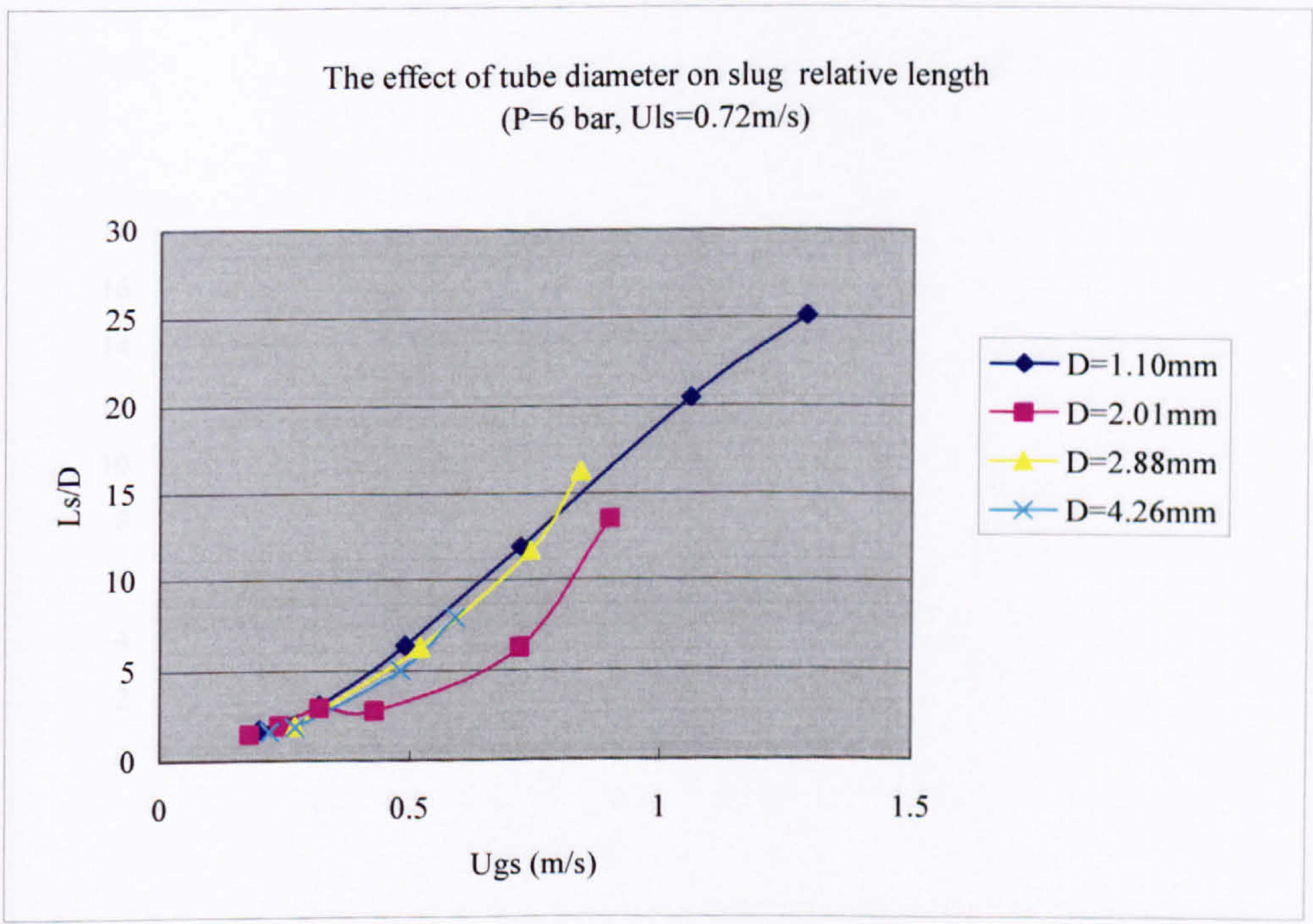

Figure G.38 The effect of tube diameter on slug length-diameter ratio at 6 bar (u_{ls}=0.72m/s).

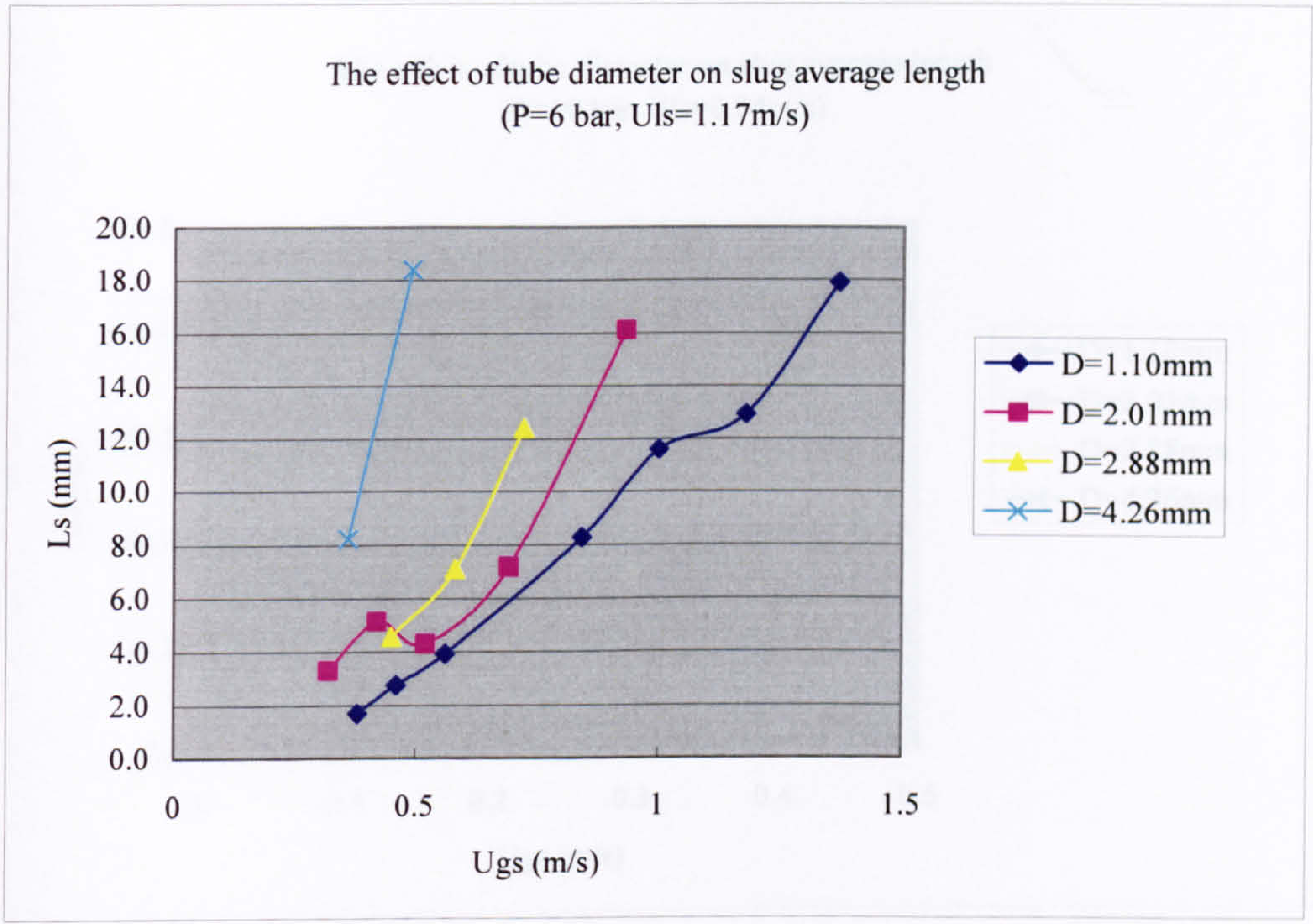

Figure G.39 The effect of tube diameter on slug average length at 6 bar (u_{ls}=1.17m/s).

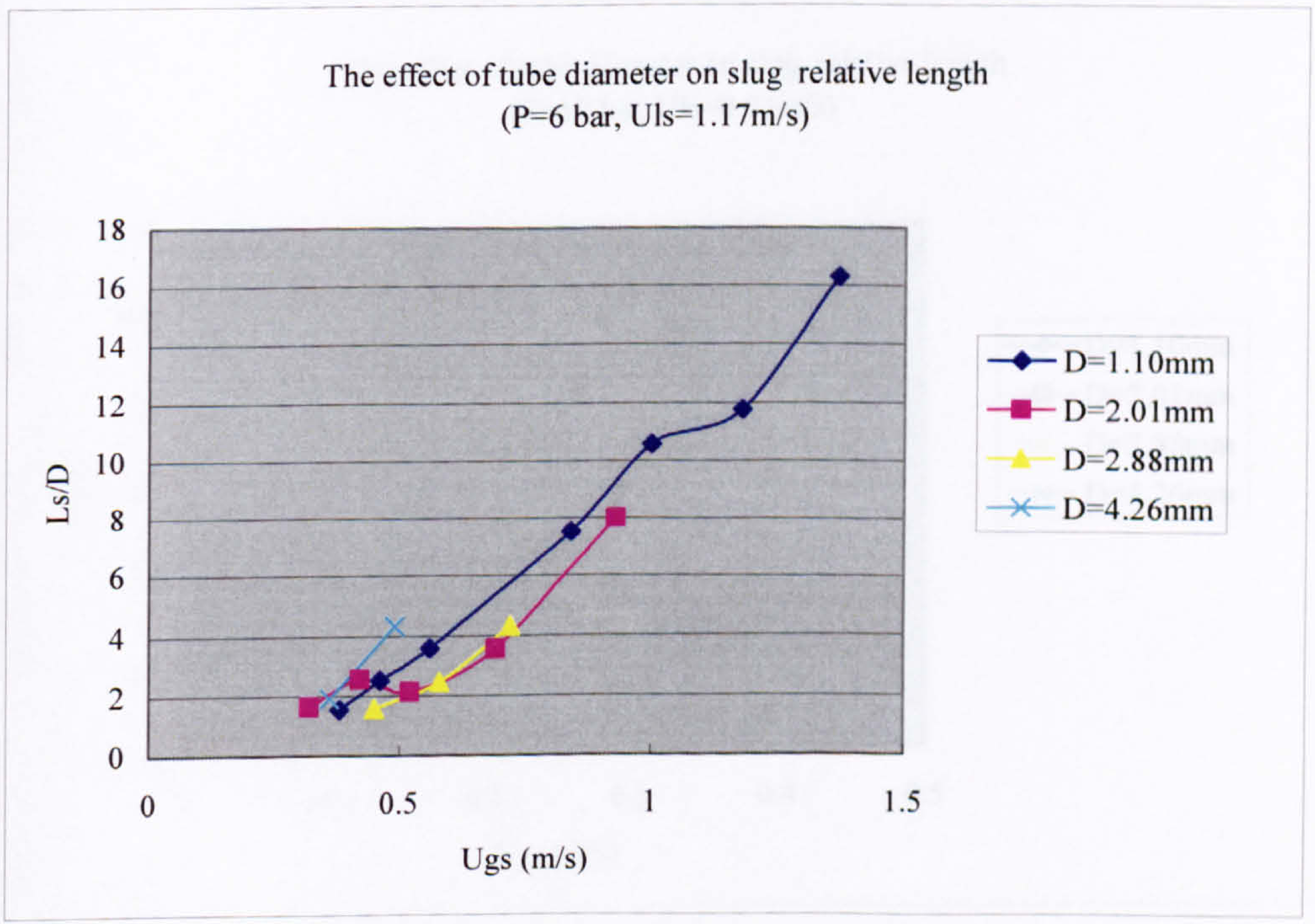

Figure G.40 The effect of tube diameter on slug length-diameter ratio at 6 bar (u_{ls}=1.17m/s).

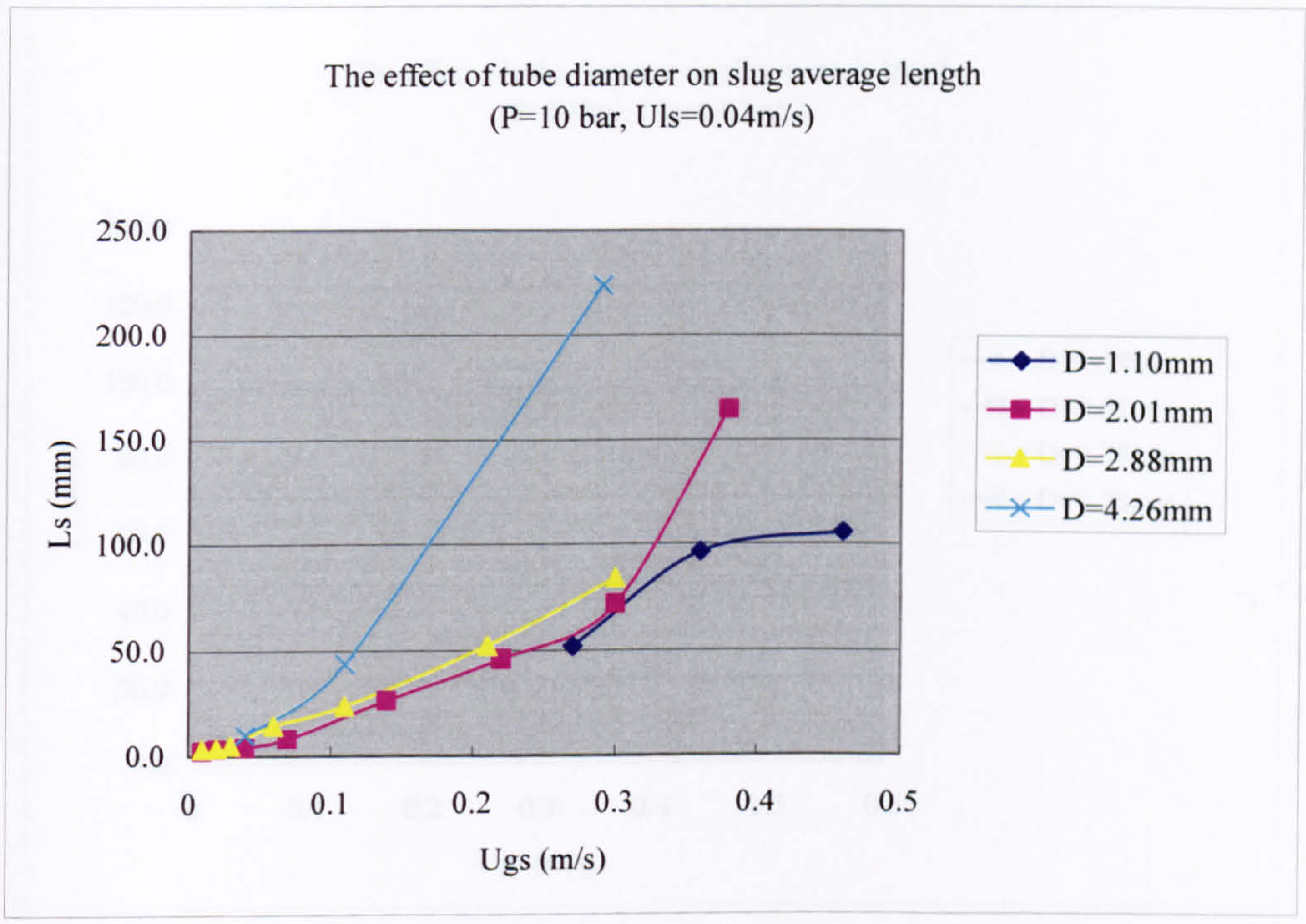

Figure G.41 The effect of tube diameter on slug average length at 10 bar (u_{ls}=0.04m/s).

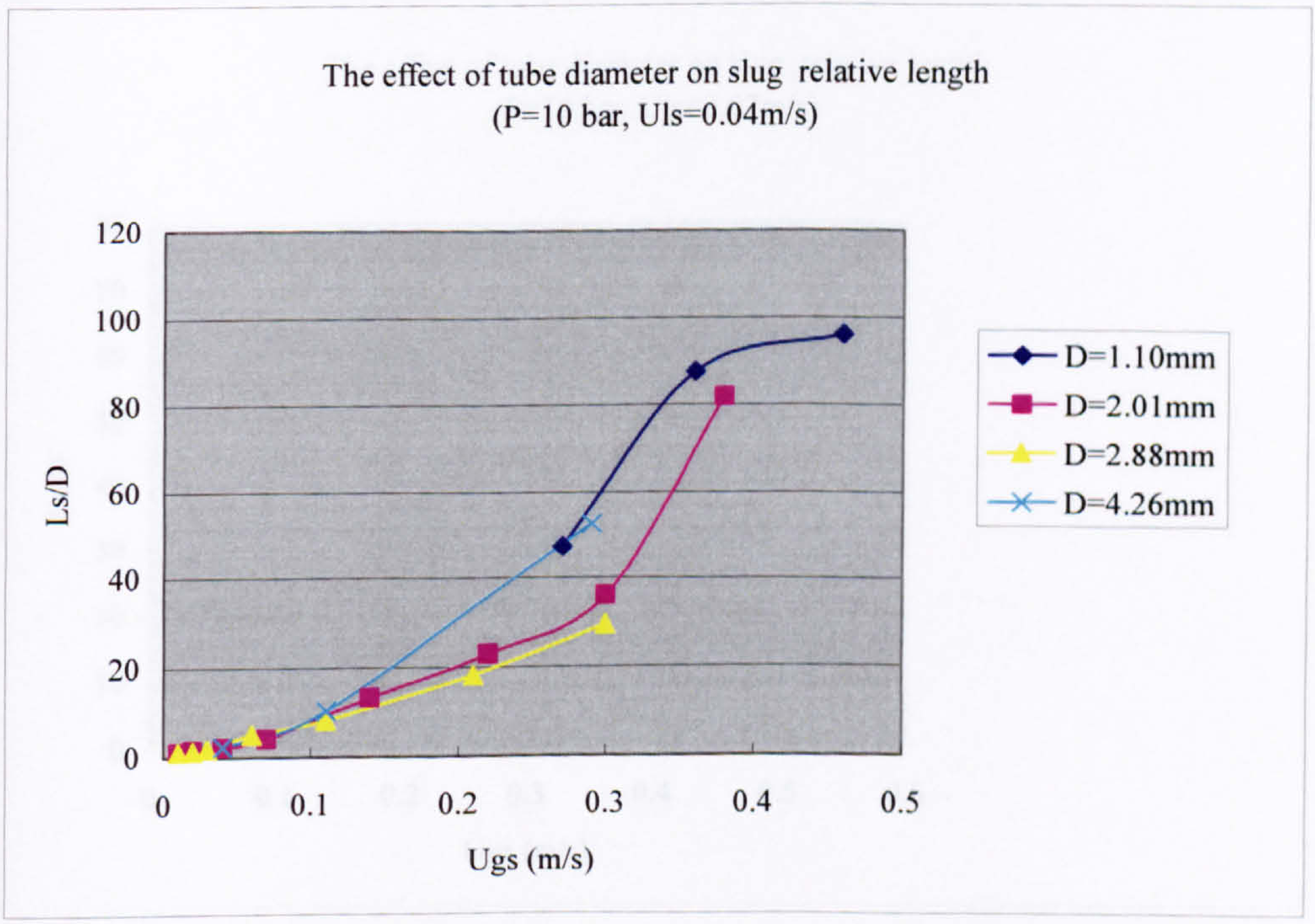

Figure G.42 The effect of tube diameter on slug length-diameter ratio at 10 bar (u_{ls}=0.04m/s).

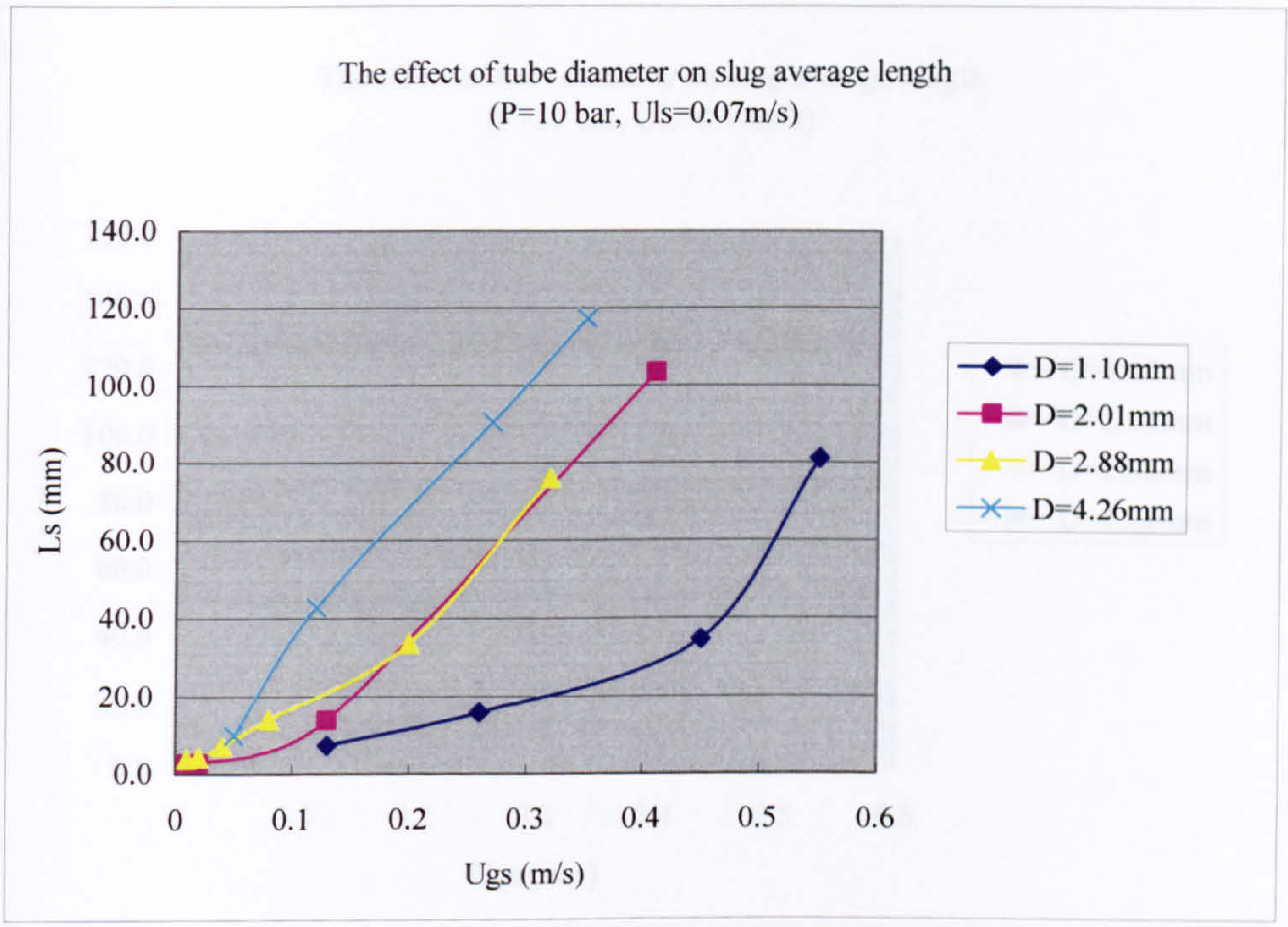

Figure G.43 The effect of tube diameter on slug average length at 10 bar (u_{ls}=0.07m/s).

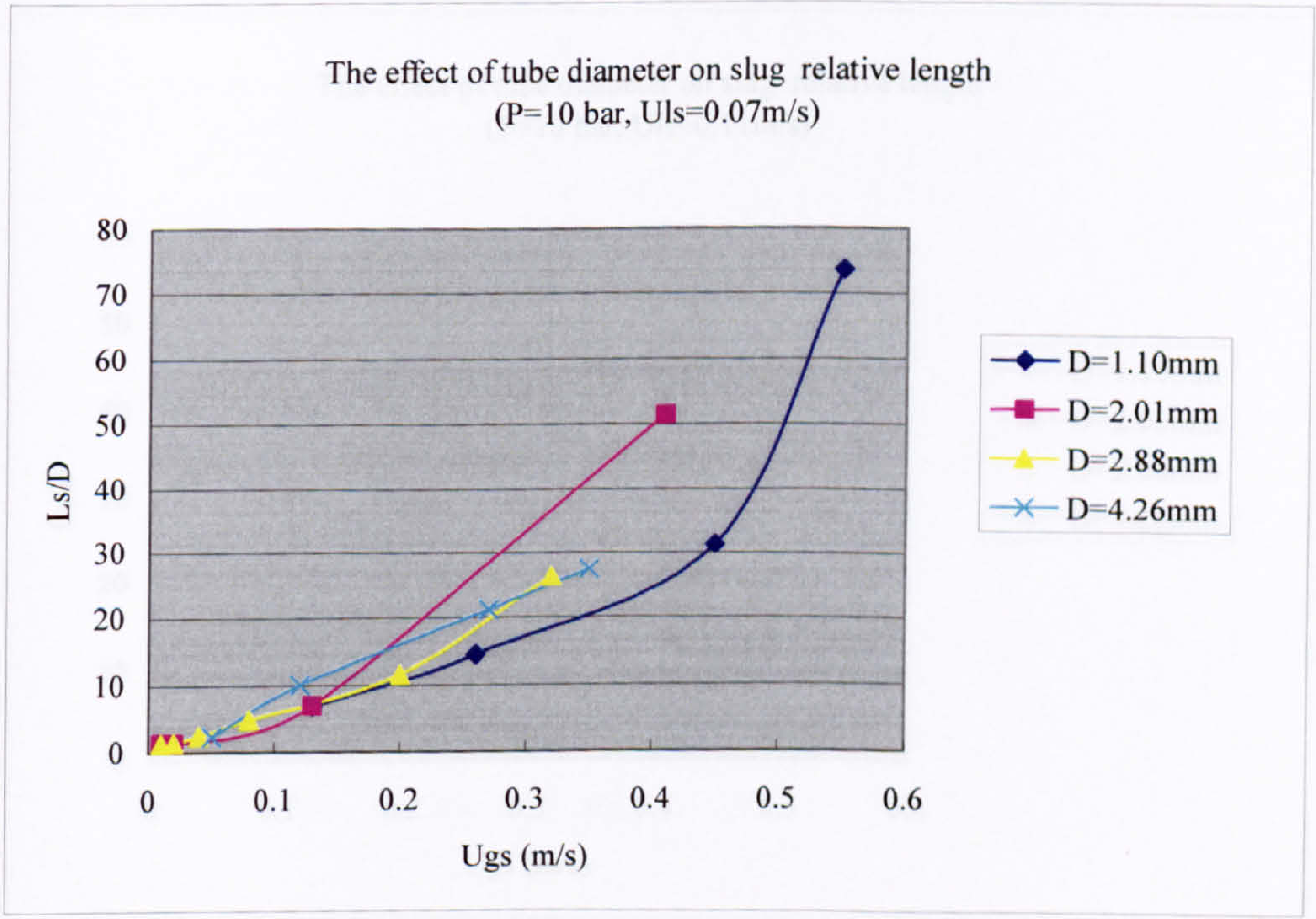

Figure G.44 The effect of tube diameter on slug length-diameter ratio at 10 bar (u_{ls}=0.07m/s).

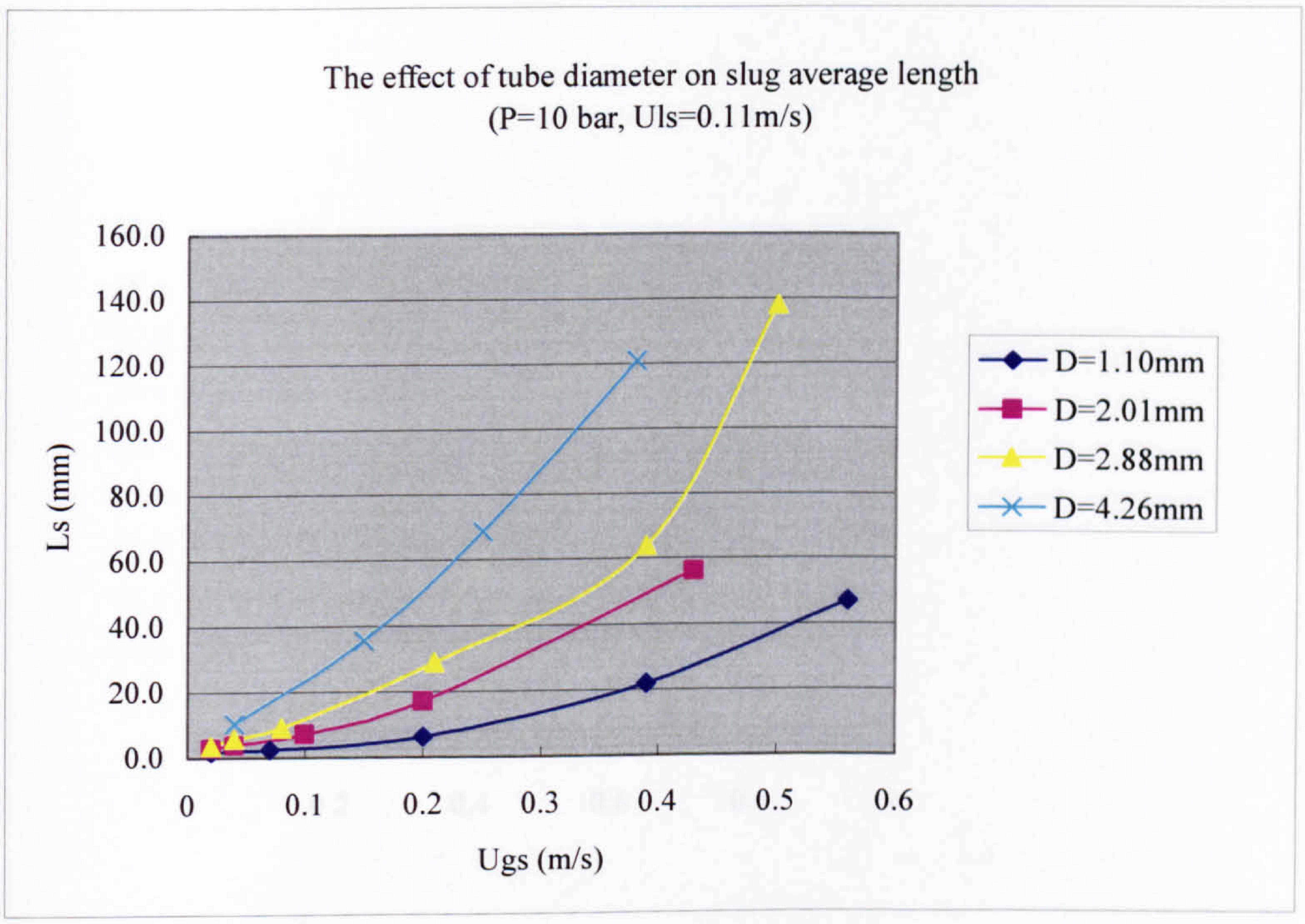

Figure G.45 The effect of tube diameter on slug average length at 10 bar (u_{ls}=0.11m/s).

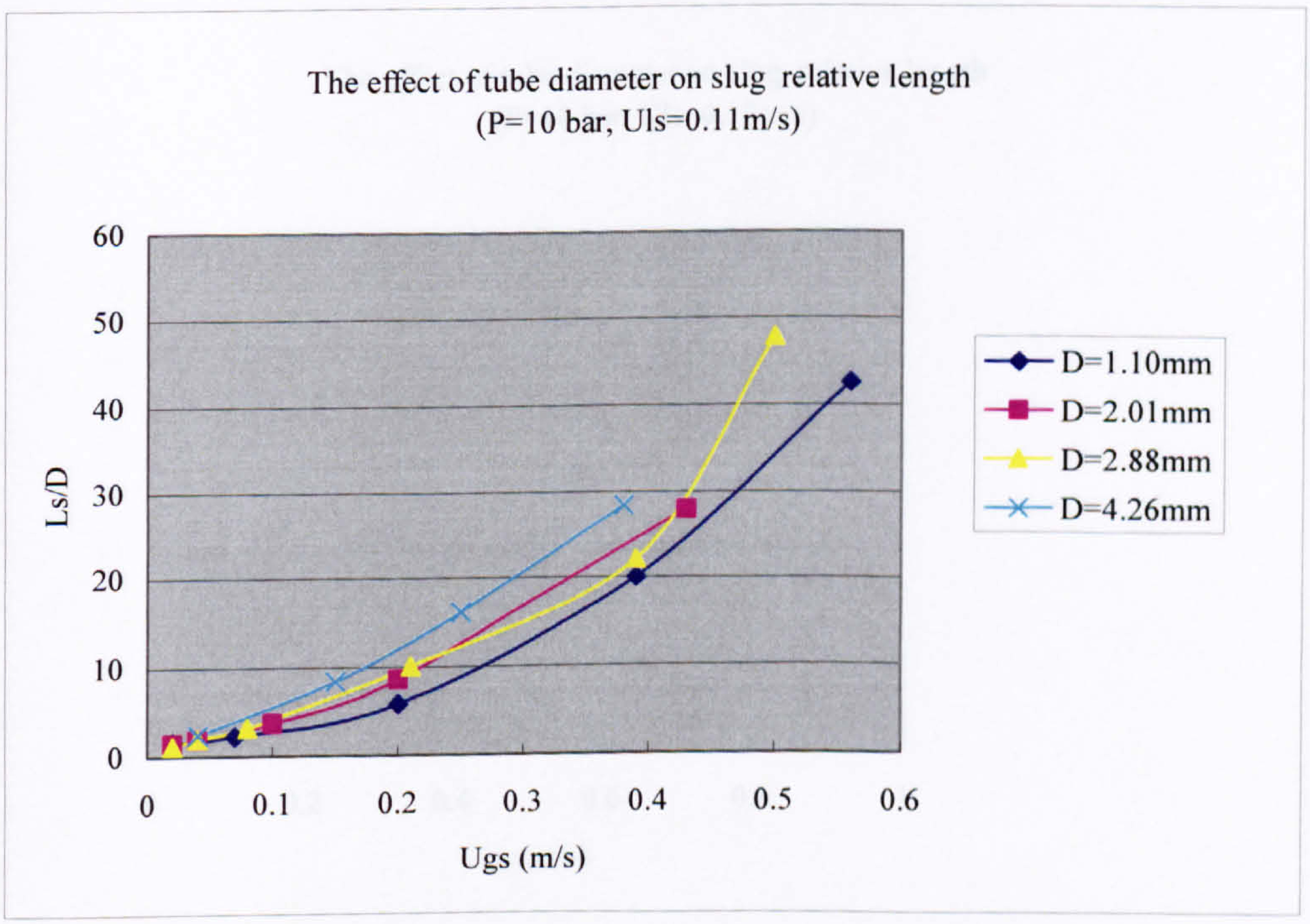

Figure G.46 The effect of tube diameter on slug length-diameter ratio at 10 bar (u_{ls}=0.11m/s).

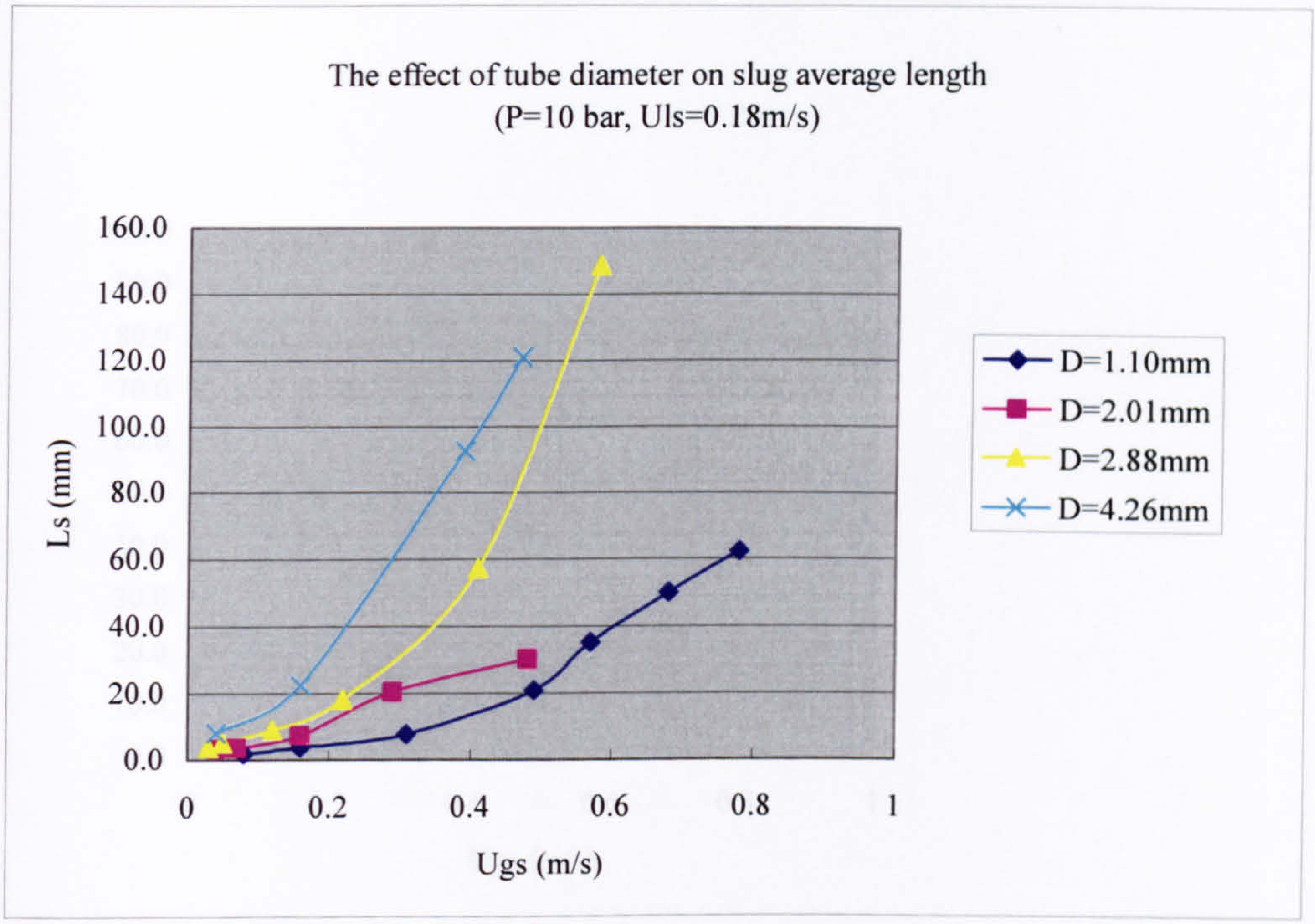

Figure G.47 The effect of tube diameter on slug average length at 10 bar (u_{ls}=0.18m/s).

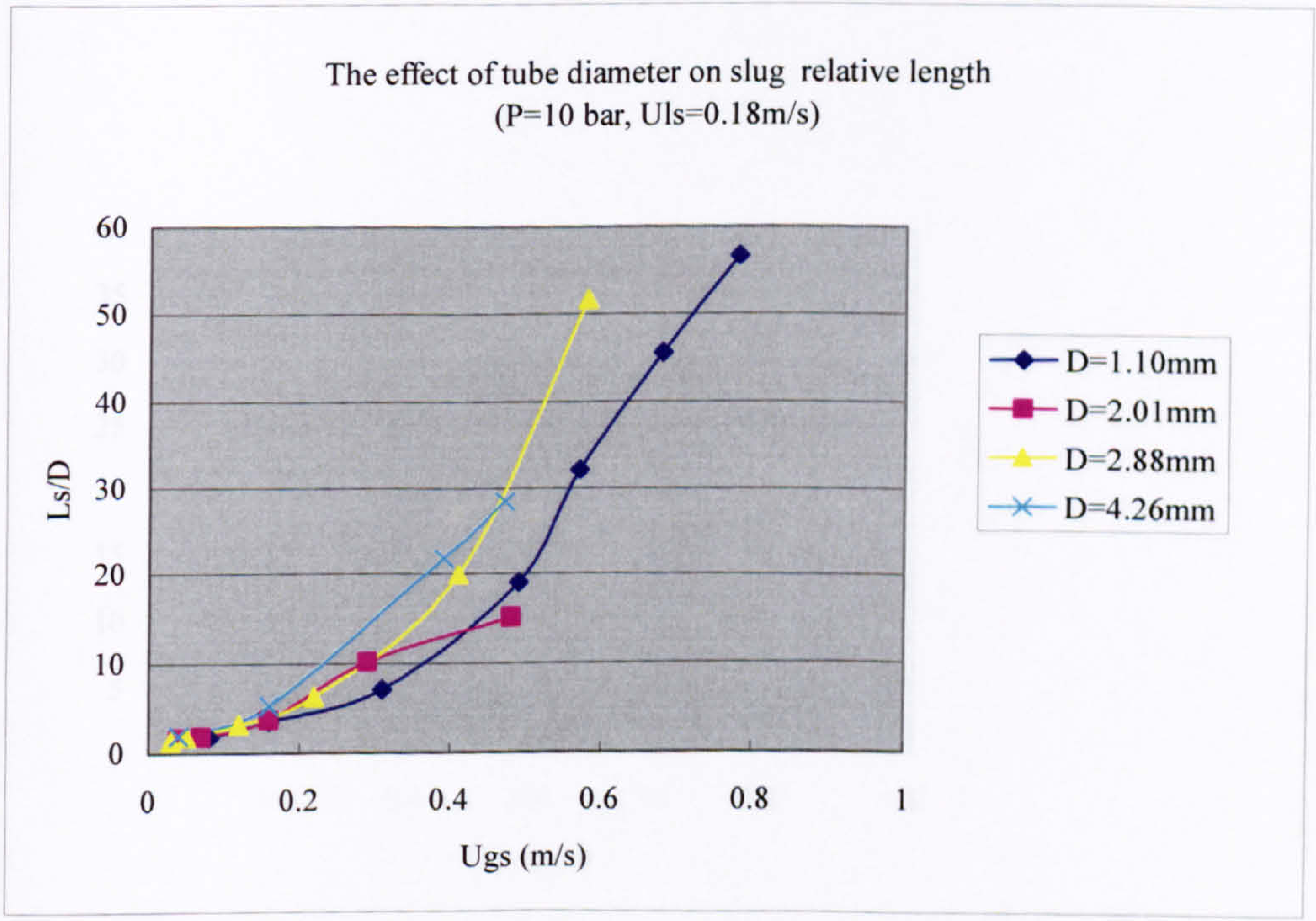

Figure G.48 The effect of tube diameter on slug length-diameter ratio at 10 bar (u_{ls}=0.18m/s).

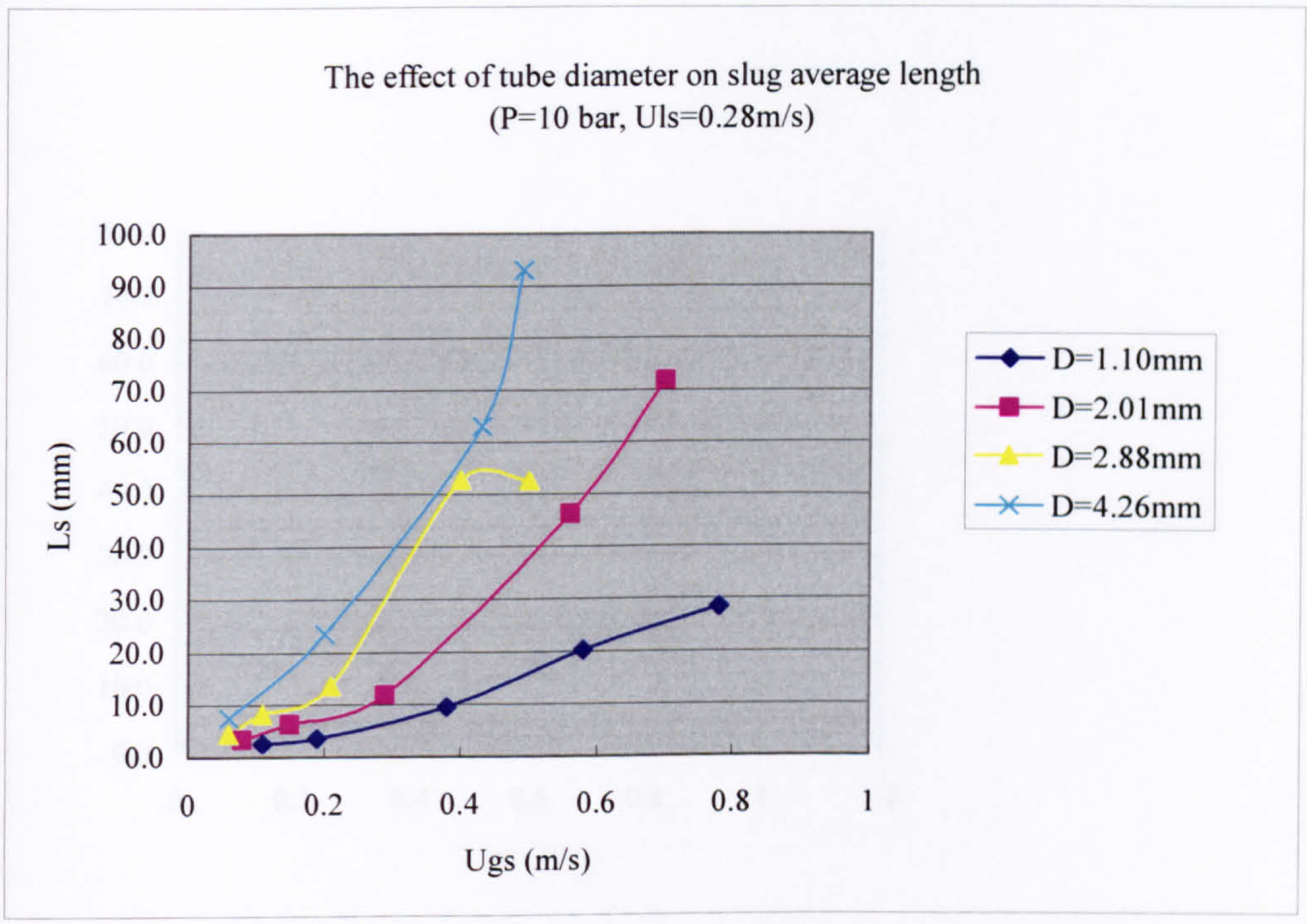

Figure G.49 The effect of tube diameter on slug average length at 10 bar (u_{ls}=0.28m/s).

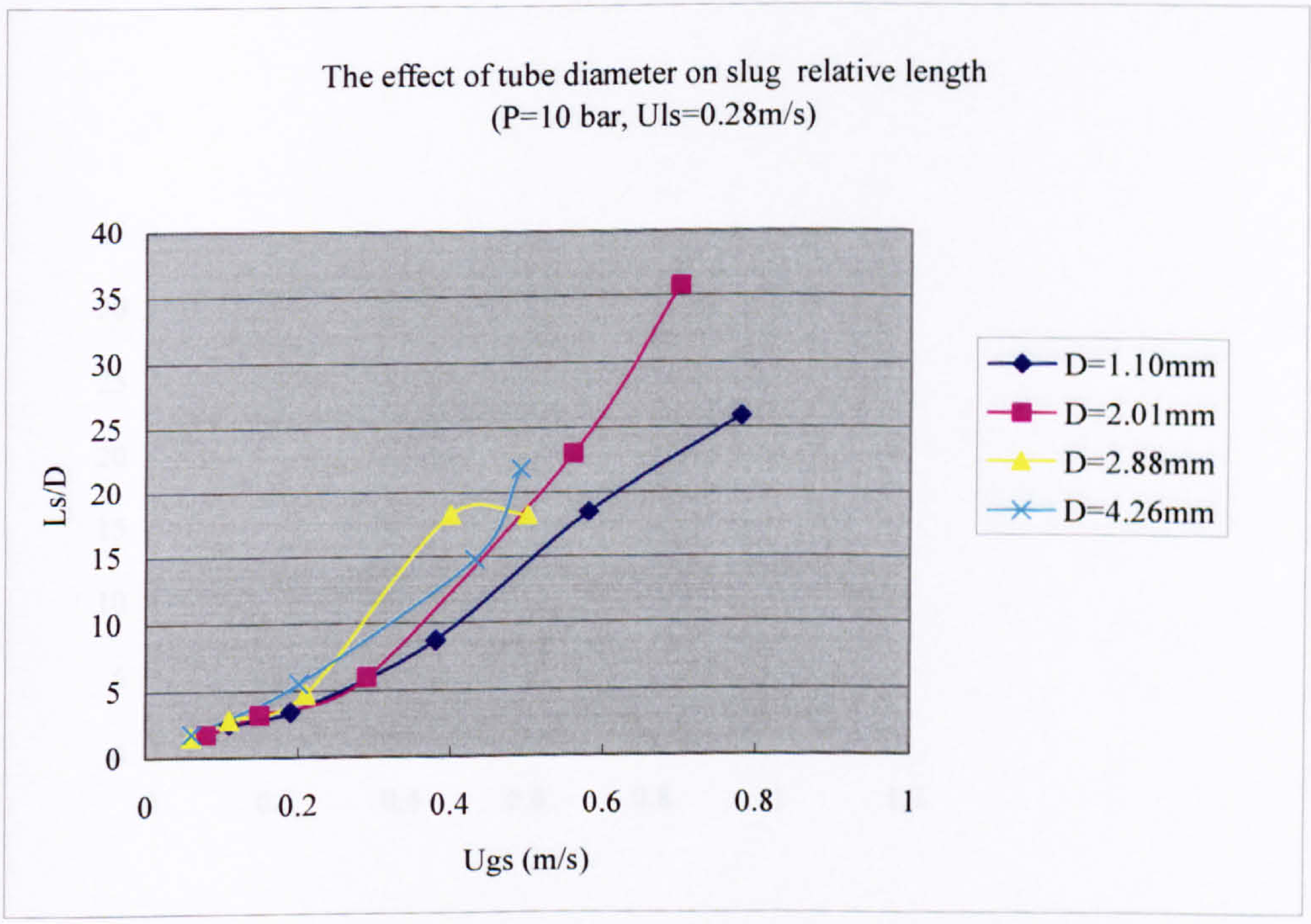

Figure G.50 The effect of tube diameter on slug length-diameter ratio at 10 bar (u_{ls}=0.28m/s).

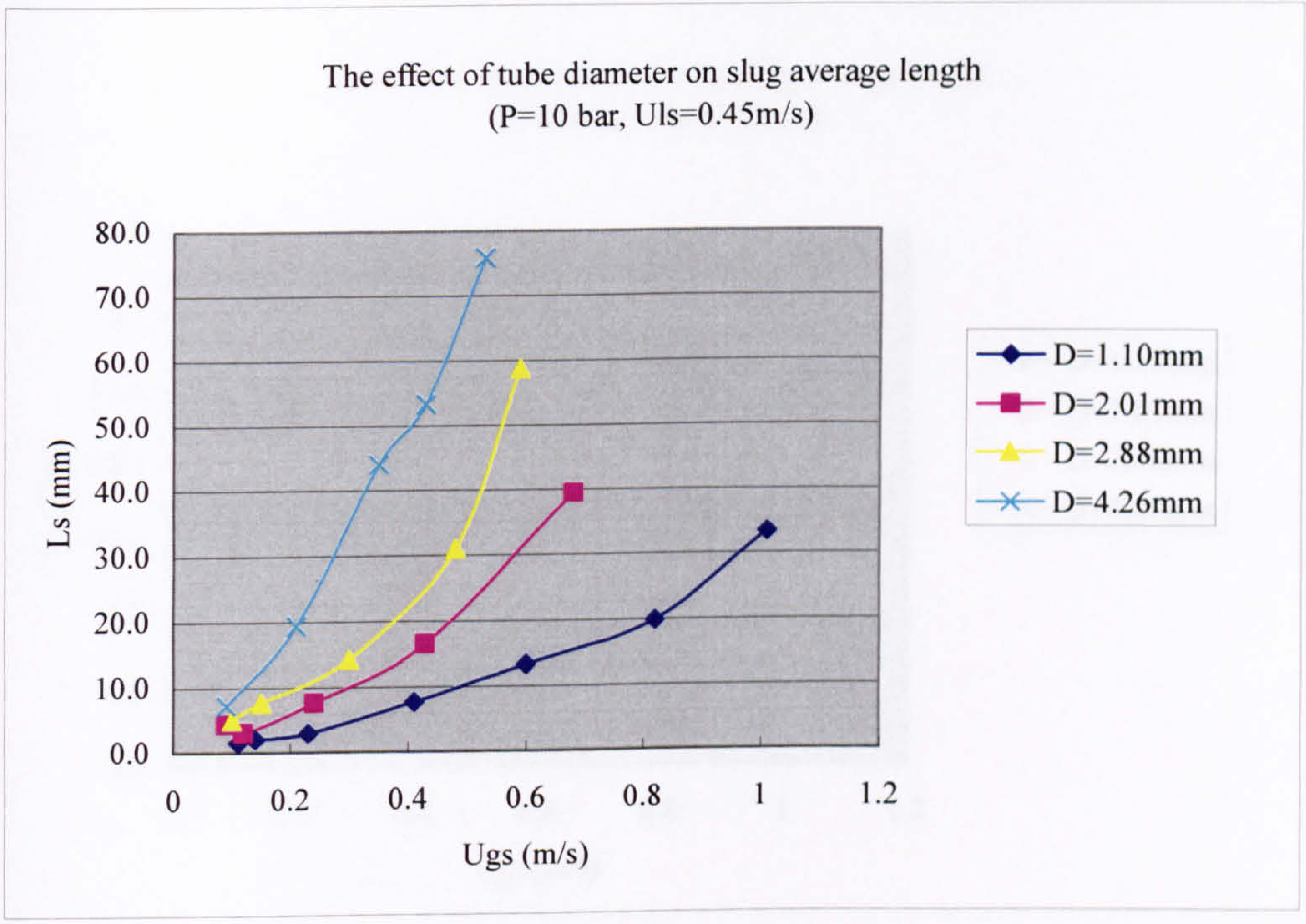

Figure G.51 The effect of tube diameter on slug average length at 10 bar (u_{ls}=0.45m/s).

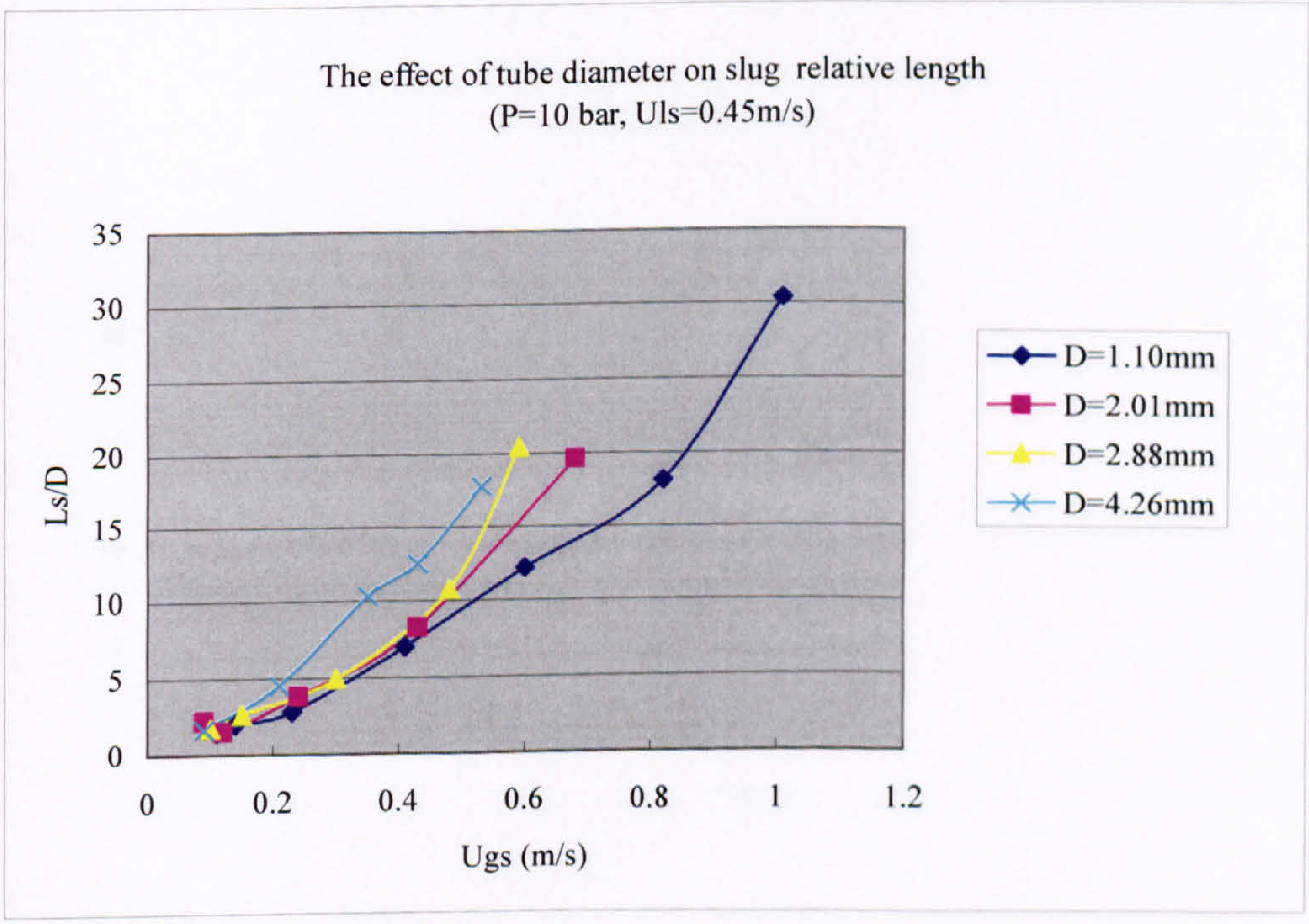

Figure G.52 The effect of tube diameter on slug length-diameter ratio at 10 bar (u_{ls}=0.45m/s).

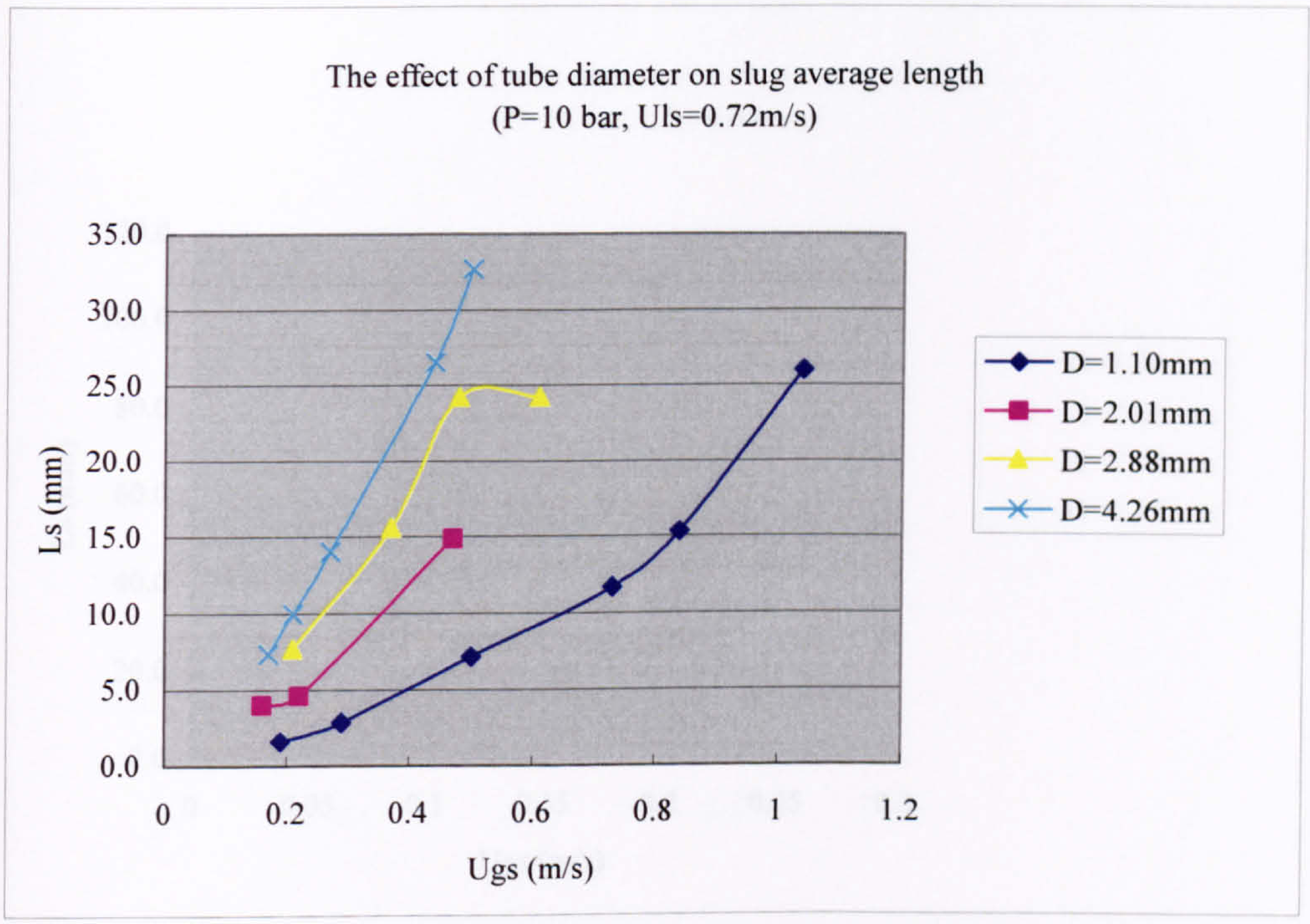

Figure G.53 The effect of tube diameter on slug average length at 10 bar (u_{ls}=0.72m/s).

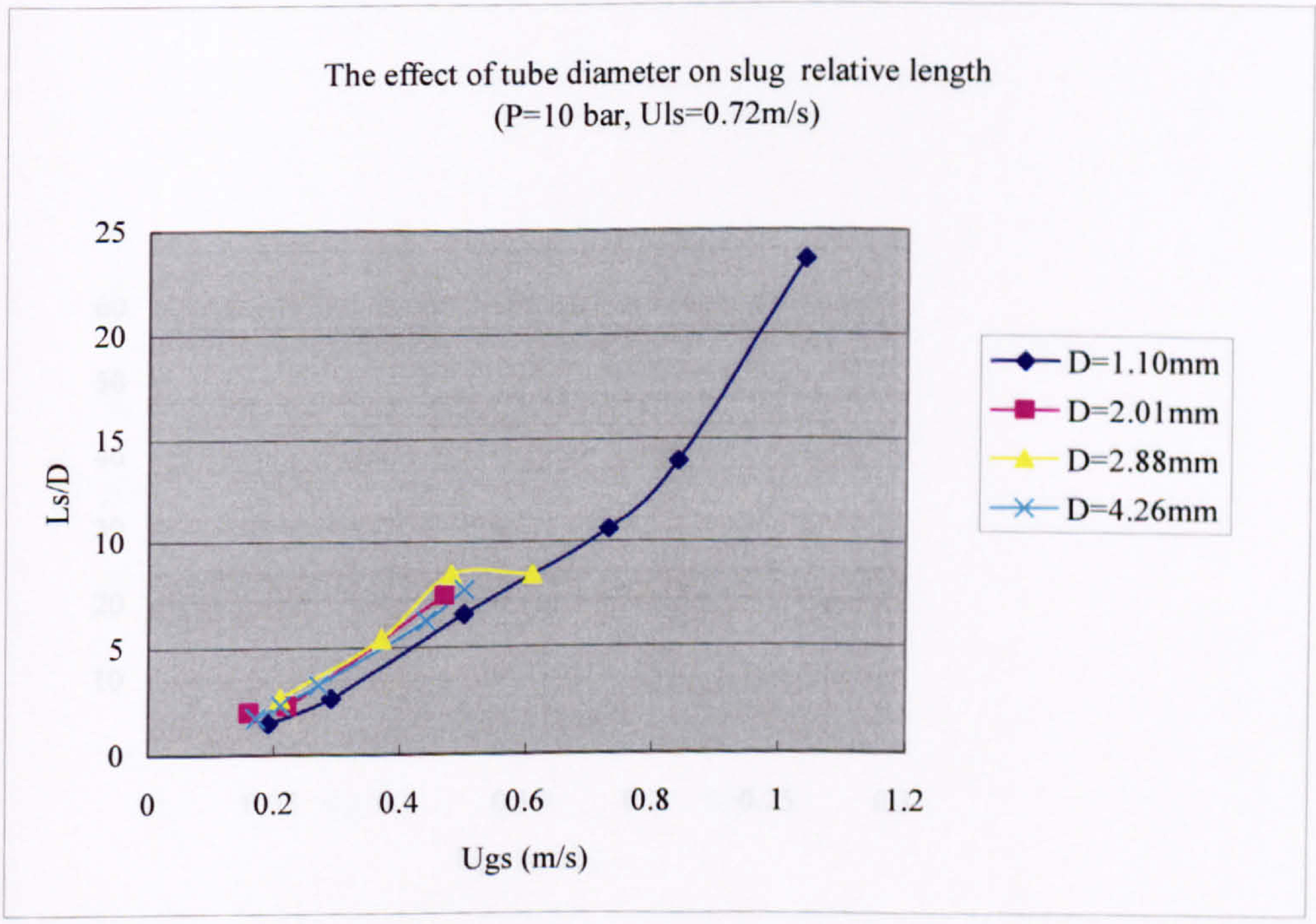

Figure G.54 The effect of tube diameter on slug length-diameter ratio at 10 bar (u_{ls}=0.72m/s).

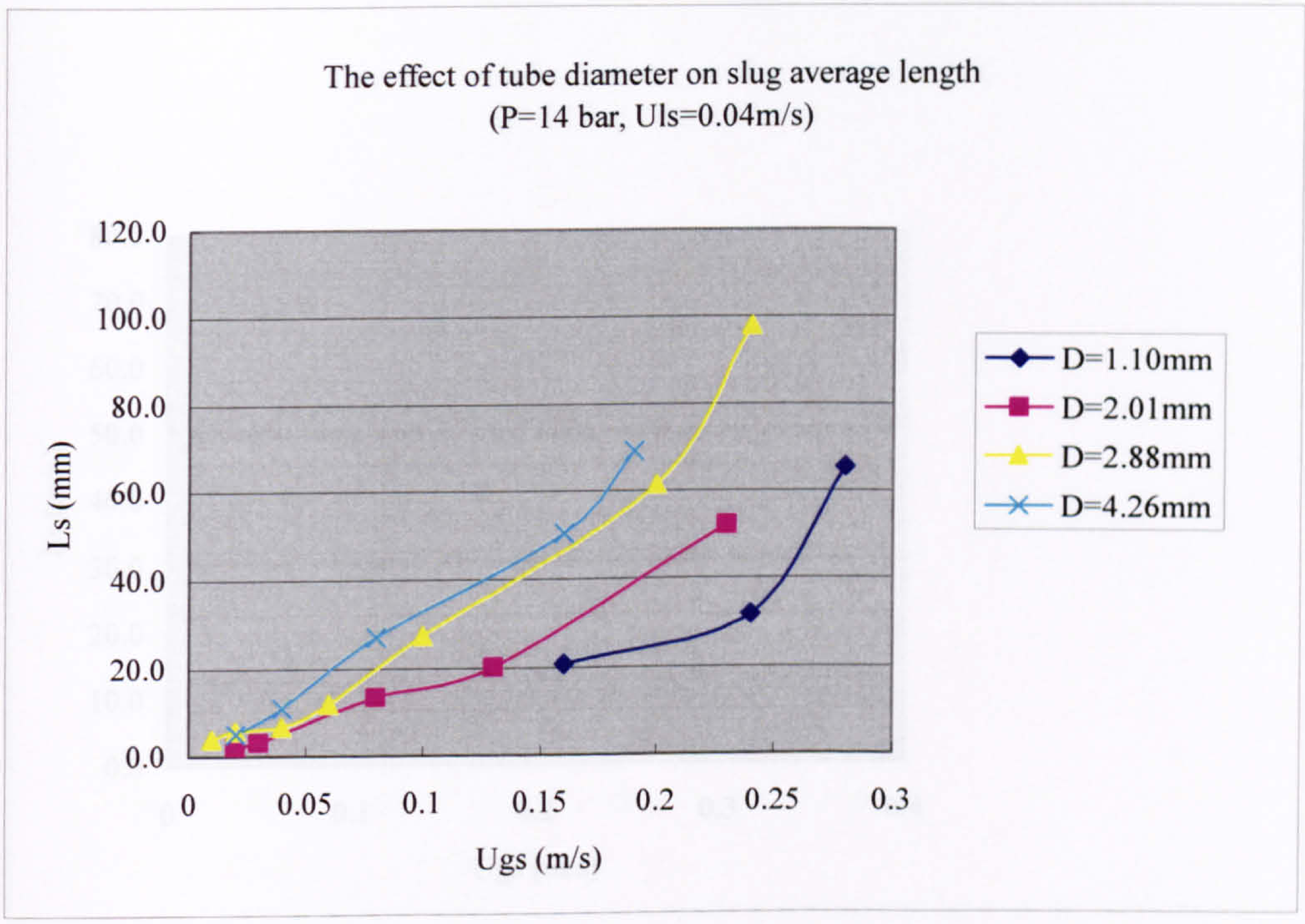

Figure G.55 The effect of tube diameter on slug average length at 14 bar (u_{ls}=0.04m/s).

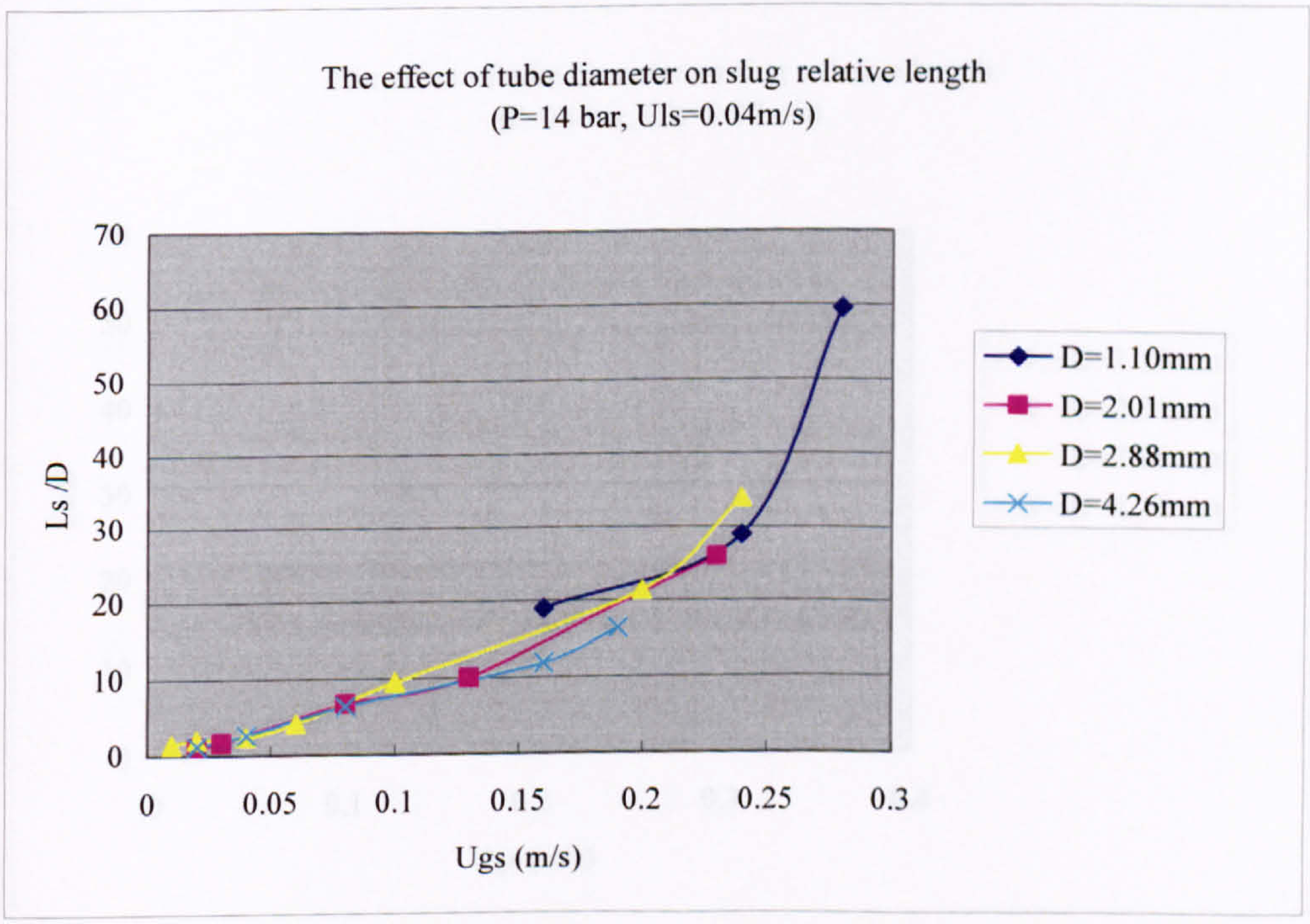

Figure G.56 The effect of tube diameter on slug length-diameter ratio at 14 bar (u_{ls}=0.04m/s).

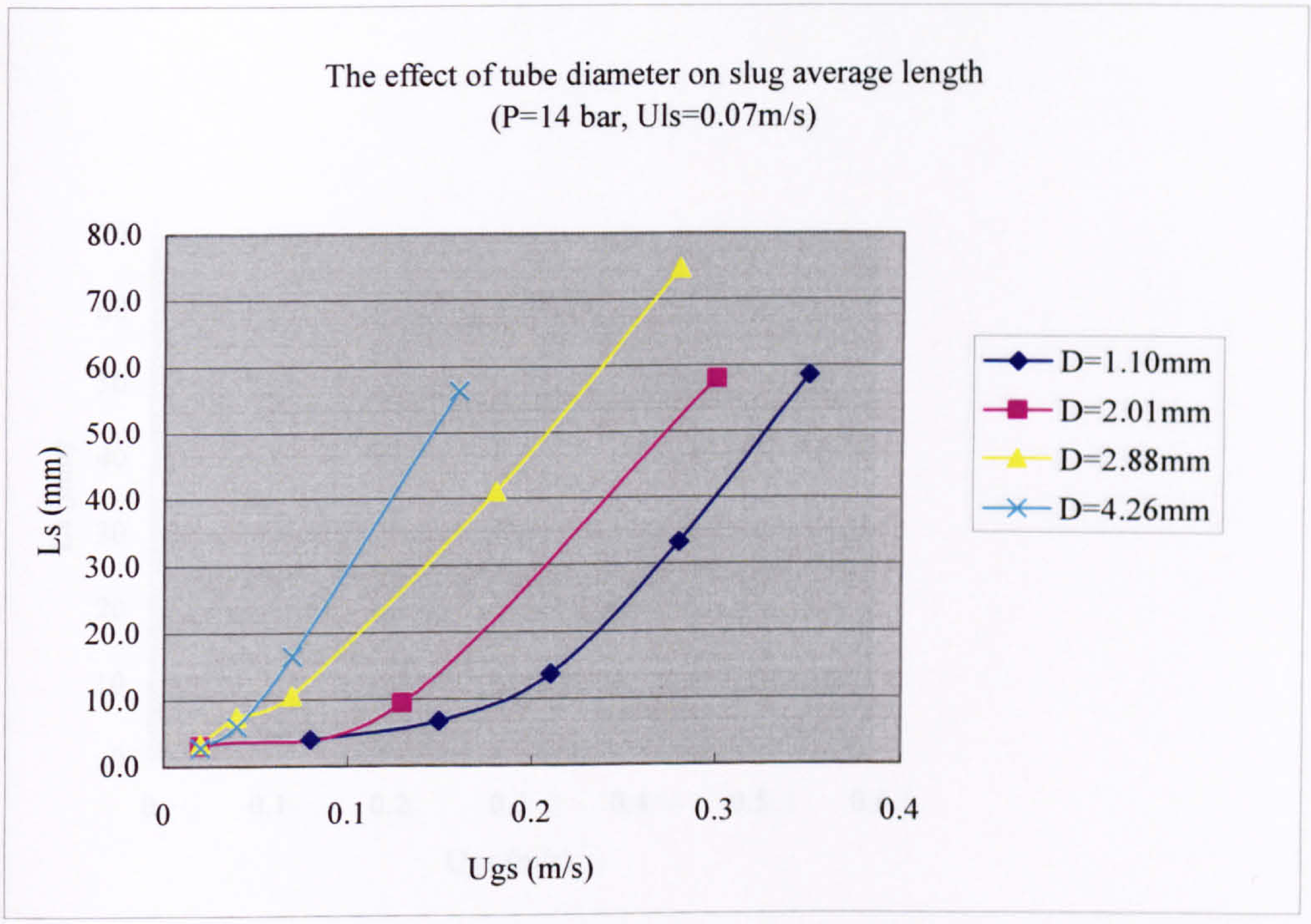

Figure G.57 The effect of tube diameter on slug average length at 14 bar (u_{ls}=0.07m/s).

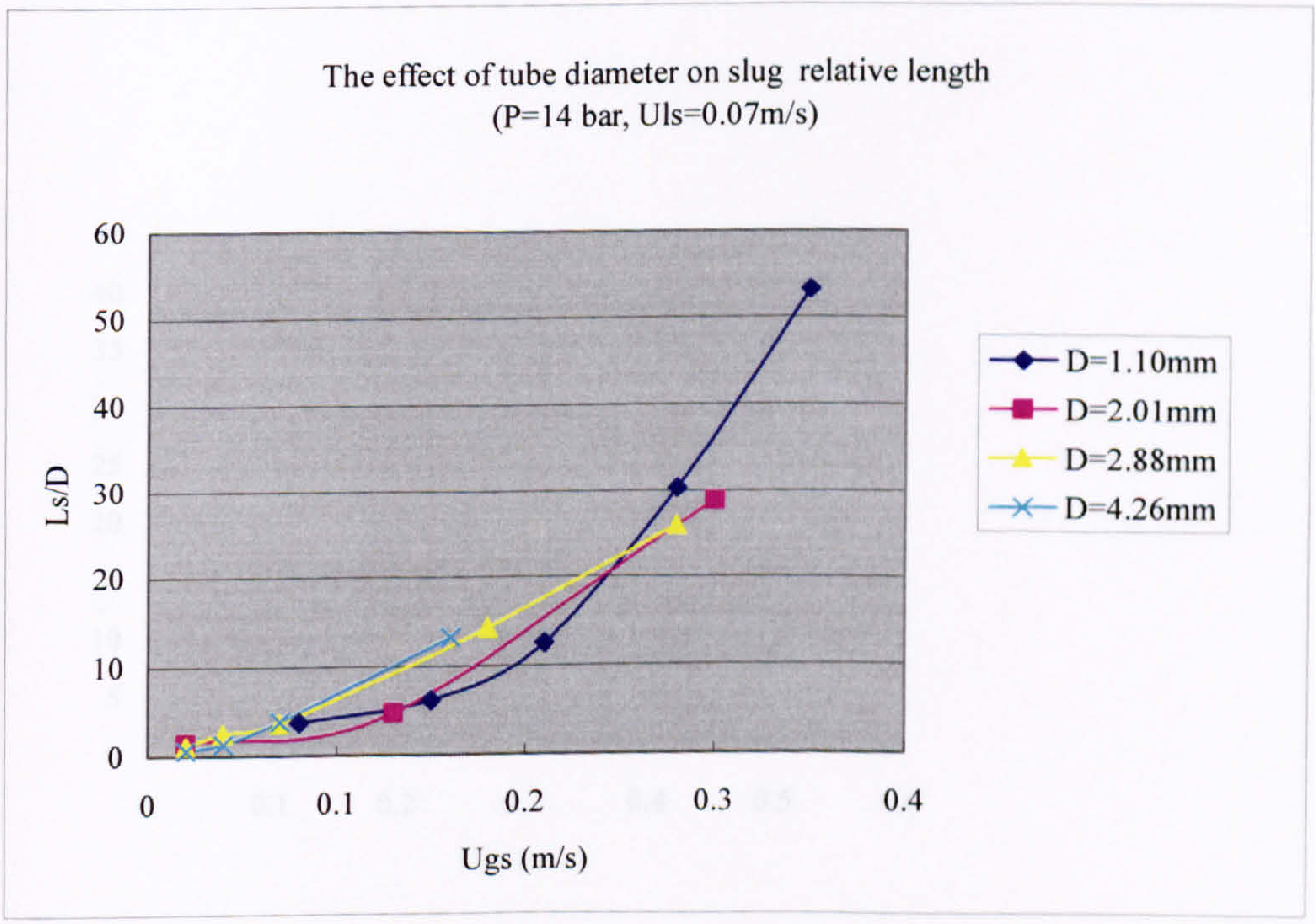

Figure G.58 The effect of tube diameter on slug length-diameter ratio at 14 bar (u_{ls}=0.07m/s).

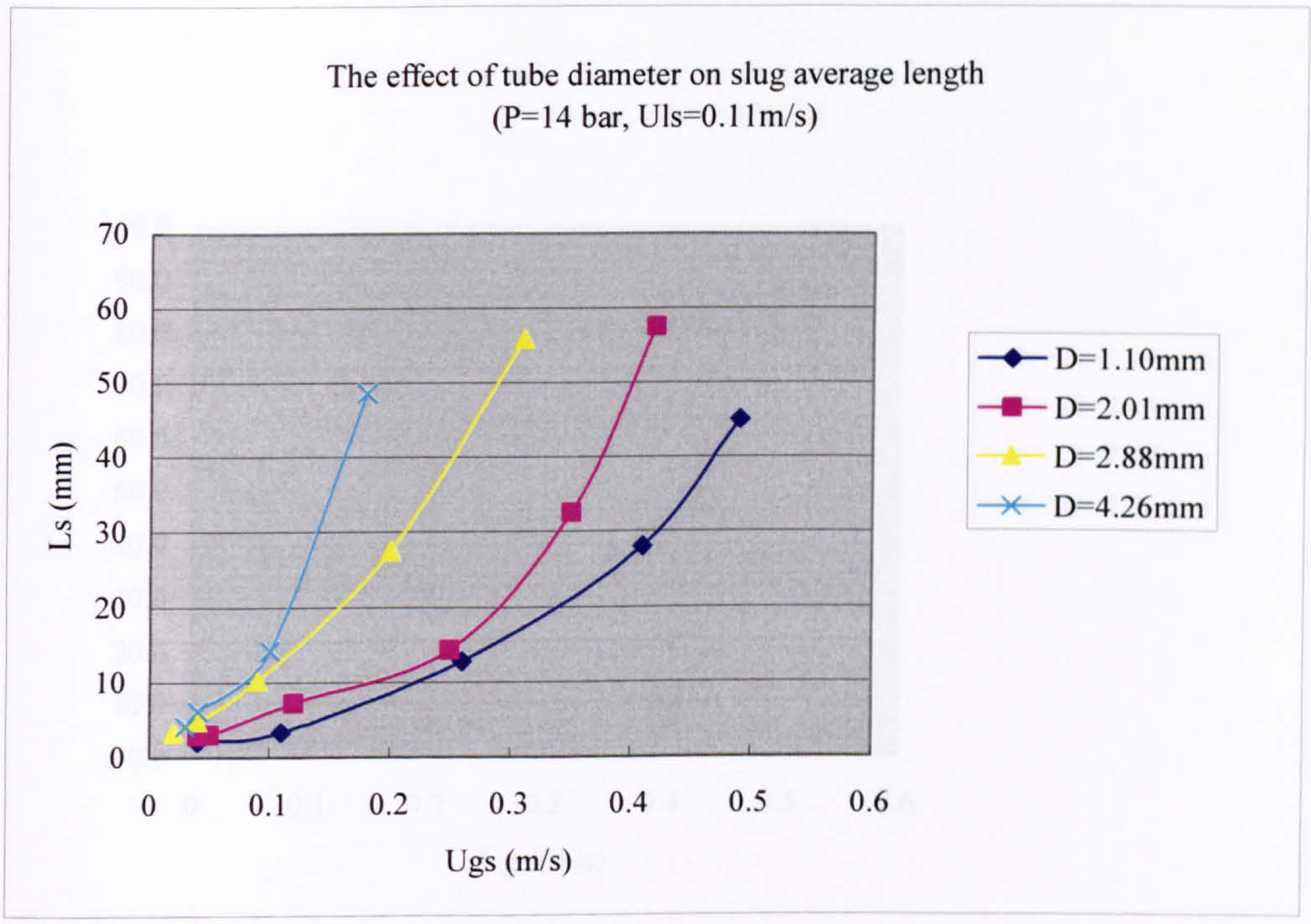

Figure G.59 The effect of tube diameter on slug average length at 14 bar (u_{ls}=0.11m/s).

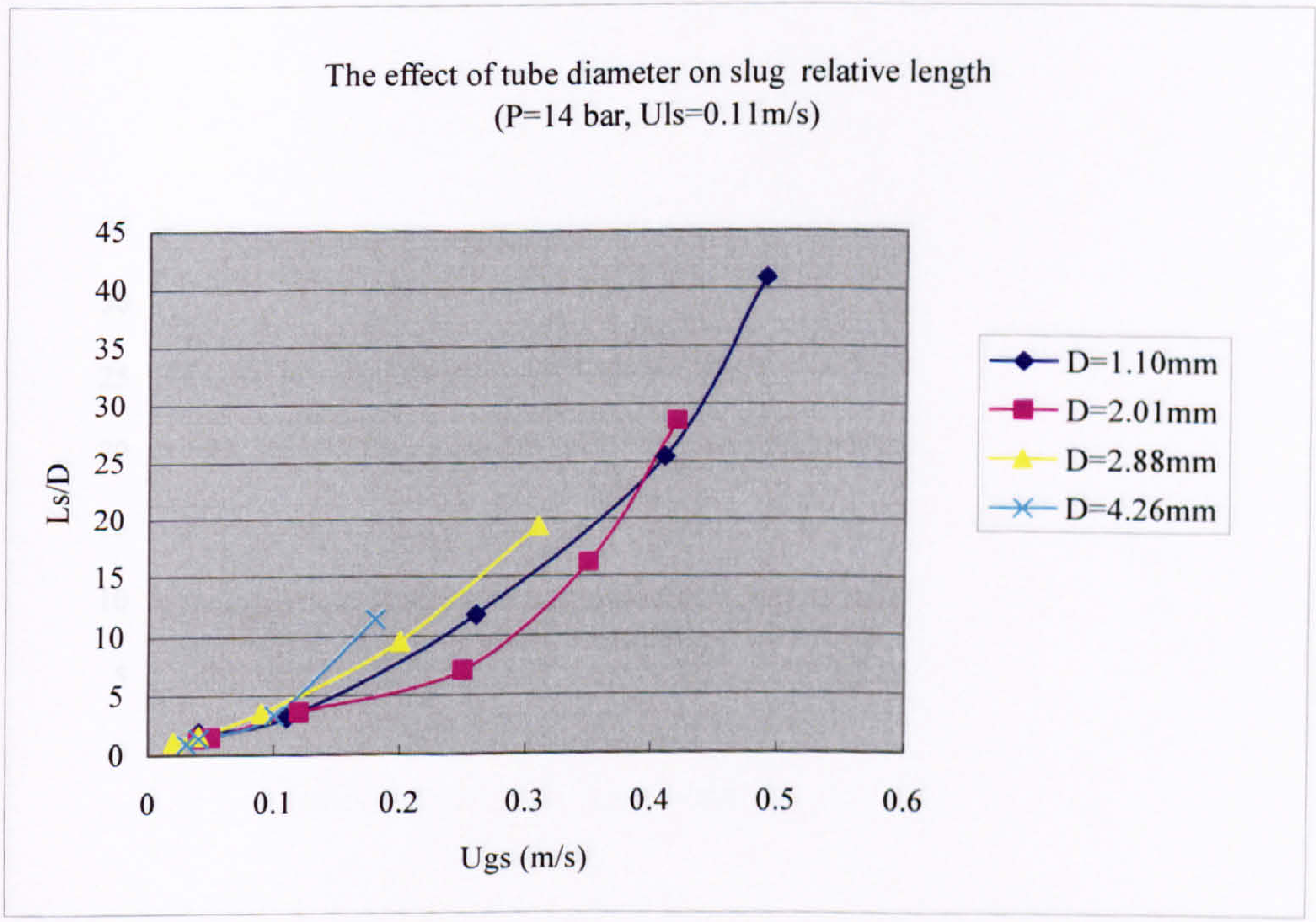

Figure G.60 The effect of tube diameter on slug length-diameter ratio at 14 bar (u_{ls}=0.11m/s).

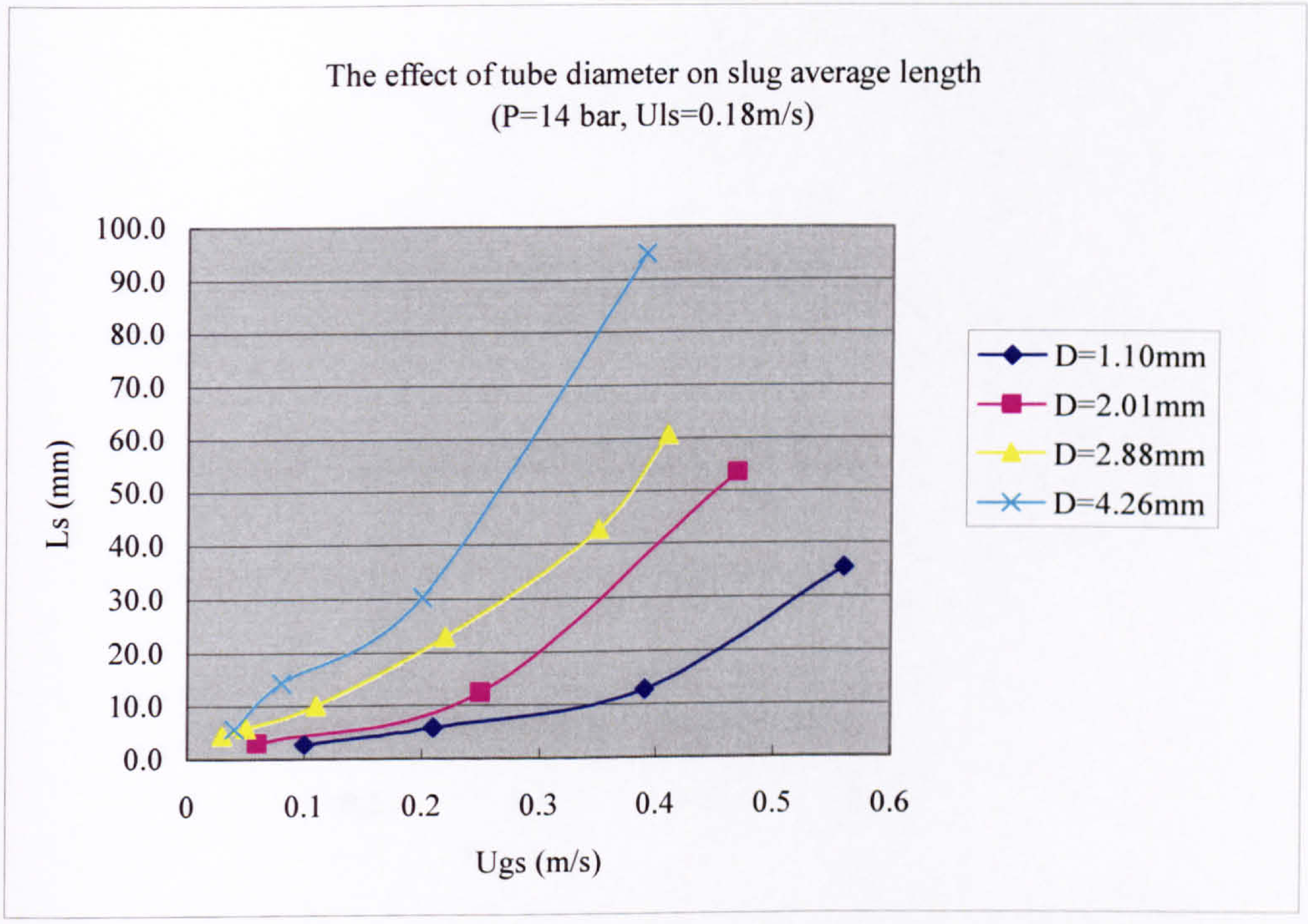

Figure G.61 The effect of tube diameter on slug average length at 14 bar (u_{ls}=0.18m/s).

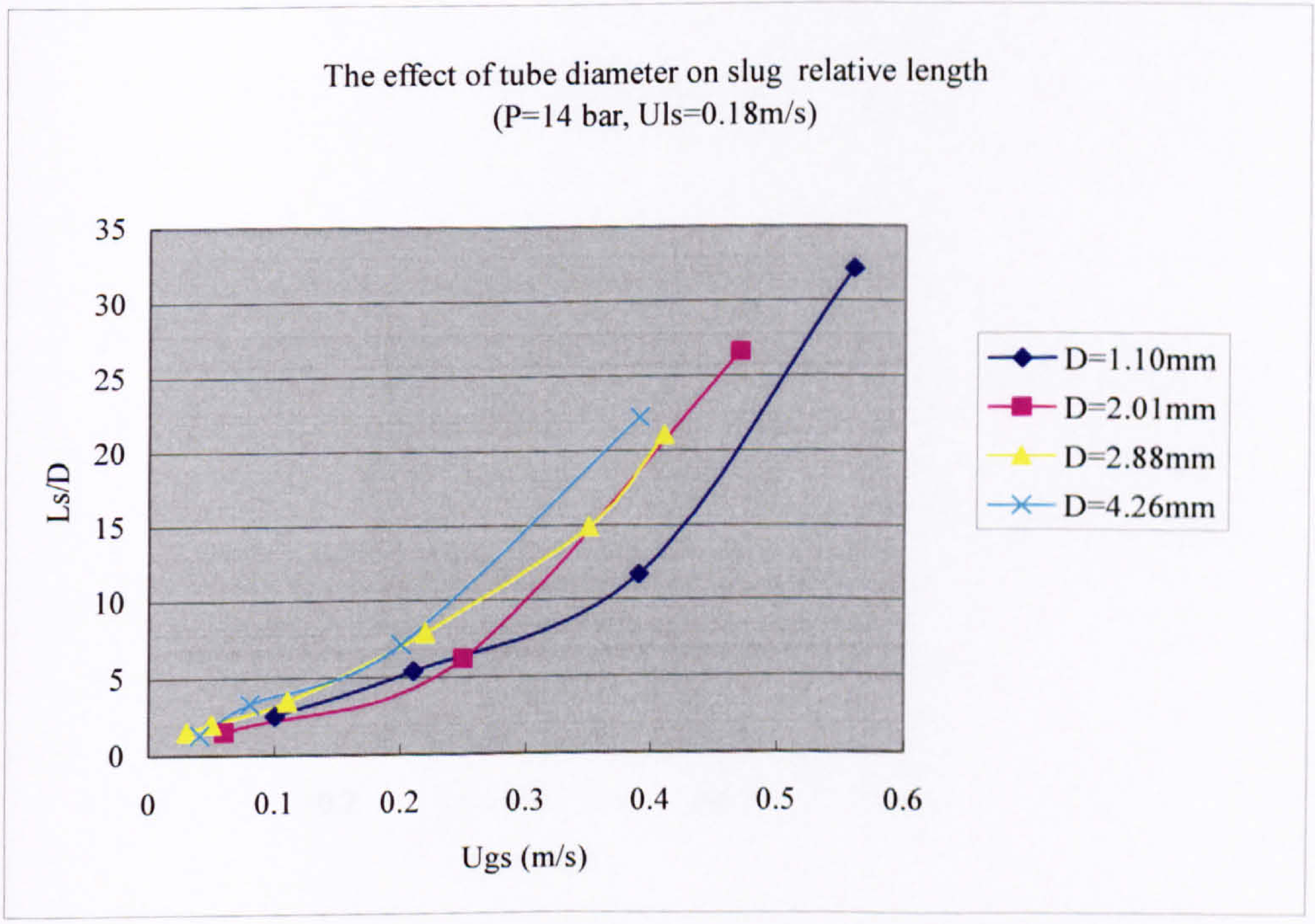

Figure G.62 The effect of tube diameter on slug length-diameter ratio at 14 bar (u_{ls}=0.18m/s).

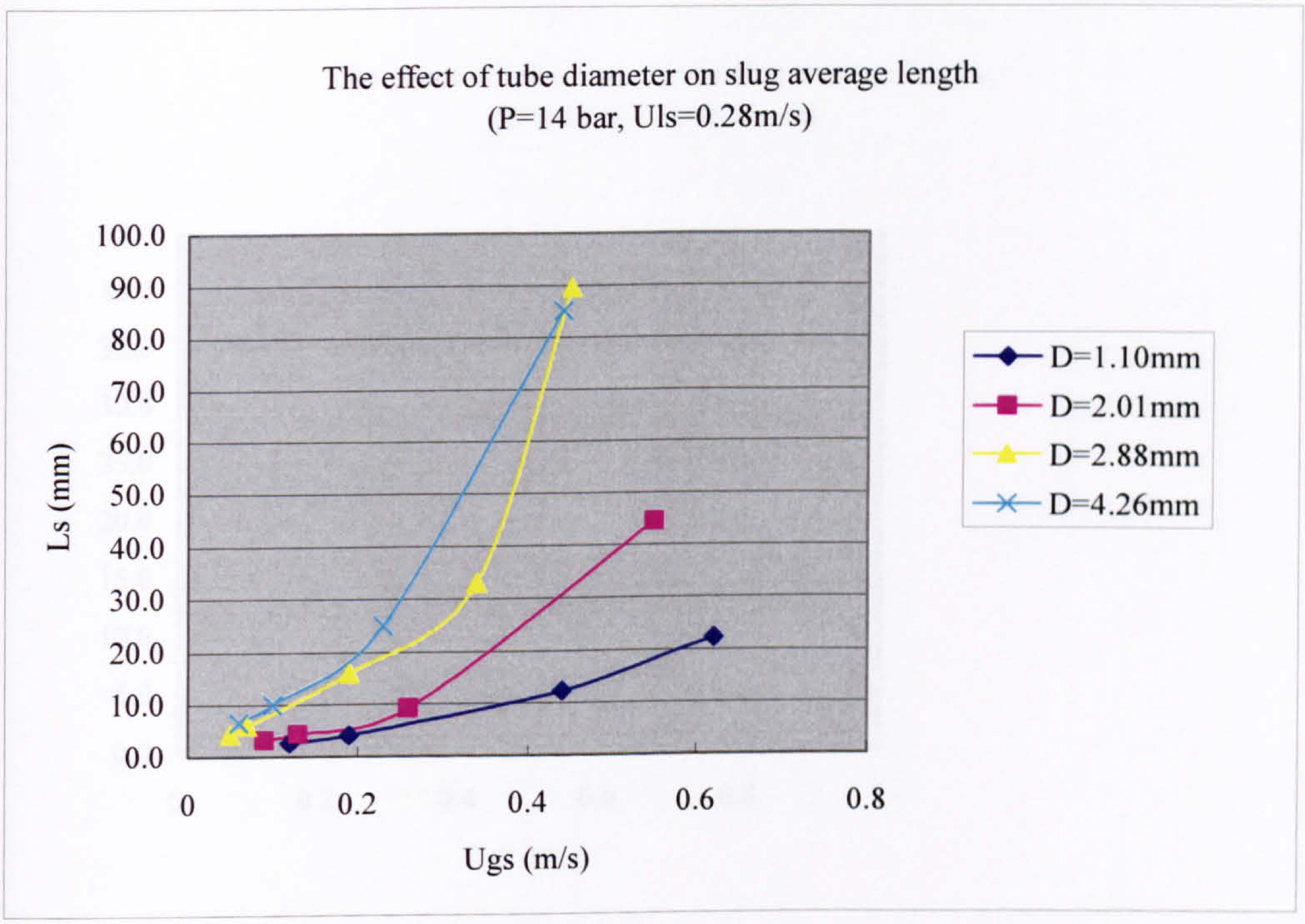

Figure G.63 The effect of tube diameter on slug average length at 14 bar (u_{ls}=0.28m/s).

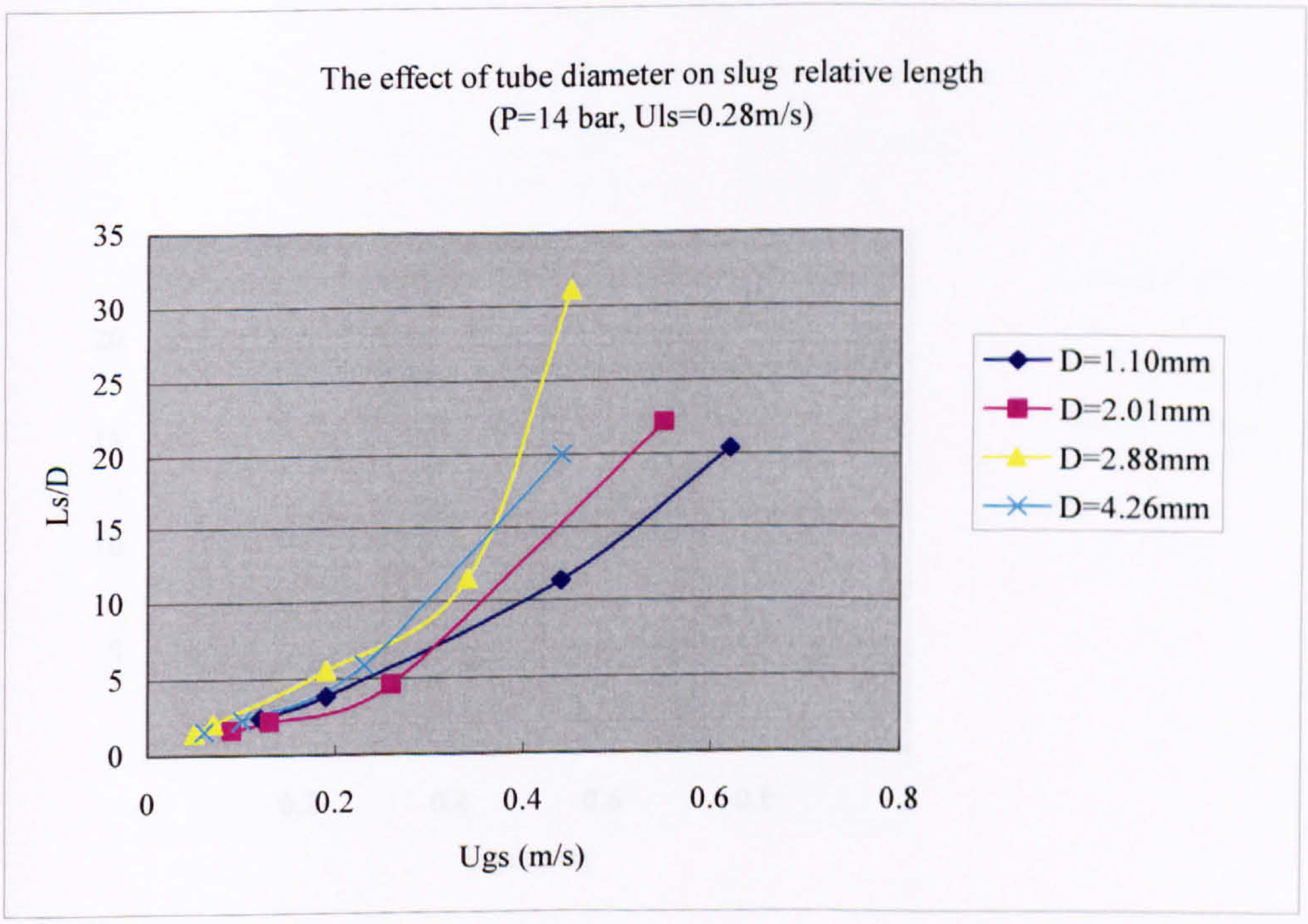

Figure G.64 The effect of tube diameter on slug length-diameter ratio at 14 bar (u_{ls}=0.28m/s).

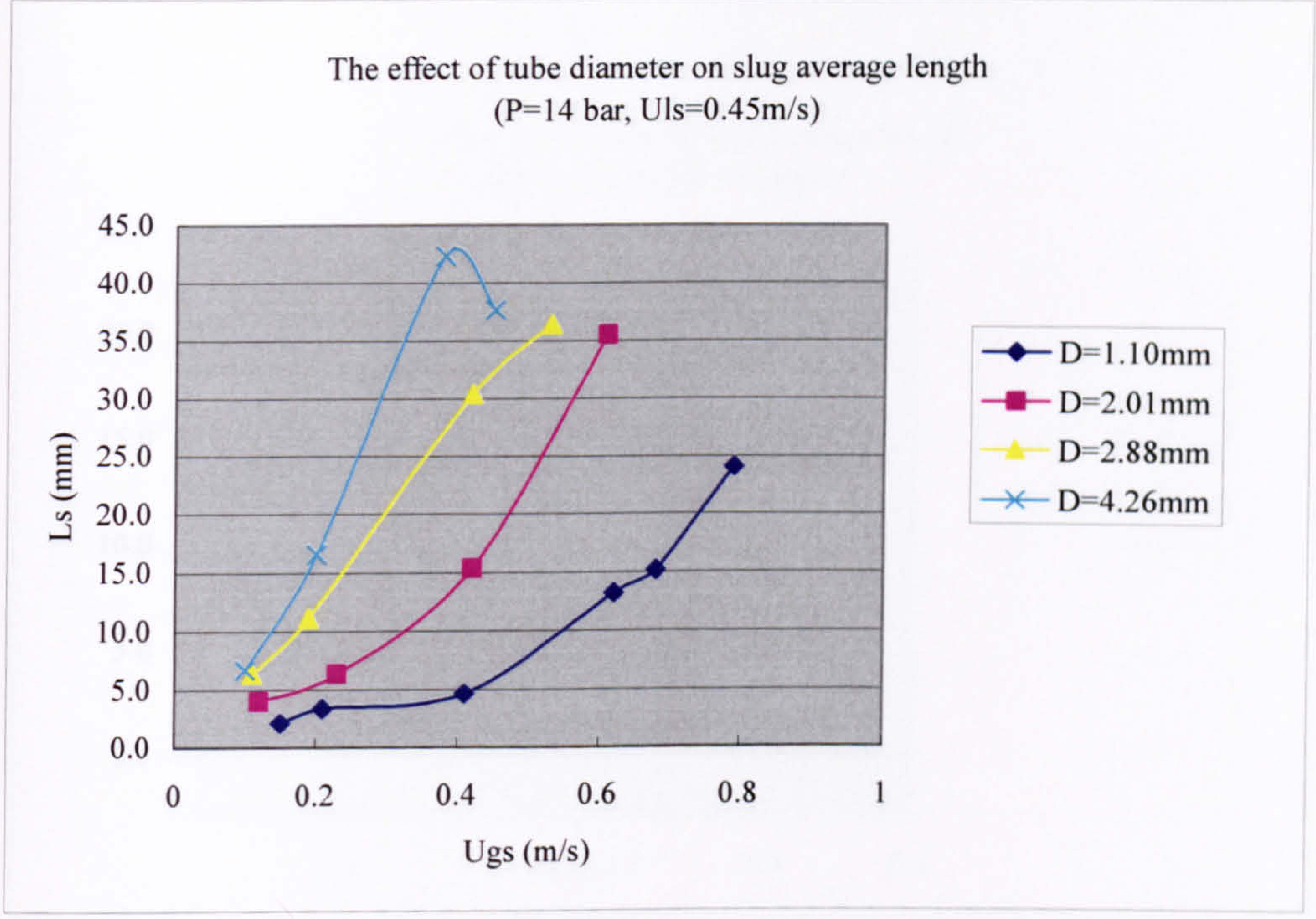

Figure G.65 The effect of tube diameter on slug average length at 14 bar (u_{ls}=0.45m/s).

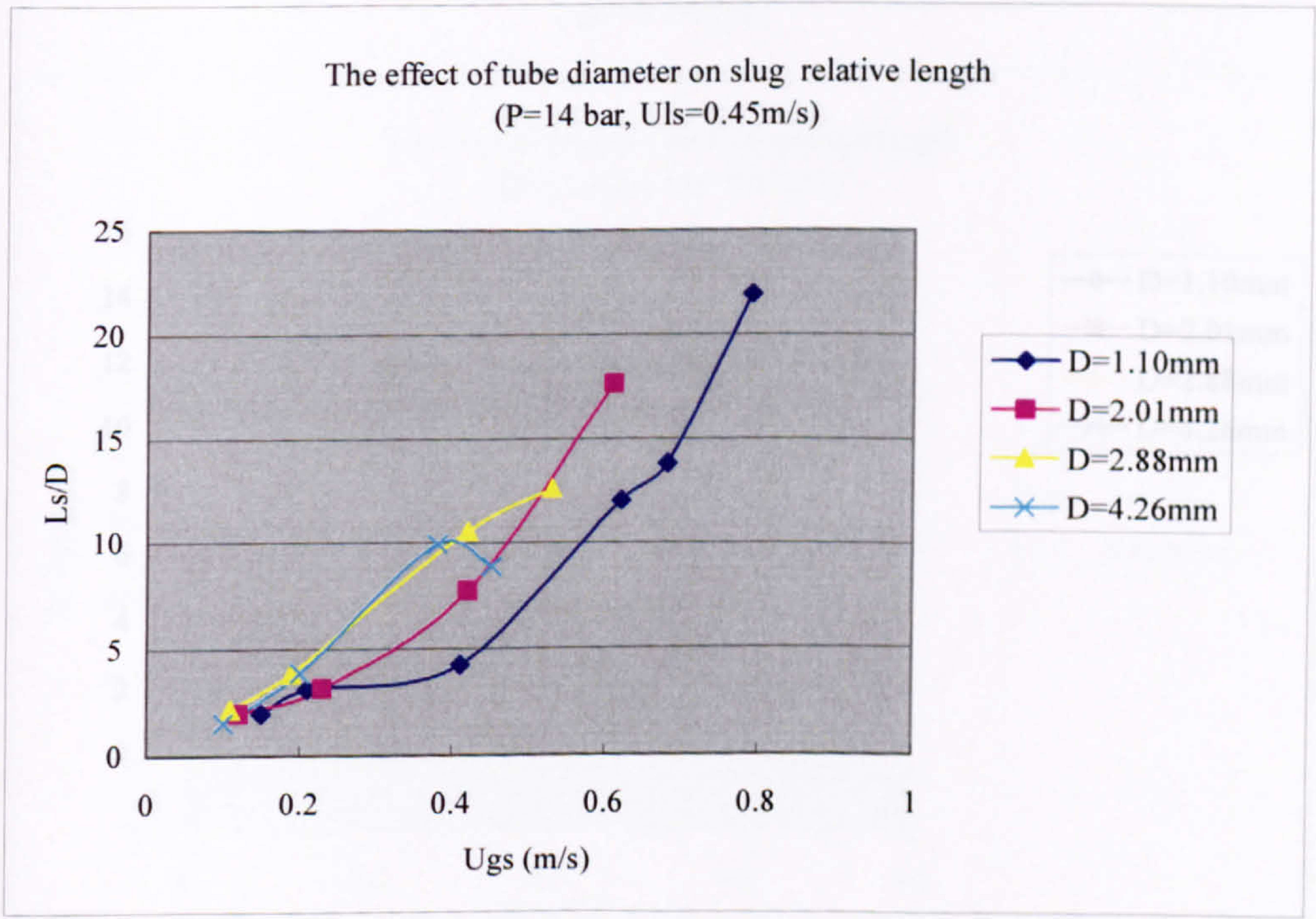

Figure G.66 The effect of tube diameter on slug length-diameter ratio at 14 bar (u_{ls}=0.45m/s).

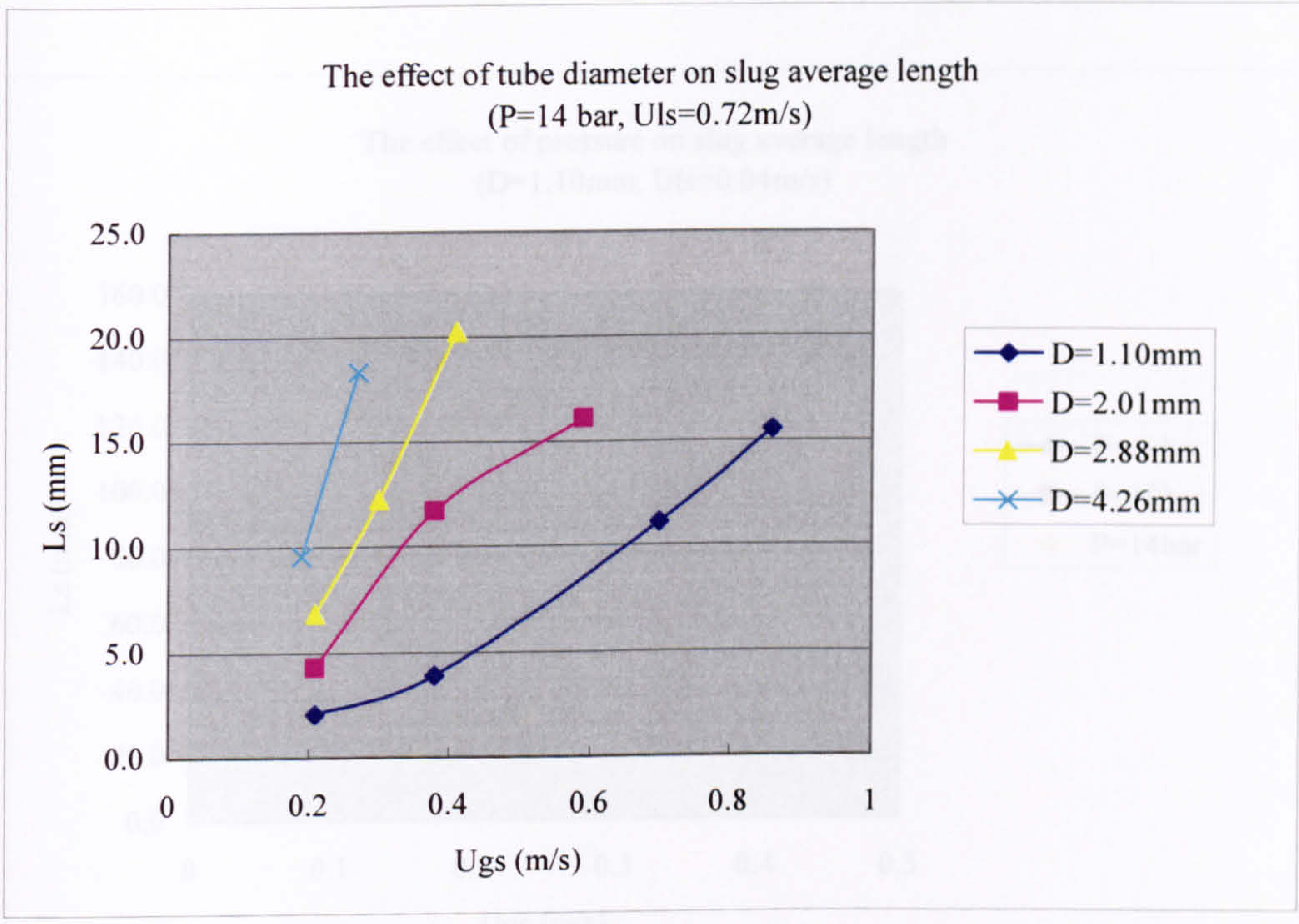

Figure G.67 The effect of tube diameter on slug average length at 14 bar (u_{ls}=0.72m/s).

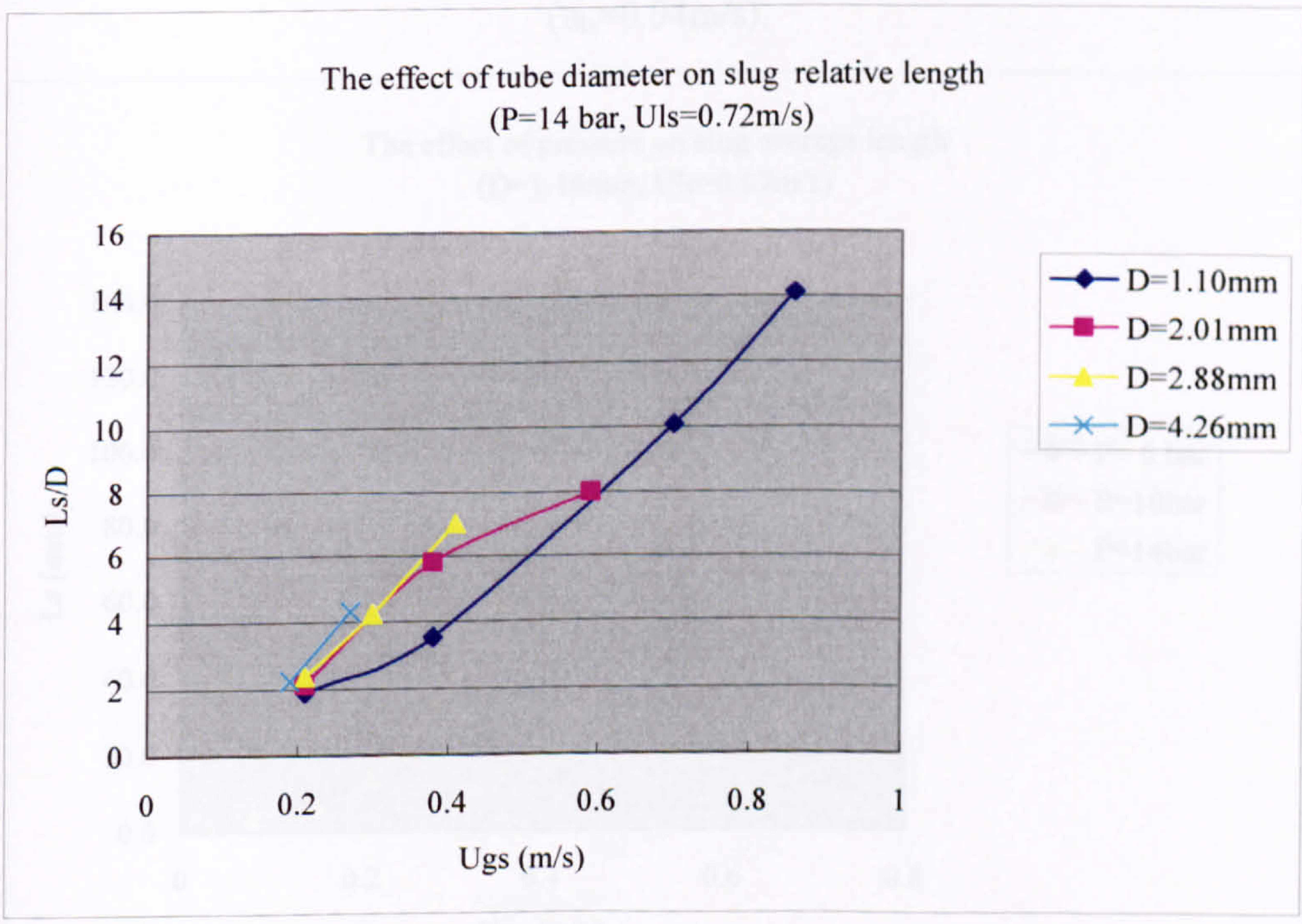

Figure G.68 The effect of tube diameter on slug length-diameter ratio at 14 bar (u_{ls}=0.72m/s).

G.3 The effect of pressure on slug length

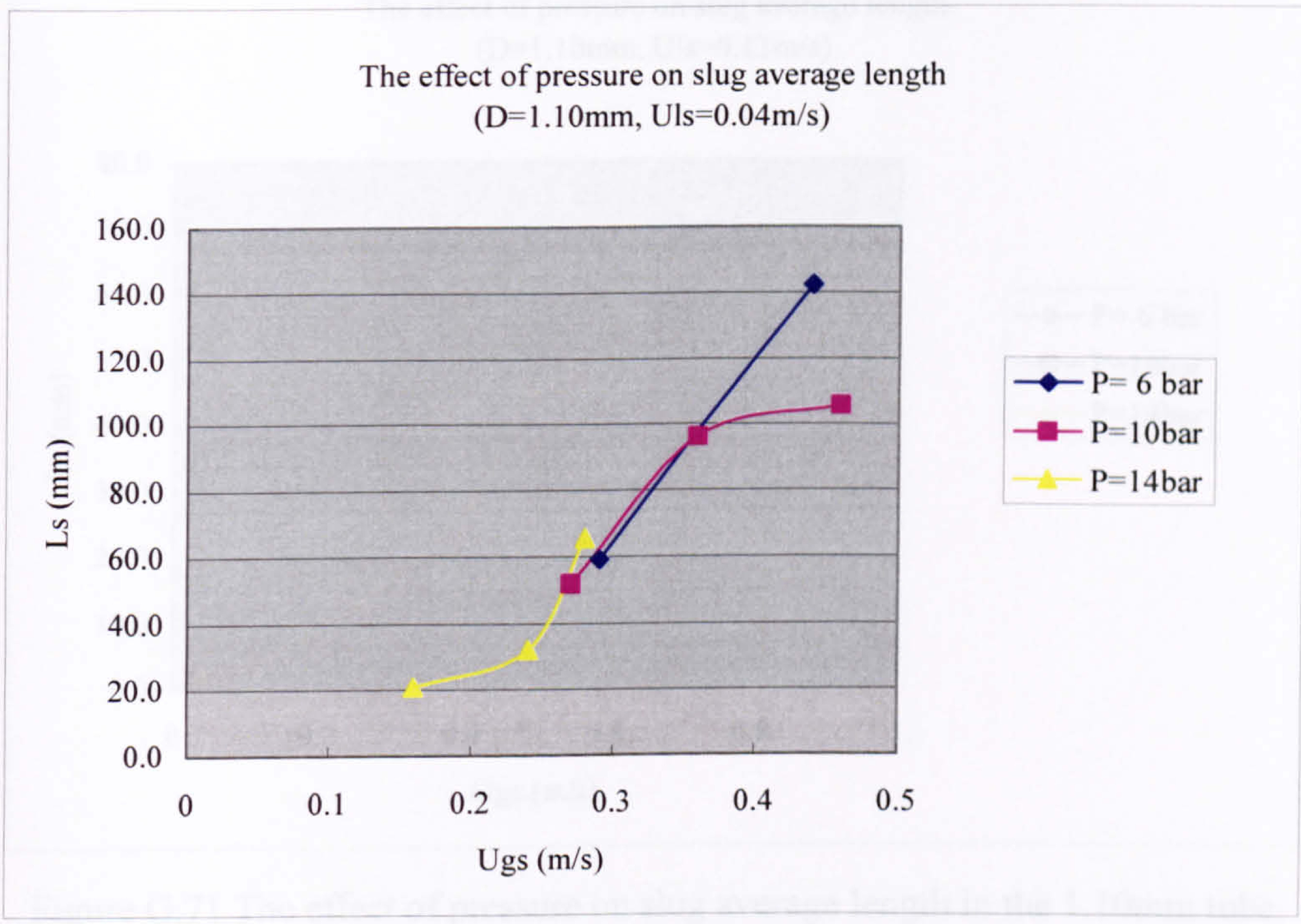

Figure G.69 The effect of pressure on slug average length in the 1.10mm tube (u_{ls}=0.04m/s).

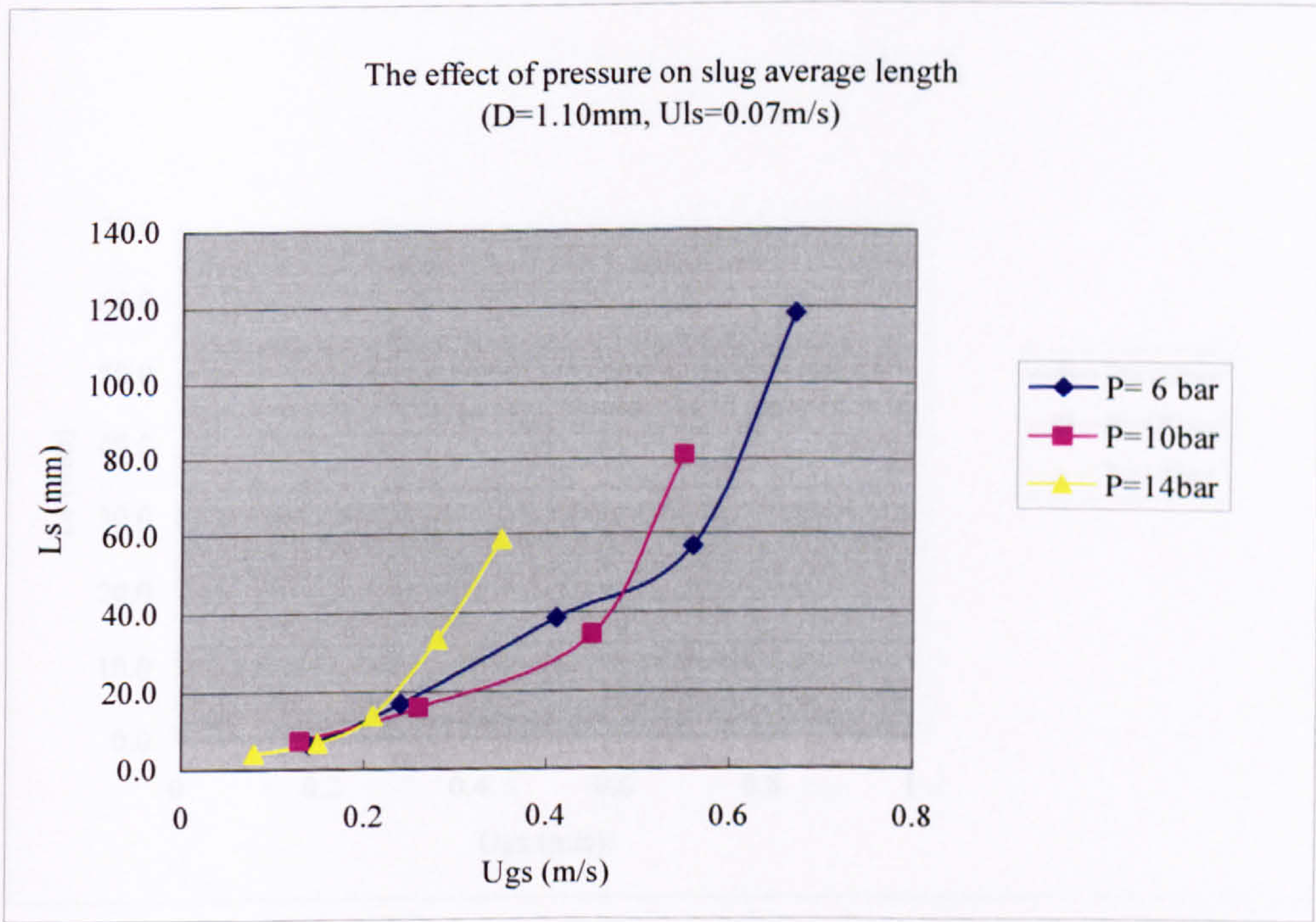

Figure G.70 The effect of pressure on slug average length in the 1.10mm tube (u_{ls}=0.07m/s).

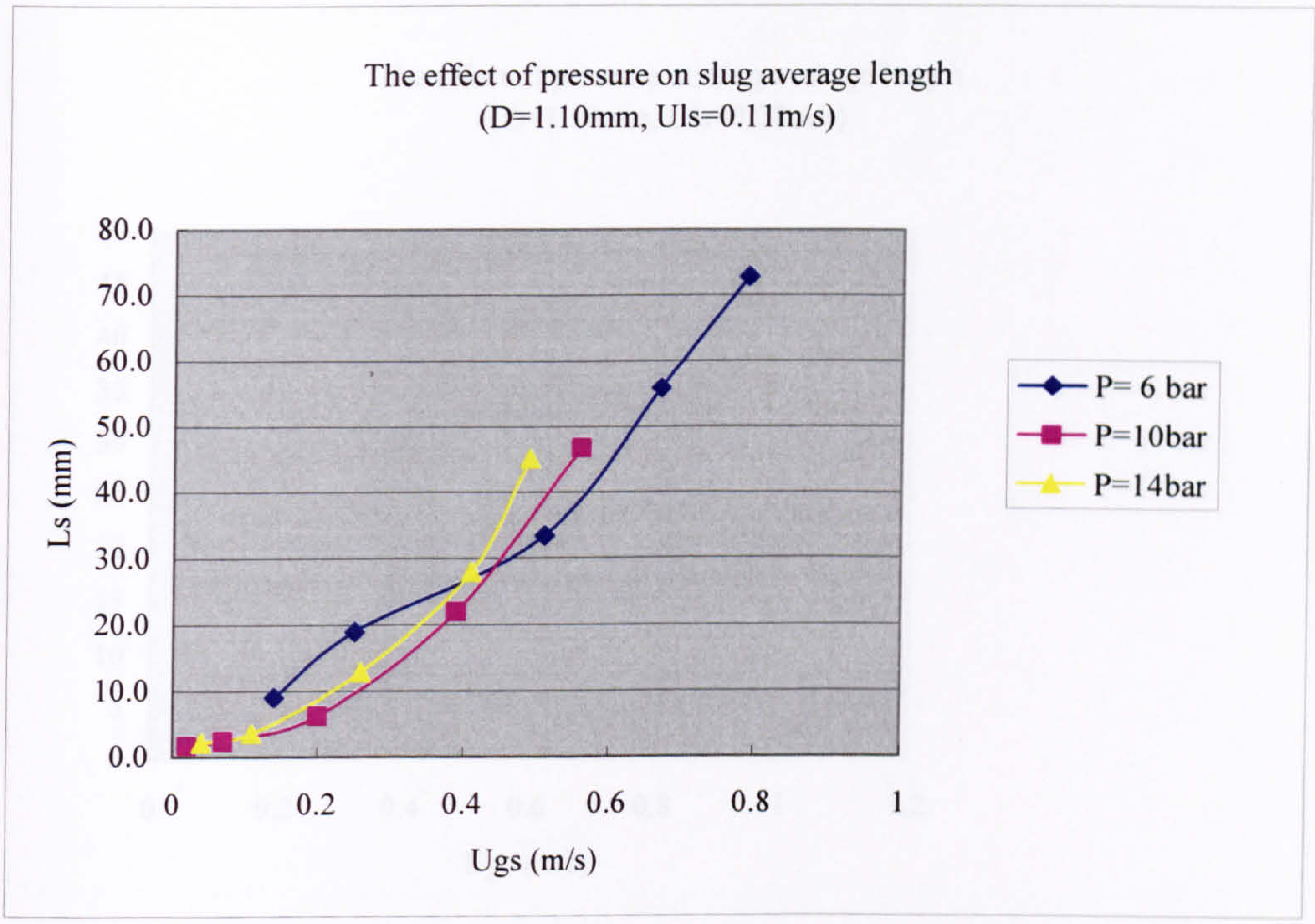

Figure G.71 The effect of pressure on slug average length in the 1.10mm tube (u_{ls}=0.11m/s).

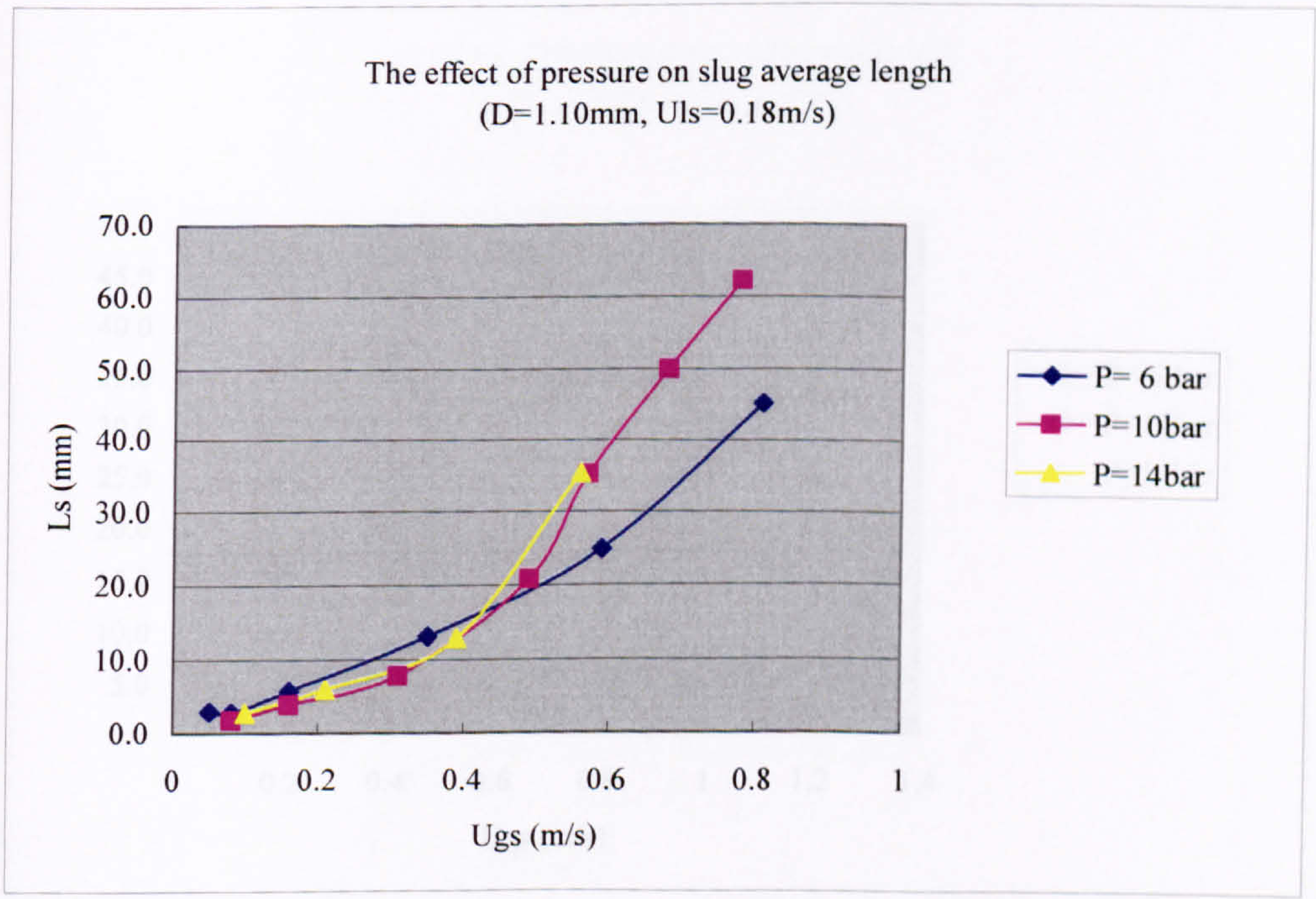

Figure G.72 The effect of pressure on slug average length in the 1.10mm tube (u_{ls}=0.18m/s).

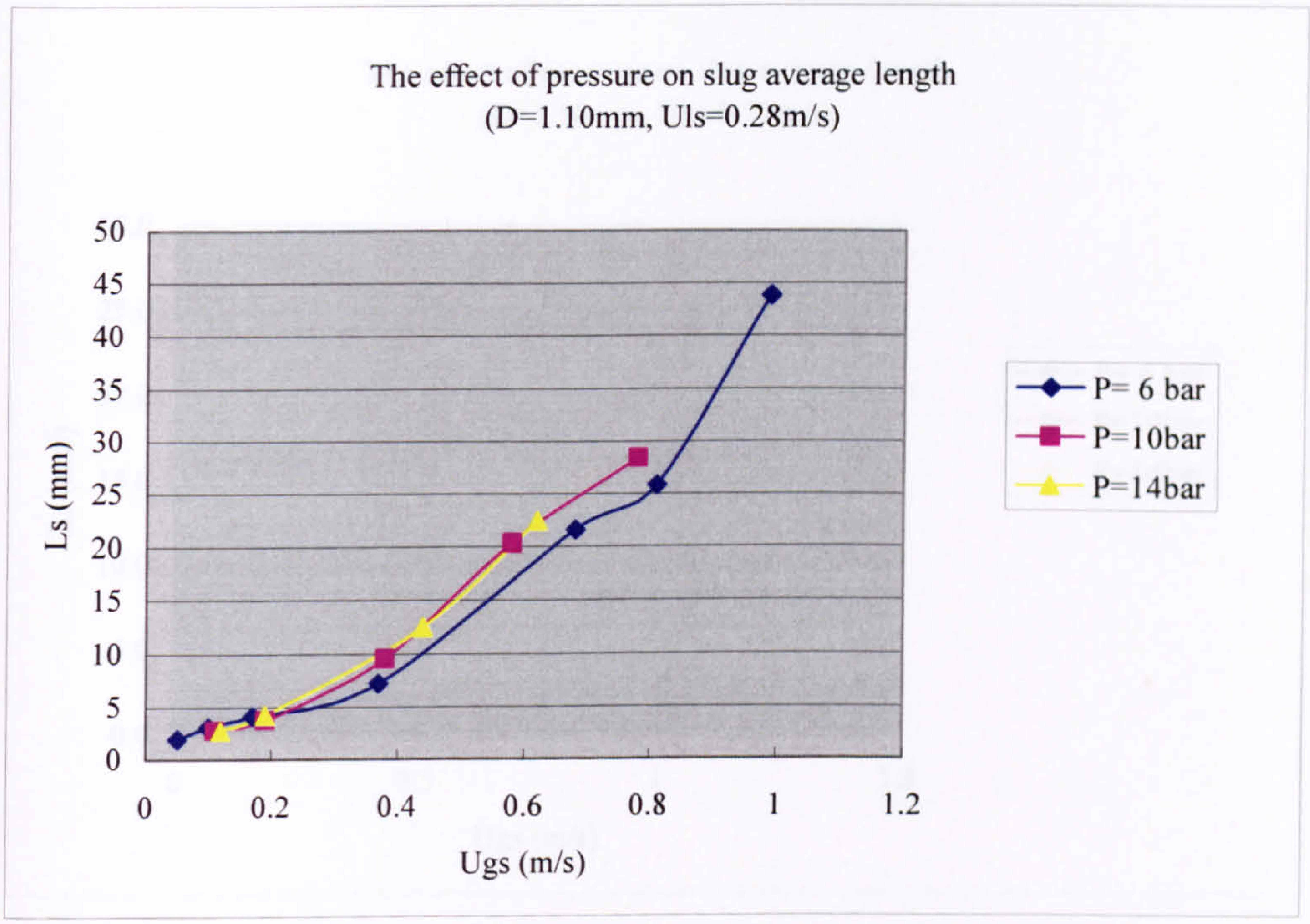

Figure G.73 The effect of pressure on slug average length in the 1.10mm tube (u_{ls}=0.28m/s).

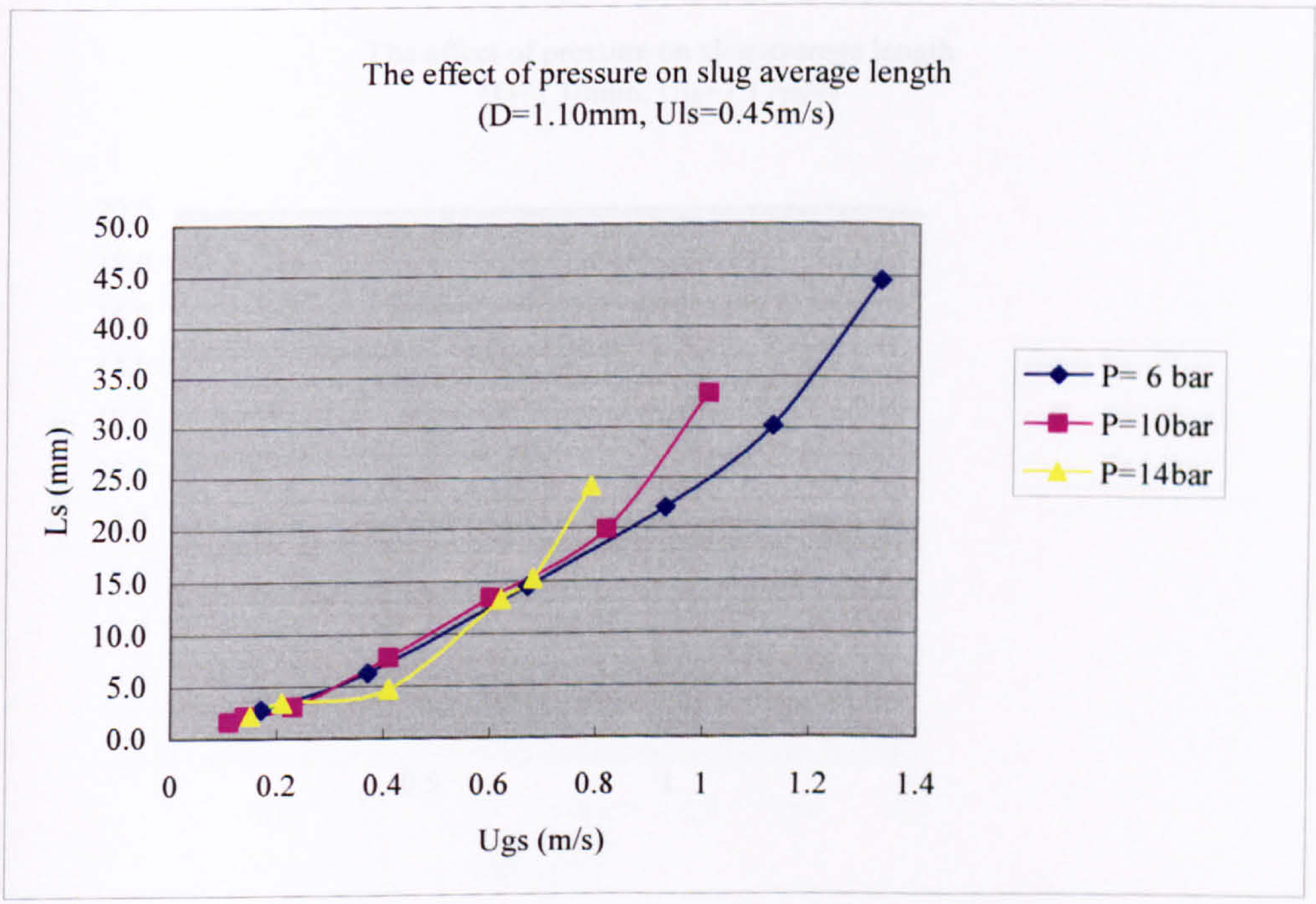

Figure G.74 The effect of pressure on slug average length in the 1.10mm tube (u_{ls}=0.45m/s).

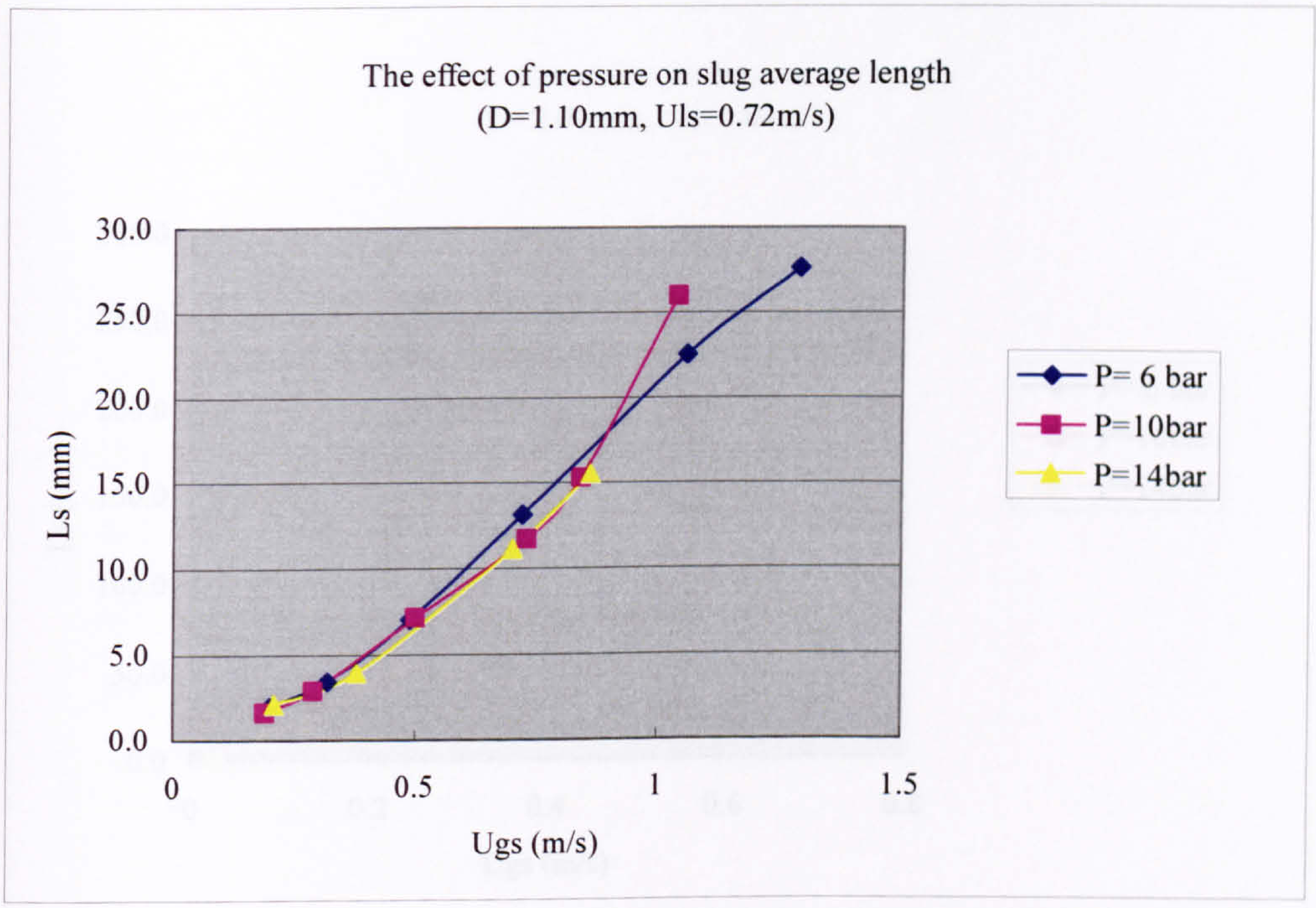

Figure G.75 The effect of pressure on slug average length in the 1.10mm tube (u_{ls}=0.72m/s).

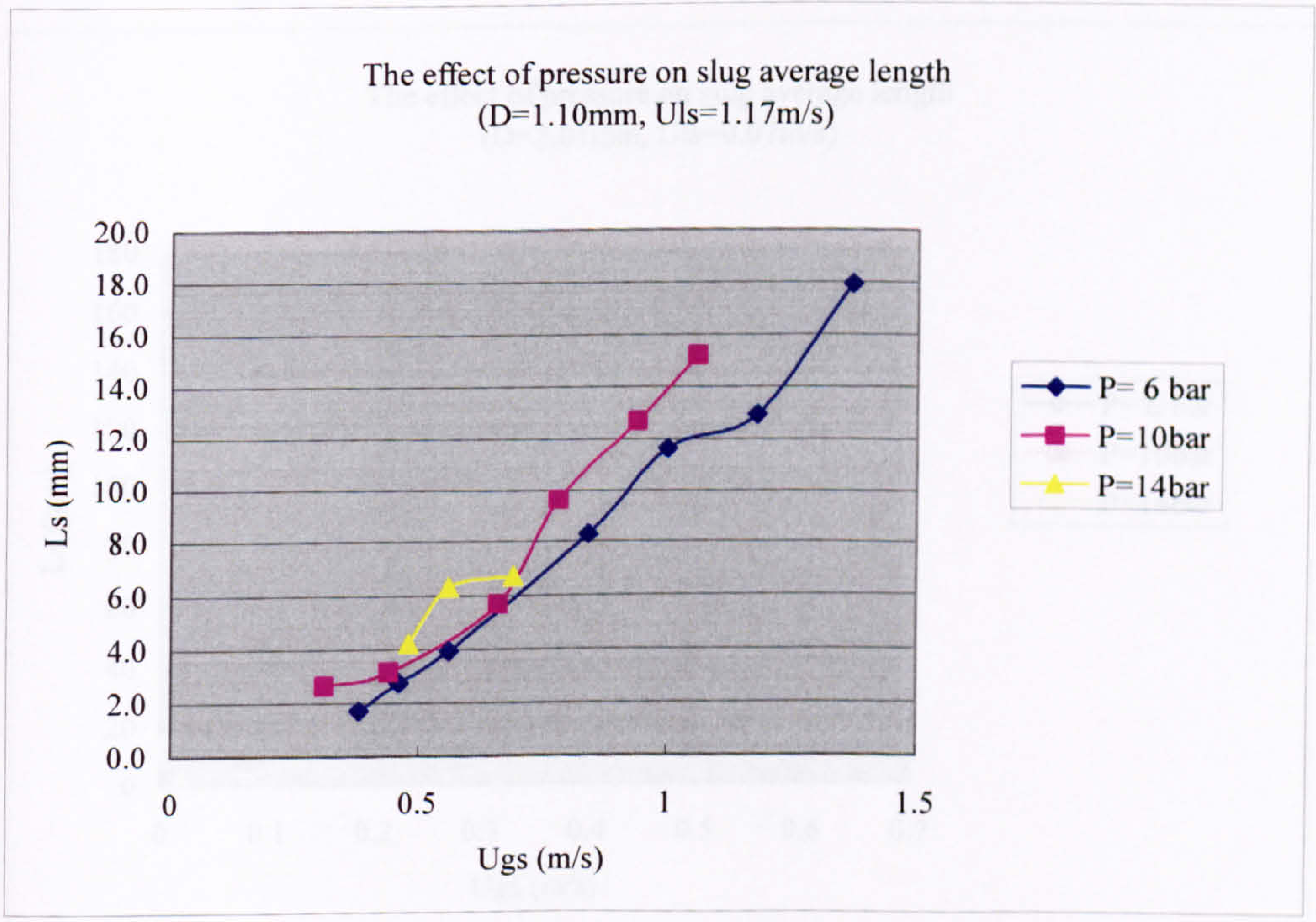

Figure G.76 The effect of pressure on slug average length in the 1.10mm tube (u_{ls}=1.17m/s).

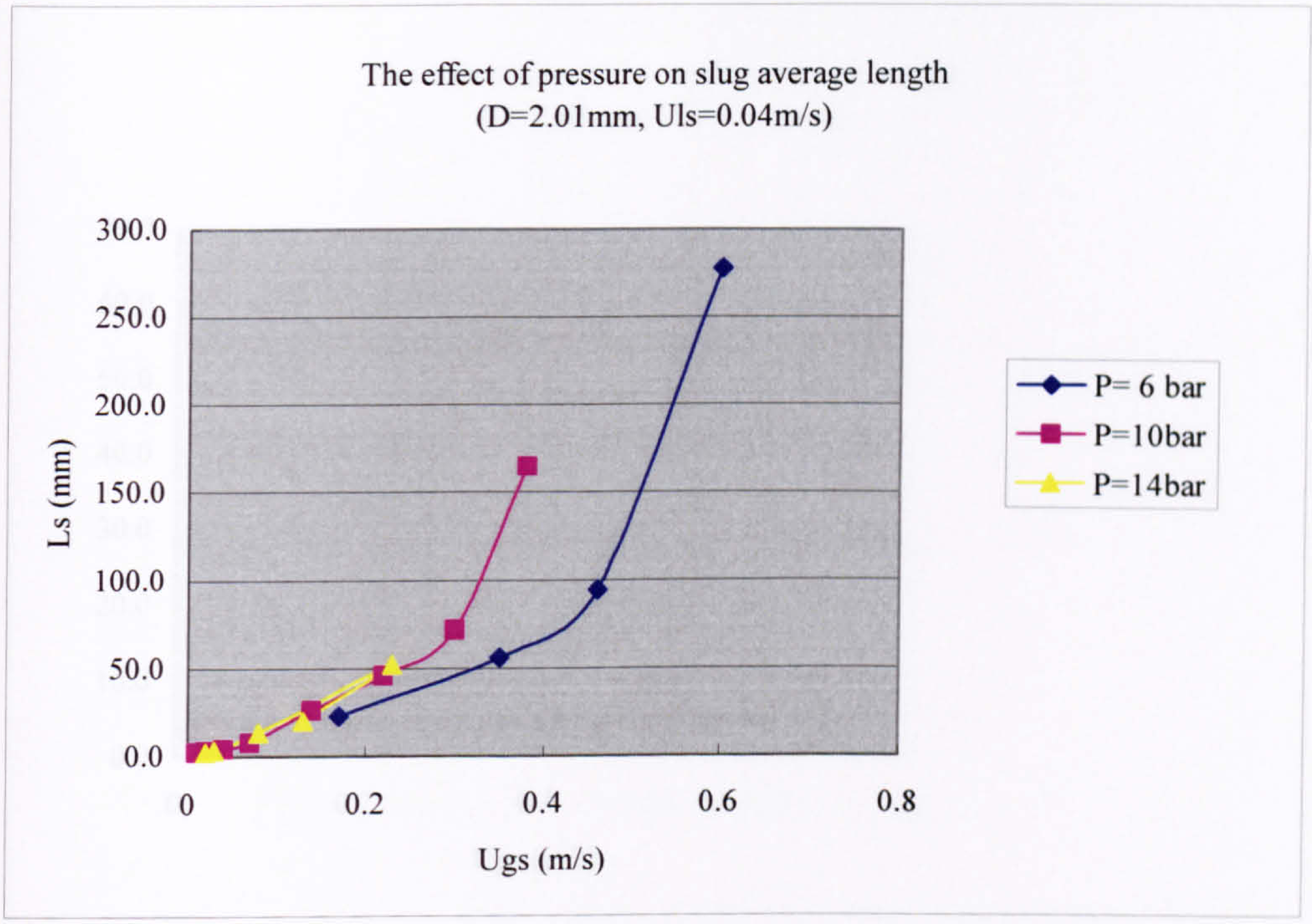

Figure G.77 The effect of pressure on slug average length in the 2.01mm tube (u_{ls}=0.04m/s).

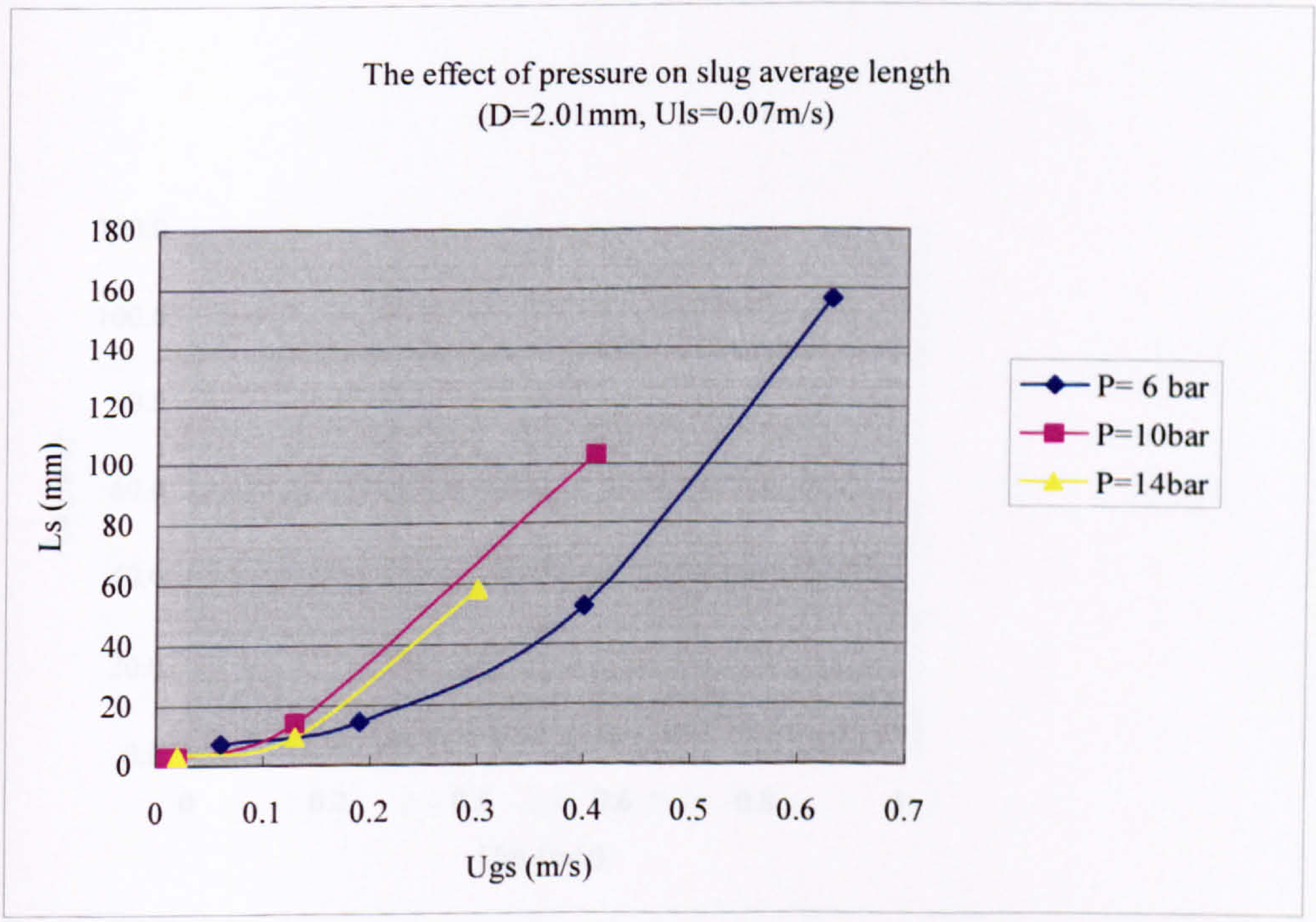

Figure G.78 The effect of pressure on slug average length in the 2.01mm tube (u_{ls}=0.07m/s).

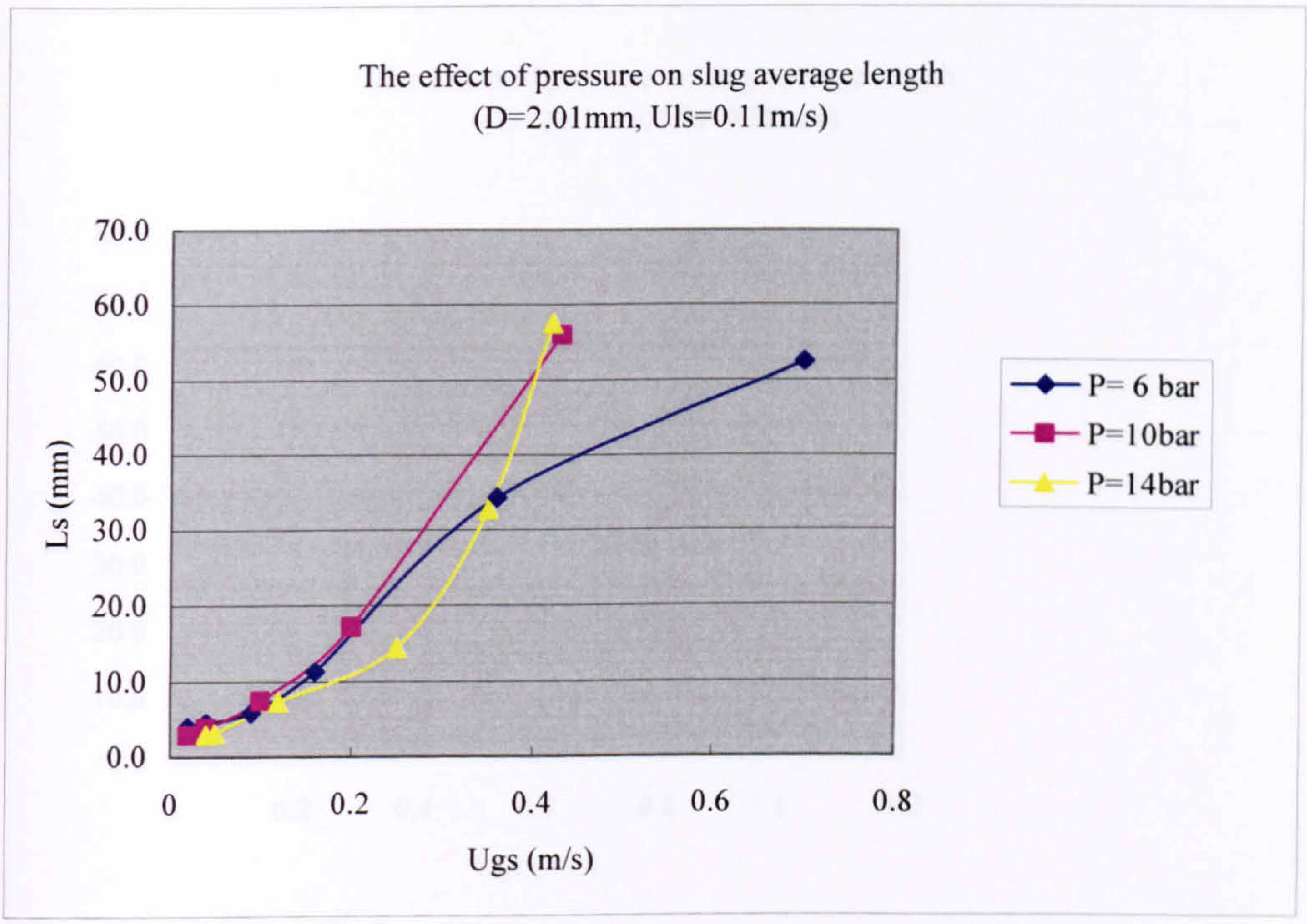

Figure G.79 The effect of pressure on slug average length in the 2.01mm tube (u_{ls}=0.11m/s).

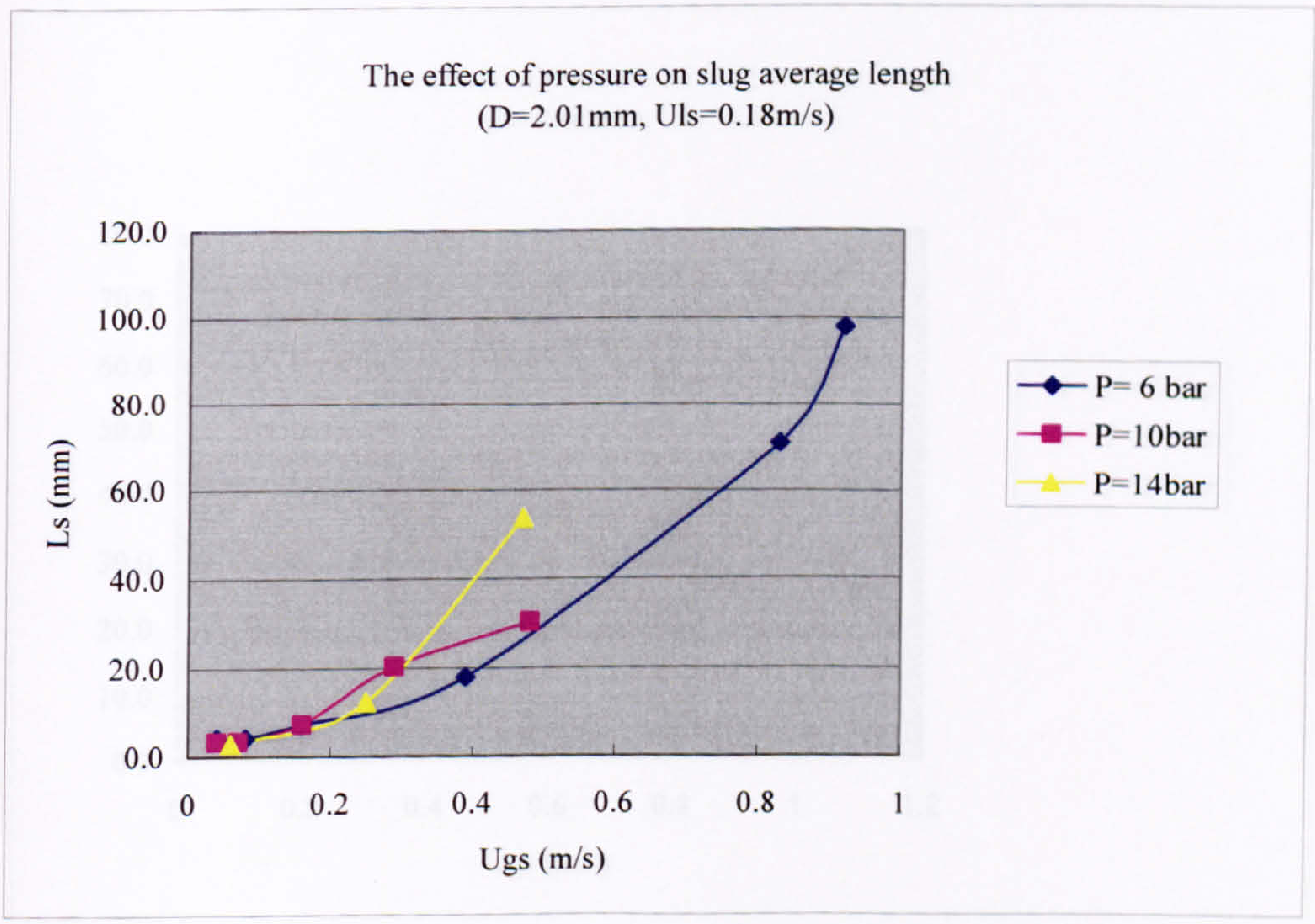

Figure G.80 The effect of pressure on slug average length in the 2.01mm tube (u_{ls}=0.18m/s).

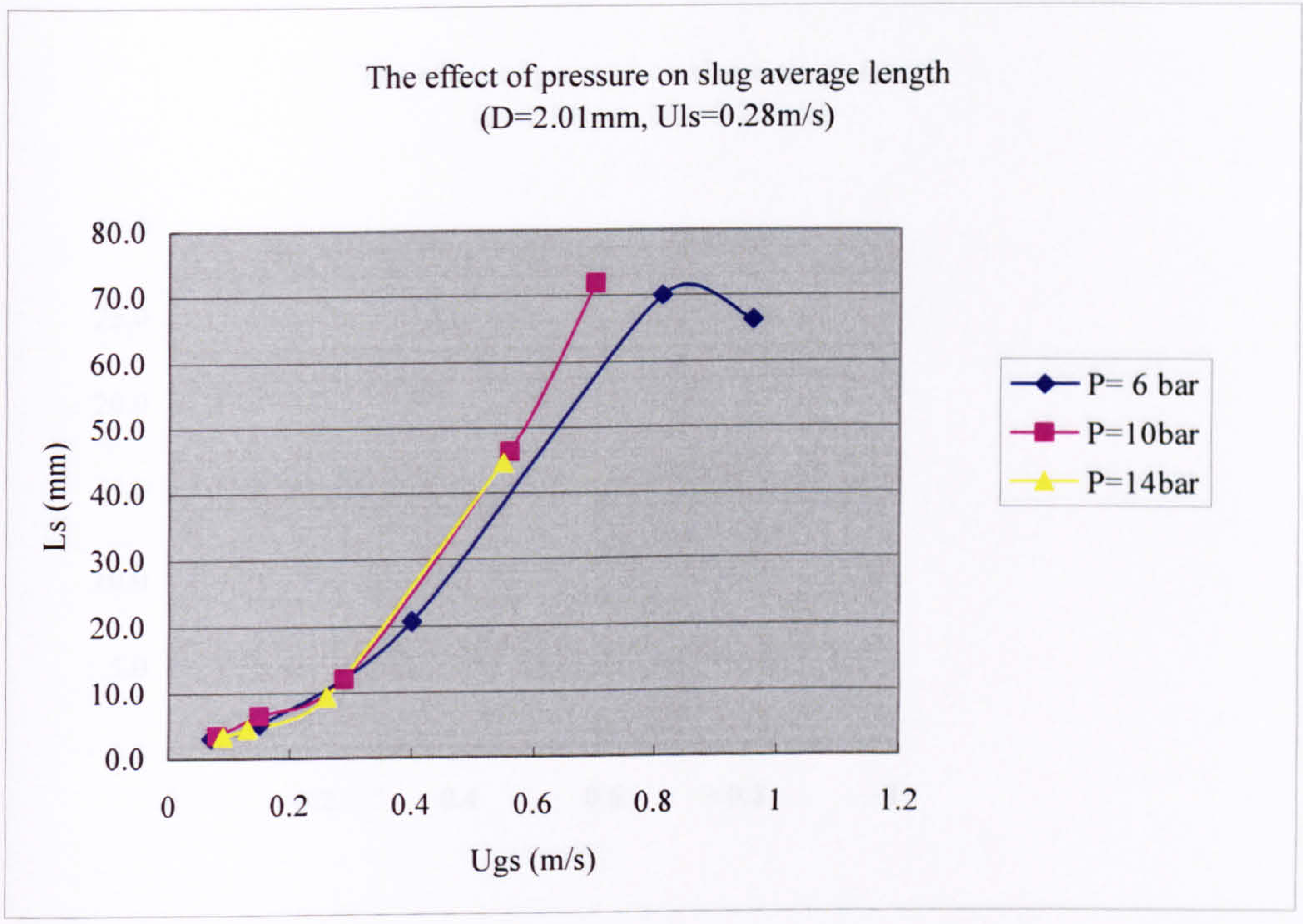

Figure G.81 The effect of pressure on slug average length in the 2.01mm tube (u_{ls}=0.28m/s).

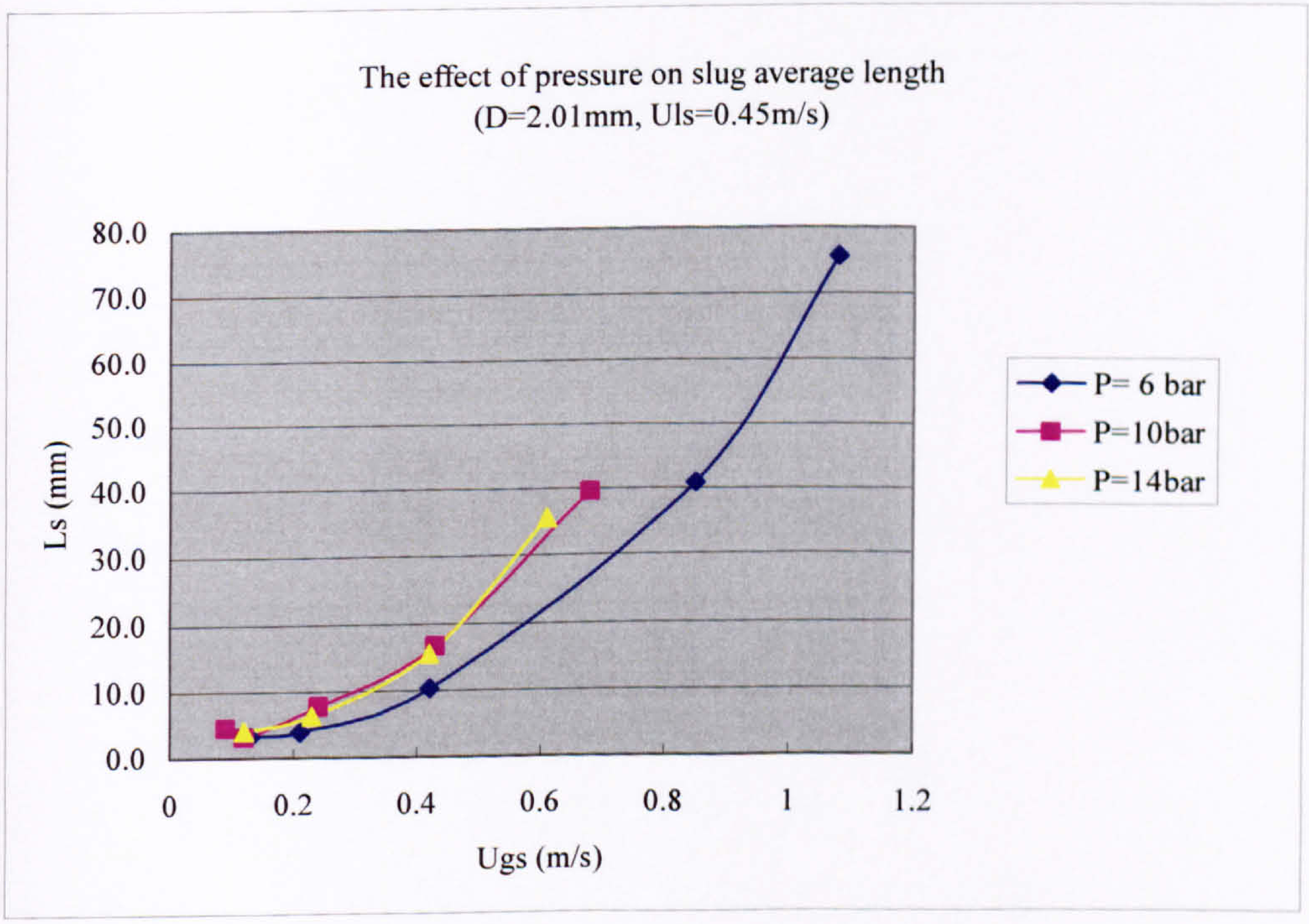

Figure G.82 The effect of pressure on slug average length in the 2.01mm tube (u_{ls}=0.45m/s).

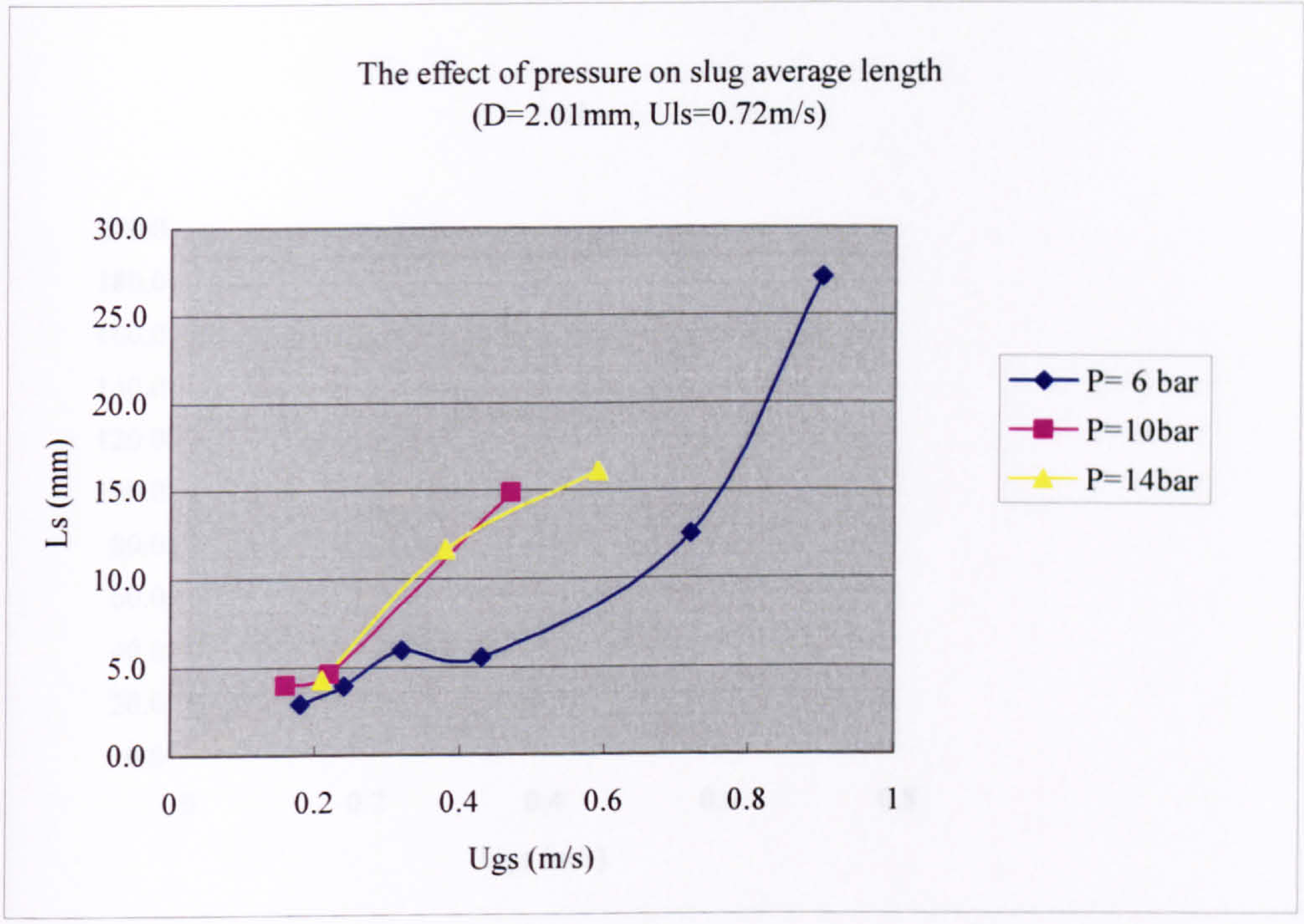

Figure G.83 The effect of pressure on slug average length in the 2.01mm tube (u_{ls}=0.72m/s).

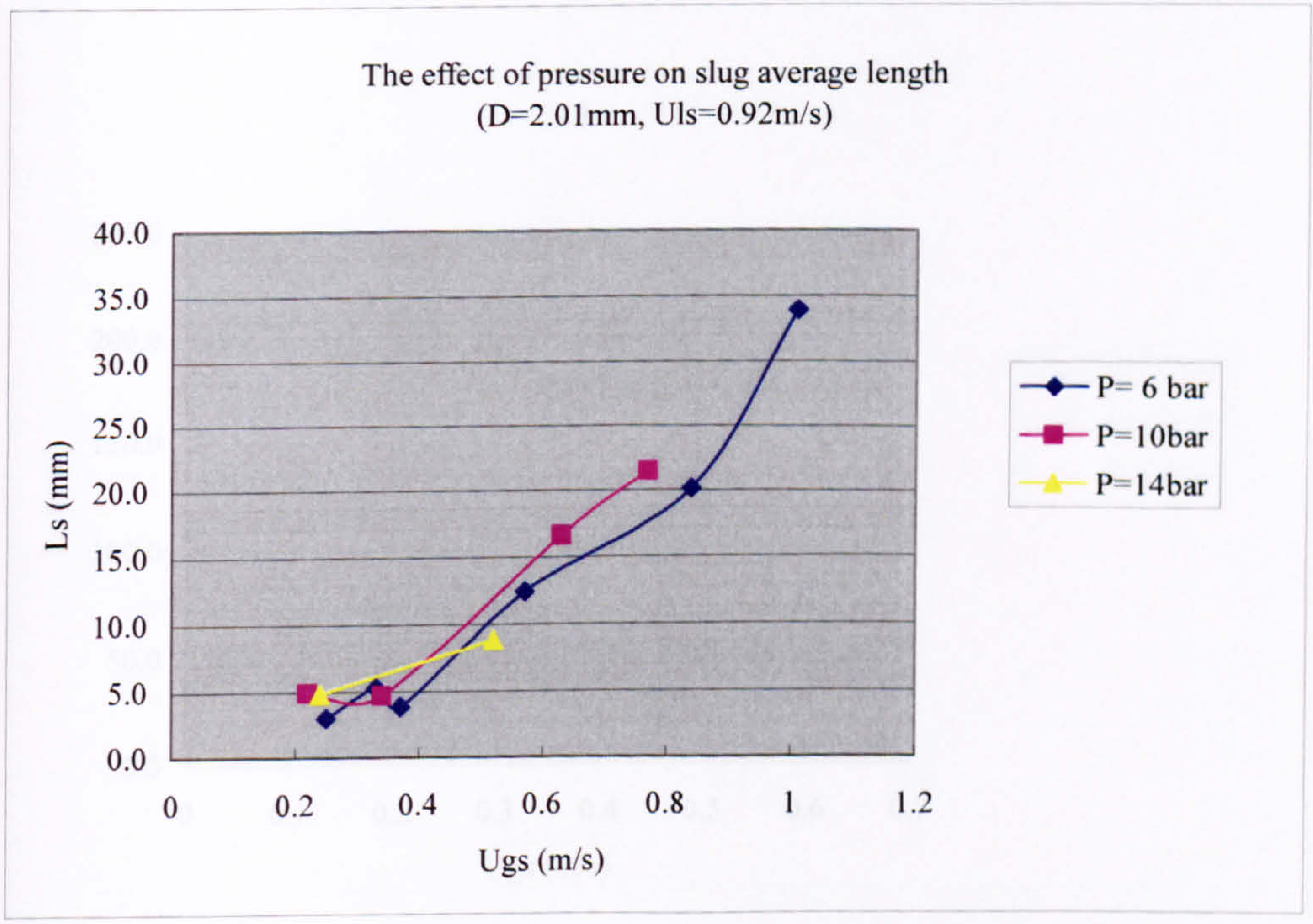

Figure G.84 The effect of pressure on slug average length in the 2.01mm tube (u_{ls}=0.92m/s).

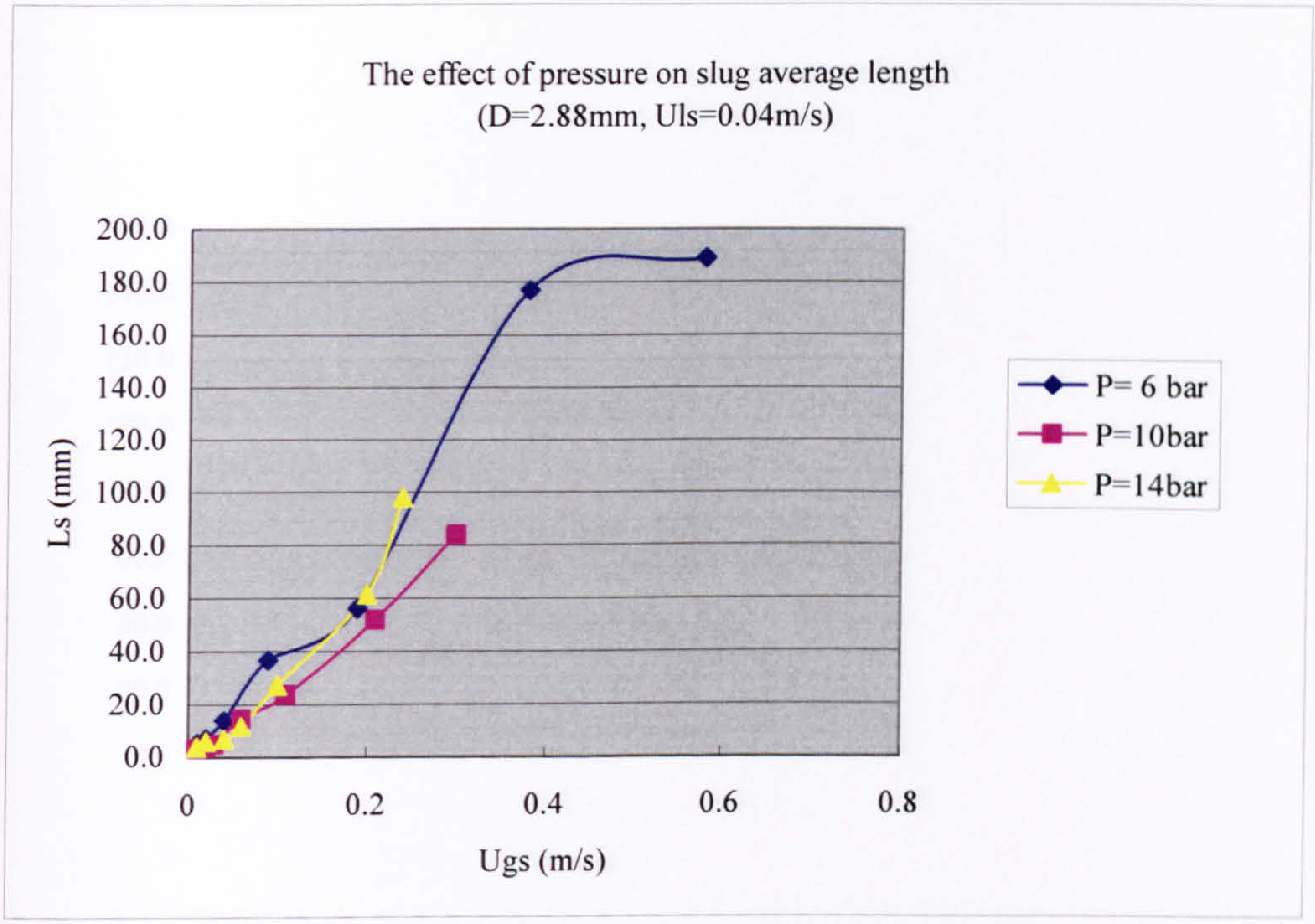

Figure G.85 The effect of pressure on slug average length in the 2.88mm tube (u_{ls}=0.04m/s).

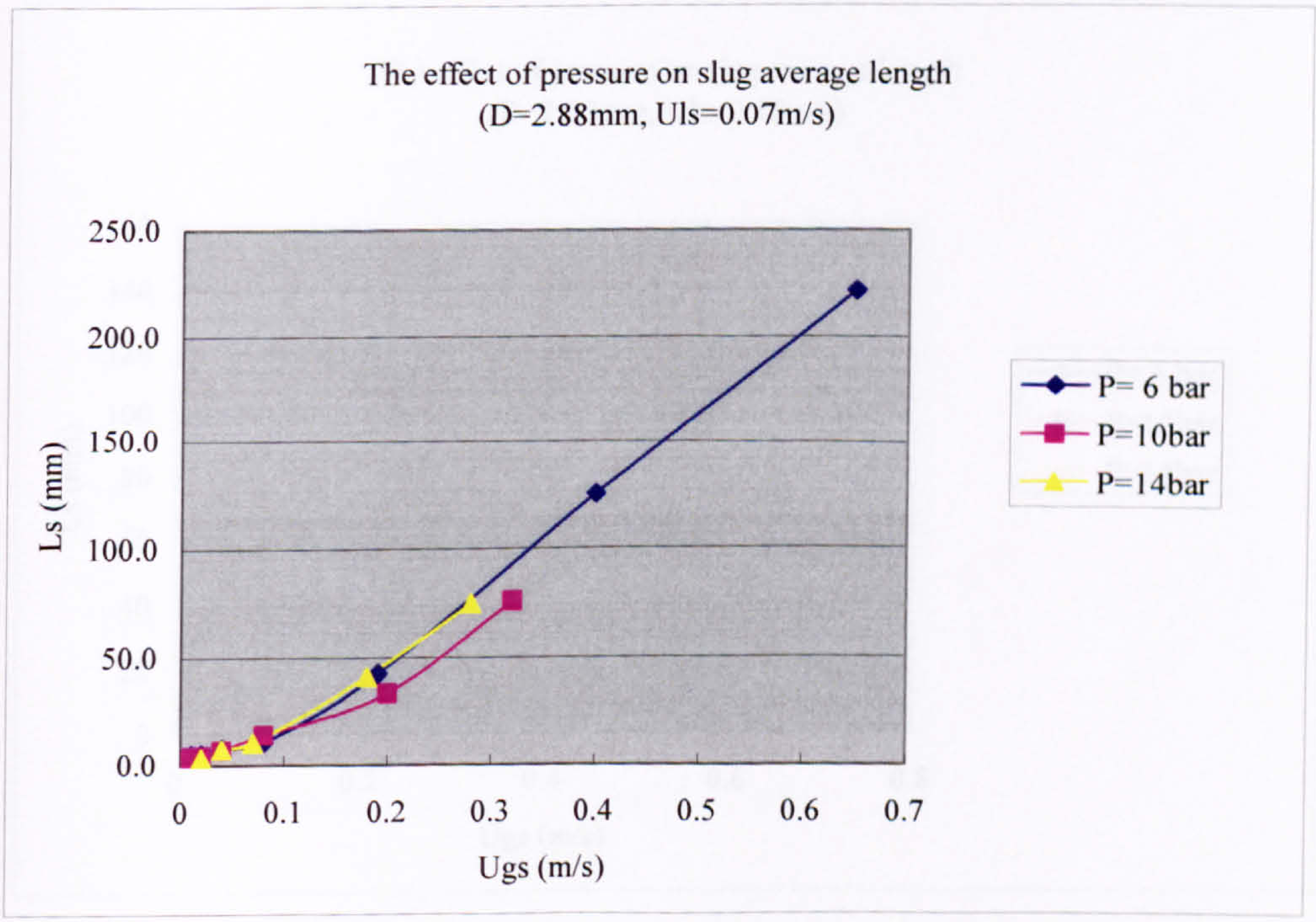

Figure G.86 The effect of pressure on slug average length in the 2.88mm tube (u_{ls}=0.07m/s).

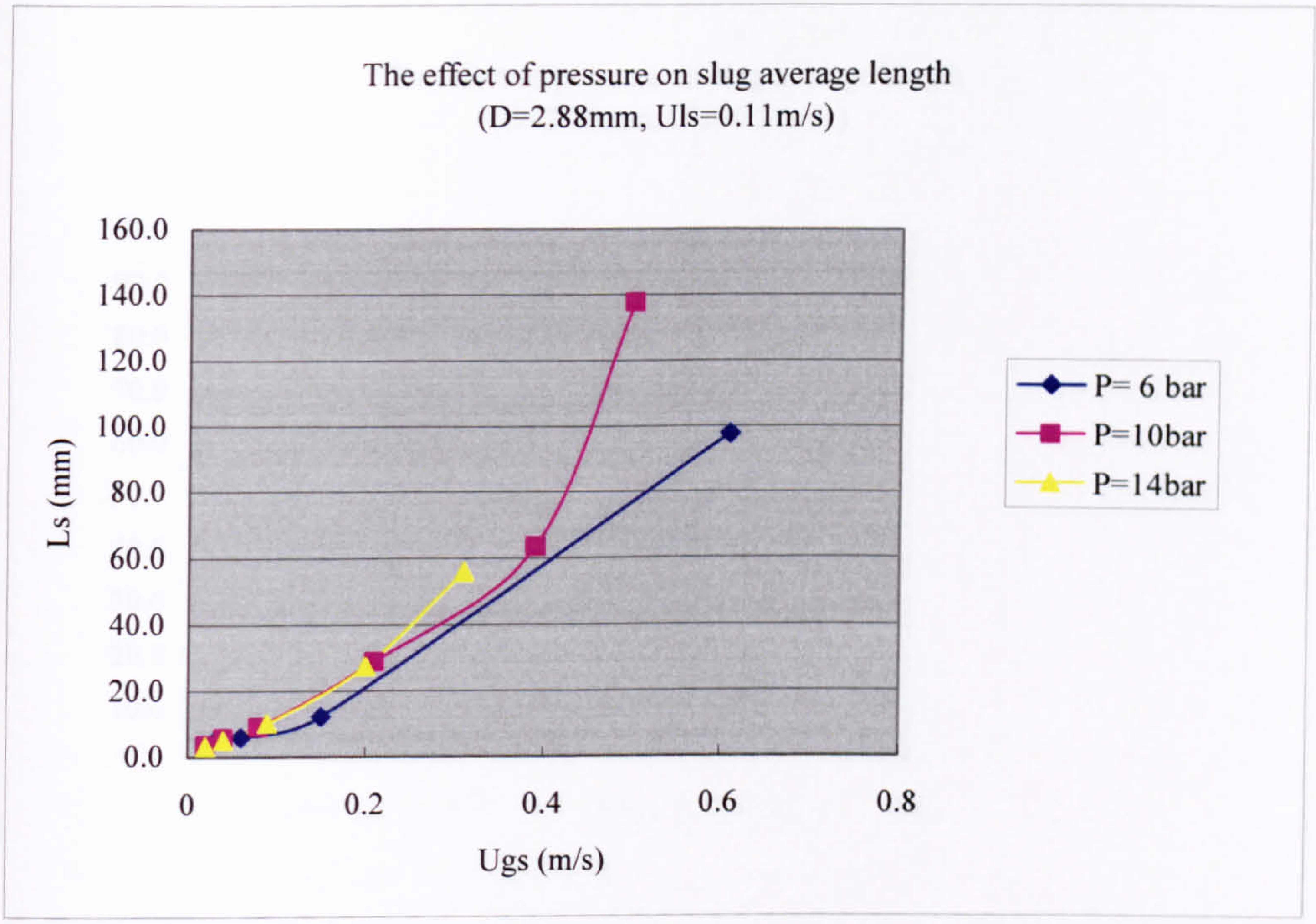

Figure G.87 The effect of pressure on slug average length in the 2.88mm tube (u_{ls}=0.11m/s).

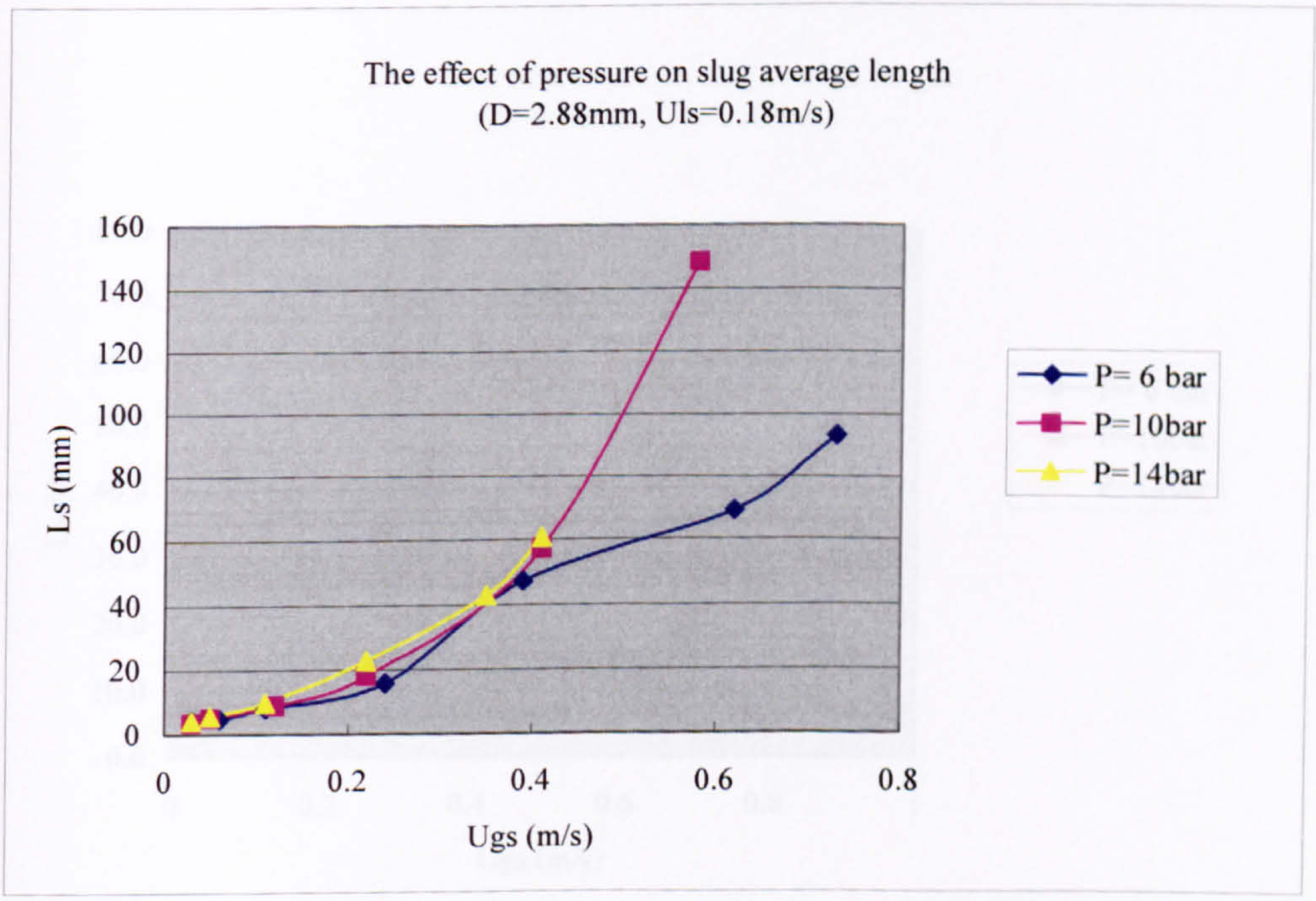

Figure G.88 The effect of pressure on slug average length in the 2.88mm tube (u_{ls}=0.18m/s).

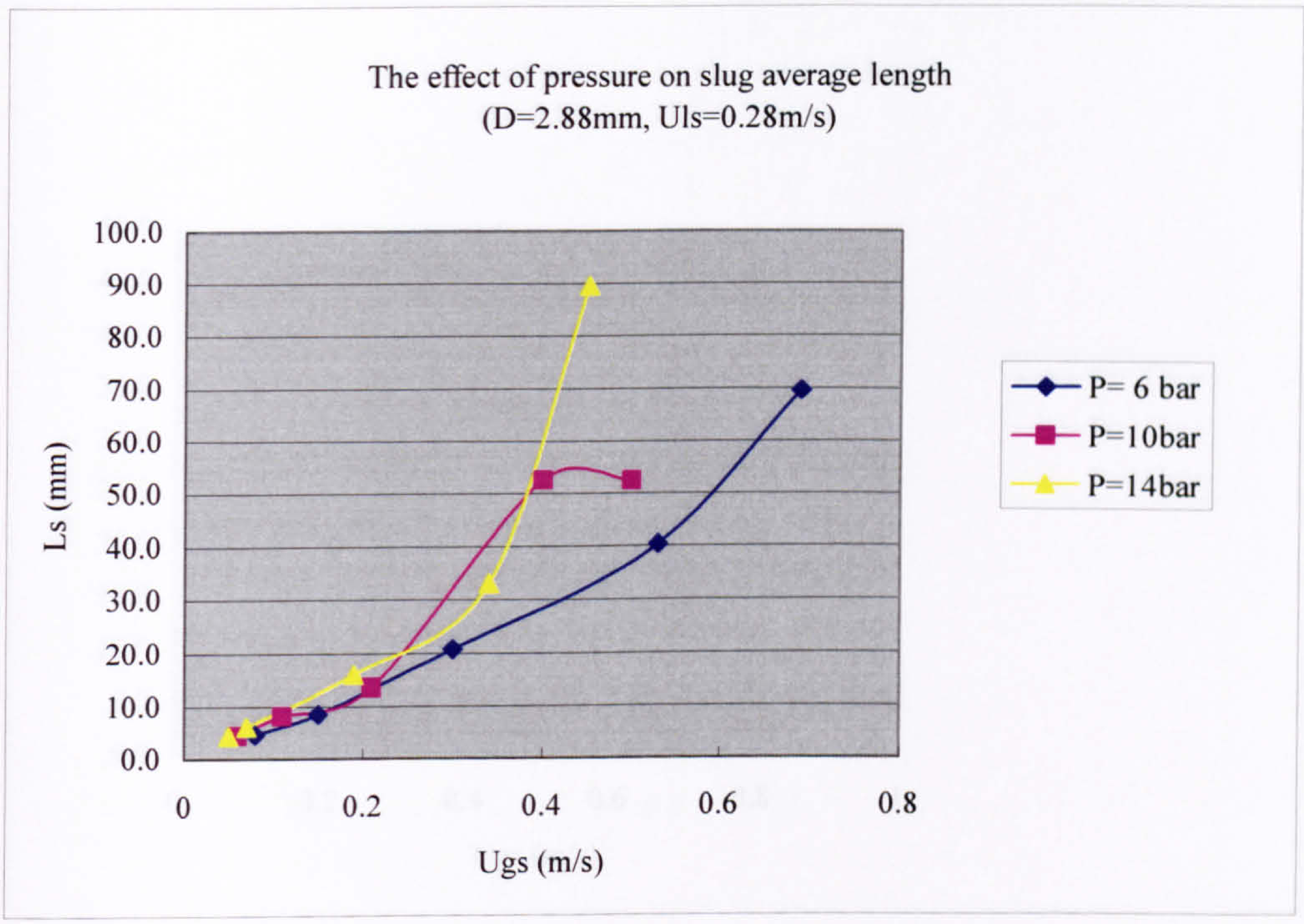

Figure G.89 The effect of pressure on slug average length in the 2.88mm tube (u_{ls}=0.28m/s).

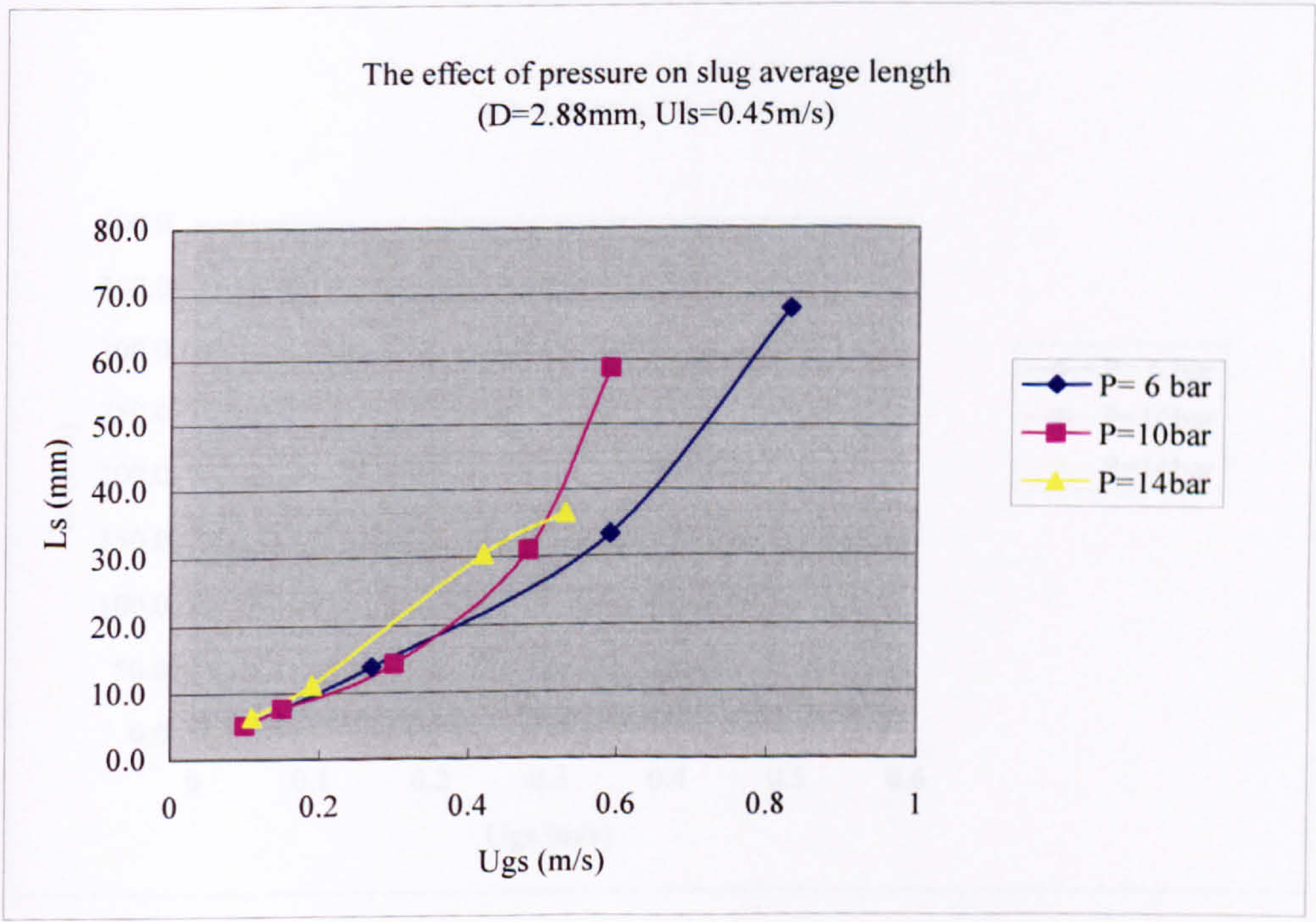

Figure G.90 The effect of pressure on slug average length in the 2.88mm tube (u_{ls}=0.45m/s).

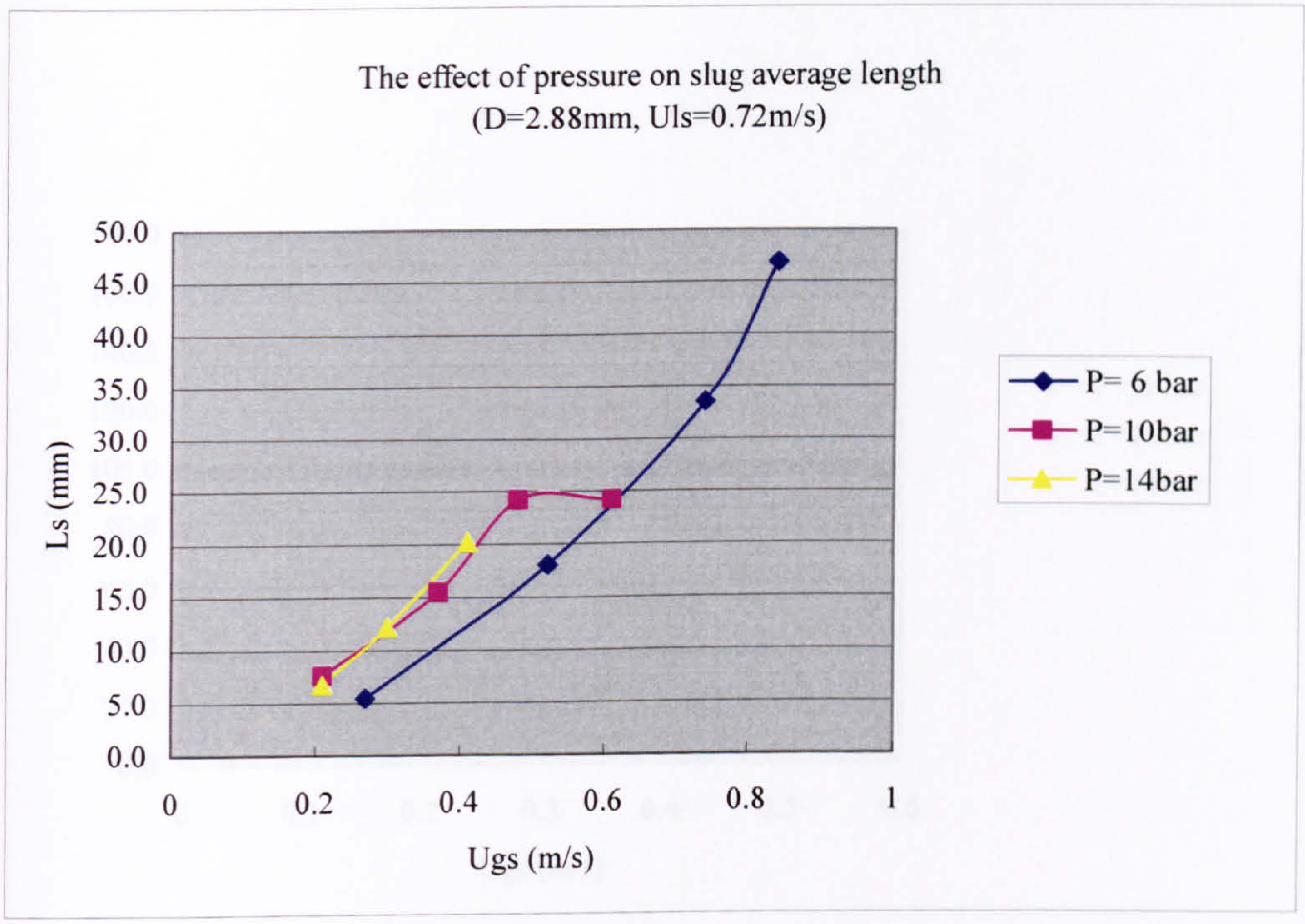

Figure G.91 The effect of pressure on slug average length in the 2.88mm tube (u_{ls}=0.72m/s).

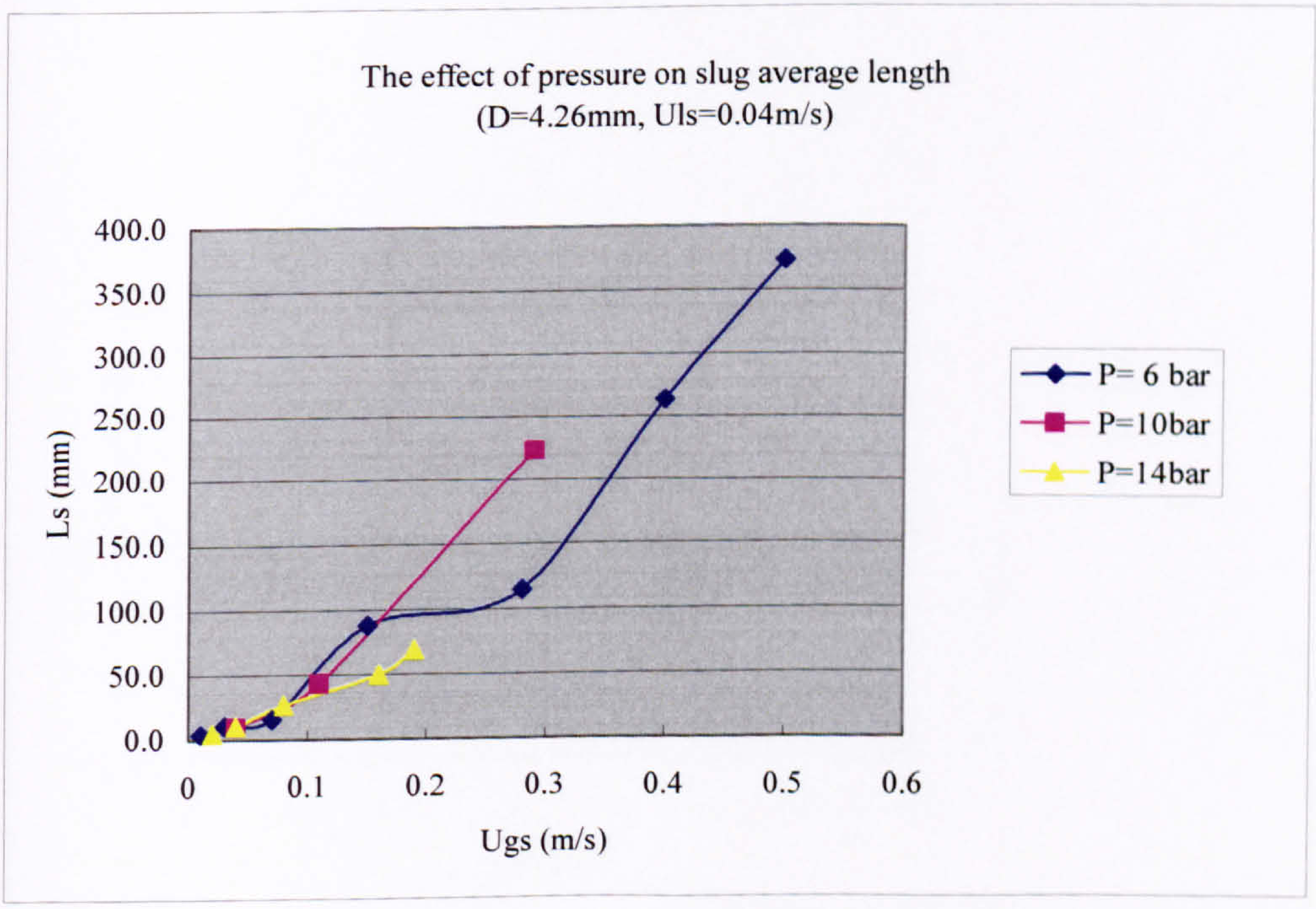

Figure G.92 The effect of pressure on slug average length in the 4.26mm tube (u_{ls}=0.04m/s).

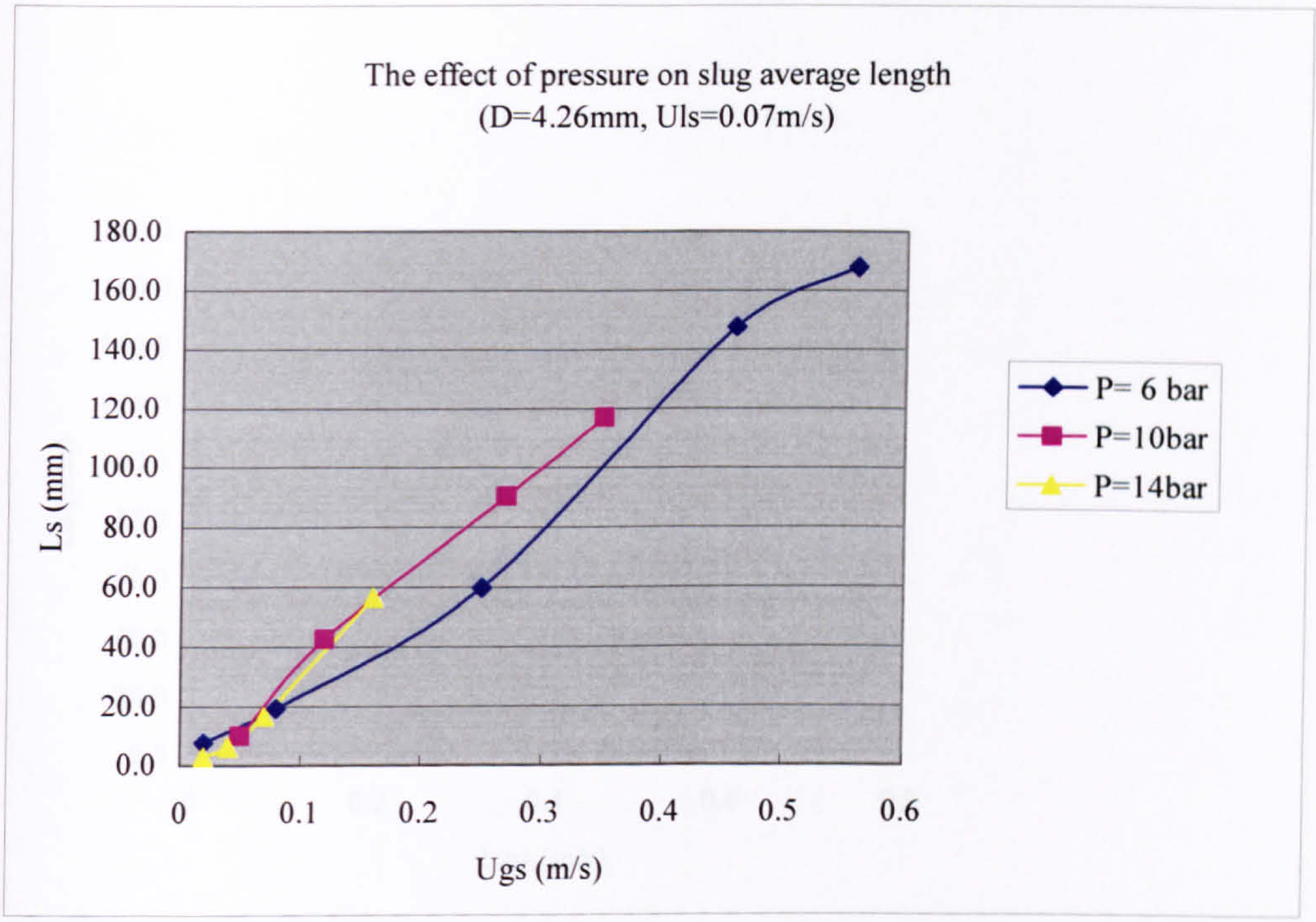

Figure G.93 The effect of pressure on slug average length in the 4.26mm tube (u_{ls}=0.07m/s).

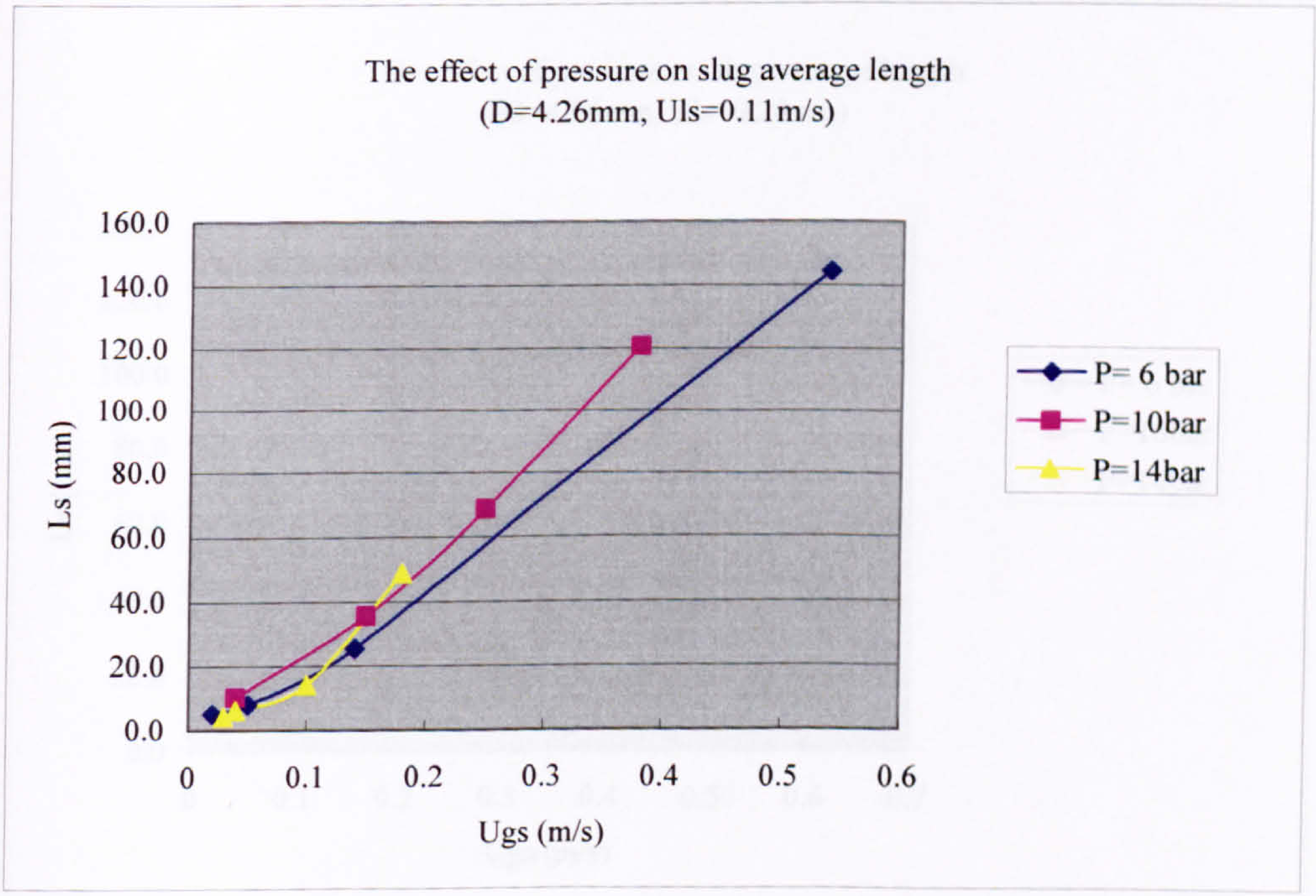

Figure G.94 The effect of pressure on slug average length in the 4.26mm tube (u_{ls}=0.11m/s).

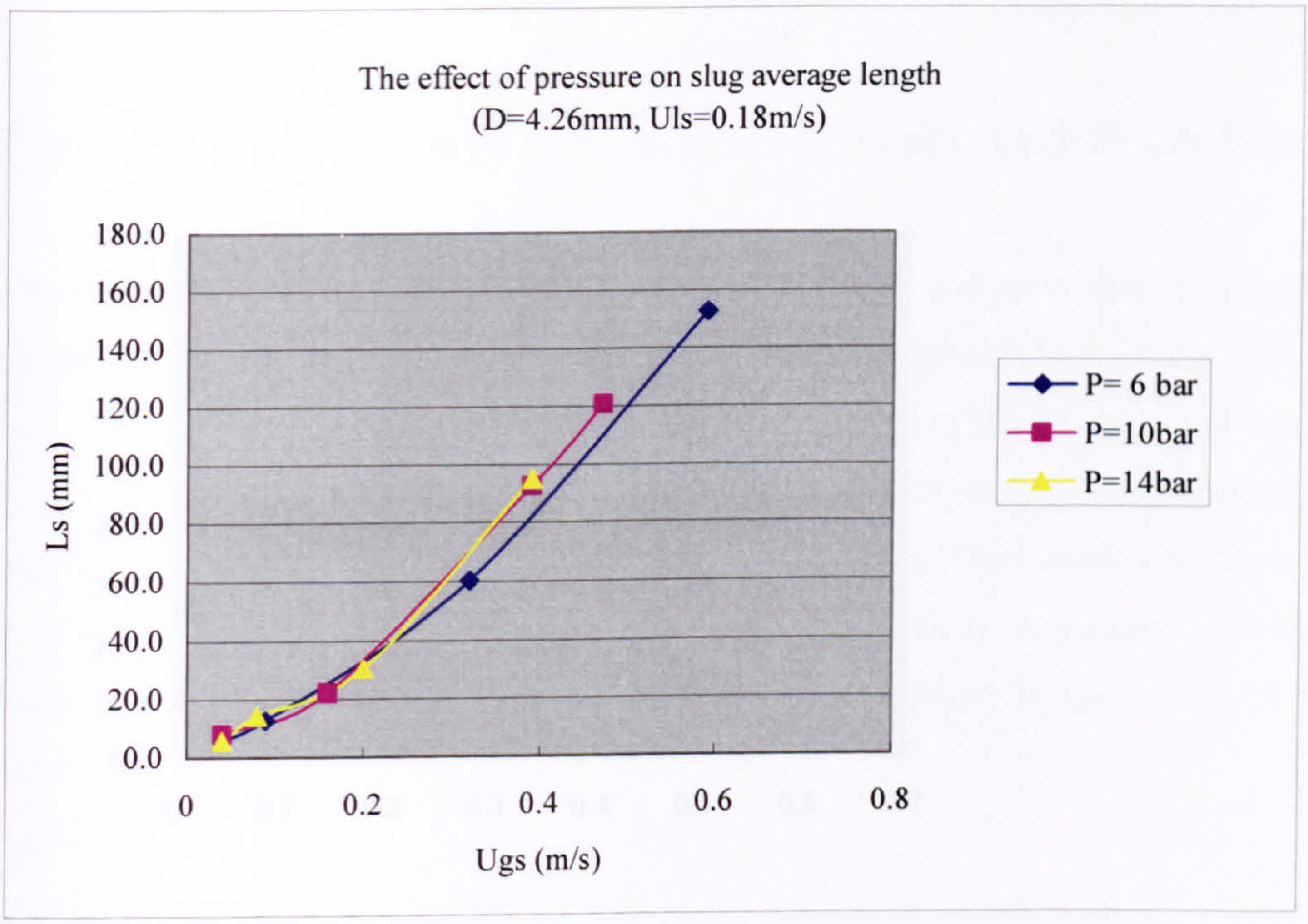

Figure G.95 The effect of pressure on slug average length in the 4.26mm tube (u_{ls}=0.18m/s).

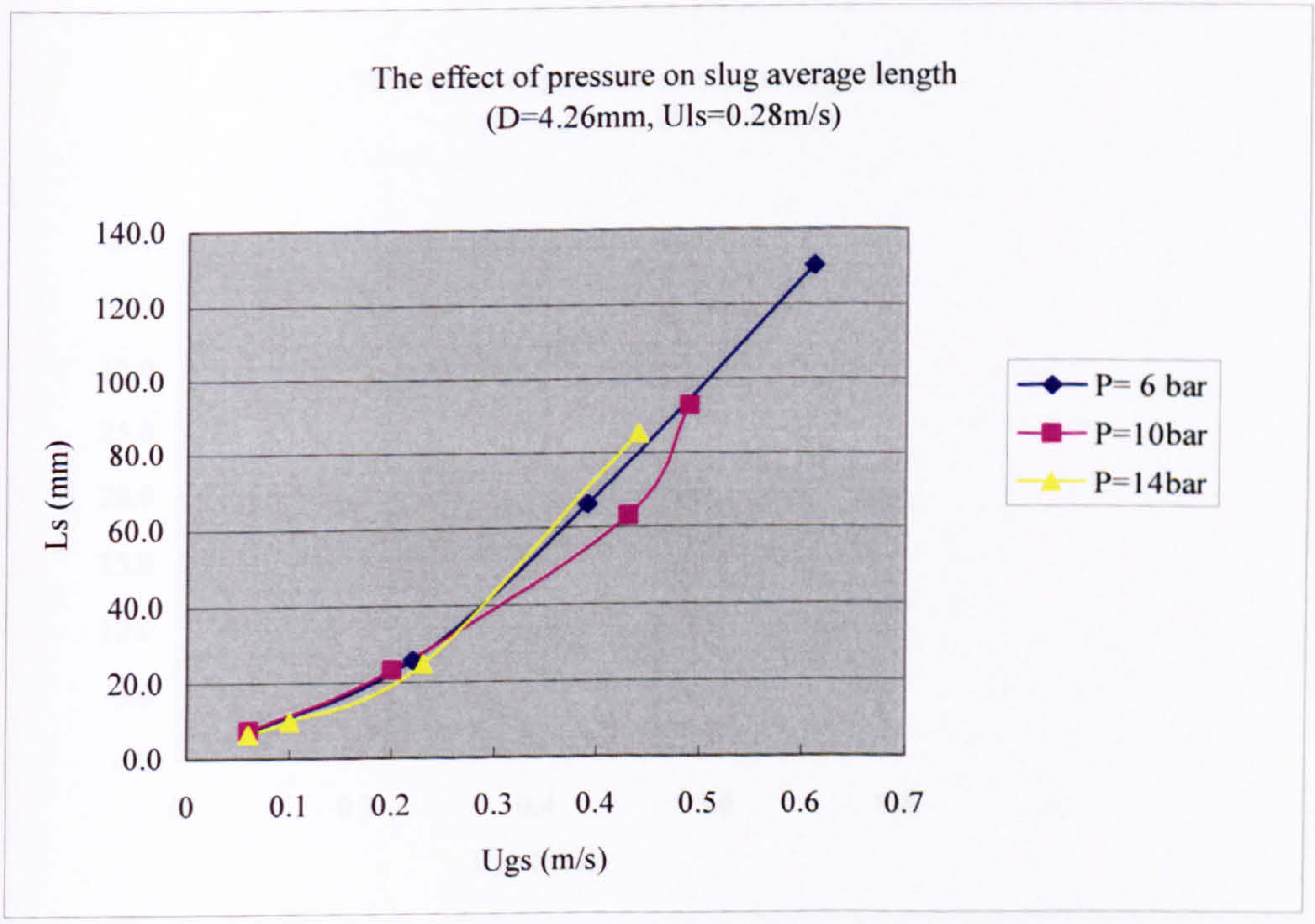

Figure G.96 The effect of pressure on slug average length in the 4.26mm tube (u_{ls}=0.28m/s).

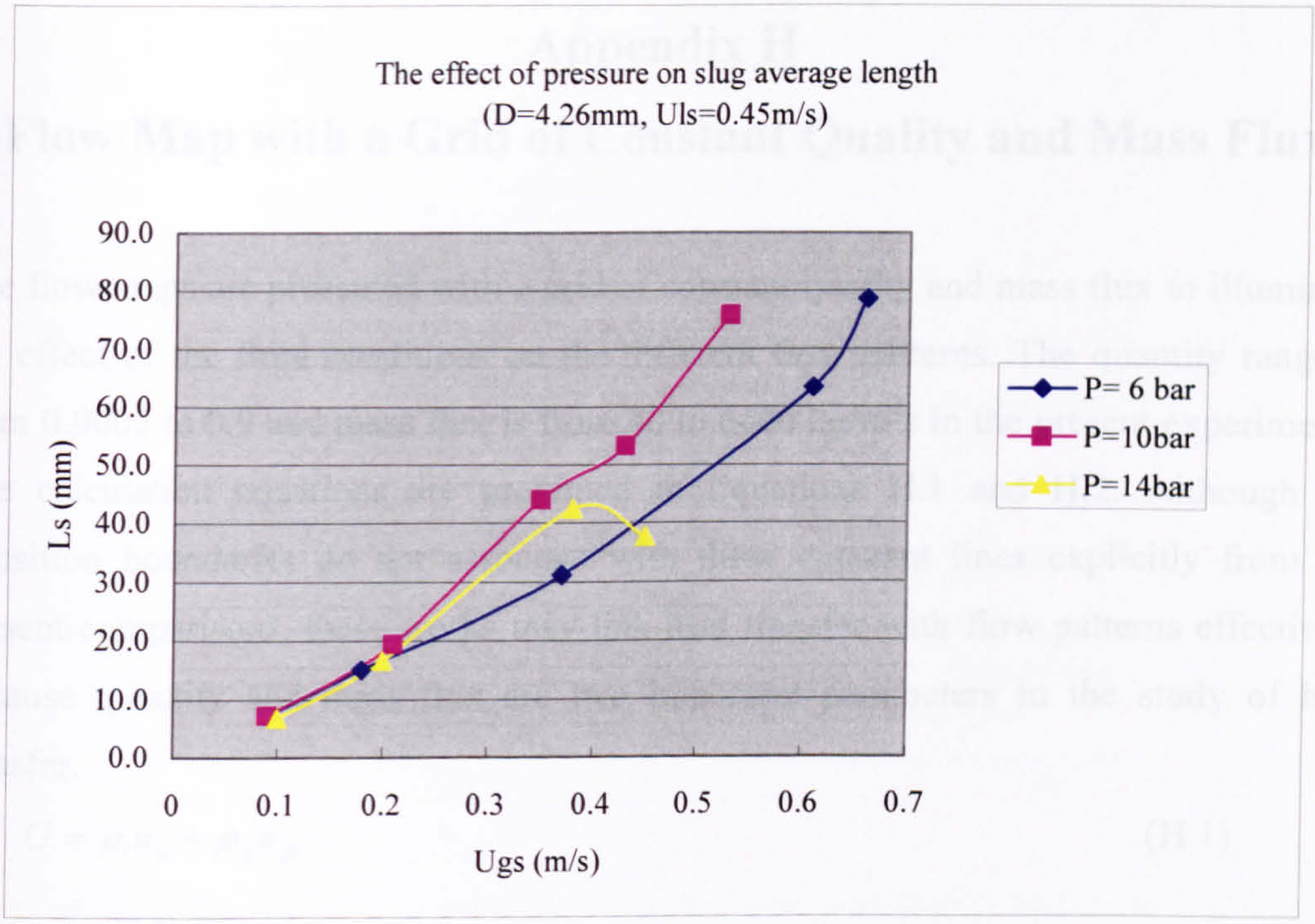

Figure G.97 The effect of pressure on slug average length in the 4.26mm tube (u_{ls}=0.45m/s).

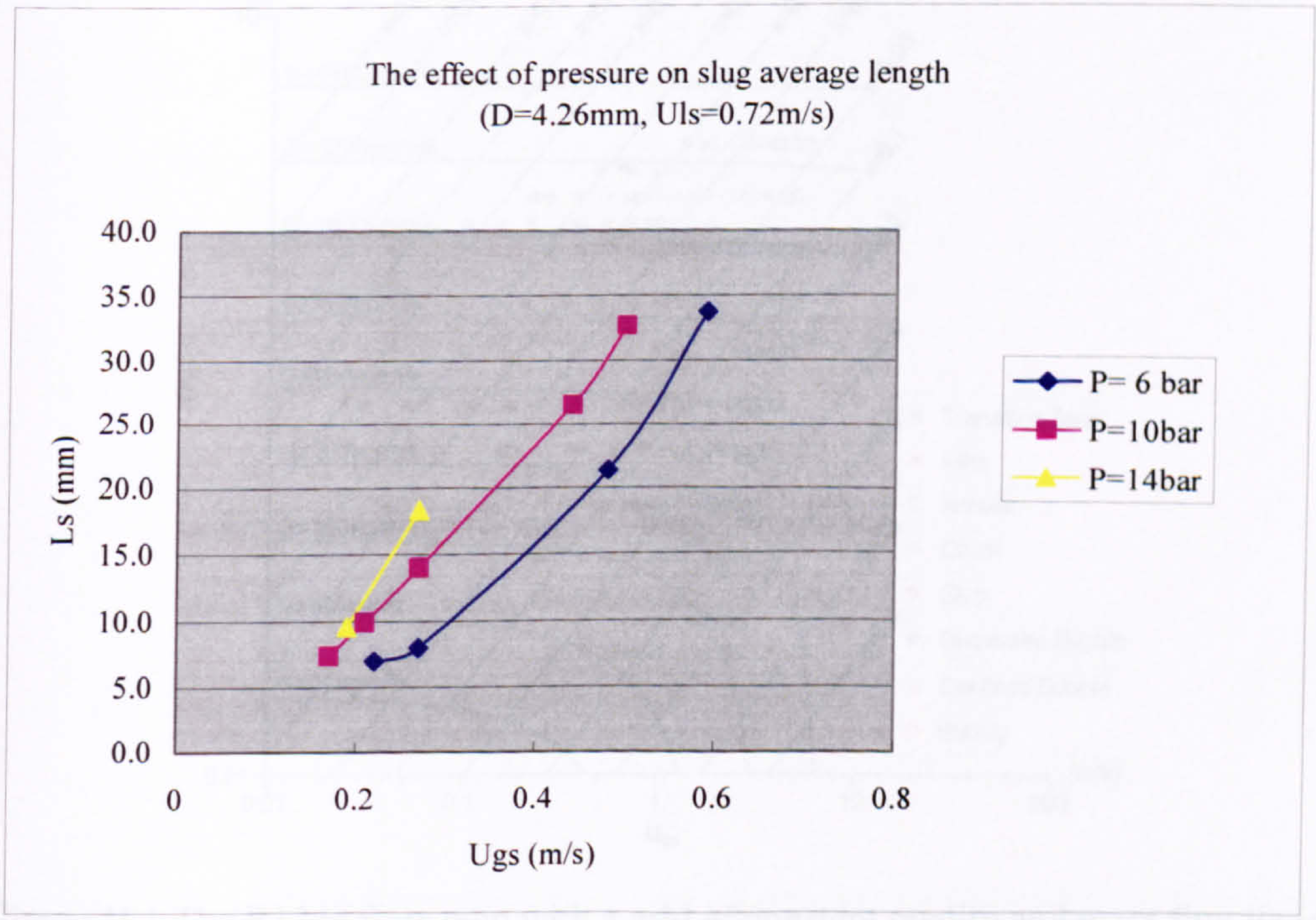

Figure G.98 The effect of pressure on slug average length in the 4.26mm tube (u_{ls}=0.72m/s).

Appendix H

Flow Map with a Grid of Constant Quality and Mass Flux

The flow maps are presented with a grid of constant quality and mass flux to illuminate the effect of the fluid conditions on the different flow patterns. The quantity range is from 0.0005 to 0.9 and mass flux is from 40 to 6400 kg/m^{2}s in the present experiments. The calculation equations are presented in Equations H.1 and H.2. Although the transition boundaries do not associate with these constant lines explicitly from the present comparisons, these works may link heat transfer with flow patterns effectively because quantity and mass flux are two important parameters in the study of heat transfer.

$$G = \rho_l u_{ls} + \rho_g u_{gs} \tag{H.1}$$

$$x = \frac{\rho_g u_{gs}}{\rho_l u_{ls} + \rho_g u_{gs}} \tag{H.2}$$

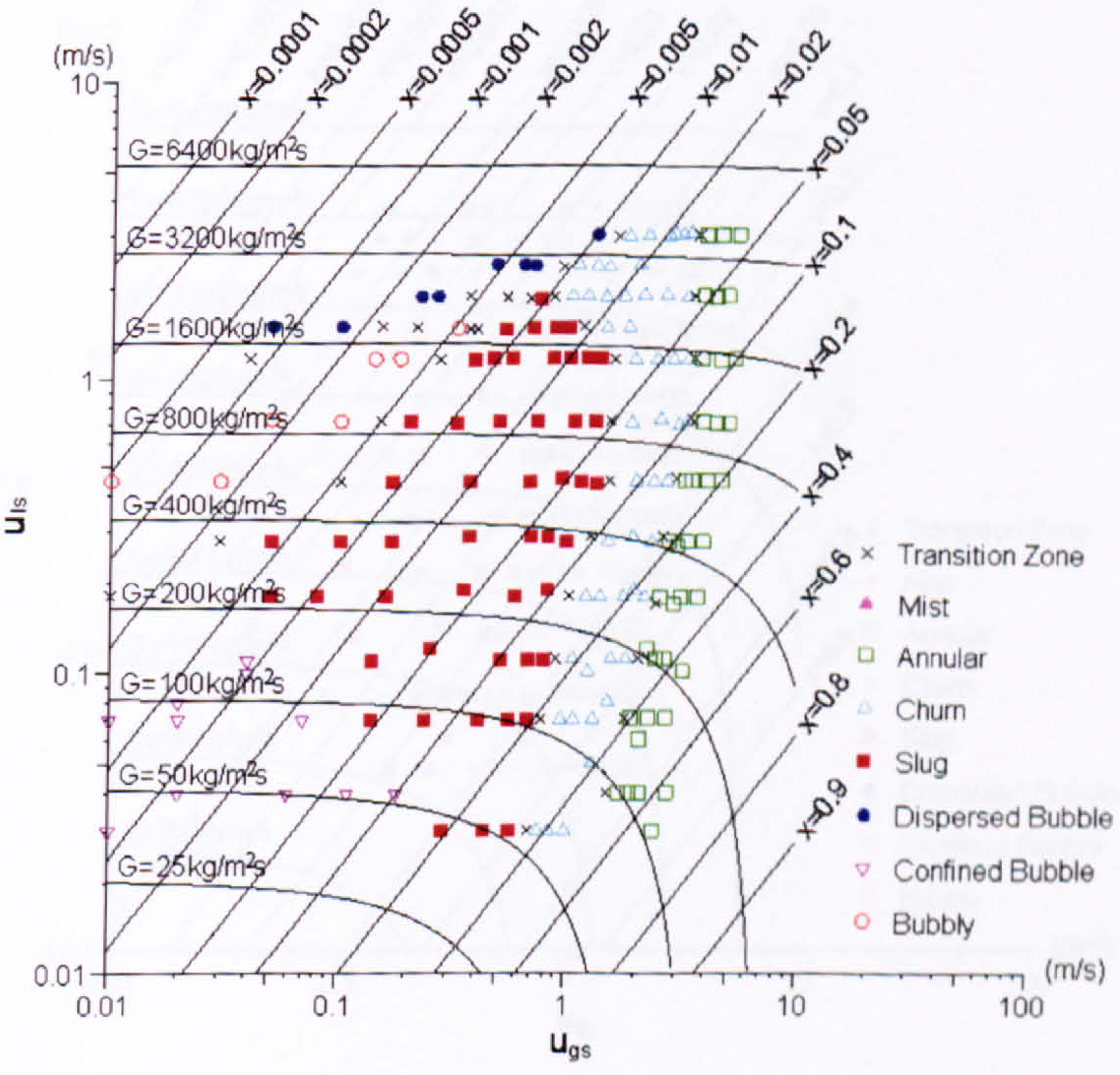

Figure H.1 The R134a flow map with a grid of constant quality and mass flux lines in the 1.10 mm diameter tube at 6 bar pressure.

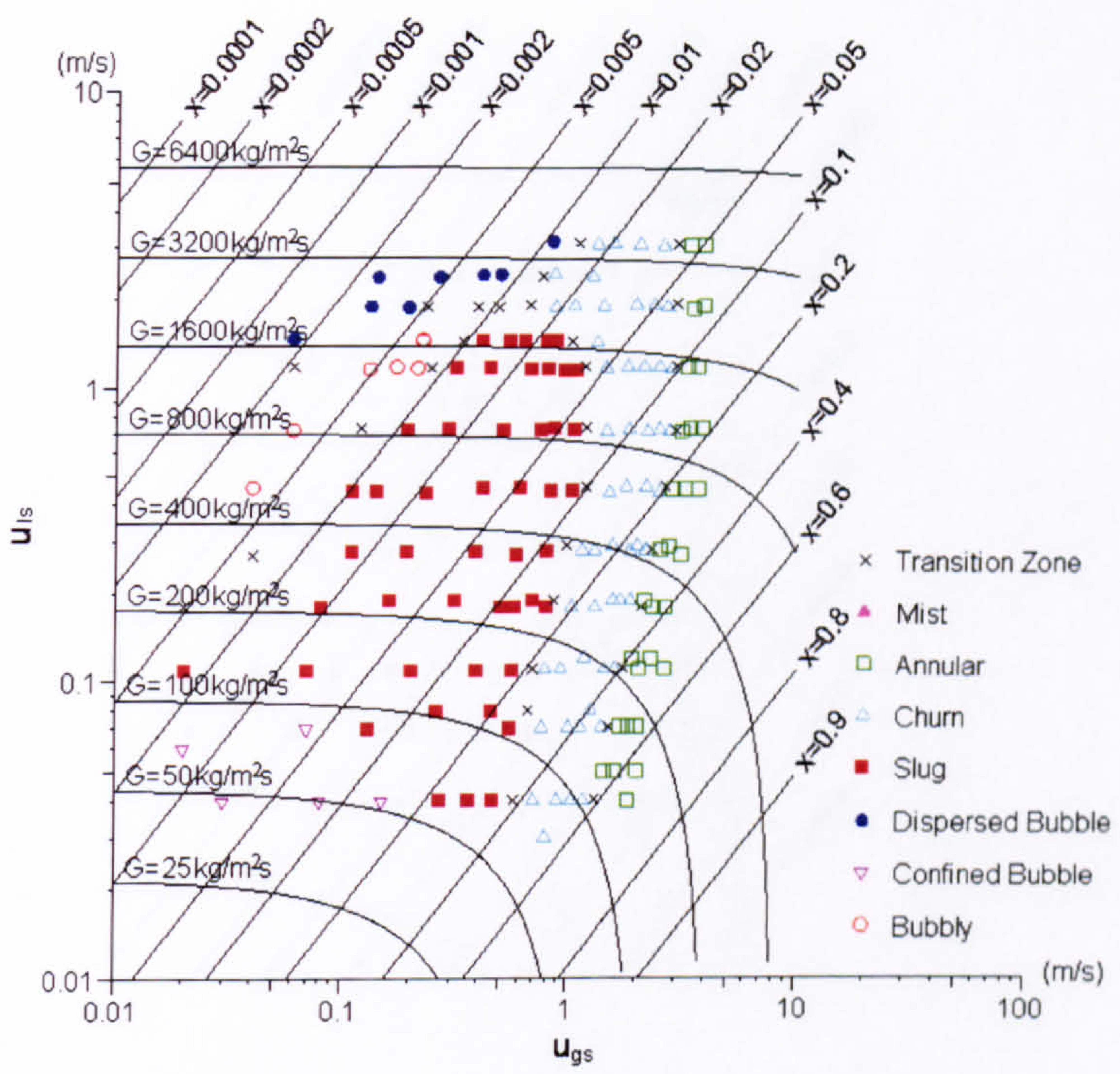

Figure H.2 The R134a flow map with a grid of constant quality and mass flux lines in the 1.10 mm diameter tube at 10 bar pressure.

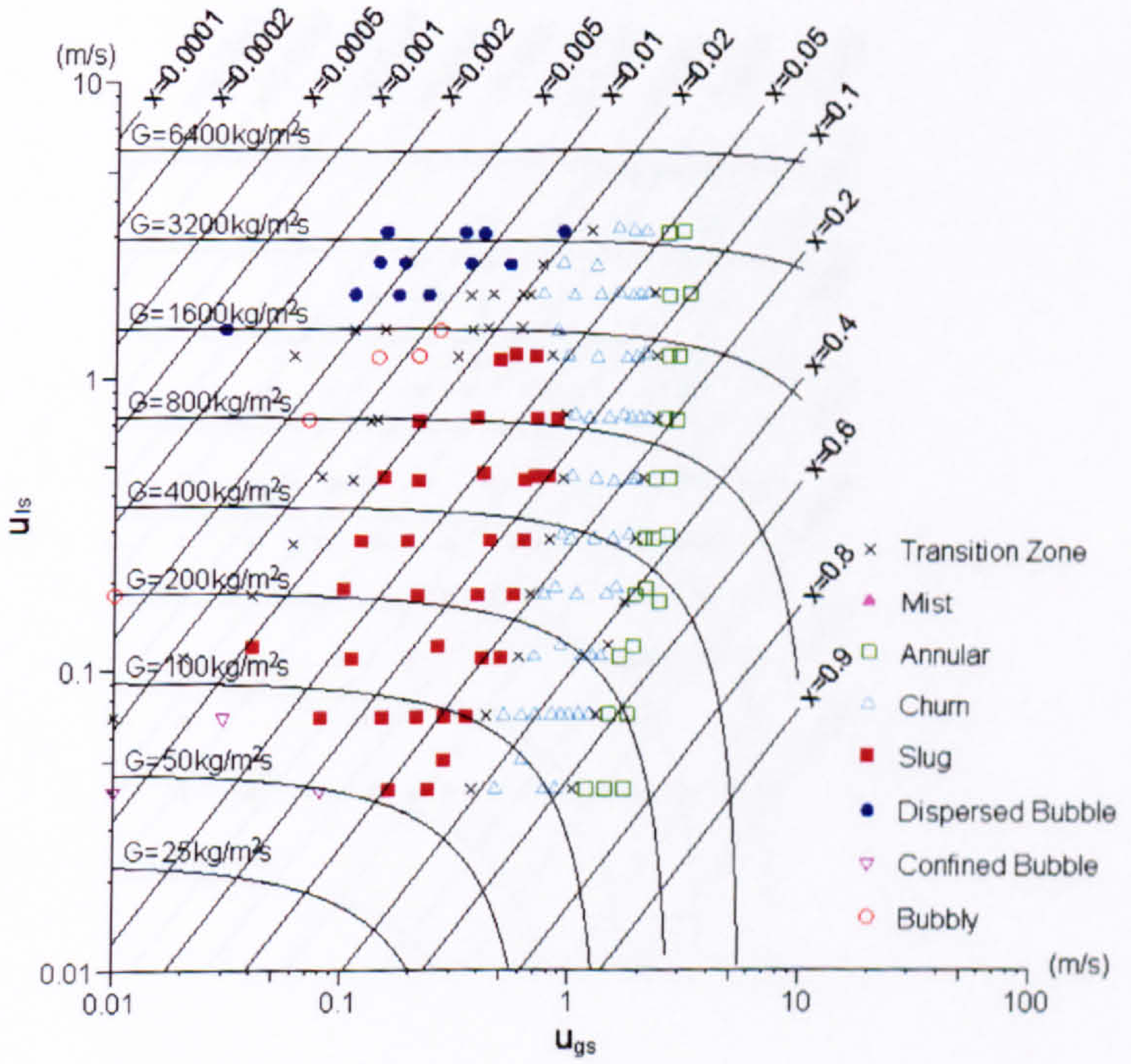

Figure H.3 The R134a flow map with a grid of constant quality and mass flux lines in the 1.10 mm diameter tube at 14 bar pressure.

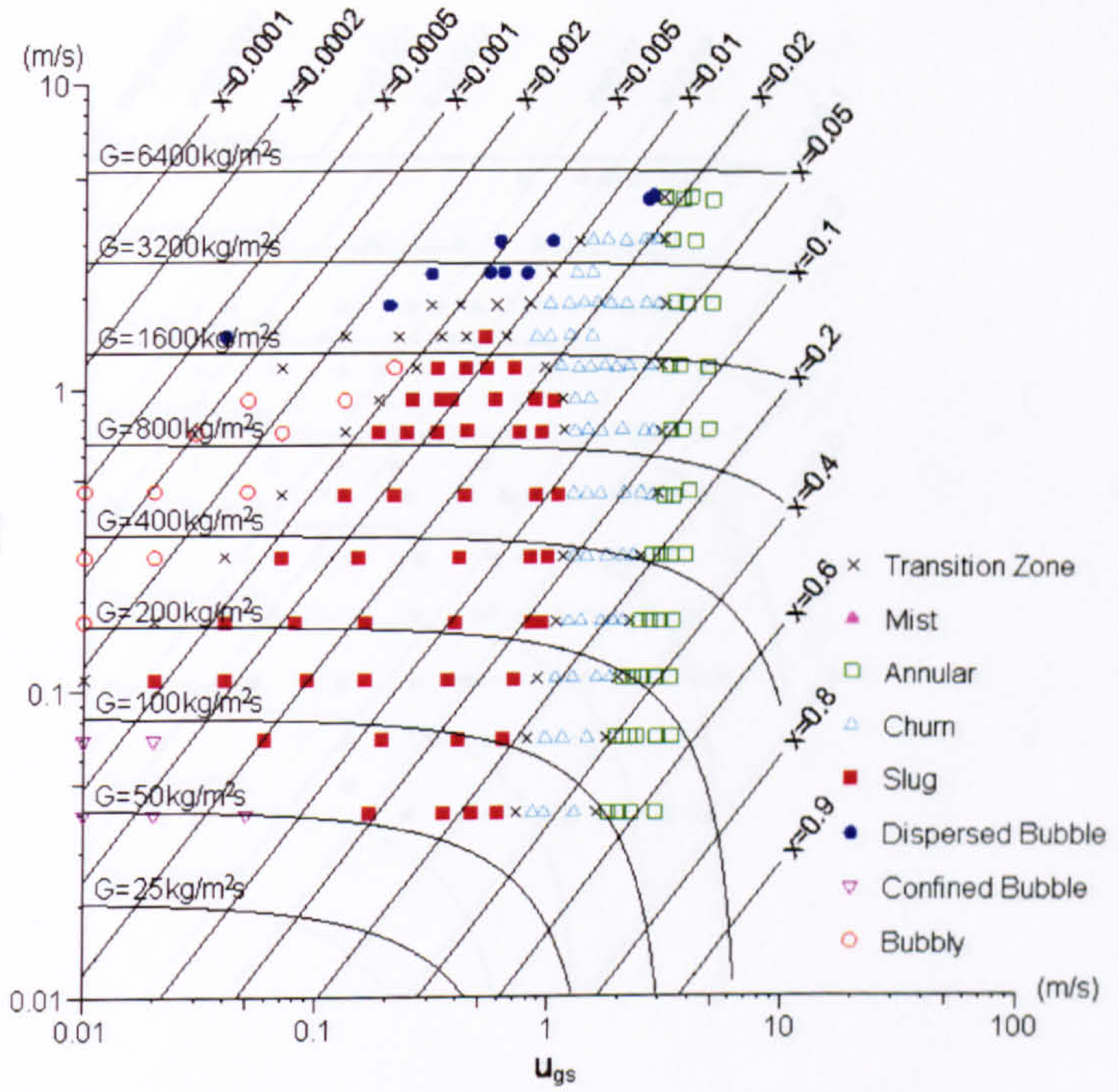

Figure H.4 The R134a flow map with a grid of constant quality and mass flux lines in the 2.01 mm diameter tube at 6 bar pressure.

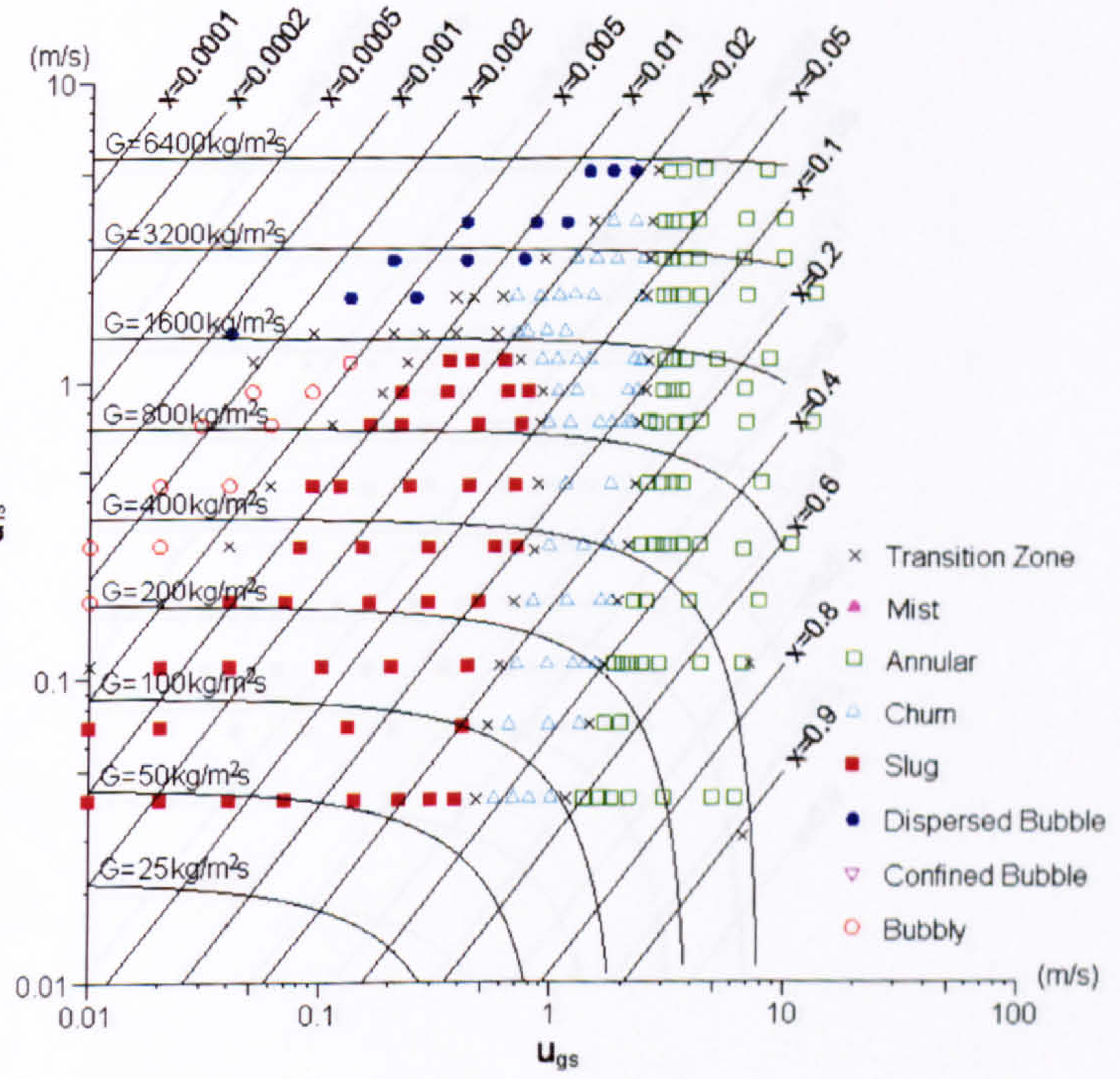

Figure H.5 The R134a flow map with a grid of constant quality and mass flux lines in the 2.01 mm diameter tube at 10 bar pressure.

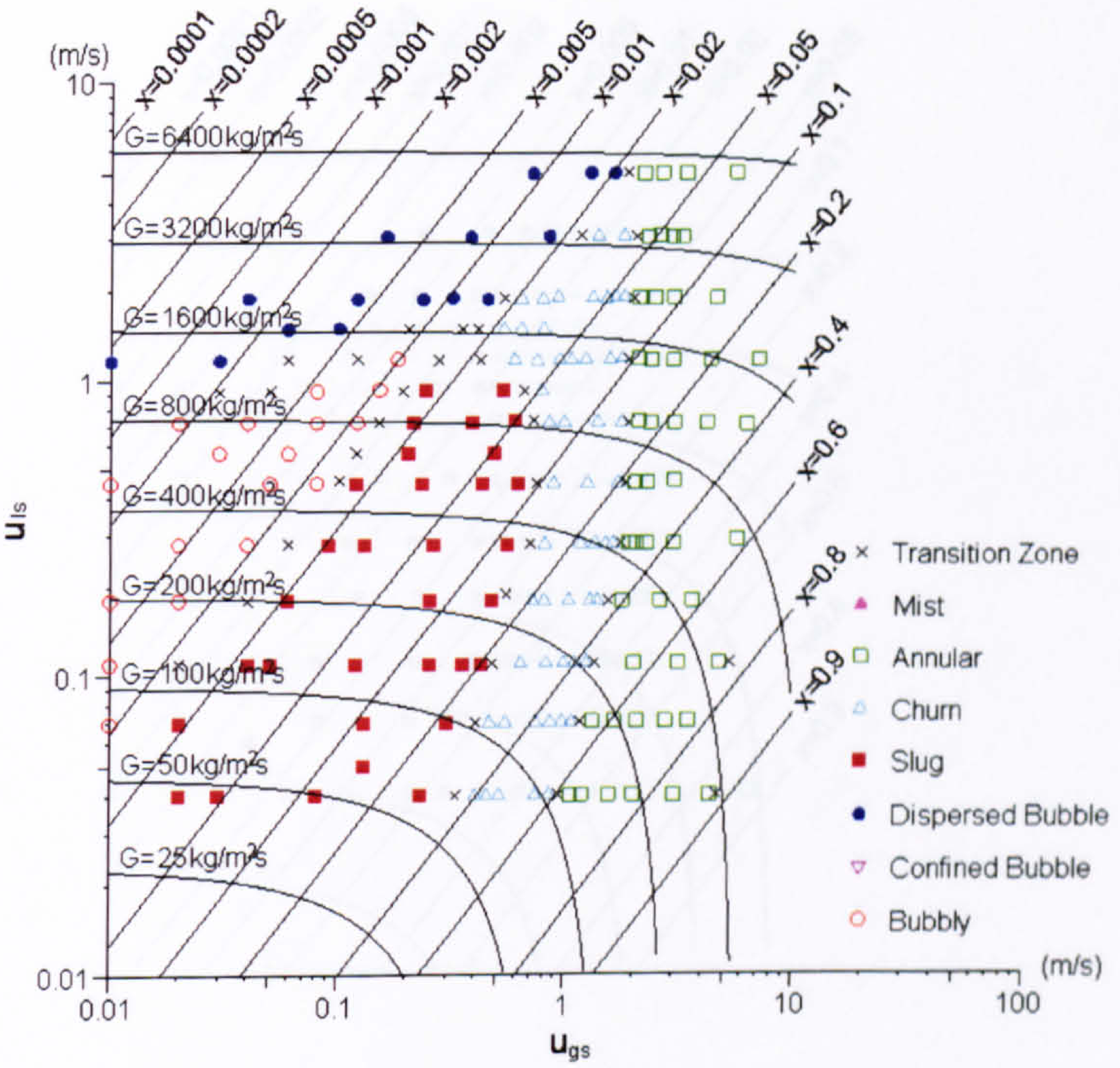

Figure H.6 The R134a flow map with a grid of constant quality and mass flux lines in the 2.01 mm diameter tube at 14 bar pressure.

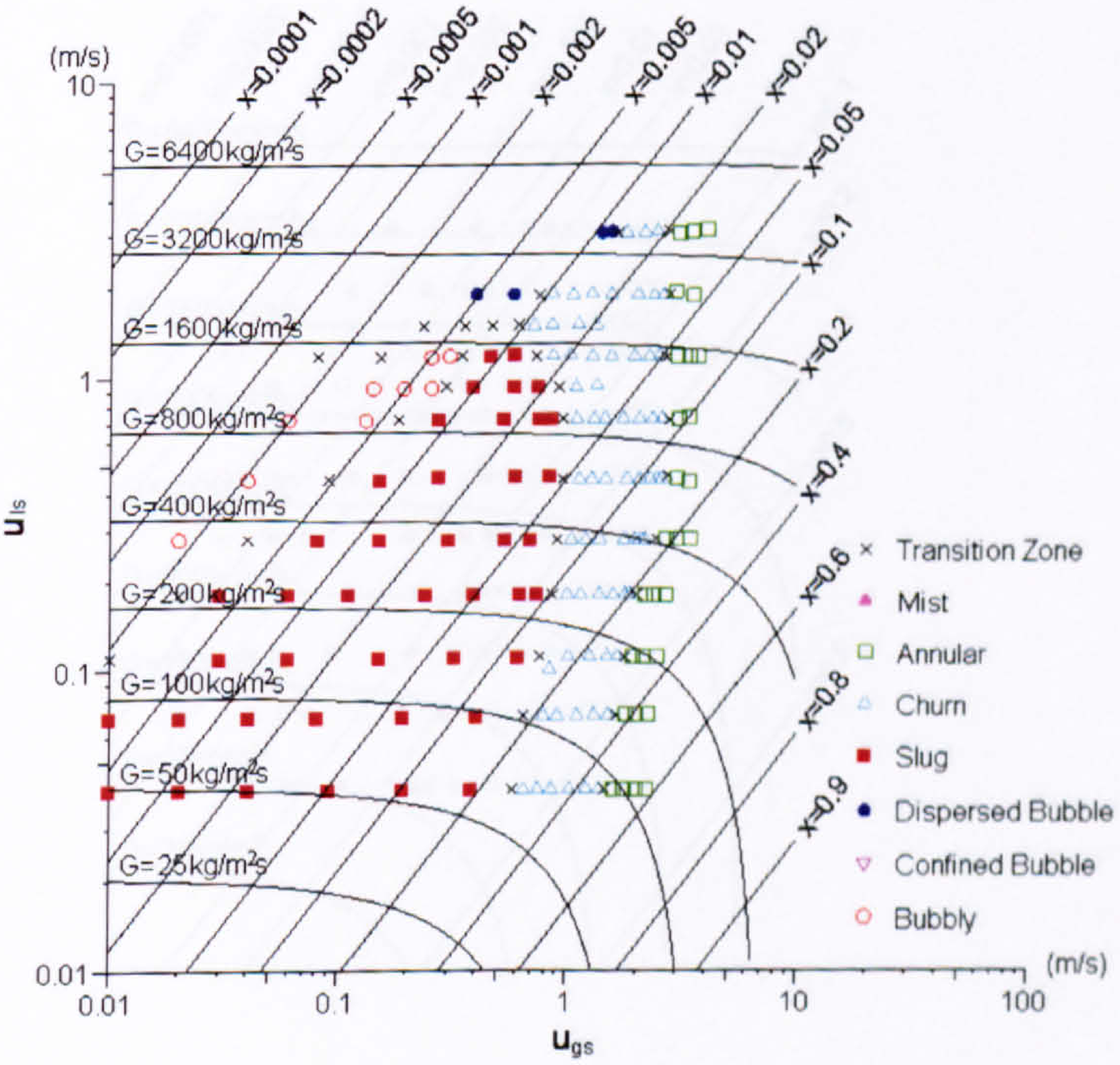

Figure H.7 The R134a flow map with a grid of constant quality and mass flux lines in the 2.88 mm diameter tube at 6 bar pressure.

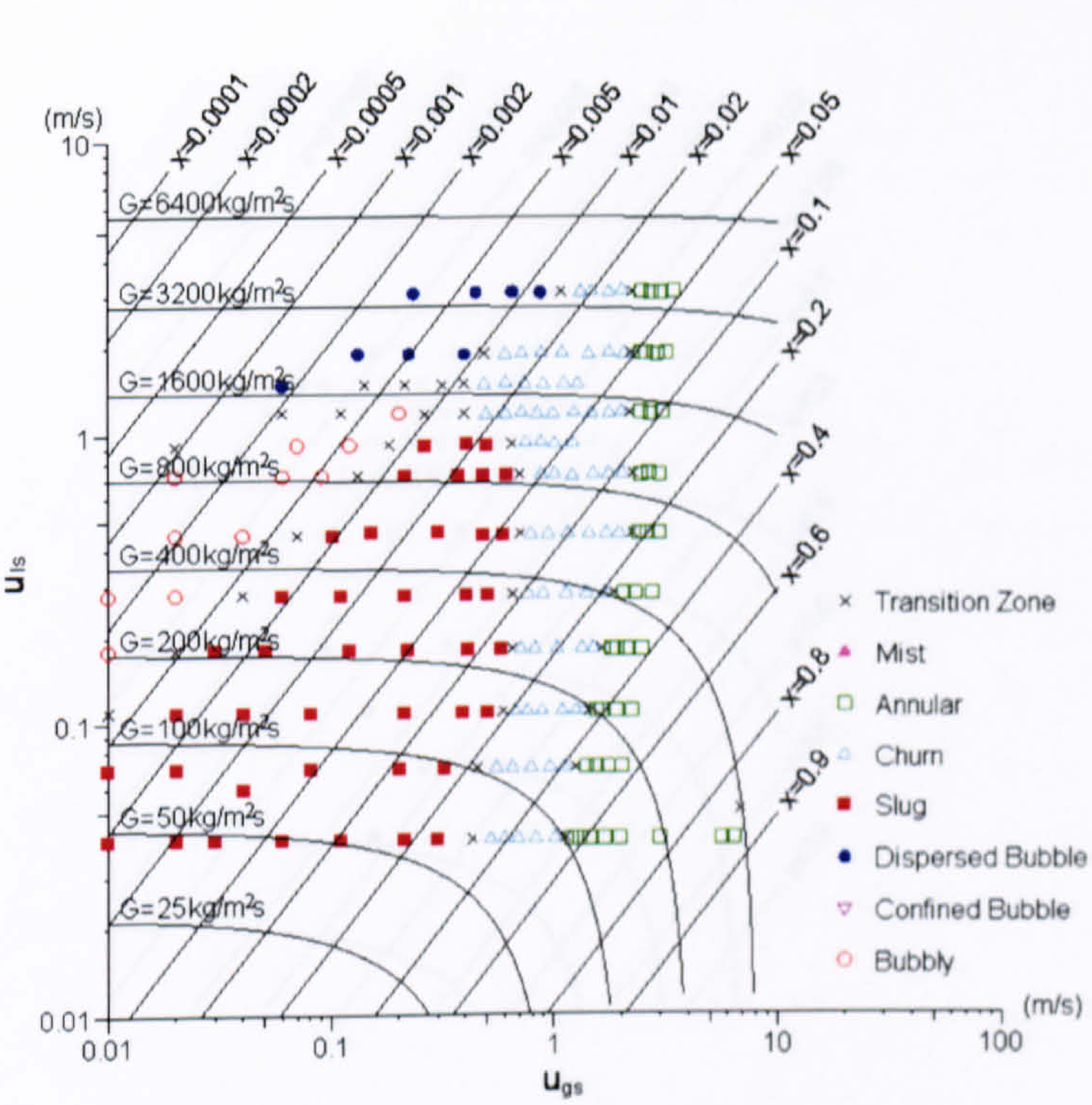

Figure H.8 The R134a flow map with a grid of constant quality and mass flux lines in the 2.88 mm diameter tube at 10 bar pressure.

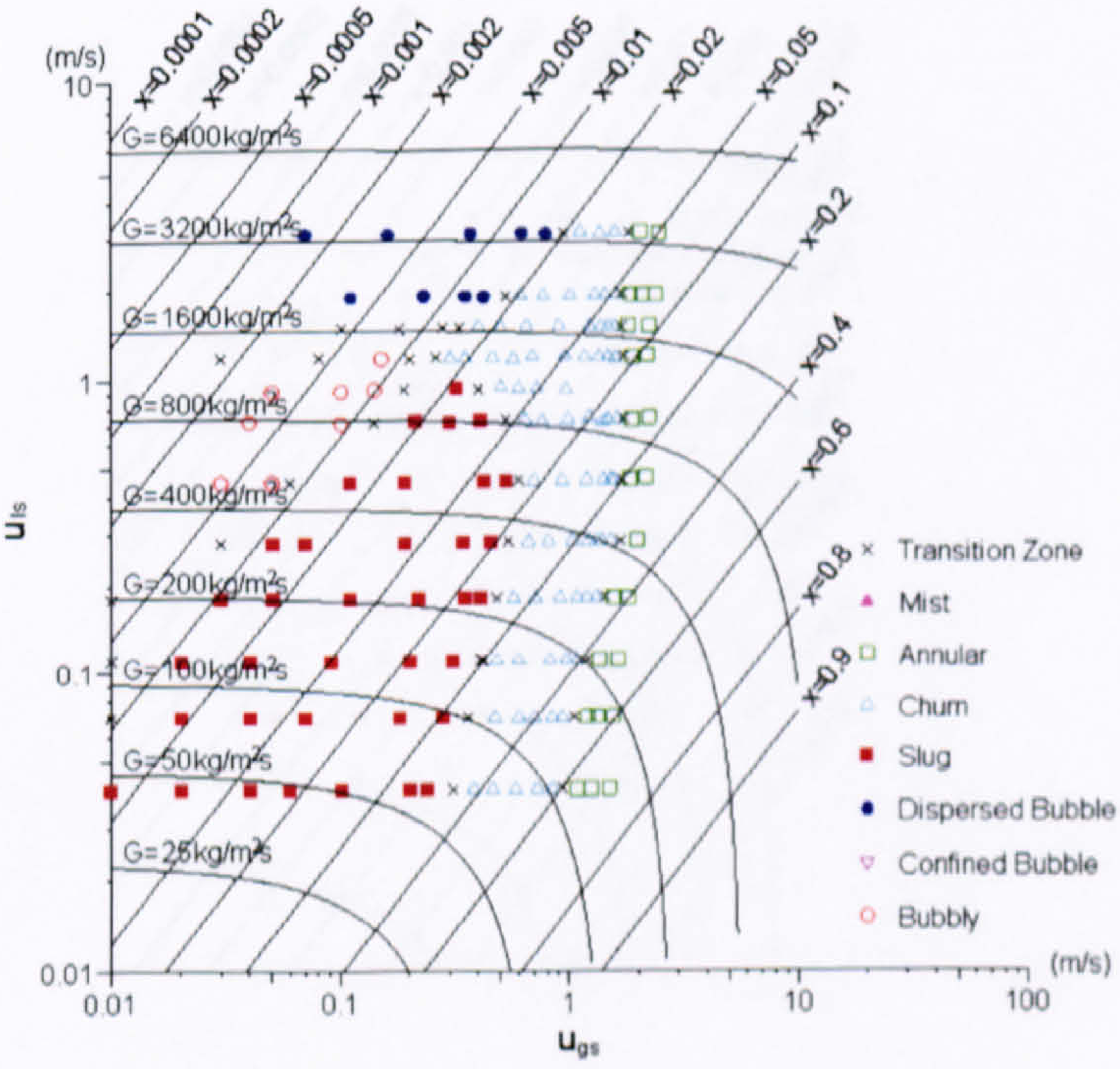

Figure H.9 The R134a flow map with a grid of constant quality and mass flux lines in the 2.88 mm diameter tube at 14 bar pressure.

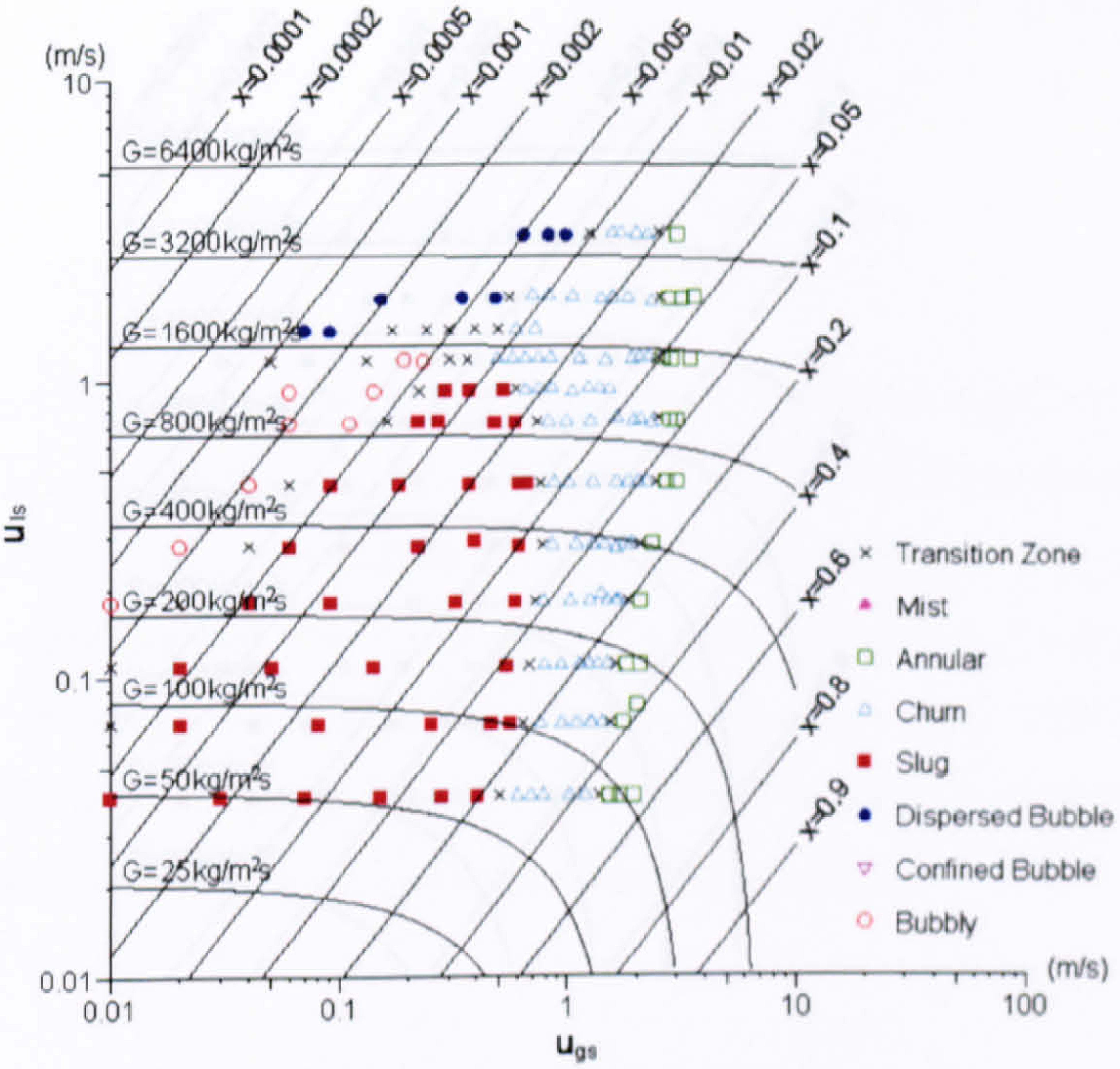

Figure H.10 The R134a flow map with a grid of constant quality and mass flux lines in the 4.26 mm diameter tube at 6 bar pressure.

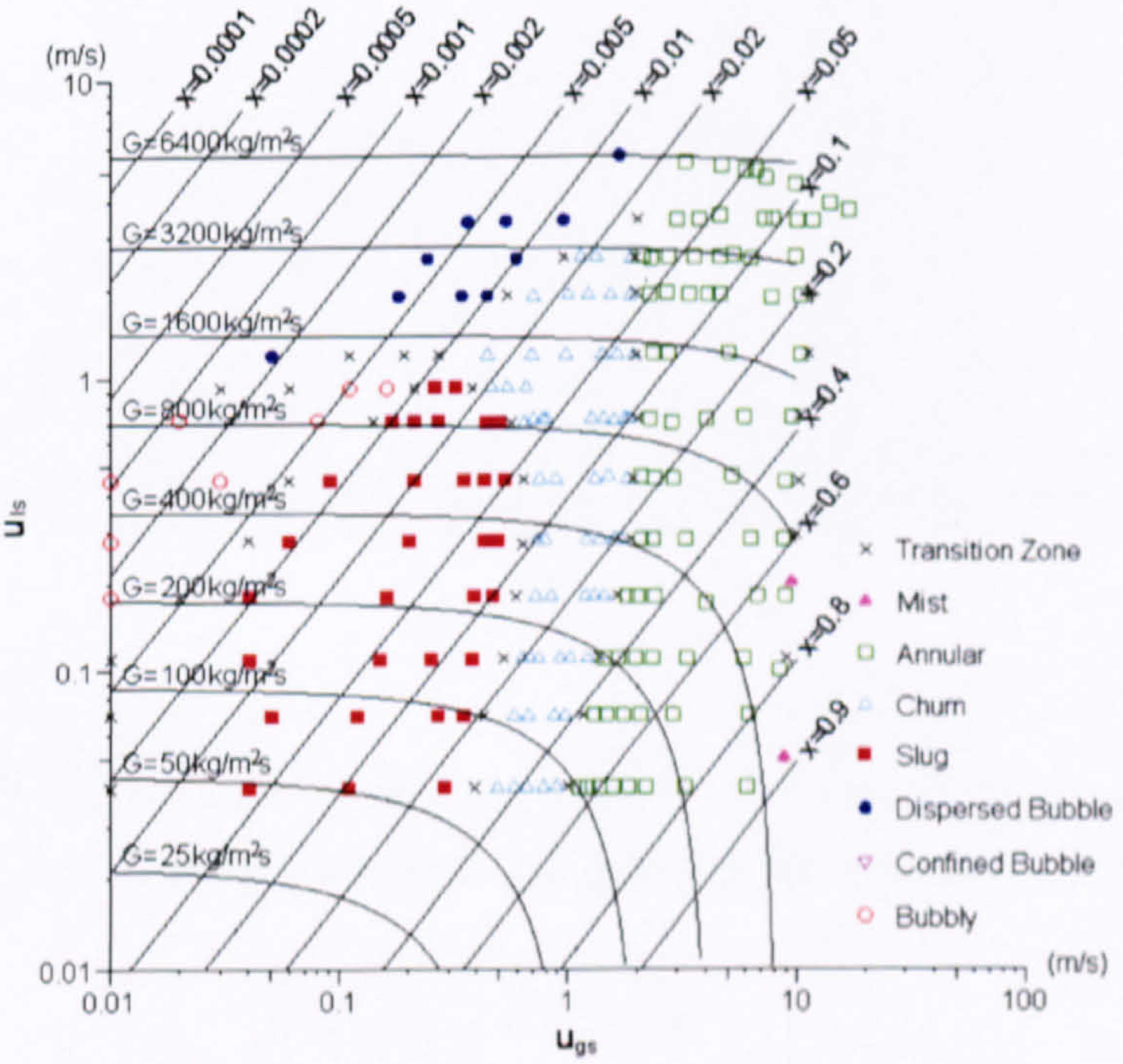

Figure H.11 The R134a flow map with a grid of constant quality and mass flux lines in the 4.26 mm diameter tube at 10 bar pressure.

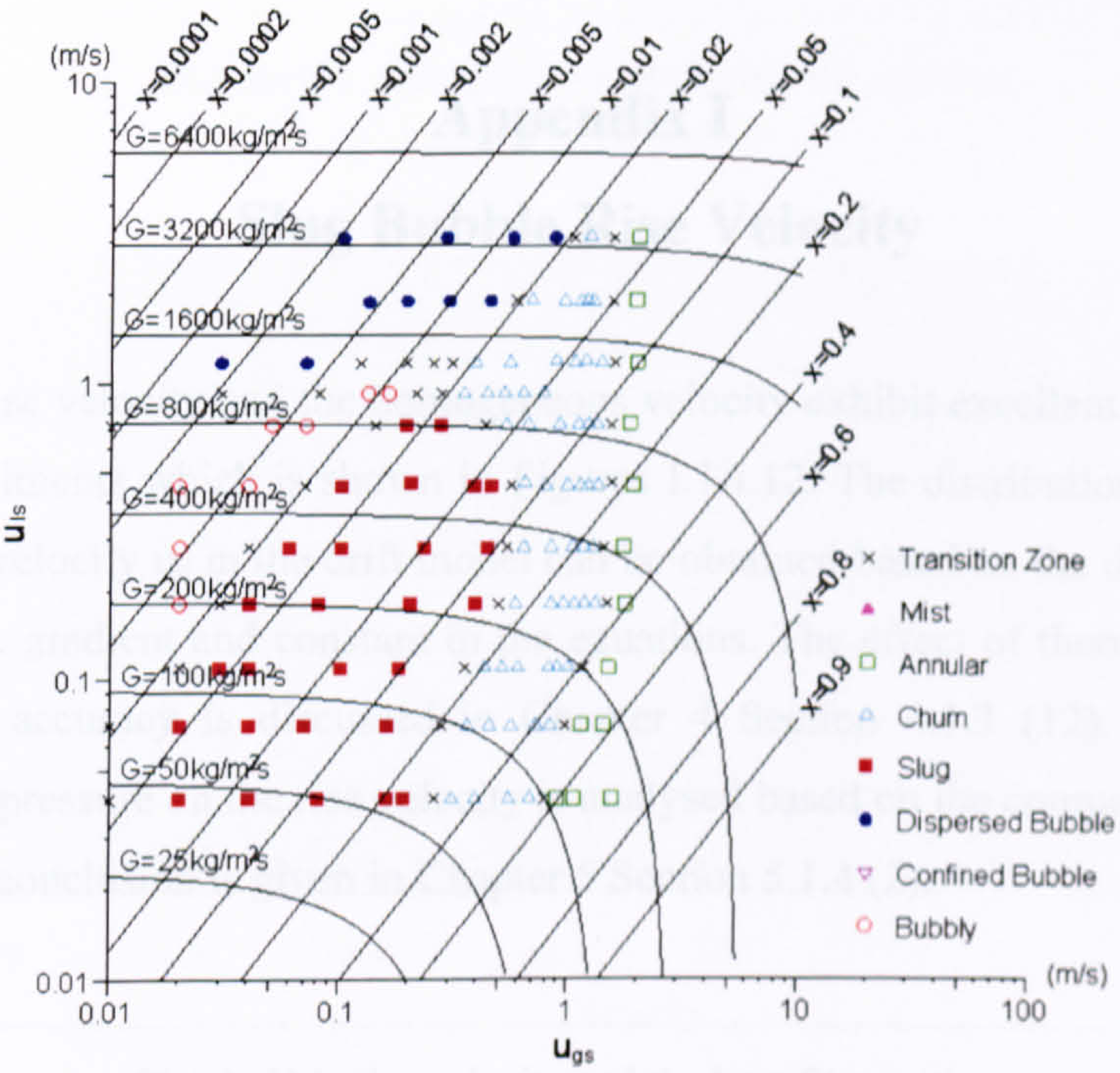

Figure H.12 The R134a flow map with a grid of constant quality and mass flux lines in the 4.26 mm diameter tube at 14 bar pressure.

Appendix I

Slug Bubble Rise Velocity

The bubble rise velocity and the homogeneous velocity exhibit excellent linearity in the present experiments which is shown in Figures I.1-I.12. The distribution parameter C_0 and the drift velocity u_d in the drift model can be obtained based on the deduced best-fit equations, i.e. gradient and constant in the equations. The effect of thermal loss on the experimental accuracy is discussed in Chapter 4 Section 4.1.3 (12). The effect of diameter and pressure on the rise velocity is analysed based on the comparisons of these figures and a conclusion is given in Chapter 5 Section 5.1.4 (2).

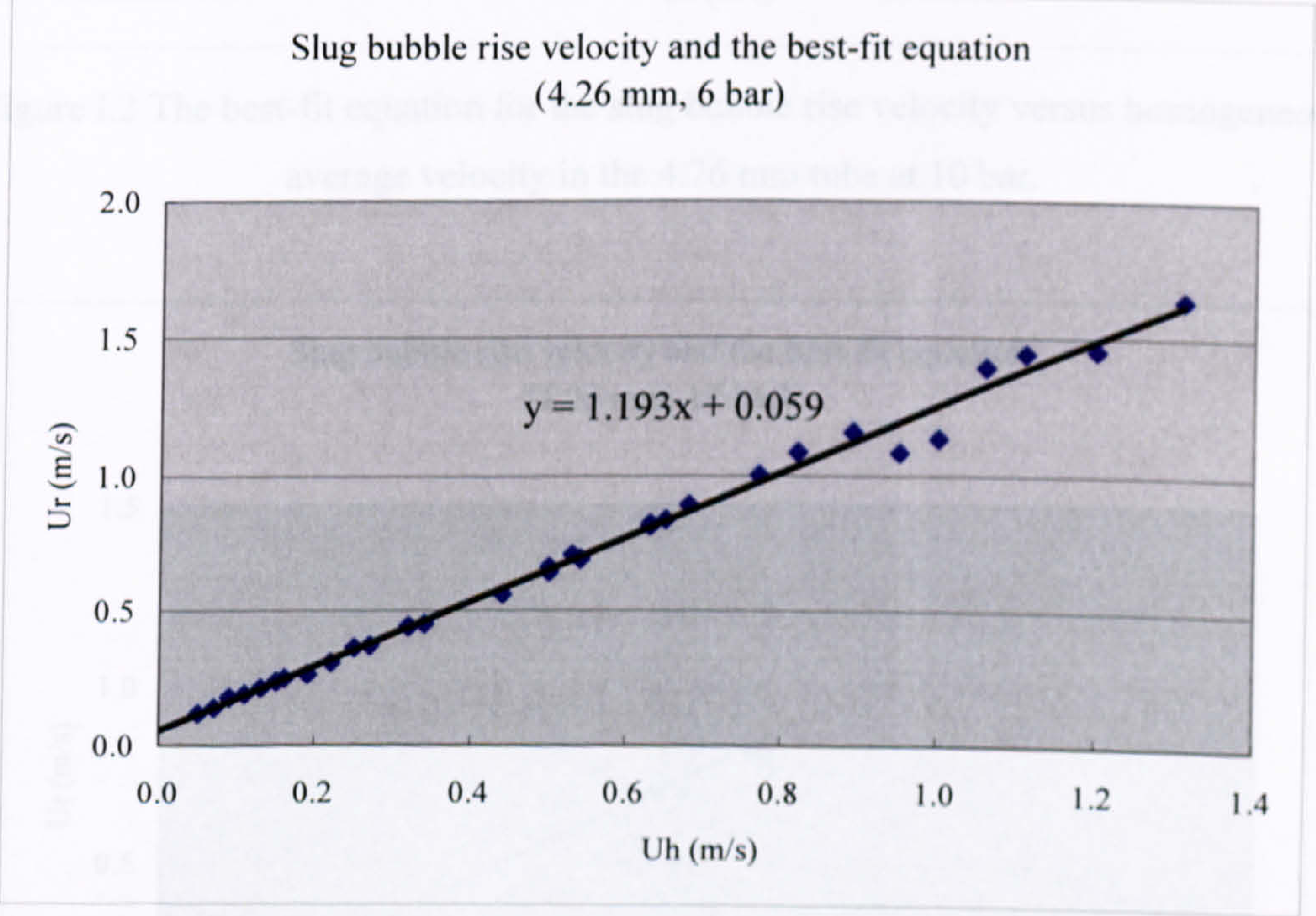

Figure I.1 The best-fit equation for the slug bubble rise velocity versus homogeneous average velocity in the 4.26 mm tube at 6 bar.

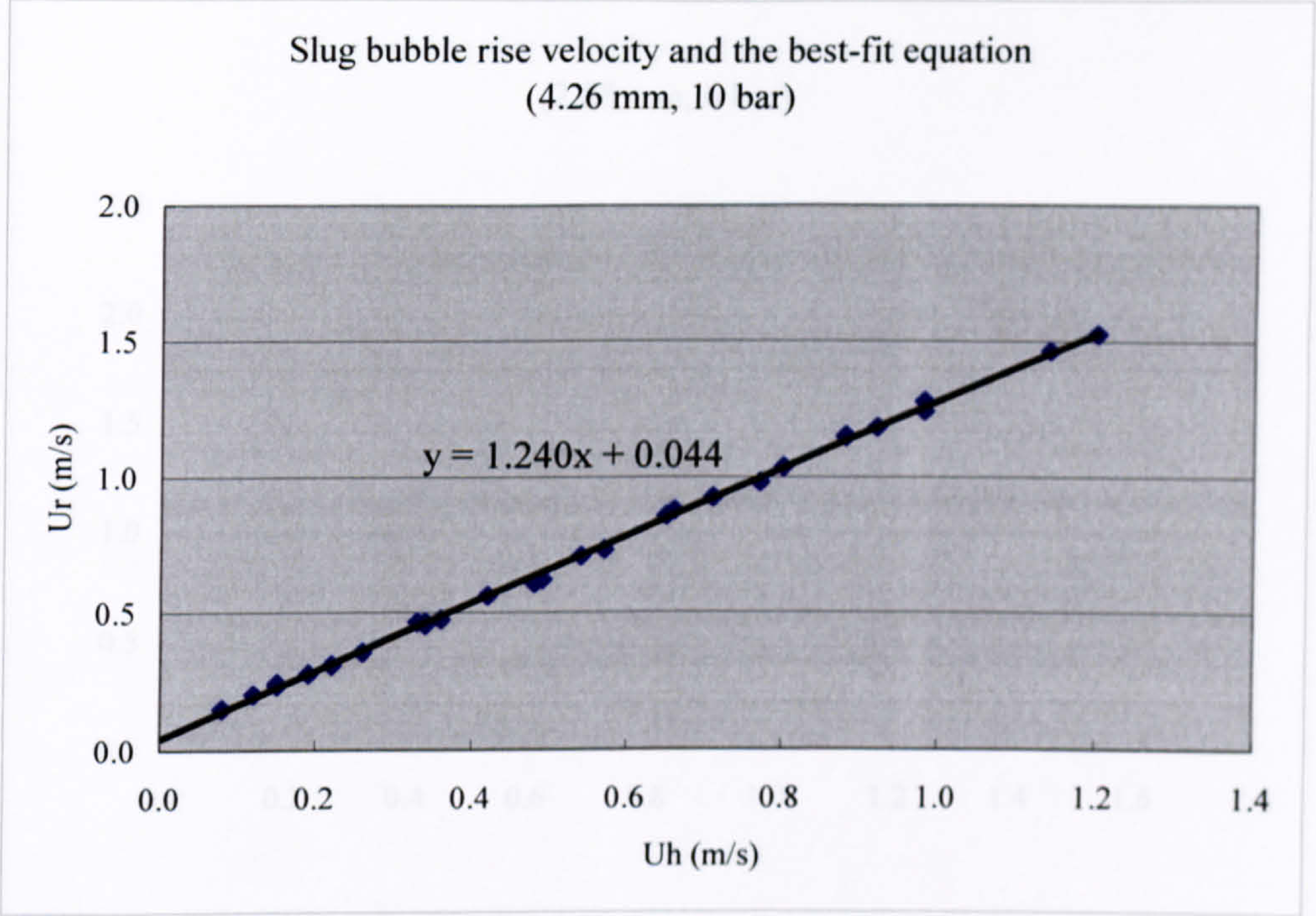

Figure I.2 The best-fit equation for the slug bubble rise velocity versus homogeneous average velocity in the 4.26 mm tube at 10 bar.

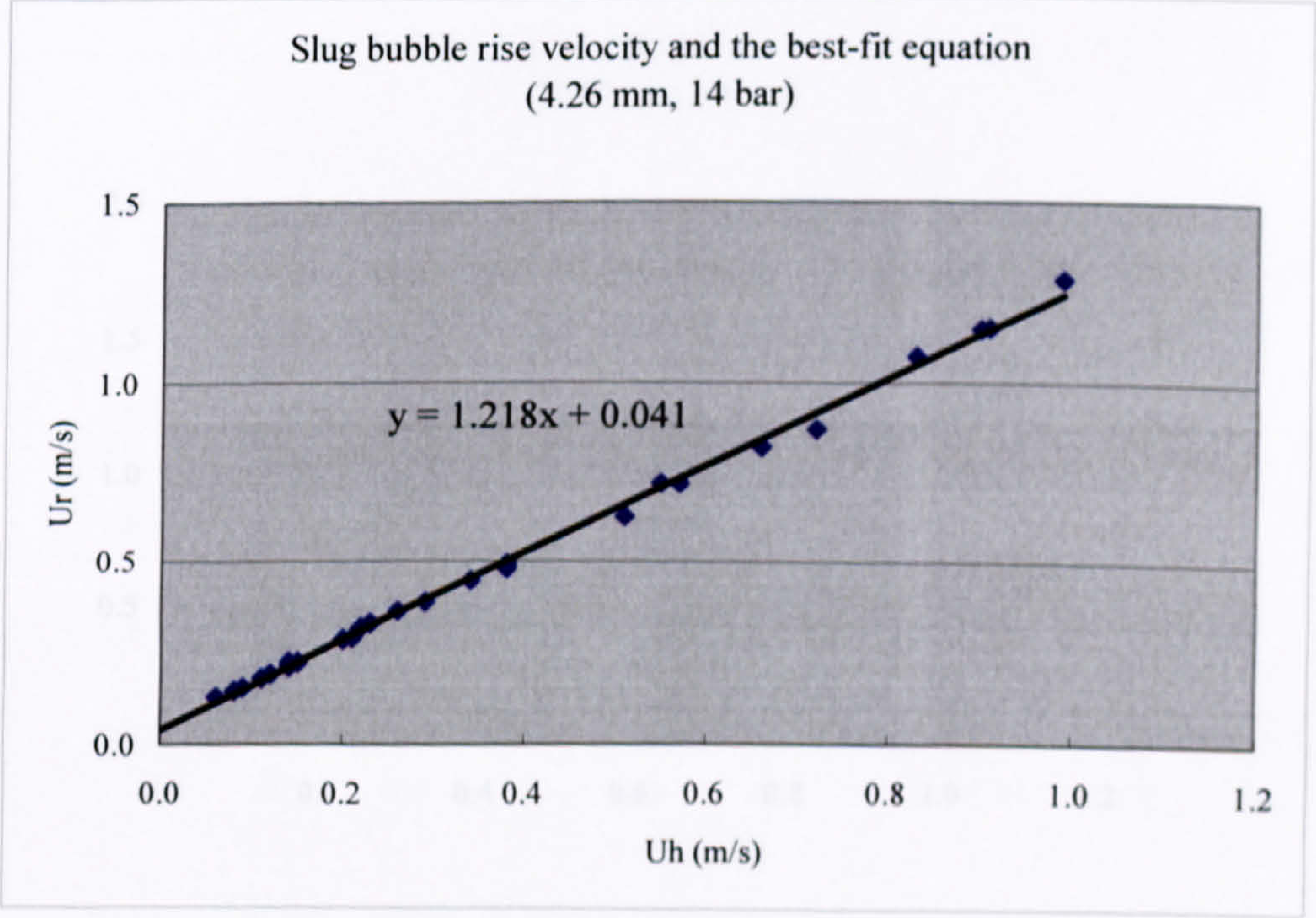

Figure I.3 The best-fit equation for the slug bubble rise velocity versus homogeneous average velocity in the 4.26 mm tube at 14 bar.

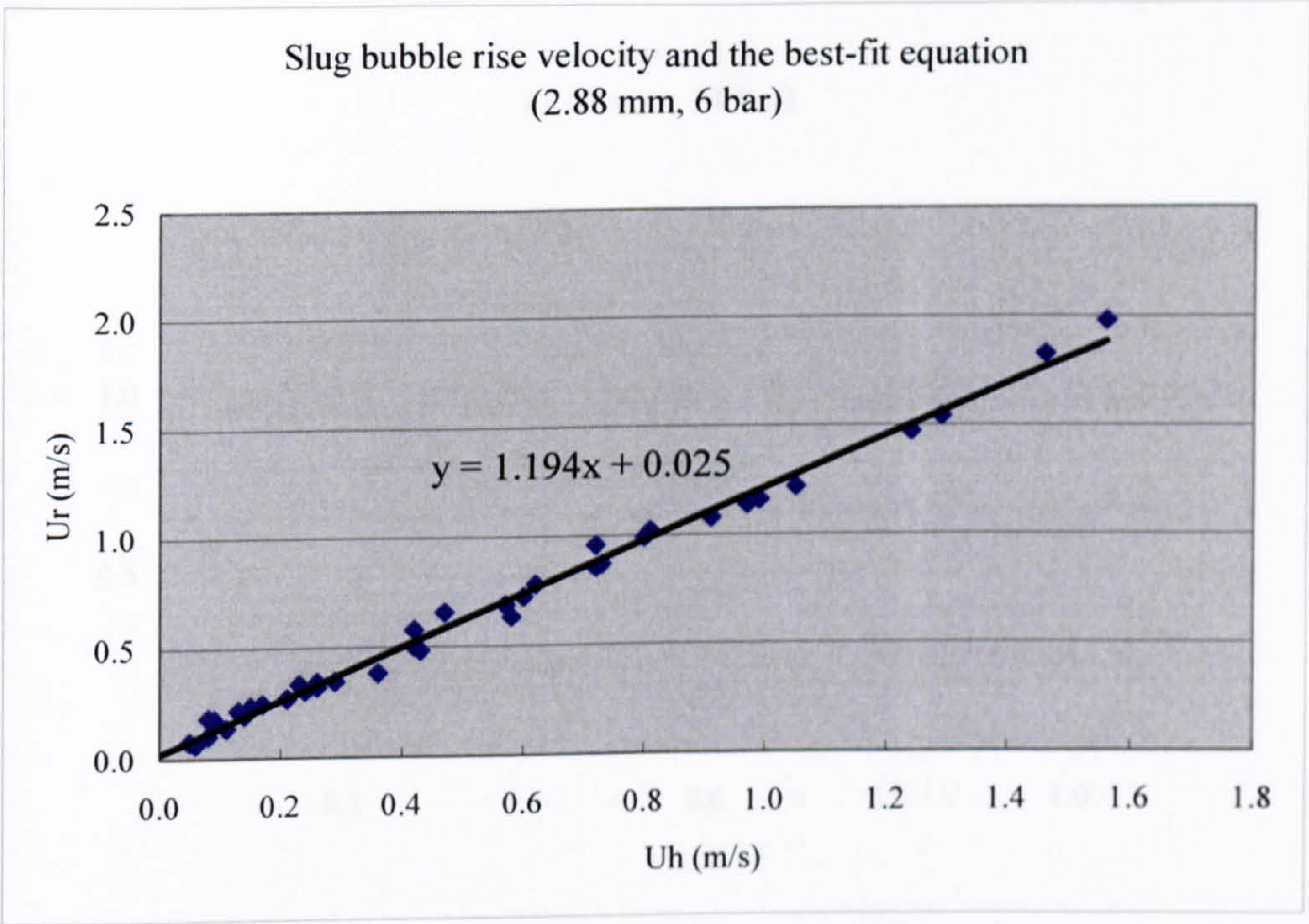

Figure I.4 The best-fit equation for the slug bubble rise velocity versus homogeneous average velocity in the 2.88 mm tube at 6 bar.

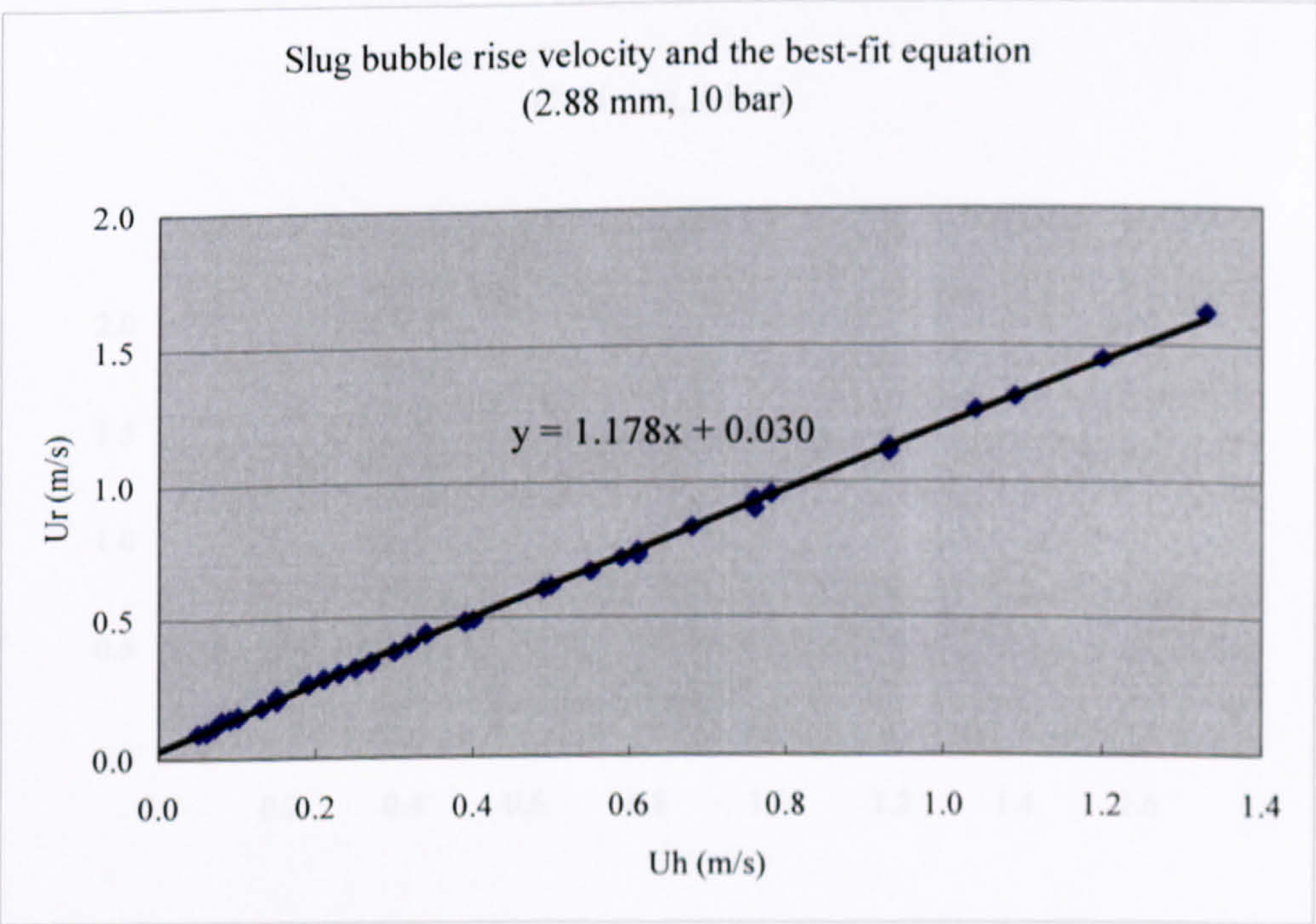

Figure I.5 The best-fit equation for the slug bubble rise velocity versus homogeneous average velocity in the 2.88 mm tube at 10 bar.

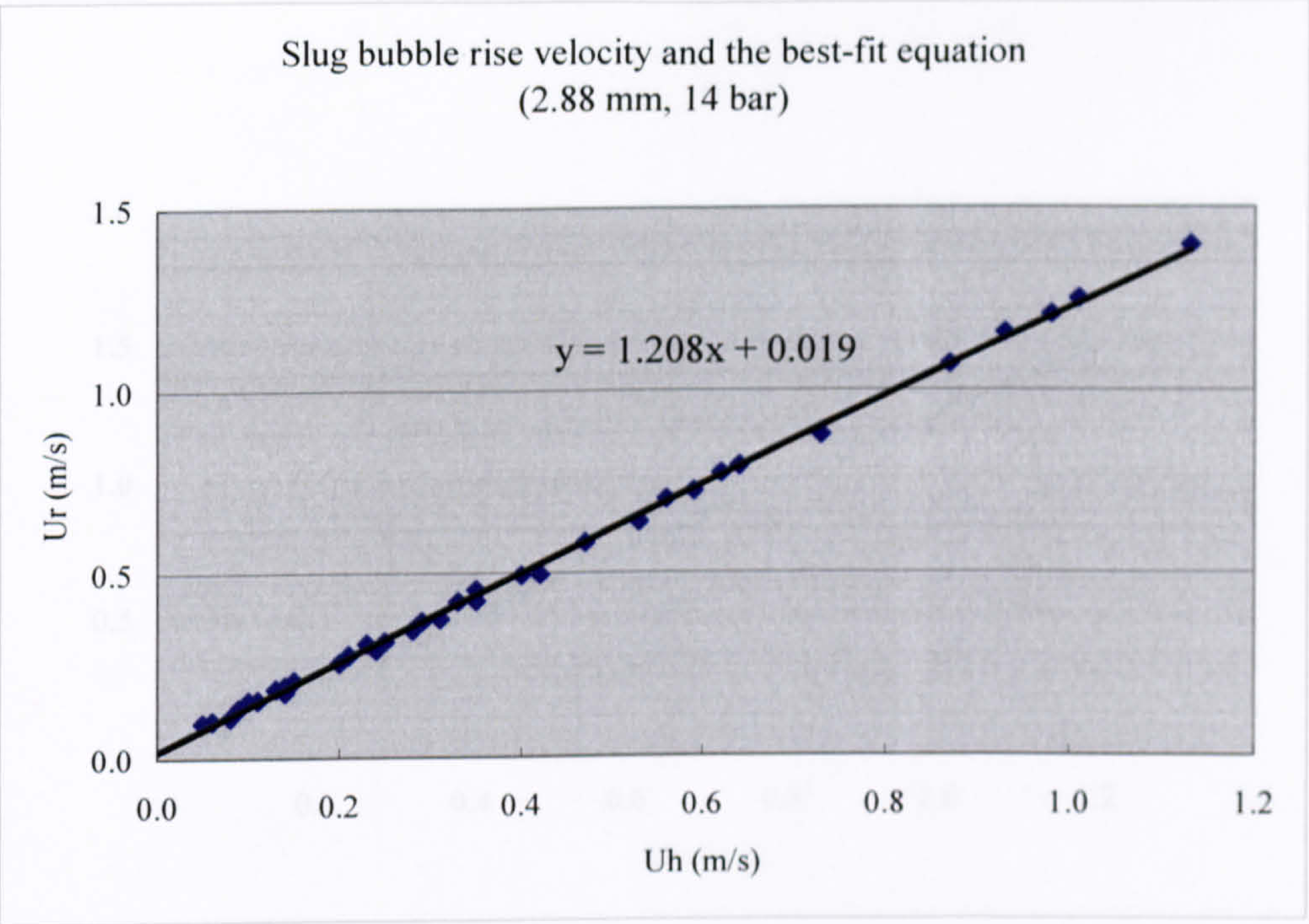

Figure I.6 The best-fit equation for the slug bubble rise velocity versus homogeneous average velocity in the 2.88 mm tube at 14 bar.

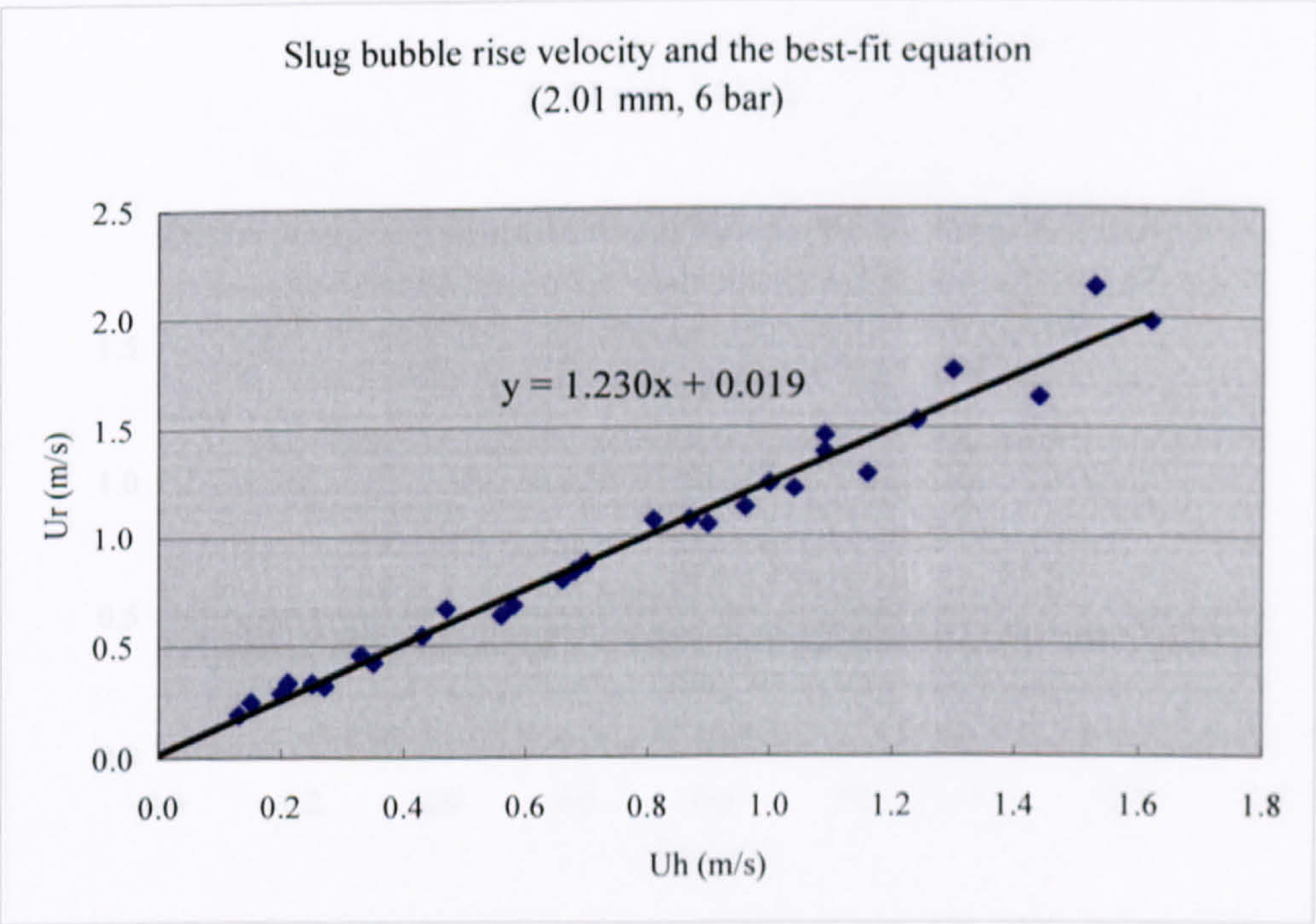

Figure I.7 The best-fit equation for the slug bubble rise velocity versus homogeneous average velocity in the 2.01 mm tube at 6 bar.

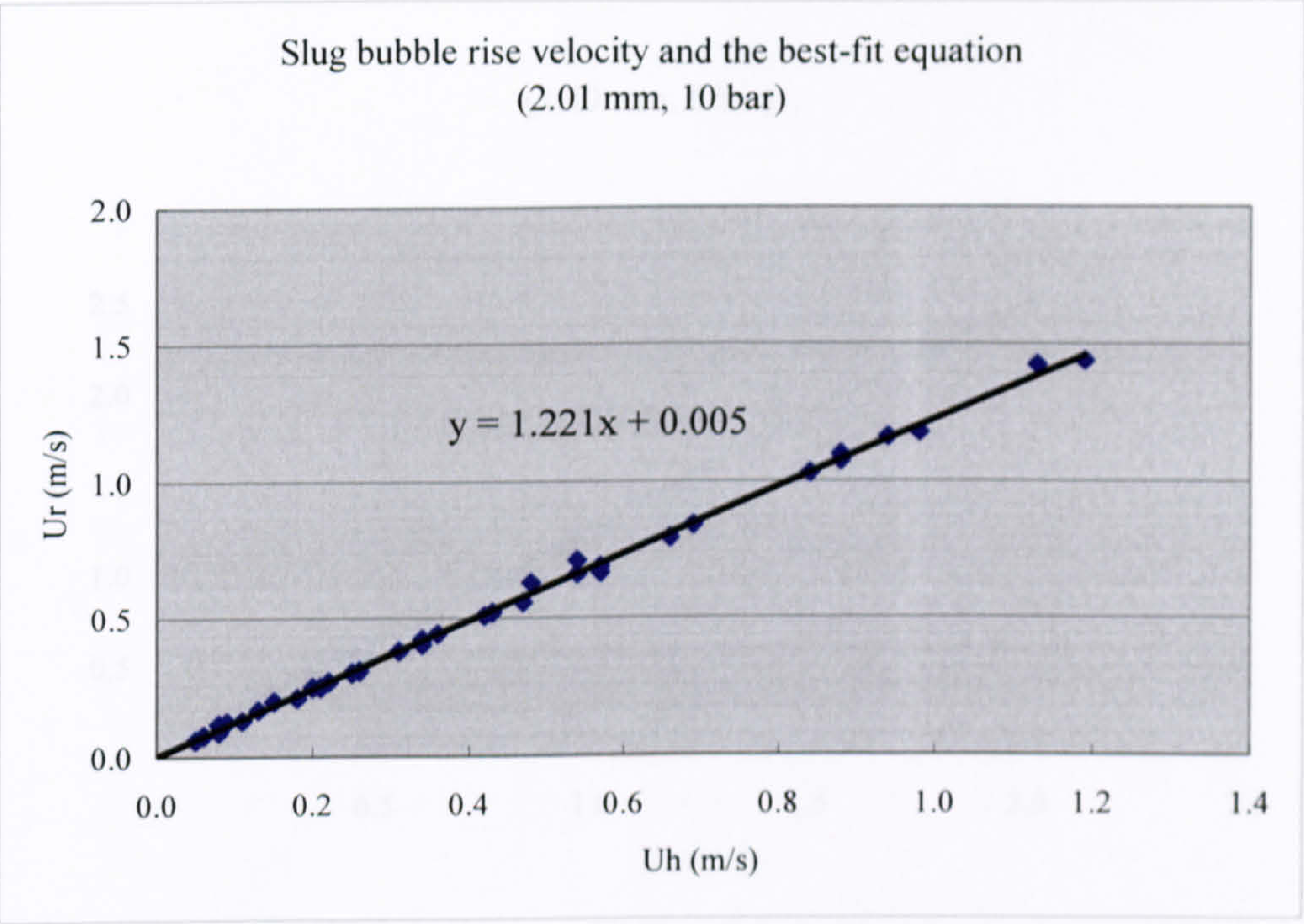

Figure I.8 The best-fit equation for the slug bubble rise velocity versus homogeneous average velocity in the 2.01 mm tube at 10 bar.

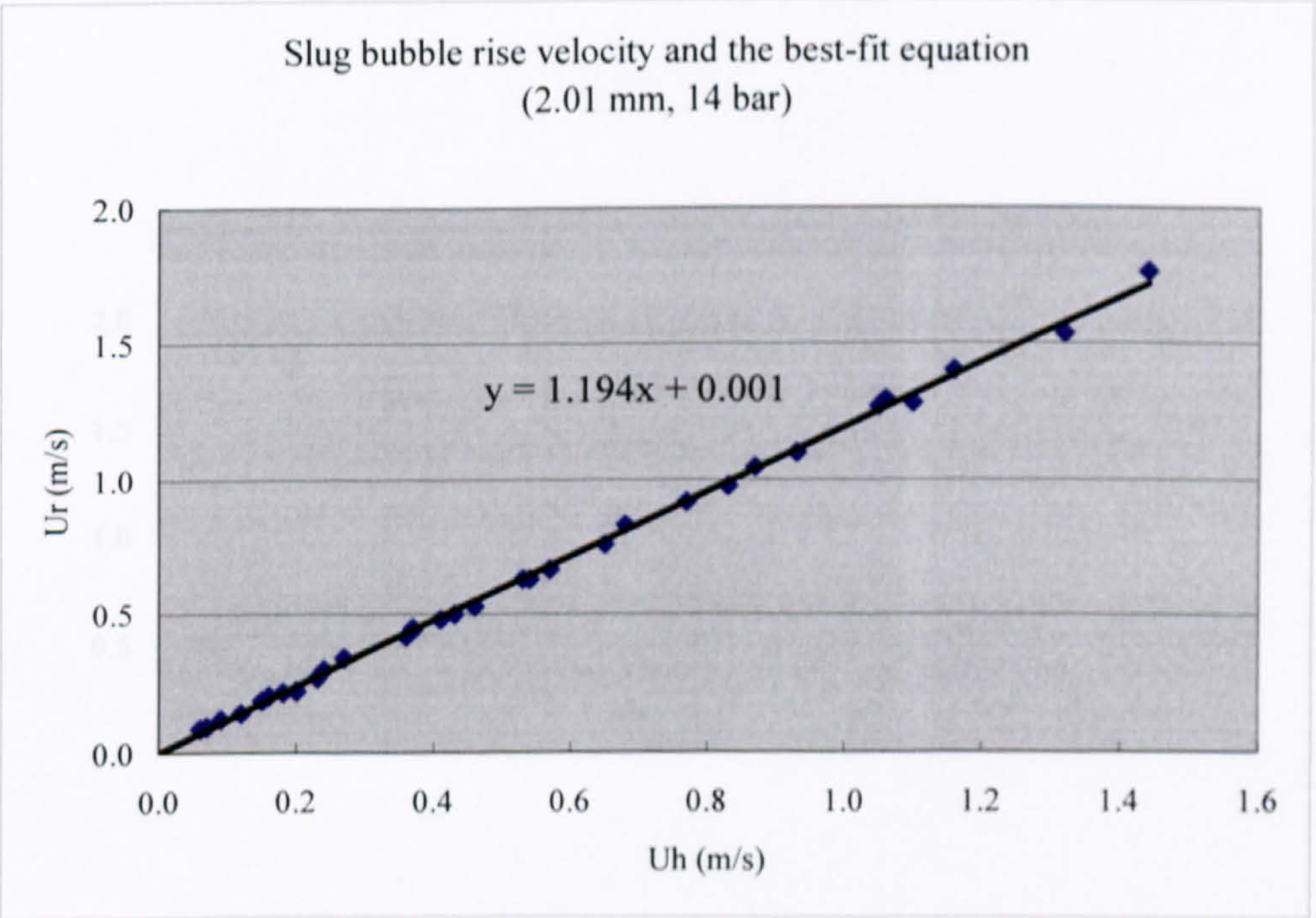

Figure I.9 The best-fit equation for the slug bubble rise velocity versus homogeneous average velocity in the 2.01 mm tube at 14 bar.

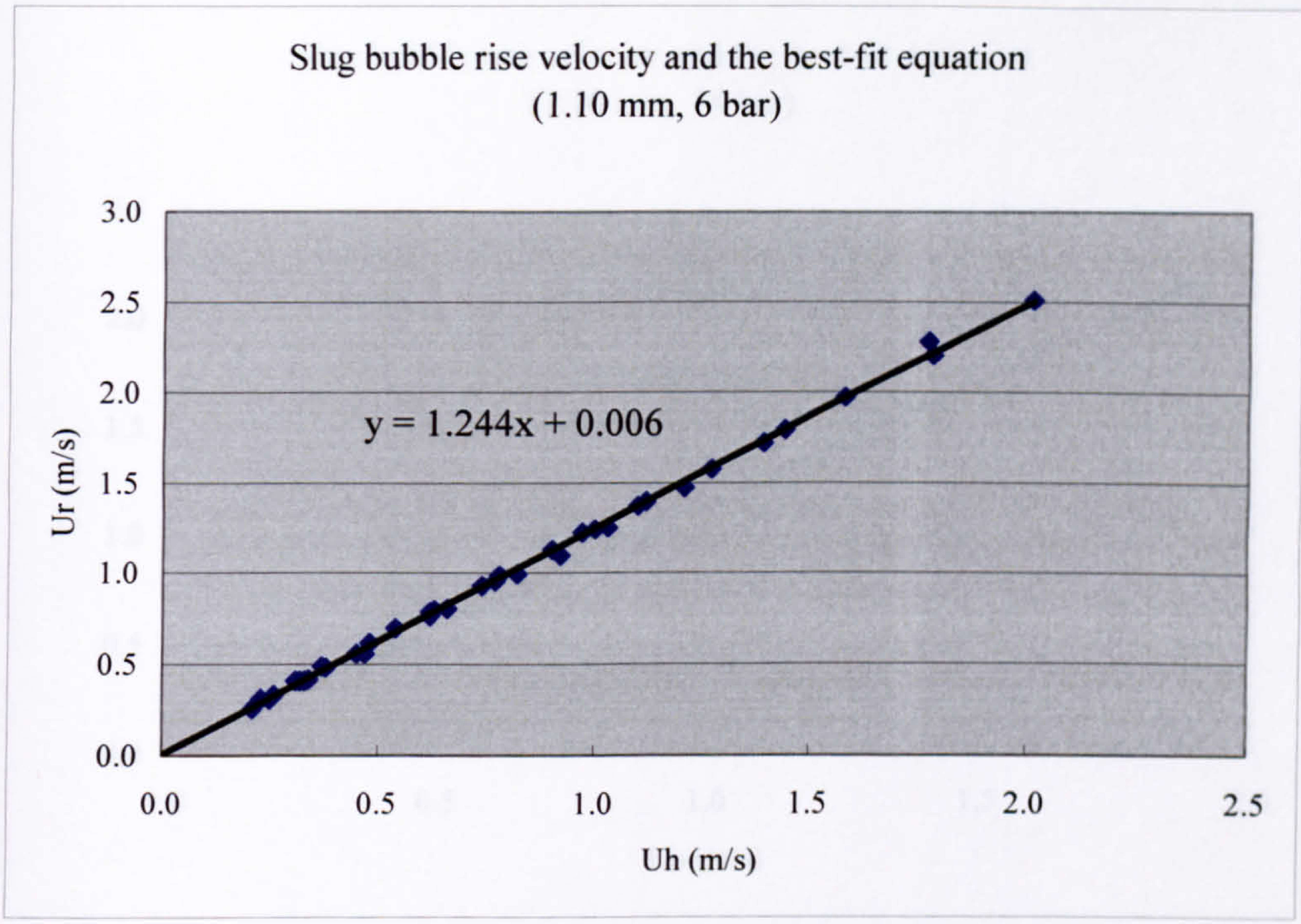

Figure I.10 The best-fit equation for the slug bubble rise velocity versus homogeneous average velocity in the 1.10 mm tube at 6 bar.

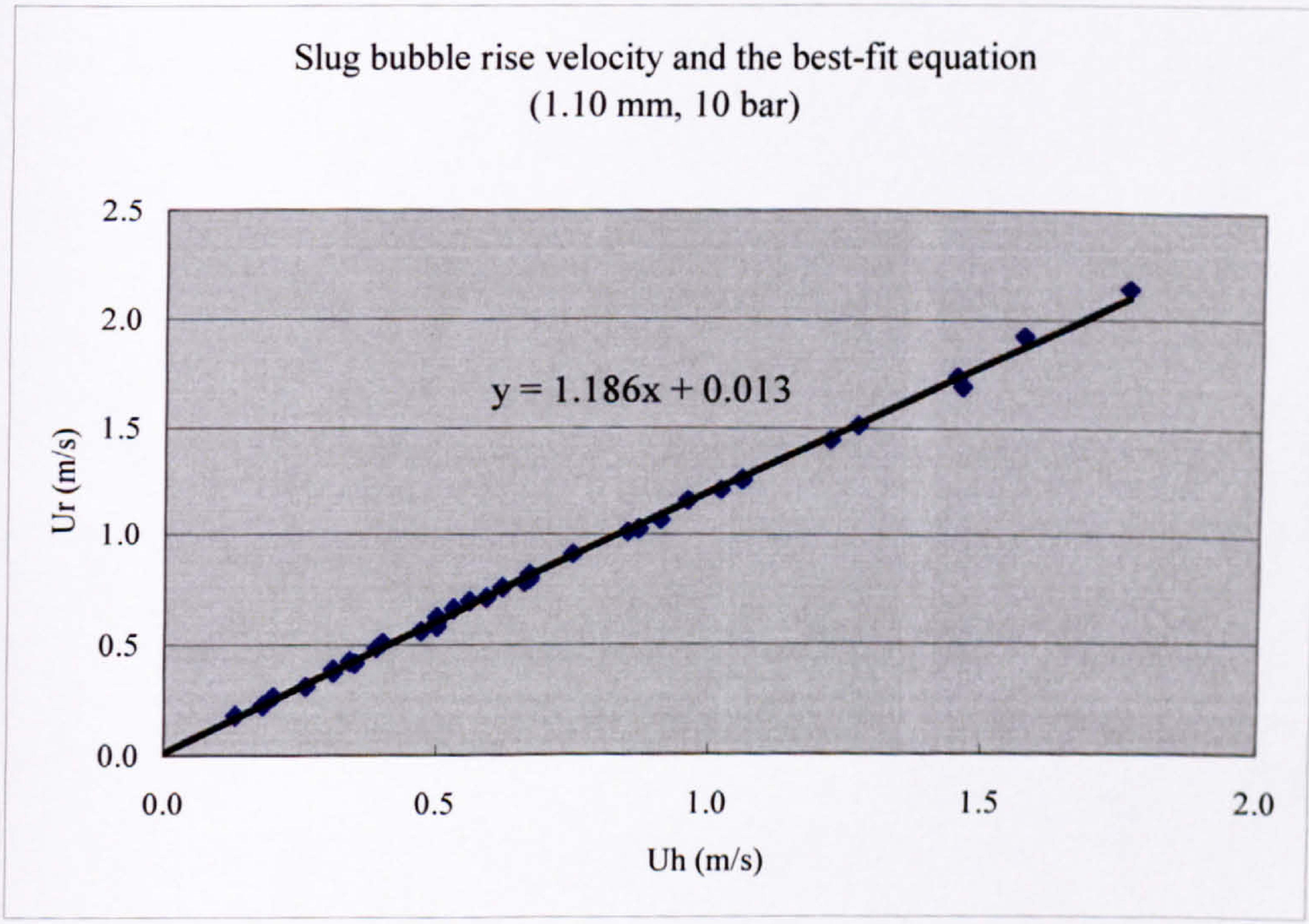

Figure I.11 The best-fit equation for the slug bubble rise velocity versus homogeneous average velocity in the 1.10 mm tube at 10 bar.

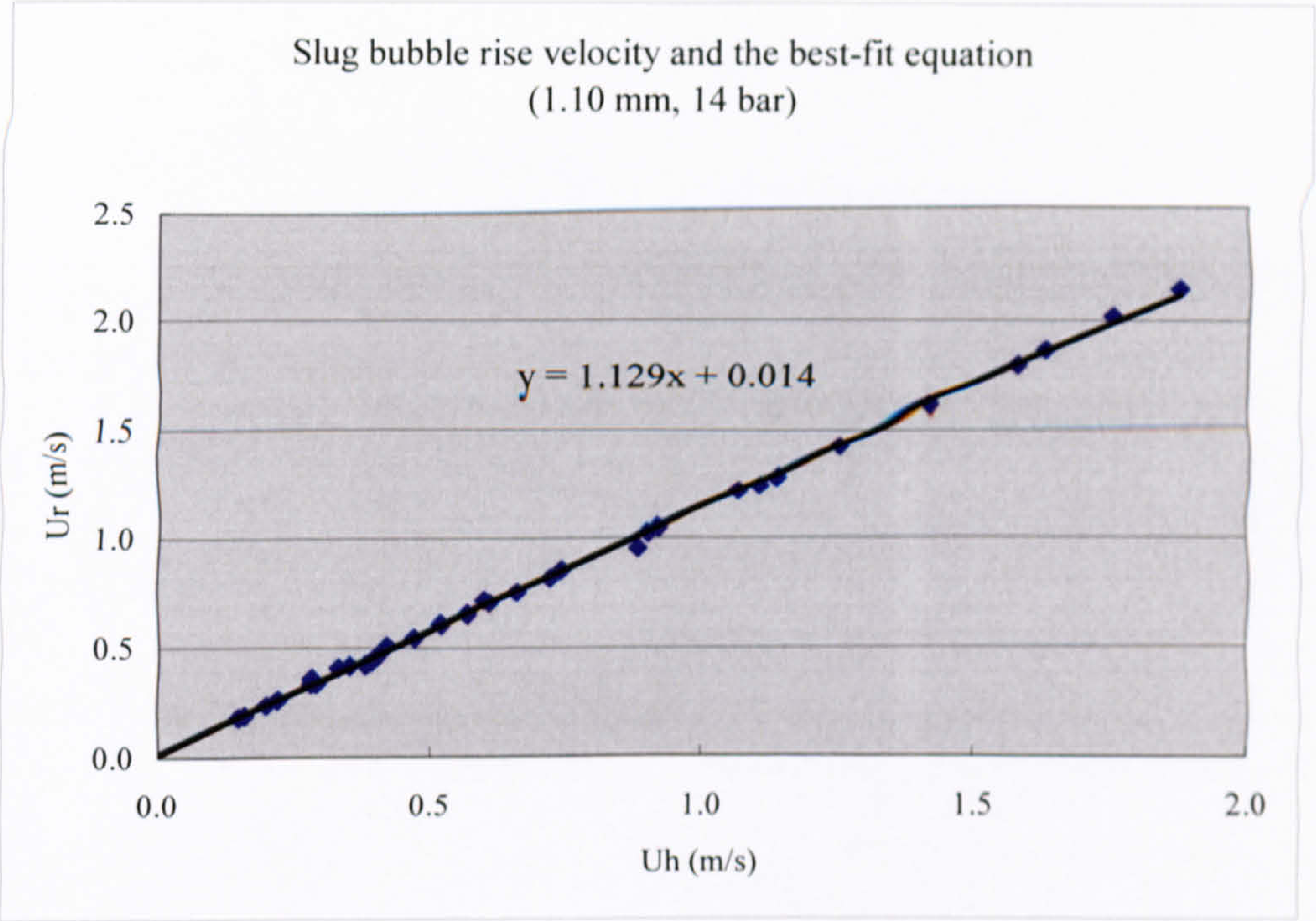

Figure I.12 The best-fit equation for the slug bubble rise velocity versus homogeneous average velocity in the 1.10 mm tube at 14 bar.

THESIS
CONTAINS
CD/DVD